Ajay Singh
Editor

Emergency Radiology

Imaging of Acute Pathologies

Third Edition

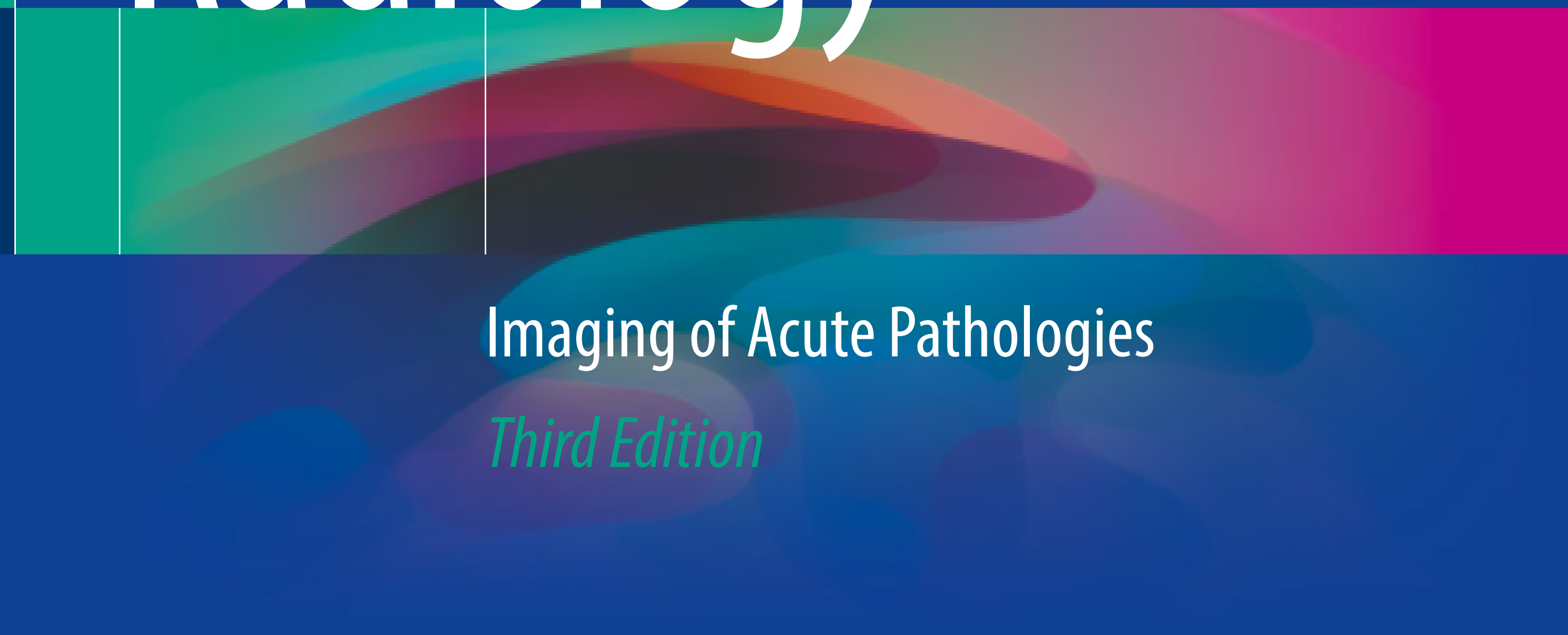

Springer

ALGrawany

Emergency Radiology

Ajay Singh
Editor

Khyati Bidani
Associate Editor

Emergency Radiology

Imaging of Acute Pathologies

Third Edition

Springer

ALGrawany

Editor
Ajay Singh
Division of Emergency Radiology, Department of Radiology, Emergency Radiology Fellowship
Massachusetts General Hospital and Harvard Medical School
Boston, MA, USA

ISBN 978-3-031-65769-6 ISBN 978-3-031-65770-2 (eBook)
https://doi.org/10.1007/978-3-031-65770-2

© The Editor(s) (if applicable) and The Author(s), under exclusive license to Springer Nature Switzerland AG 2013, 2018, 2024
This work is subject to copyright. All rights are solely and exclusively licensed by the Publisher, whether the whole or part of the material is concerned, specifically the rights of translation, reprinting, reuse of illustrations, recitation, broadcasting, reproduction on microfilms or in any other physical way, and transmission or information storage and retrieval, electronic adaptation, computer software, or by similar or dissimilar methodology now known or hereafter developed.
The use of general descriptive names, registered names, trademarks, service marks, etc. in this publication does not imply, even in the absence of a specific statement, that such names are exempt from the relevant protective laws and regulations and therefore free for general use.
The publisher, the authors and the editors are safe to assume that the advice and information in this book are believed to be true and accurate at the date of publication. Neither the publisher nor the authors or the editors give a warranty, expressed or implied, with respect to the material contained herein or for any errors or omissions that may have been made. The publisher remains neutral with regard to jurisdictional claims in published maps and institutional affiliations.

This Springer imprint is published by the registered company Springer Nature Switzerland AG
The registered company address is: Gewerbestrasse 11, 6330 Cham, Switzerland

If disposing of this product, please recycle the paper.

Preface

This book represents the culmination of years of research, collaboration, and dedication to advancing our understanding of the field. It would not have been possible without the invaluable contributions of many, especially Khyati Bidani, MD. To all who have contributed, directly or indirectly, thank you for your belief in and support of this work.

ALGrawany

Contents

1 **Imaging of Acute Aortic Conditions** 1
Jeanette Chun, Mohammad Mansouri, and Ajay Singh

2 **Emergencies of the Biliary Tract** 15
Caterina Missiroli, Khyati Bidani, Mohammad Mansouri, and Ajay Singh

3 **Acute Appendicitis** 33
Ajay Singh, Mohammad Mansouri, Benjamin M. Yeh, and Robert A. Novelline

4 **Imaging of Small Bowel** 49
Ajay Singh, Mohammad Mansouri, and Terry S. Desser

5 **Imaging of Bowel Obstruction** 67
Ajay Singh, Khyati Bidani, and Mohammad Mansouri

6 **Imaging of Acute Colonic Disorders** 77
Ajay Singh, Khyati Bidani, and Mohammad Mansouri

7 **Imaging of Genitourinary Emergencies** 97
Robin B. Levenson, Mai-Lan Ho, and Mohammad Mansouri

8 **Imaging of Acute Conditions of Male Reproductive Organs** 113
Caterina Missiroli, Mohammad Mansouri, and Ajay Singh

9 **Imaging of Blunt and Penetrating Abdominal Trauma** 127
Paul F. Von Herrmann, David J. Nickels, Mohammad Mansouri, and Ajay Singh

10 **Acute Nontraumatic Imaging in the Liver and Spleen** 145
Dale E. Hansen III, Sridhar Shankar, Mohammad Mansouri, and Ajay Singh

11 **Imaging of Acute Pancreas** 159
Caterina Missiroli, Khyati Bidani, Mohammad Mansouri, and Ajay Singh

12 **Imaging of Acute Obstetric Disorders** 169
Mohammad Mansouri and Ajay Singh

13 **Imaging of Acute Gynecologic Disorders** 181
Chris Malcolm, Amisha R. Khicha, Mohammad Mansouri, and Ajay Singh

14 **Emergency Radionuclide Imaging of the Thorax and Abdomen** 195
Blaine T. Mischen, Paul F. Von Herrmann, Cynthia Lumby, and M. Elizabeth Oates

15 **Imaging of Neck Emergencies** 215
Mohammad Mansouri, Khyati Bidani, and Ajay Singh

16 **Imaging of Acute Head Emergencies** 235
Abdul-Majid Khan, Sneha R. Patel, Mohammad Mansouri, and Ajay Singh

17 Imaging of Facial Fractures 255
Dennis Coughlin, Paul Jaffray, Mohammad Mansouri, and Ajay Singh

18 Stroke and Its Imaging Evaluation 271
Sathish Kumar Dundamadappa, Melanie Ehinger, Andrew Chen, and Mohammad Mansouri

19 Imaging of Acute Orbital Pathologies 291
Mohammad Mansouri, Khyati Bidani, and Ajay Singh

20 Imaging of Upper Extremity 307
Joshua Leeman, Jonathan E. Leeman, Mohammad Mansouri, and Ajay Singh

21 Lower Extremity Trauma 327
Rathachai Kaewlai, Mohammad Mansouri, and Ajay Singh

22 Imaging of Spinal Trauma 353
Parul Penkar, Rathachai Kaewlai, Mohammad Mansouri, Ajay Singh, Laura Avery, and Robert A. Novelline

23 Imaging of Nontraumatic Mediastinal and Pulmonary Processes 379
Brett W. Carter, Victorine V. Muse, and Mohammad Mansouri

24 Imaging of Acute Thoracic Trauma 395
Neil Patel, Mohammad Mansouri, Sridhar Shankar, and Ajay Singh

25 Imaging of Lines and Tubes 411
Ajay Singh, Mohammad Mansouri, and Chris Heinis

26 Imaging of Pediatric Emergencies 427
John J. Krol, Ashvin Singh, Paul F. Von Herrmann, Harigovinda R. Challa, Mohammad Mansouri, and Johanne E. Dillon

27 Signs in Radiology: Plain Radiographic Signs 441
Khyati Bidani, Gandharv Singh, Garima Chandra, and Ajay Singh

28 Signs in Radiology: Cross-Sectional Signs 455
Khyati Bidani, Gandharv Singh, Garima Chandra, and Ajay Singh

Index 477

ALGrawany

Contributors

Laura Avery Department of Radiology, Massachusetts General Hospital, Boston, MA, USA

Khyati Bidani Department of Radiology, Massachusetts General Hospital, Boston, MA, USA

Brett W. Carter Department of Diagnostic Radiology, The University of Texas MD Anderson Cancer Center, Houston, TX, USA

Harigovinda R. Challa Tennessee Interventional and Imaging Associates, Chattanooga, TN, USA

Garima Chandra Department of Radiology, Massachusetts General Hospital, Boston, MA, USA

Andrew Chen Department of Radiology, University of Massachusetts Medical Center, Worcester, MA, USA

Jeanette Chun Lahey Hospital and Medical Center, Burlington, MA, USA

Dennis Coughlin Department of Radiology, UMass Memorial Health Care, Worcester, MA, USA

Terry S. Desser Department of Radiology, Stanford University School of Medicine, Stanford, CA, USA

Johanne E. Dillon University of Kentucky Health Care, Lexington, KY, USA

Sathish Kumar Dundamadappa Department of Radiology, UMass Memorial Medical Center and UMass Medical School, Worcester, MA, USA

Melanie Ehinger Greensboro Radiology, Greensboro, NC, USA

Dale E. Hansen III Memphis Radiology, Germantown, TN, USA

Chris Heinis University of Massachusetts Memorial Medical Center, Worcester, MA, USA

Mai-Lan Ho Department of Radiology, Mayo Clinic, Rochester, MN, USA

Paul Jaffray GBMC Healthcare, Baltimore, MD, USA

Rathachai Kaewlai Department of Diagnostic and Therapeutic Radiology, Ramathibodi Hospital, Mahidol University, Bangkok, Thailand

Abdul-Majid Khan Department of Diagnostic Radiology, Beaumont Health System, Oakland University William Beaumont School of Medicine, Royal Oak, MI, USA

Amisha R. Khicha Department of Radiology, Wesley Medical Center, University of Kansas-Wichita, Wichita, KS, USA

John J. Krol Virtual Radiologic Associates, Eden Prairie, MN, USA

Jonathan E. Leeman Radiation Oncology, Memorial Sloan-Kettering Cancer Center, New York, NY, USA

Joshua Leeman Department of Radiology, University of Massachusetts Memorial Medical Center, Worcester, MA, USA

Robin B. Levenson Department of Radiology, Harvard Medical School, Beth Israel Deaconess Medical Center, Boston, MA, USA

Cynthia Lumby Radiology Service, VA North Texas Health Care System, Fort Worth, TX, USA

Chris Malcolm Imaging Center of Idaho, Caldwell, ID, USA

Mohammad Mansouri Department of Radiology, Massachusetts General Hospital, Boston, MA, USA

Blaine T. Mischen Department of Radiology, University of Kentucky College of Medicine, UK HealthCare, Lexington, KY, USA

Caterina Missiroli Department of Radiology, ASST Nord Milano—Bassini Hospital, Milan, Italy

Department of Radiology, Nord Milano—Bassini Hospital, Milan, Italy

Victorine V. Muse Division of Thoracic Imaging, Department of Radiology, Harvard Medical School, Massachusetts General Hospital, Boston, MA, USA

David J. Nickels Department of Radiology, University of Kentucky, Lexington, KY, USA

Robert A. Novelline Department of Radiology, Massachusetts General Hospital, Boston, MA, USA

M. Elizabeth Oates Department of Radiology, University of Kentucky College of Medicine, UK HealthCare, Lexington, KY, USA

Neil Patel University of Tennessee Health Science Center, Memphis, TN, USA

Sneha R. Patel Department of Diagnostic Radiology, Beaumont Health System, Oakland University William Beaumont School of Medicine, Royal Oak, MI, USA

Parul Penkar Department of Radiology, Massachusetts General Hospital, Boston, MA, USA

Sridhar Shankar Department of Radiology, University of Tennessee, Regional One Health Hospital, Memphis, TN, USA

Ajay Singh Division of Emergency Radiology, Department of Radiology, Massachusetts General Hospital, Boston, MA, USA

Harvard Medical School, Massachusetts General Hospital, Boston, MA, USA

Ashvin Singh Massachusetts General Hospital, Boston, MA, USA

Gandharv Singh Department of Radiology, Massachusetts General Hospital, Boston, MA, USA

Paul F. Von Herrmann Department of Radiology, North Alabama Medical Center, Florence, AL, USA

Benjamin M. Yeh Department of Radiology, University of California, San Francisco, San Francisco, CA, USA

ALGrawany

Imaging of Acute Aortic Conditions

1

Jeanette Chun, Mohammad Mansouri, and Ajay Singh

Introduction

Acute aortic conditions include, but are not limited to, aortic rupture, aortic dissection, intramural hematoma, and penetrating aortic ulcer. Prompt diagnosis of these conditions is essential for managing these conditions. Because these conditions often have similar symptoms, namely chest and abdominal pain, the imaging characteristics are key to prompt and accurate diagnosis.

Abdominal Aortic Aneurysm and Aortic Rupture

Abdominal aortic aneurysm (AAA) is seen in 5–10% of elderly male smokers. Most AAAs are true aneurysms and involve all three layers of the aortic wall. The two most common etiologies of AAA are degenerative and inflammatory (Tables 1.1 and 1.2).

Table 1.1 Causes of abdominal aortic aneurysm

Degenerative (most common)
Inflammatory (5–10% of all)
Mycotic
Syndromes: Marfan's syndrome, Ehlers–Danlos syndrome
Vasculitis: Takayasu's disease, Behcet's disease
Traumatic

Table 1.2 Normal caliber of aorta and other arteries

Vascular structure	Normal average diameter (cm)
Aortic sinuses	2.9
Ascending aorta	3
Mid-transverse arc	2.5
Mid descending	2.5
At diaphragm	2.4
Main pulmonary artery	2.7
Infrarenal	2
Common iliac	1
Common femoral	0.9
Popliteal	0.7

The most significant complication of AAA is aortic rupture. The mortality rate for ruptured AAA is 50%; thus, an accurate diagnosis is essential for prompt surgical intervention. The risk of rupture is proportional to the maximum cross-sectional diameter, with 1%/year risk for aneurysms measuring 5–5.9 cm. The risk of rupture increases up to 20%/year for an aneurysm measuring greater than 7 cm in diameter. Although AAAs are less common in females (M:F = 4:1), they are more likely to rupture when compared to males.

Ultrasound is the most commonly used imaging modality to screen for AAA and has been shown to reduce mortality. The imaging criteria to diagnose AAA include aortic caliber of more than 3 cm and an aortic caliber of more than 1.5 times the expected diameter of the abdominal aorta (Fig. 1.1). The aortic caliber is measured perpendicular to the long axis of the aorta, from outer wall to outer wall. Although ultrasound is highly sensitive in making the diagnosis of abdominal aortic aneurysm, it is not as reliable as CT in diagnosing aortic rupture. However, the demonstration of normal caliber of abdominal aorta by ultrasound makes aortic rupture an unlikely possibility.

The original version of this chapter was revised. An erratum to this chapter can be found at https://doi.org/10.1007/978-3-319-65397-6_27. An erratum to this publication is available online at https://doi.org/10.1007/978-3-319-65397-6_27.

J. Chun
Lahey Hospital and Medical Center, Burlington, MA, USA

M. Mansouri
Department of Radiology, Massachusetts General Hospital, Boston, MA, USA

A. Singh (✉)
Division of Emergency Radiology, Department of Radiology, Massachusetts General Hospital, Boston, MA, USA

Harvard Medical School, Massachusetts General Hospital, Boston, MA, USA
e-mail: asingh1@partners.org

© The Author(s), under exclusive license to Springer Nature Switzerland AG 2024
A. Singh (ed.), *Emergency Radiology*, https://doi.org/10.1007/978-3-031-65770-2_1

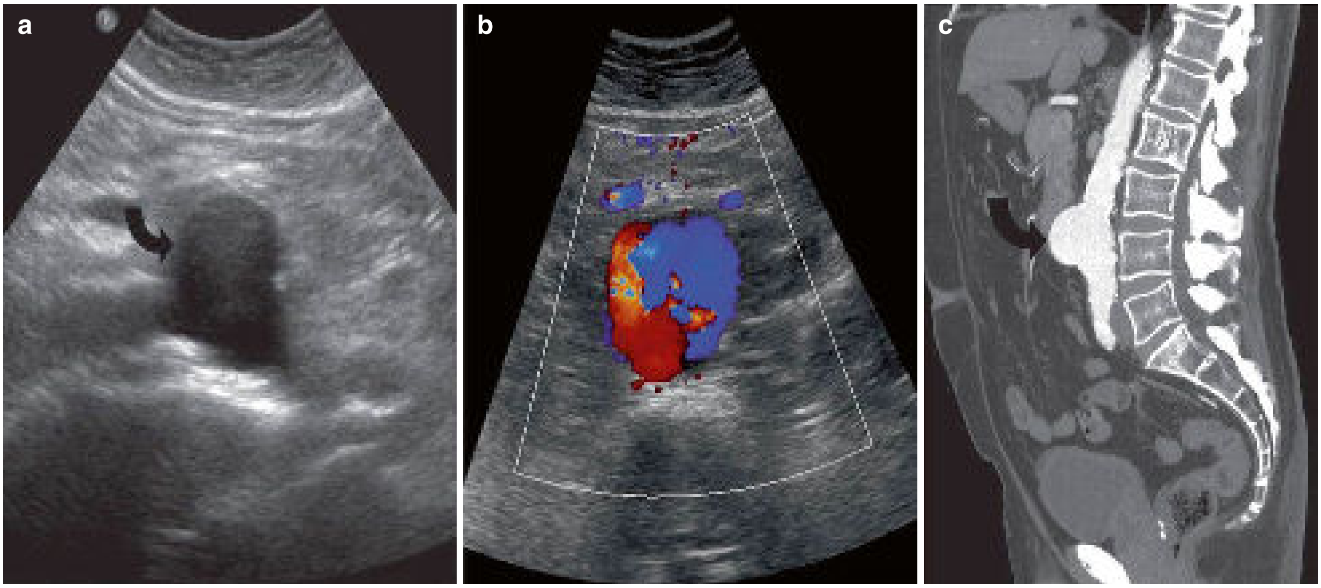

Fig. 1.1 Saccular abdominal aortic aneurysm. (**a**, **b**) US demonstrate a saccular infrarenal aortic aneurysm (*curved arrow*) with yin-yang sign on color Doppler imaging. (**c**) Sagittal reformation demonstrates the saccular infrarenal abdominal aortic aneurysm (*curved arrow*)

Most aortic aneurysm rupture involves the middle third of the aneurysm, through the posterolateral wall and into the retroperitoneum (Fig. 1.2a). However, intraperitoneal rupture into the bowel (usually the duodenum) and very rarely into the IVC may occur (Fig. 1.2b, c). Rarely, descending thoracic aortic aneurysm can rupture into the esophagus (Fig. 1.2d) as well and is mostly fatal.

Risk Factors for Aortic Rupture

Progressive aneurysmal dilatation of the aorta with increased wall tension is directly related to the risk of rupture (Fig. 1.3). The decreased proportion of thrombus-to-lumen ratio is also thought to play a part, as a larger thrombus better protects against rupture by providing protection against the high aortic pressures [1]. In addition, discontinuity in aortic wall calcification is associated with an increased risk of rupture [2].

Imaging

The imaging modality of choice is a contrast-enhanced multidetector CT (MDCT). The CT can demonstrate an AAA with surrounding retroperitoneal hemorrhage into psoas compartment, pararenal space, and perirenal space. A contrast-enhanced CT provides additional information about the aortic size, presence or absence of active extravasation, and anatomic relationships (Table 1.3). A hyperdense crescent sign and draped aorta sign are indicators of contained aortic leak or impending rupture. Focal discontinuity of intimal calcification is also a secondary sign of aortic rupture.

Hyperdense Crescent Sign

Hyperdense crescent sign is seen as a well-defined peripheral, high-density, crescent configuration within a thrombus where there is internal dissection of hemorrhage into the thrombus and ultimately reaching the aortic wall. It is a sign of acute or impending rupture (Fig. 1.4a) [1].

Draped Aorta Sign

Draped aorta sign indicates a contained aortic rupture and shows posterior aortic wall not identifiable as a separate structure and draping over the adjacent vertebral bodies (Fig. 1.4b, c, d). If rupture should occur, the most common sign of aneurysmal rupture is a retroperitoneal hematoma adjacent to the aneurysm.

ALGrawany

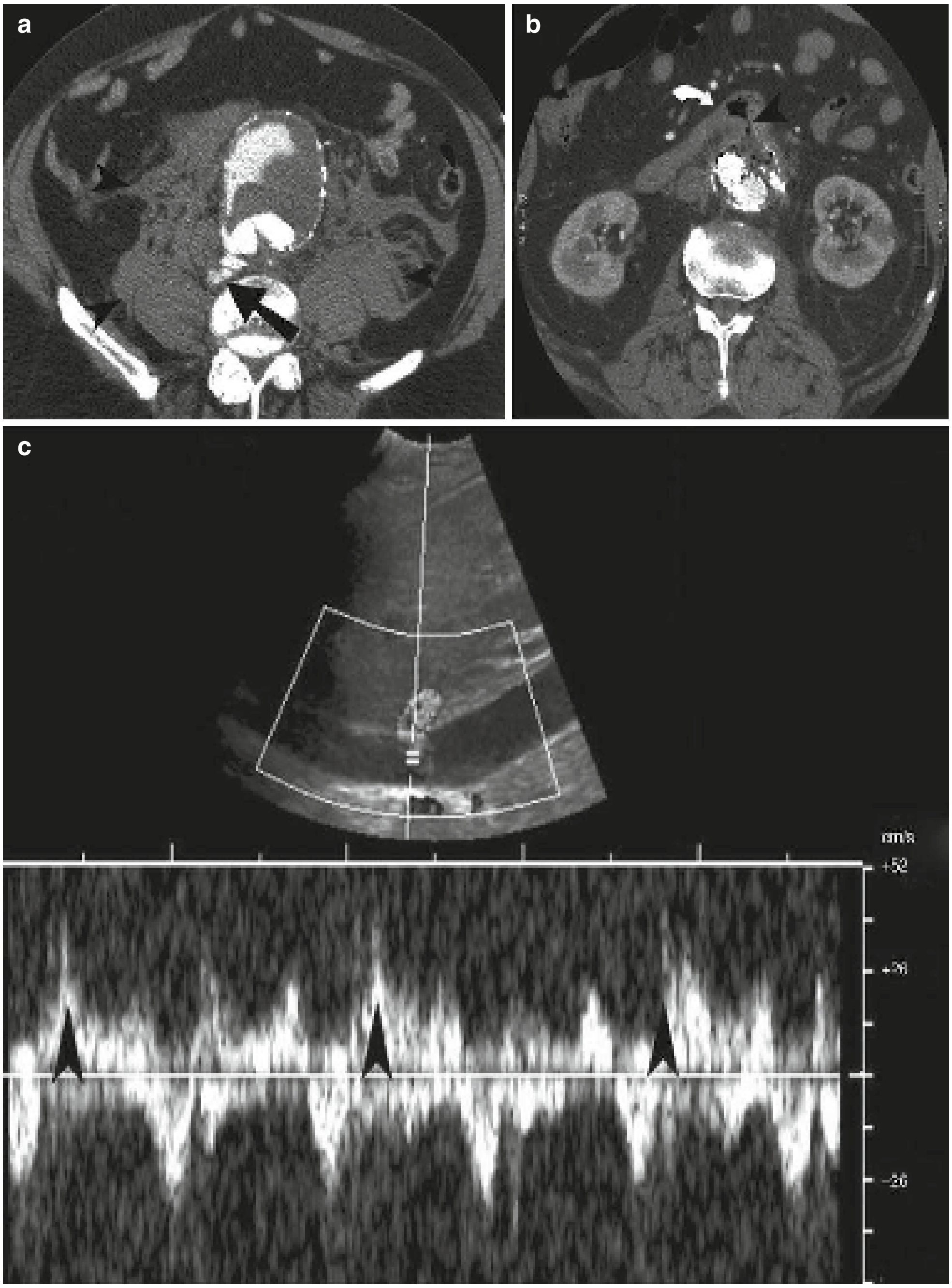

Fig. 1.2 Abdominal aortic aneurysm rupture, aorto-enteric and aortocaval fistula, and aortoesophageal fistula. (**a**) Contrast-enhanced CT scan study of the lower abdomen demonstrates active extravasation of contrast (*arrow*) from infrarenal abdominal aortic aneurysm. There is retroperitoneal hemorrhage (*arrowheads*) identified around the aortic aneurysm. (**b**) Aorto-enteric fistula. Contrast-enhanced CT scan study demonstrates communication (*arrowhead*) of the third portion of the duodenum (*arrow*) with the infrarenal abdominal aortic aneurysm sac. The patient had recently undergone endovascular stent placement. (**c**) Aortocaval fistula. Doppler US shows the combination of arterial and venous spectral waveform in the inferior vena cava lumen, in a patient with aortocaval fistula. (**d**) Contrast-enhanced CT angiogram of the chest demonstrates contained aortic perforation into the esophageal lumen. The grossly distended esophagus (arrowheads) contains a large blood clot surrounding a focus of contrast enhancement (arrow)

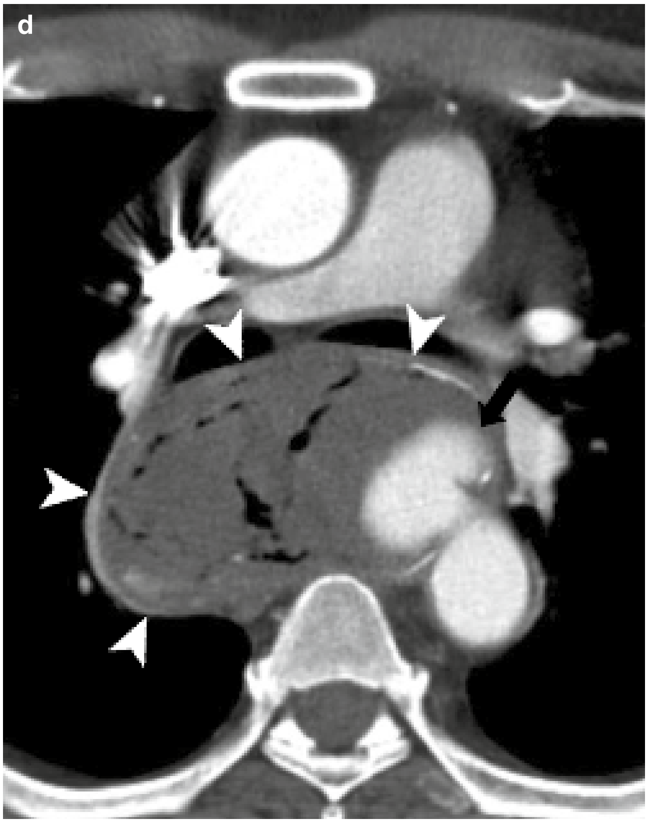

Fig. 1.2 (continued)

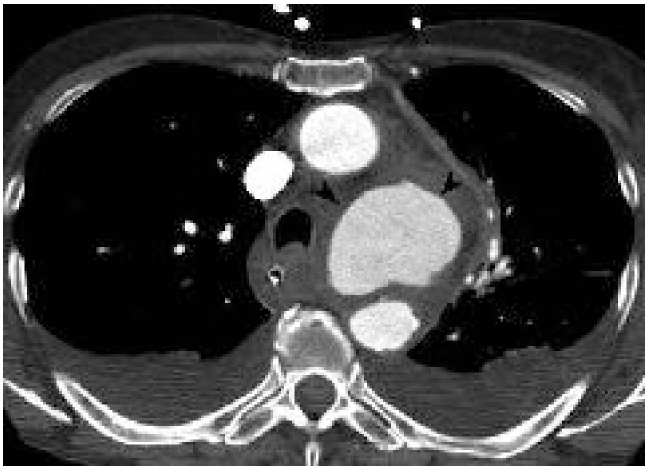

Fig. 1.3 Aortic pseudoaneurysm CTA in a 73-year-old female demonstrates a large saccular pseudoaneurysm (*arrows*) arising from the aortic arch

Table 1.3 CT findings of aortic rupture

1. Active extravasation of contrast
2. Retroperitoneal hematoma around the aortic aneurysm
3. Periaortic stranding
4. Draped aorta sign
5. Hyperdense crescent sign
6. Tangential calcium sign
7. Discontinuity of intimal calcification

Tangential Calcium Sign

The intimal calcification in the aorta points away from the circumference of the aneurysm (Fig. 1.4e).

Mycotic Aneurysm

One of the less frequent etiologies of AAA is mycotic aneurysm, which constitutes 1–3% of aortic aneurysms. However, mycotic aneurysm is known to more commonly involve aorta than any other artery. Staphylococcus and Streptococcus species are the most common pathogens of mycotic aneurysm. The cases of mycotic aneurysm due to Salmonella species are more common in East Asia and demonstrate an early tendency to rupture.

The typical imaging features of mycotic aneurysm (Fig. 1.4f) include rapidly increasing caliber of a saccular aortic aneurysm with wall irregularity, periaortic edema and soft tissue mass, and the presence of gas. Periaortic soft tissue stranding and soft tissue mass are the most common features seen on imaging of mycotic aneurysm. Calcifications and thrombus are uncommon in a mycotic aneurysm. The lack of calcification in the aortic wall is due to the nonatherosclerotic origin of the aneurysm.

Traumatic Aortic Transection

Traumatic aortic transection is usually caused by rapid deceleration injury, resulting from shearing forces. It involves a tear in all layers of the aortic wall and usually occurs in the aortic arch, most commonly between the origin of left subclavian artery and ligamentum arteriosum. CT is the imaging modality of choice, and findings include periaortic hematomas, mediastinal hematoma, pseudoaneurysm, and change

ALGrawany

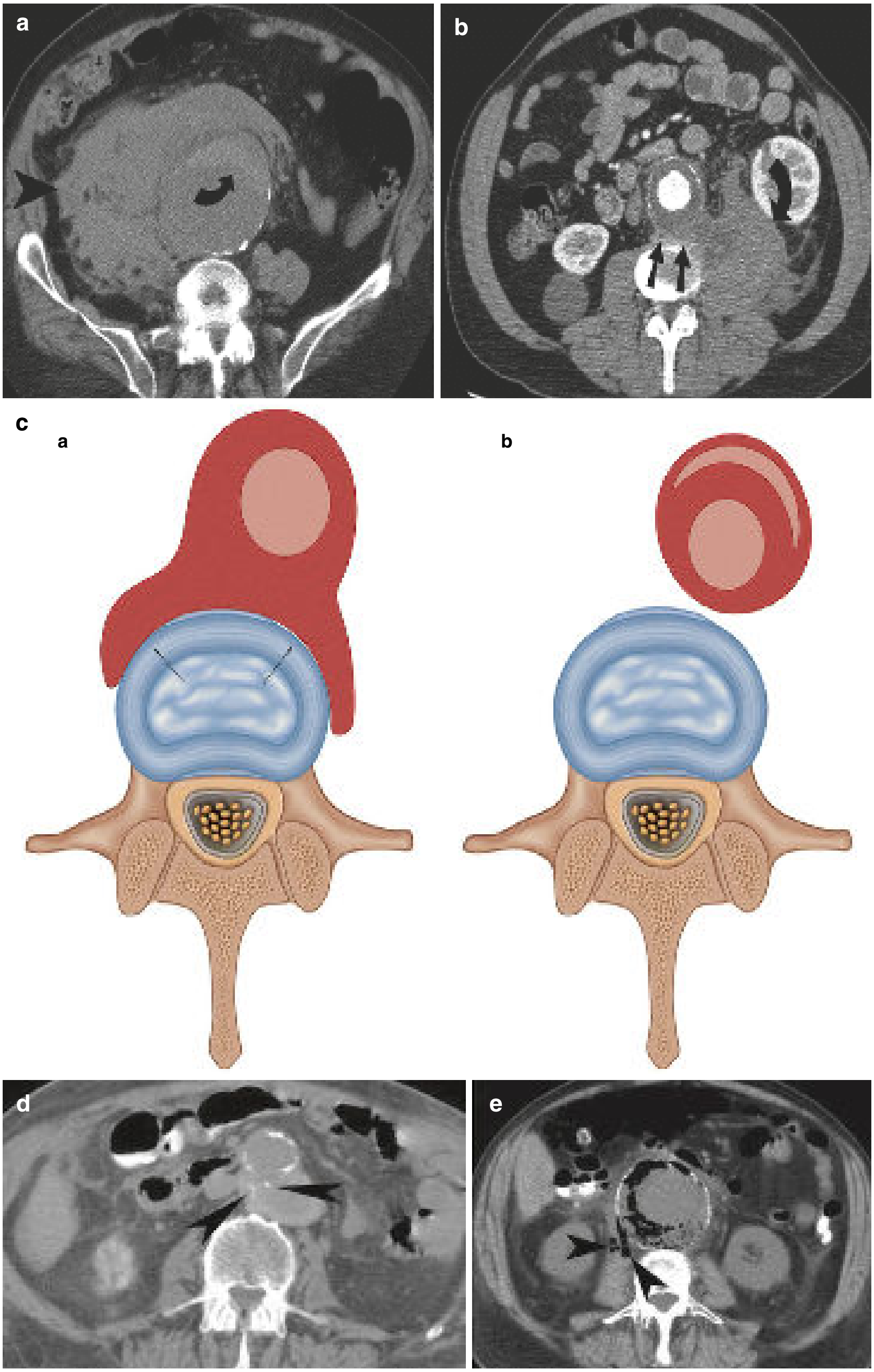

Fig. 1.4 CT features of abdominal aortic aneurysm rupture. (**a**) Hyperdense crescent sign. Noncontrast CT demonstrates large retroperitoneal hematoma (*arrowhead*) from the ruptured aortic aneurysm. A hyperdense crescent (*curved arrow*) is present in the anterior wall of the infrarenal abdominal aortic aneurysm. (**b**) Draped aorta sign. Contrast-enhanced CT demonstrates draping of the posterior wall of the aorta (*straight arrows*) on the anterior aspect of the lumbar spine. There is large retroperitoneal hematoma (*curved arrow*) identified in the psoas compartment and left posterior pararenal space. (**c**) Schematic representation of the *draped aorta sign* (*a*) and *hyperdense crescent sign* (*b*). Draped aorta sign is characterized by draping of deficient aortic wall on the anterior aspect of the vertebral body. Hyperdense crescent sign is characterized by the presence of a high-density sickle-shaped blood clot in the aortic wall. (**d**) Tangential calcium sign in a patient with contained aortic leak. Noncontrast CT demonstrates intimal calcifications (*arrowheads*) displaced from their expected location and pointing away from the aortic circumference. (**e**) Rupture of mycotic aneurysm. Noncontrast CT demonstrates air in the wall of the aortic aneurysm, secondary to clostridial infection. Breech in the aortic wall is indicated by the presence of air (*arrowheads*) outside the aortic adventitia. (**f**) Axial contrast-enhanced CT shows draping of the posterior aortic wall (arrows) along the anterior margin of the lumbar vertebral body, suggesting impending aortic rupture

Fig. 1.4 (continued)

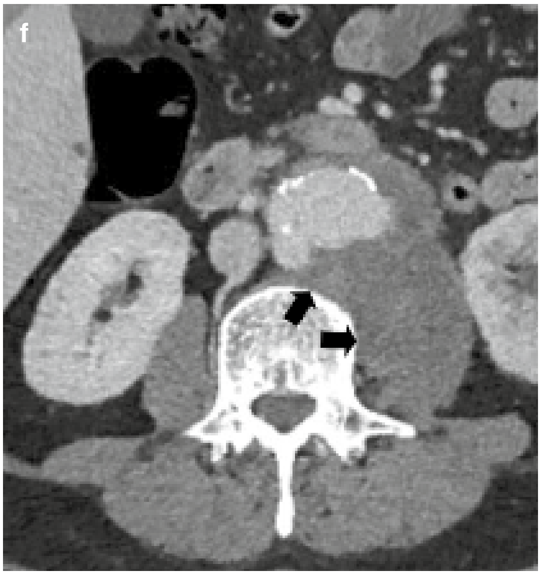

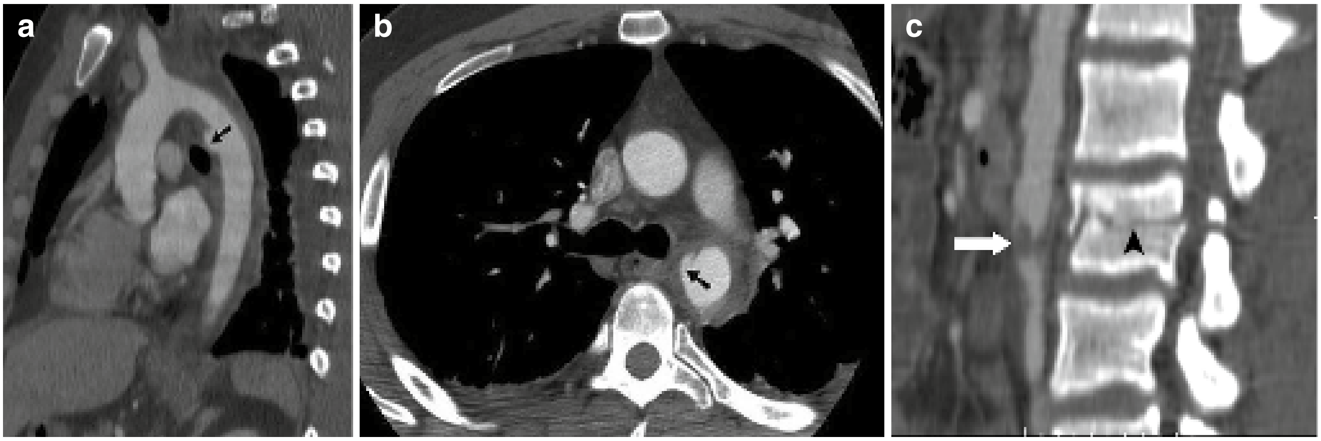

Fig. 1.5 Aortic transection. Sagittal (**a**) and axial CT (**b**) demonstrate outpouching (*arrow*) of the aorta and surrounding hemorrhage, at the junction of aortic arch and descending thoracic aorta. (**c**) Sagittal CT reformation demonstrates horizontal chance fracture through a lumbar vertebral body (arrowhead) and adjacent intimal tear of the aorta (arrow) with hemodynamically significant luminal narrowing

in aortic diameter. Transection of aorta has irregular margins with acute angles relative to the aorta (Fig. 1.5).

95 to 99% of traumatic aortic injuries are in the thoracic region. Rare case of traumatic injuries of abdominal aorta can be associated with chance fractures of the lumbar spine (Fig 1.5c).

Aortic Dissection

Aortic dissection is the most common acute presentation involving the aorta [3]. It usually originates with a tear in the intima, which causes high-pressure blood to enter and dissect the aortic wall (Table 1.4; Fig. 1.6). Based on the period from onset of symptoms to clinical presentation, aortic dissection is classified as hyperacute (symptom onset to 24 h), acute (2–7 days), subacute (8–30 days), and chronic (>30 days).

Table 1.4 Factors predisposing to aortic dissection

Hypertension (most common)
Syndromes
Marfan's syndrome
Turner syndrome
Noonan syndrome
Ehlers–Danlos syndrome
Coarctation, bicuspid aortic valve
Cocaine use
Pregnancy
Trauma

ALGrawany

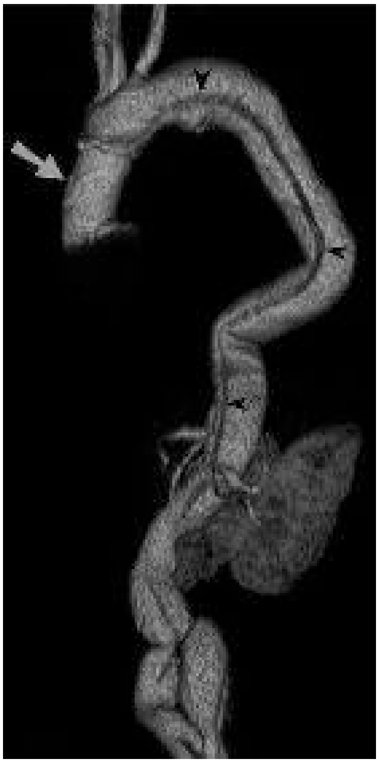

Fig. 1.6 Postoperative changes in a patient with type A aortic dissection. 3D CT image demonstrates ascending aortic graft (*arrow*) which was placed to surgically managed type A aortic dissection. The dissection flap (*arrowheads*) is visible in the aortic arch, descending thoracic aorta, and abdominal aorta

The most commonly used classification for aortic dissection is the Stanford classification system.

1. *Type A aortic dissection*: Regardless of origin and extent of dissection, a type A aortic dissection involves the ascending aorta (Fig. 1.7) [4]. The potential for complications with type A dissection necessitates urgent surgical intervention [4]. The complications include dissection into the pericardium resulting in cardiac tamponade, dissection into the coronary arteries resulting in occlusion, and aortic insufficiency with involvement of the valve [4].
2. *Type B aortic dissection*: The aortic dissection originates past the left subclavian artery [5]. Unlike type A dissection, the type B dissections are usually medically treated.

Imaging

The goals of imaging in aortic dissection include identification of:

1. Site of intimal tear site
2. Extent of dissection (for classification)

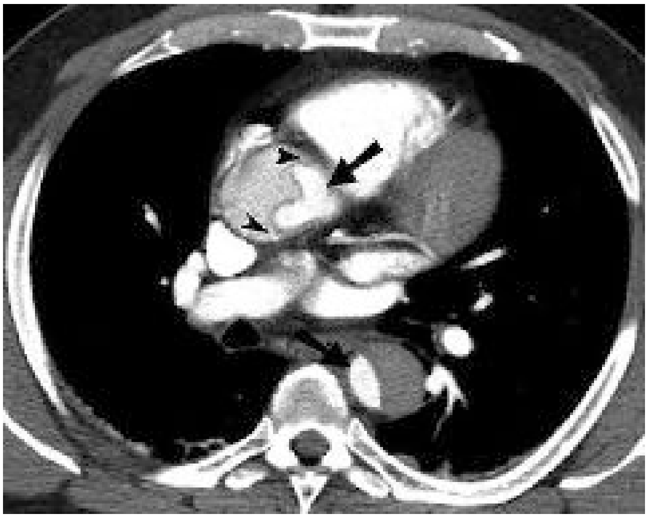

Fig. 1.7 Type A aortic dissection. Contrast-enhanced CT scan study of the chest demonstrates aortic dissection involving the ascending as well as the descending thoracic aorta. The true lumen can be identified by the smaller caliber (*arrows*) and higher acute aortic density. The beak sign (*arrowheads*) is identified in the false lumen

3. Cardiac involvement (pericardial, myocardial, and valvular)
4. Aortic rupture
5. Major branch-vessel involvement

The imaging modality of choice to evaluate aortic dissection is MDCT. It allows accurate assessment of the extent of the disease, including the origin of the dissection, involvement of the visceral branches, and presence of a false lumen [3, 4]. The most characteristic findings of aortic dissection include an intimal flap and two distinct lumens. Secondary findings include intimal displacement of calcified wall, delayed enhancement of false lumen, pericardial or mediastinal hematoma, and ischemia or infarction of distal organs supplied by the false lumen [4].

True Versus False Lumen

Once the recognition of an aortic dissection is made, it is important to distinguish between the true and false lumen for treatment purposes, especially endovascular repair. Lepage et al. evaluated signs to distinguish between the true and false lumen and determined two consistent signs: beak sign and larger cross-sectional area of false lumen as the best indicators. The beak sign is present in the false lumen and consists of an acute angle between the dissection flap and the aortic wall [5]. The larger caliber lumen is generally the false lumen and is most commonly present anteriorly to the right side in the ascending aorta (Figs. 1.7, 1.8, and 1.9). In the descending thoracic aorta, the false lumen is most often seen

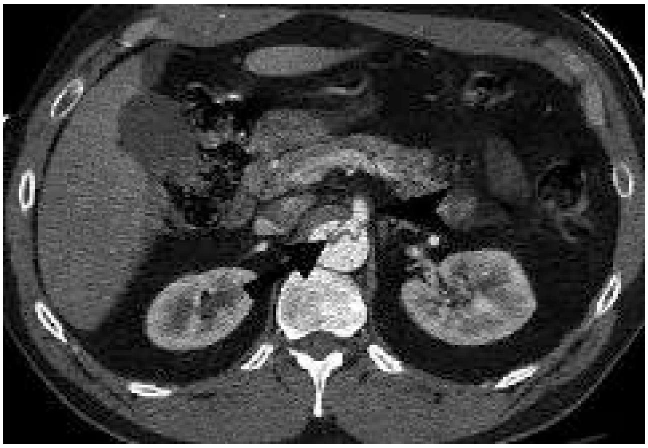

Fig. 1.8 Aortic dissection involving the abdominal aorta. Contrast-enhanced CT scan study demonstrates small caliber of the true lumen (*arrow*) supplying the superior mesenteric artery (*arrowhead*)

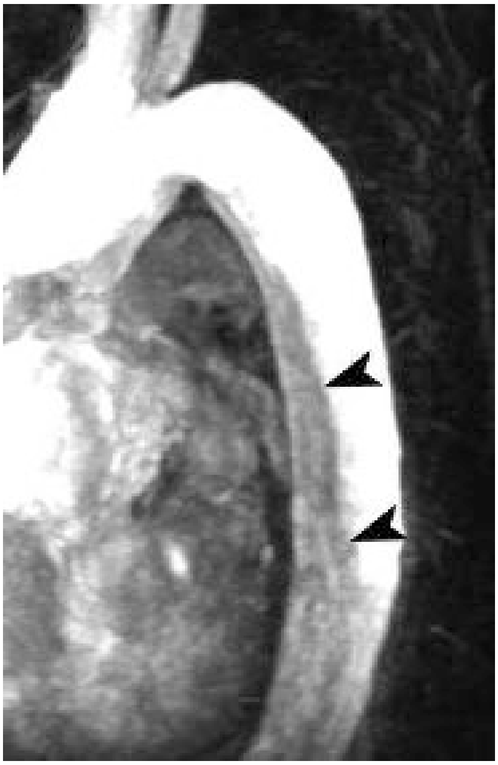

Fig. 1.9 Type B aortic dissection on MR angiogram. Gadolinium-enhanced MR angiogram demonstrates the dissection flap (*arrowheads*) present in the descending thoracic aorta

posteriorly and to the left. Cobwebs are seen in the false lumen while aortic wall calcifications are usually seen around true lumen. The true lumen may show systolic expansion and diastolic collapse during the cardiac cycle.

Intramural Hematoma

Intramural hematoma is a hematoma that has dissected through the media without an originating intimal tear (Figs. 1.10 and 1.11). The intramural hematoma may represent hemorrhage of the vasa vasorum (nutrient vessels for the vessel wall) that has dissected through the media [6]. It can be seen in hypertensive and can also be seen after blunt trauma. It can progress to rupture of the aortic wall or aortic dissection.

Unlike mural thrombus, intramural hematoma is deep to the intimal calcification and does not demonstrate the continuous flow seen with aortic dissection. Intramural hematoma can be diagnosed on CT, transesophageal echocardiography, and MRI. Since there is no intimal disruption, it cannot be diagnosed on conventional aortography. Aneurysmal dilatation, focal contrast enhancement, and intramural thickness >16 mm on CT scan indicate poor prognosis. The treatment of intramural hematoma is similar to aortic dissection.

Endoleak

Endoleak is extravasation of blood out of the endovascular stent but within the aneurysmal sac. The aneurysmal sac may enlarge and may ultimately rupture over time, especially in the setting of hypertension. CT scan is the imaging modality of choice in the detection of endoleak (Fig. 1.12).

Five types of endoleak are as follows:

Type I: Incomplete seal between graft and vessel wall in (a) proximal or (b) distal anchors.

Type II: Most common type. Retrograde blood flow into the sac from aortic branch vessels.

Type III: Relatively uncommon type. Due to separation or tear of graft material.

Type IV: Due to porosity of stent-graft material and have no CT findings.

Type V: Continued expansion of the aneurysm sac without radiographic identification of a leak.

ALGrawany

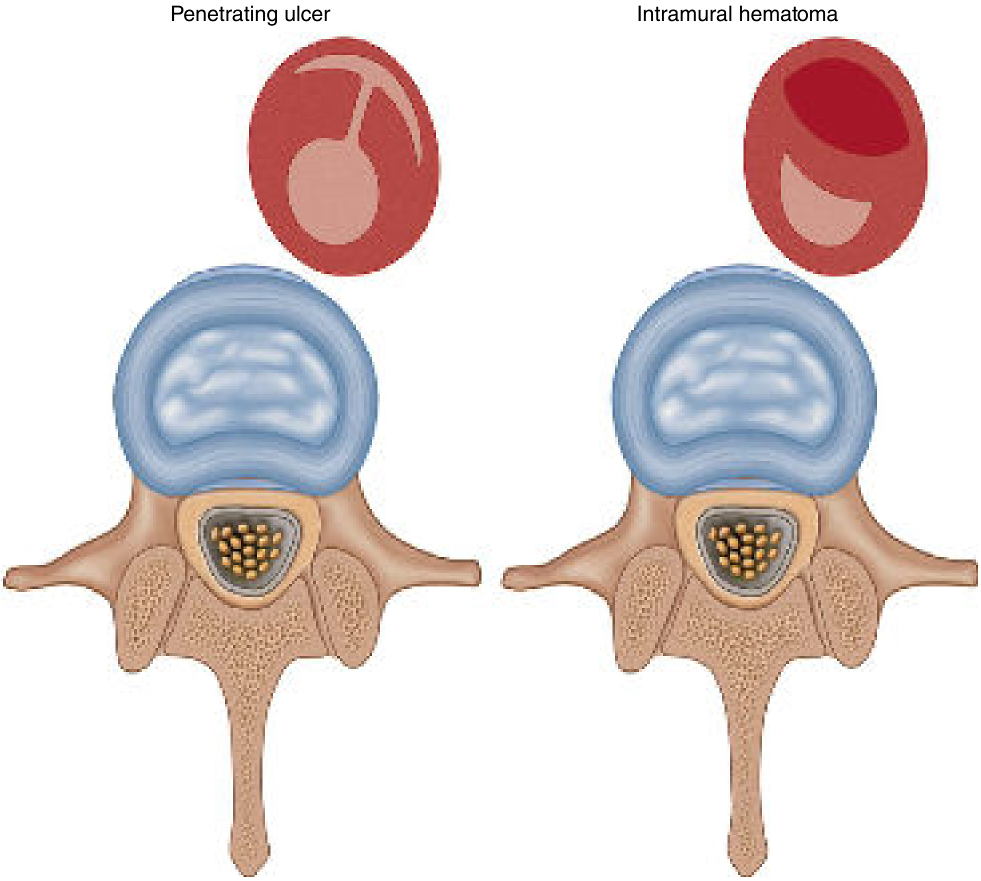

Fig. 1.10 Schematic representation of penetrating ulcer and intramural hematoma. Penetrating ulcer is characterized by communication of the arterial lumen with the hematoma located in the media. Intramural hematoma is characterized by lack of direct communication of the arterial lumen with the hematoma in the media

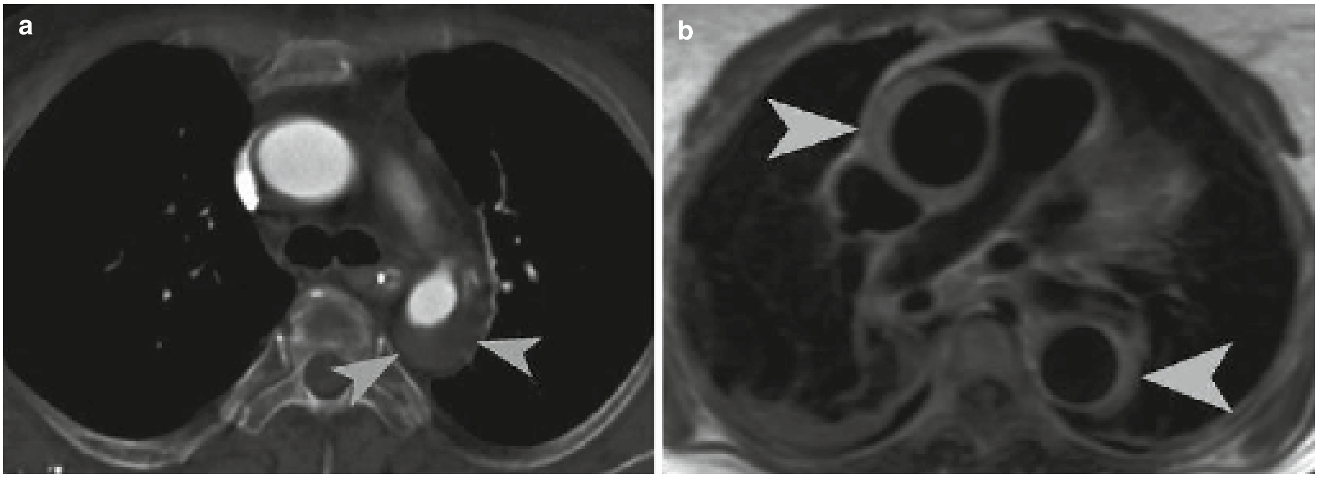

Fig. 1.11 Intramural hematoma. (**a**) Contrast-enhanced CT demonstrates asymmetric aortic wall thickening, consistent with intramural hematoma (*arrowheads*) in the descending thoracic aorta. (**b**) Noncontrast axial T1-weighted MR shows intramural hematoma (*arrowheads*) causing asymmetric aortic wall thickening in the ascending and descending thoracic aorta

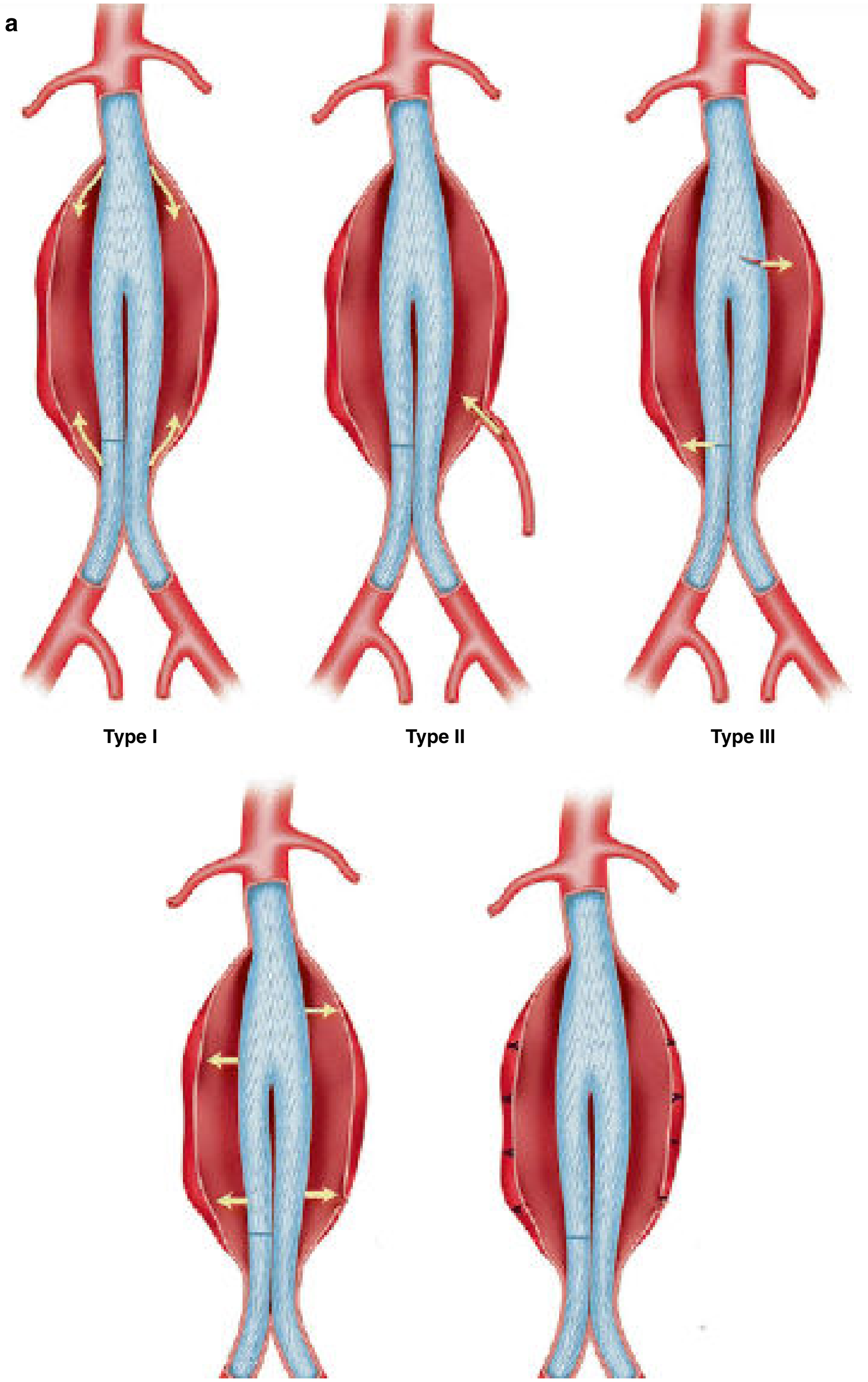

Fig. 1.12 Endoleak. (**a**) Schematic representation of endoleak types. (**b**) US demonstrates type 1b endoleak (*arrowheads*), outside the endograft. (**c**) Axial CT image demonstrates a type 2 endoleak (*arrowhead*), being fed by inferior mesenteric artery (*arrow*)

ALGrawany

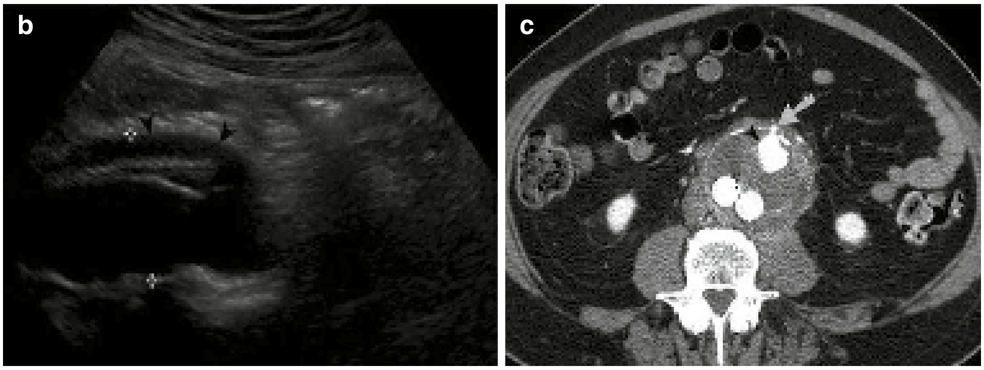

Fig. 1.12 (continued)

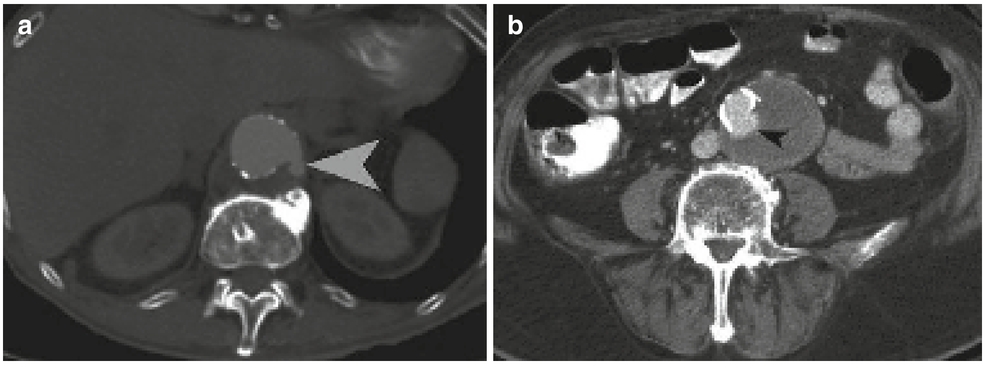

Fig. 1.13 Aortic ulcer. (**a**, **b**) Contrast-enhanced CT scan study of the abdomen demonstrates abdominal aortic aneurysm with an aortic ulcer (*arrowheads*) along with intramural hemorrhage

Penetrating Ulcer

Penetrating ulcer is characterized by atherosclerotic ulceration that has penetrated through the elastic lamina and formed a hematoma in the media. On CT scan, it is seen as an ulcer with focal hematoma and adjacent arterial wall thickening (Fig. 1.13) [7, 8]. Unlike penetrating ulcer, an atherosclerotic plaque with ulceration does not extend beyond the intima and is not associated with intramural hematoma.

Penetrating ulcer and aortic dissection are characterized by disruption of the intima, while aortic rupture is characterized by disruption of the aortic wall.

CT is the key diagnostic modality in the emergency room evaluation of acute aortic syndromes and allows different pathologies to be diagnosed for proper triage as well as treatment (Table 1.5).

Table 1.5 CT findings in acute aortic conditions

Condition	CT findings
Aortic dissection	1. Intimal flap 2. Two distinct lumens 3. Displacement of intimal calcification 4. Delayed enhancement of false lumen 5. Infarction of distal organs
Intramural hematoma	1. Thickening of aortic wall 2. Hyperdense crescent on unenhanced CT
Penetrating ulcer	1. Ulcer with focal hematoma 2. Adjacent arterial wall thickening

Teaching Points

- Most common causes of abdominal aortic aneurysm are degenerative and inflammatory.
- The imaging criteria to diagnose AAA include aortic caliber of more than 3 cm and an aortic caliber of more than 1.5 times the expected diameter of the abdominal aorta.
- There is increased risk of rupture with increasing caliber of the aneurysm and reduced thrombus-to-lumen ratio.
- Hyperdense crescent sign and draped aorta sign are indicators of contained aortic leak or impending rupture.
- The most common imaging features of mycotic aneurysm are periaortic soft tissue stranding and soft tissue mass.
- Type A aortic dissection involves the ascending aorta and is surgically managed.
- Type B aortic dissection originates past the left subclavian artery and is usually medically managed.
- Beak sign and larger cross-sectional area of lumen are indicators of false lumen.
- Intramural hematoma represents hemorrhage of the vasa vasorum and is not associated with intimal discontinuity (unlike penetrating ulcer).

Questions

1. What is the most common cause of abdominal aortic aneurysm?
   (A) Inflammatory
   (B) Marfan's syndrome
   (C) Degenerative
   (D) Traumatic
   Answer: C

2. Which of the following is the imaging criterion to diagnose abdominal aortic aneurysm?
   (A) Caliber >1.5 times the expected
   (B) Active extravasation
   (C) Hyperdense crescent sign
   (D) Draped Aorta Sign
   Answer: A

3. What is the most common predisposing factor to aortic dissection?
   (A) Drug abuse
   (B) Coarctation
   (C) Trauma
   (D) Hypertension
   Answer: D

4. Which of the following is an indicator of false lumen?
   (A) Acute angle between the dissection flap and aortic wall
   (B) Smaller lumen
   (C) Posterior location in the ascending aorta
   (D) Aortic wall calcifications around the lumen
   Answer: A

5. Aortic wall irregularity and surrounding edema are the imaging features of which of the following aortic pathology?
   (A) Aortic rupture
   (B) Mycotic aneurysm
   (C) Aortic dissection
   (D) Intramural hematoma
   Answer: B

6. CTA of an elderly man with acute chest pain in depicted in Fig. 1.14. Which of the following is a possible cause of the patient's chest pain?
   (A) Hematoma
   (B) Aneurysm
   (C) Endoleak
   (D) Penetrating ulcer
   Answer: D

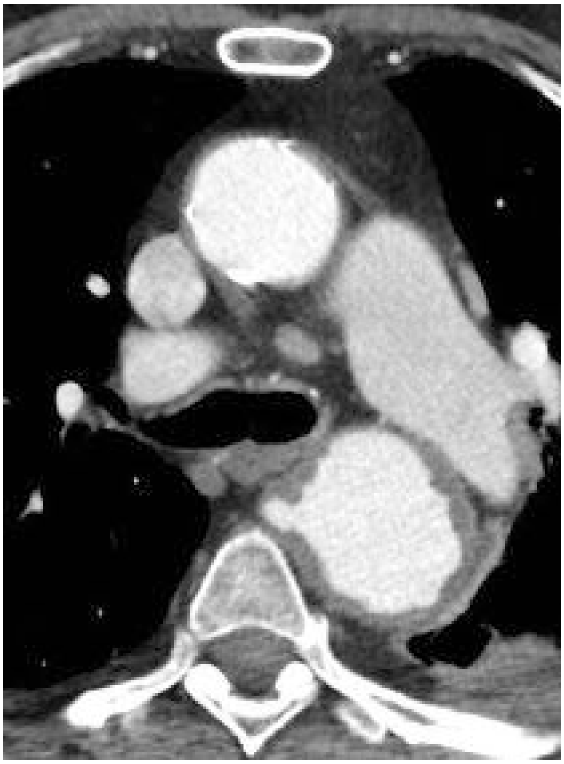

Fig. 1.14 CTA—penetrating ulcer

ALGrawany

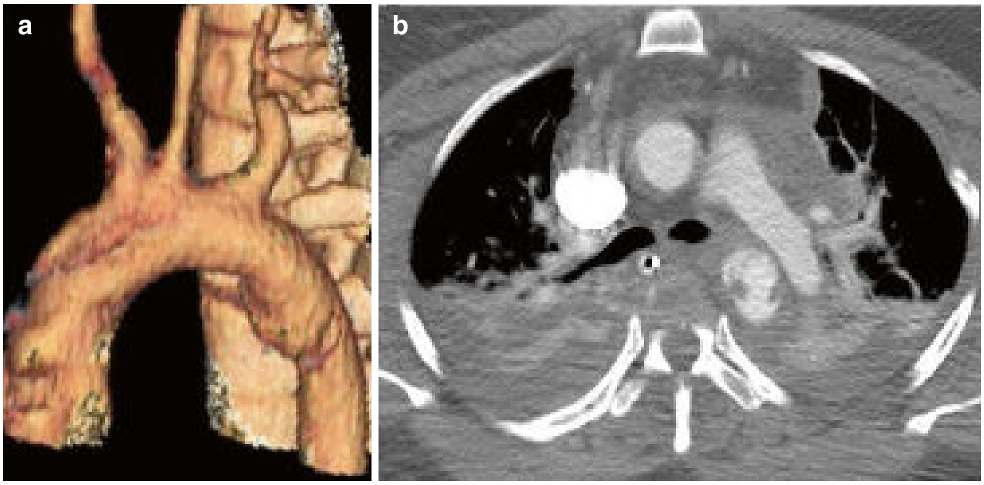

Fig. 1.15 Motor vehicle collision—transection (**a**) schematic diagram (**b**) CT image

7. Which of the following is the CT (Fig. 1.15) diagnosis of patient involved in motor vehicle collision?
   (A) Transection
   (B) Endoleak
   (C) Hematoma
   (D) Aneurysm
   Answer: A

8. What is the finding depicted on angiography (Fig. 1.16) in a patient with chest pain?
   (A) Aneurysm
   (B) Endoleak
   (C) Aortic pseudoaneurysm
   (D) Hematoma
   Answer: C

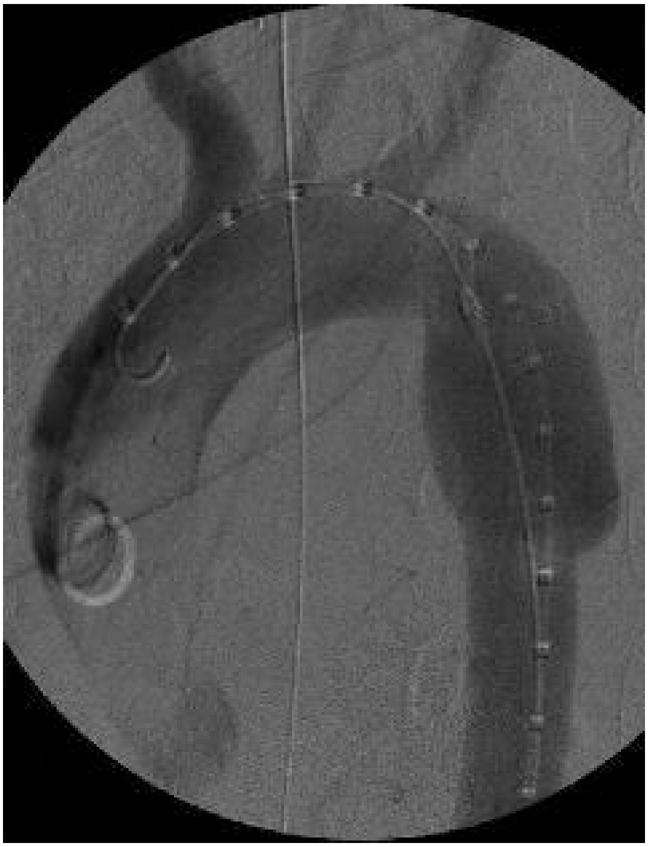

Fig. 1.16 Angiography—aortic pseudoaneurysm

References

1. Rakita D, Newatia A, Hines JJ, Siegel DN, Friedman B. Spectrum of CT findings in rupture and impending rupture of abdominal aortic aneurysms. Radiographics. 2007;27:497–507.
2. Schwartz SA, Taljanovic MS, Smyth S, O'Brien MJ, Rogers LF. CT findings of rupture, impending rupture, and contained rupture of aortic abdominal aneurysm. AJR Am J Roentgenol. 2007;188:W57–62.
3. Petasnick JP. Radiologic evaluation of aortic dissection. Radiology. 1991;180:297–305.
4. Fisher ER, Stern E, Godwin JD II, Otto C, Johnson JA. Acute aortic dissection: typical and atypical imaging. Radiographics. 1994;14:1263–71.
5. Lepage MA, Quint LE, Sonnad SS, Deeb M, Williams DM. Aortic dissection: CT features that distinguish true lumen from false lumen. AJR Am J Roentgenol. 2001;177:207–11.
6. Sawhney NS, DeMaria AN, Blanchard DG. Aortic intramural hematoma: an increasingly recognized and potentially fatal entity. Chest. 2001;120:1340–6.
7. Hayashi H, Matsuoka Y, Sakamoto I, Sueyoshi E, Okimoto T, Hayashi K, et al. Penetrating atherosclerotic ulcer of the aorta: imaging features and disease concept. Radiographics. 2000;20:995–1005.
8. Sebastià C, Pallisa E, Quiroga S, Alvarez-Castells A, Dominguez R, Evangelista A. Aortic dissection: diagnosis and follow-up with helical CT. Radiographics. 1999;19:45–60.

A L G r a w a n y

Emergencies of the Biliary Tract

2

Caterina Missiroli, Khyati Bidani, Mohammad Mansouri,
and Ajay Singh

Introduction

Gallstones are seen in 10–15% of the population, most commonly in middle-aged and elderly females. While majority of gallstones have cholesterol as the main component, a minority of stones are constituted by calcium bilirubinate and are called pigment stones. Ten to twenty percent of the gallstones contain enough calcium to be visible on plain radiograph (Fig. 2.1a). The stones are most commonly multiple and sometimes faceted. A triradiate collection of nitrogen gas within the fissures inside the gallstone produces Mercedes-Benz sign (Fig. 2.1b, c).

Typically, gallstones are seen as echogenic foci with clean distal acoustic shadowing (Fig. 2.1d). Stones larger than 2 mm should produce a shadow regardless of their composition. Mobility of stones and posterior acoustic shadowing helps to differentiate cholelithiasis from other gallbladder abnormalities including polyps, masses, and sludge. *Wall echo shadow sign* refers to the parallel echogenic lines produced by a combination of the gallbladder wall, echogenic stone, and associated distal acoustic shadowing (Fig. 2.1e). The hypoechoic line seen between the two echogenic lines represents interposed bile. This sign is seen in gallbladder filled with either a single large gallstone or multiple small gallstones.

Ultrasound has higher sensitivity than CT in diagnosing gallstones (96% in ultrasound versus 75% in CT) and is therefore the screening modality of choice. On sonography, highest possible frequency transducer should be used with the focal zone placed at the level of the stone. Although ultrasound remains the exam of choice for suspected cholecystitis, there are ever more cases of acute cholecystitis being detected today with CT in the evaluation of abdominal pain than in the past.

On T2-weighted MRI, gallstones are seen as signal voids in the high-signal intensity bile (Fig. 2.2). On T1-weighted images, signal intensity depends on stone composition. Blood clot, gas bubbles, and tumor can mimic gallstones on MRI.

Majority of the patients with gallstones are asymptomatic. Sometimes the gallstone can cause transient gallbladder outflow obstruction, leading to biliary colic. Biliary colic patients present with transient pain for 1–3 h with nausea and vomiting. The symptoms subside when the gallstone falls back into the gallbladder or passes distally into the biliary tree.

C. Missiroli
Department of Radiology, ASST Nord Milano—Bassini Hospital,
Milan, Italy

K. Bidani · M. Mansouri
Department of Radiology, Massachusetts General Hospital,
Boston, MA, USA

A. Singh (✉)
Division of Emergency Radiology, Department of Radiology,
Massachusetts General Hospital, Boston, MA, USA

Harvard Medical School, Massachusetts General Hospital,
Boston, MA, USA
e-mail: asingh1@partners.org

© The Author(s), under exclusive license to Springer Nature Switzerland AG 2024
A. Singh (ed.), *Emergency Radiology*, https://doi.org/10.1007/978-3-031-65770-2_2

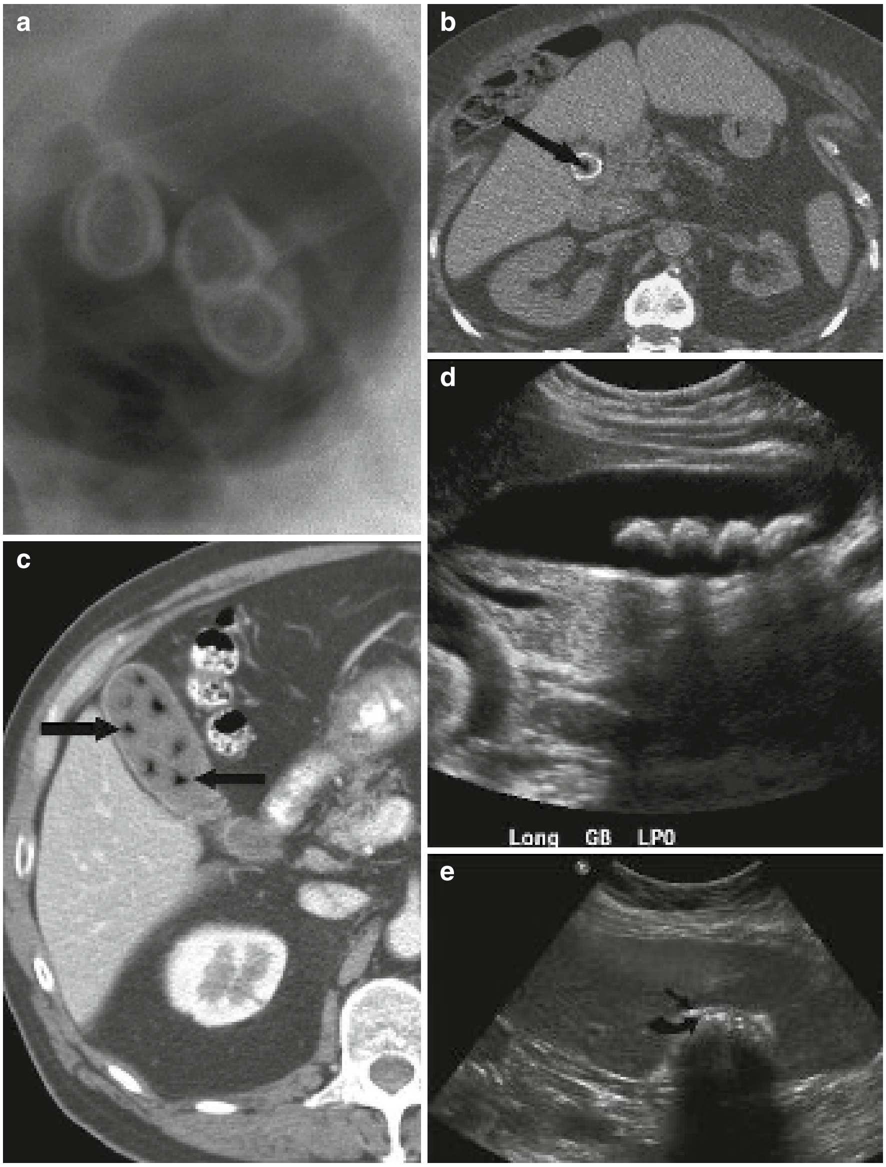

Fig. 2.1 Imaging appearance of gallstones on plain radiograph and ultrasound. (**a**) Plain radiograph demonstrates laminated radiopaque gallstones in the *right upper quadrant*. Up to a fifth of the gallstones can be seen on plain radiograph of the abdomen. (**b**, **c**) Noncontrast CT of the gallbladder shows gallstones with Mercedes-Benz sign (*arrows*). Mercedes-Benz sign is due to nitrogen collection in triradiate configuration, within fissures of a gallstone. (**d**) Ultrasound shows multiple echogenic gallstones with distal acoustic shadowing, within the gallbladder lumen. (**e**) Ultrasound shows wall echo shadow sign in a patient with multiple gallstones and chronic cholecystitis. The outer echogenic line (*straight arrow*) represents the gallbladder wall, while the inner echogenic line (*curved arrow*) represents the outer edge of gallstones

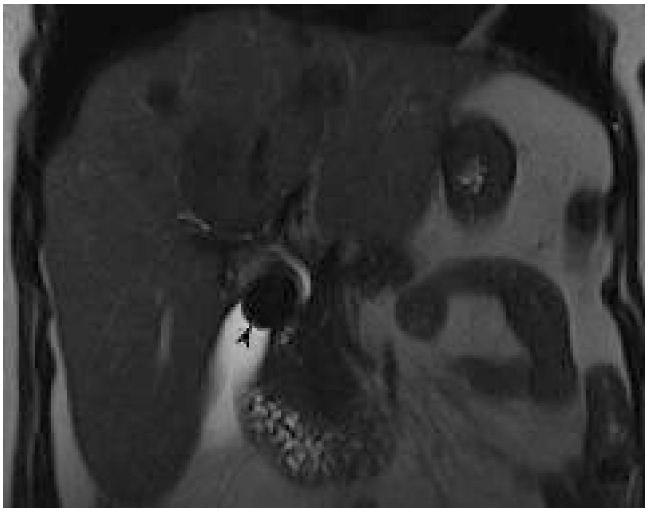

Fig. 2.2 Gallstone on MRI. T2-weighted coronal MRI shows a hypointense gallstone (*arrowhead*) in the neck of the gallbladder

Acute Cholecystitis

Acute cholecystitis usually is caused by the gallstone obstruction of the cystic duct or the gallbladder neck (one-third of cases). Acute cholecystitis without stones (5–10% of cases) can be seen in patients with adenomyomatosis, gallbladder polyp, and malignant neoplasm [1, 2]. The predisposing factors for acute acalculous cholecystitis include history of trauma, mechanical ventilation, hyperalimentation, postoperative/postpartum state, diabetes mellitus, vascular insufficiency, prolonged fasting, and burns [2].

The clinical presentation includes right upper quadrant pain for more than 6 h (vs. biliary colic), nausea, vomiting, and fever in a patient with history of gallstones. No clinical or lab finding provides high enough positive predictive value in making the diagnosis of acute cholecystitis.

ALGrawany

Imaging

Ultrasound is the first-line imaging modality in diagnosing acute cholecystitis because of wide availability, ability to detect gallstones as well as biliary ducts, and accuracy in diagnosing acute cholecystitis. The ultrasound findings of acute cholecystitis include gallstones, gallbladder wall thickening (>3 mm), gallbladder distension (>5 cm transverse dimension), and positive Murphy's sign (Fig. 2.3) [1, 3]. Positive sonographic Murphy's sign and gallstones are considered to be the most specific findings. However, sonographic Murphy's sign can be falsely negative in patients who have received analgesic medication or in the setting of gangrenous cholecystitis. Another imaging finding of acute cholecystitis is the presence of a pericholecystic fluid collection, sometimes extending to the perihepatic space [2, 4].

Gallbladder wall thickening is a finding of acute cholecystitis which can also be seen in other conditions such as hypoproteinemia, ascites, pancreatitis, right heart failure, renal failure, liver failure, and hepatitis. Striated gallbladder wall thickening is no more specific for acute cholecystitis than the observation of gallbladder wall thickening from other causes. In the clinical setting of acute cholecystitis, the presence of striated gallbladder wall thickening suggests gangrenous cholecystitis.

Cholescintigraphy (HIDA scan) is considered second-line imaging modality which can be used after equivocal ultrasound study. Cholescintigraphy has a sensitivity and specificity which is superior to ultrasound. Although it may take more than 2 h to complete the study, the use of morphine (0.04 mg/kg) allows cholescintigraphy to be completed in 1.5 h. The classic findings on cholescintigraphy include nonvisualization of the gallbladder 30 min after morphine injection and presence of a curvilinear area of increased radiotracer activity (rim sign) in the liver adjacent to the gallbladder (Fig. 2.4). False-positive results may be seen with liver disease or prolonged fasting. Delayed gallbladder filling may occur in chronic cholecystitis. Rim sign is most commonly

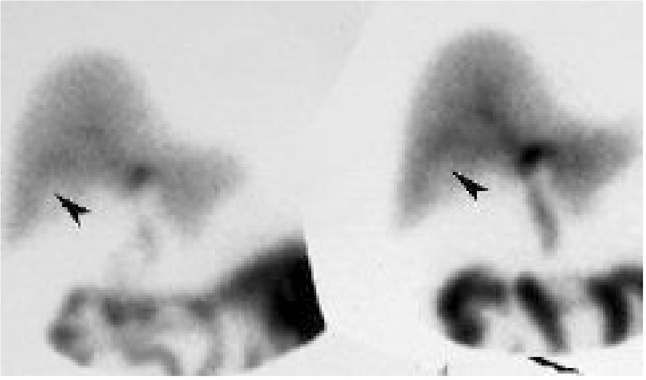

Fig. 2.4 Gangrenous cholecystitis on cholescintigraphy. Cholescintigraphy study (HIDA scan) demonstrates nonvisualization of the gallbladder and a curvilinear area of increased radiotracer activity (*rim sign*) in the pericholecystic liver parenchyma (*arrowheads*)

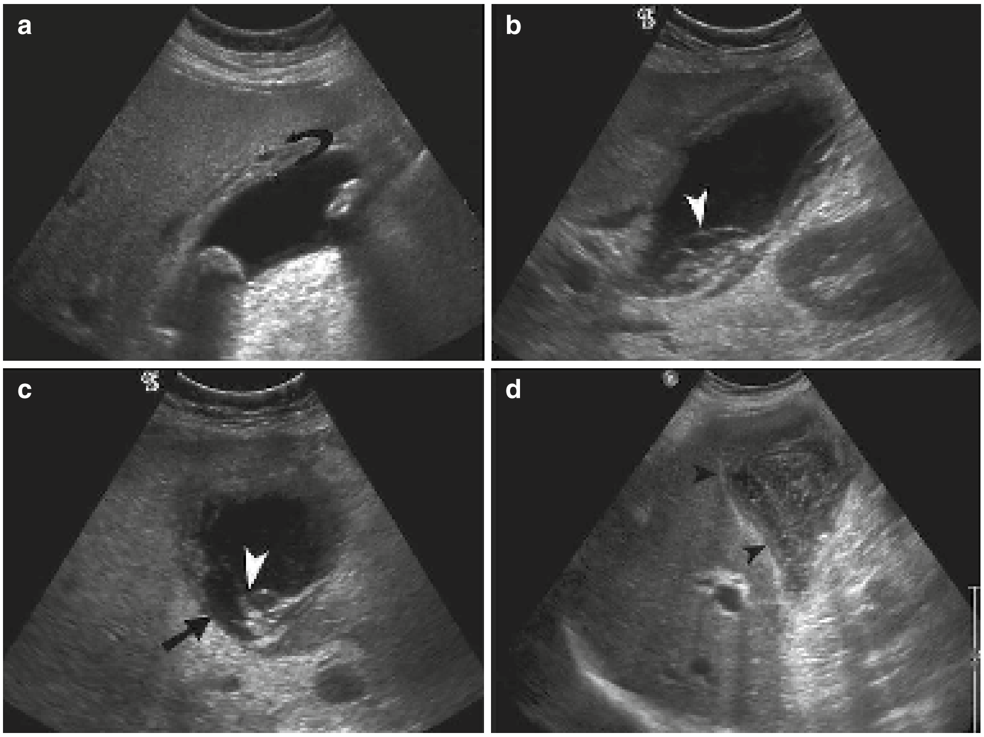

Fig. 2.3 Ultrasound imaging of acute cholecystitis. (**a**) Ultrasound in a patient with acute cholecystitis demonstrates multiple gallstones and striated thickening of the gallbladder wall (*arrow*). (**b**, **c**) Ultrasound in a patient with gangrenous cholecystitis demonstrates striated thickening of the gallbladder wall, intraluminal sludge, and sloughed mucosa (*arrowhead*). Focal thinning of the necrotic gallbladder is indicated by the *straight arrow* and appears to represent the donor site for the sloughed-off mucosa. (**d**) Ultrasound in a patient with acute cholecystitis shows gallbladder wall thickening (*arrowheads*) and complex fluid, which represented pus during cholecystostomy tube placement

seen in patients with gangrenous cholecystitis and is due to extension of inflammation beyond the gallbladder.

If ultrasound and/or cholescintigraphy show no evidence of acute cholecystitis or any other cause for the right upper quadrant pain, a contrast-enhanced CT is considered the next most appropriate imaging modality. The CT findings include gallstones, gallbladder wall thickening, gallbladder wall enhancement, increased bile attenuation (possibly indicative to empyema), distended gallbladder, and pericholecystic fluid collection (Table 2.1; Fig. 2.5) [5]. CT has lower sensitivity than US in detecting gallstones and can miss noncalcified gallstones.

Table 2.1 CT findings of acute cholecystitis

Thickening of the gallbladder wall (normal wall thickness is up to 3–4 mm)
Gallstones
Gallbladder distention (>5 cm in transverse dimension)
Pericholecystic fluid
Indistinct interface between the gallbladder wall and the liver
Pericholecystic inflammatory changes
Transient focal attenuation difference
Increased density bile

MR imaging is not a frontline imaging modality for acute cholecystitis and can be used after equivocal US study. The advantage of MR over CT is its ability to reliably study common bile duct and the lack of ionizing radiation which is especially important in pregnant population. Although, gadolinium is useful in making the diagnosis of acute cholecystitis, it should not be used in pregnant population. The important findings of cholecystitis on MR imaging are described in Table 2.2 (Fig. 2.6).

The complications of acute cholecystitis include gallbladder empyema, gangrenous cholecystitis, emphysematous cholecystitis, gallbladder perforation, Mirizzi syndrome, and gallstone ileus.

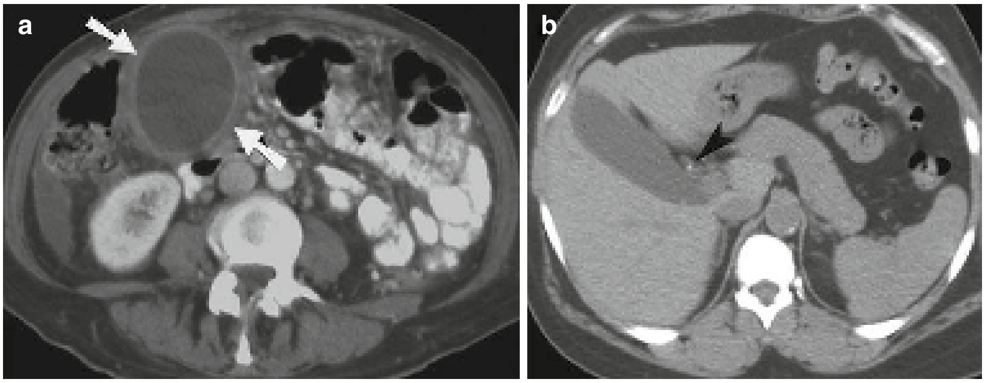

Fig. 2.5 CT findings of acute cholecystitis. (**a**) Contrast-enhanced CT shows distended gallbladder with wall thickening (*arrows*) and pericholecystic inflammatory changes. (**b**) Contrast-enhanced CT shows small calculus (*arrowhead*) causing cystic duct obstruction

Table 2.2 MR findings of acute cholecystitis

Gallbladder empyema	Low-signal intensity on T2 and high-signal intensity on T1 WI
Gallstones	Signal void on MRCP and low signal on T1–T2 WI
Gallbladder wall thickening	Enhancing wall and high signal on T1 and low to high on T2 WI
Gas within the gallbladder wall	Signal void in the wall
Pericholecystic inflammation	High intensity on T1 and T2 WI
Hemorrhage	High intensity on T1 and T2 WI
Fluid collection	High intensity on T1 and T2 WI

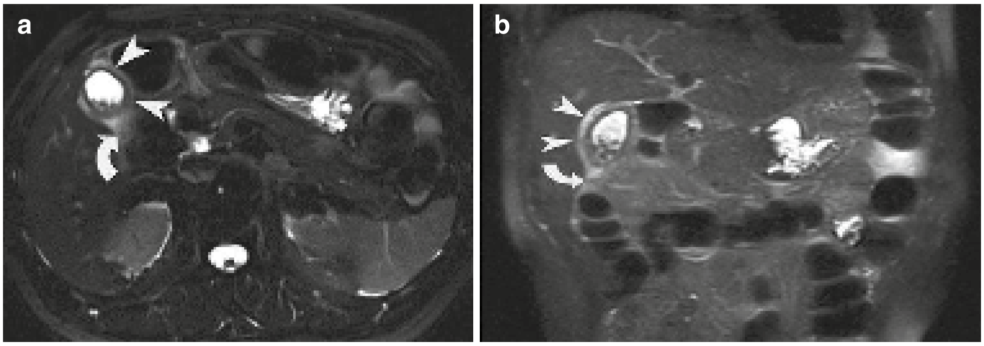

Fig. 2.6 MR findings of acute cholecystitis. (**a**, **b**) HASTE sequence shows gallbladder wall thickening (*arrowheads*), increased signal intensity (*curved arrows*), and multiple small gallstones. HASTE is a high-speed, heavily T2-weighted sequence with partial Fourier technique which has high sensitivity for fluid and a fast acquisition time (<1 s/slice)

ALGrawany

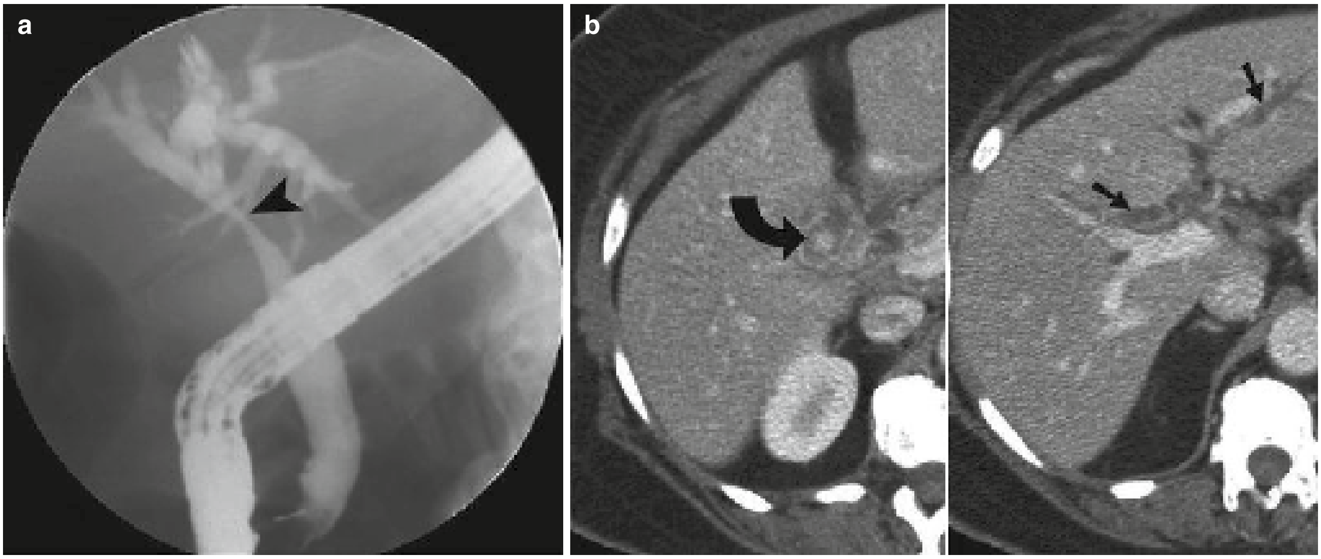

Fig. 2.7 Mirizzi syndrome. (**a**) ERCP demonstrates narrowing of the proximal CBD (*arrowhead*) due to extrinsic impression produced by calculus in the gallbladder neck. (**b**) Contrast-enhanced CT shows the calculus (*curved arrow*) in the gallbladder neck with secondary inflammation causing intrahepatic biliary ductal dilatation (*arrows*)

Mirizzi Syndrome

The obstruction of the common bile duct or common hepatic duct by calculus impacted in the Hartmann's pouch or cystic duct constitutes Mirizzi syndrome (Fig. 2.7). It is an uncommon complication of chronic cholelithiasis and occurs in patients with recurrent episodes of jaundice and cholangitis. Mirizzi syndrome or choledocholithiases should be suspected whenever there is elevated bilirubin level along with clinical symptoms of acute cholecystitis. Mirizzi syndrome can be diagnosed with ultrasonography, CT, or MRI. It is characterized by intrahepatic and common biliary dilatation to the level of the porta hepatitis, where the bile duct shows obstruction due to extrinsic impression. Caliber of distal common bile duct is normal.

Empyema

It is also called suppurative cholecystitis and occurs typically in diabetic patients, when the bile becomes infected and pus fills the distended gallbladder [1]. On imaging, gallbladder empyema is manifested as gallbladder distension, wall thickening, pericholecystic fluid accumulation, intraluminal sludge/pus, and intraluminal air (Fig. 2.8).

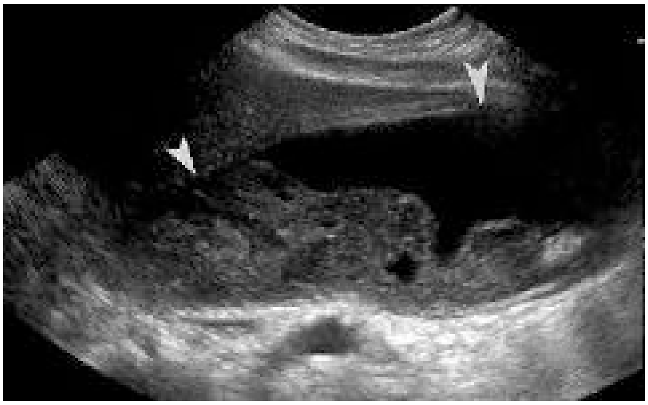

Fig. 2.8 Gallbladder empyema. Ultrasound shows marked distention (*arrowheads*) of the gallbladder lumen and intraluminal debris in a patient with gallbladder empyema

Gangrenous Cholecystitis

It is an advanced form of acute cholecystitis, most frequently seen in elderly men. It is characterized by increased intraluminal pressure, gallbladder distension, gallbladder wall necrosis, intramural hemorrhage, and abscess formation (Fig. 2.9) [1, 2]. There is an increased association of gangrenous cholecystitis with cardiovascular disease and leukocytosis of more than 17,000 WBC/mL. On ultrasonography,

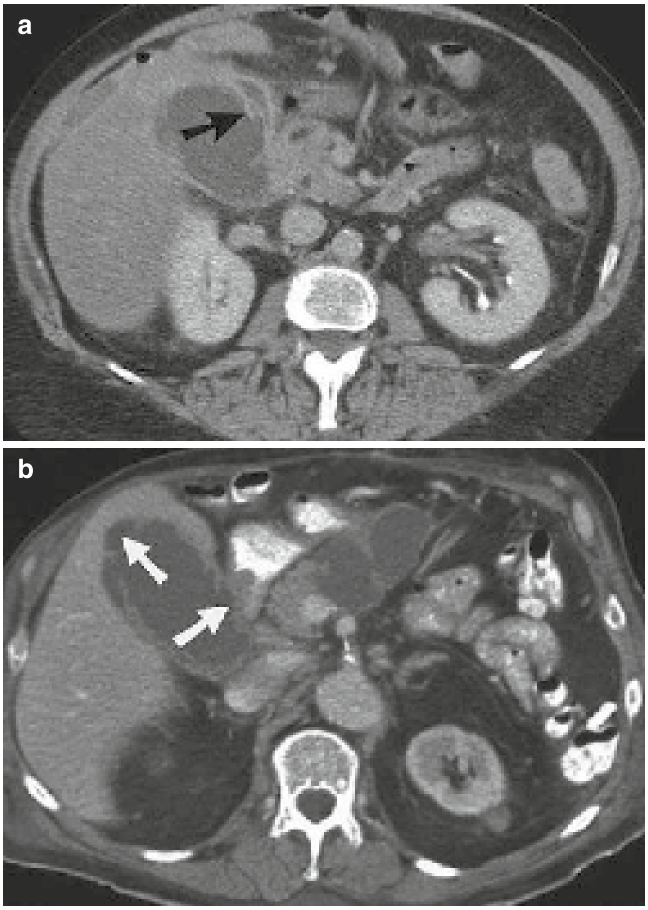

Fig. 2.9 Gangrenous cholecystitis. (**a**, **b**) Contrast-enhanced CT scan in two patients with gangrenous cholecystitis shows irregularity (*arrows*) of the gallbladder wall, gallbladder wall thickening, and pericholecystic inflammation

gangrenous cholecystitis often demonstrates heterogeneous, striated wall thickening and irregularity, and intraluminal membranes. Intraluminal membranes result from desquamation of the gallbladder mucosa (Fig. 2.10). Although CT is highly specific (>90%) in identifying patients with acute gangrenous cholecystitis, it is not very sensitive (Table 2.3). Gallbladder carcinoma may mimic the mural changes in acute cholecystitis, especially gangrenous cholecystitis. CT may be helpful in differentiating the two entities (Fig. 2.11).

Once gangrenous cholecystitis is suspected, the patients require emergency cholecystectomy or cholecystostomy to avoid life-threatening complications. These patients frequently require an open surgical procedure rather than laparoscopic cholecystectomy.

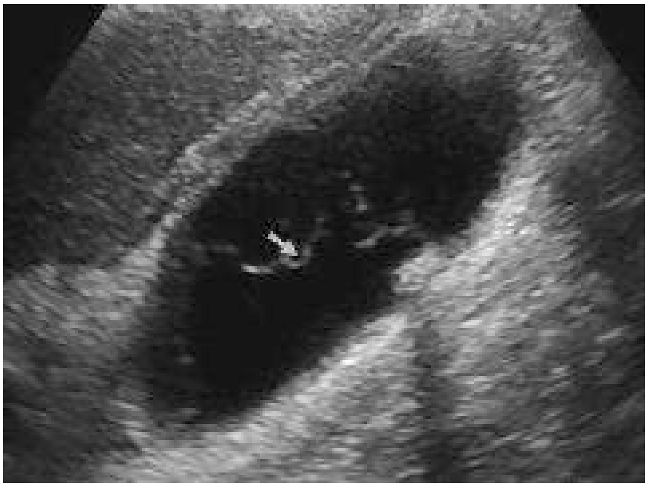

Fig. 2.10 Gangrenous cholecystitis. Ultrasound depicts sloughing of membranes (*arrow*) within the gallbladder lumen, gallbladder wall thickening, and wall edema

Table 2.3 CT findings of gangrenous cholecystitis

Gas in the gallbladder wall or lumen
Intraluminal membranes
Irregularity of wall
Pericholecystic abscess
Lack of mural enhancement
Greater degree of gallbladder distention and wall thickening

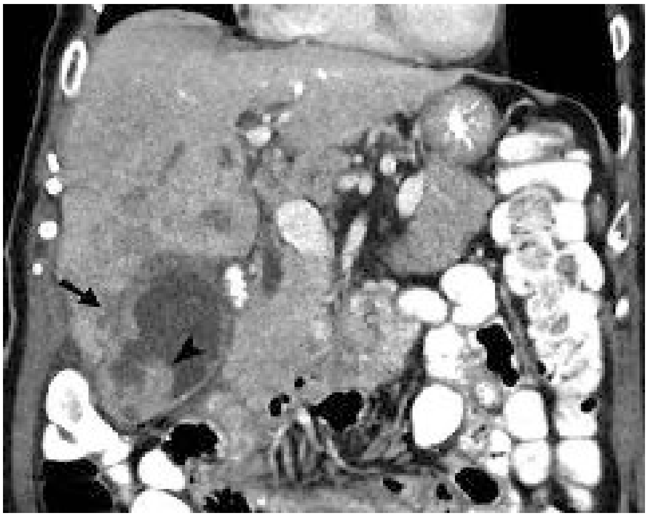

Fig. 2.11 Gallbladder carcinoma. CT scan of an 86-year-old female shows gallbladder mass (*arrowhead*) with contiguous liver extension (*arrow*) into the segment 5

ALGrawany

Emphysematous Cholecystitis

This is a rare life-threatening complication of acute cholecystitis and is characterized by gas within the gallbladder wall and/or lumen due to gas-forming bacteria. It has high mortality, especially when the diagnosis is missed. On ultrasound, gas can be recognized by the presence of dirty distal acoustic shadowing. CT reliably allows distinction of gallbladder wall gas from porcelain gallbladder (Fig. 2.12).

Perforation

This is usually a complication of acute gangrenous cholecystitis and is associated with a high mortality of 19–24% [1, 2]. It can be associated with generalized peritonitis, pericholecystic abscess, and cholecystoenteric fistula (chronic perforation).

The most common site of the gallbladder perforation is the fundus. These patients can develop pericholecystic or intrahepatic abscesses, cholecystoenteric fistulas, or biliary

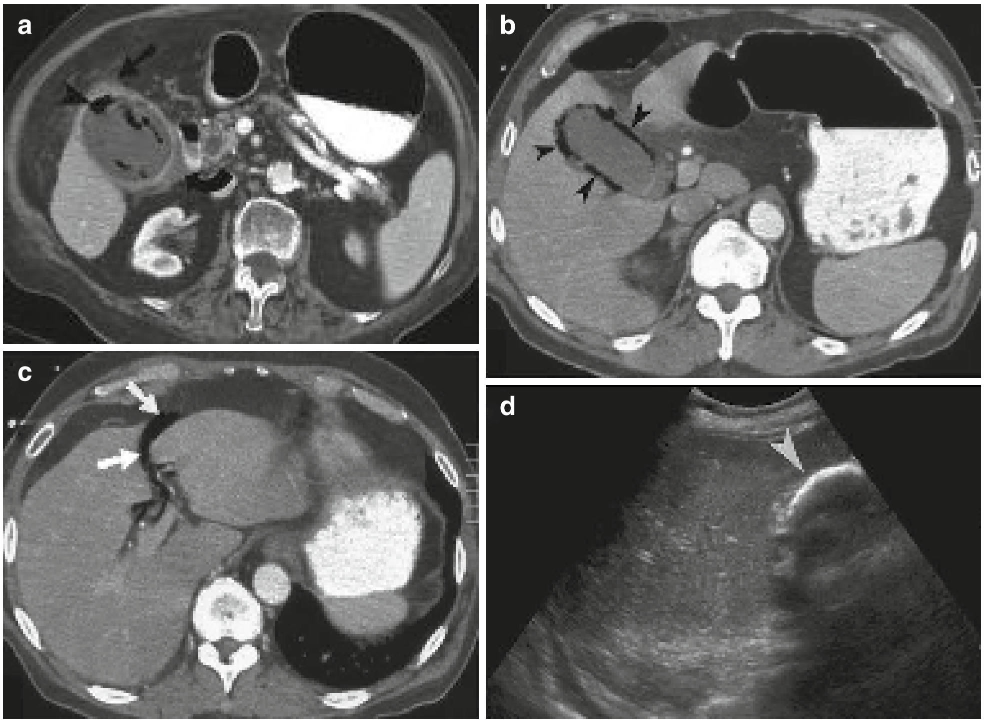

Fig. 2.12 Emphysematous cholecystitis. (**a**) Contrast-enhanced CT scan shows pericholecystic inflammation (*straight arrow*), pericholecystic fluid (*curved arrow*), and air within the gallbladder lumen (*arrowhead*). There was no air seen in the gallbladder on a previous CT study. (**b**, **c**) Contrast-enhanced CT shows air (*arrowheads*) in the wall of the gallbladder. Air is also seen to track along the ligamentum teres (*straight arrows*), indicating the presence of concomitant perforation. (**d**) Ultrasound demonstrates echogenic air (*arrowhead*) with dirty distal acoustic shadowing in the gallbladder lumen

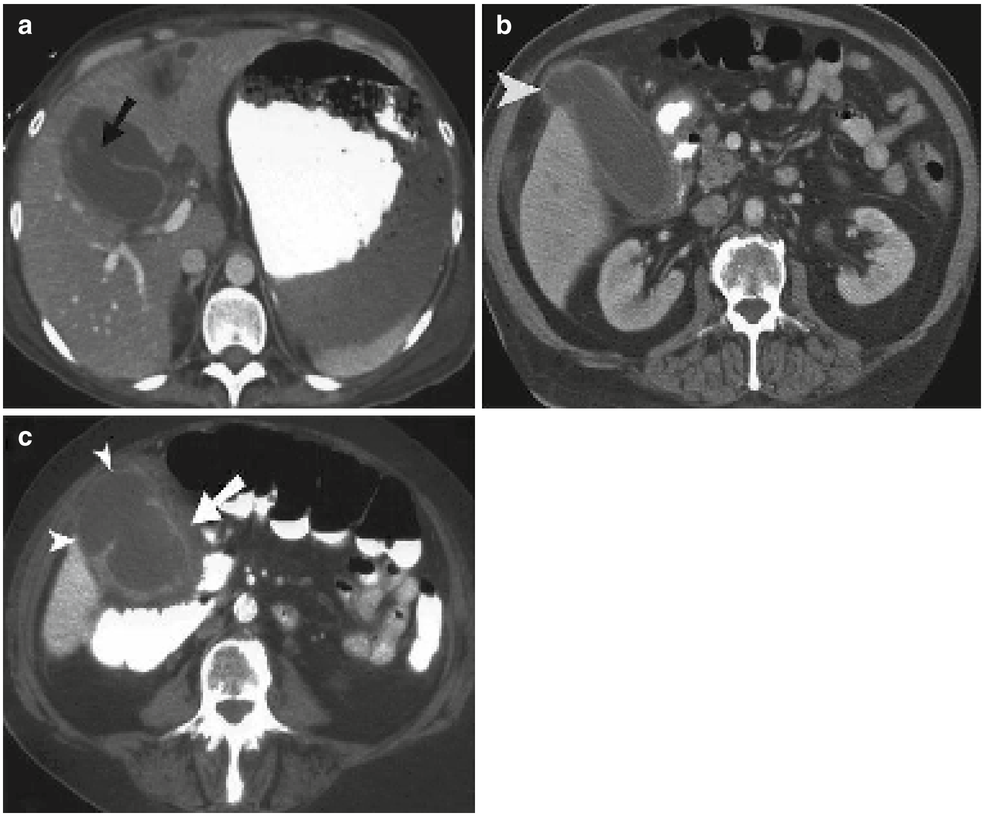

Fig. 2.13 Gallbladder perforation. (**a**) Axial contrast-enhanced CT image shows discontinuity of the gallbladder wall (*arrow*) and pericholecystic fluid. (**b**) Contrast-enhanced CT performed 3 months after cholecystostomy for acalculous cholecystitis shows CT findings of acute cholecystitis with focal perforation at the fundus (*arrowhead*). The fundal perforation was present at the site of entry of a previously placed cholecystostomy tube. (**c**) Contrast-enhanced CT demonstrates gallbladder wall perforation with intense pericholecystic inflammatory changes (*arrow*) and gallbladder wall edema. A contained perforation with bile collection (*arrowheads*) is seen anterior to the gallbladder

peritonitis. The CT findings of gallbladder perforation include gallbladder wall defect/bulge, streaky densities in the omentum or mesentery, pericholecystic fluid collection, and striated appearance of the gallbladder wall (Fig. 2.13).

The definitive treatment for gallbladder perforation is cholecystectomy (surgical or laparoscopic).

Gallbladder Torsion

It is characterized by acalculous cholecystitis and is most commonly seen in elderly women. A long or absent mesentery leading to abnormal mobility of the gallbladder predisposes to rotation of the gallbladder along its axis. If the torsion of gallbladder is partial (<180°), it leads to cystic duct obstruction. If the gallbladder torsion is complete (>180°), it leads to interruption of blood flow, leading to ischemia and gangrene.

Imaging findings may overlap with acute cholecystitis. On US, there is enlargement of the gallbladder which is abnormally oriented, with thickened wall and intramural or intraluminal gas due to gangrene [2]. On noncontrast CT, a V-shaped distortion of the extrahepatic bile duct and a twisted pedicle inferior to the liver may be observed. Contrast-enhanced CT may show poor enhancement of the gallbladder wall and twisting of the cystic artery with a whirl sign.

Biliary Ductal Obstruction

Jaundice secondary to biliary obstruction is associated with pain, nausea, and vomiting. CT is the first-line imaging modality whenever malignancy is suspected as the cause of biliary obstruction. The most sensitive noninvasive imaging test in diagnosing choledocholithiasis is MRCP (Fig. 2.14). Therefore, it is the first-line imaging modality whenever choledocholithiasis is suspected to be the cause of biliary obstruction. Ultrasound is less effective than CT or ERCP in determining the site or cause of biliary obstruction.

Although ERCP is more expensive than other modalities, it is the first-line procedure for symptomatic choledocholithiases. The complication as well as diagnostic success rate of ERCP is lower than PTC. In patients with suspected malignant biliary obstruction and negative CT, ERCP with endoscopic ultrasound can provide cytologic diagnosis. Since ERCP has a 3% complication rate and 0.4% mortality rate, the use of MRCP can decrease the use of indiscriminate ERCP. ERCP is preferred when there is high likelihood of finding choledocholithiases, which requires therapeutic

ALGrawany

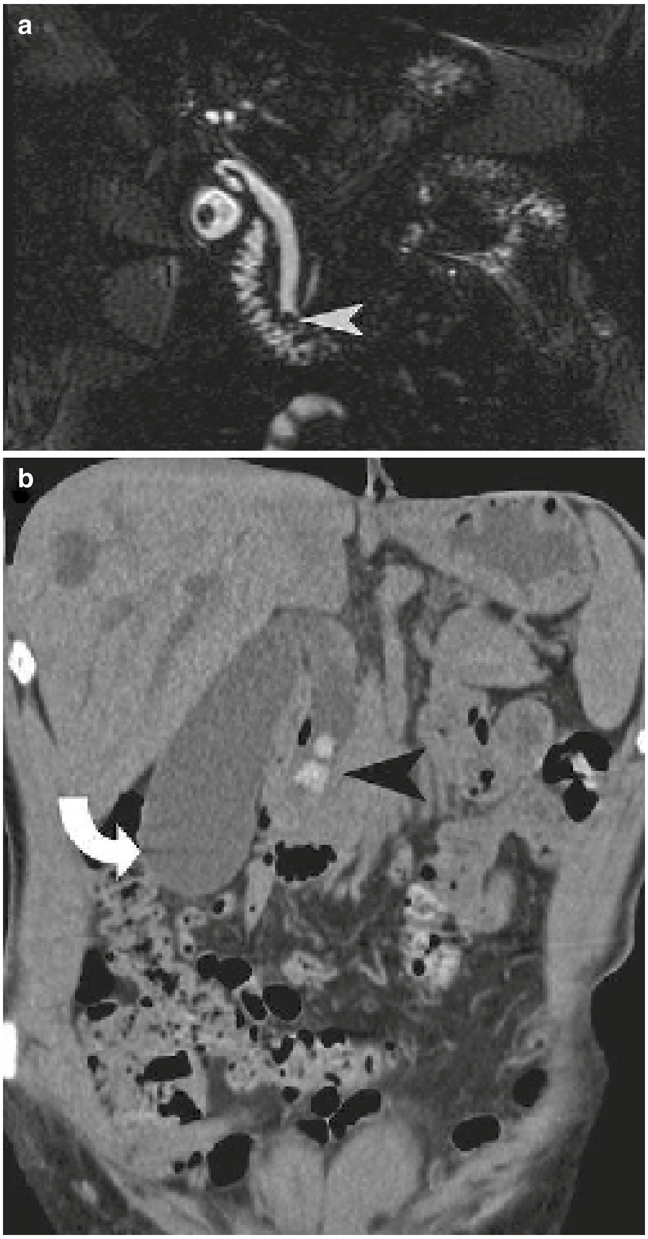

Fig. 2.14 Choledocholithiases. (**a**) MRCP shows dilatation of the CBD with choledocholithiases (*arrowhead*) at its lower end. (**b**) Coronal CT reformation shows two calculi (*arrowhead*) causing biliary obstruction at the lower end of the CBD. The gallbladder (*curved arrow*) is distended secondary to the biliary obstruction

interventions. Percutaneous transhepatic cholangiography is useful when the obstruction is present proximally in the biliary tree. In clinical practice, PTC is most commonly performed after failed ERCP.

Percutaneous biliary decompression by catheter provides the decompression of the bile duct enlargement in patients with unresectable pancreatic head neoplasm, multifocal biliary strictures, and diffuse ductal strictures [6].

Cholangitis

Bacterial cholangitis is secondary to bile stasis, biliary ductal obstruction, and increased biliary pressure, followed by colonization by bacteria. Besides choledocholithiases, other causes of cholangitis include malignancy, sclerosing cholangitis, and biliary instrumentation.

The causes of cholangitis include bacteria, parasites, and viruses (AIDS patients). The most common bacteria in patients without prior instrumentation are *Escherichia coli*, *Klebsiella pneumonia*, *Enterococcus faecalis*, and Streptococcus species. AIDS cholangiopathy is an acquired sclerosing cholangitis and is seen in patients where CD4 count is less than 100/mm^3. In posttransplant patients, bacteria (*Mycobacterium avium* complex), viruses (adenovirus, cytomegalovirus, and *Cryptosporidium parvum*), and fungi (Candida, Microsporidium) may be the cause of cholangitis [7, 8].

The classic clinical presentation (Charcot's triad) includes fever, pain, and jaundice. In immunocompromised patients, the symptoms are less typical than in immunocompetent patients.

Ultrasound is the first-line imaging tool in patients with suspected cholangitis and demonstrates biliary duct enlargement, biliary duct wall thickening, fluid collection, and abscess. On CT, the most common findings are biliary obstruction with diffuse and concentric thickening and increased enhancement of the bile duct wall. Arterial phase imaging shows nodular, patchy, wedge-shaped, or geographic inhomogeneous hepatic parenchymal enhancement. The MR findings include increased T2 signal intensity in a wedge-shaped configuration or in the parenchyma surrounding the infected biliary ducts. Wedge-shaped, peribiliary, or patchy contrast enhancement is seen most often in the arterial phase. Patchy hepatic enhancement and bulging as well as enhancing papilla are most often associated with pyogenic cholangitis. Biliary ductal wall enhancement is a common finding and best seen on delayed post-gadolinium T1-weighted images (Fig. 2.15).

The imaging findings in HIV patients are often similar to sclerosing cholangitis (Fig. 2.16). The imaging findings include intra- and extrahepatic biliary dilatation, saccular dilatations, biliary strictures, pruning, irregular thickening of the extrahepatic biliary tree wall, papillary stenosis, and cholecystitis [7].

The complications of bacterial cholangitis include sepsis, hepatic abscesses, portal vein thrombosis, biliary peritonitis, recurrent pyogenic cholangitis, sclerosing cholangitis, and suppurative cholangitis.

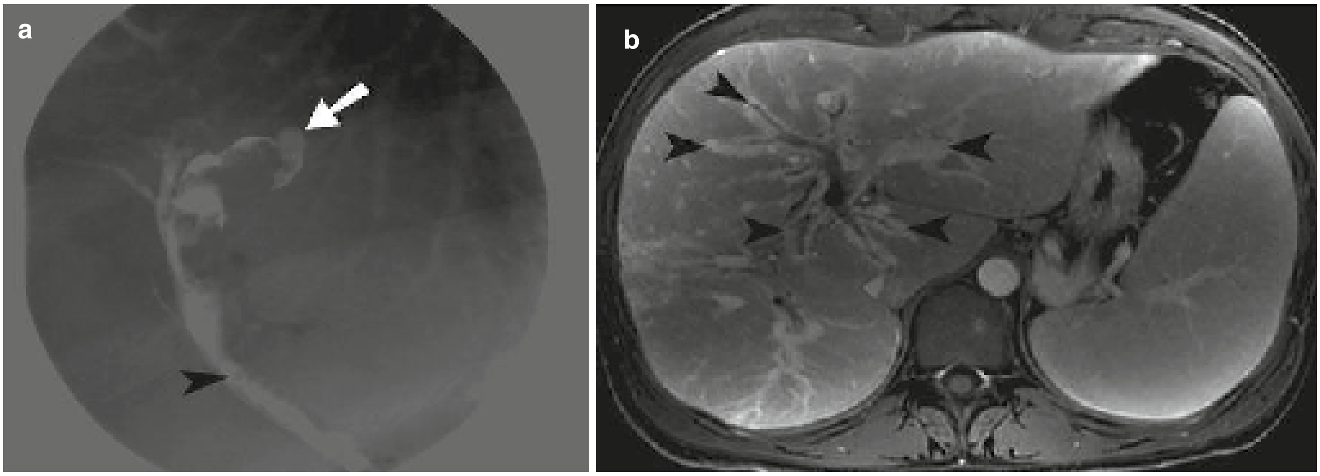

Fig. 2.15 Pyogenic cholangitis. (**a**) ERCP shows irregularity of the biliary ducts, choledocholithiases (*arrowhead*), intraductal debris, and intrahepatic abscess (*arrow*). (**b**) T1-weighted gadolinium-enhanced MR shows biliary ductal dilatation and intense enhancement (*arrowheads*) of the biliary ductal wall

Fig. 2.16 Other biliary pathologies, including sclerosing cholangitis and biliary necrosis. (**a**) Sclerosing cholangitis. ERCP shows multiple areas of biliary dilatation, strictures, and pruning in the right as well as the left hepatic ducts. (**b**) Sclerosing cholangitis. MRCP demonstrates multiple intrahepatic biliary ductal narrowing and dilatation. (**c**) Contrast-enhanced CT in a patient with hepatic artery occlusion after liver transplant demonstrates biliary necrosis. The biliary ducts (*arrowheads*) are dilated secondary to sloughed-off ductal walls

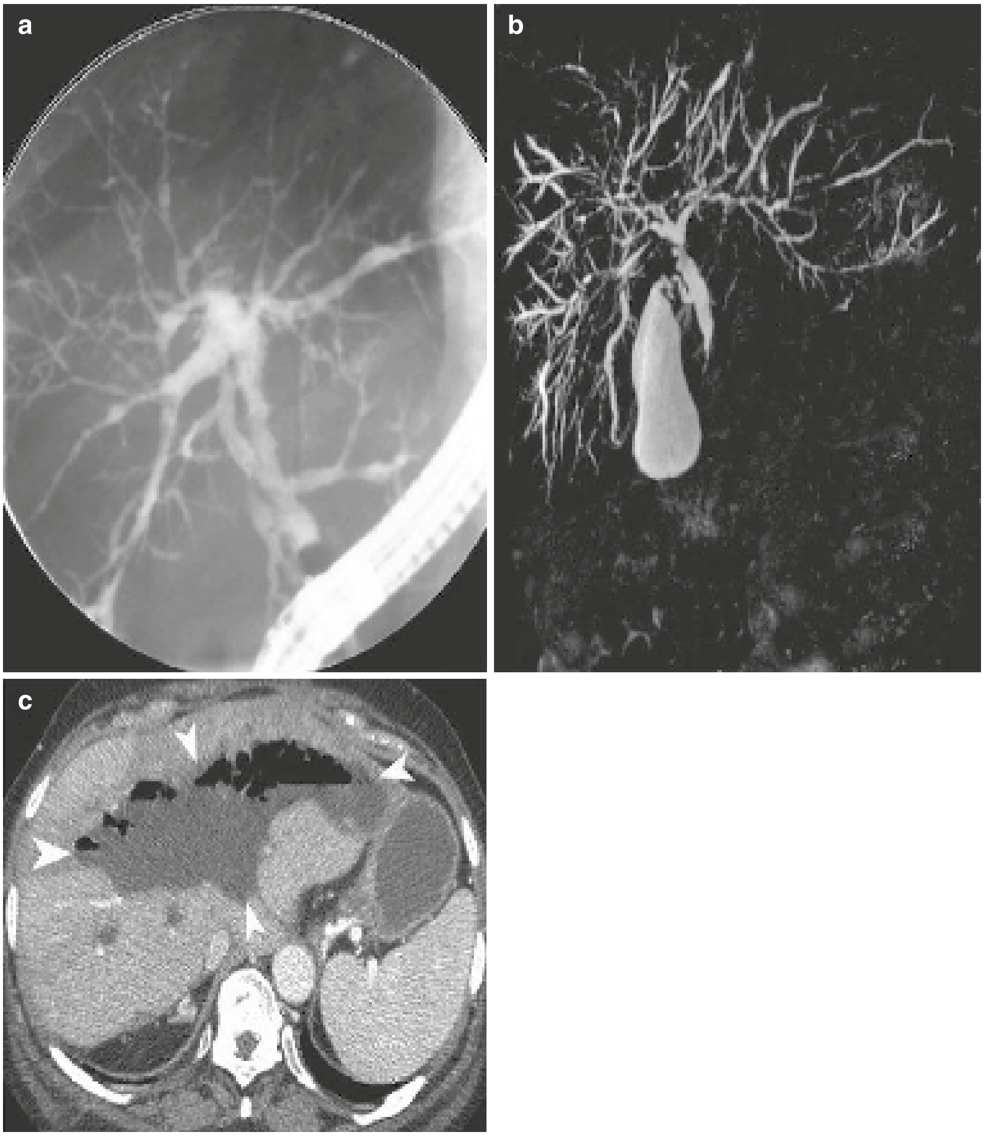

ALGrawany

Hemobilia

Hemobilia is characterized by upper gastrointestinal bleeding which originates in the biliary tree. Clinically, the classic presentation is known as Quincke's triad and is characterized by right upper quadrant pain, upper gastrointestinal bleeding, and jaundice.

The most common cause of hemobilia is blunt and penetrating abdominal trauma. The other causes include malignancy, rupture of an aneurysm, hemorrhagic cholecystitis, and blood dyscrasias (Fig. 2.17).

The imaging findings indicative of hemobilia include blood clots, appearing as filling defects in the gallbladder lumen and hemorrhagic bile, seen as altered density/signal intensity on unenhanced CT or MR imaging (increased signal on T1-weighted and decreased signal on T2-weighted images). The other findings include fluid-fluid level within the gallbladder, pseudoaneurysm, and extravasation of contrast on contrast-enhanced CT. The diagnosis can be confirmed on endoscopy or conventional angiography.

The management of hemobilia can be conservative (most common), intra-arterial embolization, or surgery.

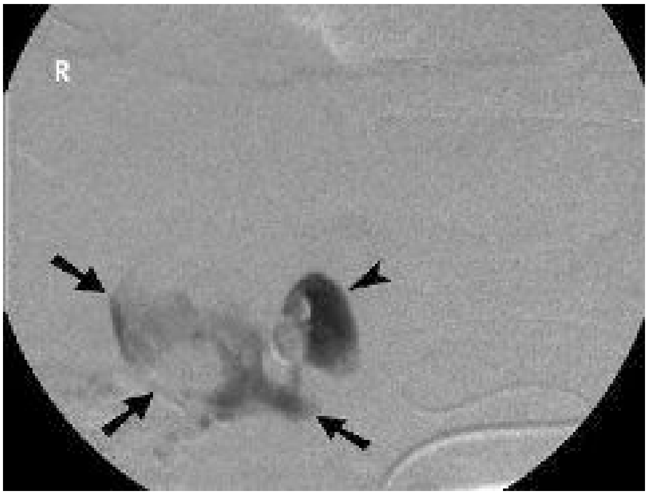

Fig. 2.17 Hemobilia. Conventional angiogram demonstrates a post-traumatic pseudoaneurysm (*arrowhead*) with active extravasation (*arrow*) of contrast. The pseudoaneurysm was subsequently embolized using endovascular coils

Gallstone Ileus

Gallstone ileus is the result of recurrent gallstone cholecystitis leading to a cholecystoenteric fistula formation. Gallstone ileus is most often seen in elderly females (70–75 years old; M:F 1:5) with history of gallstones [8, 9]. Although gallstone ileus overall accounts for less than 1% of small bowel obstructions, in elderly population it may account for up to 20% of the cases of small bowel obstruction [9, 10]. Less than half of the patients with gallstone ileus have a known history of gallbladder disease.

Since gallbladder is in anatomical contact with the duodenum and transverse colon, gallbladder perforation may create fistulous communication with these structures. The cholecystoduodenal fistula is the most common gallbladder fistula and allows passage of gallstone into the bowel. Although most stones will pass through the bowel without causing obstruction (85%), the larger stones may cause small bowel obstruction (15%) (Fig. 2.18). The most frequent site of small bowel obstruction is in the ileum because it represents the narrowest segment of the small bowel (Table 2.4). Gastric outlet or duodenal obstruction by a gallstone is rare and constitutes the Bouveret's syndrome [11].

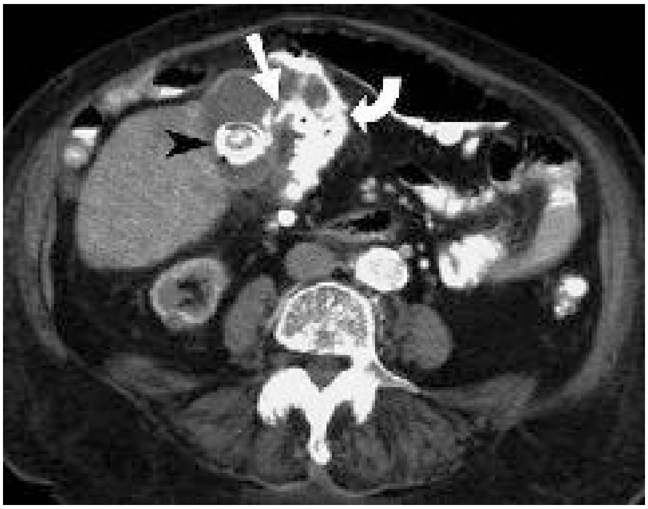

Fig. 2.18 Cholecystocolonic fistula. Axial contrast-enhanced CT image shows reflux of contrast (*straight arrow*) from the transverse colon (*curved arrow*) into the gallbladder lumen through the cholecystocolonic fistula. The gallbladder contains a gallstone (*arrowhead*) which is abutting the colonic contrast

Table 2.4 Sites of bowel obstruction in patients with gallstone ileus

1. Terminal ileum (60%)
2. Proximal ileum (30%)
3. Distal jejunum (5–10%)
4. Colon or rectum (2–4%)
5. Duodenum (1–3%)

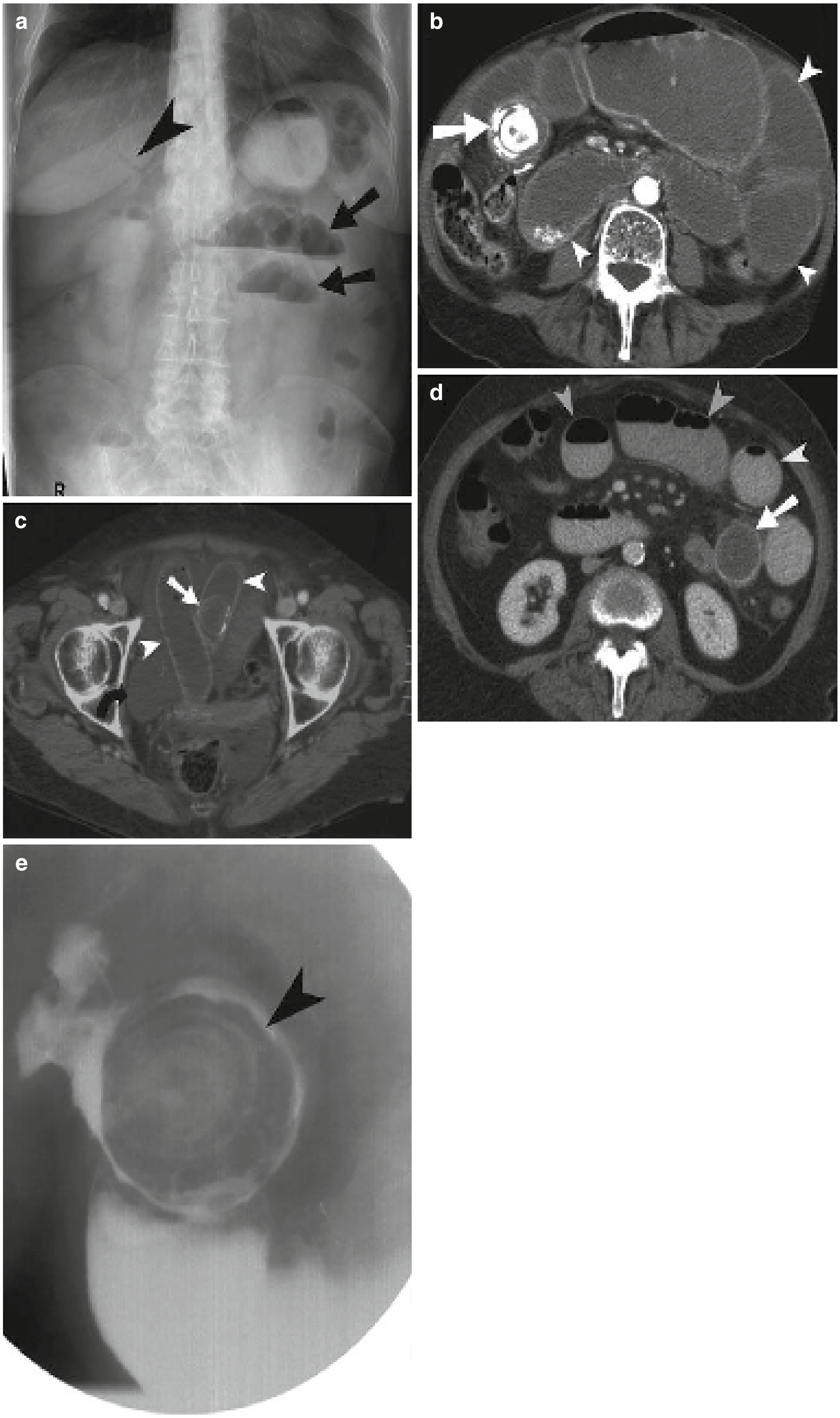

Fig. 2.19 Gallstone ileus. (**a**) Plain radiograph of a patient with gallstone ileus demonstrates pneumobilia (*arrowhead*) and multiple air-fluid levels in dilated small bowel loops (*arrows*). (**b**–**d**) Contrast-enhanced CT scan in three different patients with gallstone ileus demonstrates the obstructing gallstone (*arrows*) causing dilatation of small bowel loops (*arrowheads*). Free fluid (*curved arrow*) in the pelvis is identified in one of the patients. (**e**) Upper GI study in a patient with Bouveret's syndrome demonstrates a 6.8 cm gallstone (*arrowhead*) in the duodenal bulb with gastric outlet obstruction

A L G r a w a n y

The plain radiograph of patients with gallstone ileus may show pneumobilia (one-third of cases) and multiple air-fluid levels in small bowel loops (Fig. 2.19a). The presence of gas within the gallbladder is not always recognized on plain radiograph, and this contributes to the delay in diagnosis [12]. On ultrasound, it may be difficult to identify the gallbladder, because of the presence of air and gallbladder contraction (chronic inflammation). Ultrasound may also show bowel dilatation and rarely find the site of the bowel obstruction. However, CT better demonstrates all findings necessary to make the diagnosis. Contrast-enhanced CT in patients with gallstone ileus can show the Rigler's triad of distended small bowel loops, pneumobilia, and ectopic calcified gallstone (Fig. 2.19b–d). However, this triad may be seen in only 30–35% of patients. Cholecystoenteric fistula, which may be seen in patients without gallstone ileus, can show a contracted gallbladder containing air and associated fistulous tract.

Bouveret's syndrome (duodenal or pylorus obstruction) is an uncommon type of gallstone ileus most commonly seen in elderly women where the gallstone is lodged in the duodenum or stomach (Fig. 2.19e) [13]. Pneumobilia may be present in about 30–50% of patients with intestinal obstruction from gallstones [14]. The diagnosis of Bouveret's syndrome can be made by endoscopy (60%), upper GI series (45%), or abdominal radiograph (23%). The mortality rate is approximately 12% in recent years [13].

Intestinal obstruction in gallstone ileus typically occurs when stones larger than 2.5 cm migrate through the bowel [15]. It is recommended to obtain an early abdominal CT scan for the investigation of bowel obstruction in the elderly, as gallstone ileus is a disproportionately more common cause than in younger population [16].

Complications After Biliary Surgery

Each year, approximately 1.5 million of patients undergo cholecystectomy, and 80,000 patients undergo biliary tract surgery for various causes (obstructive jaundice or pancreaticobiliary disorders) in the USA. The complication rate of these surgeries is 14.3%, and mortality rate is 0.52% [17].

Intraperitoneal gallstone loss is not uncommon and can occur in up to 40% of cholecystectomies. Dropped gallstones can lead to abscess (perihepatic, pelvic, or abdominal wall) and biliary-enteric fistula formation (Fig. 2.20) [18].

On CT and ultrasonography, bilomas are invariably well demarcated, but most do not have an identifiable capsule (Fig. 2.21). Communication with ducts of Luschka (ducts that drain a portion of the right lobe of the liver) or cystic duct stump can lead to accumulation of bile in the subhepatic area after cholecystectomy (Fig. 2.22). Ducts of Luschka or subvesical ducts are small biliary ducts which originate from the right hepatic lobe and course along the gallbladder fossa bed. Injuries to the ducts of Luschka are the second most frequent cause of postcholecystectomy bile leaks.

Postcholecystectomy bilomas are usually well drained by image-guided percutaneous catheter placement. ERCP, PTC, and CT are the usual modalities in making the diagnosis of biliary leak. ERCP allows diagnosis as well as treatment (stenting and nasobiliary drainage) of patients with postcholecystectomy bile leak.

The other complications after cholecystectomy include biliary perforation, biliary stricture, retained surgical sponge, biliary peritonitis, and hemorrhage (Fig. 2.23).

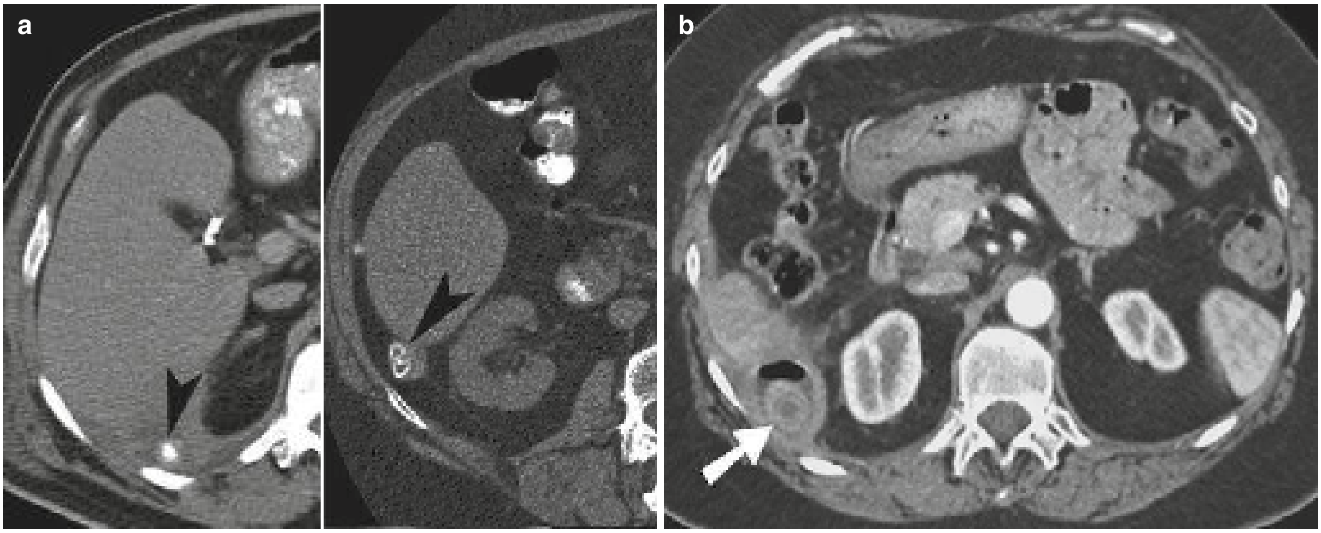

Fig. 2.20 Dropped gallstones. (**a**) Contrast-enhanced CT demonstrates dropped gallstones (*arrowheads*) incidentally detected adjacent to the caudal edge of the liver in two patients with remote history of cholecystectomy. (**b**) Contrast-enhanced CT demonstrates an abscess developing around a dropped gallstone (*arrow*) in the Morrison's pouch, in a patient where the gallstone was lost during laparoscopic cholecystectomy

Fig. 2.21 Postcholecystectomy bile leaks. (**a**) Percutaneous transhepatic cholangiogram demonstrates leakage of contrast from the cystic duct stump in a patient with recent cholecystectomy and dehiscence of cystic duct stump. (**b**, **c**) Cholescintigraphy demonstrates accumulation of radiotracer outside the biliary system, into the peritoneal cavity (*arrowheads*). (**d**) Coronal CT reformation demonstrates biloma (*arrowheads*) in the right subhepatic location

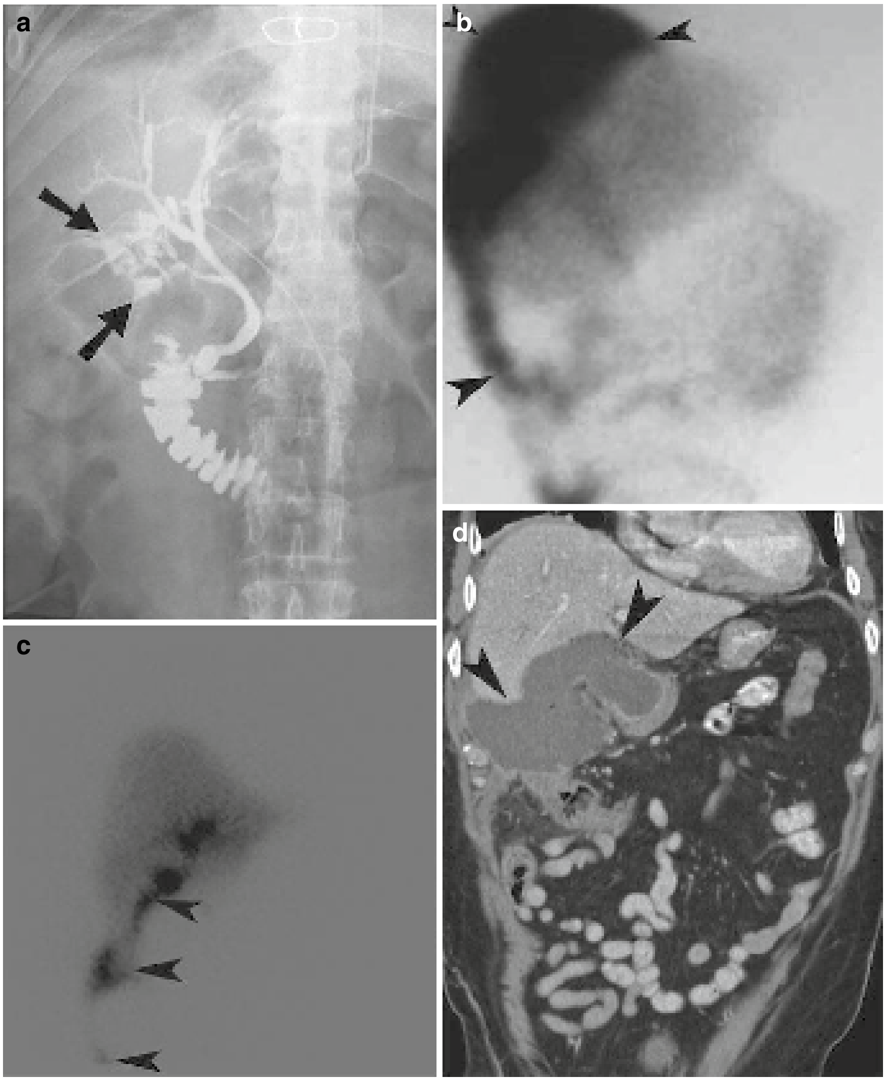

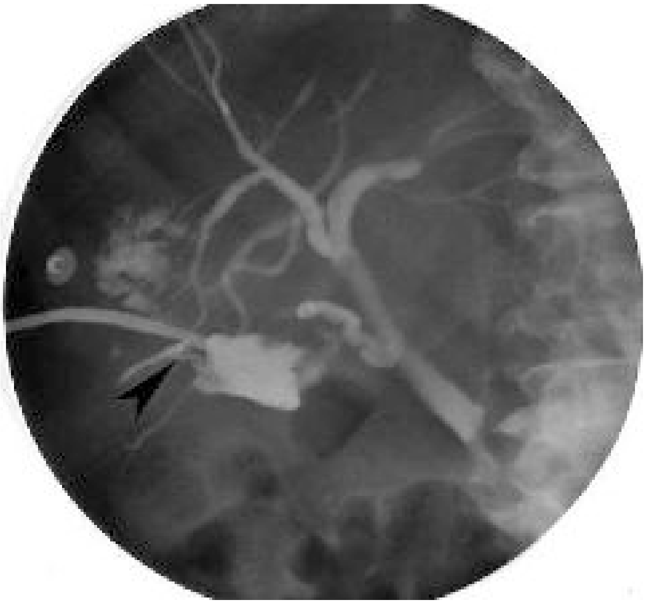

Fig. 2.22 Postcholecystectomy biloma communicating with ducts of Luschka. Pigtail catheter injection after image-guided pigtail catheter drainage of a biloma demonstrates communication of the biloma with ducts of Luschka (*arrowhead*)

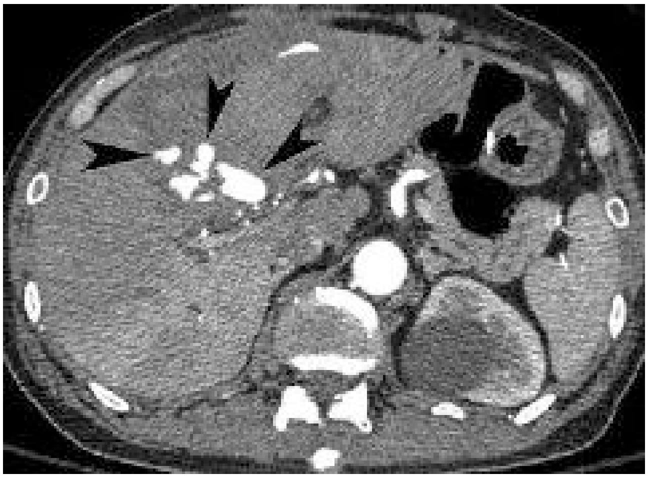

Fig. 2.23 Postcholecystectomy hemorrhage. Postcholecystectomy CT angiogram of the abdomen demonstrates active extravasation of contrast (*arrowheads*) into the gallbladder fossa

Role of MRI in Emergent Biliary Pathologies

For suspected biliary pathologies, ultrasound is the imaging modality of choice. Second-line imaging modalities include contrast-enhanced CT of the abdomen, MRI abdomen with MRCP, and cholescintigraphy which are utilized in cases of nondiagnostic US findings. MRI offers higher soft tissue resolution, non-utilization of ionizing radiation, and shorter scan times with newer techniques. MRCP is now considered first-line modality for evaluation of choledocholithiasis, unexplained biliary duct dilation, and in identification of site and cause of biliary obstruction. For biliary duct pathologies, MRCP offers sensitivity of 97–99% and specificity of 95–99%.

MRCP utilizes heavily T2-weighted images, providing increased duct-to-background contrast due to enhanced signal of slow-moving fluid in biliary system and pancreatic ducts. Commonly utilized protocols involve acquisition of a fast spin echo sequence, 2D/3D MRCP sequences, and fat-suppressed gradient echo T1 sequence. 2D MRCP utilizes breath-hold SSFSE/HASTE sequences which obtains thicker slides but are associated with less motion artifacts. 3D MRCP utilizes respiratory-triggering FSE sequences which produces thin contiguous slides. 3D technique is associated with higher acquisition time and more motion artifacts but provides high spatial resolution and signal-to-noise ratio and enables multiplanar reconstruction [19].

The typical findings of choledocholithiaisis on MRCP include calculi as hypointense rounded filling defects (Fig. 2.24) within the hyperintense bile duct. T1-weighted images can differentiate the stone type with bilirubin stones producing high-signal intensity and cholesterol stones producing low-signal intensity. MRCP is also the preferred modality for diagnosis of Mirizzi syndrome and can demonstrate stone within the gallbladder neck or cystic duct, dilated intrahepatic ducts and common bile duct proximal to the level of obstruction, and inflamed gallbladder wall. In acute cholecystitis, common MRI findings include gallbladder distension, gallbladder wall thickening, T2 hyperintense pericholecystic fluid collection, thickened gallbladder wall, and wall hyperenhancement (Fig. 2.25). Absent or irregular, heterogeneous wall enhancement is an important clue, indicating gangrenous cholecystitis [20, 21].

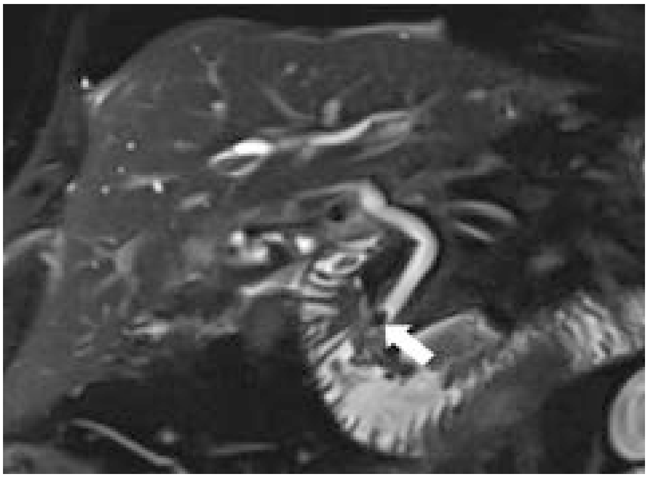

Fig. 2.24 Choledocholithiasis on MRCP. 3D MRCP image demonstrates dilated biliary duct with a 9 mm filling defect (arrow) at the lower end of the common bile duct

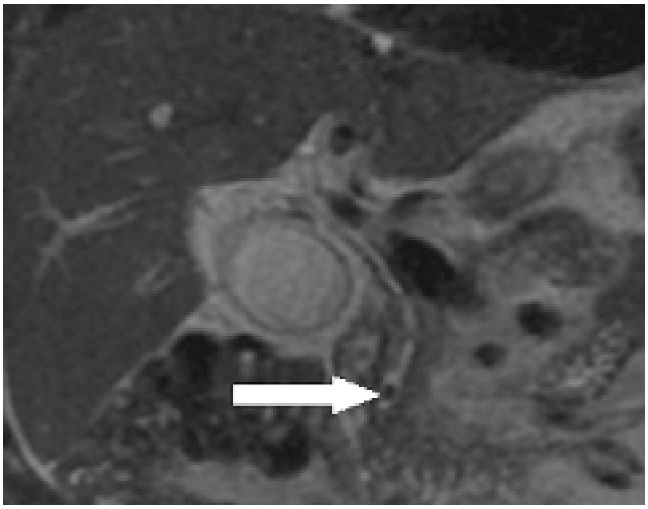

Fig. 2.25 Choledocholithiasis with acute cholecystitis on MRI. Coronal SSFSE—WI demonstrates a 7 mm filling defect (arrow) at the lower end of the common bile duct consistent with choledocholithiasis. There is gallbladder wall thickening with pericholecystic fluid collection

Teaching Points

- The ultrasound findings of acute cholecystitis include gallbladder wall thickening, gallbladder distension, pericholecystic fluid, and positive Murphy's sign.
- The findings of acute cholecystitis on cholescintigraphy include nonvisualization of the gallbladder 30 min after morphine injection and presence of a curvilinear area of increased radiotracer activity in the liver (with gangrenous cholecystitis) adjacent to the gallbladder.
- Mirizzi syndrome or choledocholithiases should be suspected whenever there is elevated bilirubin level along with clinical symptoms of acute cholecystitis.
- Gallbladder empyema is manifested as gallbladder distension, wall thickening, pericholecystic fluid accumulation, intraluminal sludge/pus, and intraluminal air.
- Gangrenous cholecystitis is characterized by increased intraluminal pressure, gallbladder distension, gallbladder wall necrosis, intramural hemorrhage, and abscess formation.
- Emphysematous cholecystitis is characterized by gas within the gallbladder wall and/or lumen.
- ERCP is the first-line procedure for symptomatic choledocholithiases.
- Ultrasound in patients with cholangitis demonstrates biliary duct dilatation, wall thickening, fluid collection, and abscess.

Questions

1. What is the maximum caliber of common bile duct in a normal 72-year-old man?
   (A) 5 mm
   (B) 6 mm
   (C) 7 mm
   (D) 8 mm
   Answer: D

2. Striated gallbladder wall thickening and intraluminal membranes in a febrile patient with positive Murphy's sign indicates which of the following?
   (A) Acute cholecystitis
   (B) Mirizzi syndrome
   (C) Emphysematous cholecystitis
   (D) Gangrenous cholecystitis
   Answer: D

3. Quincke's triad includes which of the following?
   (A) Right upper quadrant pain
   (B) Upper gastrointestinal bleeding
   (C) Jaundice
   (D) All of the above
   Answer: D

4. What is a common site of bowel obstruction in patients with Bouveret's syndrome?
   (A) Jejunum
   (B) Ileum
   (C) Rectum
   (D) Duodenum
   Answer: D

5. Saccular dilatations, strictures, and pruning are imaging findings in which of the following?
   (A) HIV cholangitis
   (B) Mirizzi syndrome
   (C) Gangrenous cholecystitis
   (D) Bacterial cholangitis
   Answer: A

6. What is the pathology depicted on the CT (Fig. 2.26) in a patient with nausea and vomiting?
   (A) Gallstone ileus
   (B) Acute cholecystitis
   (C) Gangrenous cholecystitis
   (D) Mirizzi syndrome
   Answer: A

7. T2-weighted MRI (Fig. 2.27) in a patient with right upper quadrant pain shows which of the following?
   (A) Gallbladder carcinoma
   (B) Acute cholecystitis
   (C) Gallbladder torsion
   (D) Emphysematous cholecystitis
   Answer: B

8. What is the pathology depicted on the CT (Fig. 2.28) in a diabetic patient with fever and right upper quadrant pain?
   (A) Acute cholecystitis
   (B) Gangrenous cholecystitis
   (C) Emphysematous cholecystitis
   (D) Mirizzi syndrome
   Answer: C

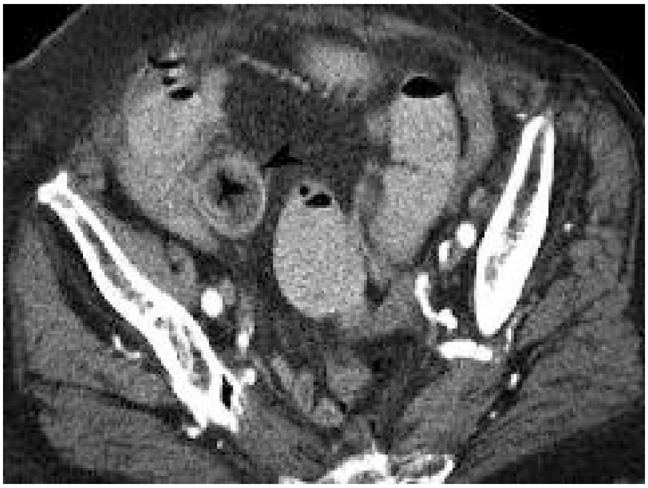

Fig. 2.26 CT—gallstone ileus

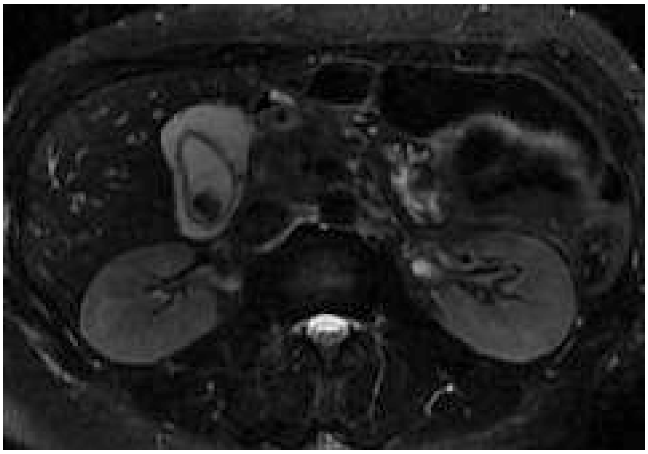

Fig. 2.27 MRI—acute cholecystitis

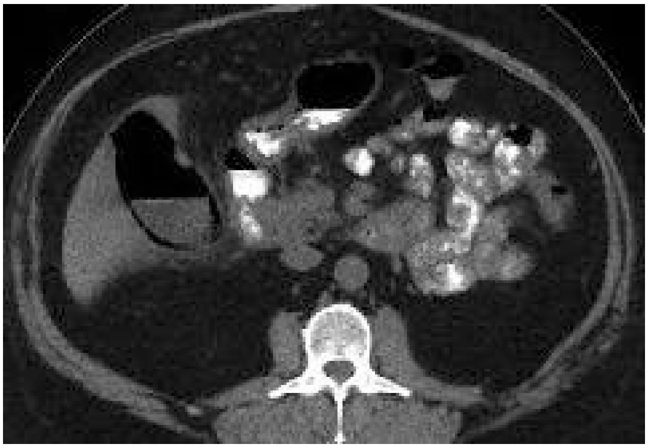

Fig. 2.28 CT—emphysematous cholecystitis

References

1. Watanabe Y, Nagayama M, Okumura A, Amoh Y, Katsube T, Suga T, et al. MR imaging of acute biliary disorders. Radiographics. 2007;27:477–95.
2. Hanbidge AE, Buckler PM, O'Malley ME, Wilson SR. From the RSNA refresher courses: imaging evaluation for acute pain in the right upper quadrant. Radiographics. 2004;24:1117–35.
3. Bortoff GA, Chen MYM, Ott DJ, Wolfman NT, Routh WD. Gallbladder stones: imaging and intervention. Radiographics. 2000;20:751–66.
4. Leopold GR. The acute abdomen: ultrasonography. Radiographics. 1985;5:273–83.
5. Teefey SA, Baron RL, Bigler SA. Sonography of the gallbladder: significance of striated (layered) thickening of the gallbladder wall. AJR Am J Roentgenol. 1991;156:945–7.
6. May GP, James EM, Bender CE, Williams HJ Jr, Adson MA. Diagnosis and treatment of jaundice. Radiographics. 1986;6:847–90.
7. Catalano OA, Sahani DV, Forcione DG, Czermak B, Liu CH, Soricelli A, et al. Biliary infections: spectrum of imaging findings and management. Radiographics. 2009;29:2059–80.
8. Murthy GD. Bouveret's syndrome. Am J Gastroenterol. 1995;90(4):638–9.
9. Delabrousse E, Bartholomot B, Sohm O, Wallerand H, Kastler B. Gallstone ileus: CT findings. Eur Radiol. 2000;10(6):938–40.
10. Madrid A. Image of the month-diagnosis. Gallstone ileus. Arch Surg. 2003;138(7):808.
11. Tuney D, Cimsit C. Bouveret's syndrome: CT findings. Eur Radiol. 2000;10(11):1711–2.
12. Swift SE, Spencer JA. Gallstone ileus: CT findings. Clin Radiol. 1998;53(6):451–4.
13. Frattaroli FM, Reggio D, Guadalaxara A, Illomei G, Lomanto D, Pappalardo G. Bouveret's syndrome: case report and review of the literature. Hepato-Gastroenterology. 1997;44(16):1019–22.
14. Herbener TE, Basile V, Nakamoto D, Butler HE, Pickering SP. Abdominal case of the day. Bouveret's syndrome. AJR Am J Roentgenol. 1997;169:252–3.
15. Romano DR, Gonzalez EM, Romero CJ, Selas PR, Diaz MM, et al. Duodenal obstruction by gallstones (Bouveret's syndrome). Presentation of a new case and literature review. Hepato-Gastroenterology. 1997;44:1351–5.
16. Coulier B, Coppens JP, Broze B. Computed tomographic diagnosis of biliary ileus. J Belg Radiol. 1998;81(2):75–8.
17. Ghahremani GG, Crampton AR, Bernstein JR, Caprini JA. Iatrogenic biliary tract complications: radiologic features and clinical significance. Radiographics. 1991;11:441–56.
18. McDonald MP, Munson JL, Sanders L, Tsao J, Buyske J. Consequences of lost gallstone. Surg Endosc. 1997;11(7):774–7.
19. Eason JB, Taylor AJ, Yu J. MRI in the workup of biliary tract filling defects. J Magn Reson Imaging. 2013;37(5):1020–34. https://doi.org/10.1002/jmri.23847.
20. Chang H, Bates DDB, Gupta A, LeBedis CA. Use of MR in pancreaticobiliary emergencies. Magn Reson Imaging Clin N Am. 2022;30(3):479–99. https://doi.org/10.1016/j.mric.2022.04.009.
21. Bidani K, Singh R, Chandra G, Rai R, Singh AK. Magnetic resonance imaging in gastrointestinal and genitourinary emergencies. Magn Reson Imaging Clin N Am. 2022;30(3):501–13. https://doi.org/10.1016/j.mric.2022.03.005.

Acute Appendicitis

3

Ajay Singh, Mohammad Mansouri, Benjamin M. Yeh,
and Robert A. Novelline

Normal Anatomy

The appendix, also known as the vermiform process or processus vermiformis, is a long (2–20 cm), narrow, tubular diverticulum, which starts from the apex of the cecum and extends posteromedially (Figs. 3.1 and 3.2). The appendix is most commonly retrocecal (58%), pelvic (22%), or paracecal (12%) [1].

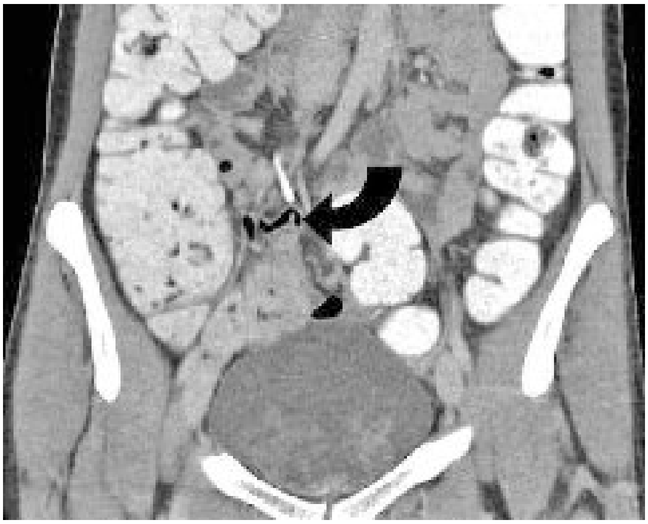

Fig. 3.1 Normal anatomy of the appendix on barium enema and CT. Coronal CT reformation of the abdomen demonstrates normal air-filled appendix (*curved arrow*) medial to the cecum. Normal appendiceal caliber is less than 7 mm

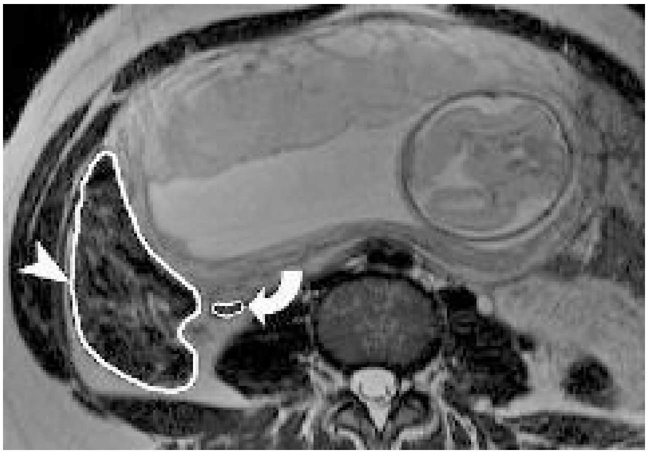

Fig. 3.2 Normal anatomy of appendix on MR imaging. Axial FSE T2-weighted sequence shows normal appendix (*arrow*) medial to the cecum (*arrowhead*). The normal appendix is low to intermediate signal intensity on T2-WI and is located between 2 and 6 o'clock position in relation to the cecum

A. Singh (✉)
Division of Emergency Radiology, Department of Radiology,
Massachusetts General Hospital, Boston, MA, USA

Harvard Medical School, Massachusetts General Hospital,
Boston, MA, USA
e-mail: asingh1@partners.org

M. Mansouri · R. A. Novelline
Department of Radiology, Massachusetts General Hospital,
Boston, MA, USA

B. M. Yeh
Department of Radiology, University of California, San Francisco,
San Francisco, CA, USA

© The Author(s), under exclusive license to Springer Nature Switzerland AG 2024
A. Singh (ed.), *Emergency Radiology*, https://doi.org/10.1007/978-3-031-65770-2_3

Pathophysiology

Appendicitis is most often due to luminal obstruction followed by bacterial invasion. Appendiceal obstruction can be caused by an appendicolith, foreign body, strictures, lymphoid hyperplasia, or rarely parasitic infections (Figs. 3.3 and 3.4). If obstruction persists, the intraluminal pressure in the appendix may rise above that of the veins, leading to venous obstruction and appendiceal wall ischemia.

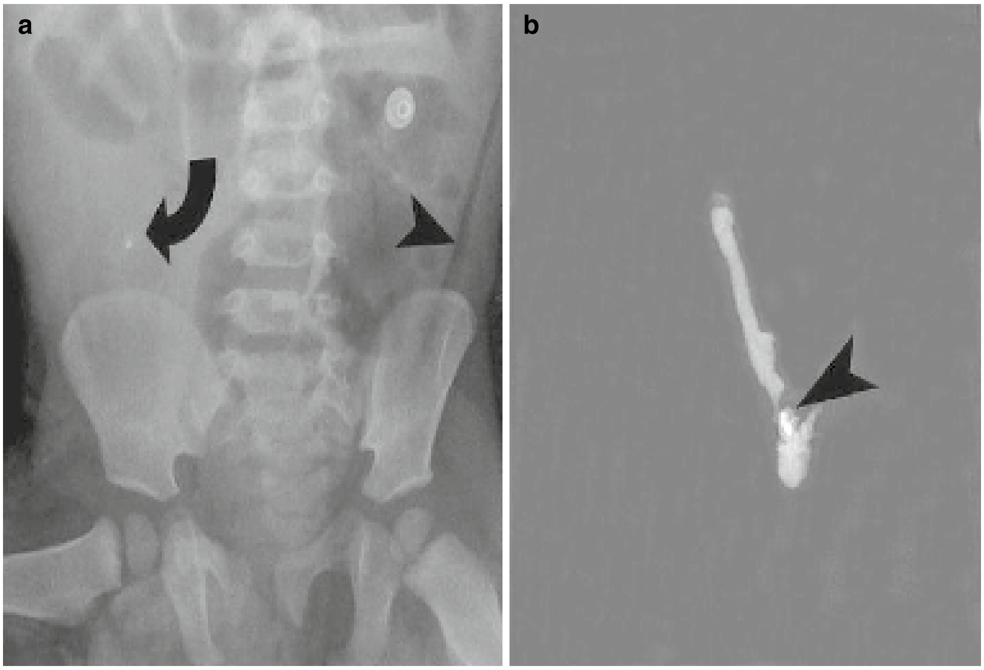

Fig. 3.3 Plain radiographic findings of acute appendicitis. (**a**) Plain X-ray of the abdomen demonstrates a small appendicolith (*curved arrow*) in the right abdomen. The properitoneal fat pad on the right is obliterated by appendiceal inflammation. The properitoneal fat pad (*arrowhead*) on the left side is well preserved. The air-containing bowel loops are displaced away from the right lower quadrant. There are changes of paralytic ileus. (**b**) Plain radiograph of the surgical specimen demonstrates an appendicolith (*arrowhead*) at the base of the appendix

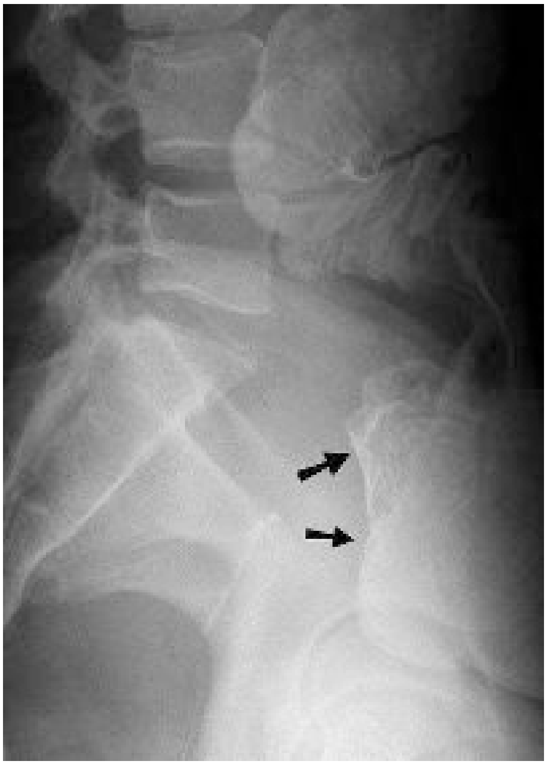

Fig. 3.4 Barium enema of acute appendicitis. Barium enema demonstrates mass effect (*arrows*) on the posterior wall of the cecum, due to inflamed retrocecal appendix

Pathological Stages of Appendicitis: Three Stages

1. Acute catarrhal appendicitis: There is early scant neutrophilic infiltrates without perforation. The inflammation of the appendix can spontaneously regress or progress to the second stage.
2. Purulent (phlegmonous) stage: Neutrophilic infiltrate, ulceration, and necrosis are seen. Spontaneous regression is rare, and there is progression to appendiceal perforation.
3. Gangrenous stage: Necrosis, ulceration, gangrene, and peritoneal inflammation are seen without the possibility of spontaneous regression.

Current Status of US, CT, and MR

- Currently, the majority of patients with clinically suspected appendicitis undergo intravenous contrast-enhanced CT with or without oral or rectal contrast before the surgery.
- Ultrasound is considered the imaging modality of choice for pediatric and pregnant patients when appendicitis is suspected.
- MR is reserved for pregnant patients when US is nondiagnostic or equivocal.

Since the first publications on the utility of CT for appendicitis in the late 1990s, there has been dramatic increase in the use of CT to evaluate right lower quadrant pain. Rao et al. found that CT performed in patients who present with suspected appendicitis improves patient care and reduces the use of hospital cost by resources $447 per patient by avoiding negative laparotomy (Table 3.1) and showed the rate of negative laparotomy decreased from 20% before to 7% after the introduction of CT [4, 5].

Table 3.1 Advantages and disadvantages of US and CT

Ultrasound	CT
1. Relatively inexpensive (technical cost = $50.28)	1. Higher cost (technical cost = $112.32) [2]
2. Wide availability	2. More restricted availability
3. Can better evaluate pelvic disease in females	3. Better identifies normal appendix (>85% in adult and 69% in children), phlegmon, and abscess [3]
4. No ionizing radiation (preferred in children and pregnancy)	4. Ionizing radiation (10 mSv)
5. Lower sensitivity compared to CT (sensitivity 75–90%)	5. More accurate for appendicitis (sensitivity 90–100%)
6. Operator dependence and technically inadequate studies due to gas	6. No operator dependence

Based on ACR appropriateness criteria, in women of childbearing age and also elderly patients with right lower quadrant pain, the threshold of imaging should be lower due to lower accuracy of clinical diagnosis. CT scan in these groups is highly accurate in diagnosing acute appendicitis and its complications.

CT Protocol

- IV contrast: 370 mg/100 cm^3 at 3.5 mL/s, followed by scanning after 150 s delay.
- 120 kV; 150 mA; slice thickness—2.5 mm.
- Targeted CT may be used with scanning from L3 to the symphysis pubis.
- Reformation (3 mm) in sagittal and coronal planes. The use of coronal reformations improves the confidence of the radiologist in visualizing the appendix and making the diagnosis of acute appendicitis [6].
- Oral (2% barium suspension) vs. rectal (1 L 3% barium suspension). The use of oral or rectal contrast is considered appropriate by ACR appropriateness criteria in the evaluation of right lower quadrant pain.

The usage of rectal as opposed to oral contrast offers the advantage of reducing the time between ordering of the scan by the physician and the time when it is performed. There is also higher likelihood of opacifying cecum and appendix with contrast. The disadvantages of rectal contrast include increased patient discomfort and the theoretical risk of rupturing the appendix from increased intraluminal pressure in the cecum. In the adult population, the appendix is seen in more than 85% cases, while in children the visualization rate is lower (69%) because of the paucity of intra-abdominal fat.

Imaging Findings on CT

1. *Appendiceal caliber*: 7 mm or more in width. This criterion alone does not have high positive predictive value because up to 42% of normal population can have an appendiceal caliber of more than 7 mm.
2. *Appendiceal wall thickness of more than 3 mm.*
3. *Appendiceal mural enhancement, homogeneous, or stratified appearance of the appendiceal wall* (Fig. 3.5).
4. *Lack of intraluminal contrast in the appendix.*
5. *Periappendiceal inflammation.*
6. *Appendicoliths* (Fig. 3.6): It is seen in 10% cases on plain radiograph and 30% on CT study. The detection of an isolated appendicolith on CT is not sufficiently specific to be the sole basis for the diagnosis of acute appendicitis [7]. The use of bone window setting can increase the detection rate of appendicolith [8].

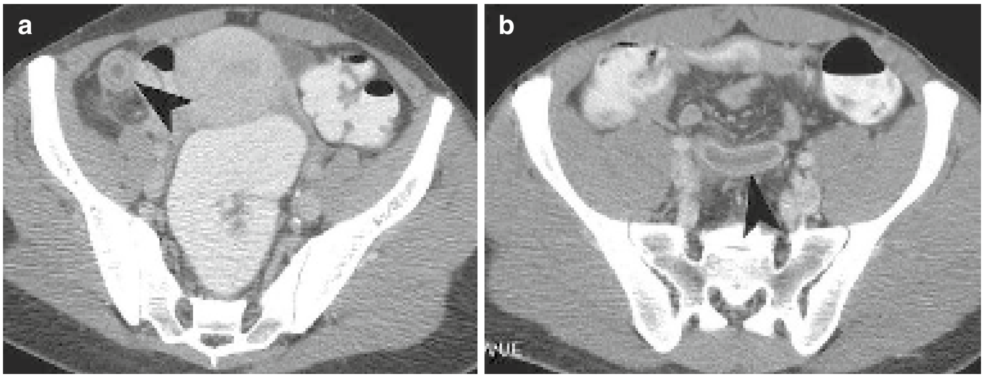

Fig. 3.5 Appendiceal wall changes in acute appendicitis. (**a**, **b**) Contrast-enhanced CT in a patient with acute appendicitis shows stratified appendiceal wall thickening (*arrowhead*). The inner hyperdense ring indicates mucosal enhancement, while the outer hyperdense ring indicates serosal enhancement

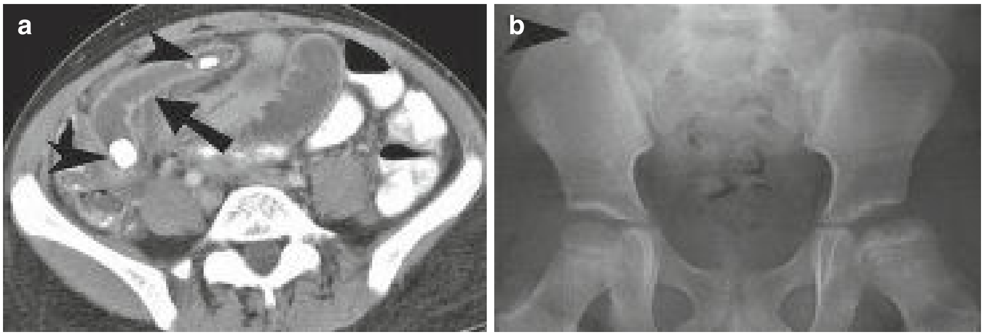

Fig. 3.6 Appendicoliths on CT and plain radiography. (**a**) Axial contrast-enhanced CT demonstrates grossly dilated appendix (*straight arrow*), containing multiple appendicoliths (*arrowheads*). The adjacent pelvic small bowel shows changes of ileus. (**b**) Plain radiograph of the abdomen demonstrates laminated appendicolith (*arrowhead*) in the right lower quadrant. Appendicoliths are seen in 10% cases of appendicitis on plain X-ray of the abdomen

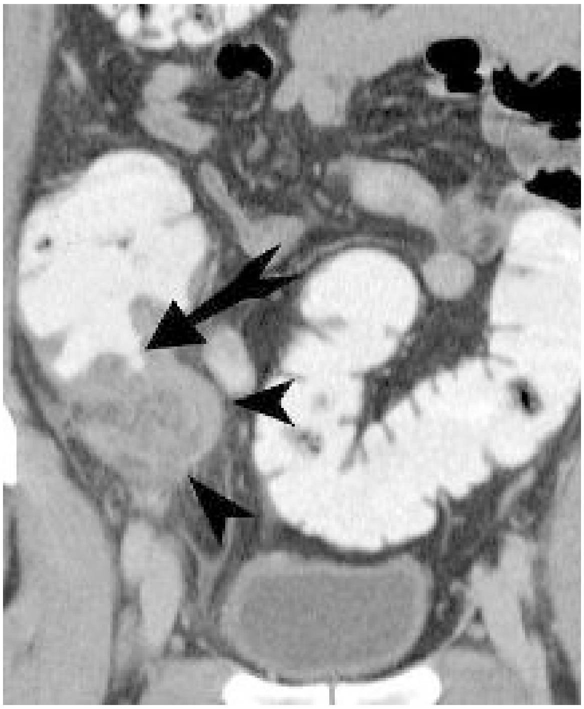

Fig. 3.7 Arrowhead sign. Contrast-enhanced CT demonstrates funneling (*straight arrow*) of contrast in the cecum with the tip pointing toward the base of the inflamed appendix (*arrowheads*) in an *arrowhead* configuration. The presence of the arrowhead sign indicates extension of inflammation from the base of the appendix into the cecal wall

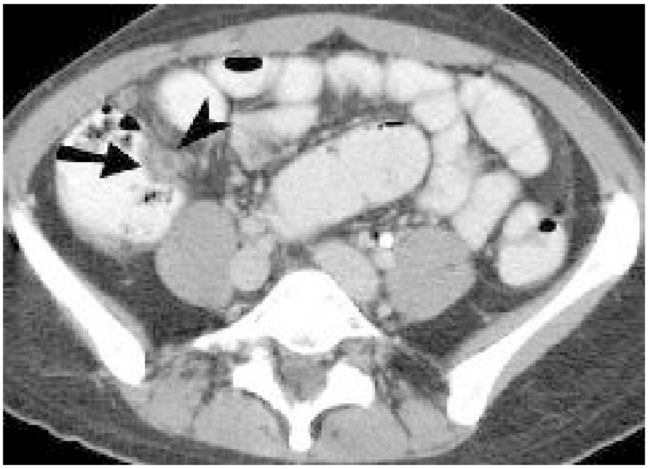

Fig. 3.8 Cecal bar sign. Contrast-enhanced CT demonstrates plaque-like thickening of the cecal wall (*straight arrow*) adjacent to the base of the inflamed appendix (*arrowhead*)

7. *Arrowhead sign*: Arrow-shaped configuration of the cecum due to funneling of intraluminal contrast into the spastic cecum (Fig. 3.7). It is an indicator of extension of inflammation from the appendix to the cecum.
8. *Cecal bar sign*: It is characterized by edema and bar-like thickening of the cecum at the base of the appendix (Fig. 3.8).

9. *Hyperdense appendix*: Hyperdense appendix is seen as high-attenuation appendix on noncontrast CT and is seen in 33% of patients with acute appendicitis [9].
10. *Maximum depth of intraluminal appendiceal fluid of more than 2.6 mm*: This can be useful in diagnosis of appendicitis when no periappendiceal inflammation is present [10].

Complications

Appendiceal perforation, abscess, and sepsis are the dreaded complications of acute appendicitis. The frequency of appendiceal perforation is 20–25%, with the highest frequency in the very young and old (40–70%). The extension of inflammation outside the appendix can lead to the formation of phlegmon and abscess. The inflammatory adhesions from appendicitis can lead to small bowel obstruction. Acute appendicitis should be in the differential diagnosis whenever there is small bowel obstruction in a patient who has no history of abdominal surgery.

The five specific CT findings of perforated appendicitis are as follows [11] (Figs. 3.9, 3.10, and 3.11):

1. Extraluminal air
2. Extraluminal appendicolith
3. Abscess
4. Phlegmon
5. Defect in the enhancing appendiceal wall (sensitivity, 64%)

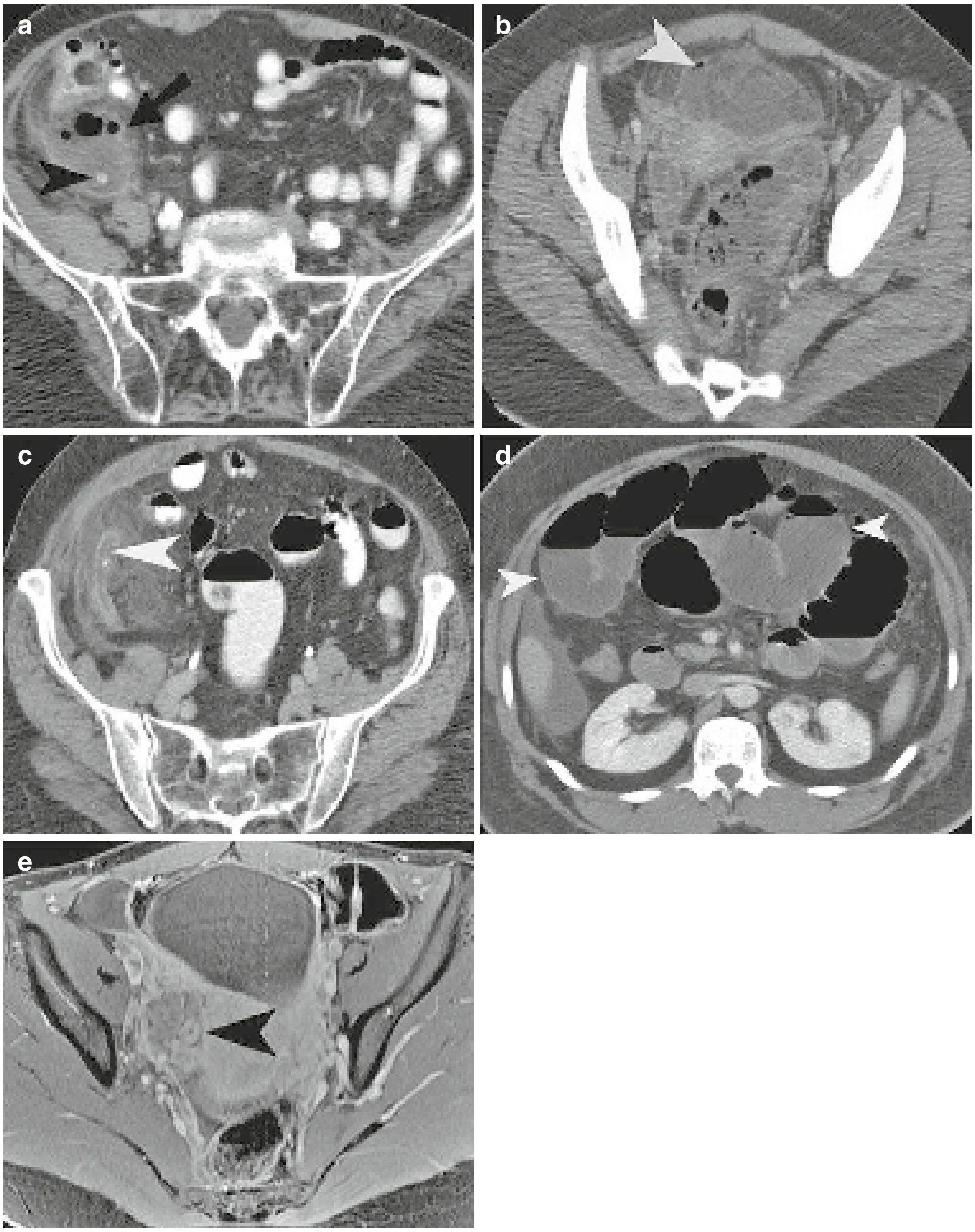

Fig. 3.9 Perforated appendicitis. (**a**) Contrast-enhanced CT demonstrates abscess (*straight arrow*) formation in the right lower quadrant from perforated appendicitis. There is an appendicolith (*arrowhead*) measuring 7 mm in diameter seen within the abscess cavity. (**b**) Contrast-enhanced CT demonstrates appendiceal perforation by the presence of tiny foci of extraluminal air (*arrowhead*) in the anterior pelvis. There is extensive inflammation present in the intraperitoneal fat. (**c**) Contrast-enhanced CT demonstrates appendiceal perforation by discontinuity of the appendiceal wall (*arrowhead*) on the medial aspect. There is tiny appendicolith seen in the appendix with surrounding inflammation seen in the right lower quadrant. (**d**) Contrast-enhanced CT demonstrates dilated small bowel loops (*arrowheads*) in a patient with small bowel obstruction caused secondary to acute appendicitis. (**e**) Gadolinium-enhanced T1-WI demonstrates a thickened appendiceal wall (*arrowhead*) to the right side of the uterus with surrounding inflammatory phlegmon

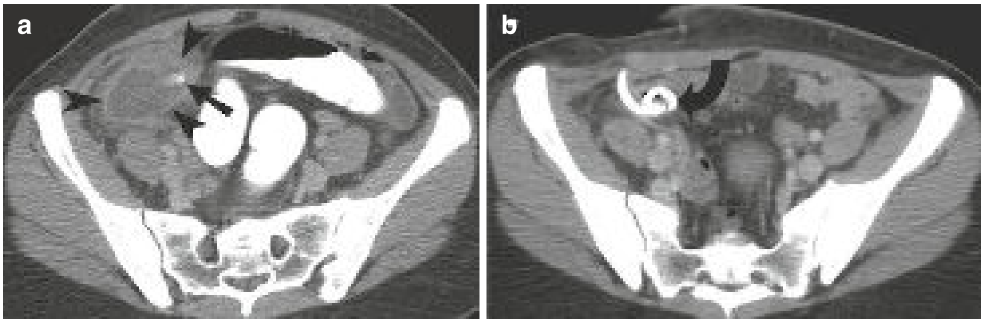

Fig. 3.10 Perforated appendicitis with abscess. (**a**) Contrast-enhanced CT scan study of the pelvis demonstrates 5-cm-diameter abscess (*arrowheads*) in the right lower quadrant, containing an appendicolith (*straight arrow*). (**b**) Axial CT image demonstrates a 10-French Dawson-Mueller pigtail drainage catheter (*curved arrow*) placed into the abscess cavity using trocar technique. Note the complete resolution of the abscess cavity following aspiration through the catheter

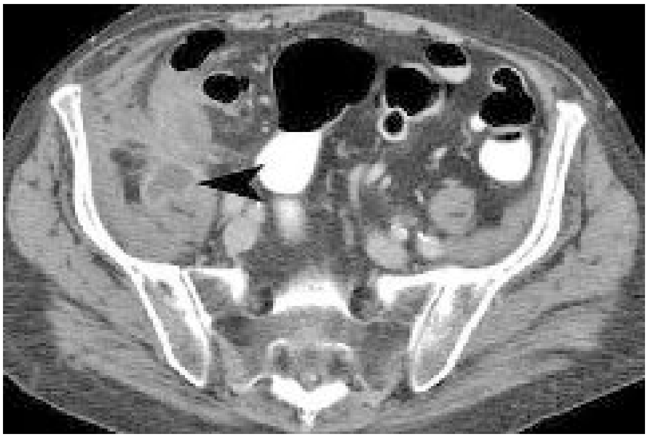

Fig. 3.11 Perforated appendicitis with psoas abscess. Contrast-enhanced CT shows ring-enhancing abscess (*arrowhead*) in the right psoas muscle, secondary to perforated appendicitis. Inflammatory phlegmon is seen in the right lower quadrant, anterior to the right psoas muscle

Ultrasound Imaging

Graded-compression ultrasound with curvilinear probes is often performed with a 3.5-MHz transducer in larger patients and 5 MHz in thinner patients. Graded-compression ultrasound is performed in the transverse plane from the tip of liver to the pelvic brim, followed by scanning in sagittal and oblique planes. The ultrasound scanning uses uniform pressure to displace gas-filled bowel from the field of view. The normal appendix can be usually seen in the majority of children but in only a minority (<10%) of adults. The presence of appendiceal perforation, leading to decompression and collapse of the appendiceal lumen, is believed to decrease the sensitivity of ultrasound in diagnosing acute appendicitis. In general, the sensitivity of ultrasound (74.2%) in the diagnosis of acute appendicitis is lower than the sensitivity reported with CT (100) [12]. In meta-analysis of head-to-head comparison studies performed between 1966 and 2006, the sensitivities of CT and graded-compression ultrasound studies were 91% and 78%, respectively [13].

Ultrasound Findings of Acute Appendicitis

1. Noncompressible and aperistaltic blind-ending tubular structure (Fig. 3.12).
2. Appendiceal caliber >6 mm between outer borders of tunica muscularis.
3. Appendicolith, indicated by clean distal acoustic shadowing.
4. Inflamed fat causes “echogenic mass effect.”
5. Periappendiceal fluid collection.
6. Reactive lymph node enlargement.
7. Increased blood flow in appendiceal wall, compared to normal gut on color Doppler ultrasound (Fig. 3.12c, d).

Table 3.2 presents a summary of imaging findings in appendicitis.

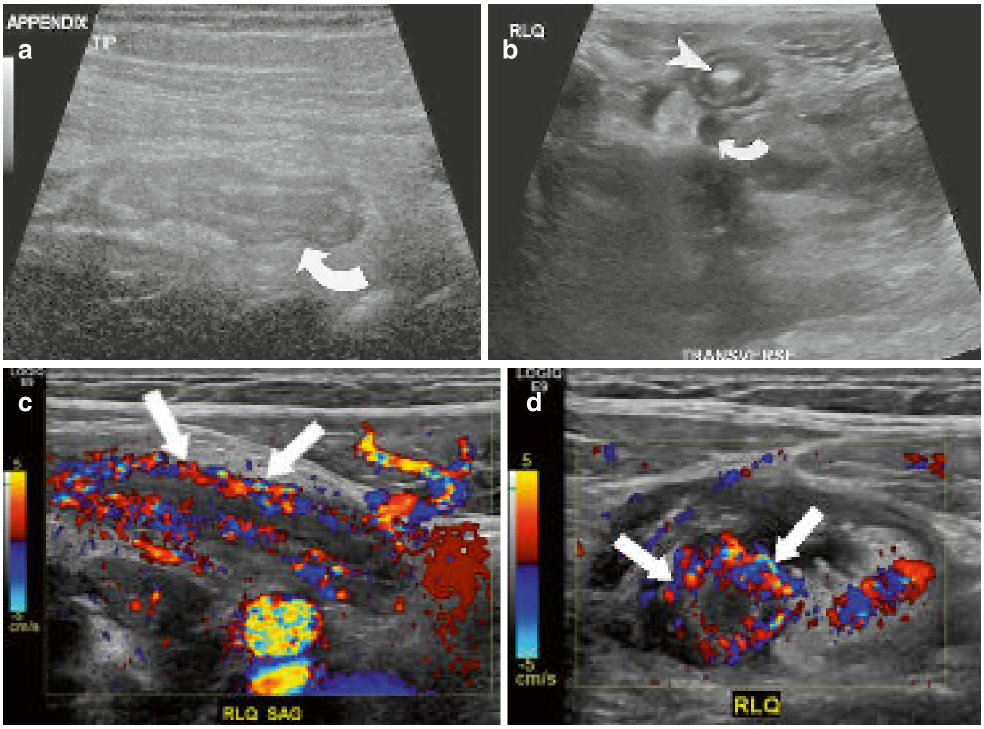

Fig. 3.12 Acute appendicitis on ultrasound imaging. (**a**) Graded-compression ultrasound image demonstrating blind-ending tubular structure measuring 12 mm in diameter with thickened wall, consistent with acute appendicitis. (**b**) Perforated appendicitis. A noncompressible tubular structure is seen in the right lower quadrant with an appendicolith (*arrowhead*). Free fluid (*curved arrows*) is seen around the inflamed appendix. Acute appendicitis on color Doppler US. Color Doppler ultrasound of the appendix on transverse (**c**) and longitudinal (**d**) planes demonstrates increased blood flow in the wall (arrows) of the dilated appendix

Table 3.2 Summary of imaging findings in appendicitis

CT	Ultrasound
Appendiceal caliber ≥7 mm	Appendiceal caliber >6 mm (between outer borders of tunica muscularis)
Lack of intraluminal contrast	Noncompressible
Hyperdense appendix	Echogenic mass effect
Appendicolith	Appendicolith
Mural enhancement (homogeneous/stratified)	Increased blood flow in appendiceal wall
Periappendiceal inflammation	Aperistaltic blind-ending tubular structure
Appendiceal wall thickness >3 mm	
Cecal bar sign Arrowhead sign	
Maximum depth of intraluminal appendiceal fluid >2.6 mm	

Variants of Acute Appendicitis

Tip appendicitis (Fig. 3.13) is characterized by the presence of inflammation of the appendiceal tip with normal appendiceal base. The proximal appendix is collapsed or filled with air/contrast [14]. Since the base of the appendix is not involved by the inflammation, there is no cecal bar sign or arrowhead sign. If the entire appendix is not demonstrated, the sensitivity to diagnose this condition may be reduced on ultrasound evaluation.

Stump appendicitis (Fig. 3.14) refers to acute appendicitis involving post-appendectomy stump. This is a rare condition with less than 40 cases reported in the world literature. It has been reported after laparoscopic as well as open appendectomy and is due to luminal obstruction of the appendiceal stump left behind after open or laparoscopic appendectomy. The CT findings include inflammatory changes around appendiceal stump.

Acute appendicitis can occur in unusual locations and has been described in the hernia sac, the left side of abdomen, and even the thorax (Fig. 3.15). The presence of inflamed appendix in inguinal hernia sac is known as Amyand's hernia (Fig. 3.16), a pathology named after Claudius Amyand, a French physician who performed the first appendectomy surgery in a patient with ruptured appendix located in right inguinal hernial. Spontaneous resolution of acute appendicitis with conservative management has been shown to be associated with high frequency of recurrence in 38% cases.

CT demonstrates a dilated and inflamed appendix (arrow) located in right inguinal hernia.

Acute Appendicitis in Pregnancy

Acute appendicitis is the most common cause of acute abdominal pain in pregnancy. The frequency of acute appendicitis in pregnancy is 1:800–1500. The accuracy of diagnosis of acute appendicitis based on clinical examination is lower in pregnant patients because of the presence of non-

Fig. 3.13 Tip appendicitis. Contrast-enhanced axial CT scan study of the pelvis demonstrates normal caliber of the appendix near the base (*arrowhead*) (**a**). There is inflammation of the appendiceal tip (*curved arrow*) on the second image (**b**)

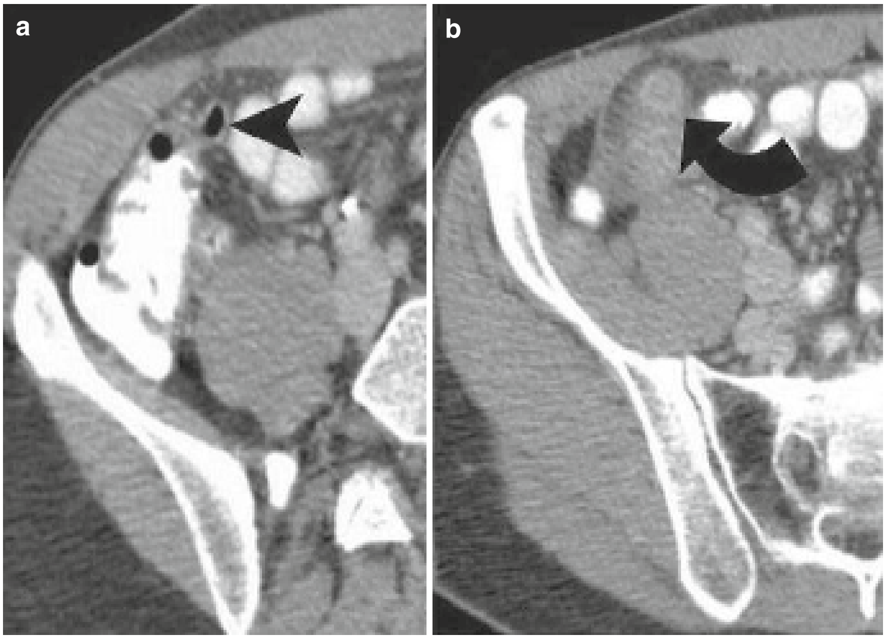

Fig. 3.14 Stump appendicitis. Contrast-enhanced axial CT scan study of the pelvis demonstrates an inflamed appendiceal stump (*curved arrow*) located posteromedial to the cecum

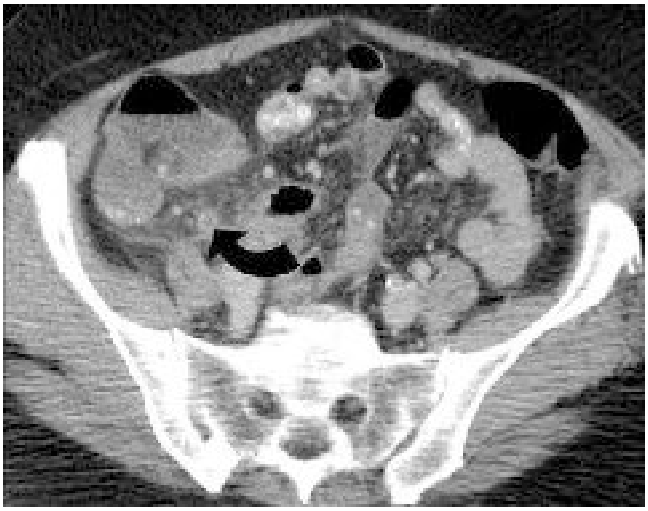

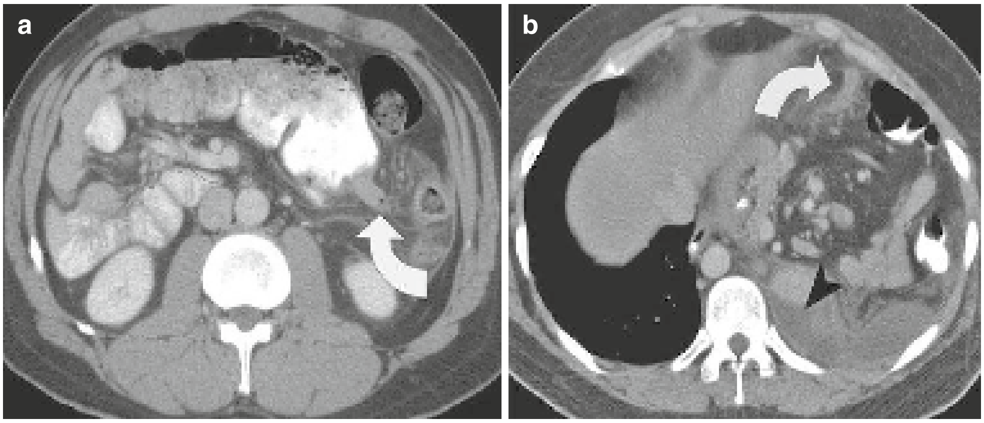

Fig. 3.15 Unusual positions of the inflamed appendix. (**a**) Contrast-enhanced CT demonstrates an inflamed left-sided appendix (*curved arrow*) in a patient with malrotation of the bowel. Note the abnormal relationship between the SMA and SMV (*oval*). (**b**) Contrast-enhanced CT shows intrathoracic location of inflamed appendix (*curved arrow*), in a patient with left diaphragmatic hernia. There is left subphrenic abscess (*arrowhead*) which required open appendectomy

specific symptoms and cranial displacement of the appendix as well as omentum by the gravid uterus (Fig. 3.17a). Leukocytosis, which is present in 80% of acute appendicitis cases in the nonpregnant population, can be physiologically present during pregnancy, thereby reducing its usefulness.

The first-line imaging modality to diagnose acute appendicitis is graded-compression ultrasound. Findings include a noncompressible, blind-ended tubular structure in right lower quadrant with a maximum diameter greater than 6 mm. If ultrasound is nondiagnostic or equivocal, then noncontrast MR is indicated. Because of ionizing radiation issues, contrast-enhanced CT is considered less appropriate than ultrasound or MR in the evaluation of appendicitis. Modifying the CT protocol to only include the lower abdomen can reduce the fetal radiation dose to 3 mGy.

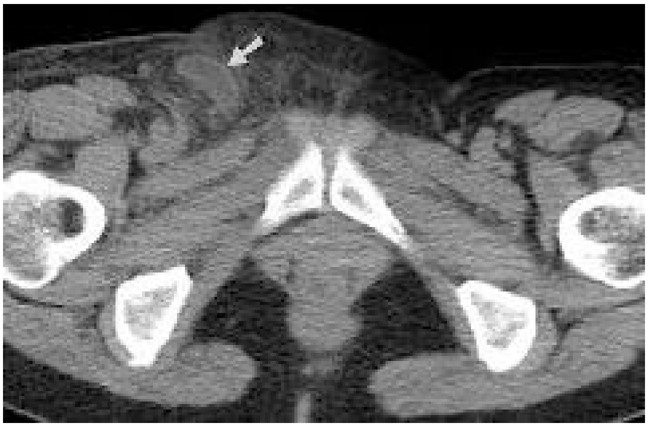

Fig. 3.16 Amyand's hernia

MR Imaging

MR is the imaging modality of choice in pregnant patients when ultrasound is nondiagnostic or equivocal. We use a four-sequence protocol, which includes T2 single-shot fast spin echo (SS-FSE), T2 FSE, short tau inversion recovery, pre-gadolinium T1, and post-gadolinium T1 sequences [15]. Three-plane SS-FSE used to localize the appendix, followed by STIR and FSE T2-weighted sequences. STIR is poor at identifying the normal appendix but excellent for identifying early edema and inflammation. STIR has high sensitivities in identifying pathologies with high T1 and T2 relaxation times.

Intravenous gadolinium-based contrast material is used only if the patient is not pregnant because gadolinium is classified as class C drug and is known to cause teratogenic effects in animals. The appendix is visualized on MR in

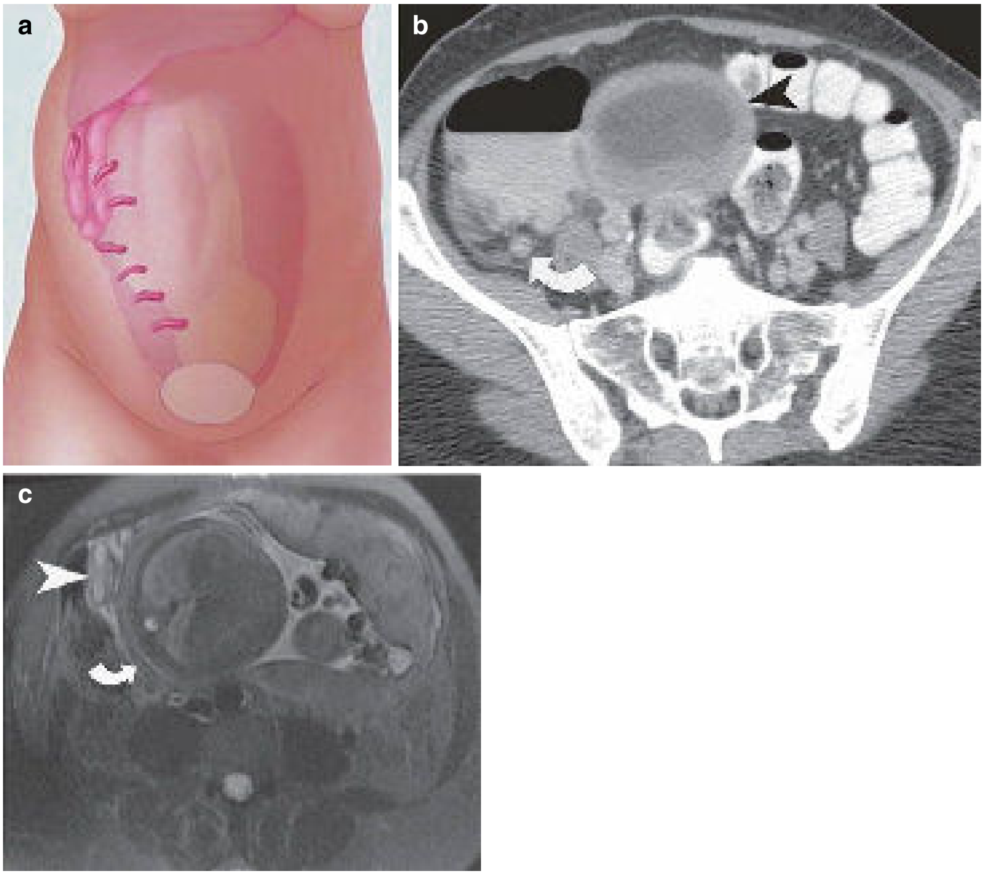

Fig. 3.17 Acute appendicitis and pregnancy. (**a**) Schematic diagram demonstrating the variable position of the appendix during pregnancy. The appendix moves out of the right lower quadrant, as the pregnancy progresses to the second trimester. (**b**) Contrast-enhanced CT demonstrates an enlarged uterus (*arrowhead*), containing gestational sac. The inflamed appendix (*curved arrow*) is present in the right lower quadrant with surrounding inflammation. (**c**) Axial T2 FSE sequence demonstrates a distended fluid-containing appendix (*arrowhead*) with surrounding free fluid. Note the right midabdominal position of the appendix, secondary to the third trimester uterus (*curved arrow*)

70–100% of patients, as opposed to 90–100% cases on CT. The sensitivity of MR for acute appendicitis is reported to be 75–100% [15–23]. Per published data, combined T2-weighted imaging and diffusion-weighted imaging yields higher accuracy in making the diagnosis of acute appendicitis.

Normal appendiceal lumen contains gas or stool which causes appendix to appear as a hypointense tubular structure on both T1- and T2-weighted imaging. The MR findings of acute appendicitis include dilated appendix, periappendiceal inflammation, appendiceal wall thickening, and intense enhancement of the appendix (Fig. 3.17b, c). The wall of the acutely inflamed appendix appears hyperintense on T2-weighted images and diffusion-weighted images (Fig. 3.18a, b), and hypointense on T1-weighted images. Appendicolith appears hypointense on both T1- and T2-weighted images.

MRI is also valuable in assessing complications of MRI including abscess formation, perforation, bowel obstruction, and peritonitis. Perforation is characterized by T2 hyperintense collection of larger volume of fluid around the appendix with or without visualization of focal discontinuity of the appendiceal wall. Extraluminal air or appendicolith, if visualized, also indicates perforation. Abscess is seen as contained T2 hyperintense collection with restricted diffusion and enhancing wall. Peritonitis, a dreaded complication, demonstrates peritoneal thickening, peritoneal enhancement, and T2-hyperintense fluid between bowel loops. Embolization of mesenteric vessels and formation of hepatic abscess are other potential complications.

The differential diagnosis of appendicitis on MR includes mucocele of the appendix, a condition caused the chronic accumulation of secretions in the appendiceal lumen, most commonly seen in patients with mucosal hyperplasia, mucinous cystadenoma, or cystadenocarcinoma of the appendix (Fig. 3.19). Dilatation of the appendix to more than 1.3 cm and presence of wall calcifications favor the diagnosis of mucocele. Figure 3.20 describes the imaging algorithm for acute appendicitis in pregnancy.

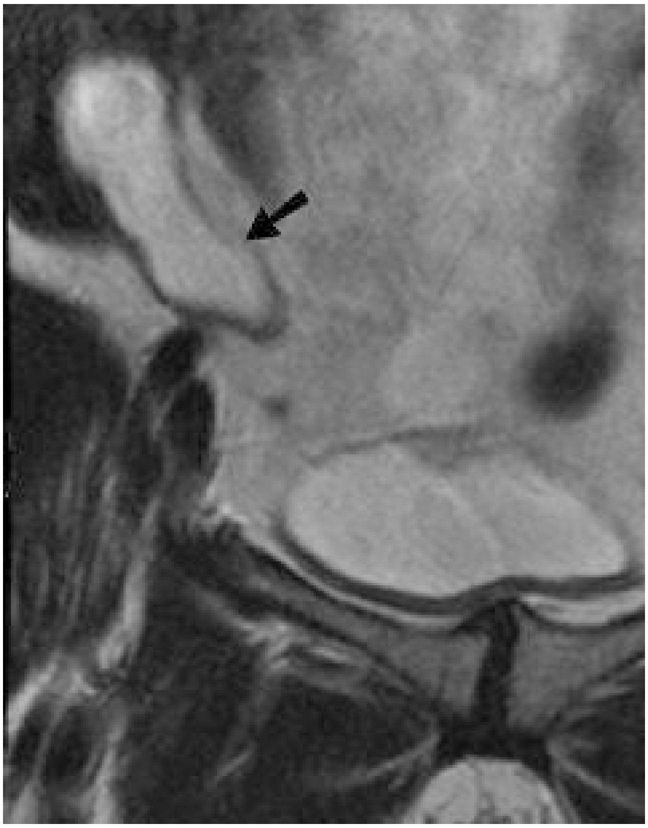

Fig. 3.19 Mucocele of appendix. MR T2-weighted coronal sequence demonstrates hyperintense tubular structure (arrow) arising from the base of the cecum. At surgery, a low-grade mucinous tumor of the appendix was found

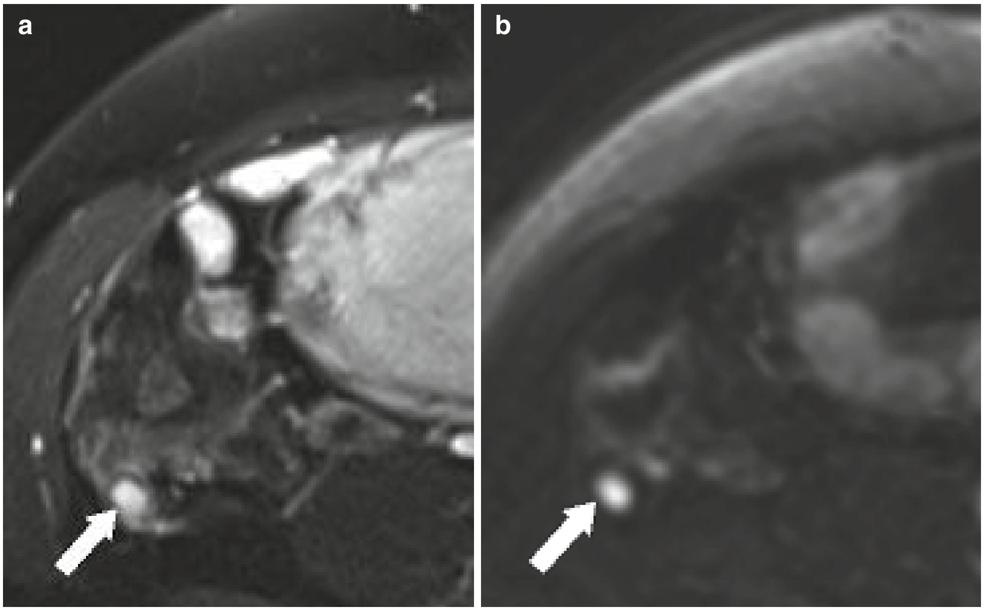

Fig. 3.18 Acute appendicitis on MRI. (**a**) Axial T2 HASTE—WI of the abdomen demonstrates hyperintense, dilated appendix (arrow) measuring 14 mm in diameter in retrocecal location. (**b**) Axial DWI ($b = 1400$ s/mm^2) of the abdomen demonstrates prominent appendix (arrow) with restricted diffusion, consistent with acute appendicitis

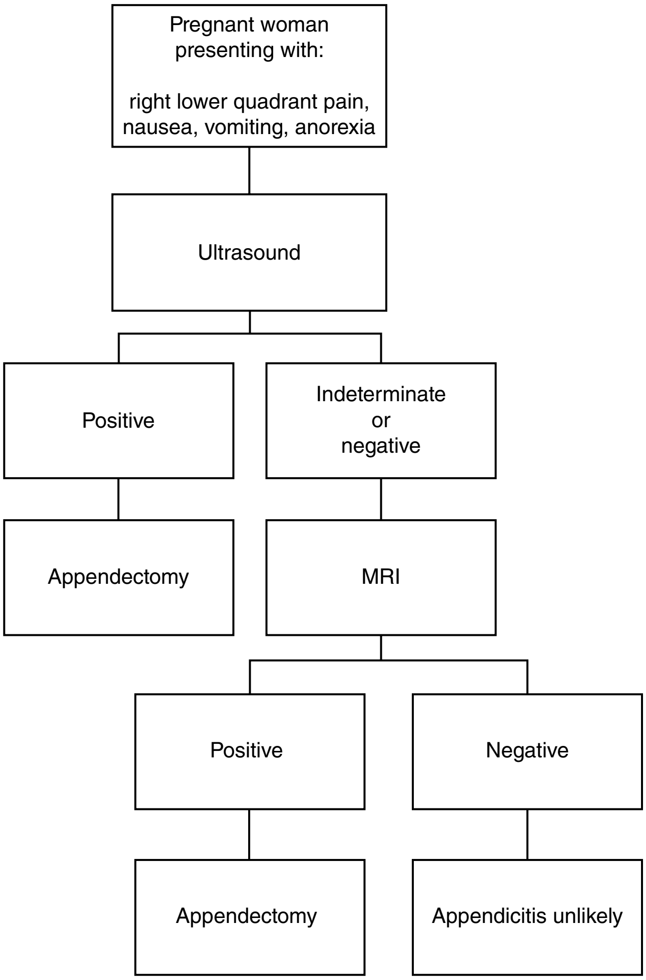
Pregnant woman presenting with:
right lower quadrant pain, nausea, vomiting, anorexia
Ultrasound
Positive
Indeterminate or negative
Appendectomy
MRI
Positive
Negative
Appendectomy
Appendicitis unlikely

Fig. 3.20 Imaging algorithm for acute appendicitis in pregnancy

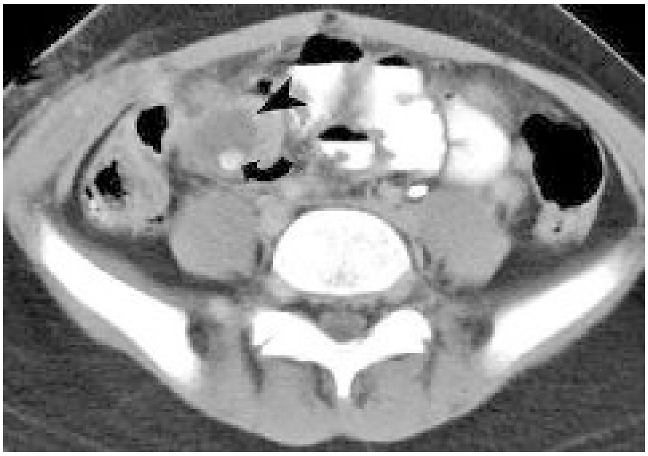

Fig. 3.21 Post appendectomy abscess and retained appendicolith. Axial contrast-enhanced CT of the lower abdomen demonstrates a well-defined abscess (*arrowhead*) in the right lower quadrant, containing an appendicolith (*curved arrow*)

Postoperative Complications and Interventional Management

A retained or dropped appendicolith is a rare postsurgical complication with less than 40 cases reported in the literature. Dropped appendicolith (Fig. 3.21) can be a nidus for future intra-abdominal abscess formation and therefore needs removal. The imaging findings include abscess containing one or more high-attenuation foci, most commonly in Morison's pouch or the paracecal region. CT-guided catheter drainage has been shown to be useful in avoiding surgery in selected cases of dropped appendicolith with abscess formation. There is a single report of successful image-guided extraction of appendicolith with Witch nitinol stone basket [24].

Image-guided pigtail catheter drainage is the primary mode of management of postoperative abscess after appendectomy and has been shown to have a high success rate in drainage of abdominal collections (Fig. 3.22).

The traditional treatment of retained appendicolith is open or laparoscopic surgery with abscess drainage and extraction of the calculus. Percutaneous retrieval of the retained appendicolith has been described using the Witch nitinol basket (Fig. 3.23). A trial of image-guided catheter drainage with or without percutaneous stone extraction may be beneficial in avoiding repeated surgery.

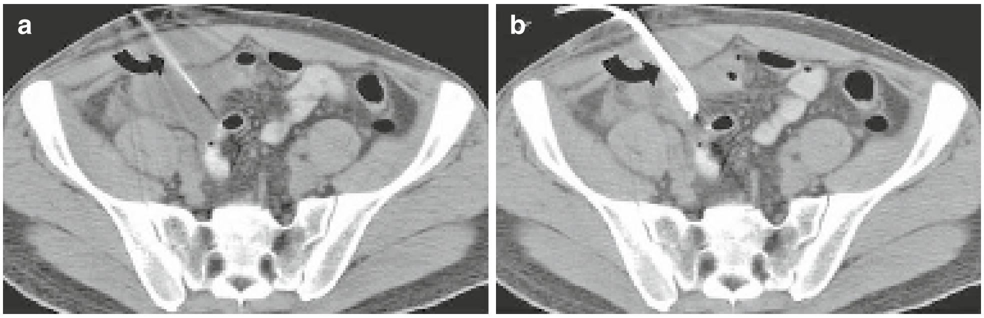

Fig. 3.22 Post appendectomy abscess drainage. (**a**) Noncontrast CT shows an 18-gauge needle (*curved arrow*) seen extending into the right lower quadrant collection at the time of the drainage procedure. (**b**) Noncontrast CT shows a 12-French pigtail catheter (*curved arrow*) placed into the collection using tandem trocar technique. Note the decrease in the size of the collection following aspiration of the catheter

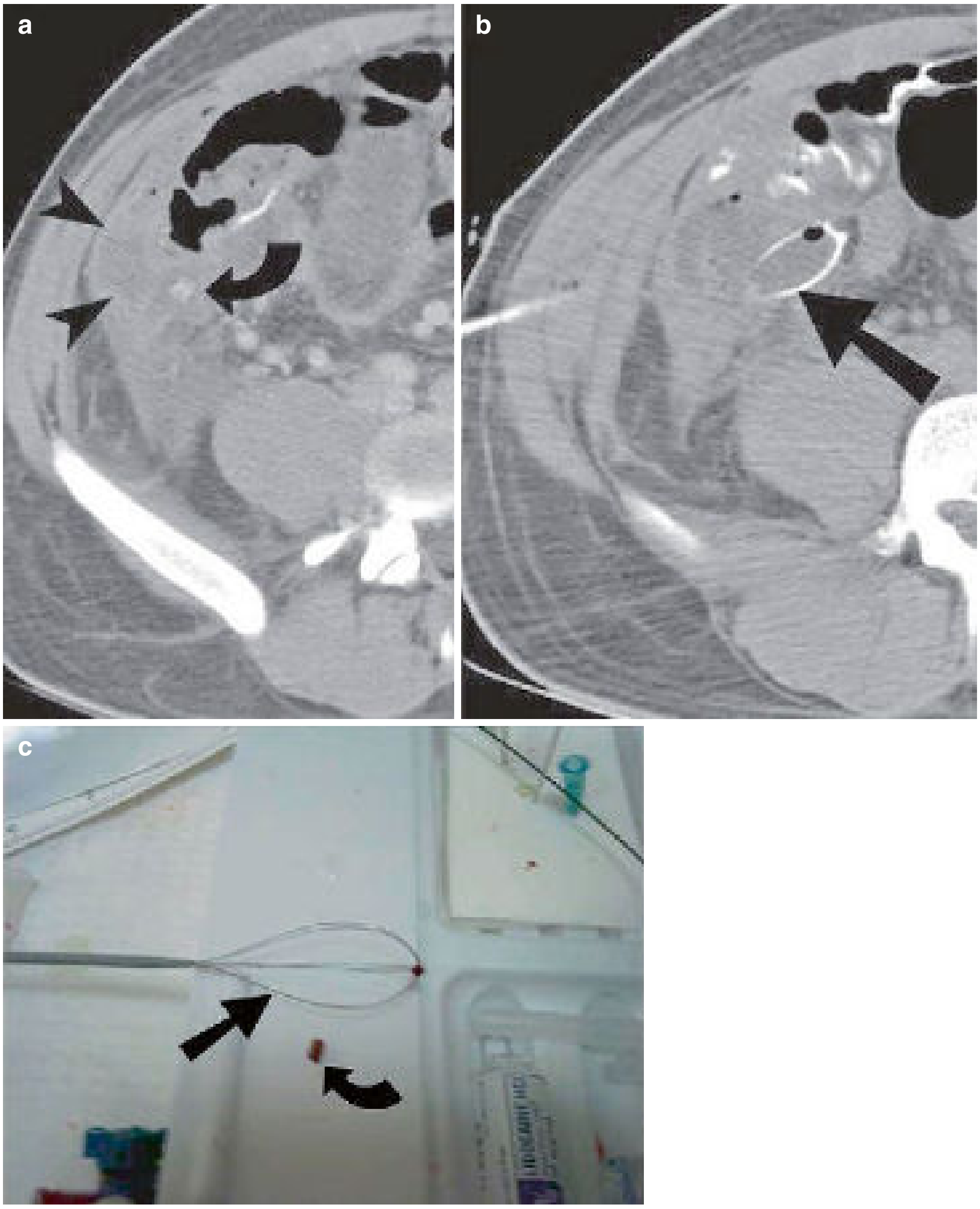

Fig. 3.23 Retained appendicolith with abscess formation after appendectomy. (**a**) Noncontrast CT scan study demonstrates the abscess cavity (*arrowheads*) in the right lower quadrant, containing a subcentimeter appendicolith (*curved arrow*). (**b**) Noncontrast CT demonstrates a Witch nitinol basket (*straight arrow*) in the abscess cavity. (**c**) Witch nitinol basket (*straight arrow*) and the appendicolith (*curved arrow*) taken out during the procedure

Appendiceal Diverticulitis

Appendiceal diverticular disease can be congenital (represents true diverticula) or acquired (represents pseudodiverticula). It clinically mimics acute appendicitis and is associated with significantly higher rates of perforation (up to 84% vs 12–30% in acute appendicitis). Appendiceal diverticulosis exhibits significant association with underlying appendiceal neoplasms including mucinous adenomas and pseudomyxoma peritonei.

On ultrasound, inflamed diverticula appears as a hypoechoic lesion next to the appendix amidst surrounding echogenic fat. Findings seen on CT include small, cystic outpouching with enhancing walls, absence of appendicolith and fluid levels, and periappendiceal abscess with adjacent non-inflamed appendix (Fig. 3.24). Detection of normal appendiceal diverticula is also an important clue (Fig. 3.25). Given the high incidence of complications (perforation, abscess formation) and associated neoplasms, treatment of choice for all cases is prophylactic appendectomy [25].

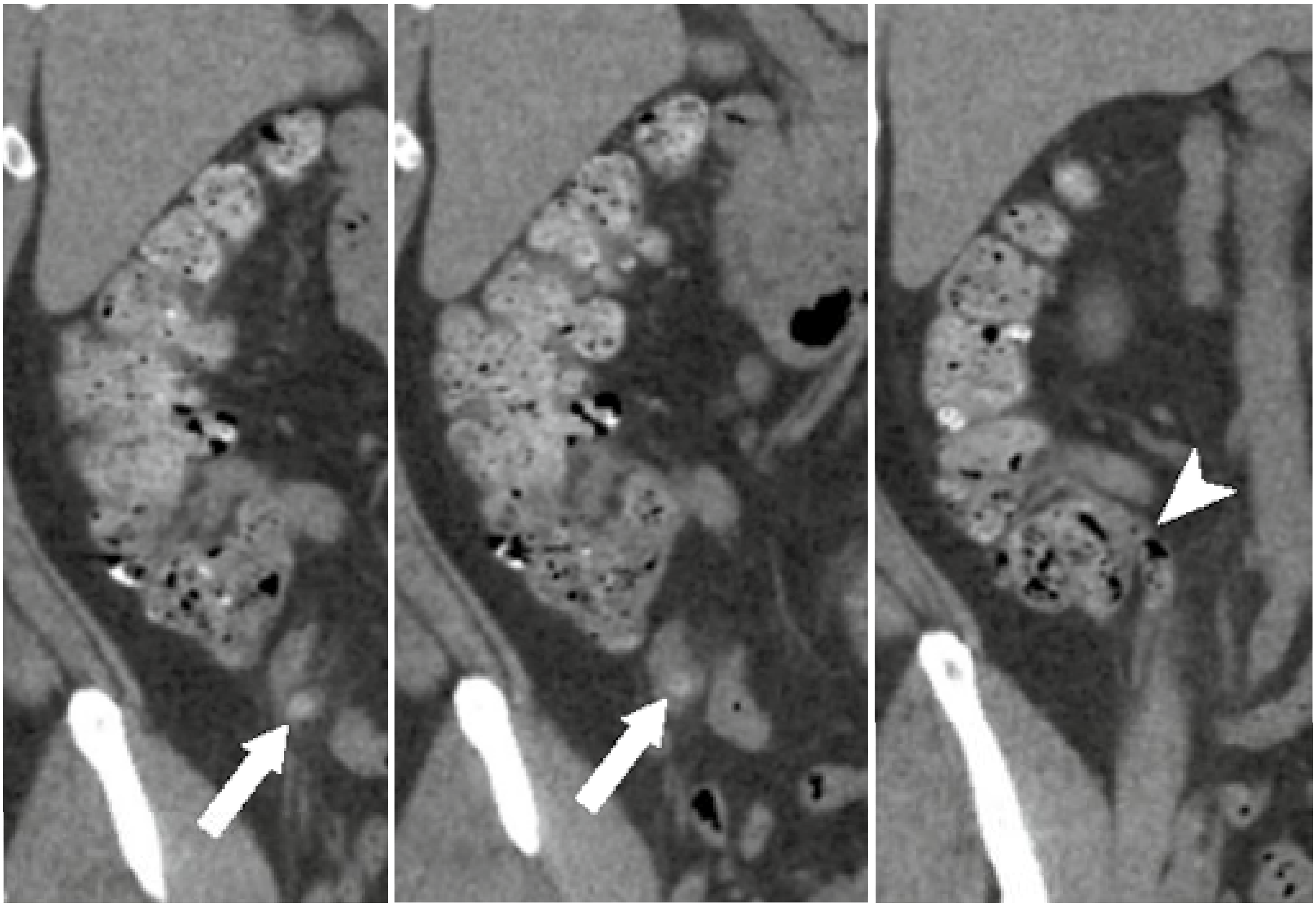

Fig. 3.24 Appendiceal diverticulitis. Three coronal contrast-enhanced CT images of the abdomen demonstrate appendiceal diverticulum (arrows) with surrounding inflammatory changes. The third image shows the origin of the appendix (arrowhead) at the base of the cecum

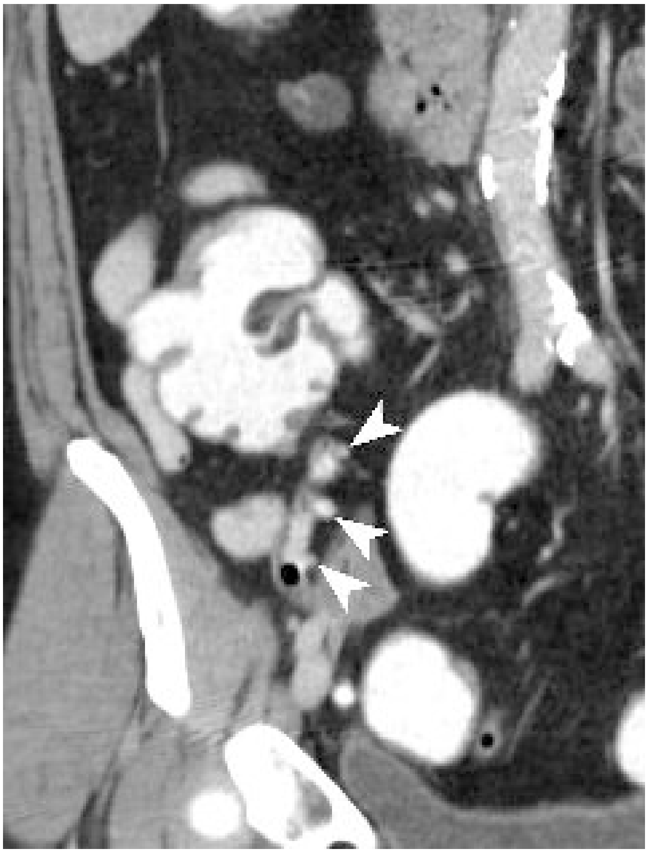

Fig. 3.25 Appendiceal diverticulosis. Coronal contrast-enhanced CT of the abdomen using intravenous and rectal contrast demonstrates multiple diverticula (arrowheads) arising from the appendix

Teaching Points

- CT is the imaging modality of choice for the evaluation of acute right lower quadrant pain.
- In CT, characteristic findings are extraluminal air, extraluminal appendicolith, abscess, phlegmon, and defect in the enhancing appendiceal wall.
- CT findings of perforated appendicitis are extraluminal air, extraluminal appendicolith, abscess, phlegmon, and appendiceal wall enhancement defect.
- Ultrasound is the first-line imaging modality in children and pregnant patients with acute right lower quadrant pain.
- In ultrasound, findings include noncompressible and aperistaltic blind-ending tubular structure, appendiceal caliber >6 mm, appendicolith, echogenic mass effect, and increased blood flow in appendiceal wall.
- MR is second-line imaging modality for acute appendicitis, mostly used after an equivocal or nondiagnostic ultrasound in pregnant patient.

Questions

1. Which of the following is the imaging finding characteristic for acute appendicitis?
   (A) Compressible appendix on ultrasound
   (B) Peristaltic tubular structure in ultrasound
   (C) Appendiceal caliber of 6 mm on CT
   (D) Bar-like thickening of the cecum on CT
   Answer: D

2. Which of the following indicates a complicated appendicitis?
   (A) Intraluminal air
   (B) Appendicolith
   (C) Phlegmon
   (D) Periappendiceal inflammation
   Answer: C

3. A pregnant woman presents to emergency department with nausea, anorexia, and right lower quadrant pain. Ultrasound is negative for acute appendicitis. What is your recommendation for further imaging?
   (A) Repeat ultrasound
   (B) MRI with intravenous contrast
   (C) MRI without intravenous contrast
   (D) CT with modified protocol
   Answer: C

4. A patient presents to emergency department with vague abdominal pain and fever. Medical history is significant for recent appendectomy. Lab data reveals leukocytosis. Postoperative CT of abdomen (Fig. 3.26) was performed. What is the next step?
   (A) Surgery
   (B) Antibiotic therapy
   (C) Magnetic resonance
   (D) Ultrasonography
   Answer: A

5. Which of the following is seen on the CT (Fig. 3.27) of a patient with right lower quadrant pain?
   (A) Amyand's hernia
   (B) Perforated appendix
   (C) Cecal bar sign
   (D) Bar-like thickening of the cecum
   Answer: B

6. The ultrasonography (Fig. 3.28) of a patient with fever and abdominal pain shows which of the following?
   (A) Phlegmon formation
   (B) Perforated appendix
   (C) Cecal bar sign
   (D) Blind-ending tubular structure
   Answer: D

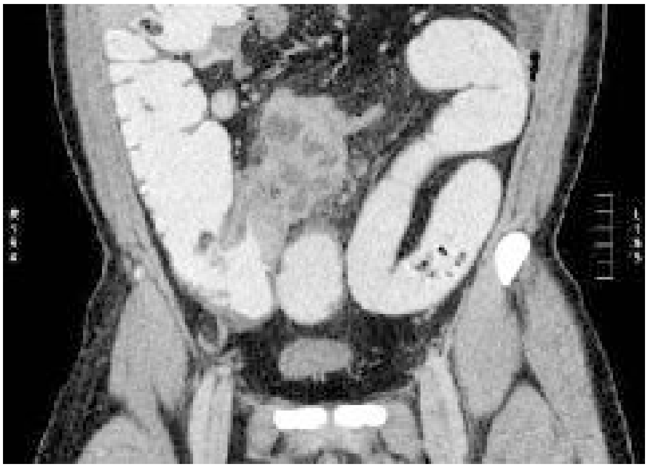

Fig. 3.26 Postoperative CT of abdomen

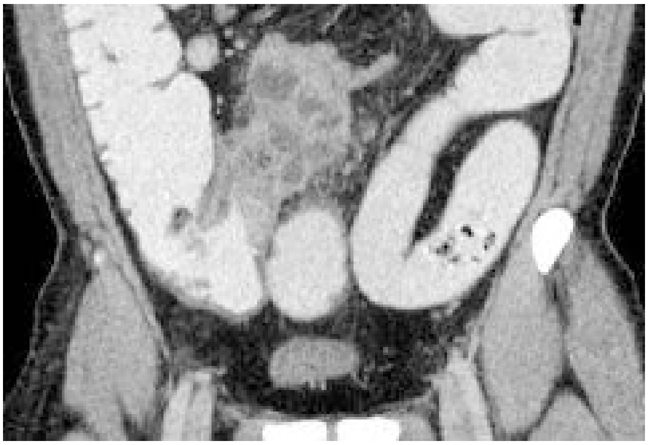

Fig. 3.27 Perforated appendix

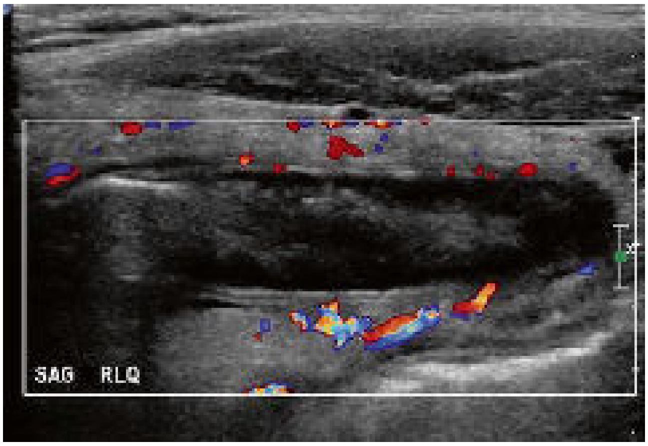

Fig. 3.28 Ultrasonography of abdomen

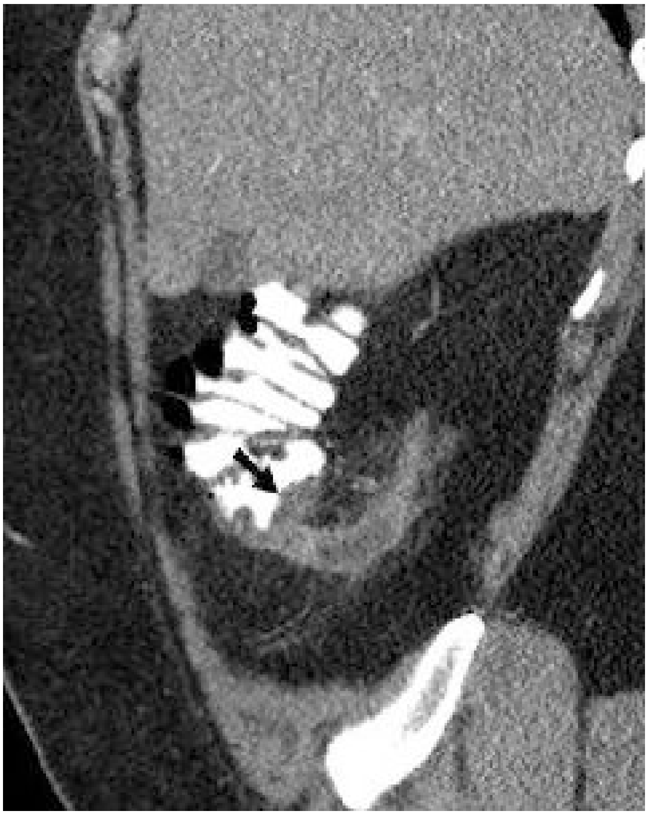

Fig. 3.29 Appendicitis

7. Which of the following finding (arrow) of appendicitis is demonstrated in the sagittal CT reformation (Fig. 3.29)?
   (A) Cecal bar sign
   (B) Phlegmon
   (C) Arrowhead sign
   (D) Abscess
   Answer: A

References

1. Collins DC. Acute retrocecal appendicitis: based on seven hundred and fifty-one instances. Arch Surg. 1938;36:729–43.
2. Saini S, Seltzer SE, Bramson RT, Levine LA, Kelly P, Jordan PF, et al. Technical cost of radiologic examinations: analysis across imaging modalities. Radiology. 2000;216:269–72.
3. Victoria T, Mahboubi S. Normal appendiceal diameter in children: does choice of CT oral contrast (VoLumen versus Gastrografin) make a difference? Emerg Radiol. 2010;17:397–401.
4. Rao PM, Rhea JT, Novelline RA, Mostafavi AA, McCabe CJ. Effect of computed tomography of the appendix on treatment of patients and use of hospital resources. N Engl J Med. 1998;338(3):141–6.
5. Rao PM, Rhea JT, Ratmer DW, Venus LG, Novelline RA. Introduction of appendiceal CT: impact on negative appendectomy and appendiceal perforation rates. Ann Surg. 1999;229:344–9.

6. Paulson EK, Harris JP, Jaffe TA, Haugan PA, Nelson RC. Acute appendicitis: added diagnostic value of coronal reformations from isotropic voxels at multi-detector row CT. Radiology. 2005;235:879–85.
7. Lowe LH, Penney MW, Scheker LE, Perez R, Stein SM, Heller RM, et al. Appendicolith revealed on CT in children with suspected appendicitis: how specific is it in the diagnosis of appendicitis? AJR Am J Roentgenol. 2000;175:981–4.
8. Alobaidi M, Shirkhoda A. Value of bone window settings on CT for revealing appendicoliths in patients with appendicitis. AJR Am J Roentgenol. 2003;180:201–5.
9. Ng SP, Cheng SM, Yang FS, Tzen CY, Huang JK. Hyperdense appendix on unenhanced CT: a sign of acute appendicitis. Abdom Imaging. 2007;32:701–4.
10. Moteki T, Horikoshi H. New CT criterion for acute appendicitis: maximum depth of intraluminal appendiceal fluid. AJR Am J Roentgenol. 2007;188:1313–9.
11. Horrow MM, White DS, Horrow JC. Differentiation of perforated from nonperforated appendicitis at CT. Radiology. 2003;227:46–51.
12. Gaitini D, Beck-Razi N, Mor-Yosef D, Fisher D, Itzhak OB, Krausz MM, et al. Diagnosing acute appendicitis in adults: accuracy of color Doppler sonography and MDCT compared with surgery and clinical follow-up. AJR Am J Roentgenol. 2008;190:1300–6.
13. van Randen A, Bipat S, Zwinderman AH, Ubbink DT, Stoker J, Boermeester MA. Acute appendicitis: meta-analysis of diagnostic performance of CT and graded-compression ultrasound related to prevalence of disease. Radiology. 2008;249(1):97–106.
14. Rao PM, Rhea JT, Novelline RA. Distal appendicitis: CT appearance and diagnosis. Radiology. 1997;204:709–12.
15. Singh AK, Desai H, Novelline RA. Emergency MRI of acute pelvic pain: MR protocol with no oral contrast. Emerg Radiol. 2009;16(2):133–41.
16. Oto A, Ernst RD, Shah R, Koroglu M, Chaljub G, Gei AF, et al. Right-lower-quadrant pain and suspected appendicitis in pregnant women: evaluation with MR imaging—initial experience. Radiology. 2005;234(2):445–51.
17. Birchard KR, Brown MA, Hyslop WB, Firat Z, Semelka RC. MRI of acute abdominal and pelvic pain in pregnant patients. AJR Am J Roentgenol. 2005;184(2):452–8.
18. Pedrosa I, Levine D, Eyvazzadeh AD, Siewert B, Ngo L, Rofsky NM. MR imaging evaluation of acute appendicitis in pregnancy. Radiology. 2006;238(3):891–9.
19. Oto A, Srinivasan PN, Ernst RD, Koroglu M, Cesani F, Nishino T, et al. Revisiting MRI for appendix location during pregnancy. AJR Am J Roentgenol. 2006;186(3):883–7.
20. Hormann M, Puig S, Prokesch SR, Partik B, Helbich TH. MR imaging of the normal appendix in children. Eur Radiol. 2002;12(9):2313–6.
21. Nitta N, Takahashi M, Furukawa A, Murata K, Mori M, Fukushima M. MR imaging of the normal appendix and acute appendicitis. J Magn Reson Imaging. 2005;21(2):156–65.
22. Incesu L, Coskun A, Selcuk MB, Akan H, Sozubir S, Bernay F. Acute appendicitis: MR imaging and sonographic correlation. AJR Am J Roentgenol. 1997;168(3):669–74.
23. Hormann M, Paya K, Eibenberger K, Dorffner R, Lang S, Kreuzer S, et al. MR imaging in children with nonperforated acute appendicitis: value of unenhanced MR imaging in sonographically selected cases. AJR Am J Roentgenol. 1998;171(2):467–70.
24. Singh AK, Hahn PF, Gervais D, Vijayraghavan G, Mueller PR. Dropped appendicolith: CT findings and implications for management. AJR Am J Roentgenol. 2008;190:707–11.
25. Williams JM, Adamo DA, Olson MC. Acute appendiceal diverticulitis: a case report [published correction appears in Radiol Case Rep. 2023 Jan 25;18(4):1641-1642]. Radiol Case Rep. 2021;16(5):1072–4. https://doi.org/10.1016/j.radcr.2021.02.034.

Imaging of Small Bowel

4

Ajay Singh, Mohammad Mansouri, and Terry S. Desser

Small Bowel of Diverticulitis

Small bowel diverticulitis is most commonly characterized by inflammation of acquired diverticula which are typically located on the mesenteric border of the bowel. Although less frequent than duodenal diverticula, jejunoileal diverticula are more prone to develop complications, including acute inflammation with perforation and abscess formation [1]. The current mode of treatment for small bowel diverticulitis is either with conservative medical management or surgical resection of the involved segment of bowel [2–4].

Small Bowel Diverticula: True Versus False Diverticula

Small bowel diverticula are most often found in the duodenum, being identified incidentally in the duodenum of 2–5% of patients undergoing upper GI barium studies and in 12.5% of patients undergoing ERCP (Figs. 4.1 and 4.2) [1, 5, 6]. The duodenum is the most common site of small bowel diverticula, followed by the jejunum, with ileal diverticula being least common. Jejunal diverticula are mostly multiple and are seven times more common than ileal diverticula [7, 8]. Small bowel diverticula are most commonly detected in the elderly in the sixth and seventh decade [9].

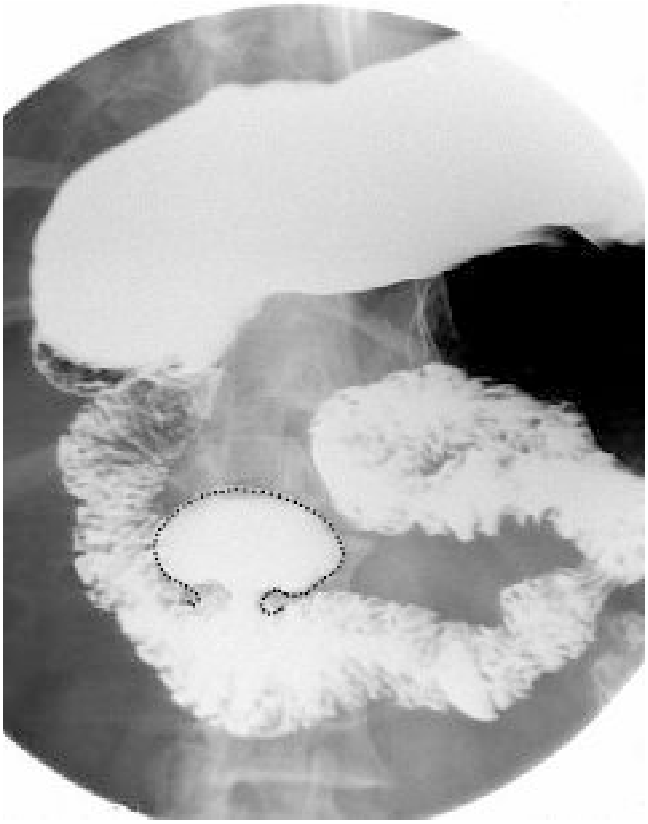

Fig. 4.1 Duodenal diverticulum. Upper GI study demonstrates an incidentally detected solitary duodenal diverticulum arising from the third portion of the duodenum

Congenital diverticula are true diverticula and are composed of all three intestinal layers and arise from the antimesenteric border of the small bowel. Meckel's diverticula, for example, are true diverticula. By contrast, pathologic acquired diverticula are "pseudodiverticula"; that is, they lack a muscular layer and result from herniation of only the mucosa and submucosa through defects in the muscular layer. It is thought that acquired diverticula tend to form at the mesenteric border where vasa recta penetrate, creating areas of relative weakness [2]. Krishnamurthy et al. found

A. Singh (✉)
Division of Emergency Radiology, Department of Radiology, Massachusetts General Hospital, Boston, MA, USA

Harvard Medical School, Massachusetts General Hospital, Boston, MA, USA
e-mail: asingh1@partners.org

M. Mansouri
Department of Radiology, Massachusetts General Hospital, Boston, MA, USA

T. S. Desser
Department of Radiology, Stanford University School of Medicine, Stanford, CA, USA

© The Author(s), under exclusive license to Springer Nature Switzerland AG 2024
A. Singh (ed.), *Emergency Radiology*, https://doi.org/10.1007/978-3-031-65770-2_4

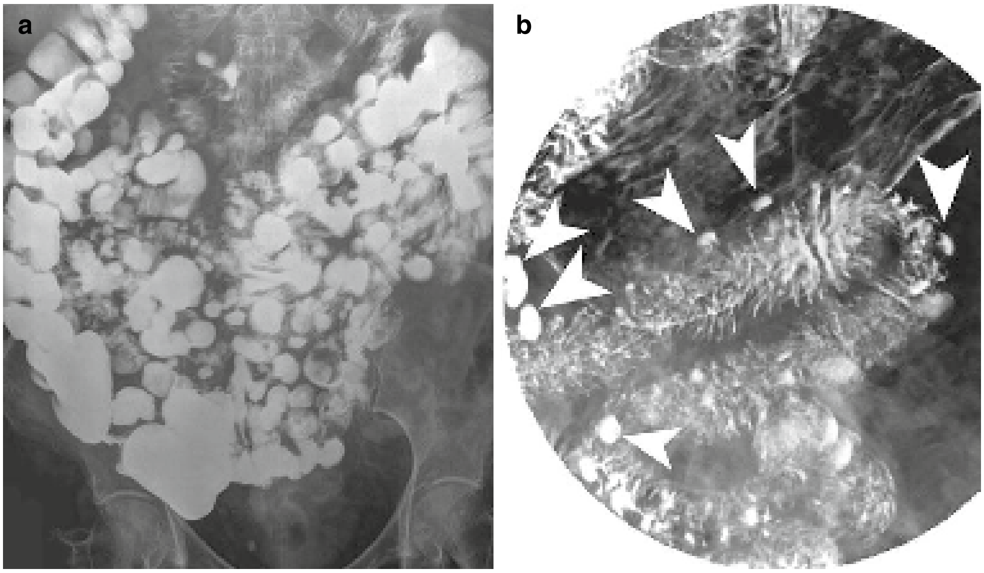

Fig. 4.2 Small bowel diverticulosis. (**a**) Small bowel follow-through examination demonstrates innumerable round collections of contrast in small bowel diverticula. (**b**) Small bowel follow-through study demonstrates multiple duodenal and jejunal diverticula (*arrowheads*) seen arising from the mesenteric border of the small bowel

histopathologic abnormalities in the wall of the jejunum of patients with jejunal diverticula, consistent with the notion that diverticula formation is associated with uncoordinated small bowel motility that results in increased intraluminal pressures [10].

Pathogenesis

Although most small bowel diverticula are of little clinical significance, approximately 10–20% will develop complications [1]. Potential sequelae include inflammation, gangrenous change, perforation, peritonitis, bleeding, obstruction, and intestinal stasis leading to blind loop syndrome [11, 12]. Jejunoileal diverticula are more likely to have complications than duodenal diverticula [1, 13]. Of the diverticula that developed complications, jejunoileal diverticula were more likely to perforate and form abscesses, whereas duodenal diverticula were more prone to bleeding [1].

Diverticula in the small bowel are less likely to develop inflammation than those in the colon, probably due to the relative sterility of small bowel contents and the lesser degree of stasis that occurs in the larger diverticula of the small bowel [2]. Stasis of diverticular contents may be promoted by foreign bodies, enteroliths, inspissation of bowel contents, or a smaller diverticular ostium which can reduce the outflow of intestinal fluid from the diverticulum [2, 11, 14]. Because small bowel diverticulitis is more commonly found at the mesenteric side of the bowel, the mesentery can close off the localized inflammatory process from the rest of the peritoneal cavity. As a result, peritonitis and pneumoperitoneum may not be detected clinically or radiologically unless there is rupture of the mesenteric peritoneum that had previously sealed off the abscess [11].

Clinical Presentation

Small bowel diverticulitis presents a diagnostic challenge on clinical exam and can mimic a host of more common abdominal pathologies including acute appendicitis, cholecystitis, perforated peptic ulcer disease, and colonic diverticulitis [12, 15]. A patient with small bowel diverticulitis may present with intermittent abdominal discomfort, acute abdominal pain, fever, chills, and leukocytosis [4, 9, 16–21]. Peritoneal signs may be appreciated on abdominal exam [9, 18].

Imaging

In the setting of small bowel diverticulitis, barium study may allow detection of air- or contrast-filled diverticula along the mesenteric small bowel wall, thickening of the bowel wall, bowel lumen obstruction, or extraluminal flow of contrast (Fig. 4.3) [12].

CT scan is the gold standard for detection and assessing the severity of diverticulitis. The CT findings are typically a focal inflammatory mass containing air, fluid, or an air-fluid level adjacent to asymmetrically thickened small bowel wall, with the presence of surrounding inflammation and mesenteric fat stranding [3, 9, 12]. The small bowel wall thickening is most prominent on the mesenteric side; however, the antimesenteric bowel border may be involved in severe cases. The inflamed diverticulum may be visible along the mesenteric border of the small bowel loop (Fig. 4.4). With small bowel diverticulitis, fecalized matter is often present within the diverticula which can aid in the identification of the inflamed diverticulum. Extrinsic compression of the common bile duct has also been observed in some cases of duodenal diverticula (known as Lemmel syndrome) or duo-

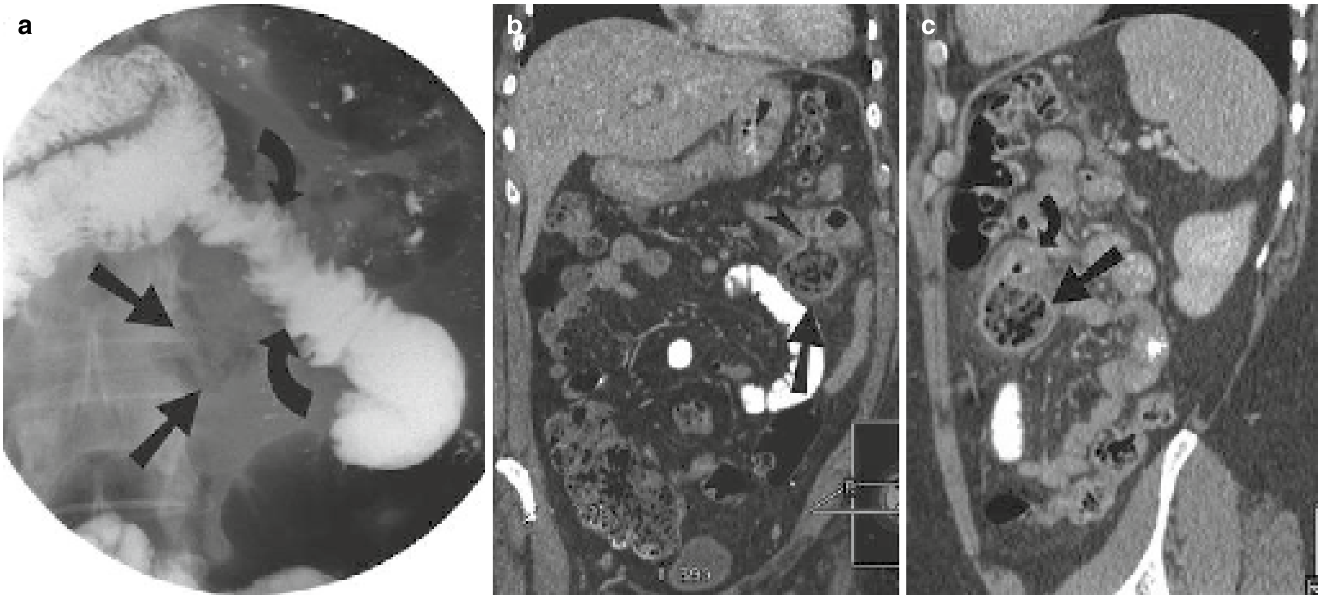

Fig. 4.3 Acute small bowel diverticulitis in an acquired jejunal diverticulum. (**a**) A small bowel follow-through study demonstrates segmental irregularity of valvulae conniventes (*curved arrows*) in the proximal jejunum. A small collection of air due to the jejunal loop represents the inflamed jejunal diverticulum (*straight arrows*). (**b**) Coronal reformation (CT) demonstrates the inflamed jejunal diverticulum (*straight arrow*) in the left upper quadrant, with its neck (*arrowhead*) arising from the antimesenteric border of a jejunal loop. (**c**) Sagittal reformation (CT) demonstrates the inflamed true diverticulum (*straight arrow*) arising on the antimesenteric border of the jejunal loop (*curved arrow*)

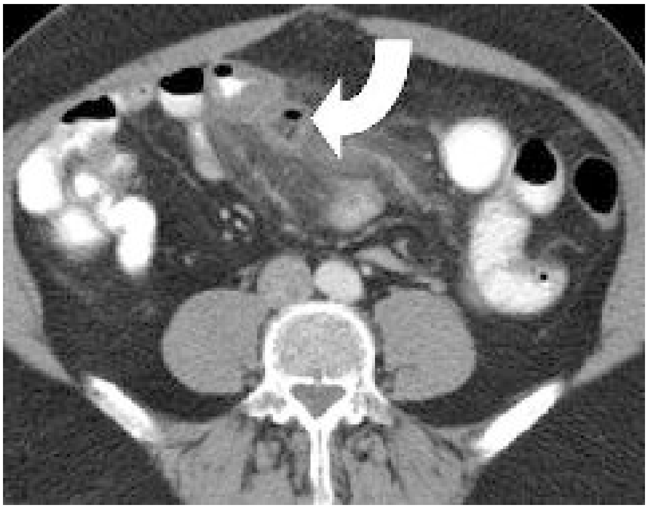

Fig. 4.4 Small bowel diverticulitis. Contrast-enhanced CT scan study of the abdomen demonstrates inflamed diverticulum (*curved arrow*) arising on the mesenteric aspect of the distal jejunal loop. There is inflammatory thickening of the adjacent small bowel wall along with inflammatory stranding in the small bowel mesentery

denal diverticulitis. The differential diagnosis on CT may include a perforated neoplasm, perforation secondary to a foreign body, NSAID-provoked ulceration, intramural hematoma, and local inflammatory bowel disease [3].

CT with multiplanar reconstruction can be employed to identify small bowel diverticula, with excellent visualization of the narrowed diverticular neck [2]. CT with coronal reformatting is especially useful for detecting single diverticula that are difficult to detect on axial views and can allow recognition of additional diverticula [3, 14].

CT Findings of Acute Small Bowel Diverticulitis

1. Inflamed diverticulum or focal inflammatory phlegmon along the mesenteric border of small bowel.
2. Asymmetrically thickened small bowel wall, more prominent along the mesenteric border.
3. Mesenteric fat stranding.

Meckel's Diverticulitis

Meckel's diverticulum is the most common congenital anomaly of the GI tract, seen in approximately 2% of the population. It is a true diverticulum and is therefore present on the antimesenteric border of the distal ileum. It is most commonly located within 100 cm of the ileocecal junction [22]. It contains hypertrophic gastric mucosa (in 25–50%) and has a lifetime complication risk of up to 4%. Heterotropic pancreatic tissue is present in approximately 10% of the cases.

The majority of cases of symptomatic Meckel's diverticulum are seen in the pediatric population. Hemorrhage is the most common complication and is most often painless. Bowel obstruction is the second most common complication and is usually seen in older children and adults. The bowel obstruction can be secondary to volvulus, intussusception, or hernia. Intestinal perforation is an uncommon presentation of Meckel's diverticulum.

Meckel's diverticulitis most often presents with abdominal pain and fever. It is secondary to acid secretion or obstruction of the mouth of the diverticulum most commonly by an enterolith, fecolith, or foreign body. Littre hernia represents Meckel's diverticulum which has herniated in a hernia sac.

Meckel's diverticulum can be seen on barium studies as a blind-ending tubular outpouching arising from the antimesenteric border of the ileum with a triradiate fold pattern at the junction of the diverticulum and ileum.

The heterotopic gastric mucosa present in a Meckel's diverticulum accumulates and secretes pertechnetate anion and is therefore detected on technetium-99m pertechnetate scan as a focal area of increased radiotracer activity (Fig. 4.5). Technetium pertechnetate scintigraphy has high sensitivity of more than 80% in the pediatric population and slightly lower sensitivity of 63% in adult population [23]. CT may show changes of small bowel diverticulitis (thickened, blind-ending, tubular structure with wall enhancement and adjacent mesenteric fat stranding) in the right iliac fossa or periumbilical region and may show volvulus or intussusception (Fig. 4.6). CT is also a valuable imaging modality for assessing other complications of Meckel's diverticulum, notably abscess formation, bowel obstruction, and perforation. Identifying normal appendix on ultrasonography or CT is important to rule out appendicitis in children with abdominal pain.

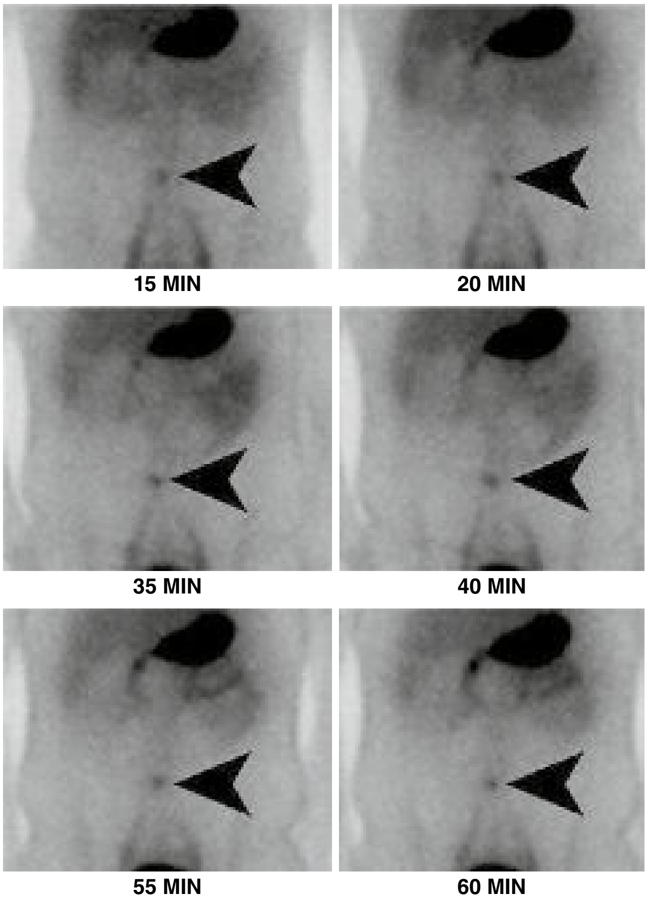

Fig. 4.5 Meckel's diverticulitis. Technetium-99m pertechnetate scan demonstrates focal increased radiotracer activity (*arrowheads*) in the lower abdomen, corresponding to the site of ectopic gastric mucosa within the inflamed Meckel's diverticulum

Treatment

Laparotomy or laparoscope-assisted surgery is typically undertaken in the setting of small bowel diverticulitis associated with perforation, abscess formation, massive GI bleed, small bowel obstruction, blind loop syndrome, or refractory abdominal pain [24, 25]. Surgical approaches include both segmental resection of the involved bowel with end-to-end anastomosis and less commonly diverticulectomy [8, 24]. Conservative management consists of antibiotic therapy, IV hydration, and bowel rest [2, 3]. However, cases have been described of patients who ultimately underwent segmental bowel resection for jejunal diverticulitis, after symptoms persisted following a period of conservative management [3].

Acute Mesenteric Ischemia

Acute mesenteric ischemia is characterized by inadequate blood flow to the bowel wall, leading to ischemia. Mesenteric arterial occlusion carries a high mortality, unless the patient undergoes emergent vascular surgery.

Clinical Presentation

Clinically the patients with arterial causes of acute mesenteric ischemia are elderly and most often present with severe dull abdominal pain and vomiting. The abdominal pain is out of proportion to the tenderness elicited on palpation. Mesenteric venous thrombosis is most often seen in younger population and present with less severe symptoms which may have been present for days or sometimes weeks. Lab studies often show metabolic acidosis, elevated lactate level, and low bicarbonate level.

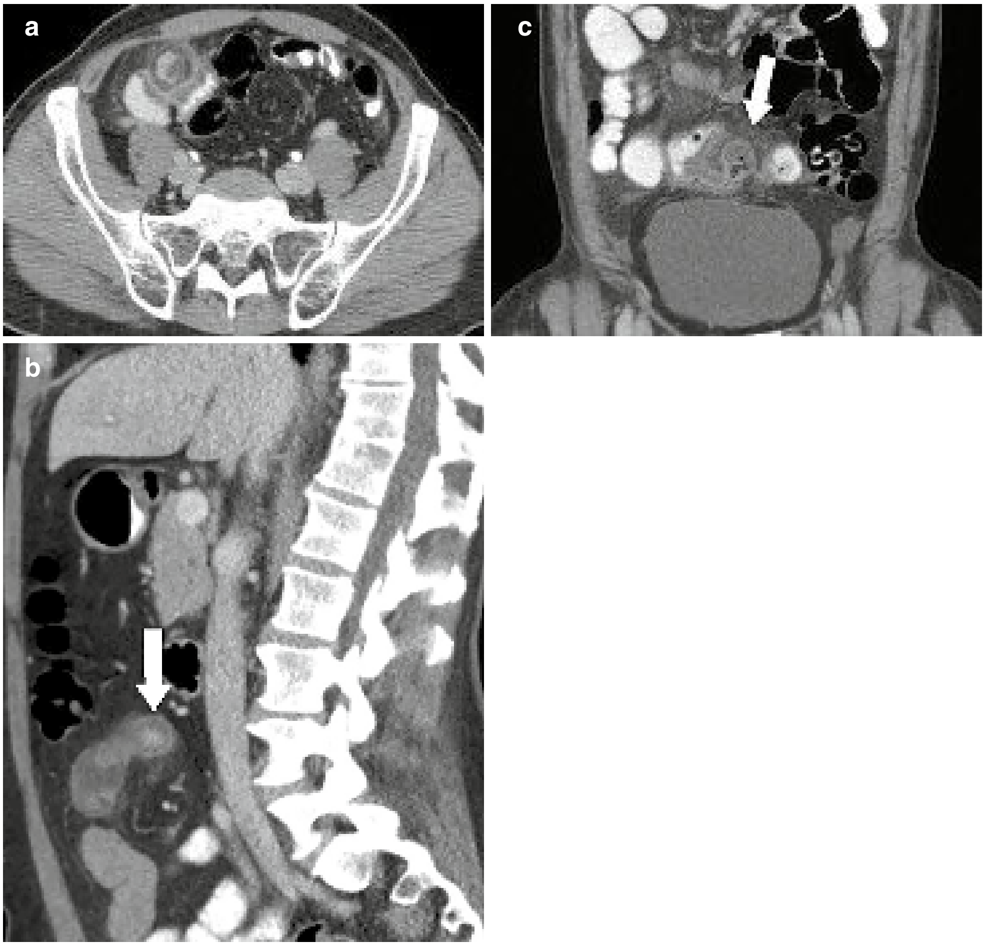

Fig. 4.6 Meckel's diverticulitis. (**a**) Axial contrast-enhanced CT demonstrates the inflamed congenital diverticulum with thickened wall arising from the antimesenteric border of the distal ileum. (**b**) Sagittal contrast-enhanced CT reformation demonstrates the inflamed Meckel's diverticulum (arrow) demonstrating thickened wall and serosal hyperenhancement. (**c**) Coronal contrast-enhanced CT reformation demonstrates the inflamed Meckel's diverticulum (arrow) with wall thickening and adjacent mesenteric edema

Pathogenesis

Superior mesenteric artery occlusion is a far more common than superior mesenteric vein occlusion as the cause of acute mesenteric ischemia. Approximately one-third of the cases are secondary to embolic occlusion and one-third secondary to thrombosis. Approximately 25% cases are caused by non-occlusive ischemia, while the remaining cases are secondary to venous occlusion [26].

Risk Factors

The risk factor for arterial occlusion is most commonly heart diseases, such as atrial fibrillation, endocarditis, and valvular heart diseases. Atrial fibrillation is the most common cause of embolism to the superior mesenteric artery. The non-occlusive bowel ischemia may be secondary to hypotensive shock, pancreatitis, bowel obstruction, dehydration, and dialysis. Mesenteric venous thrombosis is seen with hypercoagulable states, such as protein C or S deficiency, polycythemia vera, antithrombin three deficiency, sickle cell disease, pregnancy, and oral contraceptive use.

Imaging

The plain radiograph may show no abnormality in 25% of patients or show paralytic ileus. In late stage, when ischemia or infarct has developed, radiography may show obstruction, bowel wall edema, intraperitoneal free gas, or portal venous gas.

Doppler ultrasound is highly specific (92–100%) but has a low sensitivity (70–89%) for detecting vascular occlusions. Features of acute mesenteric ischemia on ultrasound are as follows:

- SMA occlusion and bowel spasm (early phase).
- Fluid-filled loops, decreased or no peristalsis, reduced bowel wall thickness, peritoneal free fluid.
- SMV and/or portal vein thrombus, decreased peristalsis, increased intraluminal secretions, and segmental wall thickening.
- Intramural gas and portal venous gas (late phase).

Contrast-enhanced CT is the imaging modality of choice as it has sensitivity of 93.3% and specificity of 95.9% in a meta-analysis of six studies published between 1996 and

2009 [27]. Although catheter angiography has been shown to have a sensitivity of 87.5%, the introduction of multidetector CT has obviated the need for this invasive test as the first-line imaging modality.

CT performed 25 and 65s after initiating contrast injection at the rate of 4 mL/s is the optimal protocol to evaluate for vascular as well as bowel wall changes. The CT angiographic phase changes management in 19% cases by showing vascular abnormality not visible on the portal venous phase [28].

The CT imaging findings include superior mesenteric artery thrombus, small-caliber superior mesenteric vein, bowel distension, and focal lack of bowel wall enhancement (Figs. 4.7 and 4.8). In the study by Kirkpatrick et al. pneumatosis intestinalis was seen in 43% cases of acute mesenteric ischemia. Bowel wall thickening and mucosal enhancement were seen in 85% and 46%, respectively [28]. Linear pattern of pneumatosis indicates more serious cause of pneumatosis and accounts for higher proportion of death from bowel infarction than cystic pattern of intramural gas (Fig. 4.9). The presence of portomesenteric venous gas favors more serious causes of pneumatosis intestinalis, such as mesenteric ischemia, and increases mortality to 50% (Fig. 4.10) [29]. The secondary findings seen on CT include ascites and mesenteric edema.

Colonic ischemia typically involves the inferior mesenteric artery territory, affecting splenic flexure and descending colon. The CT findings include reversible colonic wall thick-

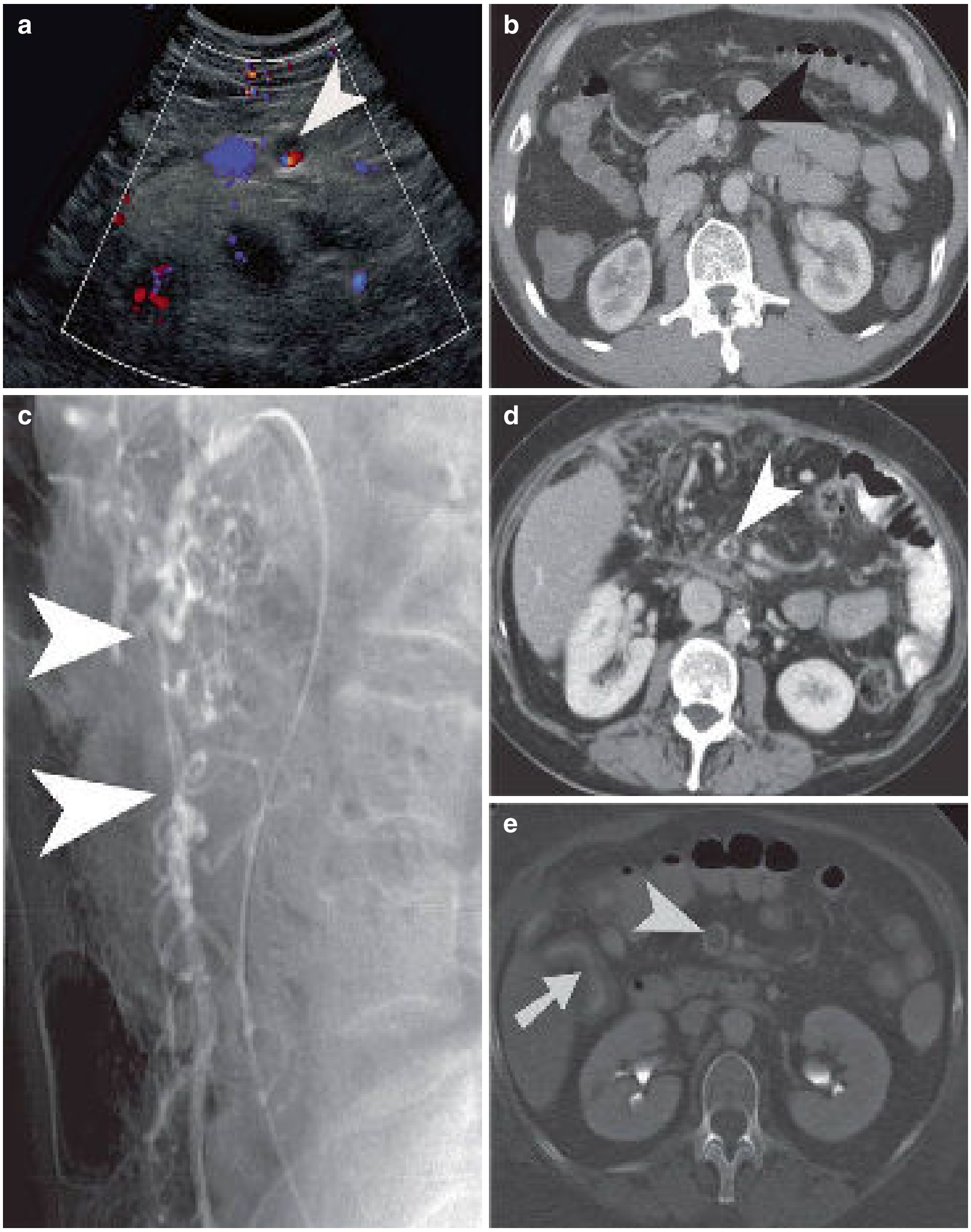

Fig. 4.7 Superior mesenteric artery and venous pathologies leading to bowel ischemia. (**a**, **b**) Color Doppler ultrasound and contrast-enhanced CT show dissection in the superior mesenteric artery (*arrowhead*). The adjacent superior mesenteric vein is patent. (**c**) Superior mesenteric arteriogram shows narrowing (*arrowheads*) of the superior mesenteric artery lumen, secondary to non-occlusive thrombosis. (**d**, **e**) Contrast-enhanced CT shows thrombosis of the superior mesenteric vein (*arrowhead*). There are edematous changes seen in the small bowel mesentery. Ischemia in the small bowel is indicated by bowel wall edema (*arrow*)

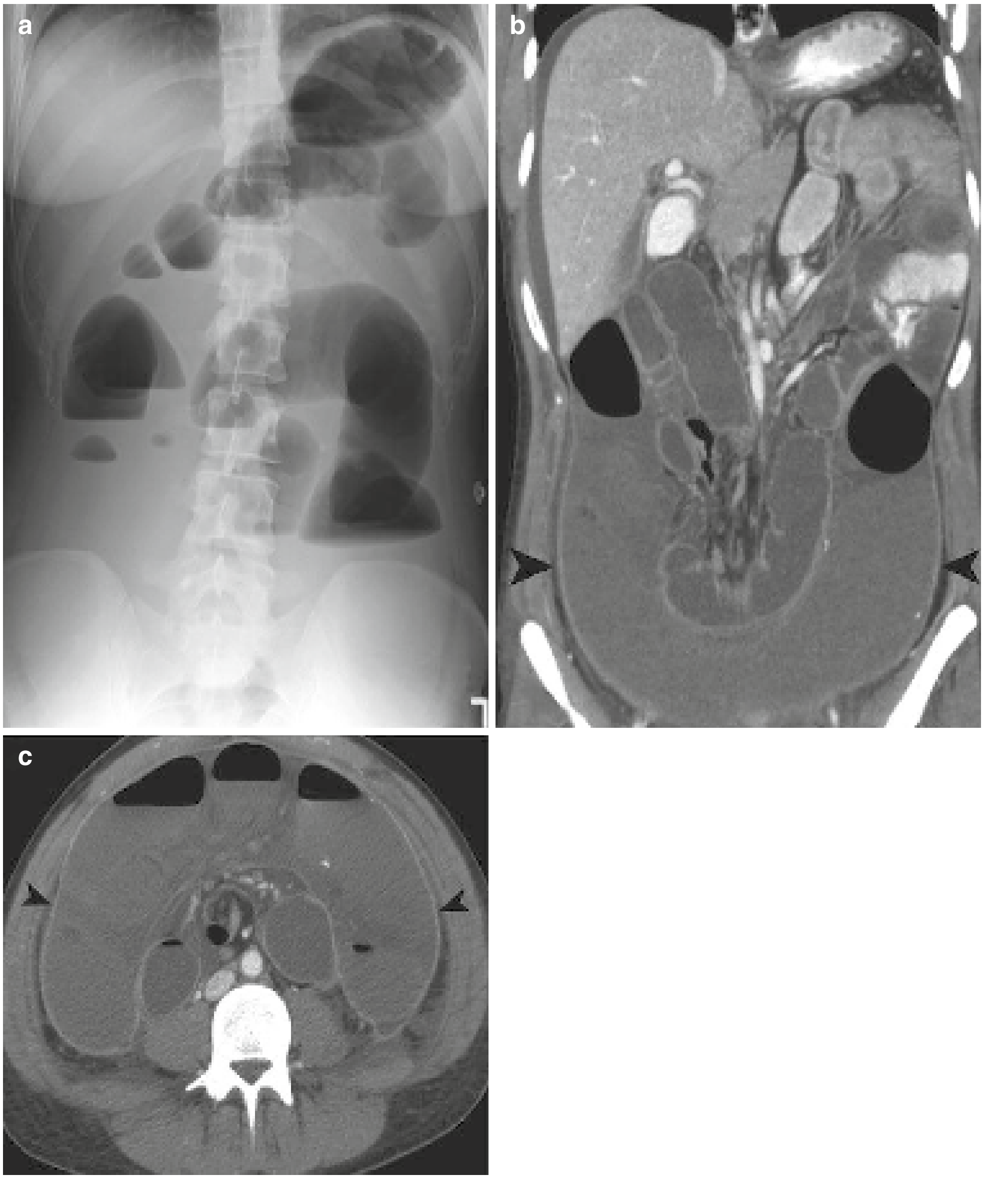

Fig. 4.8 Transmural infarction of bowel. (**a**) Plain radiograph of the abdomen demonstrates multiple air-fluid levels secondary to paralytic ileus. (**b**, **c**) Coronal CT reformation demonstrates fluid-containing, dilated small bowel loops (*arrowheads*) with no wall enhancement

ening in the distribution of inferior mesenteric artery. Colonic ischemia cases usually resolve spontaneously, and stricture formation is unusual.

Necrotizing enterocolitis is most commonly seen in premature neonates, developing in the first week of life. The imaging findings include pneumatosis, portal/mesenteric vein gas, pneumoperitoneum, and paralytic ileus.

CT Findings of Small Bowel Ischemia

1. SMA/SMV thrombus.
2. Bowel distension, bowel wall thickening, and lack of enhancement.
3. Pneumatosis (linear pattern more ominous).
4. Portal/mesenteric vein gas.
5. Ascites.

Treatment

The treatment of acute mesenteric ischemia includes emergent laparotomy and embolectomy. Resection of infarcted bowel is performed with a second-look laparotomy often used to reassess the bowel loop viability. SMV thrombus should not be resected unless the venous thrombus is acute. Anticoagulation with heparin and broad-spectrum antibiotics are utilized for mesenteric venous thrombosis. In the absence of peritoneal signs or perforation, image-guided interventions may be used.

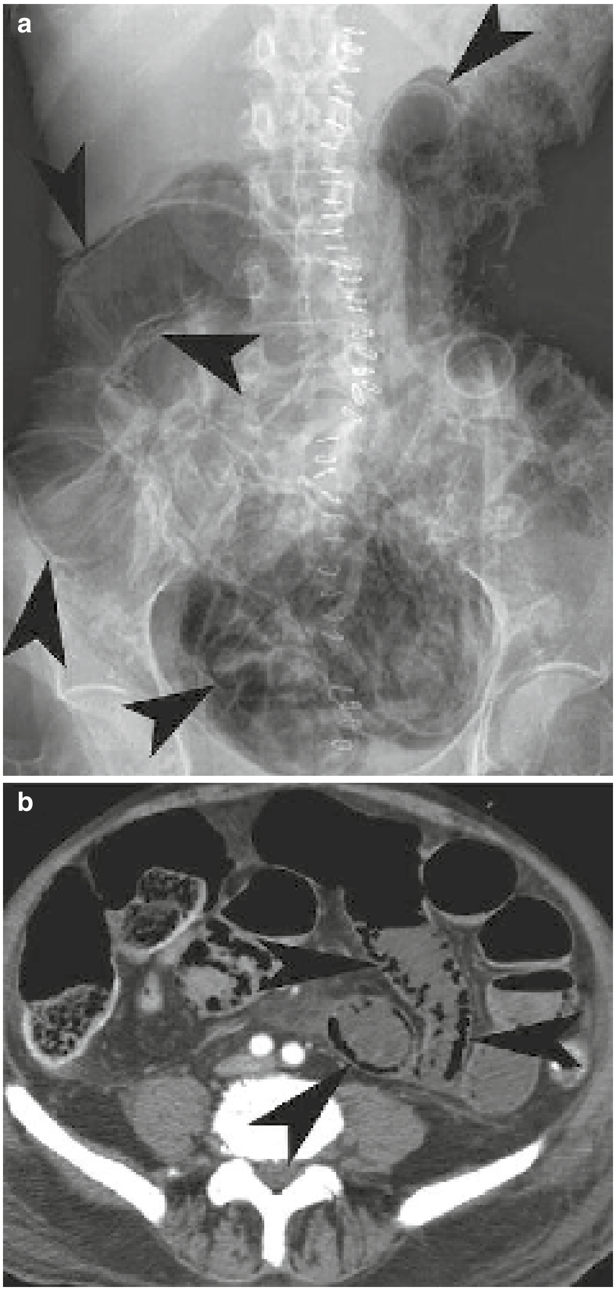

Fig. 4.9 Pneumatosis intestinalis. (**a**) Plain radiograph of the abdomen demonstrates extensive linear pneumatosis (*arrowheads*) in the small bowel wall. (**b**) Contrast-enhanced CT shows pneumatosis (*arrowheads*) in the small bowel wall, secondary to bowel wall ischemia

Pneumatosis Intestinalis

Pneumatosis intestinalis is a pathological condition in which air is present submucosally or subserosally in the bowel wall. Optimizing window settings helps easy detection of abnormal air in the bowel wall. It is an imaging finding but not a clinical diagnosis, as it is associated with a multitude of causes. Three patterns of pneumatosis have been described:

1. Bubble-like or cystoid pattern: separate bubbles of gas are present.
2. Linear pattern: gas pattern is curvilinear or crescent shape.
3. Circular pattern: circumferential gas around the bowel wall.

The causes of pneumatosis intestinalis can range from benign etiology without bowel ischemia to transmural bowel infarction, which is the most common cause (52%) [29].

Bowel obstruction can cause pneumatosis intestinalis by causing mucosal breach secondary to increased intraluminal pressure. Pneumatosis secondary to collagen vascular disease can be secondary to abnormal peristalsis and bowel wall inflammation.

Pneumatosis cystoides intestinalis is typically characterized by colonic wall gas without bowel ischemia. Pneumatosis intestinalis with cystic appearance is more likely to be due to benign cause. Pneumatosis with linear collection of air in the bowel wall is more likely to be associated with bowel ischemia and higher mortality [29]. Unlike with bowel wall ischemia, pneumatosis cystoides intestinalis does not demonstrate gas in the portal venous system.

Benign Causes of Pneumatosis Intestinalis

1. Idiopathic.
2. Mucosal injury (including from bowel obstruction, diverticulitis, inflammatory bowel disease, corrosive ingestion, G-/J-tube placement, and recent bowel wall biopsy).
3. Steroids.
4. Emphysema.

Fig. 4.10 Portal vein and superior mesenteric venous air in bowel infarction. (**a**) Noncontrast CT shows extensive air in portal vein branches (*curved arrows*). (**b**) Contrast-enhanced CT shows air in a superior mesenteric vein tributary (*arrowhead*), in a patient with bowel ischemia and portal vein gas

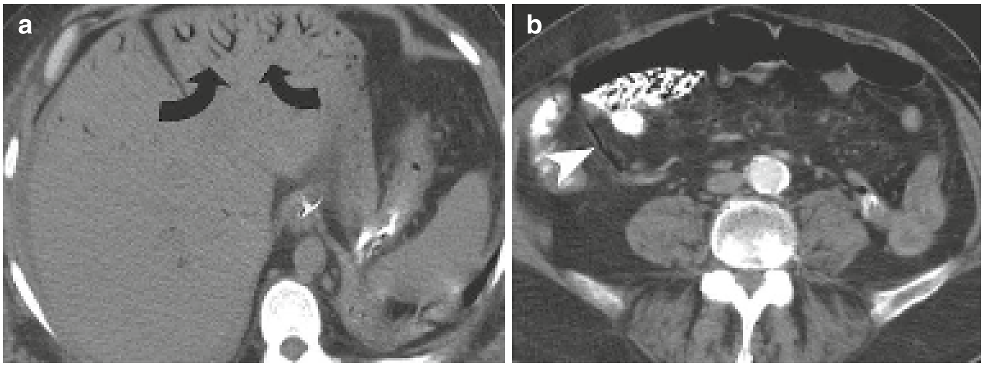

5. Collagen vascular disease (scleroderma, SLE, PAN, polymyositis, etc.).
6. Organ transplantation.
7. AIDS.

Portal Venous Gas

Although portal venous gas is often seen in patients with transmural infarction of the bowel, it can also be seen with bowel obstruction, inflammatory bowel disease, steroid use, diverticulitis, emphysema, and organ transplantation. In patients with pneumatosis intestinalis, portal venous gas is present in 25% cases and often indicates irreversible bowel wall infarction [29]. On CT, the portal venous gas is seen as branched air lucencies present peripherally in the liver. Biliary air is typically present more centrally in the liver due to the direction of flow of bile toward the porta hepatis (Figs. 4.11 and 4.12). Mesenteric venous gas is typically seen as linear or branched lucencies present adjacent to the mesenteric border of the bowel. On ultrasound study, portal vein gas can be seen as echogenic series of gas bubbles, resembling a string of pearls. Treatment is not necessarily surgery and depends on the underlying disease.

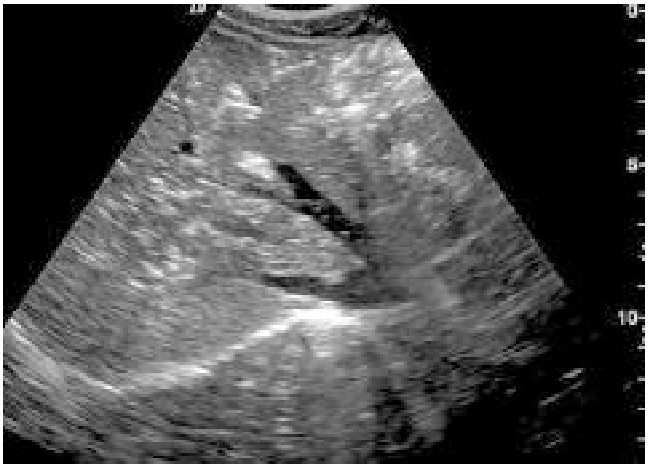

Fig. 4.11 Ultrasonographic appearance of air in the portal vein. Ultrasound shows portal venous hyperechoic foci of air seen peripherally as well as centrally in the liver

Bowel Perforation

Free air in the abdomen is most commonly seen after surgery, G-tube placement, and bowel perforation. Postoperative air progressively decreases with time and usually resolves by the seventh day. It usually takes longer time for air to resolve in asthenic patients [30]. Free air secondary to bowel perforation is most commonly due to perforated peptic ulcer and less commonly due to perforated diverticulitis, small bowel obstruction, esophageal perforation, and appendicitis (Figs. 4.13, 4.14 and 4.15).

On upright abdominal radiographs, free air is most commonly seen under the domes of the diaphragm. On decubitus film of the abdomen, free air is seen in the nondependent abdomen, adjacent to the right hepatic margin. Supine radiograph of the abdomen has a sensitivity of 56–59% in patients with known free air [31, 32].

- **Right upper quadrant gas sign**: The presence of gas in the right upper quadrant constitutes a right upper quadrant gas sign and is the most common sign of free air on supine radiograph, seen in 41% cases [32]. It is typically seen in triangular or linear configuration.
- **Ligamentum teres sign**: On supine plain radiograph of the abdomen, the falciform ligament may be outlined by air and typically extends from right upper quadrant and pointing caudally to the left lower quadrant. This is known as ligamentum teres sign and is typically seen on supine radiograph of the abdomen. The presence of air in the fissure for ligamentum teres has been described as a new sign of intraperitoneal air [33].

Fig. 4.12 Pneumobilia. (**a**) Plain radiograph of the abdomen shows centrally located air lucency in the common bile duct (*arrowhead*). (**b**) Ultrasound shows centrally located intrahepatic biliary ductal air (*arrows*)

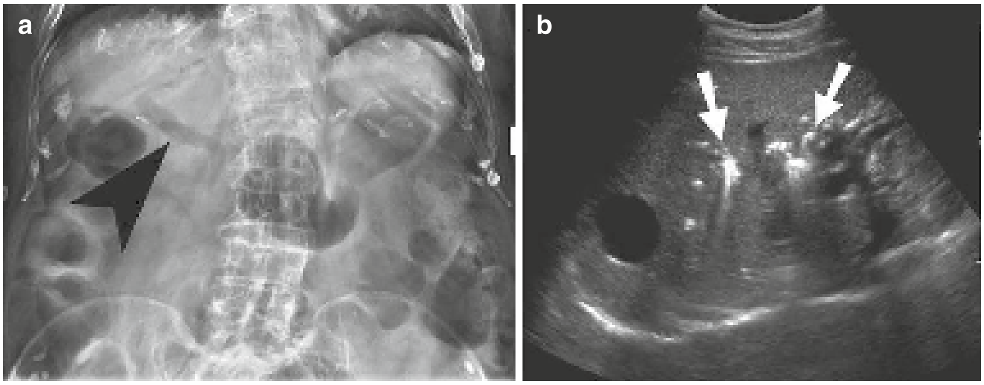

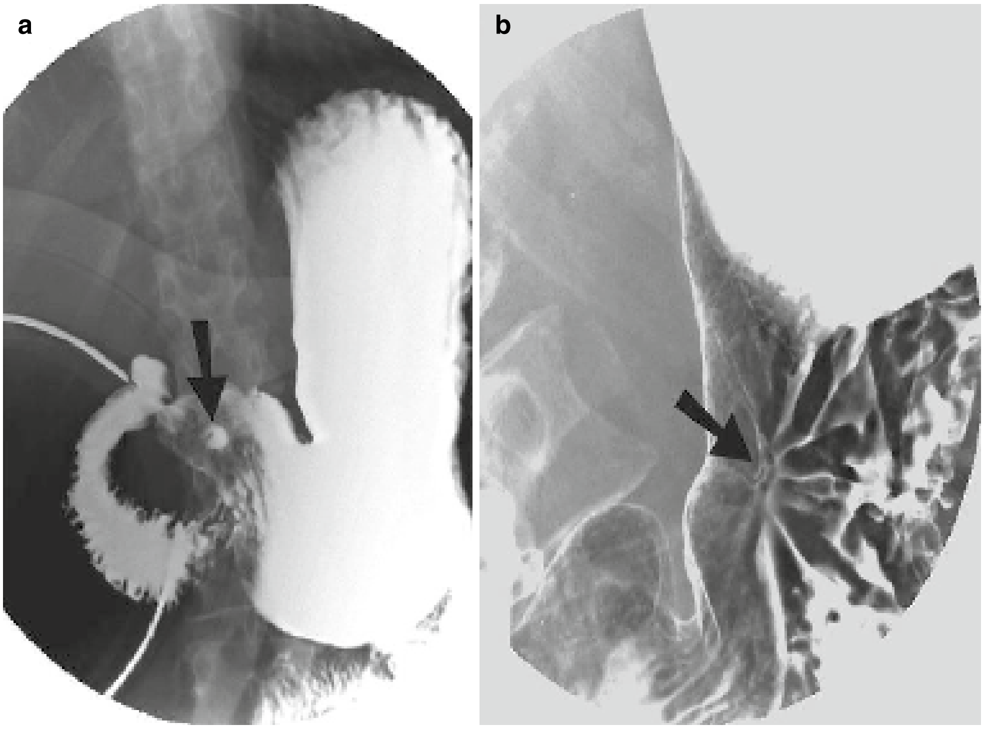

Fig. 4.13 Peptic ulcer disease. (**a**) Upper GI study demonstrates en face appearance of centrally radiopaque barium in the gastric ulcer crater (*arrow*), surrounded by a symmetric ulcer collar. (**b**) Upper GI study demonstrates smooth mucosal folds, radiating to the edge of a healing benign ulcer (*arrow*), a finding which is pathognomonic of a benign peptic ulcer

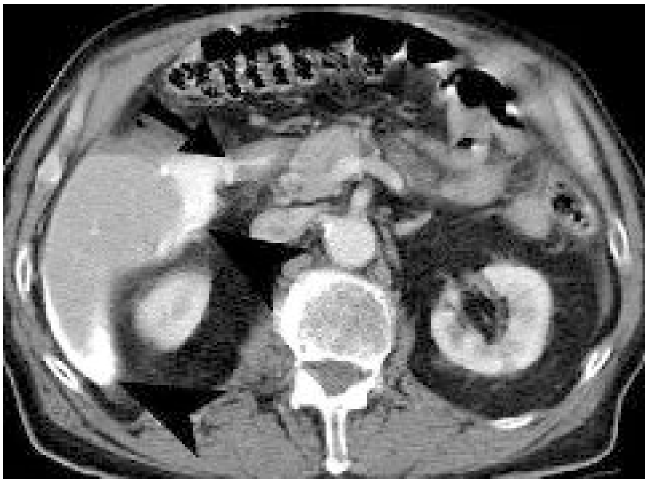

Fig. 4.14 Peptic ulcer disease with perforation. Contrast-enhanced CT shows the breech in the duodenal wall (*arrow*) with oral contrast leaking into the Morison's pouch (*arrowheads*)

- **Rigler's sign**: The second (32%) most commonly seen sign on the supine radiograph is the presence of air on either side of the bowel loops and constitutes the Rigler's sign, typically seen with large amount of free air (Figs. 4.16 and 4.17).
- **Triangle sign**: The presence of a triangular configuration of air located between three loops of bowel constitutes the triangle sign.
- **Cupola sign**: Cupola sign refers to inverted cup-shaped lucency present under the central tendon of the diaphragm, on the supine film of the abdomen (Fig. 4.18a).
- **Football sign**: When large amount of air is present on the supine radiograph of the abdomen, it can be seen as a large oval lucency on the supine radiograph of the abdomen, which is called football sign (Fig. 4.18b).

Fig. 4.15 Esophageal perforation. (**a**) Esophagram demonstrates perforation (*curved arrow*) arising from posterior esophageal wall. There is a tight stricture (*arrowhead*) present in the distal esophagus with food residue present just proximal to it. (**b**) Esophagram demonstrates esophageal perforation (*arrows*) caused by swallowed dentures

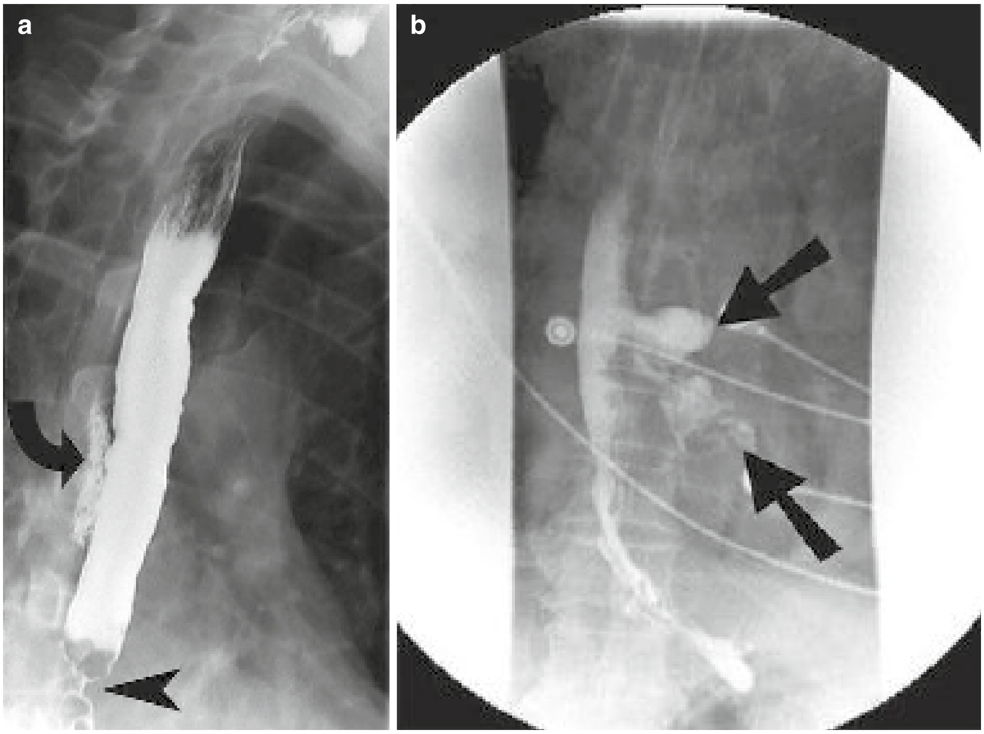

Fig. 4.16 Pneumoperitoneum: Rigler's sign. (**a**, **b**) Supine radiograph (**a**) and lateral CT scout film (**b**) demonstrate inner as well as outer wall of multiple small bowel loops (*arrowheads*). (**c**) Coronal CT reformation demonstrates large amount of free air (*arrows*) outlining the outer bowel wall margins

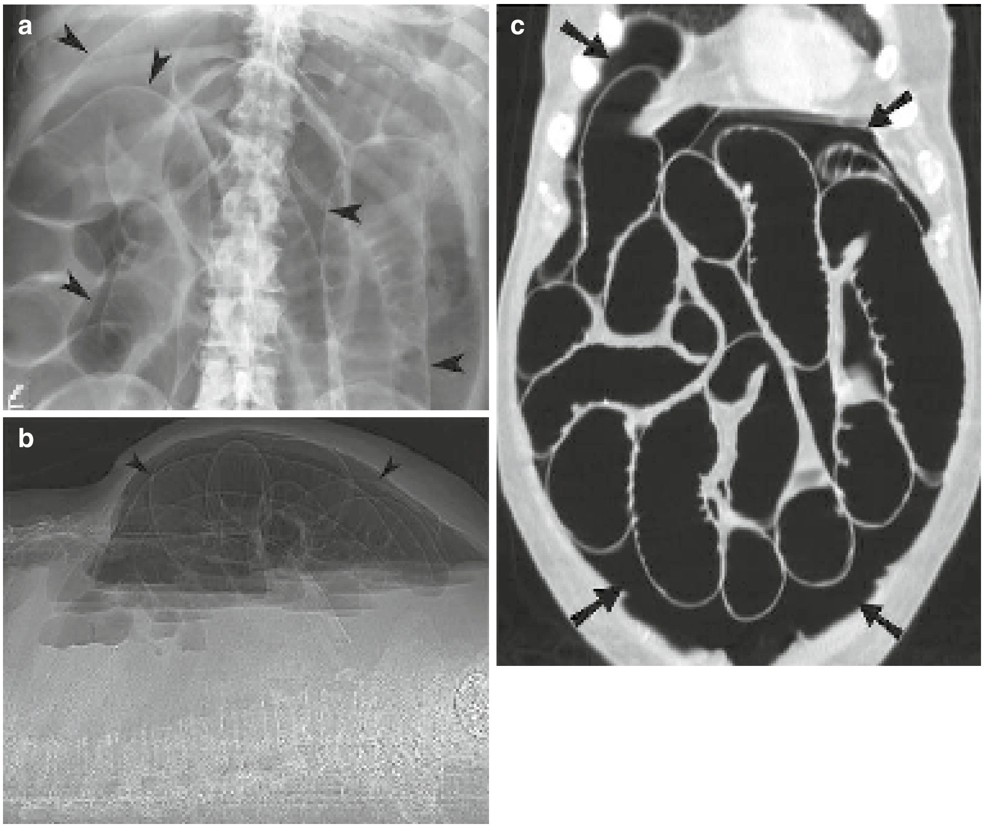

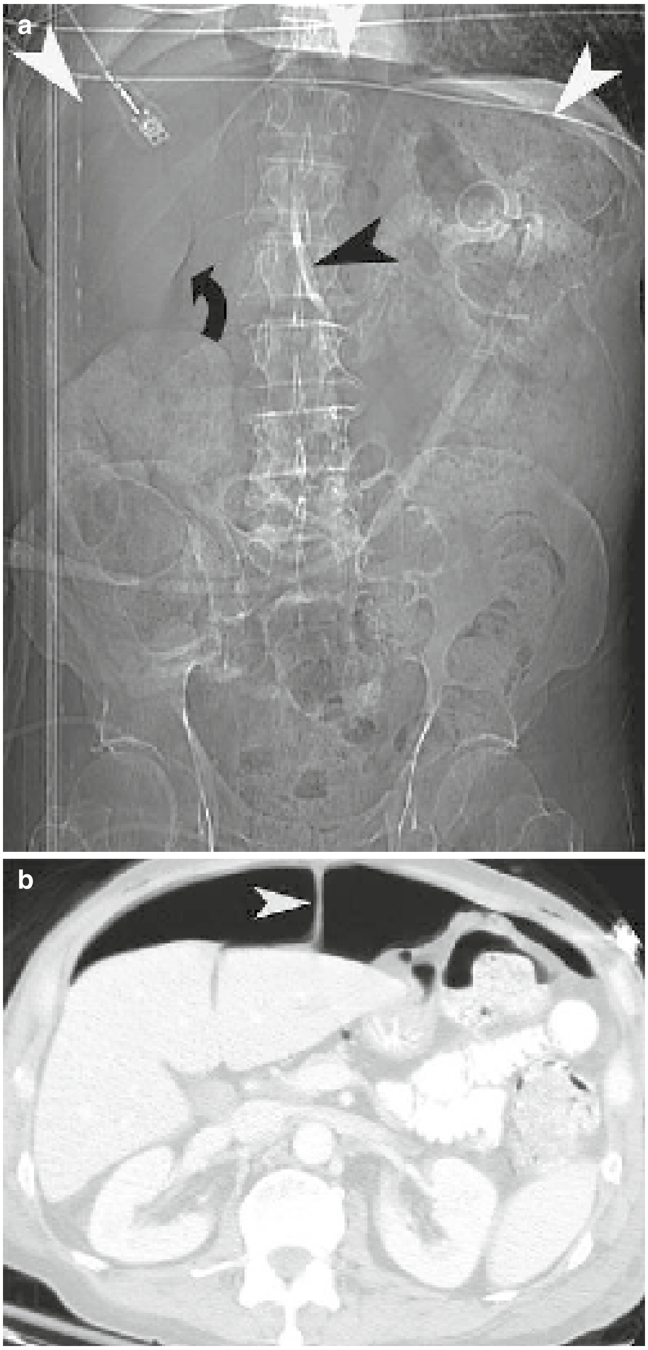

Fig. 4.17 Pneumoperitoneum: ligamentum teres sign. (**a**) Scout film of the abdomen demonstrates large amount of free air (*white arrowheads*) in the abdomen. The air is seen to outline the ligamentum teres (*black arrowhead*) as well as the undersurface (*curved arrow*) of the right lobe of the liver. (**b**) Axial CT image also demonstrates the large amount of nondependent air in the abdomen, outlining the ligamentum teres (*white arrow*)

- **Inverted v-sign**: Visualization of medial umbilical ligaments produces inverted v-sign, which is appreciated when air is present in the nondependent part of the pelvis. It is constituted by two pairs of folds: medial umbilical folds (obliterated umbilical arteries) and lateral umbilical folds (containing inferior epigastric vessels).
- **Doge's cap sign**: Doge's cap sign is produced by the presence of air in the Morison's pouch.
- **Diaphragm muscle slip sign**: This sign is produced by air outlining the undersurface of the diaphragmatic muscles.

CT is more sensitive than plain radiograph in detecting free air, which typically accumulates in the nondependent abdomen, deep to the anterior abdominal wall. Small foci of free air can often be seen between the left lobe of the liver and the rectus abdominus. In addition to extraluminal air being a highly specific finding for perforation, its location can help identify the site of perforation. Exclusive involvement of supramesocolic and inframesocolic regions suggests large bowel source, whereas presence of free air only near liver and stomach suggests upper GI source. Other CT findings include bowel wall thickening, discontinuity of the bowel wall, and presence of extraluminal contrast. Contained perforation can be a diagnostic challenge since it often does not present with pneumoperitoneum and its diagnosis depends on detection of extraluminal fecal content.

Retroperitoneal air is often caused by duodenal or rectal perforation. Unlike free air, retroperitoneal air often outlines the kidneys and/or psoas major muscles (Fig. 4.19). Also, the retroperitoneal air is less likely to change position between supine and upright films of the abdomen than free intraperitoneal air.

Infection

Although infectious enteritis is a common cause of acute diarrheal illness in the USA, it is not usually an imaging diagnosis. Most cases of acute diarrheal illness (defined as less than 14 days in duration) in adults are due to viruses, bacteria, or less commonly protozoa. Patients are managed clinically with supportive therapy, and the illness is usually self-limited. Imaging may be indicated for chronic (>30 days' duration) diarrheal illness when inflammatory bowel disease is suspected or in the setting of acute disease in an immunocompromised patient.

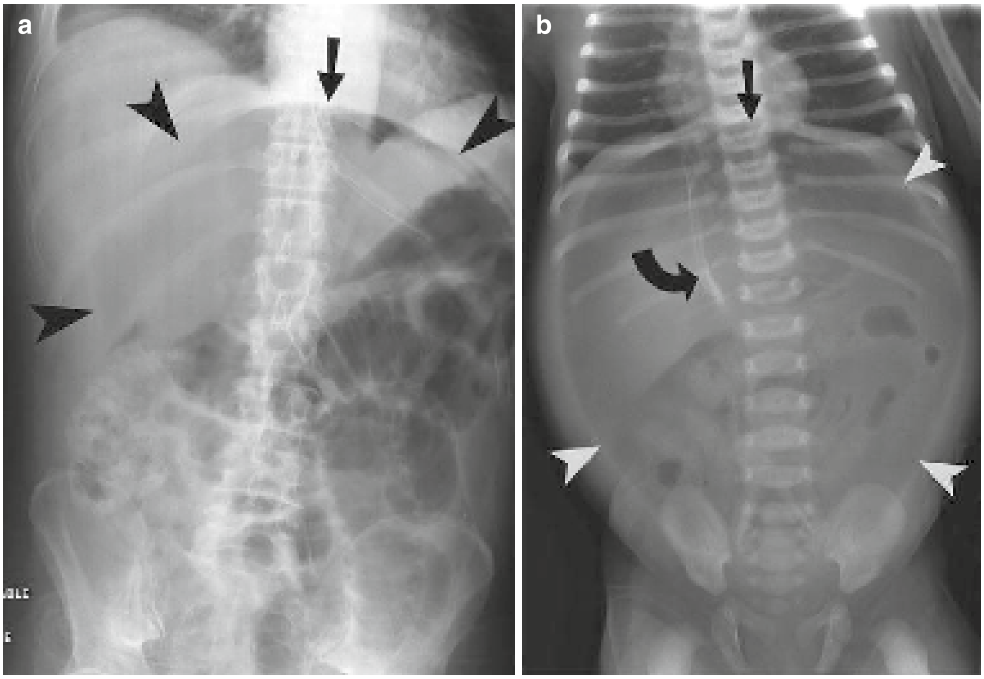

Fig. 4.18 Pneumoperitoneum: cupola sign and football sign. (**a**, **b**) Plain radiographs of the abdomen demonstrate large oval lucency (football sign, *arrowheads*) and inverted cup-shaped lucency (cupola sign, *arrow*), secondary to the free air. Ligamentum teres sign (*curved arrow*) is seen in the right upper quadrant as a sickle-shaped density outlined by air on either side

Nevertheless, infectious enteritis may be present when imaging is performed for a different suspected diagnosis, such as appendicitis or diverticulitis. Findings of infectious enteritis on CT are fairly nonspecific, with diffuse bowel wall thickening and mesenteric lymphadenopathy being the most common manifestations [34]. The proximal small bowel is the typical site of infection by Giardia lamblia, the most common parasite to cause infection in the United States. Infectious enteritis affecting the distal ileum, often in combination with the cecum, can cause a confusing clinical picture, mimicking appendicitis. Frequent pathogens causing an infectious ileocolitis include Salmonella, Yersinia, Shigella, and Campylobacter [35, 36]. *Clostridium difficile* or pseudomembranous colitis is generally self-limited and does not require imaging. On CT, findings may include wall thickening, pneumatosis, and/or portal venous gas due to loss of mucosal integrity (and not ischemia). Accordion sign may help distinguish *C. difficile* colitis from other types of colitides. Accordion sign in CT shows thickened haustral folds, with trapped oral contrast agent or bowel contents between the folds in a parallel fashion. *Clostridium difficile* colitis may develop toxic megacolon.

The clinical presentation of Campylobacter in particular may mimic that of acute appendicitis, thereby prompting CT or ultrasound imaging. The mesenteric adenitis present with this infection may be accompanied by acute inflammation of the terminal ileum, as well as an “endoappendicitis,” that is, confined to the mucosal layer and visible only microscopically. Imaging manifestations include mural thickening of the terminal ileum and cecum as well as enlarged mesenteric lymph nodes (Fig. 4.20) [37].

Important causes of enteritis in patients with HIV infection include Mycobacterium avium-intracellulare (MAI), Cytomegalovirus, and Cryptosporidium. MAI more frequently affects the jejunum, causing bowel wall thickening that can be nodular. The finding of low-density, bulky mesenteric and retroperitoneal lymphadenopathy is helpful in suggesting the diagnosis, although Whipple disease and lymphoma can have the same appearance. Cytomegalovirus enteritis is often hemorrhagic, secondary to mucosal ulcerations, which can sometimes be seen on CT. Cryptosporidium infection results in bowel wall thickening, also typically involving the proximal small bowel that can be indistinguishable from MAI and giardiasis [38].

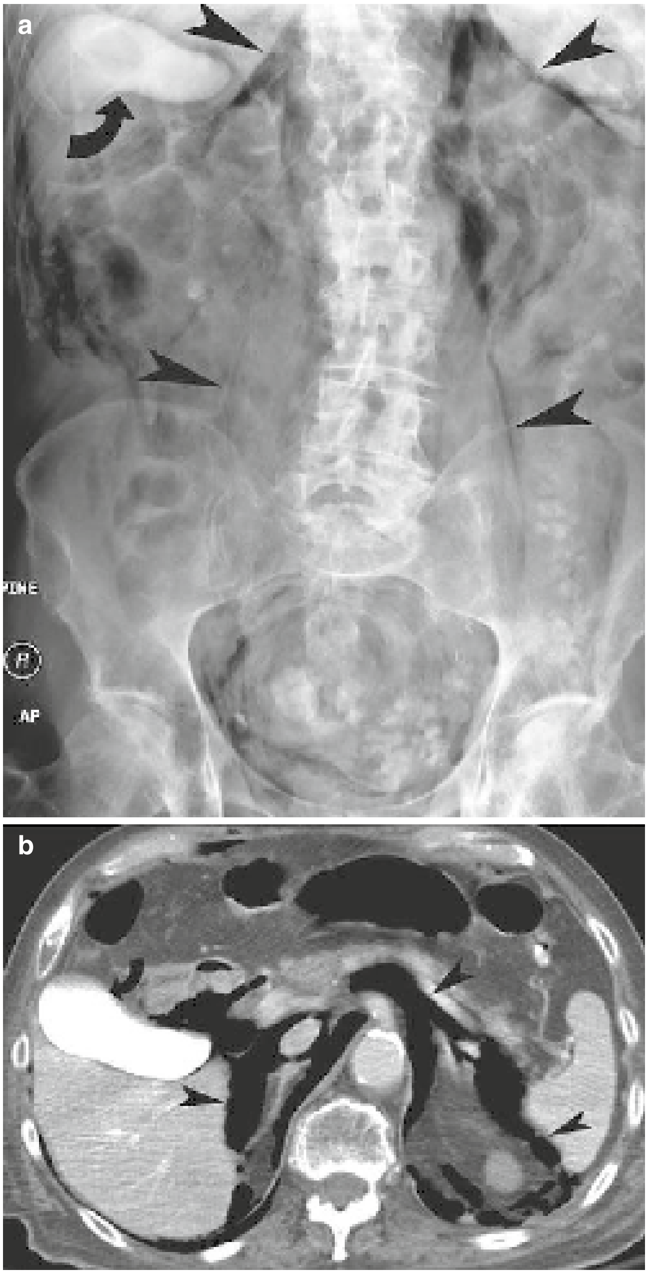

Fig. 4.19 Retroperitoneal air from perforation of the second portion of the duodenum during an ERCP study. (**a**) Plain radiograph of the abdomen demonstrates retroperitoneal air (*arrowheads*) outlining the kidneys and psoas muscles. The contrast in the gallbladder (*curved arrow*) is from the recent ERCP study. (**b**) Contrast-enhanced CT demonstrates the retroperitoneal air (*arrowheads*) and the contrast in the gallbladder (*curved arrow*)

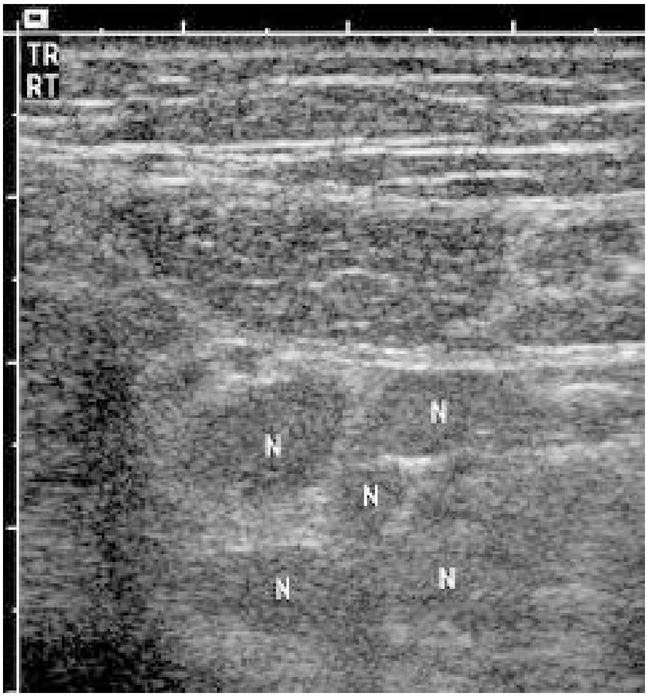

Fig. 4.20 Campylobacter ileocolitis. Ultrasound imaging demonstrates reactive mesenteric lymphadenopathy (*N*) in the right lower quadrant, in a patient with Campylobacter ileocolitis

Teaching Points

- Although less frequent than duodenal diverticula, jejunoileal diverticula are more prone to develop complications.
- Acquired small bowel diverticula are typically located on the mesenteric border of the bowel.
- Diverticula in the small bowel are less likely to develop inflammation than those in the colon.
- CT findings of small bowel diverticulitis include focal inflammatory mass containing air, fluid, or an air-fluid level adjacent to a segment of thickened small bowel, with the presence of surrounding inflammation and mesenteric fat stranding.
- Congenital diverticula (true diverticula) have three layers while acquired diverticula have two layers.
- CT findings of small bowel ischemia include SMA/SMV thrombus, bowel distension, wall thickening, lack of enhancement, pneumatosis, ascites, and portal or mesenteric vein gas.

- Pneumatosis intestinalis with linear appearance is more likely to be secondary to bowel ischemia.
- Infectious enteritis has nonspecific imaging findings. The most common manifestations are diffuse bowel wall thickening and mesenteric lymphadenopathy.

Questions

1. Which of the following is a common finding seen in the CT in patients with small bowel diverticulitis?
   (A) Asymmetrically thickened small bowel wall
   (B) Ascites
   (C) Portal venous gas
   (D) Accordion sign
   Answer: A
2. "Doge's cap sign" is produced by which of the following?
   (A) Air outlining the undersurface of the diaphragm
   (B) Air in the Morison's pouch
   (C) Portal venous gas
   (D) Air in the bowel wall
   Answer: B
3. Which of the following is most commonly seen in early phase of arterial SMA occlusion?
   (A) Decreased peristalsis
   (B) Intramural gas
   (C) Fluid-filled loops
   (D) Bowel spasm
   Answer: D
4. Parallel oral contrast with thickened colonic wall is seen in which of the following?
   (A) Campylobacter infection
   (B) Mycobacterium avium-intracellulare infection
   (C) Clostridium difficile infection
   (D) Small bowel ischemia
   Answer: C
5. The following plain radiograph (Fig. 4.21) demonstrates which sign?
   (A) Football sign
   (B) Rigler's sign
   (C) Triangle sign
   (D) Cupola sign
   (E) Inverted v-sign
   Answer: A

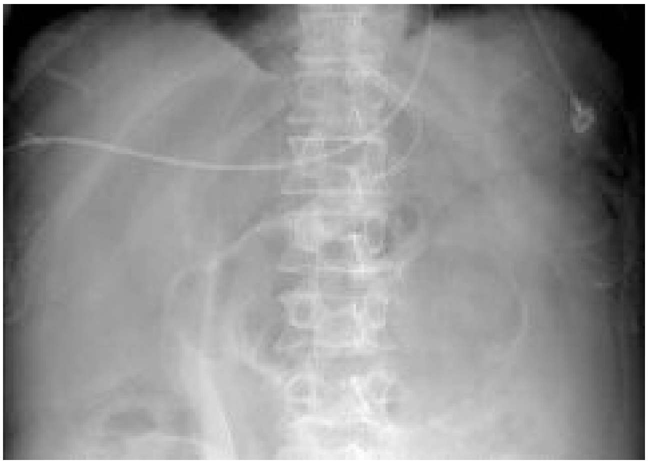

Fig. 4.21 Football sign—radiograph

6. Which sign is well demonstrated on the coronal CT reformation (Fig. 4.22)?
   (A) Ligamentum teres sign
   (B) Rigler's sign
   (C) Triangle sign
   (D) Cupola sign
   (E) Inverted v-sign
   Answer: D
7. Which imaging finding is seen in the following plain radiograph (Fig. 4.23)?
   (A) Portal vein gas
   (B) Continuous diaphragm sign
   (C) Superior mesenteric gas
   (D) Cupola sign
   Answer: B
8. The following plain radiograph (Fig. 4.24) demonstrates which sign?
   (A) Football sign
   (B) Cupola sign
   (C) Doge's cap sign
   (D) Rigler's sign
   Answer: D

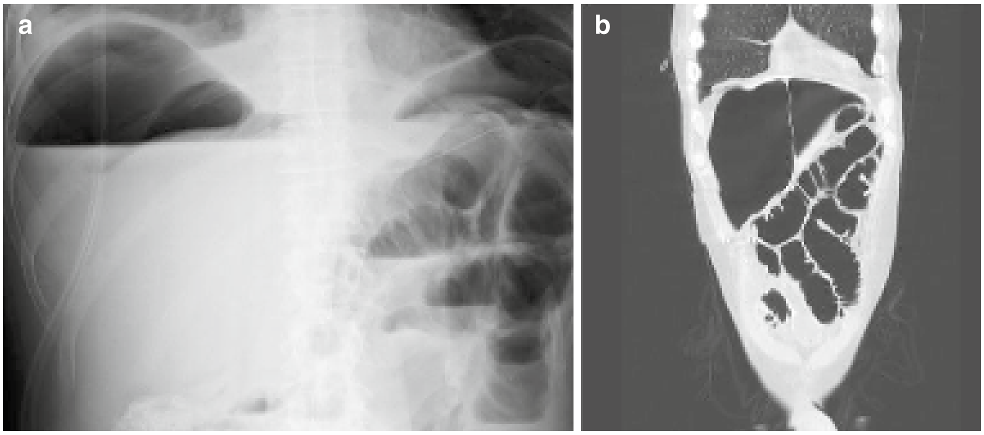

Fig. 4.22 (**a**) Plain radiograph and (**b**) Coronal CT showing Cupola sign

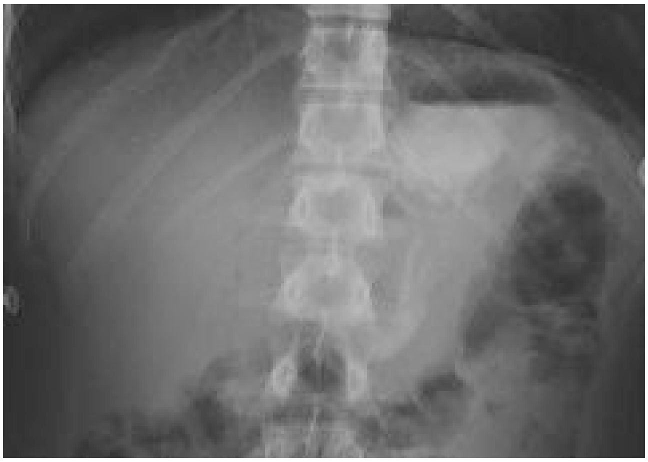

Fig. 4.23 Continuous diaphragm sign

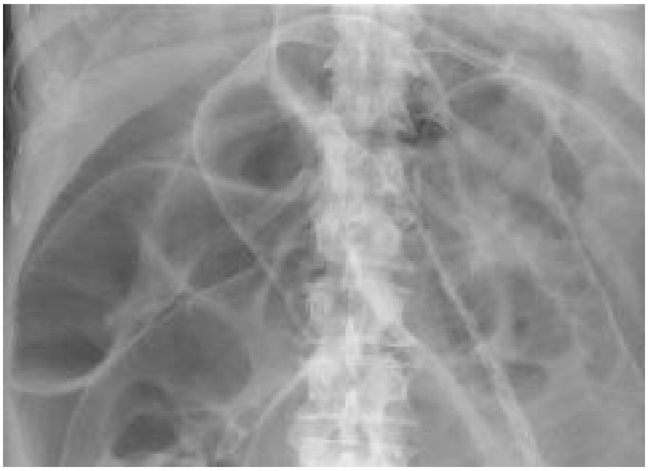

Fig. 4.24 Rigler's sign—radiograph

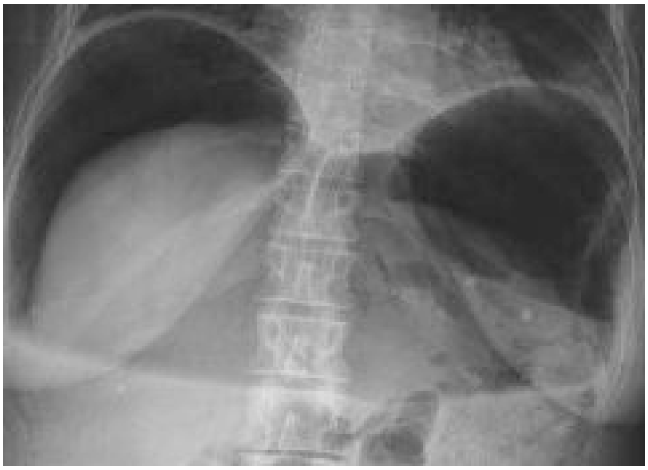

Fig. 4.25 Pneumoperitoneum—radiograph

9. What is the most clinically relevant imaging finding on the following plain radiograph (Fig. 4.25)?
   (A) Pneumoperitoneum
   (B) Pneumothorax
   (C) Bowel obstruction
   (D) Ileus
   Answer: A

10. What is the location of the abnormal air collection on the plain radiograph (Fig. 4.26)?
   (A) Intraperitoneal
   (B) Retroperitoneal
   (C) Pleural
   (D) Intramural
   Answer: B

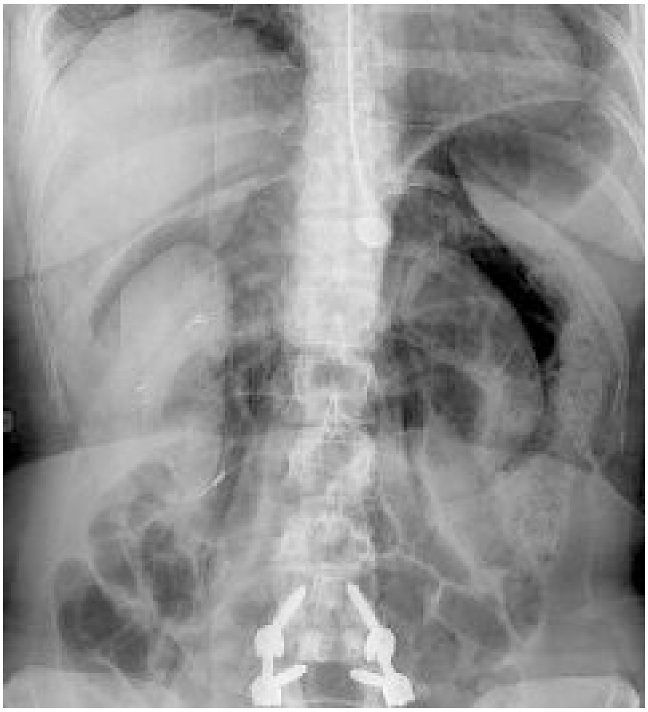

Fig. 4.26 Retroperitoneal—radiograph

References

1. Akhrass R, Yaffe MB, Fischer C, Ponsky J, Shuck JM. Small-bowel diverticulosis: perceptions and reality. J Am Coll Surg. 1997;184(4):383–8.
2. Coulier B, Maldague P, Bourgeois A, Broze B. Diverticulitis of the small bowel: CT diagnosis. Abdom Imaging. 2007;32(2):228–33.
3. Macari M, Faust M, Liang H, Pachter HL. CT of jejunal diverticulitis: imaging findings, differential diagnosis, and clinical management. Clin Radiol. 2007;62(1):73–7.
4. Lempinen M, Salmela K, Kemppainen E. Jejunal diverticulosis: a potentially dangerous entity. Scand J Gastroenterol. 2004;39(9):905–9.
5. Afridi SA, Fichtenbaum CJ, Taubin H. Review of duodenal diverticula. Am J Gastroenterol. 1991;86(8):935–8.
6. Yin WY, Chen HT, Huang SM, Lin HH, Chang TM. Clinical analysis and literature review of massive duodenal diverticular bleeding. World J Surg. 2001;25(7):848–55.
7. Maglinte DD, Chernish SM, DeWeese R, Kelvin FM, Brunelle RL. Acquired jejunoileal diverticular disease: subject review. Radiology. 1986;158(3):577–80.
8. Chendrasekhar A, Timberlake GA. Perforated jejunal diverticula: an analysis of reported cases. Am Surg. 1995;61(11):984–8.
9. Gotian A, Katz S. Jejunal diverticulitis with localized perforation and intramesenteric abscess. Am J Gastroenterol. 1998;93(7):1173–5.
10. Krishnamurthy S, Kelly MM, Rohrmann CA, Schuffler MD. Jejunal diverticulosis. A heterogenous disorder caused by a variety of abnormalities of smooth muscle or myenteric plexus. Gastroenterology. 1983;85(3):538–47.
11. Vijayaraghavan SB, Krishnaraj B, Sarveswaran V. Sonographic features of mesenteric gas. J Ultrasound Med. 2004;23(11):1507–10.
12. Peters R, Grust A, Gerharz CD, Dumon C, Furst G. Perforated jejunal diverticulitis as a rare cause of acute abdomen. Eur Radiol. 1999;9(7):1426–8.
13. Tsiotos GG, Farnell MB, Ilstrup DM. Nonmeckelian jejunal or ileal diverticulosis: an analysis of 112 cases. Surgery. 1994;116(4):726–31.
14. Pearl MS, Hill MC, Zeman RK. CT findings in duodenal diverticulitis. AJR Am J Roentgenol. 2006;187(4):W392–5.
15. Koger KE, Shatney CH, Dirbas FM, McClenathan JH. Perforated jejunal diverticula. Am Surg. 1996;62(1):26–9.
16. Williams RA, Davidson DD, Serota AI, Wilson SE. Surgical problems of diverticula of the small intestine. Surg Gynecol Obstet. 1981;152(5):621–6.
17. Kubota T. Perforated jejunal diverticulitis. Am J Surg. 2007;193(4):486–7.
18. Novak JS, Tobias J, Barkin JS. Nonsurgical management of acute jejunal diverticulitis: a review. Am J Gastroenterol. 1997;92(10):1929–31.
19. Prakash C, Clouse RE. Acute ileal diverticulitis. Am J Gastroenterol. 1998;93(3):452–4.
20. Franzen D, Gurtler T, Metzger U. Multiple recurrent perforated jejunal diverticulitis. Chirurg. 2002;73(12):1218–20.
21. Singh A, Raman S, Brooks C, Philips D, Desai R, Kandarpa K. Giant colonic diverticulum: percutaneous CT-guided treatment. J Comput Assist Tomogr. 2008;32(2):204–6.
22. Elsayes KM, Menias C, Harvin HJ, Francis IR. Imaging manifestations of Meckel's diverticulum. AJR Am J Roentgenol. 2007;189:81–8.
23. Levy AD, Hobbs CM. Meckel diverticulum: radiologic features with pathologic correlation. Radiographics. 2004;24:565–87.
24. Wilcox RD, Shatney CH. Surgical implications of jejunal diverticula. S Med J. 1988;81(11):1386–91.
25. Cross MJ, Snyder SK. Laparoscopic-directed small bowel resection for jejunal diverticulitis with perforation. J Laparoendosc Surg. 1993;3(1):47–9.
26. Trompeter M, Brazda T, Remy CT, Vestring T, Reimer P. Non-occlusive mesenteric ischemia: etiology, diagnosis, and interventional therapy. Eur Radiol. 2002;12:1179–87.
27. Menke J. Diagnostic accuracy of multidetector CT in acute mesenteric ischemia: systematic review and meta-analysis. Radiology. 2010;256(1):93–101.
28. Kirkpatrick ID, Kroeker MA, Greenberg HM. Biphasic CT with mesenteric CT angiography in the evaluation of acute mesenteric ischemia: initial experience. Radiology. 2003;229(1):91–8.
29. Lassandro F, di Santo Stefano MLM, Maria Porto A, Grassi R, Rotondo A, Scaglione M. Intestinal pneumatosis in adults: diagnostic and prognostic value. Emerg Radiol. 2010;17:361–5.
30. Felson B, Wiot JF. Another look at pneumoperitoneum. Semin Roentgenol. 1973;8:437–43.
31. Menuck L, Siemens PT. Pneumoperitoneum: importance of right upper quadrant features. AJR Am J Roentgenol. 1976;127:753–6.
32. Levine MS, Scheiner JD, Rubesin SE, Laufer I, Herlinger H. Diagnosis of pneumoperitoneum on supine abdominal radiographs. AJR Am J Roentgenol. 1991;156:731–5.
33. Cho KC, Baker SR. Air in the fissure for the ligamentum teres: new sign of intraperitoneal air on plain radiographs. Radiology. 1991;178:489–92.
34. Orchard JL, Petorak V. Abnormal abdominal CT findings in a patient with giardiasis. Resolution after treatment. Dig Dis Sci. 1995;40:346–8.

35. Puylaert JBCM, Van der Zant FM, Mutsaers JA. Infectious ileocecitis caused by Yersinia, Campylobacter, and Salmonella: clinical, radiological and US findings. Eur Radiol. 1997;7:3–9.
36. Antonopoulos P, Constantinidis F, Charalampopoulos G, Dalamarinis K, Karanicas I, Kokkini G. An emergency diagnostic dilemma: a case of *Yersinia enterocolitica* colitis mimicking acute appendicitis in a beta-thalassemia major patient: the role of CT and literature review. Emerg Radiol. 2008;15:123–6.
37. Puylaert JBCM, Lalisang RI, van der Werf SDJ, Doornbos L. Campylobacter ileocolitis mimicking acute appendicitis: differentiation of graded-compression ultrasound. Radiology. 1988;166:737–40.
38. Horton KM, Corl FM, Fishman EK. CT of nonneoplastic diseases of the small bowel: spectrum of disease. J Comput Assist Tomogr. 1999;23:417–28.

Imaging of Bowel Obstruction

5

Ajay Singh, Khyati Bidani, and Mohammad Mansouri

Small Bowel Obstruction

Small bowel obstruction is the most common disorder of the small bowel which requires hospital admission and surgical intervention. Small bowel obstruction leads to a progressive increase in the intraluminal pressure which can exceed the venous pressure and result in bowel ischemia.

The most common cause of small bowel obstruction which accounts for 60–80% cases is adhesions [1, 2]. These adhesions are most commonly due to prior surgery and less commonly due to peritonitis. Adhesions are characterized by demonstration of transition point without surrounding inflammation in a patient with prior history of abdominal or pelvic surgery.

The plain radiographic findings of small bowel obstruction include multiple air-fluid levels (>2) and dilated small bowel loops (>3 cm). More than two air-fluid levels greater than 3 cm in diameter or more than one air-fluid level in the same dilated small bowel loop are considered abnormal (Fig. 5.1a, b). String of pearl sign is seen on upright film of the abdomen in patients with small bowel obstruction and is characterized by nondependent small air bubbles located in valvulae conniventes. Plain radiography has frequently underdiagnosed or overdiagnosed small bowel obstruction. Small bowel follow-through has fallen out of favor due to the accuracy of CT scan and can be used selectively when the CT findings are equivocal (Fig. 5.1c).

CT scan has higher sensitivity (90%) than plain radiograph in making the diagnosis of small bowel obstruction and is considered the most appropriate imaging modality in diagnosing high-grade small bowel obstruction. The CT should be performed with intravenous contrast, but without oral contrast. CT enteroclysis and MR enteroclysis are both equally appropriate, first-line imaging modalities in diagnosing low-grade or intermittent small bowel obstruction. In pregnant women or children, ultrasonography and MRI are alternative imaging modalities.

CT study in patients with small bowel obstruction is characterized by small bowel loops more than 2.5 cm in caliber, transition point, and decompressed bowel loops beyond the transition zone. Although the adhesion band itself is rarely visible, the presence of a smooth transition zone often points to adhesions as the cause of the bowel obstruction. Other findings suggestive of adhesions include acute angulation of the bowel, focal crowding of bowel loops known as “matted bowel” (seen with enteroenteric or intraloop adhesions), fixed position of bowel segment on successive scans (Fig. 5.2), focal peritoneal thickening, focally increased mesenteric attenuation, vascular crowding, small bowel fecalization, fat notch sign (insinuation of mesenteric fat at the junction of dilated and non-dilated bowel loop) (Fig. 5.2), and beak sign (abrupt tapering of the bowel loop). Presence of pneumatosis on CT suggests breakdown in the mucosal integrity and ischemia. Intraperitoneal or portomesenteric gas may be seen in advanced, irreversible bowel ischemia.

Small bowel feces sign is characterized by the presence of fecal material along with air bubbles in dilated small bowel loops and is believed to be due to bacterial overgrowth and water resorption from incompletely digested food [3, 4]

A. Singh (✉)
Division of Emergency Radiology, Department of Radiology, Massachusetts General Hospital, Boston, MA, USA

Harvard Medical School, Massachusetts General Hospital, Boston, MA, USA
e-mail: asingh1@partners.org

K. Bidani · M. Mansouri
Department of Radiology, Massachusetts General Hospital, Boston, MA, USA

© The Author(s), under exclusive license to Springer Nature Switzerland AG 2024
A. Singh (ed.), *Emergency Radiology*, https://doi.org/10.1007/978-3-031-65770-2_5

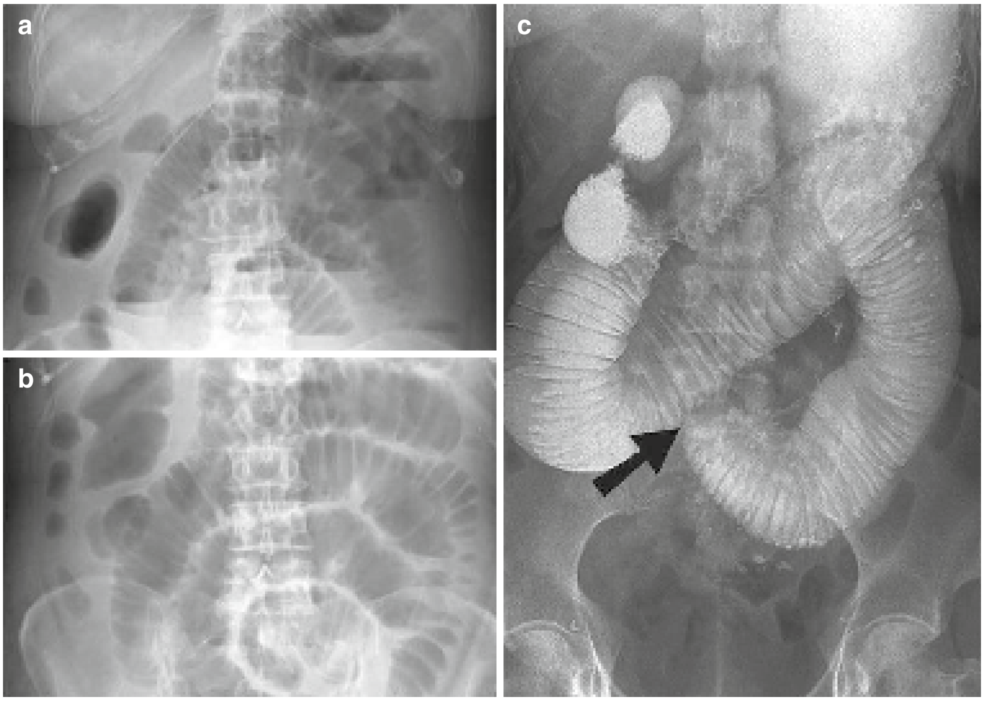

Fig. 5.1 Radiographic findings of small bowel obstruction. (**a**, **b**) Upright plain radiograph of the abdomen demonstrates dilated small bowel loops with differential air-fluid levels in a patient with high-grade obstruction. (**c**) Small bowel follow-through demonstrates dilated small bowel loops with abrupt transition in the mid-jejunum (*arrow*)

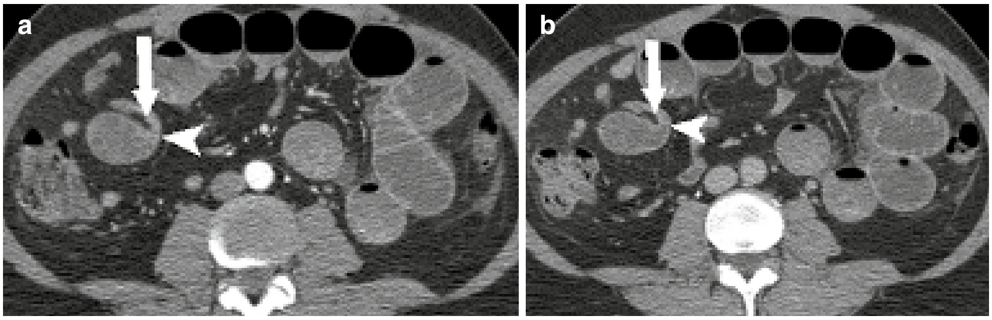

Fig. 5.2 Small bowel obstruction due to adhesions. (**a**, **b**) Contrast-enhanced CT of the abdomen in arterial and portal venous phase demonstrates persistent sudden Caliber change (arrowhead) at the site of partial small obstruction. Fat insinuation at the site of transition between dilated and non-dilated small bowel is described as the fat notch sign (arrow)

(Fig. 5.3). It is an indicator of the site of mechanical small bowel obstruction and points to the low-grade or subacute small bowel obstruction. It is present in longer segment of small bowel in patients with higher-grade obstruction and is useful in recognizing the transition point due to its close proximity. This sign has been reported in 7–82% cases of small bowel obstruction and should not be mistaken for fecal material which can be normally present in terminal ileum in patients with incompetent ileocecal valve [5]. Fecal material can also be in small bowel in patients with cystic fibrosis, with bezoars, and with infectious and metabolic bowel disease. Summary of imaging findings in small bowel obstruction are listed in Table 5.1.

The other findings of small bowel obstruction include mesenteric edema, ascites, mesenteric venous congestion, decreased bowel wall enhancement, and free extraluminal air (Table 5.2).

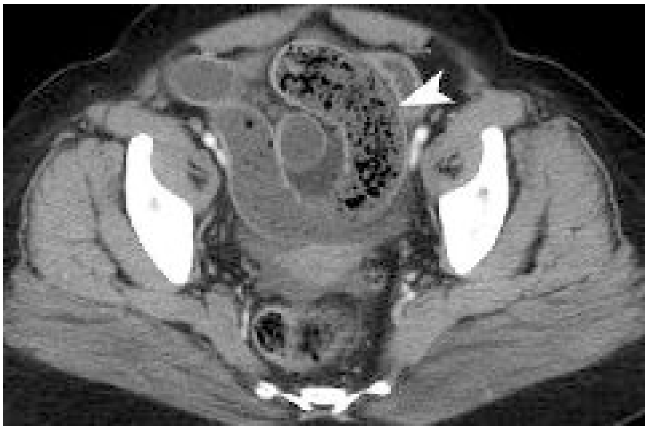

Fig. 5.3 Small bowel obstruction on CT. Contrast-enhanced CT study in a patient with small bowel obstruction demonstrates dilated small bowel loops with small bowel feces sign (*arrowhead*)

Table 5.1 Plain radiography and CT findings in small bowel obstruction

Multiple air-fluid levels (>2) and dilated small bowel loops (>3 cm) in plain radiography Small bowel loops >2.5 cm in CT
More than one air-fluid level in the same dilated small bowel loop
String of pearl sign
Transition point
Decompressed bowel loops beyond the transition zone
Small bowel feces sign
Adhesion band (rarely)

Table 5.2 Causes of small bowel obstruction

1. Adhesions (most common, 75%)
2. Crohn's disease
3. Hernia (Fig. 5.4)
4. Neoplasia
5. Rare causes: radiation, internal hernia, intussusception, volvulus, gallstone ileus, tuberculosis, hematoma, bezoars

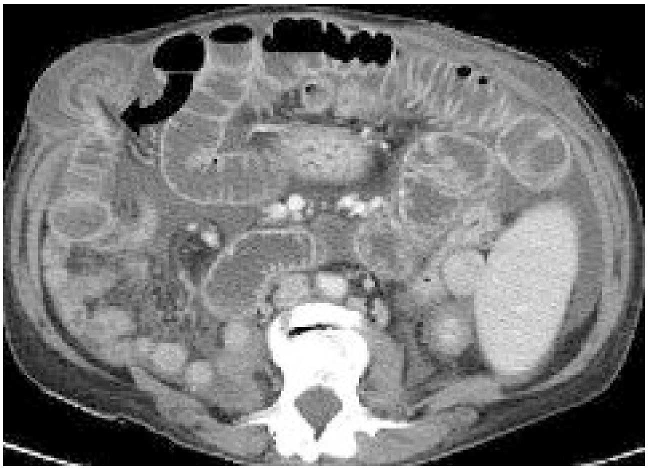

Fig. 5.4 Incarcerated hernia. Contrast-enhanced CT demonstrates small bowel obstruction secondary to bowel incarceration in hernia sac. The transition site (*curved arrow*) is located at the neck of the spigelian hernia sac

Internal Hernia

Internal hernia is characterized by herniation of small bowel through a breech in the mesentery into another compartment of the abdomen. Internal hernias cannot be reliably diagnosed on clinical exam as they are either asymptomatic or have nonspecific symptoms. Although paraduodenal hernia has traditionally been the most common type of internal hernia, the frequency of transmesenteric internal hernia has increased with increasing popularity of gastric bypass surgeries.

The internal hernia can be paraduodenal (most common), prececal, foramen of Winslow, transmesenteric, transmesocolic, intersigmoid, and retromesenteric. The right paraduodenal hernia extends in to the Waldeyer's fossa, which is located posterior to the superior mesenteric artery and transverse colon. The left paraduodenal hernia extends in to the Landzert's fossa, situated to the left of the fourth part of the duodenum.

The CT findings include sac-like cluster of small bowel obstruction, anterior displacement of stomach, and crowding of mesenteric vessels [6] (Fig. 5.5). The CT findings of transmesocolic hernia, seen after gastric bypass surgery, include clustered small bowel loops cephalic to transverse mesocolon, high position of distal jejunal anastomosis, and clustering of mesenteric vessels [7]. The right paraduodenal hernia is usually larger than left paraduodenal hernia. Transmesenteric internal hernia may also cause central displacement of colon. Similar to external hernias, internal hernias can cause bowel ischemia, strangulation, and perforation.

Fig. 5.5 Internal hernia. (**a**) Schematic representation of the right paraduodenal fossa (*1*) and left paraduodenal fossa (*2*). (**b**) CT scout film demonstrates dilated proximal small bowel (*arrowheads*) in the paraduodenal hernia. (**c**) Axial contrast-enhanced CT demonstrates dilated proximal small bowel loops (*arrowheads*) in paraduodenal hernia, without omental fat anterior to it. (**d**, **e**) Contrast-enhanced CT demonstrates clustering of small bowel loops in two different patients with paraduodenal hernia (*curved arrows*)

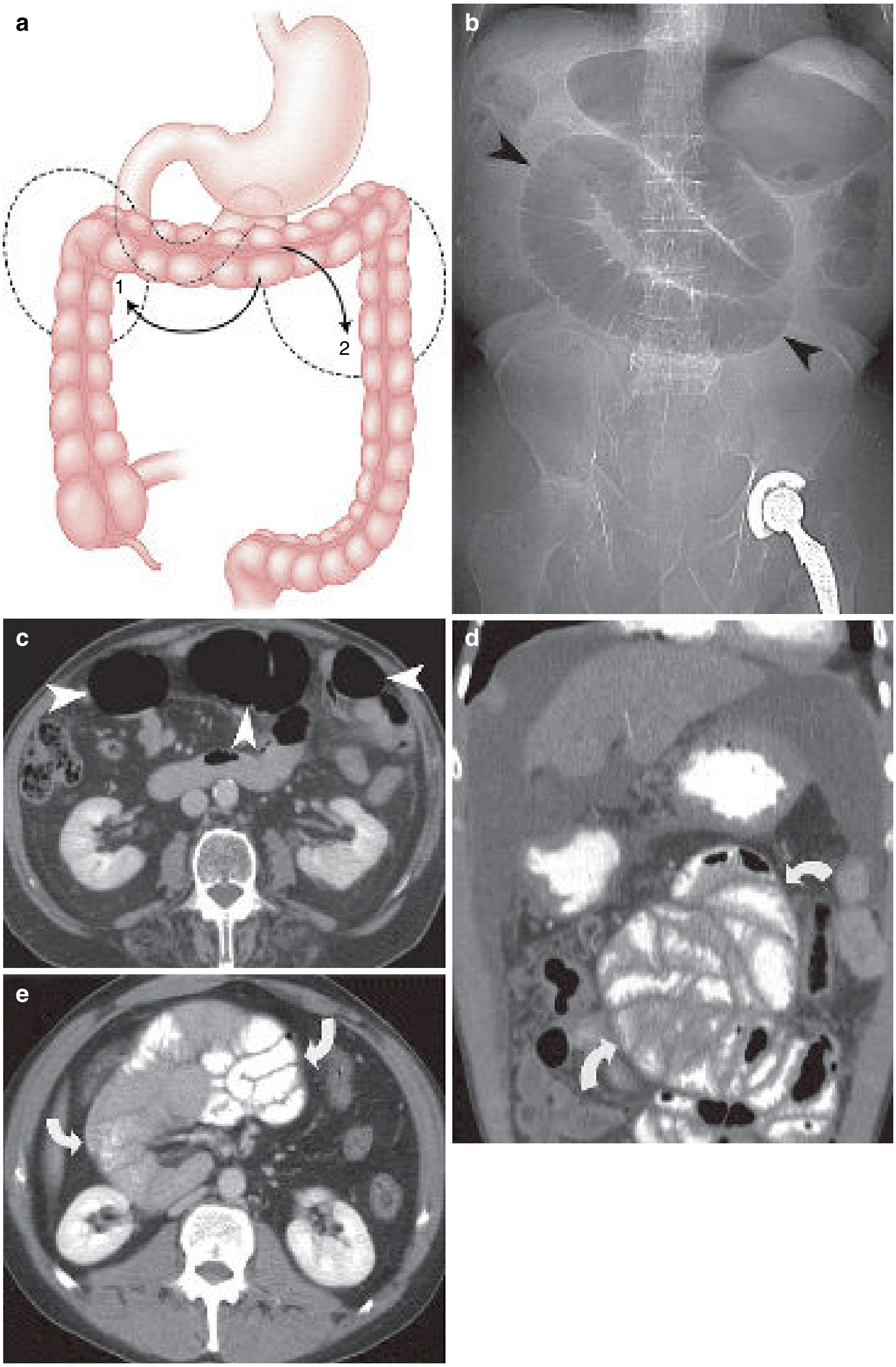

Small Bowel Volvulus

Normal mesenteric attachment is broad and prevents volvulus. Anomaly in the bowel rotation and fixation, where mesenteric base is narrow, predisposes to midgut volvulus.

On barium upper gastrointestinal study, the duodenojejunal junction is located to the left of the spine and posterior to the stomach. Corkscrew configuration of the proximal small bowel is seen with midgut volvulus.

The whirl sign is characterized by twisting of the mesenteric vessels and mesenteric fat, secondary to small

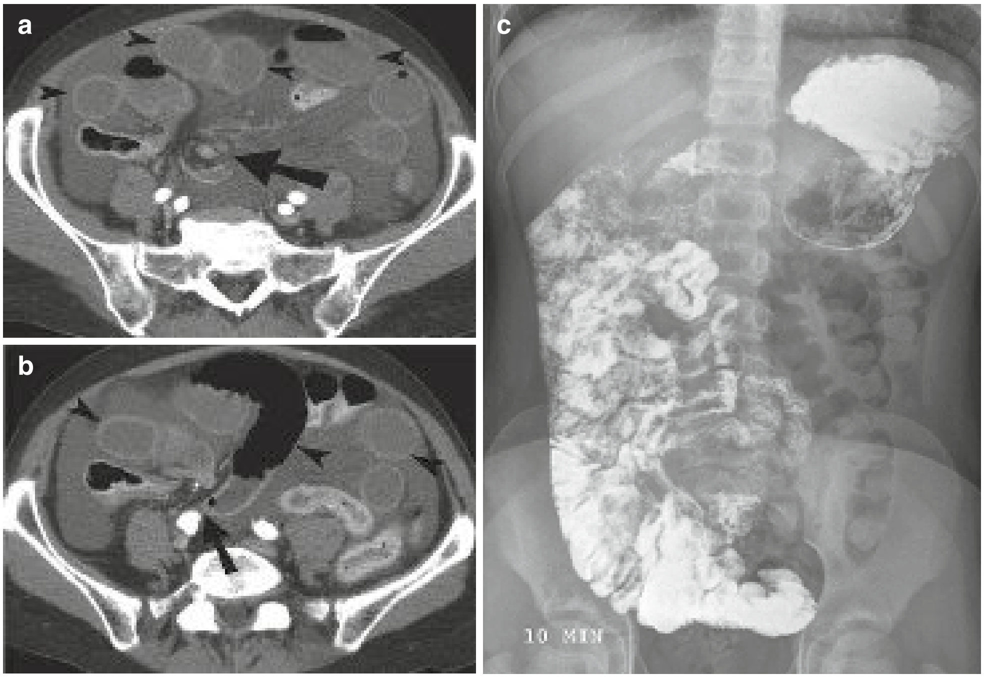

Fig. 5.6 Small bowel volvulus. (**a**, **b**) Contrast-enhanced CT demonstrates dilated small bowel loops (*arrowheads*) and whirled appearance (*arrow*) of mesentery, secondary to the volvulus. (**c**) Small bowel follow-through demonstrates the small bowel loops located to the right of midline. The air-containing colonic loops can be seen to the left of midline

bowel volvulus [8]. It occurs due to twisting of afferent and efferent small bowel loops around a fixed point (Fig. 5.6). It is best appreciated when the cross-sectional imaging plane is perpendicular to the axis of rotation. Although this sign can also be seen after surgeries which involve bowel manipulation, such as hemicolectomy, it has been shown to require surgery 25 times more likely than those small bowel obstruction patients who do not have whirl sign [9]. Northern exposure sign is the distended sigmoid colon that overlies the liver and extends superior to transverse colon.

Malrotation of Bowel

Malrotation of bowel is defined as congenital abnormal rotation and fixation of bowel. Most of the cases are isolated; however, it can be associated with situs inversus or congenital heart disease. Malrotation is often present in children with omphalocele, gastroschisis, or congenital diaphragmatic hernia. Associated congenital disorders are heterotaxy (asplenia, polysplenia), Marfan's syndrome, gastroschisis, Hirschsprung's disease, and biliary atresia. In adults, malrotation is usually an incidental finding in abdominal CT scan. CT findings include:

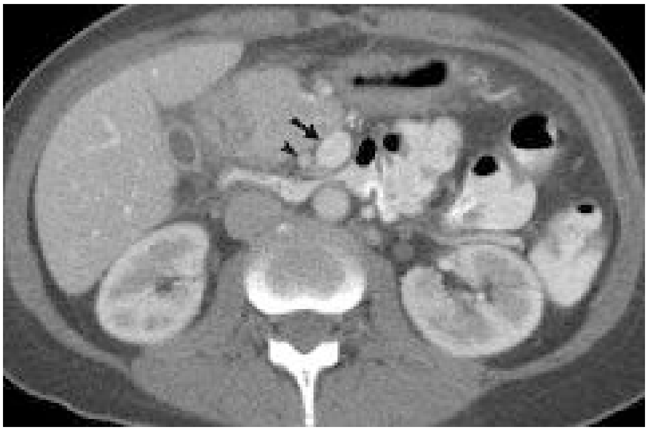

Fig. 5.7 Malrotation of bowel. Axial CT scan in a 39-year-old female shows an inversion of relationship between superior mesenteric vein (*arrow*) and artery (*arrowhead*)

1. Right-sided small bowel
2. Left-sided colon
3. Abnormal relationships between superior mesenteric vein and artery (Fig. 5.7)
4. Aplasia of the uncinate process

Patients with bowel malrotation are prone to volvulus due to short mesenteric attachment of the midgut.

Intussusception

Intussusception in children usually occurs between 6 months and 2 years and is idiopathic in almost all cases. In adults, majority of small bowel obstruction seen with intussusceptions has an underlying cause such as neoplasm, Meckel's diverticulum, or adhesions. Intussusceptions in adults can be classified as:

1. Intussusception with lead point: Persistent or recurrent which is associated with bowel obstruction. Surgery is often required.
2. Intussusception without lead point: Transient, spontaneously resolving, without bowel obstruction. Usually no treatment is required.

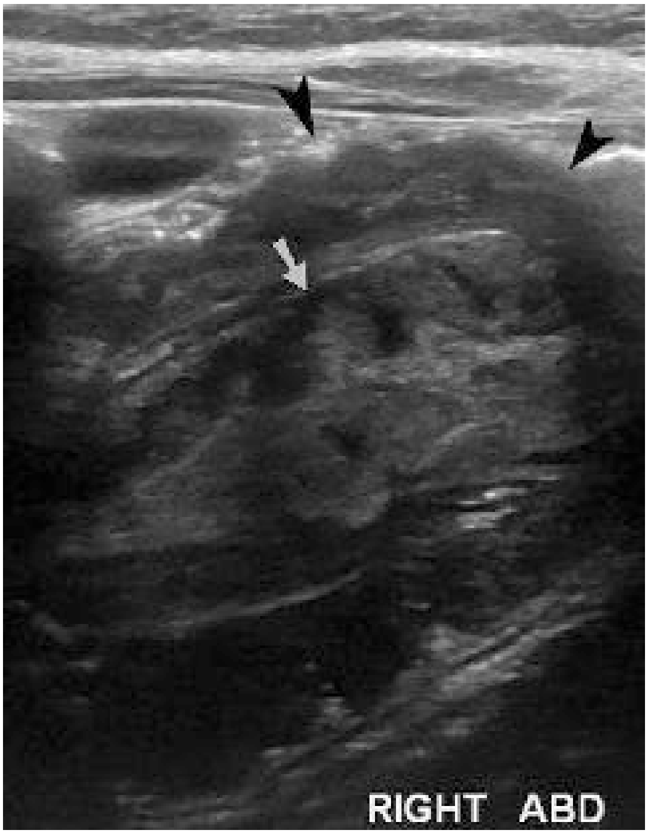

Fig. 5.8 Small bowel intussusception on ultrasound. Ultrasonography demonstrates thickened small bowel wall in the intussusceptum as well as intussuscipiens. Central echogenicity is from mesenteric fat associated with intussusceptum

Ultrasonography is highly sensitive (98–100%) and specific (88–100%) in diagnosing intussusception. Ultrasonography findings include target sign (multiple, alternating hyperechoic and hypoechoic concentric rings representing different layers of bowel wall) and crescent-in-doughnut sign on axial scans. Sandwich sign and hay-fork sign are seen on longitudinal scans (Fig. 5.8). Trapped fluid between the intussuscepted loops and absent blood flow on color-Doppler indicates bowel ischemia.

Small bowel intussusceptions (SBI) are usually transient. The findings suggestive of SBI include smaller diameter (<2.5 cm), less mesenteric fat within the lesion, and smaller length of invaginated segment. Ileocolic intussusceptions are associated with larger diameters and presence of echogenic fat and lymph nodes within the lesion. The presence of free peritoneal fluid, trapped fluid, and bowel obstruction indicate complicated cases.

The CT demonstrates a target-like appearance due to the location of intussuscepted bowel with surrounding fat-containing mesentery in the lumen of a more distal bowel (intussuscipiens) (Fig. 5.9). Wall thickening of the intussuscipiens should raise the possibility of bowel wall edema and ischemia. Dilatation of small bowel proximal to the intussusception site and collapse of the distal bowel indicate bowel obstruction.

Small bowel intussusception is usually without lead point. A lead point small bowel intussusception is usually due to benign cause (including lipoma, adenomatous polyp, and Meckel's diverticulum) rather than malignant (including metastasis, lymphoma, and adenocarcinoma) cause. Colonic intussusception is commonly associated with malignant causes (including adenocarcinoma, lymphoma, or metastasis). Benign causes include lipoma and polyps.

Partial small bowel obstruction can be treated conservatively in majority of patients with nasogastric tube placement and gastric decompression. Surgical intervention is required in patients with closed loop obstruction and in patients with suspected strangulation.

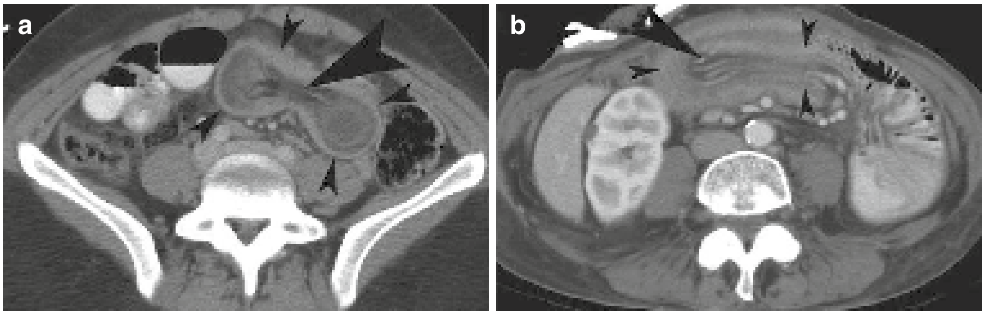

Fig. 5.9 Small bowel intussusception. (**a**, **b**) Axial contrast-enhanced CT demonstrates the mesenteric fat and mesenteric vessels in the intussusceptum (*large arrowheads*) with surrounding soft tissue density representing intussuscipiens (*small arrowheads*)

Other Causes

Gallstone ileus causes mechanical obstruction due to gallstone impaction within the bowel, most commonly at the level of terminal ileum or ileocecal junction, and constitutes up to 25% of small bowel obstruction in elderly patients (Fig. 5.10). It frequently occurs as a complication of acute cholecystitis. Fistula most commonly forms between the gallbladder and the duodenum. Rigler's triad describes plain radiographic findings of gallstone ileus which includes pneumobilia, ectopic gallstone, and evidence of small bowel obstruction (dilated bowel loops, air-fluid levels, etc.).

Duodenal hematoma is usually secondary to blunt trauma and is most often seen in children and young adults. The retroperitoneal duodenum is more prone to injury because of its immobility and rich submucosal vascularity. The diagnosis can be made either with upper GI study or CT imaging (Fig. 5.11).

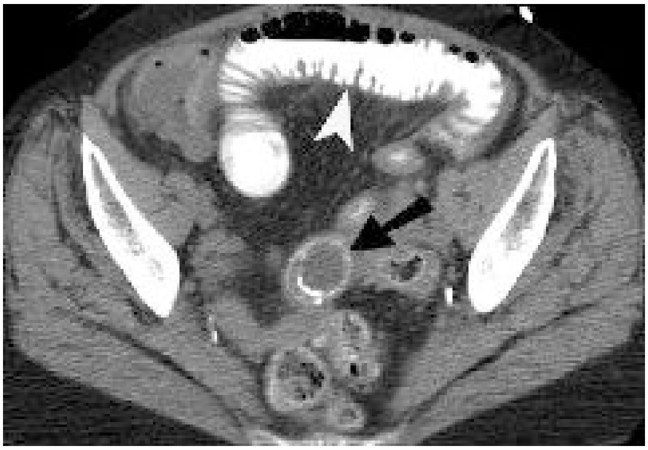

Fig. 5.10 Gallstone ileus. Contrast-enhanced CT demonstrates dilatation of small bowel (*arrowhead*) secondary to a gallstone (*arrow*) in the distal small bowel

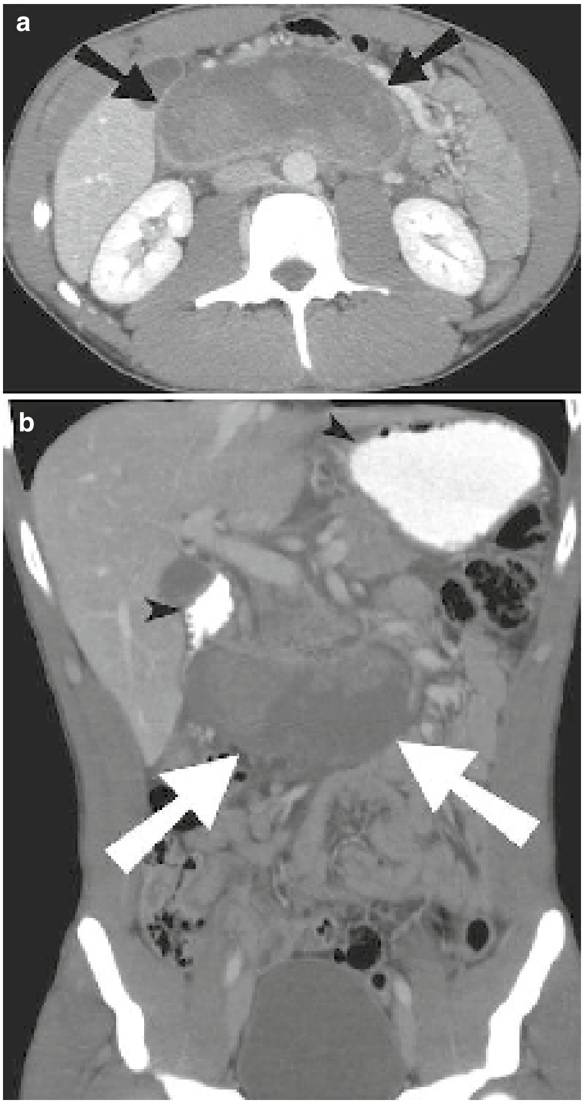

Fig. 5.11 Duodenal hematoma. (**a**, **b**) Contrast-enhanced CT demonstrates posttraumatic hematoma (*straight arrows*) in the duodenal wall, causing symptoms of proximal small bowel obstruction. (**b**) There is oral contrast (*arrowheads*) in the stomach and proximal duodenum, but not in the jejunum

Closed Loop Obstruction

Closed loop obstruction is a type of mechanical obstruction with two points of obstruction present proximally as well as distally, most commonly due to adhesions. There is progressive increase in the intraluminal pressure, as the bowel cannot be decompressed with a nasogastric tube. It is the most common cause of bowel strangulation.

On cross-sectional imaging, closed loop obstruction is characterized by U-shaped configuration of dilated small bowel, radial configuration of mesenteric vessels, and clustering of the abnormal bowel loop (Fig. 5.12). Sudden tapering of the dilated small bowel loop, known as the beak sign, and rotation of afferent and efferent bowel loops around its mesentery in cases of concurrent volvulus, known as whirl sign are also the characteristic CT findings. Small bowel strangulation is best indicated by pneumatosis intestinalis and portal venous gas.

Bowel obstruction from incarcerated hernia is characterized by dilated afferent loop extending into the hernia sac and decompressed efferent loop coming out of the hernia sac. Strangulating obstruction may demonstrate halo sign, mesenteric edema, mesenteric hemorrhage, lack of bowel enhancement, asymmetric wall enhancement, and pneumatosis.

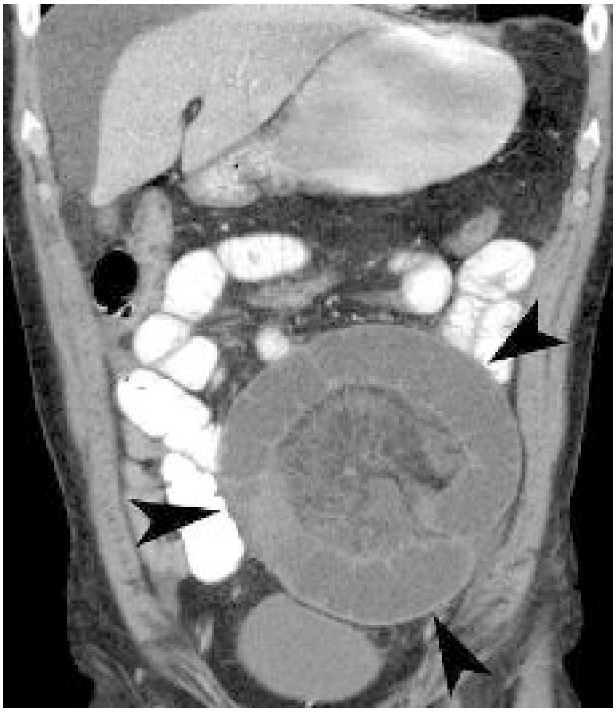

Fig. 5.12 Closed loop obstruction. Coronal CT reformation demonstrates dilated small bowel loop in circular configuration (*arrowheads*) and mesenteric vascular congestion in the left lower quadrant of the abdomen, consistent with closed loop obstruction

Teaching Points

- Contrast-enhanced CT is considered the most appropriate imaging modality in diagnosing high-grade small bowel obstruction.
- CT enteroclysis and MR enteroclysis are the imaging modalities of choice in diagnosing low-grade or intermittent small bowel obstruction.
- CT study in patients with small bowel obstruction is characterized by small bowel loops more than 2.5 cm in caliber, transition point, and decompressed bowel loops beyond the transition zone.
- Plain radiography is not the first-line imaging modality in evaluating patients with suspected small bowel obstruction.
- CT findings in internal hernia include sac-like cluster of small bowel loops with anterior displacement of stomach, and crowding of mesenteric vessels.
- Corkscrew and whirl sign are imaging features of small bowel volvulus.
- CT in intussusception demonstrates a target-like of bowel along with surrounding fat-containing mesentery in the lumen of a more distal bowel.

Questions

1. String of pearl sign is imaging characteristic of which of the following?
   (A) Internal hernia
   (B) Small bowel obstruction
   (C) Intestinal volvulus
   (D) Ileocolic intussusception
   Answer: B
2. Which of the following is the most common internal hernia in a patient with no history of abdominal surgery?
   (A) Prececal
   (B) Transmesenteric
   (C) Transmesocolic
   (D) Paraduodenal
   Answer: D
3. Which of the following is the CT finding in transmesocolic hernia after gastric bypass surgery?
   (A) Clustered small bowel loops caudal to transverse mesocolon
   (B) High position of distal jejunal anastomosis
   (C) Clustering of gastric vessels
   (D) Displacement of colon
   Answer: B

4. Which of the following descriptions is correct?
   (A) Northern exposure sign: collapsed sigmoid colon that overlie the liver
   (B) String of pearl sign: small pockets of fluid seen on upright film of the abdomen
   (C) Whirl sign: twisting of the mesenteric vessels and mesenteric fat
   (D) Small bowel feces sign: presence of fecal material in colonic bowel loops
   Answer: C

5. What is the pathology seen on the CT (Fig. 5.13) of a patient presenting with nausea and vomiting?
   (A) Paraduodenal hernia
   (B) Malrotation
   (C) Jejunitis
   (D) Bowel ischemia
   Answer: A

6. What is the location of the internal hernia (arrows) on the CT (Fig. 5.14) of a patient with acute abdomen?
   (A) Fossa of Landzert
   (B) Fossa of Winslow
   (C) Paracolic space
   (D) Retroperitoneum
   Answer: A

7. Which pathology is seen on the CT (Fig. 5.15) of a patient with cystic fibrosis?
   (A) Malrotation
   (B) Internal hernia
   (C) Volvulus
   (D) Intussusception
   Answer: D

8. What is the pathology seen on the CT (Fig. 5.16) of a patient with acute abdomen?
   (A) Intestinal malrotation
   (B) Closed loop obstruction
   (C) Sigmoid volvulus
   (D) Small bowel intussusception
   Answer: B

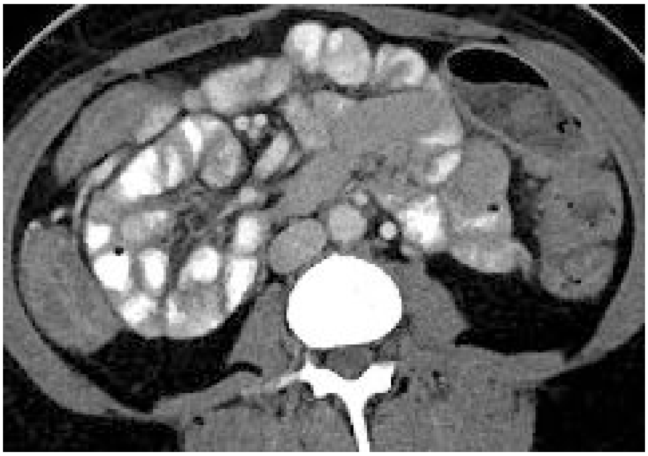

Fig. 5.13 Paraduodenal hernia—CT

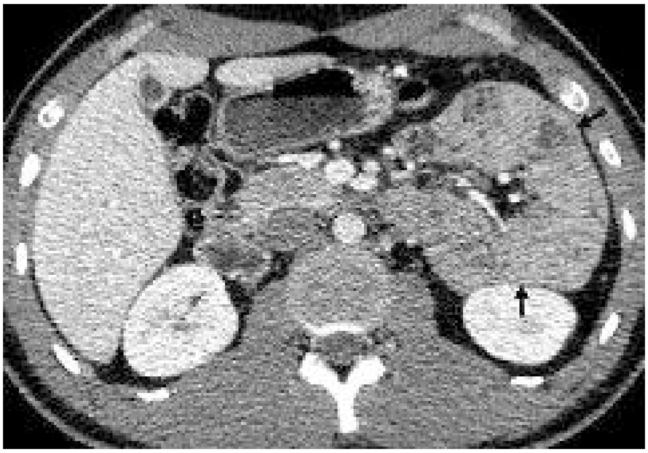

Fig. 5.14 Fossa of Landzert—CT

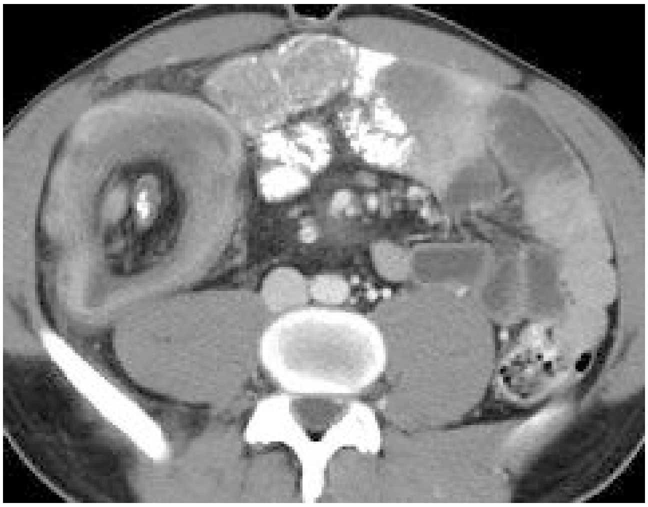

Fig. 5.15 Intussusception—CT

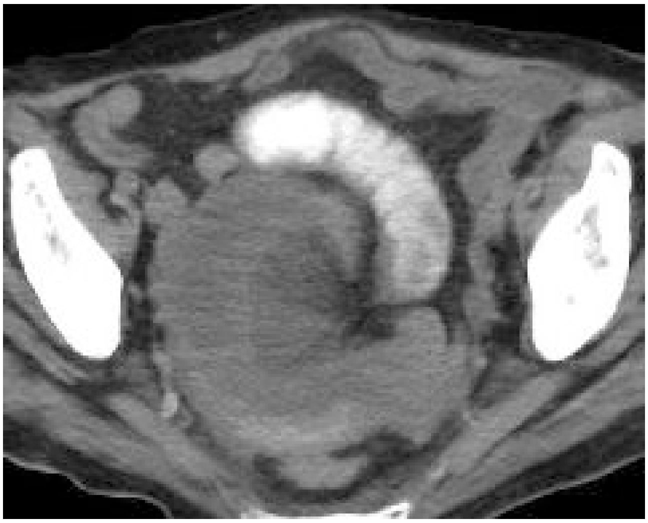

Fig. 5.16 Closed loop obstruction in abdomen

References

1. Balthazar EJ. CT of small-bowel obstruction. AJR Am J Roentgenol. 1994;162:255–61.
2. Miller G, Boman J, Shrier I, Gordon PH. Etiology of small bowel obstruction. Am J Surg. 2000;180(1):33–6.
3. Mayo-Smith WW, Wittenberg J, Bennett GL, Gervais DA, Gazelle GS, Mueller PR. The CT small bowel faeces sign: description and clinical relevance. Clin Radiol. 1995;50:765–7.
4. Fuchsjager MH. The small bowel feces sign. Radiology. 2002;225:378–9.
5. Lazarus DE, Slywotsky C, Bennett GL, Megibow AJ, Macari M. Frequency and relevance of the "small-bowel feces" sign on CT in patients with small-bowel obstruction. AJR Am J Roentgenol. 2004;183:1361–6.
6. Blachar A, Federle MP, Dodson SF. Internal hernia: clinical and imaging findings in 17 patients with emphasis on CT criteria. Radiology. 2001;218:68–74.
7. Reddy SA, Yang C, McGinnis LA, Seggerman RE, Garza E, Ford KL. Diagnosis of transmesocolic internal hernia as a complication of retrocolic gastric bypass: CT imaging criteria. AJR Am J Roentgenol. 2007;189:52–5.
8. Fisher JK. Computed tomographic diagnosis of volvulus in intestinal malrotation. Radiology. 1981;140:145–6.
9. Duda JB, Bhatt S, Dogra VS. Utility of CT whirl sign in guiding management of small-bowel obstruction. AJR Am J Roentgenol. 2008;191(3):743–7.

Imaging of Acute Colonic Disorders

6

Ajay Singh, Khyati Bidani, and Mohammad Mansouri

Acute Diverticulitis

A diverticulum is a sacculation of mucosa and submucosa through the muscularis layer of the colonic wall, where the taeniae and mesentery are absent [1, 2]. The occlusion of the neck of the diverticulum may lead to inflammation, mucosal erosions, and microperforation. Although the inflamed diverticula are most commonly seen in the sigmoid and descending colon, less commonly they may be present in the transverse or ascending colon [3].

Approximately 80% of patients with diverticulitis are more than 80 years old [2, 4]. The patients typically present with left lower quadrant pain, nausea, vomiting, fever, and leukocytosis.

Imaging

Contrast-enhanced CT is the imaging modality of choice in the evaluation of acute left lower quadrant pain. The CT can be performed with oral and/or rectal contrast and has sensitivities as high as 99% for diagnosing acute diverticulitis. CT is not only helpful in triaging the patients into surgical and nonsurgical groups, but it is also the primary imaging modality during placement of pigtail drainage catheter in patients with abscess. The CT findings of acute diverticulitis include demonstration of inflamed, fluid-filled diverticulum with mild wall thickening, and disproportionately severe surrounding inflammation (Fig. 6.1). There may be fluid in the root of sigmoid mesocolon (comma sign), engorged mesenteric vessels (centipede sign), abscesses, extraluminal air, and reactive lymphadenopathy [1–5]. Colorectal cancer can be misdiagnosed as acute diverticulitis in 1%. Colonoscopy is recommended 6–8 weeks after acute uncomplicated diverticulitis to rule out colorectal cancer.

Although graded-compression ultrasound has been shown by some to have a sensitivity of 90% for the diagnosis of diverticulitis, it has not gained widespread acceptance in the USA. Ultrasound is however considered the most appropriate test in the evaluation of left lower quadrant pain in women of childbearing age.

Complications

Complications of acute diverticulitis occur in approximately 12% of patients. The most common complications of acute diverticulitis include pericolonic abscess, peritonitis, obstruction, perforation, colovesical fistula, and strictures.

An uncommon complication of recurrent diverticulitis of the colon is giant colonic diverticula. A giant colonic diverticulum is more than or equal to 4 cm in diameter and is believed to result from narrowing of the diverticular neck, creating ball-valve mechanism where air can enter the diverticula but cannot escape out (Fig. 6.2). Complications of acute diverticulitis are summarized in Table 6.1.

Diverticulitis accounts for two-thirds of the vesicoenteric fistulas. Inflamed colon may adhere to the urinary bladder wall and may cause a fistula. These patients may have pneumaturia and fecaluria. The flow through the fistula predominantly occurs from the large bowel to the urinary bladder and is often indicated by the presence of air in the urinary bladder lumen (Fig. 6.3).

A. Singh (✉)
Division of Emergency Radiology, Department of Radiology, Massachusetts General Hospital, Boston, MA, USA

Harvard Medical School, Massachusetts General Hospital, Boston, MA, USA
e-mail: asingh1@partners.org

K. Bidani · M. Mansouri
Department of Radiology, Massachusetts General Hospital, Boston, MA, USA

© The Author(s), under exclusive license to Springer Nature Switzerland AG 2024
A. Singh (ed.), *Emergency Radiology*, https://doi.org/10.1007/978-3-031-65770-2_6

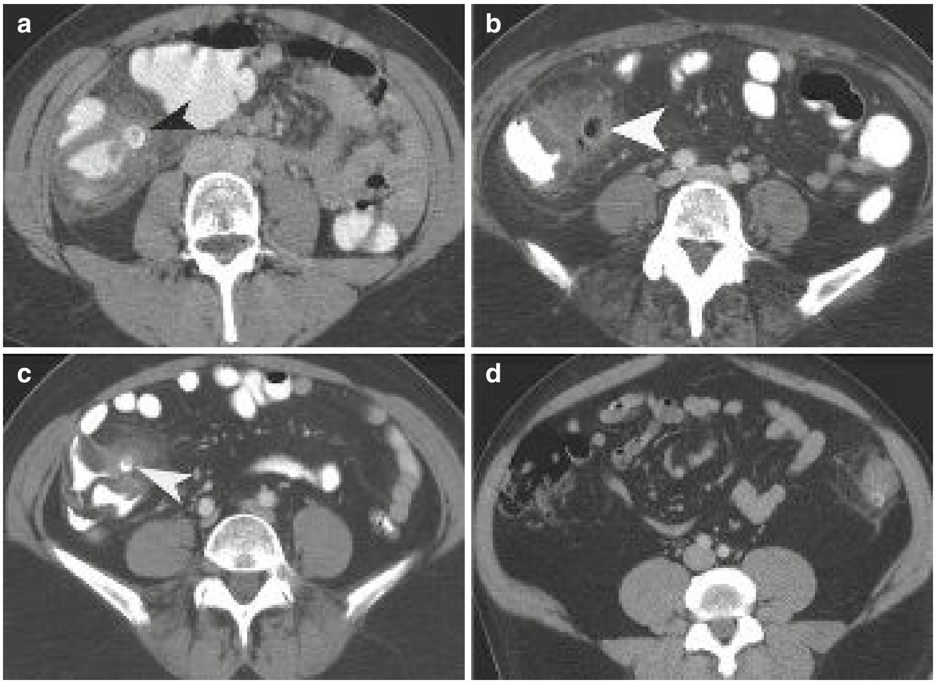

Fig. 6.1 Acute diverticulitis. (**a**–**c**) Contrast-enhanced CT scan study of the abdomen demonstrates inflamed diverticulum (*arrowheads*) arising from the ascending colon. There are pericolonic inflammatory changes seen around the inflamed colonic diverticulum. (**d**) Contrast-enhanced CT scan study of the abdomen demonstrates inflamed diverticulum arising from the distal descending colon. There is colonic wall thickening and pericolonic inflammatory changes

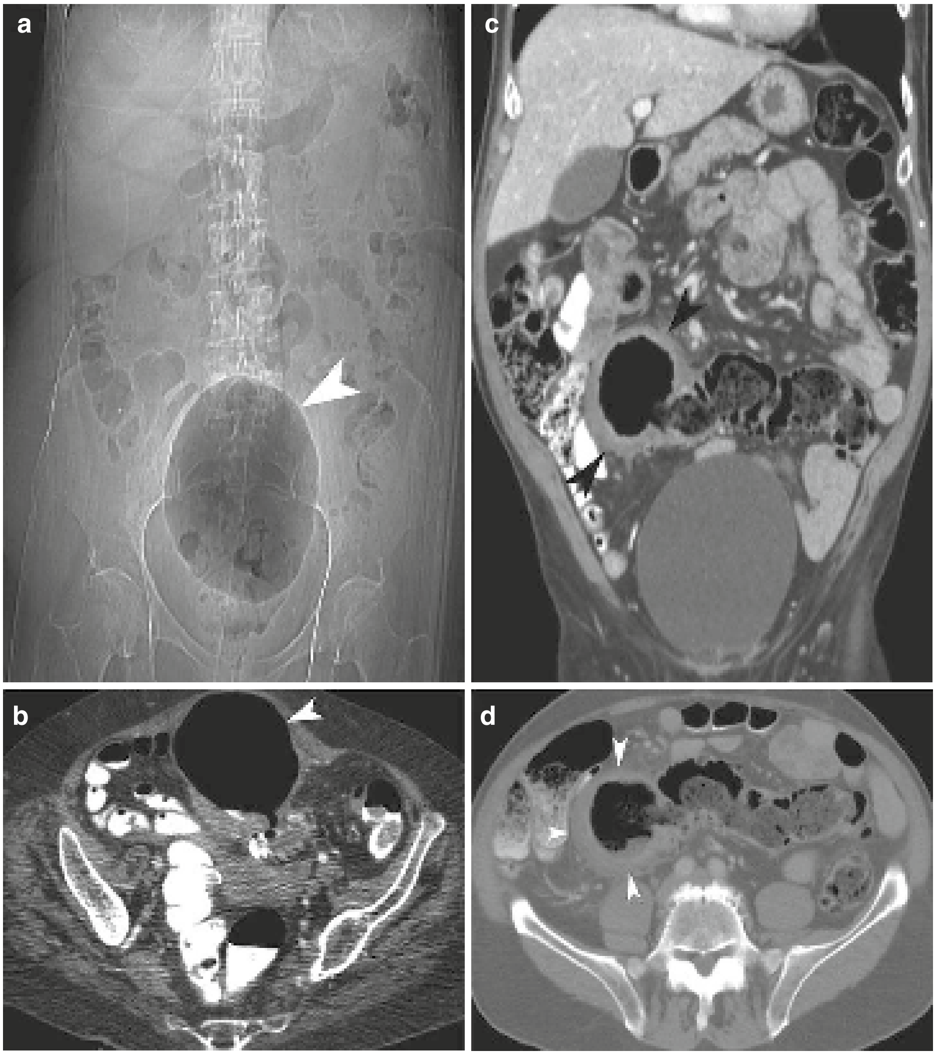

Fig. 6.2 Giant sigmoid diverticulum. (**a**) Scout film of the abdomen demonstrates a 10-cm-diameter air-containing cavity in the pelvis which corresponds to a giant sigmoid diverticulum (*arrowheads*) in a patient with recurrent episodes of diverticulitis. (**b**) Contrast-enhanced CT scan study of the pelvis demonstrates a giant sigmoid diverticulum arising from the sigmoid colon. Small amount of rectal contrast is present within the lumen of the large diverticulum. (**c**, **d**) Contrast-enhanced CT scan study demonstrates inflammatory thickening of the wall of a giant sigmoid diverticulum (*arrowheads*), arising from sigmoid colon

Treatment

The treatment of acute diverticulitis is most often conservative with antibiotic therapy. Image-guided pigtail catheter drainage is used to treat abscess and avoids the need for multistage surgery for acute diverticulitis. CT-guided catheter drainage has a 70–90% success rate in treating a post-diverticulitis abscess. Abscess less than 3 cm in diameter may be managed conservatively, without drainage or surgery. When a collection is more than 4 cm in diameter, CT-guided catheter drainage is often preferred, followed by referral for surgical treatment (Fig. 6.4). Eventual surgical resection of the segment of colon is recommended in all patients who develop abscess.

Table 6.1 Summary of acute diverticulitis complications

Pericolonic abscess (69%)
Peritonitis (27%)
Obstruction (15%)
Fistula (14%)
Strictures (2%)
Giant colonic diverticula (rare)

Segmental Omental Infarction

Omental infarction is a rare cause of acute abdomen, which most often simulates acute appendicitis on clinical exam. Patients commonly present with acute abdominal pain with gradually increasing severity. It typically occurs on the right side of the omentum due to embryologic variation in the blood supply. White blood cell count, erythrocyte sedimentation rate, and C-reactive protein are usually mildly increased. It is seen in younger age group patients than acute epiploic appendagitis. Segmental omental infarction is the result of

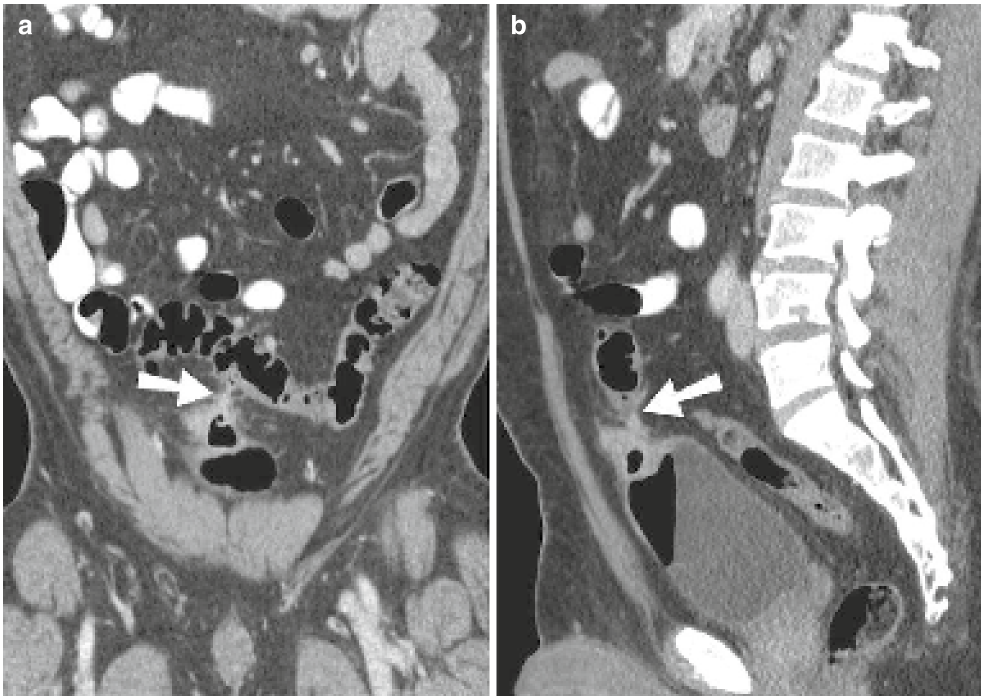

Fig. 6.3 Colovesical fistula. (**a**, **b**) Coronal and sagittal reformations of the abdomen demonstrate colovesical fistula (*arrow*) extending from the sigmoid colon to the urinary bladder dome. There is air identified within the urinary bladder lumen, secondary to the fistulous communication with the colon

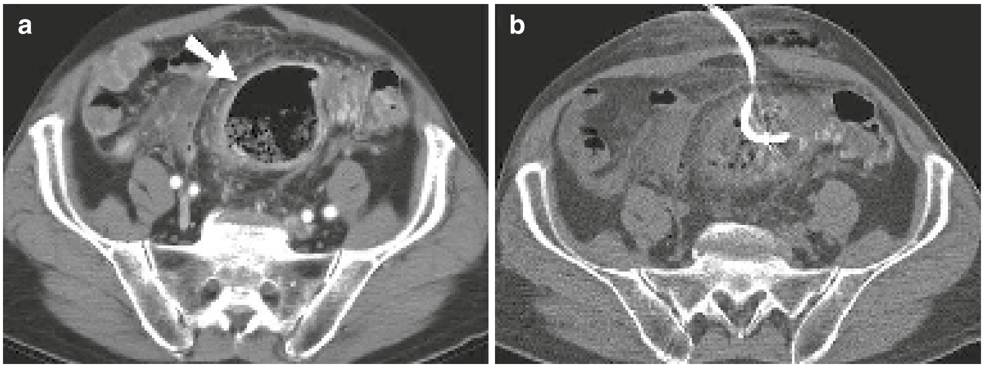

Fig. 6.4 Diverticulitis abscess. (**a**) Contrast-enhanced CT scan study of the pelvis demonstrates a well-defined abscess cavity (*arrow*) in the sigmoid mesocolon with surrounding inflammatory changes. (**b**) Contrast-enhanced CT scan study demonstrates decrease in the size of the pelvic abscess after placement of a pigtail drainage catheter

vascular compromise, either due to torsion or vascular thrombosis.

Omental torsion results in venous stasis, thrombosis, edema, congestion, and hemorrhagic necrosis. Two types of omental torsion are described in the literature:

1. Primary omental torsion: This type is idiopathic omental torsion. It occurs without any associated intra-abdominal pathology. Primary omental torsion may result from conditions which cause sudden increase in intra-abdominal pressure such as coughing, sneezing, Valsalva, or heavy meal.
2. Secondary omental torsion: The most common type. This type may occur after surgical trauma or abdominal pathology including cysts, tumors, inflammation, and hernia.

The typical CT findings of omental infarction include a cake-like inflammatory fatty mass or whirled fatty structure, most commonly in the right lower quadrant (Figs. 6.5a, b and 6.6) [6]. It might be associated with reactive bowel wall thickening. Unlike acute epiploic appendagitis, omental infarction is most commonly on the right side, may or may not about the colon, and does not demonstrate ring sign around the inflamed fat. While typical acute epiploic

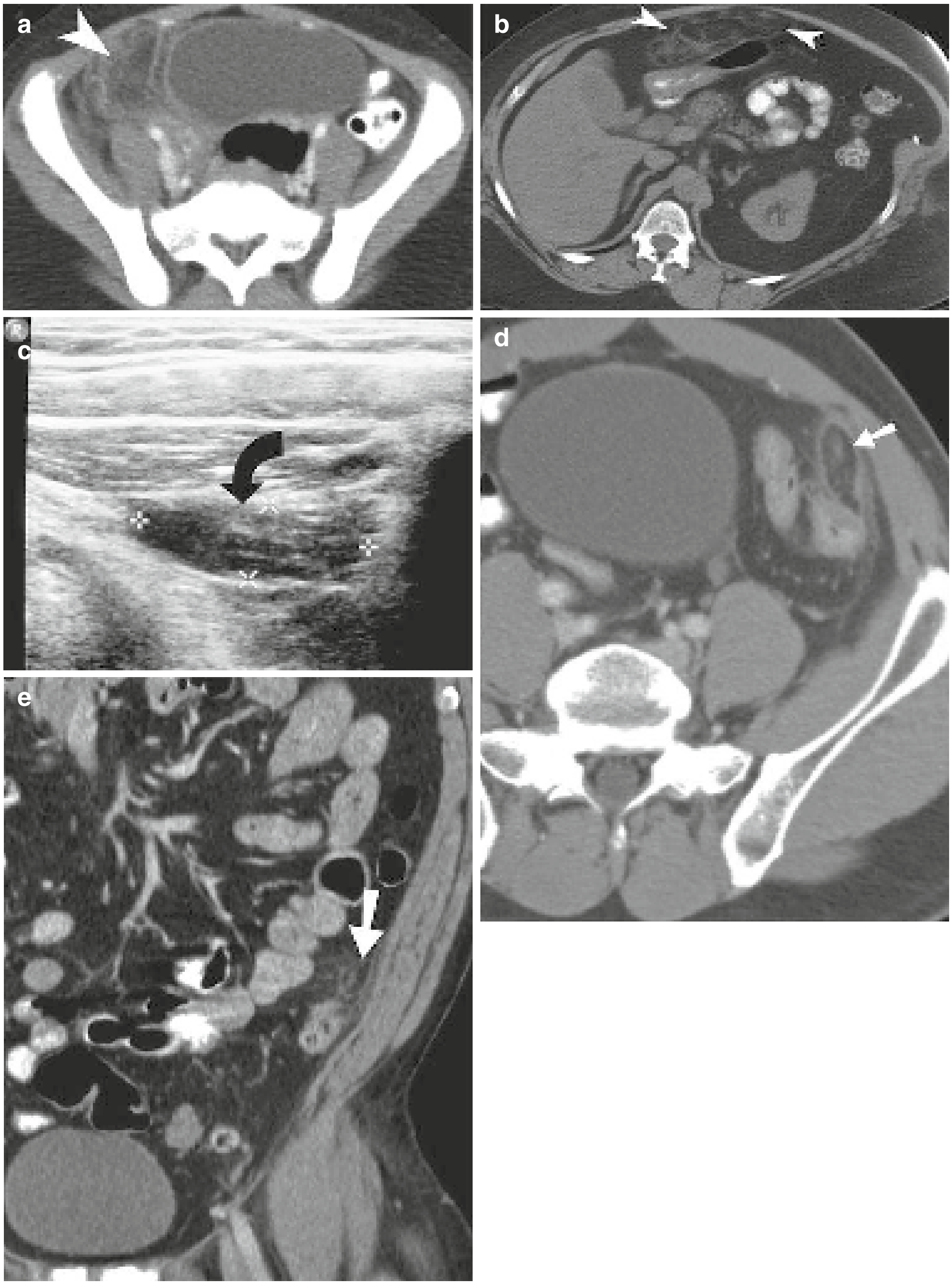

Fig. 6.5 Segmental omental infarction (**a**, **b**) and acute epiploic appendicitis (**c**–**e**). (**a**) Contrast-enhanced CT scan study demonstrates a 7-cm-diameter omental fat density inflammatory lesion (*arrowhead*) in the upper right lower quadrant of the abdomen of a 6-year-old patient. (**b**) Noncontrast CT of a patient with segmental omental infarction demonstrates a midline inflammatory fatty lesion anteroinferior to the left lobe of the liver. (**c**) Ultrasound of a patient with acute epiploic appendagitis demonstrates a focal heterogeneously hypoechoic lesion (*curved arrow*) located just deep to the left anterior abdominal wall musculature. (**d**, **e**) Axial and coronal contrast-enhanced CT scan study demonstrates an oval, fat density lesion (*straight arrow*) in relation to the sigmoid colonic wall with surrounding inflammatory changes. The high-density central dot corresponds to thrombosed or congested vessel within the torsed epiploic appendage. Omental infarction

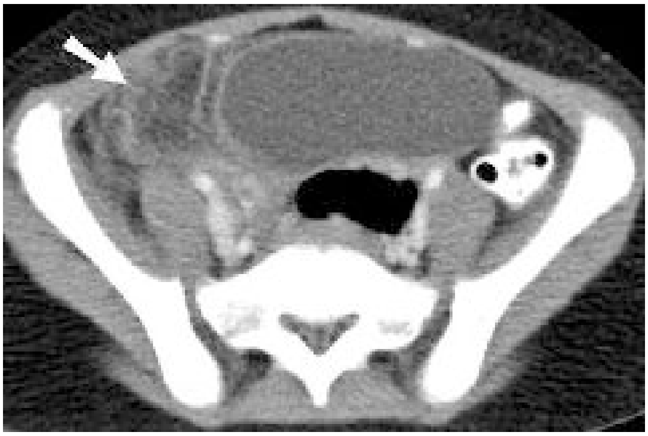

Fig. 6.6 Acute segmental omental infarction. Contrast-enhanced CT shows inflammatory focal fatty lesion (*arrow*) in the omentum. The appendix was normal and seen at a higher level

appendagitis is less than 3.5 cm in diameter, omental infarctions are much larger (typically >5 cm) [7].

Segmental omental infarction is a self-limited condition which is best managed conservatively using Motrin. Majority of the patients are asymptomatic within 10 days of the treatment.

Acute Epiploic Appendagitis

Epiploic appendages are finger-shaped fat-containing pouches which arise off the surface of the colon and are surrounded by the visceral peritoneum. The most common location of inflammation of an epiploic appendage is adjacent to the sigmoid colon and usually affects adult people in fifth to sixth decades [5]. The reason for the presence of epiploic appendagitis in the left abdomen in 80% of cases is because of the higher number of epiploic appendages present adjacent to the sigmoid colon (Table 6.2).

Torsion of epiploic appendages can lead to vascular occlusion and infarction. Inflamed epiploic appendage can cause bowel obstruction from adhesions and can get detached from colon to produce intraperitoneal loose body [5, 8]. It has also been rarely reported to cause intussusception and abscess formation.

Clinically, the patients may present with acute left lower quadrant pain, nausea, fever, and diarrhea or constipation [5]. When it involves the left lower quadrant, it is clinically most often mistaken for sigmoid diverticulitis. When it affects the cecum, it is clinically most often mistaken for acute appendicitis. Because of the clinical misdiagnoses, patients with primary epiploic appendagitis can get unnecessary hospitalization and treatment. The clinical management of acute appendagitis includes conservative treatment with pain medication.

Table 6.2 Location of acute epiploic appendagitis [7]

Location	Frequency (%)
Sigmoid colon	62
Descending colon	18
Cecum	12
Ascending colon	8
Transverse colon	0
Anterior	82
Lateral	8

Imaging

Although ultrasound has been occasionally used in diagnosing acute epiploic appendagitis, CT is the imaging tool of choice in making the diagnosis. The CT findings include a pedunculated fatty lesion, 1.5–3.5 cm in length, and associated with surrounding inflammatory stranding, hyperdense ring, high-attenuating central dot, and less commonly adjacent thickening of the colon wall (Fig. 6.5c–e) [5]. The parietal peritoneum deep to the anterior abdominal wall may be thickened. The ultrasound findings are similar to CT study and may include hypoechoic rim surrounding a hyperechoic focal lesion.

A central high-attenuation focus within the fat is a helpful finding which is believed to represent a thrombosed or congested vessel (Fig. 6.7). Since it is seen in 54% of the cases, its absence does not rule out the diagnosis of acute epiploic appendagitis. There is usually no colonic wall thickening [7]. The CT changes of acute epiploic appendagitis tend to resolve in all patients within 6 months. Table 6.3 summarizes imaging findings in acute epiploic appendagitis.

The differential diagnosis of an inflammatory fat-containing lesion on CT includes acute epiploic appendagitis, mesenteric panniculitis, acute diverticulitis, trauma, omental contusion, omental metastases, and liposarcoma. Although omental infarction can have an appearance similar to that of epiploic appendagitis, it lacks the hyperdense ring that is seen in all patients with epiploic appendagitis. Majority of the cases of acute epiploic appendagitis are self-limited and can be treated with pain management using analgesics.

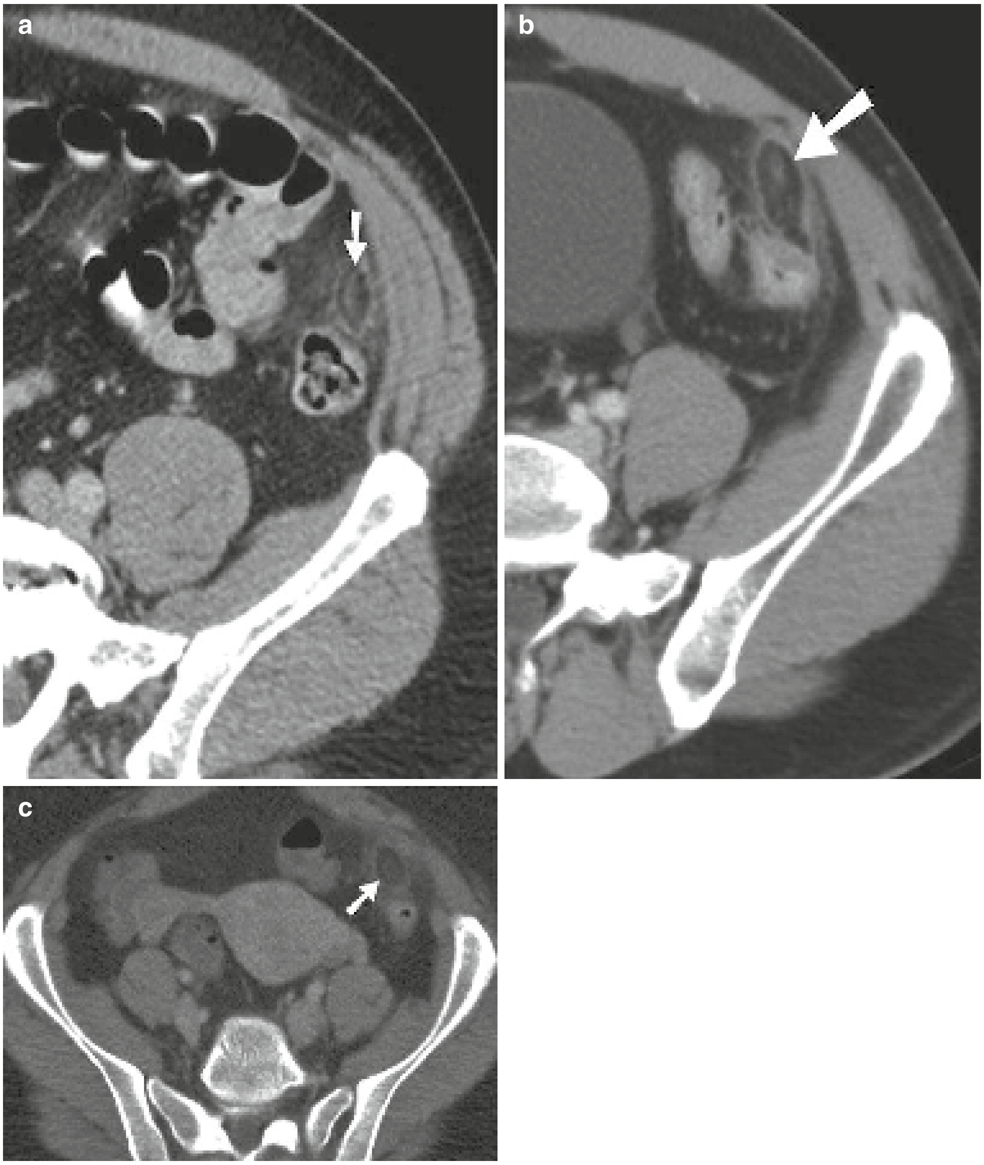

Fig. 6.7 Acute epiploic appendagitis. (**a**–**c**) CT demonstrates inflamed epiploic appendage (*arrows*) abutting the sigmoid colon. The central high density within the fatty lesion represents thrombosed or congested vessel

Table 6.3 Imaging findings in acute epiploic appendagitis

Pedunculated fatty lesion 1.5–3.5 cm in length
Surrounding inflammatory stranding
Hyperdense ring
High-attenuating central dot
Adjacent thickening of the colon wall
Thickening of parietal peritoneum

Inflammatory Bowel Disease

Crohn's disease is a chronic granulomatous inflammatory disease that involves the entire gastrointestinal tract with transmural and discontinuous lesions which most often affects the distal ileum and right colon [9]. The transmural inflammation is commonly associated with deep ulceration and sinus/fistula formation.

Ulcerative colitis is an idiopathic chronic inflammatory disease that most often demonstrates continuous involvement of the rectum and distal colon and rectum mucosa [10].

The common modes of presentation of inflammatory bowel disease include abdominal pain, diarrhea, weight loss, vomiting, and fever. The patients with Crohn's disease may have associated arthritis, ocular inflammatory diseases, gallstones, and skin lesions [11].

Imaging

For the initial presentation of suspected Crohn's disease in patients with abdominal pain, fever, and diarrhea, CT enterography is considered the most appropriate imaging modality. The second-line imaging test for suspected Crohn's

Table 6.4 Imaging findings of ulcerative colitis (Fig. 6.8)

1. Continuous involvement from rectum to colon
2. Mucosal granularity and stippling
3. Indistinctness of haustral folds
4. Collar button ulcers
5. Inflammatory pseudopolyps
6. Backlash ileitis
7. Presacral space widening (>1.5 cm)

Table 6.5 Imaging findings of Crohn's colitis (Fig. 6.9)

1. Lymphoid hyperplasia: 2 mm filling defects in the wall
2. Aphthoid ulceration: small, 1 mm diameter superficial ulcerations with radiolucent halo
3. Deep ulcerations, sinuses, and fistulas
4. Colonic wall thickening: more with Crohn's disease
5. Bowel strictures: often asymmetrical
6. Anorectal fissures, abscess, and fistulas: more commonly with Crohn's disease

disease is small bowel follow-through study. For adult and pediatric patients with known Crohn's disease, presenting with fever, abdominal pain, and leukocytosis, routine contrast-enhanced CT is considered the imaging modality of choice. CT enterography involves the use of neutral oral contrast and imaging performed 45s after intravenous contrast.

The CT findings include bowel wall enhancement, wall thickening, mural stratification, prominent vasa recta, and mesenteric inflammation. The mural stratification (target or halo sign) is produced by soft tissue density mucosa, low-density submucosa (edema or fatty infiltration), and soft tissue density muscularis propria. Imaging also allows differentiation between Crohn's disease and ulcerative colitis (Tables 6.4 and 6.5).

The imaging findings which favor Crohn's disease over intestinal tuberculosis include the presence of intra-abdominal abscess, strictures, enteroenteric fistulas, and enterocutaneous fistulas. CT findings favoring intestinal tuberculosis

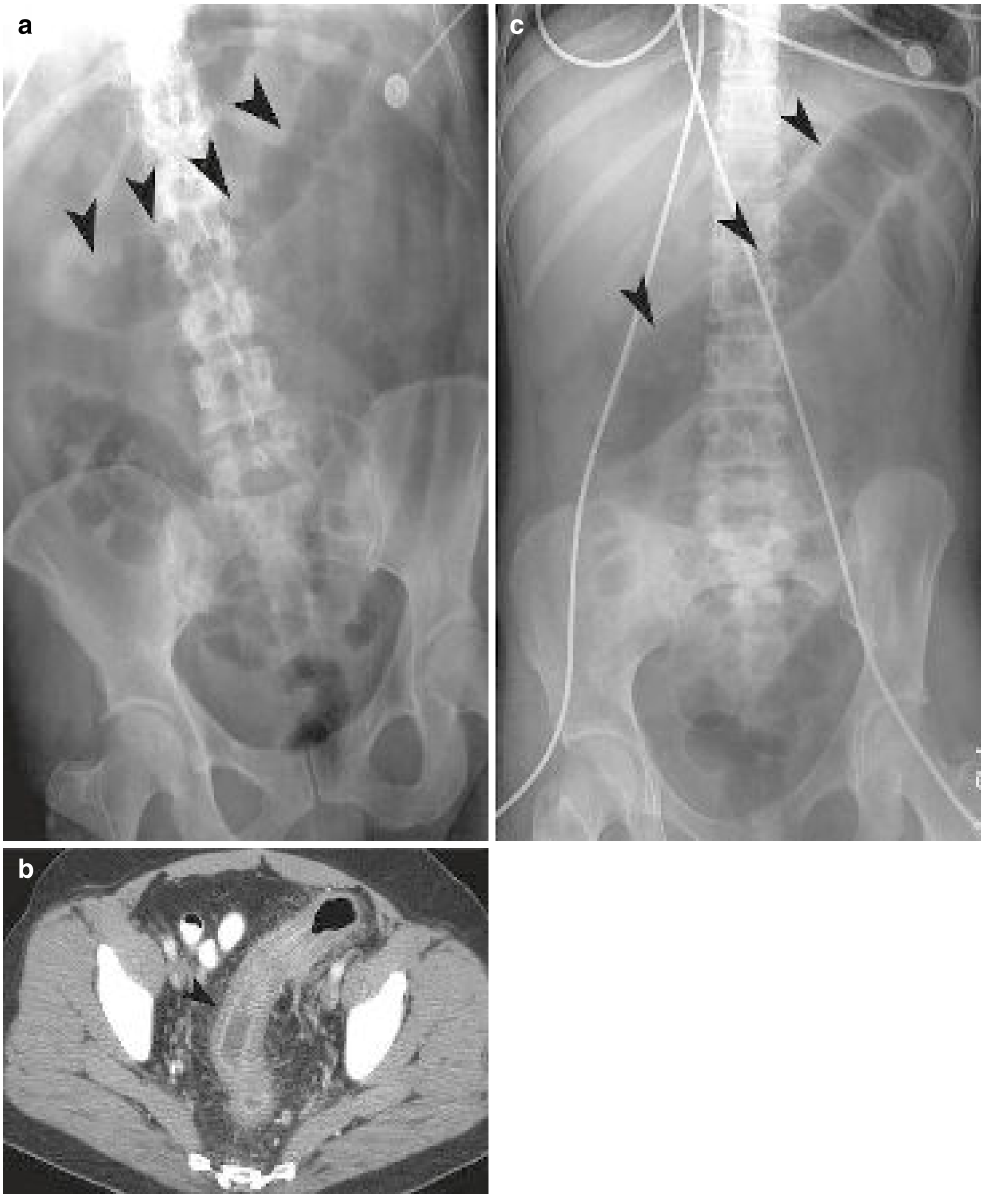

Fig. 6.8 Inflammatory bowel disease. (**a**) Plain radiograph of the abdomen demonstrates thumbprinting (*arrowheads*) involving the transverse colon in a patient with ulcerative colitis. (**b**) Contrast-enhanced CT in a patient with ulcerative colitis shows symmetrical and continuous involvement of the entire rectum and sigmoid colon by inflammatory proctocolitis (*arrowhead*). There is sigmoid wall thickening, mucosal enhancement, and pericolonic inflammatory densities. (**c**) Plain radiograph of the abdomen in a patient with Crohn's colitis demonstrates a featureless segment of the transverse colon

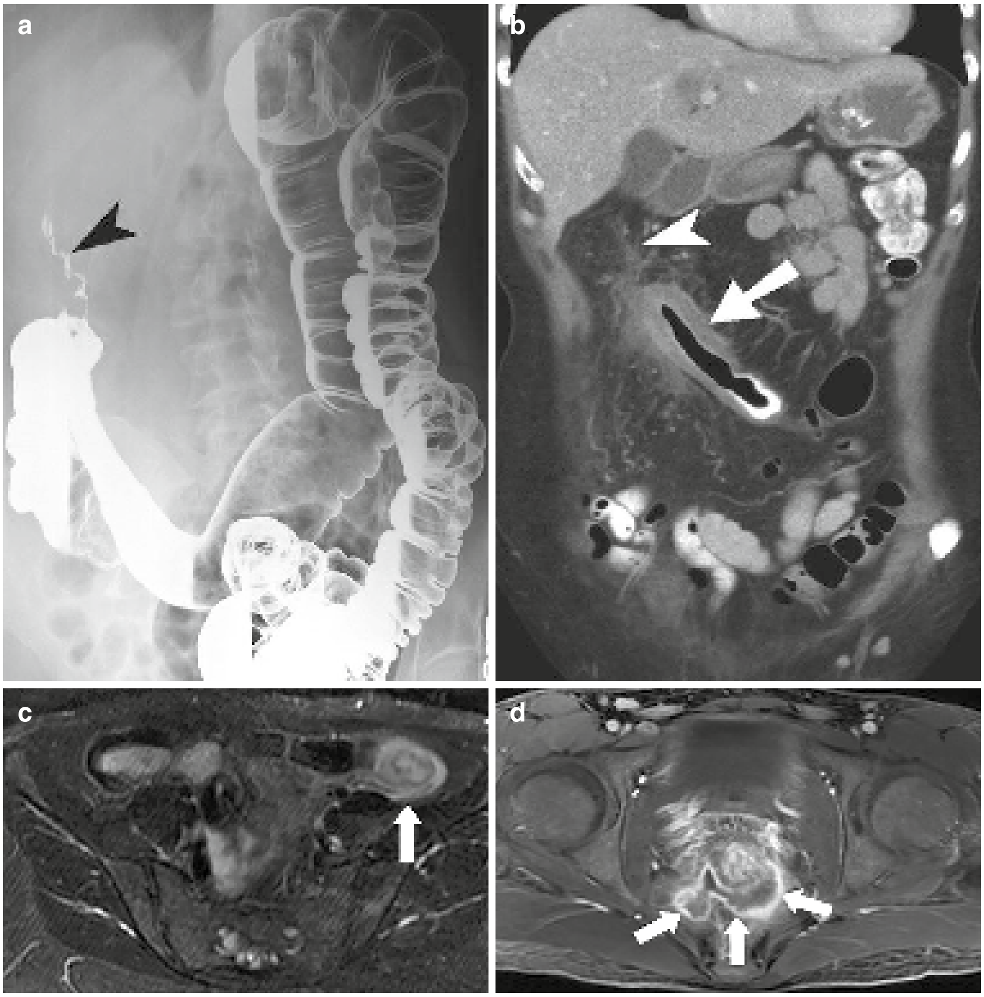

Fig. 6.9 Crohn's colitis. (**a**) Double-contrast barium enema examination demonstrates a sinus tract arising off the hepatic flexure (*arrowhead*). (**b**) Coronal CT reformation demonstrates inflammatory thickening of right transverse colon (*arrow*), secondary to Crohn's colitis. A sinus tract (*arrowhead*) is seen extending from the splenic flexure to the right subhepatic location. (**c**) Colitis in a patient with Crohn's disease. Axial STIR image demonstrates hyperintensity (arrow) in the wall of the inflamed sigmoid colon. (**d**) Perianal abscess in a patient with Crohn's disease. Postcontrast axial T1-WI demonstrates a horseshoe-shaped posterior perianal abscess with rim enhancement (arrows)

include involvement of ileocecal region or right colon, involvement of short bowel segment, presence of large and necrotic mesenteric lymph nodes, and ascites.

As per ACR appropriateness criteria, MRI displays comparable diagnostic accuracy for the diagnosis of Crohn's disease complications. Postcontrast T1-weighted images can demonstrate enhancement of walls in case of abscesses, decreased wall enhancement in case of fibrosis, and enhancing linear tracts in case of the fistulas. MRI is considered superior to CT for diagnosing fistulas and perianal disease (Fig. 6.9c, d).

In pediatric patients with Crohn's disease with mild symptoms, MR enterography is considered the most appropriate imaging modality because of its high sensitivity and specificity, similar to CT enterography. Ultrasound is the second-line imaging modality in similar clinical scenario and suffers from the disadvantage of operator dependence. Ultrasound may be useful in diagnosing colonic inflammatory diseases, in particular when equivocal results are obtained by other imaging techniques, because of its ability to see wall thickening (≥4 mm), target sign, sluggish peristalsis, and pericolonic extension of the disease. MR imaging may be also used, in particular when recurrent studies are needed, and allows excellent soft tissue contrast without radiation exposure [10].

Complications and Treatment

The complications of inflammatory bowel disease include abscess, fistulas, and bowel obstruction [2]. Acute flare-up of Crohn's disease is usually treated with anti-inflammatory drugs and steroids. Surgery is the therapeutic tool which is reserved for nonresponsive disease, complications, and very ill patients.

Pseudomembranous Colitis

Pseudomembranous colitis, also called *C. difficile* colitis, is a life-threatening condition caused by *Clostridium difficile* that produces two exotoxins and leads to colonic mucosa to generate a protein-rich membrane (pseudomembrane). Toxin A is responsible for colitis and allows toxin B to enter the

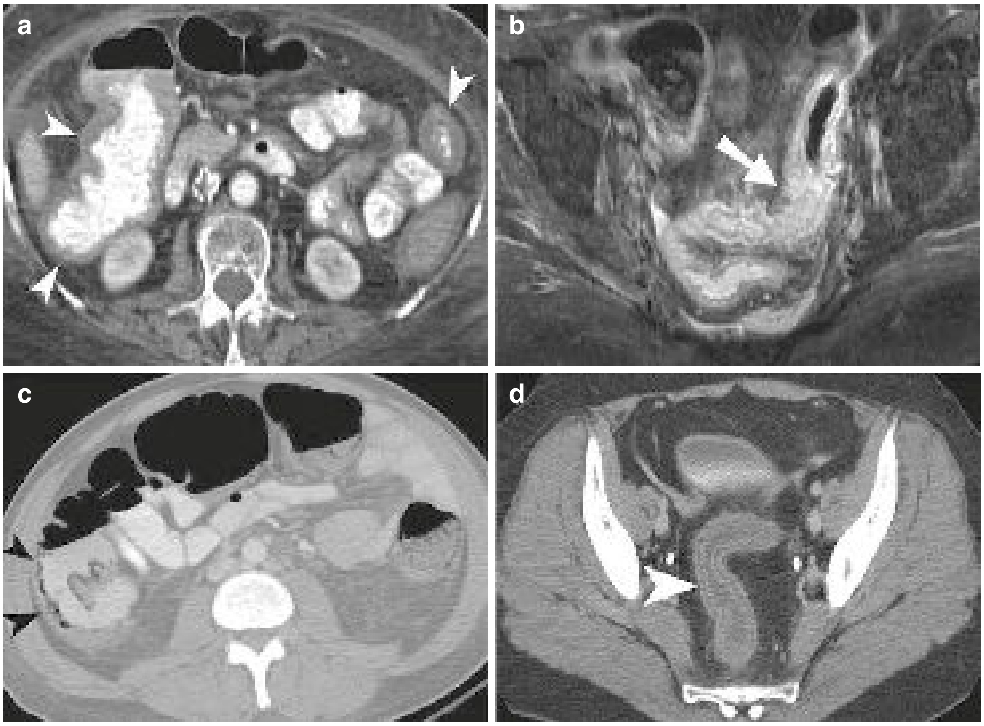

Fig. 6.10 Pseudomembranous colitis. (**a**) Contrast-enhanced CT scan study of the abdomen demonstrates diffuse thickening of the colonic wall (*arrowheads*), more prominent on the right side. (**b**) Gadolinium-enhanced T1-weighted axial image of the pelvis demonstrates enhancement and thickening of the rectal as well as sigmoid colonic wall with surrounding inflammatory changes. (**c**) Contrast-enhanced CT shows the infectious colitis affecting the right colon. There is ascending colonic wall thickening (*arrowheads*) and pneumatosis. (**d**) Contrast-enhanced CT of the pelvis shows rectosigmoidal wall thickening (*arrowhead*) from proctocolitis. The bowel wall thickening is produced by submucosal edema sandwiched between mucosal and serosal enhancements

cell. The bacterium has a widespread presence in the hospitals and is the cause of up to 20% of diarrhea associated with antibiotic therapy [12].

The disease may be asymptomatic at the beginning but then becomes clinically evident with watery diarrhea, abdominal pain and tenderness, fever, dehydration, and leukocytosis. In the life-threatening cases lethargy, tachycardia, and toxic megacolon or perforation due to necrosis may be associated. Cytoxan assay is the gold standard in detection of toxin B and has more than 90% sensitivity. Majority of cases in clinical practice are detected by colonoscopy and positive toxin B assay.

The CT findings include extensive mural thickening with prominent haustral folds (Fig. 6.10). Pneumatosis or portal venous gas may be present due to loss of mucosal integrity without any ischemia. In decreasing order of frequency, there is involvement of entire colon (most common), right colon, and left colon (least common). The barium enema findings include thumbprinting and small nodular or plaque-like filling defects. In 3% of cases, *C. difficile* colitis may become severe and develop toxic megacolon.

While the mortality of *Clostridium difficile* infection is only 2%, the cost of managing the patients in hospital is more than three billion dollars per year. The medical treatment involves the use of metronidazole for mild infection and vancomycin with or without metronidazole for severe infection. In resistant patients with elevated lactate levels and elevated WBC levels (>50,000/mm^3), surgical intervention (partial colectomy with preservation of rectum) is needed.

Typhlitis

Typhlitis is characterized by inflammation of the cecum and ascending colon in immunocompromised patients. It is also called neutropenic colitis and is most often seen in patients with leukemia, lymphoma, aplastic anemia, AIDS, renal transplantation, or other immunocompromised conditions.

CT is considered the imaging modality of choice. The CT imaging features include cecal distension, circumferential colonic wall thickening, and pericolonic wall thickening (Fig. 6.11). The other findings include pericolonic fluid, free air, and pneumatosis. The patients are treated conservatively unless they become toxic.

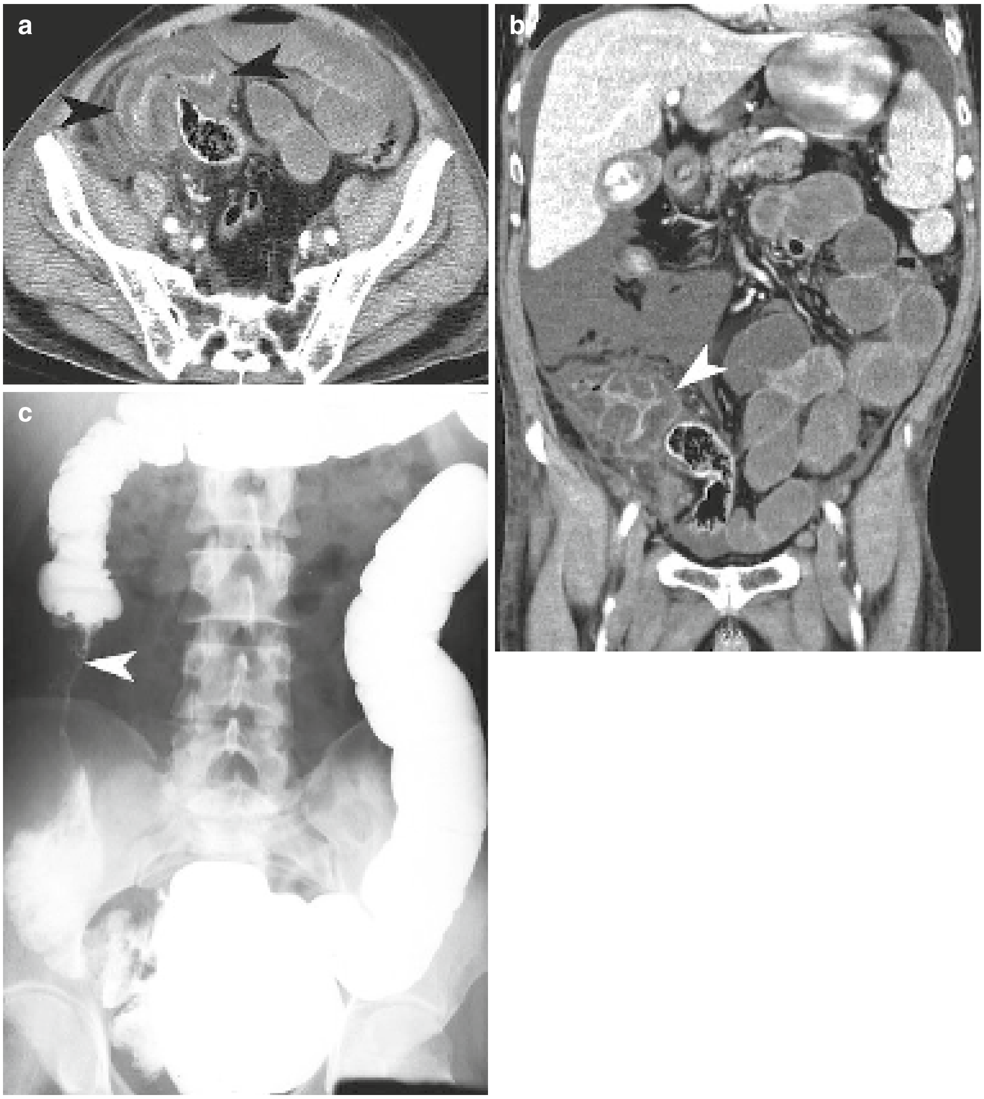

Fig. 6.11 Typhlitis (**a**, **b**) and ileocecal tuberculosis (**c**). (**a**, **b**) Axial and coronal CT images of the abdomen in a patient with chronic lymphocytic leukemia demonstrate inflammatory thickening of the cecal wall (*arrowheads*), secondary to typhlitis. (**c**) Single-contrast barium enema examination of a patient with ileocecal tuberculosis demonstrates chronic ileocecal stricture (*arrowhead*) and cranial migration of the ileocecal junction

Colonic Volvulus

Volvulus refers to torsion of a tract of free-moving bowel along its axis, usually because of a point of traction. It is more frequent in the small bowel, but may occur in the colon. Sigmoid volvulus accounts for 75% and cecal volvulus accounts for 20% of large bowel obstructions.

Cecal volvulus is a potentially life-threatening condition which accounts for up to 2% of cases of bowel obstruction, 11% of cases of intestinal volvulus, and 25–40% of colonic volvulus [13, 14]. Cecal volvulus occurs most commonly in 20–40 years and is a misnomer as the torsion occurs in the ascending colon. The two types of cecal volvulus are as follows:

1. Axial torsion which is characterized by 180°–360° twist along the long axis of the ascending colon.
2. Cecal bascule which is characterized by cecum folding anteromedially, leading to luminal occlusion.

Cecal volvulus is often predisposed by abnormal fixation of the right colon to the retroperitoneum and abnormal motility of the right colon. Other predisposing factors include prior surgery, recent colonoscopy, recent enema, pregnancy, congenital duplication cyst, and mesenteric mass.

Transverse colonic volvulus is a rare site of colonic volvulus but most likely to be life-threatening. Sigmoid volvulus usually occurs in elderly patients (>70 years) and is the most frequent type of colonic volvulus (60–75%). Main predisposing factors are high-fiber diet, pregnancy, hospitalization or institutionalization, and Chagas disease [14].

Imaging

Cecal volvulus demonstrates a dilated gas-filled colonic segment projecting in the left upper quadrant or mid-abdomen, single air-fluid level, and small bowel dilatation. On barium enema, there is a beak-like tapering at the level of the volvulus, adjacent to a dilated cecum. On CT, the "whirl sign" is the main finding, referring to the twisted appearance of the mesenteric vessels, afferent bowel, and efferent bowel loops (Figs. 6.12 and 6.13). The other signs include an abnormally enlarged cecum with decompressed distal colon.

For transverse colonic volvulus, conventional radiology is rarely useful. Barium enema or CT is frequently used to show the twist in the colon. On barium enema, a beak-shaped narrowing is seen at the level of the colonic twist (Fig. 6.14a, b).

On plain radiography, sigmoid volvulus is seen as a large air-filled bowel loop extending cranially from the pelvis to beyond the level of the transverse colon (northern exposure sign). Other radiological findings include the "coffee bean" sign, "closed loop," and "three-line" or "white-stripe" signs (describing the U-shaped closed loop appearance of the colon, between the two points of obstruction and the obliquely oriented vertical white line of the opposed walls and the space within them) (Fig. 6.14c, d) [14]. Coffee bean sign refers to a dilated C-shaped sigmoid colonic loop, extending cranial to the transverse colon and separated by a linear vertical density produced by opposing walls of sigmoid colon. CT can demonstrate the radiographic findings and few other signs (Table 6.6).

The complications of colonic volvulus include bowel wall infarction, gangrene, perforation, septic shock, and death. Symptomatic colonic obstruction in patients with splenic volvulus is characterized by 180°–720° twisting around the mesentery. Lesser degree of twisting may be asymptomatic. Although the treatment options include detorsion, cecopexy, cecostomy, and partial colectomy, if gangrenous changes are encountered, then resection of the necrotic bowel is performed.

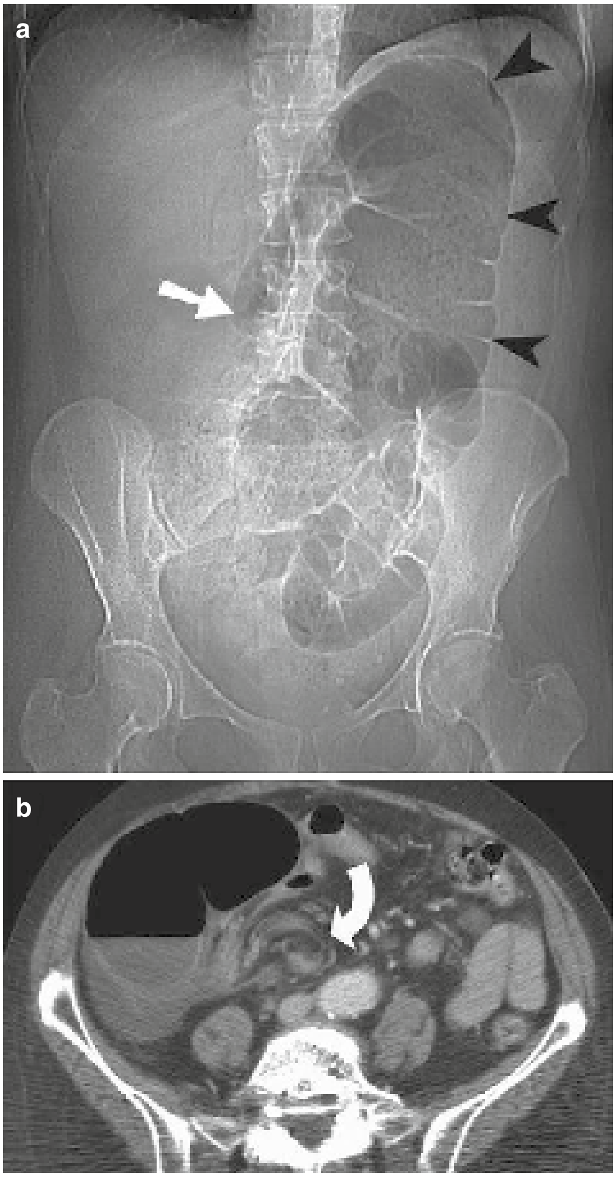

Fig. 6.12 Cecal volvulus. (**a**) Plain X-ray of the abdomen demonstrates dilatation of the cecum (*arrowheads*) which extends to the left upper quadrant. The bowel gas transition is present in the ascending colon (*arrow*). (**b**) Contrast-enhanced CT scan study of the pelvis demonstrates whirl sign in the right lower quadrant (*curved arrow*). The cecum is dilated, and there is free fluid present posterior to it

Fig. 6.13 Cecal volvulus. (**a**) Coronal CT reformation demonstrates whirled appearance of the mesentery as well as a segment of the right colon in this patient with cecal volvulus. (**b**) Coronal CT reformation demonstrates dilated sigmoid colonic loops (*arrowhead*) in this closed loop obstruction

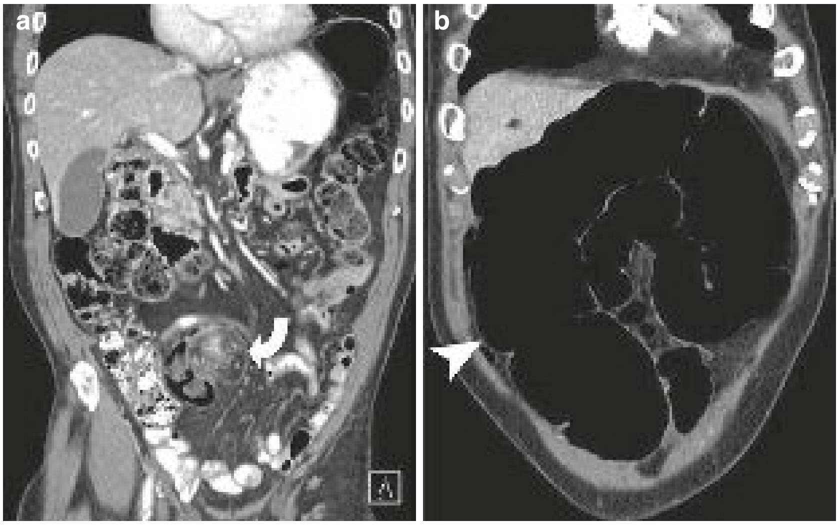

Fig. 6.14 Sigmoid volvulus. (**a**, **b**) Single-contrast barium enema examination in two patients with sigmoid volvulus demonstrates beak-like narrowing (*curved arrow*) at the rectosigmoid junction. (**c**, **d**) Plain X-ray of the abdomen demonstrates dilated loops of sigmoid colon in a coffee bean configuration (*arrowheads*) in two patients with sigmoid volvulus

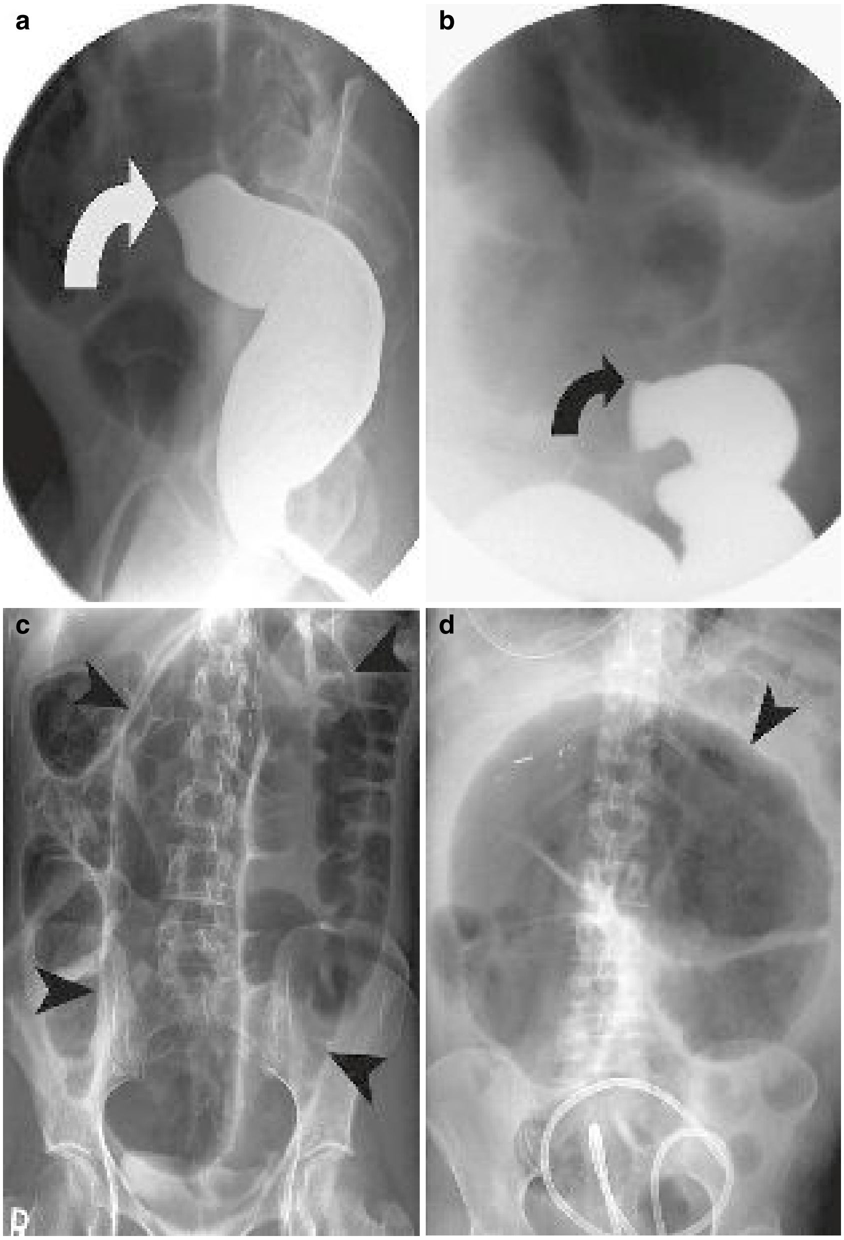

Table 6.6 CT findings of volvulus

1. Coffee bean sign
2. Whirl sign (twisting or swirling mesenteric fat and vessels)
3. X-marks-the-spot sign (crossing transition points)
4. Split-wall sign (invagination of pericolic fat giving the impression split in twisted bowel loop)

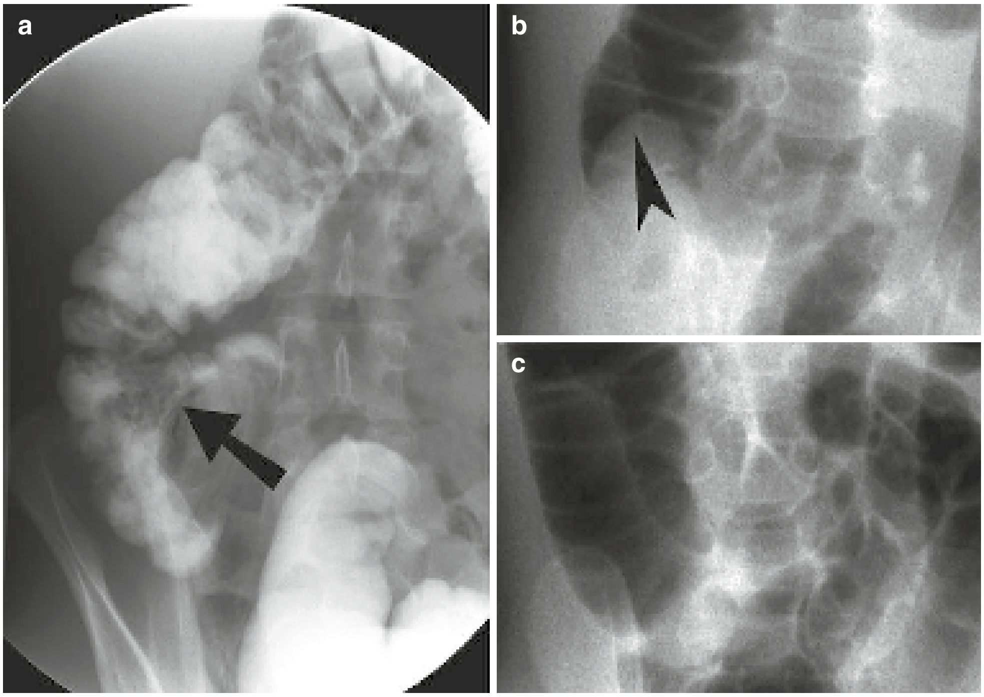

Fig. 6.15 Colonic intussusception reduction on contrast enema. (**a**) Single-contrast barium enema demonstrates a large filling defect (*arrow*) in the cecal lumen due to the presence of the intussusceptum. (**b**) Air enema demonstrates the tip of the intussusceptum (*arrowhead*) outlined by air introduced for reduction of intussusception. (**c**) The follow-up image demonstrates resolution of the ileocolonic intussusception

Intussusception

Intussusception is typically seen in the pediatric age group (2 months to 6 years), accounting for up to 90% of bowel obstruction in infants. Unlike in adults, in children majority of cases are idiopathic. Intussusception is characterized by a segment of proximal bowel and its mesentery (intussusceptum) prolapsing into a segment of contiguous distal bowel (intussuscipiens) due to peristalsis. The most frequent type of intussusception in childhood is the ileocolic intussusception and in adults is ileocolic or colocolic [15, 16]. The lead point, which is more frequent in adults than in children, can be a lipoma, adenomatous polyp, leiomyoma, or villous adenoma. Lead point is also more common in adults than in children. Majority of intussusceptions seen in small bowel on CT are transient and are idiopathic.

In plain radiograph, a crescent-shaped collection of air outlining the intussusceptum head is called "crescent sign." On barium enema, contrast trapped between intussusceptum and intussuscipiens gives a coiled spring appearance (Figs. 6.15 and 6.16). On ultrasound assessment, there is a target appearance produced by the edematous hypoechoic wall of intussuscipiens and concentric hyperechoic rings produced by layers in the wall of intussusceptum (Fig. 6.17).

Contrast enema is used in children, more for treatment than diagnosis of intussusception. Today the main diagnostic tool is ultrasound, particularly in young patients. It allows a correct diagnosis and may find an alternative one when intussusception is not present. CT is also used in doubtful cases and in adult patients.

The CT findings include the central intussusceptum, surrounded concentrically by mesenteric fat or vessels and finally intussuscipiens (Fig. 6.18). The concentric structures may produce a target- or sausage-shaped mass. A reniform-shaped mass is seen on CT in late stages and produced by progressive wall edema and vascular compromise (Table 6.7).

The treatment of intussusception includes radiological enema (with air, water-soluble material, or barium). The injection of liquid (water or saline) or air under US control is another technique that reduces radiation exposure of young patients. If no results are obtained or perforation is present, surgical resection is indicated [15]. Surgical treatment is the main therapy for adult intussusception, because of the high frequency of an underlying pathologic lead point.

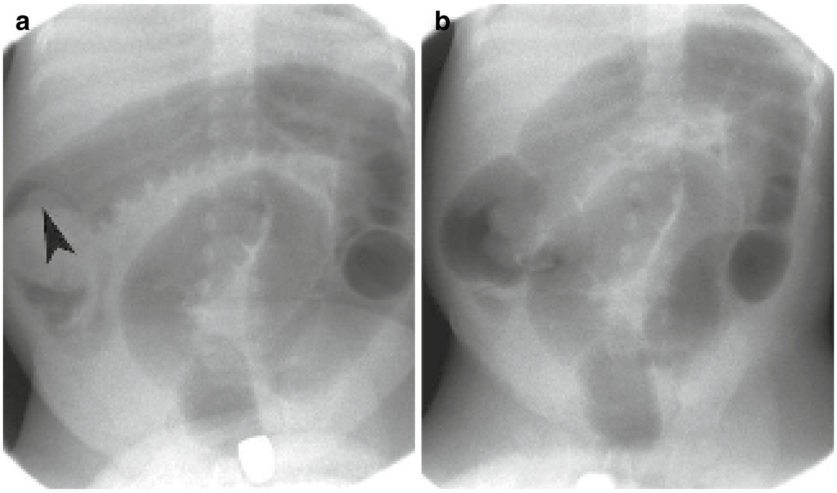

Fig. 6.16 Colonic intussusception reduction on contrast enema. (**a**, **b**) Spot images before and after contrast reduction shows the intussusceptum (*arrowhead*) outlined by air, followed by resolution of the ileocolonic intussusception

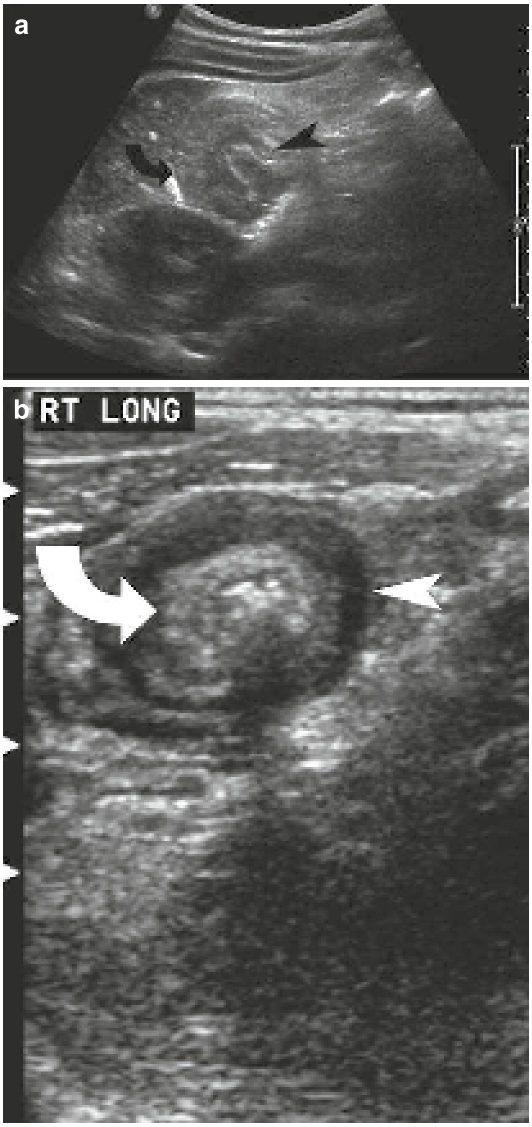

Fig. 6.17 Colonic intussusception on ultrasound and CT. (**a**) Ultrasound demonstrates concentric layers of the intussusceptum (*arrowhead*) and intussuscipiens (*curved arrow*). (**b**) Contrast-enhanced CT shows the centrally located intussusceptum (*arrowhead*), surrounded by air and intussuscipiens (*curved arrow*)

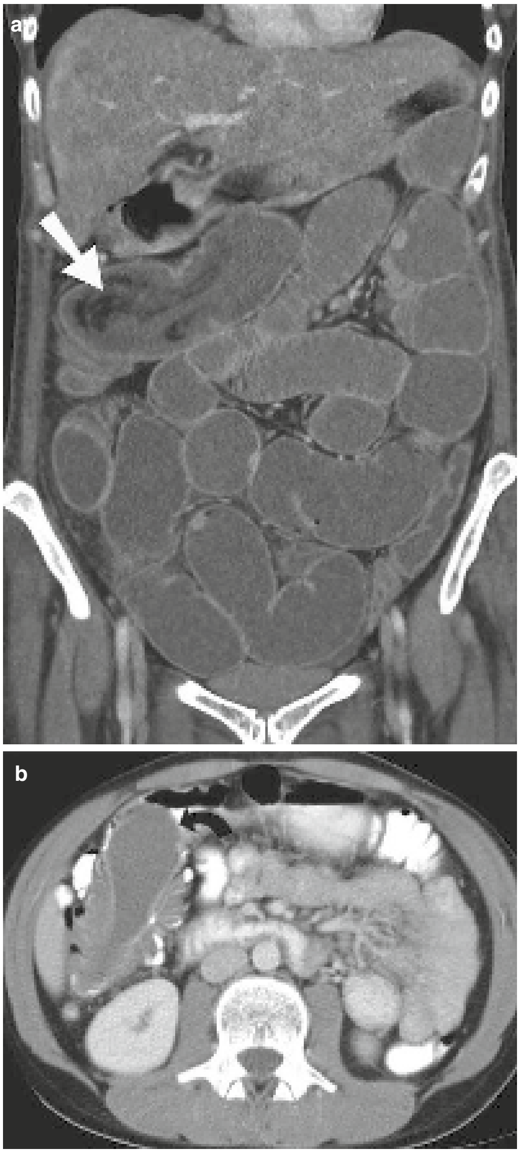

Fig. 6.18 Intussusception. (**a**) Coronal CT scan reformation demonstrates colocolonic intussusception in the hepatic flexure of the colon. The intussusceptum (*straight arrow*) is causing high-grade bowel obstruction. (**b**) Axial contrast-enhanced CT demonstrates colocolonic intussusception due to a duplication cyst (*curved arrow*)

Table 6.7 Demonstrates imaging features of intussusception in imaging modalities

Imaging modality	Findings
Ultrasonography	• Target appearance
Radiography	• Crescent sign
Barium enema	• Coiled spring appearance
CT	• Target- (or sausage-) shaped mass
	• Reniform-shaped mass

Colonic Ischemia

Ischemic colitis is the most frequent type of ischemic disease of the gastrointestinal tract (50%), most commonly involving the splenic flexure and the descending colon [13]. It mainly affects the elderly people and may manifest with reversible ischemia to irreversible ischemia (transmural infarction, gangrene, perforation, and stricture). The underlying cause of ischemia is insufficient vascular supply to the colonic wall which has the highest propensity to initially affect the mucosa. Although mucosal ischemia is reversible in the majority, it can also progress to transmural infarction.

The causes of bowel ischemia include thromboembolism, nonocclusive causes, colonic obstruction, tumors, vasculitis, radiation, and trauma [17]. Major vascular occlusion is seen on angiography in less than a tenth of the cases. Today the definitive diagnosis is usually made by colonoscopy. The plain radiograph may be normal or may show submucosal hemorrhage or edema (thumbprinting), ileus, transverse ridging, or ahaustral bowel pattern. Thumbprinting is most suggestive of colonic ischemia and is seen as thumb-shaped smooth projections into the colonic lumen (Fig. 6.19a). The initial diagnosis is most often suspected based on the CT imaging findings, most commonly in inferior mesenteric artery distribution (Table 6.8).

For mild cases, the treatment is conservative with two-thirds of all patients recovering spontaneously within 24–48 h. In patients who do not respond to conservative treatment or those who have clinical signs of frank peritonitis or bowel perforation, surgical intervention is indicated.

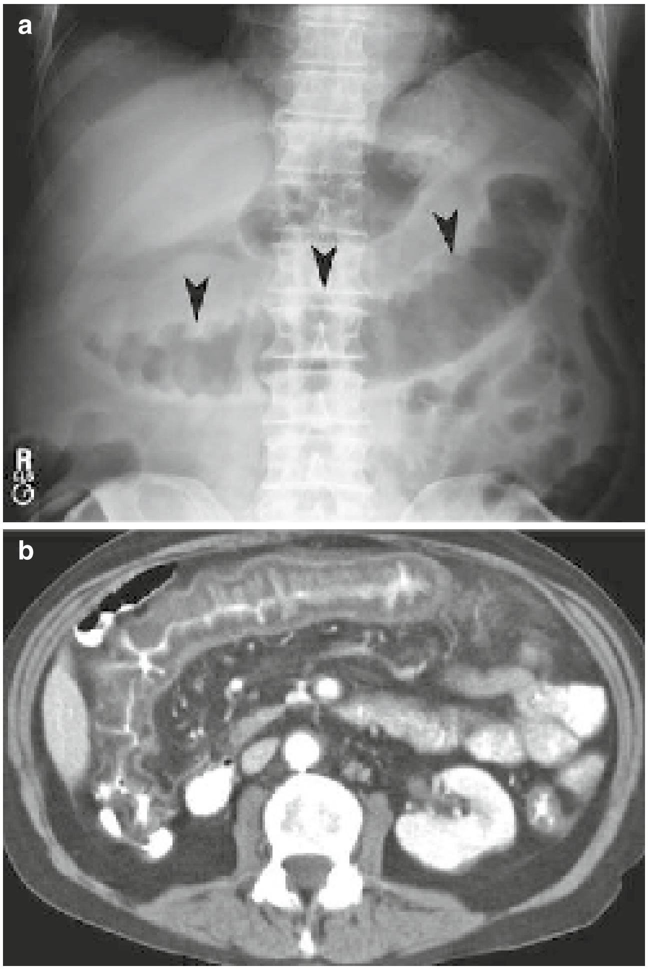

Fig. 6.19 Ischemic colitis. (**a**) Plain X-ray of the abdomen demonstrates thumbprinting and mucosal edema (*arrowheads*) in the transverse colon of a patient with ischemic colitis. (**b**) Contrast-enhanced CT scan study of the abdomen demonstrates thickening of the transverse colonic wall with stratification, secondary to mucosal and serosal enhancement. The histopathology findings were consistent with ischemic colitis

Table 6.8 CT findings of colonic ischemia

1. Symmetric bowel wall thickening (Fig. 6.19b)
2. Most commonly involving the inferior mesenteric artery territory
3. Double halo sign due to submucosal edema
4. Colonic pneumatosis (Fig. 6.20)

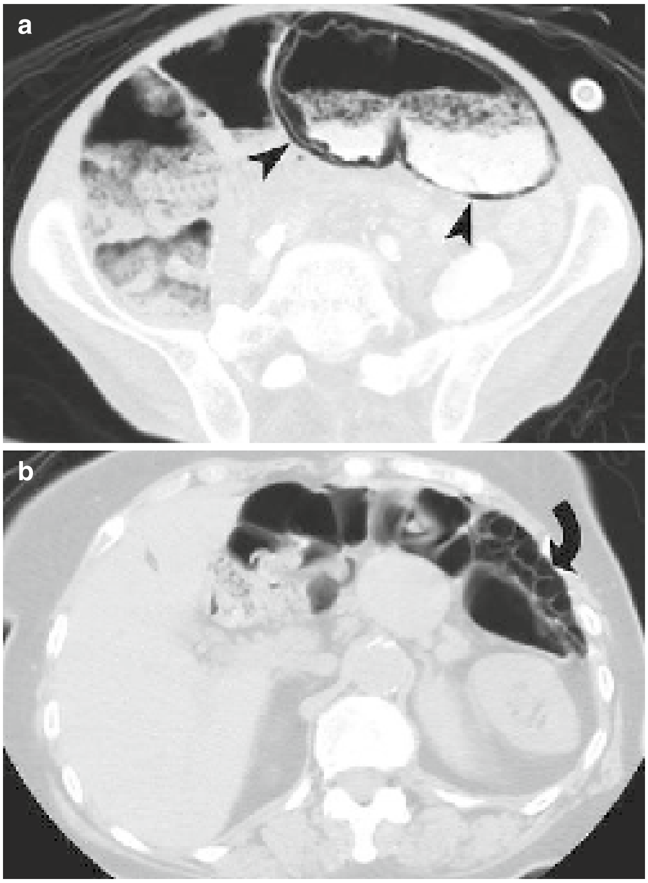

Fig. 6.20 Colonic ischemia. (**a**, **b**) CT of the abdomen (lung windows) demonstrates linear (**a**) and cystic (**b**) pneumatosis involving the transverse colon. Linear pneumatosis is believed to be associated with worse prognosis

GI Bleeding

Although most common site of gastrointestinal tract bleeding is from the esophagus, stomach, or duodenum, 30% of bleeding originates from the lower gastrointestinal tract, distal to the ligament of Treitz [18]. Upper gastrointestinal bleeding accounts for two-thirds of gastrointestinal bleedings and is most commonly due to peptic ulcers and gastritis. Lower gastrointestinal bleeding is most commonly seen in older patients than upper gastrointestinal bleeding. The main causes of bleeding in the lower intestinal tract are summarized in Table 6.9 [18].

Table 6.9 Causes of lower intestinal tract bleeding

Cause	Frequency (%)
Diverticular disease	20–55
Angiodysplasia	3–40
Tumors	8–26
Inflammatory diseases	6–22
Benign lesions of the anorectal tract	9–10

Clinically, lower gastrointestinal bleeding presents as hematochezia, which refers to passage of bright red blood. Small bleedings (<100 mL/day) may remain asymptomatic, but when blood loss is higher or acute (>500 mL or >15% blood volume), the patient may suffer hypotensive shock.

In patients with lower gastrointestinal bleeding, Tc 99m-labeled RBC scan is the investigation of choice because of its ability to detect intermittent bleeding (Fig. 6.21). Unlike Tc 99m sulfur colloid, Tc 99m-labeled RBC scan allows detection of bleeding over several hours. It is less sensitive than Tc 99m sulfur colloid in detection of bleeding. Tc 99m sulfur colloid scan has extremely high sensitivity in detecting bleeding as low as 0.05–0.1 mL/min, but has the disadvantage of being sensitive only if the bleeding occurs within 20 min of radiopharmaceutical injection.

If scintigraphy demonstrates bleeding, then conventional angiography is performed for diagnostic and therapeutic reasons. If bleeding is identified on angiography, vasopressin infusion or transcatheter embolization could be performed. To identify bleeding on angiography, the rate of bleeding must be more than 0.5 mL/min. Colonoscopy should be performed if the hematochezia has subsided and when the diagnostic yield of angiography is low.

Teaching Points

- Contrast-enhanced CT is the imaging modality of choice in the evaluation of acute left lower quadrant pain.
- For the initial presentation of suspected Crohn's disease in patients with abdominal pain, fever, and diarrhea, CT enterography is considered the most appropriate imaging modality.
- For adult and pediatric patients with known Crohn's disease, presenting with fever, abdominal pain, and leukocytosis, routine contrast-enhanced CT is considered the imaging modality of choice.
- Sigmoid volvulus accounts for 75% and cecal volvulus accounts for 20% of large bowel obstructions.

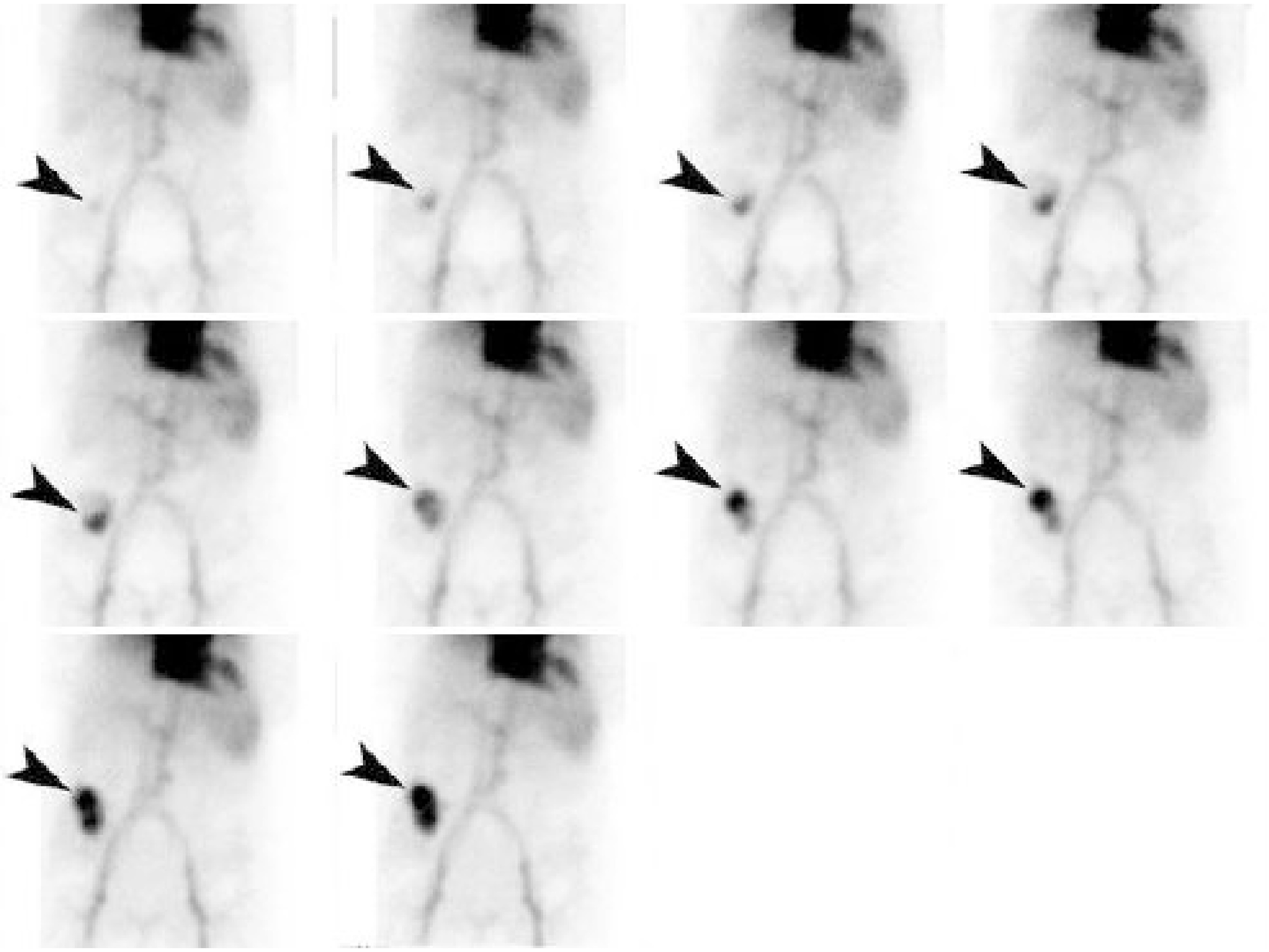

Fig. 6.21 Lower gastrointestinal bleeding on Tc 99m-labeled RBC scan. Tc 99m-labeled RBC scan demonstrates progressively increasing radiotracer activity (*arrowheads*) in the cecum

Questions

1. Which of the following is the most common complication of acute diverticulitis?
   (A) Fistula
   (B) Obstruction
   (C) Abscess
   (D) Peritonitis
   Answer: C

2. What is the most common location of acute epiploic appendagitis?
   (A) Sigmoid colon
   (B) Transverse colon
   (C) Cecum
   (D) Ascending colon
   Answer: A

3. Which of the following is most commonly associated with ulcerative colitis?
   (A) Deep ulcers
   (B) Aphthoid ulcers
   (C) Strictures
   (D) Collar button lesions
   Answer: D

4. What is the pathology depicted on the single-contrast barium enema and scout film (Fig. 6.22a, b)?
   (A) Cecal volvulus
   (B) Sigmoid volvulus
   (C) Typhlitis
   (D) Inflammatory bowel disease
   Answer: A

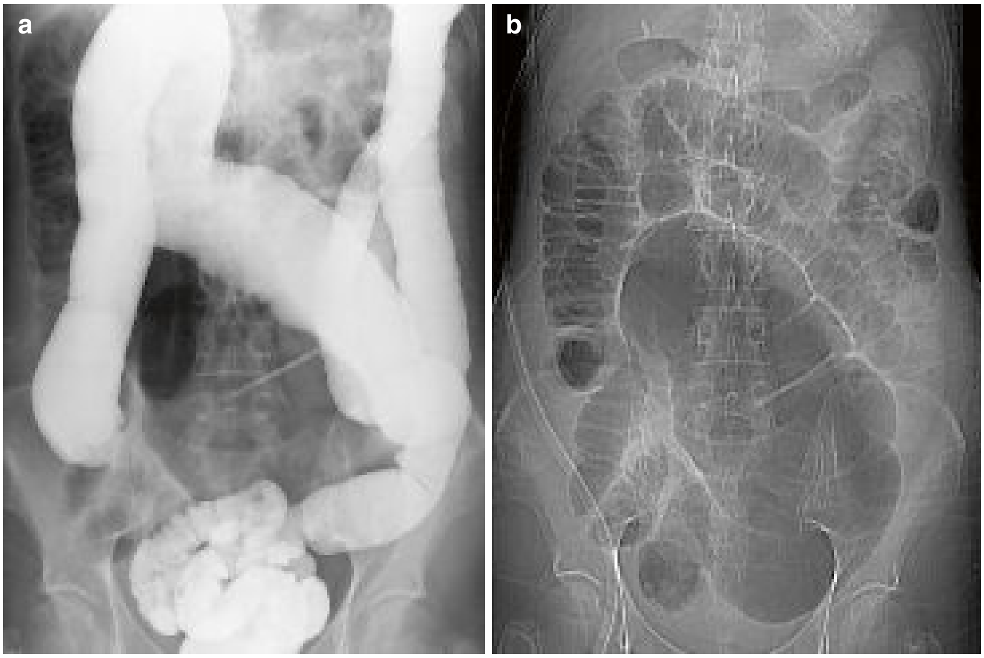

Fig. 6.22 (**a**, **b**) Cecal volvulus

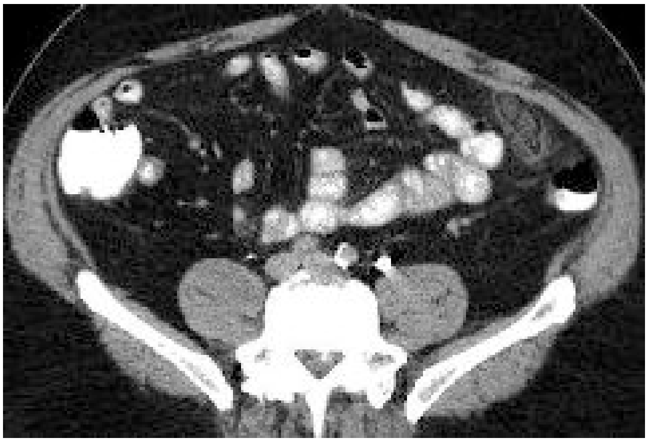

Fig. 6.23 Acute epiploic appendagitis—CT

5. What is the diagnosis in the CT (Fig. 6.23) of a patient with left lower quadrant pain?
   (A) Acute appendicitis
   (B) Acute epiploic appendagitis
   (C) Inflammatory bowel disease
   (D) Sigmoid diverticulitis
   Answer: B

6. What is the most probable diagnosis CT scan (Fig. 6.24) of a patient with bloody stools?
   (A) Ischemic colitis
   (B) Pseudomembranous colitis
   (C) Typhlitis
   (D) Inflammatory bowel disease
   Answer: B

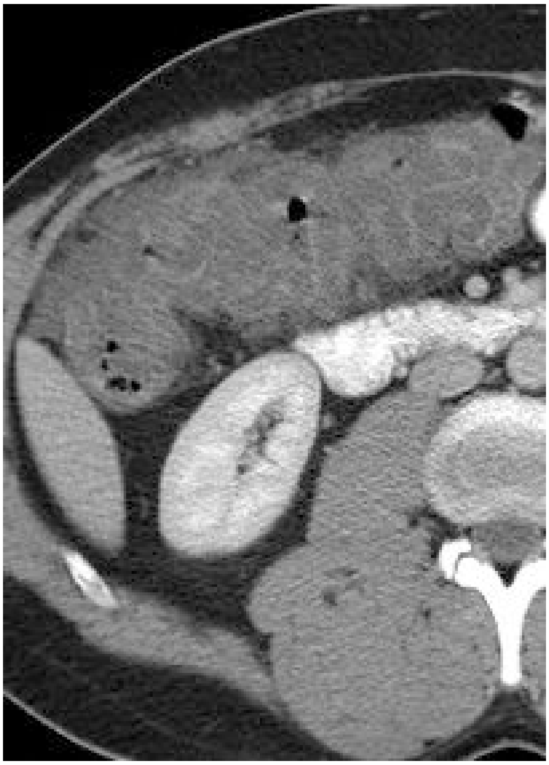

Fig. 6.24 Pseudomembranous colitis

References

1. Pereira JM, Sirlin CB, Pinto PS, Jeffrey RB, Stella DL, Casola G. Disproportionate fat stranding: a helpful CT sign in patients with acute abdominal pain. Radiographics. 2004;24:703–15.

2. Horton KM, Corl FM, Fishman EK. CT evaluation of the colon: inflammatory disease. Radiographics. 2000;20:399–418.
3. Rucker CM, Menias CO, Bhalla S. Mimics of renal colic: alternative diagnoses at unenhanced helical CT. Radiographics. 2004;24:S11–33.
4. Heverhagen JT, Klose KJ. MR imaging for acute lower abdominal and pelvic pain. Radiographics. 2009;29:1781–96.
5. Singh AK, Gervais DA, Hahn PF, Sagar P, Mueller PR, Novelline RA. Acute epiploic appendagitis and its mimics. Radiographics. 2005;25:1521–34.
6. Singh AK, Gervais DA, Lee P, Westra S, Hahn PF, Novelline RA, et al. Omental infarct: CT imaging features. Abdom Imaging. 2006;31(5):549–54.
7. Singh AK, Gervais DA, Hahn PF, Rhea J, Mueller PR. CT appearance of acute appendagitis. AJR Am J Roentgenol. 2004;183(5):1303–7.
8. Ghahremani GG, With EM, Hoff FL, Gore RM, Miller JW, Christ M. Appendices epiploicae of the colon: radiological and pathological features. Radiographics. 1992;12:59–77.
9. Furukawa A, Saotome T, Yamasaki M, Maeda K, Nitta N, Takahashi N, et al. Cross-sectional imaging in Crohn disease. Radiographics. 2004;24:689–702.
10. Rimola J, Rodríguez S, García-Bosch O, Ricart E, Pagès M, Pellisé M, et al. Role of 3.0-T MR colonography in the evaluation of inflammatory bowel disease. Radiographics. 2009;29:701–19.
11. Gore RM, Levine MS. Textbook of gastrointestinal radiology, vol. 1. 2nd ed. Philadelphia: W. B. Saunders; 2000. p. 726–45.
12. Kawamoto S, Horton KM, Fishman EK. Pseudomembranous colitis: spectrum of imaging findings with clinical and pathologic correlation. Radiographics. 1999;19:887–97.
13. Silva AC, Beaty SD, Hara AK, Fletcher JG, Fidler JL, Menias CO, et al. Spectrum of normal and abnormal CT appearances of the ileocecal valve and cecum with endoscopic and surgical correlation. Radiographics. 2007;27:1039–54.
14. Peterson CM, Anderson JS, Carenza JW, Menias CO. Volvulus of the gastrointestinal tract: appearances at multimodality imaging. Radiographics. 2009;29:1281–93.
15. del Pozo G, Albillos JC, Tejedor D, Calero R, Rasero M, de-la-Calle U, et al. Intussusception in children: current concepts in diagnosis and enema reduction. Radiographics. 1999;19:299–319.
16. Kim YH, Blake MA, Harisinghani MG, Archer-Arroyo K, Hahn PF, Pitman MB, et al. Adult intestinal intussusception: CT appearances and identification of a causative lead point. Radiographics. 2006;26:733–44.
17. Rha SE, Ha HK, Lee SH, Kim JH, Kim JK, Kim JH, et al. CT and MR imaging findings of bowel ischemia from various primary causes. Radiographics. 2000;20:29–42.
18. Laing CJ, Tobias T, Rosenblum DI, Banker WL, Tseng L, Tamarkin SW. Acute gastrointestinal bleeding: emerging role of multidetector CT angiography and review of current imaging techniques. Radiographics. 2007;27:1055–70.

Imaging of Genitourinary Emergencies

7

Robin B. Levenson, Mai-Lan Ho,
and Mohammad Mansouri

Introduction

Nontraumatic urinary tract emergencies include acute obstructive uropathy, infections which can become complicated, and acute renovascular abnormalities. Imaging plays an important role in evaluating the extent of the acute process and the location and in differentiating urinary tract emergencies from other acute conditions which may be clinical mimics.

Obstructive Uropathy

Obstructive uropathy is defined as structural or functional blockage of normal urinary outflow and may occur at any level of the urinary system. This leads to urine stasis, pressure buildup, and failure of excretion [1]. Etiologies include stones, blood clots, infection/inflammation, extrinsic compression, functional spasm, and primary or metastatic tumors. In healthy individuals, unilateral renal obstruction can be compensated for by the contralateral kidney, without measurable changes in overall excretory function. However, in patients with underlying chronic renal disease and/or bilateral obstruction, significant functional decompensation may occur. Additional complications include infection and collecting system rupture [2].

The clinical presentation of acute obstructive uropathy may include flank pain, dysuria, hematuria, oliguria, fever, and nausea/vomiting. The pain may be vague and poorly localized. In patients with fulminant uremia, lethargy and mental status changes may be present [2]. Laboratory tests and clinical findings may be inconclusive, and imaging plays an important role for diagnosis and patient management.

Imaging

Plain radiography may be used as initial screening for patients with acute abdominal or flank pain although computed tomography is the modality of choice. Radiography has 45–60% sensitivity and 70% specificity for detecting renal stones (Fig. 7.1a). Findings may be falsely negative for noncalcified stones, calcified stones less than 4 mm, and patients with large body habitus. In addition, false-positive interpretations may occur with gallstones, phleboliths, and granulomatous calcifications [1]. Other causes of obstruction, including masses and blood clots, are poorly characterized. Radiography may also be used for surgical planning including patients undergoing shock-wave lithotripsy, visualization of a stent, and for follow-up. Studies suggest that having baseline plain radiography helps physicians in follow-up [3].

Multidetector computed tomography (MDCT) is the gold standard for imaging patients with suspected obstructive uropathy. Stone or lesion size, location, and degree of obstruction can be quantified. Noncontrast CT (NCCT) has a sensitivity of 95–98% and specificity of 96–100% for detecting urinary stones [4–6]. NCCT is relatively quick, without the use of intravenous or oral contrast, making it particularly useful in the emergency setting. CT dose reduction techniques can be used with minimal effects on the sensitivity [7]. These techniques include automated tube current modulation, increased slice thickness, and decreased tube current or voltage. Most stones appear radiodense on CT. Rarely, in HIV patients who are poorly hydrated and treated with indinavir, crystalline stones develop which are radiolucent on NCCT. When findings are negative or equivocal, intravenous contrast can be administered to assess for additional renal or

---

R. B. Levenson (✉)
Department of Radiology, Harvard Medical School, Beth Israel Deaconess Medical Center, Boston, MA, USA
e-mail: rlevenso@bidmc.harvard.edu

M.-L. Ho
Department of Radiology, Mayo Clinic, Rochester, MN, USA

M. Mansouri
Department of Radiology, Massachusetts General Hospital, Boston, MA, USA

© The Author(s), under exclusive license to Springer Nature Switzerland AG 2024
A. Singh (ed.), *Emergency Radiology*, https://doi.org/10.1007/978-3-031-65770-2_7

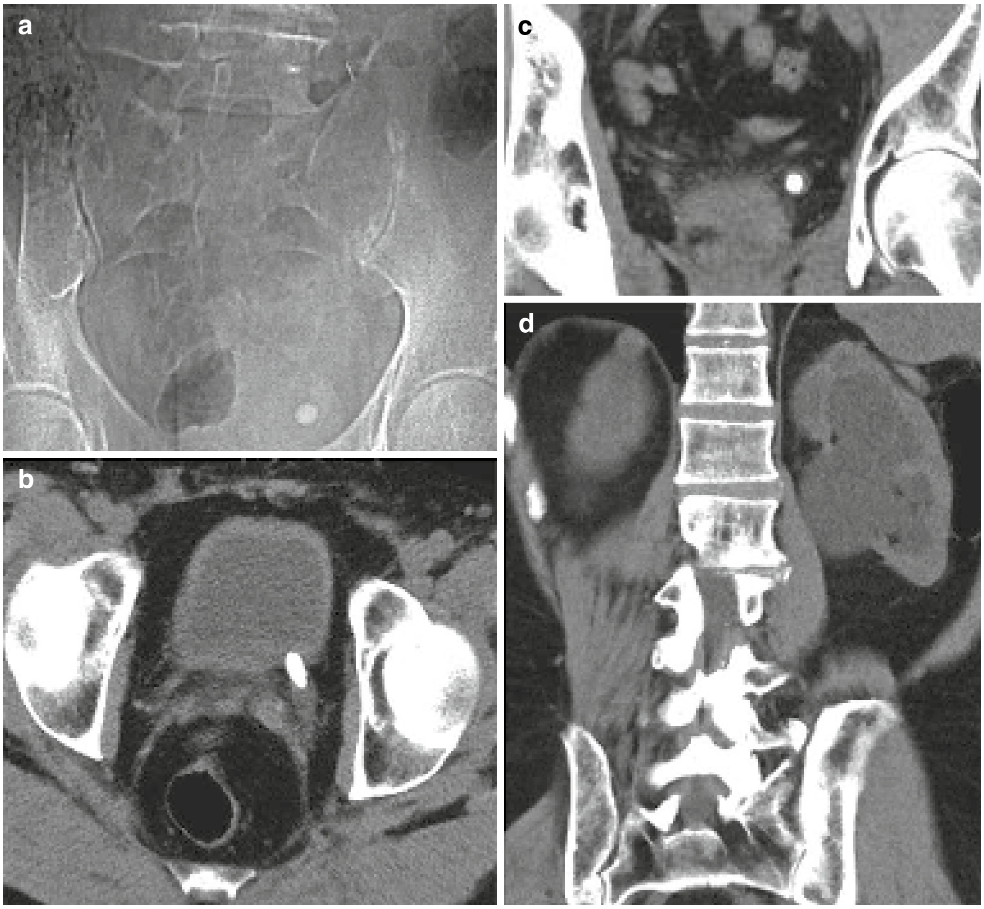

Fig. 7.1 Obstructing left UVJ stone in a 71-year-old male with elevated creatinine and hydronephrosis. (**a**) Scout view demonstrates a coarse calcification in the left pelvis corresponding to a left UVJ stone as confirmed on subsequent CT images. (**b–d**) Noncontrast-enhanced CT axial (**b**) and coronal (**c**, **d**) images show a 14 × 6 × 4 mm left UVJ stone (**b**, **c**) with soft tissue rim sign (**c**) and upstream severe left hydronephrosis (**d**)

abdominal processes. Besides urinary stones, other etiologies of intraluminal obstruction include blood clots, which are dense but lower in attenuation than calculus; masses, which measure soft tissue attenuation and enhance following contrast administration; and ureteral spasm, strictures, or injury. Extraluminal compression may be caused by retroperitoneal masses, abscess, inflammation, or posttraumatic hematoma [5, 6].

At CT evaluation for ureteral stone, one should focus at the most common locations; narrowing of the ureter occurs naturally at the ureterovesicular junction (UVJ), the pelvic brim as the ureter crosses iliac vessels, and at the ureteropelvic junction (UPJ) (see Fig. 7.1b, c) [4]. Frequently, a transition point is visible, with urinary decompression more distally. Secondary CT findings in obstructive uropathy include hydroureter, hydronephrosis, perinephric stranding, and possible enlargement of the unilateral kidney (see Fig. 7.1d; Table 7.1). Periureteral wall thickening and perinephric/periureteral fat stranding reflect acute inflammation. The "soft tissue rim sign" is due to edema of the ureteral wall at the site of stone impaction and may help differentiate a ureteral stone from a phlebolith in an adjacent vein (see Fig. 7.1c) [8]. The "comet tail sign," is thin soft tissue extending from a focus of calcification in the abdomen or pelvis, can also be used to differentiate these two entities, and typically indicates a phlebolith [7]. Renal edema may be appreciated, with decrease in Hounsfield attenuation on NCCT ("pale kidney" sign). Following contrast administration, there may be delayed excretion of contrast into the collecting system/ureter or beyond the level of obstruction ("delayed nephrogram/urogram"), which may be partial or complete (Fig. 7.2). Pyelosinus or forniceal rupture manifests as a perinephric fluid (Fig. 7.3). In cases of extrinsic compression, the ureter appears abnormally deviated due to mass effect [5, 6, 9].

Table 7.1 CT findings in acute obstructive uropathy

1. Calcified stone in the GU tract (UVJ, UPJ, and pelvic brim are most common locations)
2. Hydroureter
3. Hydronephrosis
4. Soft tissue rim sign
5. Perinephric/periureteral stranding
6. Unilateral enlarged kidney
7. Forniceal rupture
8. Pale kidney sign

Ultrasonography (US) is a useful screening examination for pregnant and pediatric patients, in whom radiation exposure is a concern. The sensitivity for urinary obstruction is 60–70%, but this is highly operator and patient dependent and involves limited ureteral assessment [10]. Renal stones are echogenic foci with or without shadowing, depending on size, composition, and technique (Fig. 7.4). At US, renal stones are best seen when the stone is greater than 5 mm. Smaller stones may blend into the echogenic renal sinus and be missed. Ureteropelvic and ureterovesical junction stones, which lie superficially within good acoustic windows, may be seen. However, mid-ureteral stones are extremely difficult to detect. The finding of hydronephrosis is suggestive but may be absent in early obstruction (false negative) or present due to alternate causes such as pregnancy and reflux (false positive) (Fig. 7.5a). One must distinguish true hydronephrosis from mimics such as parapelvic cysts, extrarenal pelvis, and pelvicaliectasis. Additional signs include absent or decreased ureteral jets and a Doppler arterial resistive index greater than 0.70 (or difference between kidneys greater than 0.10). However, these findings are neither sensitive nor specific [10]. The "twinkle artifact" in Doppler ultrasound can be used to distinguish between stones smaller than 5 mm and vascular calcifications (Fig. 7.6). "Twinkle artifact" is an area of alternating Doppler colors related to reflection from a coarse surface, like a GU stone. However this finding is not specific. Also "color comet tail artifact" in Doppler ultrasound, immediately deep to the stone, can help diagnosis. A "color comet tail artifact" is a tail-like linear band of Doppler colors which extend away from the probe.

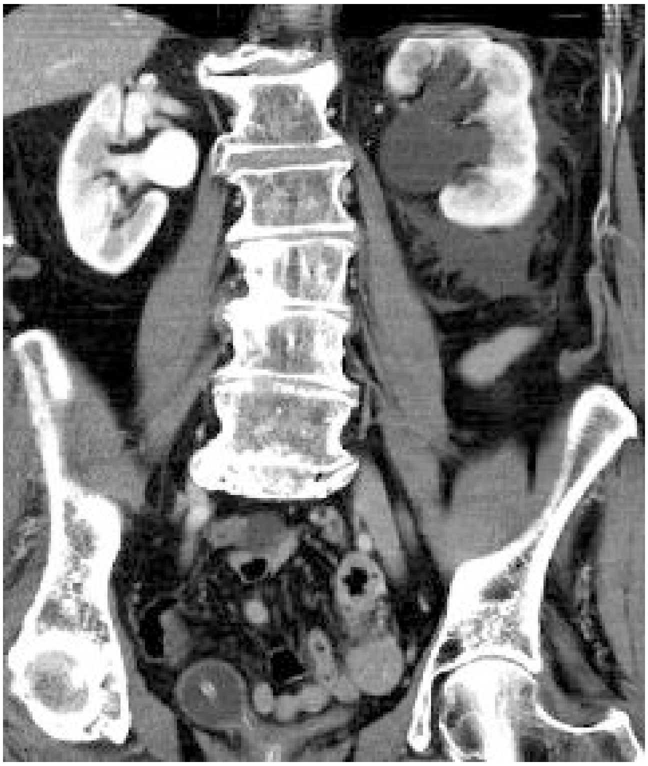

Fig. 7.2 Delayed excretion of contrast in an 87-year-old female with left abdominal pain. Contrast-enhanced coronal CT image shows left hydronephrosis and delayed excretion of contrast (delayed enhancement) from the left kidney as compared to the right in this patient with an obstructing 9 mm left UPJ stone

Magnetic resonance imaging (MRI) is an alternative to CT, particularly in pediatric and pregnant patients for whom radiation exposure is a concern. MRI offers superior soft tissue contrast, albeit with increased costs and longer scan times. Ultrafast scanning protocols have been developed to image the urinary system with good spatial resolution in multiple planes. Fluid-sensitive T2-weighted sequences, such as single-shot fast spin echo (SSFSE) and balanced steady-state free precession (SSFP), utilize urine as an intrinsic contrast agent [11]. Fat-suppressed sequences are also acquired to enable differentiation from intraperitoneal/retroperitoneal fat. Urinary calculi, which are proton poor, may appear as hypointense filling defects (see Fig. 7.5b, c). Stones smaller than 1 cm are frequently not seen—in which case diagnosis relies on signs of urinary obstruction, such as a ureteral transition point [11]. Acute obstruction frequently presents with soft tissue wall thickening, stranding, and edema, manifesting as

Fig. 7.3 Forniceal rupture in a 41-year-old female with left flank pain. (**a**) Noncontrast-enhanced axial CT image demonstrates 2 mm left UVJ stone. (**b**) Contrast-enhanced CT axial image demonstrates perinephric fluid consistent with forniceal rupture

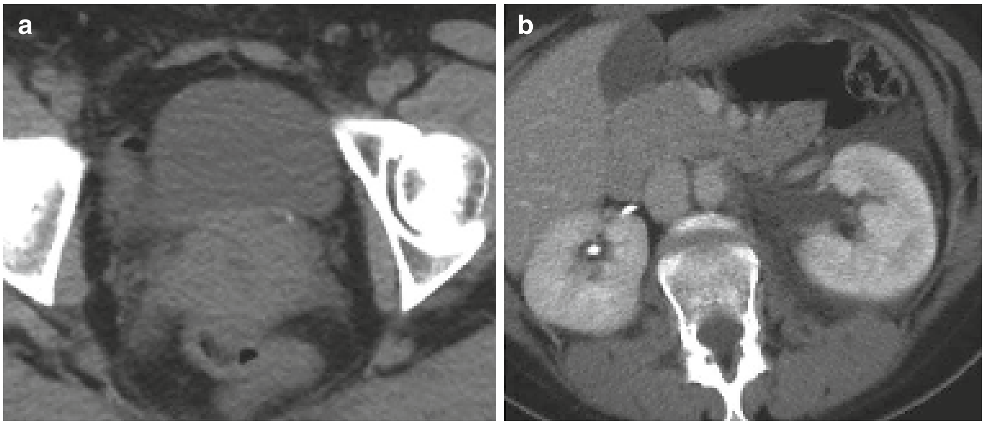

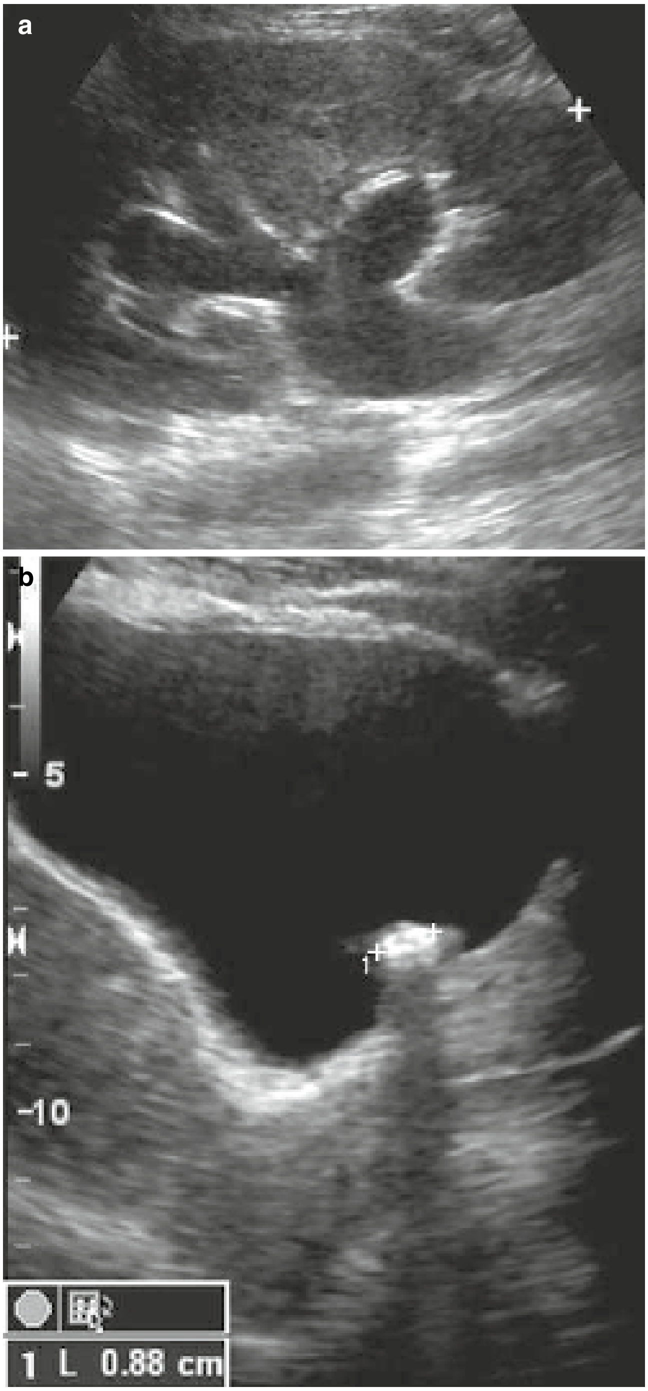

Fig. 7.4 Obstructing left UVJ stone with upstream left hydronephrosis. Ultrasound images show moderate left hydronephrosis (**a**). Shadowing echogenic focus at the left UVJ is consistent with obstructing stone (**b**)

high T2 signal and loss of renal corticomedullary differentiation. Multiphasic gadolinium-enhanced imaging can be performed using a T1-weighted spoiled gradient echo sequence. This allows assessment of the renal parenchyma, improves urinary-calculi contrast, and quantifies collecting system transit time [11]. Table 7.2 summarizes sensitivity and specificity of imaging modalities for detecting stones.

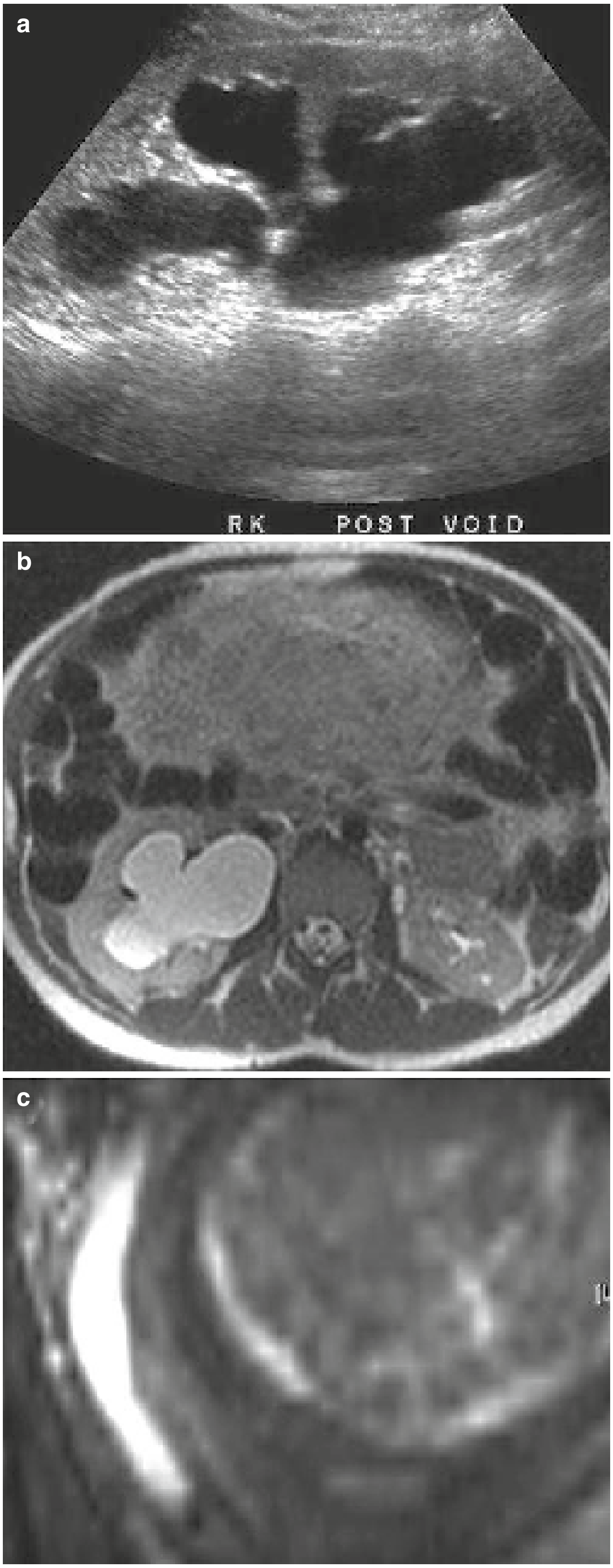

Fig. 7.5 Hydronephrosis due to ureteric stone in pregnancy. (**a**) Ultrasound shows moderate right hydronephrosis. Distal right ureter not visualized, and etiology was unclear. (**b**, **c**) Subsequent MR imaging shows moderate to severe right hydronephrosis on axial SSFSE HASTE imaging (**b**), secondary to distal right ureteric stone (**c**, coronal true FISP)

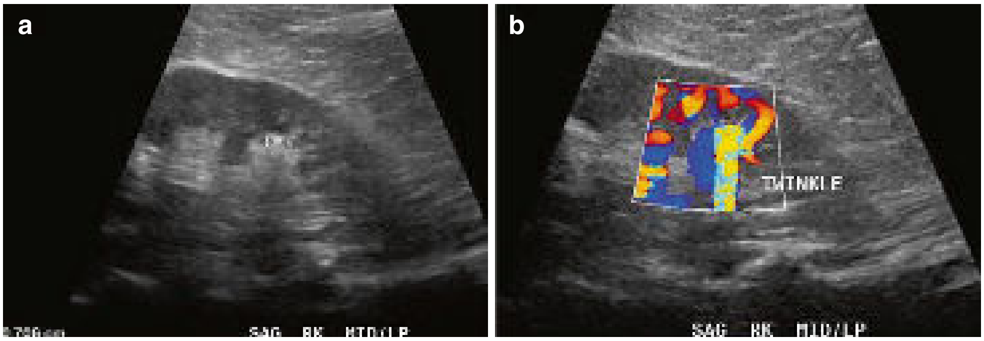

Fig. 7.6 Renal stone on color Doppler imaging. (**a**) Gray-scale ultrasound of the right kidney shows a 7 mm echogenic calculus with posterior acoustic shadowing. (**b**) Color Doppler demonstrates associated twinkle and color comet tail artifact

Table 7.2 Sensitivity and specificity of imaging modalities for detecting stones

Modality	Sensitivity (%)	Specificity (%)	Notes
Plain radiography	45–60	70	• Limited in small or noncalcified stones or large patients • May be useful in surgical planning and follow-up
US	60–70	69	• Screening tool for pregnant and pediatric patients • Mid-ureteral stones are difficult to detect
Plain radiography + US	79	71	• Useful in young females and patients with history of stones
CT	95–98	96–100	• Gold standard • Useful to differentiate causes of obstruction and to assess for alternate etiology of patient symptoms
MRI	50–60	–	• Alternate modality in pediatric and pregnant patients • Limited for small stones

Complications and Treatment

In the early stages, acute obstructive uropathy is reversible with minimal renal parenchymal damage. Urinary stones smaller than 5 mm can be managed conservatively and usually pass spontaneously. Large and/or irregularly shaped stones may become impacted, predisposing to infection and collecting system rupture which can result in hematogenous dissemination of infection (urosepsis) [2].

In urgent situations, drainage procedures such as percutaneous nephrostomy, nephroureteral stenting, and suprapubic cystostomy can be performed to decompress the urinary system proximal to the site of obstruction [2].

Infections

Urinary tract infections have accounted for approximately one million emergency department visits annually in the USA [12]. Most of these are uncomplicated and only involve the urinary bladder. However, if the infection migrates proximally or is spread hematogenously, pyelonephritis may ensue.

Acute Pyelonephritis

Urinary tract infections typically begin in the urinary bladder and migrate proximally, leading to tubulointerstitial inflammation. This ascending infection often occurs in the absence of reflux due to the virulence of the bacteria, most commonly gram-negative organisms, in particular *Escherichia coli*. Pyelonephritis can also occur if the urinary infection is spread to the kidneys hematogenously, from skin infection or endocarditis as may be seen in intravenous drug abusers. Acute pyelonephritis has an incidence of 120–130 cases annually per 100,000 females and 30–40 cases annually per 100,000 males [7].

Patients with pyelonephritis tend to present with fever, chills, and flank pain, and costovertebral angle tenderness. Symptoms often also include dysuria, urinary frequency, and urgency [12]. Additional symptoms of acute pyelonephritis may include abdominal pain, nausea, and vomiting, which overlap with many other conditions, particularly gastrointestinal. Urinalysis findings include pyuria, bacteriuria, and positive urine culture.

Imaging

The majority of patients respond well to antibiotic treatment, and imaging is often not required. However, in certain circumstances, imaging can play an important role in differentiating acute pyelonephritis from other entities causing acute symptoms (particularly if the patient has failed 72 h of antibiotic treatment), detecting structural abnormalities, and evaluating patients at high risk for complications (including pregnant, diabetic, elderly, or immunocompromised patients with history of kidney stones and genitourinary abnormalities), characterizing the severity of infection and extent of possible organ damage (Table 7.3).

Table 7.3 Summary of situations in which imaging may be indicated in acute pyelonephritis [7]

• No clinical improvement within 72 h of antibiotic therapy
• Pregnancy
• Diabetes mellitus
• Elderly
• Immunocompromised patients
• History of kidney stones
• History of genitourinary abnormalities
• Characterizing the extent of organ damage

MDCT is the preferred imaging modality to evaluate for acute bacterial pyelonephritis. Postcontrast imaging findings include one or more wedge-shaped hypodense areas extending from the papilla to the renal cortex, consistent with a striated nephrogram and representing decreased enhancement compared to the surrounding renal parenchyma (Fig. 7.7a). The findings result from stasis of contrast material within edematous tubules that demonstrate increasing attenuation over time The decreased enhancement or striation is due to reduced perfusion secondary to obstruction of the renal tubules by intraluminal inflammatory debris, interstitial edema, and vasospasm [12]. A "striated nephrogram" can also be seen in GU obstruction, renal vein thrombosis, and contusion [13] (Tables 7.4 and 7.5). On noncontrast-enhanced CT, affected regions of the kidney may be lower in density due to underlying edema, and there may be loss of the renal pyramids. The affected kidney may be enlarged [14]. Renal calculi may be present. Secondary findings due to inflammation in acute pyelonephritis may also include perinephric stranding, thickening of Gerota's fascia, and hydronephrosis [12, 14].

Variant forms of pyelonephritis include emphysematous pyelonephritis (gas in the parenchyma, collecting system, perinephric tissue), hematogenous seeding (multiple, often bilateral peripheral round hypodense foci in the setting of systemic infection), focal pyelonephritis (focal, ill-defined infection which can mimic a tumor), and hemorrhagic bacterial nephritis (wedge-shaped hyperattenuated region due to intraparenchymal hemorrhage).

Ultrasound may be used to evaluate the urinary tract in cases of infection, in particular to assess for hydronephrosis or renal abscess. Occasionally findings of pyelonephritis may be found at ultrasound, although ultrasound is not as sensitive as CT and patients with clinically suspected pyelonephritis often have negative ultrasound results. Changes in the echotexture of the renal parenchyma may be seen and include hypoechoic areas due to edema and hyperechoic regions due to hemorrhage (see Fig. 7.7b) [12]. There may be hydronephrosis, renal enlargement, and/or loss of normal corticomedullary differentiation. Regions of hypoperfusion may be seen with color Doppler. Ultrasound is limited in assessing the full extent of pyelonephritis and perinephric extension and in visualizing microabscesses [12].

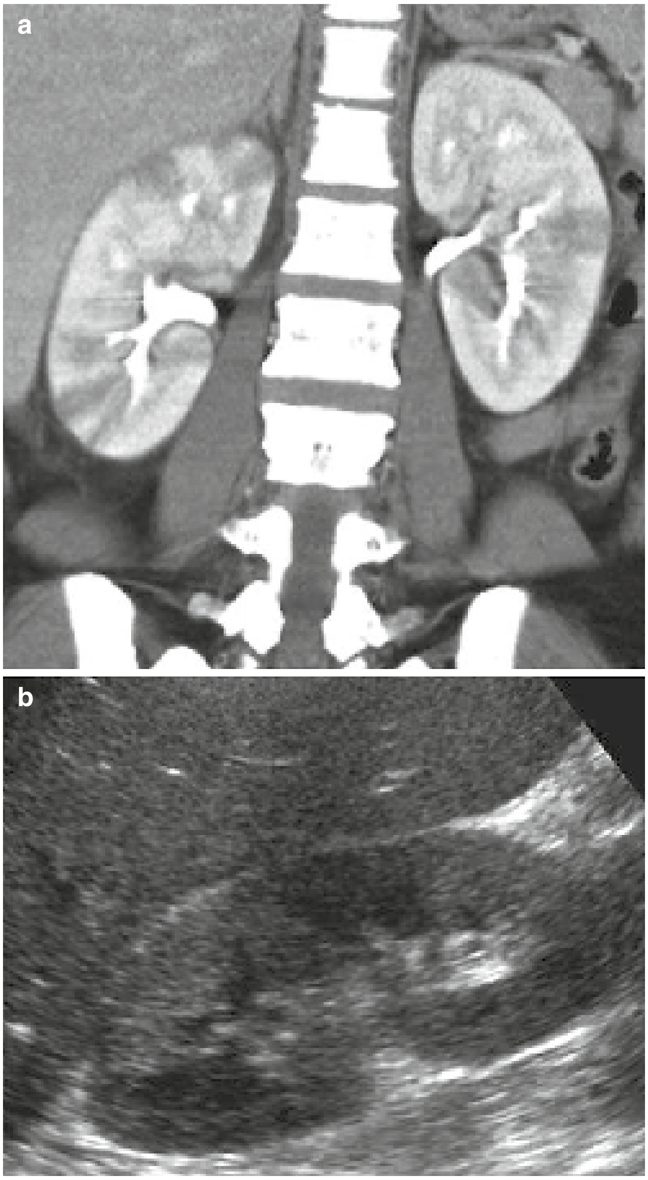

Fig. 7.7 Acute bilateral pyelonephritis in a 34-year-old female with fever, chills, and right upper quadrant pain. (**a**) Contrast-enhanced coronal CT image demonstrates bilateral, right greater than left, striated nephrograms with alternating areas of hypodensity representing decreased enhancement. No drainable fluid collection. (**b**) Ultrasound image shows wedge-shaped echogenic area in the right kidney

Table 7.4 Differential diagnosis of striated nephrogram

1. Acute pyelonephritis
2. GU obstruction
3. Renal vein thrombosis
4. Contusion

Table 7.5 Imaging of acute pyelonephritis

1. CT and MRI: striated nephrogram
2. US: often negative but can see hypoechoic or hyperechoic areas
3. Enlarged kidney

The use of MRI in the evaluation of acute renal infections tends to be limited to patients who cannot undergo intravenous contrast-enhanced CT (i.e., allergy to IV contrast material), patients in who radiation is a concern, or patients with inconclusive/equivocal CT results. MRI is much more susceptible to patient motion artifact than CT is, and it can be more difficult to obtain high-quality images in sick patients. In acute pyelonephritis, similar to that seen on CT, MRI shows wedge-shaped areas of decreased enhancement of the renal parenchyma on T1 fat-saturated postcontrast images and may show areas of decreased signal on T2-weighted images (Fig. 7.8). Renal enlargement and perinephric fluid may also be seen.

Treatment and Complications

Antibiotic therapy is the mainstay of treatment in acute bacterial pyelonephritis, and most patients respond well. However, complications of acute pyelonephritis can include renal obstruction, renal or perirenal abscess, and emphysematous pyelonephritis.

Renal Abscess

Renal or perinephric abscesses typically develop from inadequately treated pyelonephritis more commonly due to ascending infection, with diabetic patients particularly prone (75% of renal abscesses are seen in diabetic patients) and less often hematogenous spread [12]. The most common microorganisms are *E. coli* and *Proteus mirabilis*. Renal abscesses can be solitary or multiple, with multiple abscesses more commonly seen in hematogenous spread of infection [12].

Patients with renal abscess tend to have persistent symptoms of pyelonephritis despite at least 72 h treatment with antibiotics.

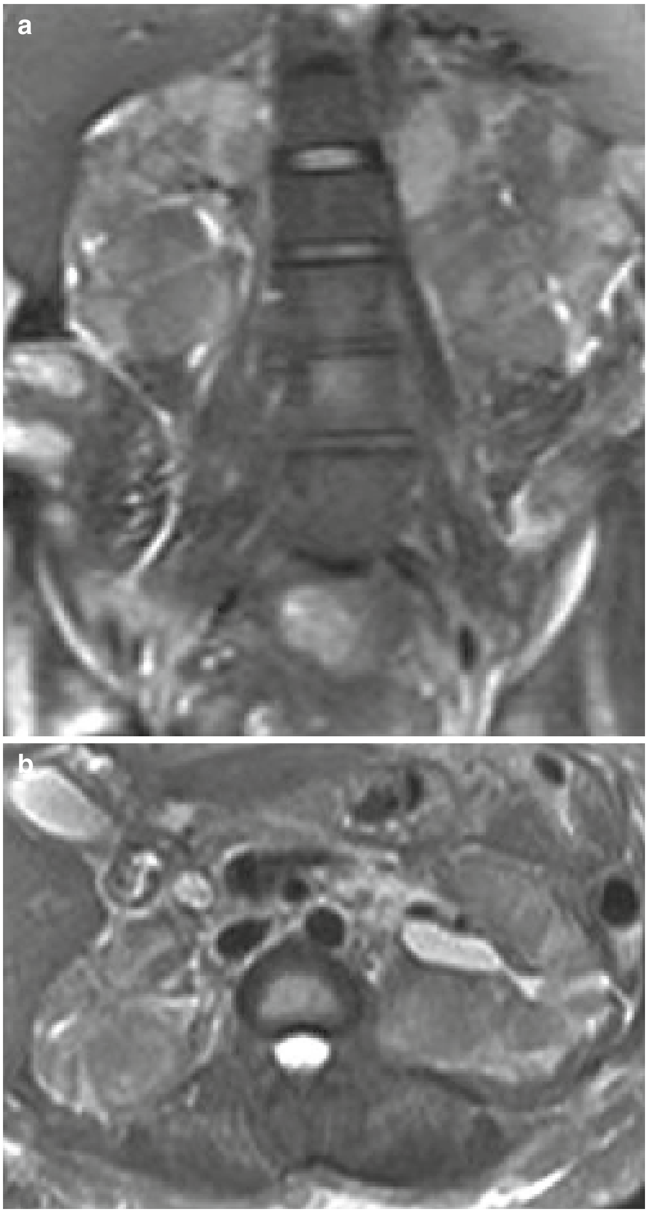

Fig. 7.8 Acute bacterial pyelonephritis due to *E. coli* infection. SSFSE (HASTE) MR coronal (**a**) and axial (**b**) images demonstrate diffuse heterogeneous signal in linear, wedge-shaped configuration in both kidneys

Imaging

CT is the preferred imaging modality to detect renal abscess in the emergent setting since some small abscesses are not seen on ultrasound. At CT, renal abscesses tend to be round and centrally hypodense, with central liquefaction, and may demonstrate significant rim enhancement at postcontrast imaging, but no internal enhancement (Fig. 7.9a). Gas may be seen within the abscess. A hypoenhancing halo may surround the abscess in the renal parenchyma during the nephrographic phase. In many cases, the entire kidney is enlarged or there may be a focal mass/bulge in the renal contour. Perinephric inflammation and thickening of Gerota’s fascia are also commonly seen. A perirenal abscess tends to manifest as a fluid collection in the perinephric space and may contain gas. Extra-parenchymal collections have been found to extend into the adjacent psoas muscle [12].

On ultrasound, a renal abscess tends to be a hypoechoic thick-walled structure with increased through transmission but less so than that seen with a simple cyst of similar size. Typically, no internal vascularity is seen. Debris may be seen within the abscess (see Fig. 7.9b).

Renal abscesses on MRI are centrally T2 hyperintense and T1 hypointense and tend to have a thick wall which shows variable enhancement on T1-weighted postcontrast imaging (Fig. 7.10). Perinephric inflammatory stranding

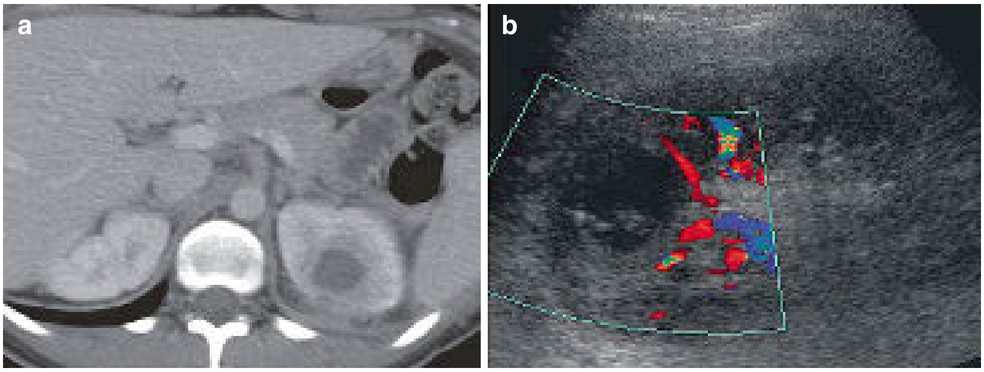

Fig. 7.9 Left renal abscess in a 26-year-old female with left flank pain and fever. (**a**) Contrast-enhanced axial CT image shows hypodense area in the left kidney with central more hypodense, necrotic core measuring 2.1 × 2.2 cm with adjacent perinephric fat stranding. (**b**). Ultrasound images of the left kidney show 2.3 × 2.1 cm hypoechoic, thick-walled structure containing echogenic internal debris and no internal vascularity

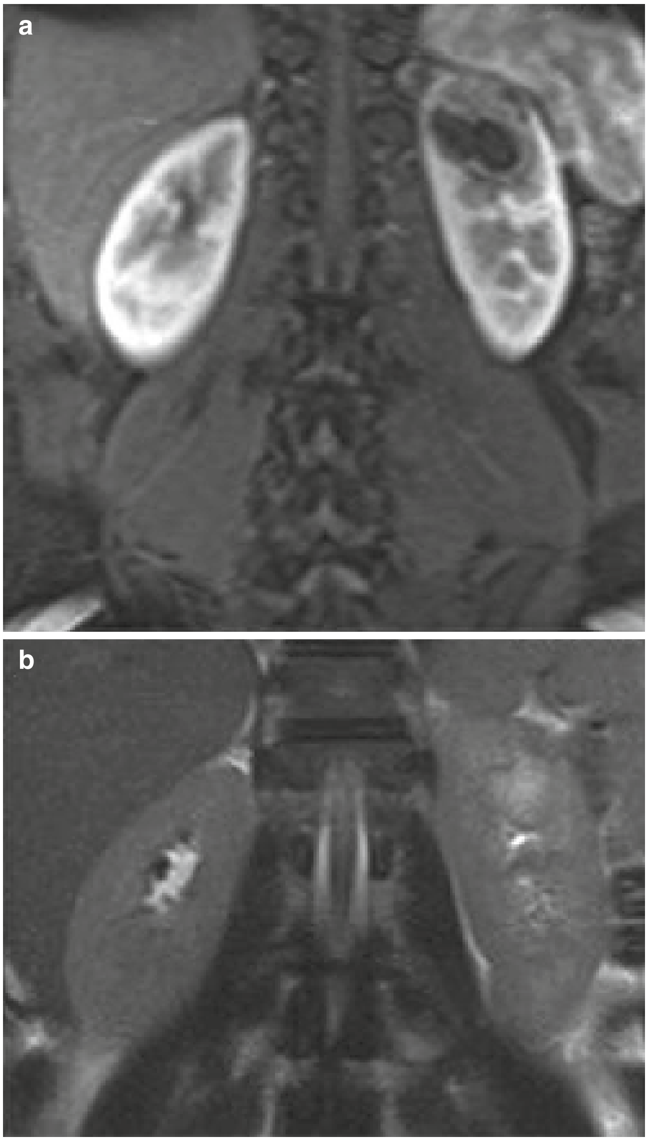

Fig. 7.10 Right renal abscess on MRI in an 18-year-old female with left upper quadrant pain and elevated WBC. (**a**) Contrast-enhanced T1-weighted coronal image demonstrates peripherally enhancing thick-walled cystic lesion. (**b**) T2-weighted coronal image shows T2 hyperintense focus in the left renal upper pole

Table 7.6 Imaging findings in renal abscess

US	CT	MRI
• Hypoechoic thick-walled structure	• Round shape	• T2 hyperintense
• Increased through transmission	• Central liquefaction	• T1 hypointense
• No internal vascularity	• Rim enhancement and no internal enhancement	• Thick wall, variable enhancement on T1
• Debris within the fluid collection	• Hypoenhancing halo surrounding the abscess	• Perinephric stranding

may also be seen. Findings may be difficult to differentiate from cystic renal cell carcinoma; the patient's clinical symptoms and subsequent resolution on follow-up imaging help make this distinction. Imaging features of renal abscess are summarized in Table 7.6.

Emphysematous Pyelonephritis

Emphysematous pyelonephritis is a life-threatening emergency of the kidneys, caused by gas-forming bacteria which infect the renal parenchyma, collecting system, and/or perinephric tissue. It is highly associated with poorly controlled diabetes mellitus, present in up to 90% of cases. Obstruction of the corresponding urinary collecting system secondary to calculus, neoplasm, and/or sloughed papilla may also be present [15, 16]. The bacteria most commonly linked to emphysematous pyelonephritis are *E. coli* (~70%) and *Klebsiella pneumoniae* [16]. Almost 50% of patients have bacteremia. If gas is localized to the renal collecting system and does not involve the renal parenchyma, the term emphysematous pyelitis is used, which is less severe than emphysematous pyelonephritis, with lower mortality.

The presenting symptoms of emphysematous pyelonephritis include fever, flank pain, and pyuria, which are nonspecific and also seen in other urinary tract infections [16]. Patients may also present with lethargy/altered mental status, acid–base abnormalities, hyperglycemia, renal failure, and, in severe cases, septic shock. Emphysematous pyelonephritis is seen more often in females than in males presumably because females are more susceptible to urinary infections. On physical exam, patients may have flank pain and, rarely, crepitus may be felt over the lower back [15].

Imaging

On radiography, evidence of gas overlying the renal shadows or radially oriented gas aligning with the renal pyramids may be seen (Fig. 7.11a). In severe cases, one may see crescentic-shaped gas collection involving Gerota's fascia. Findings may also include obscuration of the ipsilateral psoas muscle shadow [15].

CT best demonstrates the extent of gas and destruction associated with emphysematous pyelonephritis. Imaging findings include foci of gas within the renal parenchyma/collecting system, renal enlargement and destruction, fluid collections with possible gas-fluid levels, and tissue necrosis (see Fig. 7.11b) [12]. Two CT imaging types have been described:

- Type I: with streaky or mottled gas collections without fluid collections.
- Type II: with bubbly gas in the renal parenchyma/collecting system associated with renal/perirenal fluid collections [12, 15].

The presence of fluid accumulation indicates a better immune response. Mortality rates are 69% for type I and 18% in patients with type II [12, 15].

Sonographic evaluation of the kidneys in emphysematous pyelonephritis may demonstrate an enlarged kidney that contains echogenic foci with posterior dirty shadowing, indicative of gas within (Fig. 7.12). The echogenic foci representing gas may be confused with renal calculi. The true extent of emphysematous renal involvement can be underestimated on ultrasound [15]. Imaging findings in emphysematous pyelonephritis are summarized in Table 7.7.

Treatment and Complications

Initial treatment includes aggressive IV hydration, correction of electrolyte imbalances, and broad-spectrum IV antibiotics [15]. If gas is diffuse throughout the kidney, nephrectomy is often indicated. If infection is more localized and preservation of kidney is a priority, percutaneous drainage can be attempted.

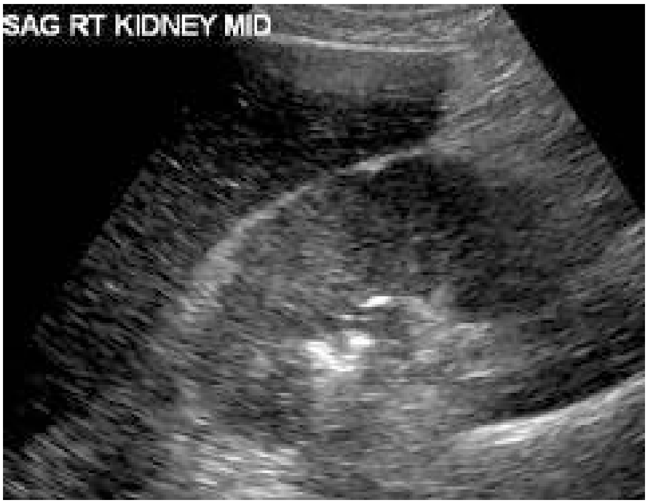

Fig. 7.12 Emphysematous pyelonephritis. Ultrasound image of the right kidney shows echogenic foci with dirty shadowing within the right kidney, consistent with gas

Fig. 7.11 Emphysematous pyelonephritis. (**a**) Scout image shows mottled lucencies projecting over the right renal shadow. (**b**) Noncontrast-enhanced axial CT image of the same patient demonstrates gas within the renal parenchyma. (Images courtesy of Leonora Mui at Columbia University Medical Center, New York, NY)

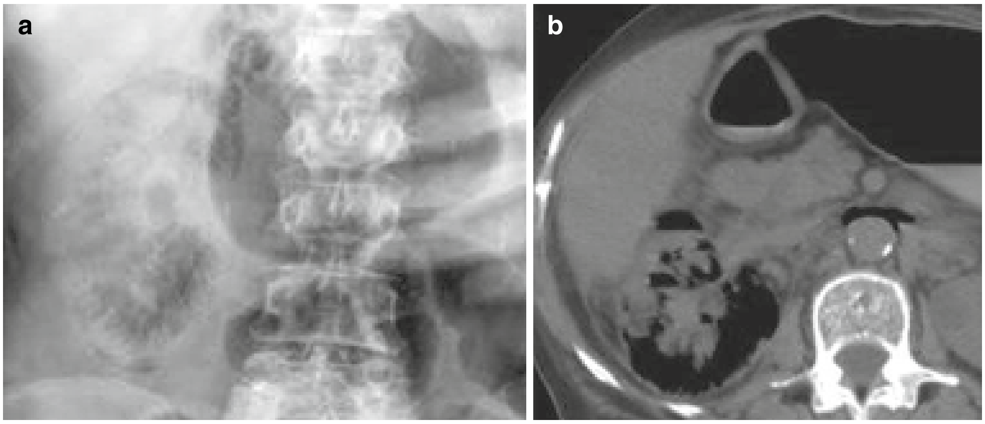

Table 7.7 Imaging findings in emphysematous pyelonephritis

Plain radiography	CT	US
Gas overlying the renal shadows	Better assessment of extent of gas and destruction	Enlarged kidney
(a) Gas aligning with the renal pyramids	Renal enlargement, destruction	Echogenic foci with posterior dirty shadowing (representing gas)
(b) Crescentic-shaped gas collection	Fluid collections, gas-fluid levels	
Obscuration of psoas muscle shadow	Tissue necrosis and gas within the parenchyma	

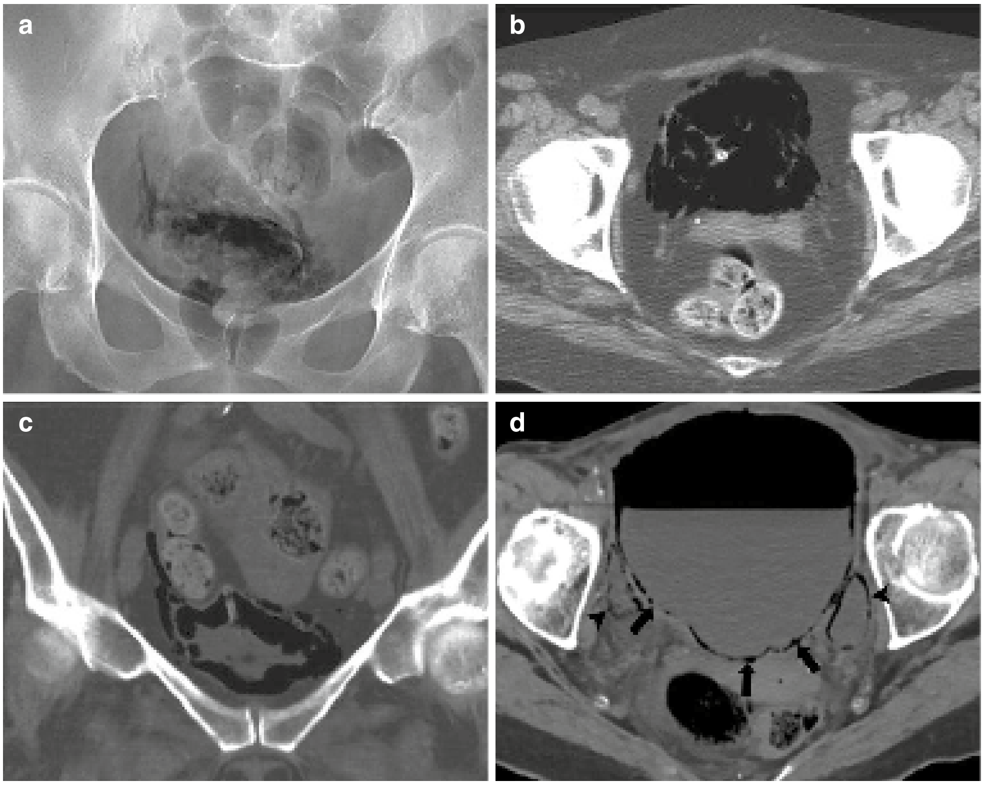

Fig. 7.13 Emphysematous cystitis. (**a**) Pelvis radiograph shows pelvic lucencies consistent with bladder gas as confirmed on CT. (**b**, **c**) CT images demonstrate extensive gas within the lumen and wall of the urinary bladder. Coronal image depicts dissection of gas in the right space of Retzius. (**d**) Emphysematous cystitis. Non-contrast CT of the pelvis demonstrating air in the wall of the urinary bladder (arrows) and bilateral urinary bladder diverticula (arrowheads)

Emphysematous Cystitis

Emphysematous cystitis is a rare infection of the bladder caused by gas-producing organisms, most commonly *E. coli*, *Enterobacter aerogenes*, and *Klebsiella pneumoniae* [17]. It tends to be seen in elderly patients with diabetes reported in over half of cases. Elderly or debilitated patients with chronic urinary retention secondary to urinary bladder outlet obstruction, neurogenic bladder, or bladder structural abnormality, as well as patients with an indwelling urinary bladder catheter, are at increased risk of developing emphysematous cystitis in part due to urinary stasis. It has been speculated that organisms within the urinary bladder cause fermentation of urinary glucose, leading to release of carbon dioxide bubbles that collect in the submucosa or lumen of the bladder [17, 18].

The presenting symptoms include dysuria, hematuria, and increased urinary frequency. The incidence of this infection is greater in females than males, 2:1 [15].

Imaging

Radiography is highly sensitive in detecting emphysematous cystitis (~97%) [19]. On radiography, one may see curvilinear lucency, consistent with gas, outlining the bladder wall, with or without intraluminal gas (Fig. 7.13a).

In patients with emphysematous cystitis (EC), gas is seen within the wall of the urinary bladder and possibly intraluminal, particularly in the absence of recent instrumentation or fistulous communication with a hollow viscous (see Fig. 7.13b, d). CT can detect cases of EC that are not apparent on radiography and can better depict the extent of disease. CT also helps differentiate emphysematous cystitis from other causes of pelvic gas, including abscess or vesicocolic fistula [15].

Treatment

Emphysematous cystitis is typically treated with early broad-spectrum antibiotics and bladder drainage with Foley catheter. Overall mortality rate is 7%. If disease progresses to involve the ureters or kidney(s), surgery may be required.

Renovascular Emergencies

Acute alternations in the renal vasculature can lead to various changes in the kidney, some of which require intervention. Renovascular emergencies include renal infarct and renal vein thrombosis.

Renal Infarction

Renal infarcts may develop secondary to thrombotic disease, embolism, aortic dissection, or trauma. Sources of thrombosis include arteriosclerosis, vasculitis, and aortic or renal artery aneurysm. Renal artery embolism is most commonly cardiac in nature but can also be iatrogenic, such as following catheterization.

The presenting symptoms in patients with renal infarction tend to be flank pain, nausea, and vomiting with possible hematuria [14]. Mild leukocytosis and fever might also be present.

Imaging

CT is the imaging modality of choice in evaluating for renal infarction. The size and location of the renal infarct depend on the size of the embolus, location of arterial occlusion, and the age of the event. At contrast-enhanced CT, findings in renal infarct are one or more wedge-shaped regions demonstrating lack of enhancement that involve both the renal cortex and medulla (Fig. 7.14) [20]. Cortical rim enhancement of the kidney can be seen adjacent to a renal infarct due to collateral capsular perfusion and usually appears several days after onset of the infarct [21]. Chronic renal infarct results in scarring and loss of renal cortex.

An acute renal infarct may have a normal gray-scale appearance on ultrasound. Alternatively, a wedge-shaped hypoechoic area may be present in the renal parenchyma, which may be difficult to distinguish from pyelonephritis without the use of color Doppler. With color Doppler, there will be absence of flow to a portion of or to the entire kidney. Imaging findings are summarized in Table 7.8.

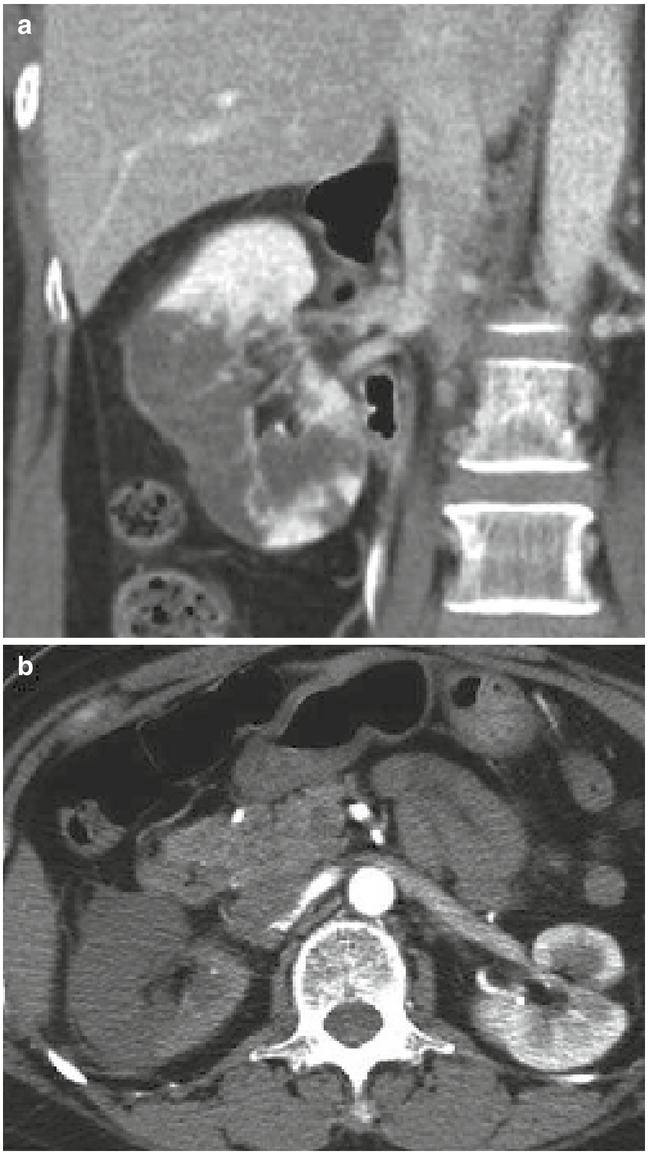

Fig. 7.14 Renal infarct in a 50-year-old female with right abdominal pain. (**a**) Contrast-enhanced coronal image of the right kidney shows wedge-shaped areas of hypodensity involving the cortex and medulla with preservation of the capsule. (**b**) Contrast-enhanced axial CT image obtained 10 days later shows lack of flow in the distal right renal artery and significantly worsened lack of right renal perfusion/enhancement

Treatment

The mainstay of treatment for acute renal infarct is anticoagulation.

Table 7.8 Imaging findings in renal infarction

CT	US
Wedge-shaped focus of nonenhancement	Normal gray-scale appearance on ultrasound in acute infarct
Cortical rim enhancement	Wedge-shaped hypoechoic area (chronic)
Scarring and loss of renal cortex suggest chronicity	Absence of flow on color Doppler

Renal Vein Thrombosis

Renal vein thrombosis is commonly due to an underlying disorder of the kidney or of the clotting system. It can also be seen in dehydration, regional neoplastic processes (involving the kidney, adrenal gland, and/or ureter) with direct extension, and trauma [20, 21].

The clinical presentation of renal vein thrombosis can vary depending on the etiology of the thrombosis. Presenting symptoms include flank pain, gross hematuria, and decrease or loss of renal function [21]. Renal vein thrombosis is more often seen on the left, which is thought to be due to the greater length of the left renal vein compared to the right. Membranous glomerulonephritis is the most common underlying disorder in adults with renal vein thrombosis [21].

Imaging

Patients suspected of having renal vein thrombosis are often first imaged with ultrasound. On ultrasound, one may see enlargement of the affected kidney and a hypoechoic renal cortex due to underlying edema. Later, the kidney decreases in size and becomes hyperechoic. On Doppler ultrasound examination, the findings include absence of venous flow, echogenic material within the renal vein lumen consistent with thrombus, reversal of arterial diastolic flow, and elevated renal artery resistive index due to high resistance.

In acute renal vein thrombosis, CT imaging demonstrates a hypoattenuating filling defect consistent with thrombus within a thickened renal vein, and the vein may be distended (Fig. 7.15). Enhancement of the thrombus suggests tumor thrombus. The kidney on the affected side may be enlarged, and there may be delay in the renal cortical nephrogram and an imaging appearance of a diminished nephrogram [20, 21]. Additionally, perinephric edema may be present. Once chronic, renal vein thrombosis leads to attenuation of the vein due to retraction of the thrombus and regional collateral vessels can be seen. Table 7.9 summarizes imaging findings in renal vein thrombosis.

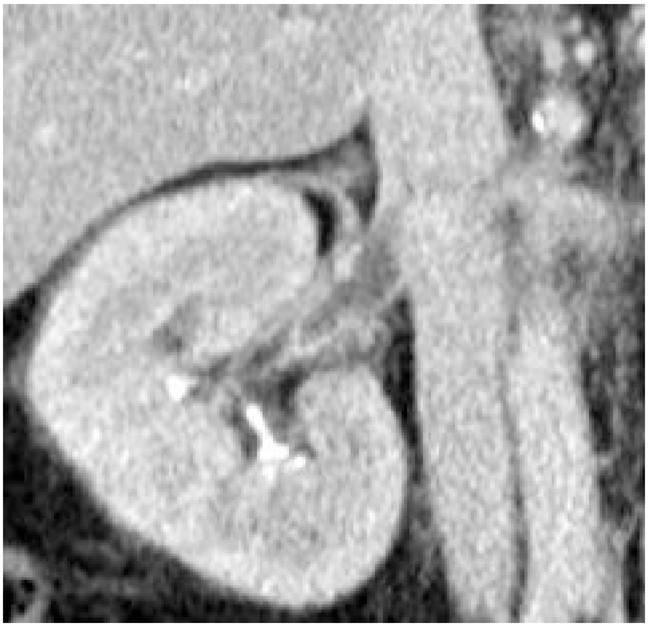

Fig. 7.15 Renal vein thrombosis in a 57-year-old female with abdominal pain and history of membranous glomerulonephritis. Contrast-enhanced coronal image shows filling defect within a distended right renal vein

Table 7.9 Imaging findings in renal infarction

US	CT
Enlargement of the affected kidney	Hypoattenuating filling defect
Hypoechoic renal cortex	Thickened renal vein
Hyperechoic cortex in later stages	Distention of the vein
At Doppler	Enlarged kidney
• Absence of venous flow	Delayed renal cortical nephrogram
• Intraluminal echogenic material in the renal vein	Diminished nephrogram
• Reversal of flow	Perinephric edema
• Elevated renal artery resistive index	

Treatment and Complications

Anticoagulation is the mainstay of treatment in renal vein thrombosis. Thrombolytic therapy has been used in cases of bilateral renal vein thrombosis with acute renal failure, large clot burden with high risk of additional embolic events, and pulmonary embolism. Complications of renal vein thrombosis include acute renal failure, extension of the thrombus into the IVC, and elevated risk of pulmonary embolism.

Renal Transplant

With increase in renal transplantation in recent years, a greater number of renal transplant patients may present to emergency departments, and it is thus important to be aware of the potential transplant complications. In the emergent setting, evaluation of renal transplant is typically performed with ultrasound. Complications may be urologic or vascular and include peritransplant fluid collections (Fig. 7.16).

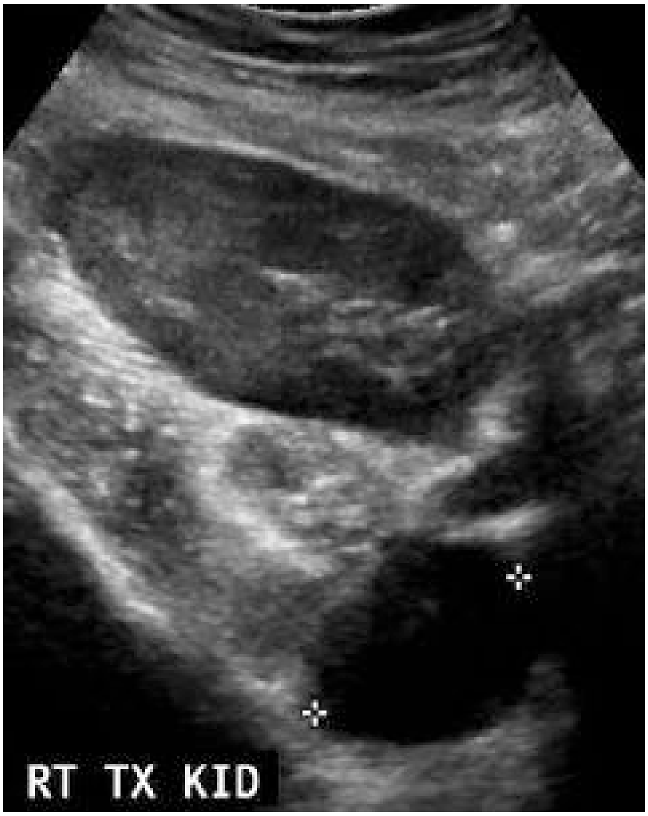

Fig. 7.16 Postoperative seroma after renal transplant. Ultrasound shows a 3.8 cm simple appearing loculated fluid collection deep to the transplant kidney

Ultrasonography

Peritransplant fluid collections can be partially differentiated based on time interval since transplantation. Small hematomas are commonly seen postoperatively and usually resolve spontaneously. They are echogenic when acute, and become less echogenic over time, and may contain septations [22].

Urinomas are well-defined, simple-appearing, anechoic collections that tend to occur between the urinary bladder and transplant kidney during the first 2 weeks after transplantation [22].

Lymphoceles are collections that tend to develop within 1–2 months posttransplantation, although may occur weeks to years thereafter and are usually seen between the transplant and the bladder. Sonographically, lymphoceles tend to be anechoic.

Large perinephric fluid collections can cause hydronephrosis, with lymphoceles being the most common [22]. All perinephric fluid collections can become infected and demonstrate more a complex cystic appearance with possible abscess formation. Peritransplant abscesses are rare and tend to develop during the first few weeks posttransplantation [22].

Renal transplant vascular complications include renal vein thrombosis and renal infarction, with imaging characteristics similar to that described above. Of note, in renal vein thrombosis, on color Doppler imaging, there may be lack of or reversal of diastolic flow in the intraparenchymal arteries, which may also be demonstrated in acute rejection or acute tubular necrosis (ATN). Renal vein thrombosis is differentiated from acute transplant rejection or ATN by lack of flow and thrombus in the main renal vein (Fig. 7.17).

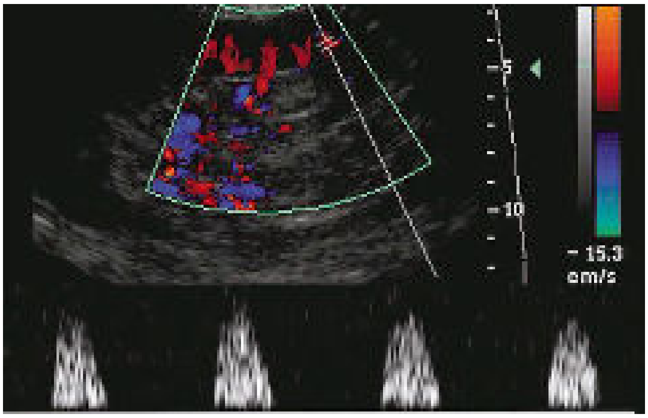

Fig. 7.17 Acute tubular necrosis on ultrasound. A 59-year-old female status post renal transplant with increasing creatinine demonstrating lack of diastolic blood flow

Teaching Points

- MDCT is the gold standard for imaging patients with suspected obstructive uropathy.
- CT findings in acute obstructive uropathy include calcified stone, hydroureter, hydronephrosis, soft tissue rim sign, perinephric/periureteral stranding, and unilateral enlarged kidney.
- Imaging findings of acute pyelonephritis include striated nephrogram and enlarged kidney.
- In CT, renal abscesses tend to be round and centrally hypodense, with central liquefaction, and may demonstrate rim enhancement at postcontrast imaging, but lack of internal enhancement.
- In emphysematous pyelonephritis, CT findings include foci of gas within the renal parenchyma or collecting system, renal enlargement, parenchymal destruction, and fluid collections with possible gas-fluid levels.
- On radiography, emphysematous cystitis findings include curvilinear lucencies consistent with gas outlining the bladder wall, with or without intraluminal gas.
- At contrast-enhanced CT, findings in renal infarct are one or more wedge-shaped regions demonstrating lack of enhancement that involve both the renal cortex and medulla, often with sparing of the renal capsule.
- In acute renal vein thrombosis, CT imaging demonstrates hypoattenuating filling defect consistent with thrombus within a thickened renal vein, and the vein may be distended.

Questions

1. Which of the following can cause striated nephrogram on CT?
   (A) Oncocytoma
   (B) Transitional cell carcinoma
   (C) Contusion
   (D) Renal cell carcinoma
   Answer: C

2. Which of the following is the description of type 2 emphysematous cystitis?
   (A) Bubbly gas and fluid accumulation
   (B) Striated bladder wall
   (C) Bladder wall thinning
   (D) Sacculations
   Answer: A

3. Which of the following statements about renal transplant ultrasonography is correct?
   (A) Hematomas tend to develop months to years after surgery
   (B) Lymphoceles are echogenic collections between transplant and bladder
   (C) Abscess formation is a common complication after surgery
   (D) Urinomas are well-defined, simple-appearing, anechoic collections
   Answer: D

4. A 22-year-old female presented with abdominal pain, dysuria, and urinary frequency. What is the imaging finding depicted on the axial and coronal contrast-enhanced CT (Fig. 7.18a, b)?
   (A) Gas formation
   (B) Renal mass
   (C) Striated nephrogram
   (D) Renal abscess
   Answer: C

5. A 90-year-old male patient presents with the history of diabetes and *Escherichia coli* urinary tract infection. CT scout radiograph and axial images are depicted below (Fig. 7.19a, b). On the axial image, dissection of gas into which space is seen?
   (A) Vesicovaginal space
   (B) Retzius space
   (C) Rectovaginal space
   (D) Pararectal spaces
   Answer: B

6. A 59-year-old-female presents with history of diabetes mellitus and malaise. CT of the right kidney is shown below (Fig. 7.20a, b). Which of the following is the most common causative agent?
   (A) *E. coli*
   (B) *Klebsiella pneumoniae*
   (C) *Staphylococcus aureus*
   (D) *Pseudomonas aeruginosa*
   Answer: A

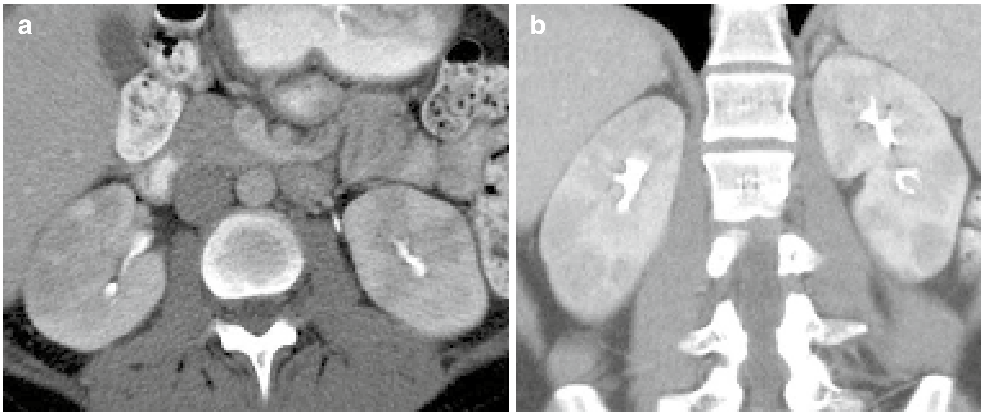

Fig. 7.18 A 22-year-old female with acute pyelonephritis. Contrast-enhanced axial (**a**) and coronal (**b**) CT images show renal cortical striated nephrogram, with alternating areas of wedge-shaped hypodensity consistent with decreased enhancement, involving the cortex and renal capsule

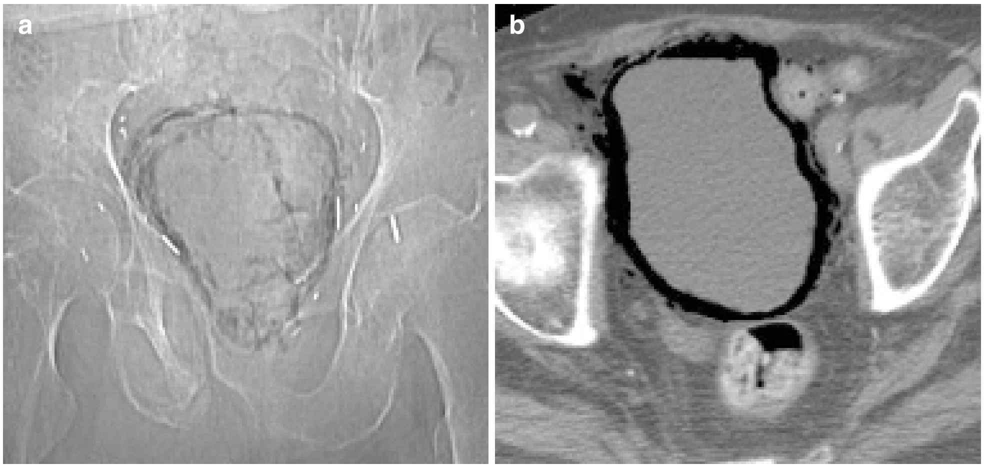

Fig. 7.19 A 90-year-old male with emphysematous cystitis. Patient presents with history of diabetes mellitus and *Escherichia coli* urinary tract infection. Scout radiograph image (**a**) demonstrates curvilinear lucency outlining the urinary bladder. Axial CT image through the lower pelvis (**b**) shows gas circumferential in the urinary bladder wall with dissection of gas into the space of Retzius, particularly on the right

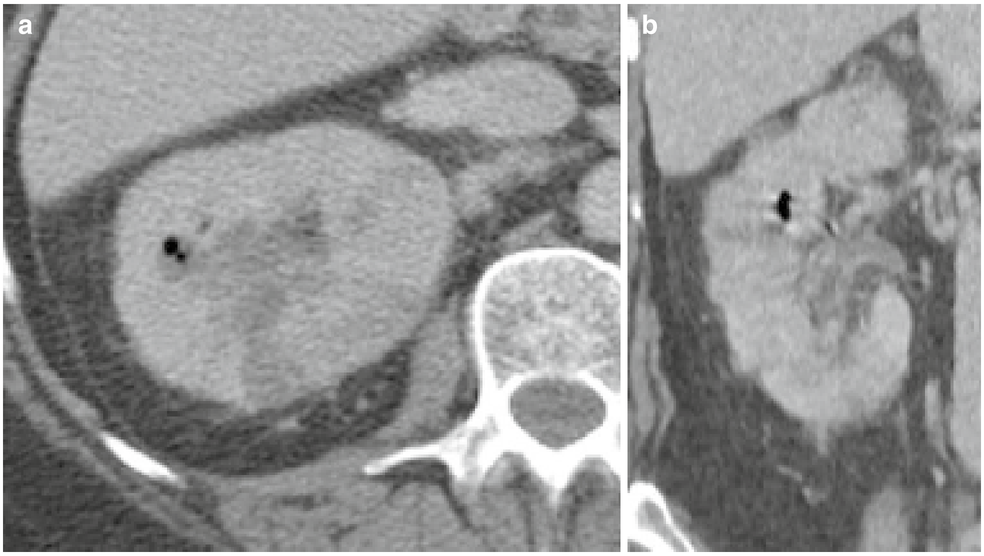

Fig. 7.20 A 59-year-old female with emphysematous pyelonephritis. Axial (**a**) and coronal (**b**) contrast-enhanced CT images show small foci of gas in the right renal collecting system

References

1. Reddy S. State of the art trends in imaging of renal colic. Emerg Radiol. 2008;15(4):217–25.
2. Dhar M, Denstedt JD. Imaging in diagnosis, treatment, and follow-up of stone patients. Adv Chronic Kidney Dis. 2009;16(1):39–47.
3. Foell K, Ordon M, Ghiculete D, Lee JY, Honey RJ, Pace KT. Does baseline radiography of the kidneys, ureters, and bladder facilitate stone management in patients presenting to the emergency department with renal colic? J Endourol. 2013;271:425–30.
4. Rucker CM, Menias CO, Bhalla S. Mimics of renal colic: alternative diagnoses at unenhanced helical CT. Radiographics. 2004;24(Suppl 1):S11–28.
5. Taourel P, Thuret R, Hoquet MD, Doyon FC, Merigeaud S, Delabrousse E. Computed tomography in the nontraumatic renal causes of acute flank pain. Semin Ultrasound CT MR. 2008;29(5):341–52.
6. Krauss T, Frauenfelder T, Strebel RT, Birzele J, Scheffel H, Seifert B, et al. Unenhanced versus multiphase MDCT in patients with hematuria, flank pain, and a negative ultrasound. Eur J Radiol. 2012;81(3):417–22.

7. Goel RH, Unnikrishnan R, Remer EM. Acute urinary tract disorders. Radiol Clin N Am. 2015;53(6):1273–92.
8. Dyer RB, Chen MY, Zagoria RJ. Classic signs in uroradiology. Radiographics. 2004;24(Suppl 1):S247–80.
9. Cullen IM, Cafferty F, Oon SF, Manecksha R, Shields D, Grainger R, et al. Evaluation of suspected renal colic with noncontrast CT in the emergency department: a single institution study. J Endourol. 2008;22(11):2441–5.
10. Moş C, Holt G, Iuhasz S, Moş D, Teodor I, Hălbac M. The sensitivity of transabdominal ultrasound in the diagnosis of ureterolithiasis. Med Ultrason. 2010;12(3):188–97.
11. Kalb B, Sharma P, Salman K, Ogan K, Pattaras JG, Martin DR. Acute abdominal pain: is there a potential role for MRI in the setting of the emergency department in a patient with renal calculi? J Magn Reson Imaging. 2010;32(5):1012–23.
12. Craig WD, Wagner BJ, Travis MD. Pyelonephritis: radiologic–pathologic review. Radiographics. 2008;28(1):255–77.
13. Saunders HS, Dyer RB, Shifrin RY, Scharling ES, Bechtold RE, Zagoria RJ. The CT nephrogram: implications for evaluation of urinary tract disease. Radiographics. 1995;15(5):1069–85.
14. Urban BA, Fishman EK. Tailored helical CT evaluation of acute abdomen. Radiographics. 2000;20(3):725–49.
15. Grayson DE, Abbott RM, Levy AD, Sherman PM. Emphysematous infections of the abdomen and pelvis: a pictorial review. Radiographics. 2002;22(3):543–61.
16. Huang JJ, Tseng CC. Emphysematous pyelonephritis: clinicoradiological classification, management, prognosis, and pathogenesis. Arch Intern Med. 2000;160(6):797–805.
17. Nemati E, Basra R, Fernandes J, Levy JB. Emphysematous cystitis. Nephrol Dial Transplant. 2005;20(3):652–3.
18. Chong SJ, Lim KB, Tan YM, Chow RK, Yip SK. Atypical presentations of emphysematous cystitis. Surgeon. 2005;3(2):109–12.
19. Grupper M, Kratvsov A, Potasman I. Emphysematous cystitis: illustrative case report and review of the literature. Medicine. 2007;86(1):47–53.
20. Urban BA, Ratner LE, Fishman EK. Three-dimensional volume-rendered CT angiography of the renal arteries and veins: normal anatomy, variants, and clinical applications. Radiographics. 2001;21(2):373–86.
21. Kawashima A, Sandler CM, Ernst RD, Tamm EP, Goldman SM, Fishman EK. CT evaluation of renovascular disease. Radiographics. 2000;20(5):1321–40.
22. Akbar SA, Jafri ZH, Amendola MA, Madrazo BL, Nis KG. Complications of renal transplantation. Radiographics. 2005;25:1335–56.

8

Imaging of Acute Conditions of Male Reproductive Organs

Caterina Missiroli, Mohammad Mansouri, and Ajay Singh

Hydrocele

There is normally 1–2 mL of fluid between the visceral and parietal layers of the tunica albuginea that surrounds the testis. The presence of abnormal amount of fluid in this space can be seen with hydrocele, hematocele, or pyocele (Figs. 8.1 and 8.2) [1]. They are usually confined to the anterolateral of the scrotum.

Hydrocele is the most common cause of painless scrotal swelling. It can be congenital (due to incomplete closure of processus vaginalis) or acquired (due to trauma or rarely tumors). Hematocele can be caused by trauma, tumor, torsion, diabetes, surgery, or atherosclerosis. Pyocele forms as the result of ruptured abscess into tunica vaginalis space or into a preformed hydrocele.

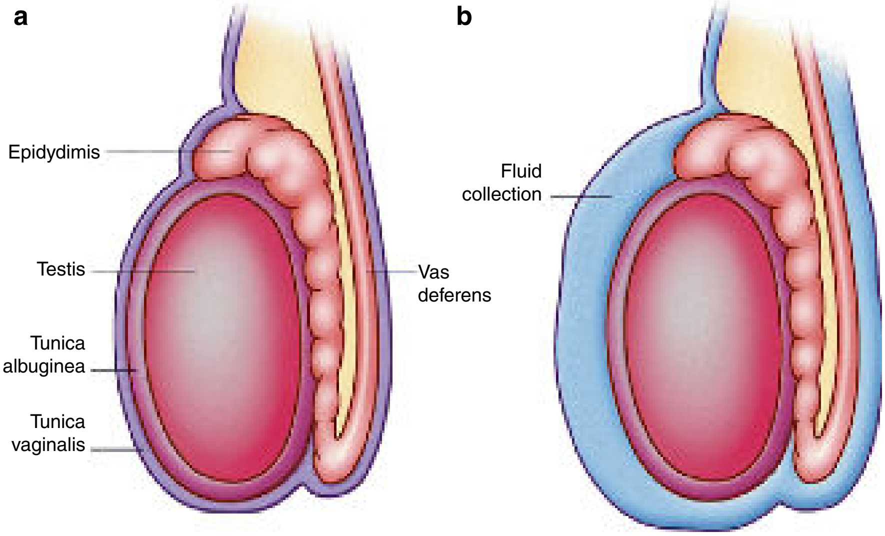

Fig. 8.1 Testicular anatomy. (**a**) Schematic diagram demonstrates normal testicular anatomy. (**b**) Hydrocele: schematic diagram demonstrates fluid between tunica albuginea and tunica vaginalis

---

C. Missiroli
Department of Radiology, ASST Nord Milano—Bassini Hospital, Milan, Italy

M. Mansouri
Department of Radiology, Massachusetts General Hospital, Boston, MA, USA

A. Singh (✉)
Division of Emergency Radiology, Department of Radiology, Massachusetts General Hospital, Boston, MA, USA

Harvard Medical School, Massachusetts General Hospital, Boston, MA, USA
e-mail: asingh1@partners.org

© The Author(s), under exclusive license to Springer Nature Switzerland AG 2024
A. Singh (ed.), *Emergency Radiology*, https://doi.org/10.1007/978-3-031-65770-2_8

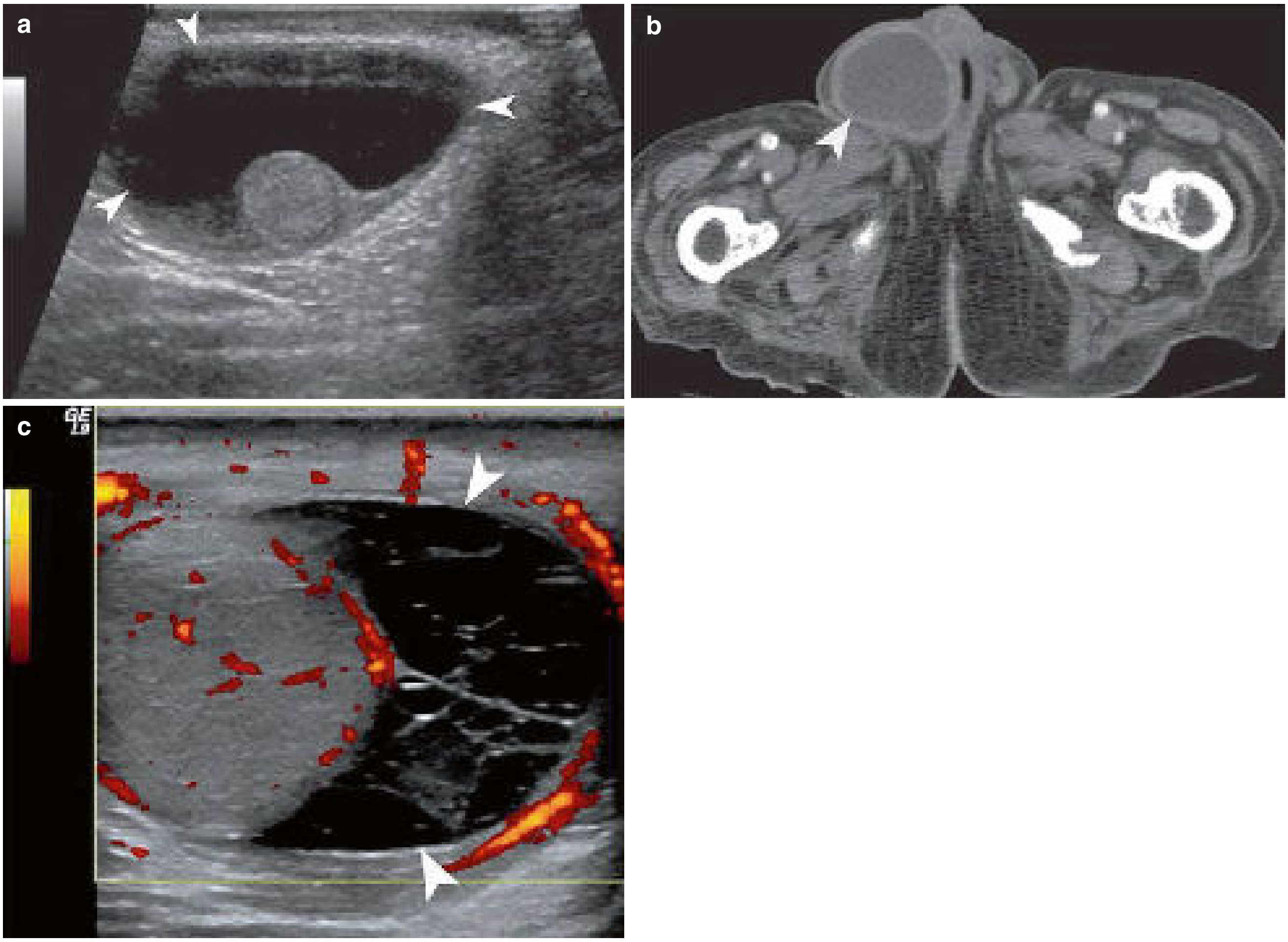

Fig. 8.2 Hydrocele and pyocele. (**a**) Hydrocele: ultrasound demonstrates anechoic fluid collection (*arrowheads*) between the parietal and visceral layers of the tunica albuginea, surrounding the testicle. (**b**) Hydrocele: contrast-enhanced axial CT imaging of the pelvis demonstrates the fluid density hydrocele (*arrowhead*) surrounded by the parietal layer of the tunica albuginea. (**c**) Pyocele: ultrasound imaging demonstrates complex fluid collection (*arrowheads*) surrounding the testicle with multiple internal septations

Ultrasound is the imaging technique of choice in determining the type of fluid collections. While hydroceles are usually anechoic collections, hematoceles and pyoceles show complex fluid with internal echoes and variable septations and loculations.

Varicocele

Varicocele is characterized by increase in the diameter of the pampiniform plexus veins (normal range 0.5–1.5 mm), resulting in a collection of tortuous elongated veins posterior to the testicle [2].

When idiopathic, it is caused by incompetent valves in the internal spermatic vein, resulting in blood flow reversal (spermatic cord to pampiniform plexus). It is usually left-sided due to venous drainage into the renal vein rather than inferior vena cava (right vein directly drain into the inferior vena cava) [2, 3]. When acquired, it is due to increased pressure on the spermatic venous system (from hydronephrosis, hepatomegaly, and abdominal tumors). In these patients, varicocele is bilateral in up to 70% of patients and more prominent in the upright position and during valsalva maneuver [2].

Color Doppler ultrasound plays an important role in the evaluation of scrotal venous morphology and demonstrates serpentine vessels larger than 2 mm in diameter, next to the epididymis head (Figs. 8.3 and 8.4) [2, 4]. The blood flow is in reversed direction and typically increases during valsalva maneuver and in upright position.

Although traditionally it is surgically treated, it can also be managed with coil embolization by interventional radiologist [5].

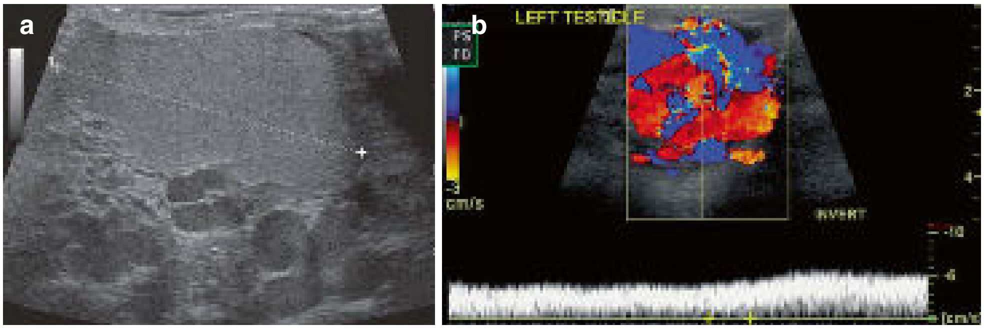

Fig. 8.3 Varicocele. (**a**, **b**) Ultrasound demonstrates extratesticular tortuous tubular structures on gray-scale imaging and color Doppler imaging

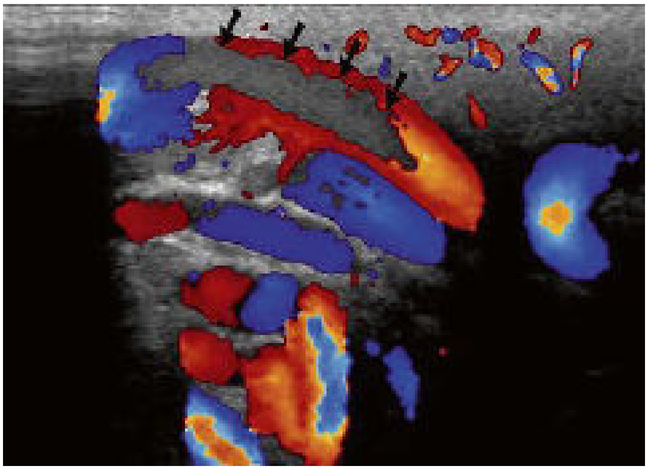

Fig. 8.4 Thrombosed varicocele. Doppler ultrasound depicts lack of blood flow (*arrows*) in a partially thrombosed extratesticular varicocele

Epididymitis and Epididymo-Orchitis

Infections of testicles and epididymitis are most common in young adults and are the result of retrograde passage of organisms (*N. gonorrhoeae*, *C. trachomatis*, or *E. coli*) from the urethra, prostate, or seminal vesicles [6, 7]. Epididymitis is the most common cause of inflammatory scrotal disease. Epididymitis and epididymo-orchitis are most commonly secondary to retrograde spread of infection from urinary tract. Infection usually originates from the head or tail and then spreads to rest of the epididymis. The clinical presentation includes pain, swelling, fever, dysuria, and urethral discharge.

The main purpose of imaging in patients with presumed inflammatory disease is to distinguish inflammation from testicular torsion or other surgically treatable causes of scrotal pain, such as abscess or testicular tumor. The ultrasound finding of inflammation includes demonstration of hyperemia, which is well displayed as low-resistance hypervascularity (RI = 0.5) with increased diastolic flow (Figs. 8.5 and 8.6). The normal epididymis demonstrates no detectable flow (even at the lowest possible flow settings), so the detection of any epididymal vascularity is abnormal and indicates hyperemia [4]. Asymmetrically increased blood flow (compared to the other side) is 100% sensitive in detecting orchitis. Epididymis and testis are usually enlarged and edematous. The sonographic findings of epididymitis include enlarged, hypoechoic, or hyperechoic epididymis and hydrocele. In complicated cases, abscess may be visualized with hypervascularity in its margins. On sonography, orchitis is seen as testicular enlargement, heterogeneous echogenicity, and hypervascularity.

Other imaging techniques are usually not necessary. MR imaging may show increased, decreased, or normal signal in epididymis and testis with associated hypervascularity and hydrocele [8]. Abscess may be present and seen as complex scrotal fluid collection.

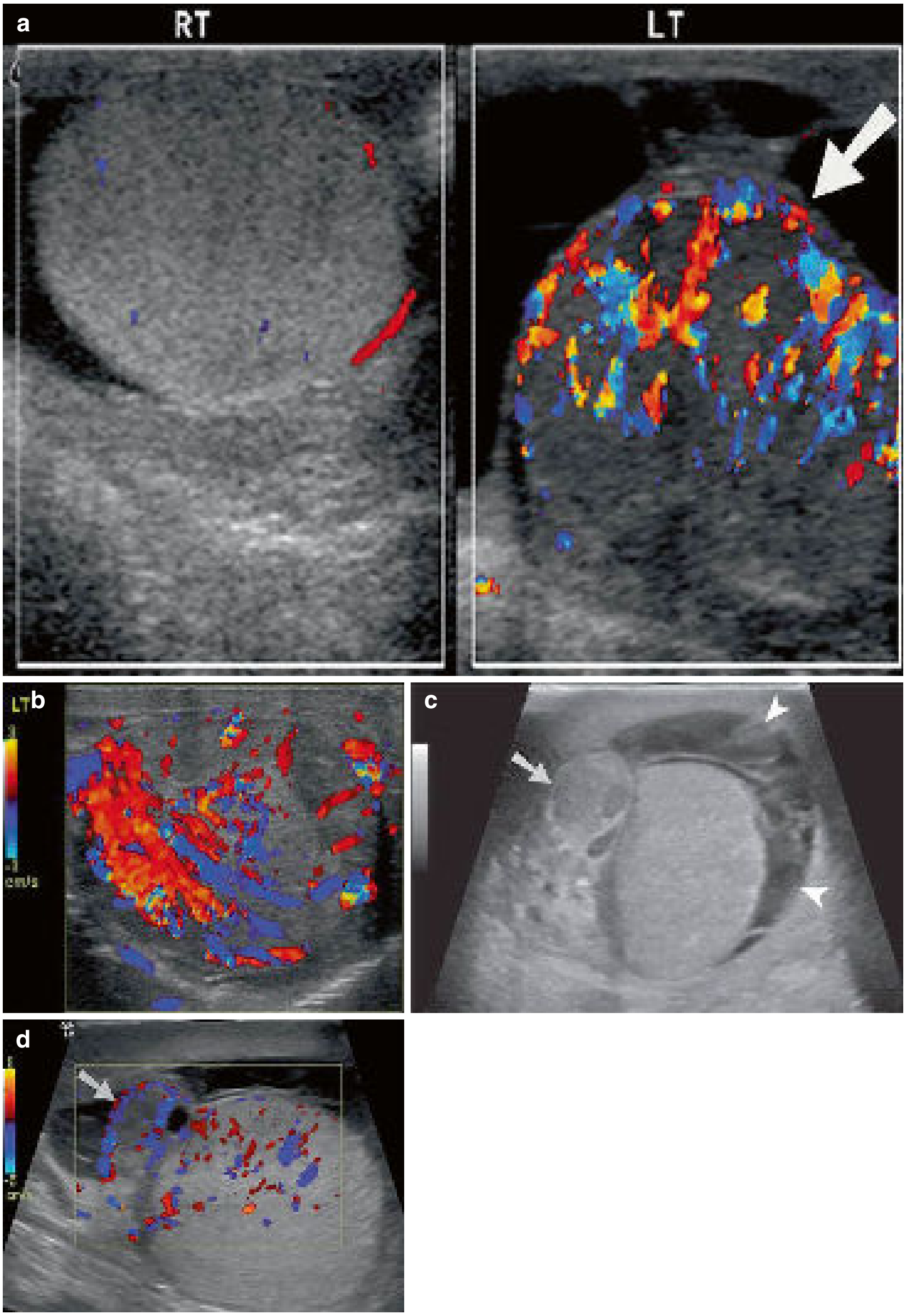

Fig. 8.5 Acute orchitis and epididymitis. (**a**, **b**) Ultrasound of the testicle demonstrates markedly increased color Doppler flow within the testicular parenchyma (*arrow*). The testicular echogenicity is mildly heterogeneous. (**c**, **d**) Ultrasound of the scrotum demonstrates enlarged epididymis (*arrow*) with increased color Doppler flow and complex hydrocele (*arrowheads*)

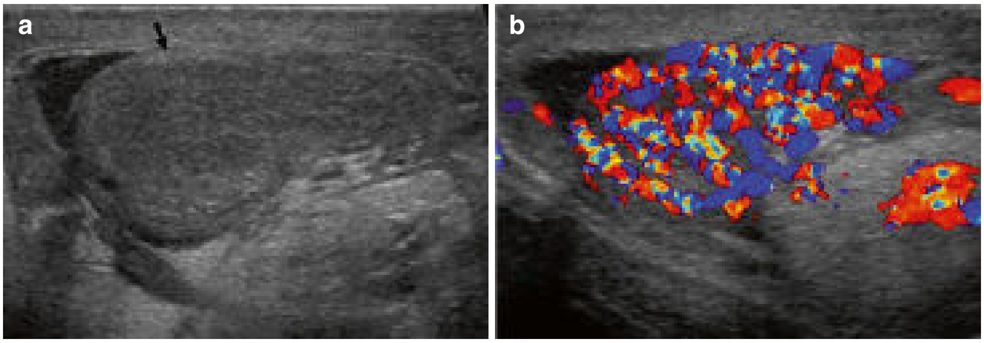

Fig. 8.6 Acute epididymitis. Testicular ultrasound with and without Doppler depicts increased size of epididymis (**a**) (*arrow*) and intense Doppler flow (**b**)

Fournier Gangrene

It is a rapidly progressing polymicrobial necrotizing fasciitis, seen most commonly in 50–60-year-old men. It involves the perineal, perianal, or genital regions and requires immediate surgical debridement as well as aggressive antibiotic treatment.

It is an infection, caused by multiple bacteria (average of more than three organisms), most commonly *Escherichia coli*, *Bacteroides*, and streptococcal species [9, 10]. Usually the infection spreads from abscess (perianal, perirectal, and ischiorectal), anal fissures or colonic perforations, urinary tract infections, and epididymitis. The predisposing factors are diabetes mellitus, alcohol abuse, urinary bladder instrumentation, trauma, surgical procedure, tumors, steroid therapy, chemotherapy, radiation therapy, prolonged hospitalization, and HIV infection [9].

On ultrasound, the findings include thickening of the scrotal skin and perineum, normal testicles due to its independent blood supply, and hyperechoic soft tissue gas producing dirty acoustic shadowing with reverberation artifacts. Scrotal and perineal hyperemia with dilated scrotal vessels can be observed on Doppler US. CT allows the evaluation of soft tissue inflammation, collections, and gas as well as complications, such as subcutaneous emphysema, abscess formation, and retroperitoneal extension (Fig. 8.7). It is also helpful in differentiating Fournier gangrene from inguinal hernia, soft tissue edema, and cellulitis. MRI may demon-

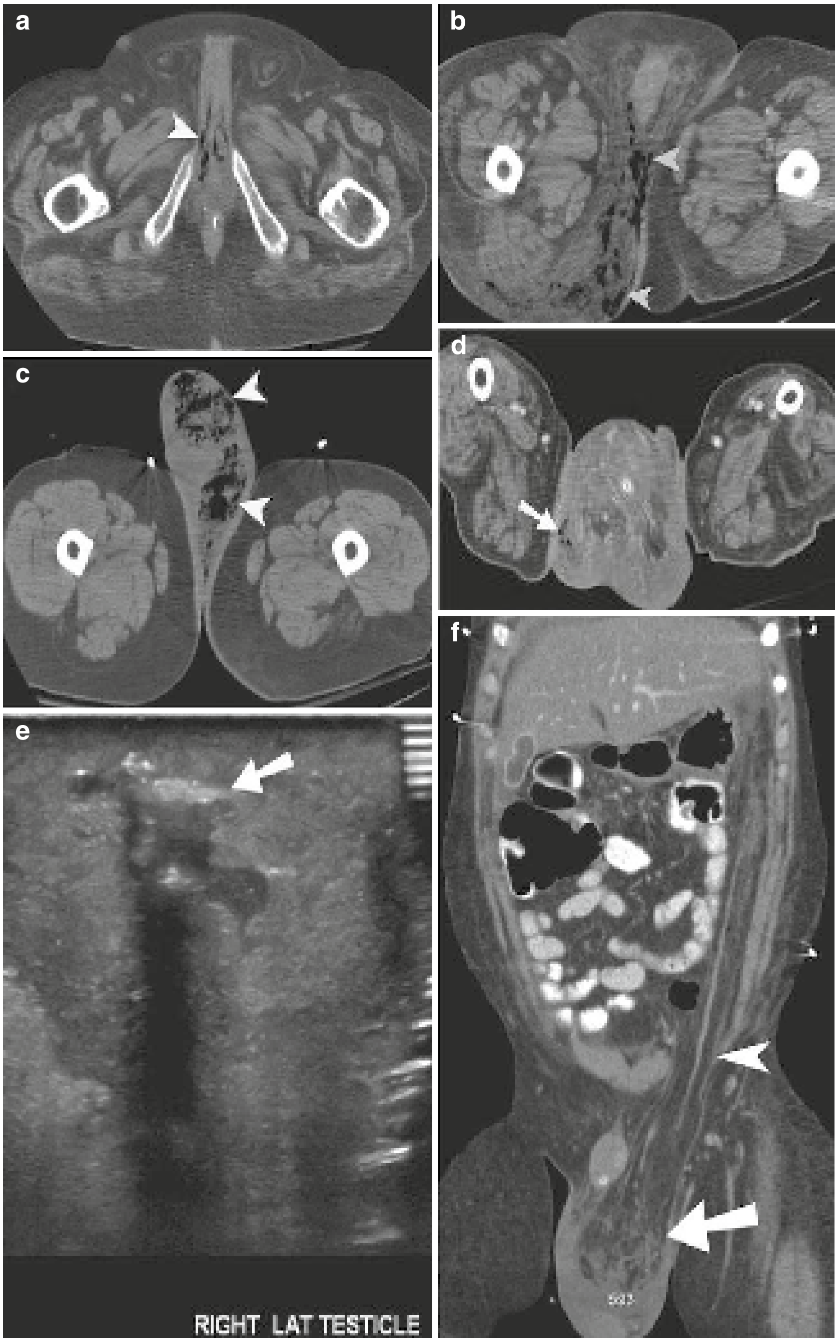

Fig. 8.7 Fournier gangrene. (**a**–**c**) Axial CT imaging of the lower pelvis demonstrates soft tissue air infiltrating in the perineum, penile shaft, and scrotal sac, secondary to anaerobic infection. (**d**, **e**) Ultrasound and CT demonstrate scrotal abscess containing foci of air (*arrow*). (**f**) Coronal CT reformation demonstrates omental fat passing through patulous left inguinal canal (*arrowhead*), into left scrotal hernia (*arrow*)

strate extensive perineal inflammation, fascial thickening, soft tissue gas, and fluid collection (possibly with air-fluid levels) or fistula.

The complications include abscess extension to thigh or abdomen, coagulopathy, diabetic ketoacidosis, sepsis, and multiple organ failure. The treatment includes hemodynamic stabilization, intravenous antibiotics, and surgical debridement of the necrotic tissues. Hyperbaric oxygen has also been used as adjuvant treatment, in patients who do not respond well to surgery.

Testicular Torsion

Spermatic cord torsion is a surgical emergency which affects 1 in 125 males in the USA and requires urgent surgery. The torsion results in vascular compromise, first of the veins and then arteries. When the torsion is between 120° and 360°, the arterial blood flow decreases. When the torsion is between 540° and 720°, the barterial occlusion occurs. Two types of torsion are as follows:

- Intravaginal torsion is the most common type and is associated with abnormal suspension of the testis by tunica vaginalis, resulting in bell-clapper deformity. This abnormality has a 2% prevalence (40–80% bilateral) and allows the testicle to rotate freely within the hemiscrotum.
- Extravaginal torsion is most frequent in newborn, where the testicle is poorly or not at all attached to the scrotal wall, permitting rotational mobility of the testicle. The resulting spermatic cord torsion is at the external inguinal ring level.

Ultrasound is the first-line imaging technique which shows low or absent vascular flow into the symptomatic cord and testis on Doppler study. Other sonographic findings suggestive of testicular torsion include spermatic cord whirlpool sign, redundant spermatic cord within the scrotal sac, and altered lie (horizontal or oblique) of the testis from its normal vertical orientation. The whirlpool sign refers to the twisting of the spermatic cord and is observed in the scrotal sac or at the external inguinal ring (Fig. 8.8). It is considered a highly reliable sign of testicular torsion, both partial and complete, even when Doppler demonstrates intact blood flow. Other findings include enlargement of the testis as well as epididymis in the first hours of onset. Although the testicular echogenicity is initially normal, with time the testis becomes heterogeneous and hypoechoic, indicating possible nonviability (Fig. 8.9). Hydrocele is frequently present on the affected side. Infarction and hemorrhage develop 24 h after torsion onset and give the testicle a heterogeneous appearance. The diagnosis may be difficult in cases with intermittent torsion where the blood flow may be normal or there may be postischemic hyperemia.

If not treated, the torsion leads to irreversible ischemia and lost of the testicle. If torsion is surgically detrosed within 6 h of symptom onset, salvage rate is as high as 80–100%. However, salvage rate drops to 20% after 12 h [2].

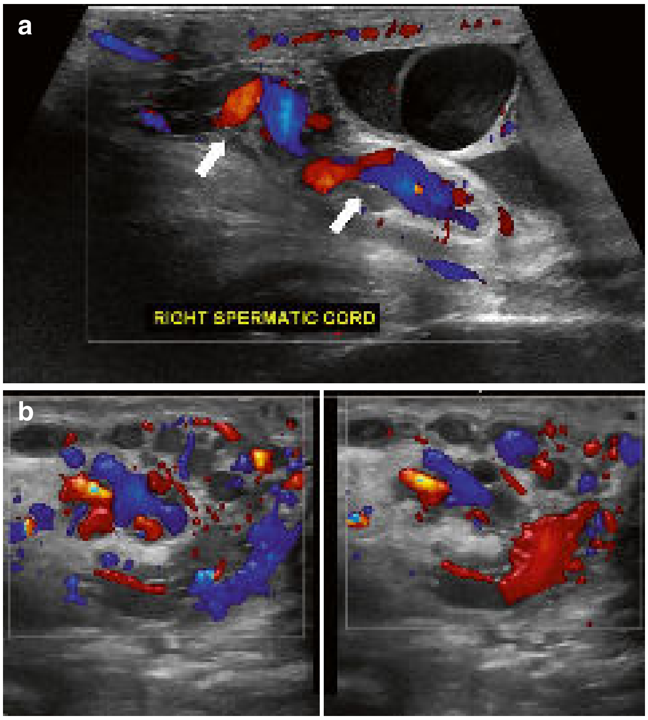

Fig. 8.8 Testicular torsion. (**a**, **b**) Ultrasound of the right scrotum demonstrates thickened spermatic cord (arrows) in the longitudinal (**a**) and cross-sectional plane (**b**) in this patient with testicular torsion. On cross-sectional imaging, the ultrasound appearance is consistent with whirlpool sign

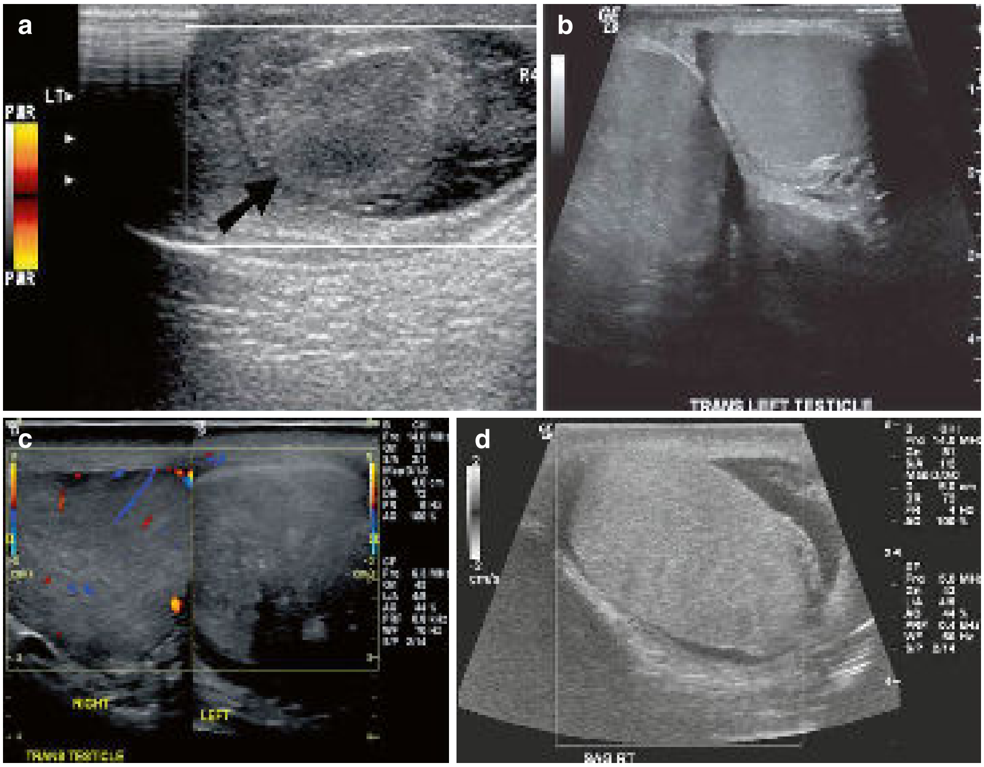

Fig. 8.9 Testicular torsion. (**a**, **b**) Gray-scale ultrasound imaging demonstrates heterogeneously hypoechoic left testicle in relation to the normal echogenicity of the right testicle (**b**). (**c**, **d**) Power Doppler and color Doppler imaging of the testicle demonstrate complete absence of flow in the testicle parenchyma. There is complex hydrocele identified caudal to the testicle (**d**)

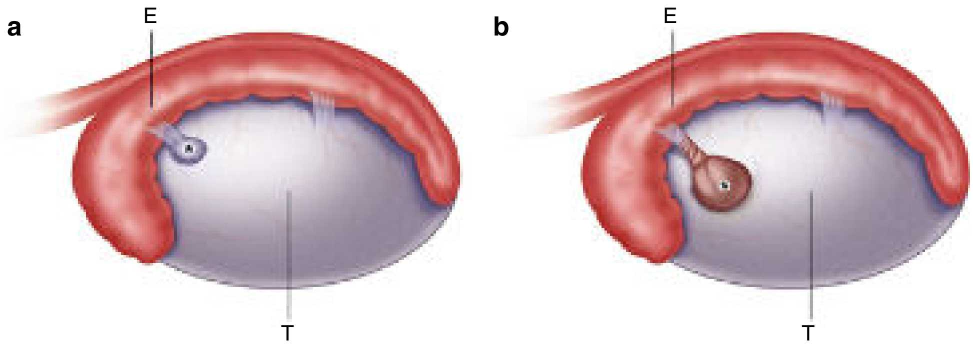

Fig. 8.10 Torsion of appendix testis. Schematic diagram shows normal (**a**) and torsed appendages (**b**). The torsed appendage is seen as enlarged avascular extratesticular mass adjacent to the epididymis

Torsion of Appendix Testis

Torsion of scrotal appendage most commonly occurs in 7–13 years old. Trauma and exercise are the most common preceding events. Clinical presentation includes pain, erythematous scrotal skin, tenderness, and edema (Fig. 8.10).

In ultrasonography, there is spherical enlargement of scrotal appendage. The torsed appendage usually appears homogenously hyperechoic; however, in 30% of patients it might become hypoechoic. On color Doppler study, no blood flow signal is present. The surrounding tissue may have increased signals. An appendiceal length above 5.6 mm is 68% sensitive and 100% specific for detecting torsion of appendage.

Scrotal Trauma

Trauma is the third most common cause of acute scrotal pain after torsion and inflammation. The primary causes are blunt, penetrating, degloving, electrical burn, and postsurgical injuries. Scrotal trauma accounts for less than 1% of all trauma-related injuries because of the anatomic location and mobility of the scrotum. The peak occurrence of scrotal trauma is in the age range of 10–30 years [11].

Blunt trauma is the most common cause of testicular injury and usually results from athletic injury (50%), motor vehicle collision (9–17%), or assault [8]. Penetrating trauma is usually due to gunshot wounds and less commonly due to stab wounds, animal attacks, and self-mutilation. In degloving injury, the scrotal skin shears off, and skin grafting may be required. The right testis is injured more often than the left one because of its greater propensity to be trapped against the pubis or inner thigh.

Ultrasonography is commonly performed for the assessment of scrotal trauma, as it shows testicular integrity, scrotal collections, and blood flow. Ultrasound can detect scrotal hematoma, hydrocele, hematocele, testicular fracture, and testicular rupture. Color Doppler ultrasound can also be helpful in differentiating posttraumatic conditions from tumors, since tumors larger than 1.5 cm are hypervascular and hematomas are avascular.

Testicular Fracture and Rupture

Fracture of the testis is an uncommon condition which is most often secondary to blunt traumatic injury. Urgent diagnosis is imperative because of the high orchiectomy rate, if the surgery is delayed for more than 3 days. Clinical diagnosis is often difficult due to presence of pain and edema.

Ultrasonography helps determine the scrotal content integrity and is highly sensitive in diagnosing testicular fracture and rupture. On ultrasound, testicular fracture is seen as linear hypoechoic band that extends across the testicular parenchyma with intact testicular contour. Testicular rupture is seen as discontinuity of the echogenic tunica albuginea, poorly defined testicular margins, and heterogeneous echotexture due to hemorrhage or infarction (Figs. 8.11 and 8.12) [11, 12]. There may be associated scrotal wall thickening and hematocele. Color Doppler images may show decreased flow or no flow and is helpful in distinguishing normal parenchyma from hematoma.

MRI may be useful to show interruption of tunica albuginea and differentiate intratesticular hematoma (no tunica albuginea disruption) from testicular rupture, which needs surgical treatment. The tunica albuginea appears as a thin, low-signal membrane on both the proton-density and

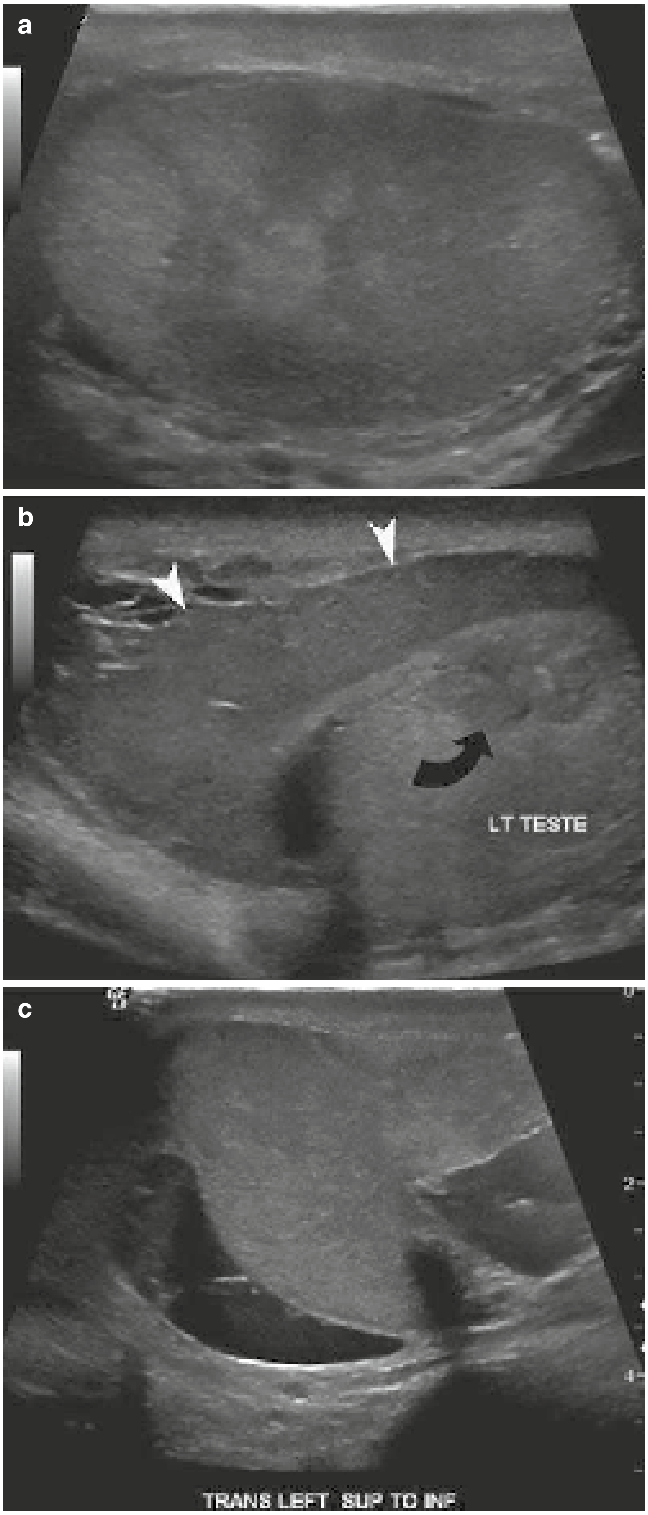

Fig. 8.11 Testicular contusion after trauma. (**a**, **b**) Ultrasound of the testicle demonstrates heterogeneous areas of low echogenicity in the testicular parenchyma, secondary to testicular contusion (*curved arrow*). There is no discontinuity identified outline of the testicle. There is associated echogenic fluid identified around the testicle, consistent with a hematocele (*arrowheads*). (**c**) Ultrasound demonstrates discontinuity of the testicular outline in a patient with testicular fracture

T2-weighted images. Testicular rupture is seen as discontinuity of this membrane, and intratesticular hematoma is seen as areas of high-signal intensity on T1-weighted images and low-signal intensity on T2-weighted images [10].

Testicular fractures are treated conservatively if normal flow is identified but require emergent surgery when there is no flow demonstrated. The timely diagnosis of rupture is critical because emergent surgery can salvage the testis in 80–90% cases of rupture. The salvage rate is lower when surgery is delayed for more than 3 days. Testicular rupture from penetrating injury is managed in the same way as rupture from blunt injury.

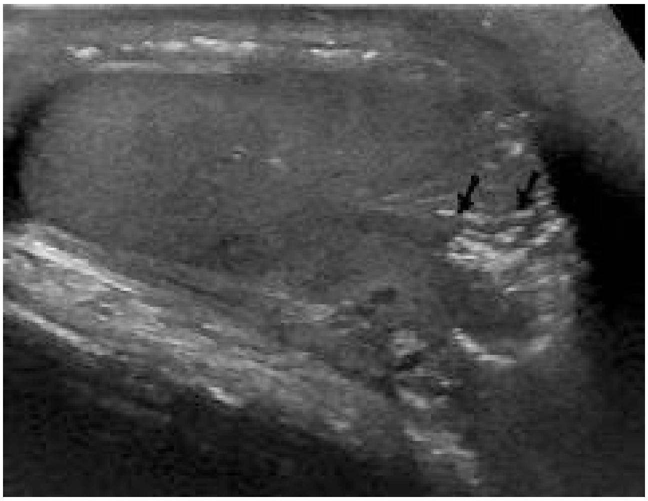

Fig. 8.12 Testicular laceration due to gunshot wound injury. Ultrasound demonstrates a heterogeneous laceration (*arrows*) of the testicular parenchyma, also containing hyperechoic gas

Penile Fracture

Penile fracture results from external force on erect penis, causing rupture of corpus cavernosum and tear of tunica albuginea. It is usually posttraumatic, often from sexual intercourse, masturbation, falling on the erect penis, rolling over in bed with an erect penis, or direct injury. Clinical presentation includes pain, bruising, and rapid detumescence. In majority of cases, the tear occurs in only one of the corpora cavernosa, often affecting the distal two-thirds of the penis. In some cases, the corpus spongiosum and the urethra (38% cases) may also be involved [13, 14].

Patients with atypical clinical presentation or severe local pain which prohibits a physical examination may require imaging. Although cavernosography can identify a corpus cavernosal tear or urethrocavernous fistula, it is an invasive method with potential complications. Ultrasound allows depiction of normal penile anatomy, tear in the tunica albuginea, and soft tissue hematoma (Figs. 8.13 and 8.14).

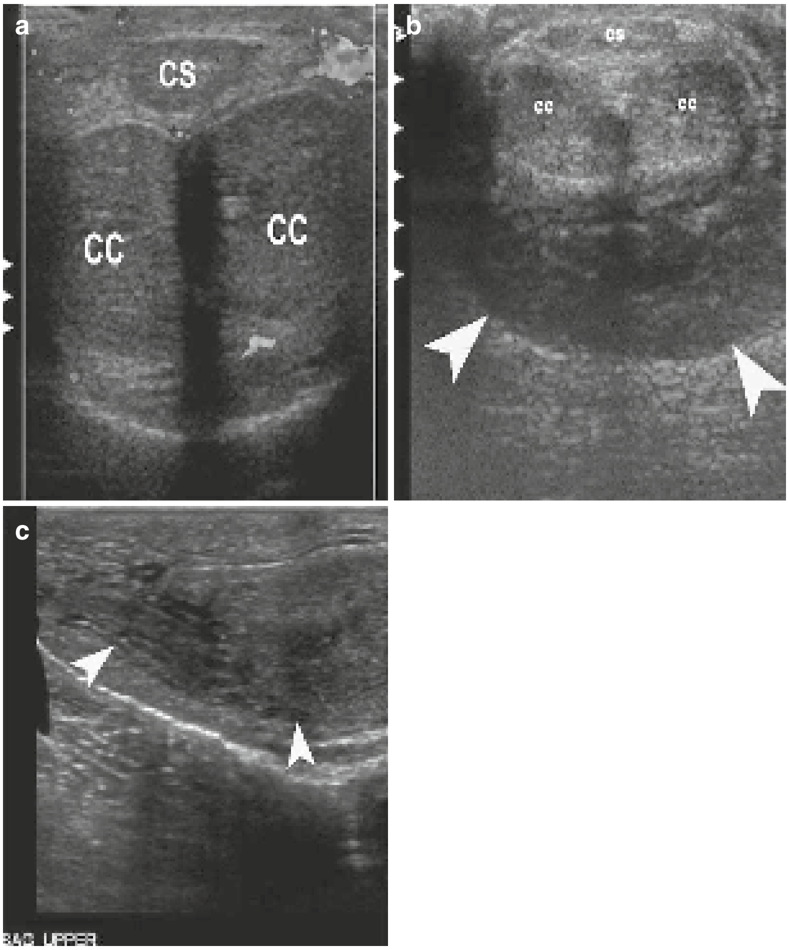

Fig. 8.13 Normal and abnormal ultrasound anatomy of the penile shaft. (**a**) Normal anatomy. Transverse ultrasound of the penile shaft demonstrates paired corpora cavernosa (*CC*) and single corpus spongiosum (*CS*). (**b**) Transverse ultrasound of the penile shaft in a patient with history of trauma demonstrates a large hematoma on the ventral aspect of the penile shaft, displacing the corpus callosum superiorly. (**c**) Sagittal image, a patient with corpora cavernosa hematoma demonstrating widening of the corpora cavernosa (*arrowheads*)

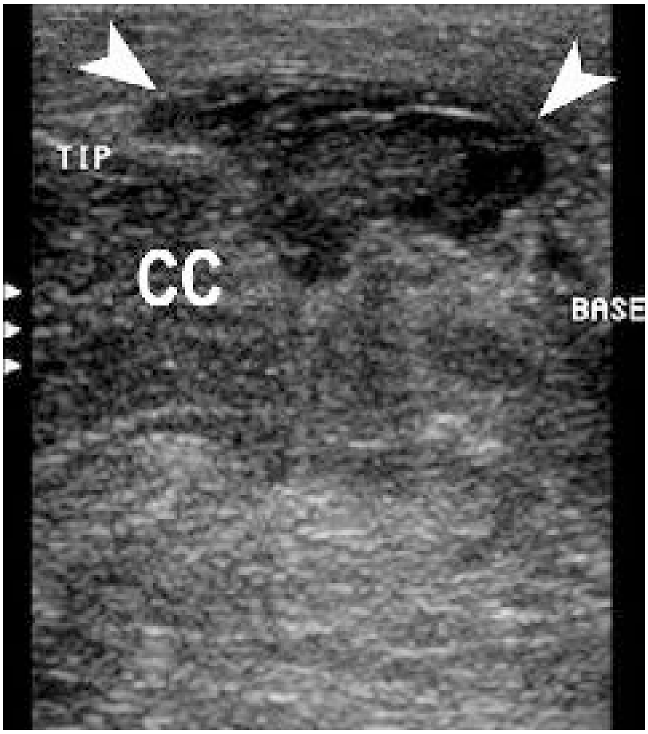

Fig. 8.14 Penile fracture. Ultrasound image in a patient with penile fracture demonstrates a hematoma located on the dorsal aspect of the corpora cavernosa with discontinuity of corpus spongiosum

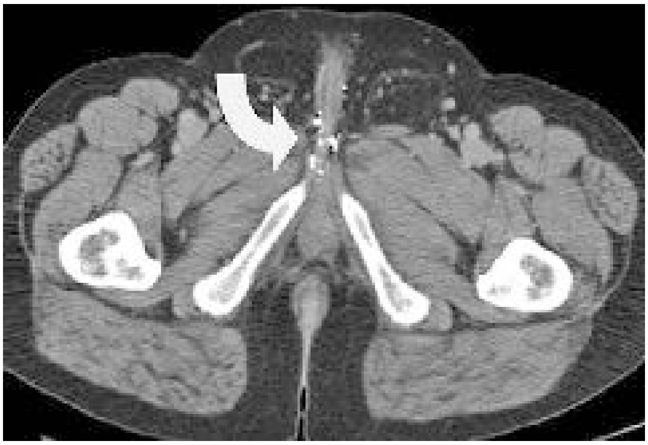

Fig. 8.15 Gunshot injury to the penile shaft. CT of the pelvis demonstrates multiple metallic fragments (*curved arrow*) seen in the penile shaft, secondary to gunshot injury. Note the limitation of CT in depiction of internal anatomy of the penile shaft

Because of its multiplanar capability and excellent tissue contrast, MR imaging can be useful in demonstrating the tunica albuginea [14]. MRI demonstrates disruption of T1 and T2 hypointense tunica albuginea, usually accompanied by T2 hyperintense hematoma. CT is generally not performed for penile injury because of its limitation in depicting internal penile anatomy (Figs. 8.15 and 8.16).

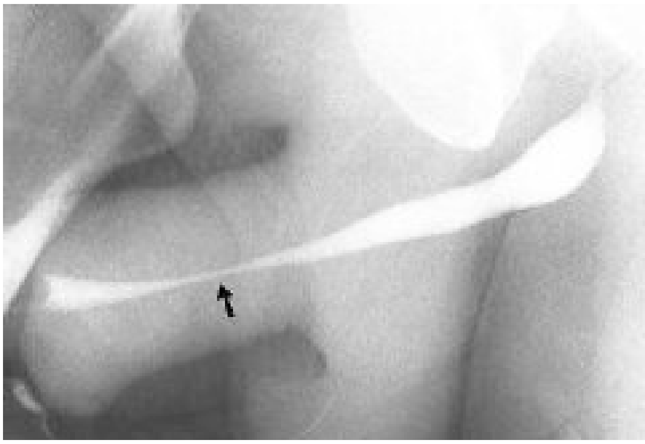

Fig. 8.16 Benign stenosis of the urethra. Retrograde urethrogram demonstrates long-segment benign narrowing of penile urethra, caused by extrinsic compression from a hematoma in the penile shaft

Surgical repair is generally recommended for patients with a suspected tear of the tunica albuginea or urethral injury. Early surgical intervention can prevent late complications such as plaque formation and erectile dysfunction [15].

Urethral Injury

Urethral injury is a common complication of pelvic trauma (motor vehicle injury and fall from height), occurring in as many as 24% of adults with pelvic fractures [16]. The urethra is vulnerable because of its close proximity to the pubic bones and the puboprostatic ligaments. The distal membranous urethra is especially at risk, and its injury may disrupt the active continence mechanism.

The most common site of urethral injury is the posterior urethra (3–25% of patients with pelvic fractures), followed by anterior urethral injury [16]. Approximately one-fifth of these patients have urinary bladder injury [14].

If urethral injury is suspected, then imaging should be performed to rule out urethral injury before a transurethral catheter is inserted. Retrograde urethrography is the most widely accepted technique to determine urethral integrity and classify urethral injury. Accurate classification of urethral injury is important because it allows effective treatment planning (Table 8.1).

CT imaging demonstrates stretched urethra, altered prostatic position, obliteration of periprostatic fat plane, and muscle hematomas (type I); extravasation of contrast agent above urogenital diaphragm is typical of type II injury and extravasation of contrast below urogenital diaphragm in type III injury [15, 17]. Urinary bladder extravasation is seen in type IV injury (Fig. 8.17).

Table 8.1 Classification of urethral injury on retrograde urethrography

Injury type	Anatomical description	Radiological findings
I	Stretched/elongated posterior urethra	Urethra is stretched but not injured
II	Disruption of the posterior urethra above urogenital diaphragm	Extravasation above the urogenital diaphragm
III	Disruption of the membranous urethra	Extravasation above and below the urogenital diaphragm
IV	Injury of the bladder neck and the proximal urethra	Extravasation into the extraperitoneal spaces and disruption of the bladder neck
Iv A	Injury of the bladder base with intact urethra (simulating type IV)	Extravasation into the urethral space associated to the lesion of the bladder base
V	Injury of the anterior urethra	Extravasation below the urogenital diaphragm

According to Goldman [2, 9]

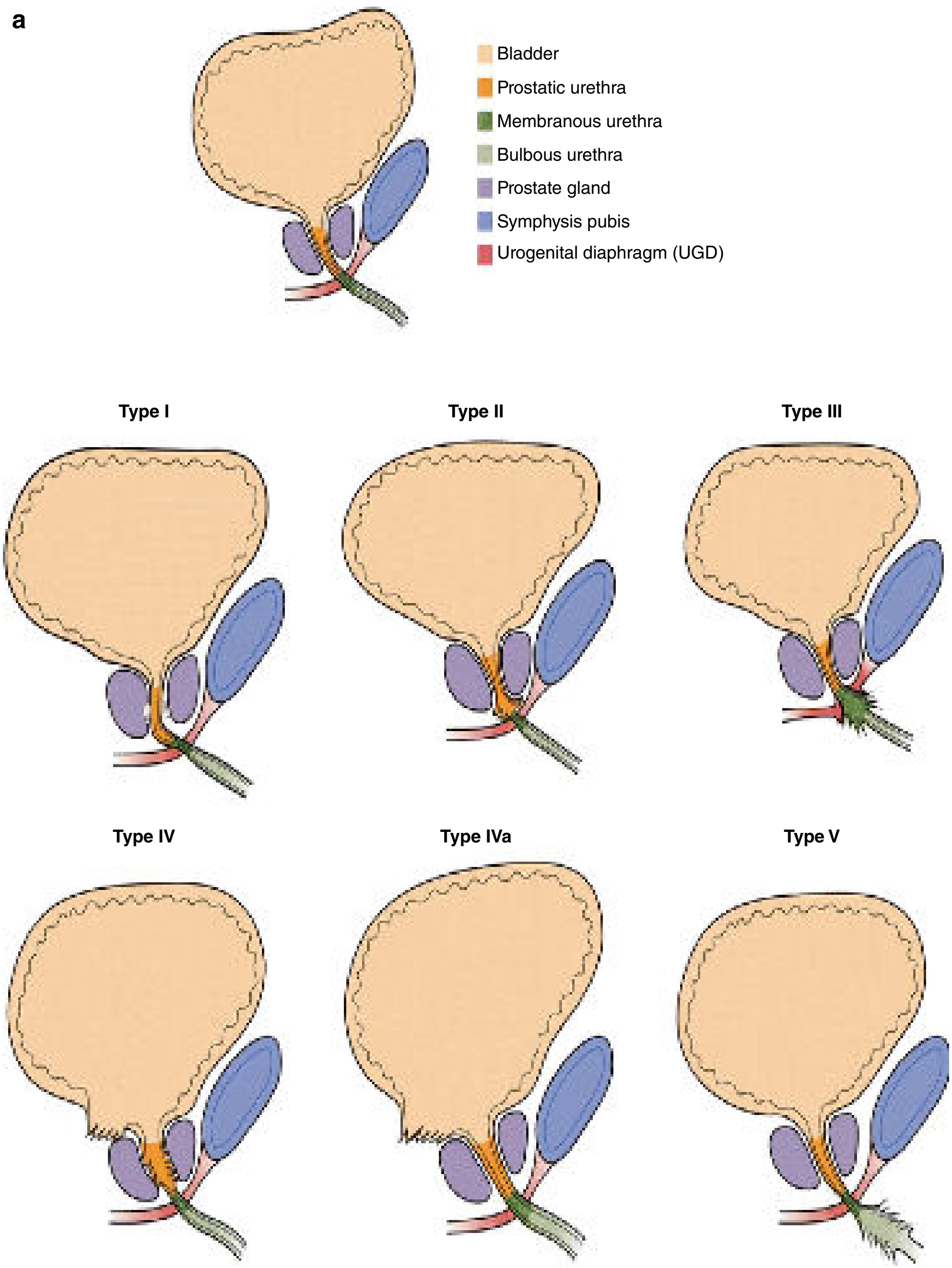
a
Bladder
Prostatic urethra
Membranous urethra
Bulbous urethra
Prostate gland
Symphysis pubis
Urogenital diaphragm (UGD)
Type I
Type II
Type III
Type IV
Type IVa
Type V

Fig. 8.17 Urethral injury. (**a**) Normal urethral anatomy and classification of urethral injury (Goldman's classification). (**b**) Cysto-urethrogram study demonstrates focal urethral stricture (*arrowhead*) and extravasation (*curved arrow*) of contrast from the proximal penile urethra in the first patient and leakage of contrast (*curved arrow*) from the penile urethra in the second patient with urethral injury

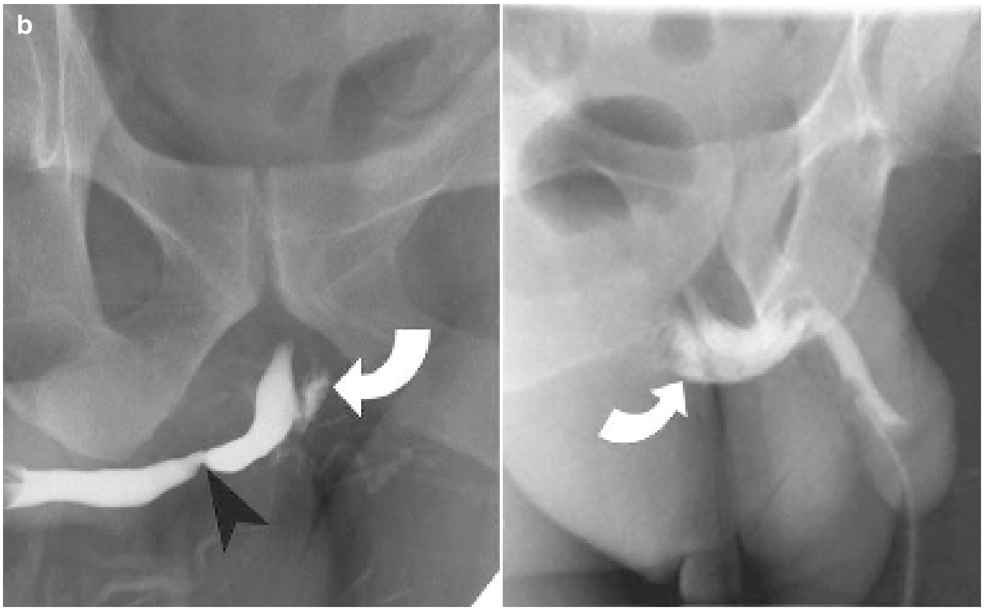

Fig. 8.17 (continued)

Late complications associated with posterior urethral injury include impotence, incontinence, strictures, and fistula, whereas those associated with anterior urethral injury include strictures and impotence. While abrupt, short-segment strictures are usually traumatic, long-segment strictures may be traumatic or postinflammatory. The diagnosis of urethral stricture is usually made by retrograde urethrography that defines location, length, number strictures, as well as the periurethral abnormalities such as stones, false tract, and diverticula [14, 15].

Immediate surgery is necessary in type IV and type V injuries because of the potential for urinary incontinence. While type I injury may be conservatively managed, complete urethral disruption (types II–III) may require immediate surgery because of risk of stricture formation in the future. In presence of short strictures, the first-line treatment is dilatation by catheter or urethrotomy, while longer and recurrent strictures require surgical resection [15].

Teaching Points

- Fournier gangrene is an infection, caused by multiple bacteria, most commonly *Escherichia coli*, Bacteroides, and streptococcal species.
- Intravaginal testicular torsion is the most common type of torsion and is associated with abnormal suspension of the testis by tunica vaginalis, resulting in bell-clapper deformity.
- On ultrasound, testicular fracture is seen as linear hypoechoic band that extends across the testicular parenchyma with intact testicular contour.
- Ultrasound allows depiction of normal penile anatomy, tear in the tunica albuginea, and soft tissue hematoma in patients with penile fracture.
- On retrograde urethrography, extravasation of contrast agent above urogenital diaphragm is seen with type II injury and extravasation of contrast below urogenital diaphragm is seen with type III urethral injury.

Questions

1. Which of the following statements is correct in ultrasonography of male reproductive organs?
   (A) Hematocele is seen as complex fluid with internal echoes.
   (B) Blood flow in varicocele decreases during valsalva maneuver.
   (C) Fournier gangrene is often seen as enlarged and edematous testicles.
   (D) In testicular torsion, the testis becomes hyperechoic after 24 h.
   Answer: A
2. Which of the following findings is the most specific in torsion of scrotal appendage?
   (A) Round shape
   (B) Homogenously hyperechoic
   (C) Increased signal of peripheral tissue
   (D) Enlargement of scrotal appendage
   Answer: D

3. Hyperintense hematoma and a disrupted tunica albuginea in MRI are seen in which of the following?
   (A) Peyronie's disease
   (B) Spermatic cord torsion
   (C) Hydrocele
   (D) Penile fracture
   Answer: D

4. T2-weighted MRI on the figure below (Fig. 8.18) shows penile fracture. The arrow indicates defect in which of the following anatomical structures?
   (A) Corpus spongiosum
   (B) Penile urethra
   (C) Tunica albuginea
   (D) Tunica media
   Answer: C

5. What is the diagnosis in ultrasonography (Fig. 8.19) in a patient with acute scrotal pain?
   (A) Epididymitis
   (B) Testicular torsion
   (C) Testicular rupture
   (D) Appendageal torsion
   Answer: B

6. What is the diagnosis on ultrasound (Fig. 8.20) in a patient with acute scrotal pain?
   (A) Testicular torsion
   (B) Varicocele
   (C) Acute orchitis
   (D) Testicular rupture
   Answer: C

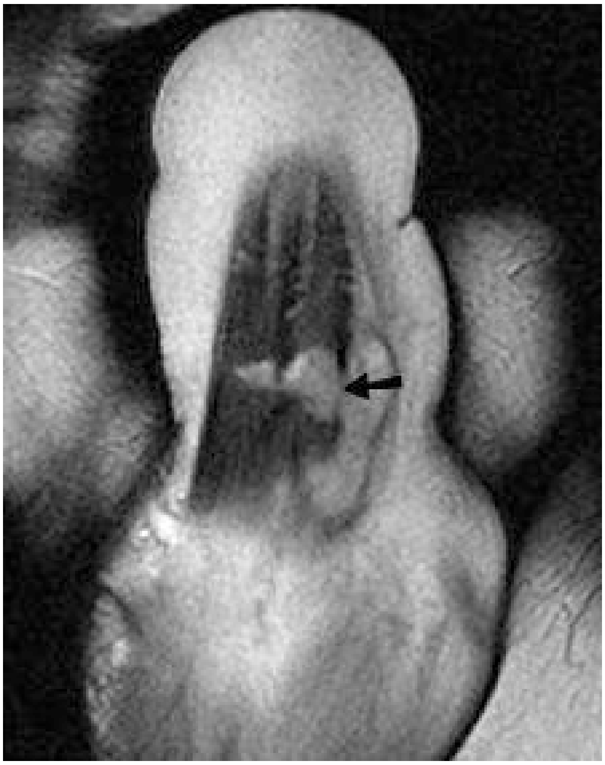

Fig. 8.18 T2-weighted MRI—Tunica albuginea

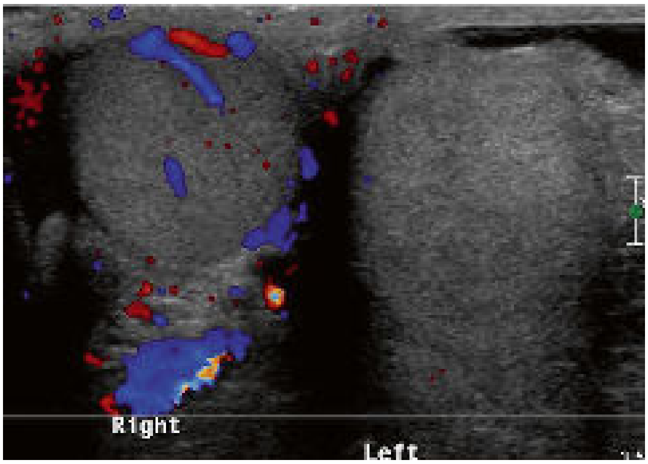

Fig. 8.19 Ultrasonography of testicular torsion

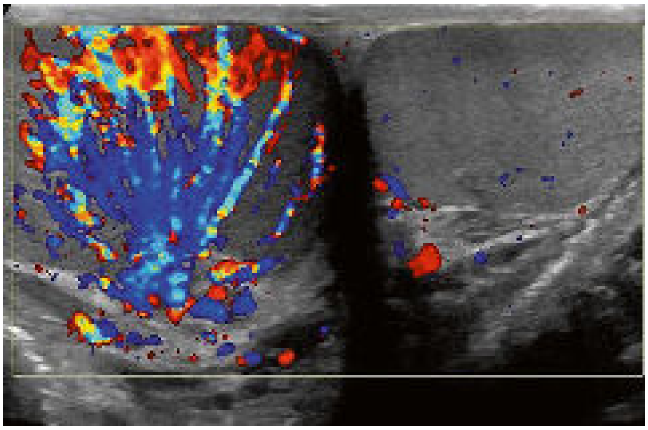

Fig. 8.20 Acute orchitis

References

1. Garriga V, Serrano A, Marin A, Medrano S, Roson N, Pruna X. US of the tunica vaginalis testis: anatomic relationships and pathologic conditions. Radiographics. 2009;29:2017–32.
2. Cokkinos DD, Antypa E, Tserotas P, Kratimenou E, Kyratzi E, Deligiannis I, et al. Emergency ultrasound of the scrotum: a review of the commonest pathologic conditions. Curr Probl Diagn Radiol. 2011;40(1):1–14.
3. Brant WE, Helms CA. Helms, fundamentals of diagnostic radiology. 2nd ed. Philadelphia: Lippincott Williams & Wilkins; 1999. p. 869–77.
4. Horstman WG, Middleton WD, Leland Melson G, Siegel BA. Color Doppler US of the scrotum. Radiographics. 1991;11:941–57.
5. Mazzucato F. Anatomia Radiologica—tecniche e metodologie in radiodiagnostica. 3rd ed. Milano: Piccin Editore; 2009. p. 2419–20.
6. Tessler FN, Tublin ME, Rzfldn MD. US case of the day. Radiographics. 1998;18:251–3.
7. Muttarak M, Lojanapiwat B. The painful scrotum: an ultrasonographical approach to diagnosis. Singap Med J. 2005;46(7):352.
8. Brant WE, Helms CA. Fundamentals of diagnostic radiology. 2nd ed. Philadelphia: Lippincott Williams & Wilkins; 1999. p. 823–6.
9. Levenson RB, Singh AK, Novelline RA. Fournier gangrene: role of imaging. Radiographics. 2008;28:519–28.
10. Cramer BM, Schlegel EA, Thueroff JW. MR imaging in the differential diagnosis of scrotal and testicular disease. Radiographics. 1991;11(1):9–21.

11. Deurdulian C, Mittelstaedt CA, Chong WK, Fielding JR. US of acute scrotal trauma: optimal technique, imaging findings, and management. Radiographics. 2007;27:357–69.
12. Bertolotto M, Pavlica P, Serafini G, Quaia E, Zappetti R. Painful penile induration: imaging findings and management. Radiographics. 2009;29:477–93.
13. Choi M-H, Kim B, Ryu J-A, Lee SW, Lee KS. MR imaging of acute penile fracture. Radiographics. 2000;20:1397–405.
14. Kawashima A, Sandler CM, Wasserman NF, LeRoy AJ, King BF Jr, Goldman SM. Imaging of urethral disease: a pictorial review. Radiographics. 2004;24:S195–216.
15. Kirkham APS, Illing RO, Minhas S, Allen C. MR imaging of nonmalignant penile lesions. Radiographics. 2008;28:837–53.
16. Ingram MD, Watson SG, Skippage PL, Patel U. Urethral injuries after pelvic trauma: evaluation with urethrography. Radiographics. 2008;28:1631–43.
17. Ali M, Safriel Y, Sclafani SJA, Schulze R. CT signs of urethral injury. Radiographics. 2003;23:951–63.
18.

9

Imaging of Blunt and Penetrating Abdominal Trauma

Paul F. Von Herrmann, David J. Nickels, Mohammad Mansouri, and Ajay Singh

Introduction

Trauma is the leading cause of morbidity and mortality among people younger than 45 years of age. Traumatic injury to the abdominal organs, with ensuing exsanguination, is the primary cause of death [1]. Of all abdominal traumatic injuries presenting to hospitals, blunt trauma comprises approximately 90% and typically results from a motor vehicle collision or a fall. Penetrating trauma accounts for the remaining 10% and is often a result of a bullet or knife injury. The evaluation of blunt or penetrating abdominal trauma can be one of the most challenging and resource-exhaustive aspects of acute trauma care.

In 1988, the American Association for the Surgery of Trauma (AAST) devised a set of organ injury scales (OISs) based on findings at surgical exploration. The OISs have now been defined by computed tomography (CT) criteria [2]. Accurate noninvasive assessment of injuries with CT is beneficial and can guide management. Since the development and application of these CT-based criteria, nonoperative management for blunt abdominal trauma has become increasingly common, particularly in hemodynamically stable patients. The accumulated evidence has demonstrated that minimally invasive management of blunt abdominal trauma, instead of laparotomy, results in improved survival rates. Analogously, managing penetrating abdominal trauma with laparotomy results in a negative or nontherapeutic procedure in 15–25% of cases, prompting a movement toward more conservative management algorithms [3].

Currently, multidetector computed tomography (MDCT) with intravenous contrast is the "gold standard" diagnostic imaging examination in hemodynamically stable patients who have intra-abdominal fluid by focused assessment with sonography for trauma (FAST) [4]. Many studies have reported that MDCT has high sensitivity, specificity, positive predictive value, negative predictive value, and accuracy in injuries to the liver, spleen, kidney and urinary bladder, hollow viscus, and major vascular structures [2–5].

FAST

FAST is a useful diagnostic tool when performed in the acute setting because it can demonstrate intra-abdominal fluid, a finding that suggests significant organ injury, with a sensitivity of 90–93% [4]. FAST is often performed after the secondary assessment or during resuscitation efforts. Identification of intra-abdominal free fluid on FAST (Fig. 9.1) in a hemodynamically unstable patient is regarded as synonymous with hemoperitoneum, thereby directing the surgeon to consider the abdomen as the major source of blood loss and prompting emergent laparotomy instead of CT. Conversely, a positive FAST in a hemodynamically stable patient should be followed by a CT scan to determine the source of the fluid. Table 9.1 summarizes the etiologies of positive FAST.

Shortcomings of FAST include its inability to qualitatively grade the extent of organ injury and its low (34–55%) sensitivity for direct demonstration of blunt abdominal injury [4]. Other limiting factors include inability to demonstrate small amounts of free fluid, operator dependence, limited accuracy in the retroperitoneum, and large body habitus.

P. F. Von Herrmann
Department of Radiology, North Alabama Medical Center,
Florence, AL, USA

D. J. Nickels
Department of Radiology, University of Kentucky,
Lexington, KY, USA

M. Mansouri
Department of Radiology, Massachusetts General Hospital,
Boston, MA, USA

A. Singh (✉)
Division of Emergency Radiology, Department of Radiology,
Massachusetts General Hospital, Boston, MA, USA

Harvard Medical School, Massachusetts General Hospital,
Boston, MA, USA
e-mail: asingh1@partners.org

© The Author(s), under exclusive license to Springer Nature Switzerland AG 2024
A. Singh (ed.), *Emergency Radiology*, https://doi.org/10.1007/978-3-031-65770-2_9

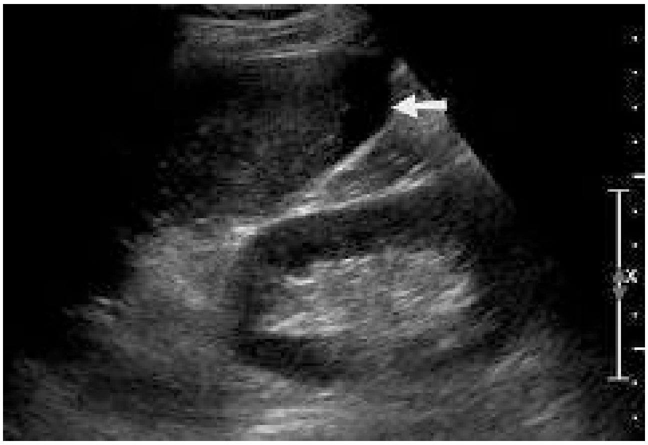

Fig. 9.1 FAST. Ultrasound image from a FAST exam shows small amount of fluid adjacent to the spleen (*arrow*)

Table 9.1 Etiologies of positive FAST

Anatomical space	Etiologies
Pericardial fluid	Preexisting fluid
	Hemopericardium
Pleural fluid	Preexisting fluid
	Hemothorax
Peritoneal fluid	Preexisting ascites
	Hemoperitoneum
	Uterine injury
	Bladder injury
	Bowel injury
	Gallbladder injury
	Ovulation
	Peritoneal dialysis
	Volume resuscitation

Liver

The liver is the most frequently injured solid abdominal organ in blunt and penetrating trauma. Hepatic injury in patients who have sustained blunt trauma has been reported to occur in 1–8% and in penetrating trauma in up to 39% [1, 6]. However, with utilization of abdominal CT in the severely injured patient, hepatic injuries can be detected in up to 25% of those with blunt trauma [7]. CT also helps in detection of associated injuries including spleen (21%), kidney (9%), and bowel (4%). Mortality rates from blunt or penetrating liver injury have been reported to range from 2.8 to 11.7% [6, 8].

Nonsurgical management is the preferred strategy for hemodynamically stable patients with blunt liver injury. Accurate characterization of the extent of the injury by CT assists the managing provider with specific information that can be followed and categorized by the AAST OIS criteria (Table 9.2).

Hepatic injuries detected by CT can be classified as lacerations, hematomas, active hemorrhage, and juxtahepatic venous injuries. Hepatic laceration is the most common type of parenchymal liver injury; it appears as an irregular, linear, or branching low-attenuation region on contrast-enhanced CT (CECT) (Fig. 9.2). Lacerations are further divided into superficial (<3 cm) or deep (>3 cm).

Table 9.2 AAST organ injury scale for liver

Grade	Description
I	Hematoma: subcapsular, <10% surface area
	Laceration: capsular tear, <1 cm in parenchymal depth
II	Hematoma: subcapsular, 10–50% surface area; intraparenchymal, <10 cm in diameter
	Laceration: 1–3 cm in parenchymal depth, <10 cm in length
III	Hematoma: subcapsular, >50% surface area or expanding or ruptured subcapsular parenchymal hematoma; intraparenchymal hematoma >10 cm or expanding or ruptured
	Laceration: >3 cm in parenchymal depth
IV	Laceration: parenchymal disruption involving 25–75% hepatic lobe or 1–3 Couinaud segments
V	Laceration: parenchymal disruption involving >75% of a hepatic lobe or >3 Couinaud segments within a single lobe
	Vascular: juxtahepatic venous injuries (i.e., central major hepatic veins or retrohepatic vena cava)
VI	Vascular: hepatic avulsion

Source: Tinkoff et al. [9]

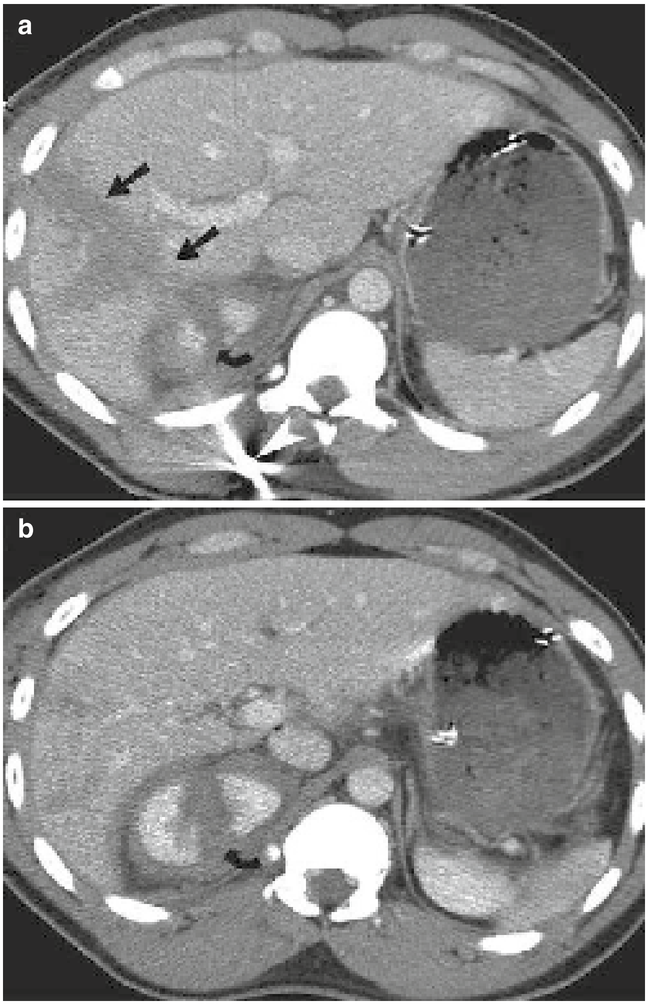

Fig. 9.2 Hepatic laceration from gunshot wound. (**a**, **b**) Contrast-enhanced CT demonstrates a deep hepatic (*straight arrow*) as well a right renal laceration (*curved arrow*). There is a bullet fragment (*white arrowhead*) located in the right posterior abdominal wall. (**c**) Contrast-enhanced CT demonstrates a metallic density bullet fragment located centrally within the right lobe of liver. The liver laceration is obscured by the extensive beam-hardening artifact produced by the bullet fragment

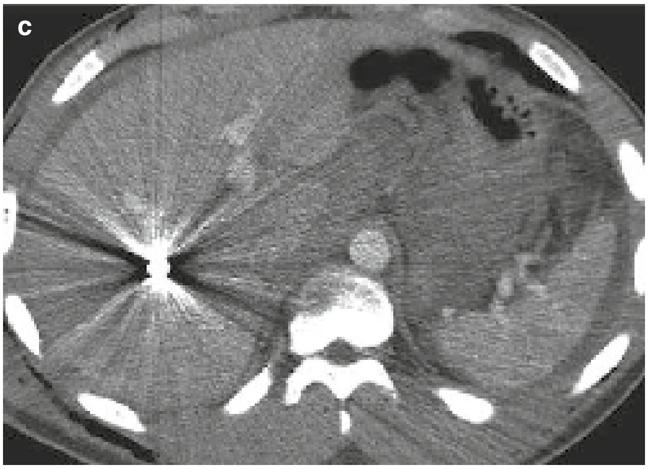

Fig. 9.2 (continued)

Hematomas that present in blunt liver trauma are designated as subscapular or intraparenchymal. On CECT, a subcapsular hematoma appears as an elliptical collection of low-attenuation blood between the capsule of the liver and the enhancing liver parenchyma (Fig. 9.3). Intraparenchymal hematomas are characterized by focal low-attenuation regions with poorly defined, irregular margins in the liver parenchyma on CECT (see Fig. 9.2). Active hemorrhage is diagnosed by identification of a focal high-attenuation area representing a collection of extravasated contrast. Active vascular extravasation can often be differentiated from clotted blood by measuring the CT attenuation coefficient. The attenuation of clotted blood ranges from 28 to 82 Hounsfield units (HU) (mean, 54 HU) (Fig. 9.4a), whereas active arterial extravasation ranges from 91 to 274 HU (mean, 155 HU) (see Fig. 9.4b) [10]. Active contrast extravasation (ACE)

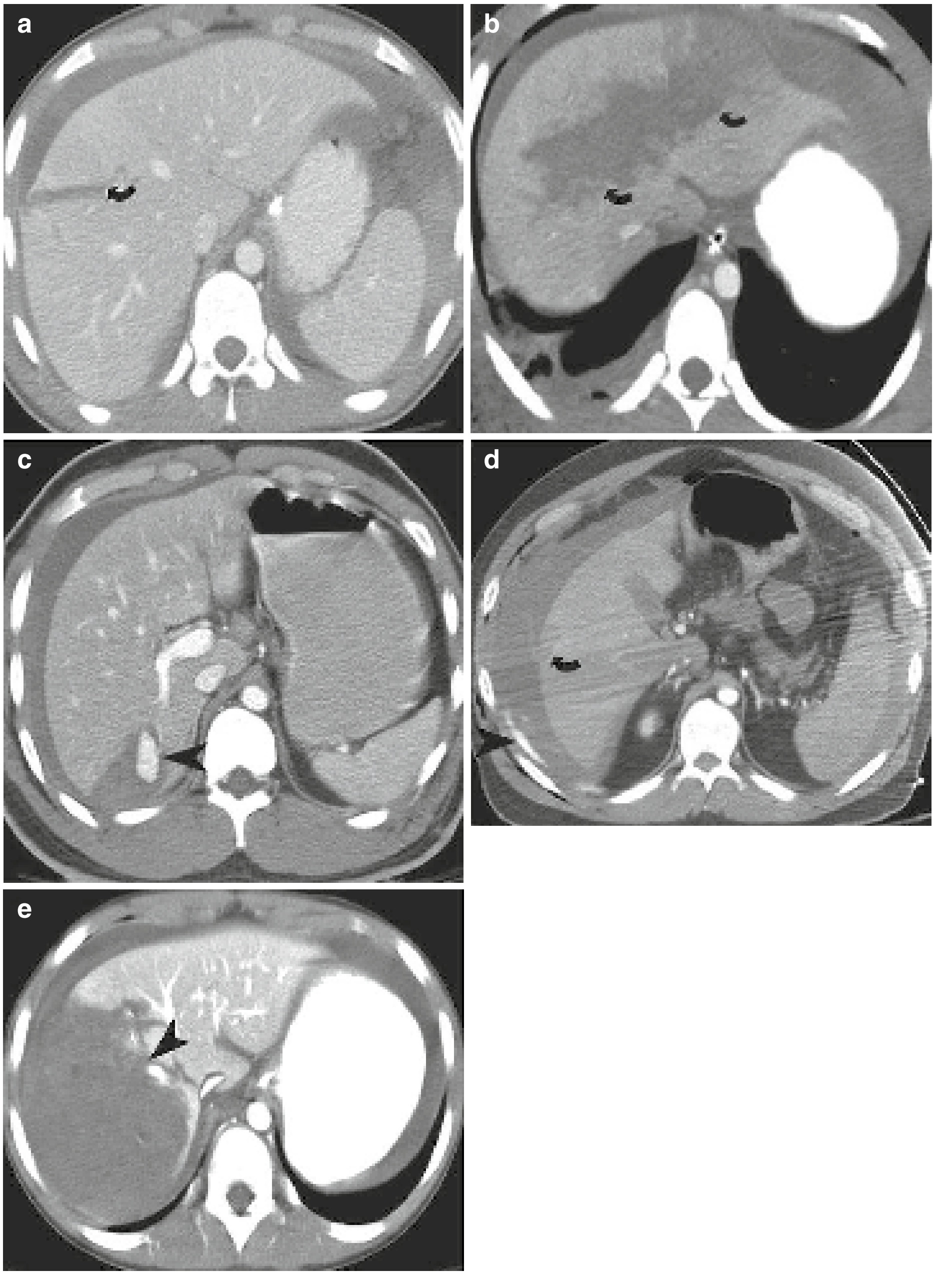

Fig. 9.3 Hepatic lacerations. (**a**, **b**) Contrast-enhanced CT in two different patients shows a deep (>3 cm) hepatic laceration (grade III and grade IV liver injury) (*curved arrows*) due to stab and gunshot injury, respectively. (**c**) Contrast-enhanced CT shows a wedge-shaped liver laceration due to stab injury and enhancing pseudoaneurysm (*arrowhead*). (**d**) Contrast-enhanced CT shows a large perihepatic hematoma and active extravasation (*arrowhead*) arising from a gunshot injury related superficial liver laceration (*curved arrow*). (**e**) Contrast-enhanced CT shows grade IV liver injury with devascularization of >25% of the right lobe of the liver (*arrowhead*)

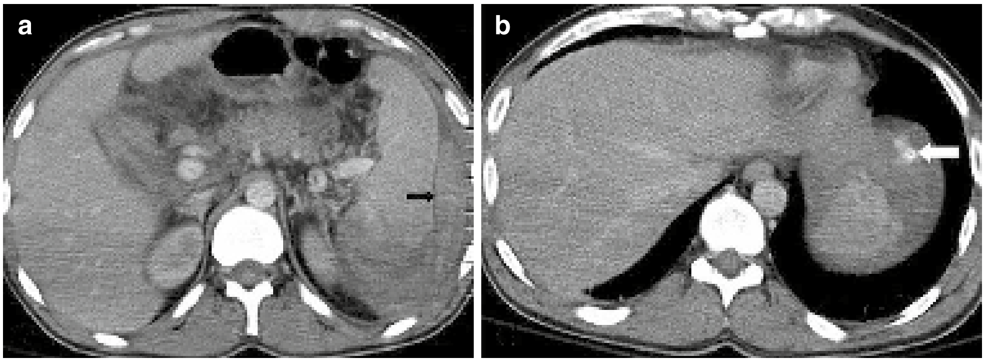

Fig. 9.4 Clotted blood versus contrast extravasation. (**a**) Contrast-enhanced CT image shows clotted blood (*arrow*) adjacent to the spleen. (**b**) Contrast-enhanced CT image shows small amount of active contrast extravasation (*arrow*) adjacent to the spleen

Table 9.3 CT findings of hepatic injuries

Classification	Findings
Lacerations	• Irregular, linear, or branching low-attenuation
	• Superficial (<3 cm) or deep (>3 cm)
Hematomas	• Subscapular: relatively lower attenuation fluid between the enhancing liver capsule and enhancing liver parenchyma
	• Intraparenchymal: focal low-attenuation regions with poorly defined and irregular margins
Active hemorrhage	• Focal high-attenuation area representing a collection of extravasated contrast
Juxtahepatic venous injuries	• Lacerations or hematomas that extend into a major venous structure

changes its appearance over time, such a pattern can be demonstrated with multiphase vascular imaging, that is, during the arterial, portal venous, or delayed phases. On later vascular phase imaging, a region of ACE will increase in size and often pool or mix with noncontrasted blood in the adjacent hematoma. Table 9.3 summarizes the CT findings of hepatic injuries.

Hepatic lacerations or hematomas that extend into a major venous structure indicate a severe injury and have been reported to require surgical management approximately 6.5 times more frequently than injuries not involving the hepatic veins or inferior vena cava (IVC) [11]. A CT finding that may indicate liver injury is periportal low attenuation paralleling the portal vein and its branches. Periportal low attenuation adjacent to a hepatic laceration may represent extension of hemorrhage into the periportal connective tissue although this finding is nonspecific. It can also represent distention of the periportal lymphatic vessels as can be seen after aggressive fluid resuscitation, tension pneumothorax, or pericardial tamponade [12].

Spleen

Currently, 60–80% of patients who sustain blunt splenic injury are managed nonoperatively with a success rate near 95% [2]. Nonoperative management of isolated splenic injury is contingent on hemodynamic stability. Inevitably, failure of nonoperative management correlates with the presence of ACE on CT scan as well as with the radiological grade of the injury per the AAST criteria [9] (Table 9.4).

CECT can accurately diagnose the four common types of splenic injury: hematoma, laceration, active hemorrhage, and vascular injuries [13]. Splenic hematomas may be classified as subcapsular or intraparenchymal. On CECT, a subcapsular hematoma appears as an elliptical, low-attenuating collection between the splenic capsule and the enhancing splenic parenchyma (Fig. 9.5). Acute lacerations have a jagged or sharp margin and appear on CECT as a linear or branching low-attenuation area.

Active hemorrhage in the spleen is represented as an irregular or linear focus of contrast extravasation on CECT. Active hemorrhage may be seen in several locations: within splenic parenchyma or subcapsular space or intraperitoneally. Differentiating between ACE (range 85–350 HU, mean 132 HU) and hematoma or clotted blood (range 40–70 HU, mean 51 HU) is accomplished by measuring the attenuation coefficient [13].

Splenic vascular injuries include posttraumatic pseudoaneurysms and arteriovenous (AV) fistulas. A splenic pseudoaneurysm will appear as a well-circumscribed focus of increased attenuation in comparison to the enhancing splenic parenchyma (Fig. 9.6). An AV fistula is best demonstrated by early splenic vein enhancement. Both of these vascular injuries are best seen on arterial phase imaging and can be difficult to detect on portal venous phase or delayed (renal excretory

Table 9.4 AAST organ injury scale for spleen

Grade	Description
I	Hematoma: subcapsular, <10% surface area
	Laceration: capsular tear, <1 cm in parenchymal depth
II	Hematoma: subcapsular, 10–50% surface area; intraparenchymal, <5 cm in diameter
	Laceration: capsular tear, 1–3 cm in parenchymal depth, not involving a trabecular vessel
III	Hematoma: subcapsular, >50% surface area or expanding; ruptured subcapsular or parenchymal hematoma; intraparenchymal hematoma >5 cm or expanding
	Laceration: >3 cm in parenchymal depth or involving trabecular vessels
IV	Laceration: involving segmental or hilar vessels producing major devascularization (>25% of spleen)
V	Hematoma: completely shattered spleen
	Laceration: hilar vascular injury that devascularized spleen

Source: Tinkoff et al. [9]

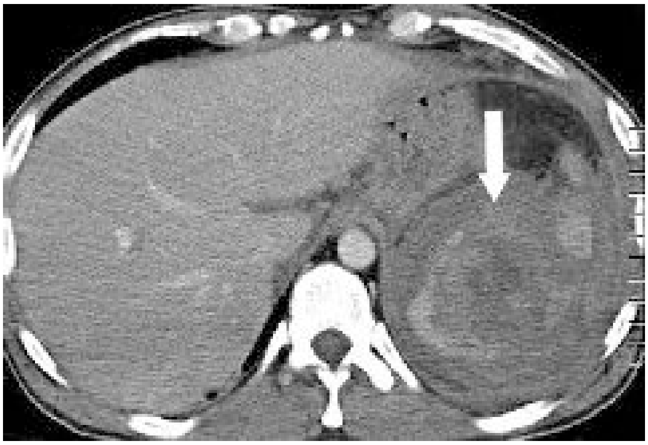

Fig. 9.5 Shattered spleen (Grade 5 injury). Contrast-enhanced CT shows shattered spleen (*arrow*) with perisplenic hematoma

phase) imaging. If a splenic pseudoaneurysm is suspected on early arterial phase imaging, it is helpful to distinguish this finding from ACE by noting the characteristics on delayed imaging. Specifically, on delayed imaging, a pseudoaneurysm will remain the same size and demonstrate similar density to the aorta, but ACE will increase in size and remain with high density. Splenic vascular lesions can be managed successfully by splenic arteriographic embolization, which improves the success rate of nonoperative management of blunt splenic injuries from 87 to 94% [14, 15]. Table 9.5 summarizes CT findings of common types of splenic injury.

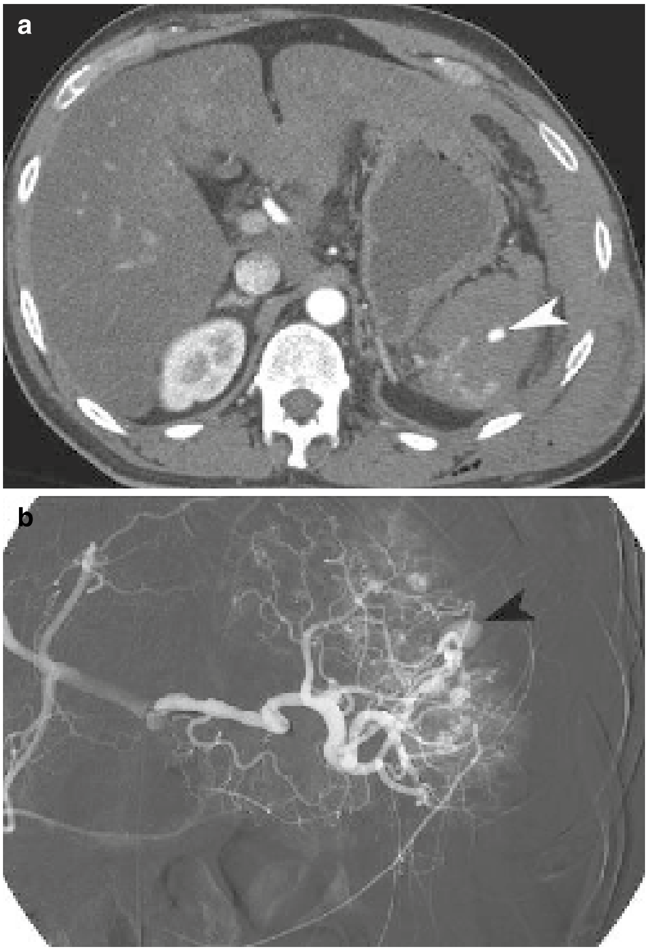

Fig. 9.6 Splenic pseudoaneurysm. (**a**) Contrast-enhanced CT demonstrates a pseudoaneurysm (*arrowhead*) within the splenic parenchymal laceration. (**b**) Conventional splenic artery angiogram demonstrates the splenic arterial branch pseudoaneurysm (*arrowhead*)

Table 9.5 CT findings of common types of splenic injury

Classification	Findings
Hematomas	• Subcapsular or intraparenchymal
Lacerations	• Linear or branching low-attenuation; jagged or sharp margins
Active hemorrhage	• Irregular or linear focus of contrast extravasation in splenic parenchyma, subcapsular space or intraperitoneally
Vascular injuries	• Posttraumatic pseudoaneurysms: well-circumscribed focus of increased attenuation in comparison to the enhancing splenic parenchyma • AV fistulas: early splenic vein enhancement

Pancreas

Pancreatic injuries have been reported as high as 12% in victims of blunt trauma and 6% in those with penetrating trauma. Typically, pancreatic injuries are associated with other intra-abdominal injuries 50–98% of the time [13]. The clinical diagnosis of pancreatic injury may be difficult, particularly when isolated. Owing to the retroperitoneal location of the pancreas, peritonitis from a pancreatic injury may take hours to days to manifest. In addition, serum and urinary amylase levels are unreliable markers for the diagnosis of pancreatic injury [16].

CECT is the modality of choice for diagnosing pancreatic injury; its reported sensitivity and specificity are as high as 85% [17]. CECT findings of pancreatic injury may be subtle, and the pancreas may appear normal immediately post-injury. Of primary importance is evaluation of the pancreatic duct because its integrity or lack of integrity directs management.

A pancreatic injury can be categorized as contusion, laceration, or transection. A pancreatic contusion may appear as diffuse enlargement of the pancreas or as focal low attenuation or heterogeneity. Pancreatic lacerations are demonstrated by linear, irregular low-attenuation areas within the normally enhancing parenchyma (Fig. 9.7). A pancreatic transection may be difficult to diagnose with CT unless there is low-attenuation fluid collection separating the two edges of the transected pancreas. Table 9.6 summarizes CT findings of common types of pancreatic injury.

The position of the pancreatic laceration in relation to the superior mesenteric artery as well as the depth of the laceration helps predict pancreatic ductal disruption, which occurs in up to 15% of pancreatic trauma [13, 17]. The superior mesenteric vessels provide a landmark for dividing the pancreas into proximal and distal portions with injury to the proximal pancreas usually associated with more severe injury. A laceration of the pancreas involving >50% of the anteroposterior diameter of the pancreatic body or tail is often associated with ductal disruption.

There are several nonspecific CT findings associated with pancreatic trauma, the most common of which is thickening or infiltration of the anterior pararenal fascia. Additional nonspecific CT findings include blood/fluid tracking along the mesenteric vessels, fluid in the lesser sac, fluid between the pancreas and splenic vein, or infiltration of the peripancreatic fat with fluid or hemorrhage [13].

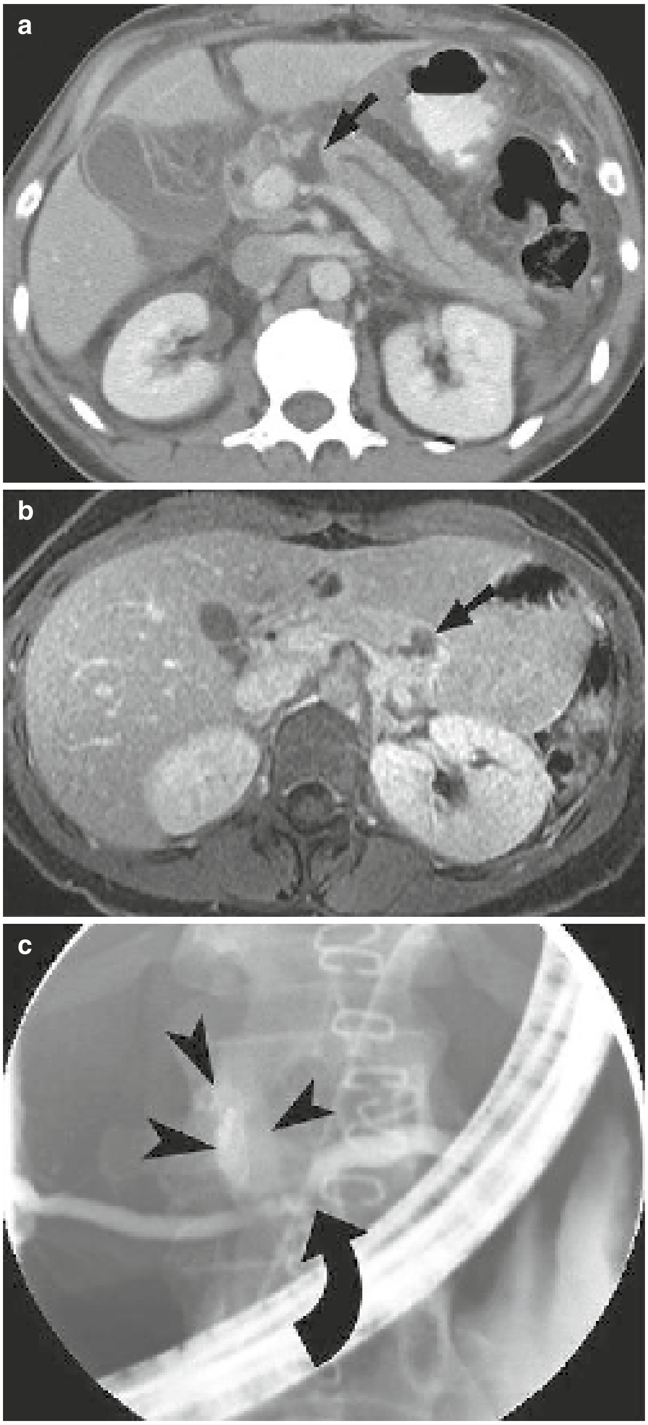

Fig. 9.7 Pancreatic injury. (**a**, **b**) Contrast-enhanced CT in two patients demonstrates pancreatic laceration (*arrow*) with disruption of the main pancreatic duct. (**c**) Endoscopic retrograde cholangiopancreatography image showing pancreatic duct discontinuity (*curved arrow*) and extravasation of contrast from the ductal disruption (*arrowheads*)

Table 9.6 CT findings of common types of pancreatic injury

Classification	Findings
Contusion	• Diffuse enlargement of the pancreas, focal low attenuation or heterogeneity
Lacerations	• Linear, irregular low-attenuation areas within the normally enhancing parenchyma
Transection	• Low-attenuation fluid collection separating the two edges of the transected pancreas

Kidney

The kidney is the most commonly injured urogenital organ in trauma. Approximately 10% of all significant blunt abdominal traumatic injuries include a renal injury, and of those, 80–90% are managed nonoperatively. The goal of conservative management is to preserve organ integrity and reduce the complication rate. Historical evidence shows that hemodynamically stable patients with kidney injuries who undergo surgical exploration have a much higher incidence of nephrectomy [4]. Blunt trauma accounts for approximately 90% of renal trauma, while penetrating trauma accounts for approximately 10%. Nonsurgical management is more commonly advocated in blunt renal injuries, but conservative protocols have also been applied to penetrating renal injuries [18, 19]. However, penetrating trauma is more frequently associated with major renal injury and frequently requires invasive treatment, as it is more often associated with hemodynamic instability and damage to surrounding abdominal organs [20]. Indications for renal imaging include gross hematuria and penetrating or blunt trauma with hematuria. The imaging modality of choice to evaluate the kidneys after trauma is CECT.

Renal injuries may be classified as lacerations, contusions, or renovascular injuries, which determine the radiological grade of the injury per AAST criteria (Table 9.7). Renal contusions are visualized as poorly marginated, round or ovoid areas of low-attenuation and show a delayed or persistent nephrogram when compared to normal adjacent renal parenchyma. Hematomas can be categorized as subcapsular or perinephric. On an unenhanced CT, a subcapsular hematoma (Fig. 9.8) is seen as an eccentric hyperattenuating fluid collection confined between the renal parenchyma and renal capsule. However, on a CECT, a subcapsular hematoma will be hypoattenuating compared to the normal enhancing renal parenchyma. A subcapsular hematoma may also exert a mass effect on the renal contour and can cause decreased perfusion in extreme cases. A perinephric hematoma is a poorly marginated, hyperattenuating fluid collection (45–90 HU) that is confined between the renal parenchyma and the Gerota's fascia [21]. Other findings associated with a perinephric hematoma are thickening of the lateroconal fascia, compression of the colon, and displacement of the kidney.

Renal lacerations are visualized as hypoattenuating, irregular wedge-shaped, or linear parenchymal defects or clefts (Figs. 9.9 and 9.10). The most severe form of renal laceration, termed a "shattered kidney," represents a kidney that is fractured into multiple fragments. It is often associated with devitalized renal tissue, injuries to the collecting system, severe hemorrhage, active arterial bleeding, and compromise in the excretion of contrast material [21]. Table 9.8 summarizes CT findings of common types of renal injury.

Table 9.7 AAST organ injury scale for kidney

Grade	Description
I	Hematoma: subcapsular, nonexpanding without parenchymal laceration
	Contusion: microscopic or gross hematuria, urologic studies normal
II	Hematoma: nonexpanding perirenal hematoma confirmed to renal retroperitoneum
	Laceration: <1 cm parenchymal depth of renal cortex without urinary extravasation
III	Laceration: >1 cm in parenchymal depth of renal cortex without collecting system rupture or urinary extravagation
IV	Laceration: parenchymal laceration extending through renal cortex, medulla, and collecting system
	Vascular: main renal artery or vein injury with contained hemorrhage
V	Hematoma: completely shattered kidney
	Vascular: avulsion of renal hilum that devascularized kidney

Source: Tinkoff et al. [9]

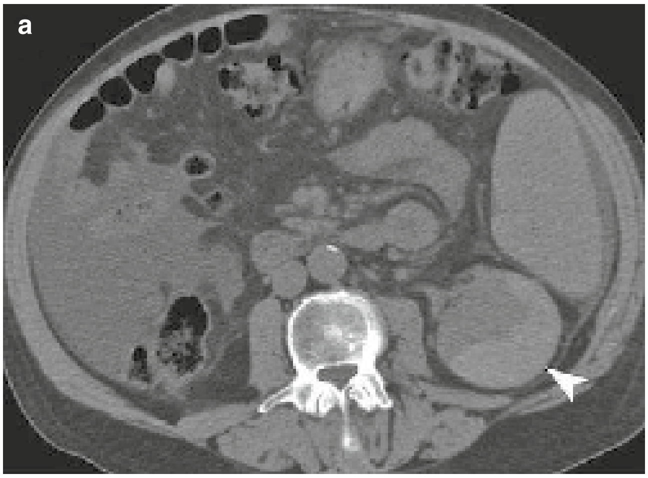

Fig. 9.8 Page kidney. (**a**, **b**) Axial and coronal contrast-enhanced CT images demonstrate subcapsular hematoma (*arrowhead*) compressing the left renal cortex

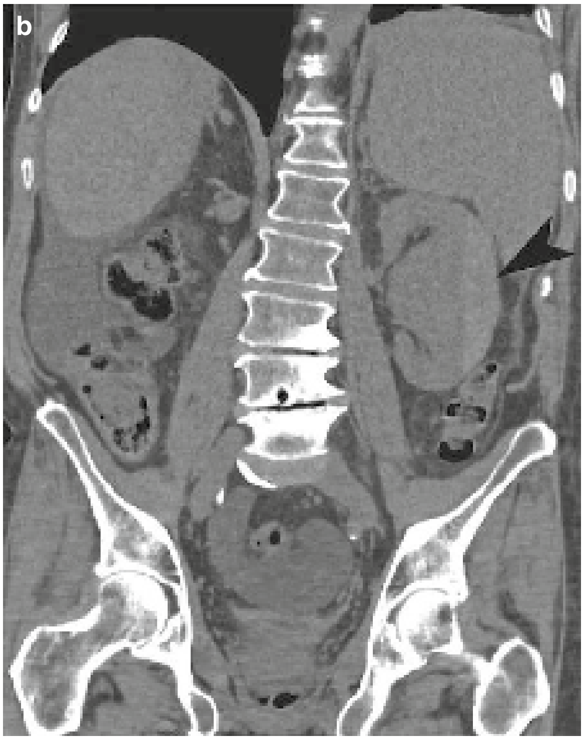

Fig. 9.8 (continued)

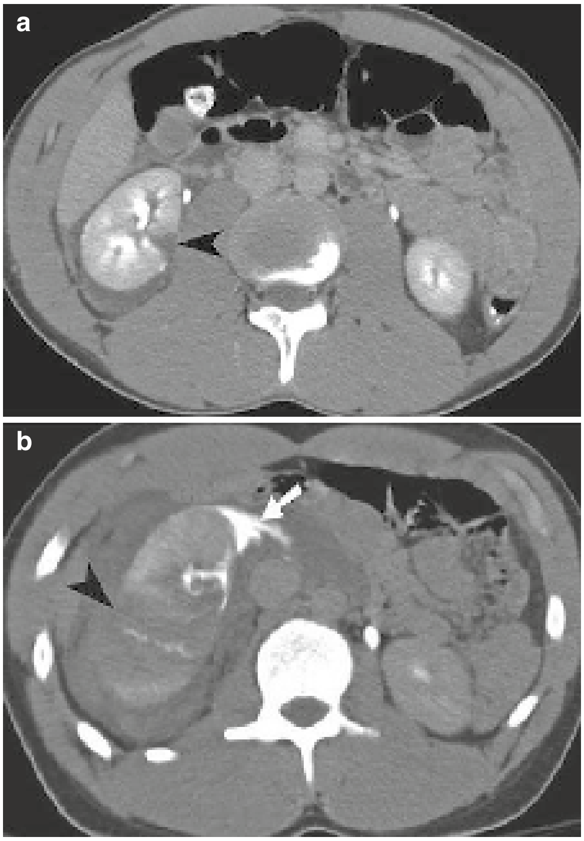

Fig. 9.9 Renal laceration. (**a**) Axial contrast-enhanced CT demonstrating a grade II laceration (*arrowhead*) with small perinephric hematoma. (**b**) Axial contrast-enhanced CT demonstrates grade V shattered kidney (*arrowhead*) and extravasation of urine (*white arrow*) into the perinephric space

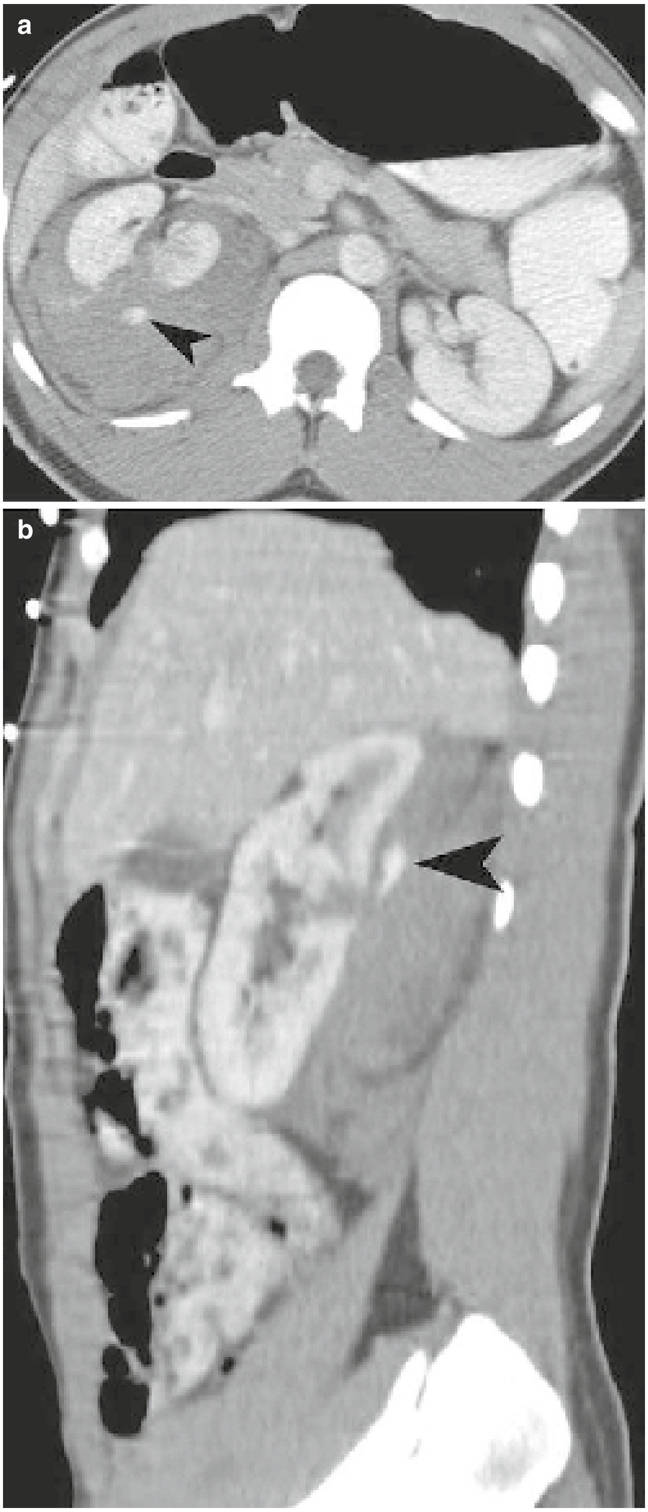

Fig. 9.10 Renal injury, CECT. (**a**, **b**) Axial and sagittal contrast-enhanced CT demonstrate right renal laceration with extravasation of contrast (*arrowheads*) into a perinephric hematoma

The depth of a renal laceration is important as it relates to the renal collecting system. If a laceration extends into the collecting system, this is consistent with a higher-grade injury (IV or V instead of III). Renal pelvis or collecting system

Table 9.8 CT findings of common types of renal injury

Classification	Findings
Lacerations	• Poorly marginated, round or ovoid areas of low-attenuation
	• Delayed or persistent nephrogram
	• The most severe form: shattered kidney
Contusion	• Subcapsular on unenhanced CT: eccentric hyperattenuating fluid collection confined between the renal parenchyma and renal capsule
	• Subcapsular on CECT: hypoattenuating compared to the normal enhancing renal parenchyma
	• Perinephric: poorly marginated, hyperattenuating fluid collection that is confined between the renal parenchyma and the Gerota's fascia
Renovascular injuries	• Renal artery or vein injury with contained hemorrhage or avulsion of renal hilum that devascularized kidney

involvement can be demonstrated by urine extravasation, which is seen as a perinephric low-density fluid collection on arterial or portal venous phase imaging. Suspected urine extravasation can be differentiated from hematoma by the presence of contrast extravasation, which is only seen on the delayed renal excretory phase images.

Urinary Bladder

Bladder injuries are caused by blunt or penetrating trauma. Blunt trauma accounts for 60–85% of bladder injuries, whereas penetrating trauma accounts for 15–40% [22]. The conventional mechanism of injury to the bladder in blunt abdominal trauma is rapid increase of the intravesical pressure resulting in a tear along the intraperitoneal portion of the bladder wall. Bladder injury is more common among those sustaining a seatbelt or steering wheel injury.

Bladder rupture should be suspected when a patient presents with gross hematuria, pelvic fluid, and/or pelvic fractures. Certain types of pelvic fractures are associated with bladder rupture; these include sacral, iliac, and pubic rami fractures as well as pubic symphysis diastasis and sacroiliac joint diastasis [23]. In patients with pelvic fractures, bladder injury occurs in approximately 10%; however, traumatic extraperitoneal ruptures of the bladder are predominantly associated with pelvic fractures [24]. CT cystography or conventional fluoroscopic cystography should be performed following CT of the abdomen and pelvis in hemodynamically stable trauma patients with:

1. Gross hematuria or
2. Pelvic fracture (other than an isolated acetabular fracture) plus microhematuria (>25 RBC/HPC) or
3. Microhematuria and pelvic fluid

CT cystography has a similar sensitivity and specificity to conventional fluoroscopic cystography and provides a more complete and more sensitive evaluation of the urinary bladder than a conventional abdominal and pelvic CT [25].

On abdominal CT, findings suggestive of urinary bladder injury or rupture include the presence of free fluid in the pelvis with no obvious source, urinary contrast extravasation, bladder wall discontinuity, and the presence of any foreign body within the bladder wall (Figs. 9.11, 9.12 and 9.13). On CT cystography, extraperitoneal injuries can be distinguished from intraperitoneal injuries by the location of the extravasation in relation to the peritoneal reflection. An extraperitoneal injury is below the peritoneal reflection and will demonstrate contrast extravasation in the classic "flame-shaped" or "molar tooth" configuration as the contrast penetrates into the paravesical tissues. In the case of intraperitoneal bladder injuries, the perforation is above the peritoneal reflection and extravasated contrast will outline bowel loops. Injuries to the neck of the bladder will show extravasation near the base of the bladder. The pattern of contrast extravasation on cystography is of foremost impor-

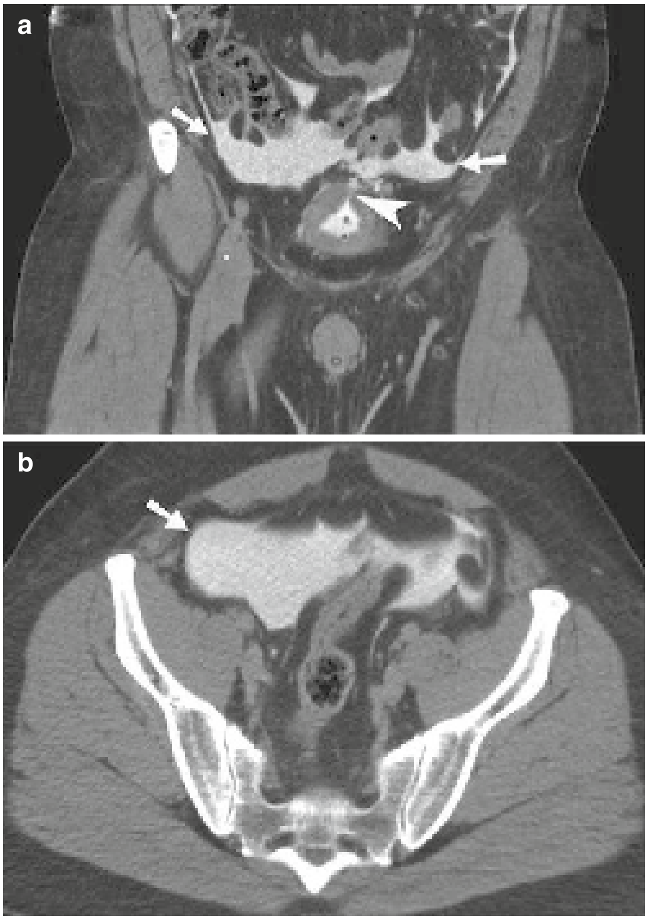

Fig. 9.11 Intraperitoneal bladder rupture. (**a**, **b**) Coronal CT cystogram image demonstrating large amount of intraperitoneal contrast (*arrows*) leaking from the dome of the urinary bladder (*arrowhead*) and outlining the small bowel loops

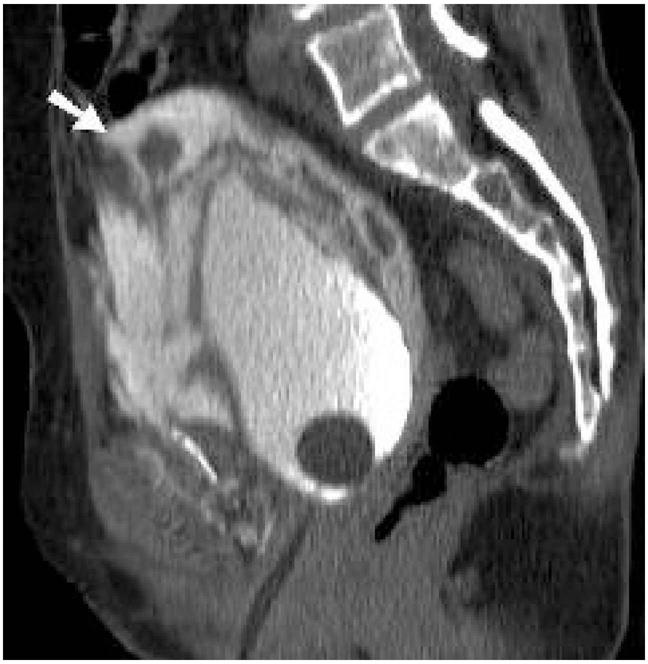

Fig. 9.12 Intraperitoneal rupture of the urinary bladder. Sagittal CT cystogram image demonstrating intraperitoneal contrast (*arrow*) and outlining the pelvis and bowel loops

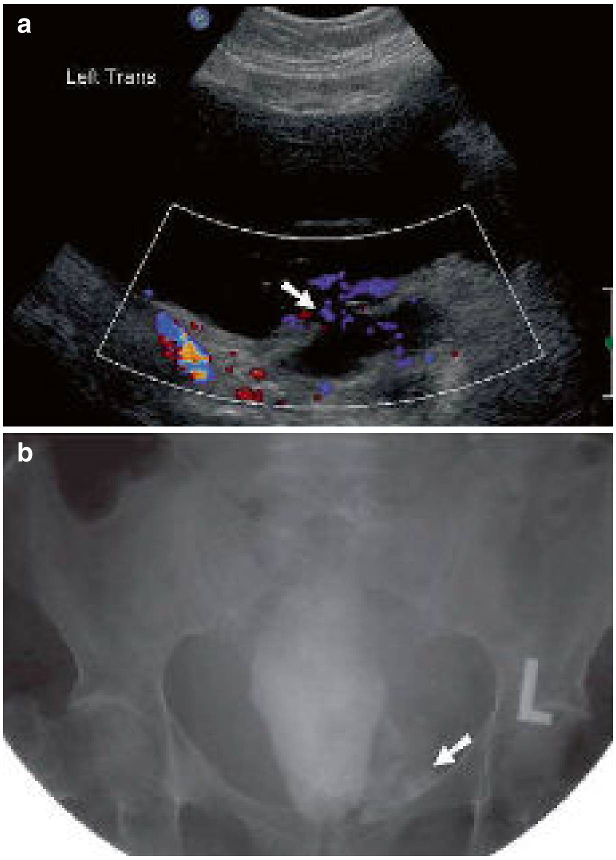

Fig. 9.13 Urinary bladder rupture. (**a**) Ultrasound image of the pelvis demonstrating direct transperitoneal communication (*arrow*) between urinary bladder and a large pelvic urinoma. (**b**) Cystogram study depicts extravasation of contrast from the urinary bladder into the extraperitoneal space (*arrow*). (**c**) CT cystogram demonstrating Foley catheter bulb (*arrow*) located outside the urinary bladder in a large pelvic hemorrhagic fluid collection

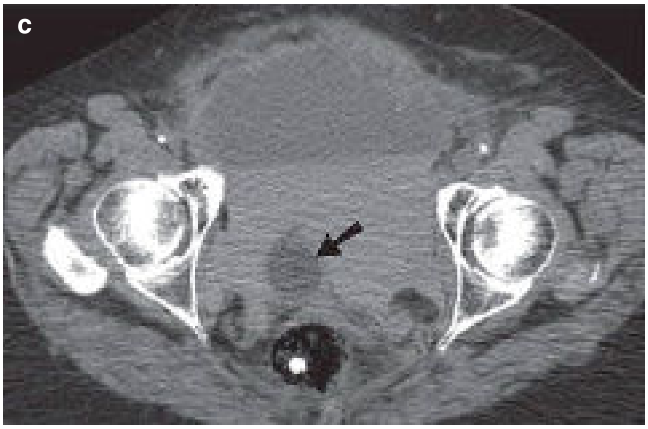

Fig. 9.13 (continued)

Table 9.9 CT findings of urinary bladder injury

Modality	Findings
Abdominal CT	• Presence of free fluid in the pelvis
	• Urinary contrast extravasation
	• Bladder wall discontinuity
	• Presence of any foreign body within the bladder wall
CT cystography	• Extraperitoneal injury: below the peritoneal reflection; "flame-shaped" or "molar tooth" configuration
	• Intraperitoneal injury: the perforation is above the peritoneal reflection; extravasated contrast may outline bowel loops

tance and will guide management of the patient. Table 9.9 summarizes CT findings of urinary bladder injury.

Urethra

Injuries to the urethra are most often caused by a displaced anterior arch pelvic fracture or iatrogenic manipulation [26]. Approximately 10–25% of patients with a pelvic fracture also have urethral trauma. Urethral injury is most often diagnosed with a retrograde urethrogram (RUG), which should be performed prior to insertion of a urethral catheter to avoid further injury. The ultimate goal of an RUG following trauma is to evaluate the integrity of the urethra and to determine if the urethra is "watertight." Contrast leakage from the urethral lumen during an RUG is diagnostic for urethral injury (Fig. 9.14). An RUG can also demonstrate strictures, which can be long-term sequelae of urethral injury.

Urethral injuries are divided into two categories based on the anatomical site of the injury. Posterior urethral injuries are located in the membranous and prostatic urethra. Anterior urethral injuries are located distal to the membranous urethra. Typically, both posterior and anterior urethral injuries are the result of blunt trauma. Penetrating trauma, which includes gunshot and stab wounds, most often affects the penile urethra (Fig. 9.15).

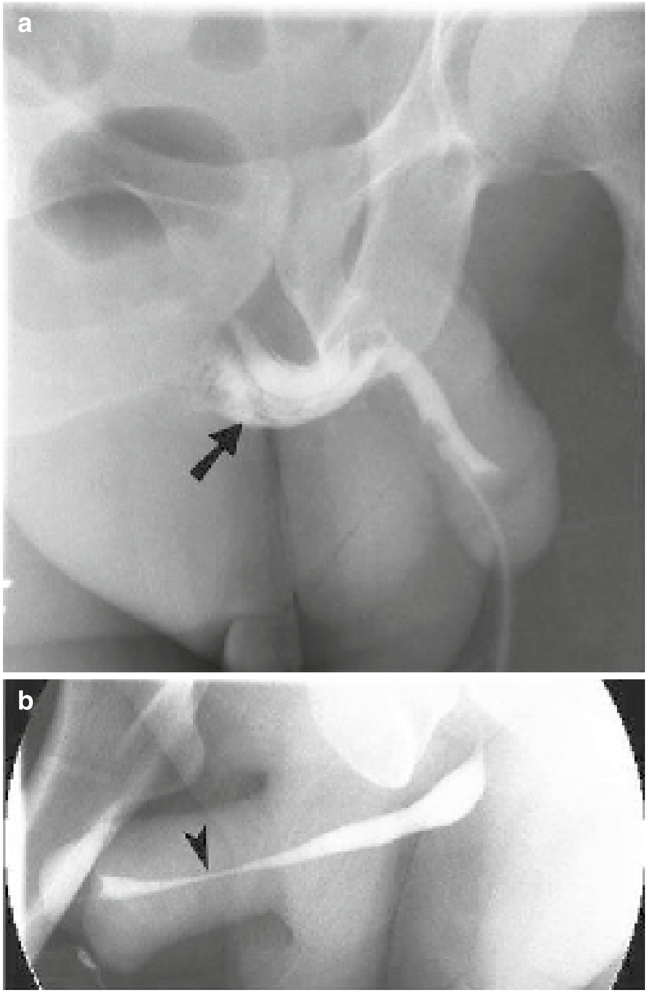

Fig. 9.14 Urethral injuries by RUG. (**a**) RUG demonstrating leakage of contrast (*arrow*) from the bulbous urethra. (**b**) RUG demonstrating urethral narrowing (*arrowhead*) due to extrinsic compression from a penile shaft hematoma. There is no disruption of the urethra in this patient

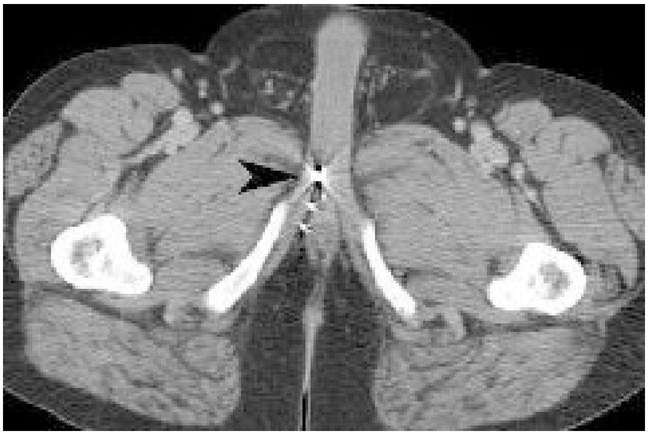

Fig. 9.15 Urethral injury from shotgun pellets. Contrast-enhanced CT demonstrates multiple metallic foreign bodies (*arrowheads*) in the corpora cavernosa and spongiosum of the penis

Table 9.10 Goldman's classification for urethral injuries

Grade	Description
I	Posterior urethra intact but stretched and elongated. Prostate and bladder apex displaced superiorly
II	Urethra disrupted above urogenital diaphragm in prostatic segment. Membranous urethra intact
III	Membranous urethra disrupted. Extension of injury to the proximal bulbous urethra and/or disruption of urogenital diaphragm
IV	Bladder neck injury with extension into the proximal urethra
IVA	Injury at the base of the bladder with periurethral extravasation simulating a type IV urethral injury
V	Partial or complete pure anterior urethral injury

Source: Ali et al. [27]

Table 9.11 AAST organ injury scale for urethra

Grade	Injury type	Description
I	Contusion	Blood at urethral meatus, urethrography normal
II	Stretch injury	Elongation of urethra without extravasation on urethrography
III	Partial disruption	Extravasation of urethrography contrast at injury site. Contrast visualized in bladder
IV	Complete disruption	Extravasation of urethrography contrast at injury site without contrast in bladder <2 cm of urethral separation
V	Complete disruption	Complete transection with >2 cm of urethral separation or extension into the prostate or vagina

Source: Ingram et al. [28]

Radiologists employ two different classification systems for grading urethral injuries. The Goldman's classification (Table 9.10) is most commonly used by urologists and includes urethral injuries as well as bladder injuries that simulate posterior urethral injury. The second classification system is the AAST Organ Injury Scale for urethral injuries (Table 9.11). Imaging of the urethra with an RUG is the reference standard for urethral injury; however, with the widespread use of CT, it is vital to be familiar with CT findings indicative of urethral injury. These findings include indistinct urogenital diaphragmatic fat plane, indistinct prostatic contour, hematoma of the ischiocavernosus and obturator internus muscles, and obscuration of the bulbocavernosus muscle [27–29].

Bowel and Mesentery

Unidentified bowel and mesenteric injuries carry significant morbidity and mortality secondary to complications arising from peritonitis. Injuries to the bowel and mesentery occur in approximately 5% of patients sustaining blunt abdominal trauma and 30% in patients sustaining penetrating trauma to the abdomen [2, 6, 13]. Similar to pancreatic injury, the initial physical examination on a patient with mesenteric injury may be misleadingly normal. Classic peritoneal signs may be present in only one-third of patients [30].

Injury to the bowel and mesentery is most often diagnosed with CECT. However, there is no single CT sign that is considered both sensitive and specific for bowel or mesenteric injury. CT findings suggestive of a mesenteric injury include contrast extravasation into the mesentery, vascular beading/abrupt termination, focal mesenteric hematoma or infiltration, bowel wall thickening, or abnormal enhancement with mesenteric hematoma (Fig. 9.16). The signs of bowel wall injury include bowel wall thickening (most sensitive but not specific), pneumoperitoneum, bowel wall defect, and contrast extravasation. In the presence of bowel perforation, CT findings may include extraluminal air or oral contrast (if administered), or moderate to large volumes of free intraperitoneal fluid without an obvious source such as solid organ injury (Fig. 9.17) [5].

Shock bowel or diffuse small bowel ischemia (Figs. 9.18 and 9.19) can occur when a patient becomes severely hypoten-

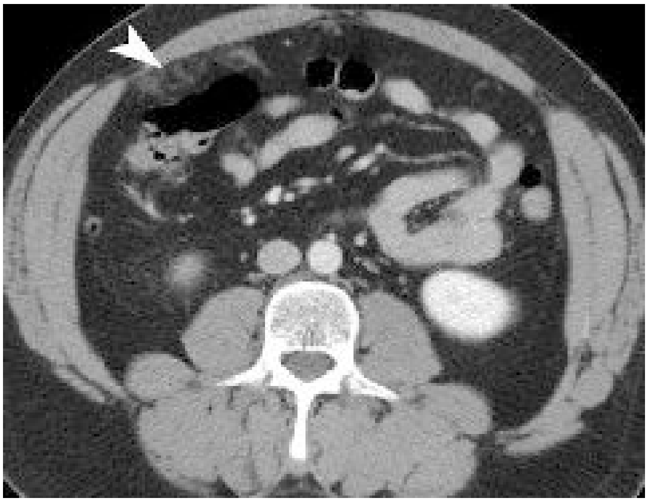

Fig. 9.16 Omental contusion. Contrast-enhanced CT demonstrates fat stranding in omental fat (*arrowhead*) due to traumatic omental contusion

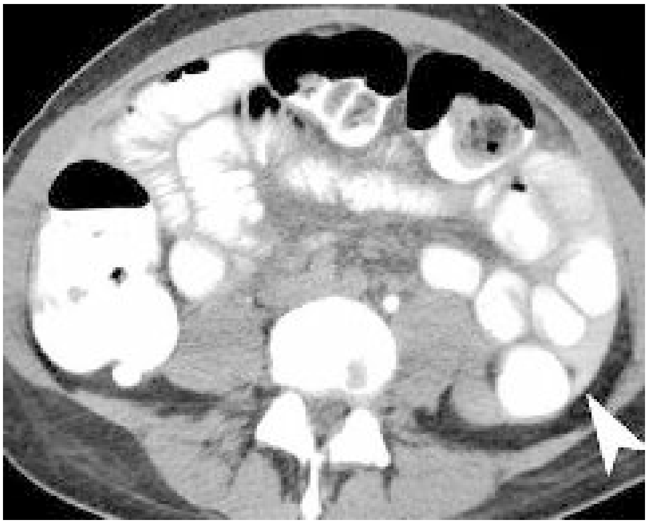

Fig. 9.17 Small bowel perforation. Contrast-enhanced CT shows extravasation of oral contrast (*arrowhead*) secondary to small bowel perforation caused by trocar during laparoscopic surgery

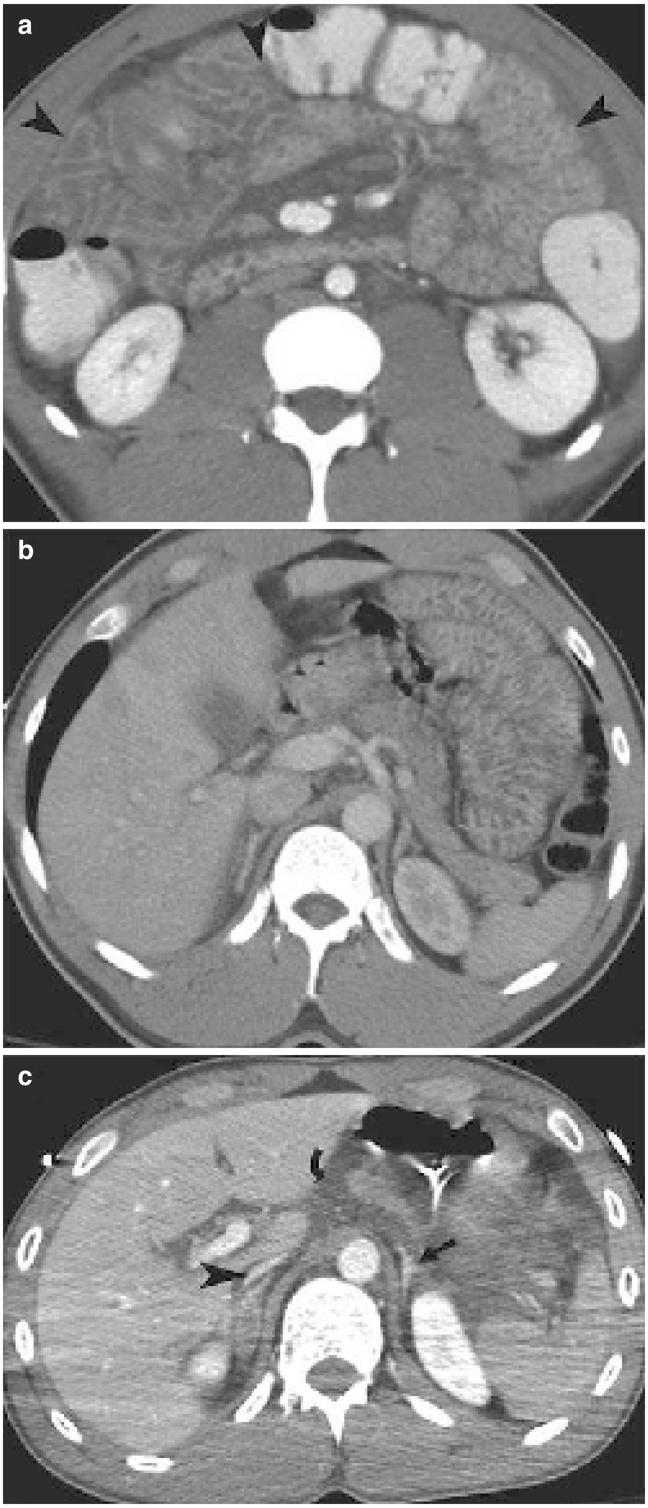

Fig. 9.18 Shock bowel syndrome. (**a**, **b**) Contrast-enhanced CT shows hyperenhancing small bowel walls (*arrowheads*) in a patient with hypovolemia after motor vehicle accident. (**c**) Contrast-enhanced CT shows hyperenhancing adrenal gland (*straight arrow*), flattened IVC (*arrowhead*), and peripancreatic fluid (*curved arrow*)

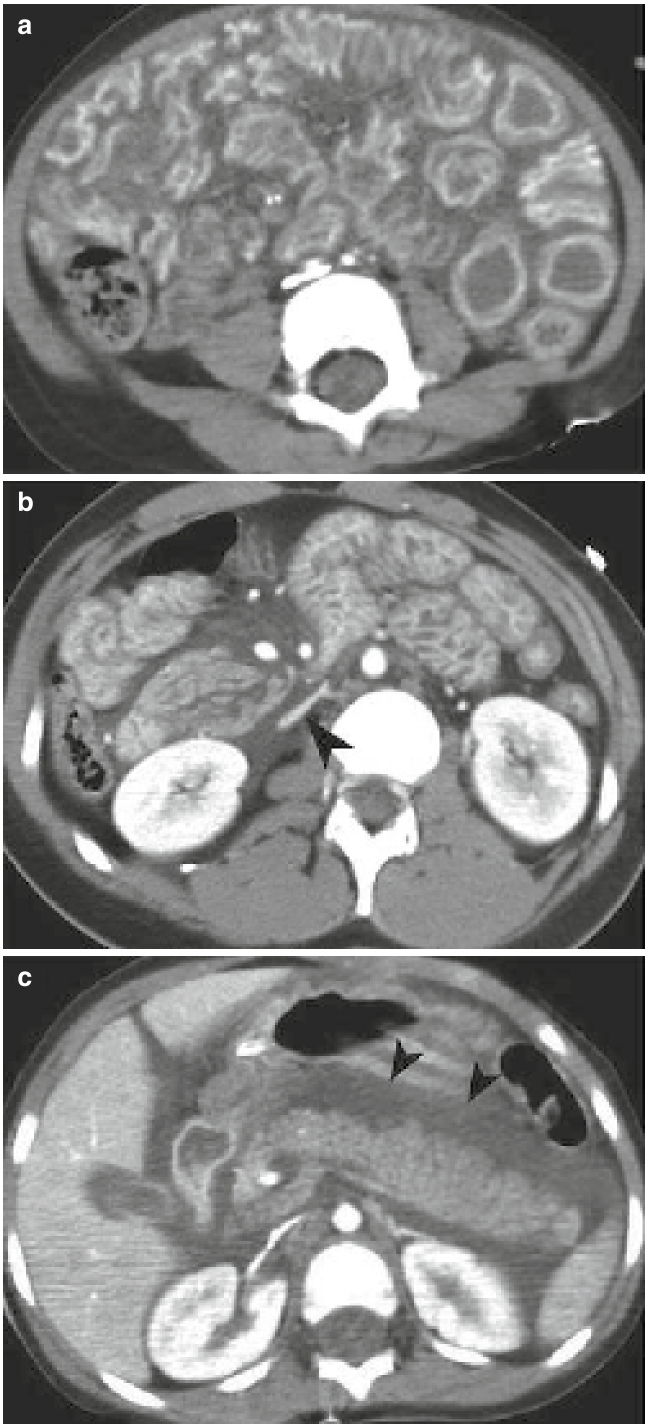

Fig. 9.19 Shock bowel syndrome. (**a**, **b**) Contrast-enhanced CT shows hyperenhancing small bowel walls and ascites. The IVC (*arrowhead*) is flattened secondary to hypovolemia. (**c**) Contrast-enhanced CT shows peripancreatic fluid (*arrowheads*) and flattened IVC

Table 9.12 CT findings of bowel and mesenteric surgery

Diagnosis	Findings
Mesenteric injury	• Contrast extravasation in the mesentery
	• Vascular beading/abrupt termination
	• Focal mesenteric hematoma or infiltration
	• Bowel wall thickening
	• Abnormal enhancement with mesenteric hematoma
	• Extraluminal air or oral contrast
	• Free intraperitoneal fluid
Shock bowel syndrome	• Diffuse thickening of the small bowel wall (7–15 mm)
	• Fluid-filled dilated small bowel
	• Increased contrast enhancement of the small bowel wall
	• Flattened vena cava

sive following hemorrhage. Shock develops from decreased circulating blood volume, which is often complicated by derangement of circulatory control and release of vasoconstrictors such as angiotensin II, adrenaline, and noradrenaline. The blood supply to the intestinal mucosa is drastically reduced during marked sympathetic stimulation and is diverted to other crucial organs such as the brain and heart. The resulting splanchnic vasoconstriction leads to intestinal hypoperfusion and, in advanced cases, intestinal ischemia. Mesenteric arterial vasoconstriction and venous constriction of the bowel wall develop after release of angiotensin II, adrenaline, and noradrenaline. The resultant decrease in both arterial perfusion and venous outflow contributes to the enhancement of the bowel mucosa in shock bowel [31]. Bowel hypoperfusion most profoundly affects the intestinal mucosa, which can lead to "third space" fluid loss into the gastrointestinal tract. CT characteristics of shock bowel are diffuse thickening of the small bowel wall (7–15 mm), fluid-filled dilated small bowel, increased contrast enhancement of the small bowel wall, and flattened vena cava. The large bowel will often appear normal in the setting of small bowel ischemia. Table 9.12 summarizes CT findings of bowel and mesenteric injury.

In addition to the aforementioned effects of the hypoperfusion complex on the bowel and mesentery, shock adrenal glands play a role in the increased sympathetic stimulation and demonstrate symmetric hyperenhancement on CT. Hypoperfusion results in the release of angiotensin II which stimulates the adrenal cortex of the adrenal glands to produce aldosterone and the adrenal medulla to produce adrenaline and noradrenaline.

Gunshot Injuries

Firearm injuries are a major public health concern in United States causing over 30,000 deaths and 67,000 non-fatal injuries each year. The most important factors determining the severity of injury include the site of entry wound and the projectile path. The most vulnerable areas include the brain and the torso. The three major types of firearms include shotguns, handguns, and rifles, and all differ in their ballistic projectiles which determine their wounding capacity. Rifles cause high-velocity injuries and handguns cause low-velocity injuries. Following impact, the more the energy dissipated within the tissue (depending upon the missile speed, missile design, and the target tissue characteristics), the more severe the wound. The wounds produced can be nonpenetrating, penetrating, or perforating.

Mechanism of injury: As the bullet comes in contact with the tissue, it transfers its kinetic energy causing crushing and laceration of the tissue at the site of contact, creating a permanent cavity of approximately the same size as bullet's caliber. High kinetic energy of the projectile also causes the tissue surrounding the bullet's wound tract to stretch radially, creating a transient secondary cavity. Inelastic or friable tissues such as liver are more prone to the effects of secondary cavity (Fig. 9.20) as compared to highly elastic tissues like lungs and bowel. The bullet characteristics such as deformation, tumbling (loss of directional stability), and fragmentation also determine the extent of tissue destruction. Full metal jacketed bullets have a tendency to stay intact, minimizing the area of damage. Semi-jacketed bullets deform into mushroom shape, increasing its surface area of contact, and therefore, increasing the size of the primary cavity as well. Some bullets can fragment on entering the body or striking the bone, with each fragment of bullet or bone, respectively, having its own projectile, causing larger area of tissue destruction. Shotgun fires multiple pellets which cause devastating soft tissue destruction from a close-range firing but multiple, superficial, low-velocity injuries from a long range.

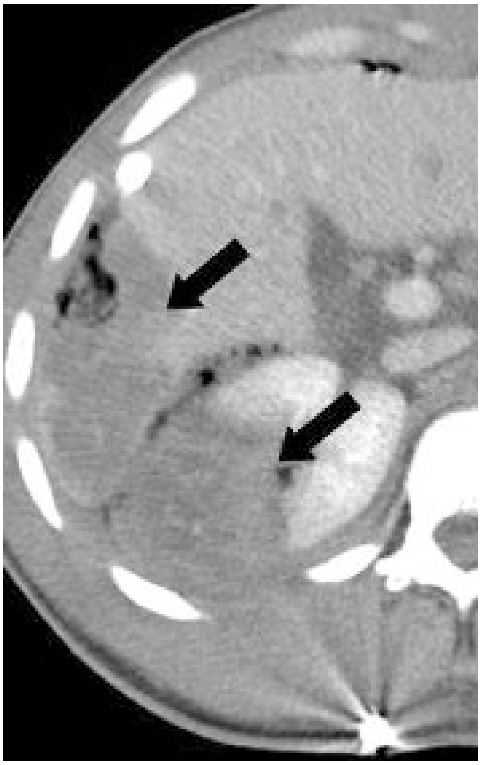

Fig. 9.20 Liver laceration from gunshot injury. Axial contrast-enhanced CT scan study of the upper abdomen demonstrates linear laceration in the liver and kidney due to high-velocity bullet injury. Note that the caliber of the laceration is several-fold bigger than the caliber of the bullet

Role of imaging: Imaging is crucial for evaluation of gunshot wounds. Plain radiography is the initial imaging modality utilized followed by CT scanning. MRI is not utilized frequently in acute settings due to longer imaging times and safety concerns in the presence of ferromagnetic fragments. Imaging is valuable for:

- Identification of entry wounds, exit wounds, and retained bullets, the sum of which should be an even number.
- Identification of the projectile tract (linear orientation of hemorrhage, gas, metal, or bone fragments).
- Identification of bullet type, ballistic debris, and bullet characteristics including deformation and fragmentation.
- Identification and evaluation of ballistic fractures.
- Evaluation of visceral injuries and active hemorrhage.

Teaching Points

- MDCT with IV contrast is not appropriate for hemodynamically unstable patients with blunt abdominal trauma.
- MDCT with IV contrast is the imaging modality of choice for hemodynamically stable patients with blunt abdominal trauma.
- Findings suggestive of mesenteric injury include ACE into the mesentery, focal mesenteric hematoma or infiltration, bowel wall thickening, or abnormal enhancement with mesenteric hematoma.
- RUG is the study of choice for the diagnosis of urethral injury.
- CT cystography or conventional cystography should be performed following abdomen/pelvis CT if bladder injury is suspected.
- Bowel perforation may show extraluminal air or oral contrast, or moderate to large volume of intraperitoneal free fluid without an obvious source.
- Shock bowel appears as diffuse thickening of the small bowel wall (7–15 mm), fluid-filled dilated small bowel, increased contrast enhancement of the small bowel wall, and flattened vena cava.

Questions

1. Which of the following is most likely to be associated with peritoneal fluid on FAST?
   (A) Injury to head of pancreas
   (B) Ovulation
   (C) Injury to middle third of rectum
   (D) Ascending colon injury
   Answer: B

2. Subcapsular hematoma which covers 40% of splenic surface is categorized as which grade based on AAST organ injury scale?
   (A) Grade 1
   (B) Grade 2
   (C) Grade 3
   (D) Grade 4
   Answer: B

3. Based on AAST organ injury scale, what is the grade of renal injury depicted on the CT [Fig. 9.21 (a) portal venous phase, (b) delayed phase]?
   (A) Grade 1
   (B) Grade 2
   (C) Grade 3
   (D) Grade 4
   Answer: C

4. Based on Goldman's classification for urethral injuries, the urethral injury depicted on the retrograde urethrogram (Fig. 9.22) can be classified as which of the following?
   (A) Grade III
   (B) Grade IV
   (C) Grade IV A
   (D) Grade V
   Answer: D

5. The area of increased density on arterial phase imaging [Fig. 9.23 (a) arterial and (b) portal venous] in the spleen most likely represents which of the following?
   (A) Pseudoaneurysm
   (B) Active extravasation of contrast
   (C) Hematoma
   (D) Calcification
   Answer: A

6. What is the pathology depicted on the CT cystogram (Fig. 9.24) in a patient involved in a motor vehicle collision?
   (A) Extraperitoneal bladder rupture
   (B) Arterial contrast extravasation
   (C) Intraperitoneal bladder rupture
   (D) Ureterocele
   Answer: C

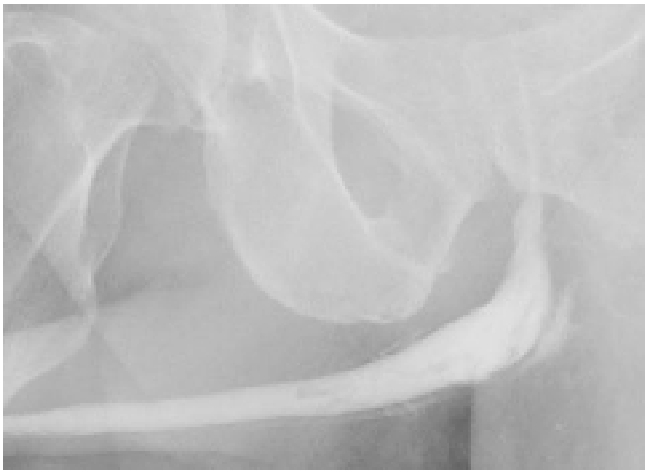

Fig. 9.22 Urethral injury—urethrogram

Fig. 9.21 Renal injury CT (**a**) and (**b**)

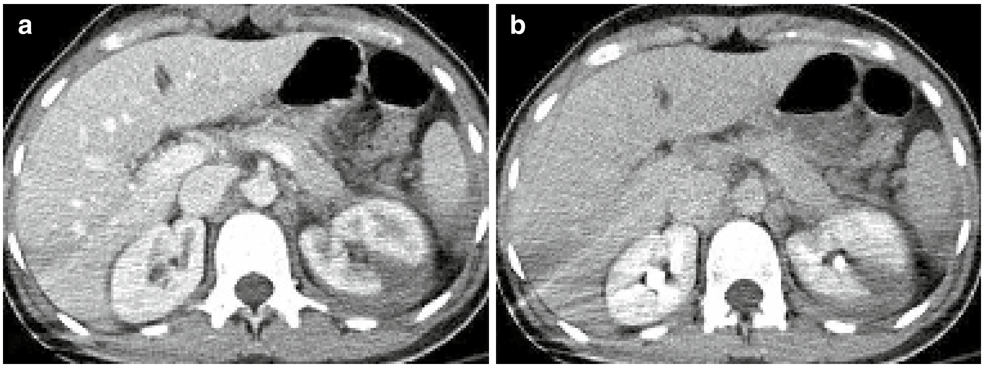

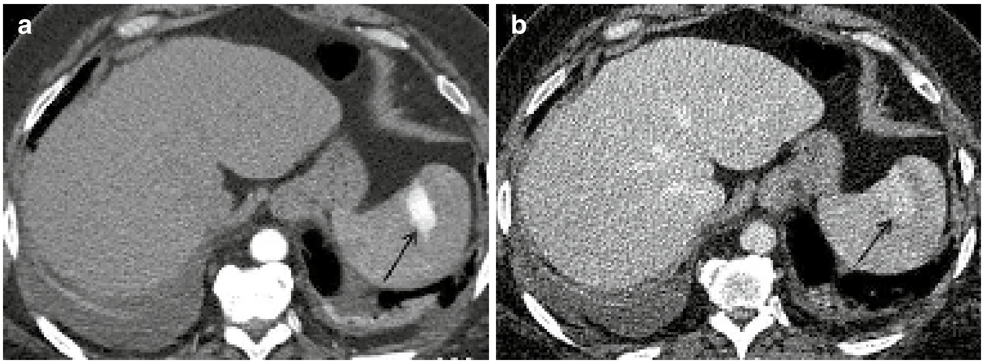

Fig. 9.23 Arterial phase imaging (**a**) and (**b**)

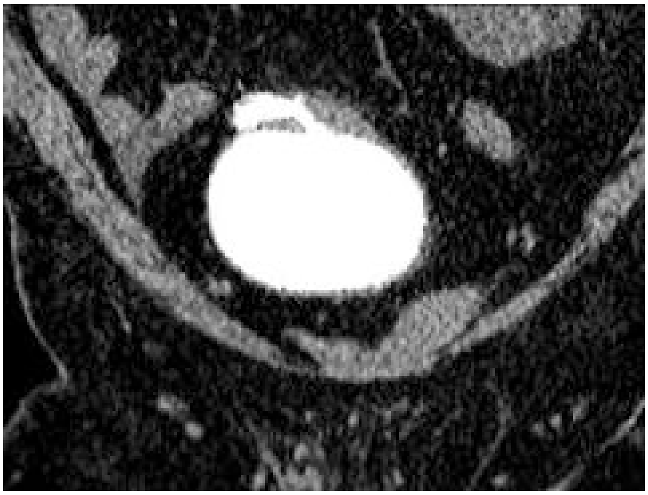

Fig. 9.24 Intraperitoneal bladder rupture—CT cystogram

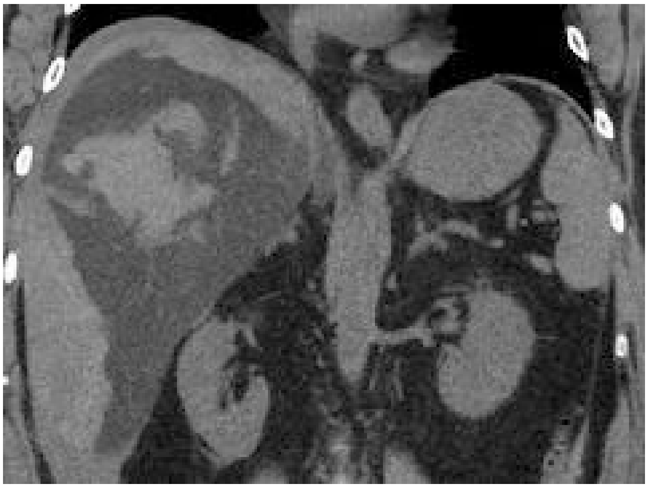

Fig. 9.25 Hepatic intraparenchymal hematoma—organ injury

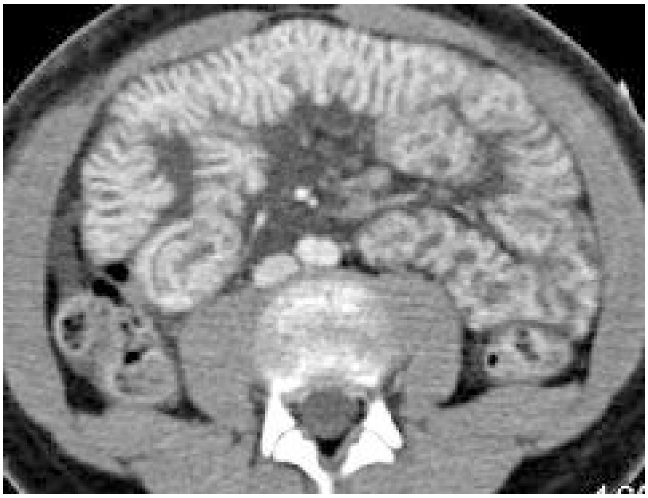

Fig. 9.26 Shock bowel syndrome

7. A hepatic intraparenchymal hematoma measuring 12 cm in width is categorized as which grade of injury according to the AAST organ injury scale (Fig. 9.25)?
   (A) Grade I
   (B) Grade II
   (C) Grade III
   (D) Grade IV
   Answer: C

8. In the acute trauma setting, the appearance of small bowel wall depicted on the CECT (Fig. 9.26) is seen with which of the following?
   (A) Enteritis
   (B) Inflammatory bowel disease
   (C) Bowel perforation
   (D) Shock bowel syndrome
   Answer: D

References

1. Sauaia A, Moore FA, Moore EE, Moser KS, Brennan R, Read RA, et al. Epidemiology of trauma deaths: a reassessment. J Trauma. 1995;38:185–93.
2. Milia DJ, Brasel K. Current use of CT in the evaluation and management of injured patients. Surg Clin N Am. 2011;91:233–48.
3. Melo EL, de Menezes MR, Cerri GG. Abdominal gunshot wounds: multi-detector-row CT findings compared with laparotomy—a prospective study. Emerg Radiol. 2012;19:35–41.
4. van der Vlies CH, Olthof DC, Gaakeer M, Ponsen KJ, van Delden OM, Goslings JC. Changing patterns in diagnostic strategies and the treatment of blunt injury to solid abdominal organs. Int J Emerg Med. 2011;4:47.
5. Butela ST, Federle MP, Chang PJ, Thaete FL, Peterson MS, Dorvault CJ, et al. Performance of CT in detection of bowel injury. AJR Am J Roentgenol. 2001;176:129–35.
6. Feliciano DV, Rozycki GS. The management of penetrating abdominal trauma. Adv Surg. 1995;28:1–39.
7. Matthes G, Stengel D, Seifert J, Rademacher G, Mutze S, Ekkernkamp A. Blunt liver injuries in polytrauma: results from a cohort study with the regular use of whole-body helical computed tomography. World J Surg. 2003;27:1124–30.
8. Yoon W, Jeong YY, Kim JK, Seo JJ, Lim HS, Shin SS, et al. CT in blunt liver trauma. Radiographics. 2005;25:87–104.
9. Tinkoff G, Esposito TJ, Reed J, Kilgo P, Fildes J, Pasquale M, et al. American Association for the Surgery of Trauma Organ Injury Scale: spleen, liver, and kidney, validation based on the national trauma data bank. J Am Coll Surg. 2008;207:646–55.
10. Willmann JK, Roos JE, Platz A, Pfammatter T, Hilfiker PR, Marincek B, et al. Multidetector CT: detection of active hemorrhage in patients with blunt abdominal trauma. AJR Am J Roentgenol. 2002;179:437–44.
11. Poletti PA, Mirvis SE, Shanmuganathan K, Killeen KL, Coldwell D. CT criteria for management of blunt liver trauma: correlation with angiographic and surgical findings. Radiology. 2000;216:418–27.
12. Shanmuganathan K, Mirvis SE. CT scan evaluation of blunt hepatic trauma. Radiol Clin N Am. 1998;36:399–411.
13. Shanmuganathan K. Multi-detector row CT imaging of blunt abdominal trauma. Semin Ultrasound CT MR. 2004;25:180–204.
14. Davis KA, Fabian TC, Croce MA, Gavant ML, Flick PA, Minard G, et al. Improved success in nonoperative management of blunt splenic injuries: embolization of splenic artery pseudoaneurysms. J Trauma. 1998;44:1008–15. discussion 1013–5.
15. Shanmuganathan K, Mirvis SE, Boyd-Kranis R, Takada T, Scalea TM. Nonsurgical management of blunt splenic injury: use of CT criteria to select patients for splenic arteriography and potential endovascular therapy. Radiology. 2000;217:75–82.
16. Craig MH, Talton DS, Hauser CJ, Poole GV. Pancreatic injuries from blunt trauma. Am Surg. 1995;61:125–8.
17. Fisher M, Brasel K. Evolving management of pancreatic injury. Curr Opin Crit Care. 2011;17:613–7.
18. Broghammer JA, Fisher MB, Santucci RA. Conservative management of renal trauma: a review. Urology. 2007;70:623–9.
19. Meng MV, Brandes SB, McAninch JW. Renal trauma: indications and techniques for surgical exploration. World J Urol. 1999;17:71–7.
20. Sica G, Bocchini G, Guida F, Tanga M, Guaglione M, Scaglione M. Multidetector computed tomography in the diagnosis and management of renal trauma. Radiol Med. 2010;115:936–49.
21. Alonso RC, Nacenta SB, Martinez PD, Guerrero AS, Fuentes CG. Kidney in danger: CT findings of blunt and penetrating renal trauma. Radiographics. 2009;29:2033–53.
22. Cass AS, Luxenberg M. Features of 164 bladder ruptures. J Urol. 1987;138:743–5.
23. Morgan DE, Nallamala LK, Kenney PJ, Mayo MS, Rue LW 3rd. CT cystography: radiographic and clinical predictors of bladder rupture. AJR Am J Roentgenol. 2000;174:89–95.
24. Tonkin JB, Tisdale BE, Jordan GH. Assessment and initial management of urologic trauma. Med Clin N Am. 2011;95:245–51.
25. Wirth GJ, Peter R, Poletti PA, Iselin CE. Advances in the management of blunt traumatic bladder rupture: experience with 36 cases. BJU Int. 2010;106:1344–9.
26. Koraitim MM, Marzouk ME, Atta MA, Orabi SS. Risk factors and mechanism of urethral injury in pelvic fractures. Br J Urol. 1996;77:876–80.
27. Ali M, Safriel Y, Sclafani SJ, Schulze R. CT signs of urethral injury. Radiographics. 2003;23:951–63.
28. Ingram MD, Watson SG, Skippage PL, Patel U. Urethral injuries after pelvic trauma: evaluation with urethrography. Radiographics. 2008;28:1631–43.
29. Ramchandani P, Buckler PM. Imaging of genitourinary trauma. AJR Am J Roentgenol. 2009;192:1514–23.
30. Donohue JH, Crass RA, Trunkey DD. The management of duodenal and other small intestinal trauma. World J Surg. 1985;9:904–13.
31. Lubner M, Demertzis J, Lee JY, Appleton CM, Bhalla S, Menias CO. CT evaluation of shock viscera: a pictorial review. Emerg Radiol. 2008;15:1–11.

Acute Nontraumatic Imaging in the Liver and Spleen

10

Dale E. Hansen III, Sridhar Shankar,
Mohammad Mansouri, and Ajay Singh

Introduction

Each year, more than 120 million patients visit the emergency room in the USA. The single most common cause of presentation in the emergency room patient is abdominal pain. Our job as radiologists is to help pinpoint a diagnosis and triage patients in the right direction. The following review covers acute nontraumatic disease processes of the liver and spleen.

Acute Hepatitis

Broadly speaking, acute hepatitis is any acute insult to the liver resulting in the influx of inflammatory cells [1]. The differential diagnosis for hepatitis is long, ranging from an acute viral hepatitis to autoimmune hepatitis [2]. The imaging findings of the various causes of hepatitis are relatively nonspecific, and teasing out a specific diagnosis must often be left to the clinician. The imaging findings in acute viral hepatitis are discussed below, though these findings could be seen in any acute hepatitis.

The "classic" ER case of acute hepatitis is one with right upper quadrant pain, jaundice, and fever [2]. In severe cases of fulminant hepatic failure, patients may present with severe coagulopathy and mental status changes [2]. Morbidity and mortality in severe cases can be as high as 50%. Laboratory evaluation can help determine the diagnosis of hepatitis and possibly a specific cause. The aminotransferases are nearly always elevated, usually significantly so. Viral hepatitis panels help determine if an acute viral infection is the cause. Finally, history is crucial in determining any patient's risk for hepatitis. Historical factors suggesting acute hepatitis include IV drug use, food poisoning, other autoimmune disease, alcoholism, obesity, diabetes, acetaminophen overdose, or radiation.

Imaging

As mentioned earlier, imaging of acute hepatitis is fairly nonspecific. Ultrasound will often demonstrate hepatomegaly with diffuse decreased echogenicity of the hepatic parenchyma [3]. This decreased echogenicity leads to a relative hyperechoic appearance of the portal branches, resulting in the classic "starry sky" appearance (Fig. 10.1a). However, this appearance is nonspecific and can be seen in normal patients, leukemia, lymphoma, and hepatic congestion. There may be associated reactionary gallbladder wall thickening as well. Unfortunately, a normal appearance to the liver does not exclude acute hepatitis [3]. Ultrasonography in alcoholic liver disease demonstrates hepatic steatosis, enlarged, hyperechogenic liver with acoustic attenuation and reduced penetration, and decreased visualization of the portal area, hepatic vein, and diaphragm.

The original version of this chapter was revised. An erratum to this chapter can be found at https://doi.org/10.1007/978-3-319-65397-6_27. An erratum to this publication is available online at https://doi.org/10.1007/978-3-319-65397-6_27.

D. E. Hansen III
Memphis Radiology, Germantown, TN, USA

S. Shankar
Department of Radiology, University of Tennessee, Regional One Health Hospital, Memphis, TN, USA

M. Mansouri
Department of Radiology, Massachusetts General Hospital, Boston, MA, USA

A. Singh (✉)
Division of Emergency Radiology, Department of Radiology, Massachusetts General Hospital, Boston, MA, USA

Harvard Medical School, Massachusetts General Hospital, Boston, MA, USA
e-mail: asingh1@partners.org

© The Author(s), under exclusive license to Springer Nature Switzerland AG 2024
A. Singh (ed.), *Emergency Radiology*, https://doi.org/10.1007/978-3-031-65770-2_10

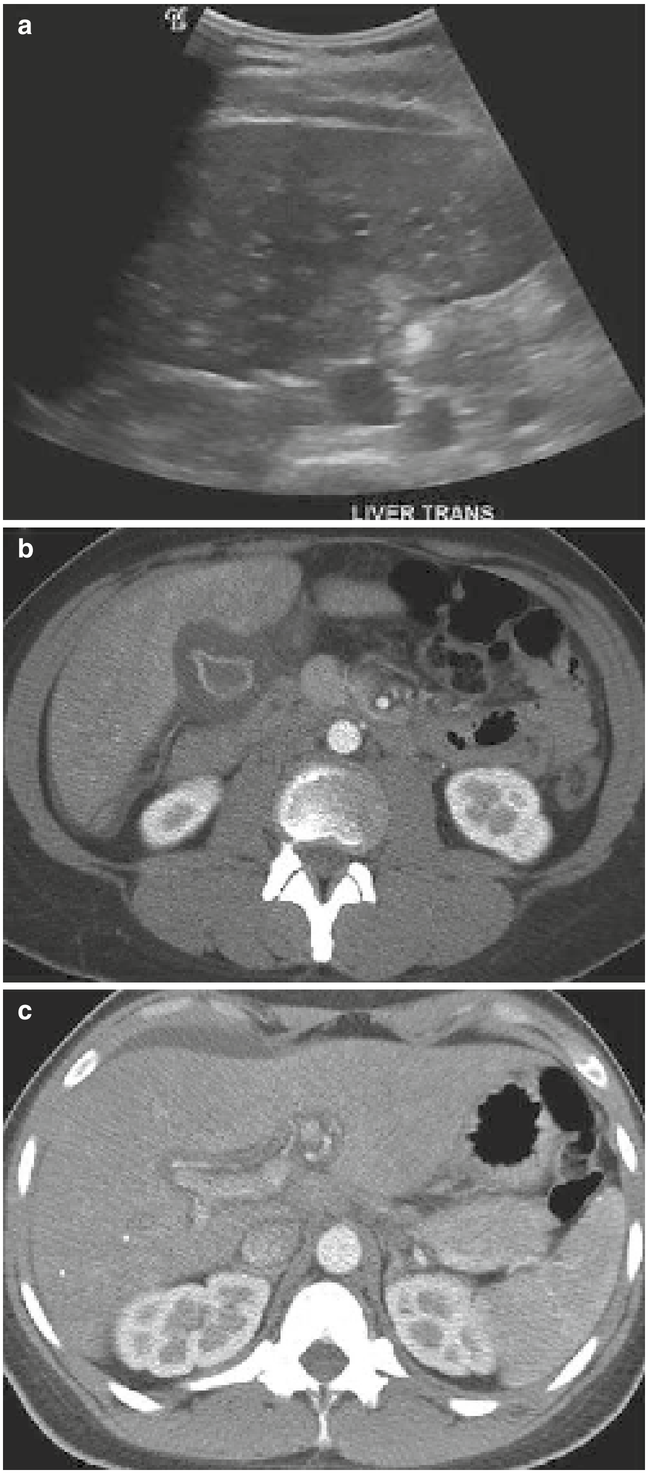

Fig. 10.1 Acute hepatitis C. (**a**) Ultrasound of the liver shows "starry sky" appearance due to decreased parenchymal echogenicity and relative increase in periportal echogenicity. (**b**, **c**) Contrast-enhanced CT demonstrates periportal edema, gallbladder wall edema, and pericholecystic fluid

Contrast-enhanced CT study will often demonstrate a heterogeneous appearing liver [3]. The hypoattenuating regions represent areas of necrosis or periportal edema. The more hyperattenuating regions usually represent focal areas of sparing or, in the more chronic case, areas of nodular regeneration. Other findings include hepatomegaly, periportal edema, gallbladder wall thickening, reactive lymphadenopathy in the porta hepatis, and ascites (see Fig. 10.1b, c). On MRI, T2-weighted images will show hyperintense regions of periportal edema; these same areas will be low intensity on T1 images [3]. Patchy enhancement of the liver parenchyma on arterial phase and gallbladder wall thickening may also be seen in MRI. CT in alcoholic liver disease may demonstrate liver enlargement and decreased attenuation. Normally Hounsfield Unit (HU) of liver should be at least 8 HU greater than spleen HU. In alcoholic liver disease, the HU of liver may be 10 HU less than that of spleen on unenhanced scans or 25 HU less than spleen HU on contrast-enhanced CT. On MRI, signal dropout on out of phase images or fat-suppressed sequences may be seen.

Fulminant hepatitis, the most devastating and life-threatening form, is characterized by a small liver with massive areas of hypoattenuation associated with expansive necrosis [4, 5]. Secondary findings of ascites, splenomegaly, and portal vein dilatation may be noted. Although generally not intended to diagnose hepatitis, HIDA scans in patients with right upper quadrant pain and suspected cholecystitis can be useful in determining the cause of gallbladder wall thickening (Fig. 10.2). Impaired clearance of the blood pool with no excretion of radiotracer into the biliary system suggests marked hepatocellular dysfunction consistent with acute hepatitis.

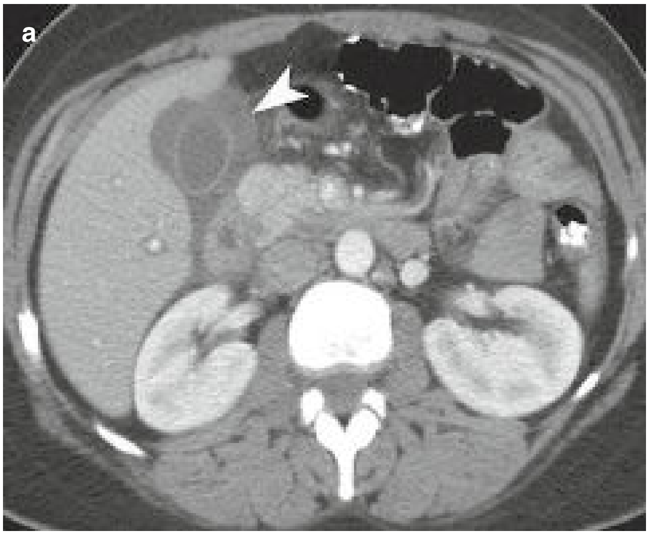

Fig. 10.2 Acute hepatitis B. (**a**) Contrast-enhanced CT demonstrates gallbladder wall edema (*arrowhead*) and pericholecystic fluid. The gallbladder wall, though prominent, is not as thickened as in the previous case. (**b**) HIDA scan showing uptake in the gallbladder (*curved arrow*) and excretion into small bowel loops. The presence of radiotracer into the gallbladder lumen rules out cystic duct

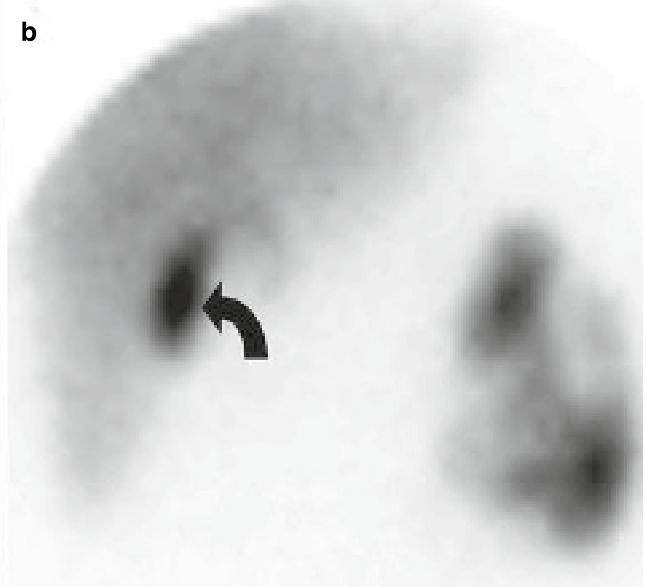

Fig. 10.2 (continued)

Hepatic Abscess

Liver abscesses can be polymicrobial, with *Escherichia coli* being by far the most common pathogen, or they can be due to fungal infection or *Entamoeba histolytica*. Fungal infection of the liver is most commonly seen in the patient with AIDS, hematologic malignancy, or organ transplant [3]. Candida is the most frequent causative organism. Cryptococcus, histoplasmosis, aspergillus, and mucormycosis are less commonly seen. Liver abscesses are most often caused by spread of biliary infection or by hematogenous spread, superinfection of necrotic liver, or iatrogenic causes. Clinical symptoms include right upper quadrant pain, fever, and jaundice. Leukocytosis and increased liver enzymes may also be present. Overall, pyogenic abscesses are a fairly dangerous entity, with an associated 2% mortality rate [3].

Pyogenic abscesses are generally treated by radiologists, with CT-guided drainage being the mainstay of treatment.

Imaging

Pyogenic Abscess

Pyogenic abscesses can further be subdivided into two categories: microabscesses versus macroabscesses, with 2 cm being the cutoff between the two [3]. Ultrasound and CT are the mainstays of imaging.

In the setting of microabscesses, ultrasound will show a small (<2 cm), possibly scattered hypoechoic focus or foci, or heterogeneous echotexture. With macroabscesses, the ultrasound appearance can be quite varied, ranging from hypoechoic to hyperechoic with varying degrees of internal septation and debris. Internal gas, indicated by high-intensity echoes and dirty posterior shadowing, helps seal the diagnosis [3].

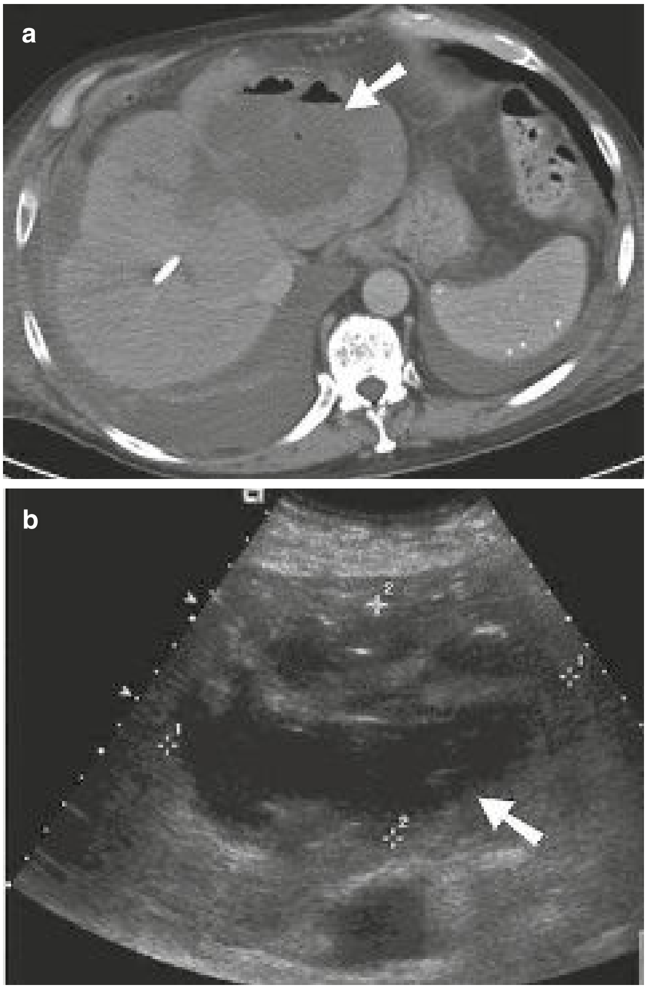

Fig. 10.3 Pyogenic hepatic abscess after liver transplant. (**a**) Contrast-enhanced CT through the liver demonstrates a large, irregular hypodense collection (*arrow*) in the left lobe of liver, containing air. This is virtually diagnostic of an abscess. An internal biliary stent is also seen. (**b**) Gray-scale ultrasound in the same patient showing a complex collection (*arrow*) within the liver. This patient went on to have percutaneous drainage of the abscess under CT guidance

CT, with microabscesses, will demonstrate small, hypoattenuating lesions with faint peripheral enhancement and surrounding edema [3]. The cluster sign depicts multiple small coalescing hypoattenuations. The double target sign includes a low-attenuation central collection surrounded by a hyperattenuation ring and hypoattenuation outer zone. Larger abscesses will also be hypoattenuating, often with irregular margins, rim enhancement, and internal gas (Figs. 10.3, 10.4 and 10.5).

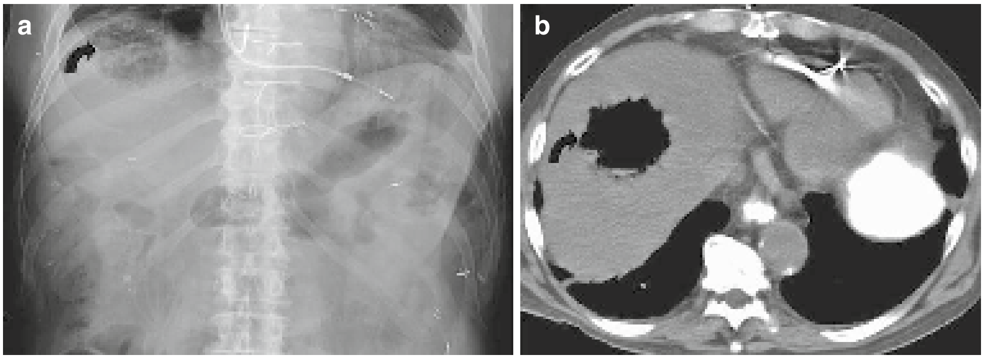

Fig. 10.4 Hepatic abscess. (**a**) Plain film of the upper abdomen demonstrates a round collection of gas in the right upper quadrant (*curved arrow*). This would be an atypical appearance and location of bowel gas. (**b**) Contrast-enhanced CT through the upper abdomen confirms a large collection of air within the liver with some layering debris (*curved arrow*), diagnostic of abscess

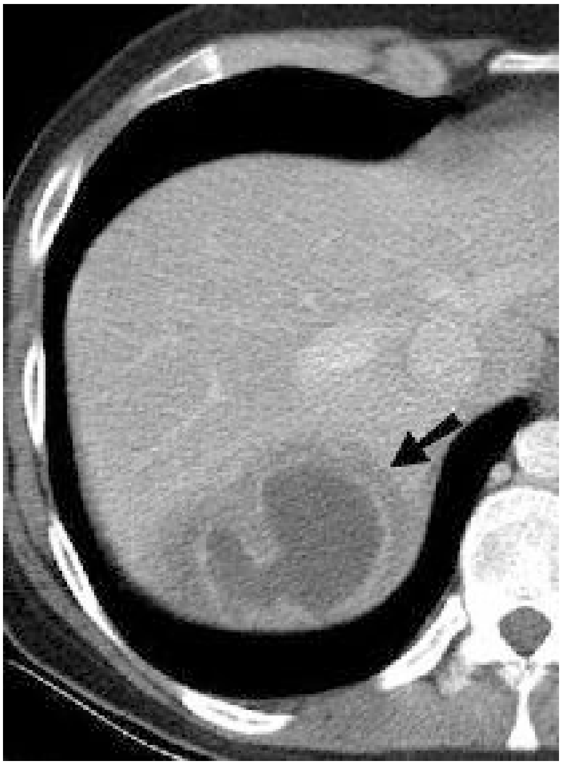

Fig. 10.5 Double target sign in liver abscess. CECT demonstrates a fluid attenuation central abscess surrounded by a hyperattenuation ring and hypoattenuation outer zone of edema (*arrow*)

Fungal Abscess

Fungal abscess occurs in immunosuppressed patients, especially in patients with prolonged neutropenia. Candida is the most common organism. At ultrasound, four appearances of fungal infection have been described:

1. A "wheel within a wheel" appearance featuring a central hypoechoic zone of fungal necrosis surrounded by echogenic inflammatory cells. There may also be a thin hypoechoic rim of fibrosis.
2. A "bull's-eye" appearance with a central echogenic nidus with a surrounding hypoechoic region. This appearance is seen in patients with active infection.
3. Simply a hypoechoic nodule without other distinguishing features. Unfortunately, this is the most common appearance and also the least specific.
4. An echogenic focus with posterior shadowing. This appearance is typically seen during early resolution.

At contrast-enhanced CT, the typical finding is multiple, small (typically less than 1 cm), hypoattenuating lesions throughout the liver. The lesions typically enhance centrally (though less than the surrounding liver) and may occasionally enhance peripherally. MRI will demonstrate multiple small lesions throughout the liver which are extremely T2 hyperintense and mildly hypointense on T1-weighted images (Fig. 10.6). Gadolinium-enhanced T1-weighted images will show hypointense lesions when compared to the surrounding liver.

Amebic Abscess

Amebic abscess is caused by Entamoeba histolytica and is transmitted by the fecal-oral route. Although amebic abscesses may appear very similar to pyogenic abscesses, one helpful clue is the tendency for amebic abscesses to spread beyond the liver. Findings of a right pleural effusion or intraperitoneal rupture suggest the diagnosis of amebic abscess [6].

Amebic abscesses are typically oval abscesses seen near the capsule, generally hypoechoic and homogeneous on ultrasound, with low-level internal echoes and no wall echoes. There may be increased through transmission. Contrast-enhanced CT will show a complex fluid collection with rim enhancement and peripheral edema. Internal septa or fluid-debris levels may be identified [3, 6]. The abscess wall is usually between 3 and 15 mm thick, with contrast enhancement and surrounded by a rim of edema. MRI, if utilized, will generally show

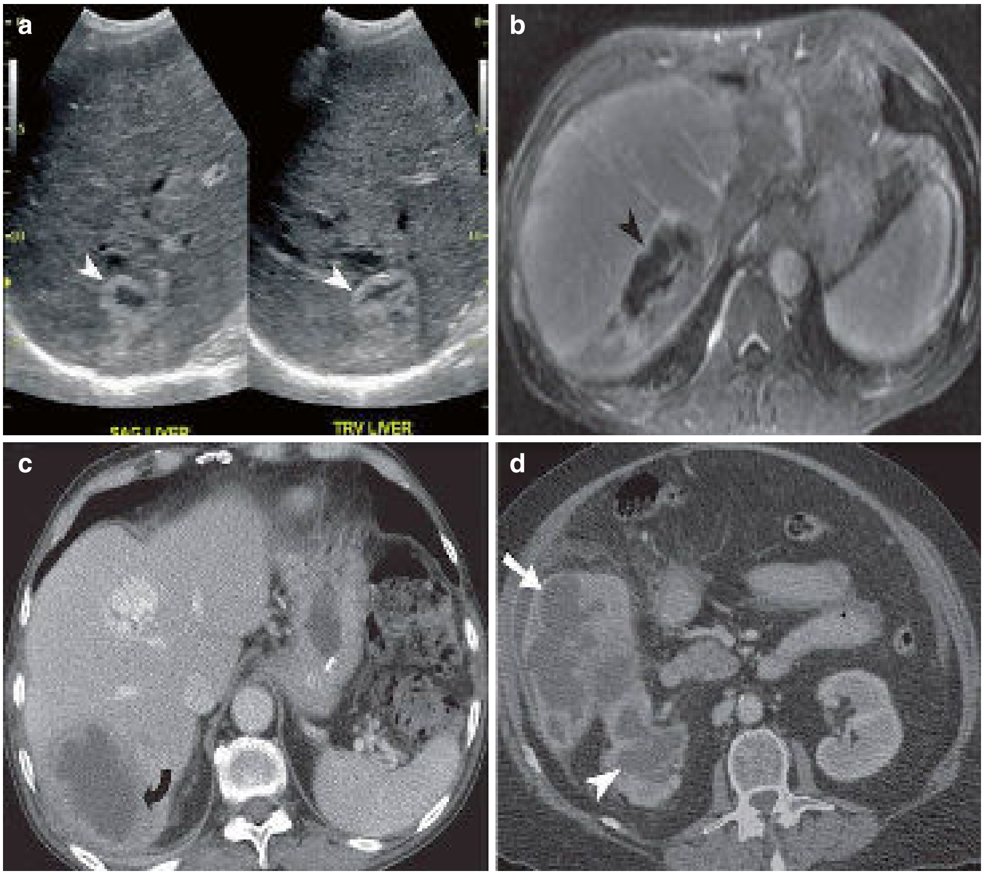

Fig. 10.6 Hepatic abscesses. (**a**) Transverse and sagittal gray-scale ultrasound images of the liver demonstrate a hypoechoic lesion with a hyperechoic rim (*white arrowhead*). (**b**) Gadolinium-enhanced T1-weighted MRI in the same patient shows a necrotic lesion (*black arrowhead*) in the right lobe of the liver with faint peripheral enhancement. This is a case of treated enterococcal abscess. (**c**) Contrast-enhanced CT of the abdomen shows a fluid density lesion with an irregular wall, consistent with abscess (*curved arrow*). Incidentally note is made of a hemangioma, located more anteriorly in the right lobe of liver. (**d**) Contrast-enhanced CT abdomen through the inferior aspect of the liver demonstrates an irregular abscess (*arrow*), communicating with pyonephrosis (*arrowhead*)

a high-intensity T2 lesion with low intensity on T1. Fifty percent will have surrounding edema, best appreciated on the T2 sequence [3].

Hydatid Cyst

Though rarely seen in the USA, hydatid cysts are endemic to the Mediterranean Basin. The disease is spread through ingesting the eggs of *Echinococcus granulosus*, a tapeworm. Dogs act as a reservoir for the spread of disease. Hydatid cysts often go undetected, but patients may present secondary to cyst rupture, mass effect of the cyst, or superimposed infection [2]. Hydatid cyst rupture can be divided into the following categories:

- Contained ruptures: The pericyst remains intact.
- Communicating rupture: Pericyst ruptures and the contents spill into the biliary or bronchial tree.
- Direct rupture occurs when the membranes as well as the pericyst break and the contents spill into the peritoneal, pleural, or pericardial spaces.

Histologically, hydatid cysts consist of three layers. The outer pericyst is composed of compressed liver; the middle ectocyst, a thin membrane; and the inner endocyst, a germinal layer [3].

Imaging

Imaging characteristics of hydatid cysts vary from a cystic lesion to a solid pseudotumor. The classic appearance is the "water lily sign," which is actually wavy bands of delaminated endocyst. Daughter cysts and peripheral calcifications are commonly seen.

On CT, hydatid cysts will generally present as hypoattenuating lesions with a distinguishable wall. Fifty percent will have peripheral wall calcifications, and a daughter cyst can be identified in 75% (Fig. 10.7) [3]. Calcified wall usually represents absence of active infection. In *E. granulosus*, the daughter cysts and curvilinear mural calcification are seen. *E. multilocularis*, which is the more invasive pathogen, multiple small-clustered cystic and solid components are seen along with central calcifications. MRI is excellent for delineating the pericyst, which will be hypointense on both T1- and T2-weighted images secondary to fibrosis and calcification. The hydatid matrix will generally be extremely T2 hyperintense and T1 hypointense. The daughter cyst, if identified, will be T1 and T2 hypointense.

Fitz-Hugh–Curtis Syndrome

Fitz-Hugh–Curtis syndrome is a fairly uncommon sequel of advanced pelvic inflammatory disease in which there is intraperitoneal spread of infection from the pelvis into the right upper quadrant. These patients present with fever, vaginal discharge, cervical motion tenderness, and right upper quadrant pain [2]. The differential diagnosis includes other causes of "perihepatitis" such as perforated cholecystitis, radiation changes, and perforated abscess [7].

Imaging findings include early arterial enhancement of the anterior surface of the liver on contrasted CT with findings of PID in pelvis (pyosalpinx, inflammation) [7, 8]. Enhancement may remain on delayed phase, which represents capsular fibrosis. Ultrasound will typically appear normal [2].

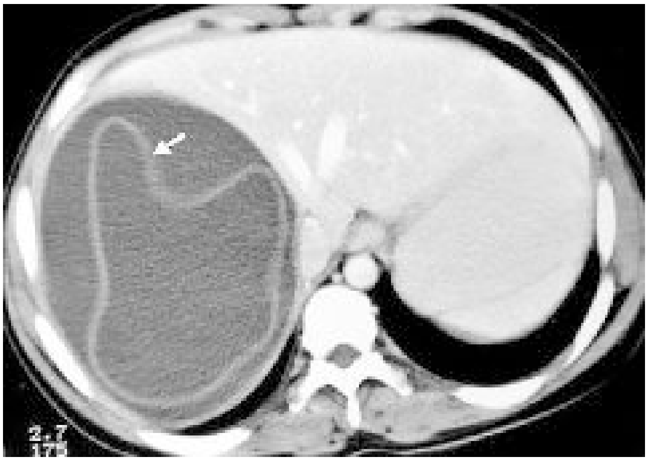

Fig. 10.7 Hydatid cyst. Contrast-enhanced CT of the abdomen demonstrates a large, cystic lesion within the right lobe of the liver. Internally, there is a delaminated endocyst (*arrow*); this is equivalent to the water lily sign described on ultrasound

Hepatic Infarct

Hepatic infarcts are generally rare because of the dual blood supply of the liver [9]. They are generally seen after insult to the hepatic artery or portal vein thrombus in the setting of chronic hepatic arterial insufficiency [10]. However, the one occasion when hepatic infarcts are more common is after liver transplant. In this setting, the hepatic artery plays a larger role in supplying blood to the liver. Any insult to the hepatic artery, without the "backup" of the portal vein, will therefore result in infarction.

The causes of hepatic infarction include trauma, shock, hypercoagulable state, post-TIPS, and posttransplant status. Because the hepatic artery is the sole blood supply to the bile ducts, hepatic arterial occlusion can lead to biliary necrosis with the eventual formation of bile lakes [10, 11].

Imaging

On CT, hepatic infarcts are generally seen as wedge-shaped peripheral areas of hypoattenuation, often paralleling the bile ducts (Fig. 10.8a) [9–11]. These areas may show heterogeneous enhancement, with lack of enhancement in any necrotic regions. Gas may be seen within the infarct, secondary to either necrosis or superinfection. Bile lakes, or bilomas after biliary necrosis, may be seen as irregular, hypoattenuating regions, often in posttransplant patients with hepatic arterial compromise (see Fig. 10.8b). Arterial phase imaging can be used to evaluate the hepatic artery for any insult. Conversely, portal venous phase imaging will help assess for any portal vein thrombus. One etiologic clue is to search for associated splenic infarcts, which would suggest either systemic hypoperfusion (shock) or embolic disease.

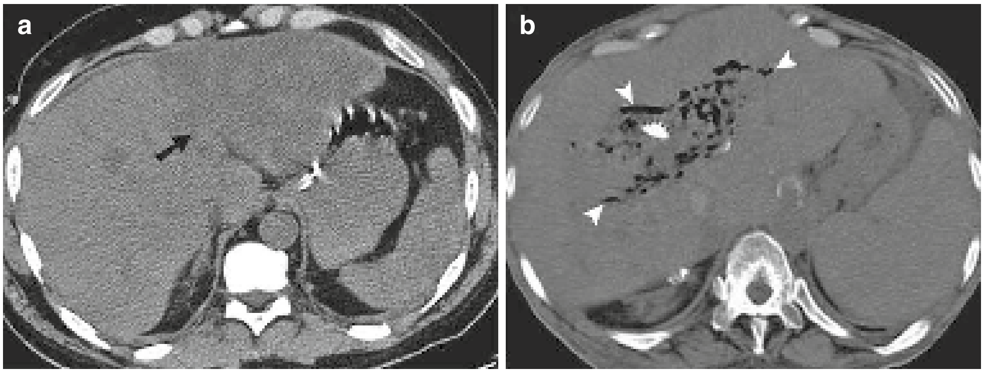

Fig. 10.8 Liver infarct after Whipple procedure and liver transplant. (**a**) Noncontrast CT demonstrates a large, hypoattenuating region occupying the left lobe of the liver, consistent with a large hepatic infarct. *Arrow* denotes a well-delineated transition between normal liver and infarcted liver. (**b**) Noncontrast CT of the transplant liver shows debris within a dilated biliary tree (*arrowheads*). The patient had hepatic arterial thrombosis, resulting in biliary necrosis

Budd–Chiari Syndrome

Budd–Chiari syndrome is caused by occlusion of the hepatic veins or inferior vena cava. This impairs venous outflow, causing hepatic congestion, decreased portal venous flow, and eventual necrosis and atrophy [12]. There are multiple causes of Budd–Chiari, the most common being a hypercoagulable state. Nearly all patients have some degree of abdominal pain, and ascites is nearly always present.

Budd–Chiari syndrome can present with fulminant, acute, subacute, or chronic liver failure. The most common form is the subacute form, in which there has been some time to develop collateral vessels. Rarely, patients can present with fulminant hepatic failure with massive necrosis, ascites, and encephalopathy. Hepatic encephalopathy in fulminant form occurs within 8 weeks after onset of jaundice. The changes consistent with portal hypertension (splenomegaly and varices) may be seen in more subacute to chronic forms. The caudate lobe of the liver is generally spared secondary to separate venous drainage into the IVC. Cirrhosis is a common complication of Budd–Chiari syndrome.

Imaging

Ultrasound, CT, and MRI are all useful in imaging Budd–Chiari syndrome. Color Doppler ultrasound is extremely helpful in detecting diminished or absent venous outflow from the liver as well as in detecting echogenic thrombus with the hepatic veins or IVC. Doppler ultrasonography has the sensitivity of 87% in detecting Budd–Chiari syndrome. The secondary findings of splenomegaly and ascites may be seen as well.

In the acute phase of Budd–Chiari syndrome, unenhanced CT will generally show an enlarged liver with decreased attenuation [10, 12]. The IVC may appear hyperattenuating on noncontrast imaging secondary to the presence of a thrombus [9]. After contrast enhancement, the classic pattern is early arterial enhancement of the caudate lobe and central liver with diffuse peripheral hypoattenuation secondary to necrosis and/or steatosis (Fig. 10.9). On the portal venous phase images, there may be a “flip–flop,” with contrast washout from the central liver and peripheral enhancement due to flow from capsular veins [10]. Hypoattenuating clot may be seen within the hepatic veins or IVC. More chronically, the liver will appear dysmorphic with peripheral atrophy, caudate hypertrophy, and heterogeneous enhancement secondary to fibrosis and nodular regeneration [10, 12]. Secondary findings of portal hypertension including splenomegaly, ascites, and varices may be seen as well.

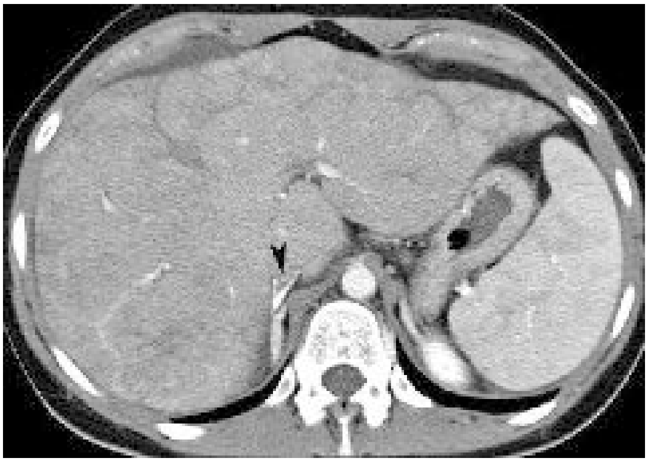

Fig. 10.9 Budd–Chiari syndrome. Contrast-enhanced CT shows areas of hypoattenuating fibrosis and multiple regenerating nodules as well as trace ascites anteriorly. A thrombus (*arrowhead*) can be seen within the inferior vena cava with some contrast passing around the thrombus

On MRI, acute phase imaging will show decreased T1 signal and heterogeneously increased T2 signal at the liver periphery [12]. Chronically, effected portions of the liver will become fibrotic, resulting in hypointensity on both T1- and T2-weighted images.

Treatment includes treatment of underlying disease, anticoagulant therapy, vascular intervention, or transplantation.

Spontaneous Nontraumatic Hepatic Hematoma

Spontaneous hepatic hematoma without trauma is a fairly rare entity, usually seen in the setting of hepatic neoplasm. By far the two most common etiologies are hemorrhage into a hepatic adenoma and hepatocellular carcinoma, though several other less common etiologies include focal nodular hyperplasia, amebic abscess, metastases, and hemangioma [13].

The findings on CT include hyperattenuating hematoma seen within the liver in the acute phase, though in more chronic phases this may become hypoattenuating.

Adenomas are classically related to females taking oral contraceptives (4 cases/10,000 users) [13]. They may also rarely be seen in the setting of diabetes, glycogen storage disease, iron deposition disease, and anabolic steroid use. Eighty percent of adenomas are solitary, and they are nearly always asymptomatic until they rupture [14]. Because adenomas generally have poor connective tissue support, incomplete capsules, and high peripheral vascularity, they are a perfect setup for extensive hemorrhage.

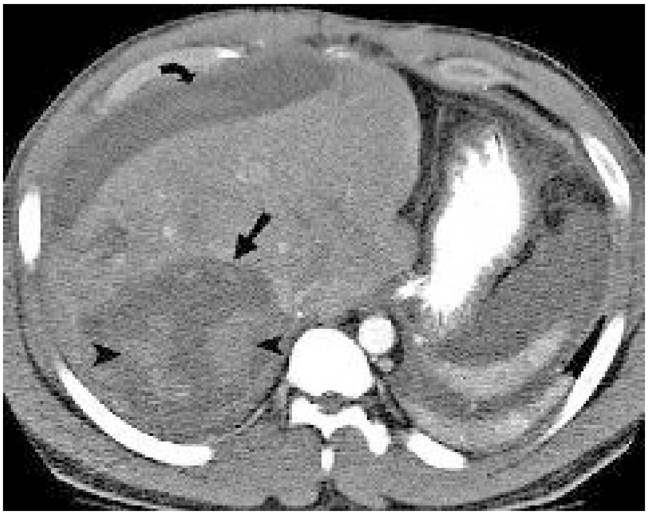

Fig. 10.10 Hemorrhagic adenoma. Contrast-enhanced CT of the abdomen demonstrates areas of mixed attenuation adenoma (*arrow*) within the right lobe of the liver (*arrowheads*), containing hemorrhagic areas (*arrowheads*). There is also subcapsular hematoma (*curved arrow*) anterior to the liver and fluid around the spleen from hemoperitoneum

Unenhanced CT will show a hypoattenuating tumor containing areas of hyperattenuating blood (Fig. 10.10). Subcapsular hematoma and intraperitoneal hematoma may also be visualized. Ten percent of adenomas will contain fat [14]. The appearance on MRI is variable depending on the age of the hematoma.

Treatment of a hemorrhagic adenoma is generally surgical resection of the tumor with a margin of normal liver. Nonhemorrhagic adenomas are generally prophylactically removed if they are larger than 4 cm [14].

Portal Vein Thrombosis

Portal vein thrombosis is most commonly seen in cirrhosis (in 16% of patients), often as a complication of hepatocellular carcinoma. Other entities such as hypercoagulable states, myeloproliferative disease, embolic phenomenon, and infection can also result in portal vein thrombosis [15]. As discussed previously, patients with portal vein thrombosis may also present with a liver infarct if there is superimposed hepatic arterial insufficiency.

Imaging

Ultrasound is perhaps the most commonly used technique for identifying portal vein thrombosis and discriminating the source. Bland thrombus can be distinguished from tumor thrombus because bland thrombus will have no internal flow, whereas tumor thrombus will have internal flow (Fig. 10.11). Secondary findings of cirrhosis, hepatic mass, splenomegaly, and ascites may be seen and help determine the etiology.

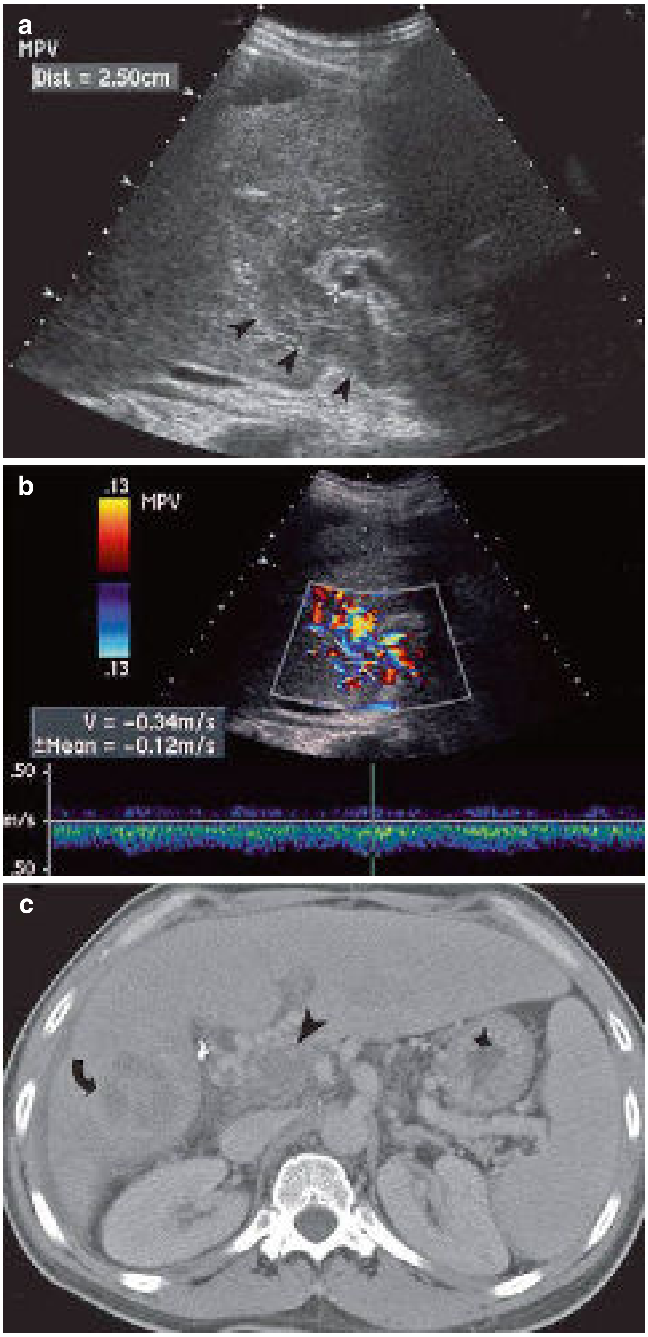

Fig. 10.11 Hepatocellular carcinoma and portal vein thrombus in a patient with hepatitis C. (**a**, **b**) Gray-scale and color Doppler ultrasound of portal vein thrombosis. There is echogenic thrombus within an enlarged portal vein (*arrowheads*). There is arterial flow within the thrombus, consistent with tumor thrombus. (**c**) Contrast-enhanced CT of the same patient shows low-density thrombus within the portal vein (*arrowhead*) as well as a hepatocellular carcinoma in the right lobe of the liver (*curved arrow*)

On unenhanced CT, hyperattenuating thrombus can be seen within the portal vein. After contrast administration, obstruction of contrast flow can be seen in the portal vein on the portal venous images with the thrombus visualized as a filling defect [15]. In acute venous thrombosis there is associated expansion and peripheral enhancement of the vein. In subacute and chronic thrombosis, cavernous transformation of the portal vein is seen which is characterized by tortuous venous collaterals at the portal area that replace the portal vein. If there is any hepatic lesion seen in the setting of cirrhosis and portal vein thrombosis, one should be very careful about calling it anything other than hepatocellular carcinoma.

Acute Liver Failure

Acute liver failure (ALF) is characterized by severe acute liver injury, hepatic encephalopathy (altered mental status, asterixis), and synthetic liver dysfunction with international normalized ratio (INR) >1.5 in a patient without pre-existing liver disease or cirrhosis. Most common etiologies include viral and drug-induced hepatitis. Other etiologies include autoimmune hepatitis, Budd–Chiari syndrome, Wilson's disease, malignant infiltration, and acute fatty liver of pregnancy.

Imaging

CT scan of the abdomen in patients with acute liver failure can demonstrate hepatomegaly, heterogenous hepatic parenchyma, surface nodularity, ascites, venous occlusion, and splenomegaly. Surface nodularity can be observed in about 17% of patients with acute failure, more commonly in patients presenting with symptoms for a longer duration or with massive necrosis.

Splenic Infarct

Though uncommon, splenic infarction is a recognized cause of abdominal pain. Embolic cause from atrial fibrillation is the most common cause of splenic infarct. Other infarcted organs, including the liver, may be seen as well in patients with embolic infarcts of the spleen. Other causes include malignancy and hypercoagulable states [16]. Complications include pseudocyst formation, infection, hemorrhage, and splenic rupture.

Imaging

The imaging modality of choice for imaging splenic infarction is contrast-enhanced CT (Figs. 10.12 and 10.13). The CT

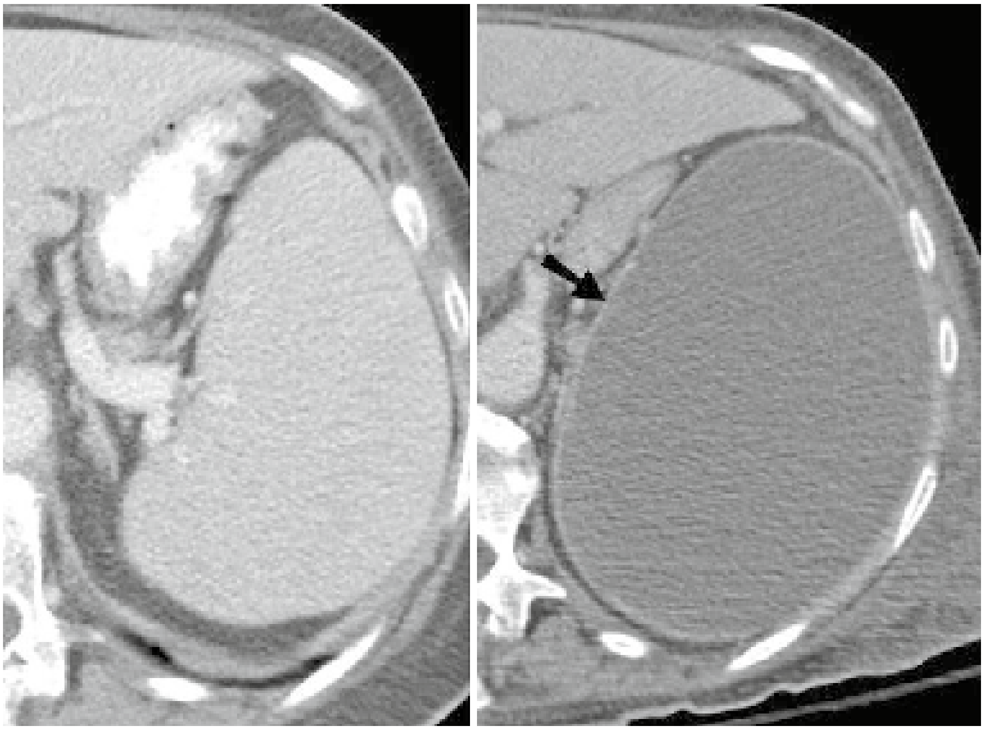

Fig. 10.12 Splenic infarct before and after. *Left-side* image shows a normal spleen. Image on the *right* in the same patient demonstrates diffuse decreased density within the spleen (*arrow*) secondary to infarct of the entire spleen

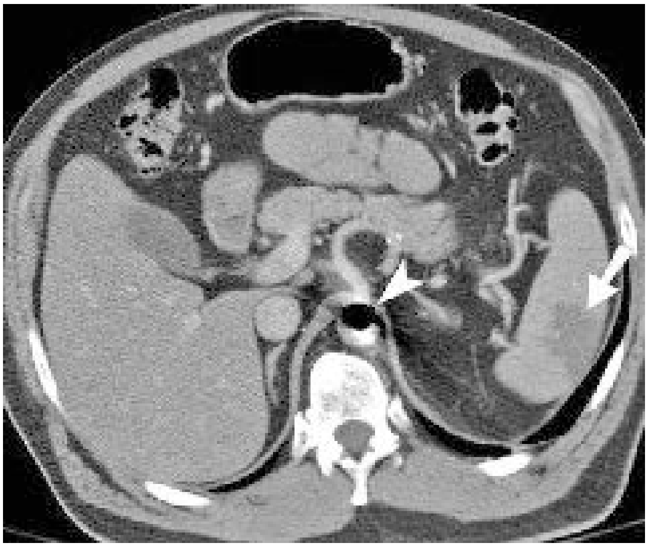

Fig. 10.13 Splenic infarct secondary to intra-aortic balloon pump. Contrast-enhanced CT demonstrates a wedge-shaped hypodense region within the spleen consistent with infarct (*arrow*). Intra-aortic balloon pump (*arrowhead*) is seen in the aorta adjacent to the origin of the celiac trunk

appearance is typically a wedge-shaped, hypoattenuating region within the spleen. Perisplenic fluid, a left-sided pleural effusion, and associated infarcts in other organs are other signs, each present in 30% of cases. Splenic infarct may also mimic other splenic lesions, such as tumors or abscesses. Fine needle biopsy or clinical correlation may be necessary to differentiate these lesions. Care must be taken to differentiate a splenic infarction from early, heterogeneous perfusion of the spleen; more delayed images will help differentiate the two. Ultrasound may show wedge-shaped, hypoechoic regions within the spleen but is not very sensitive [16, 17]. MRI will show a region of low T1 and T2 intensity which does not enhance [18].

Splenic Torsion

Splenic torsion is a very uncommon diagnosis, usually seen in the setting of a wandering spleen. With wandering spleen, the spleen can "wander" outside of its usual position in the left upper quadrant due to laxity of splenic ligaments. Annual incidence is reported to be less than 0.2%. Patients with a wandering spleen can get spontaneous torsion and may present with an acute abdomen secondary to torsion splenic ischemia [19]. Clinical presentation includes abdominal pain, nausea, vomiting, fever, leukocytosis, and palpable mass.

Imaging

On abdominal radiography, the normal splenic outline in the left upper quadrant may be absent and a soft tissue mass in the mid-abdomen may be demonstrated. Like torsion to other organs, splenic torsion is diagnosed when there is evidence of decreased blood flow. Color Doppler ultrasound will show decreased vascular flow to a spleen which may be in an ectopic position. CT may show an ectopic spleen with poor enhancement and decreased attenuation on noncontrasted studies (Fig. 10.14). Treatment usually includes splenectomy.

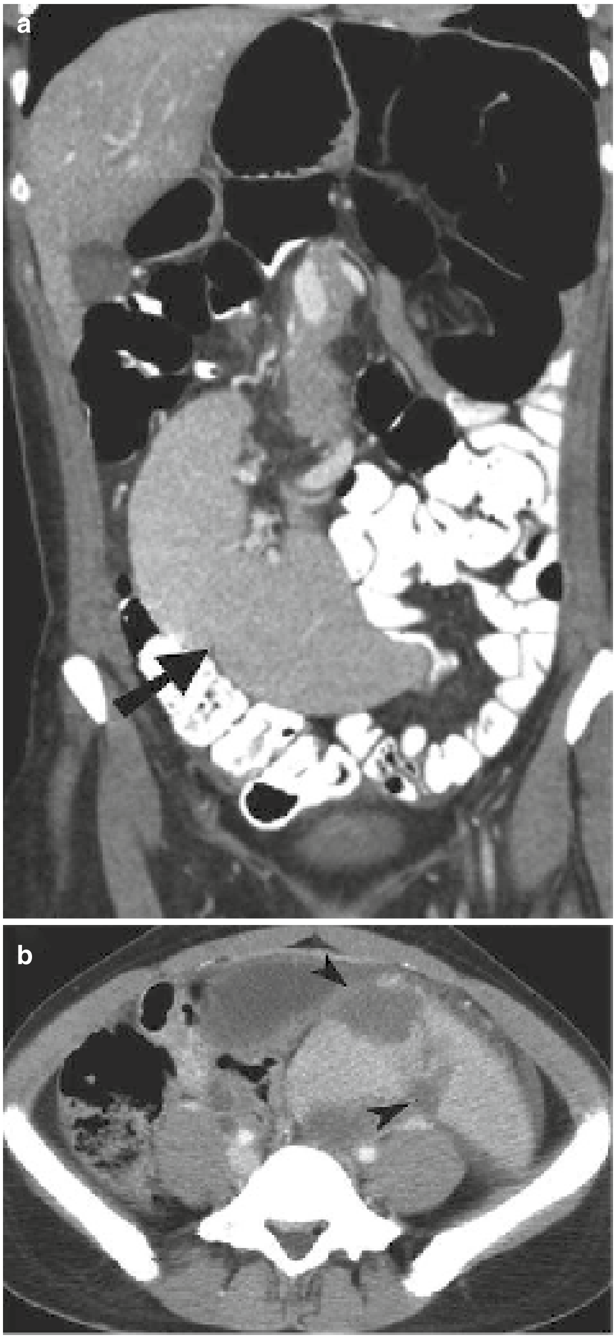

Fig. 10.14 Wandering spleen and splenic torsion. (**a**) Coronal CT reformation with oral and IV contrast demonstrates an ectopic location of the spleen (*arrow*) within the pelvis due to ligamentous laxity. There is normal enhancement of the spleen. (**b**) Contrast-enhanced CT through the pelvis demonstrates an ectopic location of the spleen. Additionally, there are multiple hypodense regions within the spleen (*arrowheads*) consistent with infarcts from vascular compromise

Hematoma

Spontaneous, nontraumatic splenic hematoma or rupture is a rare pathology, seen most often in patients with splenomegaly, from either malignancy (leukemia or lymphoma) or infection (infectious mononucleosis, CMV infection, and malaria) [20].

Like hematomas in other locations, spontaneous splenic hematomas are most easily diagnosed with CT as heterogeneous pseudo-masses within the spleen and often extending outside of the splenic parenchyma. The spleen itself may be enlarged with a sizeable hematoma, giving onion skin appearance (Fig. 10.15). Hemoperitoneum may also be present if there is extension of hematoma outside of the spleen.

Teaching Points

- The most common ultrasound appearance of a fungal infection in the liver is a hypoechoic nodule.
- The imaging findings of acute hepatitis include increased echogenicity of the portal tracts and gallbladder wall thickening.
- Imaging characteristics of hydatid cyst vary from cystic lesion to a solid pseudotumor.
- Common findings associated with splenic infarction include wedge-shaped hypodensity, perisplenic fluid, left-sided pleural effusion, and infarcts in other organs.

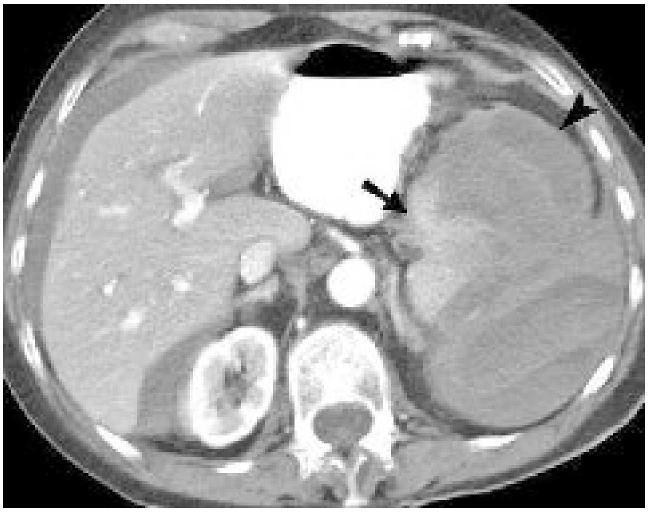

Fig. 10.15 Spontaneous splenic hematoma. Contrast-enhanced CT of the abdomen demonstrates a large subcapsular splenic hematoma (*arrowhead*) compressing the spleen (*arrow*) in a patient with no history of trauma. There is associated high-density fluid around the liver, hemoperitoneum

- Hepatocellular carcinoma should be suspected in a patient with cirrhosis with portal vein thrombus, intrahepatic hematoma, and subcapsular hematoma.
- Imaging findings in acute Budd–Chiari include contrast washout from the central areas of the liver on enhanced CT during the portal venous phase and sparing of the caudate lobe.
- In patients with portal vein thrombosis, a bland thrombus will have no internal flow, whereas tumor thrombus will have internal flow.
- In splenic infarct, the CT appearance is typically a wedge-shaped, hypoattenuating region within the spleen.

Questions

1. Cluster and double target signs are seen in which of the following liver lesions?
   (A) Pyogenic abscess
   (B) Fungal abscess
   (C) Hydatid cyst
   (D) Hepatic infarct
   Answer: A

2. Rupture of pericyst and spillage of the hydatid contents into the biliary tree are characteristics of which of the following?
   (A) Contained ruptures
   (B) Direct rupture
   (C) Communicating rupture
   (D) Superimposed infection
   Answer: C

3. Which of the following is associated with acute portal vein thrombosis?
   (A) Cavernous transformation
   (B) Hypoattenuating thrombus
   (C) Tortuous venous collaterals
   (D) Peripheral enhancement of the vein
   Answer: D

4. Early arterial enhancement of the caudate lobe and central liver with diffuse peripheral hypoattenuation in contrast-enhanced CT is characteristic of which of the following lesions?
   (A) Hepatic infarct
   (B) Hepatic abscess
   (C) Budd–Chiari syndrome
   (D) Portal vein thrombosis
   Answer: C

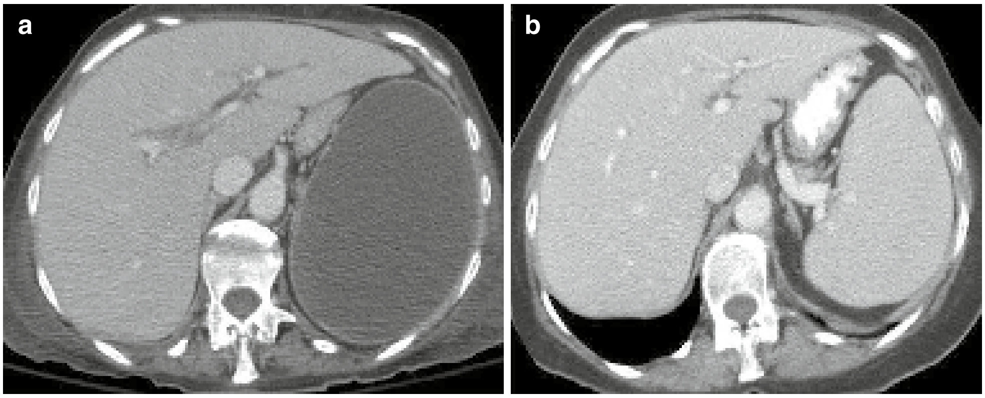

Fig. 10.16 (**a**) Splenic infarction CT. (**b**) Splenic infarction after 6 month

5. What pathology is seen in the patient whose current CT (Fig. 10.16a) and comparison CT from 6 months ago (see Fig. 10.16b) are shown?
   (A) Splenic infarction
   (B) Splenic volvulus
   (C) Budd–Chiari syndrome
   (D) Splenic neoplasm
   Answer: A

6. What is the cause of fever and abdominal pain on the CT (Fig. 10.17) of a patient who recently traveled Peru?
   (A) Hepatitis
   (B) Amebic abscess
   (C) Liver hemangioma
   (D) Fitz-Hugh–Curtis
   Answer: B

7. What is the CT (Fig. 10.18) diagnosis in a patient with history of alcoholism?
   (A) Amebic abscess
   (B) Hemosiderosis
   (C) Hepatitis
   (D) Budd–Chiari syndrome
   Answer: D

8. What is the pathology depicted on the CT (Fig. 10.19) of a patient with fever of unknown origin?
   (A) Liver abscess
   (B) Liver hemangioma
   (C) Liver abscess and hemangioma
   (D) Liver metastases
   Answer: C

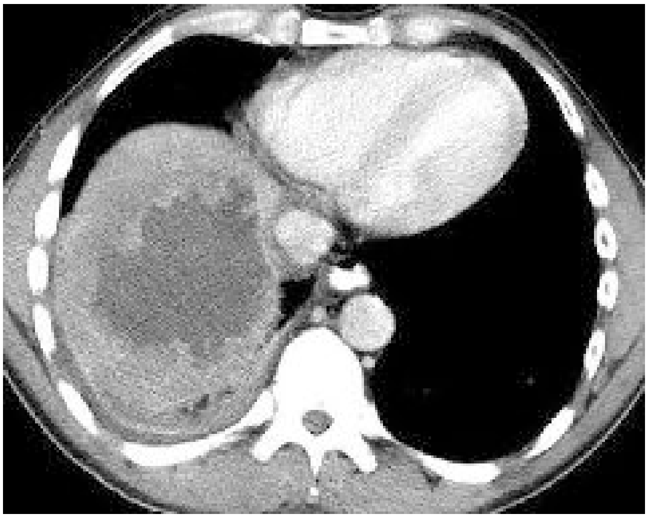

Fig. 10.17 Amebic abscess—CT

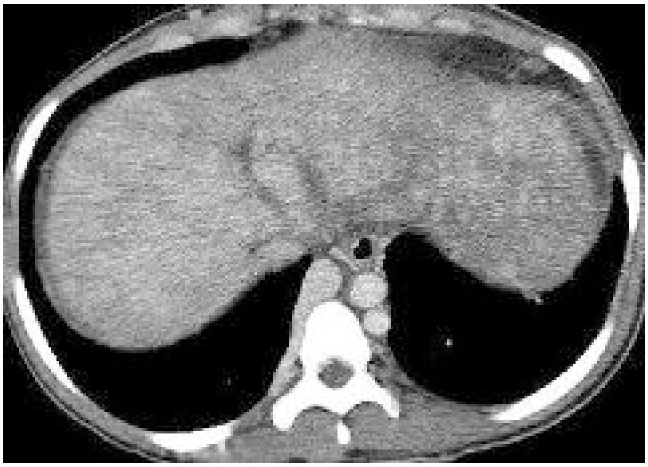

Fig. 10.18 Budd–Chiari syndrome

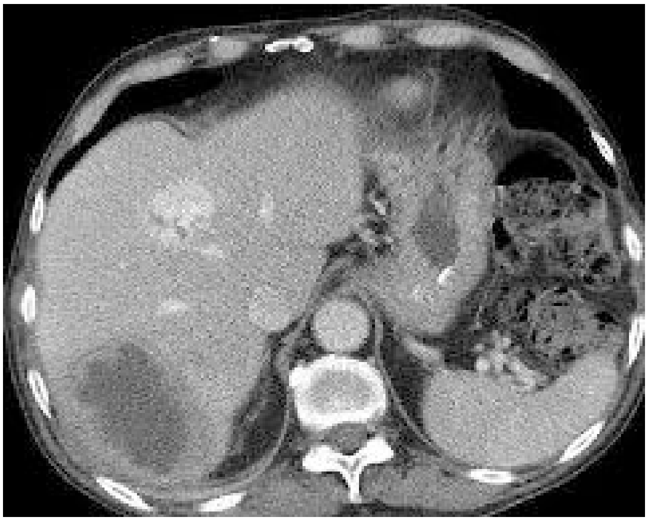

Fig. 10.19 Liver abscess and hemangioma

References

1. Kumar V, Abbas AK, Fausto N. Robins and Cotran: pathologic basis of disease. 7th ed. Philadelphia: Saunders; 2004.
2. Kasper DL, et al. Harrison's principles of internal medicine. 16th ed. New York: McGraw-Hill; 2005.
3. Mortele KJ, Segatto E, Ros PR. The infected liver: radiologic–pathologic correlation. Radiographics. 2004;4:937–55.
4. Itai Y, Sekiyama K, Ahmadi T, Obuchi M, Yoshiba M. Fulminant hepatic failure: observation with serial CT. Radiology. 1997;202:379–82.
5. Murakami T, Baron RL, Peterson MS. Liver necrosis and regeneration after fulminant hepatitis: pathologic correlation with CT and MR findings. Radiology. 1996;198:239–42.
6. Radin DR, Ralls PW, Colletti PM, Halls JM. CT of amebic liver abscess. AJR Am J Roentgenol. 1988;150:1297–301.
7. Kim S, Kim TU, Lee JW, Lee TH, Lee SH, Jeon TY, et al. The perihepatic space: comprehensive anatomy and ct features of pathologic conditions. Radiographics. 2007;27:129–43.
8. Joo SH, Kim MJ, Lim JS, Kim JH, Kim KW. CT diagnosis of Fitz-Hugh and Curtis syndrome: value of the arterial phase scan. Korean J Radiol. 2007;8:40–7.
9. Kawamoto S, Soyer PA, Fishman EK, Bluemke DA. Nonneoplastic liver disease: evaluation with CT and MR imaging. Radiographics. 1998;18:827–48.
10. Torabi M, Hosseinzadeh K, Federle MP. CT of nonneoplastic hepatic vascular and perfusion disorders. Radiographics. 2008;28:1967–82.
11. Smith GS, Birnbaum BA, Jacobs JE. Hepatic infarction secondary to arterial insufficiency in native livers: CT findings in 10 patients. Radiology. 1998;208:223–9.
12. Cura M, Haskal Z, Lopera J. Diagnostic and interventional radiology for Budd Chiari syndrome. Radiographics. 2009;29:669–81.
13. Casillas VJ, Amendola MA, Gascue A, Pinar N, Levi JU, Perez JM. Imaging of nontraumatic hemorrhagic hepatic lesions. Radiographics. 2000;20:367–78.
14. Grazioli L, Federle MP, Brancatelli G, Ichikawa T, Olivetti L, Blachar A. Hepatic adenomas: imaging and pathologic findings. Radiographics. 2001;21:877–92.
15. Gallego C, Velasco M, Marcuello P, Tejedor D, Campo LD, Friera A. Congenital and acquired anomalies of the portal venous system. Radiographics. 2002;22:141–59.
16. Antopolsky M, Hiller N, Salameh S, Goldshtein B, Stalnikowicz R. Splenic infarction: 10 years of experience. Am J Emerg Med. 2009;27:262–5.
17. Goerg C, Schwerk W. Splenic infarction: sonographic patterns, diagnosis, follow-up, and complications. Radiology. 1990;174:803–7.
18. Elsayes KM, Narra VR, Mukundan G, Lewis JS, Menias CO, Heiken JP. MR imaging of the spleen: spectrum of abnormalities. Radiographics. 2005;25:967–82.
19. Herman TE, Siegel MJ. CT of acute splenic torsion in children with wandering spleen. AJR Am J Roentgenol. 1991;156:151–3.
20. Furlan A, Fakhran S, Federle MP. Spontaneous abdominal hemorrhage: causes, CT findings, and clinical implications. AJR Am J Roentgenol. 2009;193:1077–87.

Imaging of Acute Pancreas

11

Caterina Missiroli, Khyati Bidani, Mohammad Mansouri,
and Ajay Singh

Acute Pancreatitis

The cause of acute pancreatitis is believed to be pancreatic autodigestion by pancreatic enzymes. In adults, 70–80% of cases of pancreatitis are due to biliary stones or alcohol [1, 2]. Approximately 75–80% of patients with acute pancreatitis have a mild clinical course and will recover completely with conservative treatment. Others develop severe course associated with morbidity, mortality, and prolonged hospital stay. In children, the most frequent causes are blunt trauma, drugs (steroids and furosemide), infection (mumps, coxsackievirus, ascariasis, *E. coli*), or hereditary disorders, such as hemolytic-uremic syndrome, gene mutation (cationic trypsinogen), and biliary tract anomalies [3, 4]. Causes of acute pancreatitis are summarized in Table 11.1.

Autoimmune pancreatitis is a rare cause of pancreatitis with the incidence rate of 1.4 per 100,000 individuals per year. Clinical presentation is nonspecific and includes jaundice, upper abdominal pain, weight loss, and fatigue. Diagnosis is based on serology, histology, imaging, other organ involvement, and effect of steroid.

Table 11.1 Causes of acute pancreatitis

Common causes (70–80%)
• Cholelithiasis • Alcohol abuse
Uncommon causes (10–15%)
• Hypercalcemia • Hypertriglyceridemia • Post-ERCP • Drug induced • Trauma • Infection • Tumors
Idiopathic (10–20%)

Classification

The Atlanta classification for acute pancreatitis was introduced in 1992 and classified acute pancreatitis into mild and severe groups [5]. Mild pancreatitis results in edematous pancreatic parenchyma, which results in uneventful recovery with conservative management. Severe pancreatitis is associated with organ failure and complications such as pseudocyst formation, pancreatic necrosis, and pancreatic abscess formation. In 2008, Acute Pancreatitis Classification Working Group revised the Atlanta classification system to improve clinical assessment as well as clarify appropriate terms for pancreatic/peripancreatic fluid collections. This classification defines pancreatitis into two categories, including interstitial edematous pancreatitis and necrotizing pancreatitis with pancreatic parenchymal necrosis and/or peripancreatic necrosis (Fig. 11.1).

The classification defines four types of collections associated with pancreatitis. These are acute peripancreatic fluid collection (<4 weeks old), pseudocyst (>4 weeks old), acute postnecrotic collection (<4 weeks old), and walled-off necrosis (>4 weeks old). Revised Atlanta classification also classifies the severity of acute pancreatitis into mild, moderately severe, and severe (Table 11.2).

C. Missiroli
Department of Radiology, Nord Milano—Bassini Hospital,
Milan, Italy

K. Bidani · M. Mansouri
Department of Radiology, Massachusetts General Hospital,
Boston, MA, USA

A. Singh (✉)
Division of Emergency Radiology, Department of Radiology,
Massachusetts General Hospital, Boston, MA, USA

Harvard Medical School, Massachusetts General Hospital,
Boston, MA, USA
e-mail: asingh1@partners.org

© The Author(s), under exclusive license to Springer Nature Switzerland AG 2024
A. Singh (ed.), *Emergency Radiology*, https://doi.org/10.1007/978-3-031-65770-2_11

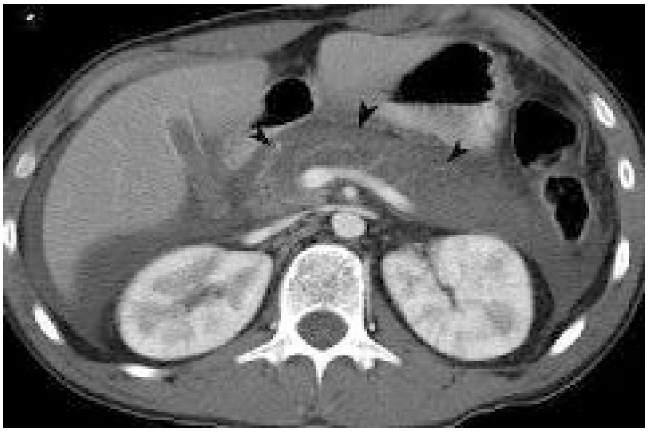

Fig. 11.1 Necrotizing pancreatitis. Contrast-enhanced CT demonstrates nonenhancement of pancreatic head, neck, and body (*arrowheads*). There is peripancreatic inflammation, extending to the anterior pararenal space

Table 11.2 Revised Atlanta classification of acute pancreatitis

Grade	Definition
Mild	No organ failure; no local/systemic complications
Moderately severe	Organ failure for less than 48 h and/or local or systemic complications; no persistent organ failure
Severe	Persistent organ failure for more than 48 h; single-organ failure; multiple-organ failure with or without local and/or systemic complications

Table 11.3 CT severity index

CT finding	CT grade	Score
Normal pancreas	A	0
Focal or diffuse enlargement of the pancreas	B	1
Inflammatory changes in peripancreatic fat	C	2
Single fluid collection	D	3
≥2 collections and/or gas in/adjacent to pancreas	E	4
Necrosis (%)	Score	
<30	2	
30–50	4	
>50	6	

Balthazar et al. described CT severity index, giving scores from 0 to 4 for various findings of acute pancreatitis (Table 11.3) [6]. A composite score of 6 is associated with >50% frequency of pancreatic necrosis.

Imaging

When imaging is required, contrast-enhanced CT and ultrasound are both considered first-line imaging modality for the initial assessment of acute pancreatitis in patients with elevated amylase and/or lipase but no fever or evidence of fluid loss (Fig. 11.2). Ultrasound is primarily used to assess for gallstones, and contrast-enhanced CT is the most appropriate imaging modality for the assessment of pancreatic parenchyma in children and adults. For the assessment of pancreatitis in patients who are not improving after 48 h of presentation, contrast-enhanced CT and MRI with MRCP are considered the appropriate first-line and second-line imaging modalities, respectively (Fig. 11.3).

Ultrasound is often limited by technical factors such as obesity and bowel gas, thereby limiting its usefulness for purposes other than biliary assessment. The CT imaging findings of acute pancreatitis include pancreatic enlargement, ill definition of the peripancreatic fat planes, extrapancreatic fluid collection, dilated pancreatic duct, and pancreatobiliary calculus (Figs. 11.4 and 11.5). Interstitial edematous pancreatitis is seen on CT as localized or diffuse pancreatic enlargement with homogeneous or heterogeneous enhancement. Necrotizing pancreatitis is characterized by lack of pancreatic parenchymal enhancement. The extent of pancreatic necrosis is categorized as less than 30%, 30–50%, and more than 50% of the pancreas. Areas of no or poor enhancement in less than 30% of the pancreas categorized as necrosis may on a follow-up CT actually represent changes of edematous pancreatitis rather than necrosis.

MRI is useful in stable patients because of the capacity of identifying as well as grading the inflammatory process and detecting ducts and their obstruction or disruption when present [1, 2, 7]. The detection of the type fluid composition is also possible on MRI in patients with complicated pancreatitis (e.g., hemorrhagic, necrotic) (Figs. 11.6 and 11.7). Table 11.4 describes imaging findings in acute pancreatitis.

On ultrasonography, autoimmune pancreatitis presents with enlarged, hypoechoic pancreas. CT is the most helpful imaging modality and can depict diffuse pancreatic parenchymal enlargement, diminished enhancement in the arterial phase, and increased or prolonged enhancement in the delayed or venous phase. Capsule-like low-density rim around the pancreas is a characteristic finding (Fig. 11.8). MRI shows hypointense signal on T1- and hyperintense signal on T2-weighted images.

The complications of acute pancreatitis include hemorrhage, necrosis, abscesses, pseudocyst, and pseudoaneurysm [2] (Figs. 11.9, 11.10, 11.11 and 11.12). Symptomatic collections and pseudocysts are often best treated with image-guided catheter drainage. ERCP is used for diagnosis as well as treatment of stone-related pancreatitis and is often used when a stone is seen obstructing the pancreatobiliary duct on MRCP (Figs. 11.13 and 11.14).

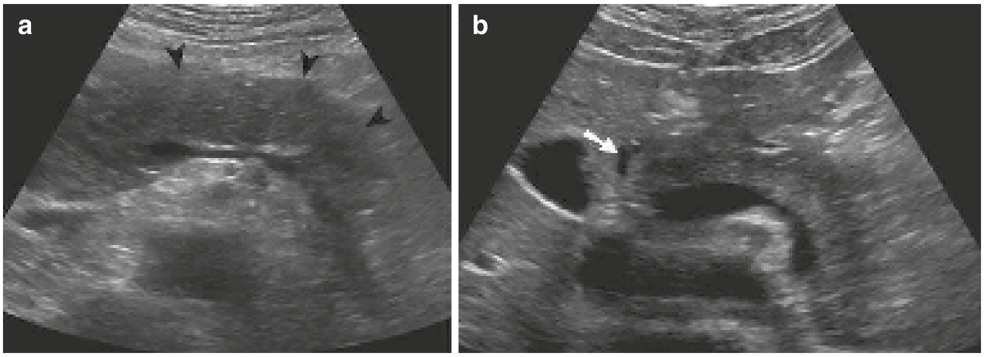

Fig. 11.2 Acute edematous pancreatitis. (**a**) Ultrasound shows pancreatic enlargement (*arrowheads*) with hypoechogenicity of the pancreatic parenchyma caused by pancreatic parenchymal edema. (**b**) Ultrasound shows hypoechoic pancreatic parenchyma and small peripancreatic fluid (*white arrow*)

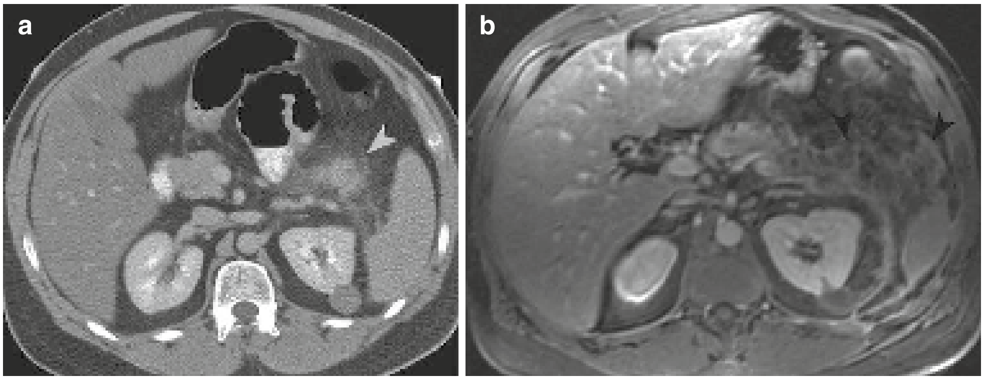

Fig. 11.3 Acute edematous pancreatitis. (**a**) Contrast-enhanced CT image shows fat stranding around the pancreatic tail (*arrowhead*) due to edematous pancreatitis. (**b**) Contrast-enhanced MR shows heterogeneous inflammation (*arrowhead*) around the pancreatic tail with thickening of the lateroconal fascia

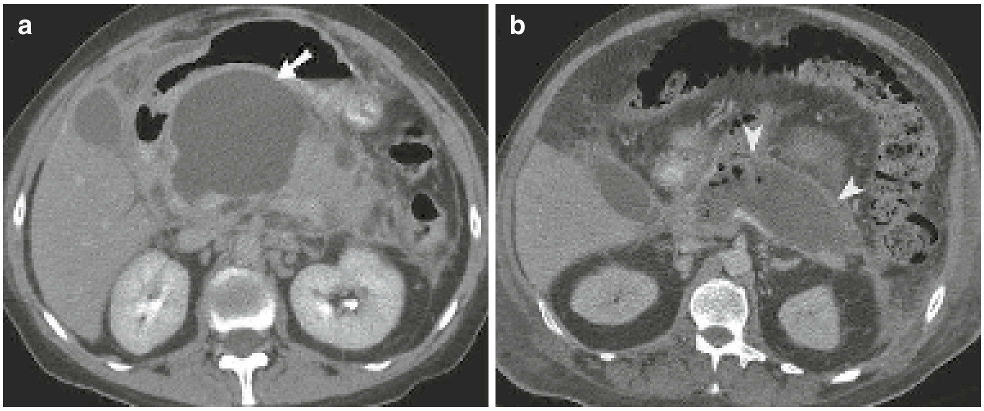

Fig. 11.4 Pancreatic collections. (**a**) Contrast-enhanced CT shows pancreatic enlargement due to a dominant pancreatic head collection (*arrow*). (**b**) Contrast-enhanced CT shows pancreatic parenchymal necrosis with intrapancreatic fluid (*arrowheads*) and air

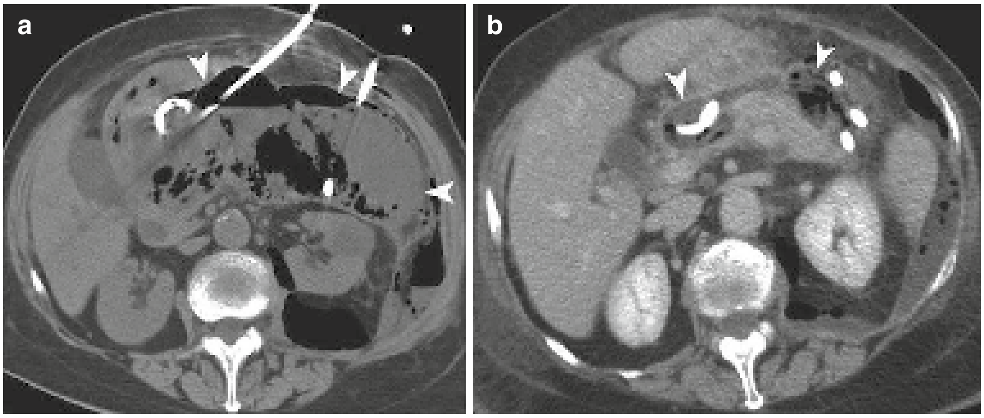

Fig. 11.5 Pancreatic collection. (**a**) Noncontrast CT obtained immediately after image-guided pigtail catheter placement demonstrates a large lesser sac fluid- and air-containing collection (*white arrowheads*). There are collections also seen in left posterior pararenal space and left paracolic gutter. (**b**) Follow-up contrast-enhanced CT image shows marked improvement in the lesser sac fluid collection (*white arrowheads*)

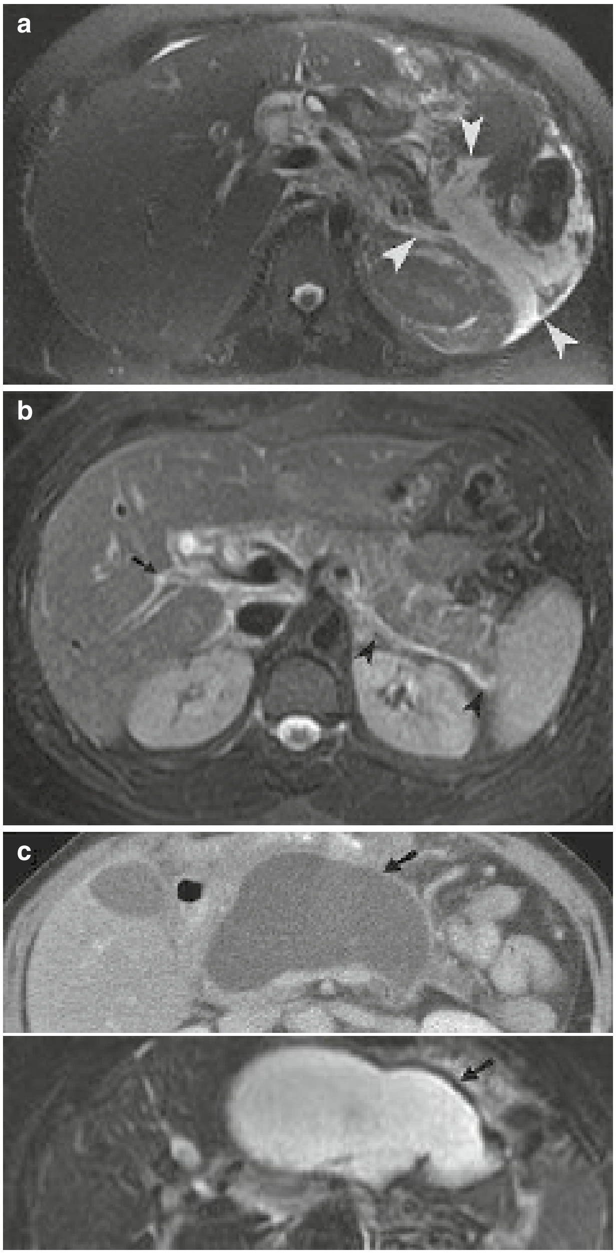

Fig. 11.6 Acute pancreatitis on MRI. (**a**) TSE-T2-weighted sequence shows extensive hyperintense peripancreatic inflammatory process (*arrowheads*) in the left anterior pararenal space. (**b**) Post-gadolinium T1-weighted sequence in a patient with amylase level of 2300 units per liter shows peripancreatic inflammation (*arrowheads*) and periportal edema (*arrow*). (**c**) Contrast-enhanced CT and corresponding FSE-T2-weighted MRI sequence show pancreatic necrosis and large homogeneous fluid collection (*arrows*) within the pancreas

Table 11.4 Imaging findings in acute pancreatitis

Imaging modality	Notes
Ultrasonography	• First-line imaging modality • Assess for gallstones and biliary system
CT	• First-line imaging modality if patient not improving after 48 h • Good for assessment of pancreatic parenchyma • Pancreatic enlargement • Ill definition of the peripancreatic fat planes • Extrapancreatic fluid collection • Dilated pancreatic duct • Pancreatobiliary calculus
MRI	• First-line imaging modality if patient not improving after 48 h • Useful in stable patients and grading the inflammatory process • Detection of fluid composition

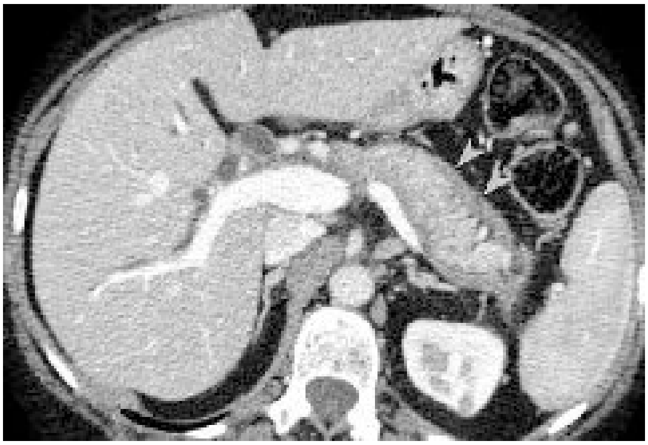

Fig. 11.8 Autoimmune pancreatitis. Contrast-enhanced CT depicts diffuse pancreatic parenchymal enlargement and a surrounding capsule-like low-density rim (*arrowheads*)

Fig. 11.7 Pseudocyst with bleeding. (**a**, **b**) Noncontrast-enhanced CT and T2-weighted MR image shows a large lesser sac pseudocyst (*arrowheads*) containing blood clots from recent bleeding

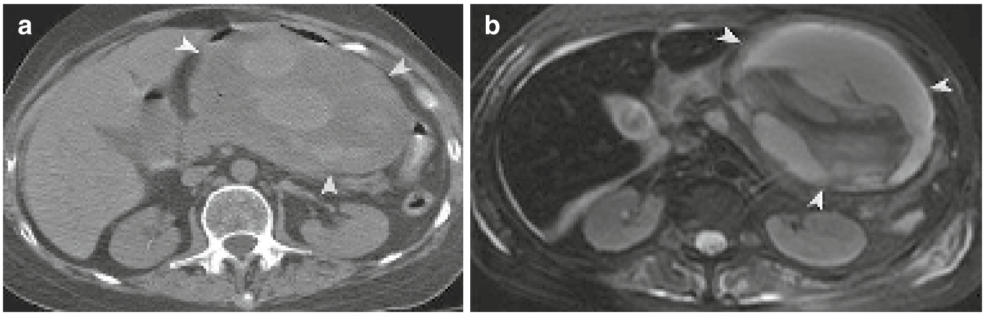

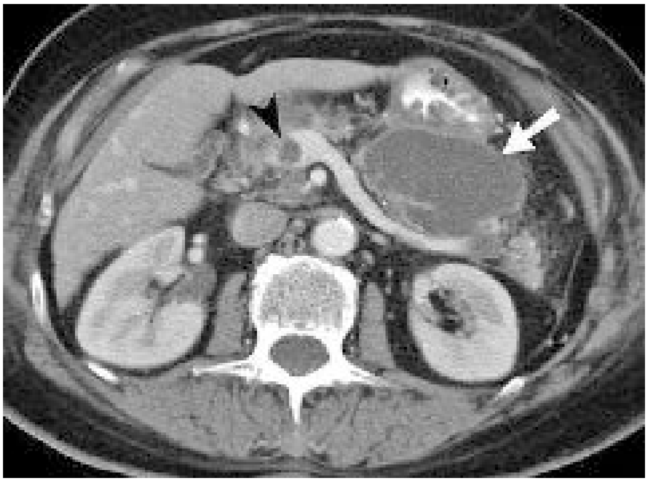

Fig. 11.9 Portal vein thrombosis. Contrast-enhanced CT image shows a thrombus in the main portal vein (*arrowhead*) which developed secondary to acute pancreatitis. There is an intrapancreatic collection (*arrow*) seen within the pancreatic body

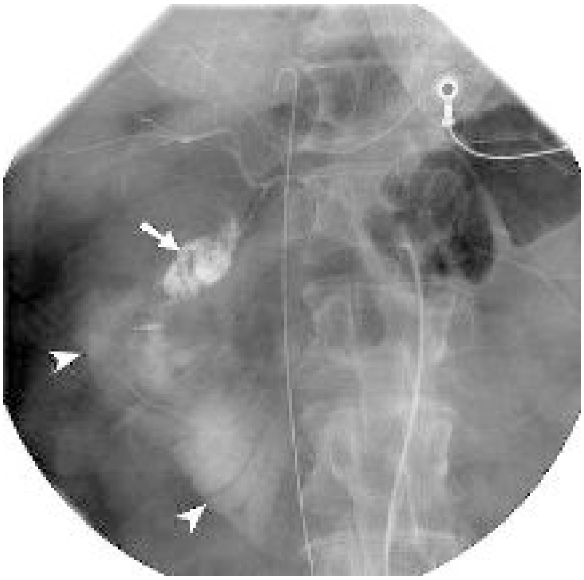

Fig. 11.11 Gastroduodenal artery aneurysm. Conventional angiogram demonstrates contrast extravasation (*arrowheads*) into the duodenal lumen from a large gastroduodenal artery aneurysm (*arrow*)

Fig. 11.10 Postpancreatitis gastroduodenal artery aneurysm. Digital subtraction angiographic images show the presence of an aneurysm (*arrow*) along the course of the gastroduodenal artery. The second image obtained after aneurysm coiling (*arrowhead*) demonstrates contrast extravasation (*curved arrow*)

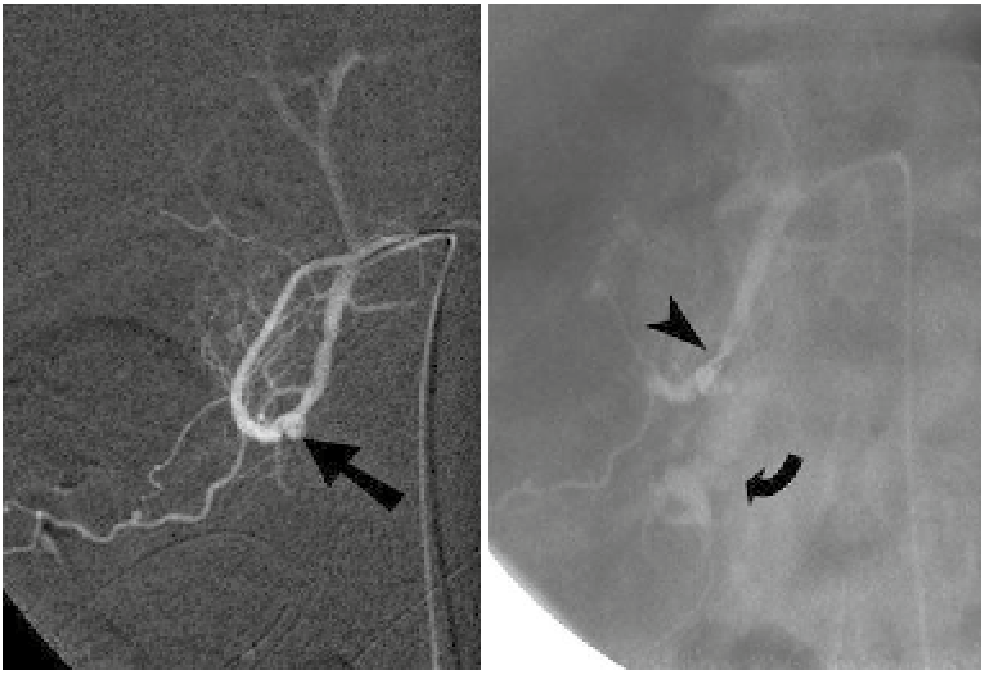

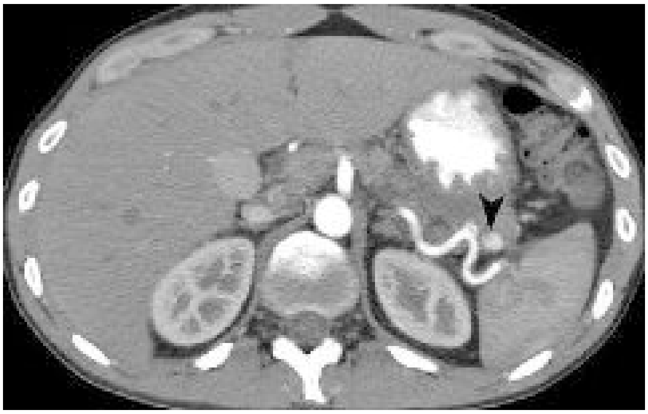

Fig. 11.12 Splenic artery aneurysm. Contrast-enhanced CT shows a subcentimeter pseudoaneurysm (*arrowhead*) within the pancreatic tail, adjacent to the splenic artery

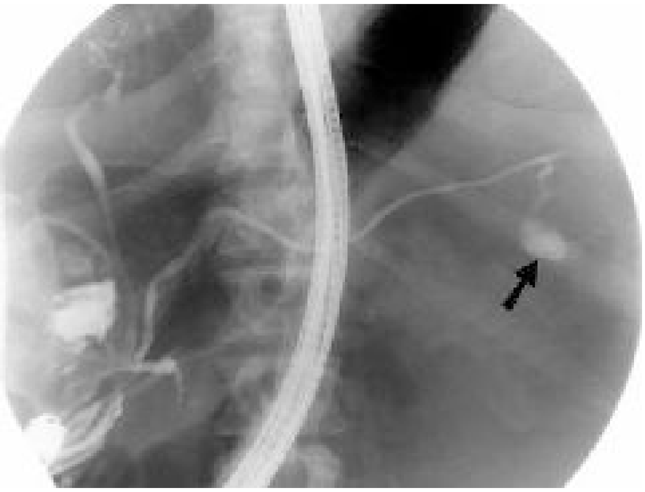

Fig. 11.13 Pancreatic duct leak. ERCP spot film shows the presence of contrast leaking (*arrow*) the main pancreatic duct, in the tail of the pancreas. The resultant collection was drained using image-guided pigtail catheter drainage

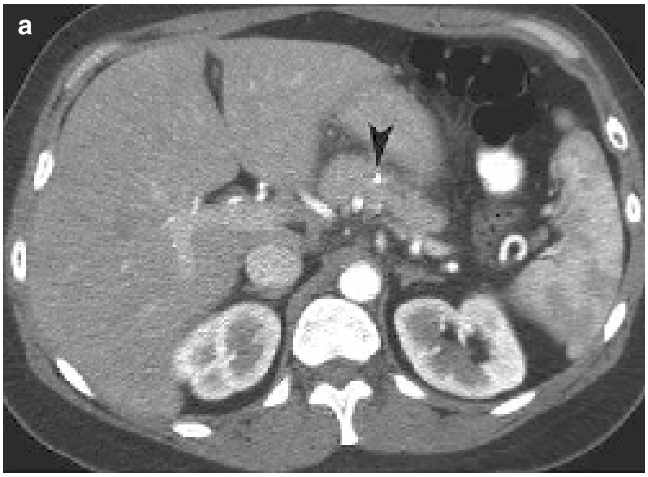

Fig. 11.14 Pancreatic duct stone. (**a**) Contrast-enhanced CT shows a small calculus (*arrowhead*) in the main pancreatic duct, causing ductal obstruction and pancreatitis. (**b**) MRCP shows main pancreatic ductal obstruction (*arrowhead*) caused by the calculus, located 8 cm from the ampulla

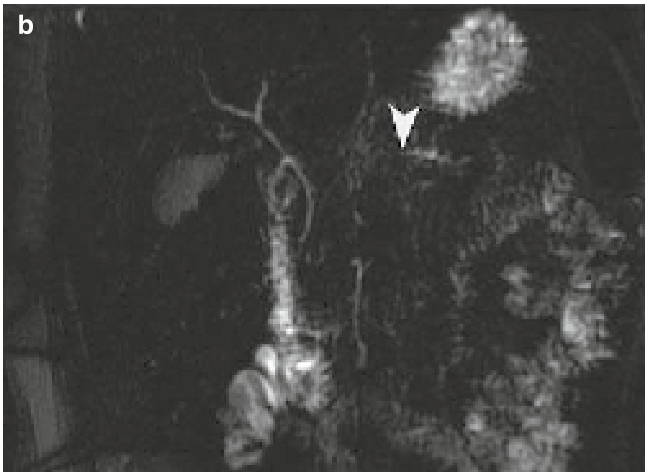

Fig. 11.14 (continued)

Acute Pancreatitis in Pancreatic Cancer

Pancreatic inflammation is possible in the presence of a neoplasm, usually adenocarcinoma, lymphoma, or metastasis. Acute pancreatitis is caused by neoplasm in 1–2% of the cases [3]. The pancreatitis is usually due to ductal obstruction by a pancreatic head mass.

In patients over the age of 40 with first episode of pancreatitis and no identifiable cause, contrast-enhanced CT should be used to exclude an underlying neoplastic process. The diagnosis of the pancreatic neoplasm is usually delayed because of the inflammatory changes masking the tumor. Imaging findings useful in making the diagnosis of underlying neoplasm include significant enlargement of ducts, pancreatic head enlargement disproportionate to the rest of the gland, lymphadenopathy, metastasis, and vascular involvement. The definite diagnosis can be made with endoscopic or image-guided biopsy.

Traumatic Injuries

Pancreatic injury is relatively uncommon, accounting for 2% of all abdominal traumas. In patients with pancreatic injury, the mortality is high, ranging from 9 to 34% [4, 8]. Majority of the patients have associated other visceral organ injury, which is the major cause of mortality within 48 h after injury.

The pancreatic injury may involve the duct (type I) or duct as well as pancreatic parenchyma (type II) (Table 11.5; Figs. 11.15 and 11.16). In children, the common causes of pancreatic injury include bicycle accident and abuse. In adults, motor vehicle accident is the most common cause, followed by less common causes such as sports injury, fall, and blow to the abdomen [8].

Ultrasonography may demonstrate localized enlargement of the pancreas or diffuse edema. Peripancreatic fluid may be seen in pancreatic contusion. Main pancreatic duct needs to be delineated on ultrasound, because most of the complications of trauma are due to rupture or stenosis of this structure.

Contrast-enhanced CT is the most frequently used imaging tool in trauma patients and is the best technique for the diagnosis of pancreatic injuries in stable patients [9]. The sensitivity of CT in detecting pancreatic trauma is approximately 80%. CT tends to underestimate the severity of

Table 11.5 Grading of pancreatic injury

	Grading of injuries
I	No ductal injury, hematoma, and minor laceration
II	Hematoma and major laceration/contusion, no ductal injury
III	Distal laceration/transaction with duct injury
IV	Proximal laceration/transaction with biliary duct injury and ampullary lesion
V	Massive head injury

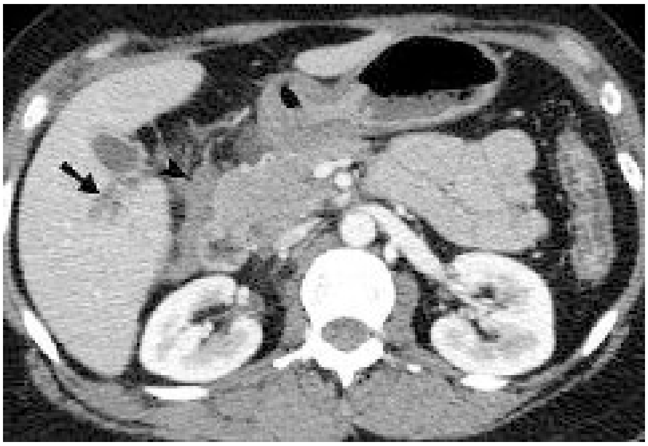

Fig. 11.16 Post-traumatic pancreatic and liver injury. CECT demonstrates peripancreatic hemorrhage around the pancreatic head (*arrowhead*). Liver laceration is seen in the right lobe of the liver (*arrow*)

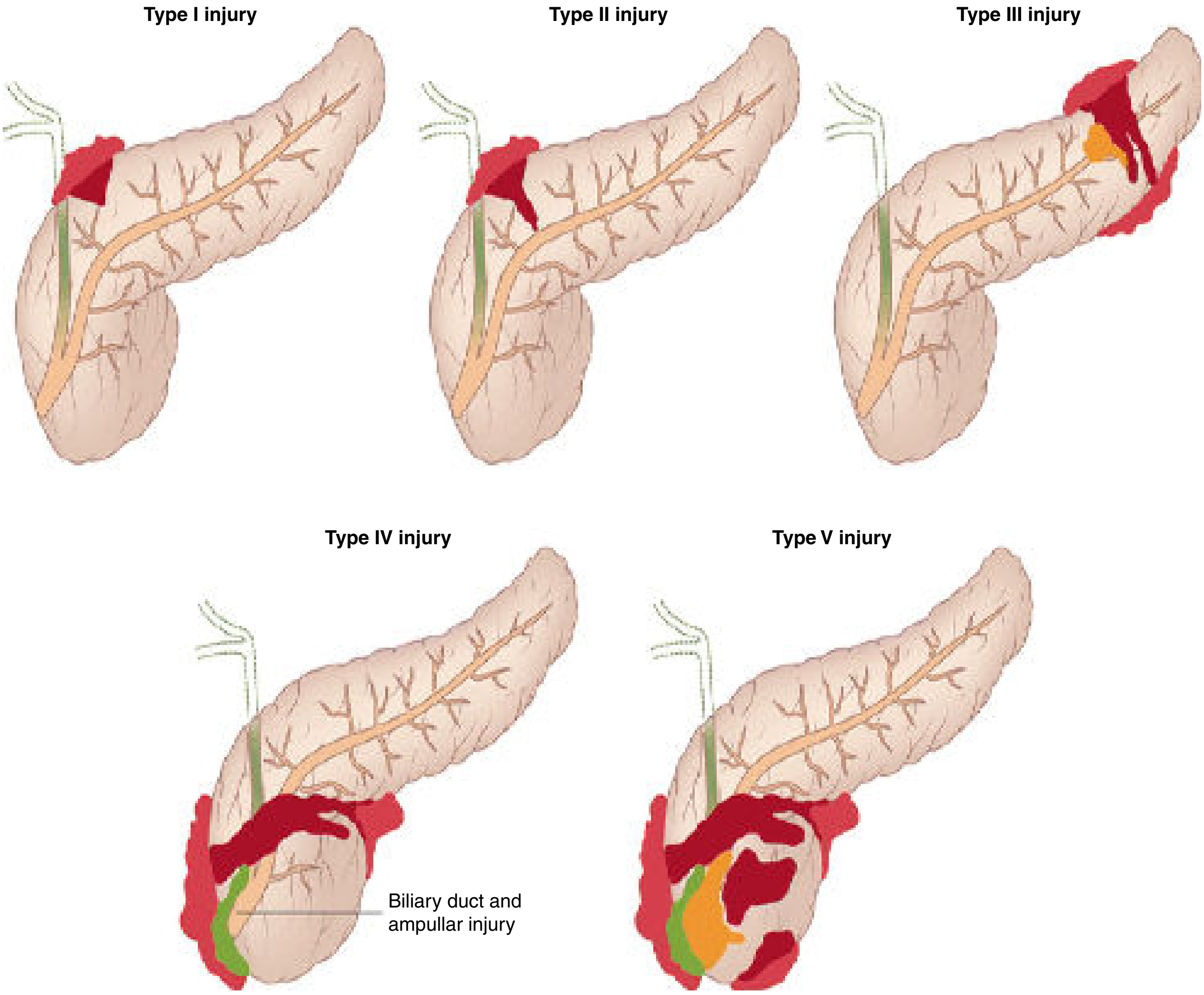

Fig. 11.15 Grading of pancreatic injury

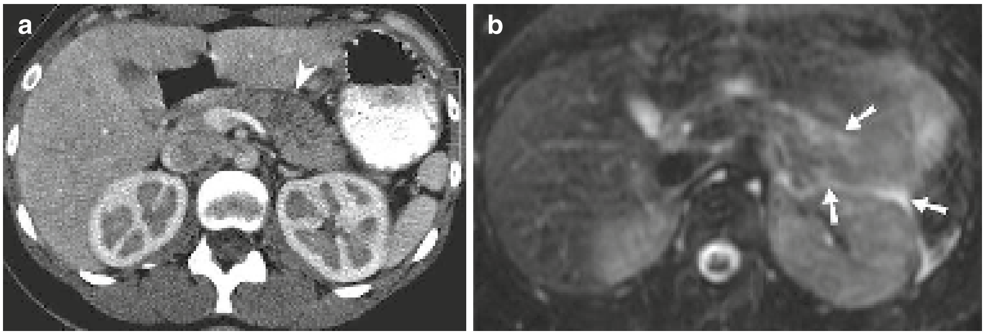

Fig. 11.17 Pancreatic contusion. (**a**) Contrast-enhanced CT demonstrates a low-density contusion (*arrowhead*) in the pancreatic body in a patient with a history of blunt trauma. (**b**) T2-weighted sequence demonstrates prepancreatic hyperintensity (*arrows*) produced by edema in the retroperitoneum

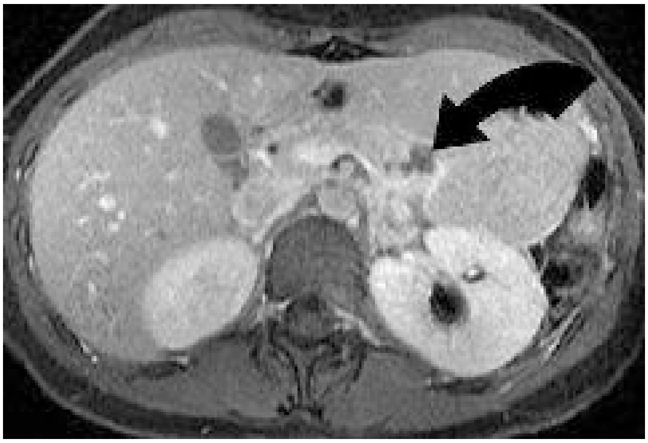

Fig. 11.18 Pancreatic laceration. Contrast-enhanced MRI study demonstrates pancreatic laceration (*arrow*) which had disrupted the main pancreatic duct

pancreatic injury. The CT findings of pancreatic trauma include pancreatic lacerations (seen as linear hypodensity), edema, or hemorrhage.

Pancreatic contusions are seen as focal or diffuse hypodensity in the pancreas (Fig. 11.17). A pancreatic laceration of more than one-half the diameter of the pancreatic thickness indicates the presence of main pancreatic ductal injury. The presence of fluid between the splenic vein and the pancreas is a helpful CT finding for the diagnosis of pancreatic injury after blunt abdominal trauma [10].

Documenting the integrity of the pancreatic duct is important for triaging the patient and predicting the prognosis. MRCP is the best noninvasive modality in the evaluation of the pancreatic duct. T2-weighted MRI sequence is sensitive in the detection of pancreatic parenchymal injury as well as peripancreatic inflammation (Fig. 11.18). ERCP allows evaluation of the pancreatic duct integrity and placement of patent. The imaging findings of pancreatic trauma include pancreatic enlargement, hypoattenuating laceration/contusion, pancreatic duct discontinuity, peripancreatic stranding, fluid collection, and hematoma.

Complications occur in 30–60% of patients with pancreatic injury and include fistulas, pancreatitis, pseudocysts, abscess, hemorrhage, sepsis, and multiorgan failure. Surgical treatment is required for penetrating traumas and severe blunt injuries (grades III–V), active hemorrhage, and ductal transection [11]. Image-guided drainage can be used for pseudocyst, infected collection, and postoperative seroma.

Autoimmune Pancreatitis

Autoimmune pancreatitis (AIP) is a chronic inflammatory condition of the pancreas of autoimmune etiology and typically responds very well to the glucocorticoid therapy. It often presents with recurrent acute pancreatitis or painless jaundice. Radiologically, sometimes it can resemble pancreatic ductal adenocarcinoma, and it is critical to distinguish the two in such cases. AIP can be a primary pancreatic disorder, manifestation of systemic autoimmune disease, or a part of IgG4-related disorders.

Imaging

The most characteristic finding of AIP seen on CT/MRI is diffuse enlargement of pancreas with homogenous enhancement in the delayed phase instead of normal arterial or pancreatic phase. However, during pancreatic phase, punctate foci of enhancements can be seen within the lesion which represents the normal parenchyma. Rim of band like hypoenhancement around the lesion (known as capsule rim sign) in both pancreatic and delayed phase, if seen, is suggestive of fibrosis and is a highly specific finding of AIP (Fig. 11.19a) [12].

On MRI, the lesion appears hypointense on T1-weighted images and hyperintense on T2-weighted and diffusion-weighted images. Loss of normal lobulated texture of the pancreas can also be observed. Capsule rim sign on MRI

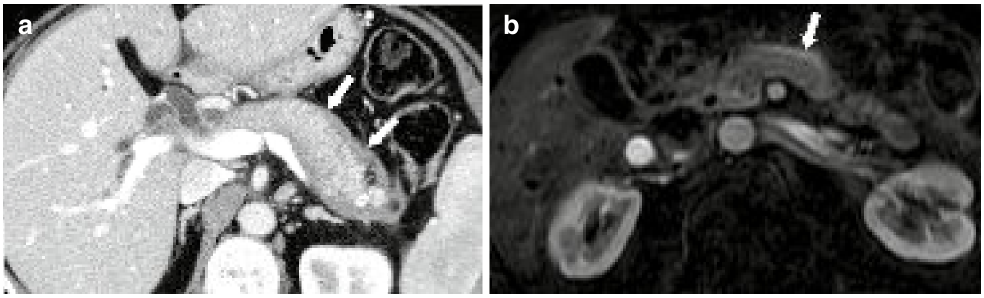

Fig. 11.19 Autoimmune pancreatitis. (**a**) Contrast-enhanced CT of the abdomen demonstrates a rim of hypoenhancement (arrows) around the pancreas, consistent with the capsular rim sign. (**b**) Post-contrast T1-WI demonstrates hyperenhancing outer capsule (arrow) and loss of pancreatic lobulation

appears as hypointense rim on T1- and T2-weighted images with delayed enhancement (Fig. 11.19b). Capsule rim can sometimes be confused with peripancreatic fluid collection; however, peripancreatic fluid will be hyperintense on T2-weighted images and will not enhance. On diffusion-weighted images, the lesion demonstrates hyperintensity due to restricted diffusion with low ADC values. Significant increase in the ADC value has been noted following steroid treatment [12].

The MRCP findings include diffuse irregular narrowing of the main pancreatic duct, long stricture (involving more than a third of length), or multiple strictures of pancreatic duct without significant upstream dilation. Involvement of intrapancreatic portion of common bile duct usually suggests associated IgG4-related sclerosing cholangitis. Penetrating duct sign, also known as icicle sign, refers to the smooth tapering of the main pancreatic duct stenosis and suggests benign stricture of AIP. This sign helps in differentiating AIP from pancreatic ductal carcinoma, which is associated with abrupt pancreatic duct cut off usually with significant upstream dilation. Ductal changes of AIP often resolve following adequate treatment with steroids [12].

Teaching Points

- In adults, 70–80% of cases of pancreatitis are due to biliary stones or alcohol.
- The revised Atlanta classification system divides acute pancreatitis into acute edematous pancreatitis and necrotizing pancreatitis.
- In patients over the age of 40 with first episode of pancreatitis and no identifiable cause, contrast-enhanced CT should be used to exclude an underlying neoplastic process.
- CT findings in acute pancreatitis include pancreatic enlargement, ill definition of the peripancreatic fat planes, extrapancreatic fluid collection, and dilated pancreatic duct.
- MRI is useful in grading the inflammatory process, and detection of fluid composition.
- The CT findings of pancreatic trauma include pancreatic lacerations (seen as linear hypodensity), edema, or hemorrhage.
- According to CT severity index, a composite score of 6 is associated with >50% frequency of pancreatic necrosis.

Questions

1. In traumatic pancreatic injury, laceration of distal pancreas with ductal injury is seen in which of the following grades?
   (A) Grade 1
   (B) Grade 2
   (C) Grade 3
   (D) Grade 4
   Answer: C

2. Which of the following imaging modalities is indicated if patient with acute pancreatitis does not improve after 48 h of conservative treatment?
   (A) US
   (B) CT
   (C) MRI
   (D) MRCP
   Answer: B

3. Which complication of pancreatitis is depicted on the CT (Fig. 11.20)?
   (A) Splenic infarct
   (B) Splenic artery pseudoaneurysm
   (C) Bowel perforation
   (D) Splenic artery pseudoaneurysm and splenic infarct
   Answer: D

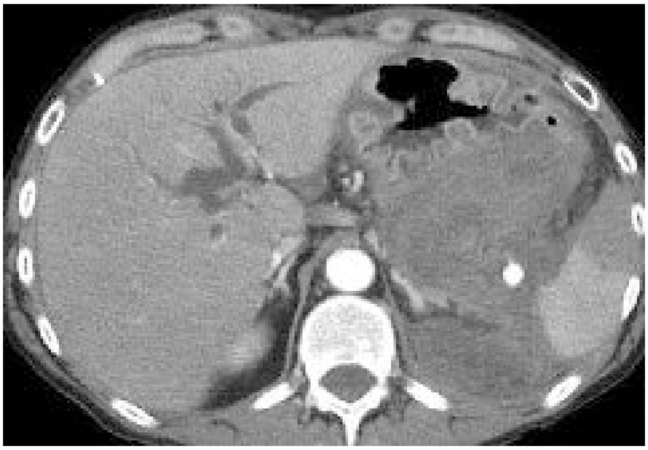

Fig. 11.20 Pancreatitis on CT

4. What is the further course of management of patient whose CECT (Fig. 11.21) is depicted below?
   (A) Embolization
   (B) Catheter drainage
   (C) Biopsy
   (D) Conservative management
   Answer: A

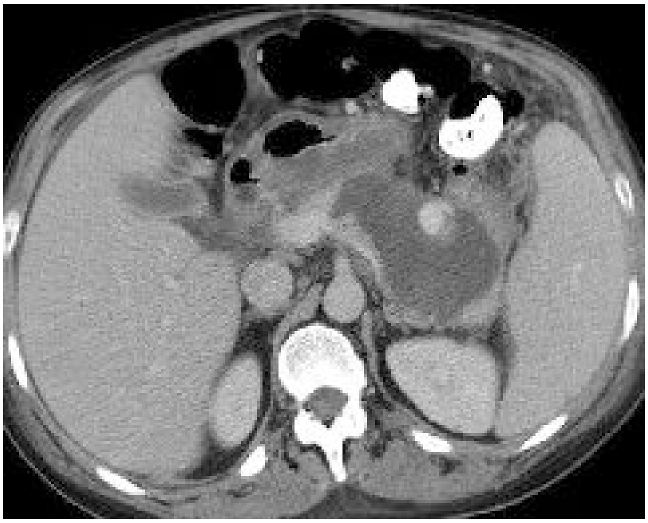

Fig. 11.21 Embolization CECT

References

1. Kim YS, Kim Y, Kim SK, Rhim H. Computed tomographic differentiation between alcoholic and gallstone pancreatitis: significance of distribution of infiltration or fluid collection. World J Gastroenterol. 2006;12(28):4524–8.
2. Xiao B, Zhang XM, Tang W, Zeng NL, Zhai ZH. Magnetic resonance imaging for local complications of acute pancreatitis: a pictorial review. World J Gastroenterol. 2010;16(22):2735–42.
3. Shanbhogue AKP, Fasih N, Surabhi VR, Doherty GP, Shanbhogue DKP, Sethi SK. A clinical and radiologic review of uncommon types and causes of pancreatitis. Radiographics. 2009;29:1003–26.
4. Vaughn DD, Jabra AA, Fishman EK. Pancreatic disease in children and young adults: evaluation with CT. Radiographics. 1998;18:1171–87.
5. Thoeni RF. The revised Atlanta classification of acute pancreatitis: its importance for the radiologist and its effect on treatment. Radiology. 2012;262(3):751–64.
6. Balthazar EJ, Robinson DL, Megibow AJ, Ranson JHC. Acute pancreatitis: value of CT in establishing prognosis. Radiology. 1990;174:331–6.
7. Vanzulli GA. Role of MR imaging in the diagnostic work-up of acute pancreatitis. JOP. 2006;7(1):110–2.
8. Linsenmaier U, Wirth S, Reiser M, Körner M. Diagnosis and classification of pancreatic and duodenal injuries in emergency radiology. Radiographics. 2008;28:1591–602.
9. Gupta A, Stuhlfaut JW, Fleming KW, Lucey BC, Soto JA. Blunt trauma of the pancreas and biliary tract: a multimodality imaging approach to diagnosis. Radiographics. 2004;24:1381–95.
10. Lane MJ, Mindelzun RE, Sandhu JS, McCormick VD, Jeffrey RB. CT diagnosis of blunt pancreatic trauma: importance of detecting fluid between the pancreas and the splenic vein. AJR Am J Roentgenol. 1994;163(4):833–5.
11. Henarejos A, Cohen DM, Moossa AR. Management of pancreatic trauma. Ann R Coll Surg Engl. 1983;65:297–300.
12. Ogawa H, Takehara Y, Naganawa S. Imaging diagnosis of autoimmune pancreatitis: computed tomography and magnetic resonance imaging. J Med Ultrason (2001). 2021;48(4):565–71. https://doi.org/10.1007/s10396-021-01145-8.

12

Imaging of Acute Obstetric Disorders

Mohammad Mansouri and Ajay Singh

Introduction

The aims of a first-trimester ultrasound study include localization of the gestational sac, detection of embryonic demise, detection of multiple pregnancies, and confirmation of gestational age. The American College of Obstetrics and Gynecology and the American College of Radiology do not recommend routine ultrasound screening in the first trimester of pregnancy. Typically, the endovaginal probes used for the assessment of first trimester of pregnancy give more information than transabdominal probes and are typically 5–7.5 MHz [1]. Transabdominal probes used in first trimester are often 3.5–5 MHz.

Gestational Age

Fertilization typically occurs within 24 h in the fallopian tube. The zygote migrates and implants on days 22–25 of the menstrual cycle, 4 days prior to the first missed period. The gestational sac progressively increases in size at the age of 1–1.5 mm per day for the first 2 months.

The gestational age is not same as the fertilization age. The fertilization age is counted from the time of fertilization, while the gestational age is 2 weeks more than the fertilization age:

$$\text{Menstrual age} = 30\ \text{days} + \text{gestational sac diameter}\left(1\ \text{mm is equal to } 1\ \text{day}\right)$$

Once the embryonic pole is detected, the crown-rump length (CRL) measurement is considered the most accurate measurement of gestational age (accuracy ±5 days till ≤8 + 6 weeks and ±7 days from 9 + 0 to 13 + 6 weeks). The mean sac diameter is used to measure the gestational age between 5 and 6 weeks of pregnancy or when the embryo is not identified. The biparietal diameter, femur length, head circumference, and abdominal circumference are used for the measurement of gestational age in the second (14 + 0 to 27 + 6 weeks) and third trimesters (28 + 0 weeks onwards) of pregnancy. Biparietal diameter is considered the most reliable marker due to its high reproducibility, except in cases of skull shape variations when head circumference is considered more reliable. Head circumference is also useful for the assessment of growth disorders. Abdominal circumference is the least reliable. Margin of error in determining gestational age using these biomarkers significantly increases past 22 weeks (±14 to 21 days) due to biologically variable fetal growth in advanced gestations.

Normal Pregnancy

Intradecidual sign refers to focal anechoic eccentrically positioned focus within the endometrium, surrounded by thick echogenic wall (Fig. 12.1a). It is due to the presence of a blastocyst embedded in thickened endometrium. Although it can be seen as early as 3.5 weeks of menstrual age, Laing et al. found low sensitivity of 34–66% for this sign [2]. It is a useful sign, especially when the endometrial cavity can be reliably separated from the gestational sac [3, 4].

The gestational sac is eccentric to the endometrial canal and measures 1 mm in diameter when a 4-week blastocyst cavity is present. It is possible to see the gestational sac along with the yolk sac (in chorionic cavity) on ultrasound at 4.5–5-week gestational age (Table 12.1), when it measures up to 1 cm in diameter. The embryo and the amniotic cavity are very small at this gestational age. The gestational sac

---

M. Mansouri
Department of Radiology, Massachusetts General Hospital,
Boston, MA, USA

A. Singh (✉)
Division of Emergency Radiology, Department of Radiology,
Massachusetts General Hospital, Boston, MA, USA

Harvard Medical School, Massachusetts General Hospital,
Boston, MA, USA
e-mail: asingh1@partners.org

© The Author(s), under exclusive license to Springer Nature Switzerland AG 2024
A. Singh (ed.), *Emergency Radiology*, https://doi.org/10.1007/978-3-031-65770-2_12

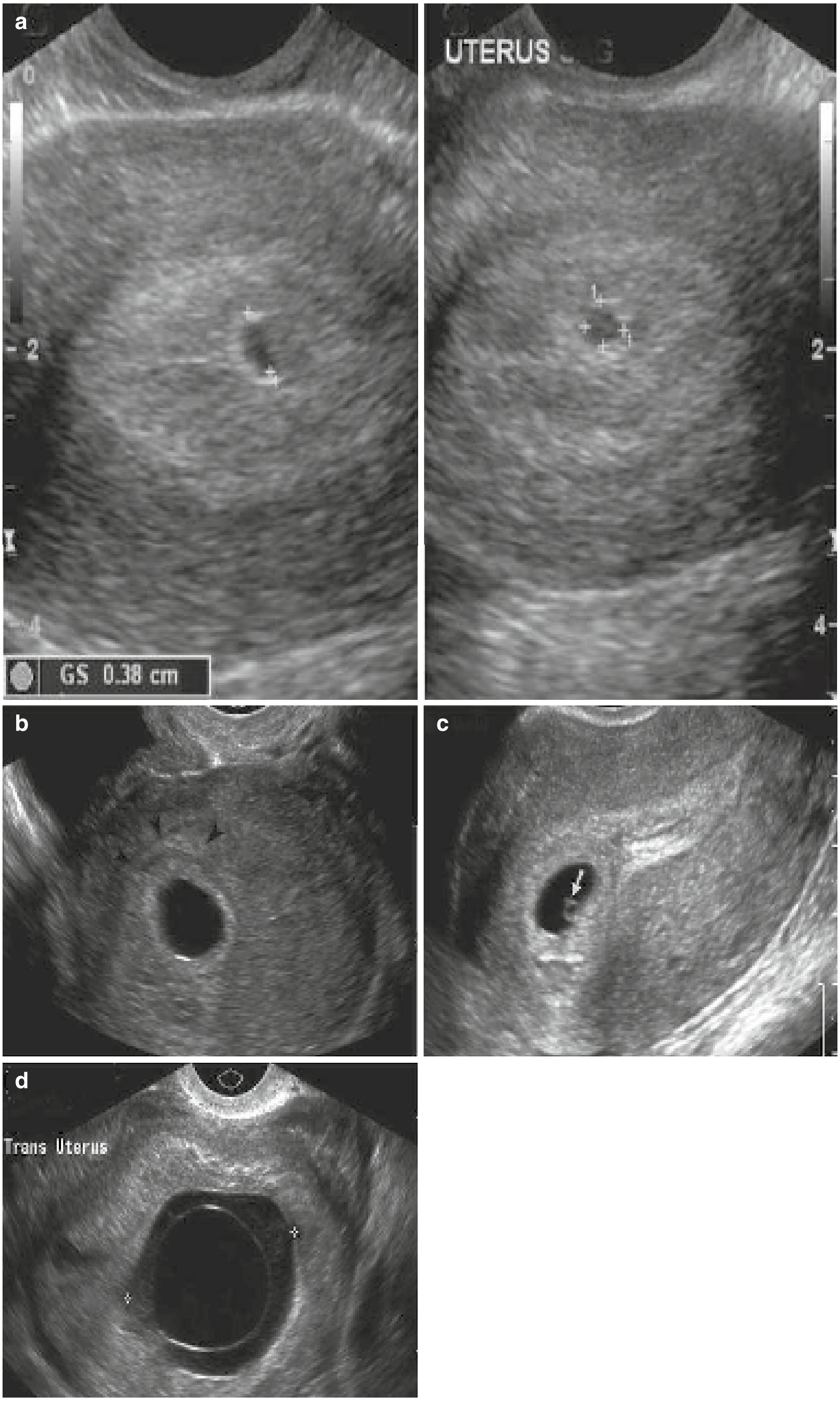

Fig. 12.1 Normal pregnancy. (**a**) Intradecidual sac sign: ultrasound demonstrating a 4-week gestational sac in thickened endometrium, without any identifiable yolk sac or embryo. (**b**) Double-decidual sac sign: ultrasound demonstrating concentric hyperechoic rings produced by chorion and decidua (*arrowheads*), around the gestational sac. (**c**) Six weeks: ultrasound demonstrates a yolk sac (*arrow*) and tiny embryo within a 6-week-old pregnancy. (**d**) Nine weeks: ultrasound demonstrates the anechoic amniotic cavity separated from chorionic cavity by the amnion. The chorionic cavity has low-level echoes due to the presence of high protein concentration

Table 12.1 First-trimester important sonographic milestones on transvaginal ultrasound (TVUS)

Gestational sac	4.5–5 weeks
Yolk sac	5 weeks
Cardiac activity	5.5–6 weeks
Measurable crown-rump length (CRL)	6 weeks

Table 12.2 Criteria for abnormal yolk sac

1. More than 5.6 mm (between 5 and 10 weeks) in diameter
2. Less than 2 mm in diameter (between 8 and 12 weeks)
3. Absence of yolk sac in a gestational sac more than 8 mm in diameter
4. Absence of yolk sac in the presence of embryo during early pregnancy

typically grows at a rate of 1.1 mm/day and measures 1.6 cm by 6 weeks.

Double-decidual sac sign refers to the presence of two concentric rings: the inner one representing chorion and the outer one representing the decidua (see Fig. 12.1b). The presence of double-decidual sign does not exclude the presence of ectopic pregnancy. It is seen in majority of the pregnancies and is best seen when the gestational sac is approximately 10 mm in diameter.

Yolk sac is the first element identified within the gestational sac, typically at 5 weeks of gestation. It is usually less than 5 mm in diameter and spherical in shape (see Fig. 12.1c). A yolk sac which is too small or too large is considered to be abnormal (Table 12.2). The number of yolk sac is equal to the number of amniotic sac. Table 12.3 summarizes imaging indicators of poor prognosis in early pregnancy.

The amnion is barely appreciable when the crown-rump length is 2 mm, at gestational age of 6 weeks. It is normal to see an amnion as a separate membrane between 2 and 4 months of gestation (see Fig. 12.1d). The chorionic fluid is more echogenic than the amniotic fluid because of the presence of a high protein concentration. The amniotic cavity progressively increases in size and fills the subchorionic cavity by 14–16 weeks. Double bleb refers to the visualization of two concentric blebs due to the presence of a yolk sac and amniotic sac.

Although the embryonic cardiac activity begins at day 26 of menstrual age, they are first seen on sonography when the crown-rump length is 5 mm, at approximately 6.2 weeks. If the crown-rump length is less than 5 mm and no embryonic cardiac pulsations are demonstrated, then the ultrasound should be repeated. The embryonic cardiac activity of less than 80 beats/min is associated with high risk of embryonic demise.

The reliable criteria to verify the presence of early intrauterine pregnancy include demonstration of yolk sac within the gestational sac and presence of an embryo with cardiac activity (Table 12.4).

Table 12.3 Indicators of poor prognosis in early pregnancy

1. Irregular, low-lying gestational sac
2. Calcified, >7 mm yolk sac
3. Empty, enlarged, or expanded amnion
4. Amorphous shaped embryo
5. Cardiac pulse rate of <85 beats/min
6. Hydropic changes in chorionic villi
7. Large, subchorionic hemorrhage occupying >2/3 of the gestational sac circumference

Table 12.4 Morphologic findings of pregnancy and the corresponding gestational ages when they appear

Last menstrual period	0 week
Conception	2 weeks
Gestational sac	4.5 weeks (in all by 5 weeks)
Yolk sac	5–5.5 weeks
Embryo	5.7–6.1 weeks
Embryonic cardiac pulsations	6.2 weeks; lower limit is 100 beats/min
Amniotic membrane	6.5–7 weeks
Spine	7–8 weeks
Limb buds, head curvature separates from body	8 weeks
Intrinsic embryonic motion	8–8.5 weeks

Typically, transabdominal ultrasound is positive for pregnancy when beta-hCG level is more than 3600. Intrauterine pregnancies should be seen on transvaginal ultrasound in all when the beta-hCG level is more than 2000.

Abnormal Gestational Sac

Anembryonic gestation refers to the presence of gestational sac without an embryo. It is due to embryonic death with continued development of the trophoblast and is often due to underlying chromosomal abnormality.

The most important criteria for detection of anembryonic pregnancy are the absence of embryo when the mean sac diameter on transvaginal ultrasound study is more than 18 mm and the absence of yolk sac when the mean sac diameter is more than 13 mm on transvaginal sonography (Figs. 12.2 and 12.3; Table 12.5). Since these criteria are not foolproof, a follow-up ultrasound should be performed in 7–10 days' time to rule out the possibility of normal pregnancy.

When the fetal pole is more than 6 mm in diameter and no fetal cardiac pulsations are demonstrated, the findings are suggestive of silent miscarriage. If the fetal pole is less than 6 mm in diameter and no fetal cardiac pulsations are demonstrated, then the patient should be rescanned in a week's time to distinguish live from failed pregnancy. If no fetal cardiac activity is seen on 1-week follow-up ultrasound study, then the findings indicate a silent miscarriage.

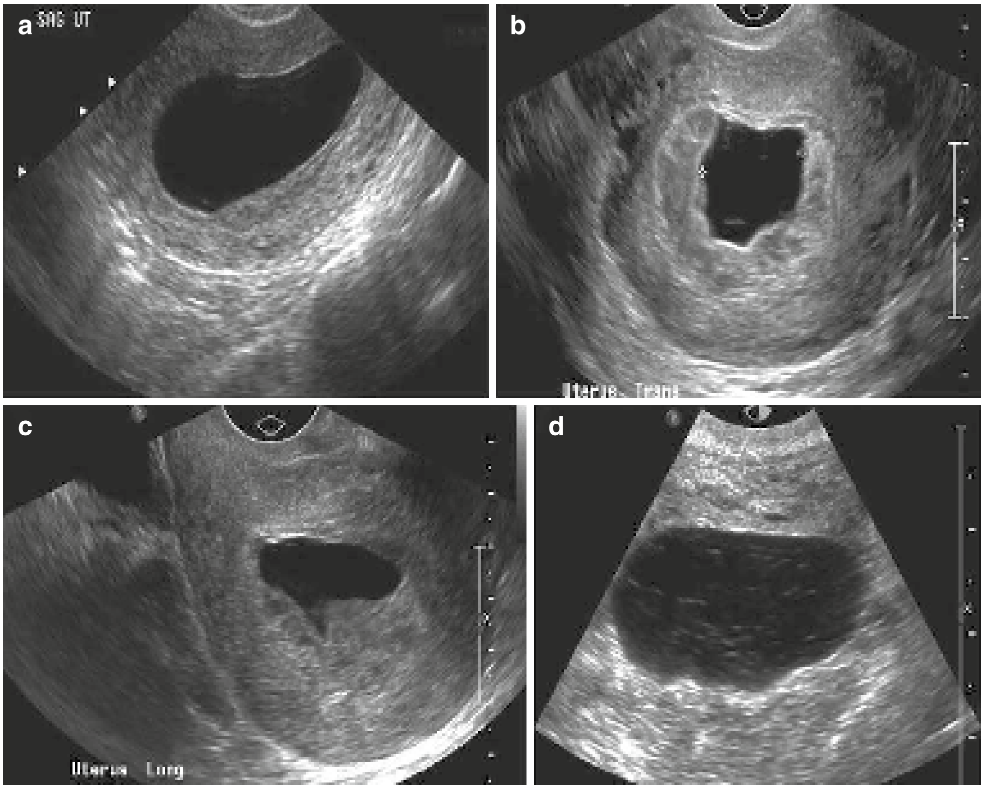

Fig. 12.2 Abnormal gestational sac: anembryonic pregnancy. (**a**) Ultrasound demonstrates anembryonic gestational sac in 8-week-old pregnancy. Lack of embryo in a gestational sac measuring more than 13 mm in diameter is considered abnormal on transvaginal ultrasound. (**b**, **c**) Ultrasound shows irregular outline of the anembryonic gestational sac on transvaginal ultrasound. (**d**) Ultrasound shows anembryonic 8-week gestational sac, containing low-level internal echoes

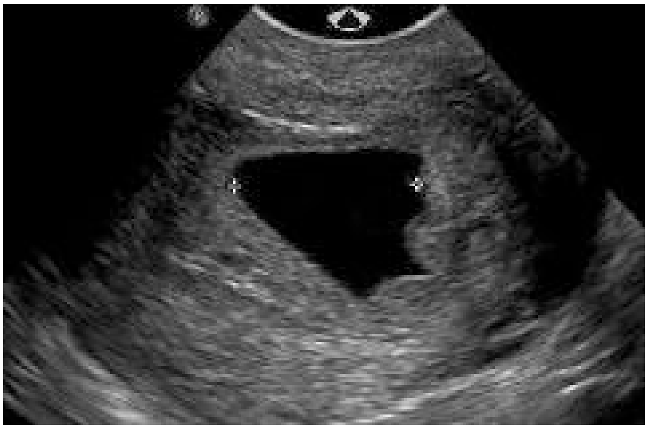

Fig. 12.3 Anembryonic pregnancy. Ultrasound demonstrates irregular appearance of gestational sac without any embryo. The absence of embryo when the mean sac diameter on transvaginal ultrasound study is more than 18 mm indicates anembryonic pregnancy

Table 12.5 Imaging findings of anembryonic pregnancy

1. Absent embryo when mean sac diameter is 18 mm
2. Absent yolk sac when the mean sac diameter is 13 mm
3. Low-lying gestational sac
4. Irregular shape of the gestational sac (see Fig. 12.2b, c)
5. Thin decidual reaction of less than 2 mm thickness
6. Absence of double-decidual sac sign
7. Presence of fluid-fluid level or debris within the gestational sac (see Fig. 12.2d)

Small sac size, defined by difference of less than 5 mm between mean sac diameter and crown-rump length, is associated with high miscarriage rates. Missed abortion refers to retention of pregnancy for more than or equal to 2 months.

Pregnancy Termination Failure

Termination of pregnancy could be performed within 72 h with more than 80% success rate with the use of oral misoprostol and mifepristone. In case of failed termination, the sonographic features include presence of intrauterine mass and increased vascularity. The lack of blood flow, however, does not exclude the presence of retained products of conception. The absence of color Doppler flow favors that the products of conception are nonviable and therefore will pass out spontaneously without the use of dilatation and curettage (Fig. 12.4a, b). Retained products of conception typically produce irregular interface between endometrium and myometrium. If no endometrial mass or fluid is seen and the endometrial stripe thickness is less than 10 mm, retained products of conception are very unlikely. MR imaging may show intracavitary uterine mass with variable enhancement and junctional zone obliteration (see Fig. 12.4c, d).

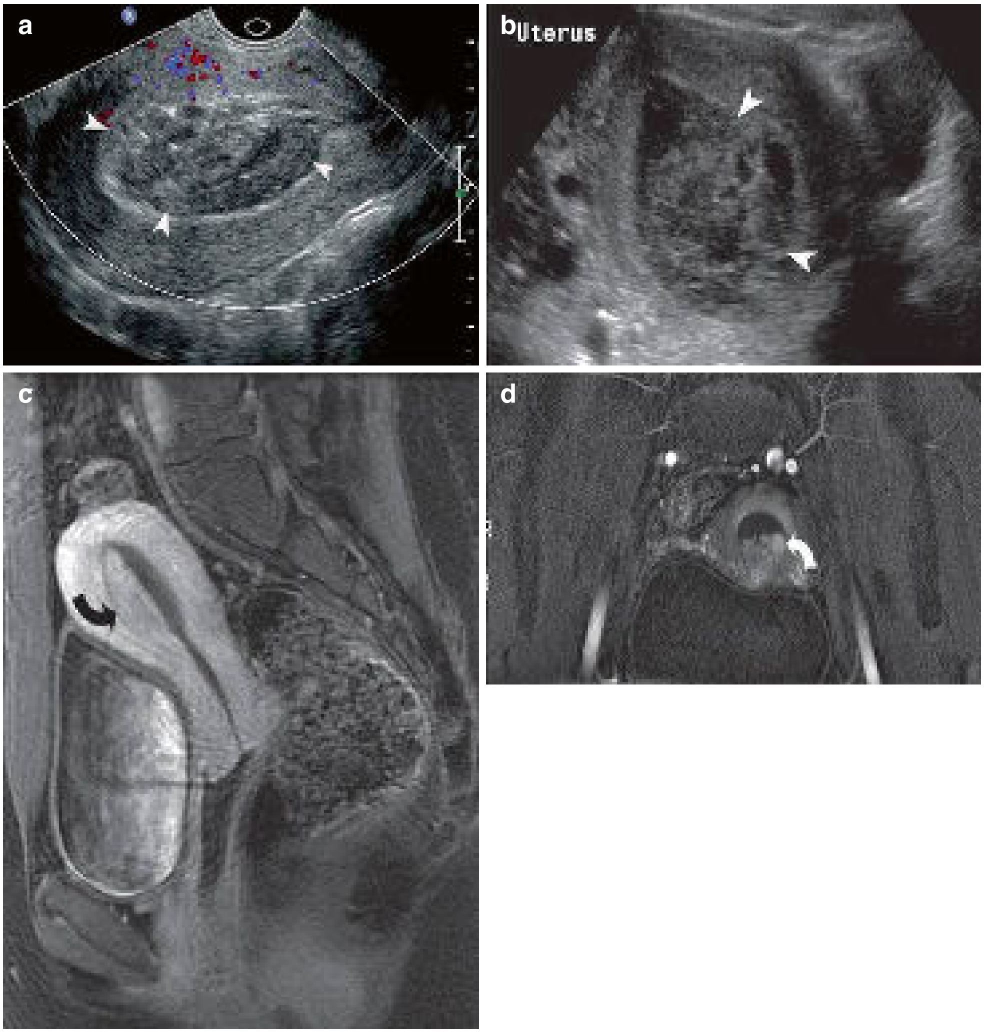

Fig. 12.4 Retained products of conception. Ultrasound demonstrates retained blood clots (**a**) (*arrowheads*) and products of conception (**b**) (*arrowheads*) present within the endometrial cavity. Gadolinium-enhanced MRI (**c**, **d**) demonstrates enhancement of the retained products of conception (*curved arrows*)

Subchorionic Hemorrhage

Subchorionic hemorrhage is the most common type of intrauterine chorionic bleed, and it refers to separation of the chorionic membrane from the decidua vera by a hematoma. The incidence is reported to be between 4 and 22%. Up to 70% of cases are associated with spontaneous resolution by the end of second trimester. The subchorionic hemorrhage is initially isoechoic or hyperechoic to the placenta and progressively becomes hypoechoic (Fig. 12.5). Associated complications of subchorionic hematoma include early and late pregnancy loss, placental abruption, preterm premature rupture of the membranes, and preterm delivery. The earlier the gestational age and larger the size of the hemorrhage, the more are the chances of pregnancy loss and other adverse outcomes from subchorionic hemorrhage. We typically describe the size of subchorionic hemorrhage in relation to the proportion (<1/3, 1/3–2/3, >2/3, etc.) of circumference of the gestational sac covered by the hematoma. The rate of abortion is reported to be 7.7% for small hematomas (<1/3 the circumference of the gestational sac), 9.2% for medium hematomas (1/3–1/2 the circumference of the gestational sac), and 18.8% for large hematomas (>2/3 the circumference of the gestational sac).

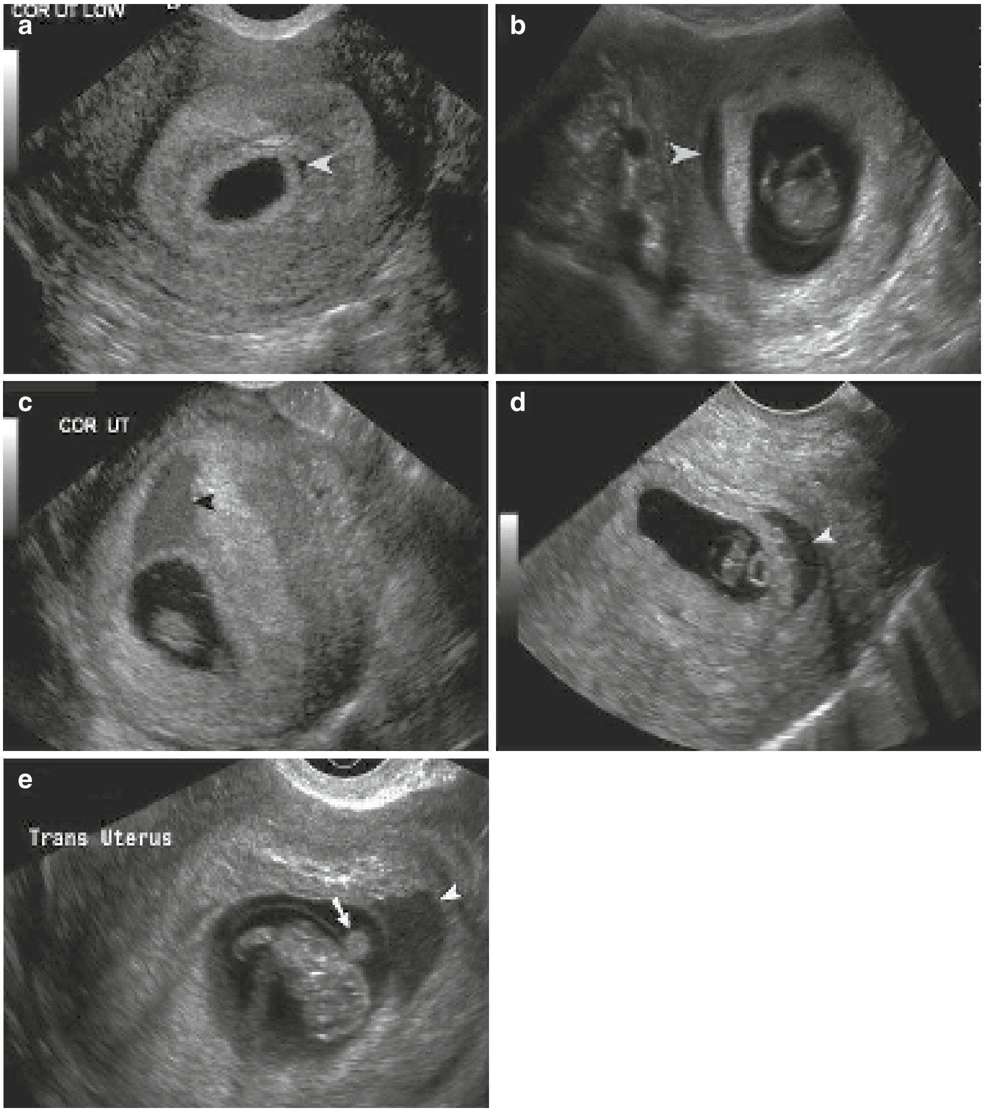

Fig. 12.5 Subchorionic hemorrhage. (**a**–**e**) Ultrasound demonstrates sickle-shaped subchorionic hemorrhage (*arrowhead*) in five different patients. An abnormally large and echogenic yolk sac (*arrow*) is identified within the chorionic cavity (**e**)

Ectopic Pregnancy

Ectopic pregnancy is one of the most serious and potentially fatal causes of acute pelvic pain. It most commonly presents around 6 weeks' gestation. It accounts for 1.4–2% of all pregnancies and 4.5% of all in vitro pregnancies. Ectopic pregnancy is responsible for 15% of maternal deaths. The most common location of ectopic pregnancy is in the ampulla, followed by isthmus, fimbria, and cornua of the fallopian tube, in descending frequency. The second most common site of ectopic pregnancy which occurs in approximately 2% is in the intramural portion of the fallopian tube. The presence of a mass within the ovary is unlikely to be ectopic pregnancy because of the rarity of ectopic pregnancy within the ovary. The risk factors for ectopic pregnancy include pelvic inflammatory disease, history of ectopic pregnancy, endometriosis, pelvic surgery, infertility treatment, early age at first intercourse, and uterotubal abnormalities. The use of intrauterine device does not increase the risk of ectopic pregnancy.

Ectopic gestational sac can be seen on ultrasound study in anywhere from one-fourth to two-thirds of the cases. The combination of adnexal mass and pelvic free fluid in patients with suspicion of ectopic pregnancy has a high positive predictive value. In up to one-third of patients with proven ectopic pregnancy, the adnexal ultrasound study is normal, while in one-fifth of the cases, a live embryo can be seen within the adnexa. High suspicion of ectopic pregnancy should be raised when there is no intrauterine pregnancy identified on ultrasound, in a patient with menstrual age of more than 5 weeks and a positive beta-hCG level. Hemoperitoneum can be very subtle on ultrasonography. However, it is a very sensitive finding (93%) for ruptured ectopic pregnancy. This finding should be reported immediately as intraperitoneal bleeding can be fatal. Right upper quadrant should always be scanned in

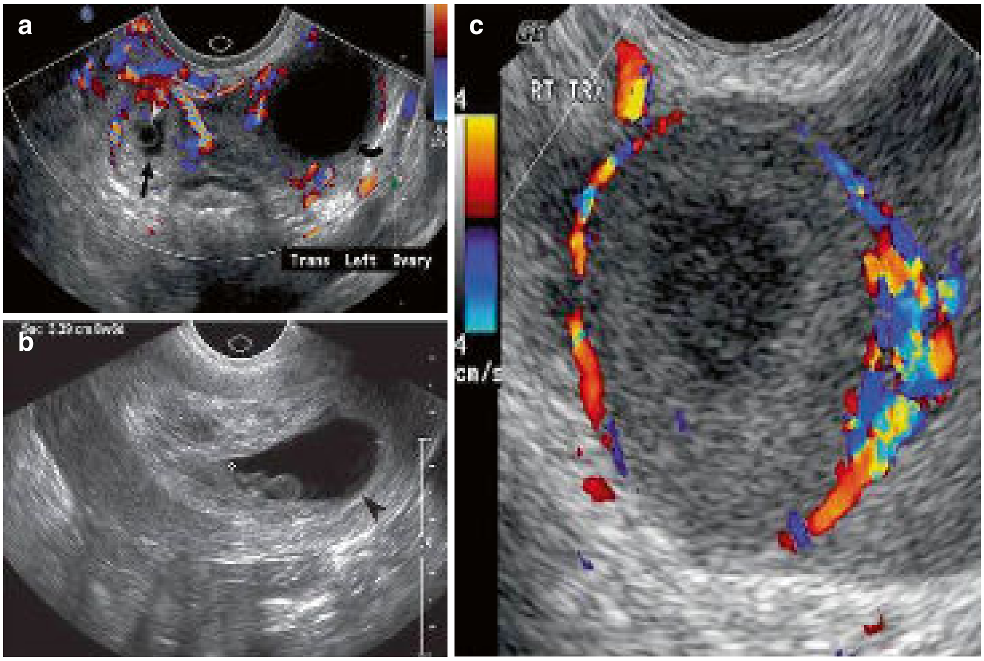

Fig. 12.6 Ectopic pregnancy. (**a**) Left adnexal ectopic pregnancy is indicated by the presence of gestational sac (*arrow*) and yolk sac (*arrowhead*), adjacent to the left ovary (*curved arrow*). (**b**) Sagittal ultrasound image demonstrates ectopic pregnancy in the cervical canal (*arrowhead*). (**c**) Hemorrhagic luteal cyst seen in the left ovary in a patient who had a recent abortion. The rarity of ectopic pregnancy within the ovary makes that diagnosis very unlikely in this case

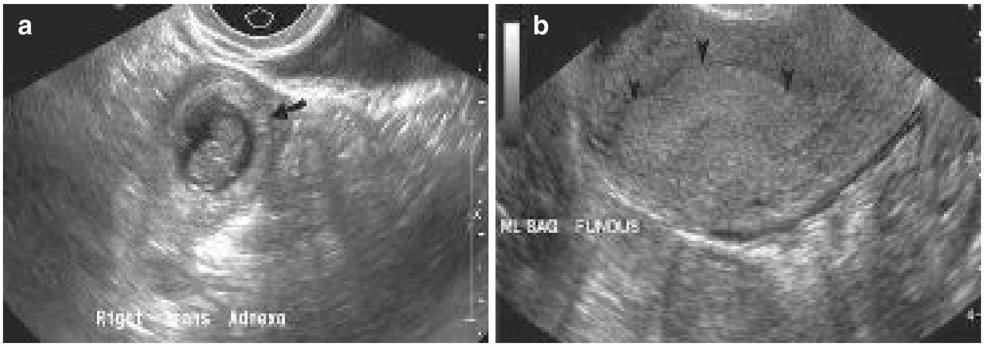

Fig. 12.7 Ectopic pregnancy. (**a**) Ectopic tubal ring is indicated by an ectopic gestational sac (*arrow*) surrounded by echogenic trophoblast in the right pelvic adnexa. (**b**) There is decidual reaction (*arrowheads*) identified within the uterus of the same patient with ectopic pregnancy

the search for hemoperitoneum. Morison's pouch is the most dependent part of the peritoneum and may contain a large volume of blood.

Ectopic tubal ring consists of a 2–4 mm echogenic rim surrounding a hypoechoic center and is present in 49–68% of cases [5]. The echogenic rim is produced by trophoblast around the chorionic sac, which is more echogenic than the ovarian parenchyma (Figs. 12.6 and 12.7). The color Doppler flow in the fallopian tube on the affected side is typically high velocity with low impedance. The lower resistive index in the affected fallopian tube is believed to be due to invasion of the trophoblast [6, 7]. The ring-of-fire sign refers to increased color Doppler flow, which can be seen with ectopic pregnancy as well as corpus luteum. The presence of flow within the ectopic pregnancy indicates viable tissue and can be treated with either methotrexate or laparoscopic surgery. Since there are a significant number of patients who have intrauterine pregnancy even when the beta-hCG is more than 2000 and ultrasound fails to demonstrate a gestational sac, these patients should not be automatically considered to have ectopic pregnancy.

Interstitial Ectopic Pregnancy

In these patients, the pregnancy is in the intramural portion of the fallopian tube and is surrounded by myometrial tissue which has richer blood supply, which allows the pregnancy to progress into the second trimester. The clinical significance of interstitial ectopic pregnancy is that it has a tendency to rupture later, leading to higher mortality than other cases of ectopic pregnancy.

The ultrasound finding of interstitial ectopic pregnancy is thinning of the myometrium on one side of the gestational sac, which is present eccentrically in the fundus, in relation to the endometrial cavity. Typically, the myometrial thickness on the outer aspect of the gestational sac is less than 5 mm (Fig. 12.8).

Interstitial line sign is characterized by the extension of echogenic line from the interstitial ectopic pregnancy to the endometrial echo complex. It has an 80% sensitivity in making the diagnosis of an interstitial ectopic pregnancy, compared to 40% sensitivity for eccentric gestational sac [8].

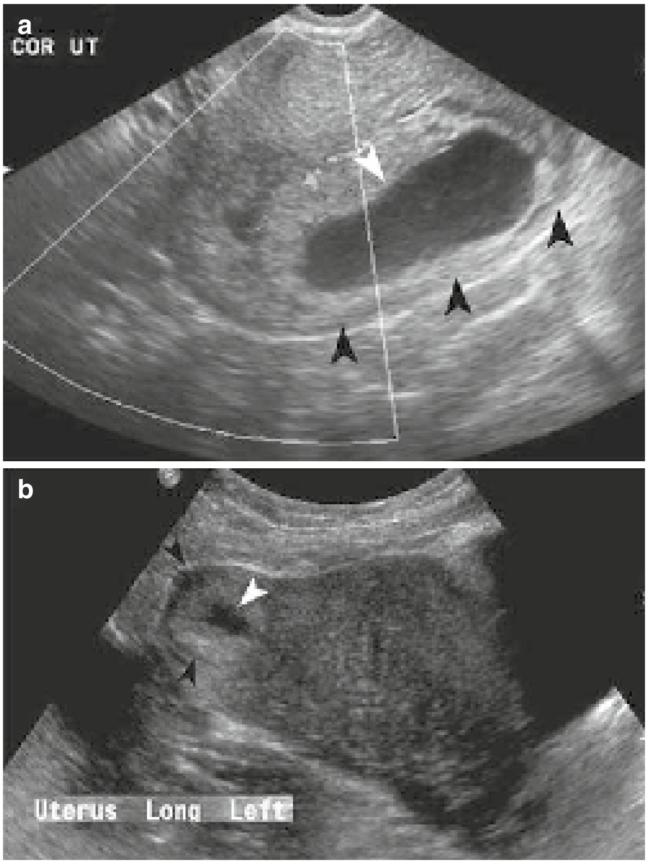

Fig. 12.8 Cornual ectopic pregnancy. (**a**, **b**) Ultrasound demonstrates eccentric gestational sac (*white arrowhead*) with thinning of the myometrium (*black arrowhead*) to less than 5 mm

Heterotopic Pregnancy

Heterotopic pregnancy refers to the simultaneous presence of intrauterine as well as ectopic pregnancy (Figs. 12.9 and 12.10). The frequency of heterotrophic pregnancy has increased with the usage of ovulation induction medications. The extrauterine pregnancy is most commonly within the fallopian tube (94%) [9]. The frequency of heterotrophic pregnancy, which was estimated to be about 1 in 30,000 in general population, has now increased to as much as 1 in 100, in patients undergoing fertility treatment. The current frequency of heterotrophic pregnancy is between 1 in 4000 and 1 in 7000 [10, 11]. Treatment is usually surgical. Alternative treatment is US-guided injection of potassium chloride to a nonviable and nonruptured ectopic pregnancy. The beta-hCG is often within the normal range due to the coexisting intrauterine pregnancy.

Fig. 12.9 Heterotopic pregnancy. (**a**, **b**) T2-weighted MRI demonstrates heterogeneous right adnexal ectopic pregnancy (*arrowheads*) and intrauterine pregnancy (*arrow*)

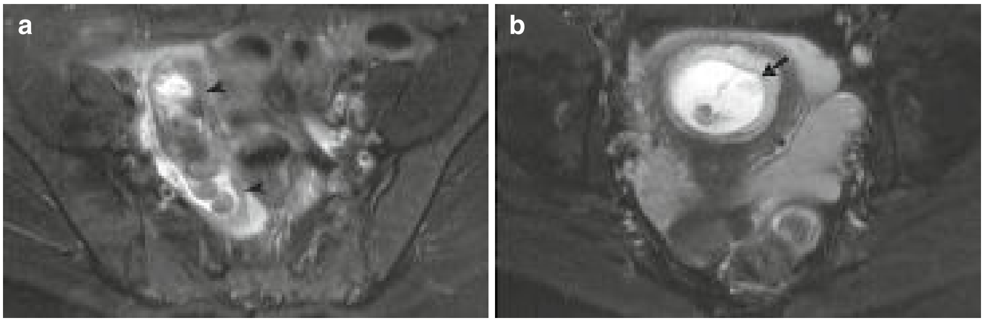

Fig. 12.10 Heterotopic pregnancy. (**a**) Ultrasound of the adnexa demonstrates heterotopic pregnancy (*arrowhead*) located adjacent to the ovary. (**b**) Ultrasound depicts an intrauterine gestational sac, containing a yolk sac

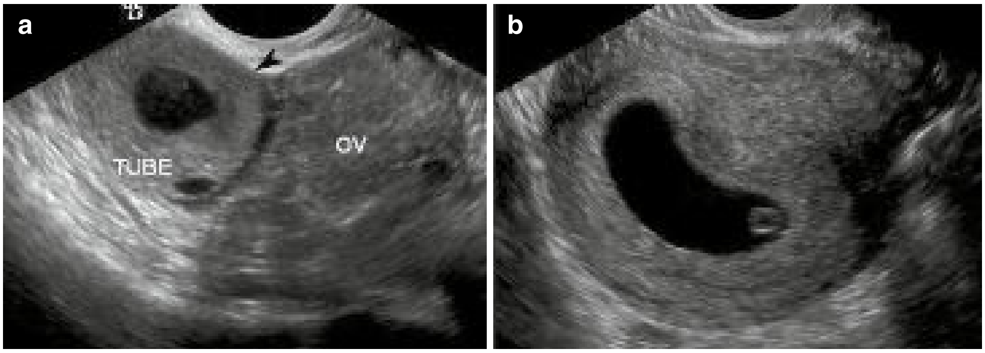

Molar Pregnancy

Partial H mole is caused by two sperms penetrating the ovum, resulting in a total of 69 chromosomes, instead of 46. A complete H mole is usually caused by a single sperm fertilizing an ovum, which has lost its chromosomes. The sperm replicates its chromosomes to produce 46 chromosomes. Approximately 20% of complete H moles and 2% of partial H mole lead to gestational trophoblastic disease. Abnormal bleeding for more than 6 weeks after any pregnancy should be evaluated with beta-hCG measurement to exclude a new pregnancy or gestational trophoblastic disease. The classic clinical triad of hypertension, hyperemesis, and excessive uterine growth may not be present until the second trimester.

Ultrasound alone is not enough in diagnosing molar pregnancy and has a sensitivity of only 34%. The sensitivity is higher for complete H mole (58%) than partial H mole (17%) [12]. Almost two-thirds of the molar pregnancy cases will be missed in ultrasound evaluation because the sonographic appearance is that of missed abortion or anembryonic pregnancy. The diagnostic ultrasound appearance of molar pregnancy is that of cystic spaces caused by hydropic villi. The heterogeneous mass produced by the molar pregnancy may have a snowstorm appearance (Figs. 12.11 and 12.12a, b). In partial mole, enlarged placenta with scattered cysts may create a "Swiss cheese" appearance. The ovaries are enlarged, and theca lutein cysts are seen in up to 40% of cases due to overstimulation by beta-hCG. Theca lutein cysts are typically multiloculated and bilateral (see Fig. 12.12c).

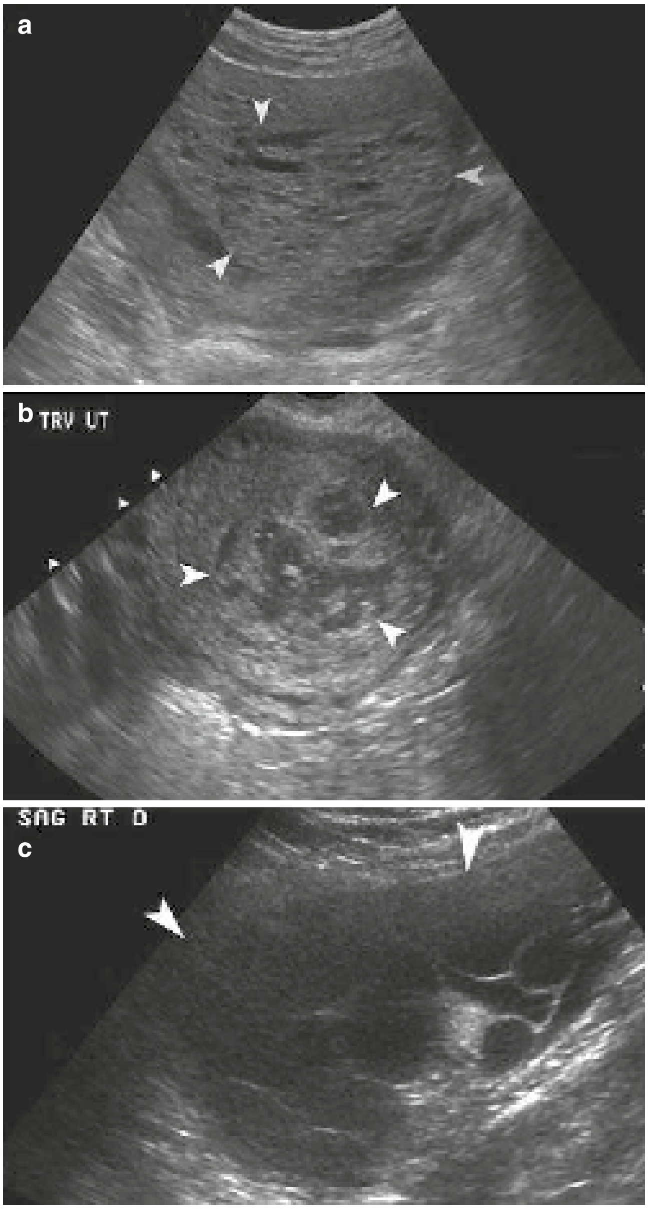

Fig. 12.12 Molar pregnancy. (**a**, **b**) Ultrasound of the uterus in two patients demonstrates heterogeneous echogenicity mass (*arrowheads*) located within the uterus. (**c**) Ultrasound of a patient with molar pregnancy demonstrates an enlarged ovary (*arrowheads*) measuring more than 8 cm in diameter and containing multiple large theca lutein cysts

Fig. 12.11 Molar pregnancy. (**a**, **b**) Ultrasound demonstrates heterogeneous (*arrowhead*) solid as well as cystic (hydropic villi) areas distending the endometrial cavity with increased color Doppler flow

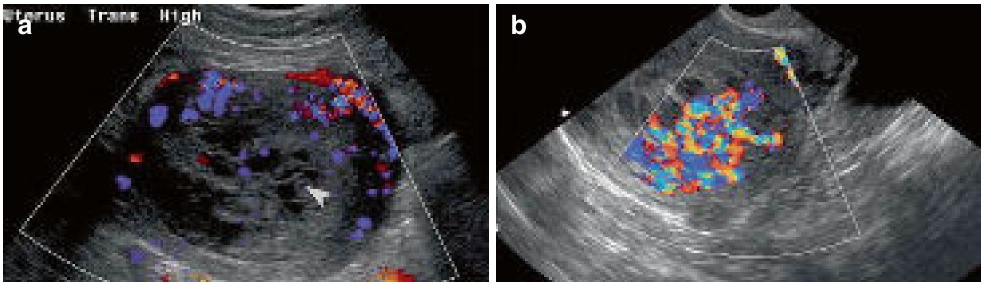

Placenta Previa

Placenta previa refers to abnormally low-lying placenta, covering the cervical internal os partially or completely. Placenta previa can be classified as marginal (placenta reaches the edge of cervix), partial (placenta partially overlies the cervical opening), or complete (placenta completely covers the cervical os).

Diagnosis depends on sonographic evidence of placenta overlaying cervical internal os during the second or third trimester (Fig. 12.13a, b). Transvaginal ultrasound is preferred over transabdominal ultrasound. The extent of placenta covering the internal os (in millimeters) should also be reported. On routine 18–20-week ultrasound, placenta previa is a relatively common finding and is much less predictive. Therefore, follow-up ultrasound is required at 32–34 weeks gestation for confirmation.

Teaching Points

- The yolk sac and embryo should be visualized on transvaginal ultrasound when the mean sac diameters are 13 mm and 18 mm, respectively.
- Lack of embryonic cardiac pulsations in an embryo measuring 6 mm in diameter warrants a follow-up ultrasound to evaluate for embryonic demise.
- The crown-rump length is the preferred mode of measurement of gestational age in the first trimester of pregnancy, whenever possible.
- Embryonic heart rate of less than 80 is associated with poor outcome in the first trimester.
- The ring-of-fire sign refers to increased color Doppler flow, which can be seen with ectopic pregnancy as well as corpus luteum.
- The diagnostic ultrasound appearance of molar pregnancy is that of cystic spaces caused by hydropic villi.

Questions

1. Where is the least common site of ectopic pregnancy?
   (A) Ampulla
   (B) Isthmus
   (C) Fimbria
   (D) Cornua
   Answer: D

2. Which of the following is the imaging finding seen in anembryonic pregnancy?
   (A) Presence of debris within the gestational sac
   (B) Presence of double-decidual sac sign
   (C) Decidual reaction of more than 2 mm thickness
   (D) Absence of fluid–fluid level in the gestational sac
   Answer: A

3. What is the imaging diagnosis (Fig. 12.14) of a patient with positive beta-hCG and abdominal pain?
   (A) Corpus luteal cyst
   (B) Ectopic pregnancy
   (C) Endometrioma
   (D) Functional ovarian cyst
   Answer: C

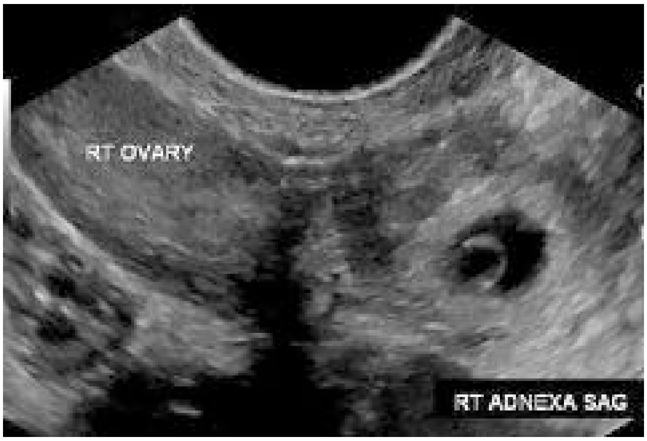

Fig. 12.14 Endometrioma—abdomen

Fig. 12.13 Placenta previa. (**a**) Ultrasound of the pelvis demonstrates placenta previa extending over the internal os (arrow). Hemorrhagic blood products are seen in the endocervical canal. (**b**) Sagittal ultrasound of the pelvis demonstrates complete placenta previa (arrows) in third-trimester pregnancy

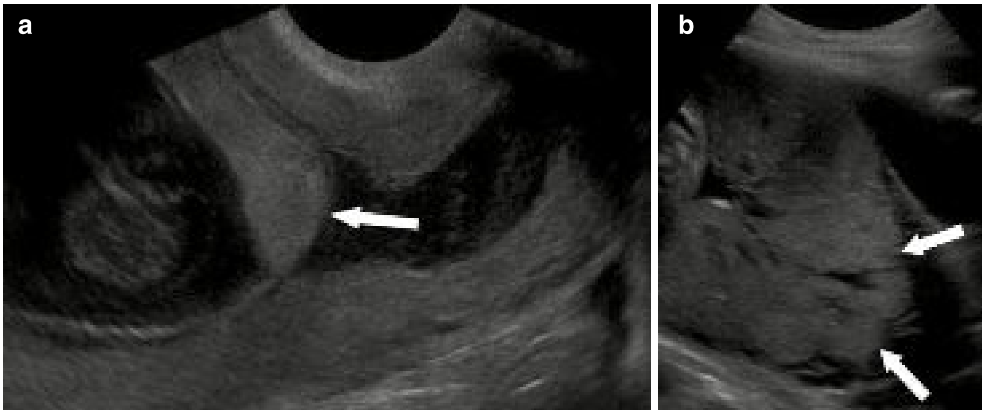

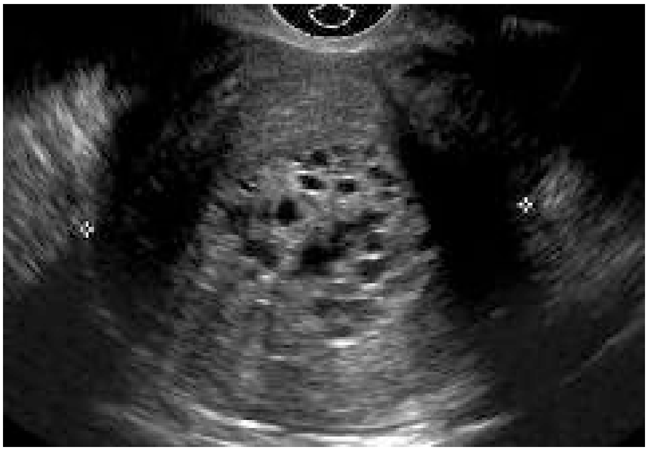

Fig. 12.15 Hydatidiform mole—ultrasound

4. What is the pathology seen on the ultrasound (Fig. 12.15) of a patient with hyperemesis?
   (A) Endometrial carcinoma
   (B) Hydatidiform mole
   (C) Endometritis
   (D) Degenerating fibroid
   Answer: B

References

1. Kaur A, Kaur A. Transvaginal ultrasonography in first trimester of pregnancy and its comparison with transabdominal ultrasonography. J Pharm Bioallied Sci. 2011;3(3):329–38.
2. Laing FC, Brown DL, Price JF, Teeger S, Wong ML. Intradecidual sign: is it effective in diagnosis of an early intrauterine pregnancy? Radiology. 1997;204:655–60.
3. Yeh HC. Efficacy of the intradecidual sign and fallacy of the double decidual sac sign in the diagnosis of early intrauterine pregnancy. Radiology. 1999;210(2):579–82.
4. Yeh HC, Goodman JD, Carr L, Rabinowitz JG. Intradecidual sign: a US criterion of early intrauterine pregnancy. Radiology. 1986;161:463–7.
5. Fleischer AC, Pennell RG, McKee MS, Worrell JA, Keefe B, Herbert CM, et al. Ectopic pregnancy: features at transvaginal sonography. Radiology. 1990;174(2):375–8.
6. Szabó I, Csabay L, Belics Z, Fekete T, Papp Z. Assessment of uterine circulation in ectopic pregnancy by transvaginal color Doppler. Eur J Obstet Gynecol Reprod Biol. 2003;106(2):203–8.
7. Kirchler HC, Kölle D, Schwegel P. Changes in tubal blood flow in evaluating ectopic pregnancy. Ultrasound Obstet Gynecol. 1992;2(4):283–8.
8. Ackerman TE, Levi CS, Dashefsky SM, Holt SC, Lindsay DJ. Interstitial line: sonographic finding in interstitial (cornual) ectopic pregnancy. Radiology. 1993;189:83–7.
9. Reece EA, Petrie RH, Sirmans MF, Finster M, Todd WD. Combined intrauterine and extrauterine gestations: a review. Am J Obstet Gynecol. 1998;146:323–30.
10. Hann LE, Bachman DM, McArdle CR. Coexistent intrauterine and ectopic pregnancy: a reevaluation. Radiology. 1984;152:151–4.
11. Rizk B, Tan SL, Morcos S. Heterotopic pregnancy after in vitro fertilization and embryo transfer. Am J Obstet Gynecol. 1991;164:161–4.
12. Sebire NJ, Rees H, Paradinas F, Seckl M, Newlands E. The diagnostic implications of routine ultrasound examination in histologically confirmed early molar pregnancies. Ultrasound Obstet Gynecol. 2001;18:662.

13

Imaging of Acute Gynecologic Disorders

Chris Malcolm, Amisha R. Khicha, Mohammad Mansouri,
and Ajay Singh

Introduction

Pelvic pain is one of the most common causes for presentation to the emergency department. A variety of gynecological processes may be the etiology for pelvic pain; hemorrhagic ovarian cysts, pelvic inflammatory disease, ovarian torsion, endometriosis, cystitis, ovarian vein thrombosis, and ovarian hyperstimulation syndrome are a few of the most commonly encountered pathologies. Before medical imaging is performed for the evaluation of pelvic pain, it is important to obtain relevant clinical history and review available laboratory information. The patient's age and pregnancy status are of particular importance in the differential diagnosis; therefore, serum beta-hCG laboratory evaluation is performed if there is even a remote possibility of pregnancy.

Transvaginal and transabdominal ultrasound are the workhorse modalities for the evaluation of pelvic pain when a gynecological etiology is suspected. Transvaginal and/or transabdominal ultrasound are both considered equally appropriate when evaluating pelvic pain; this is true whether the serum beta-hCG is positive or negative and whether a gynecologic or nongynecologic etiology is suspected.

Magnetic resonance imaging may be appropriate in the evaluation of pelvic pain in pregnant and nonpregnant women when ultrasound is nondiagnostic. The limitations of MR include limited availability, long imaging time, high cost, and motion artifacts from peristalsing bowel.

CT is not the frontline imaging modality in the evaluation of pelvic pain when a gynecologic etiology is suspected. It is the most appropriate imaging modality for acute pathologies of the gastrointestinal or urinary tract.

Functional Ovarian Cysts

The normal ovary in the preovulation period shows multiple simple follicles including a dominant follicle which usually measures less than 2.5 cm. At ovulation, the dominant follicle ruptures, releasing an egg and a small amount of free fluid. Following ovulation, the dominant follicle becomes the corpus luteum cyst, which usually measures less than 2.5 cm in maximal diameter and demonstrates a peripheral ring of increased vascularity on Doppler ultrasound. The regressing corpus luteum eventually forms the corpus albicans [1].

During the ovarian cycle, multiple events may occur which would prompt a visit to the emergency department. Many women experience varying degrees of pain during rupture of the dominant follicle at ovulation; the term mittelschmerz ("middle pain") is used to describe this pain accompanying rupture of the normal dominant follicle with release of the egg. A woman may experience pain from peritoneal irritation from the cyst rupture or pain due to hemorrhage into a cyst. Most ruptured ovarian cysts or hemorrhagic ovarian cysts are physiologic [2].

Imaging

Simple ovarian cysts are anechoic without septations on ultrasound. In premenopausal women, if these simple cysts are less than or equal to 5 cm, they are mostly benign. In general, the incidence of malignancy in simple cysts <7.5 cm is very low. In postmenopausal patients, simple cysts less than 1 cm do not require follow-up. If the features of an ovarian cyst are

---

C. Malcolm
Imaging Center of Idaho, Caldwell, ID, USA

A. R. Khicha
Department of Radiology, Wesley Medical Center, University of Kansas-Wichita, Wichita, KS, USA

M. Mansouri
Department of Radiology, Massachusetts General Hospital, Boston, MA, USA

A. Singh (✉)
Division of Emergency Radiology, Department of Radiology, Massachusetts General Hospital, Boston, MA, USA

Harvard Medical School, Massachusetts General Hospital, Boston, MA, USA
e-mail: asingh1@partners.org

© The Author(s), under exclusive license to Springer Nature Switzerland AG 2024
A. Singh (ed.), *Emergency Radiology*, https://doi.org/10.1007/978-3-031-65770-2_13

concerning for malignancy (i.e., thick septations, mural nodularity, or contrast enhancement), surgical consultation would be recommended regardless of the sonographic appearance.

A ruptured ovarian cyst does not have a specific appearance, and often the only finding is the presence of free fluid in the pelvis. Almost half of the women will have some free fluid in the pouch of Douglas on ultrasound during normal ovulation; therefore, correlation with patient symptoms is necessary.

Hemorrhagic ovarian cysts on ultrasound classically have a hypoechoic appearance with a reticular pattern of internal echoes sometimes described as lacelike, spiderweb, or fishnet. Hemorrhagic cysts in premenopausal patients which measure greater than 5 cm should undergo follow-up imaging in 6–12 weeks on days 3–10 of the menstrual cycle (Fig. 13.1). Postmenopausal patients should never have a hemorrhagic cyst [1]. Hemoperitoneum resulting from a ruptured hemorrhagic ovarian cyst may be demonstrated as a large amount of complex fluid in the pelvis on ultrasound. CT reveals hyperdense fluid within the peritoneal space and possible hyperdense sentinel clot adjacent to the hemorrhagic cyst. On MRI, hemorrhagic cyst is most often T2 hyperintense, and hemorrhagic ascites is T1 hyperintense (Fig. 13.2) [3]. Table 13.1 summarizes the imaging findings in ovarian cysts.

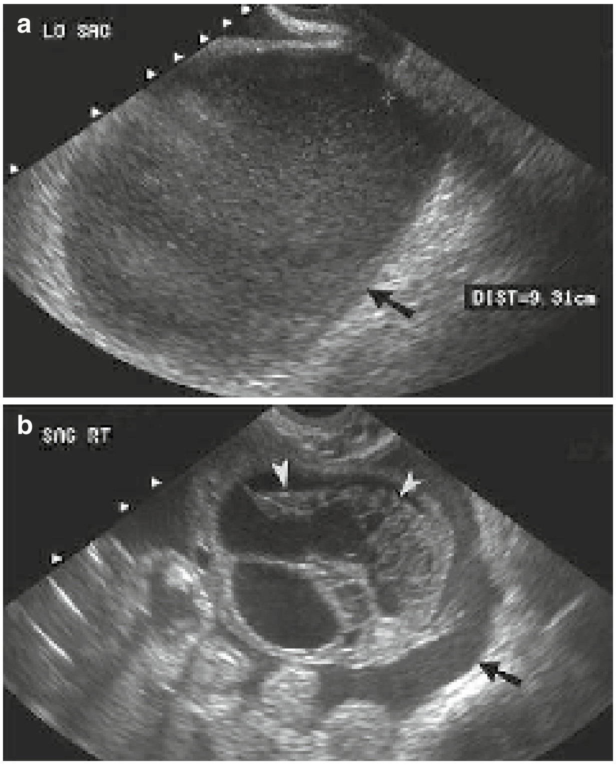

Fig. 13.1 Corpus luteal cyst. (**a**) Sagittal grayscale transabdominal ultrasound image of the pelvis demonstrates a large, cystic lesion (*arrow*) with relatively homogeneous internal echogenicity and posterior acoustic enhancement. (**b**) Ultrasound study demonstrates a hemorrhagic functional ovarian cyst containing a blood clot (*arrowhead*). There is surrounding hemorrhagic fluid (*straight arrow*) that is also seen in the adnexa. (**c**) Axial T2-weighted MR image of the pelvis shows a T2 hyperintense corpus luteal cyst in the left hemipelvis (*arrow*). Note the thin wall and lack of internal septations or nodularity

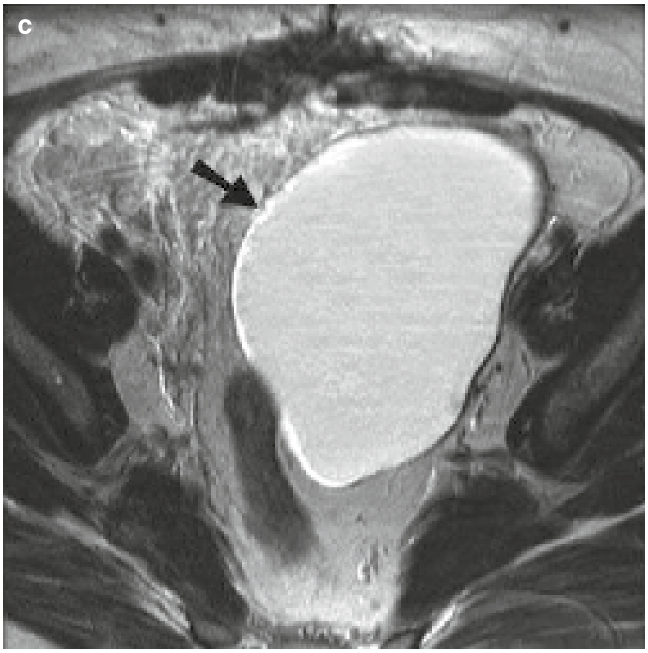

Fig. 13.1 (contimued)

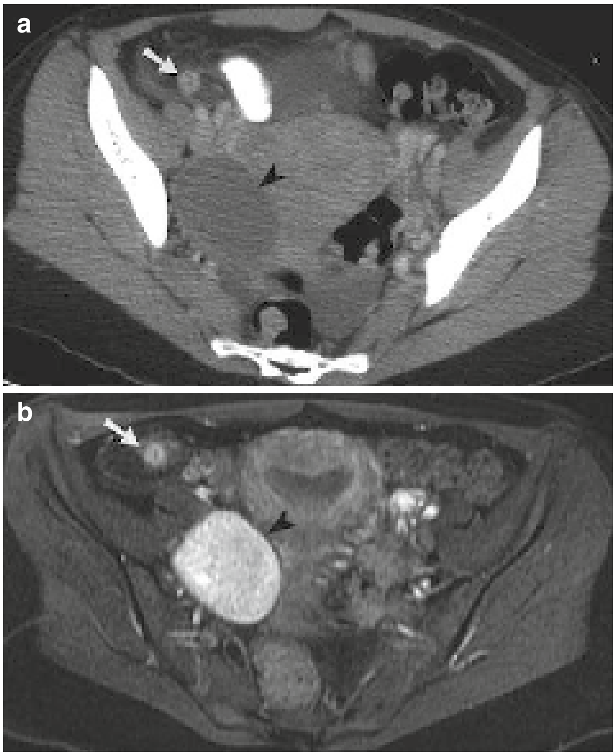

Fig. 13.2 Hemorrhagic ovarian cyst and appendicitis. (**a**) Contrast-enhanced axial CT image through the pelvis demonstrates an enlarged appendix with surrounded inflammatory fat stranding in the right lower quadrant (*arrow*). An oval, rim-enhancing ovarian cyst is identified to the right of the uterus (*arrowhead*), along with small amount of free fluid. (**b**) Axial contrast-enhanced, T1-weighted MR image with fat saturation obtained through the pelvis demonstrates a hyperenhancing, enlarged appendix with surrounding inflammatory changes in the adjacent mesenteric fat (*arrow*). The nonenhancing internal component of the hemorrhagic right ovarian cyst (*arrowhead*) is homogeneously T1 hyperintense, consistent with methemoglobin

Table 13.1 Summary of imaging findings in ovarian cysts

Simple cyst
• US: Anechoic without septations
Ruptured cyst
• US: No specific appearance, free fluid in the pelvis
Hemorrhagic cyst
• US: Hypoechoic appearance with a reticular pattern of internal echoes
• CT: Hyperdense fluid in the peritoneal space; hyperdense sentinel clot adjacent to the hemorrhagic cyst
• MRI: Hemorrhagic cyst is T2 hyperintense, hemorrhagic ascites is T1 hyperintense

Pelvic Inflammatory Disease: Tubo-Ovarian Abscess and Pyosalpinx

Pelvic inflammatory disease (PID) is usually caused by bacterial infection with *Chlamydia trachomatis* or *Neisseria gonorrhoeae* [4]. Infection begins in the vagina and spreads to the endometrium causing endometritis. The infection then extends into the fallopian tube. The resulting inflammatory changes, edema, and exudate result in obstruction of the fallopian tube and formation of a pyosalpinx [5]. The infection then extends out along the fimbria and enters the ovary (often via a ruptured corpus luteum), leading to tubo-ovarian abscess [6]. The disease can spread in the peritoneal space to involve various organs including the liver and right paracolic gutter (Fitz-Hugh–Curtis syndrome).

The symptoms are often nonspecific and may include fever, pelvic pain, cervical/adnexal tenderness (chandelier sign), vaginal discharge, dyspareunia, nausea, and vomiting. Up to 35% of the patients with PID have no symptoms [7].

Imaging

Pelvic ultrasound is the modality of choice when PID is suspected, due to high sensitivity and specificity with relatively low cost. Because the symptoms of PID are nonspecific, CT is often the first study performed, especially when the differential diagnosis is wide and includes other suspected pathologies such as diverticulitis or appendicitis (Fig. 13.3a). Pelvic MRI also has high sensitivity and specificity for pelvic inflammatory disease; however, it is usually not considered a first-line imaging modality (Figs. 13.3b, 13.4 and 13.5) [4].

On ultrasound, the fallopian tubes often become distended with fluid in patients with PID. In acute disease, the fallopian tube walls measure 5 mm or thicker and demonstrate abundant color flow with reduced flow resistance on the Doppler images (resistive index near 0.5). As the fluid-filled fallopian tubes distend, they become tortuous and fold on themselves; these folds have the appearance of incomplete septa. The thickened tube wall, fluid-filled lumen, and thickened mucosal folds can produce the “cogwheel sign” [5]. In pyosalpinx, fluid-debris levels containing low-level echoes are often visualized in the distended tubes. If the ovary cannot be visualized separate from this inflammatory mass, then the diagnosis of a tubo-ovarian abscess should be suggested rather than pyosalpinx. Folding of the tube over on itself makes the appearance of a partial septation, which

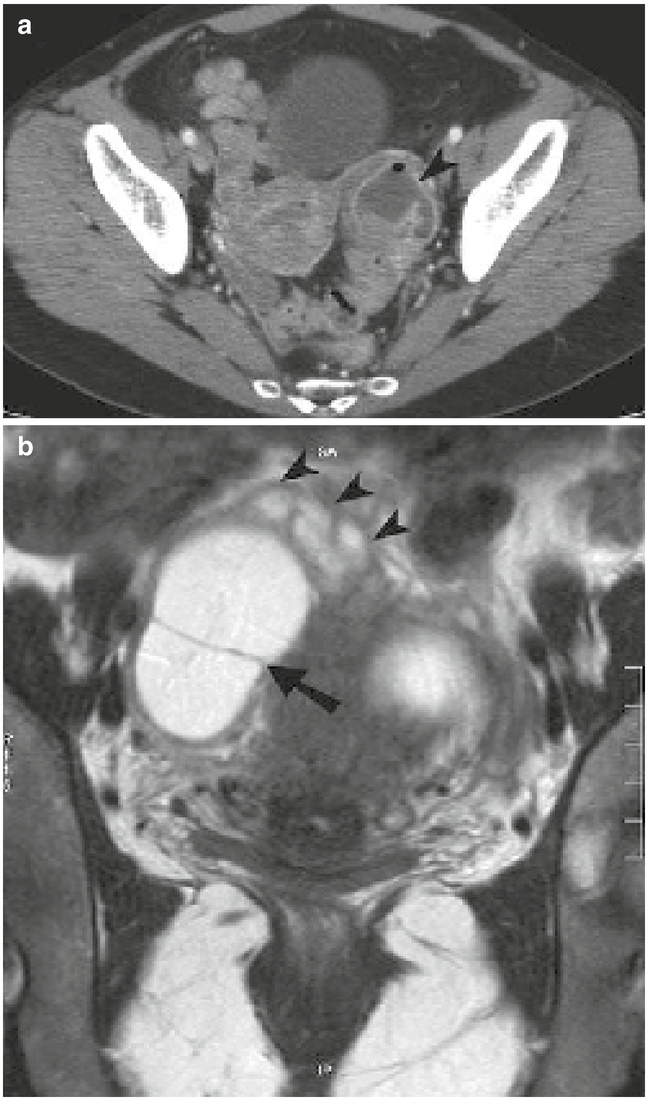

Fig. 13.3 Tubo-ovarian abscess. (**a**) Axial contrast-enhanced CT image through the pelvis shows a left adnexal lesion containing a peripherally enhancing tubo-ovarian abscess (*arrowhead*) with a small focus of nondependent air. The ovary and fallopian tube are not distinguishable as separate structures. (**b**) Coronal noncontrast T2-weighted MR image of the pelvis demonstrates a large T2 hyperintense right adnexal abscess with a thick peripheral capsule and an internal septation (*arrow*). A mildly dilated, serpiginous fallopian tube (*arrowheads*) with a thick wall is seen extending into the abscess

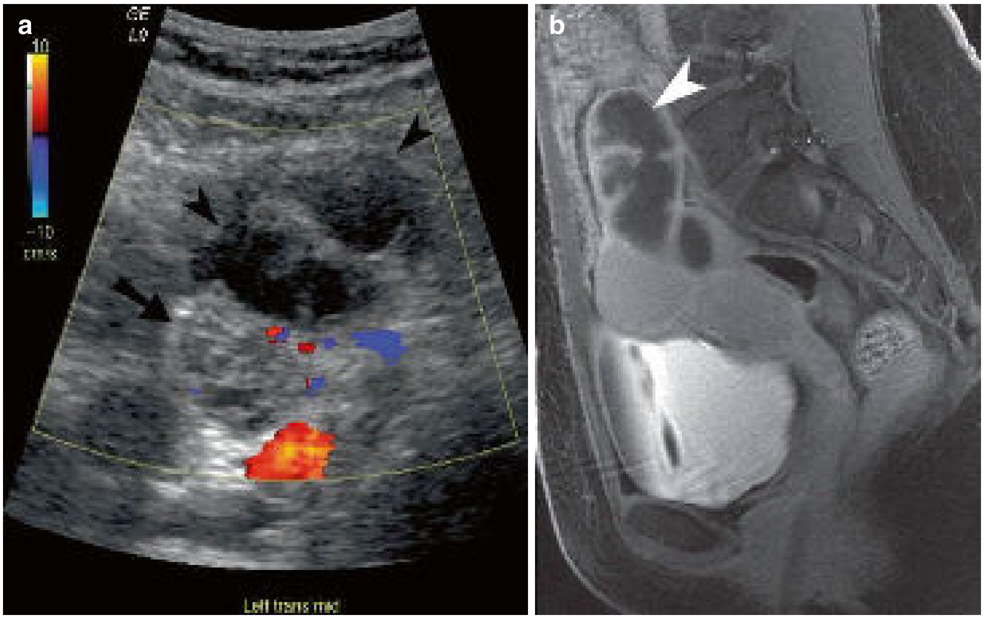

Fig. 13.4 Pyosalpinx. (**a**) Transvaginal ultrasound image demonstrates a dilated fallopian tube (*arrowheads*) located adjacent to the ovary (*arrow*). (**b**) Sagittal contrast-enhanced T1-weighted MR image with fat saturation demonstrates a dilated fallopian tube (*arrowhead*) with incomplete internal septations and prominent contrast enhancement of the thickened tube wall

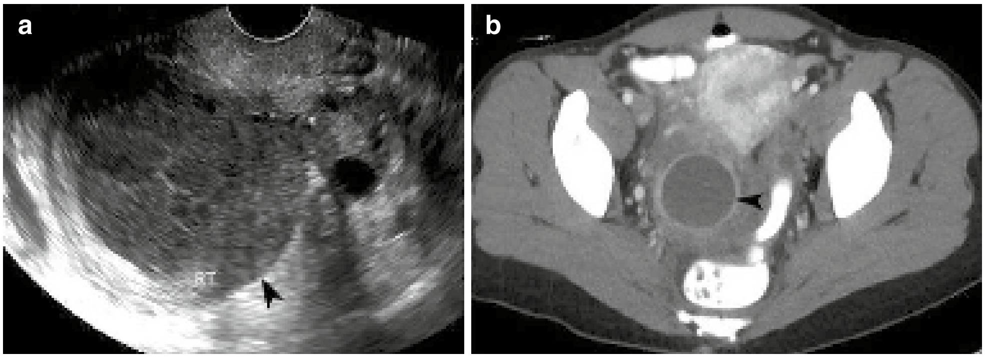

Fig. 13.5 Tubo-ovarian abscess. (**a**) Ultrasound demonstrates complex ovarian cyst with internal echoes and septations in the right pelvic adnexa (*arrowhead*). (**b**) Contrast-enhanced CT of the same patient demonstrates tubo-ovarian abscess with enhancing rim and surrounding inflammation in the right pelvic adnexa (*arrowhead*)

gives a more confident diagnosis of pyosalpinx. In chronic tubal disease, the luminal distention increases, the tube wall becomes thin, and mucosal folds are much more spread out resulting in a "beads-on-a-string" sign when visualized in cross section [5].

On CT, the findings of PID include dilated fallopian tubes, enlarged ovaries, inflammatory changes in the adjacent pelvic fat, thickening of the uterosacral ligaments, and peritoneal hyperenhancement [4, 7, 8]. The secondary findings which may include small bowel ileus/obstruction, perihepatitis (Fitz-Hugh–Curtis syndrome), and ureteral obstruction can be better evaluated on CT [4].

Pelvic infection with *Actinomyces israelii* is associated with the use of intrauterine contraceptive device. Tubo-ovarian abscesses with actinomycosis usually appear solid and may contain small rim-enhancing lesions. This infection spreads by direct extension, demonstrating linear, enhancing lesions which often have an appearance resembling carcinomatosis.

On MRI, a tubo-ovarian abscess usually presents as a mass which is T1 hypointense, often with hyperintense hemorrhage or proteinaceous debris. There is often a thin rim of T1 hyperintense signal along the inner portion of the abscess, secondary to hemorrhage within a layer of granulation tissue [8]. The abscess is usually hyperintense on T2-weighted sequence. On the postcontrast images, there is enhancement of the abscess wall and adjacent fat stranding [9]. Tubo-ovarian abscesses are hyperintense on diffusion-weighted images and demonstrate diffusion restriction [10]. Table 13.2 summarizes imaging findings in PID.

Table 13.2 Summary of imaging features of PID

Ultrasonography
• Modality of choice
• Distended fallopian tubes, with fluid
• Fallopian tube wall thickness >5 mm
• Abundant color flow with reduced flow resistance on Doppler
• Cogwheel and beads-on-a-string signs
CT
• Often the first study performed
• Dilated fallopian tubes
• Enlarged ovaries
• Inflammatory changes in the adjacent pelvic fat
• Thickening of the uterosacral ligaments
• Peritoneal hyperenhancement
MRI
• T1 hypointense mass
• Hyperintense hemorrhage or proteinaceous debris
• Thin rim of T1 hyperintense signal along the inner portion of the abscess
• Abscess is hyperintense on T2-weighted sequence
• Enhancement of the abscess wall in postcontrast images
• Hyperintense on diffusion-weighted images

Endometriosis

In endometriosis, endometrial tissue develops outside the uterine cavity, possibly due to metastatic implantation of endometrial cells from retrograde menstruation [11]. The most common locations for endometriosis include the ovaries (endometriomas, also known as "chocolate cysts"), uterosacral ligament, rectosigmoid colon, vagina, and bladder. The ectopic endometrial tissue in endometriosis infiltrates adjacent structures causing an intense desmoplastic reaction, fibrosis, adhesions, and muscular hyperplasia. These changes can result in dysmenorrhea, dyspareunia, dyschezia, dysuria, back pain with menses, and hematuria [12–14].

Laparoscopy is the gold standard for the diagnosis, staging, and treatment of endometriosis; however, in cases where there is limited mobility of pelvic structures due to extensive fibrosis and adhesions, laparoscopic evaluation may be limited. The goal of imaging is lesion mapping for presurgical planning and postsurgical response evaluation. Transvaginal ultrasound is the first-line imaging technique for the initial evaluation of suspected endometriosis.

Imaging

On ultrasound, deeply infiltrating endometrial implants are hypoechoic compared to myometrium. The endometriomas demonstrate diffuse low-level internal echoes and no internal blood flow in Doppler ultrasonography. Doppler can be used to exclude internal vascularity. Complex endometriomas can include punctate echogenic foci in the periphery. More complex lesions feature larger peripheral nodules or coalescent debris.

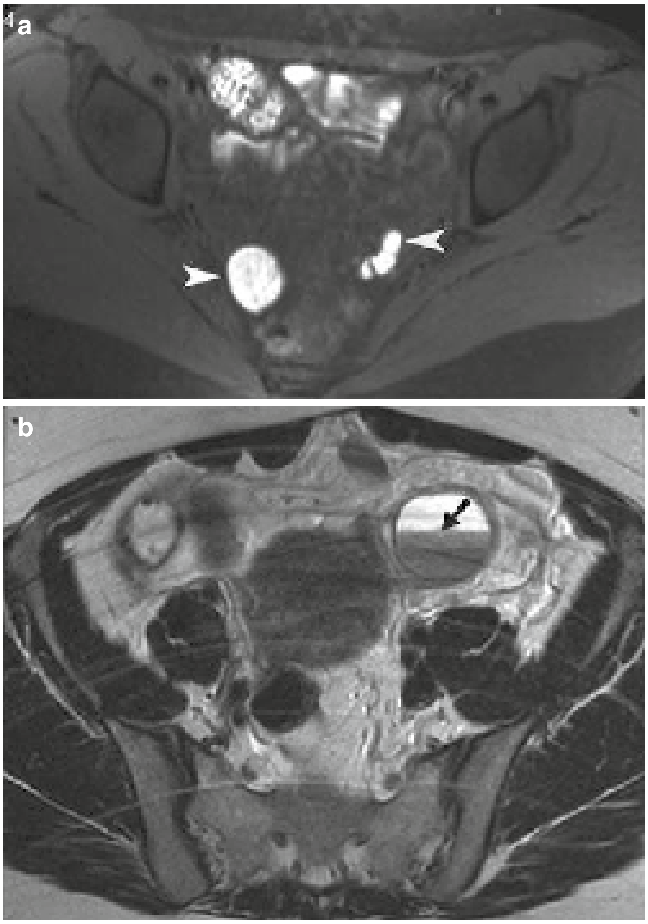

Fig. 13.6 Endometriosis. (**a**) Axial noncontrast T1-weighted MR image with fat saturation obtained through the pelvis showing multiple endometriotic cysts along bilateral pelvic side walls (*arrowheads*). The implants appear T1 hyperintense due to methemoglobin content. (**b**) Axial noncontrast T2-weighted MR image of the pelvis demonstrates a left ovarian endometrioma with a fluid/fluid level (*arrow*). The dependent contents of the endometrioma demonstrated characteristic "T2 shading" (hypointensity)

MRI is probably the most specific imaging modality for diagnosing endometriomas. MRI is best for looking at hemorrhagic content, which is hyperintense on fat-suppressed T1-weighted images and hypointense on T2-weighted images (Fig. 13.6a). The surrounding desmoplastic reaction is hypointense on T1-weighted and T2-weighted sequence [12, 13]. Endometriomas are classically T1 hyperintense and T2 hypointense (described as "T2 shading") (see Fig. 13.6b). Endometriosis may rarely be a cause of hemoperitoneum, which can result from rupture of an endometrioma or infiltration and subsequent rupture of the uterine artery [14]. Treatment is often conservative. Malignancy may occur in 1% of endometriomas, mostly in women older than 45 years old and with lesions larger than 9 cm. Table 13.3 summarizes the imaging features of endometriosis.

Table 13.3 Summary of imaging findings in ovarian cysts

Ultrasonography
• Deeply infiltrating endometrial implants are hypoechoic compared to myometrium
• Endometriomas demonstrate diffuse low-level internal echoes and no internal blood flow
MRI
• The hemorrhagic content is hyperintense on fat-suppressed T1-weighted images and hypointense on T2-weighted images
• The surrounding desmoplastic reaction is hypointense on T1-weighted and T2-weighted sequence
• Endometriomas are classically T1 hyperintense and T2 hypointense (T2 shading)

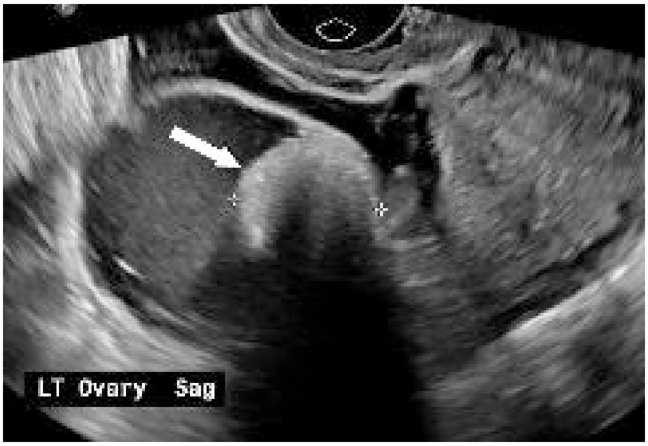

Fig. 13.7 Ovarian dermoid. Ultrasound study demonstrates hyperechoic focal lesion with distal acoustic shadowing due to dermoid plug, consistent with iceberg sign

Ovarian Torsion

Patients with ovarian torsion usually present with acute, severe lower abdominal pain. However, it may happen in the subacute or chronic settings as well. Ovarian torsion occurs when the adnexa twists on the vascular pedicle, often resulting in interruption of the venous flow and enlargement of the ovary. As the torsion progresses, the arterial blood flow is interrupted, and ovarian ischemia occurs [15]. The ovary has a dual arterial blood supply which includes the ovarian artery and ovarian branches of the uterine artery. Any ovarian mass or large cyst may place the adnexa at risk of torsion [2, 16].

Torsion is most commonly seen in reproductive-age women with an ovarian mass or cyst found in up to 80% of cases of torsion. Symptoms of torsion are nonspecific and most commonly include acute abnormal pain. Patients may also experience nausea and vomiting with fever occasionally developing several hours late [17]. Because the clinical presentation is nonspecific, correct diagnosis is often delayed [18].

Presence of ovarian masses significantly increases the risk of ovarian torsion. Of women presenting with torsion due to an ovarian mass, 46% are associated with ovarian neoplasm and 48% with ovarian cysts. Among neoplasms, ovarian dermoids are encountered most frequently. Sonographic findings of dermoid cysts include echogenic dermoid plug, dermoid mesh (multiple small hyperechoic foci within the cyst), tip of the iceberg sign (a hyperechoic focus with obscuration of distal structures) (Fig. 13.7), and fat-fluid level.

Imaging

Ultrasound is the preferred initial imaging modality when ovarian torsion is suspected. If the ovaries appear normal in size and morphologic on ultrasound, then torsion can be excluded [19]. The most common finding is ovarian enlargement of greater than 4 cm. The ovary may have a teardrop configuration with multiple small follicles displaced to the periphery of the ovary. The "follicular ring sign" is the echogenic rim around the peripheral follicles.

Although the absent vascular flow on color Doppler imaging is highly suggestive of torsion, normal Doppler flow does not exclude torsion because early torsion is often intermittent or partial [2, 16]. The "whirlpool sign" refers to visualization of twisted or circular vessels in the vascular pedicle; this is highly specific for adnexal torsion [15, 20].

Occasionally on CT and MRI, twisting of the vascular pedicle can be directly visualized; this finding is highly specific for adnexal torsion (Figs. 13.8 and 13.9) [21]. Most other findings are nonspecific and can include an adnexal mass, ipsilateral deviation of the uterus, lack of contrast enhancement, and ascites. On MRI, diffusion-weighted imaging reveals diffusion restriction when ischemia is present. Ovarian enlargement and edema from torsion result in T2 hyperintensity in the central ovarian stroma, which also shows multiple peripheral follicles. Table 13.4 summarizes the imaging features of ovarian torsion.

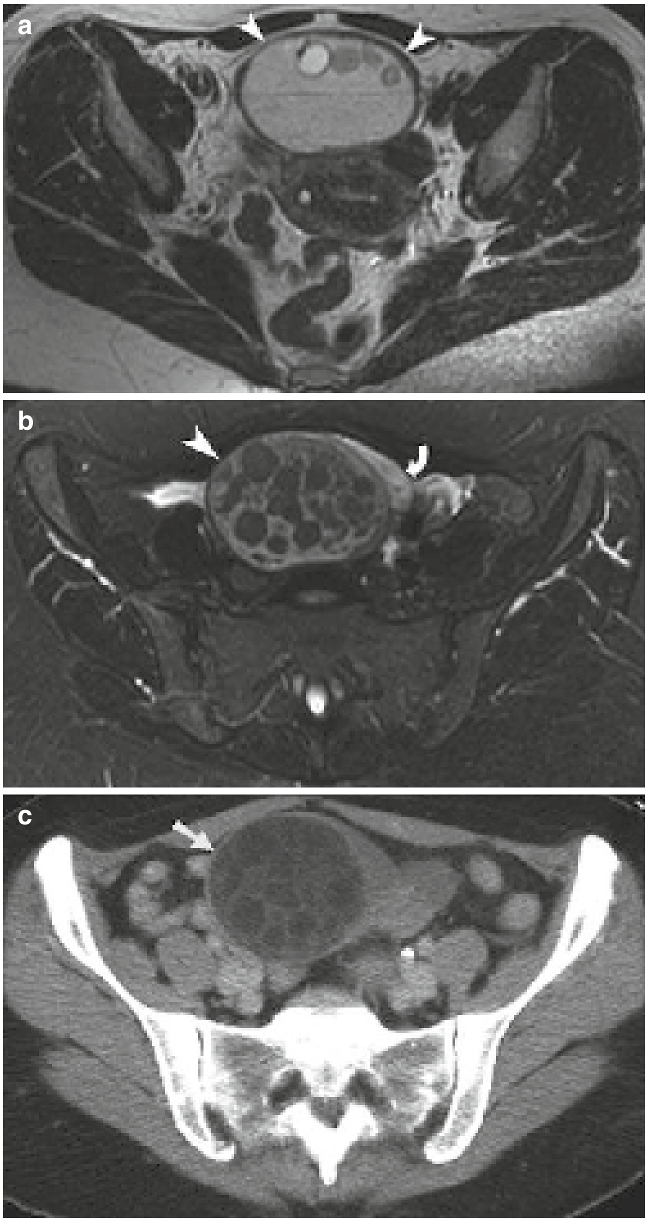

Fig. 13.8 Ovarian dermoid. (**a**) Axial noncontrast T2-weighted MR image of the pelvis demonstrates a well-circumscribed, round lesion (*arrowheads*) located anterior to the uterus. The majority of the contents of this mature teratoma appear T2 hyperintense, but there are multiple round lobules within the lesion. (**b**) Axial noncontrast STIR MR image of the pelvis again demonstrates a round, well-circumscribed ovarian dermoid located midline in the pelvis (*arrowhead*). There are multiple round, internal lobules which demonstrate signal dropout due to the fat content. A rim of edematous ovarian tissue lateral and anterior to the dermoid shows T2 hyperintensity (*curved arrow*). (**c**) Axial contrast-enhanced CT image of the pelvis again shows the immature teratoma with multiple internal fat density lobules demonstrating the characteristic fat attenuation, which is diagnostic of an ovarian dermoid (*arrow*)

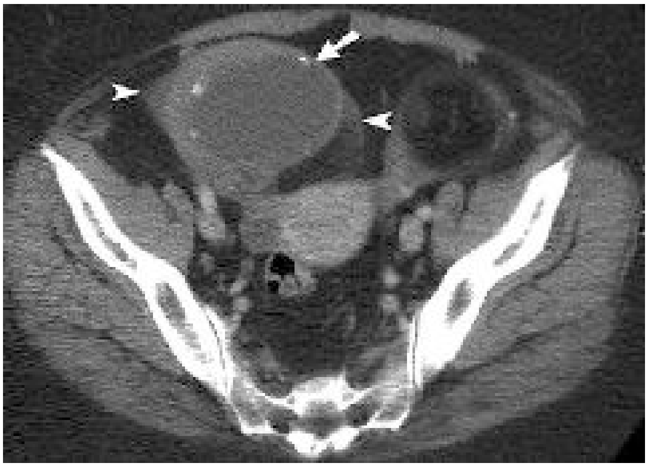

Fig. 13.9 Ovarian torsion of a dermoid cyst. Contrast-enhanced CT depicts a fluid density dermoid cyst (*arrow*) in the right ovary. There are discontinuous calcifications seen in the wall of the cyst with surrounding inflammatory changes (*arrowheads*). There is an incidental fat-containing dermoid seen in the left ovary

Table 13.4 Imaging features of ovarian torsion

Ultrasonography
• Preferred initial modality
• Normal size of ovaries can exclude torsion
• Most common finding: ovarian enlargement >4 cm
• Absent vascular flow on Doppler study
• "Whirlpool sign": highly specific for torsion
CT
• Visualization of vascular pedicle
• Nonspecific findings (adnexal mass, ipsilateral deviation of the uterus, lack of contrast enhancement, and ascites)
MRI
• Restricted diffusion in ischemia in MRI
• T2 hyperintensity due to ovarian enlargement and edema

Cystitis

Cystitis can be of multiple etiologies including bacterial infection, mechanical irritation (Foley catheter), medication effects (cyclophosphamide), radiation, or idiopathic (interstitial cystitis). When uncomplicated cystitis is suspected, no medical imaging is generally indicated [22]. However, imaging may be indicated if there is concern for malignancy, calculi, or urine flow obstruction.

The imaging findings of uncomplicated cystitis included diffuse bladder wall thickening and pericystic inflammation. The normal bladder wall thickness of the distended (>200 mL) urinary bladder is 1.1–4.5 mm [23]. Although

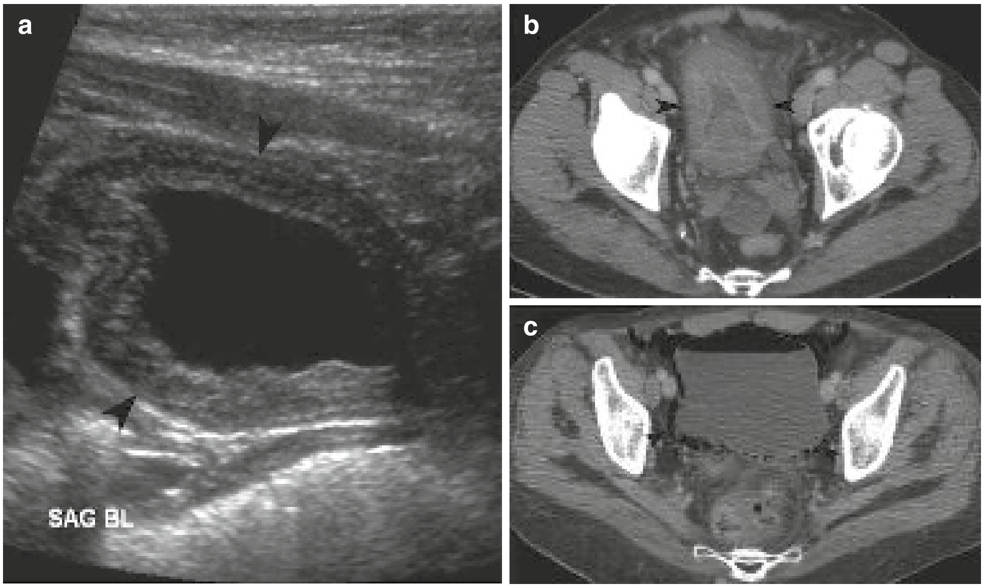

Fig. 13.10 Cystitis. (**a**) Transabdominal grayscale ultrasound image demonstrates inflammatory thickening of the urinary bladder wall (*arrowheads*). (**b**) Axial contrast-enhanced CT image of the pelvis shows marked thickening and hyperenhancement of the wall of the urinary bladder (*arrowheads*). There is also extensive inflammatory stranding in the adjacent fat. (**c**) Axial contrast-enhanced CT evidence of the pelvis demonstrates extensive emphysema within the urinary bladder wall (*arrowheads*). Extraluminal air is also seen anterior to the urinary bladder (*curved arrows*)

bladder wall thickening can be evaluated with ultrasound, CT, or MRI, pericystic inflammation can only be appreciated on CT or MRI (Fig. 13.10a, b). Immunocompromised patients are at increased risk of emphysematous cystitis, which is best recognized by the presence of air within the urinary bladder wall (see Fig. 13.10c) [24].

Ovarian Hyperstimulation Syndrome

Ovarian hyperstimulation syndrome (OHSS) is a rare complication which occurs in women undergoing infertility treatment with gonadotropic hormones. Symptoms include abdominal pain, nausea, vomiting, abdominal distention, and dizziness. The imaging findings include ascites and enlargement of ovaries which contain large peripheral cysts (Fig. 13.11). Pleural effusions may also be present [15, 25].

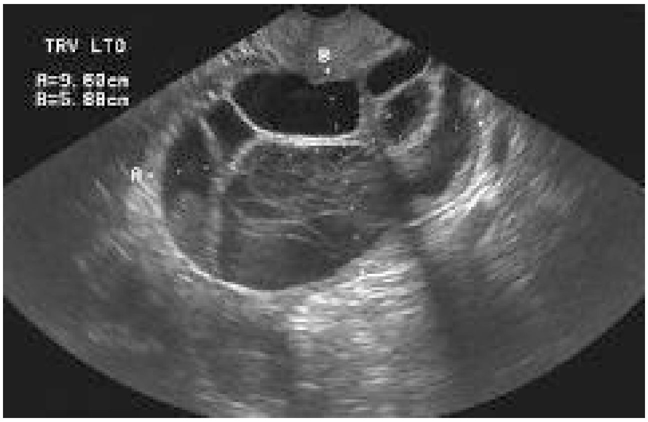

Fig. 13.11 Ovarian hyperstimulation syndrome. Ultrasound study demonstrates a markedly enlarged ovary measuring more than 9 cm in diameter and containing multiple cysts, some of which are hemorrhagic

Ovarian Vein Thrombosis

Ovarian vein thrombosis most often occurs in postpartum or postoperative patients. The symptoms include fever and abdominal pain. Most cases involve the right ovarian vein which appears enlarged with central filling defect and surrounding fat stranding. Contrast-enhanced CT is the most sensitive modality for diagnosis (Fig. 13.12) [25].

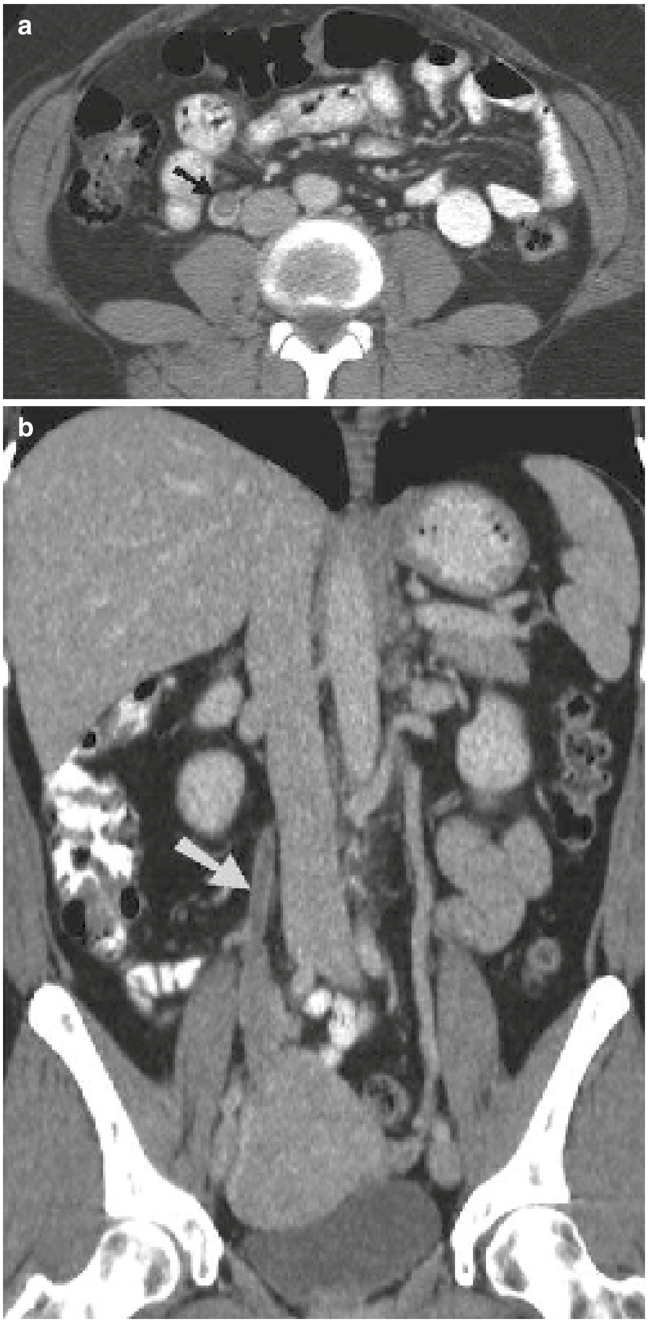

Fig. 13.12 Gonadal vein thrombosis. (**a**) Axial contrast-enhanced CT image of the abdomen demonstrates a low-density intraluminal thrombus within an abnormally expanded right gonadal vein (*arrow*). (**b**) Coronal contrast-enhanced CT image of the abdomen and pelvis shows a tubular intraluminal thrombus in a segment of the right gonadal vein (*arrow*). The vein is abnormally expanded, and a small amount of contrast is seen surrounding the thrombus

Symptomatic Fibroids

Uterine fibroids represent benign masses of uterine smooth muscle and connective tissue proliferation. Fibroids may be the cause for acute pelvic pain in the setting of infarction, torsion (pedunculated subserosal fibroid), or prolapse (pedunculated submucosal fibroid).

Fibroids undergo degeneration when its blood or nutrient supply becomes inadequate, commonly seen with increased fibroid size (>5 cm), pregnancy, and menopause. On ultrasound, the presence of cystic features within a fibroid indicates internal degeneration. The sensitivity and specificity for the detection of fibroid degeneration are higher with MRI (Figs. 13.13, 13.14 and 13.15). A solid fibroid on MRI appears homogenously T2 hypointense and T1 isointense when compared to outer myometrium. Degenerating fibroids are also associated with heterogeneous contrast enhancement relative to typical fibroids. High T2 signal intensity of leiomyomas with poor or no enhancement on contrast-enhanced T1-weighted sequence suggests the presence of ischemia or hemorrhagic necrosis [26]. Degeneration can be of various types including hyaline, cystic, myxoid, and red (hemorrhagic).

Hyaline degeneration, the most common type, displays signal voids on MRI due to associated dystrophic calcification. The deposited collagen or proteinaceous material in the extracellular space between smooth muscle fibers appears T2 hypointense and T1 isointense with minimal or no enhancement on contrast-enhanced images, much like a nondegenerated fibroid.

Cystic degeneration is an uncommon type and commonly occurs secondary to severe forms of other underlying degeneration, such as hyaline degeneration. Hyperintense T2 signal without associated enhancement represents edema and cystic areas.

Myxoid degeneration, a rare form, is associated with accumulation of myxoid matrix and extracellular mucin within the fibroid. On MRI, these areas exhibit hyperintensity on T2 images and enhancement on postcontrast images.

Red degeneration usually occurs in the setting of pregnancy or in patients on oral contraceptives and is due to obstruction of draining veins. Varying signal intensities are produced within the fibroid due to the presence of hemorrhagic products of different ages. The peripheral obstructed veins may be seen as a peripheral rim of low T2 and high T1 signal intensity. Postcontrast images will demonstrate no enhancement.

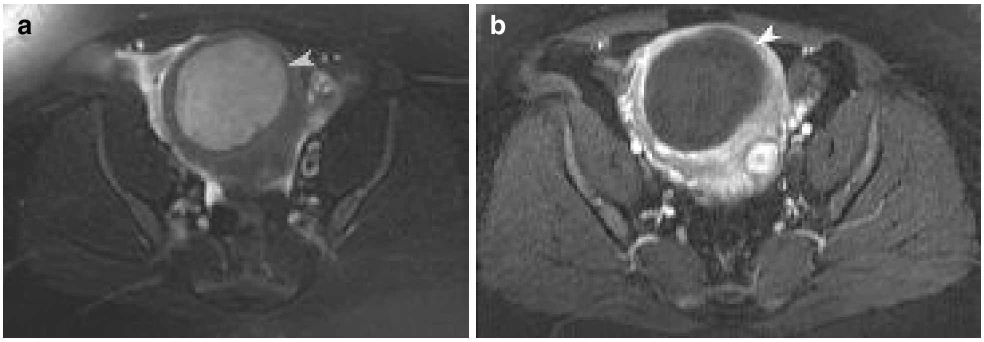

Fig. 13.13 Degenerating uterine fibroid. (**a**) Axial T2-weighted MR image with fat saturation obtained through the pelvis demonstrates a well-circumscribed, T2 hyperintense leiomyoma (*arrowhead*) with cystic degeneration. (**b**) Axial contrast-enhanced T1-weighted MR image with fat saturation shows no enhancement within the round, well-circumscribed leiomyoma (*arrowhead*)

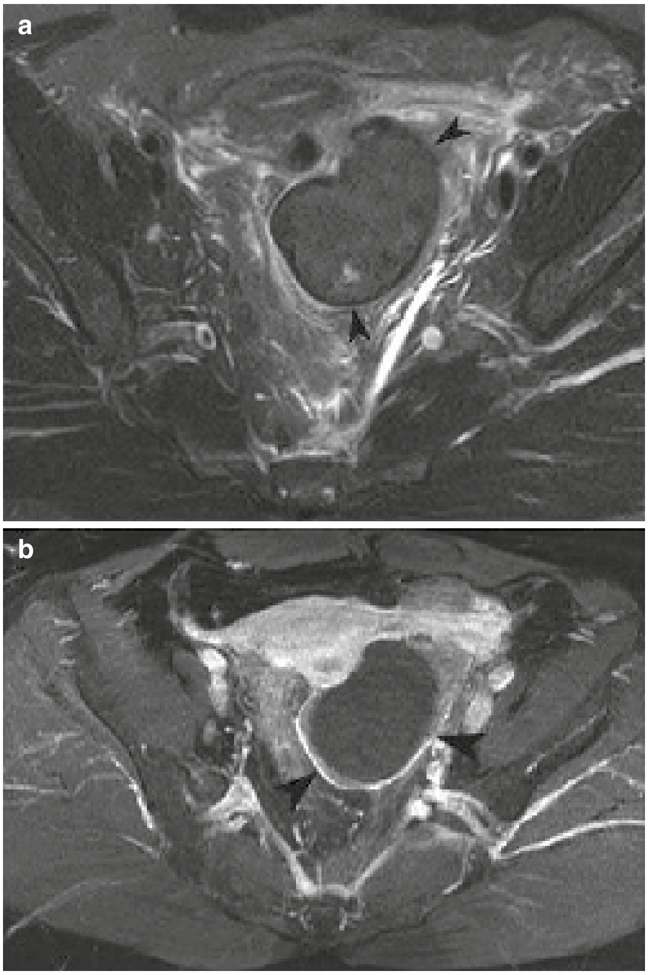

Fig. 13.14 Degenerating uterine fibroid. (**a**) Axial noncontrast T2-weighted MR image with fat saturation obtained in the pelvis demonstrates a hypointense mass with a peripheral rim of low signal intensity, which is characteristic of a leiomyoma undergoing red degeneration (*arrowheads*). (**b**) Axial postcontrast T1-weighted MR imaging with fat saturation confirms that there is no contrast enhancement within the subserosal leiomyoma undergoing degeneration (*arrowheads*)

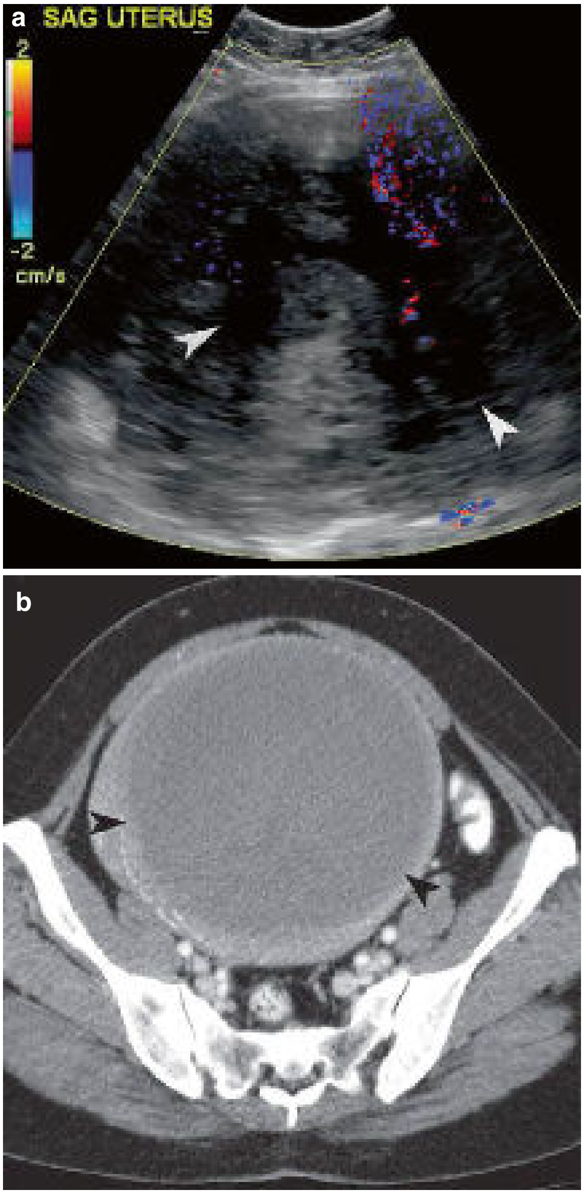

Fig. 13.15 Degenerating fibroid. (**a**) Pelvic ultrasound with color flow demonstrates a large heterogeneous mass with irregular cystic areas (*arrowheads*) within the degenerating fibroid. (**b**) Axial contrast-enhanced CT demonstrates a large, necrotic, well-circumscribed uterine leiomyoma, which does not enhance (*arrowheads*)

Hematometrocolpos and Hydrometrocolpos

While hematometrocolpos represents accumulation of blood within the vagina, hydrometrocolpos represents the presence of fluid within the vagina and uterus. The cause may be congenital imperforate hymen or acquired, such as neoplastic obstruction, postpartum infection, or iatrogenic cervical stenosis. Imaging by sonography, CT, or MRI will most commonly demonstrate cystic distension of the vagina and/or uterine cavity with a possible fluid-debris level posterior to the bladder (Fig. 13.16) [27, 28].

Teaching Points

- Ultrasound is the primary modality utilized for imaging of acute pelvic disorders.
- Ovarian torsion is most common in women of reproductive age and almost always occurs in the setting of an ovarian abnormality such as a mass or cyst.
- Although a less convenient and more expensive modality, the sensitivity and specificity for MRI are high with advanced anatomical delineation for most acute pelvic processes.
- Hemorrhagic ovarian cysts on ultrasound classically have a hypoechoic appearance with a reticular pattern of internal echoes sometimes described as lacelike, spiderweb, or fishnet.
- In pelvic inflammatory disease, ultrasound demonstrates the distended fallopian tubes, containing fluid.
- Deeply infiltrating endometrial implants on ultrasound are hypoechoic compared to myometrium.
- The most common finding in ovarian torsion is ovarian enlargement of greater than 4 cm.

Questions

1. Which of the following statements is correct?
   (A) Hemorrhagic ovarian cysts on ultrasound classically have a hyperechoic appearance with a reticular pattern of internal echoes
   (B) On MRI, acute hemorrhagic cyst is most often T2 hypointense
   (C) Folding of the tube over itself is a characteristic finding in pyosalpinx
   (D) Tubo-ovarian abscesses with actinomycosis are the result of hematogenous spread
   Answer: C

2. Which of the following statements is correct regarding ovarian torsion?
   (A) Normal morphologic appearance of ovaries on US excludes ovarian torsion
   (B) The most common finding on ultrasonography is the whirlpool sign
   (C) T2 hypointensity in the central ovarian stroma can be seen on MRI
   (D) Torsion most commonly occurs in postmenopausal women
   Answer: A

3. Which of the following is correct?
   (A) For the diagnosis of fibroids, ultrasonography is more sensitive and specific than MRI
   (B) Ovarian vein thrombosis most often occurs in postpartum or postoperative patients

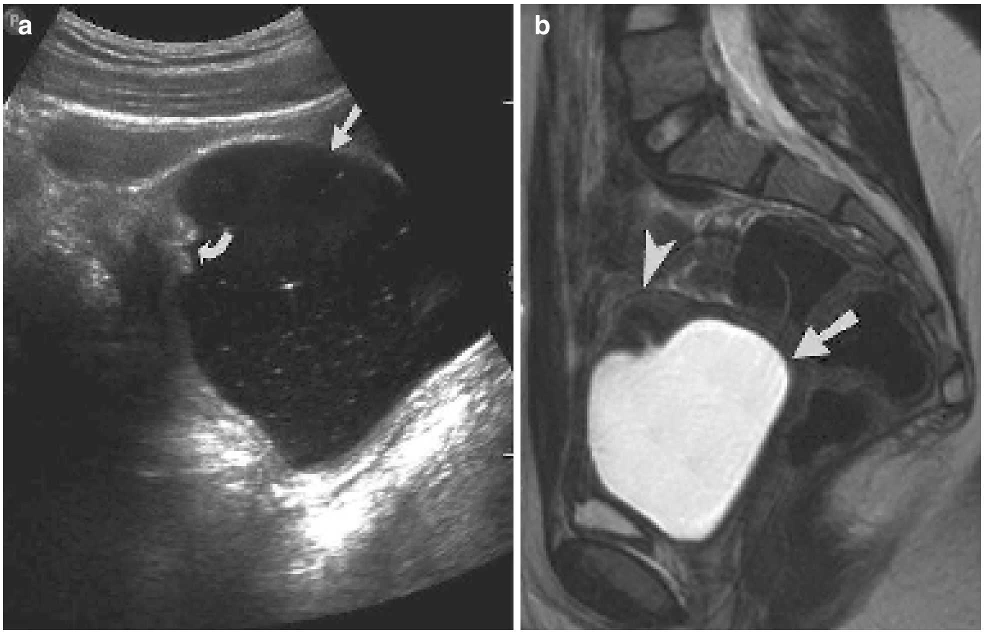

Fig. 13.16 Hematocolpos due to imperforate hymen. (**a**) Transabdominal ultrasound shows a large hypoechoic fluid collection with floating internal echogenic debris within a markedly distended vaginal cavity (*arrow*). The cervix can be seen along the superior aspect of the fluid collection (*curved arrow*). (**b**) Sagittal T2-weighted images of the pelvis demonstrate a large, T2 hyperintense fluid collection within the distended vaginal cavity (*arrow*). The uterus (*arrowhead*) can be seen displaced superiorly by the distended, fluid-filled vagina

(C) Red degeneration in fibroids usually occurs in the postmenopausal setting
(D) Imaging findings in ovarian hyperstimulation syndrome include ascites and normal-sized ovaries
Answer: B

4. What is the imaging diagnosis on the T1-weighted MR (with and without fat saturation) images depicted below (Fig. 13.17a, b)?
(A) Fibroma
(B) Ectopic pregnancy
(C) Endometrioma
(D) Dermoid cyst
Answer: D

5. CT of a patient with cystic ovarian neoplasm with acute pain is depicted below. What imaging finding on the CT (Fig. 13.18) indicates ovarian torsion?
(A) Inflammatory stranding to the right of ovarian cyst
(B) Corpus luteum
(C) Intratumoral hemorrhage
(D) Thick wall of the cyst
Answer: A

6. In a patient with acute pelvic pain, what is the CT imaging diagnosis (Fig. 13.19)?
(A) Ovarian torsion
(B) Bowel obstruction
(C) Hydrosalpinx
(D) Ectopic pregnancy
Answer: C

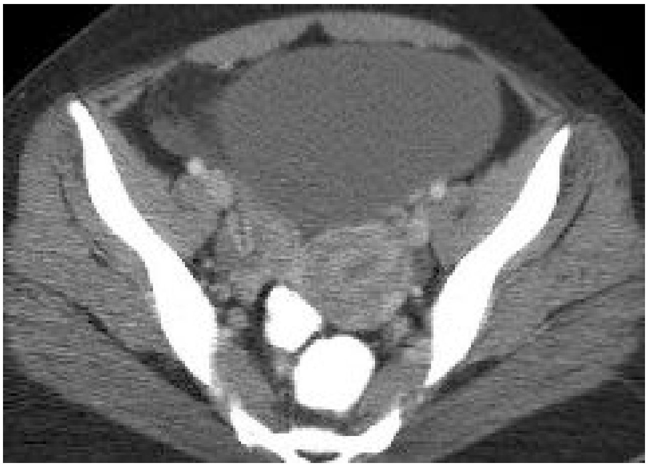

Fig. 13.18 Inflammatory stranding to the right of ovarian cyst-CT

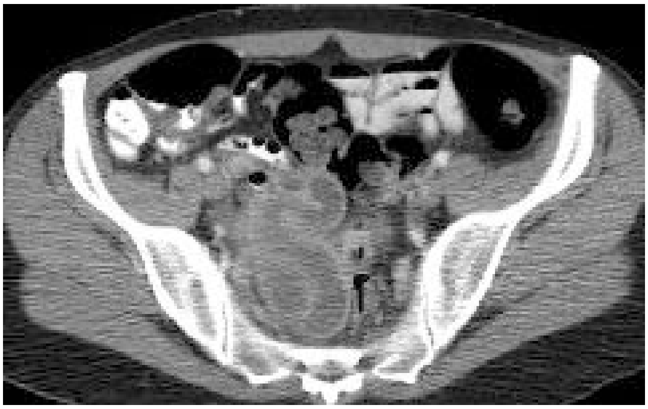

Fig. 13.19 Hydrosalpinx CT imaging

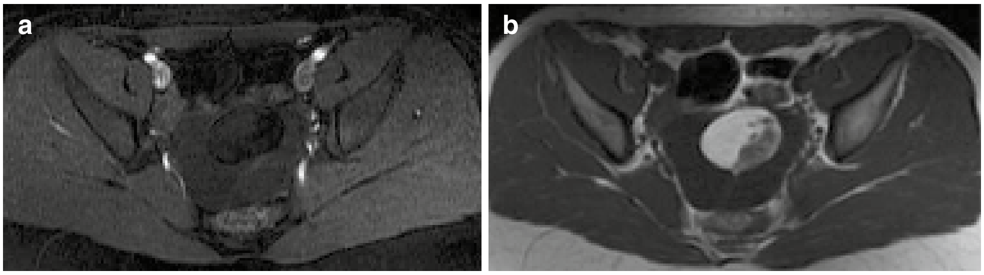

Fig. 13.17 (**a**, **b**) Dermoid cyst with and without fat saturation

References

1. Levine D, Brown DL, Andreotti RF, Benacerraf B, Benson CB, Brewster WR, et al. Management of asymptomatic ovarian and other adnexal cysts imaged at US Society of Radiologists in Ultrasound Consensus Conference Statement. Ultrasound Q. 2010;26(3):121–31.
2. Bottomley C, Bourne T. Diagnosis and management of ovarian cyst accidents. Best Pract Res Clin Obstet Gynaecol. 2009;23(5):711–24.
3. Tamai K, Koyama T, Saga T, Kido A, Kataoka M, Umeoka S, et al. MR features of physiologic and benign conditions of the ovary. Eur Radiol. 2006;16(12):2700–11.
4. Horrow MM. Ultrasound of pelvic inflammatory disease. Ultrasound Q. 2004;20(4):171–9.
5. Timor-Tritsch IE, Lerner JP, Monteagudo A, Murphy KE, Heller DS. Transvaginal sonographic markers of tubal inflammatory disease. Ultrasound Obstet Gynecol. 1998;12(1):56–66.
6. Lambert MJ, Villa M. Gynecologic ultrasound in emergency medicine. Emerg Med Clin N Am. 2004;22(3):683–96.
7. Sam JW, Jacobs JE, Birnbaum BA. Spectrum of CT findings in acute pyogenic pelvic inflammatory disease. Radiographics. 2002;22(6):1327–34.
8. Kim SH, Kim SH, Yang DM, Kim KA. Unusual causes of tubo-ovarian abscess: CT and MR imaging findings. Radiographics. 2004;24(6):1575–89.
9. Singh AK, Desai H, Novelline RA. Emergency MRI of acute pelvic pain: MR protocol with no oral contrast. Emerg Radiol. 2009;16(2):133–41.
10. Kilickesmez O, Tasdelen N, Yetimoglu B, Kayhan A, Cihangiroglu M, Gurmen N. Diffusion-weighted imaging of adnexal torsion. Emerg Radiol. 2009;16(5):399–401.
11. Woodward PJ, Sohaey R, Mezzetti TP Jr. Endometriosis: radiologic–pathologic correlation. Radiographics. 2001;21(1):193–216. questionnaire 288–94.
12. Chamie LP, Blasbalg R, Pereira RMA, Warmbrand G, Serafini PC. Findings of pelvic endometriosis at transvaginal US, MR imaging, and laparoscopy. Radiographics. 2011;31(4):E77–100.
13. Marcal L, Nothaft MA, Coelho F, Choi H. Deep pelvic endometriosis: MR imaging. Abdom Imaging. 2010;35(6):708–15.
14. Bennett GL, Slywotzky CM, Cantera M, Hecht EM. Unusual manifestations and complications of endometriosis—spectrum of imaging findings: pictorial review. AJR Am J Roentgenol. 2010;194(6 Suppl):WS34–46.
15. Chang HC, Bhatt S, Dogra VS. Pearls and pitfalls in diagnosis of ovarian torsion. Radiographics. 2008;28(5):1355–68.
16. Chiou S-Y, Lev-Toaff AS, Masuda E, Feld RI, Bergin D. Adnexal torsion: new clinical and imaging observations by sonography, computed tomography, and magnetic resonance imaging. J Ultrasound Med. 2007;26(10):1289–301.
17. Galinier P, Carfagna L, Delsol M, Ballouhey Q, Lemasson F, Le Mandat A, et al. Ovarian torsion. Management and ovarian prognosis: a report of 45 cases. J Pediatr Surg. 2009;44(9):1759–65.
18. Hiller N, Appelbaum L, Simanovsky N, Lev-Sagi A, Aharoni D, Sella T. CT features of adnexal torsion. AJR Am J Roentgenol. 2007;189(1):124–9.
19. Patel MD, Dubinsky TJ. Reimaging the female pelvis with ultrasound after CT. Ultrasound Q. 2007;23(3):177–87.
20. Vijayaraghavan SB. Sonographic whirlpool sign in ovarian torsion. J Ultrasound Med. 2004;23(12):1643–9. quiz 1650–1.
21. Rha SE, Byun JY, Jung SE, Jung JI, Choi BG, Kim BS, et al. CT and MR imaging features of adnexal torsion. Radiographics. 2002;22(2):283–94.
22. Johansen TEB. The role of imaging in urinary tract infections. World J Urol. 2004;22(5):392–8.
23. Blatt AH, Titus J, Chan L. Ultrasound measurement of bladder wall thickness in the assessment of voiding dysfunction. J Urol. 2008;179(6):2275–8. discussion 2278–9.
24. Chang C-B, Chang C-C. Emphysematous cystitis: a rare cause of gross hematuria. J Emerg Med. 2011;40(5):506–8.
25. Bennett GL, Slywotzky CM, Giovanniello G. Gynecologic causes of acute pelvic pain: spectrum of CT findings. Radiographics. 2002;22(4):785–801.
26. Wilde S, Scott-Barrett S. Radiological appearances of uterine fibroids. Indian J Radiol Imaging. 2009;19:222–31.
27. Dykes T, Siegel C, Dodson W. Imaging of congenital uterine anomalies: review and self-assessment module. AJR Am J Roentgenol. 2007;189(3):S1–10.
28. Kim TH, Lee HH, Chung SH. Presenting features of pyometra including an increase in iatrogenic causes. J Low Genit Tract Dis. 2011;15(4):316–7.

Emergency Radionuclide Imaging of the Thorax and Abdomen

14

Blaine T. Mischen, Paul F. Von Herrmann, Cynthia Lumby, and M. Elizabeth Oates

Introduction

Nuclear medicine (NM) utilizes a variety of unsealed radioactive compounds, known as radiopharmaceuticals or radiotracers. Given in small (tracer) quantities, radiopharmaceuticals typically consist of two components: a radionuclide (also called a radioisotope) and a molecular or cellular carrier; the latter determines the biodistribution upon administration to a patient. The most common routes of administration in clinical practice are intravenous (IV), inhalation, and oral.

Based on its respective radionuclide, a radiopharmaceutical emits specific gamma rays, which can be detected and processed into medical images by gamma camera systems; this is termed scintigraphy. The resulting scintigraphic images depict the biodistribution of the administered radioactivity within the patient's body, thereby reflecting normal or abnormal physiological function combined with a low-resolution anatomical representation of the organs/organ systems of interest. The physiological data are complementary to the anatomical data and, in certain conditions, prove more beneficial than the anatomical data alone.

In the emergency setting, appropriate triage and timely diagnosis are of utmost importance. Emergency physicians increasingly rely on medical imaging for diagnosis and management; decisions to admit or discharge patients often hinge on the radiological diagnosis. NM examinations are generally underutilized in the emergency setting for several fundamental reasons. Emergency physicians tend to be less familiar with the NM options and are less experienced with their respective appropriateness and advantages. Common logistical challenges include limited availability and longer duration of the imaging examination compared to other types of imaging. Specifically, there may be difficulty obtaining radiopharmaceuticals during evenings, nights, and weekends. In many institutions, NM personnel are typically only on-site during regular working hours; at some institutions, the NM technologists are "on call," while in others, there is no availability during the off-hours. Nuclear pharmacies are often at a different location and require transport of the radiopharmaceutical, which also delays study completion. This lack of ready access is likely one of the major determinants that leads emergency physicians to request fewer NM examinations. Even when available, however, scintigraphic examinations generally require more time than radiography (X-ray), ultrasound (US), or computed tomography (CT) and may require transport to a different location within the facility.

Nevertheless, NM can play important primary and secondary roles in diagnosis and management in the emergency setting. Within the radiological armamentarium, selected scintigraphic examinations offer significant value because those negative examinations exclude diagnoses with high certainty, while positive examinations direct appropriate management. Currently, common radionuclide imaging examinations of the thorax and abdomen in the emergency setting include ventilation/perfusion (V/Q) lung scintigraphy, myocardial perfusion imaging (MPI), hepatobiliary scintigraphy (HBS), and RBC gastrointestinal (GI) bleeding, as well as Meckel's diverticulum scintigraphy (Table 14.1). This chapter reviews their appropriate utilization, highlights their advantages and disadvantages, and illustrates each by way of representative case examples. Multiple-choice questions at the end of the chapter are provided for self-assessment.

B. T. Mischen (✉) · M. E. Oates
Department of Radiology, University of Kentucky College of Medicine, UK HealthCare, Lexington, KY, USA
e-mail: blaine.mischen@uky.edu

P. F. Von Herrmann
Department of Radiology, North Alabama Medical Center, Florence, AL, USA

C. Lumby
Radiology Service, VA North Texas Health Care System, Fort Worth, TX, USA

© The Author(s), under exclusive license to Springer Nature Switzerland AG 2024
A. Singh (ed.), *Emergency Radiology*, https://doi.org/10.1007/978-3-031-65770-2_14

Table 14.1 Common clinical indications for emergency radionuclide imaging of the thorax and abdomen

Clinical indication	Examination	Radiopharmaceuticals	Typical time to completion	Sensitivity	Specificity	Positive predictive value	Negative predictive value	References
Acute pulmonary embolism	V/Q lung scintigraphy	*Ventilation*: ^{133}Xe gas, inhaled, or ^{99m}Tc DTPA aerosol, inhaled *Perfusion*: ^{99m}Tc MAA, IV	30–60 min	70–85% for high-probability interpretation	96–98% for normal/very-low-probability interpretation	96–99% for high-probability interpretation with high clinical suspicion	97–98% for normal/very-low-probability interpretation	[1–4]
Acute coronary syndrome	Myocardial perfusion imaging	^{99m}Tc sestamibi IV or ^{99m}Tc tetrofosmin IV	1–2 h	90–100%	63–71%	90%	96–100%	[3, 5–7]
Cystic duct obstruction (acute cholecystitis) and common bile duct obstruction	Hepatobiliary scintigraphy	^{99m}Tc IDA analog, IV	1–4-h delayed imaging up to 24 h	40–99%	64–100%	85%	95%	[4, 8, 9]
Cystic/bile duct injury	Hepatobiliary scintigraphy for bile leak	^{99m}Tc IDA analog, IV	1–4 h	100%	90–100%	91–100%	100%	[10]
Acute gastrointestinal bleeding	GI bleeding study	^{99m}Tc RBCs, IV	1–2 h	78–97%	70–100% for diagnosis, 88–97% for localization	75–77%	76%	[11–14]
GI bleeding from suspected Meckel's diverticulum	Meckel's diverticulum scintigraphy	^{99m}Tc sodium pertechnetate, IV	30–60 min	60–85%	95–96%	100%	74%	[15, 16]

Acute Pulmonary Embolism: Ventilation/Perfusion Lung Scintigraphy

Pulmonary embolism (PE) is a potentially fatal complication of deep venous thrombosis. In acute PE, thrombus dislodges from the vein, migrates to the pulmonary vasculature, and lodges in a main pulmonary artery or segmental branch. Thromboemboli reduce the cross-sectional area of the pulmonary arterial vascular bed, thus potentially resulting in hypoxia and hemodynamic compromise. Diagnosing acute PE can be very difficult clinically due to nonspecific symptoms and confounding clinical presentations mimicking other acute thoracic and abdominal conditions.

Both CT angiography (CTA) and ventilation/perfusion (V/Q) lung scintigraphy are well-accepted modalities for the imaging evaluation of suspected acute PE. Currently, CTA is performed in the vast majority of patients. However, V/Q lung scintigraphy remains relevant because radionuclide imaging of the lungs provides physiological information regarding not only regional pulmonary arterial perfusion but also bronchoalveolar ventilation. V/Q lung scintigraphy also spares the patient exposure to potentially nephrotoxic iodinated contrast and results in lower radiation dosimetry [1, 3].

Table 14.2 Typical ventilation/perfusion (V/Q) lung scintigraphy technical protocol

1. Obtain contemporaneous chest radiography in posterior-anterior (PA) and lateral projections
2. Have patient inhale 5–20 mCi (200–750 MBq) of ^{133}Xe gas or 25–35 mCi (900–1300 MBq) of ^{99m}Tc diethylenetriaminepentaacetic acid (DTPA), aerosolized by a nebulizer, from which the patient receives approximately 0.5–1.0 mCi (20–40 MBq) into the lungs
3. Acquire ventilation images in posterior projection (^{133}Xe gas) or anterior, posterior, bilateral anterior oblique, and bilateral posterior oblique projections (^{99m}Tc DTPA aerosol)
4. Administer 4 mCi (148 MBq) of ^{99m}Tc macroaggregated albumin (MAA) IV with the patient supine or as close to supine as possible
5. Acquire perfusion images in anterior, posterior, bilateral anterior oblique, and bilateral posterior oblique projections

Although V/Q lung scintigraphy protocols vary by institution, ventilation images, using one of the two routinely available radiopharmaceuticals, are typically acquired first. The perfusion phase using a standard radiopharmaceutical follows (Table 14.2). Perfusion imaging is based on the principle of capillary blockade. The radioactive macroaggregated albumin (MAA) particles are larger than the capillaries and lodge in the precapillary arterioles; thus, their biodistribution reflects pulmonary arterial blood flow to both lungs. On these scintigraphic images, pulmonary segments with normal perfusion demonstrate uniform perfusion throughout (Fig. 14.1), while those with decreased perfusion demonstrate lower radioactivity than normal segments (Figs. 14.2 and 14.3). Classically, underlying lung disease presents as mildly to markedly abnormal perfusion that is "matched" by (or shows even more pronounced) abnormal ventilation (see Fig. 14.2). Acute PE affects perfusion only while ventilation should be preserved, resulting in the so-called V/Q mismatch pattern (Fig. 14.3). The modified PIOPED II criteria can be used to interpret V/Q lung scintigraphy (Table 14.3) [1].

In selecting the optimal radiological approach for suspected acute PE, the emergency physician should take into account multiple factors, not the least of which include sensitivity and specificity of the different imaging examinations, technical availability, and patient safety. For a patient with acute symptomatology, conventional chest radiography remains first line. Patients with significantly abnormal chest

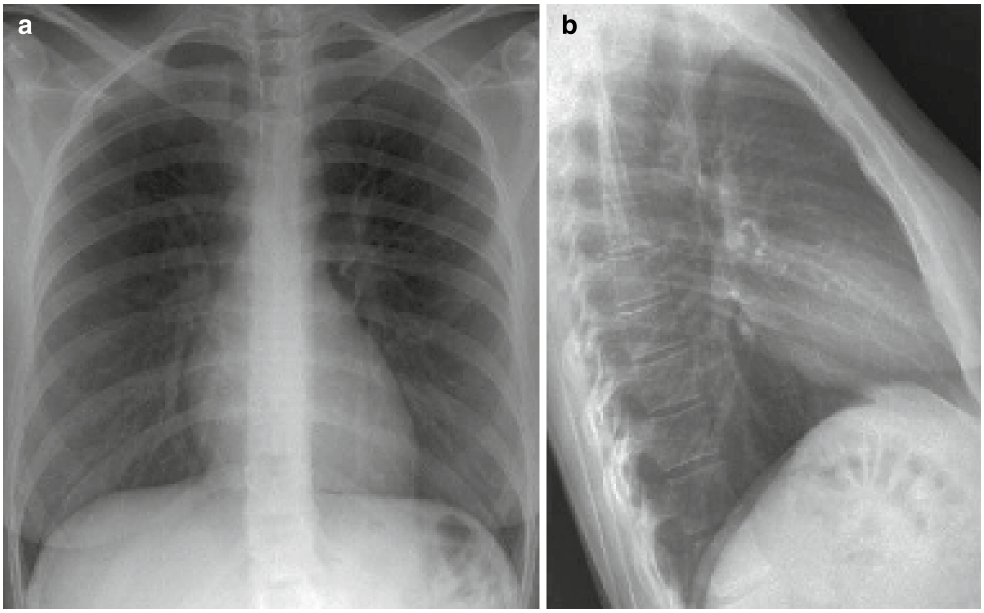

Fig. 14.1 Normal. Normal posterior-anterior (**a**) and lateral (**b**) chest radiographs. Normal ventilation (**c**) and perfusion (**d**) scintigraphy performed with ^{133}Xe gas (ventilation) and ^{99m}Tc MAA (perfusion)

Fig. 14.1 (continued)

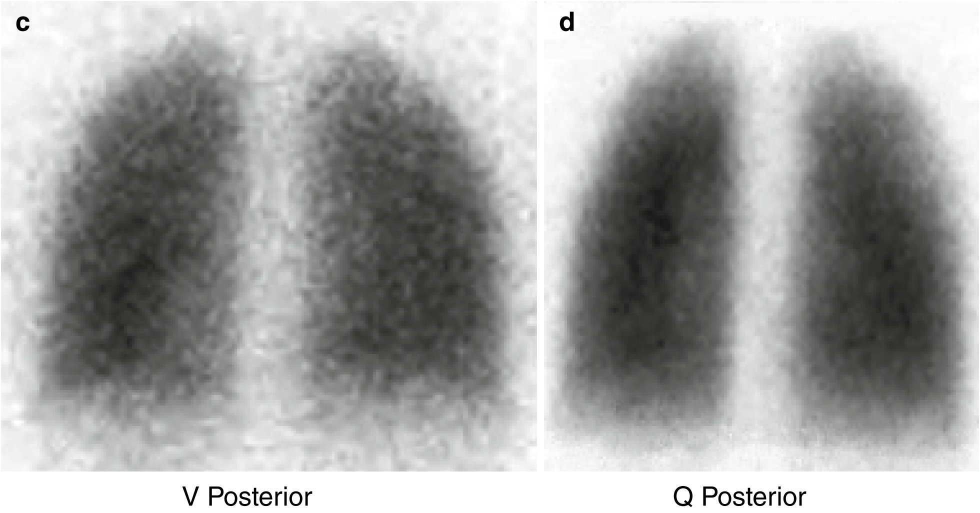
c
d
V Posterior
Q Posterior

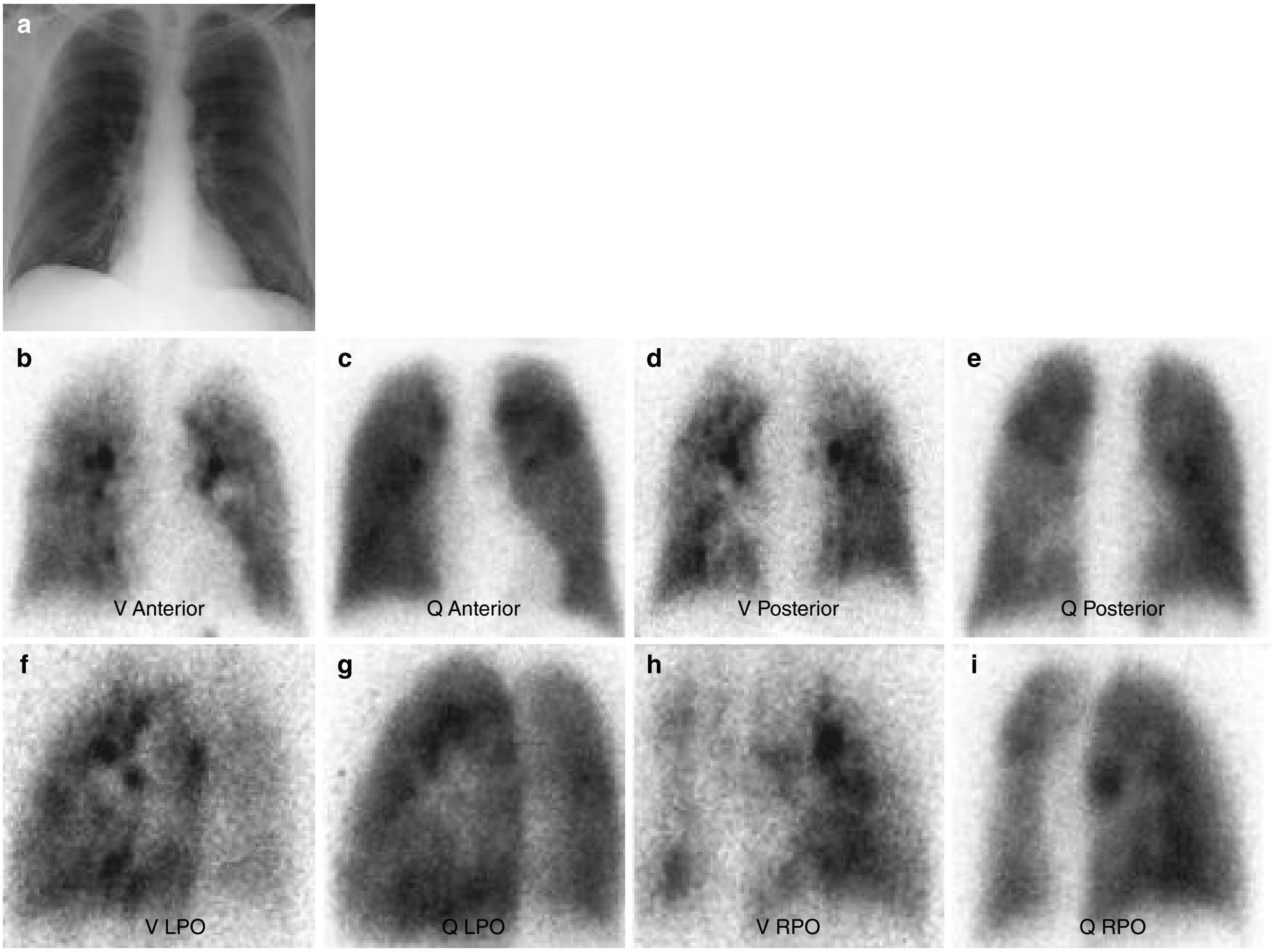
a
b
c
d
e
V Anterior
Q Anterior
V Posterior
Q Posterior
f
g
h
i
V LPO
Q LPO
V RPO
Q RPO

Fig. 14.2 Multiple matched V/Q abnormalities related to underlying airway disease. Normal PA chest radiograph (**a**). Heterogeneous ^{99m}Tc DTPA ventilation (**b**, **d**, **f**, **h**) and heterogeneous ^{99m}Tc MAA perfusion (**c**, **e**, **g**, **i**)

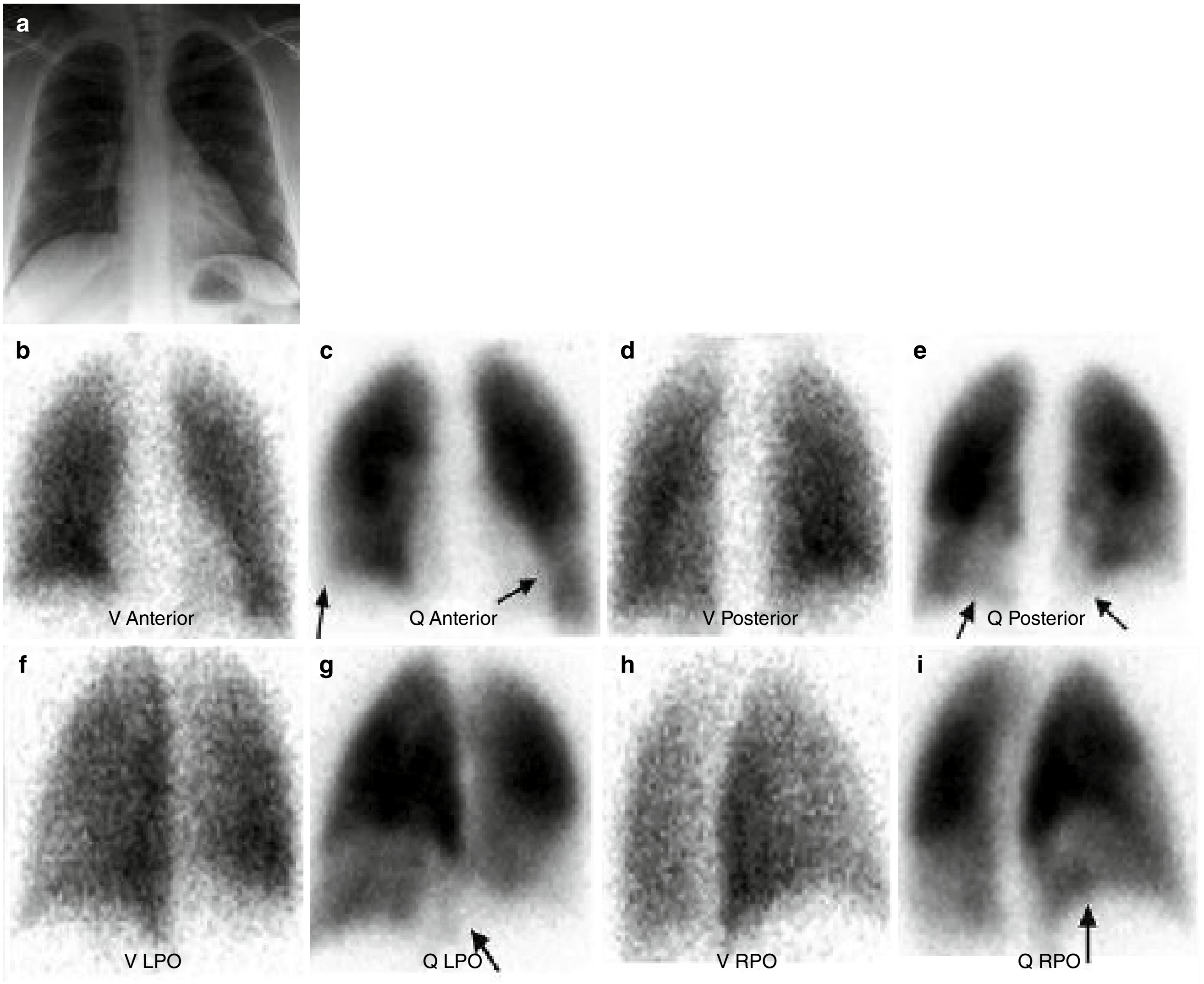

Fig. 14.3 High probability for acute PE as evidenced by multiple V/Q mismatches. Normal PA chest radiograph (**a**). Normal ^{99m}Tc DTPA ventilation (**b**, **d**, **f**, **h**) and abnormal ^{99m}Tc MAA perfusion (**c**, **e**, **g**, **i**) with multiple bilateral lower lobe segmental perfusion defects (*arrows*)

Table 14.3 Modified PIOPED II

Interpretation	Patterns on V/Q lung scintigraphy
PE absent: "normal"	No perfusion defects
PE absent: "very low probability"	Nonsegmental perfusion defects (e.g., cardiomegaly, enlarged hila, elevated hemidiaphragm)
	Perfusion defect smaller than corresponding chest X-ray abnormality
	Two or more V/Q matching defects with corresponding normal chest X-ray and otherwise relatively normal perfusion
	Three or fewer small segmental perfusion defects
	Triple-matched V/Q/X-ray abnormality in upper/mid-lung
	Stripe sign (i.e., preserved perfusion to pleural surface)
	Large pleural effusion with otherwise normal perfusion
Nondiagnostic for PE: "low probability" or "intermediate probability"	All other patterns, including triple-matched V/Q/X-ray abnormality in lower lung
PE present: "high probability"	Two or more segmental V/Q mismatching defects without corresponding chest X-ray abnormalities

Simplified criteria for interpretation of V/Q lung scintigraphy for diagnosis of acute PE
Adapted from Parker et al. and Sostman et al. [1, 2]

radiographs should be directed to CTA and are not well suited for V/Q lung scintigraphy because there is a greater likelihood of a nondiagnostic interpretation due to confounding underlying pulmonary conditions such as chronic obstructive lung disease, pneumonia, pleural effusion(s), atelectasis, perihilar mass, or hilar fibrosis (Fig. 14.4) [17]. Concomitantly, there can be considerable interobserver variability of V/Q interpretations, especially in the low and intermediate probability categories. CTA has the distinct advantage of evaluating the entire chest and upper abdomen and can delineate alternative thoracic or abdominal pathologies.

Second, in most institutions today, CTA is available around-the-clock with an on-site CT technologist who can perform the examination in a timely manner. During the standard workday, V/Q lung scintigraphy can be performed relatively quickly; however, during the off-hours, the NM technologist usually needs to travel to the hospital, and the radiopharmaceuticals may need to be prepared in-house

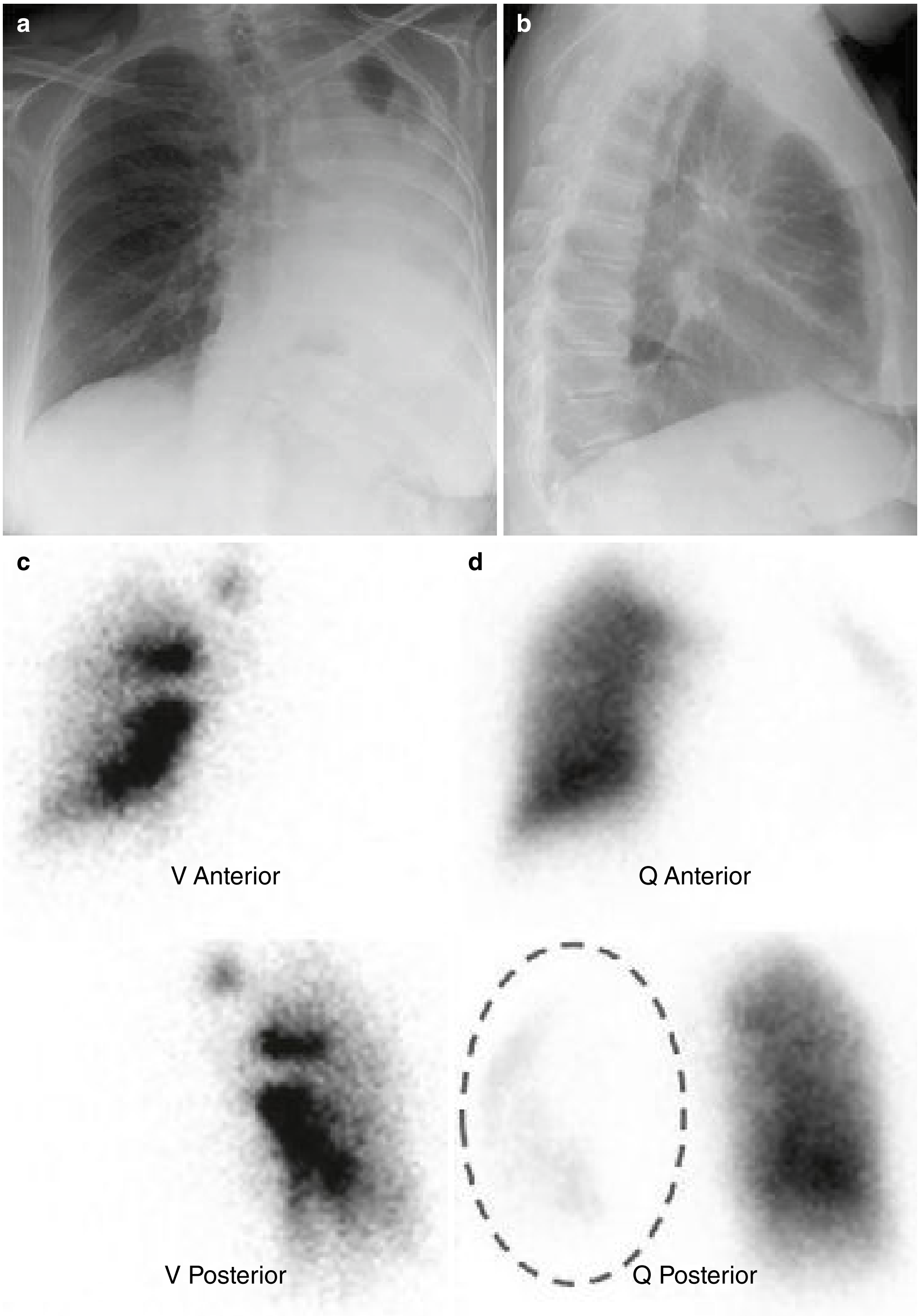

Fig. 14.4 Abnormal V/Q scan secondary to left hilar mass. Whole lung-matched defect. Opacification of the left lung on posterior-anterior (**a**) and lateral (**b**) chest radiographs. Abnormal left whole lung on ^{99m}Tc DTPA ventilation (**c**) and ^{99m}Tc MAA perfusion (**d**) scintigraphy. Note faint perfusion in the left lung (*dashed outline*) but absent ventilation

or, most often, delivered from an outside nuclear pharmacy, all requiring additional time. The patient will need to be transported to the NM imaging suite, which is typically located at a distance from the emergency department.

Third, there is much concern about radiation dosimetry, and the risks related to iodinated contrast are well established [3]. With CTA, there is higher radiation exposure to the patient, particularly to the female breast. The tissue dose to the breasts of nonpregnant women can be 10–60 mGy (1–6 rad) and is likely higher in pregnancy. Conversely, the breast dose from V/Q lung scintigraphy can be much lower than 0.31 mGy (0.031 rad) or almost 200 times less than CTA. During the first trimester of pregnancy, the fetal dose can be halved by using a modified V/Q lung scintigraphy protocol resulting in reduced administered activity. In a pregnant person, the perfusion study can be performed first, and if normal, the ventilation portion does not need to be completed [1, 3]. The fetal dose depends on the stage of gestation, which should be considered when determining the appropriate imaging study. Thus, for selected patients with special medical considerations such as pregnancy, breastfeeding, poor renal function, or iodinated contrast allergy, V/Q lung scintigraphy may represent the most appropriate imaging option.

In summary, V/Q lung scintigraphy can be considered a primary imaging approach in patients with suspected acute PE when there is:

1. Normal chest radiography
2. No concurrent cardiopulmonary process
3. Available NM facilities and personnel
4. Relative contraindication to CTA regarding radiation exposure or use of iodinated contrast

Acute Coronary Syndrome: Myocardial Perfusion Imaging

Acute coronary syndrome (ACS) accounts for approximately 10% of all emergency department visits, making it one of the most commonly encountered medical emergencies. ACS refers to a spectrum of clinical presentations ranging from ST-segment elevation myocardial infarction to unstable angina. Clinical presentation, electrocardiography (ECG), and cardiac biomarkers, such as troponin, guide initial risk stratification. Troponin has become the favored biomarker for determination of myocardial necrosis because of the high sensitivity and specificity. However, myocardial biomarkers can only diagnose infarction and cannot identify ischemia in the absence of necrosis; also, laboratory evidence lags behind the physiological event. By convention, patients are stratified into three risk groups: high, moderate, and low.

The majority of patients with chest pain have no history of coronary artery disease and no ischemic ECG changes. Risk of ACS in such patients is low; however, it is not zero. Identification of high-risk patients within this cohort can be difficult clinically. Thus, many patients without ischemia are admitted for observation and further testing. Conversely, despite a low threshold for admission, a significant minority of patients with atypical symptoms of ACS who actually have acute myocardial infarction are initially triaged as low risk and are inadvertently discharged home [18].

Myocardial perfusion imaging (MPI) can be effectively used as a triage tool in patients with chest pain of unclear etiology [6]. MPI typically utilizes one of the two available ^{99m}Tc radiopharmaceuticals, ^{99m}Tc sestamibi or ^{99m}Tc tetrofosmin (Table 14.4). The biodistribution within the left ventricular myocardium is generally proportional to coronary arterial blood flow at the time of IV administration; these radiotracers do not redistribute for several hours. Normally, there is uniform myocardial perfusion (Fig. 14.5). If a patient with ACS is injected at rest while experiencing coronary-related chest pain, the distribution of the perfusion agent will be altered and will demonstrate diminished regional perfusion corresponding to the vascular territory involved (Fig. 14.6). However, acute or prior myocardial infarction may produce a similar perfusion defect on rest MPI; therefore, differentiation between ischemia and infarction may not be possible with rest MPI alone.

Rest MPI in symptomatic patients has reported sensitivities of 90–100% with negative predictive value (NPV) of greater than 99% for identifying patients without cardiac events [7]. The high sensitivity of rest MPI is dependent on the presence of chest pain during radiotracer injection; that is, MPI in patients injected after cessation of chest pain does not yield the same sensitivity, and that subgroup should undergo stress testing. Thus, the high NPV of rest MPI in patients with chest pain allows the emergency physician to establish confidently the absence of myocardial ischemia or infarction as the etiology of the symptomatology. Specifically, negative rest MPI directs disposition of patients who might otherwise have a prolonged hospital stay, and, conversely, positive rest MPI identifies high-risk patients who might be categorized incorrectly as low risk and might have a delayed diagnosis of ACS.

Table 14.4 Typical rest with chest pain myocardial perfusion imaging (MPI) technical protocol

1. Administer 25 mCi (925 MBq) of ^{99m}Tc sestamibi or ^{99m}Tc tetrofosmin IV while the patient has chest pain at rest
2. Wait for 15–30 min
3. Perform single-photon emission computed tomography (SPECT) or SPECT/CT imaging
4. Evaluate rest-only images

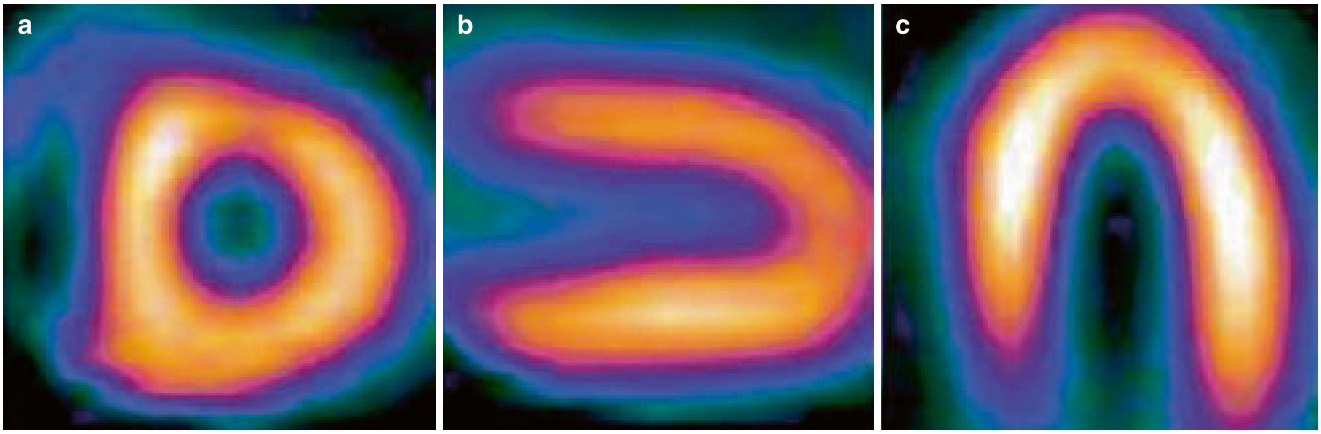

Fig. 14.5 Normal rest MPI. Uniform ^{99m}Tc sestamibi activity throughout the left ventricular myocardium. (**a**) Short-axis, (**b**) vertical long-axis, and (**c**) horizontal long-axis images

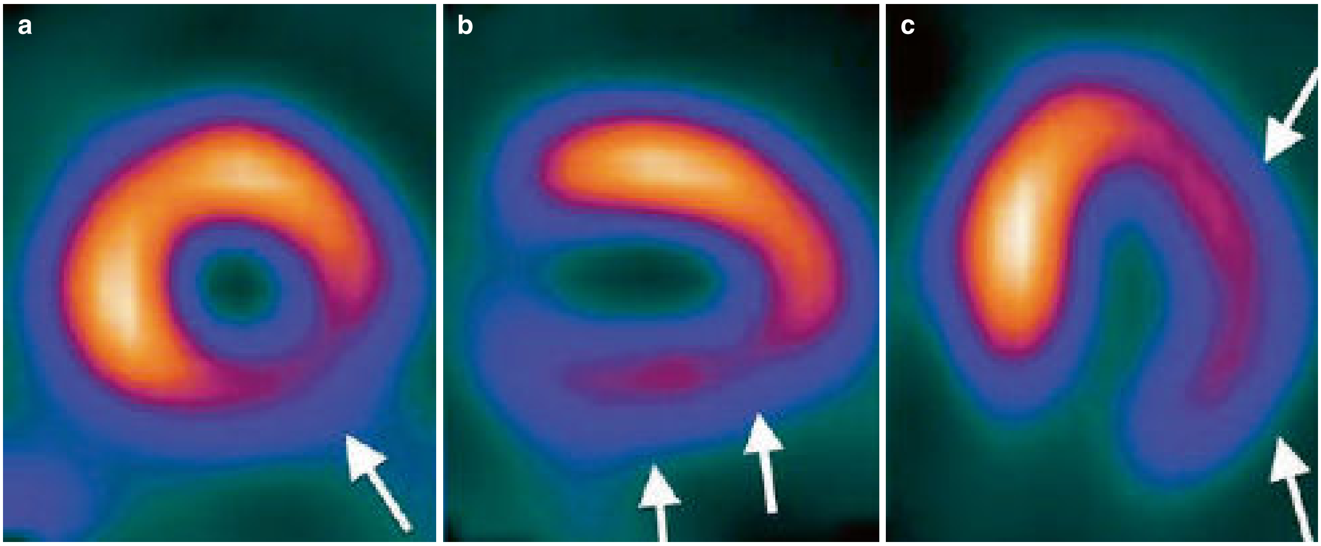

Fig. 14.6 Abnormal rest MPI. High-grade occlusion of left circumflex coronary artery as etiology of active chest pain during ^{99m}Tc sestamibi administration IV. Large, moderately severe perfusion defect in the inferior-lateral wall extending from apex to base (*arrows*). (**a**) Short-axis, (**b**) vertical long-axis, and (**c**) horizontal long-axis images

Incorporation of MPI into the acute chest pain diagnostic algorithm is beneficial. The ERASE trial [19, 20] demonstrated that MPI in the emergency setting reduced unnecessary admissions without increasing inappropriate discharges. MPI as a triage tool is most effective when used on low-risk patients who are experiencing active chest pain (i.e., hemodynamically stable, no ECG changes, no prior coronary disease). Together, concordantly negative rest MPI and negative biomarkers identify patients who can safely be discharged or, alternatively, undergo early stress testing with or without hospital admission depending on those results. MPI is the only commonly available imaging technique that provides a direct and accurate assessment of myocardium at risk [7]. The greatest benefit of MPI lies in its high NPV, which assists the emergency physician in effectively excluding ACS in low-risk patients, lowering costs, shortening length of hospital stay, and decreasing morbidity [21].

In summary, in conjunction with biomarkers such as troponin, MPI can be used as a triage tool to establish the absence of myocardial ischemia or infarction as the etiology of active chest pain in patients who meet the following criteria:

1. Hemodynamically stable
2. Chest pain of unclear etiology
3. No ischemic ECG changes
4. Considered low risk for ACS

Acute Biliary Conditions: Hepatobiliary Scintigraphy

Cystic Duct Obstruction (Acute Cholecystitis) and Common Bile Duct Obstruction

Greater than 95% of acute cholecystitis is caused by complete obstruction of the cystic duct, typically related to one or multiple gallstones. The blockage results in potentially fatal pathophysiologic changes including lymphatic and venous obstruction, mucosal congestion and edema, acute inflammatory leukocyte infiltration, hemorrhage and necrosis, and, finally, complications of gangrene, perforation, and abscess [9, 22]. Therefore, early diagnosis and appropriate management are essential to reduce mortality and morbidity.

Hepatobiliary scintigraphy (HBS), colloquially known as HIDA scanning or cholescintigraphy (Table 14.5), provides a physiologic map of hepatocellular function and bile flow. Given IV, the ^{99m}Tc iminodiacetic acid (IDA) analog is extracted by the liver and is rapidly secreted into the bile. Normally, radioactive bile enters the biliary system including the gallbladder and passes into the small bowel within 1 h (Fig. 14.7).

In acute cholecystitis, there is a high likelihood that the cystic duct is obstructed. Thus, the hallmark finding of acute cholecystitis on HBS is nonvisualization of the gallbladder yet prompt visualization of the common bile duct and duodenum (Fig. 14.8). Complicated acute cholecystitis is supported by the pericholecystic rim sign, which is manifested by increased hepatic radiotracer activity adjacent to the gallbladder fossa. The rim sign is seen in approximately 20% of HBS with a nonvisualized gallbladder and is strongly associated with complicated acute cholecystitis; furthermore, approximately 40% have a gangrenous or perforated gallbladder (see Fig. 14.8). Delayed gallbladder visualization suggests chronic cholecystitis with resistance to bile flow within the cystic duct without true obstruction (Fig. 14.9). Causes of false-positive and false-negative interpretations of HBS for acute cholecystitis are listed in Table 14.6.

Sensitivity and specificity for the accurate HBS diagnosis of acute cholecystitis increase with time. For conventional HBS, the false-positive rate decreases from 10% when imaging is completed at 1 h to less than 1% when imaging is continued to 4 h, and the specificity improves from 88 to 99% [22]. Consequently, delayed imaging became the standard

Table 14.5 Typical hepatobiliary scintigraphy technical protocol for acute cholecystitis or common bile duct obstruction

1. Patient should be fasting for 4 h; if fasting longer than 24 h, administer sincalide (synthetic CCK, 0.02 ucg/kg, IV) over 30 min, 15 min prior to hepatobiliary tracer injection, to prepare gallbladder
2. Administer 4 mCi (148 MBq) of ^{99m}Tc IDA analog IV
3. Acquire anterior images dynamically at 1 frame/min for 60 min or until gallbladder and small bowel are visualized
4. After 60 min, if small bowel is visualized without gallbladder visualization, administer morphine sulfate (0.04 mg/kg IV) preceded by a 2 mCi (74 MBq) booster of ^{99m}Tc IDA analog IV; if small bowel is not visualized, morphine sulfate is contraindicated
5. Acquire anterior images dynamically at 1 frame/minute for 30 min; additional anterior, left anterior oblique, and/or right lateral static images can be acquired after the 30-min dynamic images
6. If no small bowel is visualized or if there is poor clearance from the liver parenchyma, delayed anterior, left anterior oblique, and/or right lateral static images should be acquired after an additional 2–4 h or up to 24 h

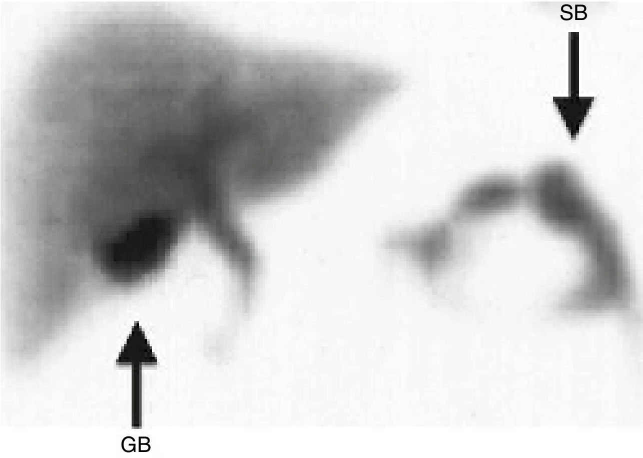

Fig. 14.7 Normal. Anterior image 20 min after ^{99m}Tc IDA analog IV. Visualization of gallbladder (*GB*) and small bowel (*SB*)

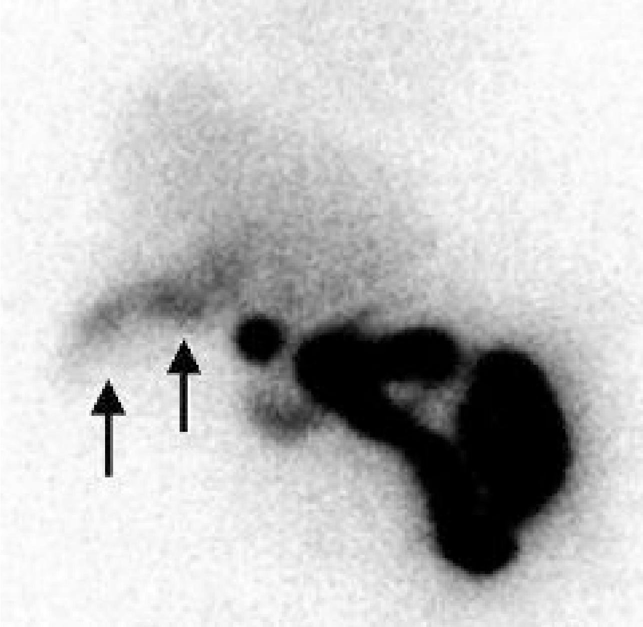

Fig. 14.8 Acute gangrenous cholecystitis. Anterior image at 2 h after IV ^{99m}Tc IDA analog. Nonvisualization of gallbladder with pericholecystic rim sign (*arrows*)

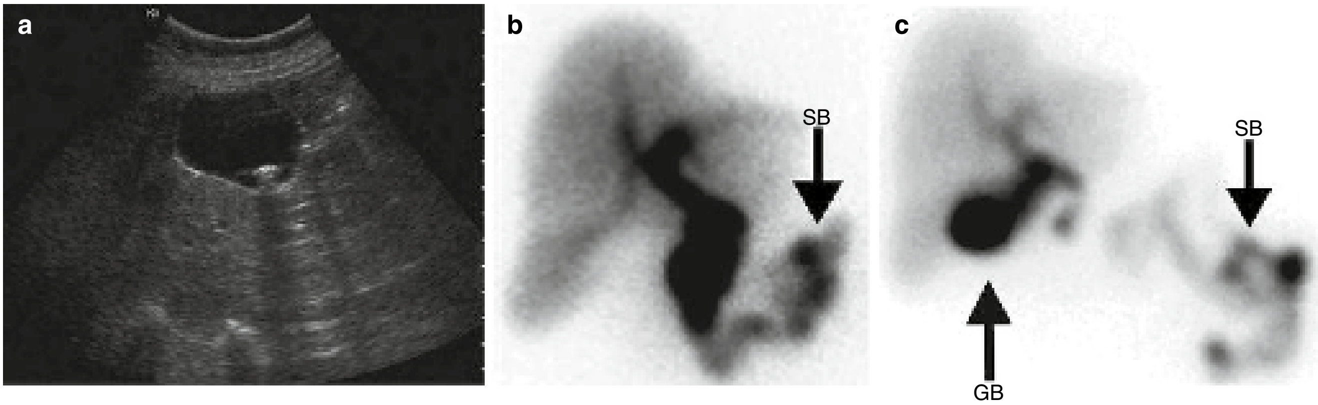

Fig. 14.9 Chronic calculous cholecystitis. Gallstones by ultrasound (**a**). On HBS, gallbladder nonvisualization at 1 h (**b**) after ^{99m}Tc IDA analog IV, but visualization (*GB*) at 20 min following morphine sulfate IV (**c**). Note small bowel (*SB*)

Table 14.6 False positives and false negatives on HBS for acute cholecystitis

Causes of false-positive interpretations (nonvisualized gallbladder)	Causes of false-negative interpretations (apparently visualized gallbladder)
Recent meal (<4 h)	Acalculous cholecystitis
Prolonged fasting (>24 h)	Perforated acute cholecystitis with bile leak
High-grade common bile duct obstruction	Accessory cystic duct or dilated cystic duct sign simulating gallbladder
Chronic cholecystitis	Duodenal diverticulum or bowel loop-simulating gallbladder (misinterpretation)
Severe hepatocellular disease	
Cystic duct cholangiocarcinoma	
Pancreatitis (rare)	

protocol to differentiate acute cholecystitis from chronic cholecystitis, with the latter condition often demonstrating delayed gallbladder visualization. The administration of IV morphine sulfate during HBS shortens the duration and increases the specificity for acute cholecystitis. By constricting the sphincter of Oddi, morphine sulfate raises pressure within the common bile duct, thereby diverting bile through a patent cystic duct and facilitating gallbladder visualization (see Fig. 14.9). The small bowel must be visualized to apply the morphine augmentation protocol. It is important to determine if opioid medications were given to the patient in the emergency department to ensure that additional opiates are not administered inadvertently. Morphine-augmented cholescintigraphy has a high accuracy and is as accurate as delayed imaging [9].

When compared to ultrasonography for the diagnosis of acute cholecystitis, HBS has superior sensitivity (88% vs. 50%), specificity (93% vs. 88%), positive predictive value (85% vs. 64%), negative predictive value (95% vs. 80%), and accuracy (92% vs. 77%) [8, 23]. However, as discussed earlier in this chapter, logistical challenges limit the availability of NM during off-hours and impact the clinical application of this excellent scintigraphic technique. Thus, right upper quadrant ultrasonography reigns as the first-line modality for acute cholecystitis, and it can provide information regarding alternative non-biliary diagnoses.

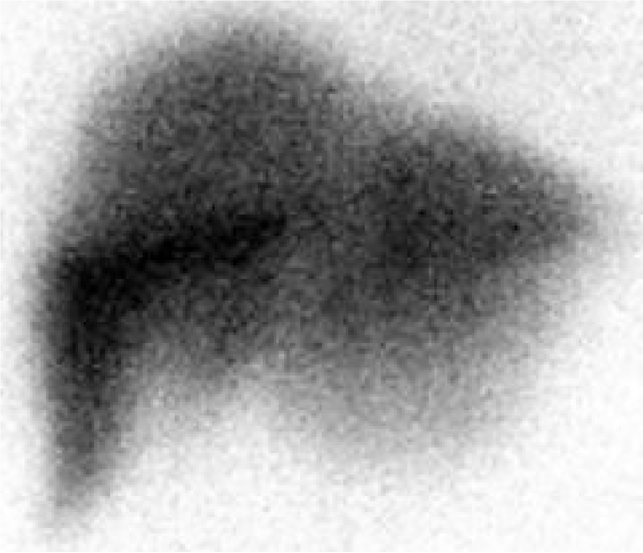

Fig. 14.10 Complete common bile duct obstruction. On HBS, uniform liver activity without biliary or small bowel activity at 24 h after ^{99m}Tc IDA analog IV

When bile fails to flow from the liver, the differential diagnosis includes acute high-grade/complete common bile duct obstruction, often related to distally impacted gallstone(s), versus underlying hepatocellular dysfunction. HBS can continue up to 24 h; however, the clinical context may direct management after only a few hours of imaging. The classic HBS finding of common bile duct obstruction is a persistent liver ("hepatogram") without excretion into the bile ducts and nonvisualization of the small bowel (Fig. 14.10) [22]. Ultrasonography may be normal early on because it may take the common bile duct up to 72 h to dilate in response to a distal obstruction. It should be noted that the patency of the cystic duct cannot be established by HBS when bile flow from the liver is severely impaired. For example, total bilirubin greater than 10 mg/dL may not result in a diagnostic study.

Bile Duct Injury

Bile duct injuries commonly occur after blunt abdominal trauma and are secondary to a shearing injury of the biliary system. Additionally, bile duct injuries can be iatrogenic after cholecystectomy or liver transplant. Bile duct injuries may lead to bile peritonitis, which may require days or weeks to develop; thus, the clinical diagnosis may be elusive. While CT and ultrasonography can identify and localize intra-abdominal fluid collections, they cannot characterize them as containing bile.

HBS is the noninvasive standard for diagnosis of bile leak [24]. As discussed earlier in this chapter, HBS uses ^{99m}Tc IDA analogs. For evaluating bile leaks, the technical protocol is modified (Table 14.7). HBS can detect free or localized bile collections (bilomas) as well as provide information on the rate and extent of the leak. Leaks may be slow or fast, active or intermittent. If radioactive bile extravasates outside of the normal biliary and gastrointestinal tracts, there is an active bile leak (Fig. 14.11). The precise site of bile leakage is possible with HBS, which may allow less invasive measures for management. Furthermore, based on HBS findings, management may be conservative or may progress to percutaneous drainage, endoscopic retrograde cholangiography, or laparotomy.

In the emergency setting, particularly after blunt or penetrating trauma, HBS may be appropriate to identify an active bile leak or to characterize an abnormal fluid collection visualized on CT. For example, a liver laceration with significant bile duct injury may require different initial management compared to one without bile duct injury [25].

Table 14.7 Typical hepatobiliary scintigraphy technical protocol for bile leak

1. Administer 4 mCi (148 MBq) of ^{99m}Tc IDA analog IV
2. Acquire anterior images dynamically at 1 frame/minute for 60–90 min or until liver is cleared or bile leak is identified
3. Acquire anterior and posterior, right and left anterior oblique, and/or right lateral static images up to 24 h, as needed; if available, consider SPECT/CT
4. Image biliary drains, if present

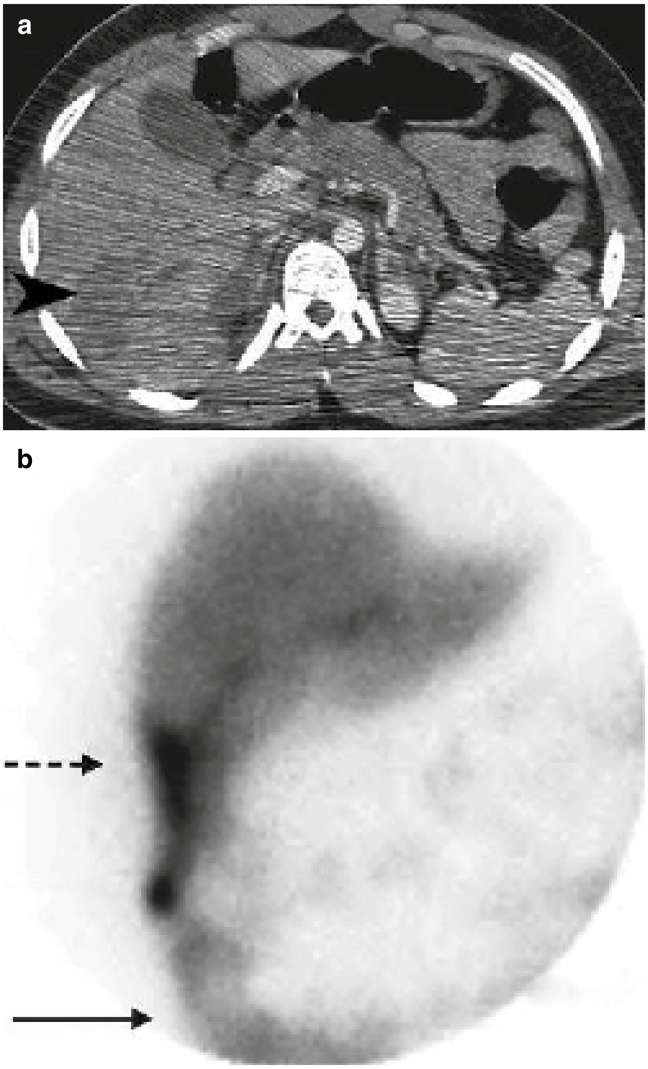

Fig. 14.11 Active bile leak. Liver laceration in right lobe (*arrowhead*) on CT (**a**) after blunt trauma. On hepatobiliary scintigraphy at 30 min after ^{99m}Tc IDA analog IV (**b**), free leakage of bile (*dashed arrow*) into the right paracolic gutter (*long arrow*) and throughout the peritoneal cavity without expected intraluminal small bowel activity

In summary, by providing a physiologic map of the biliary system, HBS should be strongly considered and utilized whenever available in the acute emergency setting to:

1. Provide a more specific diagnosis of acute cholecystitis as compared to ultrasonography
2. Establish patency and integrity of the hepatobiliary-small bowel system; evaluate for high-grade common bile duct obstruction
3. Detect active bile leak, particularly after trauma

Gastrointestinal Hemorrhage: GI Bleeding and Meckel's Diverticulum Scintigraphy

GI Bleeding Study

Acute GI hemorrhage can be a life-threatening event and requires prompt diagnosis and appropriate intervention. Upper GI hemorrhage is defined as bleeding that originates proximal to the ligament of Treitz, whereas lower GI hemorrhage occurs distal to this landmark. Upper GI hemorrhage typically presents with either hematemesis or melanotic stools, whereas lower GI hemorrhage usually presents with hematochezia.

Endoscopy is a well-tolerated and generally successful first-line approach for patients with suspected upper GI hemorrhage; esophageal, gastric, or duodenal bleeding sites can be visualized and treated directly. Suspected lower GI hemorrhage presents different challenges. Prompt localization of the bleeding site is crucial to patient management; time to diagnosis is an important determinant of outcome in high-risk lower GI hemorrhage [26]. Endoscopy is an option, but is more limited in an unprepared colon that might be filled with blood from a proximal source, and the small bowel cannot be examined. Two diagnostic imaging modalities are available to identify and localize the lower GI source: ^{99m}Tc RBC scintigraphy and angiography. Despite the well-documented sensitivity, only 10–15% of patients presenting with lower GI hemorrhage are evaluated with scintigraphy [12].

Table 14.8 Typical dynamic red blood cell scintigraphy technical protocol

1. Remove aliquot of blood for radiolabeling
2. Radiolabel red blood cells with ^{99m}Tc sodium pertechnetate by in vitro kit method
3. Administer 25 mCi (925 MBq) of ^{99m}Tc-labeled red blood cells IV
4. Acquire anterior images dynamically at 1 frame every 10–60 s for 60–90 min
5. Review images in cinematic mode

Dynamic GI bleeding scintigraphy utilizes ^{99m}Tc-labeled red blood cells (RBCs) (Table 14.8) and can effectively identify and localize slow or rapid, active or intermittent lower GI bleeding. Radiolabeled RBCs that extravasate from the normal circulatory system (referred to as the blood pool) are relatively easily identified because of a high target-to-background ratio of the imaging study. The extravasated radiolabeled RBCs will move (antegrade or retrograde) in the bowel lumen over time, aiding in pinpointing the site of origin (Fig. 14.12).

RBC scintigraphy offers several advantages over angiography in localizing bleeding sites. First, bleeding rates as low as 0.1–0.3 mL/min are detectable with scintigraphy; catheter-based angiography or CTA requires rates at least tenfold higher [27]. Second, RBC scintigraphy allows examination of the entire lower GI tract continuously for whatever period of time is needed and tolerated by the patient's clinical condition. Continuous imaging for long periods of time allows for the detection of intermittent GI bleeding [14, 28]. Third, there are fewer complications compared with more invasive angiography, and the radiation exposure is significantly lower. Last, RBC scintigraphy can direct angiographic confirmation, expediting intervention.

As a noninvasive modality with high sensitivity, scintigraphy has been assessed as an important prognostic tool in GI hemorrhage. Negative results predict good clinical outcome [26]; positive results predict greater hospital morbidity and mortality [26]. Positive results are accurate in localizing the

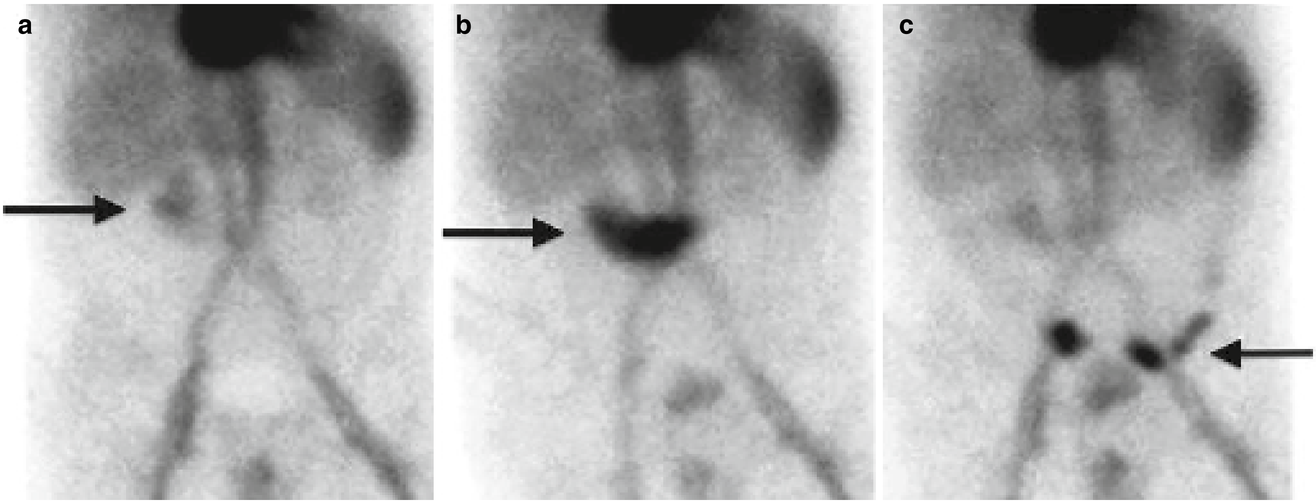

Fig. 14.12 Active bleed in proximal transverse colon. Selected images at 6 min (**a**), 38 min (**b**), and 50 min (**c**) after ^{99m}Tc RBCs IV. Active extravasation into right upper quadrant (**a**, *arrow*) with movement into mid-abdomen (**b**, *arrow*) and further movement distally into the descending colon and sigmoid colon (**c**, *arrow*) over time

bleeding site in approximately 75% [27]. False positives include horseshoe kidney, hepatic hemangiomata, ischemic bowel, uterine leiomyomata, and aneurysmal and collateral vasculature [14, 28].

In summary, RBC scintigraphy should be considered as the primary imaging approach in patients presenting with GI bleeding under the following conditions:

1. Hemodynamically stable
2. Localization of the source desired to direct intervention

Meckel's Diverticulum Scintigraphy

Meckel's diverticulum scintigraphy can identify bleeding from a Meckel's diverticulum containing ectopic gastric mucosa (Table 14.9). The clinical presentation is typically an occult bleed, which may result in anemia, usually not an emergency; however, in some cases, acute bleeding may lead to hypovolemic shock and be life-threatening. Bleeding from a Meckel's diverticulum is the most common cause of lower GI bleed in an otherwise healthy young child. Meckel's diverticulum is the most common congenital abnormality in the GI tract, occurs in 1–2% of the population, and is found in the antimesenteric mid- to distal ileum when there is incomplete involution of the omphalomesenteric duct. The diverticulum may contain heterotopic tissues ranging across gastric, pancreatic, and/or colonic types. Gastric cells take up ^{99m}Tc sodium pertechnetate ("free" ^{99m}Tc); thus, scintigraphy using this radiotracer can identify a bleeding source if it is a Meckel's diverticulum containing ectopic gastric mucosa (Fig. 14.13). Medications such as histamine H2 blockers or proton pump inhibitors may increase imaging sensitivity by inhibiting secretion of gastric acid and limiting release of ^{99m}Tc pertechnetate (Fig. 14.14) [15].

In summary, Meckel's diverticulum scintigraphy has a very high sensitivity and specificity for the detection of a gastric mucosa containing Meckel's diverticulum and should be utilized as first-line imaging studies under the following conditions.

1. Hemodynamically stable
2. Gastrointestinal bleeding in a child

Table 14.9 Typical Meckel's diverticulum scintigraphy technical protocol

1. Premedicate with histamine H2 blockers or proton pump inhibitors (optional)
2. Administer children 0.05 mCi/kg (1.85 MBq/kg) or adults 10 mCi (370 MBq) of ^{99m}Tc sodium pertechnetate IV
3. Acquire anterior images of the abdomen and pelvis dynamically at 30–60-s intervals for 30–60 min
4. Acquire anterior and right lateral static images of the mid-abdomen and pelvis after the patient voids

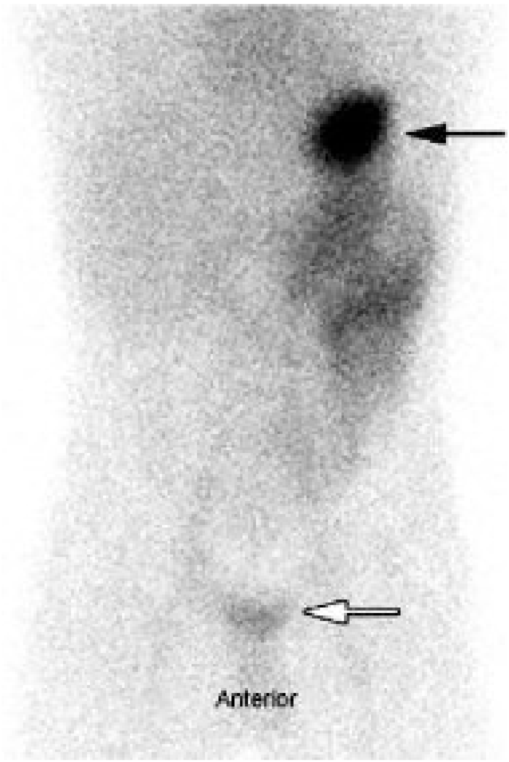

Fig. 14.13 Negative ^{99m}Tc sodium pertechnetate scan for Meckel's diverticulum. Note normal activity in the stomach (*arrow*) as well as normal intraluminal small bowel activity in the left abdomen. Normal activity is seen in the post-void bladder (*open arrow*)

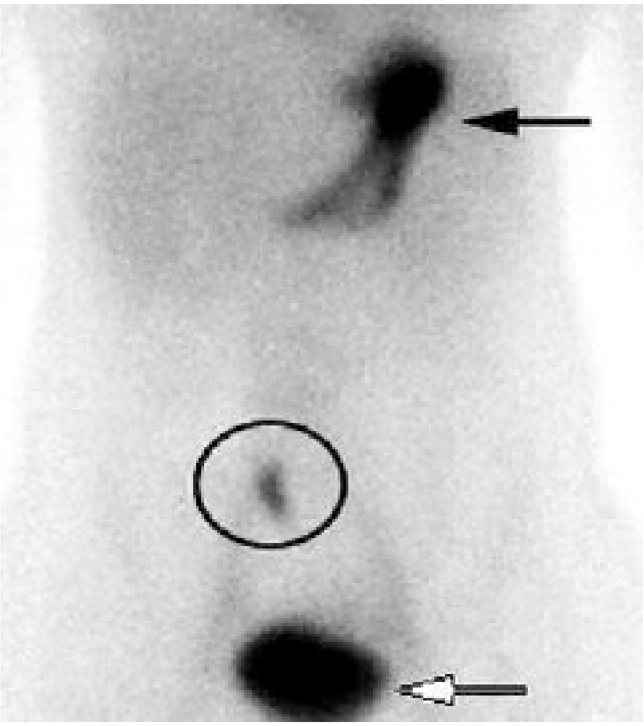

Fig. 14.14 Positive ^{99m}Tc sodium pertechnetate scan for Meckel's diverticulum (circle). Note the normal stomach (*solid arrow*) and bladder (*open arrow*)

Teaching Points

- Ventilation/perfusion (V/Q) lung scintigraphy should be considered as the primary imaging approach in patients with suspected acute PE and normal chest radiography, no concurrent cardiopulmonary process, relative contraindications to iodinated contrast for CTA, or concerns related to radiation dosimetry.
- Rest myocardial perfusion imaging (MPI) is most effective as a triage tool when applied to low-risk patients who present with active chest pain; negative rest MPI and concordantly negative biomarkers identify patients who can safely be discharged or, conversely, positive rest MPI may lead to early stress testing to determine the need for admission.
- Hepatobiliary scintigraphy (HBS) provides a physiologic map of bile flow, uncovering normal or obstructive patterns, and boasts superior diagnostic capabilities as compared to ultrasonography for the diagnosis of acute cholecystitis. HBS can detect subtle bile duct injuries, particularly in the setting of blunt trauma or postoperative situations.
- Dynamic ^{99m}Tc-labeled red blood cell (RBC) scintigraphy can pinpoint the source of active or intermittent lower gastrointestinal hemorrhage and directs angiographic or surgical intervention.
- Meckel's diverticulum scintigraphy can identify an occult source of gastrointestinal bleed from a gastric mucosa-containing Meckel's diverticulum, particularly in young children.

Questions

1. A 40-year-old patient who is allergic to iodinated contrast presents with acute dyspnea. He undergoes chest radiography and a V/Q lung scan to assess for acute pulmonary embolism. Based on the images shown (Fig. 14.15), what is the probability of acute pulmonary emboli?
   - (A) Very low
   - (B) Low
   - (C) Intermediate
   - (D) High

Answer: D. High probability. Normal posterior-anterior (**a**) and lateral (**b**) chest radiographs. Normal ^{99m}Tc DTPA ventilation (**c**, **e**, **g**, **i**) and markedly abnormal ^{99m}Tc MAA perfusion (**d**, **f**, **h**, **j**). Note the multiple large mismatched segmental perfusion defects in both lungs.

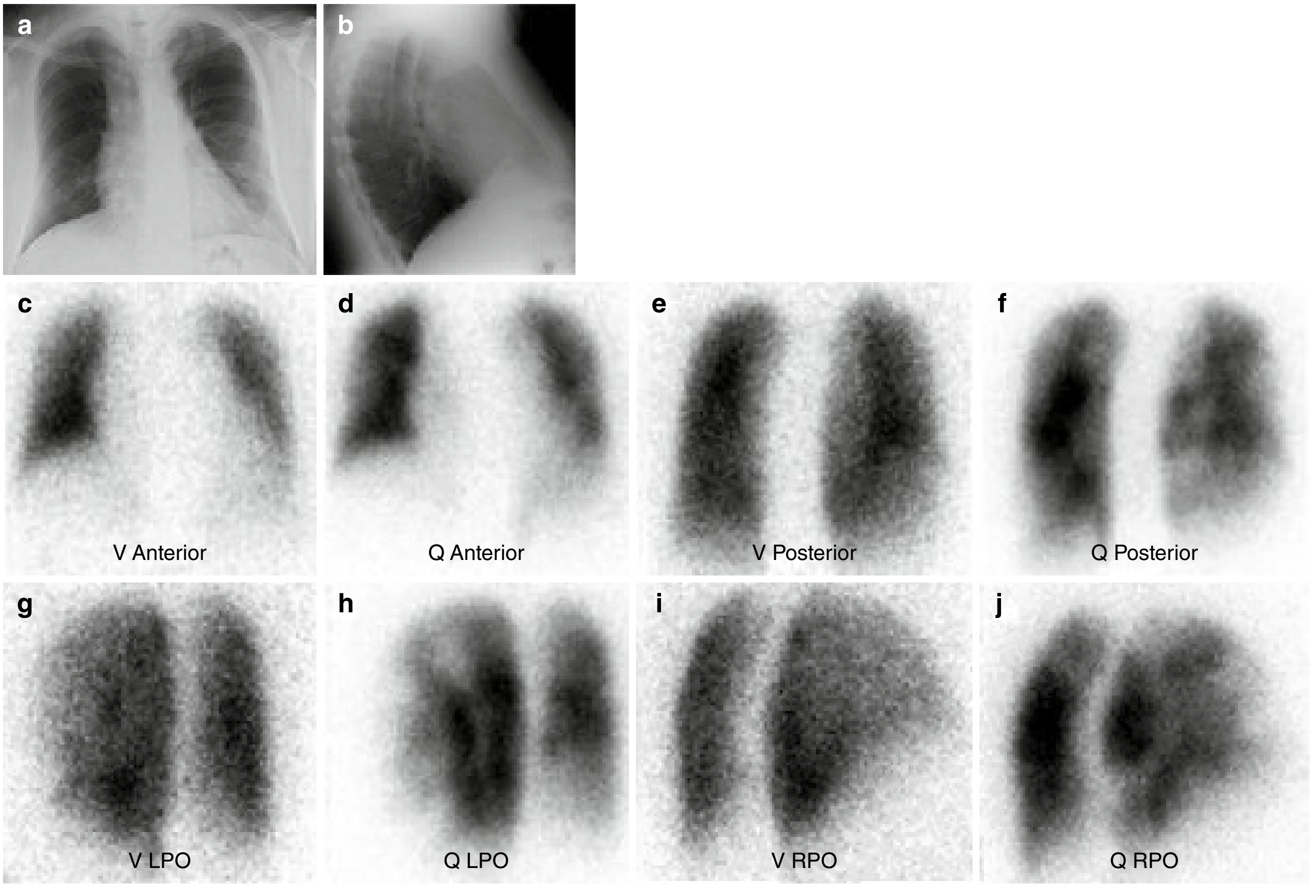
a
b
c
V Anterior
d
Q Anterior
e
V Posterior
f
Q Posterior
g
V LPO
h
Q LPO
i
V RPO
j
Q RPO

Fig. 14.15 Chest radiography and a V/Q lung scan

2. A 56-year-old patient presents to the emergency department with acute chest pain. The rest myocardial perfusion images (Fig. 14.16) demonstrate a defect signaling ischemia or infarct in which vascular territory? (**a**) Short-axis, (**b**) vertical long-axis, and (**c**) horizontal long-axis images.
   (A) Left anterior descending coronary artery
   (B) Right coronary artery
   (C) Left circumflex artery
   (D) Left main coronary artery

Answer: A. Myocardial perfusion images from a rest-only scan show large severe defects involving the anterior, septal, and apical walls (arrows). (**a**) Short-axis, (**b**) vertical long-axis, and (**c**) horizontal long-axis images.

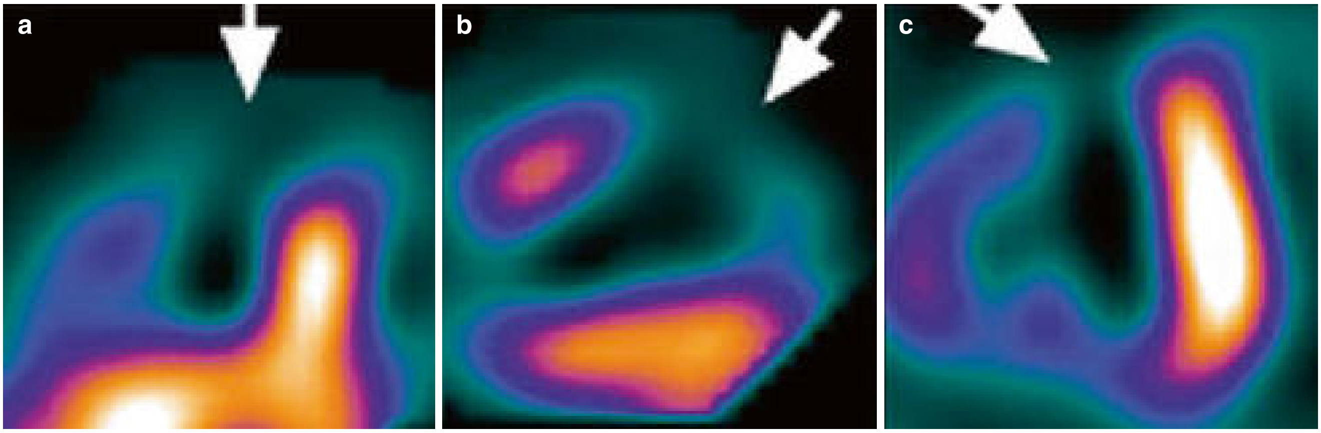

Fig. 14.16 Myocardial perfusion images

3. A 39-year-old patient underwent a laparoscopic cholecystectomy for chronic cholecystitis and had been discharged home. Two days later, they presented to the ED with severe right upper quadrant pain. The patient went to the operating room, was found to have a bile leak from a duct of Luschka, and had abdominal drain placement. The images (Fig. 14.17) are from the hepatobiliary scan. What is the best interpretation?
   (A) No active bile leak
   (B) Active bile leak
   (C) Liver failure
   (D) Common bile duct obstruction

Answer: B. Active bile leak draining into a right-sided abdominal drainage catheter (solid arrows) and bile also flows along its normal pathway into the small bowel (outlined arrow).

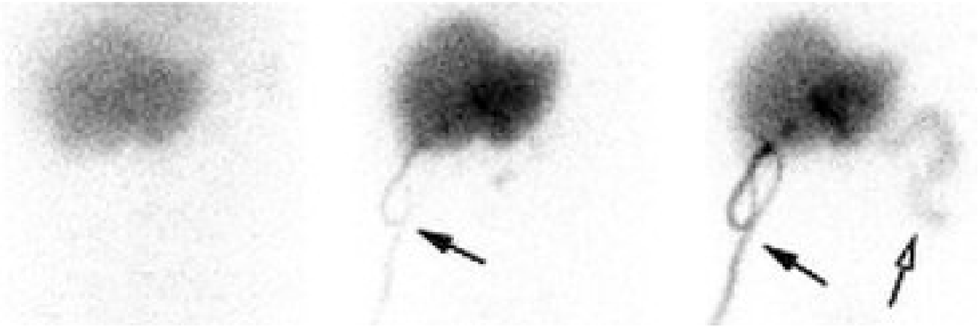

Fig. 14.17 Active bile leak-hepatobiliary scan

4. A 50-year-old patient with hematochezia and hypotension is evaluated with upper endoscopy and colonoscopy; however, no source of bleeding is identified. A GI bleeding scan is performed (Fig. 14.18). Localize the source of bleeding.
   (A) Duodenum
   (B) Small bowel
   (C) Large bowel

   What arterial vascular territory supplies the bleeding site?
   (A) Celiac artery
   (B) Superior mesenteric artery
   (C) Inferior mesenteric artery

Answers: B and B. Small bowel and superior mesenteric artery, respectively. The bleeding site is the jejunum, which is supplied by the superior mesenteric artery. Note that the active extravasation in the left mid-abdomen has a serpentine pattern and increases over time, consistent with active bleed in the jejunum (arrows). Normal bladder activity is visualized due to vicarious excretion.

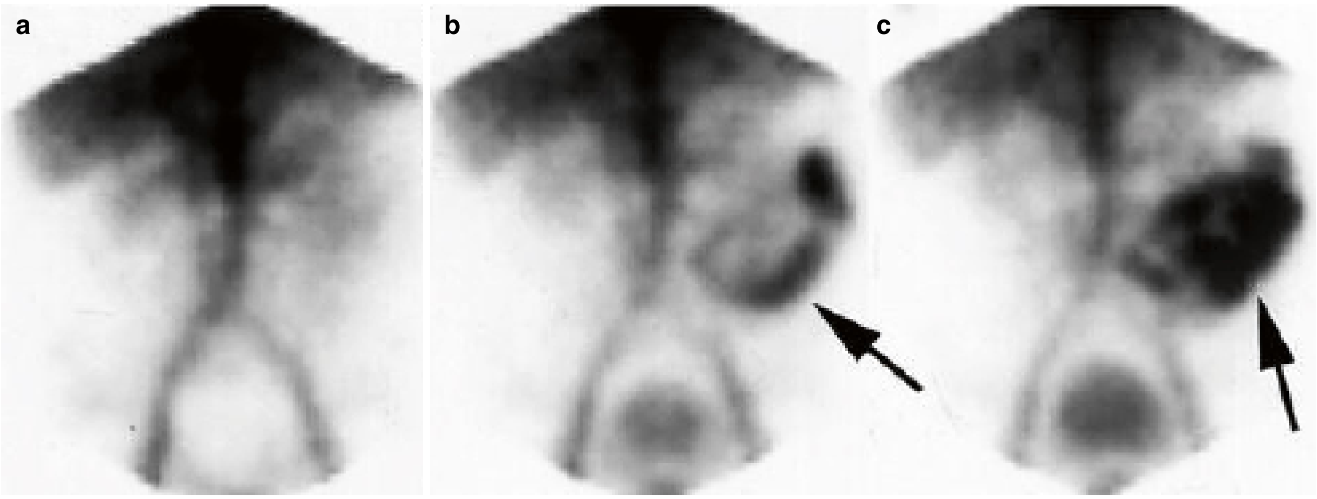

Fig. 14.18 Superior mesenteric artery

5. An 8-year-old child presents with dark red stools and anemia. A Meckel's scan is performed (Fig. 14.19). Is this study positive or negative for a Meckel's diverticulum?
   (A) Positive
   (B) Negative

Answer: A. The study is positive. Uptake in the right lower quadrant superior to the bladder, which appears simultaneously with the stomach, is characteristic of a Meckel's diverticulum (solid arrows). Note the normal uptake in the stomach (open arrows) and bladder (arrowheads).

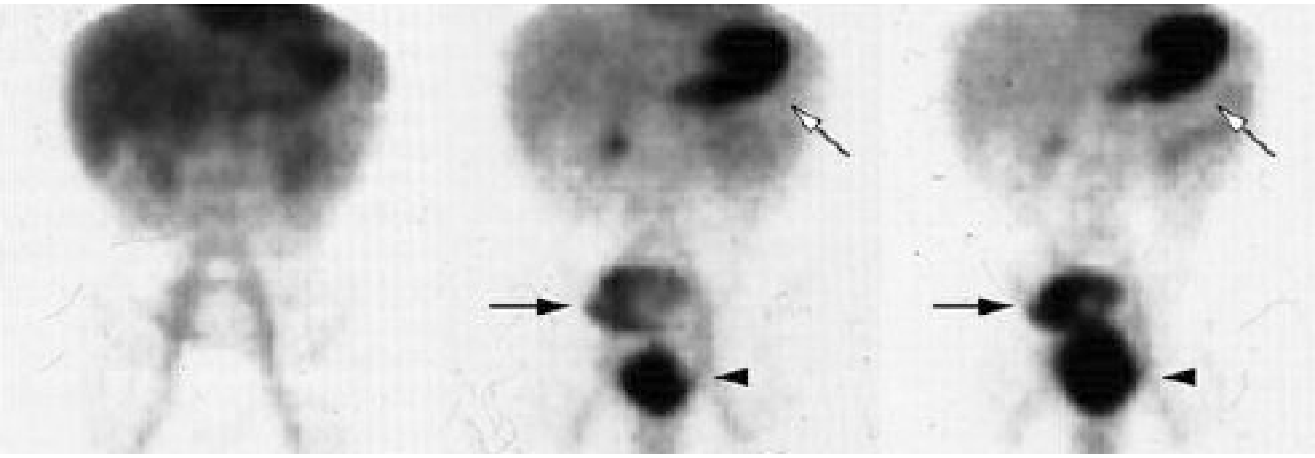

Fig. 14.19 Meckel's scan in the stomach

References

1. Parker JA, Coleman RE, Grady E, et al. SNM practice guideline for lung scintigraphy 4.0 [published correction appears in J Nucl Med Technol. 2016 Dec;44(4):271]. J Nucl Med Technol. 2012;40(1):57–65.
2. Sostman HD, Miniati M, Gottschalk A, Matta F, Stein PD, Pistolesi M. Sensitivity and specificity of perfusion scintigraphy combined with chest radiography for acute pulmonary embolism in PIOPED II. J Nucl Med. 2008;49:1741–8.
3. Amini B, Patel CB, Lewin MR, Kim T, Fisher RE. Diagnostic nuclear medicine in the ED. Am J Emerg Med. 2011;29:91–101.
4. Uliel L, Mellnick VM, Menias CO, Holz AL, McConathy J. Nuclear medicine in the acute clinical setting: indications, imaging findings, and potential pitfalls. Radiographics. 2013;33:375–96.
5. Taban Sadeghi M, Mahmoudian B, Ghaffari S, et al. Value of early rest myocardial perfusion imaging with SPECT in patients with chest pain and non-diagnostic ECG in emergency department. Int J Cardiovasc Imaging. 2019;35(5):965–71.
6. Rybicki FJ, Udelson JE, Peacock WF, Goldhaber SZ, Isselbacher EM, Kazerooni E, et al. 2015 ACR/ACC/AHA/AATS/ACEP/ASNC/NASCI/SAEM/SCCT/SCMR/SCPC/SNMMI/STR/STS appropriate utilization of cardiovascular imaging in emergency department patients with chest pain. J Am Coll Radiol. 2015;13:e1–e29.
7. Dedic A, Genders TS, Nieman K, Hunink MG. Imaging strategies for acute chest pain in the emergency department. AJR Am J Roentgenol. 2013;200(1):W26–38.
8. Chatziioannou SN, Moore WH, Ford PV, Dhekne RD. Hepatobiliary scintigraphy is superior to abdominal ultrasonography in suspected acute cholecystitis. Surgery. 2000;127:609–13.
9. Ziessman HA. Hepatobiliary scintigraphy in 2014. J Nucl Med. 2014;55:967–75.
10. Kousik V, Bhattacharya A, Yadav TD, Mittal BR. Hepatobiliary scintigraphy-role in preliminary diagnosis and management of biliary tract injuries. Clin Nucl Med. 2020;45(1):e1–7.
11. Brunnler T, Klebl F, Mundorff S, Eilles C, Reng M, von Korn H, et al. Significance of scintigraphy for the localisation of obscure gastrointestinal bleedings. World J Gastroenterol. 2008;14:5015–9.
12. Currie GM, Kiat H, Wheat JM. Scintigraphic evaluation of acute lower gastrointestinal hemorrhage: current status and future directions. J Clin Gastroenterol. 2011;45:92–9.
13. Dam HQ, Brandon DC, Grantham VV, Hilson AJ, Howarth DM, Maurer AH, et al. The SNMMI procedure standard/EANM practice guideline for gastrointestinal bleeding scintigraphy 2.0. J Nucl Med Technol. 2014;42:308–17.
14. Strate LL, Gralnek IM. ACG clinical guideline: management of patients with acute lower gastrointestinal bleeding [published correction appears in Am J Gastroenterol. 2016 May;111(5):755]. Am J Gastroenterol. 2016;111(4):459–74.
15. Spottswood SE, Pfluger T, Bartold SP, Brandon D, Burchell N, Delbeke D, et al. SNMMI and EANM practice guideline for Meckel diverticulum scintigraphy 2.0. J Nucl Med Technol. 2014;42:163–9.
16. Swaniker F, Soldes O, Hirschl RB. The utility of technetium 99m pertechnetate scintigraphy in the evaluation of patients with Meckel's diverticulum. J Pediatr Surg. 1999;34:760–4. discussion 765.
17. Freeman LM, Stein EG, Sprayregen S, Chamarthy M, Haramati LB. The current and continuing important role of ventilation-perfusion scintigraphy in evaluating patients with suspected pulmonary embolism. Semin Nucl Med. 2008;38:432–40.
18. Kontos MC, Tatum JL. Imaging in the evaluation of the patient with suspected acute coronary syndrome. Semin Nucl Med. 2003;33:246–58.
19. Raff GL, Hoffmann U, Udelson JE. Trials of imaging use in the emergency department for acute chest pain. JACC Cardiovasc Imaging. 2017;10(3):338–49.
20. Udelson JE, Beshansky JR, Ballin DS, Feldman JA, Griffith JL, Handler J, et al. Myocardial perfusion imaging for evaluation and triage of patients with suspected acute cardiac ischemia: a randomized controlled trial. JAMA. 2002;288:2693–700.
21. Kontos MC, Schmidt KL, McCue M, Rossiter LF, Jurgensen M, Nicholson CS, et al. A comprehensive strategy for the evaluation and triage of the chest pain patient: a cost comparison study. J Nucl Cardiol. 2003;10:284–90.
22. Ziessman HA. Interventions used with cholescintigraphy for the diagnosis of hepatobiliary disease. Semin Nucl Med. 2009;39:174–85.
23. Rodriguez LE, Santaliz-Ruiz LE, De La Torre-Bisot G, et al. Clinical implications of hepatobiliary scintigraphy and ultrasound in the diagnosis of acute cholecystitis. Int J Surg. 2016;35:196–200.
24. Fleming KW, Lucey BC, Soto JA, Oates ME. Posttraumatic bile leaks: role of diagnostic imaging and impact on patient outcome. Emerg Radiol. 2006;12:103–7.
25. Melamud K, LeBedis CA, Anderson SW, Soto JA. Biliary imaging: multimodality approach to imaging of biliary injuries and their complications. Radiographics. 2014;34(3):613–23.
26. O'Neill BB, Gosnell JE, Lull RJ, Schecter WP, Koch J, Halvorsen RA, et al. Cinematic nuclear scintigraphy reliably directs surgical intervention for patients with gastrointestinal bleeding. Arch Surg. 2000;135:1076–81. discussion 1081–2.
27. Mellinger JD, Bittner JG, Edwards MA, Bates W, Williams HT. Imaging of gastrointestinal bleeding. Surg Clin N Am. 2011;91:93–108.
28. Howarth DM. The role of nuclear medicine in the detection of acute gastrointestinal bleeding. Semin Nucl Med. 2006;36:133–46.

15

Imaging of Neck Emergencies

Mohammad Mansouri, Khyati Bidani, and Ajay Singh

Foreign Body in the Pharynx and Esophagus

The most common foreign bodies in the pharynx and esophagus include coins, fish bones, batteries, tooth fragment, buttons, and plastic pieces. Although most small foreign bodies will pass through the gastrointestinal tract without producing symptoms, those which cause symptoms most commonly lodge above the cricopharyngeus.

Button batteries are associated with the risk of injuries much severe than those seen with other foreign bodies because button batteries conduct electricity when both its anode and cathode come in contact with esophageal tissue. Electric energy generated is sufficient to produce ulceration, liquefactive necrosis, and esophageal perforation. The maximum damage to the esophageal wall is observed at the site of anode. Additionally, leaked alkaline contents and mercury of the battery can cause caustic damage in the esophagus and systemic toxicity, respectively. Other serious complications include formation of tracheoesophageal fistula, fatal aorto-esophageal fistula, vocal cord paralysis, and tracheal and esophageal stenoses. The narrowest parts of esophagus including gastroesophageal junction, thoracic inlet, and at aortic arch impression of esophagus are the most common sites for impaction of foreign body. If the battery transits through the gastroesophageal junction, the risk of complications is much less and observation with serial radiographs is considered adequate [1, 2].

On frontal radiographs, the radiopaque, round button batteries demonstrate double-rim sign or halo sign representing the two disks of the battery (anode and cathode), which helps differentiate it from a coin (Fig. 15.1). In cases of unclear diagnosis, lateral radiographs can demonstrate step-off sign caused by the smaller diameter of anode [2].

Investigation of a patient with pain after eating fish leads to demonstration of fish bone in 21% of the cases, most commonly in the oropharynx [3]. The most common site of impaction of fish bone is the base of the tongue. If no fish bone is demonstrated, the symptoms will usually resolve spontaneously. The complications of fish bone include perforation and sepsis. The most definitive test for

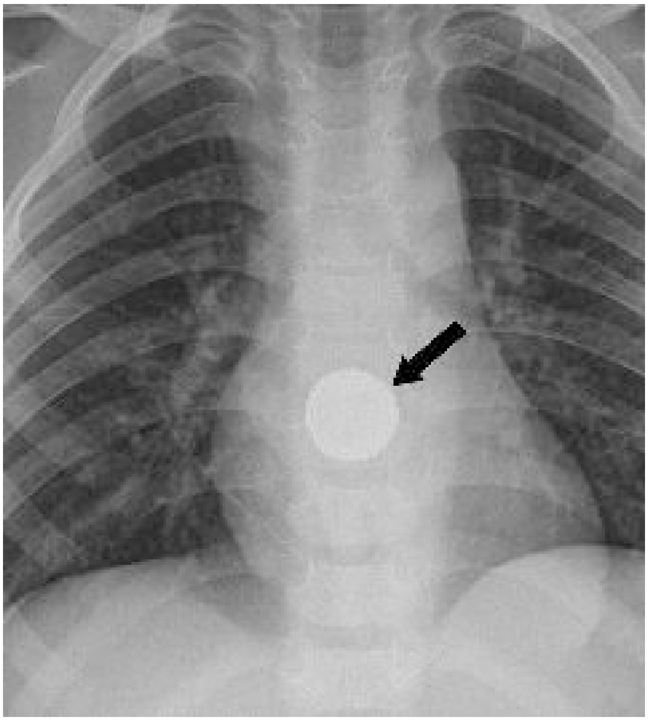

Fig. 15.1 Button battery in the thoracic esophagus. Plain radiograph of the chest demonstrates double-rim sign or halo sign representing the two disks of the battery

M. Mansouri · K. Bidani
Department of Radiology, Massachusetts General Hospital,
Boston, MA, USA

A. Singh (✉)
Division of Emergency Radiology, Department of Radiology,
Massachusetts General Hospital, Boston, MA, USA

Harvard Medical School, Massachusetts General Hospital,
Boston, MA, USA
e-mail: asingh1@partners.org

© The Author(s), under exclusive license to Springer Nature Switzerland AG 2024
A. Singh (ed.), *Emergency Radiology*, https://doi.org/10.1007/978-3-031-65770-2_15

evaluation of foreign body in the pharynx is rigid endoscopy. The density of the fish bone depends on a type of fish eaten by the patient. Fish such as salmon, trout, skate, and herring have lower radiopaque bone density and are difficult to see on radiographic assessment.

Plain radiography is recommended as the initial imaging modality; however, its sensitivity for detecting fish bone is only 32%, and false-negative rate is 47%. Biplane radiography improves the sensitivity of plain radiography [4]. The radiographic findings seen on lateral view of the neck include prevertebral soft tissue swelling, soft tissue air, and demonstration of radiopaque bone (Figs. 15.2 and 15.3). It is important to include at least the sixth cervical vertebra, so as to evaluate the cricopharyngeus for foreign body. The plain radiograph may be obtained by asking the patient to sing "E," which raises the larynx and brings more of the upper esophagus into the field of view. CT is highly sensitive and specific (both above 90%) in detecting foreign bodies, which can be improved with 3D reconstruction. Positive and negative predictive values for CT are 75% and 97%, respectively [4]. CT is also valuable in detecting possible complications.

Radiopaque coins are the most commonly ingested foreign body in the pediatric patient. In patients with symptoms related to the esophageal coin, immediate removal with endoscopy is recommended, while in asymptomatic patients with esophageal coin, conservative management for 12–24 h is recommended, with the hope of spontaneous passage of the coin [5]. The management of esophageal coin in asymptomatic patients where the coin is located below the thoracic inlet includes next radiograph. If the follow-up X-ray demonstrates persistent esophageal coin, then endoscopic removal is required [6].

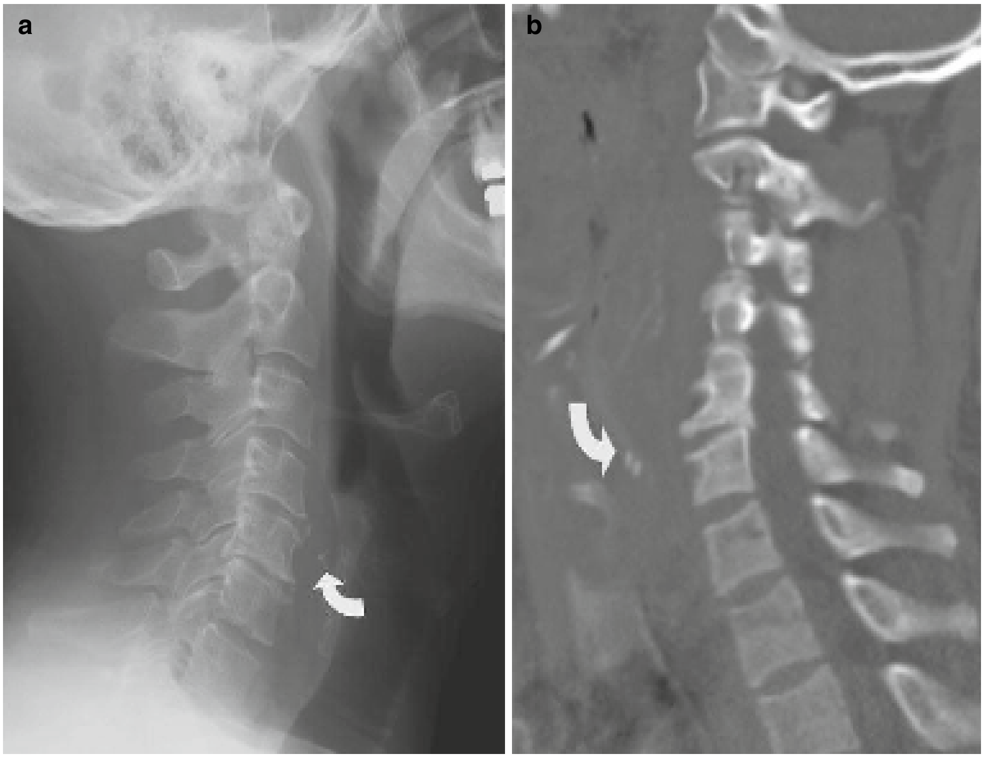

Fig. 15.2 Fish bone in the hypopharynx. (**a**, **b**) Lateral view of the neck and sagittal CT reformation demonstrating fish bone (*curved arrow*) in the prevertebral soft tissue, at the level of the C5 vertebra

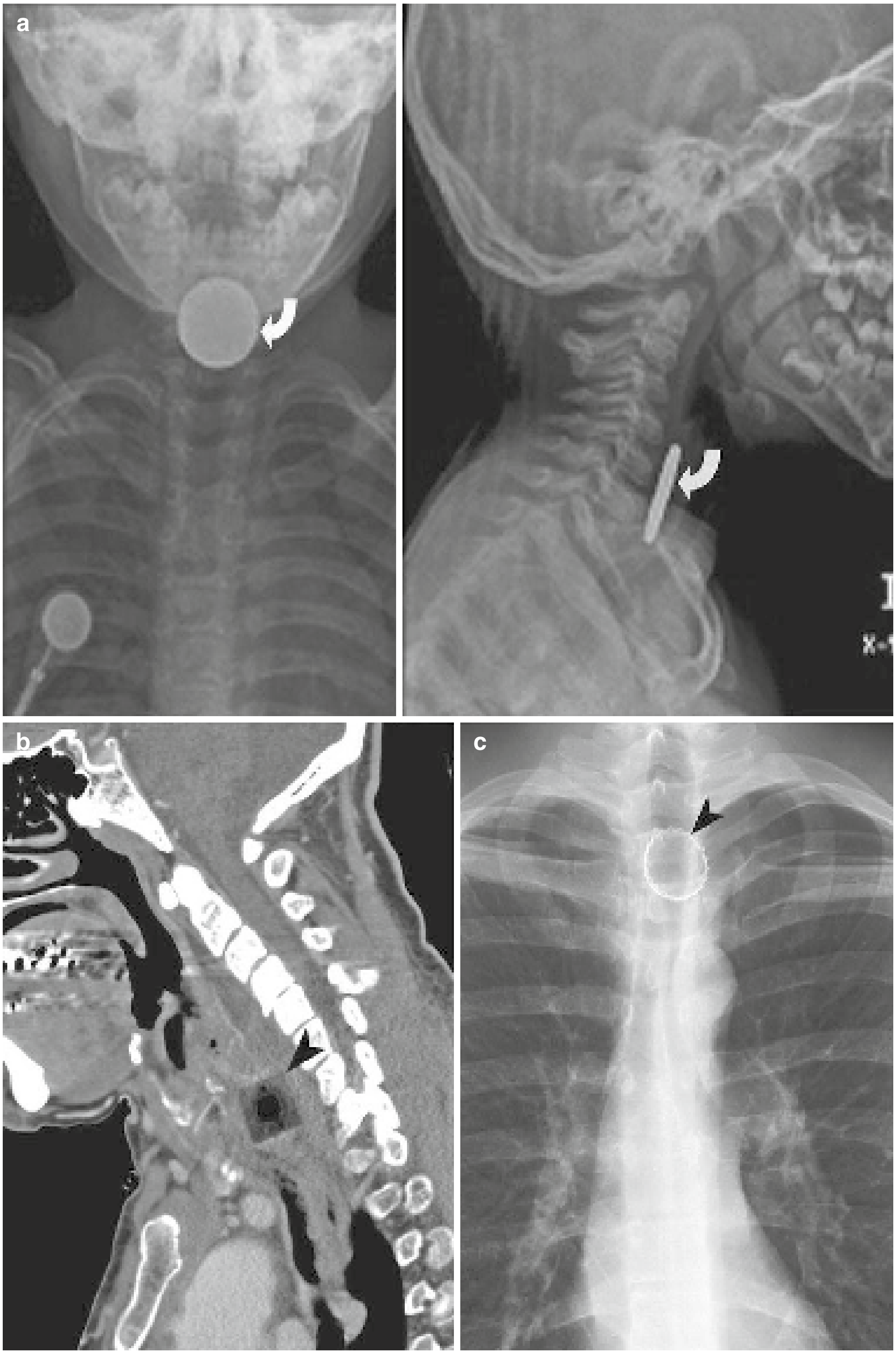

Fig. 15.3 Foreign body in the hypopharynx. (**a**) AP and lateral radiographs of the neck demonstrating radiopaque coin (*curved arrow*) lodged in the prevertebral soft tissues, above the cricopharyngeus. (**b**) Sagittal CT reformation of the neck demonstrates a plastic foreign body (*arrowhead*) in the prevertebral soft tissues, lodged just proximal to the cricopharyngeus muscle. (**c**) AP radiograph of the neck demonstrates radiopaque bottle cap (*arrowhead*) lodged in the hypopharynx soft tissues, above the cricopharyngeus

Infections

Oral cavity infections are most often related to periodontal diseases. Periodontal infection originates from gingivitis and leads to periodontal pocket of infection, seen as radiolucency around the root of the teeth. Infections from periodontal disease can extend into the submandibular or sublingual space, depending on whether the roots of the teeth extend above or below the mylohyoid muscle insertion. Cortical destruction is more common on the lingual aspect of the mandible than the buccal aspect because of the thinner cortex on the lingual aspect. Odontogenic infection from incisors, canines, and first premolar tends to involve the lingual space. The second and third mandibular molar roots extend below mylohyoid muscle insertion and therefore tend to involve the submandibular space.

Infection in buccal space arises from maxillary incisor, canine, premolar, and first molar. Masticator space infections arise from the second maxillary molar. Infection from the third maxillary molar tends to involve the parapharyngeal space.

On contrast-enhanced CT scan study, bony erosions can be identified around the root of the affected teeth, with extension of the abscess into the soft tissues of the floor of the mouth (Fig. 15.4) [7].

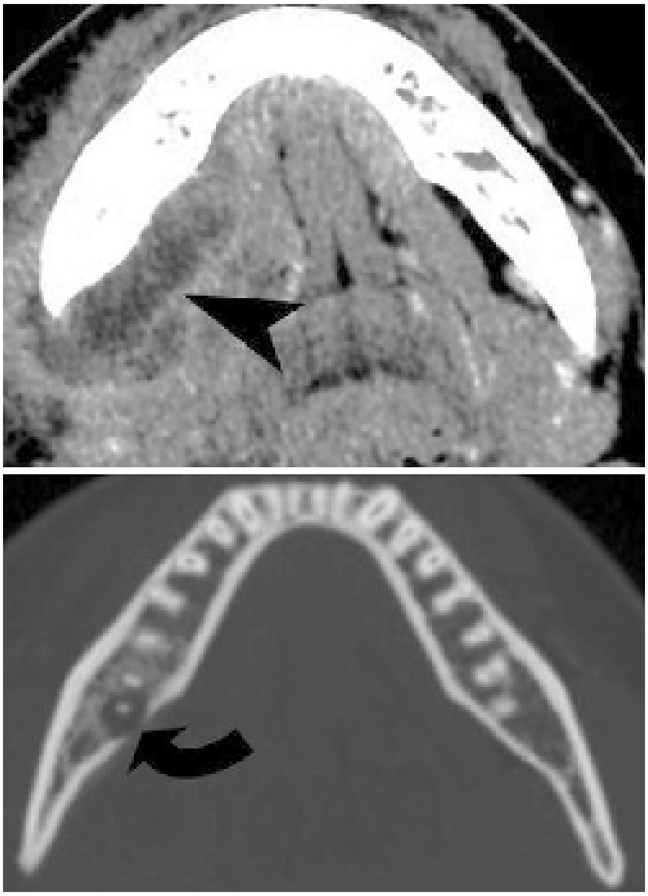

Fig. 15.4 Periodontal abscess. Contrast-enhanced CT scan study of the mandible demonstrates periodontal abscess (*curved arrow*) with extension of the abscess into the right submandibular triangle (*arrowhead*)

MRI is more sensitive for detecting complications of odontogenic infections such as osteomyelitis or extraosseous abscess. MRI can differentiate osteomyelitis and subperiosteal abscess, from bone infarct with hemorrhage in sickle cell disease. Ludwig's angina can be well demonstrated on MRI by the presence of soft tissue edema and rim-enhancing abscess.

Sialadenitis

Sialadenitis refers to viral or bacterial infection of salivary gland, most commonly affecting the parotid gland. The frequency of viral infection (mumps) has drastically decreased due to the widespread use of immunization. The viral causes of sialadenitis include mumps virus (most common), HIV, coxsackievirus, parainfluenza virus, and herpesvirus. Bacterial infection can be caused by obstruction of Wharton's duct (submandibular gland) or Stensen's duct (parotid gland) by sialolithiases. The most common organisms causing sialadenitis include *Staphylococcus aureus*, *Streptococcus viridans*, *Haemophilus influenzae*, *Streptococcus pyogenes*, *Pseudomonas aeruginosa*, and *Escherichia coli*. Sjögren's syndrome most commonly is associated with parotid sialadenitis, keratoconjunctivitis sicca, and xerostomia.

Salivary gland duct obstruction secondary to sialolithiases most commonly involves the submandibular gland. The stones are most commonly composed of calcium phosphate or calcium carbonate and are usually radiopaque enough to be visible on plain radiography. Eighty to ninety-five percent of submandibular gland sialolithiases are radiopaque and therefore seen on plain radiography [8]. Sialography is the imaging modality of choice for demonstration of the salivary gland ducts.

The salivary gland can be imaged using plain radiography, sialography, ultrasonography, and CT scan. CT allows excellent comparison with contralateral salivary gland, demonstrating sialolithiases, distinguishing intrinsic from extrinsic inflammatory process, and defining abscess/phlegmon formation. Sialadenitis is typically seen on CT as salivary gland enlargement, surrounding inflammatory changes, and ductal dilatation with calculi (Figs. 15.5, 15.6 and 15.7) [9].

On MRI, sialadenitis is characterized by salivary gland edema and abnormal enhancement, sometimes with rim-enhancing abscess, inflammation of the surrounding soft tissues, and signal void due to sialolithiasis within the obstructed duct.

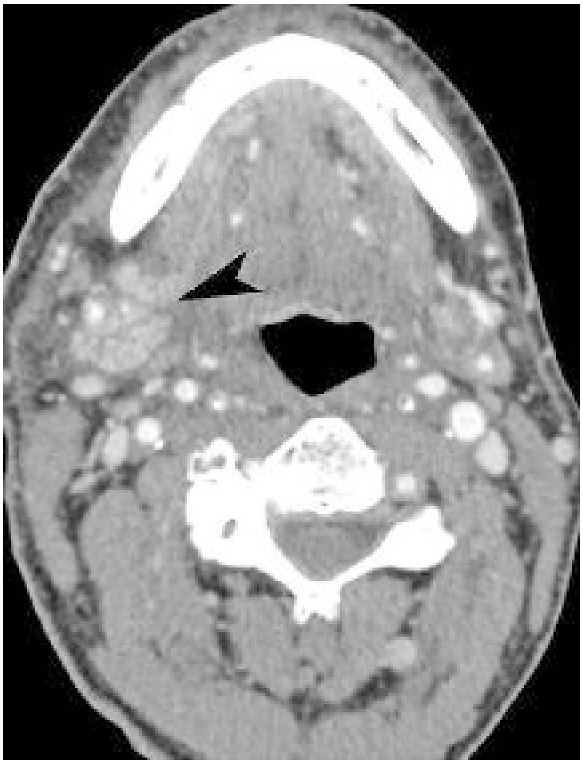

Fig. 15.5 Sialadenitis. Contrast-enhanced CT scan study of the floor of the mouth demonstrates unilateral enlargement of the right submandibular gland (*arrowhead*) with surrounding edema

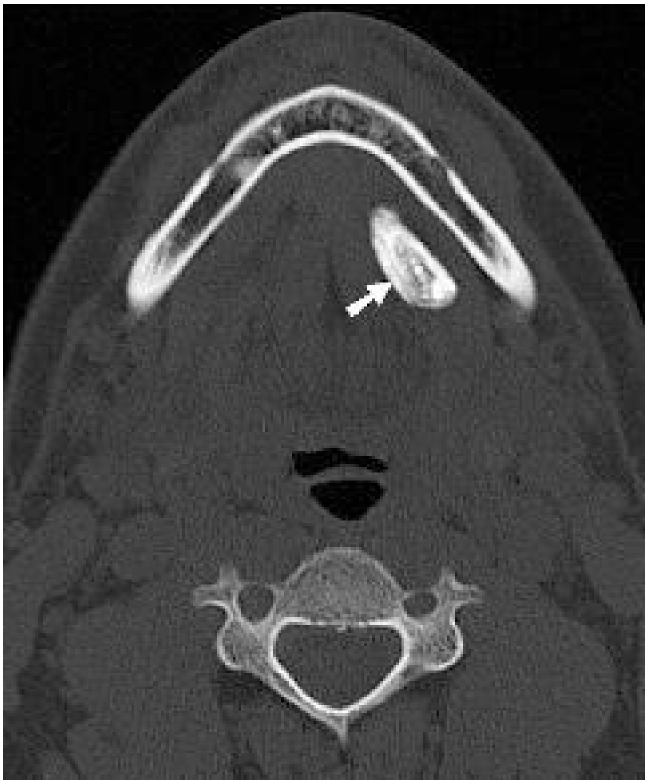

Fig. 15.6 Sialolithiasis in Wharton's duct. CT demonstrates a large sialolith (*arrow*) in the duct of the left submandibular gland (Wharton's duct)

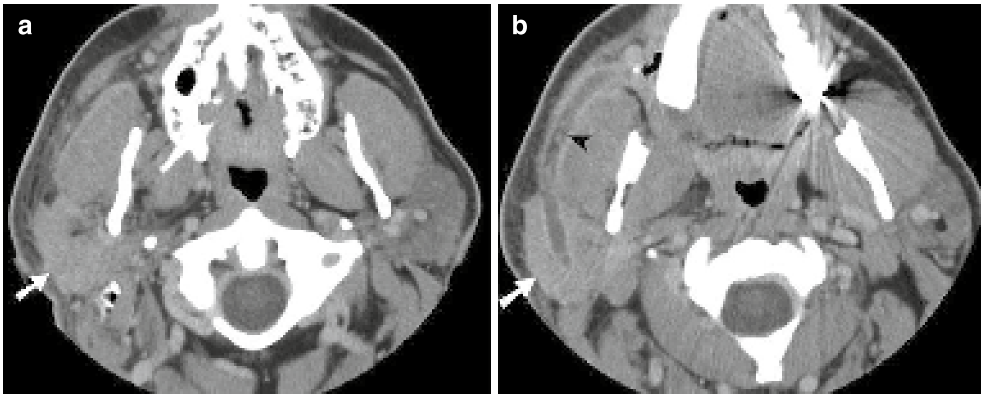

Fig. 15.7 Sialolithiasis in Stensen's duct. (**a**) Contrast-enhanced CT shows asymmetric prominence of right parotid gland (*white arrow*) with surrounding edema. (**b**) There is dilatation of right Stensen's duct (*arrowhead*), which is obstructed by a 3 mm sialolith (*curved arrow*)

Danger Space and Retropharyngeal Space Abscess

Danger space is located posterior to the retropharyngeal space and is bounded anteriorly by the alar fascia and posteriorly by the prevertebral fascia. The clinical significance of danger space infection is that the infection can directly spread to the posterior mediastinum, on either side of midline.

The retropharyngeal space is located between the buccopharyngeal fascia (visceral fascia surrounding the pharynx) and alar fascia. It is bounded laterally by the parapharyngeal space and carotid sheath. Inferiorly it extends to the level of the tracheal bifurcation, and superiorly it extends to the base of the skull.

The plain radiographic findings include prevertebral soft tissue thickening, which is indicated by retrotracheal space (at C6) more than 14 mm in children and 22 mm in adults. Contrast-enhanced CT is the definitive test for demonstration of the size, location, and extent of the abscess in the deep spaces of the neck. It is not possible to distinguish retropharyngeal space from danger space abscess, unless the abscess is seen extending below the T4 vertebra (Fig. 15.8).

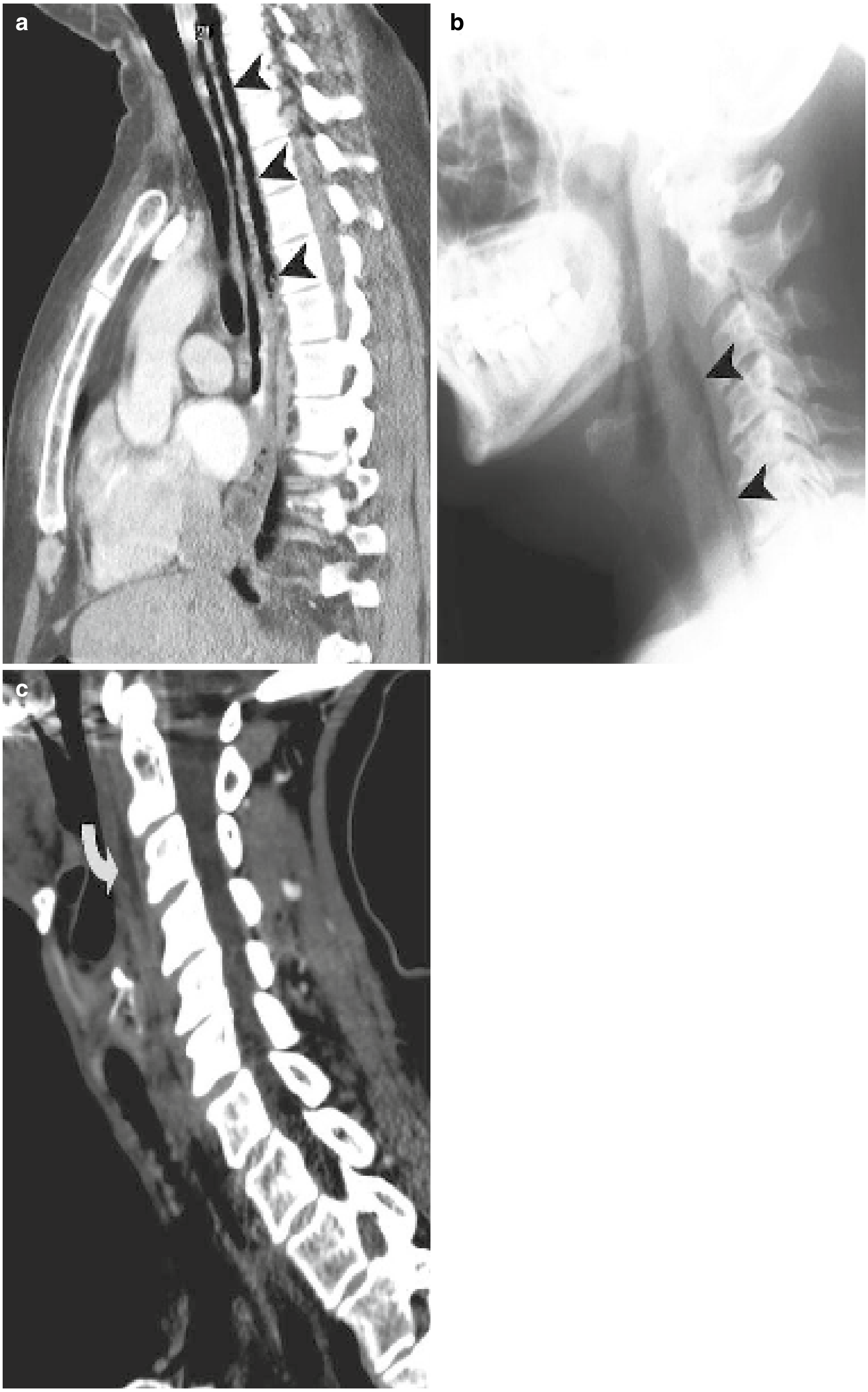

Fig. 15.8 Danger space abscess (**a**, **b**) and retropharyngeal abscess (**c**). (**a**) Sagittal information on the neck and chest demonstrates air-containing abscess cavity (*arrowheads*) located posterior to the esophagus and extending from the neck into the mediastinum. (**b**) Plain radiograph of the neck also demonstrates the containing abscess cavity (*arrowheads*) in the prevertebral soft tissues. (**c**) Sagittal CT reformation demonstrates low-density retropharyngeal abscess (*curved arrow*) in the prevertebral soft tissues

Retropharyngeal Abscess

It is most commonly seen before the age of 6 years and is most often caused by *Staphylococcus*, *Streptococcus*, and *Haemophilus*. It most often arises secondary to suppurative changes in retropharyngeal lymph nodes draining tonsillitis, pharyngitis, or otitis media [10]. These suppurative lymph nodes can rupture and result in retropharyngeal abscess. The retropharyngeal abscess may also be caused by spine surgery, discitis, vertebral osteomyelitis, or pharyngeal perforation.

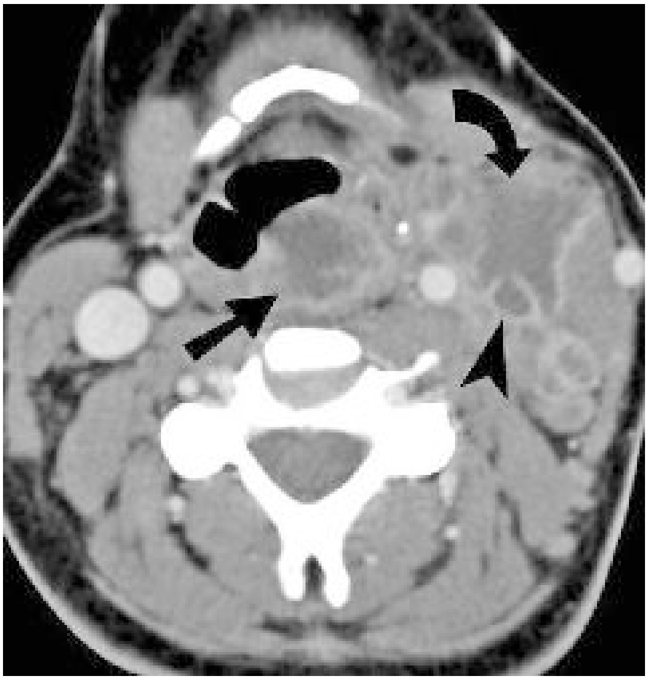

Fig. 15.9 Lemierre's syndrome. Contrast-enhanced CT scan study of the neck demonstrates retropharyngeal abscess (*straight arrow*) with extension on the left side to produce left internal jugular vein (*arrowhead*) thrombophlebitis. The septic thrombus in the left internal jugular vein is also producing abscess (*curved arrow*) in the soft tissues of the left anterior triangle of the neck

Contrast-enhanced CT is the imaging modality of choice and can show prevertebral soft tissue swelling and loculated abscess with enhancing wall (Fig. 15.9). It can also show other findings such as discitis/osteomyelitis, airway compromise, thrombophlebitis, and epidural abscess.

On MRI, retropharyngeal space has a bow-tie-shaped distension, displacing the posterior pharyngeal wall anteriorly. Retropharyngeal space shows T2 hyperintensity and T1 hypointensity due to edema/cellulitis. The abscess shows restricted diffusion and rim enhancement.

Lemierre's Syndrome

Lemierre's syndrome, also called postanginal sepsis or necrobacillosis, is characterized by thrombophlebitis in the neck, most often due to *Fusobacterium necrophorum* infection [11]. Other *Fusobacterium* species are responsible for 11%, and other gram-negative organisms are responsible in 8% of cases of Lemierre's syndrome [12]. It most commonly affects young adults after a complicated pharyngitis with parapharyngeal or peritonsillar abscess formation. These abscesses provide optimal surroundings for the growth of the anaerobic bacteria, which proliferate to involve the adjacent internal jugular vein. The thrombophlebitis of the internal jugular vein can cause embolization of the infected clot to the lungs and septicemia.

The imaging findings of septic thrombophlebitis and associated abscess can be demonstrated on US or CT study. Ultrasonography is less sensitive than CT in detecting recently formed thrombosis or investigating deep tissues around the clavicle and mandible. The acute internal jugular vein thrombus can be seen on contrast-enhanced CT as low-density filling defect with distension of the vein (see Fig. 15.9). Contrast-enhanced CT can also demonstrate the septic microemboli to the lungs indicated by multiple peripheral round- or wedge-shaped nodules and lung abscess formation. Other pulmonary findings include consolidation, pleural effusion, and empyema. MRI is the most sensitive modality for visualizing anatomical structures of the region, thrombosis, and septic emboli.

Tonsillitis and Peritonsillar Abscess

Peritonsillar abscess is a complication of acute tonsillitis, due to extension of infection through the tonsillar capsule to the potential space between the capsule and the superior constrictor muscle. Approximately 45,000 cases of acute tonsillitis occur annually in the USA. It represents the most common deep soft tissue infection of the neck, most commonly caused by *Staphylococcus*, *Streptococcus*, *Haemophilus*, *Pneumococcus*, *Fusobacterium*, and *Peptostreptococcus*. Symptoms include fever, dysphagia, and cervical lymphadenopathy.

Imaging is most often performed in cases of complicated tonsillitis, where peritonsillar infection is suspected. The imaging findings include palatine tonsillar enlargement, striated enhancement, peritonsillar liquefaction, and loculated abscess formation (Fig. 15.10). The definitive treatment of peritonsillar abscess is surgical incision and drainage in the emergency room after intravenous antibiotics. MRI in peritonsillar abscess shows rim-enhancing loculated fluid collection in the peritonsillar area. Restricted diffusion is seen on DWI.

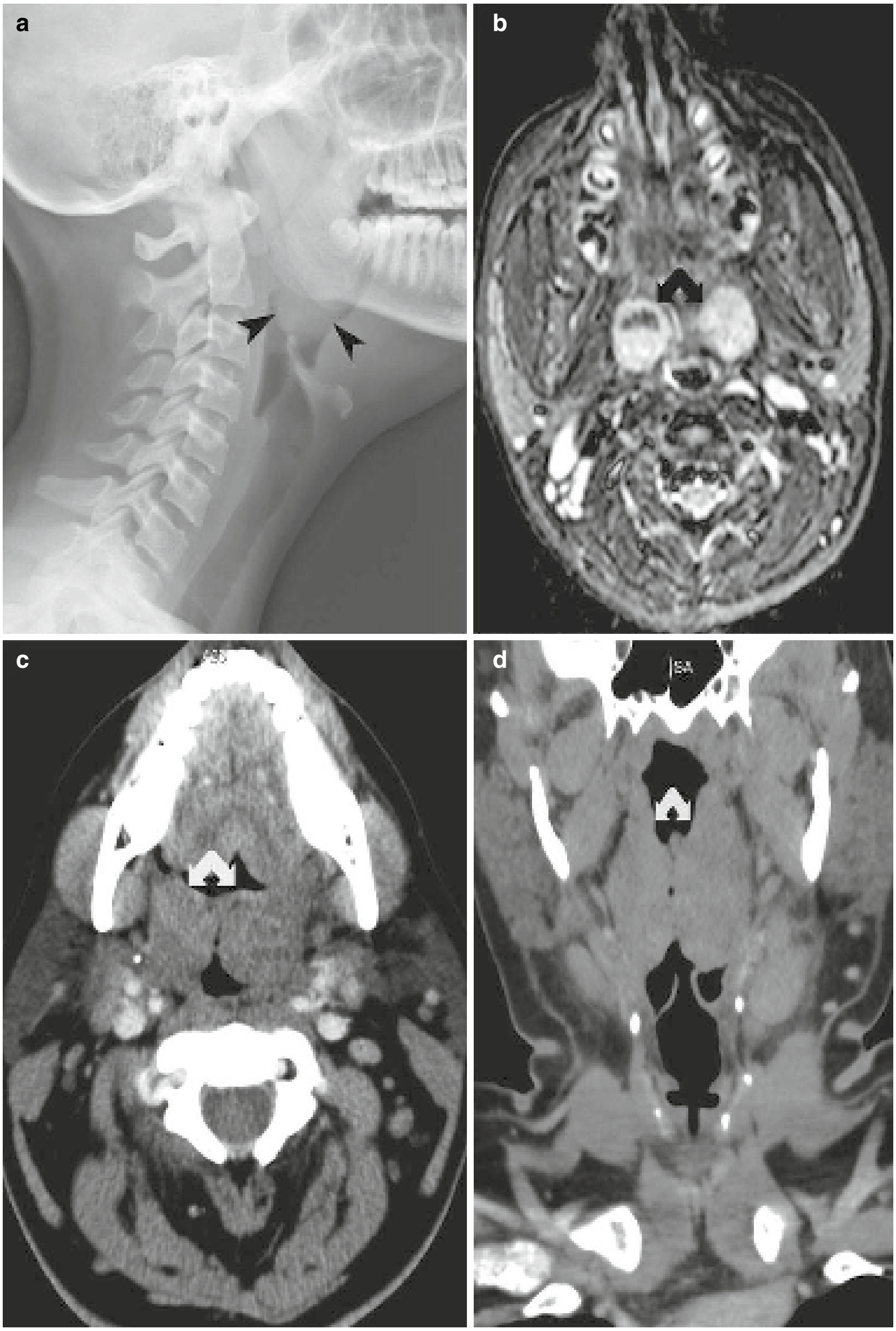

Fig. 15.10 Tonsillitis and peritonsillar abscess. (**a**) Lateral radiograph of neck demonstrates enlargement of the pharyngeal tonsils (*arrowheads*) in the lateral wall of the oropharynx. (**b–d**) Contrast-enhanced T1-weighted MRI and noncontrast CT (axial and coronal) demonstrate bilateral palatine tonsillar enlargement (*bifid arrow*). (**e**) Contrast-enhanced CT scan study of the upper neck demonstrates left peritonsillar abscess (*curved arrow*), producing mass effect on the oropharyngeal airway. (**f**) Contrast-enhanced T1-weighted MRI of the upper neck demonstrates left peritonsillar abscess (*arrowhead*) with mass effect on the oropharyngeal airway

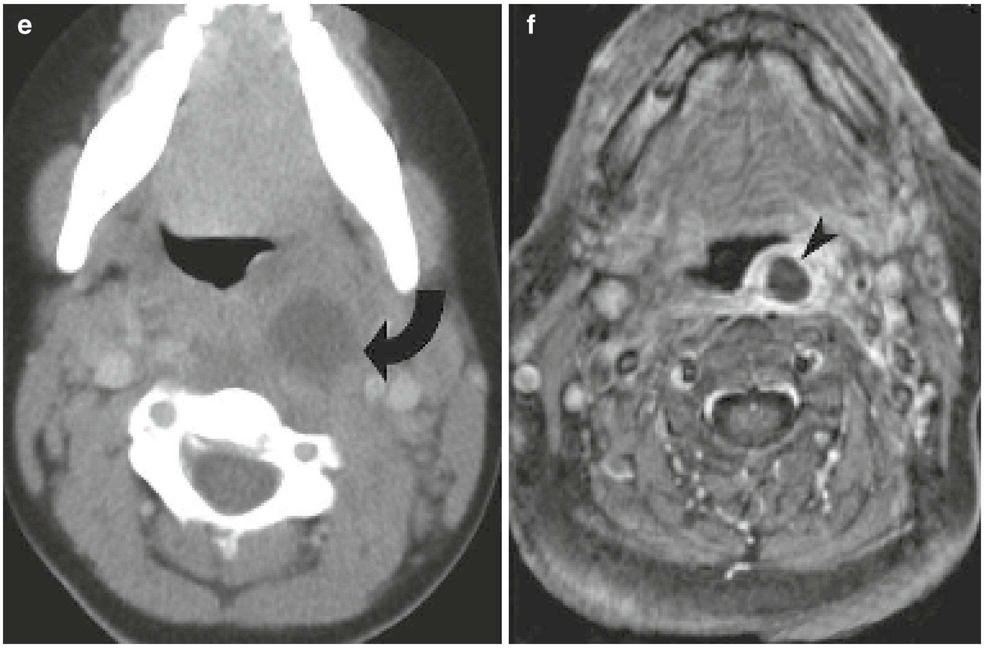

Fig. 15.10 (continued)

Adenoidal Hypertrophy

Adenoidal hypertrophy is common in the 6-month to 6-year age group. Clinical examination and flexible nasopharyngoscopy can be performed to evaluate the adenoidal size. Nasal endoscopy may be complementary to lateral radiograph of the neck in the evaluation of adenoids [13]. Although its role is controversial, lateral radiograph of the neck was shown to be a reliable diagnostic test in the evaluation of hypertrophied adenoids (Fig. 15.11) [13, 14].

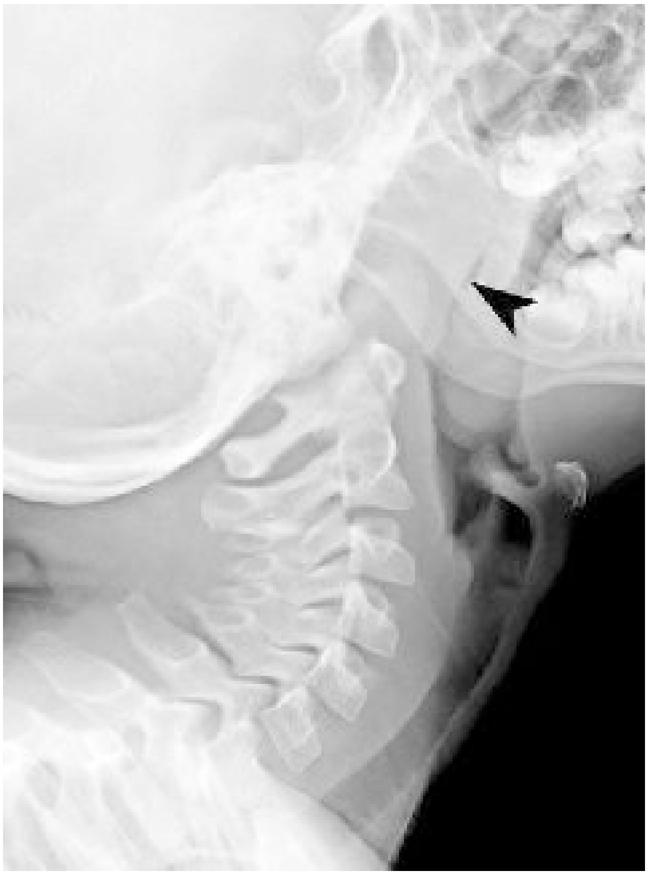

Fig. 15.11 Adenoidal hypertrophy. Lateral radiograph of the neck demonstrates gross adenoidal hypertrophy (*arrowhead*) along the posterior wall of the nasopharynx with severe compromise of the nasopharyngeal airway

Croup

Croup is a viral infection of the airways and is typically characterized by acute laryngotracheobronchitis. It is most commonly caused by parainfluenza or respiratory syncytial virus. It is most commonly seen in the age group of 6 months to 3 years. It is associated with reactive subglottic edema, which extends from true vocal cords to the conus elasticus, which can be seen on high-KV radiographs of the neck.

Normal AP radiograph of the neck shows shouldering in the subglottic larynx (Fig. 15.12a). Patients with croup will most often have subglottic edema, indicated by the steeple sign. The steeple sign is characterized by inverted V-shaped configuration of the subglottic larynx with loss of subglottic shouldering or convexity (see Fig. 15.12b). Steeple sign indicates subglottic edema. It can be absent in croup and present due to other causes of inflammation of the upper airway. The lateral radiograph may also show distension of hypopharynx,

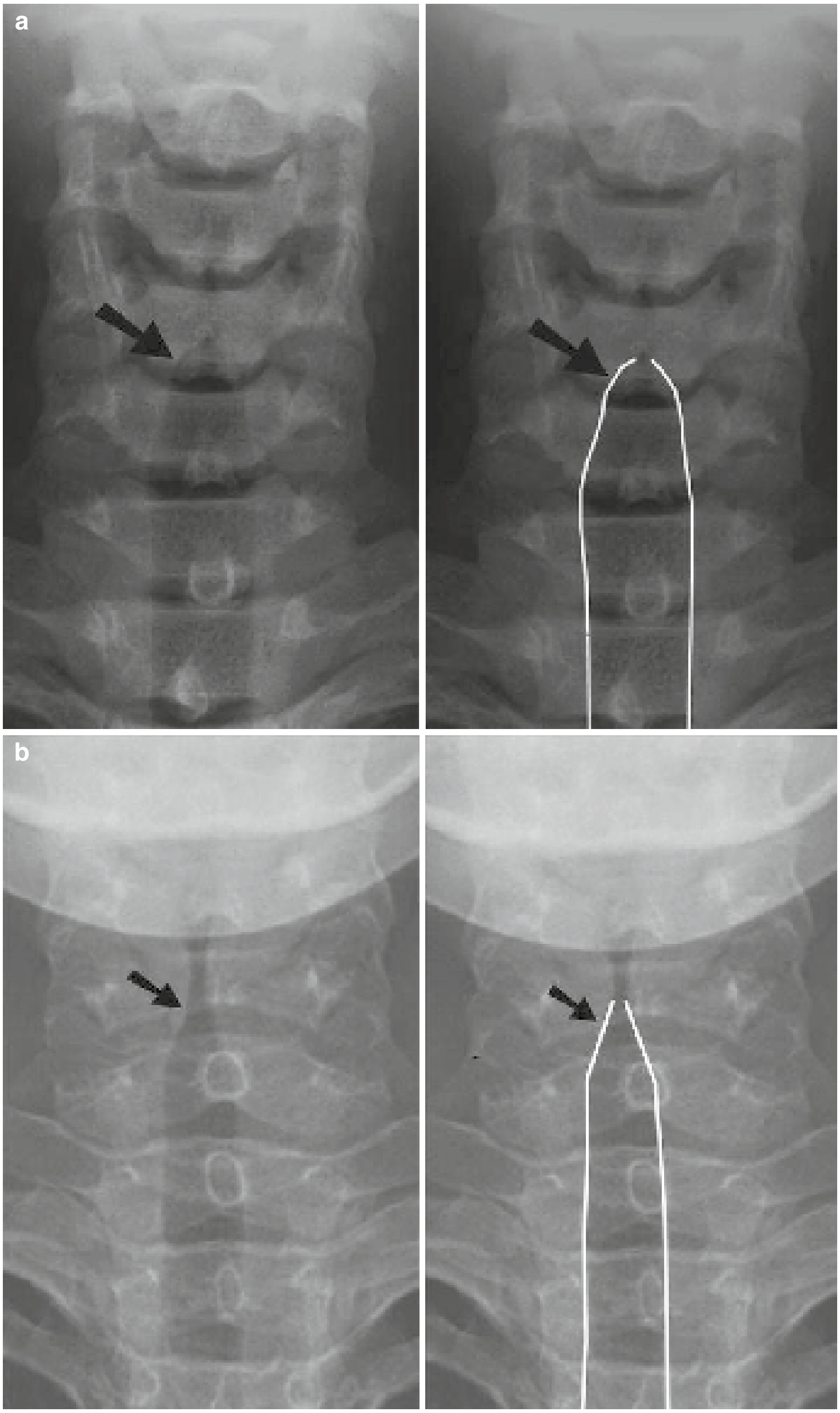

Fig. 15.12 Steeple sign. (**a**) Normal AP radiograph of the neck demonstrates normal shouldering (*straight arrow*) seen in the subglottic laryngeal airway. (**b**) AP radiograph of the neck in a patient with croup demonstrates steeple-shaped narrowing (*straight arrow*) of the subglottic laryngeal airway

secondary to the subglottic narrowing, which measures 1–1.5 cm in length [15]. For obtaining lateral view, the head should be in neutral or slight extension position to avoid pseudothickening of soft tissues and reduce patient distress.

Croup is a self-limited disease with excellent prognosis with conservative management.

Epiglottitis

Epiglottitis is life threatening which can cause rapid airway compromise, especially in children. Unlike croup, epiglottitis is seen in older children, most often at the group of 6–7 years. *H. influenzae* epiglottitis is more rapidly progressive than other kinds of epiglottitis and therefore has high risk of upper airway occlusion. Symptoms include abrupt onset of stridor, dysphagia, fever, and sore throat. Imaging may be performed when the clinical diagnosis is not certain. Anxiety and crying can worsen the respiratory distress, so it is better to minimize patient anxiety. Intubation equipment should be nearby if epiglottitis is suspected. Supine position is an alternate position if the patient cannot tolerate upright position during radiography. The lateral radiograph of the neck shows thumb-like enlargement of the epiglottis and thickened aryepiglottic folds (Fig. 15.13). Contrast-enhanced CT can show enlargement of the epiglottitis, mucosal enhancement, and adjacent cellulitis/abscess formation.

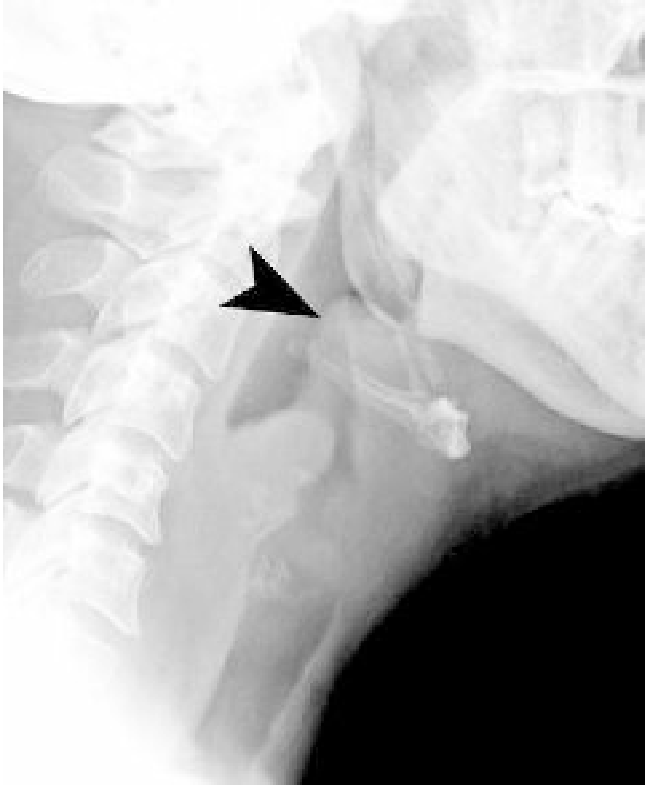

Fig. 15.13 Epiglottitis. Lateral radiograph of the neck demonstrates gross enlargement of the epiglottis (*arrowhead*) as well as the aryepiglottic fold, resulting in narrowing of the supraglottic laryngeal airway

Thyroglossal Duct Cyst

Thyroglossal duct cyst is the most common congenital anomaly of the neck and is caused by incomplete regression of the thyroglossal duct. It is most commonly seen in the first decade of life. These epithelial-lined cysts are commonly midline (except infrahyoid cysts) in position and are located in close proximity to the hyoid bone. Infrahyoid location is the most common (65%) location of the thyroglossal duct cysts. The infrahyoid cysts which are not midline in location are most often located within 2 cm of midline. The complications of thyroglossal duct cysts include infection and malignant transformation (papillary carcinoma of thyroid).

The thyroglossal duct cysts can be imaged with ultrasound, CT, or MRI. On ultrasound imaging, four patterns of thyroglossal duct cyst have been described by Ahujaa et al. These four patterns include anechoic (28%), homogeneously hypoechoic with internal debris (18%), pseudosolid (28%), and heterogeneous (28%). The majority showed posterior enhancement (88%), midline (63%), and infrahyoid in location (83%) [16].

The CT findings include a well-defined low-attenuation cystic lesion with thin wall, most commonly in infrahyoid location (Fig. 15.14). The cystic lesion has a low signal intensity on T1 and high signal intensity on T2-weighted images. The differential diagnosis of TDC in adults includes dermoid cyst, branchial cleft cyst, lymphadenopathy, thymic cyst, lymphangioma, and cystic thyroid nodule.

Fig. 15.14 Thyroglossal duct cyst. (**a**, **b**) Axial CT and sagittal C2 formation demonstrates well-defined infrahyoid cystic lesion with enhancing wall (*curved arrows*). (**c**) Contrast-enhanced CT scan study of the upper neck demonstrates midline thyroglossal duct cyst and infrahilar location. The enhancing irregular lesion with calcification identified within the cyst represents papillary thyroid carcinoma (*arrowhead*)

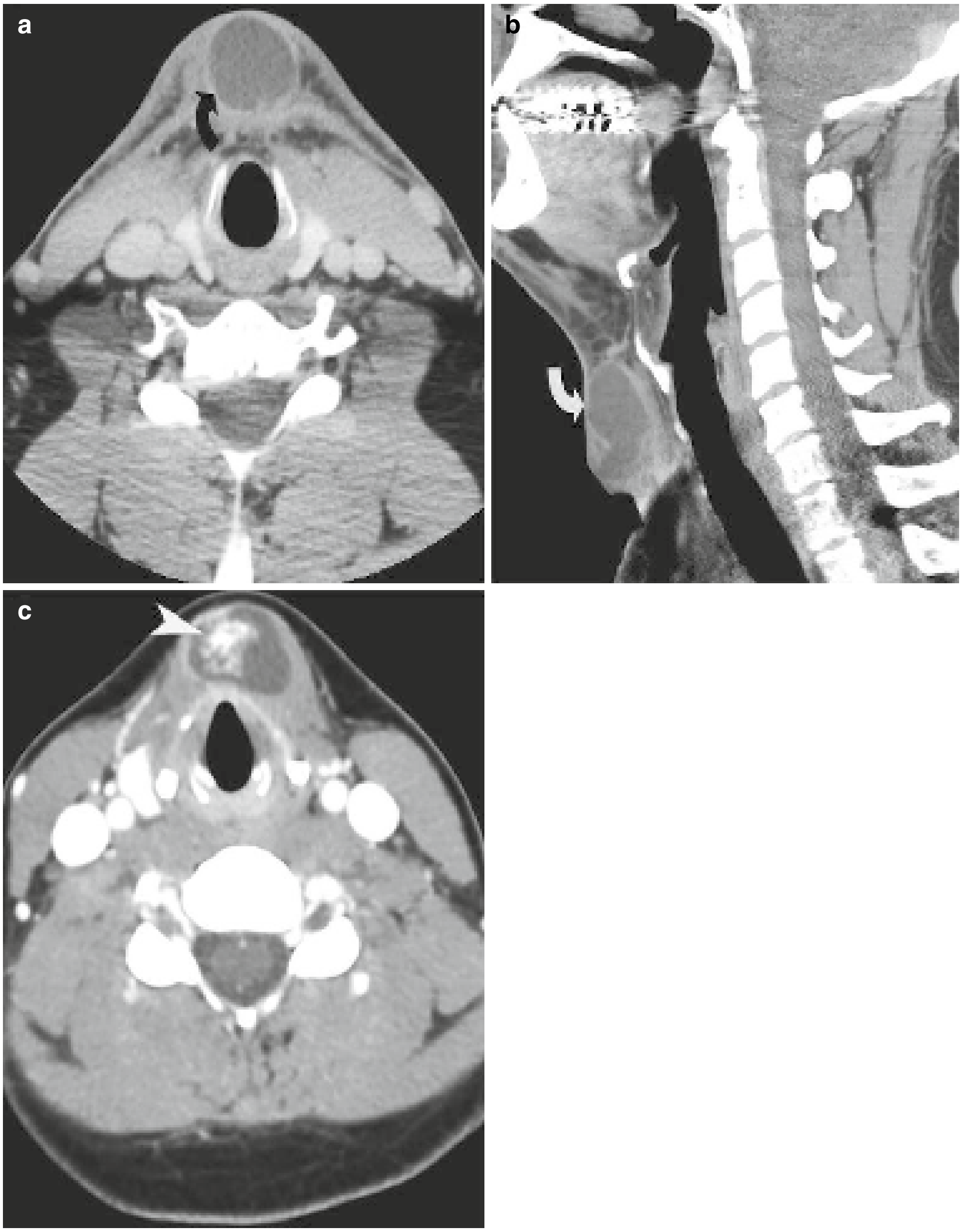

Branchial Cleft Cyst

The second branchial cleft accounts for 95% of the anomalies and is located in relation to the proximal third of the sternocleidomastoid muscle (Table 15.1). Cysts are the most common anomalies of the second branchial cleft, followed by sinuses and fistulas. Branchial cleft cysts are most commonly seen in 10–40-year age group as a painless cystic mass in the upper neck. On CT, it is typically seen as a cystic lesion with thin wall, in relation to the anterior border

Table 15.1 Branchial cleft cyst locations

Branchial cleft cyst	Location
First	External auditory canal (type 1) and submandibular gland (type 2)
Second	Anterior border of upper third of sternocleidomastoid muscle
Third	Larynx and pyriform sinus
Fourth	Various locations, including thyroid gland and mediastinum

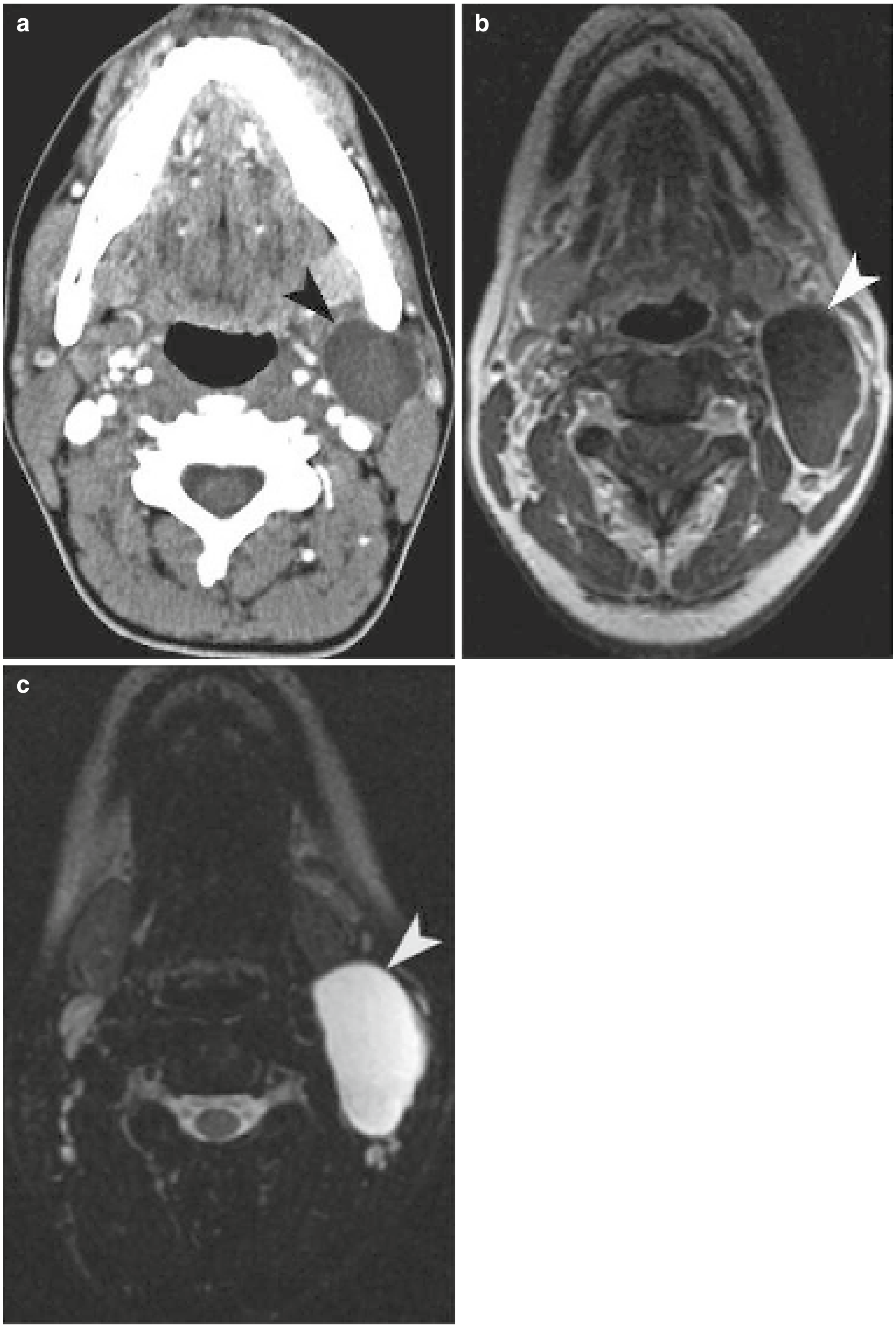

Fig. 15.15 Branchial cleft cyst. (**a**) Contrast-enhanced CT scan study of the upper neck demonstrates a second branchial cleft cyst (*arrowhead*) located in tear medial to the sternocleidomastoid muscle, at the level of the angle of the mandible. (**b**, **c**) Noncontrast T1-weighted and T2-weighted sequence of the upper neck demonstrates a well-defined second branchial cleft cyst (*arrowheads*) on the *left side*

of the sternocleidomastoid, at the level of the angle of mandible (Fig. 15.15). Infected cyst may show wall thickening and enhancement. The differential diagnosis of paramedian cystic mass of the neck includes dermoid, laryngocele, plunging ranula, lymphangioma, thymic cyst (Fig. 15.16), and necrotic lymph node. Sinuses or fistulas present with skin drainage from recurrent infection or abscess formation.

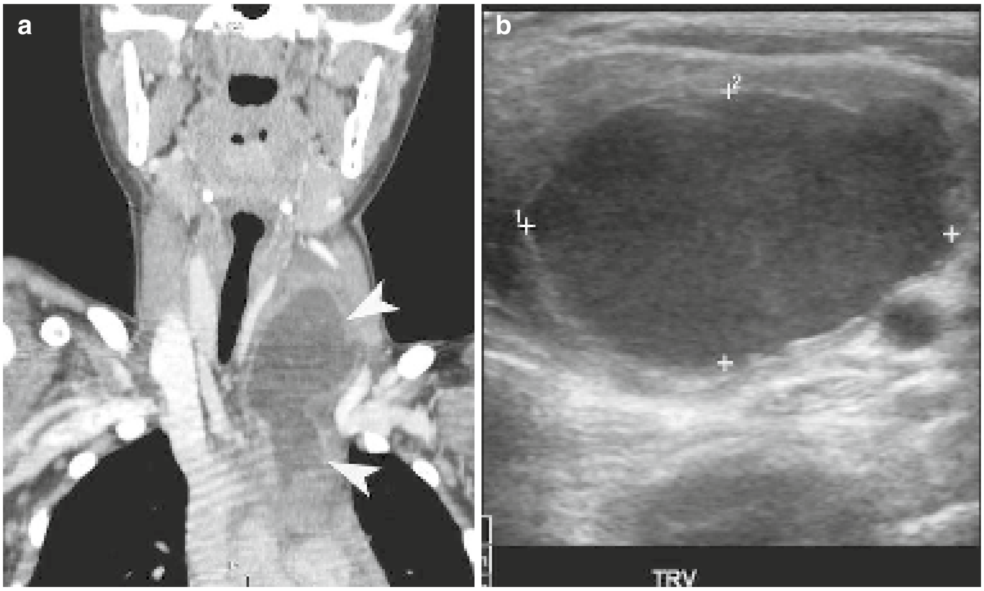

Fig. 15.16 Infected thymic cyst. (**a**) Coronal CT reformation demonstrates a large left-sided thymic cyst (*arrowheads*) extending from the left superior mediastinum to the left supraclavicular neck. (**b**) Ultrasound of the infected thymic cyst demonstrates low-level internal echoes within the cyst

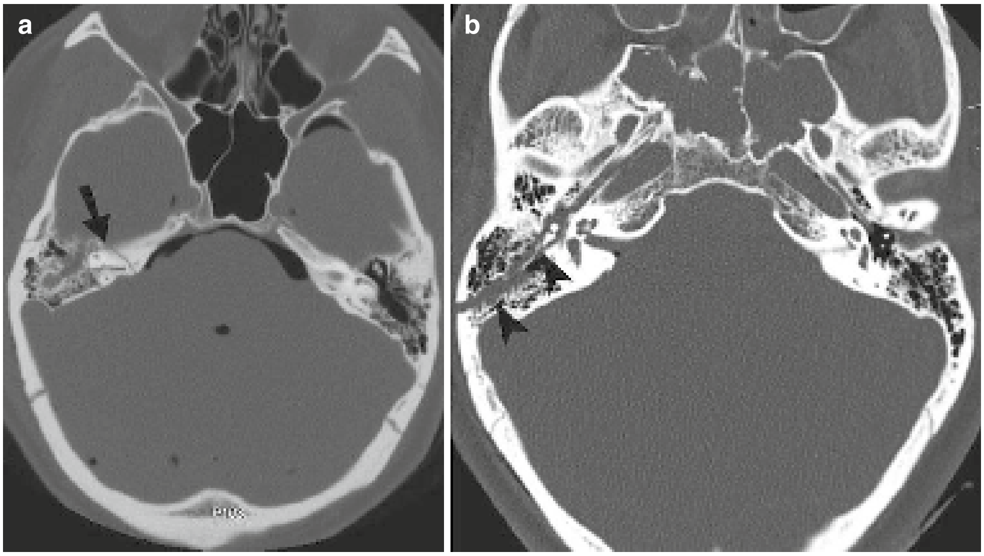

Fig. 15.17 Petrous temporal fracture. (**a**) Axial CT scan study of the petrous temporal bone demonstrates transversely oriented fracture (*straight arrow*) of the right petrous temporal bone. There is pneumocephalus identified due to communication of the mastoid air cells with the extra-axial spaces. (**b**) Axial CT scan study of the petrous temporal bone demonstrates a longitudinally oriented fracture line (*arrowheads*) through the right petrous temporal bone

Temporal Fracture

CT is the imaging modality of choice for the evaluation of temporal bone fracture and ossicular disruption. Temporal bone fractures are classified as either longitudinal or transverse, depending on whether the fracture plane is parallel to the long axis or perpendicular to the long axis of the petrous temporal bone. If components of both fracture planes exist, it is called a mixed subtype. Longitudinal fractures occur more frequently and account for 50–80% of fractures [17]. The injuries associated with petrous temporal bone fracture include seventh cranial nerve injury, CSF leak, sensorineural deafness, conductive deafness, and brain contusion.

Transverse fractures of the temporal bone are often the result of trauma to the occipital or craniocervical junction. The transversely oriented fracture can cause sensorineural deafness because of the involvement of the vestibulocochlear apparatus (Fig. 15.17a). This fracture can also be associated with injury to the seventh cranial nerve, along its labyrinthine course.

The longitudinal fractures are the most common type of petrous temporal fractures (see Fig. 15.17b). It is often the result of direct trauma to the temporal region and is therefore associated with fractures of the squamous temporal bone. The fracture line may pass through the facial nerve canal and may also cause disruption of the ossicular chain, resulting in

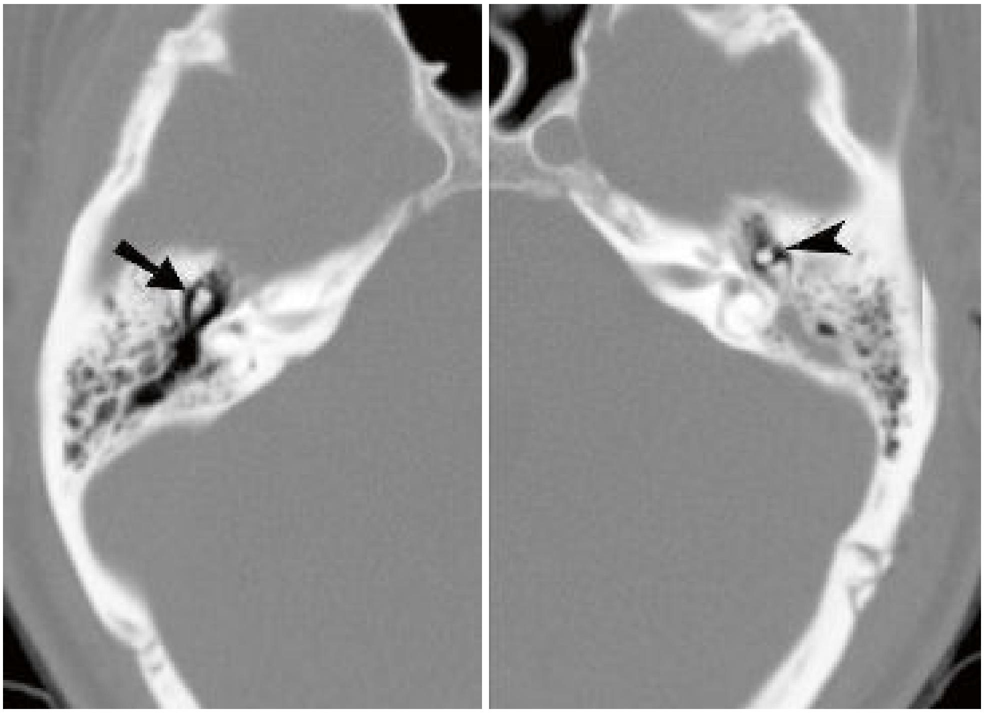

Fig. 15.18 Ossicular disruption. Axial noncontrast CT scan study of the petrous temporal bone demonstrates normal orientation of the right middle-ear ossicles (*straight arrow*). The CT scan study demonstrates left-sided incudostapedial ossicular disruption (*arrowhead*), indicated by the presence of air between the malleus and incus

conductive deafness. Incudostapedial joint disarticulation is the most common post-traumatic abnormality of the middle-ear ossicles (Fig. 15.18). Reconstruction of the ossicular chain is performed when there is conductive hearing loss of more than 30 dB that persists 6 months after trauma [18].

Alternative classification is based on the involvement of labyrinthine structures. This type of classification may help predicting patients who are at higher risk for long-term sensorineural hearing loss and vascular and facial nerve injuries. The patients with intralabyrinthine fracture are at higher risk for severe complications.

Hyoid Fracture

The hyoid bone consists of body, two greater cornua directed posteriorly, and two lesser cornua projected superiorly. Hyoid bone fractures are clinically important because of its proximity to the airway and associated soft tissue injuries (Fig. 15.19). These fractures tend to involve the central part of the bone. Majority of isolated hyoid bone fractures are due to strangulation. Therefore, hyoid bone fracture in cases of suspected homicide strongly suggests strangulation injury [19]. Fractured hyoids are more likely in older patients where they are fused. The fractured hyoid bones tend to be longer in the anterior-posterior plane and more steeply sloping when compared with unfractured hyoids [17].

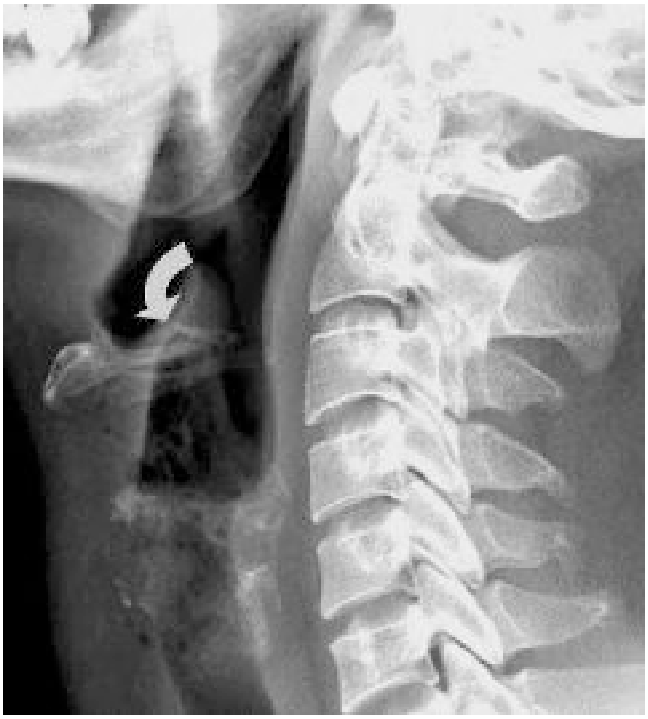

Fig. 15.19 Hyoid bone fracture. Lateral radiograph of the neck demonstrates fracture of the greater cornua (*curved arrow*)

Cholesteatoma

Majority of cholesteatomas are acquired and are believed to arise secondary to middle-ear infection, from the tympanic membrane. It is made up of densely packed squamous keratinized squamous epithelial cells, which are continuously collecting inside the shell formed by the epithelial cells. The shell is formed by tympanic membrane retraction with obstruction of the neck by keratin.

CT is the imaging modality of choice and most often demonstrates the cholesteatoma in the Prussak's space with erosion of the scutum and medial displacement of the ossicles (Fig. 15.20). This classic appearance of cholesteatoma arises from the pars tensa and constitutes more than 80% of the cholesteatomas. The less common (less than 20%) pars tensa cholesteatomas extend medial to the incus and displace the ossicles laterally.

MRI does not allow the anatomical precision as CT study but may allow better tissue characterization for scar, granulation tissue, cholesteatoma (hyperintense on DWI), and cholesterol granuloma (T1 hyperintense). On MRI, cholesteatoma is T1 hypointense and T2 hyperintense, with hyperintensity on diffusion-weighted sequence.

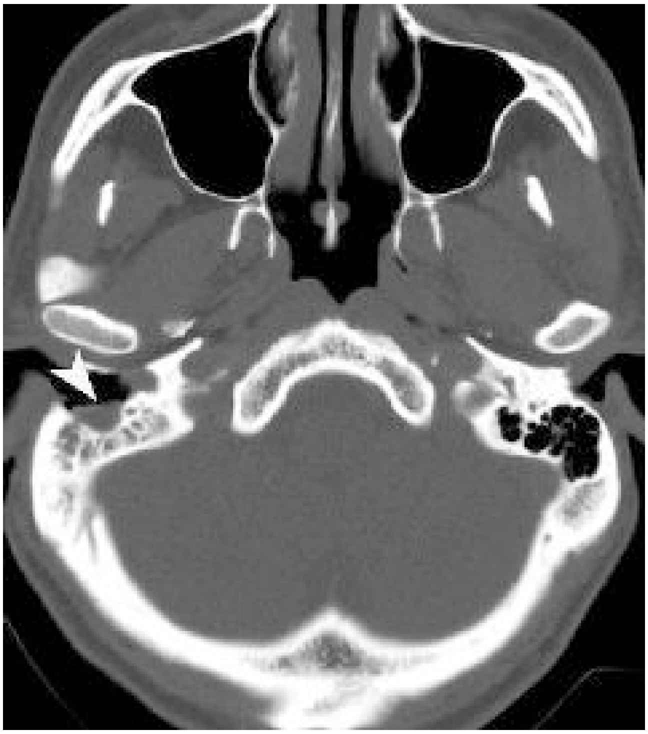

Fig. 15.20 Cholesteatoma. Soft tissue density cholesteatoma (*arrowhead*) is identified on the right side with associated destruction of the bony walls and opacification of the mastoid air cells

Petrous Apicitis

Petrous apicitis refers to the infection of the petrous temporal apex, resulting in osteomyelitis. It can be seen as a complication of mastoiditis or middle-ear infection and is less commonly seen in today's practice because of the early use of antibiotics. *Pseudomonas* is most often responsible for petrous apicitis.

The classic clinical presentation includes headache, sixth cranial nerve palsy, and otorrhea. This is described as Gradenigo syndrome and is characterized by abducent nerve paralysis as it passes through the Dorello's canal. The complications of petrous apicitis include dural venous sinus thrombosis, extradural abscess, meningitis, as well as brain abscess formation.

CT scan study is the imaging modality of choice and is characterized by the presence of bony erosion with ill-defined margins and peripheral enhancement. MRI is more sensitive for the evaluation of the extension of inflammation to the dura and intracranial extension. The MRI findings include hyperintensity on T2-weighted images due to the presence of fluid as well as granulation tissue and post-gadolinium enhancement due to the presence of inflammation (Fig. 15.21) [20].

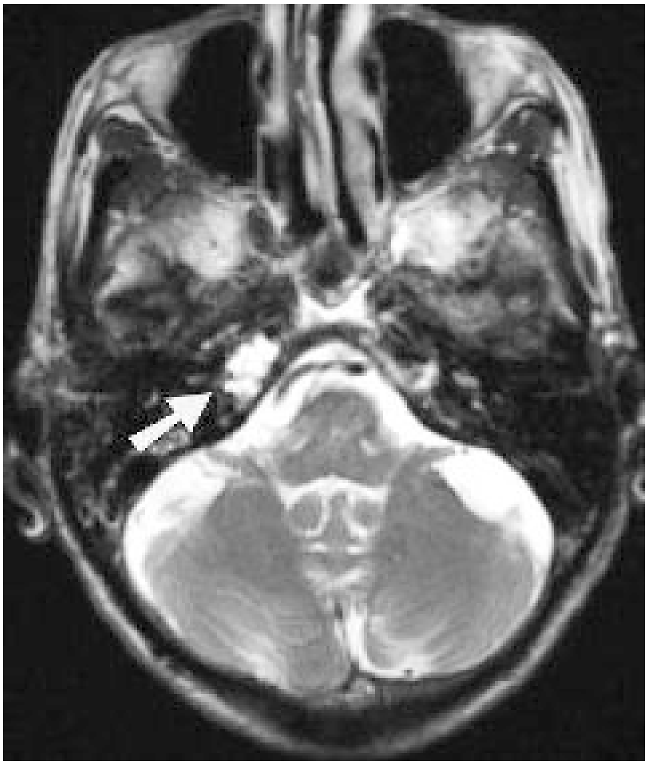

Fig. 15.21 Petrous apicitis. T2-weighted MRI petrous temporal bone demonstrates high signal intensity (*straight arrow*) in the right petrous apex

Mastoiditis

Mastoiditis refers to infection of the mastoid air cells of the temporal bone. Because of their close anatomical relationship with the middle ear, mastoiditis is often caused by extension of the otitis media. Mastoiditis can progress from infection of the mucosa lining of the mastoid air cells to osteomyelitis and formation of abscess cavity, which in turn may extend outside the confines of the mastoid cortex. The complications of acute mastoiditis include dural sinus thrombosis, osteomyelitis, brain abscess, subdural abscess, and epidural abscess.

Acute mastoiditis is most commonly seen in young children and is often secondary to acute otitis media. The CT findings include opacification of the mastoid air cells, which in later stages can be associated with bony destruction, bony dehiscence, and abscess formation. Bezold's abscess refers to dehiscence of mastoid wall with extension of inflammation into the soft tissues of the neck and abscess formation (Fig. 15.22).

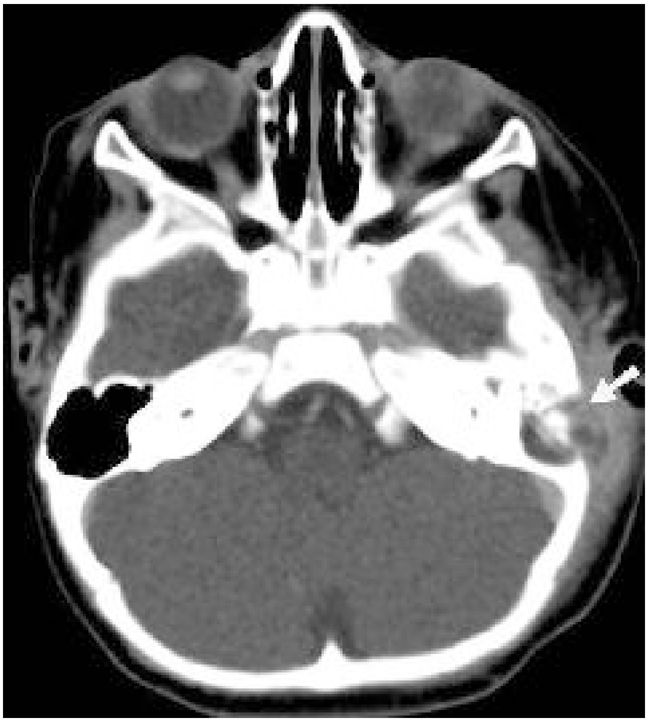

Fig. 15.22 Mastoiditis and Bezold's abscess. Axial contrast-enhanced CT scan study of the petrous temporal bone demonstrates destruction of the left mastoid air cells with extension of abscess (*straight arrow*) into the soft tissues over the left mastoid process

Teaching Points

- Unlike retropharyngeal abscess, danger space abscess can extend below T4 vertebra.
- The radiographic findings of foreign body in the pharynx include prevertebral soft tissue swelling, soft tissue air, and demonstration of radiopaque foreign body.
- The contrast-enhanced CT findings of oral cavity infections include bony erosions around the root of the affected teeth, with extension of the abscess into the soft tissues in the floor of the mouth.
- Lemierre's syndrome is characterized by thrombophlebitis in the neck, most often due to *Fusobacterium necrophorum* infection.
- Eighty to ninety-five percent of submandibular gland sialolithiases are radiopaque and therefore seen on plain radiography.
- Sialadenitis is seen on CT as salivary gland enlargement, surrounding inflammatory changes, and ductal dilatation with calculus.

Questions

1. Which of the following is the most accurate diagnostic modality for foreign body in the pharynx?
   (A) Plain radiography
   (B) CT
   (C) MRI
   (D) Rigid endoscopy
   Answer: D
2. Which of the following is the benefit of MRI in infections of head and neck?
   (A) Differentiates osteomyelitis from bone infarct in sickle cell disease
   (B) Demonstrates Ludwig's angina
   (C) Differentiates subperiosteal abscess from bone infarct in sickle cell disease
   (D) All of the above
   Answer: D

3. Which of the following statements is correct about Lemierre's syndrome?
   (A) It is most commonly due to *Acinetobacter*
   (B) Hyperdense intravascular filling defect is seen on contrast-enhanced CT
   (C) Doppler US is more sensitive than CT in detecting thrombosis
   (D) It commonly occurs after a complicated pharyngitis in youth
   Answer: D

4. Which of the following statements is correct?
   (A) Four patterns of thyroglossal duct cyst are anechoic, homogeneously hypoechoic with internal debris, pseudosolid, and heterogeneous
   (B) Majority of thyroglossal duct cysts are midline in location
   (C) Third branchial cleft cysts are the most common type of branchial cleft cysts
   (D) Transverse temporal fractures are more common than longitudinal fractures
   Answer: A

5. What is the pathology indicated by the arrow on the CT (Fig. 15.23), in a patient with acute pain while swallowing?
   (A) Abscess
   (B) Fish bone
   (C) Epiglottitis
   (D) Tonsillitis
   Answer: B

6. Which abnormality is depicted on the CT scout radiograph (Fig. 15.24) in a patient with difficult endotracheal intubation?
   (A) Fracture of frontal teeth
   (B) Facial fracture
   (C) Dislodged denture
   (D) Atlantoaxial subluxation
   Answer: C

7. What is the imaging diagnosis (Fig. 15.25) in a 25-year-old patient with left neck swelling?
   (A) First branchial cleft cyst
   (B) Second branchial cleft cyst
   (C) Third branchial cleft cyst
   (D) Fourth branchial cleft cyst
   Answer: B

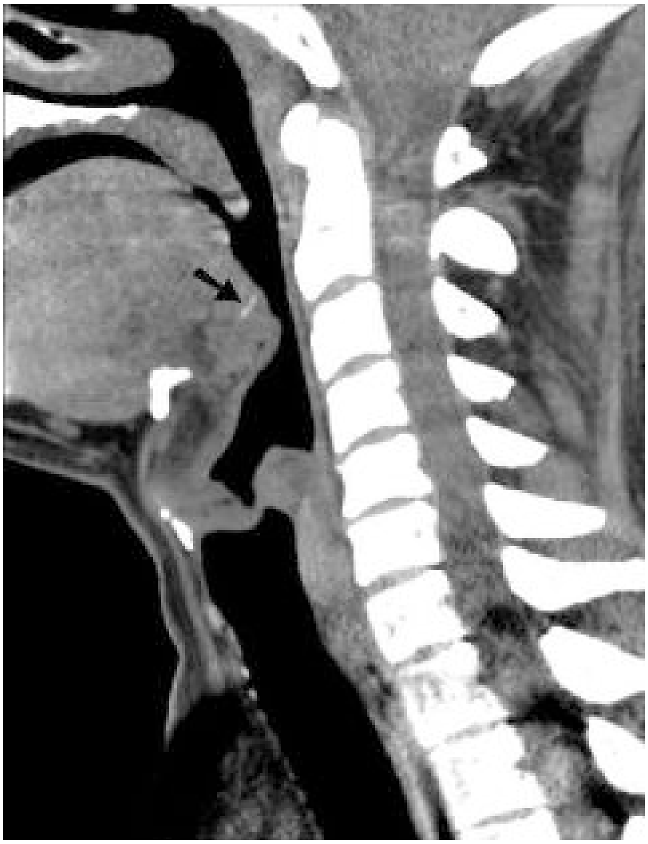

Fig. 15.23 Fish bone—CT scan

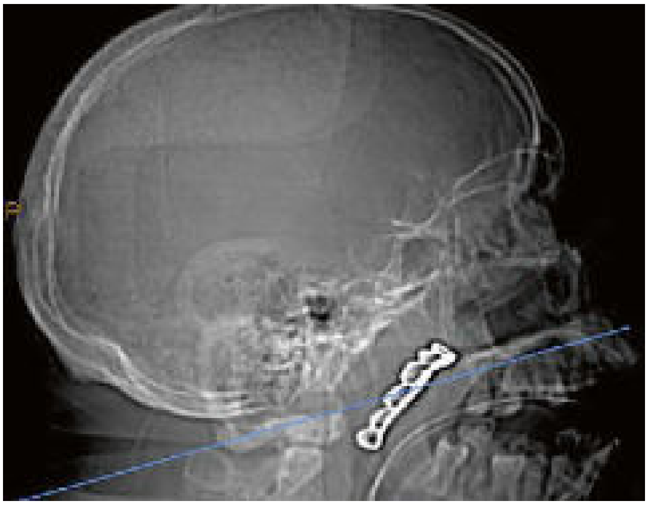

Fig. 15.24 CT scout radiograph—dislodged denture

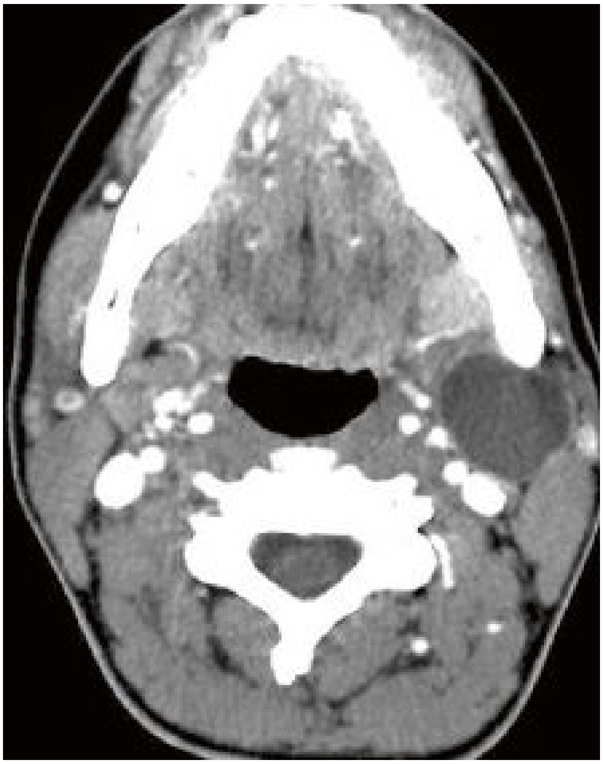

Fig. 15.25 2nd Branchial clef cyst

References

1. Fuentes S, Cano I, Benavent MI, Gómez A. Severe esophageal injuries caused by accidental button battery ingestion in children. J Emerg Trauma Shock. 2014;7(4):316–21. https://doi.org/10.4103/0974-2700.142773.
2. Semple T, Calder AD, Ramaswamy M, McHugh K. Button battery ingestion in children-a potentially catastrophic event of which all radiologists must be aware. Br J Radiol. 2018;91(1081):20160781. https://doi.org/10.1259/bjr.20160781.
3. Knight LC, Lesser THJ. Fish bones in the throat. Arch Emerg Med. 1989;6:13–6.
4. Kim HU. Oroesophageal fish bone foreign body. Clin Endosc. 2016;49(4):318–26.
5. Waltzman ML. Management of esophageal coins. Curr Opin Pediatr. 2006;18(5):571–4.
6. Sharieff GQ, Brousseau TJ, Bradshaw JA, Shad JA. Acute esophageal coin ingestions: is immediate removal necessary? Pediatr Radiol. 2003;33(12):859–63.
7. Capps EF, Kinsella JJ, Gupta M, Bhatki AM, Opatowsky MJ. Emergency imaging assessment of acute, nontraumatic conditions of the head and neck. Radiographics. 2010;30:1335–52.
8. Isacsson G, Isberg A, Haverling M, Lundquist PG. Salivary calculi and chronic sialadenitis of the submandibular gland: a radiographic and histologic study. Oral Surg Oral Med Oral Pathol. 1984;58(5):622–7.
9. Zenk J, Iro H, Klintworth N, Lell M. Diagnostic imaging in sialadenitis. Oral Maxillofac Surg Clin N Am. 2009;21(3):275–92.
10. Shefelbine SE, Mancuso AA, Gajewski BJ, Ojiri H, Stringer S, Sedwick JD. Pediatric retropharyngeal lymphadenitis: differentiation from retropharyngeal abscess and treatment implications. Otolaryngol Head Neck Surg. 2007;136(2):182–8.
11. Screaton NJ, Ravenel JG, Lehner PJ, Heitzman ER, Flower CD. Lemierre syndrome: forgotten but not extinct—report of four cases. Radiology. 1999;213(2):369–74.
12. Sinave CP, Hardy GJ, Fardy PW. The Lemierre syndrome: suppurative thrombophlebitis of the internal jugular vein secondary to oropharyngeal infection. Medicine. 1989;68:85–94.
13. Saedi B, Sadeghi M, Mojtahed M, Mahboubi H. Diagnostic efficacy of different methods in the assessment of adenoid hypertrophy. Am J Otolaryngol. 2011;32(2):147–51.
14. Mary Kurien M, Lepcha A, Mathew J, Ali A, Jeyaseelan L. X-rays in the evaluation of adenoid hypertrophy: it's role in the endoscopic era. Indian J Otolaryngol Head Neck Surg. 2005;57(1):45–7.
15. Mozhdeh SM. The steeple sign. Radiology. 2000;216:428–9.
16. Ahujaa AT, Kinga AD, Kinga W, Metrewelia C. Thyroglossal duct cysts: sonographic appearances in adults. AJNR Am J Neuroradiol. 1999;20:579–82.
17. Kennedy TA, Avey GD, Gentry LR. Imaging of temporal bone trauma. Neuroimaging Clin N Am. 2014;24(3):467–86.
18. Lee D, Honrado C, Har-El G, Goldsmith A. Pediatric temporal bone fractures. Laryngoscope. 1998;108:816–21.
19. Pollanen MS, Chiasson DA. Fracture of the hyoid bone in strangulation: comparison of fractured and unfractured hyoids from victims of strangulation. J Forensic Sci. 1996;41(1):110–3.
20. Lee YH, Lee NJ, Kim JH, Song JJ. CT, MRI and gallium SPECT in the diagnosis and treatment of petrous apicitis presenting as multiple cranial neuropathies. Br J Radiol. 2005;78:948–51.

Imaging of Acute Head Emergencies

16

Abdul-Majid Khan, Sneha R. Patel, Mohammad Mansouri,
and Ajay Singh

Introduction

In the management of acute intracranial emergencies, triage of patients is key, and therefore, proper diagnosis on early imaging can go a long way in directing the appropriate workup and management.

Pseudo-Subarachnoid Hemorrhage

Increased density in the subarachnoid spaces at the basal cisterns is typically seen in patients with diffuse subarachnoid hemorrhage. However, it is imperative to examine the brain parenchyma for signs of increased cerebral edema, as the increased density in the subarachnoid space may well be due to engorged dural, arterial, and venous vessels from brain swelling (Fig. 16.1). Other CT mimics of subarachnoid hemorrhage include intrathecal contrast injection, infectious meningitis, leakage of intravascular contrast into the subarachnoid spaces, infarction, subdural hematoma, status epilepticus, spontaneous intracranial hypotension, polycythemia, and after myelography.

The pathologic cause of the increased cisternal density is not definitively known, but is postulated to be secondary to a combination of factors, including displacement of normally hypodense cerebrospinal fluid, engorgement of the superficial vasculature, and edematous and hypodense adjacent brain [1].

A.-M. Khan · S. R. Patel
Department of Diagnostic Radiology, Beaumont Health System,
Oakland University William Beaumont School of Medicine,
Royal Oak, MI, USA

M. Mansouri
Department of Radiology, Massachusetts General Hospital,
Boston, MA, USA

A. Singh (✉)
Division of Emergency Radiology, Department of Radiology,
Massachusetts General Hospital, Boston, MA, USA

Harvard Medical School, Massachusetts General Hospital,
Boston, MA, USA
e-mail: asingh1@partners.org

© The Author(s), under exclusive license to Springer Nature Switzerland AG 2024
A. Singh (ed.), *Emergency Radiology*, https://doi.org/10.1007/978-3-031-65770-2_16

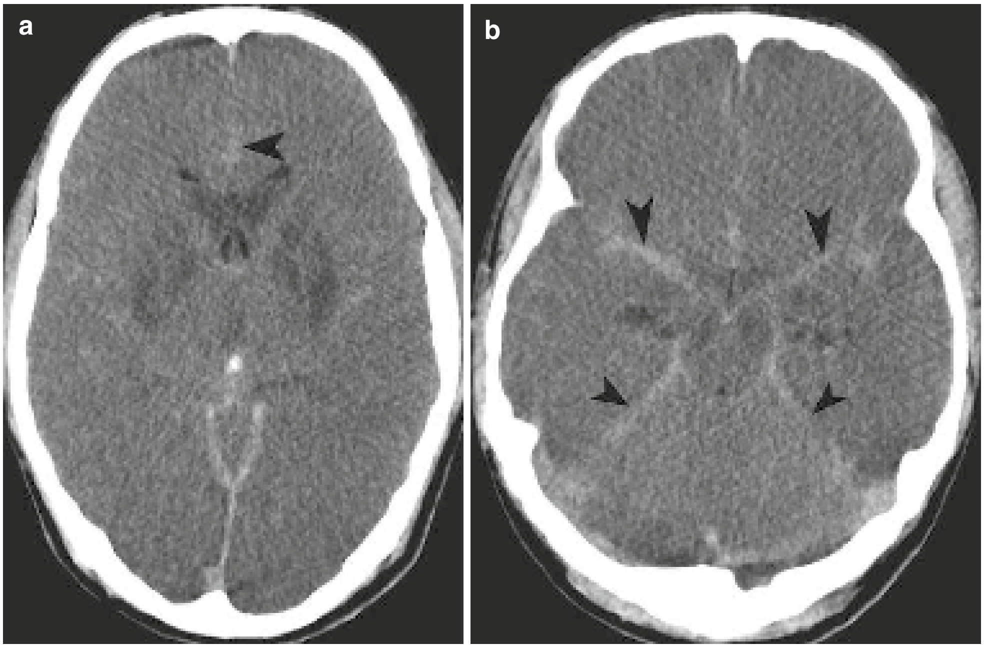

Fig. 16.1 Cerebral edema. (**a**) Noncontrast axial CT image of the brain shows diffuse hypodensity in the brain parenchyma, with loss of the gray-white interface compatible with brain edema. (**b**) Extra-axial high attenuation (*arrowheads*) has the appearance of subarachnoid hemorrhage but is simply secondary to brain swelling

Carbon Monoxide Poisoning

Patients found unresponsive and brought for acute neuroimaging can have a whole host of imaging findings, some subtle and others obvious. Initial symptoms include headache, nausea, dizziness, fatigue, and impaired manual dexterity. Loss of consciousness and death can occur with carboxyhemoglobin levels between 30 and 70%. Carbon monoxide poisoning is one potentially subtle imaging finding which, if detected early, can significantly improve the clinical prognosis of the patient.

Carbon monoxide poisoning is a typically symmetric anoxic encephalopathy, with a much higher affinity for hemoglobin than oxygen. Cerebral injury has a predilection for the globi pallidi (Fig. 16.2) [2]. The cerebral white matter may or may not be also involved, depending on the duration of exposure. If diagnosed within 6 h on initial injury, long-term neuropsychiatric morbidity can be curtailed. Standard treatments include hyperbaric oxygen and 100% oxygen with tight-fitting mask for more than 6 h. Neurological abnormalities can occur even with normal MRI.

Differential considerations include Creutzfeldt–Jakob disease, Wilson's disease, and Leigh syndrome, all entities which can affect the globi pallidi, although all of these have more widespread gray matter involvement than CO poisoning.

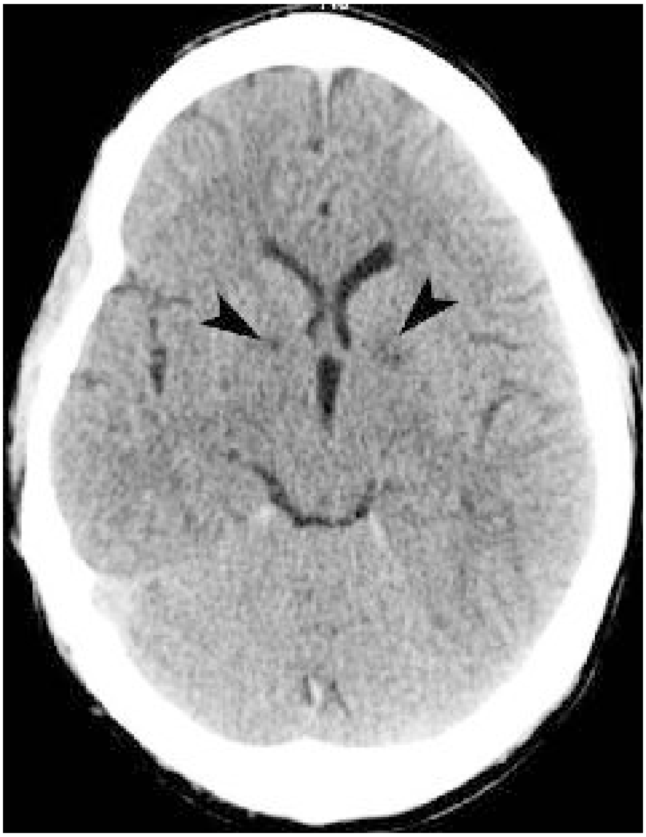

Fig. 16.2 Carbon monoxide poisoning. Noncontrast axial CT image of the brain shows subtle areas of decreased attenuation in bilateral globi pallidi (*arrowheads*), compatible with ischemic injury in the setting of carbon monoxide poisoning

Central Nervous System Infections

Cerebral abscesses are typically located at the corticomedullary junction and have thin, regular capsule formation that appears hypointense on T2-weighted images. MRI is the most sensitive imaging modality to detect brain abscess. The causes of brain abscess include bacterial, fungal, or tuberculosis. The disease evolves from an early cerebritis and extensive T2 signal intensity abnormality to liquefaction and capsule formation. On CT with contrast, ring-enhancing lesions can be seen.

Blood culture can identify the organism in 25% of cases. CSF remains sterile in most of the cases; however, LP can be done to identify concomitant meningitis or abscess rupture into the ventricles. In these situations, contraindications to LP should be carefully investigated to avoid brain herniation.

The medial temporal lobe involvement by focal process can be from arterial ischemia, which originates from the PCA territory; pyogenic infection, which can arise from otogenic infection; and herpes encephalitis, which has a predilection for the hippocampal formation [3]. If the focal abnormality involves the lateral temporal lobe, MCA territory arterial ischemia should be considered. If the edema involves the entire temporal lobe, one has to consider tumor. If otogenic infection is left untreated, there can be dural breach, leading to empyema, cerebritis, and abscess formation (Figs. 16.3, 16.4 and 16.5).

Parasitic infection, such as neurocysticercosis, paragonimiasis, and echinococcus infection, should be considered when there is history of travel to an endemic region. Neurocysticercosis is the most common parasitic infection involving the central nervous system in developing countries and is endemic to Mexico, South America, Africa, Eastern Europe, and Asia. The patient’s symptoms depend on host response rather than active parasites. The neurocysticercosis involving the central nervous system is of four types:

- Meningeal
- Parenchymal
- Ventricular
- Mixed

While the meningeal cysts form mostly in the basal meninges, parenchymal cysts are usually found in the cerebral cortex. The white matter is rarely involved. Ventricular cysts are seen in 15% of patients with neurocysticercosis, most commonly involving the fourth ventricle. In approximately one-fifth of cases of ventricular disease, there is associated parenchymal involvement.

Parenchymal neurocysticercosis is typically seen as 1 cm (range, 4–20 mm) diameter spherical shape lesion with a 2–3 mm mural nodule produced by the scolex. The presence of surrounding edema and enhancement of capsule indicates that the parasite is in degenerative or colloidal state. Noncontrast CT is useful in detecting calcified or intraparenchymal cystic lesions, but can miss subarachnoid or intraventricular lesions. MRI is generally more sensitive but is not sensitive for calcified lesions. Using both modalities is preferred for staging of the disease. On T1-weighted sequence, the fluid in the cystic lesion is hypointense to white matter and hyperintense to cerebrospinal fluid (see Fig. 16.3e, f). On T2-weighted sequence, the cystic fluid is markedly hyperintense. There is usually no enhancement in the earlier vesicular stage, when the larva is still viable and the cyst is antigenically inert. In nodular calcified stage, cystic lesion is calcified and does not show any enhancement. DWI helps detect scolex, which may be impossible to detect on regular MRI or CT.

Overall, common causes of leptomeningeal enhancement include bacterial, viral, fungal, and parasitic meningitis, and neoplasms (also called carcinomatous meningitis), which could be primary (such as medulloblastoma, ependymoma, glioblastoma, and oligodendroglioma) or secondary (such as lymphoma and breast cancer).

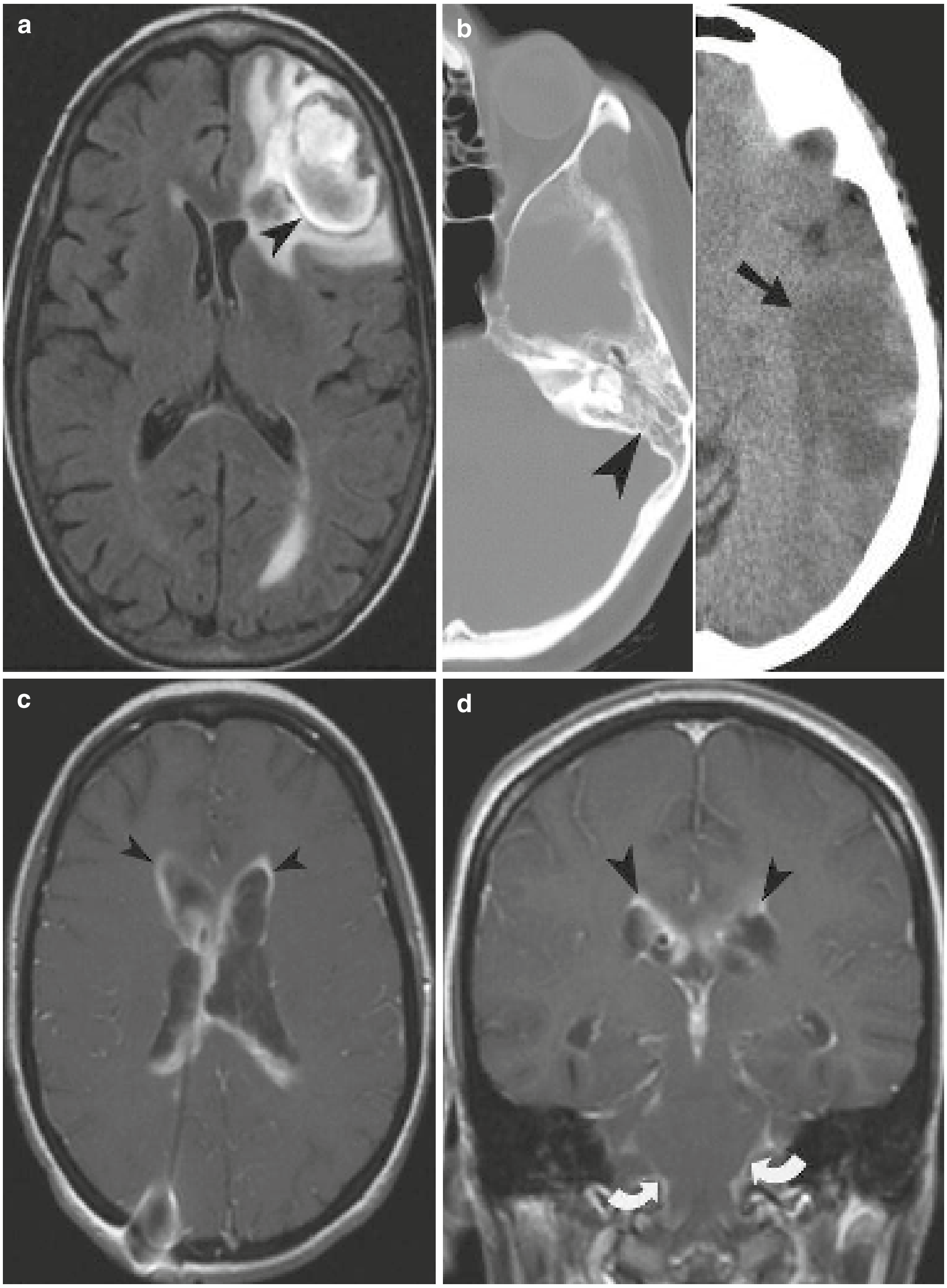

Fig. 16.3 Intracranial infection: brain abscess, ventriculitis, meningitis, and neurocysticercosis. (**a**) FLAIR sequence demonstrates left frontal brain abscess (*arrowhead*) from fungal infection with surrounding edema. The wall of the abscess is thinner on the medial aspect, a feature of brain abscess which is the result of limited vascular supply on the medial aspect. (**b**) Noncontrast axial CT image of the brain shows confluent decreased attenuation (*arrowhead*) in the left temporal lobe, from a combination of abscess and edema (*arrow*). Bone windows at the same level show fluid in mastoid air cells (*arrowhead*). (**c**, **d**) Contrast-enhanced T1-weighted MRI shows extensive ependymal enhancement of the ventricular wall (*arrowheads*). There is also enhancement of the basal cisterns (*curved arrows*). The defect seen in the right parietal bone is from a ventriculostomy catheter which had become infected and was taken out. (**e**, **f**) T1-weighted sequence demonstrates multiple spherical parenchymal neurocysticercosis (*arrowheads*) containing scolex, at the gray-white matter junction. Post-gadolinium T1-weighted (**f**) sequence shows rim enhancement of the multiple cystic lesions in the supratentorial compartment

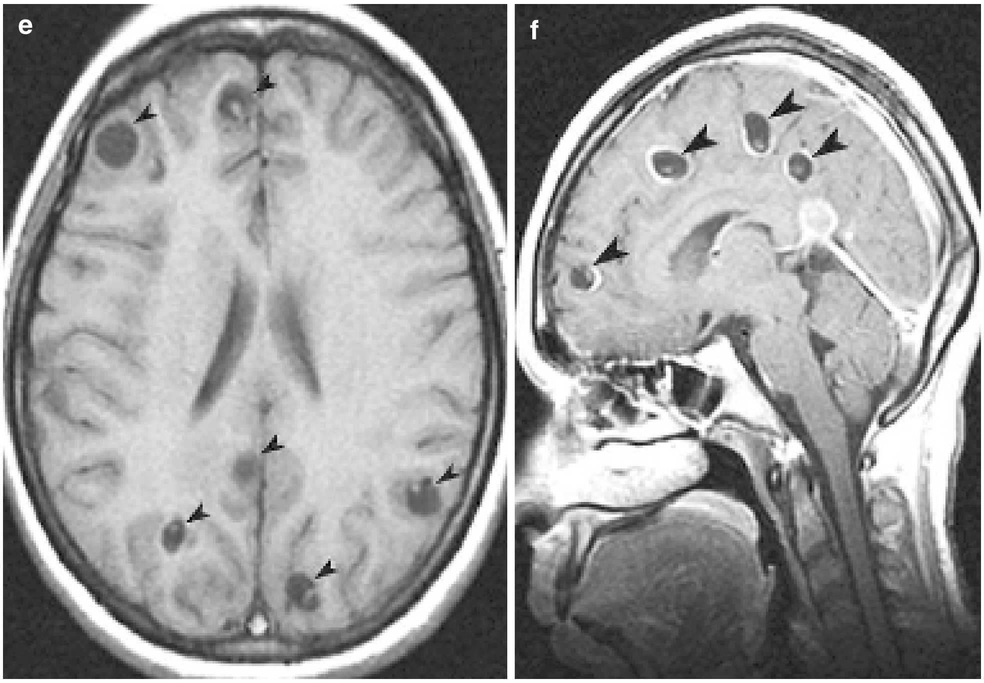

Fig. 16.3 (continued)

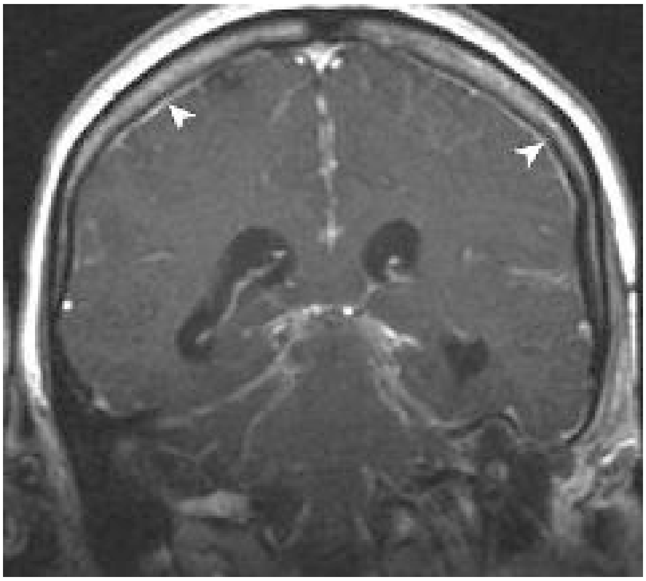

Fig. 16.4 Bacterial meningitis. Contrast-enhanced T1-weighted MRI shows intense leptomeningeal enhancement (*arrowheads*), consistent with meningitis

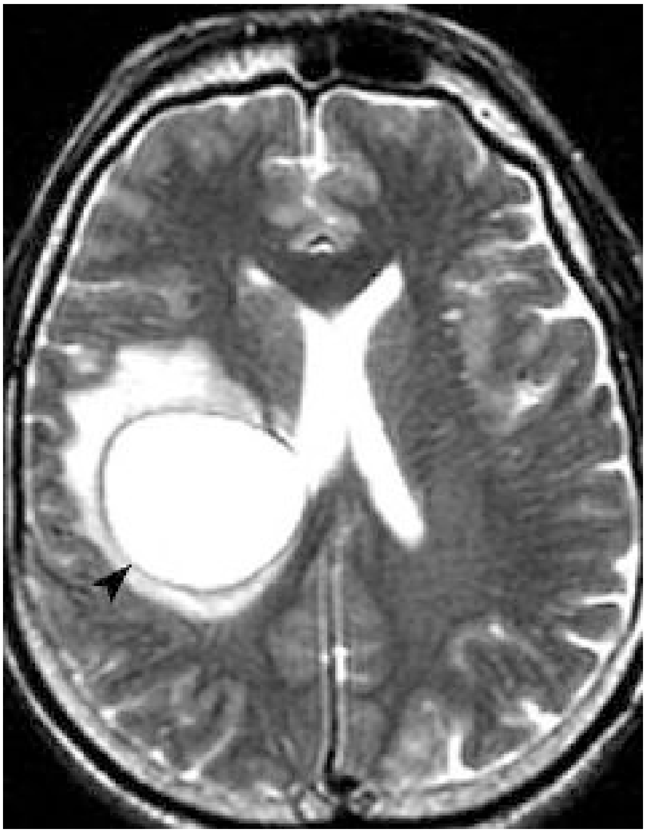

Fig. 16.5 Hydatid cyst. T2-weighted MRI of brain demonstrates thin-wall cystic lesion in the cerebral white matter with surrounding edema

Herpes Encephalitis

Herpes simplex virus infection is ubiquitous in the general population, usually contracted initially via oronasopharyngeal contact. The virus then lies dormant within the trigeminal ganglion and spreads retrogradely. HSV encephalitis is the most common viral infection in the central nervous system. What precipitates viral reactivation in the CNS is not known, although some patients have been found to have a viral prodrome prior to full manifestation [4]. Patients usually present with fever, headache, seizure, and a gradual onset of altered mental status, over the course of a few days. Infrequently, there are focal neurological signs. Bilateral involvement is usually asymmetric, involves insula, and usually does not go further than the lateral putaminal border.

Fortunately, there are many imaging features for HSV encephalitis that are characteristic. The limbic system is a characteristic location (Fig. 16.6). CT often shows asymmetric insular edema. On MRI, the enhancement is typically gyriform. Restricted diffusion is often seen in the limbic system. Hemorrhage is a late feature. If a patient has these features, a presumptive diagnosis of herpes encephalitis should lead the clinical team to start IV acyclovir, as prompt antiviral therapy has been shown to improve outcomes.

The differential possibilities include infarction, especially if the symptoms are very acute in onset; postictal states can cause swelling and patchy areas of enhancements, mimicking HSV encephalitis, especially if the focus is on the temporal lobes, and limbic encephalitis, especially if the onset of symptoms is more gradual, such as over the course of months rather than days in herpetic encephalitis.

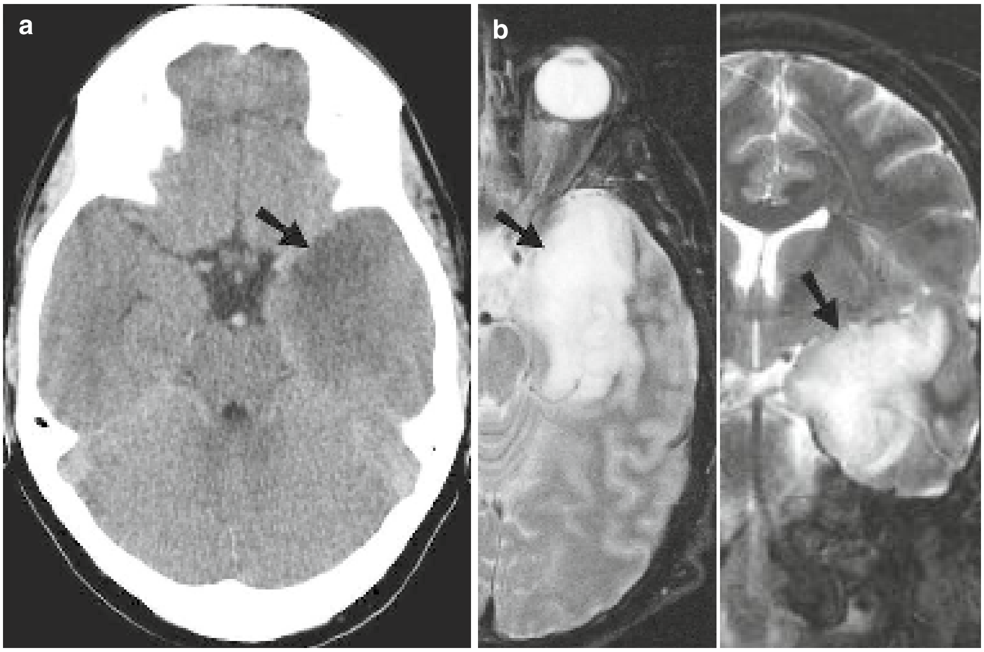

Fig. 16.6 Herpes encephalitis. (**a**) Noncontrast axial CT image of the brain shows decreased attenuation in the medial left temporal lobe (*arrow*). (**b**) Axial and coronal T2-weighted images show edema (*arrows*) in the medial temporal lobe, with contrast-enhanced T1-weighted images demonstrating patchy areas of enhancement

Tension Pneumocephalus

Tension pneumocephalus, a serious and potentially life-threatening condition, is due to increased air pressure in the subdural space causing mass effect on the frontal lobes and leading to neurological deterioration. The pathogenesis is described as a ball-and-valve mechanism. Another possible mechanism is inverted soda bottle phenomenon, in which CSF leaks which causes negative intracranial pressure and air replaces the lost CSF. There is communication of the extracranial and intracranial spaces with ingress of air intracranially due to lower intracranial pressure, and the egress of air is blocked by an obstruction. Most cases occur due to head trauma, but tension pneumocephalus can also occur due to skull base surgery, paranasal sinus surgery, CSF shunting, evacuation of a subdural hematoma, or posterior fossa surgery.

Patients with tension pneumocephalus often have headache, nausea, vomiting, seizures, and, most importantly, a diminishing level of consciousness. Hemiparesis, cranial nerve palsies, meningism, and aphasia may be seen in the physical examination. Imaging findings are characteristic, but not pathognomonic: prominent bifrontal subdural air collections that cause a mass effect on both frontal lobes, with widening of the interhemispheric spaces between the frontal lobes (Mt. Fuji sign) (Fig. 16.7) [5, 6].

The peaking sign is more common in pneumocephalus rather than tension pneumocephalus and is defined as bilateral compression of the frontal lobes caused by the bridging veins entering the superior sagittal sinus, which may result in subdural air collection. The air bubble sign is also more common in pneumocephalus and shows multiple air bubbles around the cisterns, caused by a tear in the arachnoid membrane.

If a patient who has had recent surgery has this imaging appearance and is clinically deteriorating, a diagnosis of tension pneumocephalus should be highly considered. Treatments include burr hole placement, craniotomy, needle aspiration, and closure of dural defects.

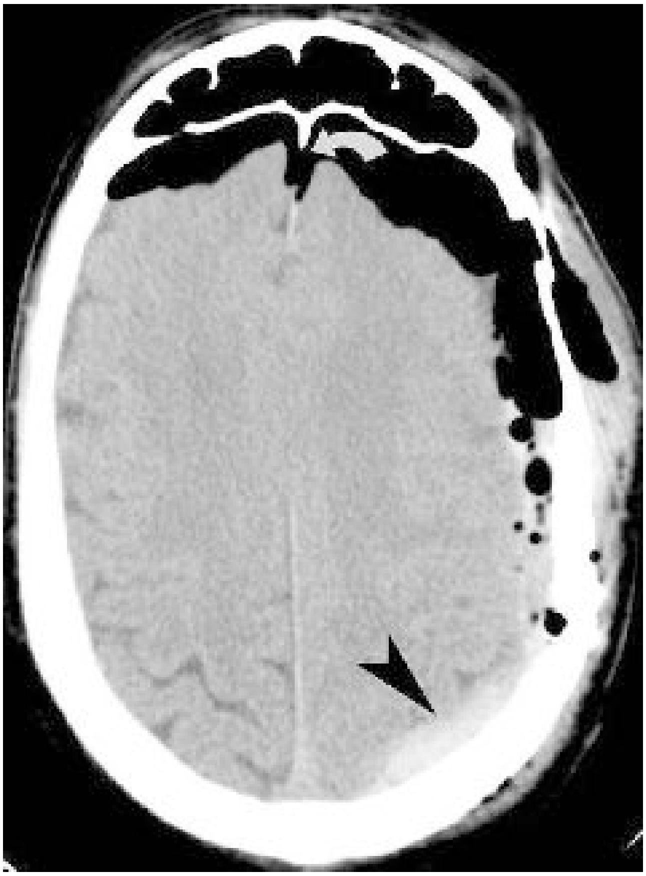

Fig. 16.7 Tension pneumocephalus. Noncontrast CT of the head shows prominent bifrontal subdural air collections with mass effect on both frontal lobes and widening of the interhemispheric space (Mt. Fuji sign) (*curved arrow*). A hyperdense left-sided subdural hematoma (*arrowhead*) is seen over the left parietal lobe

Giant MCA Aneurysm

Giant intracranial aneurysms are aneurysms that have a diameter greater than 2.5 cm. Most giant aneurysms are saccular rather than fusiform [7]. They tend to occur at branch points, arising de novo in defects in the intima or arising from enlarging smaller aneurysms due to hemodynamic stress. While ruptured giant aneurysms have typical symptoms of the "worst headache of my life," unruptured giant aneurysms have a sinister clinical presentation, often presenting due to mass effect on the adjacent structures or due to thromboemboli. Any large hyperdense mass in the vicinity of the cisterns and subarachnoid spaces should at least raise the possibility of a cerebral aneurysm (Fig. 16.8). Aside from size, other imaging features of giant cerebral aneurysms are rim calcifications, a laminated and adjacent parenchymal hypodensity due to edema from pulsation.

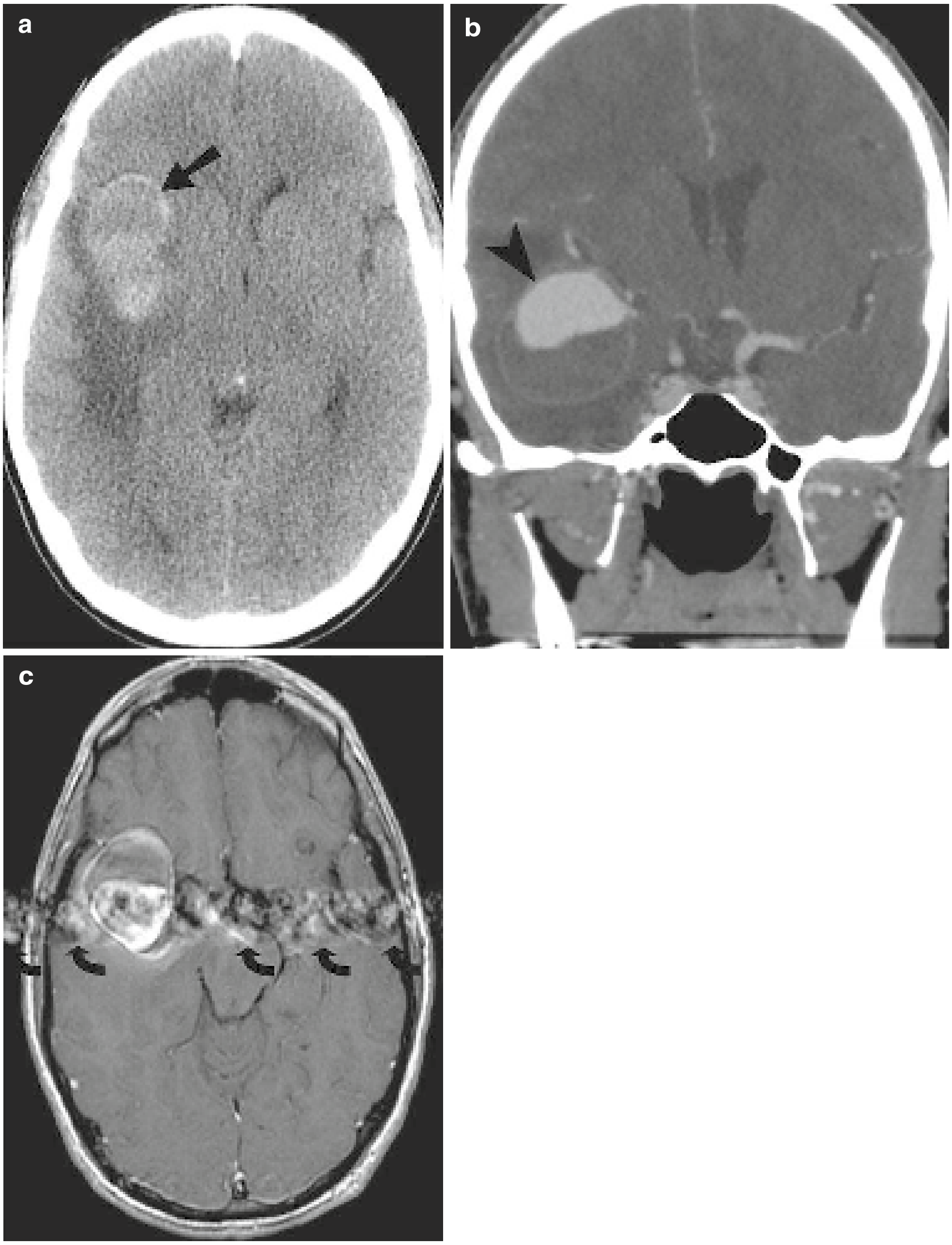

Fig. 16.8 MCA aneurysm. (**a**) Noncontrast axial CT image of the brain demonstrates a heterogeneously hyperdense lesion (*arrow*) in the right Sylvian cistern with edema within the right temporal lobe. (**b**) Coronal CTA image shows a 4.5 cm diameter, partially thrombosed aneurysm (*arrowhead*) arising off the M2 segment of the right MCA. (**c**) Axial T1-weighted images with contrast show pulsation artifacts (*curved arrows*) in the phase-encoding direction, indicative of a high-flow process in the aneurysm

Spontaneous Intracranial Hypotension

Spontaneous intracranial hypotension is characterized by low CSF pressure and postural headaches in the absence of prior trauma, surgery, or lumbar puncture [8]. It is usually due to an occult CSF leak from small meningeal defects. Clinical presentation is a new onset of headache with prompt and striking relief of pain in the supine position and recurrence of pain in the sitting or standing position. Headache may be associated with nausea, vomiting, vertigo, blurred vision, photophobia, neck stiffness, and occipitocervical pain with neck flexion. There should be no recent history of dural puncture, and the findings should not be attributable to other disorders. Imaging findings on CT or MR brain imaging include bilateral subdural hematomas, diffuse pachymeningeal enhancement, caudal displacement of the cerebellar tonsil and brainstem, decreased size of the ventricles and basal cisterns, sagging of the brain, engorgement of venous structures, and enlargement or hyperemia of the pituitary gland (Fig. 16.9) [9]. The condition is generally self-limited, but treatment of associated subdural hematoma or headaches may be needed. Persistent headaches may be treated with the use of autologous epidural blood patch if conservative measures fail.

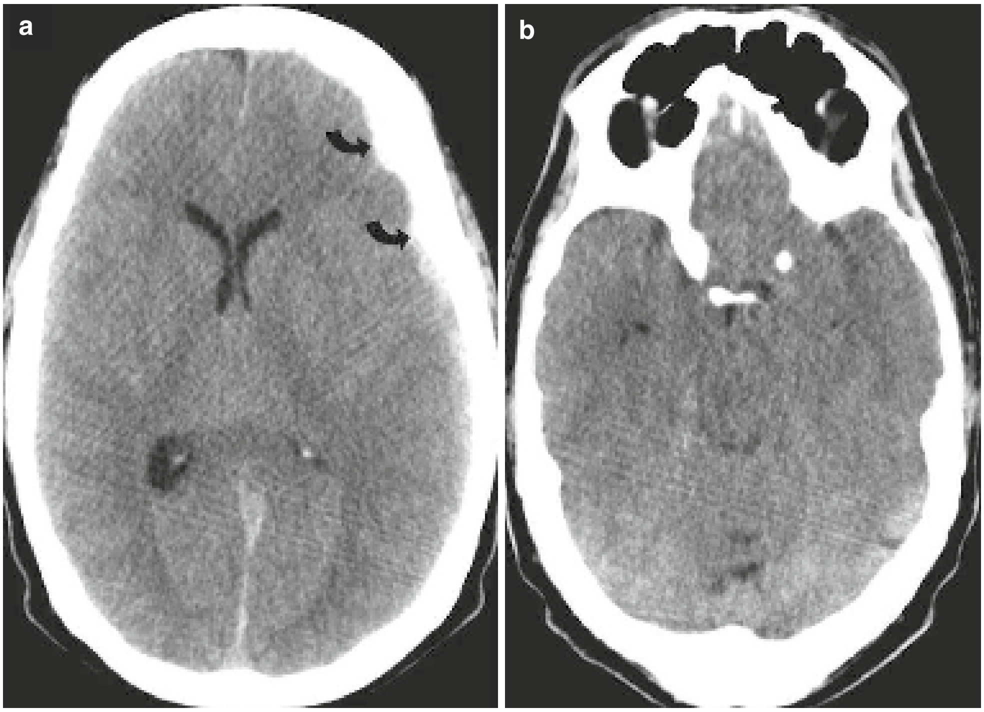

Fig. 16.9 Intracranial hypotension. (**a**) Unenhanced axial CT images of the brain demonstrate effacement of the basal cisterns, brainstem sagging, and left-sided subdural hematoma (*curved arrow*). (**b**) Unenhanced sagittal T1 MRI image of the brain demonstrates sagging of the brainstem and descent of the cerebellar tonsils

Extra-Axial Hemorrhages

Extra-axial hemorrhages are classified into three main compartments: epidural, subdural, and subarachnoid (Fig. 16.10) [10].

Traumatic subarachnoid hemorrhage is the most common extra-axial hemorrhage associated with head trauma. It is caused by traumatic injuries of veins and arteries at the base of the brain, and there is less hemorrhage compared to subarachnoid hemorrhage due to aneurysm rupture.

Subdural hematomas occur between the inner dural layer and the arachnoid. Approximately half are due to shearing of the bridging veins, and the other half are due to tear of the cortical arteries. The hemorrhage is crescentic in shape acutely and crosses sutures commonly but cannot cross the midline. Interhemispheric location in children suggests non-accidental trauma.

Epidural hematomas occur in the potential space between the calvarium and the outer dural layer. The most common cause is a temporal bone fracture and arterial laceration (usu-

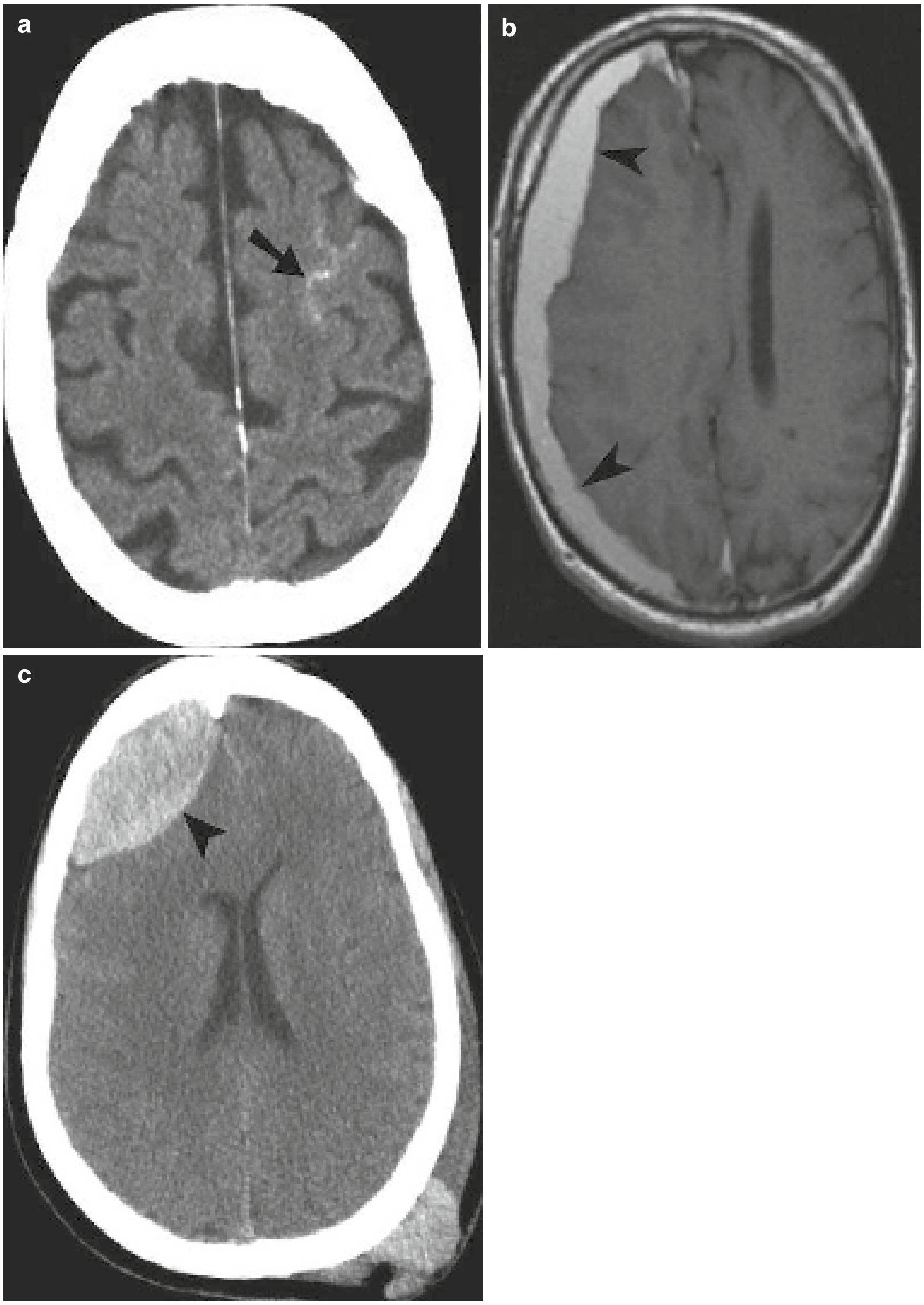

Fig. 16.10 Intracranial hemorrhage. (**a**) Noncontrast CT demonstrates subarachnoid hemorrhage (*arrow*) in the sulci over the left frontal convexity. (**b**) Unenhanced axial T1 MRI image of the brain demonstrates a hyperintense subdural fluid collection (*arrowheads*) along the right cerebral convexity consistent with a subacute subdural hematoma. (**c**) Noncontrast CT demonstrates a biconvex-shaped epidural hematoma (*arrowhead*) over the right frontal convexity produced by countercoup injury. It is producing mass effect over the right lateral ventricle

Table 16.1 Summary of imaging findings in extra-axial hemorrhages

Traumatic subarachnoid hemorrhage	Subdural hematomas	Epidural hematomas
Most common extra-axial hemorrhage	Half are due to shearing of the bridging veins	Most common cause is a temporal bone fracture and arterial laceration
Traumatic injuries of veins and arteries	Other half are due to tear of the cortical arteries	Biconvex in configuration
Less hemorrhage compared to aneurysm rupture	Crescentic in shape	Limited by sutures
	Crosses sutures commonly but cannot cross the midline	Lucid interval may be present

ally the middle meningeal artery) with smaller percentage associated with dural venous sinus tear. The hemorrhage is biconvex in configuration and is limited by sutures due to the firm adherence of the dura to the inner table and its attachment to the sutures. In less than 50% of cases, there is a lucid interval in which the patient is knocked out by the initial concussion and then lapses into unconsciousness again after recovery. Prompt recognition and treatment can significantly decrease morbidity and mortality associated with epidural hemorrhages (Table 16.1).

Herniation Syndromes

The brain, CSF, and blood coexist in a rigid and non-expandable container: the cranium. When most other organs enlarge, there is generally some room for expansion; however, the brain, when it expands due to edema, tumor, or hemorrhage, has very little space in which to expand. If the intracranial pressure increases enough, it will cause the brain to herniate from one compartment to another (Fig. 16.11a–d) [11].

Subfalcine herniation, the most common type of herniation, occurs when the cingulate gyrus and pericallosal branches of the anterior cerebral artery herniate beneath the falx cerebri. There is effacement of the ipsilateral ventricle and enlargement of the contralateral ventricle due to continuous production of CSF by the choroid plexus. There are possible compression of the ipsilateral anterior cerebral artery or internal cerebral veins and risk of infarction.

Uncal herniation occurs when the medial temporal lobe tissue (uncus and hippocampus) is displaced medially through the free edge of the tentorium cerebelli and compresses the brainstem and adjacent structures (posterior cerebral artery, oculomotor nerve, and anterior choroidal artery). There is compression of the ipsilateral oculomotor nerve, causing a fixed and dilated pupil, and ipsilateral posterior cerebral artery, causing an infarct in its distribution. Complications also include periaqueductal necrosis; midbrain (Duret) hemorrhages; hemorrhages in the tegmentum of the pons and midbrain, as a result of stretching of the upper branches of the basilar artery; and compression of the contralateral cerebral peduncle against the free edge of the tentorium, Kernohan-Woltman notch.

Tonsillar herniation occurs due to mass effect in the posterior fossa leading to obstruction of the fourth ventricle, hydrocephalus, and inferior displacement of the cerebellar tonsils and cerebellum through the foramen magnum. There is compression of the medulla resulting in depression of the vital centers for respiration and cardiac rhythm control.

Less common herniations include central transtentorial herniation, due to end result of downward displacement of the cerebral hemispheres and basal nuclei with possible complete obliteration of the basal cisterns, and ascending transtentorial (superior vermian) herniation, caused by a slowly growing cerebellar or brainstem process forcing upward herniation of the vermis and cerebellar hemispheres through the tentorium (Table 16.2).

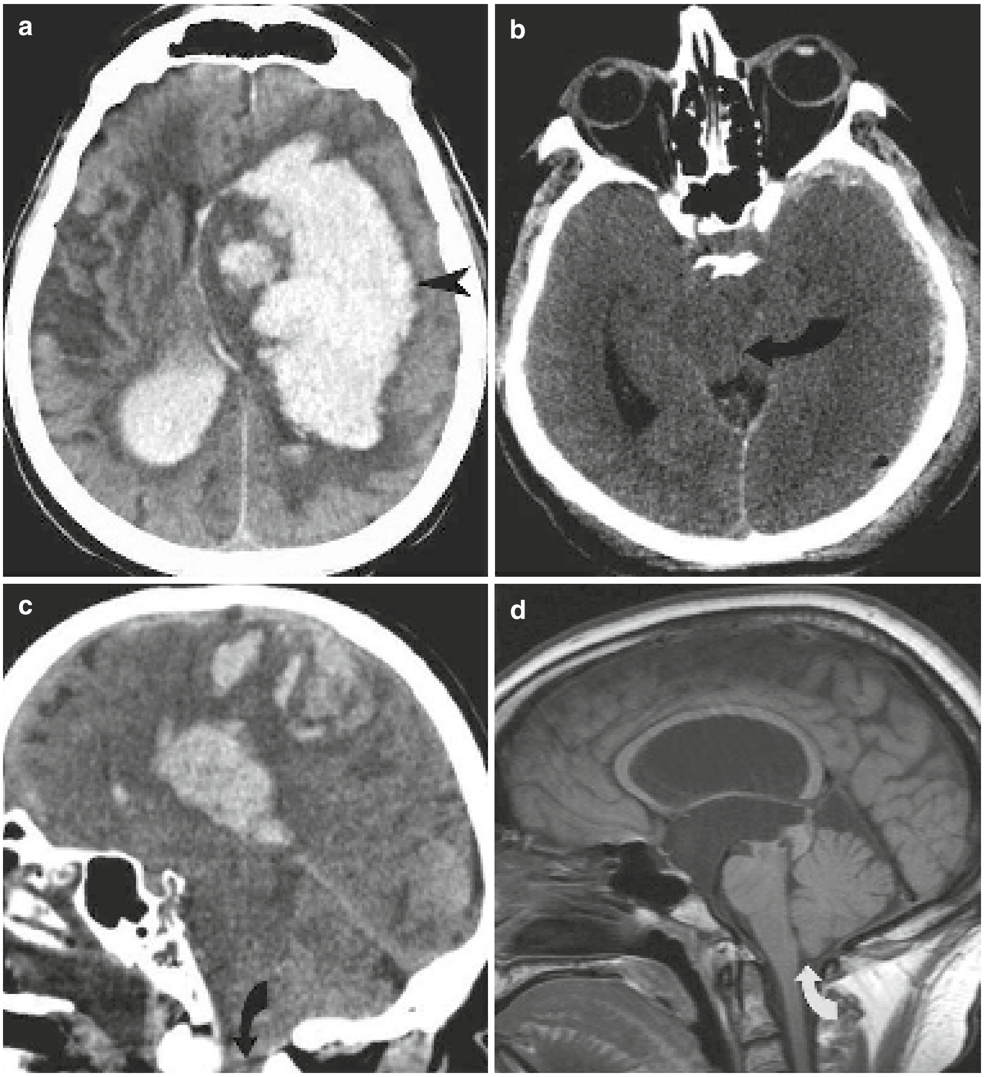

Fig. 16.11 Intraparenchymal hemorrhage. (**a**) Unenhanced axial CT image of the brain shows a large intraparenchymal hemorrhage (*arrowhead*) within the left cerebral hemisphere causing rightward subfalcine herniation. There is compression of the ipsilateral ventricle and dilatation of the contralateral ventricle and intraventricular hemorrhage. (**b**) Noncontrast CT in a patient with uncal herniation from left subdural hemorrhage demonstrates medial temporal lobe (uncus) (*curved arrow*) displaced medially through the free edge of the tentorium cerebelli and compressing the midbrain. (**c**, **d**) CT and MRI demonstrate tonsillar herniation (*curved arrows*) in two patients from parenchymal hemorrhage (**c**) and hydrocephalus (**d**). (**e**) Noncontrast axial CT images demonstrate intraparenchymal hemorrhage within the temporal and frontal lobes compatible with traumatic hemorrhagic contusions (*arrowheads*). Subarachnoid (*arrow*) and subdural blood is also seen, often coexistent with contusions. (**f**) Noncontrast CT of the head in a patient with gunshot injury demonstrates the entry wound (*arrowhead*), bullet track through the midbrain (*curved arrow*), and exit wound (*straight arrow*). There is pneumocephalus as well as subarachnoid hemorrhage

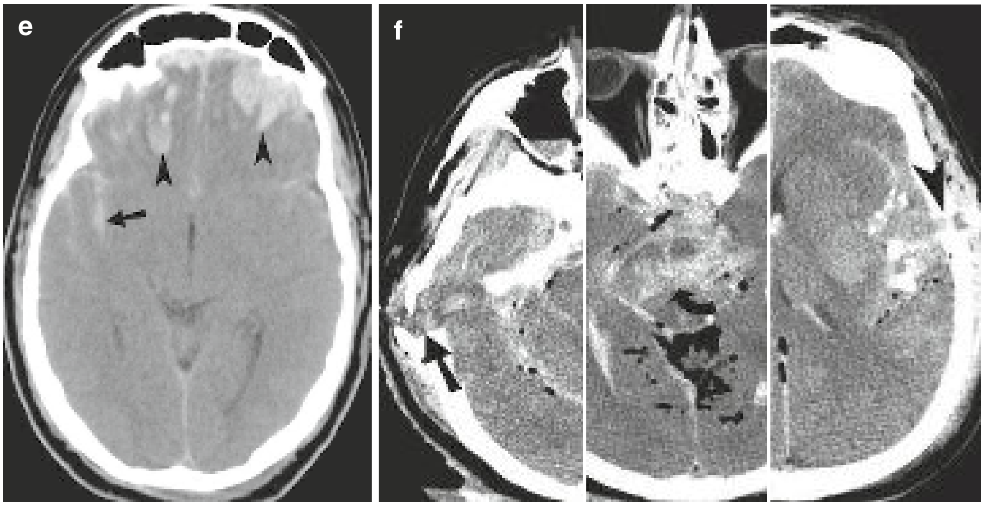

Fig. 16.11 (continued)

Table 16.2 Summary of imaging findings in herniation syndromes

Subfalcine herniation	Uncal herniation	Tonsillar herniation
Most common type of herniation	Medial temporal lobe tissue is displaced medially through the free edge of the tentorium cerebelli and compresses the brainstem and adjacent structures	Mass effect in the posterior fossa leading to obstruction of the fourth ventricle, hydrocephalus, and inferior displacement of the cerebellar tonsils and cerebellum through the foramen magnum
Cingulate gyrus and pericallosal branches of the anterior cerebral artery herniate beneath the falx cerebri	Compression of the ipsilateral oculomotor nerve	Compression of the medulla
Effacement of the ipsilateral ventricle		
Enlargement of the contralateral ventricle		
Compression of the ipsilateral anterior cerebral or internal cerebral veins		

Cerebral Contusions

Contusions represent acceleration/deceleration injuries to the brain involving the peripheral surfaces of the brain due to trauma. They are the second most common primary traumatic neuronal injury after diffuse axonal injury. The location of the contusions is characteristic, namely, the anterior and inferior surfaces of the temporal and frontal lobes (see Fig. 16.9e, f) [12]. These parts of the brain are the most mobile areas and have more fixed proximal portions and thus brush up against the irregular inner calvarial surfaces of the anterior and inferior frontal bone of the anterior cranial fossa and the greater sphenoid wing and temporal bone in the middle cranial fossa. Less frequently, contusions can occur in the parasagittal cerebral hemispheres, as the parenchyma contuses along the rigid interhemispheric falx.

It is important in the setting of contusions, both hemorrhagic and nonhemorrhagic, to get short-term follow-up, as new lesions may appear within the first few days, and existing injuries may become larger. An important differential to exclude is venous occlusive disease, as sinus thrombosis can often have a similar appearance and location. The treatment is to prevent secondary injury, such as hematoma formation, mass effect, or herniation—all of which may require surgical intervention.

Cortical Laminar Necrosis

Cortical laminar necrosis is focal or diffuse necrosis of one or more cortical lamina. It can be associated with hypoxia, infarction, metabolic encephalopathy, infections, and medications. Cortical laminar necrosis is important to know for two reasons: one, it is a hallmark of subacute injury, i.e., roughly 14–21 days after initial insult; two, the cortical hyperdensity (or hyperintensity on T1 MRI) is secondary to *hypoxic* ischemic injury rather than hemorrhagic injury. This patient was a 35-year-old female who earlier had a cesarean section and, approximately 3 months postpartum, presented to the emergency department with signs and symptoms of hypertensive urgency. The patient's labile response to blood pressure correction led to a severe pressure drop, which precipitated worsening mental status changes. Subsequent head

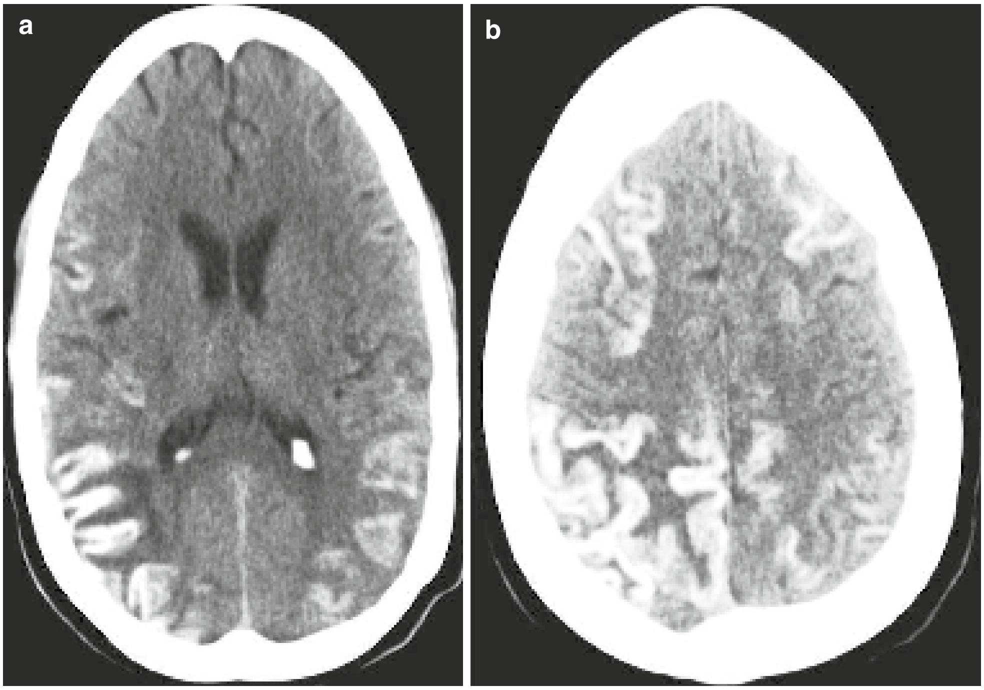

Fig. 16.12 Cortical laminar necrosis. (**a**, **b**) Noncontrast axial CT images of the brain demonstrate extensive, diffuse cortical gyral wavy hyperdensities, most consistent with cortical laminar necrosis. Although incompletely understood, the hyperdensity and hyperintensity on CT are not due to blood or calcification

CT exams demonstrated patchy hypodensities in the parietal and occipital lobes. Three weeks after presentation, findings had progressed to laminar necrosis.

The differential diagnosis includes cerebritis, low-grade cortical neoplasm, and Sturge-Weber. Hyperdense gyri may or may not be present on CT, but the characteristic high signal intensity on T1 sequence is most sensitive (Fig. 16.12) [13]. Subacute infarcts are infrequently imaged, and so knowledge of the myriad imaging appearances, coupled with appropriate history, can often aid clinicians in treatment and prevent needless tests (i.e., neoplasm or infectious disease workups).

Overall, the presence of cortical laminar necrosis is indicative of a poor clinical prognosis. Interestingly, although incompletely understood, the hyperdensity and hyperintensity on CT and MRI are not due to blood or calcification, but felt to be due to reactive gliosis and fat-laden macrophages. To our knowledge, there is no association in the literature between CLN and hypertension or hypertensive crisis.

Cerebral Arterial Air Embolism

Aside from the airway, the paranasal sinuses, and the mastoid and petrous temporal bones, the head should not have air within it. Cerebral air emboli can be venous or arterial. Venous air emboli can occur due to central catheter placement or other instrumentation related to venous access such as from a CT injector. Intracranially, air is often seen in the cavernous sinus and superficial maxillofacial venous branches. If minimal, patients are often asymptomatic, but it is still worthwhile to alert the clinicians of the presence of venous air.

Arterial cerebral air embolism, however, is an infrequent but potentially devastating entity with serious sequelae. Arterial air emboli can cause an inflammatory response that can result from the air itself or due to a reduction in perfusion distal to the obstruction [14].

Arterial air emboli are often the result of trauma, surgery, or procedures such as lung biopsy. Air can reach the arterial system through the pulmonary vein (and ultimately the systemic circulation) via a biopsy needle or broncho-venous fistula of any cause, by way of the systemic venous side by traversing the pulmonary microvasculature (even without an arteriovenous communication) or through any form of right-to-left shunt. The air detected on CT scan can reabsorb rapidly and therefore will not be apparent on a follow-up study (Fig. 16.13).

Patients often present with generalized seizures and focal neurological deficits. Treatment is 100% oxygen, aggressive fluid resuscitation, and hyperbaric oxygen therapy. Prompt diagnosis and clinician communication can initiate aggressive treatment and mitigate the extent of damage.

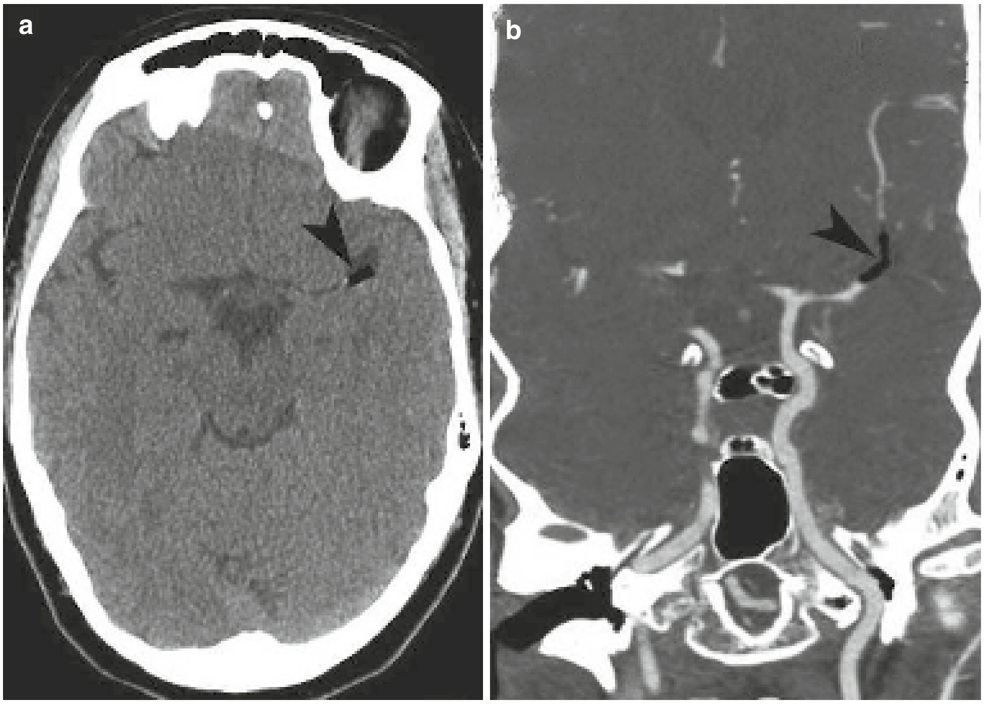

Fig. 16.13 Air embolism. (**a**, **b**) Noncontrast axial CT and CT angiogram of the brain demonstrate a focal area of intravascular air (*arrowhead*) within the M1 (Sylvian) segment of the left middle cerebral artery, compatible with arterial air embolism

Obstructive Hydrocephalus

Obstructive hydrocephalus is caused by obstruction to the flow of CSF at the level of foramen of Monro, third ventricle, aqueduct of Sylvius, or fourth ventricle. The imaging findings of obstructive hydrocephalus include prominence of ventricular system above the occlusion. The most common site of obstruction is aqueduct of Sylvius and results in prominence of the lateral and third ventricle. Obstruction to the outflow of the fourth ventricle results in additional prominence of the fourth ventricle, which loses its triangular configuration and appears round. The supratentorial cisterns, fissures, and sulci are much less prominent due to ventricular dilatation. Periventricular edema may occur due to transependymal spread of fluid (Fig. 16.14).

Fig. 16.14 Obstructive hydrocephalus. (**a**, **b**) Noncontrast CT of the head demonstrates acute obstructive hydrocephalus with transependymal edema (*curved arrows*), caused by posterior fossa hemorrhage (**a**) and colloid cyst at the foramen of Monro (*arrowhead*) (**b**). (**c**) T2-weighted MRI shows acute obstructive hydrocephalus with transependymal edema (*curved arrows*) around the lateral ventricles

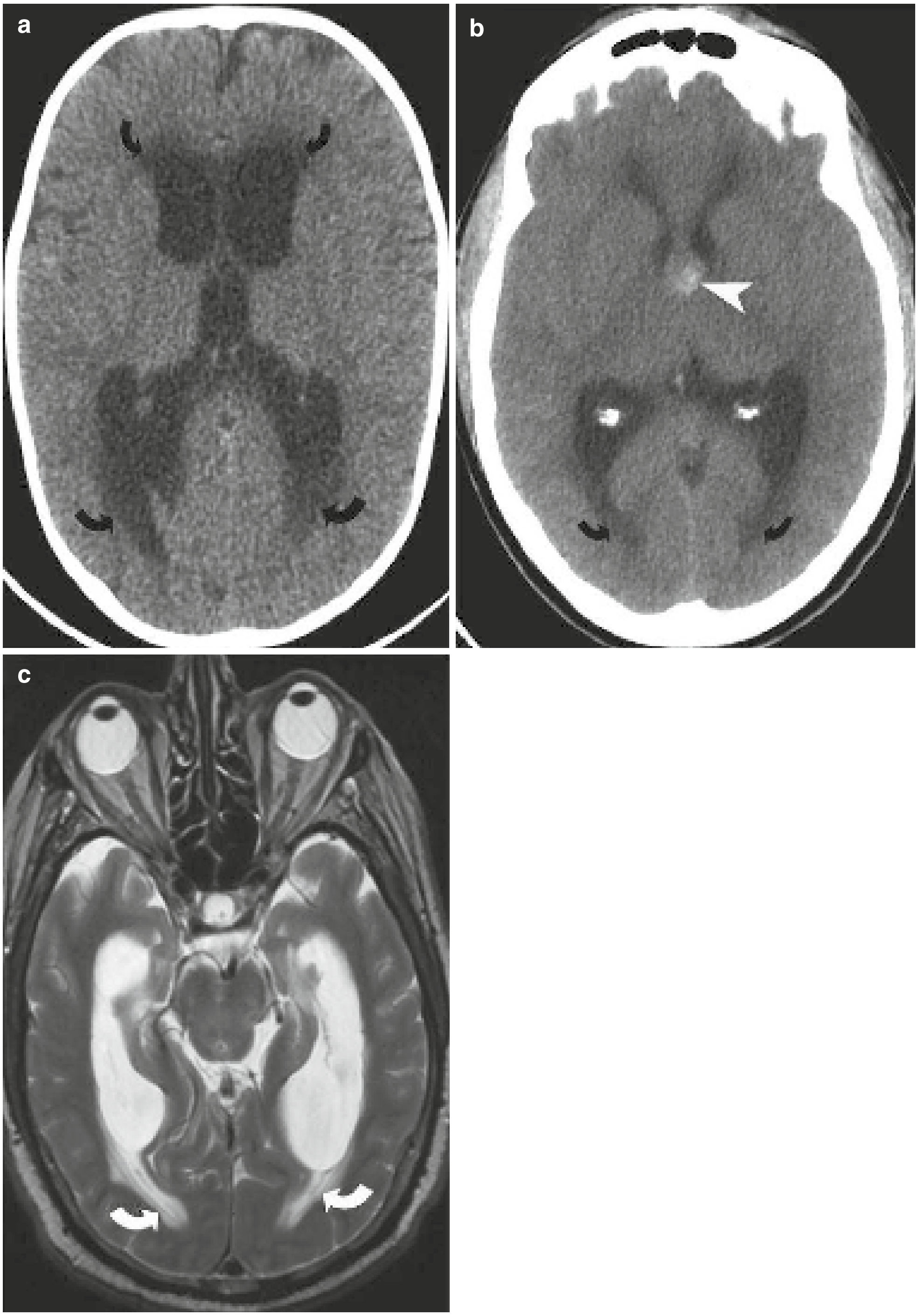

Acute Hypertensive Encephalopathy

It is seen in patients with severe hypertension and is believed to be due to abnormal cerebrovascular autoregulation. It is also called posterior reversible encephalopathy syndrome.

On CT imaging, there is bilateral cortical or subcortical low density, most commonly in the posterior circulation. The occipital lobes and posterior parietal lobes are most commonly involved by the process, which is more often patchy than confluent (Fig. 16.15). On MR imaging, the patchy lesions are bright on T2-weighted and FLAIR sequences. The differential diagnosis includes cerebral infarcts, progressive multifocal encephalopathy, demyelinating disease, and metabolic derangements (dialysis).

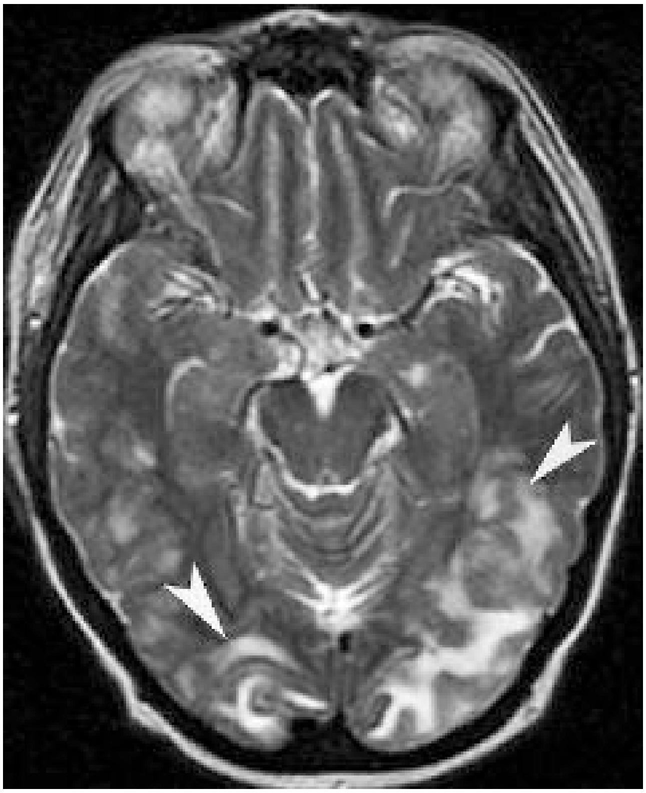

Fig. 16.15 Acute hypertensive encephalopathy. T2-weighted MR image demonstrates patchy and confluent hyperintensities (*arrowheads*) in both occipital lobes

CSF Leak

Majority (90%) of the cases are post-traumatic, often occurring through the floor of anterior cranial fossa and resulting in CSF rhinorrhea. Fracture of temporal bone may result in otorrhea, accounting for 20% of the cases. Eighty percent of CSF leaks occur within 48 h for the traumatic event and 95% occur within 3 months.

CT cisternogram is the gold standard in demonstrating CSF leak from the base of the skull. If the CSF leak is intermittent, then the timing of the study is important in detecting the leak. A positive study will show contrast material leaking through the dural and osseous defect (Fig. 16.16). Since the anatomical site of defect is more difficult to see on radionuclide cisternograms (indium 111 diethylenetriaminepentaacetic acid), they are used as second-line imaging modality. The biological half-life of 2.8 days prolonged imaging for up to 3 days after radiotracer administration.

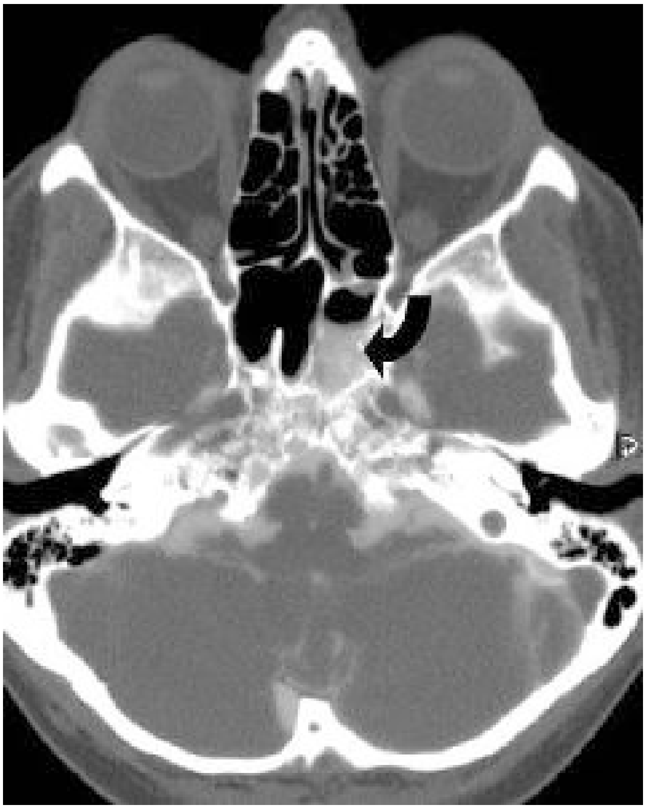

Fig. 16.16 Post-traumatic CSF leak. CT cisternogram study demonstrates radiopaque contrast leaking through dural and osseous defect in sphenoid sinus wall. The contrast is seen collecting in the left sphenoid sinus (*curved arrow*)

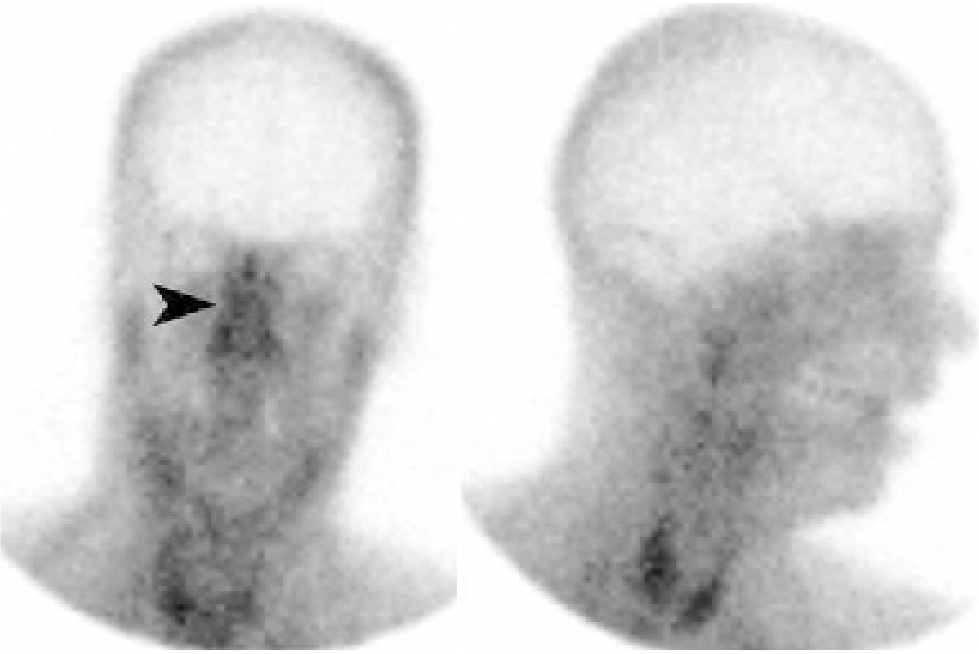

Fig. 16.17 Brain death. Tc99m HMPAO study demonstrates hot nose sign (*arrowhead*) in this patient with no intracranial uptake (*light bulb sign*) of radiotracer

Brain Death

The best imaging test to confirm brain death is a neurolite study. Brain death is characterized by irreversible loss of brain function with marked brain swelling and obliteration of sulci. The intracranial pressure exceeds the vascular perfusion pressure and leads to irreversible ischemia. The EEG of a patient with brain death is isoelectric due to cessation of physiologic functions.

Normal brain shows uptake of Tc99m HMPAO, and Tc99m ECD does cross the blood–brain barrier, in proportion to the regional blood flow. On Tc99m ECD (neurolite) or Tc99m HMPAO (Ceretec) study, there is no flow to the intracranial supratentorial as well as infratentorial structures after brain death. These patients will typically show increased radiotracer in the nasal area (hot nose sign). The absence to radiotracer in the intracranial region produces a light bulb sign (Fig. 16.17).

Basilar Skull Fractures

Skull base fractures are frequently encountered in the setting of traumatic head injuries. Temporal bone is most frequently involved (40%) followed by sphenoid (23%), occipital (15%), and ethmoid (11%) bones. The fractures can be classified as laterobasal, frontobasal, posterior basal, and basioccipital. Thin-slice CT is the preferred modality for evaluation of skull base fractures.

Laterobasal fractures involve the temporal bone, including petrous and mastoid segments. Traditional classification classifies the temporal fractures as longitudinal (most common), transverse, and mixed (Fig. 16.18a, b). New classification classifies the fractures as otic capsule sparing (91.5%) and otic capsule violating (8.5%). Otic capsule-sparing fractures are associated with higher risk of facial nerve injury, sensorineural hearing loss, and CSF leak.

Frontobasal fractures are associated with significant neurologic sequelae. Frontobasal fractures can be classified as type I (isolated linear anterior skull base fractures), type II (linear fractures of frontal bone extending to the skull base), and type III (complex comminuted fractures). Common complications include CSF leak and orbital apex syndromes.

Posterior basal fractures can involve clivus, squamous, and condylar occipital bone. The fractures can be classified as longitudinal, transverse, and oblique. Longitudinal fractures are associated with higher mortality rates. High incidence of associated cranial nerve palsies and vascular injuries has been reported.

Teaching Points

- Parenchymal neurocysticercosis is typically seen as 1 cm diameter spherical shape lesion with a 2–3 mm mural nodule produced by the scolex.
- In herpes encephalitis, MRI shows gyriform enhancement with restricted diffusion in the limbic system.
- In tension pneumocephalus, Mt. Fuji sign is prominent bifrontal subdural air collections that cause a mass effect on both frontal lobes, with widening of the interhemispheric spaces between the frontal lobes.
- Any large hyperdense mass in the vicinity of the cisterns and subarachnoid spaces should at least raise the possibility of a cerebral aneurysm.

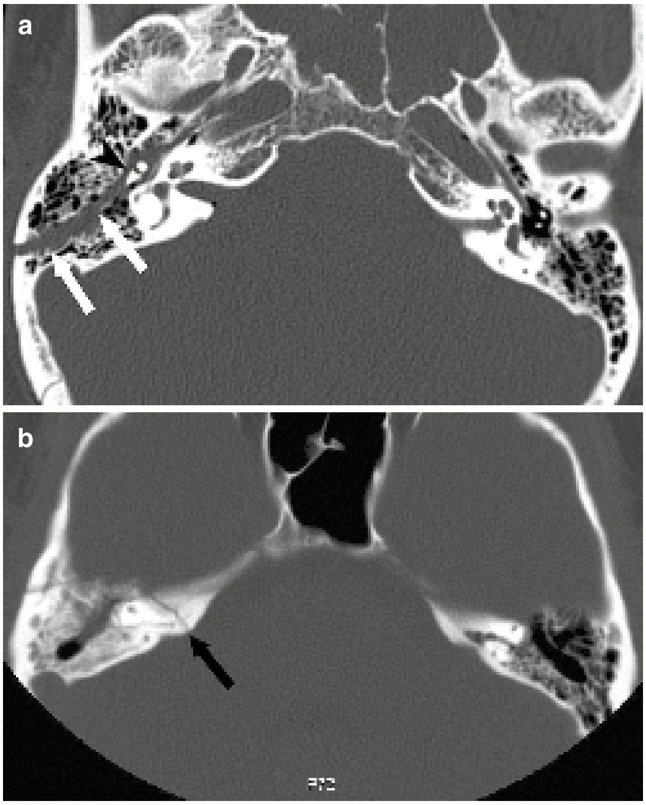

Fig. 16.18 Temporal bone fracture. (**a**) Non-contrast CT of the temporal bone demonstrates longitudinal fracture of the petrous temporal bone (arrows) with fracture line passing through the middle ear cavity. There is no disruption of the middle ear ossicles (arrowhead). (**b**) Non-contrast CT of the temporal bone demonstrates transverse fracture of the petrous temporal bone (arrow)

- In spontaneous intracranial hypotension, imaging findings include bilateral subdural hematomas, diffuse pachymeningeal enhancement, caudal displacement of the cerebellar tonsil and brainstem, decreased size of the ventricles and basal cisterns, and enlargement of the pituitary gland.
- The best imaging test to confirm brain death is a neurolite study.

Questions

1. Which of the following can cause pseudo-subarachnoid hemorrhage?
   (A) Intrathecal contrast injection
   (B) Infectious meningitis
   (C) Status epilepticus
   (D) Polycythemia
   (E) All of the above
   Answer: E

2. Which of the following statements is correct about neurocysticercosis?
   (A) On T1-weighted sequence, the fluid in the cystic lesion is hyperintense to white matter
   (B) On T1-weighted sequence, the fluid in the cystic lesion is hypointense to cerebrospinal fluid
   (C) On T2-weighted sequence, the cystic fluid is markedly hyperintense
   (D) There is usually subtle enhancement in the earlier vesicular stage
   Answer: C

3. Which of the following statements is correct in tension pneumocephalus?
   (A) Peaking sign is more common in tension pneumocephalus
   (B) Air bubble sign is more common in tension pneumocephalus
   (C) Mt. Fuji sign is defined as prominent bifrontal subdural air collections that cause a mass effect on both frontal lobes
   (D) Most cases are iatrogenic
   Answer: C

4. What is the imaging diagnosis (Fig. 16.19) of a patient with a recent onset of headache?
   (A) Neurocysticercosis
   (B) Hydatid cyst
   (C) Brain abscess
   (D) Hemangioblastoma
   Answer: A

5. What is the imaging diagnosis of a patient (Fig. 16.20) presenting with headache, fever, and multiple cranial nerve palsies?
   (A) Encephalitis
   (B) Pneumococcal meningitis
   (C) Neurocysticercosis
   (D) Ventriculitis
   Answer: B

6. What is the imaging diagnosis of a patient (Fig. 16.21) presenting with fever, headache, and altered mental status?
   (A) Infarction
   (B) Oligodendroglioma
   (C) Brain abscess
   (D) Ventriculitis and meningitis
   Answer: D

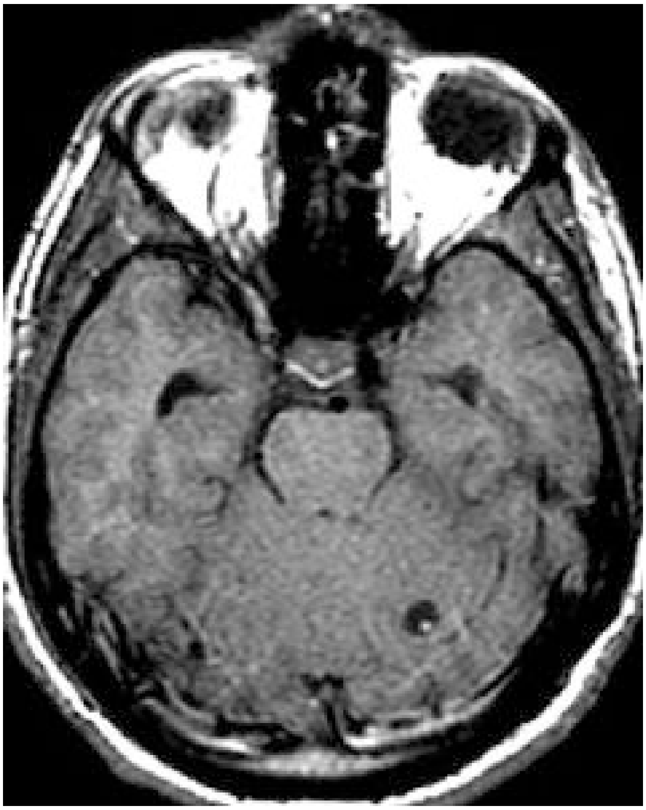

Fig. 16.19 Neurocysticercosis

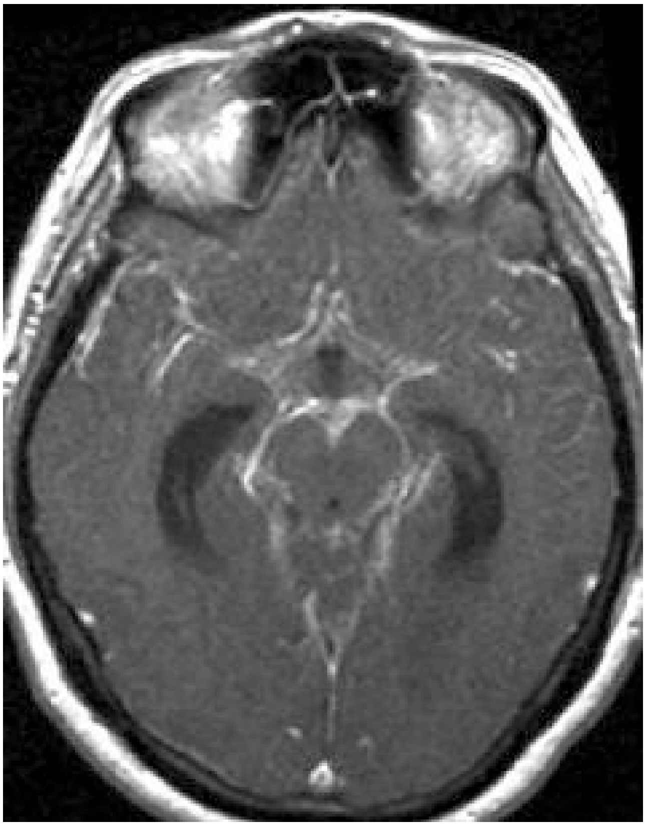

Fig. 16.20 Pneumococcal meningitis

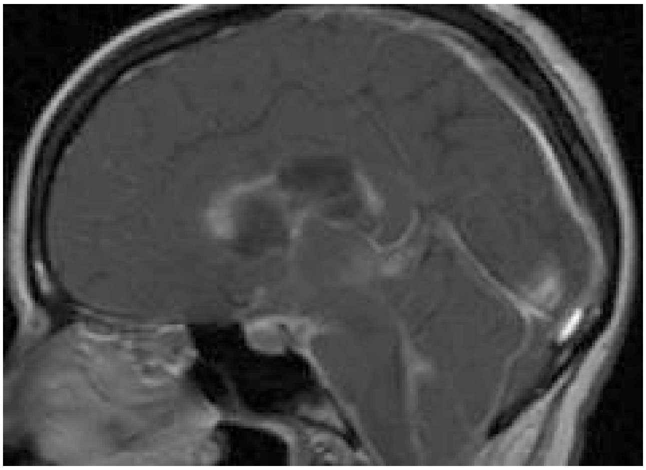

Fig. 16.21 Ventriculitis and meningitis—imaging diagnosis

References

1. Given CA 2nd, Burdette JH, Elster AD, Williams DW 3rd, et al. Pseudo-subarachnoid hemorrhage: a potential imaging pitfall associated with diffuse cerebral edema. AJNR Am J Neuroradiol. 2003;24:254–6.
2. Sener RN. Acute carbon monoxide poisoning: diffusion MR imaging findings. AJNR Am J Neuroradiol. 2003;24:1475–7.
3. Paolini S, Ralli G, Ciappetta P, Raco A. Gas-containing otogenic brain abscess. Surg Neurol. 2002;58(3–4):271–3.
4. Baringer JR. Herpes simplex infections of the nervous systems. Neurol Clin. 2008;26(3):657–74. viii.
5. Sinclair AG, Scoffings DJ. Imaging of the post-operative cranium. Radiographics. 2010;30:461–82.
6. Michel SJ. The Mount Fuji sign. Radiology. 2004;232:449–50.
7. Mehta RI, Salamon N, Zipser BD, Mehta RI. Best cases from the AFIP: giant intracranial aneurysm. Radiographics. 2010;30:1133–8.
8. Jacobs MB, Wasserstein PH. Spontaneous intracranial hypotension: an uncommon and underrecognized cause of headache. West J Med. 1991;155:178–80.
9. Watanabe A, Horikoshi T, Uchida M, Koizumi H, Yagishita T, Kinouchi H. Diagnostic value of spinal MR imaging in spontaneous intracranial hypotension syndrome. AJNR Am J Neuroradiol. 2009;30:147–51.
10. Osborn AG, Salzman KL, Barkovich J. Trauma. In: Diagnostic imaging brain. 2nd ed. London: Amirys Publishing Inc; 2005. p. 2–3.
11. Coburn MW, Rodriguez FJ. Cerebral herniations. Appl Radiol. 1998;27:10–6.
12. Kim JJ, Gean AD. Imaging for the diagnosis and management of traumatic brain injury. Neurotherapeutics. 2011;8(1):39–53.
13. Kinoshita T, Ogawa T, Yoshida Y, Tamura H, Kado H, Okudera T. Curvilinear T1 hyperintense lesions representing cortical necrosis after cerebral infarction. Neuroradiology. 2005;47:647–51.
14. Yang MS, Yang TH, Ou CH, Chan SW, Chen TI, Tu CW, et al. Iatrogenic and fatal air arterial embolism during CT scan. J Chin Med Assoc. 2011;74:188–91.

Imaging of Facial Fractures

17

Dennis Coughlin, Paul Jaffray, Mohammad Mansouri,
and Ajay Singh

Introduction

Facial trauma is a common presentation to the emergency department, usually as a result of blunt trauma. The trauma can range from a simple, isolated nondisplaced fracture to complex displaced facial fractures. Multiple fracture patterns have been described that make it easier to efficiently detect, document, and communicate the diagnosis in patients with multiple fractures. René Le Fort made the earliest and most famous classification in 1901, and since that time, multiple other fracture patterns have been described [1]. While these can be present in pure form, often they coexist, particularly in the setting of high-impact trauma.

Paralleling this development in facial trauma classification has been that of surgical fixation. After the advent of antibiotics, the most commonly used treatment of complex facial fractures is open reduction. A primary reason for improvement in surgical treatment of facial fractures is the introduction and refinement of the concept of functional units of the face. This concept was first described by Sicher and DuBrul in 1970 [2]. Through experience, surgeons have learned that reducing these functional units leads to the best anatomical and functional outcome for facial fractures [3–5].

While physical exam is an essential component in the workup of a trauma patient, this is often difficult due to the patient's mental state, distracting injuries, and associated comorbidities. Imaging plays a central role in the workup of the trauma patient. This is particularly true with the advent of modern multidetector CT scans.

Imaging of Craniofacial Trauma

Historically, initial assessment of facial trauma was performed with a facial radiograph series. Typical series included Caldwell, straight PA, Waters, Towne, lateral, and SMV views [6]. Radiographs are still being utilized, but their use has progressively diminished as CT technology continues to improve. In many institutions, the use of CT has largely replaced radiographs in the evaluation of the trauma patient. MRI is rarely used in the immediate workup of the trauma patient but can aid in evaluating complications.

Older generation CT scanners acquired axial images with subsequent patient repositioning required to obtain series in other planes. With improvement of imaging technology, helical acquisition on modern multi-slice CT scanners rapidly obtains a volume of data, which can be used to obtain reformations in any plane. Multiplanar imaging greatly aids in the detection and appropriate description of facial injuries.

Our CT trauma protocol for imaging of the head and maxillofacial region involves acquiring a data volume at 0.6 mm slice thickness from immediately below the mental protuberance to the skull vertex without intravenous contrast. Maxillofacial thin overlapping axial reconstructions as well as coronal and sagittal reformats, typically 2 × 1.5 mm, are generated using both bone and soft tissue algorithms. In addition, volume-rendered 3D images are generated.

In order to reduce CT dose, first, patients should be selected carefully. Inappropriate CT referrals should be elim-

---

The original version of this chapter was revised. An erratum to this chapter can be found at https://doi.org/10.1007/978-3-319-65397-6_27. An erratum to this publication is available online at https://doi.org/10.1007/978-3-319-65397-6_27.

D. Coughlin
Department of Radiology, UMass Memorial Health Care,
Worcester, MA, USA

P. Jaffray
GBMC Healthcare, Baltimore, MD, USA

M. Mansouri
Department of Radiology, Massachusetts General Hospital,
Boston, MA, USA

A. Singh (✉)
Division of Emergency Radiology, Department of Radiology,
Massachusetts General Hospital, Boston, MA, USA

Harvard Medical School, Massachusetts General Hospital,
Boston, MA, USA
e-mail: asingh1@partners.org

© The Author(s), under exclusive license to Springer Nature Switzerland AG 2024
A. Singh (ed.), *Emergency Radiology*, https://doi.org/10.1007/978-3-031-65770-2_17

inated. Second, range of scan should be limited to the area of interest. Unnecessary contrast phases should be eliminated. Using a large pitch, automated current modulation, adaptive dose shielding, and updated image reconstruction algorithms are other helpful techniques of CT dose reduction in craniofacial trauma.

Craniofacial Anatomy

Anatomically, the face is divided into upper, middle, and lower thirds (Fig. 17.1). The upper third is comprised of the frontal bone and extends to its zygomatic, maxillary, and nasal sutures. The middle third extends from the frontal bone to the upper teeth of the maxilla. The mandible represents the lower third. The "midface" is comprised of the maxilla, zygoma, nasal, lacrimal, vomer, inferior concha, and palatine bones (Table 17.1). The frontal, sphenoid, and ethmoid bones form portions of both the cranium and face. The facial bones are relatively weak owing to their multiple sinus cavities but are reinforced with a series of vertical and horizontal buttresses. They are able to withstand forces in the vertical direction but are much weaker in the horizontal and lateral directions. The goal of the surgeon is to restore alignment and integrity of these buttresses when they fracture. There are four vertical and four horizontal facial buttresses (variously termed struts of mastication, midfacial buttresses, or structural pillars).

The floor of the anterior cranial fossa (ACF) is formed by the cribriform plate of the ethmoid, the frontal bone, and the lesser wing of the sphenoid. The frontal bone forms the majority of the floor of the ACF and also comprises the majority of the orbital roof. The lesser wing of the sphenoid forms the posterior margin of the ACF. The floor of the middle cranial fossa (MCF) is formed by the greater wing of the sphenoid and the squamosal portion of the temporal bone [7].

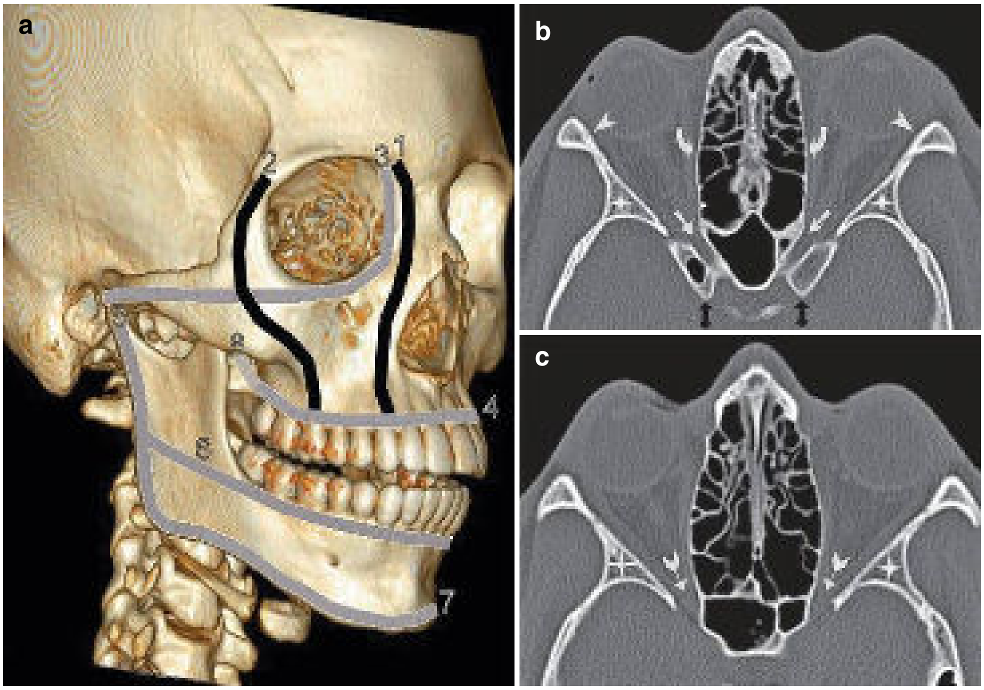

Fig. 17.1 Normal CT anatomy and facial buttresses. (**a**) 3D surface-rendered image demonstrating the four vertical and four transverse buttresses (*1* medial maxillary, *2* lateral maxillary, *3* upper transverse maxillary, *4* lower transverse maxillary, *5* posterior vertical, *6* upper transverse mandibular, *7* lower transverse mandibular, and *8* posterior maxillary). (**b**, **c**) Axial CT demonstrates the normal anatomy of the facial bones (*arrowhead* zygomatic arch, *curved arrow* lamina papyracea, *white straight arrow* optic canal, *black straight arrow* anterior clinoid process, *star* greater wing of sphenoid, and *white arrow* superior orbital fissure)

Table 17.1 Craniofacial bones

Upper third	Middle third	Lower third
Frontal bone: – Zygomatic – Maxillary – Nasal sutures	Maxilla Zygoma Nasal Lacrimal Vomer Inferior concha Palatine	Mandible

Orbital Fractures

The orbit is shaped like a cone with the apex posterior and the base anterior. The apex of the orbit is at the convergence of the superior and inferior orbital fissures. The anterior orbital rim is composed of the frontal, maxillary, and zygomatic bones.

Fractures of the orbit can affect the orbital rim, orbital walls (Table 17.2), or orbital apex. Orbital apex fractures are an important fracture to detect due to proximity to the optic nerve and are more commonly seen with complex injury. The most common isolated orbital fractures are the so-called blowout fractures that occur in the medial and inferior orbital walls.

Table 17.2 Characteristics of orbital wall fractures

Orbital floor fractures	Most common Common association with medial wall fractures Inferior displacement of fracture fragment into maxillary sinus Complications: • Inferior rectus muscle entrapment (Fig. 17.6) • Orbital fat herniation • Enophthalmos • Infraorbital nerve injury • Orbital dystopia
Medial wall fractures	Second most common Occurs through lamina papyracea Orbital emphysema: indirect sign of nondisplaced lamina papyracea fractures Complications: • Medial rectus muscle entrapment • Intraorbital fat herniation
Orbital roof fractures	Most commonly seen in children (high cranium-to-midface ratio, redeveloped frontal sinus) Fracture fragments can be undisplaced, displaced superiorly, or displaced inferiorly Complications: • Superior rectus and superior oblique muscle entrapment • Intracranial injuries: dural tears, pneumocephalus, CSF leak, meningitis, cerebral edema • Ocular injuries: orbital compartment syndrome, optic neuropathy, lid lacerations, corneal abrasion
Lateral wall fractures	Least common Associated with zygomatic-orbital complex fractures Complications: • Enophthalmos

Blowout Fractures

A blowout fracture is a fracture of the orbital wall that displaces outwardly. In 1957, Smith and Regan proposed a mechanism of increased intraorbital pressure secondary to a direct frontal blow to the globe [8]. The forces are transmitted through the orbital walls with fracturing of the weakest sections while the orbital rim remains intact [9]. Enophthalmos may occur as a result of blowout fractures and is best repaired after the edema has resolved. The lamina papyracea is the thinnest bone but is reinforced with buttressing from the ethmoid air cells. The inferior orbital wall is made weaker by the presence of the infraorbital groove and is the most common site of a fracture. The fracture fragment can displace inferiorly into the maxillary sinus, resulting in herniation of intraorbital fat, and/or extraocular muscles. The "trapdoor" blowout fracture, which is more common in pediatric age group, occurs when the hinge fragment springs back into place often trapping the inferior rectus muscle. Entrapment of the inferior rectus muscle results in limitation of upward/outward gaze, while entrapment of the medial rectus muscle results in limitation in the lateral gaze.

The coronal and sagittal reformations are most useful for detecting orbital floor fracture. Axial and coronal images best detect fractures of the medial wall (Figs. 17.2 and 17.3).

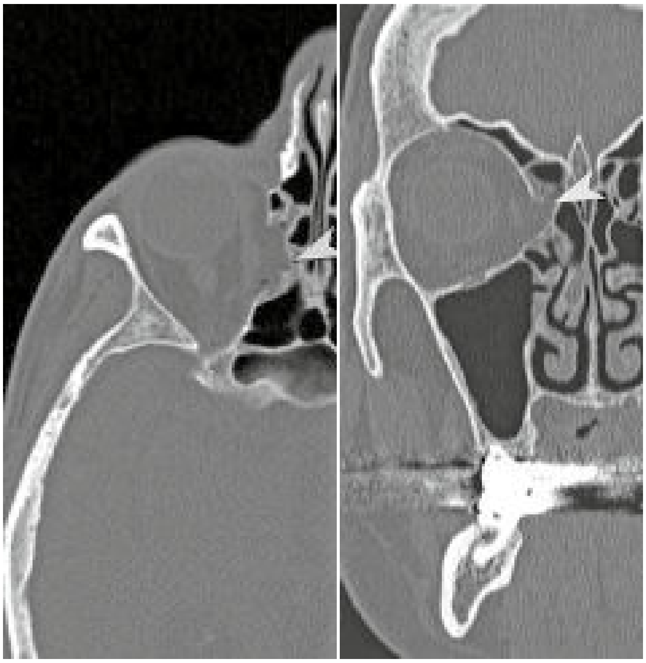

Fig. 17.2 Medial orbital wall blowout fracture. Axial and coronal CT images demonstrate a fracture (*arrowhead*) of the right medial orbital wall (lamina papyracea). Note the herniation of orbital fat through the defect in the right medial orbital wall

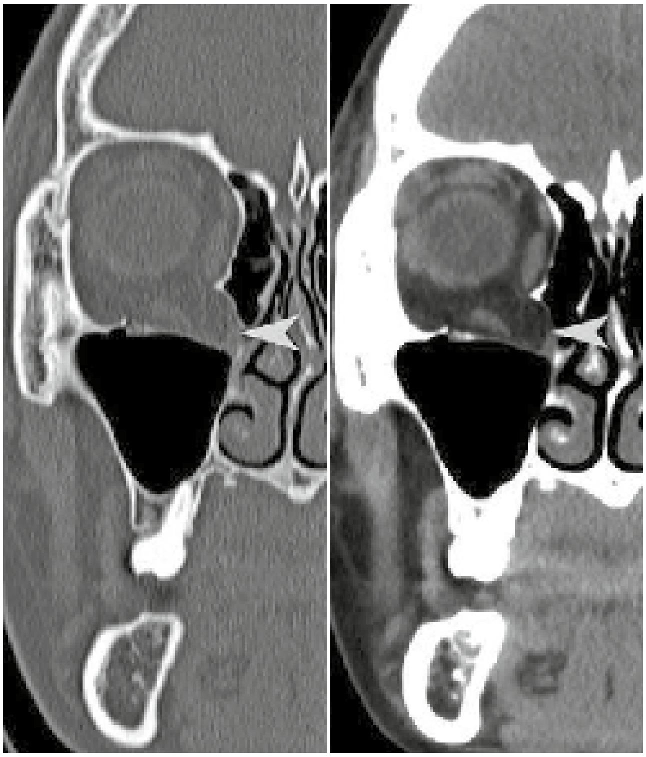

Fig. 17.3 Orbital floor lateral hinge blowout fracture. Coronal and sagittal images in bone and soft tissue algorithm demonstrating a right orbital floor blowout fracture. The displaced fragment hinges laterally at the infraorbital fissure. Note herniation of the orbital contents (*arrowhead*), including the inferior rectus muscle

It is important to note the site of fracture, fracture displacement and/or fracture angulation, and presence or absence of herniated orbital contents as they are predictors of persistent diplopia. Surprisingly, large fractures have a lower risk for entrapment, compared with small- and medium-sized orbital fractures.

Blow-in Fractures

The blow-in fracture is less common compared to blowout fractures and is defined as an inwardly displaced fracture of the orbital wall and/or rim resulting in a reduced orbital volume. These are generally the result of high-energy trauma and are most commonly seen in association with other fractures [10, 11]. A "pure" blow-in fracture is one limited to the orbital walls while the orbital rim remains intact (Figs. 17.4 and 17.5). "Impure" blow-in fractures, which are much more common, involve inward displacement of the orbital rim (Table 17.3). Superior rim fractures, owing to their location and higher impact forces, are usually more severe and associated with head injuries and frontal sinus fractures. Inferomedial blow-in rim fractures are the most common and seen with NOE fractures. Blow-in fractures commonly lead to proptosis and increase the risk of optic nerve injuries.

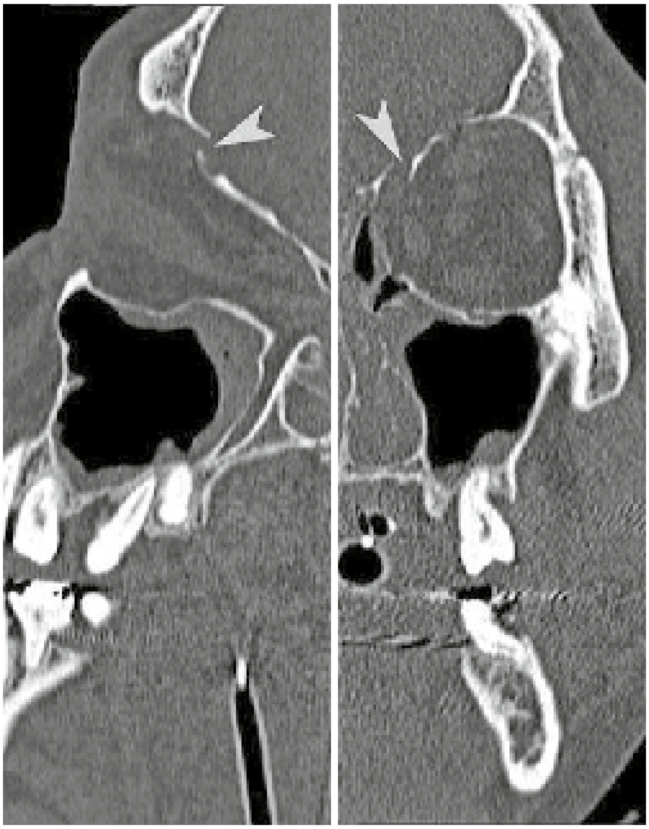

Fig. 17.4 Orbital roof blow-in fracture. Coronal and sagittal CT reformations demonstrate a "pure" orbital blow-in fracture (*arrowhead*) of the left orbital roof. The orbital rim is intact

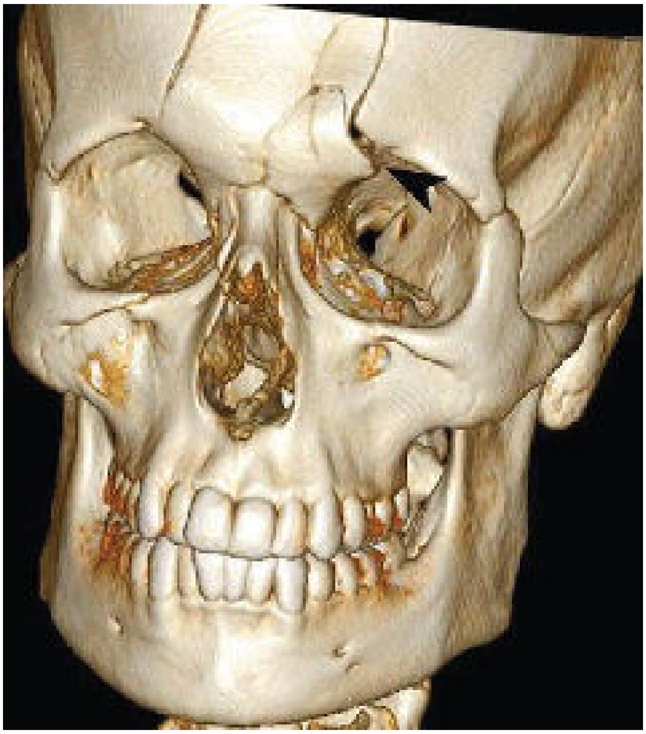

Fig. 17.5 Orbital rim blow-in fractures. Surface-rendered image demonstrating orbital rim blow-in fracture of the superomedial orbital rim associated with a frontal fracture (*arrowhead*)

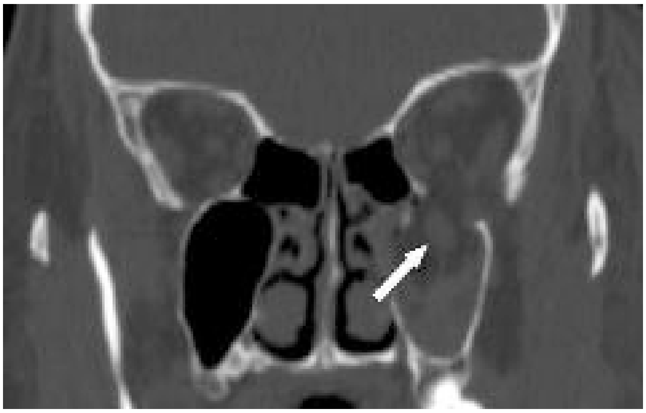

Fig. 17.6 Orbital floor fracture with inferior rectus muscle entrapment. Coronal CT reformation demonstrates blow-out fracture of the left orbital floor with herniation of the inferior rectus muscle (arrow) through the fracture defect

Table 17.3 Blow-in fractures

Pure blow-in fracture	Limited to the orbital walls Orbital rim remains intact Less common
Impure blow-in fracture	Inward displacement of the orbital rim More common

Fractures of the orbital apex may result in superior orbital fissure syndrome [12]. Symptoms include diplopia, ophthalmoplegia, ptosis, proptosis, and anesthesia in the ophthalmic nerve distribution. If there is associated blindness due to optic nerve injury (optic canal), it is termed orbital apex syndrome.

Zygoma Fractures

The zygoma (malar bone) is a dense solid bone that articulates with the frontal, maxillary, sphenoid, and temporal bones and forms the malar prominence (cheek), an important component of the facial contour. Since the zygoma is a solid bone, a direct blow to the cheek usually results in fractures of its relatively weaker articulation points. As the majority of the lateral orbital wall is formed by the zygoma, fractures to this region usually involve the orbit.

Zygomaticomaxillary Complex Fractures

While it is also called malar, tripod, tetrapod, and zygomatic complex fracture, the generally accepted and most commonly used term is zygomaticomaxillary complex (ZMC) fracture. It has a tendency to fracture at the weaker articulations with the frontal, sphenoid, maxillary, and temporal bones, resulting in disruption of the lateral maxillary and upper transverse maxillary buttresses [13]. Fractures of the ZMC may result in increased or decreased orbital volume.

While damage to the infraorbital nerve will result in loss of sensation to the eyelid and lateral nose, injury to the zygomatic nerve will result in sensory impairment to the lateral midface. Displaced fractures may result in flattening of the malar prominence and facial asymmetry and may require surgery. Treatment can be conservative in the mildly displaced fractures.

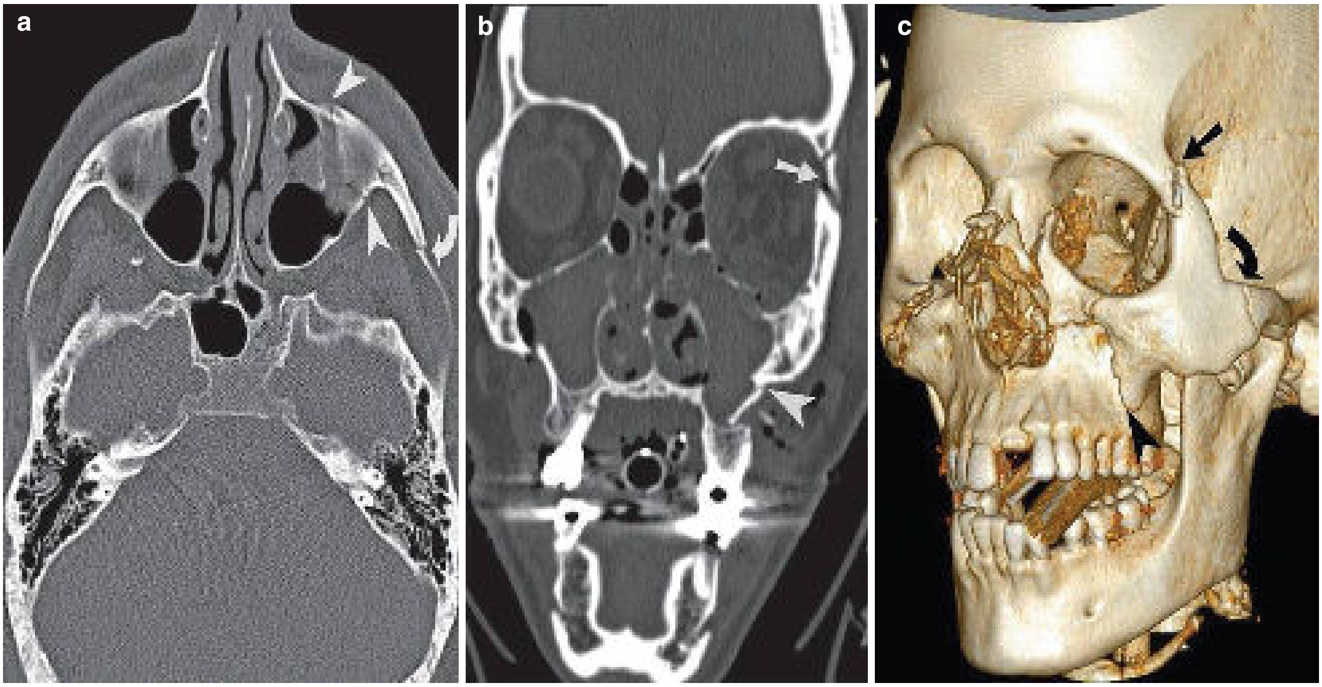

Fig. 17.7 ZMC fracture. (**a**, **b**) Axial and coronal CT demonstrates fractures of the anterior/posterolateral antral walls (*arrowheads*), orbital floor, lateral orbital rim, and zygomatic arch (*curved arrow*). (**c**) Surface-rendered image demonstrates fractures of the left zygomaticotemporal suture (*curved arrow*), zygomaticofrontal suture (*straight arrow*), and zygomaticomaxillary suture (*arrowhead*)

Fig. 17.8 Displaced and angulated ZMC fracture. (**a**, **b**) Axial image and surface-rendered image showing the zygoma complex posterolaterally displaced and internally rotated with displaced zygomaticomaxillary fracture (*arrowheads*) and zygomaticotemporal fracture (*curved arrows*). There is also fracture of the coronoid process of the mandible

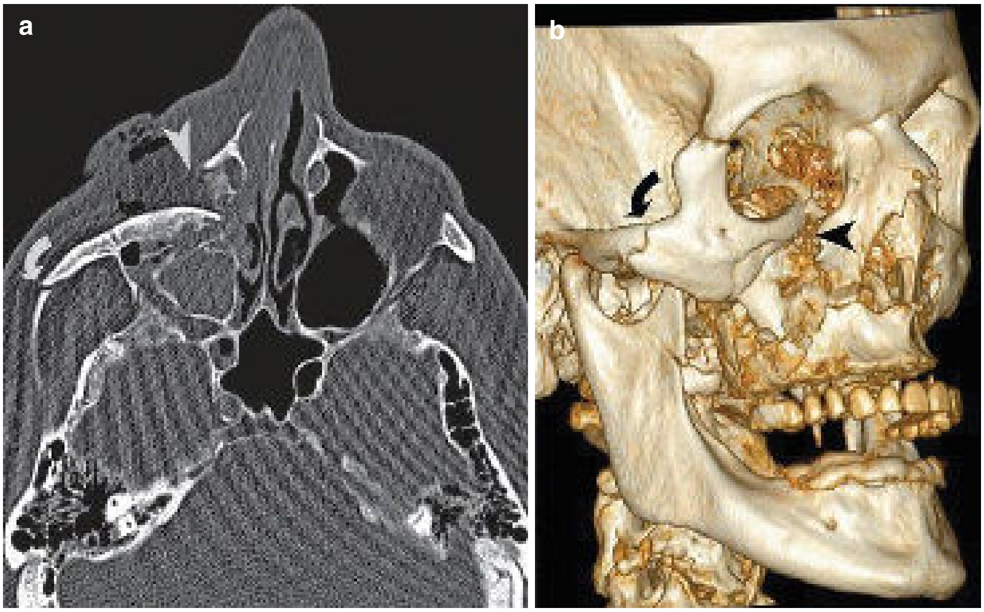

Because of its complex articulation, the ZMC fragment can rotate in any plane along the fracture lines. The goal of imaging is to evaluate the extent of the fractures, the position and displacement of the ZMC fragment, and the status of the zygomatic arch (Figs. 17.7 and 17.8). The fractures may be associated with ocular injuries.

Isolated Fractures

A focused direct blow may result in an isolated arch fracture. The direction of the force usually results in a depressed V-shaped fracture with the apex directed toward the infratemporal fossa. Segmented fractures may result as well

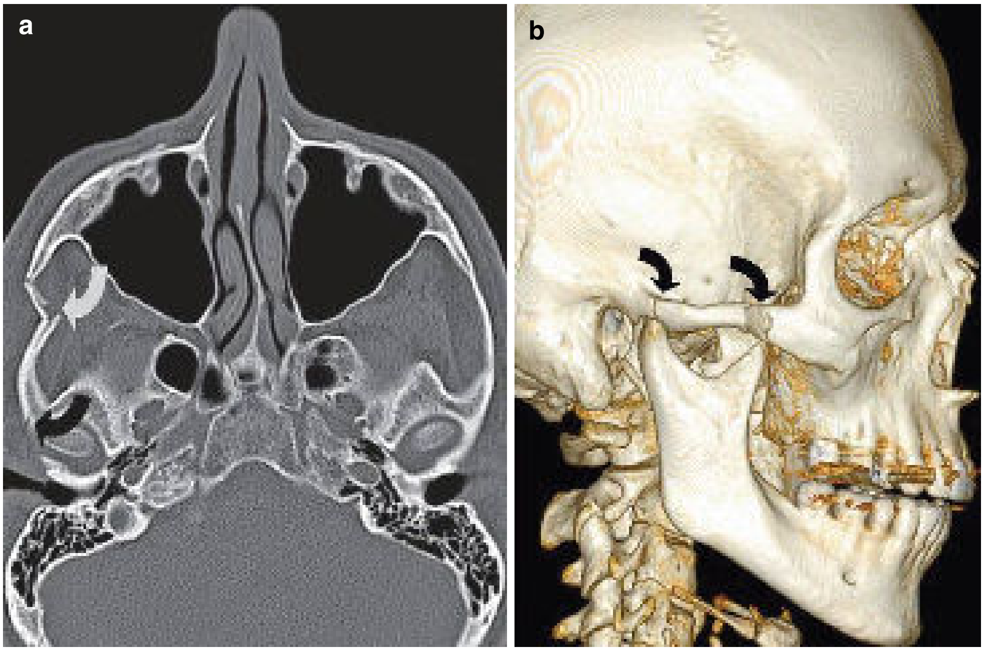

Fig. 17.9 Zygomatic arch fracture. (**a**, **b**) Axial CT and surface-rendered image demonstrates a depressed, segmental fracture of the zygomatic bone (*curved arrows*)

(Fig. 17.9). Complications result from impingement of the temporal muscle and injury to the zygomatic nerve.

Nasal Fractures

The bridge of the nose is formed by the paired nasal bones, the frontal process of the maxilla, and the nasal processes of the frontal bone. The ethmoid is comprised of multiple delicate buttressing bones and air cells and is bounded laterally by the orbits and maxillary sinuses. The nasal septum is formed by the vertical plate of the ethmoid and vomer posteriorly and cartilaginous septum anteriorly. The lateral nasal wall is formed by three longitudinal elevations called conchae (turbinates). The superior and middle turbinates are part of the ethmoid, while the inferior turbinate is a separate bone.

Fractures of the nasal bones are the most common facial fractures seen in the emergency imaging of trauma cases. The nasal bones form a portion of the nasal bridge and, if fractured, may result in facial deformity. Injury can range from isolated nasal bone fractures to more complex patterns involving multiple bones (Figs. 17.10 and 17.11). Radiographs are still routinely ordered if there is suspicion of an isolated nasal fracture. On CT, attention to the nasal septum is important to evaluate for the presence of a septal hematoma, which may lead to complications of ischemic necrosis or abscess formation. Associated anterior nasal spine fractures may be present. Close reduction may be possible immediately after trauma. Open reduction is done in comminuted fractures, severe injuries, and marked soft tissue damage. Presence of bone fragment in the maxillary sinus may cause sinusitis. Nasal septal hematoma may cause necrosis, saddle nose deformity, and abscess formation.

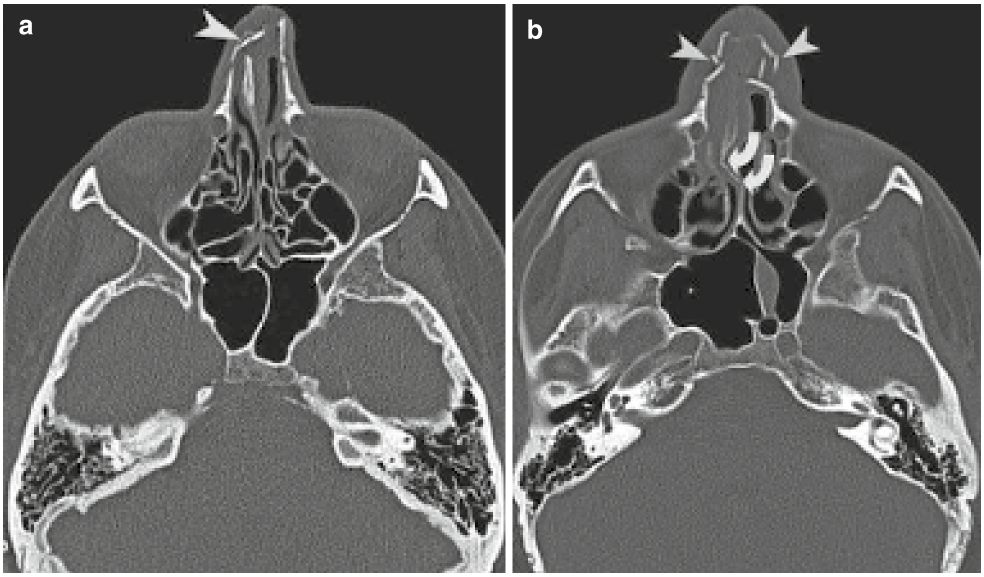

Fig. 17.10 Nasal bone fracture. (**a**) Axial CT demonstrates comminuted, displaced, and angulated right nasal bone fractures (*arrowhead*). (**b**) Axial CT demonstrates fractures that involve the nasal bones (*arrowheads*), frontal process of the maxilla, and nasal septum (*curved arrows*). Note the posterior displacement with telescoping of the nasal septum

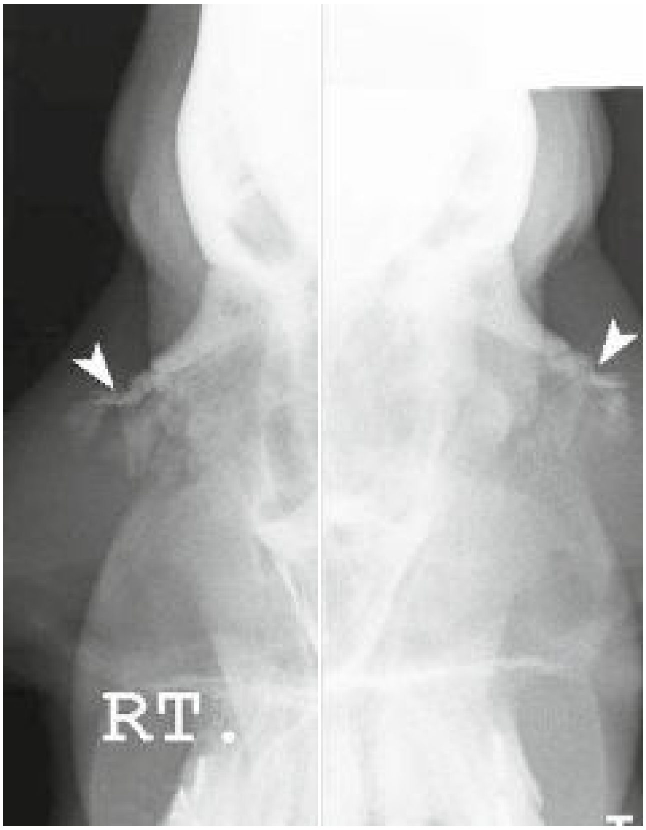

Fig. 17.11 Nasal bone fractures. Lateral view radiographs demonstrate comminuted fractures of bilateral nasal bones

Naso-Orbital-Ethmoid Fractures

A high-impact force to the central face may disrupt the medial maxillary and upper transverse maxillary buttresses, referred to as naso-orbital-ethmoid (NOE) fractures. They account for 15% of pediatric and 5% of adult facial fractures. A classification system developed by Markowitz and Manson is based on the degree of injury to the medial maxillary buttress at the insertion of the medial canthal ligament (Table 17.4) [14]. The posterior extension of the medial maxillary buttress is made up of thin delicate bones offering little support, which results in impaction and posterior telescoping of the midface. Depressed and displaced fractures may result in flattening of the nasal bridge and telecanthus. Frequency of NOE fractures has decreased due to routine airbag use.

Axial and coronal images provide the most information (Figs. 17.12 and 17.13). It is important to evaluate the medial maxillary buttress at the level of the lacrimal fossa, the site of medial canthal ligament attachment. Reconstruction of the attachment of the medial canthal ligament is essential to avoid telecanthus, enophthalmos, and dysfunction of the lacrimal system. It is also important to comment on the posterior extension of these buttresses—medial orbital walls and floor. Additional associated injuries may include nasofrontal duct injury, cribriform plate fracture, frontal sinus involvement, orbital apex involvement, and associated ocular injuries.

Table 17.4 Manson classification of NOE fractures

Type 1	Most common Single fragment
Type 2	Comminuted Intact insertion of medial canthal tendon
Type 3	Uncommon Comminuted Lateral displacement or avulsion of medial canthal ligament

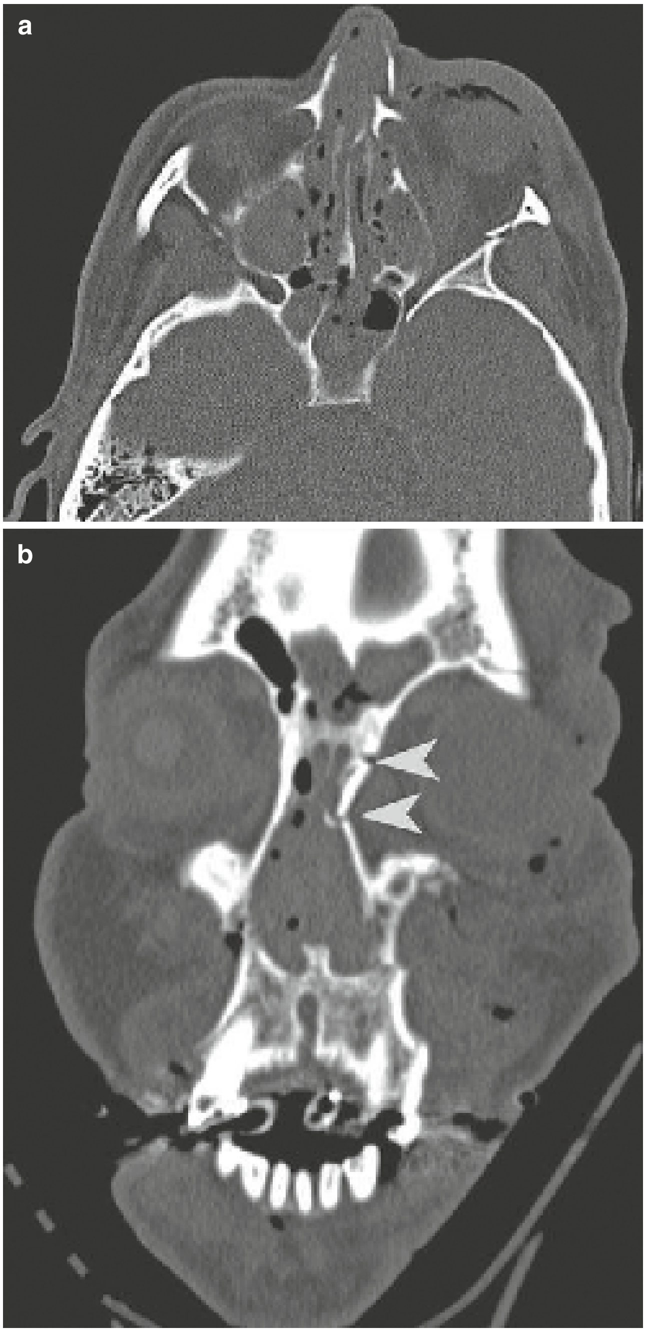

Fig. 17.12 Naso-orbital-ethmoid (NOE) fracture. (**a**) Axial CT image at the level of the lacrimal fossa demonstrates a comminuted fracture and disruption of the left medial maxillary buttress. (**b**) Coronal images at the level of the lacrimal fossa demonstrating disruption of the left medial maxillary buttress (*arrowheads*)

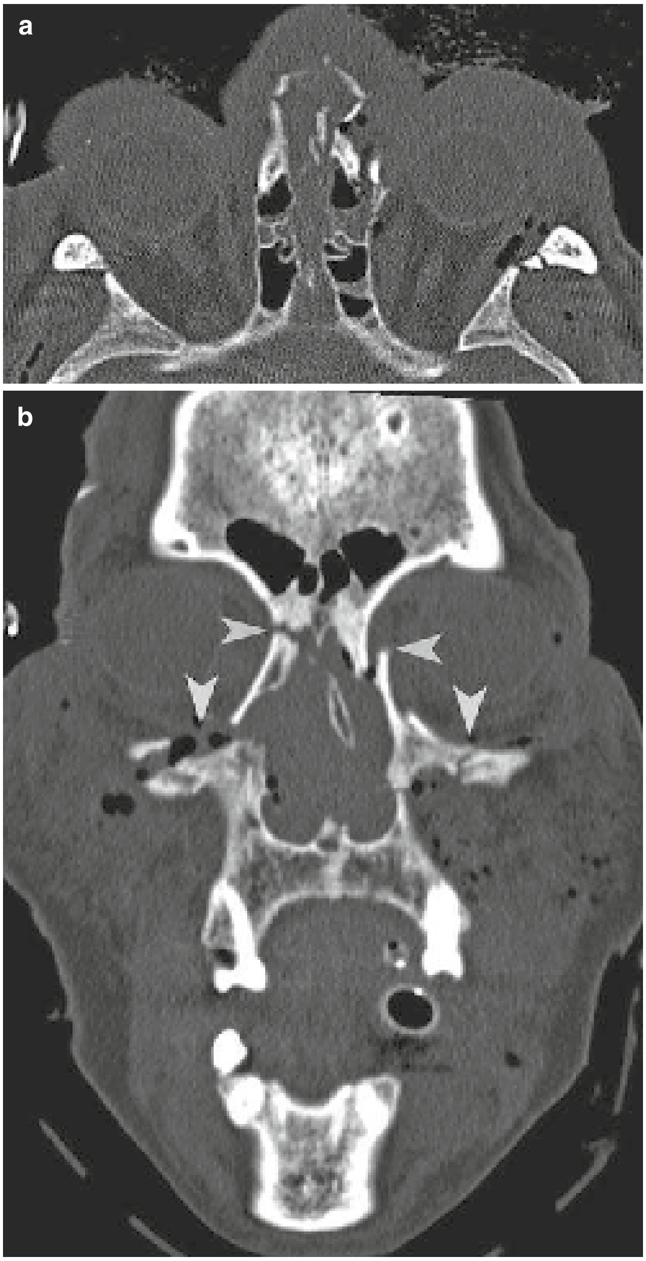

Fig. 17.13 NOE fracture. (**a**, **b**) Axial and coronal CT image in a patient with facial smash injury demonstrates NOE, Le Fort II (*arrowheads*), and bilateral ZMC fractures. The fractures have resulted in disruption of the medial maxillary, lateral maxillary, and upper transverse buttresses. There is posterior displacement of the central face and lateral displacement of the medial maxillary buttresses

Frontal Fractures

The frontal bone progressively pneumatizes throughout childhood. The anterior table forms the forehead and the superior orbital rims. The posterior table forms the anterior wall of the anterior cranial fossa. This strong bone forms the transverse frontal buttress and provides the anchor for the vertical maxillary buttresses. Due to its strength, a large

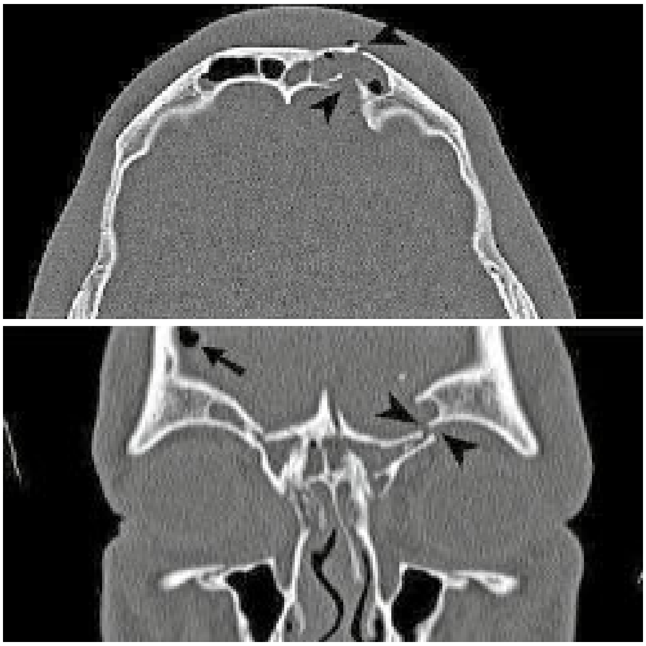

Fig. 17.14 Anterior and posterior table frontal fractures. Axial CT and surface-rendered images demonstrate comminuted fractures involving both the anterior and posterior tables (*arrowheads*). Pneumocephalus suggests dural disruption (*straight arrow*)

force is required to fracture the frontal bone [15]. The frontal sinus drains to the nose via the nasofrontal ducts. Injury to the nasofrontal duct can lead to later complications including frontal sinus mucocele, frontal sinusitis, osteomyelitis with anaerobes, or intracranial extension leading to brain abscess. Complications may develop years after the trauma. Surgeons may obliterate the frontal sinus (cranialization) to prevent these complications [16, 17].

Depressed outer table fractures will result in forehead deformities although this may be masked by the edema. Fractures of the posterior table are rarely isolated and may result in dural tear and CSF rhinorrhea. Fractures of the cribriform plate may result in anosmia. Fractures of the lateral frontal sinus floor usually involve the orbital roof.

CT is important to evaluate the extent of the fracture and whether it involves the anterior table, posterior table, or both (Figs. 17.14 and 17.15). When evaluating posterior table fractures, one should look for displacement, depression, pneumocephalus (suggesting dural disruption), and intracranial injury.

Management has become increasingly conservative. A patent outflow tract indicates salvageable frontal sinus. If the outflow tract cannot be restored, the sinus is eradicated. Posterior table fractures may need to be cranialized. Follow-up with CT scans to exclude possible complications may be useful.

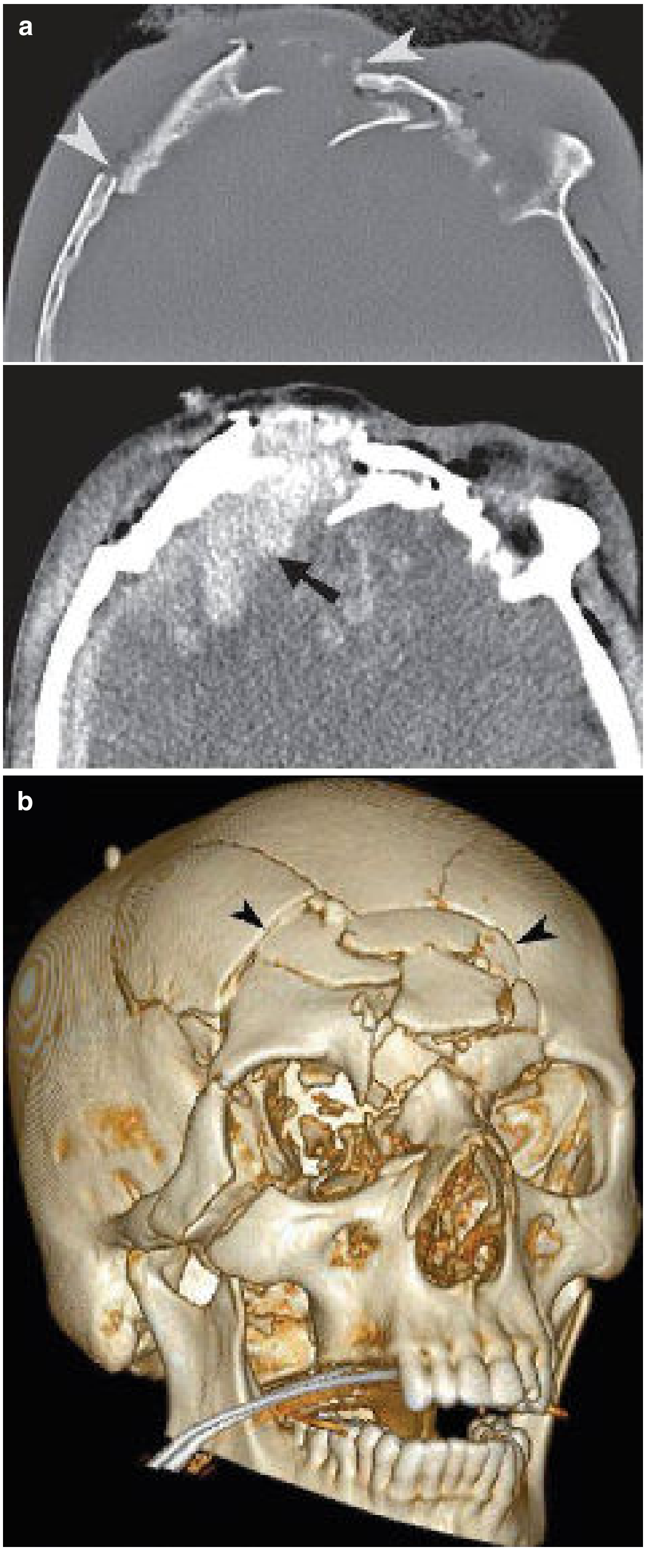

Fig. 17.15 Comminuted frontal fracture with intracranial injury. (**a**, **b**) Severely comminuted open frontal bone fractures (*arrowheads*) with associated intracranial subdural hemorrhage and frontal lobe contusion (*straight arrow*)

Maxillary Fractures

The maxilla, palatine, and nasal bones form the majority of the midface. The anterior maxillary wall forms the flat portion of the face between the nose and cheek. The maxilla contains the maxillary antrum, which is bordered by thin walls, resulting in predictable fracture patterns.

Le Fort Fractures

In 1901, René Le Fort published results of experiments performed on cadavers in which he demonstrated predictable fracture patterns of the midface [1]. Le Fort fractures are often seen in combination with other fractures [18].

Le Fort type I fractures result from trauma at a level immediately superior to the alveolar process of the maxilla. The horizontal fracture line extends through the anterior maxillary wall, medial antral wall, lateral antral wall, and pterygoid plates. There is depression of the lower transverse maxillary buttress, the hard palate. Type I fractures disrupt both medial and lateral maxillary buttresses (Fig. 17.16).

Le Fort type II fractures result from trauma at the level of the nasal bones with disruption of the (inferior) lateral and (superior) medial maxillary buttresses. These are also referred to as pyramidal fractures, with the entire maxilla moving with respect to the skull base. Type II fractures extend across the nasal bridge, inferomedial orbital rim, and zygomaticomaxillary suture and posteriorly through the maxillary sinus to the level of the pterygoid plates (Fig. 17.17).

Le Fort type III fractures result from a force delivered at the orbital level. The (superior) medial, (superior) lateral,

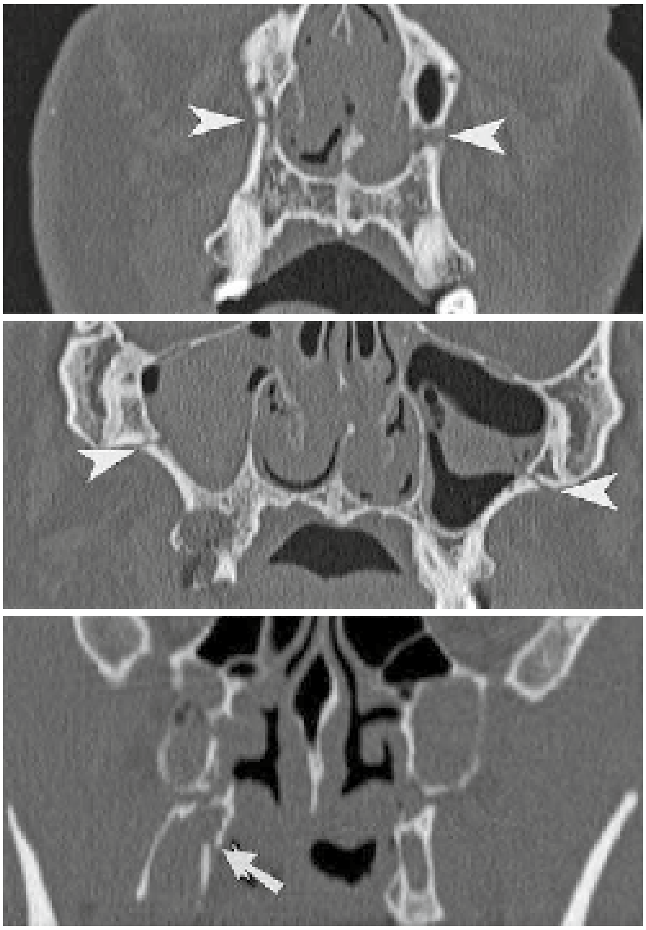

Fig. 17.16 Le Fort I fracture. Sequential coronal images from anterior to posterior showing a horizontal fracture through the medial maxillary buttresses (*arrowheads*), medial and lateral antral walls (*arrowheads*), and extending to the pterygoid plates (*straight arrow*)

Fig. 17.17 Le Fort II fracture. (**a**, **b**) Coronal CT reformation and surface-rendered image demonstrate multiple comminuted pyramid-shaped fracture of the midface. There are fractures of medial orbital walls (*straight arrow*), orbital floor (*curved arrows*), and lateral antral wall (*arrowhead*)

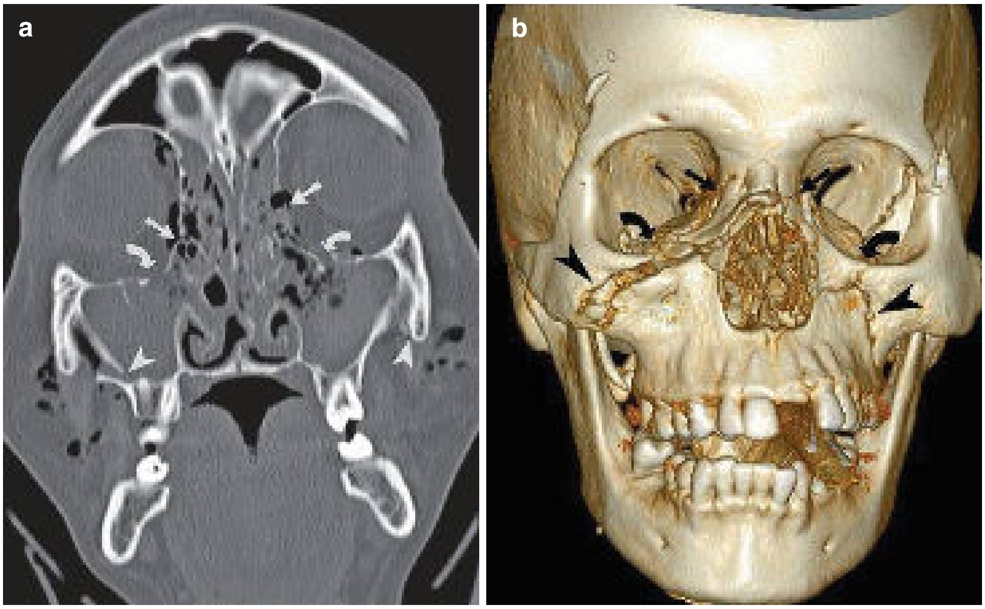

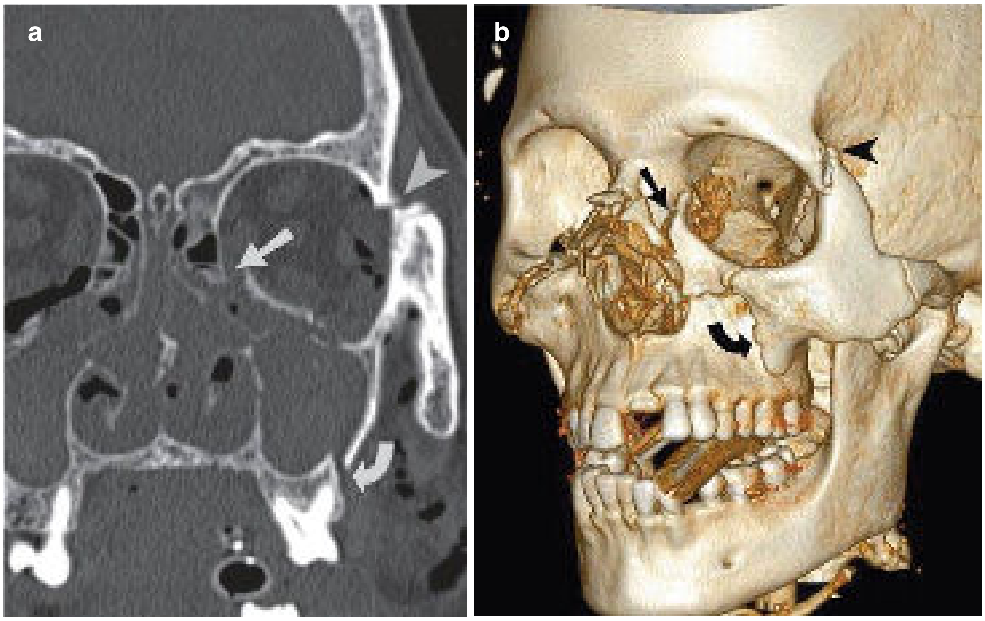

Fig. 17.18 Left hemi-Le Fort II and III fractures. (**a**, **b**) Coronal CT reformation and surface-rendered image demonstrates fractures through the left medial orbital wall (*straight arrow*), orbital floor, lateral antral wall (*curved arrow*), and zygomaticofrontal suture (*arrowhead*). The posterior extension and involvement of the posteromedial orbital wall distinguish these fractures from the ZMC fracture

and upper transverse maxillary buttresses are disrupted, resulting in craniofacial dissociation. The fracture line extends across the nasal bridge, zygomaticofrontal suture, zygomaticotemporal suture, and orbital walls, terminating posteriorly at the level of the pterygopalatine fossa, pterygoid process, or pterygoid plates. It is distinguished from the ZMC fracture by involvement of the medial orbital wall and posterior extension (Fig. 17.18).

Type I fractures may result in a free-floating palate. Type II injuries may demonstrate step deformities at the nasal bridge and infraorbital rim. Type III injuries may demonstrate craniofacial instability. With posterior displacement, type II and III injuries may demonstrate the characteristic “dish-face” deformity, a concave appearance of the face.

Type I injuries can be associated with dentoalveolar and mandible fractures. Type II and III injuries often demonstrate associated ZMC and NOE fractures. Type III injuries can be associated with skull fractures and intracranial injuries. Table 17.5 summarizes Le Fort fractures.

Table 17.5 Le Fort fractures

	Type I	Type II	Type III
Trauma level	Superior to the alveolar process of the maxilla	Nasal bones with disruption of the lateral and medial maxillary buttresses	Orbital level
Disruption	Medial and lateral maxillary buttresses	Inferior lateral and superior medial maxillary buttresses	Superior medial, lateral, and upper transverse maxillary buttresses
Results	Free-floating palate	Step deformities at the nasal bridge and infraorbital rim Possibly “dish-face” deformity	Craniofacial instability Possibly “dish-face” deformity
Associated injuries	Dentoalveolar and mandible fractures	ZMC and NOE fractures	ZMC and NOE fractures Skull fractures and intracranial injuries

Dentoalveolar and Maxillary Sagittal Fractures

The hard palate is formed by the horizontal process of the maxilla and palatine bone. Fractures may affect the alveolus and/or palate in isolation or in combination with other more complex fractures [19, 20]. The World Health Organization (WHO) has developed an injury classification system of dentoalveolar fractures:

- Fracture of the tooth: enamel infraction, enamel fracture, enamel-dentin fracture, complicated crown fracture, uncomplicated crown-root fracture, complicated crown-root fracture, root fracture
- Injury to the periodontal tissue: concussion, subluxation (loosening), extrusive luxation (peripheral dislocation, peripheral avulsion), lateral luxation, intrusive luxation (central dislocation), avulsion (exarticulation)
- Injury to the supporting bone: comminution of the mandibular, fracture of the mandibular or maxillary alveolar socket wall, fracture of the mandibular or maxillary alveolar process, jaw fracture
- Injuries to the gingival or oral mucosa: laceration of gingival or oral mucosa, contusion of gingiva or oral mucosa, abrasion of gingival or oral mucosa [21]

A classification system of maxillary sagittal fractures, developed by Hendrickson, is based on the fracture pattern through the palate:

1. Anterior and posterolateral alveolar
2. Sagittal
3. Parasagittal
4. Para-alveolar
5. Complex
6. Transverse [22]

Palatal fractures are commonly associated with Le Fort I (100%), Le Fort II and III (55%), dental (55%), and mandible (48%) fractures.

Clinically, the presence of mobility of multiple teeth suggests a fracture of the alveolar process. Facial, chest, and abdominal radiographs may be helpful to evaluate for displaced, swallowed, or aspirated teeth and bone fragments. Panoramic radiographs can evaluate the teeth and the integrity of the periodontal ligament. When evaluating CT scans with dentoalveolar injury, it is important to note fractures of teeth, dental extrusion or intrusion, displacement, tooth socket fractures, tooth fragments lodged in soft tissues, and associated mandibular or other facial fractures.

Mandible Fractures

The mandible is formed by a horizontal U-shaped body and two vertical rami. The alveolar process arises from the body and contains the mandibular teeth. The superior portion of each ramus has two processes: a posterior condylar process and an anterior coronoid process, separated by the mandibular notch. The body and rami join at the angle of the mandible. The prominent position of the mandible in the lower third of the face makes it vulnerable to fracture. They commonly occur bilaterally. The mandible fractures can be divided into the following regions: symphyseal, parasymphyseal, alveolar, body, angle, ramus, condylar process, and coronoid processes. Condylar process fractures are common, particularly the neck. In the setting of bilateral parasymphyseal fractures, the genioglossus, geniohyoid, and digastric muscles retract the symphysis posteriorly and inferiorly. The condylar head is often displaced medially in patients with condylar neck fractures due to the unopposed action of the lateral pterygoid muscle. CT angiogram of neck is indicated in fracture dislocation of condyle to assess for vascular injuries such as dissection.

As with most current imaging of craniofacial trauma, MDCT acquisition with axial, coronal, sagittal, and 3D volume-rendered reformats allows complete evaluation of mandibular fractures as well as associated injuries (Figs. 17.19 and 17.20). Treatment consists of intermaxillary (maxillomandibular) fixation, repair of the anterior segment (teeth-bearing, symphysis, and body), and reducing the posterior mandible (angle, ramus, coronoid, and condyle).

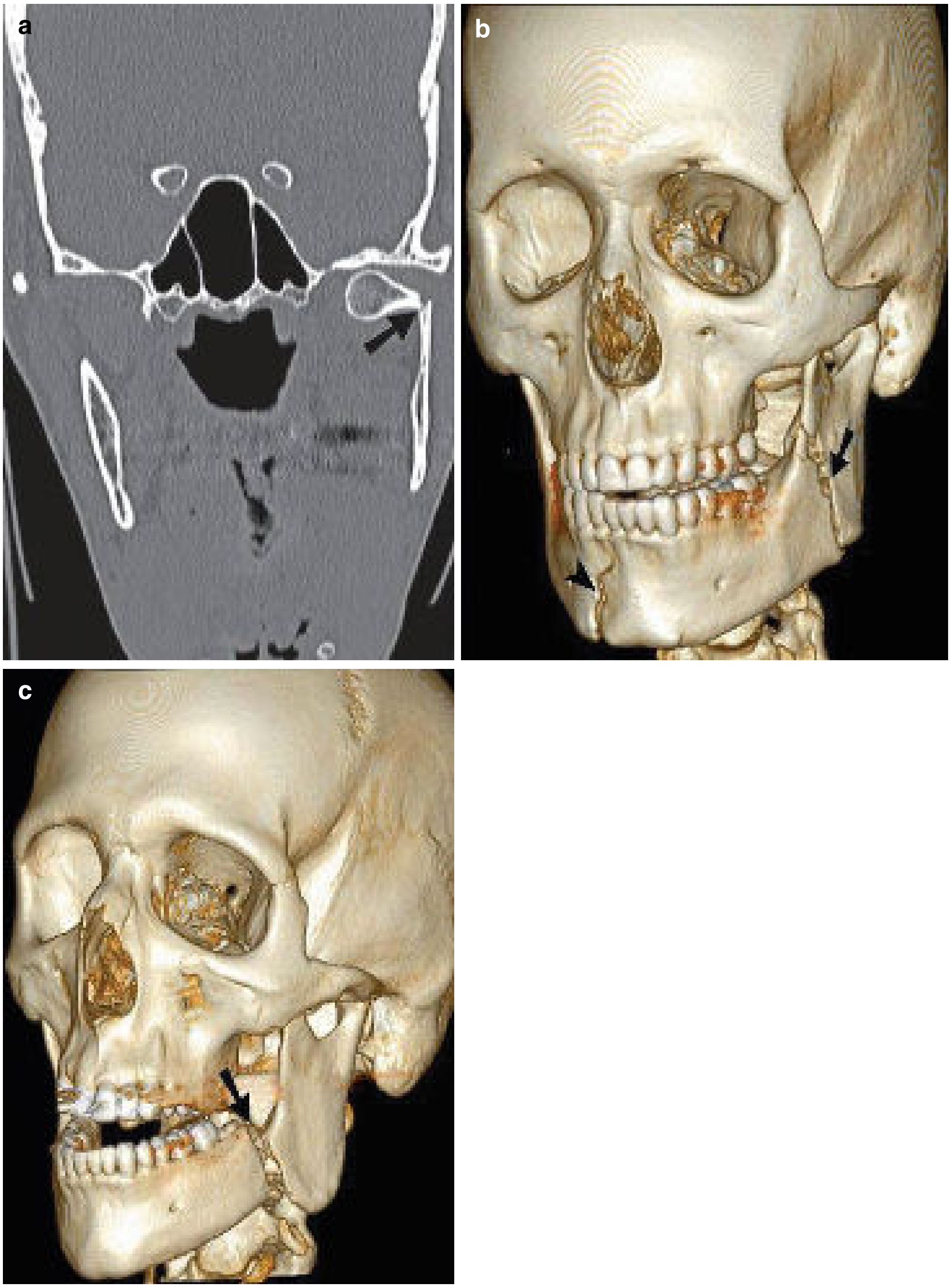

Fig. 17.19 Mandible fractures. (**a**) Coronal CT reformation shows angulated subcondylar fracture (*straight arrow*) with medial dislocation of the left mandible condylar head. (**b**) Surface-rendered CT image demonstrates right parasymphyseal (*arrowhead*) and left mandibular angle (*straight arrow*) fractures. (**c**) Surface-rendered CT image demonstrates displaced left mandibular angle fracture (*straight arrow*)

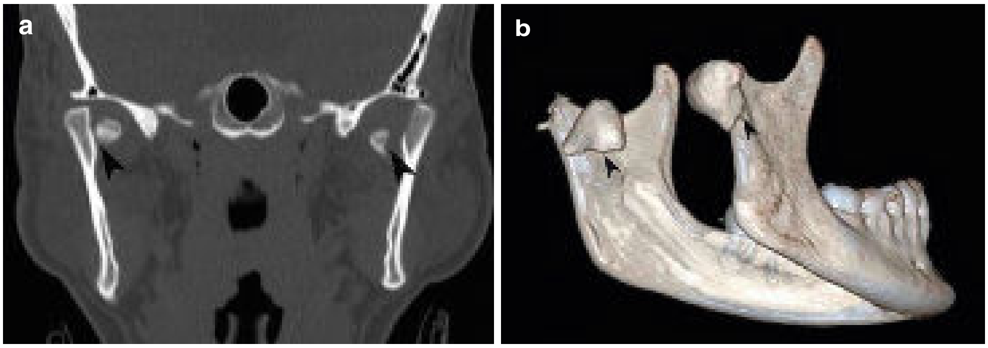

Fig. 17.20 Bilateral mandible subcondylar fractures. CT demonstrates bilateral subcondylar fractures on coronal (**a**) and surface-rendered images (**b**)

Questions

1. Which of the following statements is correct?
   (A) Impure blow-in orbital fractures are limited to the orbital walls
   (B) Pure blow-in orbital fractures are more common than impure fractures
   (C) Superior rim fractures are usually more severe
   (D) Nasal bone fractures are the second most imaged fractures in emergency setting
   Answer: C

2. Which of the following statements is correct regarding Manson classification of naso-orbital-ethmoid fractures?
   (A) Type 2 is the most common type
   (B) Type 2 consists of a single fragment
   (C) In type 1, insertion of medial canthal tendon is intact
   (D) Type 3 involves lateral displacement or avulsion of medial canthal ligament
   Answer: D

3. Which of the following injury pattern is classically associated fracture with palatal fractures?
   (A) Le Fort I
   (B) Le Fort II
   (C) Le Fort III
   (D) Le Fort IV
   Answer: A

4. What is the abnormality detected on the volume-rendered CT depicted below (Fig. 17.21)?
   (A) Le Fort I
   (B) Zygomaticomaxillary complex fracture
   (C) Naso-orbital-ethmoid fracture
   (D) Mandibular fracture
   Answer: B

5. In a patient with a history of motor vehicle collision (Fig. 17.22a, b), how would you characterize his mid facial fractures?
   (A) Le Fort I
   (B) Le Fort II
   (C) Le Fort III
   (D) Both Le Fort II and III
   Answer: D

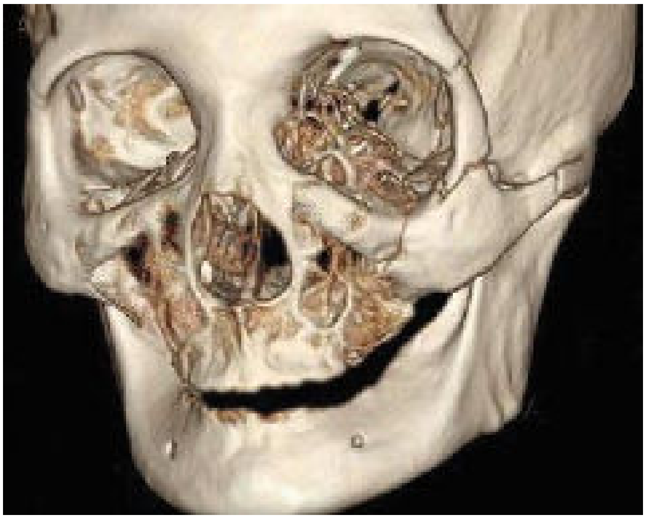

Fig. 17.21 Zygomaticomaxillary complex fracture

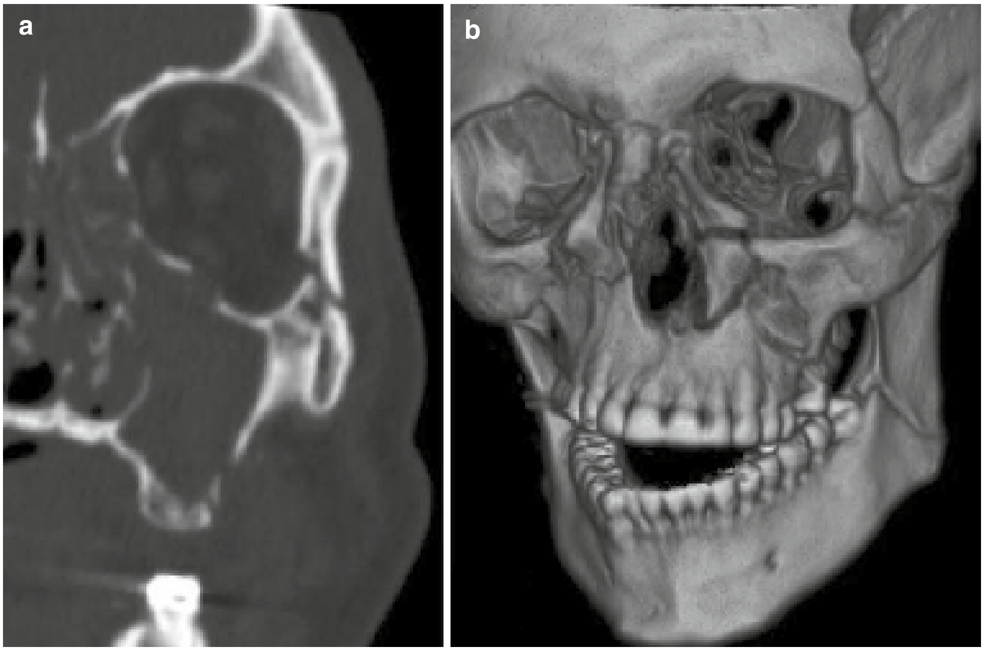

Fig. 17.22 (**a**, **b**) Mid facial fractures Le Fort II and III

References

1. LeFort R. Etude experimentale sur les fractures de la machoire superieure. Rev Chir. 1901;23:208–27.
2. Sicher H, Debrul EL. Oral anatomy. 5th ed. St. Louis: Mosby; 1970. p. 78.
3. Gentry LR, Manor WF, Turski PA, Strother CM. High resolution of the CT analysis of the facial struts in trauma: 1 and 2: normal anatomy and osseous and soft-tissue complications. AJR Am J Roentgenol. 1983;140:523–32.
4. Manson P, Hoopes JE, Su CT. Structural pillars of the facial skeleton: an approach to the management of le fort fractures. Plast Reconstr Surg. 1980;66(1):54–61.
5. Fonseca R, Barber HD, Powers M, Frost DE. Oral and maxillofacial trauma. St. Louis: Elsevier/Saunders; 2005.
6. Dolan K, Jacoby CG, Smoker WRK. The radiology of facial fractures. Radiographics. 1984;4:575–663.
7. Moore K, Dalley AF, AMR A. Clinically oriented anatomy. 6th ed. Baltimore: Lippincott Williams & Wilkins; 2010.
8. Smith B, Regan WF. Blow-out fracture of the orbit, mechanism and correction of internal orbital fracture. Am J Ophthalmol. 1957;44:733–9.
9. Rhee J, Kilde J, Yoganadan N, Pintar F. Orbital blowout fractures: experimental evidence for the pure hydraulic theory. Arch Facial Plast Surg. 2002;4:98–101.
10. Chirico P, Mirvis SE, Kelman SE, Karesh JW. Orbital "blow-in" fractures: clinical and CT features. J Comput Assist Tomogr. 1989;13(6):1017–22.
11. Antonyshyn O, Gruss JS, Kassel EE. Blow-in fractures of the orbit. Plast Reconstr Surg. 1989;84(1):10–20.
12. Rohrich RJ, Hackney FL, Parikh RS. Superior orbital fissure syndrome: current management concepts. J Craniomaxillofac Trauma. 1995;1(2):44–8.
13. Hopper R, Salemy S, Sze RW. Diagnosis of midface fractures with CT: what the surgeon needs to know. Radiographics. 2006;26:783–93.
14. Markowitz B, Manson PN, Sargent L, Vander Kolk CA, Yaremchuk M, Glassman D, et al. Management of the medial canthal tendon in nasoethmoid orbital fractures: the importance of the central fragments in classification and treatment. Plast Reconstr Surg. 1991;87(5):843–53.
15. Ioannides C, Freihofer HP. Fractures of the frontal sinus: classification and its implications for surgical treatment. Am J Otolaryngol. 1999;20(5):273–80.
16. Stanley R, Becker TS. Injuries of the nasofrontal orifices in frontal sinus fractures. Laryngoscope. 1987;97(6):728–31.
17. Gonty A, Marciani RD, Adornato DC. Management of frontal sinus fractures: a review of 33 cases. J Oral Maxillofac Surg. 1999;57:372–9.
18. Fraioli R, Branstetter BF 4th, Deleyiannis FW. Facial fractures: beyond le fort. Otolaryngol Clin N Am. 2008;41:51–76.
19. Andreasen JO, Bakland LK, Flores MT, Andreasen FM, Andersson L. Traumatic dental injuries: a manual. 3rd ed. Malden: Wiley-Blackwell; 2011. p. 260–2.
20. Antoniades K, Dimitriou C, Triaridis C, Karabouta I, Layaridis N, Karakasis D. Sagittal fracture of the maxilla. J Craniomaxillofac Surg. 1990;18(6):260–2.
21. World Health Organization. Application of the international classification of diseases to dentistry and stomatology. IDC-DA. 3rd ed. Geneva: World Health Organization; 1995.
22. Hendrickson M, Clark N, Manson PN, Yaremchuk M, Robertson B, Slezak S, et al. Palatal fractures: classification, patterns and treatment with rigid internal fixation. Plast Reconstr Surg. 1998;101:319–32.

Stroke and Its Imaging Evaluation

18

Sathish Kumar Dundamadappa, Melanie Ehinger,
Andrew Chen, and Mohammad Mansouri

Introduction

Stroke, defined as the sudden onset of persistent neurologic deficit, is a significant cause of morbidity and mortality in the USA. It is the fourth leading cause of death, accounts for 130,000 deaths each year in the USA, and is the leading cause of serious long-term disability. Approximately 795,000 people have a stroke in the USA. In addition, stroke is associated with overall $36.5 billion cost to the society [1]. Ischemic infarction is by far the most common etiology comprising 88% of stroke. Intracranial hemorrhage makes up an additional 10%–15%, with less common etiologies accounting for the remainder. Mortality rates vary with etiology, with a 38% and 8%–12% 30-day mortality seen in hemorrhagic and ischemic strokes, respectively.

Ischemic Stroke

Ischemia is by far the most common cause of stroke. Ischemic causes can be further subdivided into atherosclerotic, cardiogenic, hemodynamic, or cryptogenic sources. Atherosclerotic causes are the most common subtype as thrombi are formed in vessels with abnormal endothelium, usually directly at atherosclerotic plaque.

Emboli travel distally from the site of origin from the heart or intra/extracranial vessels. Arterial emboli are often produced at the site of atherosclerotic plaque that dislodge and travel downstream creating an artery-to-artery embolism. Common sites for thromboembolic disease include the carotid bifurcation, carotid siphon, proximal portions of the anterior/middle cerebral arteries, subclavian artery, origin of the vertebral artery, distal vertebral artery, and basilar artery. Cardioembolic events may occur in the setting of relative stasis of blood resulting in thrombus formation within the heart.

Occlusion of small perforating end arteries results in lacunar infarcts, which are infarcts less than 20 mm in diameter and that frequently occur in the deep cerebral white matter, basal ganglia, internal capsule, pons, thalami, or corona radiata (Fig. 18.1) [1]. Occlusion of terminal branches causes cortical infarcts.

Ischemic stroke is associated with the presence and extent of coronary artery disease, especially with calcified plaque. Furthermore, subclinical coronary artery disease is common in patients with acute embolic stroke or transient ischemic attack [1].

Less common etiologies, representing less than 5% of acute stroke, include vasculopathies, immune-related diseases, hypercoagulable states, arterial dissection, global hypoperfusion, venous infarction, and mitochondrial disorders (Table 18.1).

S. K. Dundamadappa (✉)
Department of Radiology, UMass Memorial Medical Center and UMass Medical School, Worcester, MA, USA
e-mail: sathish.dundamadappa@umassmemorial.org

M. Ehinger
Greensboro Radiology, Greensboro, NC, USA
e-mail: melanie.ehinger@umassmemorial.org

A. Chen
Department of Radiology, University of Massachusetts Medical Center, Worcester, MA, USA
e-mail: andrew.chen@umassmemorial.org

M. Mansouri
Department of Radiology, Massachusetts General Hospital, Boston, MA, USA

© The Author(s), under exclusive license to Springer Nature Switzerland AG 2024
A. Singh (ed.), *Emergency Radiology*, https://doi.org/10.1007/978-3-031-65770-2_18

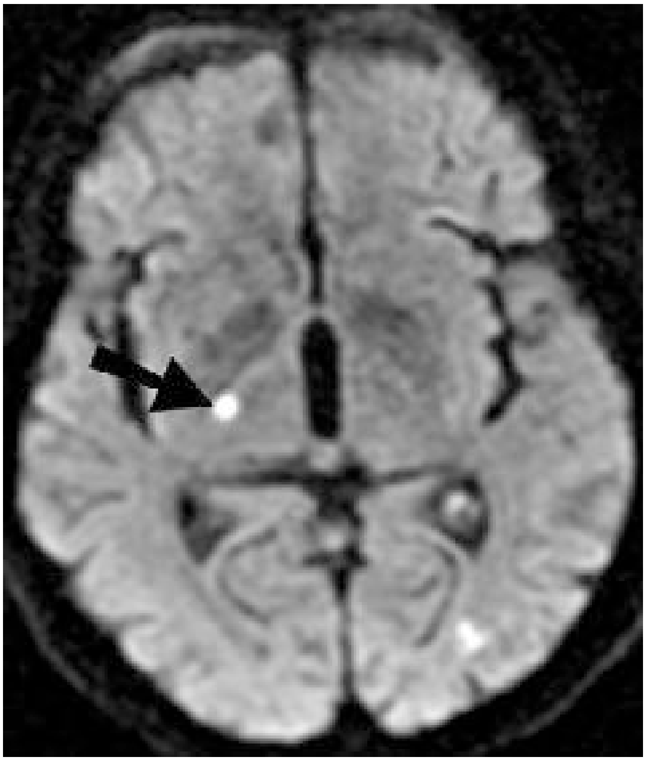

Fig. 18.1 Acute infarct. Diffusion-weighted images showing acute lacunar infarct (*arrow*) in posterior limb of right internal capsule

Table 18.1 Causes of ischemic stroke

Atherosclerotic
Cardiogenic
Hemodynamic
Cryptogenic
Vasculopathies
Immune-related diseases
Hypercoagulable states
Arterial dissection
Global hypoperfusion
Venous infarction
Mitochondrial disorders

Concept of Penumbra

Once vascular supply to the brain has been compromised, there is a window of opportunity for reversing ischemic symptoms depending upon the level to which the blood flow has dropped. Normal cerebral flow ranges between 60 and 100 mL/100 g/min, with varying degrees of hypoperfusion seen at lower flow rates. Brain parenchyma can compensate for a decrease in perfusion by increasing oxygen extraction to a cerebral blood flow (CBF) of approximately 20–23 mL/100 g/min. While blood flow of 10–20 mL/100 g/min may be reversible for a period of hours, more severe perfusion deficit (below 10 mL/100 g/min) may lead to infarction within minutes. Ischemic brain tissue can functionally be divided into three components—infarct core, penumbra, and oligemic region (Fig. 18.2, Table 18.2). When a cerebral artery is occluded, a core of brain tissue with severe perfusion deficit dies rapidly while the surrounding brain tissue (ischemic penumbra) with moderately reduced blood flow may lose electrical activity. Tissue in the penumbra may be salvageable with reperfusion; otherwise, the tissue in penumbra will progress to infarction. Mildly reduced blood flow to the oligemic region surrounds the penumbra and is more likely to survive unless perfusion is further hemodynamically altered.

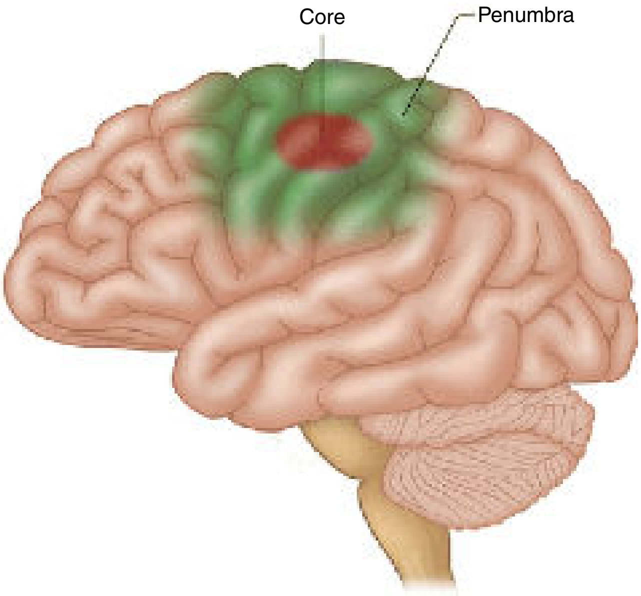

Fig. 18.2 Schematic diagram shows an acute infarct and the surrounding penumbra

Table 18.2 Features of penumbra

• Hypoperfused abnormal brain tissue with cellular dysfunction but not death
• Area within the same ischemic vascular territory as the infarct core
• Salvaging of the area is associated with better clinical outcomes

Imaging Workup of Acute Ischemic Stroke

In the past, imaging was primarily used to exclude hemorrhage and evaluate for surgically amenable lesions. The role of imaging has changed dramatically over the last decade and currently involves detection as well as extent of the infarct and penumbra.

Goals in acute stroke imaging are to assess the 4 "Ps" (Fig. 18.3) [2]:

Fig. 18.3 Goals in acute stroke imaging

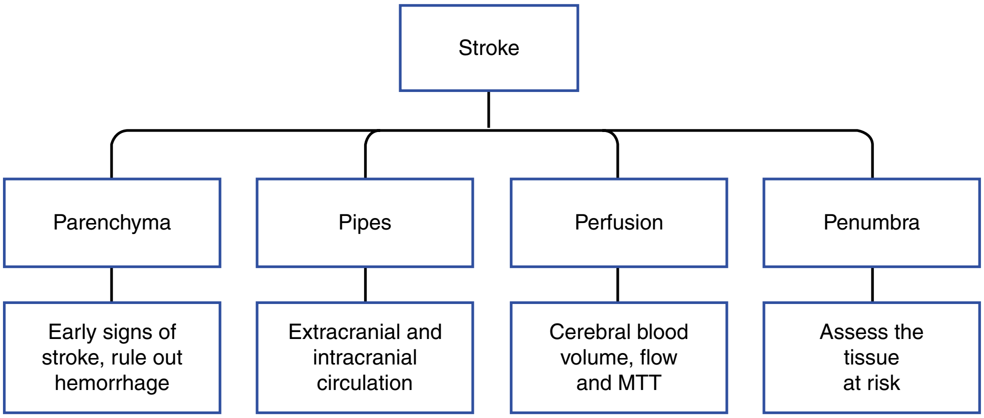
Stroke
Parenchyma
Pipes
Perfusion
Penumbra
Early signs of stroke, rule out hemorrhage
Extracranial and intracranial circulation
Cerebral blood volume, flow and MTT
Assess the tissue at risk

- *Parenchyma*: Assess early signs of acute stroke and rule out hemorrhage.
- *Pipes*: Assess extracranial and intracranial circulation for intravascular thrombus, occlusion, severe stenosis, and presence/degree of collateral circulation.
- *Perfusion*: Assess cerebral blood volume, cerebral blood flow, and mean transit time (MTT).
- *Penumbra*: Assess tissue at risk of dying if ischemia continues without recanalization.

Table 18.3 CT signs of early ischemia

Sign	Description
Dense artery sign	Linear hyperdensity in the vessel
MCA “dot” sign	Hyperdensity in distal MCA and its branches
Loss of gray-white differentiation	Obscuration of lentiform nucleus, insular ribbon sign, and loss of definition of cortical regions
Hypodensity	Seen by 24 h, followed by swelling, especially in larger infarctions

CT imaging, including noncontrast CT (NCCT), CT angiography (CTA), and CT perfusion (CTP), is the most often used initial imaging modality in stroke evaluation. At our institution, NCCT followed by multiphasic CTA is the initial study in stroke evaluation. Multiphasic CTA helps in the assessment of the degree of collateral supply, which has prognostic significance. CTP is performed in select cases to help stratify patients for treatment.

Noncontrast CT

Sensitivity of NCCT is 60%–70% in the first 3–6 h, and virtually all infarcts are seen by 24 h. Despite its relative insensitivity to acute infarcts in the emergency setting, NCCT remains the widely used initial imaging study in acute stroke. It is used to rule out intracranial hemorrhage and other stroke mimics.

CT signs of early ischemia include (Table 18.3, Fig. 18.4):

- *Dense artery sign*: Acute thrombus or embolus in a cerebral artery may produce linear hyperdensity in the vessel affected. Hyperdense MCA sign is associated with large MCA territory infarct and is seen in one-third of the hyperacute infarcts. In addition, patients with hyperdense MCA sign respond better to endovascular intervention [1]. MCA “dot” sign refers to hyperdensity in distal MCA and its branches in Sylvian fissure.
- *Loss of gray-white differentiation*: In MCA territory infarcts, there is often obscuration of lentiform nucleus (basal ganglia are more sensitive to ischemia due to their end-artery blood supply) and insular ribbon sign (insula is especially sensitive to ischemia due to its distance from collateral flow). Peripherally, acute infarction results in loss of definition of regions of cortex (cortical sign) in the affected vascular territory.
- *Hypodensity*: This becomes more apparent and well circumscribed by 24 h. Variable amount of cerebral swelling develops after 24 h and usually peaks at 3–5 days. The degree of swelling depends on the restoration of flow.

The detection of early acute ischemic stroke on NCCT may be improved by using variable window width and center-level settings to accentuate the contrast between normal and edematous tissue [3]. Multiplanar reformats and thin slices may also help in identifying subtle infarcts (e.g., coronal reformats for superior cerebellar infarcts).

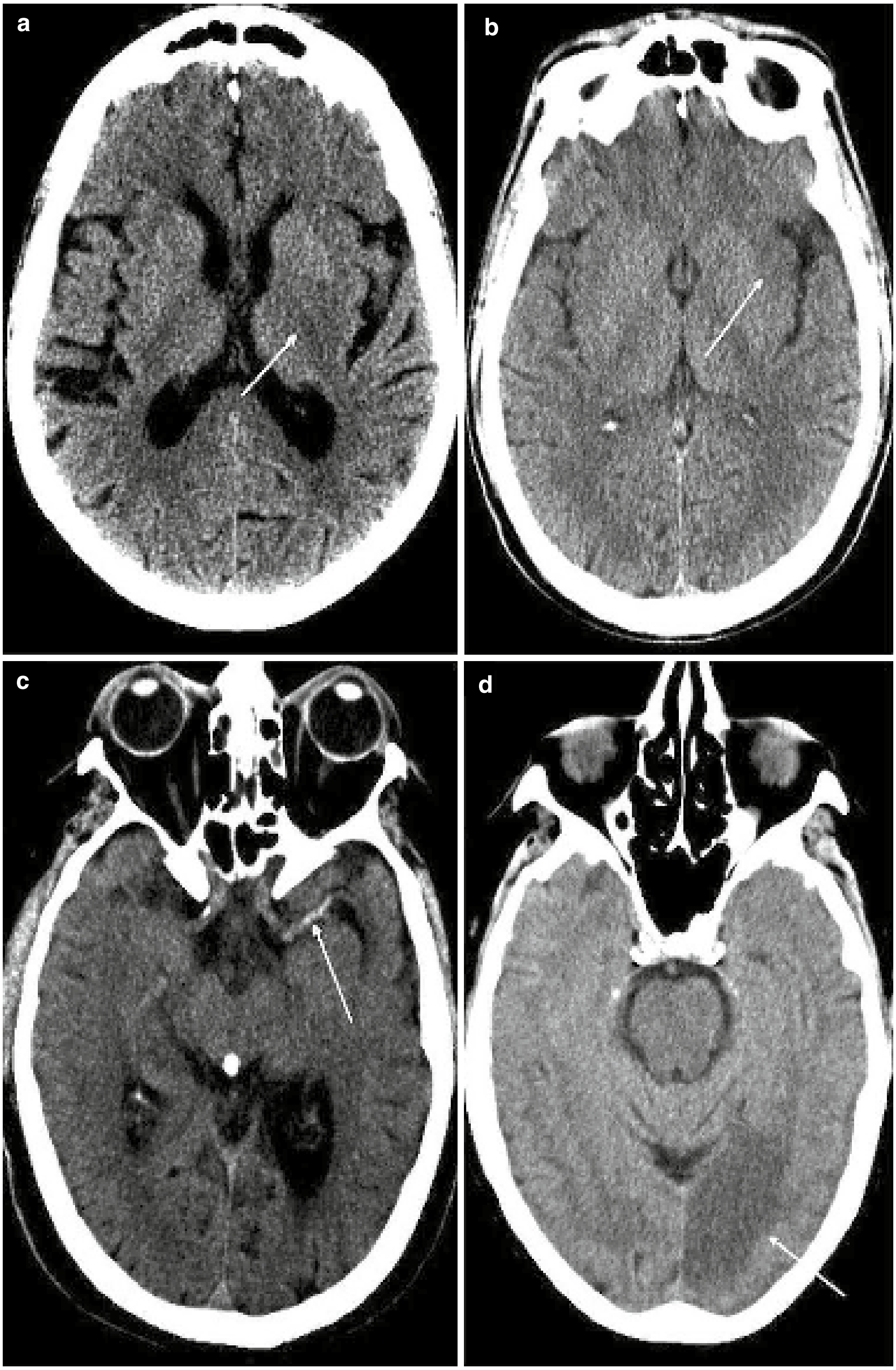

Fig. 18.4 CT signs of acute infarction. (**a**) Hypodense lentiform nucleus (*arrow*), (**b**) loss of "insular ribbon" (*arrow*), (**c**) hyperdense middle cerebral artery (*arrow*), (**d**) hypodensity in arterial territory (*arrow*)

CT Angiography

CTA is fast and noninvasive and allows for evaluation of etiology of acute ischemic stroke (such as thrombosis, occlusion, severe stenosis, and dissection). CTA has more than 98% sensitivity, specificity, and accuracy in detecting large vessel occlusion [1]. Both source images and 3D images should be reviewed. Though not very accurate, clot morphology like ulceration can also be assessed. When calcified plaques are present, the window can be widened for better evaluation.

Proximal occlusion of arteries is associated with worse clinical outcome, longer hospital and ICU stay, and higher hospitalization costs [1]. Assessing CTA collaterals with multiphasic CTA is widely accepted to be useful in prognostication and also in patient selection for endovascular treatment. Patients with better collaterals have smaller admission DWI infarct size and better clinical outcomes.

CT Perfusion

CTP is a functional imaging technique that can be rapidly performed to evaluate ischemic but potentially salvageable penumbral tissue. CTP is based on the entry and washout of an intravenous iodinated bolus of contrast. The routing use of perfusion in acute stroke imaging is controversial, and its accuracy and impact on outcome are yet to be validated. In our institution, we use it in select cases. CTP findings alone are probably insufficient to make therapeutic decision, but when considered with other clinical/imaging factors may help in borderline cases.

Severely diminished cerebral blood volume (CBV) has been demonstrated as a good correlate to the area of restricted diffusion on MRI and hence is considered a measure of the infarct core. Decreased cerebral blood flow (CBF) and increased mean transit time (MTT) are seen in areas of the brain either at risk for or undergoing infarct. Occasionally, increased CBV (luxury perfusion) may be seen in ischemic region due to autoregulatory vasodilatation and recruitment of collateral vessels. The combination of low CBF and normal/increased CBV probably represents an area at risk for ischemia (penumbra) but currently compensated by dilated collateral vessels (Figs. 18.5 and 18.6).

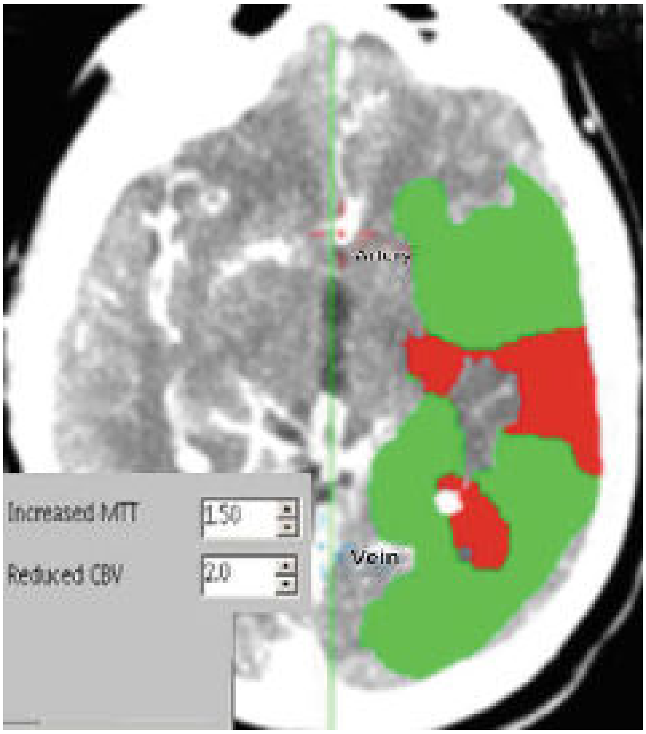

Increased MTT 1.50

Reduced CBV 2.0

Fig. 18.5 Color-coded summary maps from CT perfusion study showing large penumbra (shown in *green*) in the left MCA territory. The red color indicates severely reduced cerebral blood volume

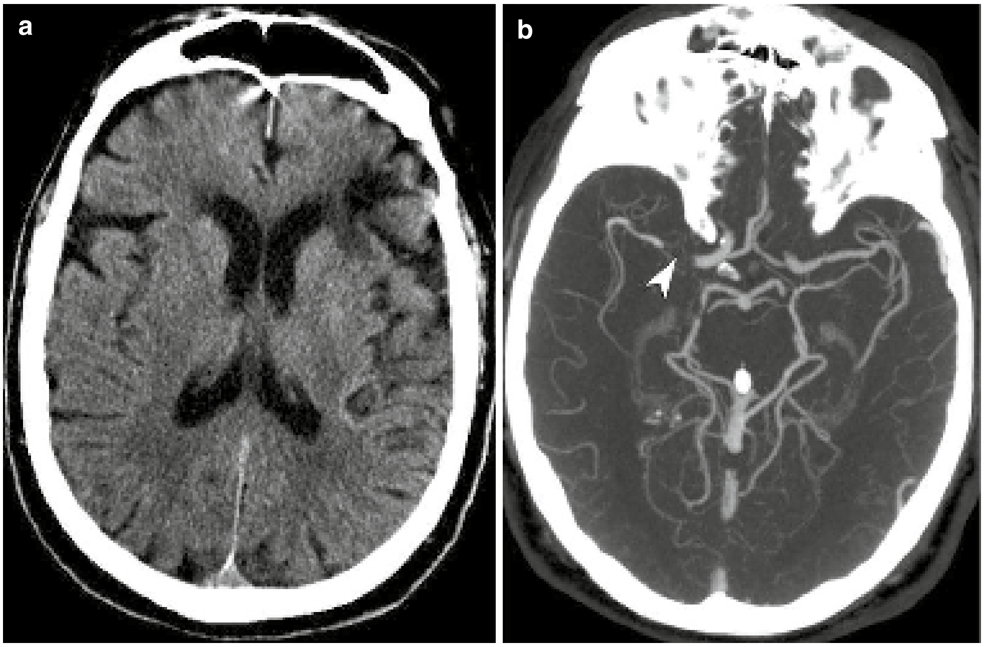

Fig. 18.6 Perfusion imaging in acute stroke. (**a**) Noncontrast CT shows no evidence of acute infarction in the right middle artery territory. (**b**) CTA showing focal occlusion of the M1 segment of the right middle cerebral artery (arrowhead). (**c–e**) Perfusion imaging shows mismatch between CBV (**c**) and MTT/CBF defects (**d** and **e**, respectively)

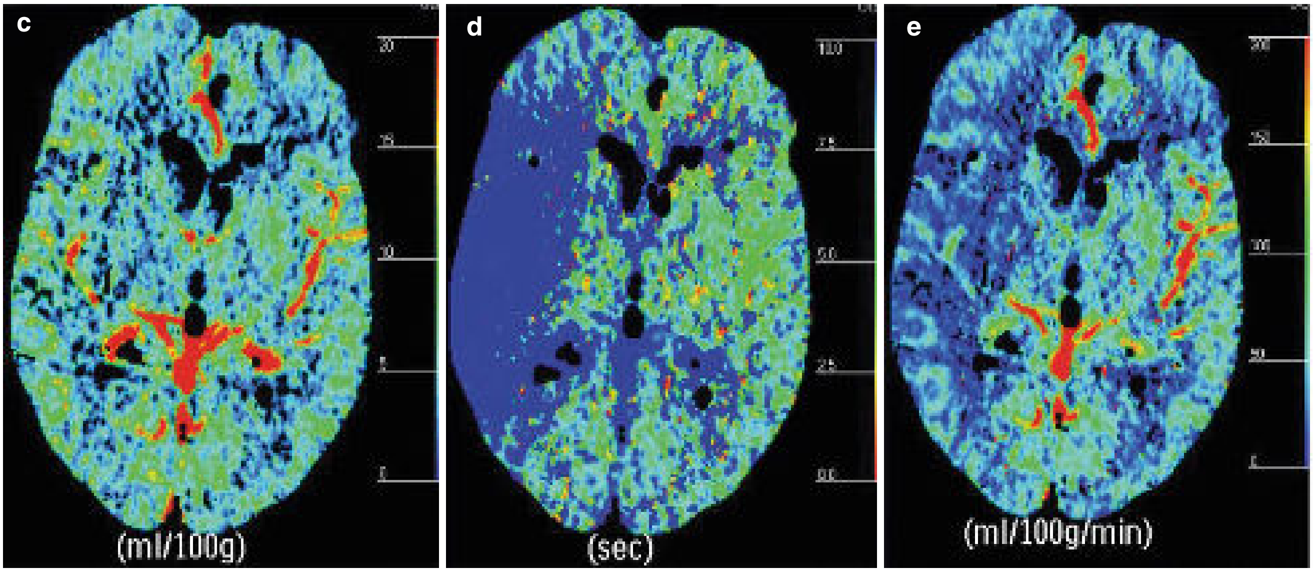

Fig. 18.6 (continued)

MR Imaging

MR imaging is more sensitive and specific than CT for detection of acute stroke. Its sensitivity and specificity range from 91% to 100% and 86% to 100%, respectively, in the detection of ischemia within 6 h of stroke onset [1]. The most sensitive imaging sequence for detecting ischemia is diffusion-weighted MR imaging (DWI), with changes in acute infarction detected within minutes of onset of the symptoms. Cytotoxic edema of acute ischemia results in reduced water diffusion in the extracellular matrix. DWI detects this restriction of microscopic motion. The location and size of the infarct play an important role in the sensitivity of DWI series. Vertebrobasilar lesions have higher false-negative rate, compared to 2% of anterior circulation lesions. High-resolution DWI series should be obtained if small infarct is suspected [1].

Acute infarct is seen as bright signal intensity on DWI due to restricted diffusion as well as secondary to increased water content (T2 effect), with corresponding decrease on apparent diffusion coefficient (ADC) sequence (Figs. 18.7a and 18.8). DWI is positive in the acute phase with increasing intensity that peaks at 7 days. The time to normalization of DWI signal has been reported in literature to range from 14 to 72 days [4, 5]. ADC sequence initially has low signal intensity, with maximum hypointensity occurring at 24 h. Signal intensity then increases and normalizes between the seventh and 11th days [6].

Additional findings in acute infarct include the presence of lesion in arterial distribution, hyperintense signal on T2-weighted and fluid-attenuated inversion recovery sequence, subcortical white matter hypointensity on T2-weighted sequence (see Fig. 18.7b), exaggerated intravascular enhancement, and findings of vascular occlusion (lack of normal flow void on long TE sequence and high arterial signal on FLAIR sequence related to slow flow/occlusion) (see Fig. 18.7c). However, T2 signal can be normal in the first 8 h after ictus. With time, infarcts become hyperintense on T2-weighted sequence, with maximum hyperintensity reached between 7 and 30 days.

Fig. 18.7 Acute infarction on MRI. (**a**) Acute right PCA territory infarct, which is not apparent on T2-weighted sequence, is clearly seen on DWI (*arrow*). (**b**) T2-weighted sequence shows acute left PCA territory infarction (*arrows*). (**c**) Left ICA occlusion: T2-weighted sequence shows hyperintense signal within left ICA (*arrow*), indicating the presence of thrombus in the arterial lumen

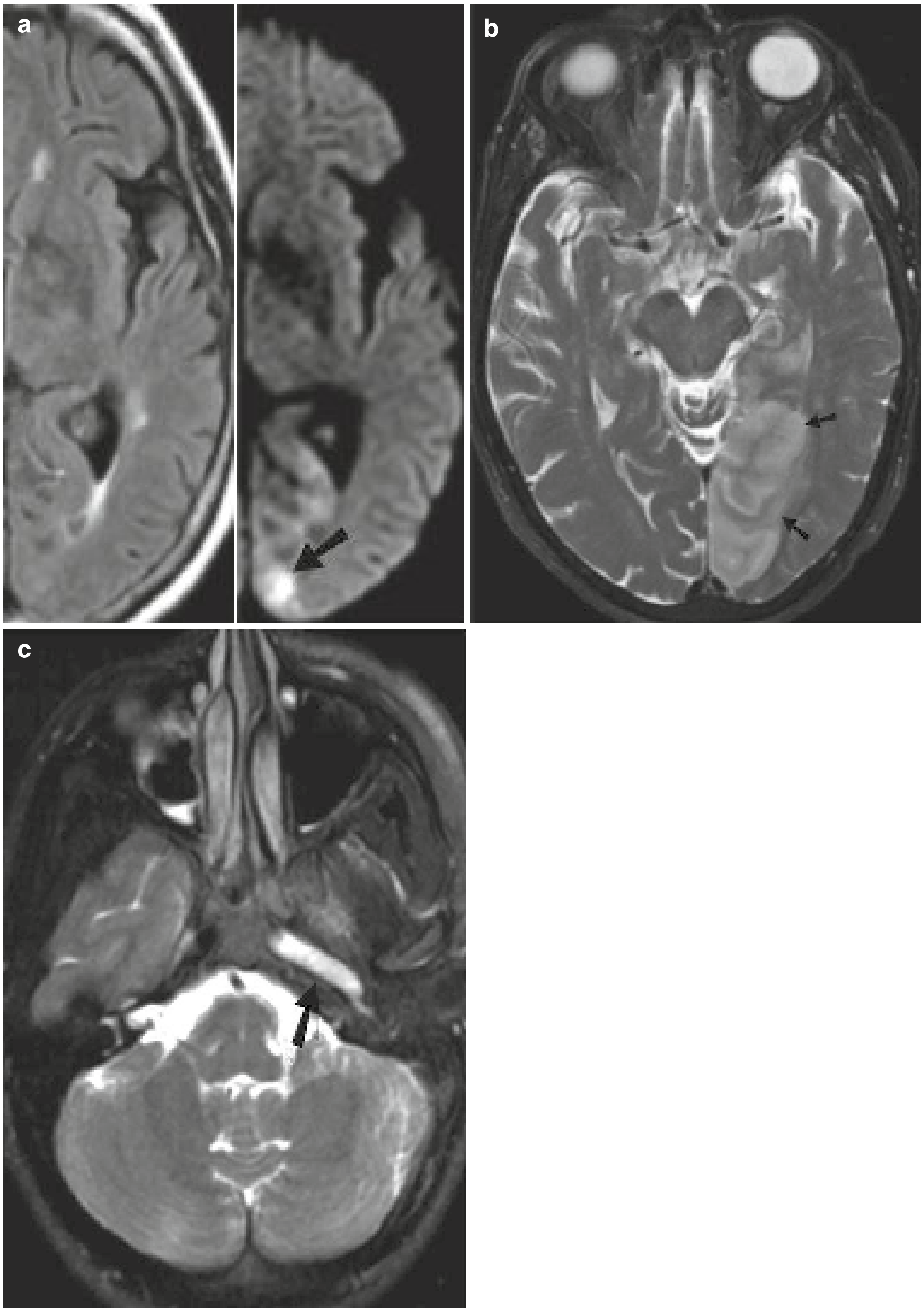

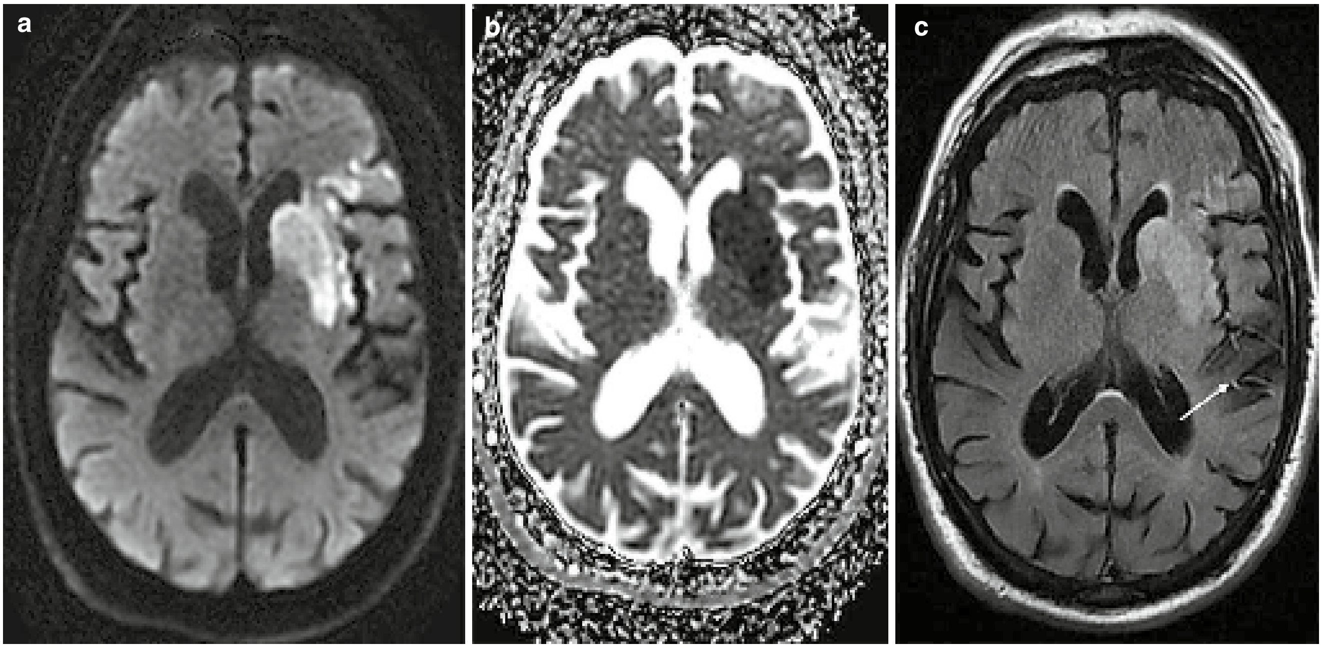

Fig. 18.8 Acute infraction on MRI. (**a**) Hyperintense on diffusion-weighted images, (**b**) hypointense on ADC maps, (**c**) hyperintense on T2 FLAIR image. Note FLAIR hyperintensity in left middle cerebral artery branches (*arrow*) secondary to slow flow or occlusion

MR Perfusion Imaging

MR perfusion is increasingly becoming a less common technique for acute stroke evaluation. The major deterrent is the time it takes to get the patient to the magnet. MR perfusion imaging techniques include exogenous contrast-enhanced method or an endogenous method (arterial spin labeling). Exogenous dynamic susceptibility-weighted (T2*-weighted) sequence is the most commonly used technique in acute stroke evaluation. The technique involves tracking of the tissue signal loss caused by T2* effects of paramagnetic contrast agent to create a hemodynamic time–signal intensity curve. As in dynamic CT perfusion imaging, various parametric maps (CBV, MTT, CBF, TTP) are calculated from this curve by using a deconvolution technique. The core of infarct demonstrated by restricted diffusion is compared against CBF or MTT maps for mismatch, which represents the penumbra, tissue at risk (Fig. 18.9).

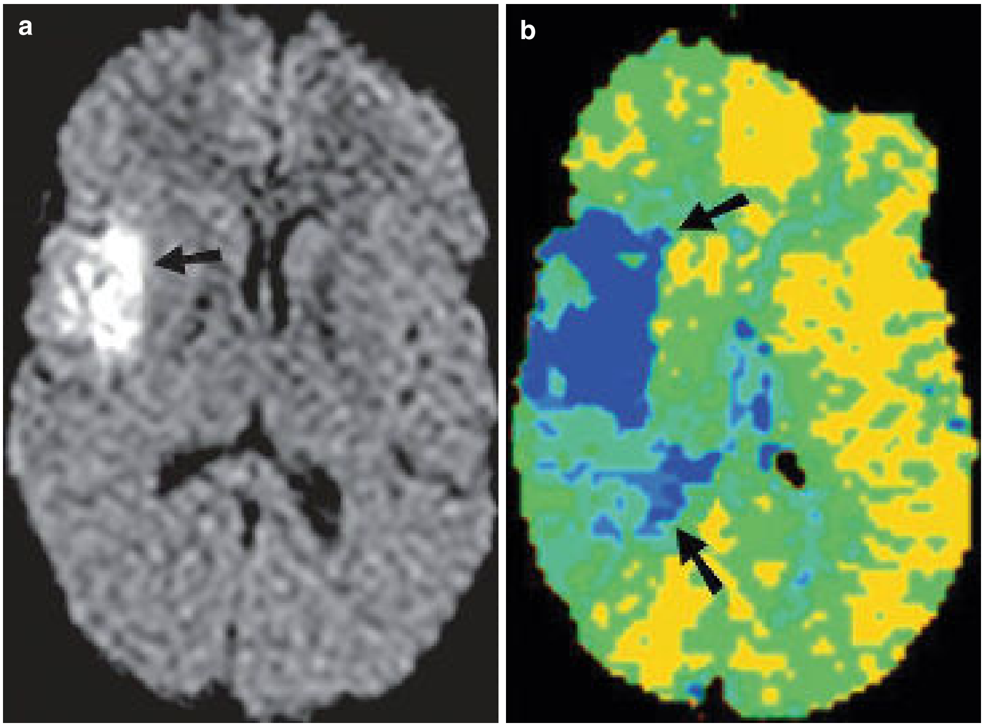

Fig. 18.9 Acute infarction on MR. (**a**) Diffusion-weighted sequence shows a hyperintense acute infarct in the right MCA territory. (**b**) MR perfusion image shows a large defect (*arrows*), suggesting the presence of a penumbra

Hemorrhagic Transformation

Though small hemorrhagic transformation is not uncommon, clinically significant parenchymal hematomas within untreated infarction are less common (2%–9%) in the acute stage. It is thought to be due to reperfusion of ischemic tissue during the first 2 weeks, occurring more commonly in larger infarcts and cardioembolic infarcts. Anticoagulant and thrombolytic agents increase the incidence of hemorrhagic transformation.

The European Cooperative Acute Stroke Study (ECASS) classification of hemorrhagic transformation stratified the size of these hemorrhages with the clinical outcome [7].

Hemorrhagic infarct (HI) (Fig. 18.10): petechial hemorrhages without space-occupying effect.

HI1: small petechiae

HI2: more confluent petechiae parenchymal hematoma (PH) (Fig. 18.11): hemorrhage (coagulum) with mass effect

PH1: <30% of the infarcted area with mild space-occupying effect.

PH2: >30% of the infarcted area with significant space-occupying effect (Fig. 18.12).

Only PH2 independently modifies the risk of a worse clinical outcome both early and late after stroke onset. PH1 has increased risk of early deterioration but not of a worse long-term outcome. HI is not associated with worse early or late outcome [8].

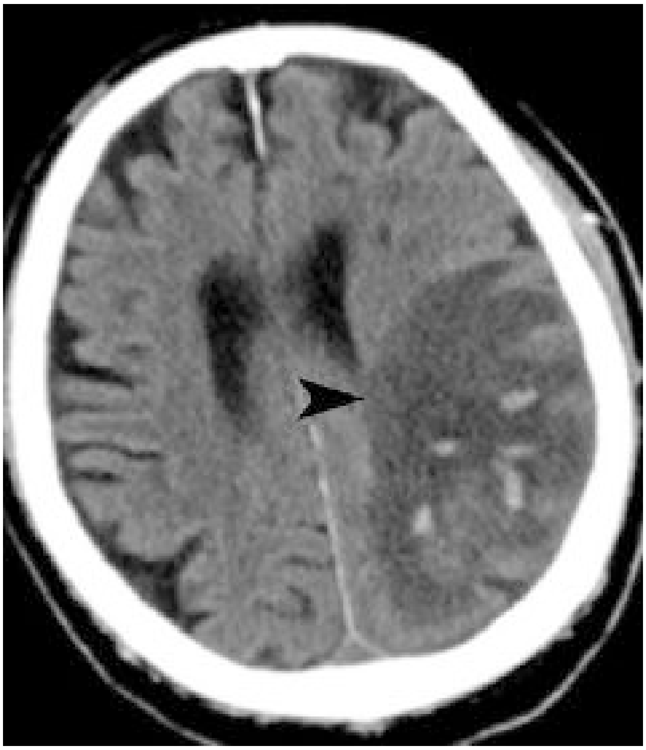

Fig. 18.10 Acute infarct with hemorrhage. Noncontrast CT shows petechial hemorrhages with left parietal infarct (*arrowhead*) (ECASS HI2)

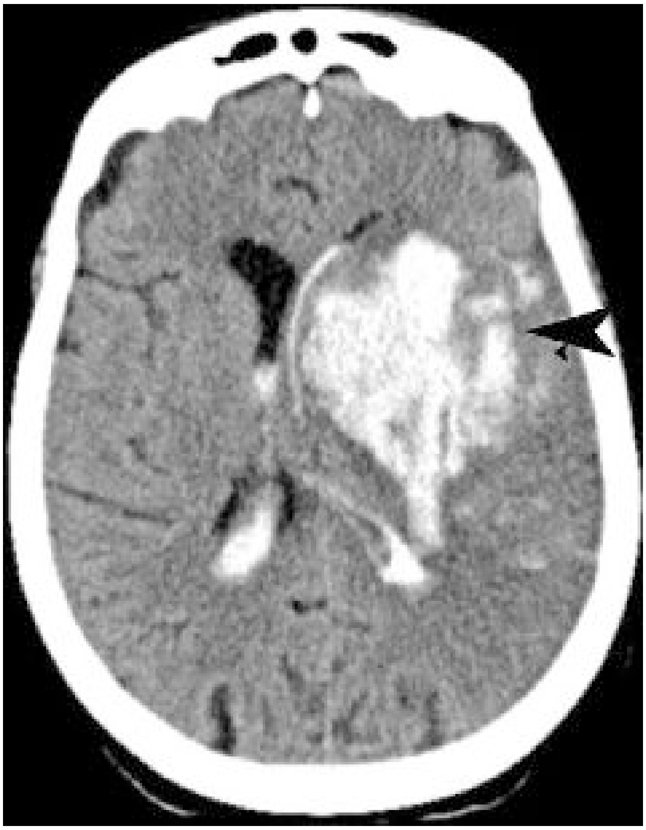

Fig. 18.11 Acute infarct with hemorrhage. Noncontrast CT shows intraparenchymal as well as intraventricular hemorrhage (*arrow*) within left MCA territory infarction (ECASS PH2), following IV tPA

Fig. 18.12 European Cooperative Acute Stroke Study (ECASS) classification of hemorrhagic transformation

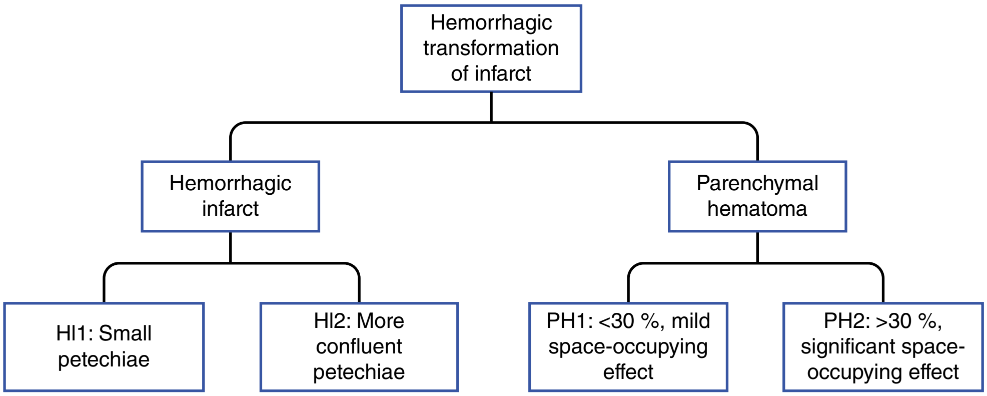
Hemorrhagic transformation of infarct
Hemorrhagic infarct
Parenchymal hematoma
HI1: Small petechiae
HI2: More confluent petechiae
PH1: <30 %, mild space-occupying effect
PH2: >30 %, significant space-occupying effect

Infarction from Septic Emboli

This is a subset of embolic infarctions, mostly seen with intravenous drug abuse, infective endocarditis, and cardiac valve abnormalities. The most common MRI finding in early stages of septic emboli is that of ordinary embolic infarction. Eventually, changes related to infection show up, with disproportionate edema, enhancement, cerebritis, and finally frank abscess formation. Like other embolic infarctions, these show a higher tendency to bleed.

Watershed Infarction

Watershed or boundary zone infarctions occur from hypoperfusion at the junction between arterial territories and have two patterns (Fig. 18.13):

- *Superficial border zone*: These are infarctions of the cortex and adjacent white matter located at the boundary zone between leptomeningeal collaterals from adjacent

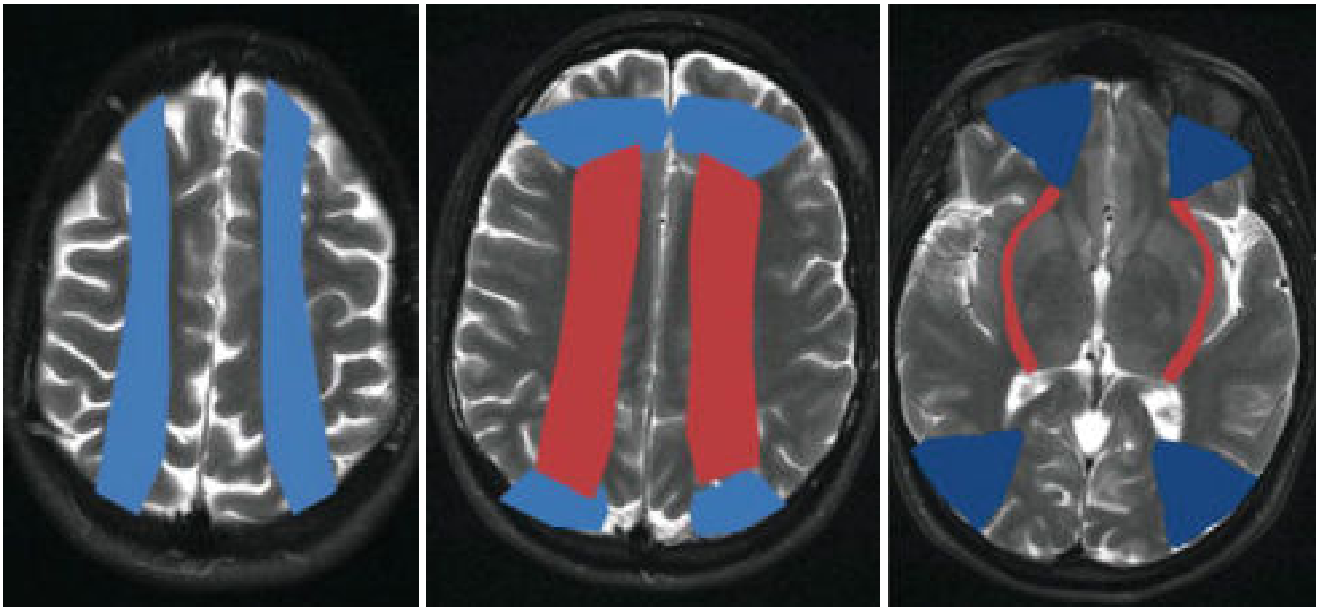

Fig. 18.13 Schematic representation of the superficial (*colored red*) and internal (*colored blue*) watershed zones in the cerebral hemispheres

arterial territories (ACA/MCA, MCA/PCA, and ACA/PCA).

- *Internal border zone*: They occur in the corona radiata and centrum semiovale, between lenticulostriate perforators and deep-penetrating cortical branches of the MCA and between deep white matter branches of the MCA and the ACA.

Infarct Evolution

Subacute stage approximately extends from 2 to 14 days following the initial ischemic event. In this stage, the infarcts become better circumscribed. Mass effect peaks by 3–5 days and then diminishes. When there is hemorrhagic transformation, MR signal characteristics of blood change with age. Contrast enhancement seen typically in this stage can be gyral or patchy (Fig. 18.14). It typically begins toward the end of the first week, when mass effect has resolved, and persists for approximately 6–8 weeks. This discordance between enhancement and mass effect is a useful radiologic observation, because enhancing lesions with significant mass effect are unlikely to represent cerebral infarction [9].

The chronic stage of cerebral infarction begins weeks to months after the initial ischemic event, when the integrity of the blood–brain barrier is restored and edema has resolved. The infarcts are smaller and better defined than seen in earlier stages and no longer enhance. Gliosis or encephalomalacia and volume loss are the hallmarks of this stage.

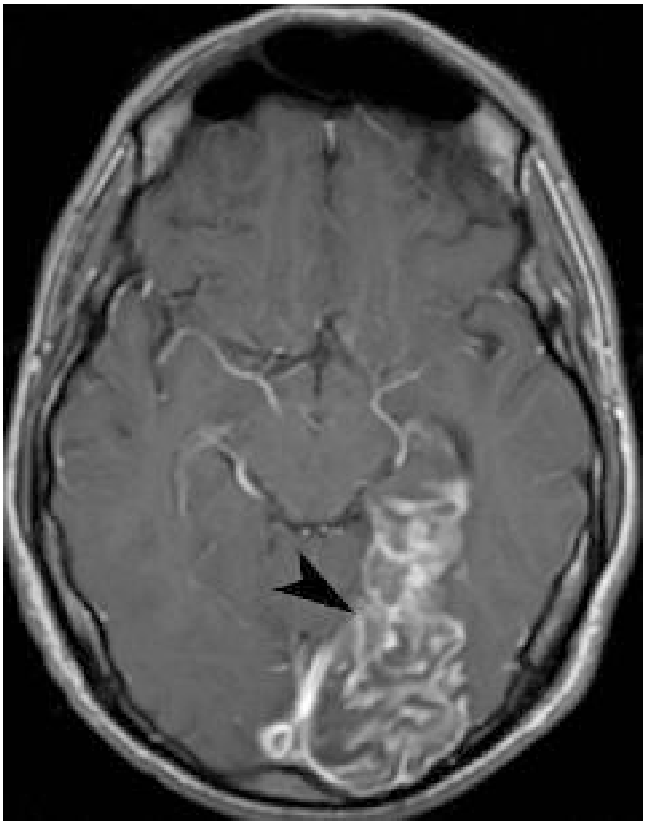

Fig. 18.14 Subacute infarction on MR. Contrast-enhanced T1-weighted image showing enhancing subacute infarct in left PCA territory (*arrowhead*)

Posttreatment Imaging

After treatment, CT is generally used to evaluate infarct progression or look for posttreatment hemorrhagic conversion. Special attention is paid to history and timing of any previous angiographic intervention, as dense contrast from this procedure can mimic blood.

Nontraumatic Intracranial Hemorrhage

Nontraumatic intracranial hemorrhage (ICH) accounts for about 15% of strokes in the USA. The hemorrhages are typically parenchymal or subarachnoid but may be subdural, intraventricular, or rarely epidural. Further discussion in this section is limited to parenchymal hemorrhage. Clinical presentation usually includes sudden-onset focal neurologic deficit, headache, altered mental status, nausea, and vomiting.

Etiology

The causes of nontraumatic and noninfarct-related parenchymal ICH include hypertension, vascular malformations, amyloid angiopathy, neoplasm, coagulopathies, drug abuse, anticoagulants, thrombolytics, and venous thrombosis. Rarer causes like vasculitis and reversible cerebral vasoconstrictive syndrome can also be considered (Table 18.4).

Hypertension is the most prevalent and modifiable risk factor for spontaneous ICH. The most frequent anatomic locations for hypertensive ICH are the putamen (Fig. 18.15), globus pallidus, external capsule, subcortical white matter, thalamus, internal capsule, and in the cerebellum and brain stem. On CT, the presence of white matter microvascular ischemic changes and lacunar infarcts may be associated with hypertension as the underlying cause of the acute hemorrhage.

Table 18.4 Etiologies of nontraumatic ICH

Hypertension (most common)
Vascular malformations
Amyloid angiopathy
Neoplasm
Coagulopathies
Drug abuse
Anticoagulants
Thrombolytics
Venous thrombosis
Vasculitis
Reversible cerebral vasoconstrictive syndrome

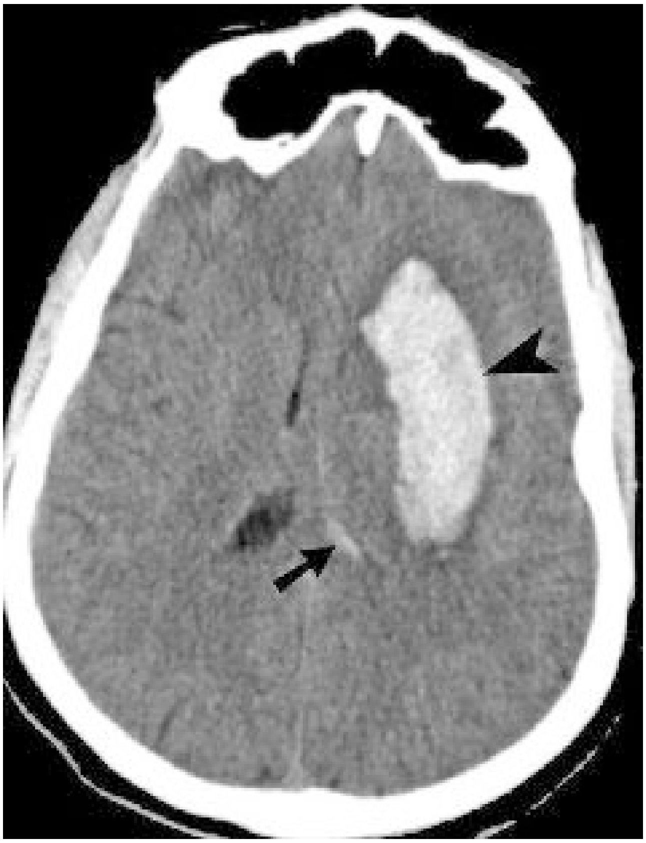

Fig. 18.15 Hypertensive hemorrhage. Noncontrast CT of the head demonstrates intraparenchymal hypertensive hemorrhage (*arrowhead*) in the left basal ganglia region with small intraventricular extension (*arrow*)

Cerebral amyloid angiopathy refers to the deposition of β-amyloid in small- and midsized arteries (and less frequently veins) of the cerebral cortex and the leptomeninges. Its prevalence is approximately 5%–8% in people in the seventh decade and 55%–60% of people who are 90 years or older [10]. It has been reported to account for 5%–20% of nontraumatic cerebral hemorrhages in elderly patients [11]. The hemorrhages are typically lobar (parieto-occipital predominance) of different ages and affect elderly normotensive patients.

In a population-based study, 12% of all cases of ICH were on anticoagulation medications at the time of their hemorrhage, compared with only 4% of age-, race-, and gender-matched control [12].

Vascular malformations are the leading cause of spontaneous ICH in young adults. Arteriovenous malformations (AVMs) and cavernous malformations (CMs) account for most of the clinically evident hemorrhages. Brain tumors may have associated ICH, in up to 15% of patients, but rarely is hemorrhage the presenting symptom of a previously undiagnosed brain mass [13]. Hemorrhagic primary brain tumors are generally high-grade tumors like glioblastoma multiforme and anaplastic astrocytoma. The intracerebral metastases that are most likely to hemorrhage are those caused by choriocarcinoma, melanoma, thyroid carcinoma, and renal cell carcinoma. However, most hemorrhagic metastases are caused by breast and lung carcinomas, as they are more common causes of brain metastases in the general population.

Illicit drugs associated with ICH include cocaine, amphetamines, phenylpropanolamine, phencyclidine, ephedrine, and pseudoephedrine. The predominant underlying mechanism is abrupt hypertension or in some cases vasculitis. Appearance on brain imaging is similar to long-standing hypertension, but they usually occur in younger patients.

Hemorrhage from cerebral venous thrombosis is typically cortical in location, with subcortical extension [14]. Flame-shaped irregular zones of lobar hemorrhage in the parasagittal frontal and parietal lobes are typical findings in superior sagittal sinus thrombosis, whereas hemorrhage in the temporal or occipital lobes is more typical of transverse sinus thrombosis.

Imaging Evaluation

Noncontrast CT of the head is generally the initial investigation given the wide availability and high sensitivity for acute hemorrhage. Acute hematoma is hyperdense on CT with density between 50 and 70 Hounsfield units. After the third day, the blood density gradually decreases from periphery to the central region. CT also provides information on the location, size, intraventricular extension, mass affect, hydrocephalus, or midline shift.

Contrast-enhanced MR imaging is the next imaging step in the subset of patients to evaluate for an underlying lesion. MR imaging of hemorrhage is more complex than CT, and the signal characteristics of the hematoma vary with its age (Table 18.5). Gradient-recalled echo or susceptibility-weighted sequences are sensitive for the detection of hemorrhage. Five stages of hemorrhage can be identified by MRI.

An important role of imaging is to evaluate for an underlying lesion. Heterogeneity of the hematoma (Fig. 18.16), enhancing component, hypodense filling defect on CT (Fig. 18.17), disproportionate surrounding edema, unusual or lobar location, unusual age, known primary tumor, additional enhancing lesions, abnormal calcification, and incomplete peripheral hypointense rim on T2 images suggest an underlying mass lesion. Contrast-enhanced MRI is more sensitive in the detection of enhancing tumor component in or adjacent to the hematoma. Follow-up imaging may show delayed evolution of blood breakdown products, persistent edema, mass effect, or serpiginous flow voids. The underlying lesion may become more apparent as the hematoma resolves.

Table 18.5 MR findings of hemorrhagic products

Stage of hematoma	Time	Signal on T1WI	Signal on T2WI
Hyperacute	First 6 h	Low	High
Acute	Up to 3 days	Iso to low	Low
Early subacute	4–7 days	High	Low
Late subacute	1 week to several months	High	High
Chronic	Months to years	Low	Low

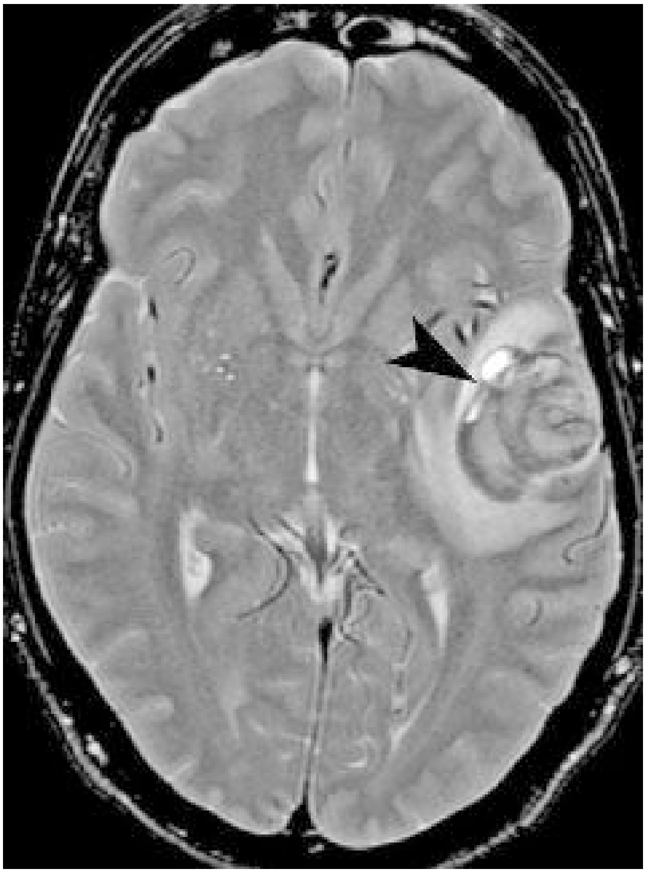

Fig. 18.16 Hemorrhagic primary intracranial tumor. T2-weighted image shows marked heterogeneity (*arrowhead*) of the hematoma in a patient with hemorrhagic glioblastoma multiforme

Underlying vascular malformation may be suggested by younger age of the patient and prominent vessels or linear calcification adjacent to the hematoma (Figs. 18.18 and 18.19). Catheter angiography is used to diagnose small AVMs that may be occult on both CT and MR, to fully characterize an AVM, and to perform therapeutic intervention. Repeat angiography after resorption of the hematoma is appropriate in selected patients with a high index of suspicion and a negative initial cerebral angiogram [11]. Cavernomas show characteristic "popcorn ball" morphology on MRI with complete T2 hypointense rim.

The direct signs of cerebral venous thrombosis can be seen on noncontrast CT (sensitivity of about 33%) and include visualization of hyperattenuating thrombus in

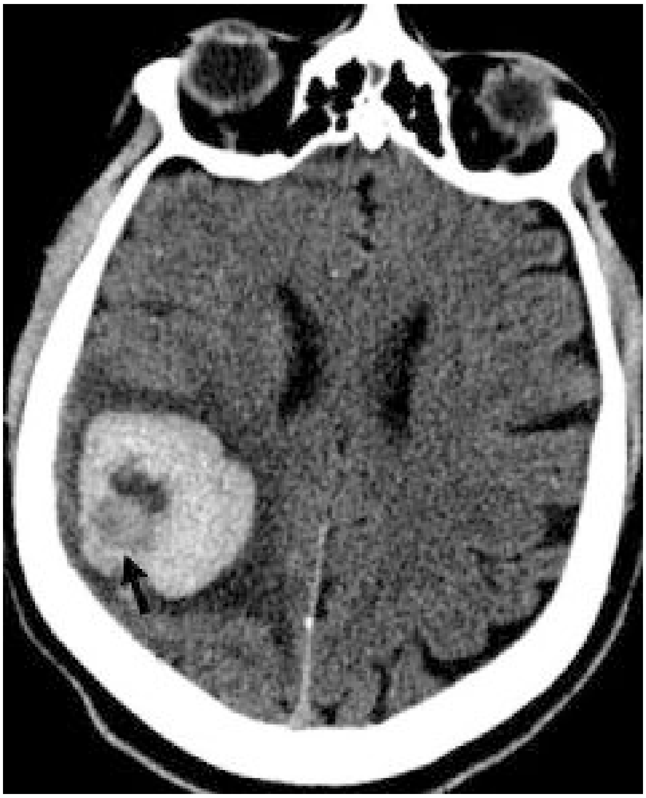

Fig. 18.17 Hemorrhagic metastatic melanoma. Noncontrast CT shows eccentric relatively hypodense mass within the hematoma (*arrow*) in a patient with known melanoma

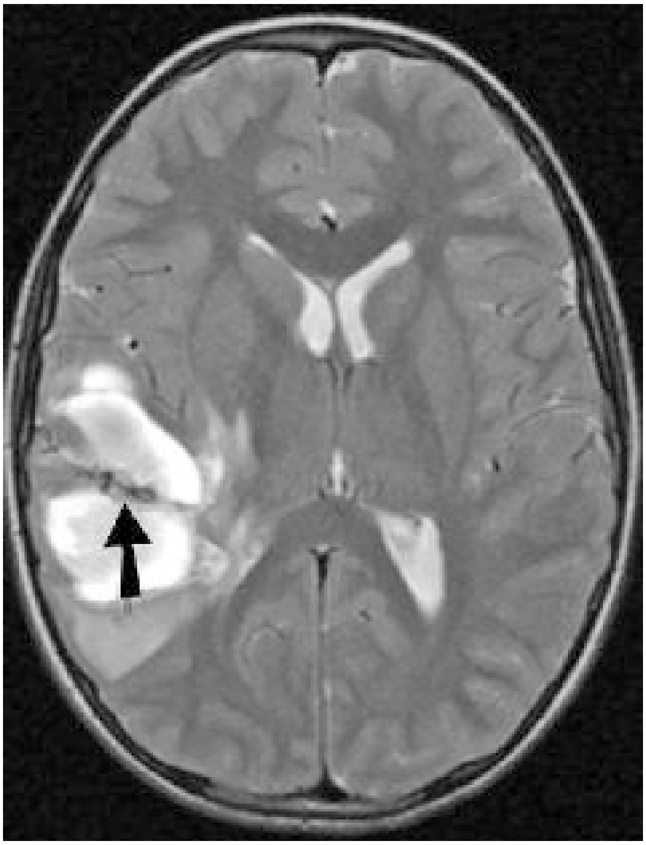

Fig. 18.18 Hemorrhagic AVM. T2-weighted sequence shows hyperintense subacute hematoma. Flow voids from vessels (*arrow*) are seen within the hematoma, suggesting the presence of an underlying vascular abnormality

Fig. 18.19 Arteriovenous malformation. (**a**) T2-weighted MR demonstrates extensive signal voids in the left occipital lobe arteriovenous malformation. (**b**) A subsequent CT demonstrates intraparenchymal hemorrhage in the left occipital lobe

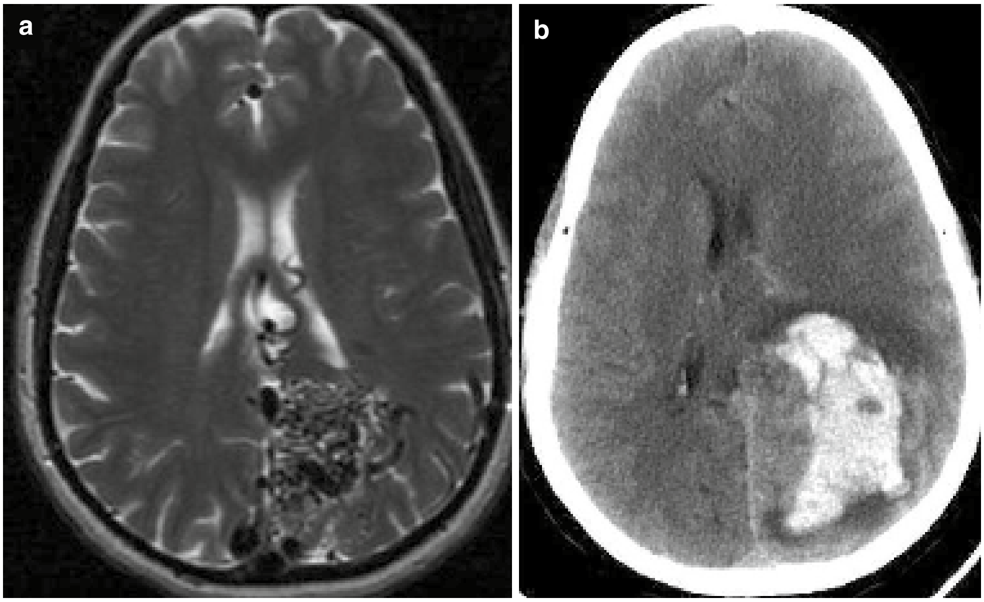

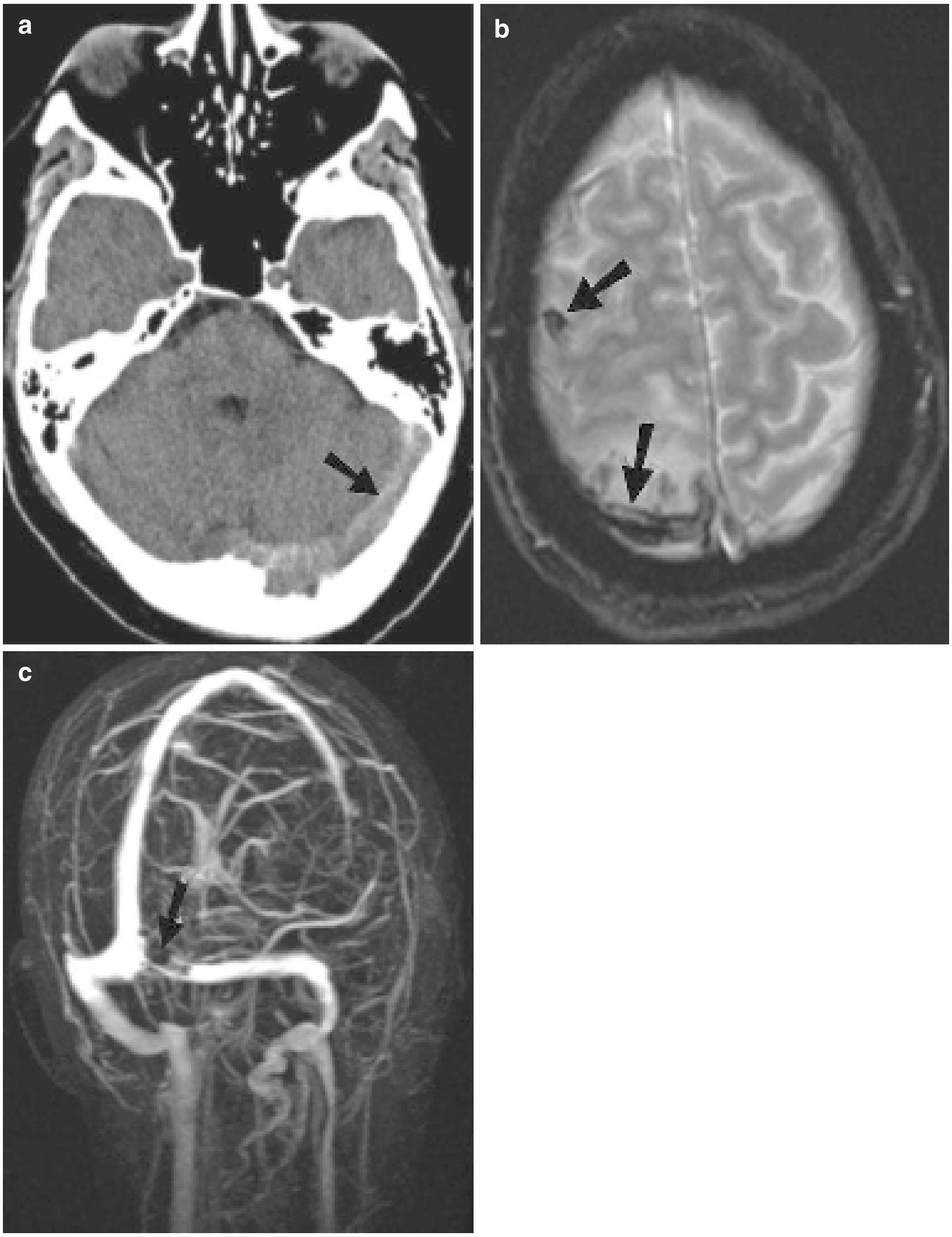

Fig. 18.20 Venous thrombosis, different patients. (**a**) Noncontrast CT shows hyperdense left transverse sinus, (*arrow*), secondary to thrombosis. (**b**) Gradient echo T2-weighted MR sequence shows blooming of thrombosed cortical veins (*arrows*). (**c**) MR venogram shows a focal filling defect within proximal left transverse sinus, from intraluminal thrombus

dural sinus (dense clot sign) (Fig. 18.20) [15]. The "cord sign" represents direct visualization of a hyperattenuating thrombosed cortical vein. Given this limited sensitivity of noncontrast CT, if the location of hematoma or the clinical features raise the possibility of venous thrombosis, further evaluation should be done by MRI and MRV or CTV. Contrast-enhanced CT can show "the empty delta sign," which represents the filling defect (nonenhancing thrombus) surrounded by the enhancing dural sinus wall. On MRI, thrombosed veins bloom on gradient-recalled images. There may also be intraluminal abnormal signal in the vein depending on the stage of the thrombus. Venographic techniques better demonstrate the thrombus and also show venous collaterals and resultant adjacent dural enhancement. Catheter angiogram can be done for confirmation and intervention.

Subarachnoid Hemorrhage

Subarachnoid hemorrhage (SAH) is most commonly of traumatic etiology, but in 85% of nontraumatic SAH cases, it occurs due to ruptured aneurysm [11]. Risk factors for aneurysmal SAH include smoking and hypertension, and it occurs more frequently in females. Less common causes include AVM, vasculitis, venous thrombosis, reversible cerebral vasoconstriction syndrome, and extension of parenchymal/intraventricular hemorrhage into subarachnoid space [16]. Saccular aneurysm is the most common type of cerebral aneurysm. Fusiform aneurysms are less common and are most often the result of atherosclerosis and dissection or found in association with congenital conditions. Septic emboli may result in mycotic aneurysms which are typically small and located in distal arterial branches. Aneurysms can be seen in feeding arteries, nidus, or draining veins of AVM. Common presenting symptoms include severe headache, vomiting, seizure, nuchal rigidity, focal neurological deficit, and altered level of consciousness.

Aneurysms are considered to be acquired lesions, occurring most frequently at the vascular bifurcations. The common locations of aneurysms are anterior communicating artery, clinoid/supraclinoid ICA, middle cerebral artery bifurcation or trifurcation, basilar artery (tip and the origin of superior cerebellar arteries), and vertebral artery (at the origin of the posterior inferior cerebellar arteries). Incidence of unruptured aneurysm is about 5% [17]. When the aneurysms are multiple, the distribution of SAH and irregular/lobulated contour of the aneurysm are helpful in determining the ruptured aneurysm.

Approximately 10%–15% of patients with SAH secondary to aneurysm rupture die before reaching the medical care, and 25% of the rest die over the succeeding 2 weeks [18]. The risk of rebleeding in untreated aneurysm is about 4% within the first 24 h, 20% within 2 weeks, and 50% within 1 month [19].

Imaging Evaluation

The cornerstone of the diagnosis is a noncontrast head CT, which has a diagnostic yield of approximately 90%. SAH is seen as diffuse hyperdensity in subarachnoid space (Figs. 18.21 and 18.22). If hemorrhage is brisk, focal hematoma may form in the subarachnoid space. Careful attention should be paid to areas where a small amount of blood can be easily overlooked, such as posterior aspects of the Sylvian fissures, interpeduncular cistern, deep cerebral sulci, occipital horns of the lateral ventricles, and foramen magnum.

Exuberant inflammatory exudates in the subarachnoid space and recent iodinated contrast administration can result in subarachnoid hyperdensity and mimic SAH. Diseases causing diffuse cerebral edema as well as intracranial mass lesions and severe obstructive hydrocephalus can result in an appearance similar to SAH due to apposition of pial surfaces and resultant engorgement of pial veins [20].

Distribution of SAH, focal clot in subarachnoid space, and parenchyma hematoma may help in localization of ruptured aneurysm on NCT. The aneurysm may be seen as a relatively hypodense area within the dense SAH. On CT, SAH generally resolves by 5–7 days. Smaller bleeds may resolve earlier. Focal clot, if present, may persist for a longer time.

Generally, a lumbar puncture is performed to evaluate for xanthochromia in patients who have suspected SAH and a negative CT scan. Xanthochromia is representative of the presence of bilirubin in the CSF and requires at least 12 h to develop [18].

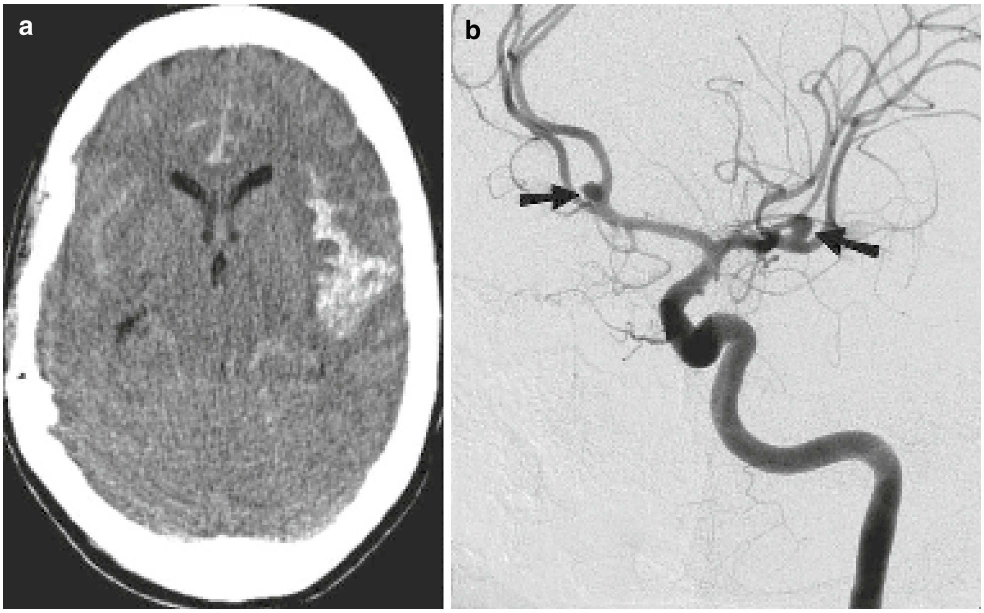

Fig. 18.21 Subarachnoid hemorrhage from ruptured circle of Willis aneurysm. (**a**) Noncontrast shows bilateral subarachnoid hemorrhage, most prominently involving the left Sylvian fissure. (**b**) Subsequent digital subtraction angiogram shows left MCA and anterior communicating artery aneurysms (*arrows*). Given the focal hematoma in left Sylvian fissure and lobulated contour, left MCA aneurysm is likely the source of bleeding

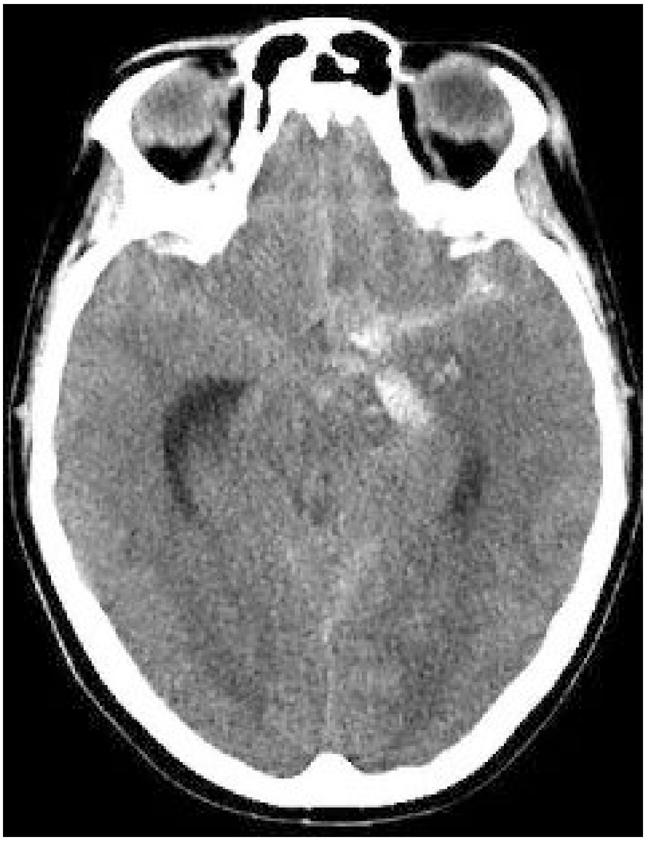

Fig. 18.22 Ruptured left ICA aneurysm. Noncontrast CT demonstrates subarachnoid hemorrhage in the left basal cisterns

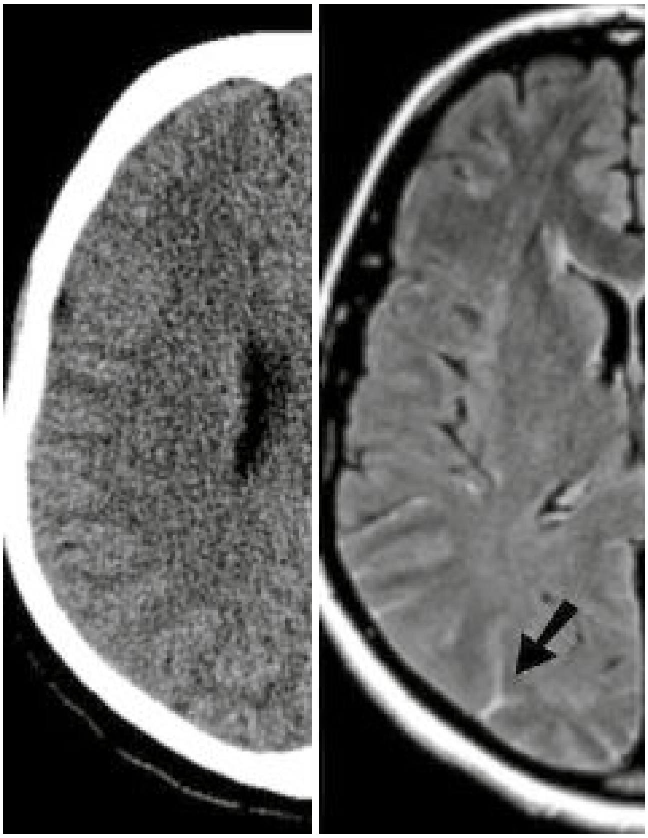

Fig. 18.23 Subacute SAH. Noncontrast CT fails to show sulcal hyperdensity, but FLAIR image clearly shows sulcal hyperintensity from subarachnoid hemorrhage (*arrow*)

Computed Tomography Angiography (CTA)

CTA is generally the next investigation in SAH evaluation. The sensitivity of multidetector CTA is reported to be 94.8% and the specificity 95.2% for the detection on a per aneurysm basis and 99.0% and 95.2% on a per patient basis, respectively [21]. In this study, a cutoff size of 2 mm was found as the inflection point at which CTA became less able to detect aneurysms. CTA demonstrates the location of aneurysm and evaluates for the presence of thrombus and wall calcification. On CTA, saccular aneurysm is seen as rounded contrast-filled outpouching of the vessel wall.

MRI

SAH has different MR imaging features than other intracranial hemorrhages. This is due to mixing of blood with CSF and resultant dilution, antifibrogenic elements in CSF, and relatively high oxygen saturation of CSF (which limits the amount of paramagnetic deoxyhemoglobin) [17]. Due to relative lack of magnetic inhomogeneity of SAH, gradient-recalled images are less sensitive for the detection of SAH. T2-weighted fluid-attenuated inversion recovery (FLAIR) is the most sensitive sequence for SAH and shows subarachnoid hyperintensity. Larger amount of blood can demonstrate blooming on gradient-recalled images. Also, T1 images may show slight inhomogeneity of CSF with mild hyperintensity. FLAIR is comparable in its sensitivity to CT in the detection of acute SAH. In our experience, it is better than CT in subacute stage (Fig. 18.23). However, FLAIR is prone to artifacts, especially in the posterior fossa and adjacent to metallic hardware. Also, other leptomeningeal inflammatory and neoplastic processes can result in subarachnoid hyperintensity in FLAIR images. SAH also causes reactive contrast enhancement in the meninges.

Magnetic Resonance Angiography (MRA)

The reported sensitivity of MRA in the detection of aneurysms 3 mm or larger is 90%, but this number falls precipitously for smaller aneurysms with reported sensitivity of less than 40%. MRA may be impractical in acute settings as most of the patients are ill and may not be able to lay still. This is a good modality to follow up unruptured aneurysms.

Catheter Angiogram

This is the gold standard for aneurysm evaluation. If there is high suspicion for SAH and the noninvasive imaging fails to show an aneurysm, DSA should be done for further evaluation.

Angiogram can be negative in up to 10% of SAH, possibly due to vasospasm or clot filling up the aneurysm. A repeat catheter angiogram is usually performed at about the seventh day to look for aneurysms missed on the first study.

Vasospasm

After initial treatment and diagnosis of SAH, clinical deterioration can occur due to recurrent hemorrhage, hydrocephalus, vasospasm, and stroke. Vasospasm represents the leading cause of mortality and usually begins approximately 3 days after the initial bleed [17]. The proposed causes of SAH include reactive vasoconstriction, decreased vascular autoregulation, reversible vasculopathy, and relative hypovolemia [22]. The radiologic findings often precede such clinical deficits and thus offer the opportunity to potentially intervene to prevent neurologic injury.

The methods for diagnosing vasospasm include transcranial Doppler (TCD) ultrasonography, CTA, CTP, and DSA (gold standard). The validity of TCD as a monitor for VS has been controversial and is best, an adjunct to other tests. CTA has relatively good sensitivity and specificity in discovering severe VS of proximal arteries (Fig. 18.24a). It also has a high negative predictive value. MTT is reported to be the most helpful perfusion CT parameter for the diagnosis of vasospasm (see Fig. 18.24b) [21]. DSA is the gold standard for the diagnosis of vasospasm. Endovascular treatment options for vasospasm include intra-arterial vasodilator and angioplasty.

Stroke imaging has made significant progress in the last several years and is evolving. With technologic advances, together with better anatomic depiction, increased emphasis will be on functional imaging to determine tissue viability and appropriateness of therapy.

Teaching Points

- Goals in acute stroke imaging are to assess parenchyma, pipes, perfusion, and penumbra.
- CT signs of early ischemia include dense artery sign, loss of gray-white differentiation, and hypodensity.
- The most sensitive imaging sequence for detecting ischemia is DWI, with changes in acute infarction detected within minutes of onset of the symptoms.
- Noncontrast CT of the head is generally the initial investigation given the wide availability and high sensitivity for acute hemorrhage.
- Contrast-enhanced MR imaging is the next imaging step in acute hemorrhage to evaluate for an underlying lesion.

Questions

1. Which of the following hemorrhagic transformation is associated with worse clinical outcome after stroke onset?
   (A) HI1
   (B) HI2
   (C) PH1
   (D) PH2
   Answer: D

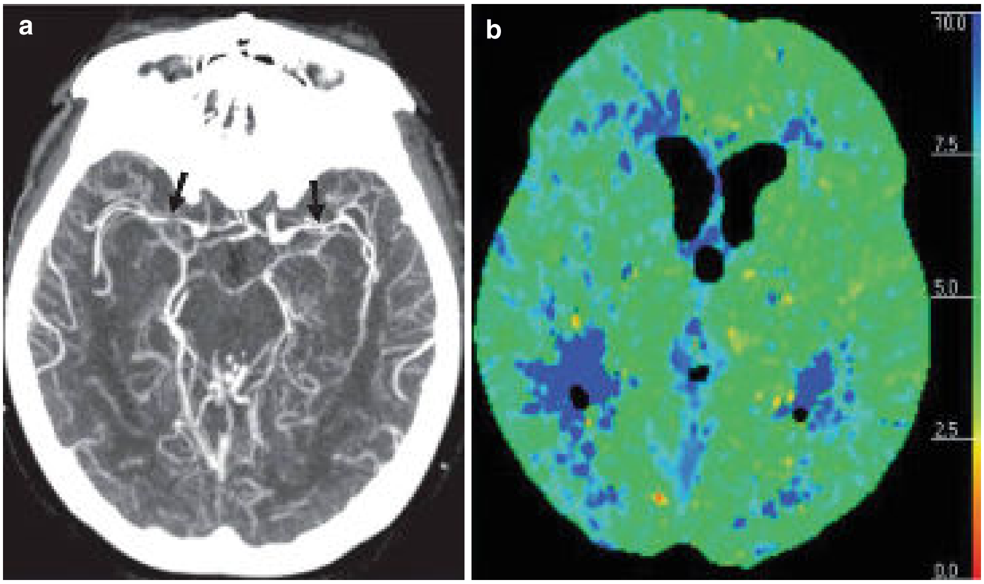

Fig. 18.24 Intracranial vasospasm. (**a**) CT angiogram shows vasospasm in bilateral middle cerebral arteries (*arrows*) and bilateral proximal posterior cerebral arteries. (**b**) Mean transit time (MTT) map from CT perfusion study shows prolonged MTT, more so on the left

2. What is the most common cause of nontraumatic ICH?
   (A) Smoking
   (B) Hypertension
   (C) Diabetes
   (D) Vascular malformations
   Answer: B

3. Which is the "reference standard" to exclude hemorrhage in acute stroke prior to thrombolytic therapy?
   (A) NECT
   (B) Susceptibility-weighted MR imaging
   (C) NIH stoke scale
   (D) Presence of headache
   Answer: A

4. Which is the best measure of infarct volume that aids in the decision for thrombolytic therapy?
   (A) Well-formed hypodensity on NECT
   (B) Hypoenhancement in arterial territory in source CTA images
   (C) Diffusion-weighted MR imaging
   (D) Markedly reduced CBV on perfusion study
   Answer: C

5. What Is True Regarding Nontraumatic SAH?
   (A) MRI has poor sensitivity
   (B) Vasospasm is most common between 3 and 10 days
   (C) Perimesencephalic bleed commonly results from aneurysm in anterior inferior cerebellar artery
   (D) Most of the causative aneurysms are congenital in origin

Answer: B

6. Which of the following imaging feature suggests a lesion underlying a parenchymal hemorrhage?
   (A) Marked heterogeneity
   (B) Contrast-enhancing component
   (C) Hypodense filling defect on CT
   (D) All the above
   Answer: D

References

1. Young JY, Schaefer PW. Acute ischemic stroke imaging: a practical approach for diagnosis and triage. Int J Card Imaging. 2016;32(1):19–33.
2. Rowley HA. The four ps of acute stroke imaging: parenchyma, pipes, perfusion, and penumbra. AJNR Am J Neuroradiol. 2001;22(4):599–601.
3. Srinivasan A, Goyal M, Al Azri F, Lum C. State-of-the-art imaging of acute stroke. Radiographics. 2006;26(Suppl 1):S75–95.
4. Burdette JH, Ricci PE, Petitti N, Elster AD. Cerebral infarction: time course of signal intensity changes on diffusion-weighted MR images. AJR Am J Roentgenol. 1998;171(3):791–5.
5. Huang IJ, Chen CY, Chung HW, Chang DC, Lee CC, Chin SC, et al. Time course of cerebral infarction in the middle cerebral arterial territory: deep watershed versus territorial subtypes on diffusion-weighted MR images. Radiology. 2001;221(1):35–42.
6. Eastwood JD, Engelter ST, MacFall JF, Delong DM, Provenzale JM. Quantitative assessment of the time course of infarct signal intensity on diffusion-weighted images. AJNR Am J Neuroradiol. 2003;24(4):680–7.
7. Hacke W, Kaste M, Fieschi C, Toni D, Lesaffre E, von Kummer R, et al. Intravenous thrombolysis with recombinant tissue plasminogen activator for acute hemispheric stroke. The European Cooperative Acute Stroke Study (ECASS). JAMA. 1995;274(13):1017–25.
8. Berger C, Fiorelli M, Steiner T, Schabitz WR, Bozzao L, Bluhmki E, et al. Hemorrhagic transformation of ischemic brain tissue: asymptomatic or symptomatic? Stroke. 2001;32(6):1330–5.
9. Atlas SW. Magnetic resonance imaging of the brain and spine. Philadelphia: Lippincott Williams & Wilkins; 2008.
10. Masuda J, Tanaka K, Ueda K, Omae T. Autopsy study of incidence and distribution of cerebral amyloid angiopathy in Hisayama, Japan. Stroke. 1988;19(2):205–10.
11. Fischbein NJ, Wijman CA. Nontraumatic intracranial hemorrhage. Neuroimaging Clin N Am. 2010;20(4):469–92.
12. Woo D, Sauerbeck LR, Kissela BM, Khoury JC, Szaflarski JP, Gebel J, et al. Genetic and environmental risk factors for intracerebral hemorrhage: preliminary results of a population-based study. Stroke. 2002;33(5):1190–5.
13. Salmaggi A, Erbetta A, Silvani A, Maderna E, Pollo B. Intracerebral haemorrhage in primary and metastatic brain tumours. Neurol Sci. 2008;29(Suppl 2):S264–5.
14. Leach JL, Fortuna RB, Jones BV, Gaskill-Shipley MF. Imaging of cerebral venous thrombosis: current techniques, spectrum of findings, and diagnostic pitfalls. Radiographics. 2006;26(Suppl 1):S19–41; discussion S42–3;
15. Poon CS, Chang JK, Swarnkar A, Johnson MH, Wasenko J. Radiologic diagnosis of cerebral venous thrombosis: pictorial review. AJR Am J Roentgenol. 2007;189(6 Suppl):S64–75.
16. Linn FH, Rinkel GJ, Algra A, van Gijn J. Incidence of subarachnoid hemorrhage: role of region, year, and rate of computed tomography: a meta-analysis. Stroke. 1996;27(4):625–9.
17. Yousem DM, Grossman RI. Neuroradiology: the requisites. 3rd ed. Philadelphia: Mosby; 2010.
18. Manno EM. Subarachnoid hemorrhage. Neurol Clin. 2004;22(2):347–66.
19. Kassell NF, Torner JC, Haley EC Jr, Jane JA, Adams HP, Kongable GL. The international cooperative study on the timing of aneurysm surgery. Part 1: overall management results. J Neurosurg. 1990;73(1):18–36.
20. Provenzale JM, Hacein-Bey L. CT evaluation of subarachnoid hemorrhage: a practical review for the radiologist interpreting emergency room studies. Emerg Radiol. 2009;16(6):441–51.
21. Wintermark M, Ko NU, Smith WS, Liu S, Higashida RT, Dillon WP. Vasospasm after subarachnoid hemorrhage: utility of perfusion CT and CT angiography on diagnosis and management. AJNR Am J Neuroradiol. 2006;27(1):26–34.
22. Marshall SA, Kathuria S, Nyquist P, Gandhi D. Noninvasive imaging techniques in the diagnosis and management of aneurysmal subarachnoid hemorrhage. Neurosurg Clin N Am. 2010;21(2):305–23.

19

Imaging of Acute Orbital Pathologies

Mohammad Mansouri, Khyati Bidani, and Ajay Singh

Introduction

There are 30,000 hospital admissions per year secondary to traumatic eye injuries, which occur commonly in patients with blunt or penetrating facial trauma. Majority of the traumas are secondary to motor vehicle collision or sports-related injury. Ocular trauma accounts for 7.5% for eye admissions in the hospitals and 3% of all emergency room visits in the USA [1]. Ocular trauma is the leading cause of noncongenital unilateral blindness in <20-year-olds and overall the second leading cause of blindness. It is estimated that eye injuries result in blindness in 1.6 million people and unilateral blindness or decreased vision in about 19 million people each year. Open-globe injury risk is highest for young adults and lowest for seniors [2].

Patients with significant eye injuries may have grossly normal eyes on physical exam and may subsequently become apparent. Prompt diagnosis is important in preserving visual acuity and preventing complications.

Traumatic injuries range from simple ecchymosis of the eyelid and subconjunctival hemorrhage to more serious lesions, including hyphema, choroidal or retinal rupture, optic nerve contusion, and rupture of the globe. Most common ocular injuries are superficial corneal ulcerations and foreign bodies. The more serious injuries include globe rupture, anterior chamber hemorrhage possibly complicated by glaucoma, intraocular foreign body, corneal perforation, post-traumatic cataract, and retinal detachment (RD). The most common trauma histories are motor vehicle accidents, sports-related accidents, industrial accidents, falls, and violent trauma.

Classification and Mechanism

The visual pathway traumatic injuries by location can be divided into:

1. Intraocular
2. Intraorbital
3. Intracanalicular
4. Intracranial

Normal Anatomy (Fig. 19.1)

Orbit is a pyramid-shaped structure, constituted by seven bones. The medial wall is the thinnest and has four bones, namely, frontal process of maxilla, lacrimal bone, sphenoid, and lamina papyracea of the ethmoid. The lateral wall is constituted by the sphenoid wings and zygoma. The orbital roof is constituted by the orbital process of the frontal bone and lesser wing of the sphenoid. The floor is the weakest wall, constituted by maxilla, zygoma, and palatine bones.

Anterior chamber (AC) is crescent shaped between the lens and the cornea, measuring 2.5–3.5 mm in depth (see Fig. 19.1). It is isointense to the vitreous on T1- and T2-weighted sequences. The posterior chamber lies between the posterior surface of the iris and anterior surface of the vitreous.

The vitreous constitutes two-thirds volume of the eye (4 cm^3) and serves as the shock absorber. Because of 98% water content, it has longer relaxation times than most tissues but shorter than that of water.

The intraocular lens measures 9 mm in diameter and 4 mm in thickness. Anterior to the lens is the aqueous humor and posterior to the lens is the vitreous humor. It is the least hydrated organ (67%) in the body and is therefore darker on MRI than surrounding tissues.

M. Mansouri · K. Bidani
Department of Radiology, Massachusetts General Hospital, Boston, MA, USA

A. Singh (✉)
Division of Emergency Radiology, Department of Radiology, Massachusetts General Hospital, Boston, MA, USA

Harvard Medical School, Massachusetts General Hospital, Boston, MA, USA
e-mail: asingh1@partners.org

© The Author(s), under exclusive license to Springer Nature Switzerland AG 2024

A. Singh (ed.), *Emergency Radiology*, https://doi.org/10.1007/978-3-031-65770-2_19

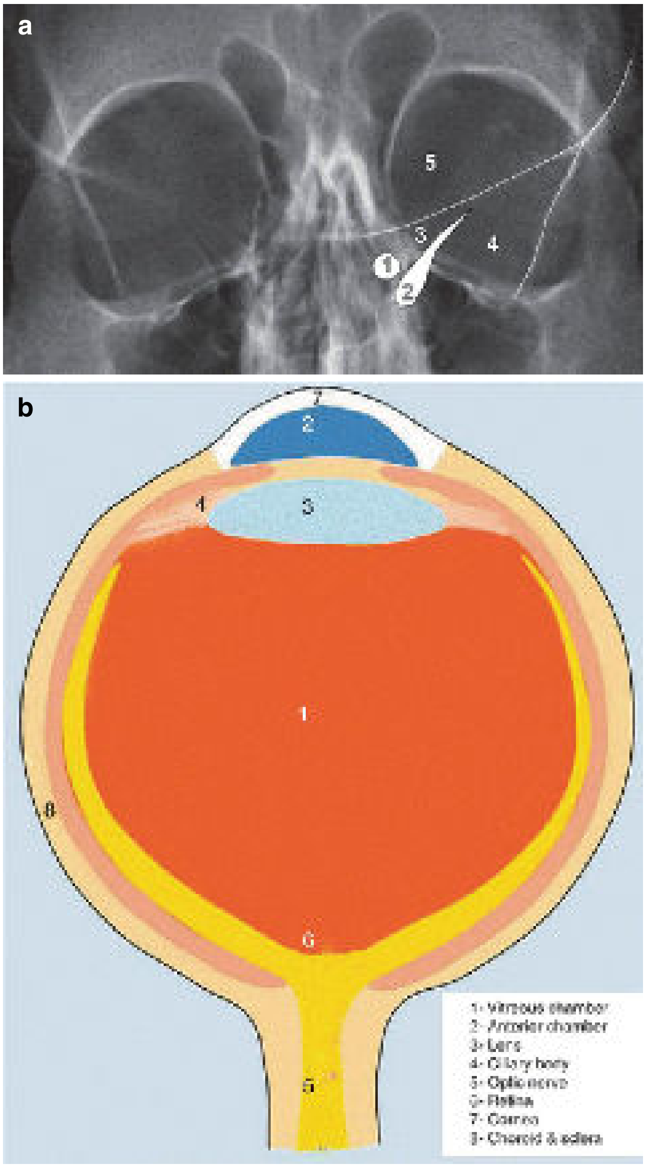

Fig. 19.1 Normal orbital and ocular anatomy. (**a**) Plain radiograph (Waters' view) demonstrates osseous anatomy. The superior orbital fissure (*2*) separates the roof from the lateral wall of the orbit. The lateral wall of the orbit is constituted by the greater wing of the sphenoid (*4*). The roof is constituted by the orbital plate of the frontal bone (*5*) and lesser wing of the sphenoid (*3*). The optic canal (*1*) is located in the roof, within the lesser wing of the sphenoid. The floor is separated from the lateral wall by the inferior orbital fissure. (**b**) Drawing illustrates the axial anatomy of the globe. On imaging, it is not possible to distinguish sclera, choroids, and retina, unless retinal or choroidal detachment is present. The lens separates the aqueous humor from vitreous humor

The walls of the globe include sclera (outer layer), uvea (middle layer), and retina (inner layer). It is not possible to distinguish between these three layers on CT or MRI in normal eye. Tenon's capsule surrounds the eyeball from optic nerve to the ciliary muscle.

Imaging

Radiographic assessment of the orbits can detect two-thirds of the orbital fractures but has very limited sensitivity for soft tissue injuries. Ultrasound may demonstrate hyphema, lens dislocation, globe rupture, intraocular foreign bodies, and vitreous and retinal hemorrhage. However, ultrasound is contraindicated in patients where there is suspicion of globe rupture. MRI is not the primary modality in the evaluation of intraocular foreign body due to risk of damage by motion of a ferromagnetic foreign body and artifact produced by ferromagnetic foreign bodies. MRI is contraindicated if there is suspicion of metallic foreign body in the orbit. MRI can be used in patients with subtle open-globe injuries or organic foreign bodies that are difficult to see on CT.

CT is the modality of choice for traumatized eye and suspected ferromagnetic foreign body due to its wide availability in emergency departments, rapid scan time, no/minimal motion artifact, and high sensitivity in the detection of foreign bodies [3]. The presence of foreign bodies may cause artifacts and limit the imaging findings. Table 19.1 summarizes the advantages and disadvantages of imaging modalities in the assessment of orbit.

Table 19.1 Advantages and disadvantages of imaging modalities in the assessment of orbit

Imaging modalities	Advantages	Disadvantages
Radiography	Assessment of the orbital fractures or radiopaque foreign bodies	Low sensitivity Limited information on orbital soft tissue
US	Demonstrates – Hyphema – Lens dislocation – Globe rupture – Foreign bodies – Vitreous hemorrhage – Retinal hemorrhage	Contraindicated if globe rupture is suspected
CT	Modality of choice for traumatized eye and suspected ferromagnetic foreign body Widely available Rapid scan time Minimal motion artifacts High sensitivity	Ionizing radiation
MRI	Subtle open-globe injuries Organic foreign bodies	Contraindicated in metallic foreign-body suspicion Not widely available Time consuming Poor definition of bones

Imaging Protocol

CT: Orbital protocol (0.625–1.25 mm slice thickness)

- Noncontrast CT
- Performed as part of the facial CT in axial plane
- Sagittal and coronal reformations performed at 1 mm interval
- Soft tissue and bone algorithm reconstructions

MRI: Orbital protocol (3 mm slice thickness)

1. Axial and coronal T1 through orbits without fat sat
2. Coronal FSE T2 through orbits with fat sat
3. Post-gadolinium axial T1 with fat sat through orbits
4. Coronal T1 chiasm through globes with fat sat
5. Sagittal T1, axial FLAIR, axial T2, axial DWI through whole brain
6. Optional T1 axial through whole brain

Anterior Segment Injury and Lens Dislocation

Trauma accounts for more than half of the lens subluxation-dislocation. It is caused by disruption of the zonular attachments, which hold the lens in place. The lens is most commonly dislocated posteriorly, often lying in dependent vitreous humor. Spontaneous atraumatic dislocation, which is often bilateral, is associated with Marfan's syndrome, homocystinuria, sulfite oxidase deficiency, hyperlysinemia, ED syndrome, aniridia, and congenital glaucoma. Most patients with lens dislocation will have a pars plana vitrectomy/lensectomy with an intraocular lens implantation.

The patients with traumatic hyphema have hemorrhage in anterior chamber, usually from the tear of ciliary body and iris. Corneal lacerations are usually associated with penetrating trauma. Blunt trauma can disrupt the lens capsule, which leads to edema and cataract. Post-traumatic cataract is most often localized and not associated with significant loss of vision [4].

Imaging: Anterior chamber injuries are characterized by decrease in the depth of the anterior chamber, when compared with the normal eye. Hyphema on unenhanced CT may be seen as hyperattenuation in the anterior chamber. A dislocated lens is seen as high-attenuation lenticular structure in the vitreous on CT, where it is generally free floating (Figs. 19.2 and 19.3). A ruptured lens capsule often results in decreased attenuation and subtle increase in the size of the lens.

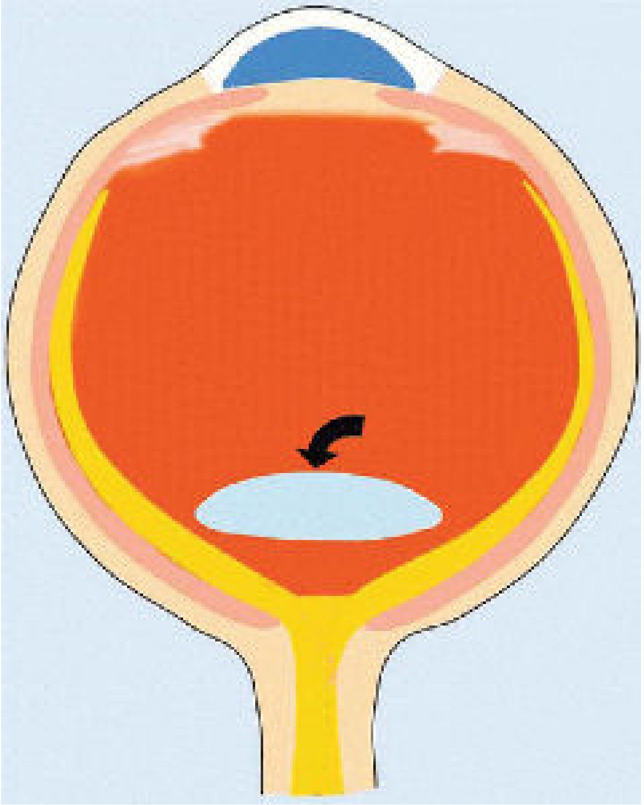

Fig. 19.2 Intraocular dislocation. Drawing illustrates the dislocated lens located posteriorly in the vitreous chamber

Fig. 19.3 Lens dislocation from penetrating trauma. (**a**) Axial CT shows posterior subluxation of the lens, increase in the depth of the anterior chamber, and vitreous hemorrhage (*arrowhead*). (**b**) Superior dislocation of the right lens (*arrowhead*) seen in a patient with right lateral orbital wall fracture and overlying soft tissue contusion from blunt trauma

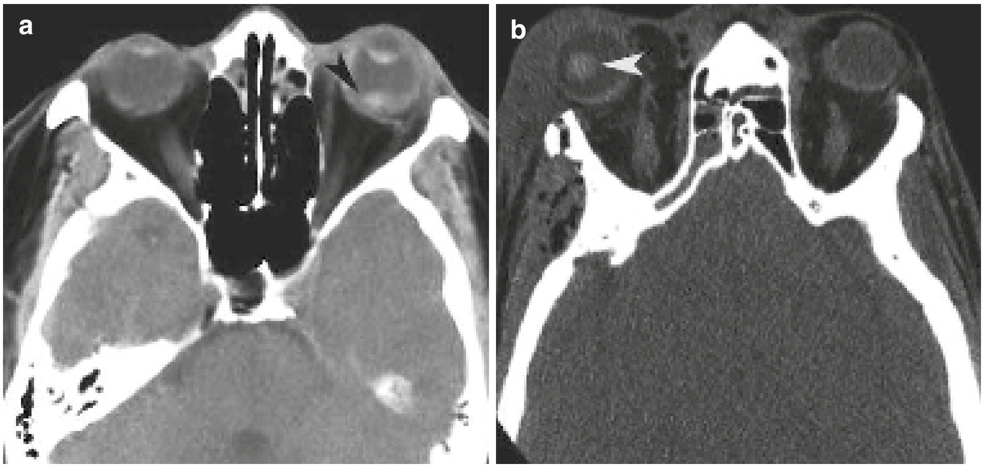

Open-Globe Injury

Traumatic rupture of the globe results in loss of vitreous and posterior displacement of lens, causing deepening of the anterior chamber. Vitreous prolapse is associated with retinal detachment (RD), iridodialysis or ciliary body cleft, and contusion cataract (41%) [5]. Globe ruptures (5% of blunt injuries) are associated with grades III and IV hyphema.

Superior nasal limbus is the most common site of globe rupture because lower temporal quadrant is the most exposed site to trauma. The risk of trauma-induced globe ruptures is highest in eyes after cataract surgery and in females. The rupture of the globe most often occurs at the site of insertion of intraocular muscles because the sclera is thinnest at this site.

Imaging: The CT findings of globe rupture include vitreous hemorrhage, globe contour deformity, obvious loss of globe volume, absence of lens, intraocular air/foreign body, scleral discontinuity, increased depth of anterior chamber, and RD/CD (Figs. 19.4, 19.5, 19.6, 19.7, and 19.8). Flat tire sign is characterized by flattening of the posterior contour of the globe due to posterior collapse of the sclera and volume loss in the vitreous chamber.

Because of the decompression of the vitreous chamber, the lens may move back without disruption of the zonular attachments. This finding is seen as asymmetrically deep anterior chamber on CT. Discrepancy in the depth of AC of 2 mm or more is abnormal. Absolute depth of AC measuring >5 mm is abnormal (normal AC depth = 2.5–3.5 mm). In the study by Arey et al., the sensitivity of CT to diagnose open-globe injury was 56–68%, and the positive predictive value was 86%–100% [6]. MRI has higher sensitivity and can be used when clinical suspicion remains despite a negative CT. US is contraindicated if open-globe injury is suspected.

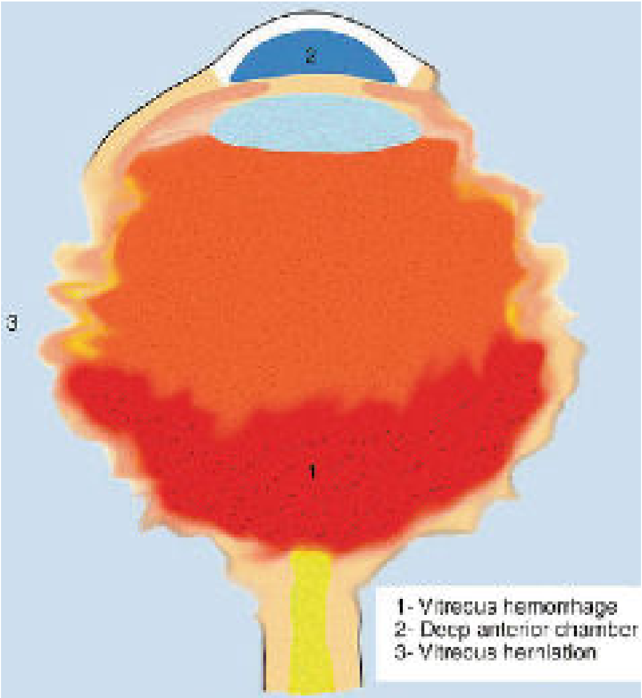

Fig. 19.4 Ruptured globe. Drawing illustrates the imaging findings of distorted outline of the globe, increase in the depth of the anterior chamber with posterior location of the lens, and vitreous hemorrhage

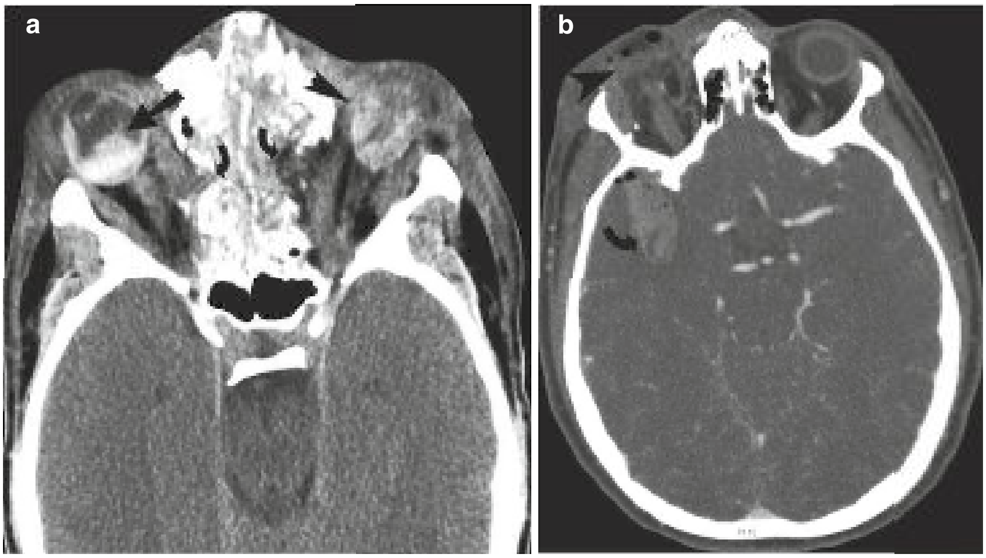

Fig. 19.5 Traumatic globe rupture. (**a**) Bilateral ruptured globes and orbital blowout fractures from wrench chain trauma. Axial CT shows bilateral open-globe injuries with vitreous hemorrhage. There is obvious distortion of the outline of the left globe (*arrowhead*). The right intraocular lens (*arrow*) is dislocated into the vitreous chamber. There are bilateral blowout fractures involving the medial orbital walls (*curved arrows*). (**b**) Axial CT demonstrates globe rupture caused by shrapnel from a pipe bomb explosion. There is gross contour deformity and deflation of the globe (*arrowhead*). There is intracranial hemorrhage (*curved arrow*) caused by the shrapnel

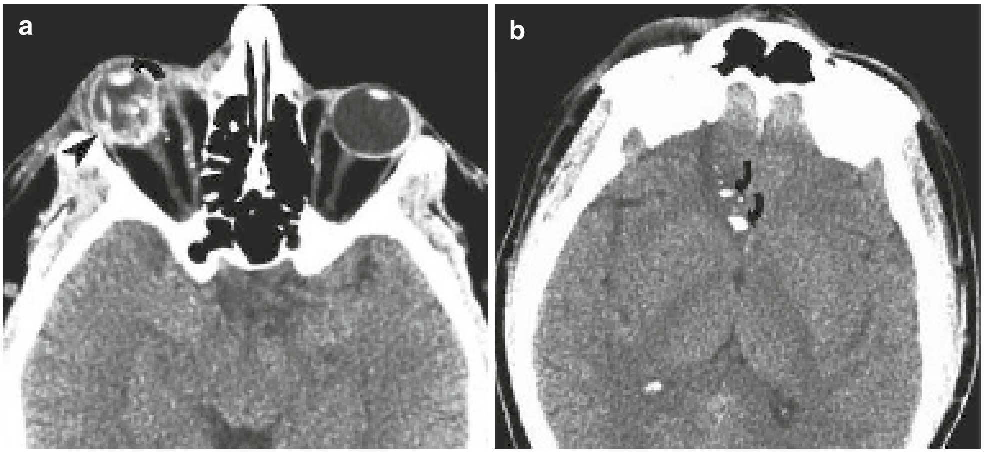

Fig. 19.6 Right globe rupture from bullet injury. (**a**) Axial CT shows increase in the depth of the anterior chamber (*curved arrow*), extensive vitreous compartment hemorrhage, and distortion in the shape of the globe (*straight arrow*). (**b**) Axial CT of the cerebral hemisphere shows the track of the bullet illustrated by bone fragments (*curved arrows*)

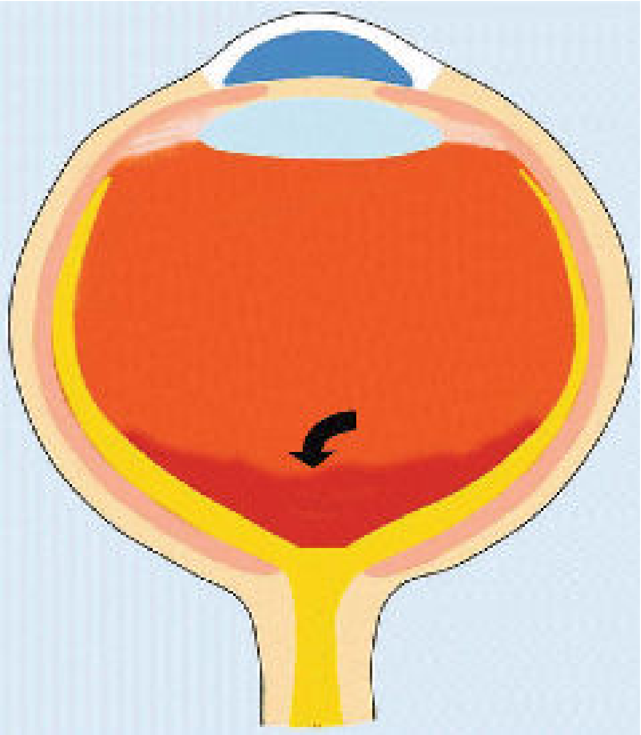

Fig. 19.7 Vitreous chamber hemorrhage. Drawing illustrates vitreous chamber hemorrhage (*curved arrow*), which can be an isolated finding or associated with globe rupture, lens dislocation, or orbital fractures

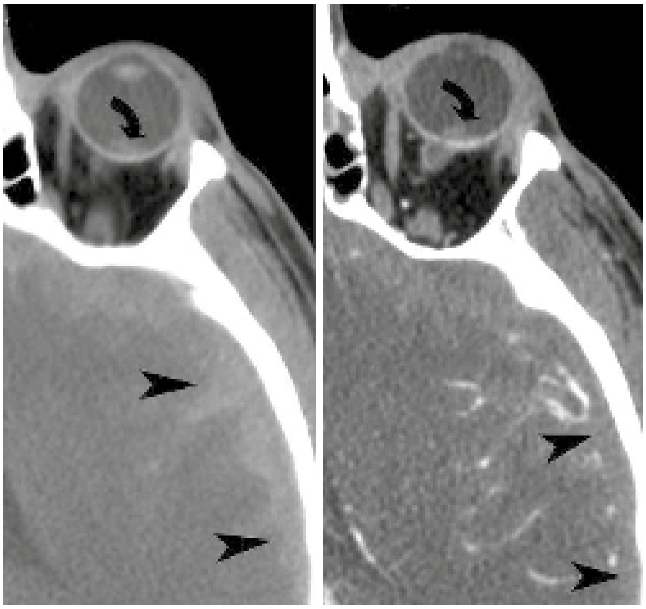

Fig. 19.8 Vitreous chamber hemorrhage from blunt trauma in a 28-year-old male. Noncontrast axial CT and contrast-enhanced CT demonstrate left vitreous hemorrhage (*curved arrows*) and left subdural hemorrhage (*arrowheads*)

Nontraumatic mimics of open-globe injury include coloboma, staphyloma, congenital glaucoma, an elongated globe from myopia, phthisis bulbi, and mass effect from an orbital mass or hematoma.

Intraocular Foreign Body

Intraocular foreign bodies are present in 10%–17% of ocular injuries. However, they are often clinically overlooked, if not clinically suspected. While small nonreactive foreign bodies (gold, platinum, aluminum, and glass) can be left in the orbit, other foreign bodies made up of iron and copper must be removed due to risk of siderosis from iron and chalcosis from copper. Organic materials, such as wood, can cause infection, abscess/chronic inflammation, and retinal toxicity and therefore need to be removed.

Enucleation is usually necessary when a large foreign body enters the eye with resulting hemorrhage, lens dislocation, and vitreous loss. Intracranial injury should be excluded with imaging before performing enucleation.

Imaging: The high density of metallic foreign body is best diagnosed on CT (Figs. 19.9, 19.10, and 19.11). The density of wood is highly variable, thereby resulting in lower sensitivity of CT and MRI in the detection of organic foreign body (42% vs. 57%) [7]. Wooden foreign bodies are most often of lower density and therefore can be mistaken for air. Geometric shape of air density should raise the suspicion of wooden foreign body. The sensitivity of helical CT and T1-weighted MRI sequence for the detection of intraocular glass is 57% and 11%, respectively [8]. The sensitivity of CT for the detection of more than 1.5 mm diameter glass fragment is much higher than a 0.5 mm fragment. MRI is contraindicated when a metallic foreign body is suspected. US can demonstrate foreign bodies but is less sensitive than CT or MRI. Intraocular air may cause false positive in foreign-body detection with US. Radiography plays a limited role in eye trauma. However, if penetrating eye injury is suspected, its sensitivity for detecting intraocular foreign body may be as high as 96%.

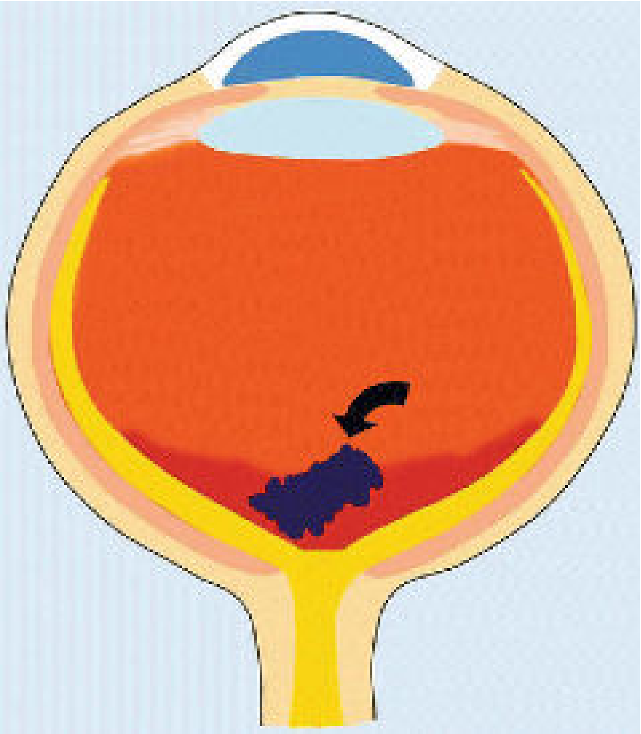

Fig. 19.9 Intraocular foreign body. Diagram illustrates an intraocular foreign body and hemorrhage in the vitreous chamber

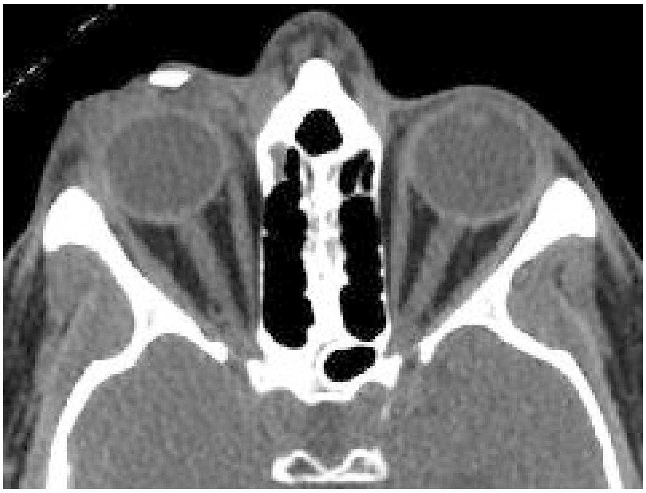

Fig. 19.11 Foreign body in the preseptal space. CT demonstrates extensive preseptal soft tissue edema and an 8 mm glass fragment in the upper lid of a patient who was involved in a motor vehicle collision

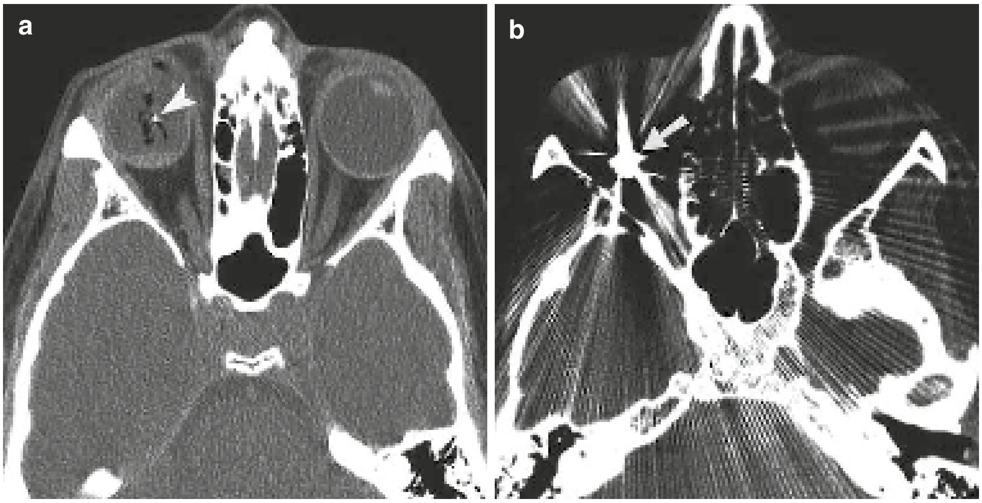

Fig. 19.10 Metallic intraocular foreign body. (**a**) Axial CT shows intraocular-dependent vitreous hemorrhage, and intraocular and bullet fragment (*arrowhead*) from gunshot injury. (**b**) Axial CT at a more caudal level shows an intraconal metallic foreign body (*arrow*), producing streak artifacts at the posterior ocular wall

Mimics of intraocular foreign bodies include ocular calcifications (such as optic drusen, scleral plaques in elderly patients, and cataract) and materials used to treat retinal detachment (such as scleral bands, silicon oil, and gas).

Retinal Detachment

The retina is firmly attached anteriorly at the ora serrata and posteriorly at the optic disk. RD refers to the separation of the sensory retina from retinal pigmented epithelium. It can be caused by mass, vitreoretinopathy, toxocara endophthalmitis, Coats' disease, senile macular degeneration, and trauma.

Imaging: Exudative RD results in subretinal fluid rich in protein, resulting in high-density fluid on CT than seen with a rhegmatogenous RD. RD is seen on CT and MRI as a characteristic V-shaped configuration with apex at the optic disk and anterior end at the ora serrata (Figs. 19.12 and 19.13). On coronal MRI, it is seen as characteristic folding membranes converging at the optic disk.

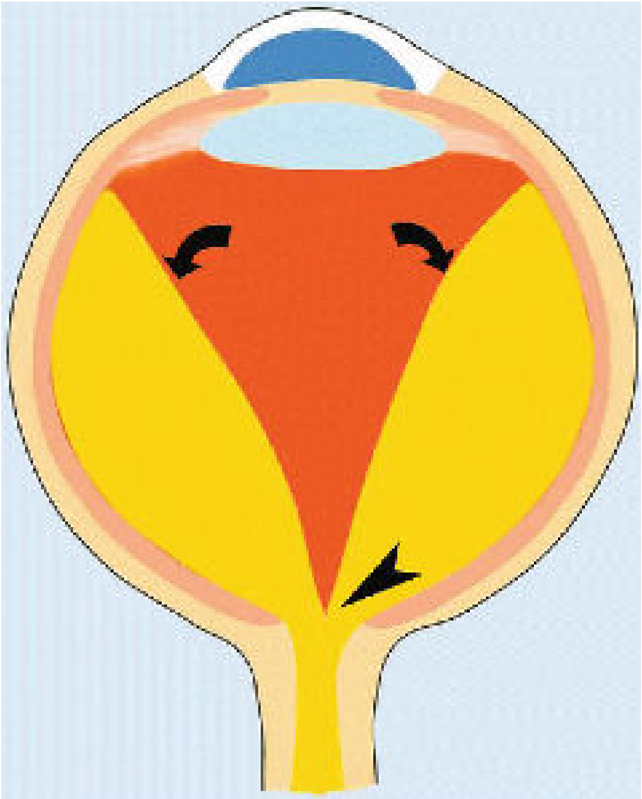

Fig. 19.12 Retinal detachment. Diagram illustrates V-shaped retinal detachment (*curved arrow*) arising posteriorly from the optic disk (*arrowhead*)

Fig. 19.13 Acute retinal detachment in a 39-year-old male. Axial CT (**a**) and axial FLAIR (**b**) sequence show retinal detachment with subretinal hemorrhage (*bifid arrow*), which is of high density on CT and hyperintense on FLAIR sequence

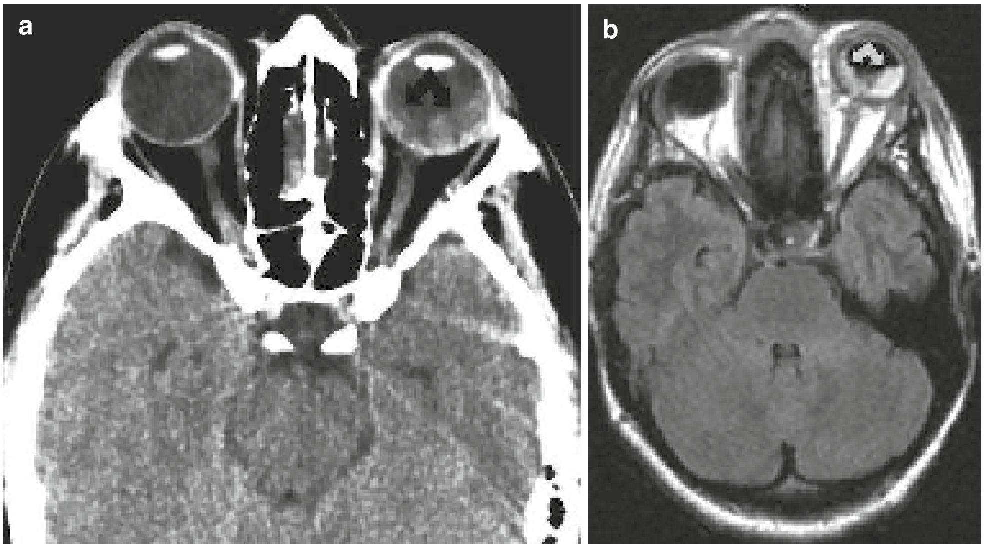

Choroidal Detachment

CD is caused by accumulation of serous fluid or blood in potential subchoroidal space. CD happens when an injury decreases the intraocular pressure, which reduces suprachoroidal space pressure, and allows fluid or blood to accumulate and detach the choroid. The causes include intraocular surgery, trauma, or inflammatory disorders. Unlike RD, it does not extend to the optic disk and is restricted by anchoring effect of short posterior ciliary arteries and nerves.

Imaging: CT is the imaging modality of choice and shows focal, biconvex, lenticular mass in the ocular wall, which is posteriorly restricted by short posterior ciliary arteries and nerves (Figs. 19.14 and 19.15a).

MRI shows choroidal hematoma as a focal, well-demarcated lenticular mass in the wall of the eyeball (see Fig. 19.15b). Within the first 48 h, the hematoma is isointense to slightly hypointense to the vitreous body on T1-weighted images. After 5 days, choroidal hematoma appears hyperintense on T1-weighted images. Choroidal hematoma usually increases in signal intensity on T1- as well as T2-weighted images and becomes hyperintense by the second week on all MRI sequences.

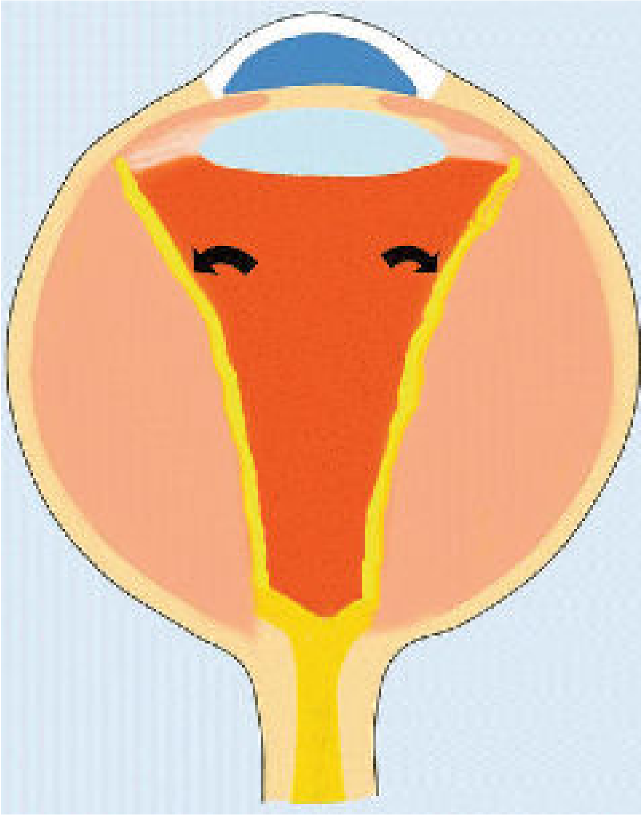

Fig. 19.14 Choroidal detachment. Diagram illustrates fluid accumulation, which is confined by choroid (*curved arrows*) on the inside and sclera on the outside

Fig. 19.15 Choroidal detachment from blunt trauma in a 92-year-old female. (**a**) Axial CT shows choroidal detachment (*arrow heads*) with high-density blood in the subchoroidal space. There is preseptal soft tissue contusion extending lateral to the left lateral orbital wall. (**b**) T2-weighted MRI sequence demonstrates acute choroidal detachment with hypointense subchoroidal fluid (*arrowheads*), indicating the presence of acute blood products

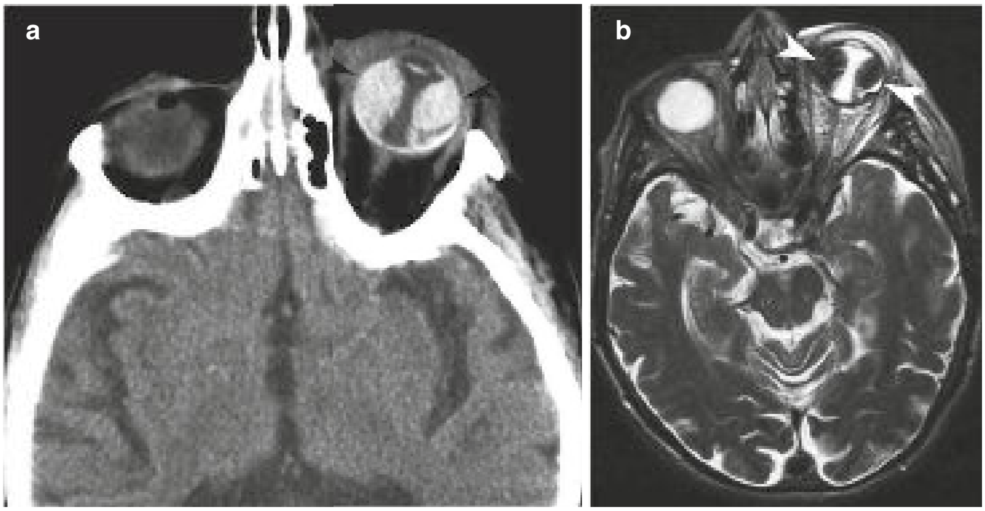

Associated Injuries

The injuries associated with ocular trauma include retrobulbar hemorrhage, optic nerve injury, orbital wall fractures, herniation of intraorbital contents through the orbital fracture, muscle entrapment/contusion, intraorbital emphysema, intracranial injuries, and maxillofacial fractures (Figs. 19.16, 19.17, 19.18, and 19.19). Orbital floor is the most common, and orbital roof is the least common site for orbital wall fracture. Type 2 and 3 Le Fort fractures involve the orbital walls.

Le Fort II fracture is a pyramidal shaped fracture of the maxilla with superior extension to the inferior orbital rim and medial orbital wall. Le Fort III fracture is called craniofacial dissociation and involves the orbital floor, medial wall, as well as lateral wall.

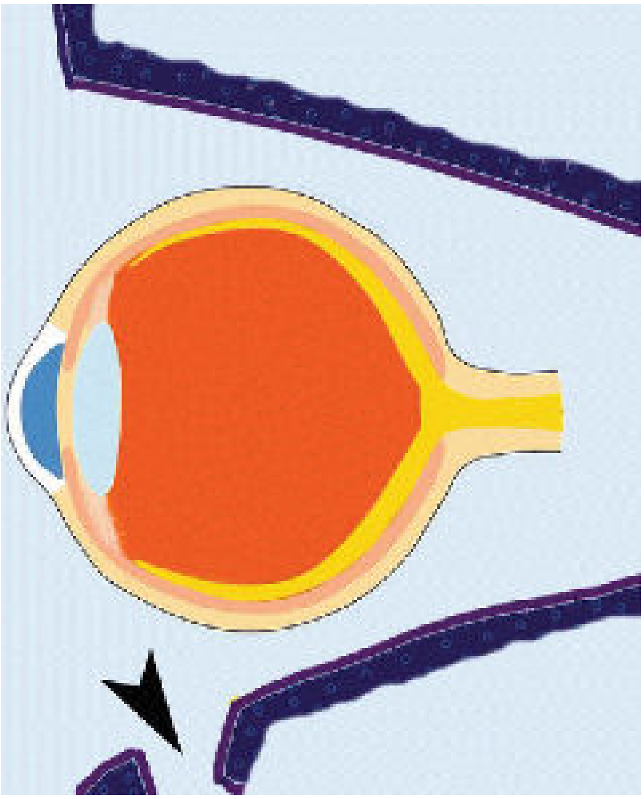

Fig. 19.16 Orbital blowout fracture. Diagram illustrates orbital floor fracture (*curved arrowhead*), which is the most common orbital wall to fracture from blunt force causing increase in the intraorbital pressure

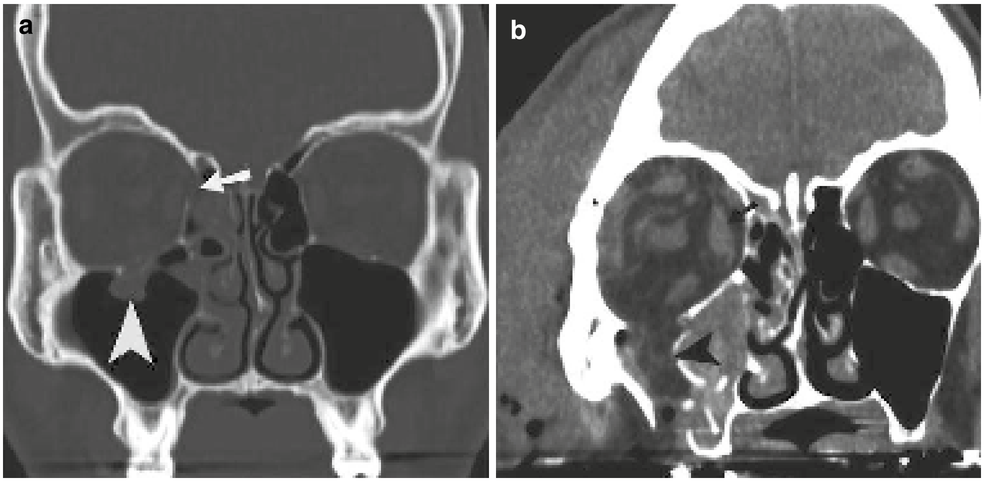

Fig. 19.17 Orbital blowout fracture. (**a**) Coronal CT reconstruction shows fracture of the medial (*arrow*) and inferior orbital wall. There is herniation (*arrowhead*) of intraorbital fat into the right maxillary sinus. (**b**) Coronal CT reconstruction in a different patient demonstrates the asymmetric right medial rectus muscle thickening (*arrow*). There is herniation of intraorbital fat (*arrowhead*) through the inferior orbital wall fracture

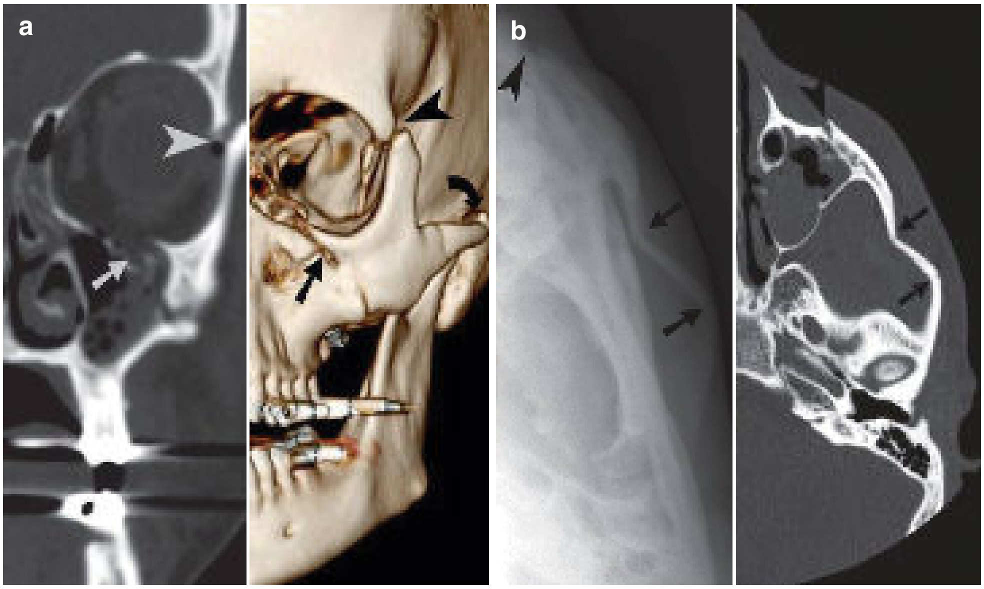

Fig. 19.18 Orbital wall fractures. (**a**) Coronal CT reformation and 3D reconstruction in a patient show zygomaticomaxillary fracture involving the lateral orbital rim (*arrowhead*), zygomatic arch (*curved arrow*), and inferior orbital rim (*straight arrow*). (**b**) Base-of-skull radiograph and axial CT demonstrate zygomaticomaxillary fracture involving the zygomatic arch (*straight arrows*) and orbital floor (*arrowhead*)

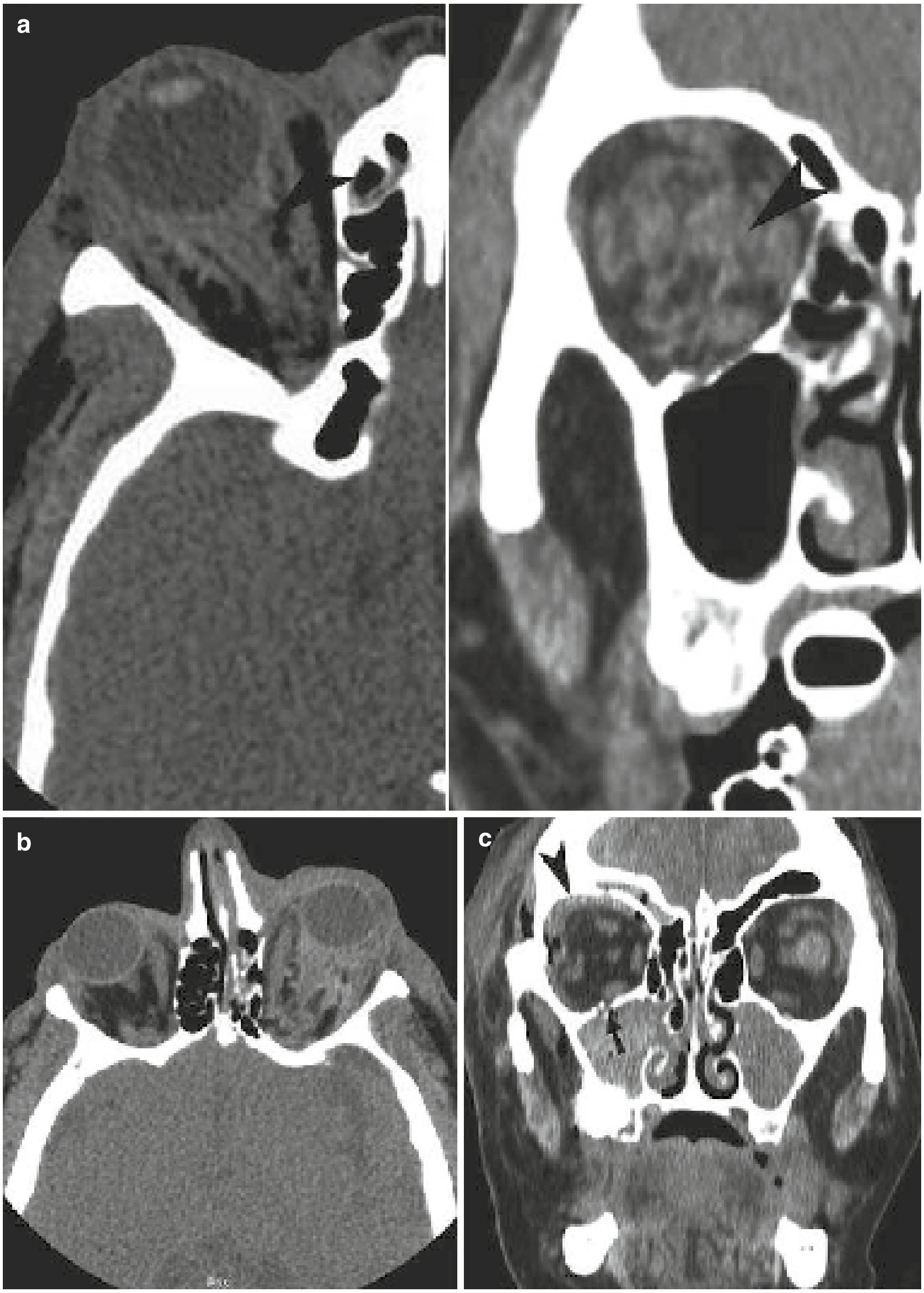

Fig. 19.19 Intraconal and extraconal hemorrhage after blunt trauma. (**a**) Axial and coronal CT shows right proptosis secondary to intraconal hemorrhage (*arrowheads*). There is scleral thickening at the optic disk, secondary to scleral contusion. (**b**) Axial CT in a patient who was punched in the left eye shows left retrobulbar hemorrhage leading to proptosis. (**c**) Coronal CT reconstruction in a patient who fell down an elevator shaft demonstrates extraconal hemorrhage (*arrowhead*) along the superior orbital wall. There is also inferior orbital wall fracture (*arrow*) with hemorrhage in the right maxillary sinus

Acute Fulminant Invasive Fungal Sinusitis

Acute fulminant invasive fungal sinusitis (AFIFS), mainly affecting severely immunocompromised patients, is caused by *Aspergillus* species or zygomycetes (*Rhizopus*, *Mucor*, *Rhizomucor*) and is associated with high morbidity and mortality. Mortality rate can reach as high as 50%–80%. Tissue infarction occurring as a result of fungal invasion of blood vessels is characteristic. Through inhalation of spores, infection first affects the nose and paranasal sinuses and then spreads to orbits and subsequently to intracranial space via angioinvasion.

Imaging

CT and MR imaging are the most commonly utilized modalities. Middle nasal turbinate is the most commonly involved site followed by maxillary, ethmoid, and sphenoid sinuses, respectively. CT finding includes unilateral mucosal thickening of the nasal cavity, perimaxillary fat infiltration, and unilateral sinus opacification. Late findings include bony erosion, pterygopalatine fossa involvement, orbital involvement, and intracranial extension. Characteristic MR imaging finding includes lack of contrast enhancement (LoCE) of paranasal sinus mucosa secondary to mucosal ischemia. This demonstration of hypointensity and non-enhancement of involved turbinates is referred to as "black turbinate sign." T1- and T2-WI are useful for characterization of soft tissues and bone involvement, fat-saturated T2-WI is the most useful sequence for pathology demonstration, and diffusion-weighted imaging is valuable for characterization of optic nerve and cerebral infarction.

Orbit remains the most commonly involved extrasinus site. Orbital spread can occur through nasolacrimal duct, lamina papyracea, ethmoidal foramina, or inferior orbital fissure. Imaging findings include orbital fat stranding in intra- or extraconal space, thickening and displacement of involved extraocular muscles (especially medial rectus), or intraorbital inflammation/abscess formation. Fat-saturated T2-WI allows superior visualization of retro-orbital fat infiltration. Proptosis can be seen with diffuse infection. Mucormycosis is the most common cause of orbital apex syndrome, and infection can spread to the orbital apex via sphenoid sinus. Orbital apex involvement provides an easy route for intracranial spread to the cavernous sinus region. Optic nerve involvement is also known to occur [9].

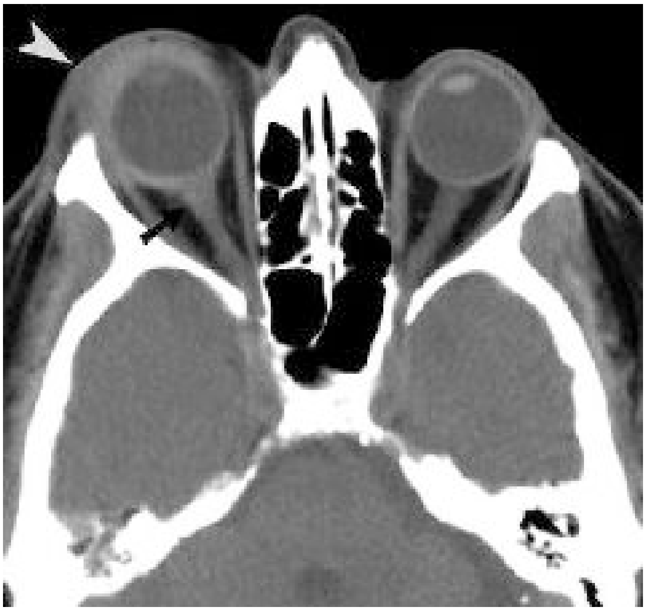

Fig. 19.20 Optic nerve contusion. Axial CT shows thickening and increased density (*arrow*) of the right optic nerve with adjacent scleral thickening. There is also right preseptal contusion (*arrowhead*) caused by blunt trauma

Optic Nerve Injury

Optic nerve injury can be due to compression from an optic canal fracture or more commonly due to compromised vascular supply to the optic nerve. It is usually associated with other orbital or facial fractures or involves the skull base. Injury to the optic nerve can be seen as hyperintensity of the optic nerve on T2-weighted images (Fig. 19.20). Emergent surgery may be indicated.

Carotid Cavernous Fistula

It is most commonly caused by post-traumatic tear in the internal carotid artery with communication with the cavernous sinus. Because of the reversal of flow in the venous tributaries of the cavernous sinus, there is prominence of the superior ophthalmic vein on CT imaging. The diagnosis can be confirmed on CT angiogram or conventional angiogram (Fig. 19.21). Early filling of the superior ophthalmic vein during arterial phase is seen on CT angiography or conventional catheter angiography.

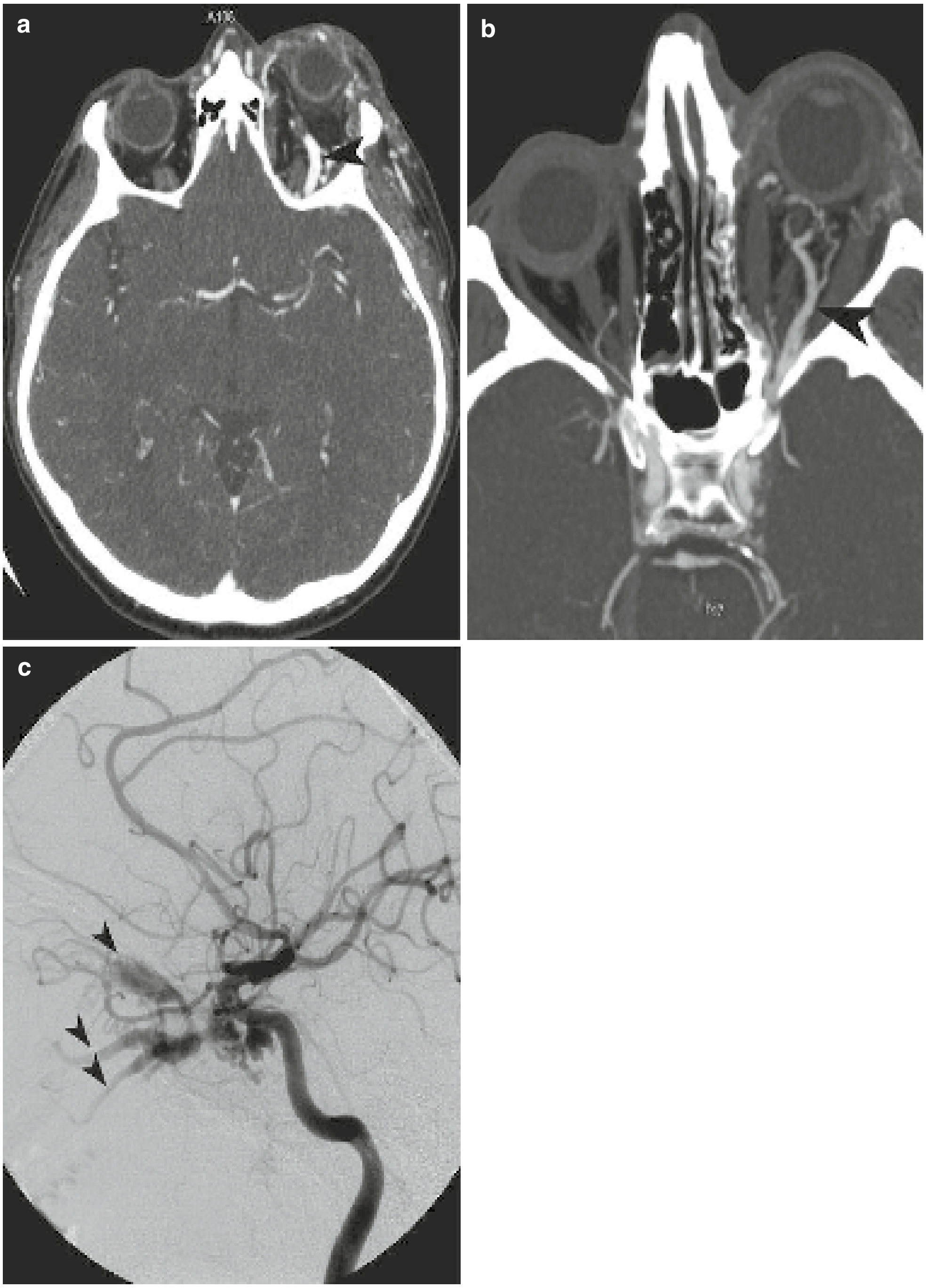

Fig. 19.21 Post-traumatic carotid cavernous fistula. (**a**, **b**) Contrast-enhanced CT demonstrates prominence of the left superior ophthalmic vein (*arrowhead*) secondary to carotid cavernous fistula. (**c**) Left internal carotid angiogram demonstrates communication with the cavernous sinus as well as its venous tributaries

Orbital Infections

Orbital infections are classified as preseptal (periorbital) or postseptal (orbital), depending on their location in relation to orbital septum. The orbital septum is a periosteal reflection off the bony margin of the orbit. Based on noncontrast CT, it is not possible to distinguish preseptal edema from periorbital cellulitis. Contrast-enhanced CT or MRI can be used to distinguish these two entities. Periorbital cellulitis is treated less aggressively, compared to postseptal infection, with antibiotic therapy.

The postseptal infections can be intraconic, extraconic (between periosteum and recti muscles), and subperiosteal (between orbital wall and periosteum). Preseptal cellulitis is clinically a less severe infection compared with postseptal, which may be complicated by vision loss, ophthalmoplegia, intracranial spread of infection (such as brain abscess or meningitis), or cavernous sinus thrombosis.

Orbital Subperiosteal Abscess

Orbital subperiosteal abscess is most often caused by maxillary, ethmoidal, or frontal sinusitis due to close anatomic relationship with the orbit. Spread of the infection can cause loss of vision, endophthalmitis, cavernous sinus thrombosis, brain abscess, and meningitis.

The CT findings include opacification of the ethmoidal and maxillary sinuses with rim-enhancing, lenticular shaped subperiosteal abscess, most commonly along the medial orbital wall (Fig. 19.22). MRI will demonstrate rim enhancement with internal T2 hyperintensity and restricted diffusion. Occasionally, air is present within the subperiosteal abscess. Unlike ethmoidal sinusitis, which causes subperiosteal abscess along the medial orbital wall, frontal sinusitis most often causes the subperiosteal abscess to be along the orbital roof.

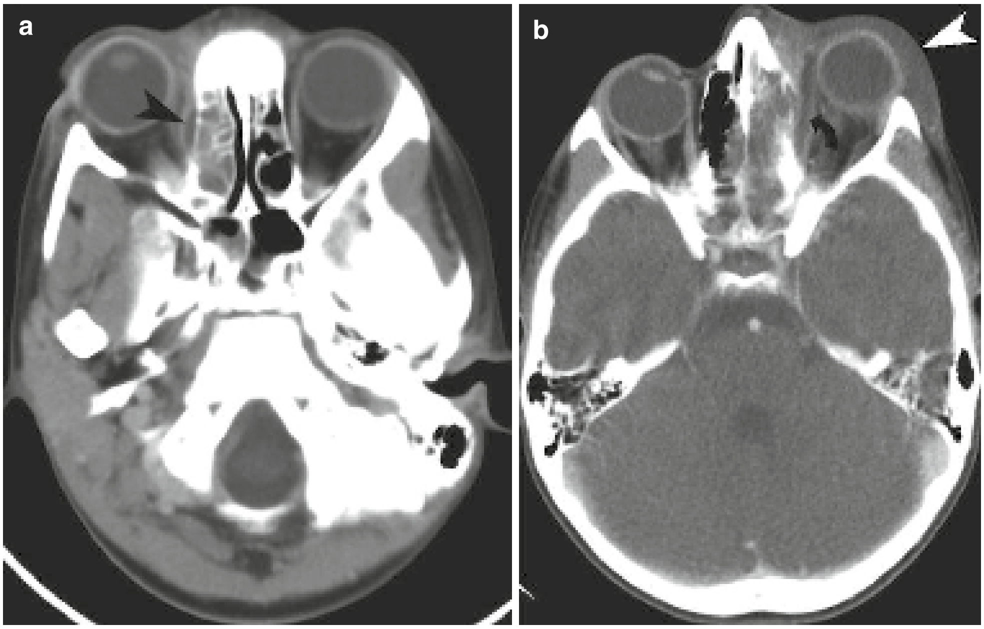

Fig. 19.22 Orbital abscess. (**a**) Contrast-enhanced CT demonstrates orbital subperiosteal abscess (*arrowhead*) along the right medial orbital wall, secondary to ethmoidal sinusitis. (**b**) Contrast-enhanced CT shows left ethmoidal sinusitis with abscess (*curved arrow*) formation along the left medial orbital wall, leading to proptosis. The abscess has extended beyond the subperiosteal confines to involve extraconic compartment medial to the medial rectus. There is also extension of inflammation anteriorly to cause periorbital cellulitis (*arrowhead*)

Optic Neuritis

Optic neuritis refers to acute inflammatory or demyelinating disorder of the optic nerve. Although majority of the cases are idiopathic, some cases are due to multiple sclerosis. Majority of the patients are in the 15–50-year age group and have rapid progression of visual loss within 2 weeks. Although the diagnosis is typically made on clinical examination, MRI imaging is used when there are atypical clinical features.

The MRI features include T2 hyperintensity with enlarged optic nerve. It frequently enhances on postcontrast T1-weighted imaging (Fig. 19.23). There may be associated white matter abnormalities on T2-weighted sequence, which can predict the subsequent development of multiple sclerosis. The 5-year risk of developing subsequent multiple sclerosis is 51% in patients with three or more lesions and 16% in patients without white matter abnormalities [9, 10].

Teaching Points

- CT is the imaging modality of choice in the detection of intraocular foreign bodies, globe rupture, lens dislocation, intra/extraconal injury, and associated orbital/facial injuries.
- The role of MRI is more limited in the evaluation of acute ocular trauma; however, it can be utilized when a ferromagnetic foreign body is excluded by radiography or CT imaging.
- Ultrasound is contraindicated when globe rupture is suspected.
- Retinal detachment is seen on CT and MRI as a characteristic V-shaped configuration with apex at the optic disk and anterior end at the ora serrata.
- CT in choroidal detachment shows focal, biconvex, lenticular mass in the ocular wall, which is posteriorly restricted by short posterior ciliary arteries and nerves.
- Orbital infections are classified as preseptal (periorbital) or postseptal (orbital), depending on their location in relation to orbital septum.
- The CT findings in orbital subperiosteal abscess include opacification of the ethmoidal and maxillary sinuses with rim-enhancing, lenticular shaped subperiosteal abscess, most commonly along the medial orbital wall.
- The MRI features in optic neuritis include T2 hyperintensity with enlarged optic nerve.

Questions

1. In patients with optic neuritis without white matter abnormalities, what is the 5-year risk of developing multiple sclerosis?
   (A) 1–10%
   (B) 11–20%
   (C) 21–30%
   (D) 31–40%
   Answer: B

2. Early filling of the superior ophthalmic vein in arterial phase is a sign of which of the following abnormalities?
   (A) Infection
   (B) Fistula
   (C) Thrombosis
   (D) Aneurysm
   Answer: B

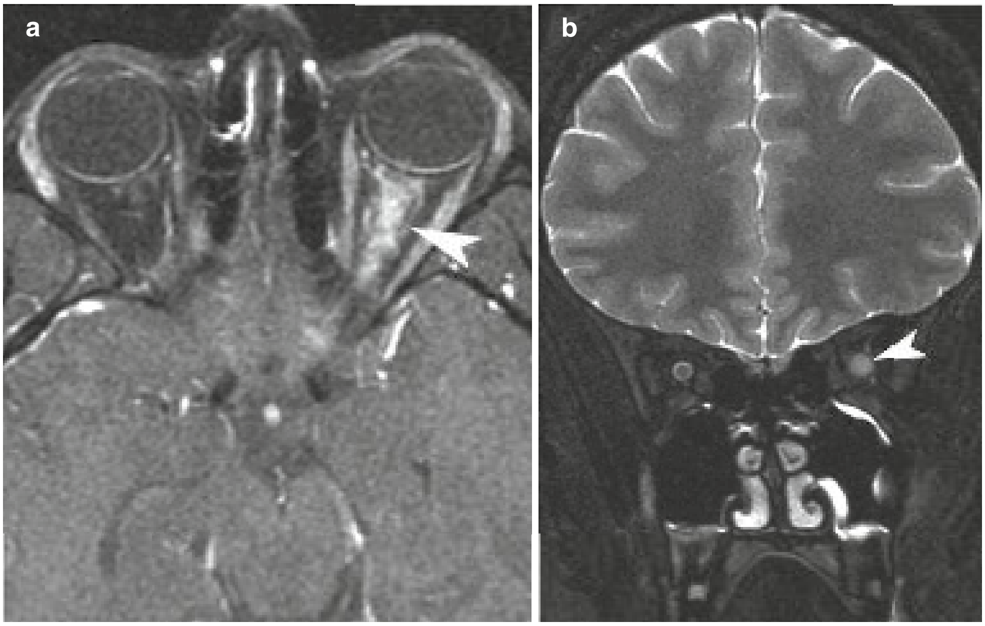

Fig. 19.23 Optic neuritis. Axial post-gadolinium T1-weighted (**a**) and coronal T2-weighted (**b**) sequences demonstrate thickening and enhancement of the left optic nerve (*arrowhead*)

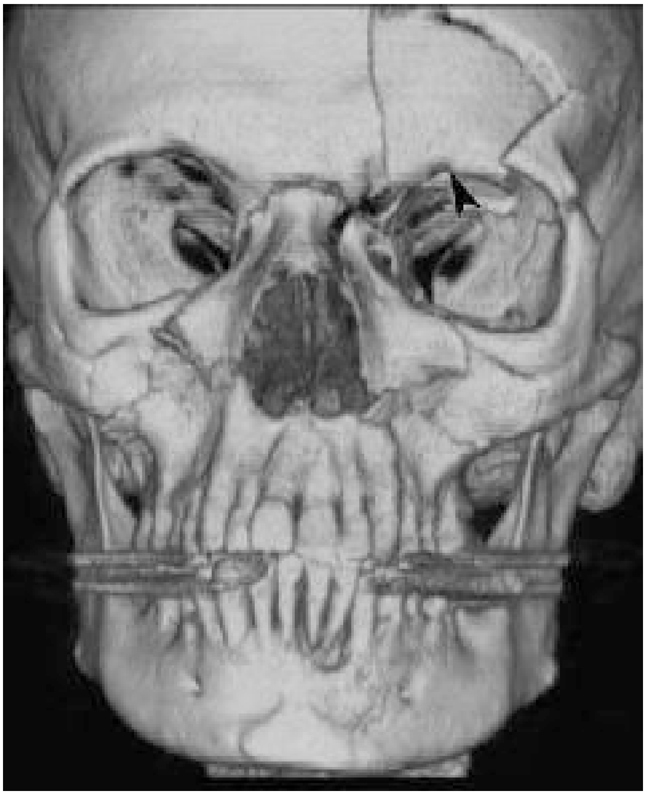

Fig. 19.24 Le Fort injury

3. Which of the following statements is correct regarding intraocular foreign bodies?
   (A) Scleral plaques in elderly can mimic foreign bodies
   (B) MRI is the best imaging modality
   (C) Wooden foreign bodies usually have high density
   (D) MRI is more sensitive in the detection of glass, compared with CT
   Answer: A

4. What kind of orbital injury is depicted by the arrowhead (Fig. 19.24) in a patient with Le Fort injury who was involved in a motor vehicle collision?
   (A) Naso-orbital-ethmoid fracture
   (B) Optic canal fracture
   (C) Orbital blowout fracture
   (D) Orbital blow-in fracture
   Answer: D

5. What CT finding is shown below in a patient with history of blunt trauma (Fig. 19.25)?
   (A) Le Fort II
   (B) Le Fort III

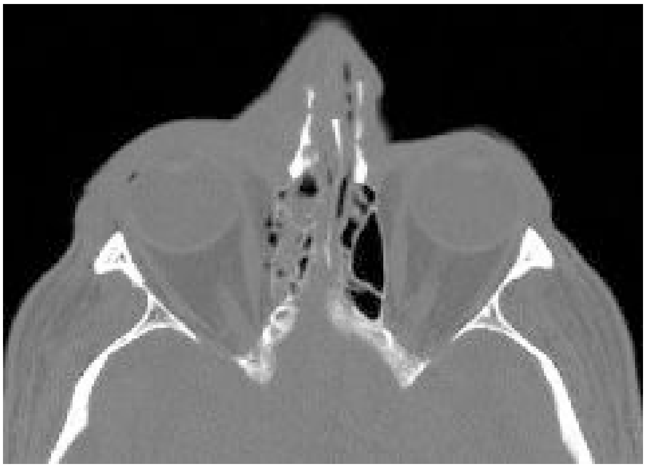

Fig. 19.25 Orbital blow-out fracture

   (C) Orbital blowout fracture
   (D) Orbital blow-in fracture
   Answer: C

References

1. Maltzman BA, Pruzon H, Mund ML. A survey of ocular trauma. Surv Ophthalmol. 1976;21(3):285–90.
2. Schrader WF. Epidemiology of open globe eye injuries: analysis of 1026 cases in 18 years. Klin Monatsbl Augenheilkd. 2004;221(08):629–35.
3. Lakits A, Prokesch R, Scholda C, Bankier A. Orbital helically computed tomography in the diagnosis and management of eye trauma. Ophthalmology. 1999;106(12):2330–5.
4. Canavan YM, Archer DB. Anterior segment consequences of blunt ocular injury. Br J Ophthalmol. 1982;66(9):549–55.
5. Viestenz A, Kuchle M. Blunt ocular trauma. Part II. Blunt posterior segment trauma. Ophthalmology. 2005;102(1):89–99; quiz 100–1.
6. Arey ML, Mootha VV, Whittemore AR, Chason DP, Blomquist PH. Computed tomography in the diagnosis of occult open-globe injuries. Ophthalmology. 2007;114:1448–52.
7. Nasr AM, Haik BG, Fleming JC, Al-Hussain HM, Karcioglu ZA. Penetrating orbital injury with organic foreign bodies. Ophthalmology. 1999;106(3):523–32.
8. Gor DM, Kirsch CF, Leen J, Turbin R, Von Hagen S. Radiologic differentiation of intraocular glass: evaluation of imaging techniques, glass types, size, and effect of intraocular hemorrhage. AJR Am J Roentgenol. 2001;177(5):1199–203.
9. Khullar T, Kumar J, Sindhu D, Garg A, Meher R. CT imaging features in acute invasive fungal rhinosinusitis—recalling the oblivion in the COVID era. Curr Probl Diagn Radiol. 2022;51(5):798–805. https://doi.org/10.1067/j.cpradiol.2022.02.001.
10. Optic Neuritis Study Group. Visual function 5 years after optic neuritis: experience of the optic neuritis treatment trial. The optic neuritis study group. Arch Ophthalmol. 1997;115(12):1545–52.

Imaging of Upper Extremity

20

Joshua Leeman, Jonathan E. Leeman,
Mohammad Mansouri, and Ajay Singh

Introduction

A vast number of traumatic injuries can involve the upper extremity. In this chapter, the specific injuries seen most commonly in a busy emergency department are described, with emphasis on the mechanism of injury, radiographic appearance, and complications. Radiographic appearances of injuries will be emphasized as the radiograph is typically the initial imaging tool utilized in the emergency setting, and frequently the diagnosis can be made using radiography alone.

Scapulothoracic Dissociation

Scapulothoracic dissociation is a rare but devastating and potentially life-threatening injury. The mortality can be as high as 10%. It most commonly results from severe lateral traction of the shoulder girdle in the case of a motorcyclist who holds on to the handlebars while being thrown from the vehicle. Trauma history usually involves trauma to heart, chest wall, and lungs. It is usually accompanied by avulsion of the brachial plexus and rupture of the subclavian or axillary artery. Associated orthopedic conditions include scapula fracture, clavicle fracture, acromioclavicular dislocation, sternoclavicular dislocation, and flail extremity.

Imaging

On frontal radiograph, there is lateral displacement of the scapula, as indicated by wide separation (>1 cm) between the medial edge of the scapula and the spinous processes. The injury is often accompanied by other osseous injuries including acromioclavicular separation, sternoclavicular dislocation, and distracted fracture of the clavicle. Adjacent soft tissue masses representing hematomas suggest severe injury to vascular structures [1]. Angiogram helps detect injury to the vessels.

As it is the result of severe trauma, scapulothoracic dissociation is often overlooked initially because of concomitant hemodynamic shock or head injuries. Brachial plexus avulsion can result in flail arm, which usually requires above-the-elbow amputation.

Clavicle Fracture

Clavicle fractures represent 50% of fractures involving the shoulder girdle [2]. They are usually the result of a direct fall on the shoulder during athletic activity or falling on an outstretched hand. Fractures of the clavicle are common in the pediatric population and can also result from anterior pressure on the shoulder during childbirth.

Symptoms include pain, sagging shoulder, inability to lift the arm, "bump" over the break, tenderness on the collarbone, and skin changes such as bruising and swelling.

The original version of this chapter was revised. An erratum to this chapter can be found at https://doi.org/10.1007/978-3-319-65397-6_27. An erratum to this publication is available online at https://doi.org/10.1007/978-3-319-65397-6_27.

J. Leeman
Department of Radiology, University of Massachusetts Memorial Medical Center, Worcester, MA, USA

J. E. Leeman
Radiation Oncology, Memorial Sloan-Kettering Cancer Center, New York, NY, USA

M. Mansouri
Department of Radiology, Massachusetts General Hospital, Boston, MA, USA

A. Singh (✉)
Division of Emergency Radiology, Department of Radiology, Massachusetts General Hospital, Boston, MA, USA

Harvard Medical School, Massachusetts General Hospital, Boston, MA, USA
e-mail: asingh1@partners.org

© The Author(s), under exclusive license to Springer Nature Switzerland AG 2024
A. Singh (ed.), *Emergency Radiology*, https://doi.org/10.1007/978-3-031-65770-2_20

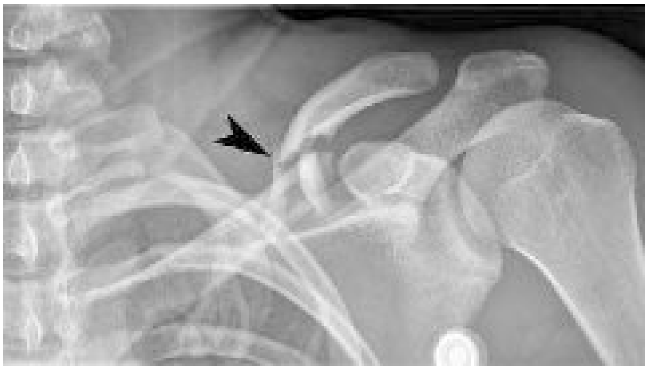

Fig. 20.1 Clavicle fracture. AP view of the clavicle shows a comminuted fracture at the distal third of the clavicle (*arrowhead*)

Imaging

The majority of fractures occur in the middle third of the clavicle and are easily detectable on radiography. Because of the unopposed action of the sternocleidomastoid muscle, there is often superomedial displacement of the medial segment of the clavicle. The inferior displacement of the lateral clavicle fragment results from the weight of the upper extremity (Fig. 20.1).

Complications

Clavicle fracture can be associated with injury to the subclavian artery, subclavian vein, or brachial plexus. There may be associated sternoclavicular or acromioclavicular subluxation, as well as pneumothorax. Malunion and nonunion can lead to shortening of the shoulder girdle and chronic pain [3].

Sternoclavicular Dislocation

Sternoclavicular dislocation accounts for only 2%–3% of shoulder girdle dislocations and can occur after indirect blunt trauma to the shoulder [4]. The dislocation allows for free rotation of the head of the clavicle with the intact costoclavicular ligament serving as a fulcrum. Anterior dislocation from an anterolateral blow is significantly more common than posterior dislocation from a posterolateral blow. Stanmore triangle classification is a useful tool to classify and manage patients with instability of the sternoclavicular joint. It is mainly based on the presence of trauma, laxity, and articular, capsular, and muscle involvement.

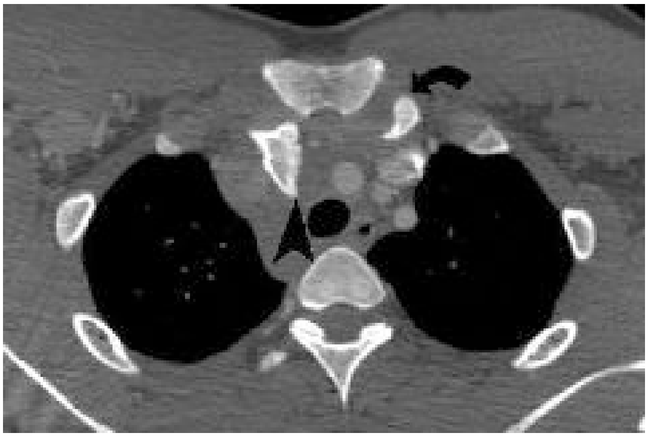

Fig. 20.2 Posterior dislocation of clavicle. Axial CT image depicts posterior dislocation of the right clavicle head (*arrowhead*), which is now situated within the superior mediastinum. The left sternoclavicular articulation (*curved arrow*) is normal

Imaging

Sternoclavicular dislocation can result in asymmetry of the clavicular heads. Compared to plain radiography, CT can better distinguish anterior from posterior dislocation. It is also able to detect associated injury to mediastinal structures such as great vessels, recurrent laryngeal nerve, trachea, and esophagus, in patients with posterior dislocation (Fig. 20.2). 3D reconstruction can help showing the abnormal anatomical structures. MRI is a useful modality to show intra-articular disc injuries, ligament disruption, and injuries to the adjacent neurovascular structures.

Acromioclavicular Dislocation

Acromioclavicular dislocation is a common injury usually resulting from direct trauma in contact sports, such as football or hockey. Dislocation can also result from a fall on an outstretched hand.

AP radiographs with a 10°–15° cephalic tilt (Zanca view) are recommended for assessment of the acromioclavicular region. Dislocations are classified into the following types (Table 20.1):

- Type 1: Isolated sprain of the acromioclavicular ligament (AC). Plain films are normal aside from soft tissue swelling.

Table 20.1 Classification of acromioclavicular dislocation

Types	Description
Type 1	Isolated sprain of the AC ligament Normal plain films
Type 2	Subluxation with rupture of the AC ligament Sprain of the CC ligament
Type 3	Complete rupture of AC and CC ligaments Superior migration of the clavicle >5 mm above the acromion Coracoid fracture and injuries to the insertion of the trapezius or deltoid muscles

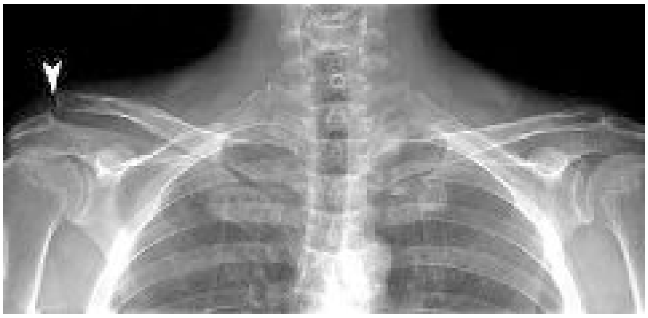

Fig. 20.3 Acromioclavicular dislocation. AP view shows a type III acromioclavicular injury with elevation of the acromion more than 5 mm from its normal position (*arrowhead*). This degree of displacement indicates rupture of both CC and AC ligaments

- Type 2: Subluxation with rupture of the AC ligament and sprain of the coracoclavicular ligament (CC). The distal clavicle will typically be situated <5 mm superiorly to the acromion.
- Type 3: Complete rupture of AC and CC ligaments with superior migration of the clavicle >5 mm above the acromion (Fig. 20.3). Coracoid fracture and injuries to the insertion of the trapezius or deltoid muscles can occur as a result of type 3 dislocations.

Glenohumeral Joint Dislocation

Because of its inherent instability, the glenohumeral joint is the most commonly dislocated joint in the body. Anterior dislocation is far more common than posterior and often results from an anterior blow to an abducted arm and less frequently from a direct injury to the shoulder. Posterior dislocation may be a consequence of electric shock or seizure and can therefore be bilateral. Inferior glenohumeral dislocation, known as luxatio erecta, results from hyperabduction of the arm and is suspected in a patient with an abducted arm, with the wrist resting on the head. Superior dislocation from an upward blow on an adducted arm represents the rarest type and is almost always associated with rotator cuff tear.

Imaging

In the setting of anterior glenohumeral dislocation, the AP radiograph will show the humeral head situated medial and inferior with respect to the glenoid, such that it lies directly inferior to the coracoid process (Fig. 20.4a). If posteriorly dislocated, the AP view will depict an increased distance between the humeral head and the glenoid and loss of the normal overlap of the humeral head and glenoid. However, it should be noted that a large effusion may have an identical appearance. The axillary projection (45° posterior oblique with 45° of inferior angulation), scapular Y projection (60° anterior oblique), and true AP (Grashey view) in external rotation afford an excellent appraisal of the congruence of the glenohumeral joint (Fig. 20.4b). These latter views are often best for distinguishing between an anterior and posterior dislocation when the AP view is confusing.

Anteroinferior dislocation, or subcoracoid dislocation, can result in fracture of the posterolateral aspect of the humeral head (Hill–Sachs lesion), best seen as a linear or wedge-shaped defect that is evident on radiography (Fig. 20.4c). As the humeral head impacts against the glenoid rim, fracture of the anteroinferior glenoid (Bankart lesion) with avulsion of the labroligamentous complex can also occur. With nonoperative treatment, anterior dislocations will recur in approximately 50% of cases [5].

Conversely, a reverse Bankart lesion, or posteroinferior fracture of the glenoid rim, can result from posterior dislocation. In the evaluation of glenohumeral dislocation, CT is most appropriate for identifying bony fragments or associated vascular injury, while MRI can more clearly identify soft tissue damage (Fig. 20.4d and Table 20.2).

Fig. 20.4 Glenohumeral dislocation. (**a**) AP view of the shoulder illustrates the typical appearance of anterior glenohumeral dislocation with the humeral head situated in a subcoracoid position (*top*). A postreduction AP view shows a wedge-shaped defect at the posterolateral aspect of the humeral head typical of a Hill–Sachs lesion (*arrow*). (**b**) Scapular Y view clearly demonstrates anterior dislocation of the humeral head, which now lies under the coracoid process. (**c**) Axial CT shows wedge-shaped Hill–Sachs deformities on the posterolateral aspects of both humeral heads (*arrows*) after bilateral anterior dislocations. (**d**) MIP reconstruction of contrast-enhanced CT shows abrupt occlusion of the axillary artery (*arrowhead*) caused by anterior glenohumeral dislocation

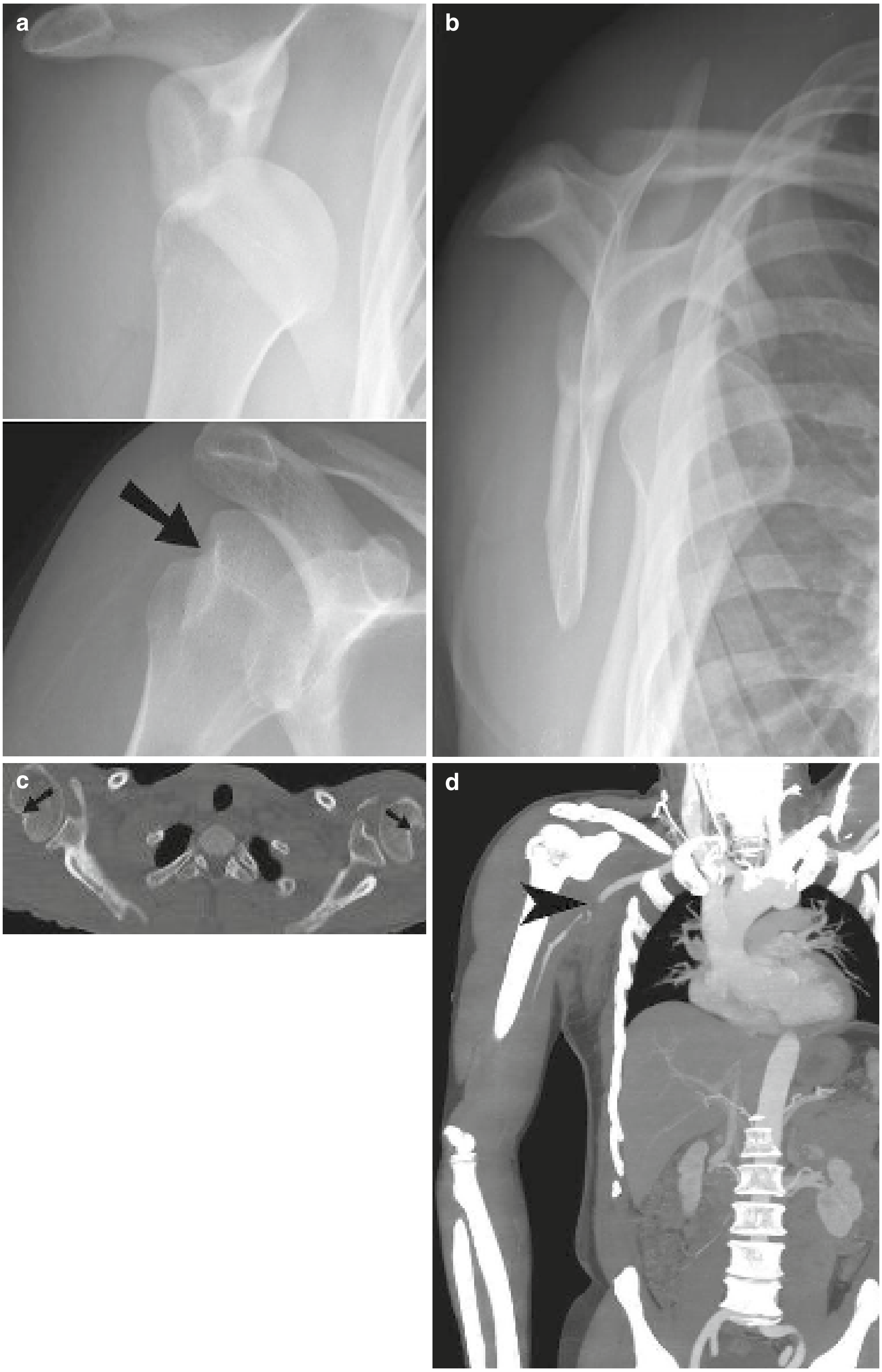

Table 20.2 Classification of glenohumeral joint dislocation

Dislocations	Description
Anteroinferior (subcoracoid dislocation)	More common Due to anterior blow to an abducted arm Results in Hill–Sachs lesion Best seen as a linear or wedge-shaped defect on radiography Can cause Bankart lesion with avulsion of the labroligamentous complex High recurrence rate without operation
Posterior	Consequence of electric shock or seizure Can be bilateral Can cause reverse Bankart lesion
Inferior (luxatio erecta)	Results from hyperabduction of the arm Suspected in a patient with an abducted arm, with the wrist resting on the head
Superior	Due to upward blow on an adducted arm Rarest type Associated with rotator cuff tear

Scapular Fracture

An isolated fracture of the scapula is uncommon and is usually the consequence of direct blunt trauma. It is usually accompanied by tenderness, fracture crepitus, and an adducted upper extremity.

Imaging

Fractures of the scapular body can be horizontal, vertical, or comminuted. Radiologic evaluation starts with true AP and lateral scapular views. However, CT is optimal for delineation of these fractures and identification of associated fractures.

Since scapular fractures are often accompanied by other injuries, they are frequently missed on AP chest radiographs as the associated injuries are either more clinically urgent (lung contusion, pneumothorax, widened mediastinum) or more obvious (clavicle and rib fractures).

Variations in the anatomy of scapula can be confused with a fracture, especially in youth. For example, epiphyseal lines at the acromion and coracoid can be mistakenly read as fractures. Comparison films may not be helpful as ossification centers may be asymmetric. In approximately 8% of the adult population, the ossification center in acromion remains unfused.

Proximal Humerus Fractures

A fracture of the proximal humerus represents a common injury in the elderly population, most often occurring after a fall on an outstretched hand. Alternatively, a direct blow to the lateral shoulder can cause a head-splitting fracture by forcing the humeral head directly into the glenoid fossa. Most commonly, proximal humeral fractures occur at the surgical neck.

Table 20.3 The Neer classification of the proximal humerus fractures

Classification	Description
One-part fracture	Fracture lines involve 1–4 parts None are displaced
Two-part fracture	Fracture lines involve 2–4 parts One part is displaced
Three-part fracture	Fracture lines involve 3–4 parts Two parts are displaced
Four-part fracture	Fracture lines involve more than 4 parts Three parts are displaced with respect to the fourth part

Imaging

The Neer classification system describes the severity of proximal humerus fractures according to the displacement of the four bone segments (greater tuberosity, lesser tuberosity, head, and surgical neck) [6]. Displacement is defined as >1 cm or >45° of separation from the anatomic position of the bone fragment. The majority of fractures are one-part fractures that are not associated with significant displacement of any segments (Table 20.3).

Since the anterior circumflex humeral artery is closely associated with the surgical neck of the humerus, fractures may compromise the blood supply to the humeral head and result in avascular necrosis (AVN). Other complications of displaced fractures include rotator cuff tear and nonunion.

Supracondylar Fractures

Pediatric supracondylar fractures of the humerus are most frequently caused by axial loading on the elbow from a fall on an outstretched hand. Low-impact falls can also result in supracondylar fractures in osteoporotic elderly patients.

Imaging

The radiographic findings include an elevated anterior or posterior fat pad, caused by hemarthrosis. A posterior fat pad sign may represent the sole finding in a patient with radiographically occult fracture [7]. Anterior displacement of the anterior humeral line which ordinarily transects the middle third of the capitellum is also a common finding (Fig. 20.5).

Supracondylar fractures are traditionally classified by the Gartland system: class I is a nondisplaced fracture; class II fractures have anterior cortical disruption; and class III fractures have both anterior and posterior disruption [8].

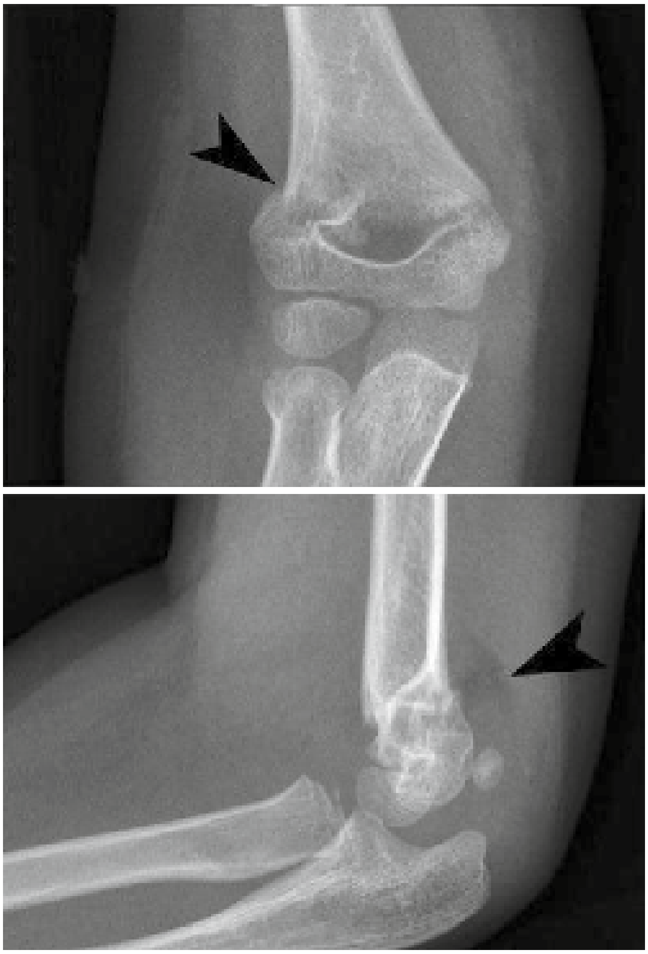

Fig. 20.5 Supracondylar fracture. AP projection of the elbow depicts a focal cortical step-off of the supracondylar humerus (*arrowhead*), indicative of supracondylar fracture (*top*). A lateral projection of the elbow shows the elevated posterior fat pad (*arrowhead*), which normally should not be seen and indicates an effusion. Also, the anterior humeral line passes through the anterior margin of the capitellum

Radial Head Fractures

Radial head fractures are usually the result of axial loading from a fall on an outstretched hand where the radial head is forced into the capitellum. They account for approximately 33%–50% of elbow fractures, and about half of them are nondisplaced fractures. Less commonly, it occurs secondary to posterior elbow dislocation. Fractures are classified into four types: type I is nondisplaced, type II is a displaced marginal fracture, type III fracture is comminuted, and type IV fracture is associated with elbow dislocation (Table 20.4).

Table 20.4 Radial head fractures

Classification	Description
Type I	Nondisplaced fracture
Type II	Displaced marginal fracture
Type III	Comminuted fracture
Type IV	Elbow dislocation

Imaging

On radiography, the fracture line may be subtle or radiographically occult. AP, lateral, and radiocapitellar views (angled 45° cephalad) may be obtained. Lateral radiographs may reveal anterior and posterior fat pad signs, which indicate hemarthrosis and are suggestive of an underlying radial head fracture. The radial head should be aligned with the capitellum in all views, and any disruption of the radiocapitellar line indicates radial head dislocation.

Radial head fractures can be associated with elbow dislocation and fractures of the capitellum or coronoid process. Avulsion of the medial epicondyle may also result from excessive, valgus stress.

Medial and Lateral Condyle Fractures

Fractures of the humeral condyles represent a small fraction of elbow injuries with lateral fractures being more common than medial. Fractures of the condyles in the pediatric population are often Salter–Harris type IV fractures with involvement of epiphysis, physis, and metaphysis. Either condyle may be fractured as a result of a direct force applied to the elbow at an angle during flexion. These fractures are associated with instability and capsular and ligament injuries on the opposite side of the joint.

Radiographic findings may be subtle in the immature elbow, particularly distinguishing between condylar fractures and epicondylar fractures, which are extra-articular. Comparison with the contralateral extremity anatomy may be valuable. Stress views may be helpful with the application of valgus or varus forces under anesthesia. MRI, arthrography, or oblique radiographic views may also reveal slight displacement [9].

Associated injuries include elbow dislocation or associated fracture of the radial head. Additionally, fracture nonunion, valgus deformity, or ulnar neuritis can complicate recovery [10].

Medial Epicondyle Avulsion

Avulsion of the medial epicondyle of the humerus is a common sports-related injury in adolescents. It is the result of extreme valgus force on the apophysis secondary to contraction of the forearm flexors during pitching or arm wrestling. This fracture is also described in children.

If avulsion involves a bony fragment, it may be apparent on AP radiography. If bone is not fractured, then MRI or ultrasound is essential to assess for soft tissue injury.

Because of its close association with the medial epicondyle, damage to the ulnar nerve may occur.

Elbow Dislocation

Elbow dislocation is almost always caused by a fall on an outstretched hand triggering a posterior dislocation. Injury progresses in three stages: Stage 1 is associated with posterolateral ulnar subluxation with disruption of the lateral ulnar collateral ligament (UCL). A stage 2 injury is characterized by perching of the coronoid process inferior to the trochlea. When the coronoid rests posterior to the trochlea, the injury is classified as stage 3.

Ligamentous disruption can be best visualized on T2-weighted MR imaging and reveals complete tear of the lateral UCL. The other findings may include disruption of the radial collateral ligament as well as injury to the brachialis muscle or tendon.

Complex dislocations may be associated with fractures (radial head, radial neck, coronoid process, or capitellum) or neurovascular injury (brachial artery or ulnar nerve). Late complications include myositis ossificans, leading to limitation of range of motion of the elbow.

Forearm Fracture Dislocations

Galeazzi fracture dislocation involves fracture through the midshaft of the radius with associated subluxation or dislocation of the distal radioulnar joint (Fig. 20.6a). In an adult, a radial fracture is almost always accompanied by injury to the distal radioulnar joint. The Galeazzi fracture dislocation is uncommon in children, with only approximately 5% of pediatric radial shaft fractures accompanied by disruption at the distal radioulnar joint [9].

Bowing fracture is an incomplete fracture of long bones seen exclusively in pediatric patients. Radius and ulna are the most common affected bones (Fig. 20.7). Plain radiography demonstrates bowing of the bone if the view is obtained in a different plane to the direction of bowing. No fracture line or cortical injury is seen on the plain radiograph. Diaphysis of the paired bone is commonly fractured or sometimes dislocated.

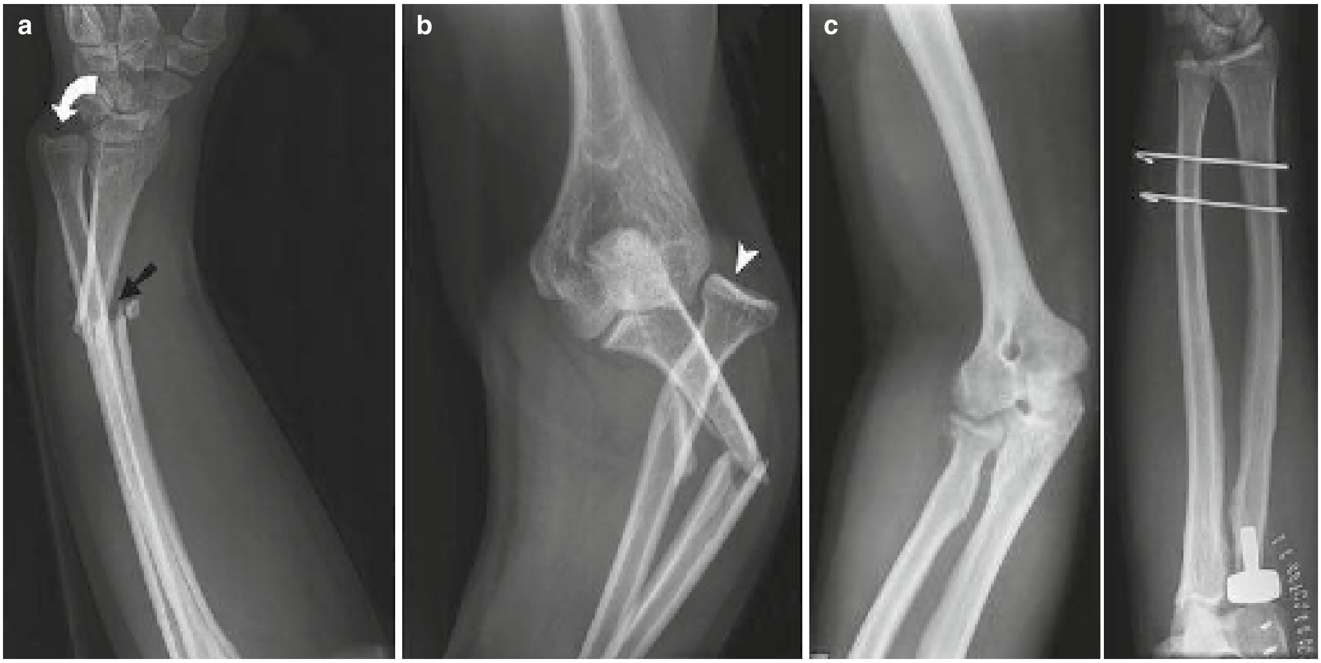

Fig. 20.6 Forearm fracture dislocations. (**a**) Galeazzi fracture dislocation: lateral view of the forearm depicts a fracture of the shaft of the radius (*straight arrow*) with associated disruption at the distal radioulnar joint (*curved arrow*). (**b**) Monteggia fracture dislocation: radiograph demonstrates fracture of the proximal ulnar shaft with dislocation of the radial head (*arrowhead*). (**c**) AP view of the elbow (*left*) shows a subtle nondisplaced radial head fracture as a component of the Essex–Lopresti complex. After surgical repair, a radial head prosthesis is in place, and there is normal alignment at the distal radioulnar joint with K-wire fixation (*right*)

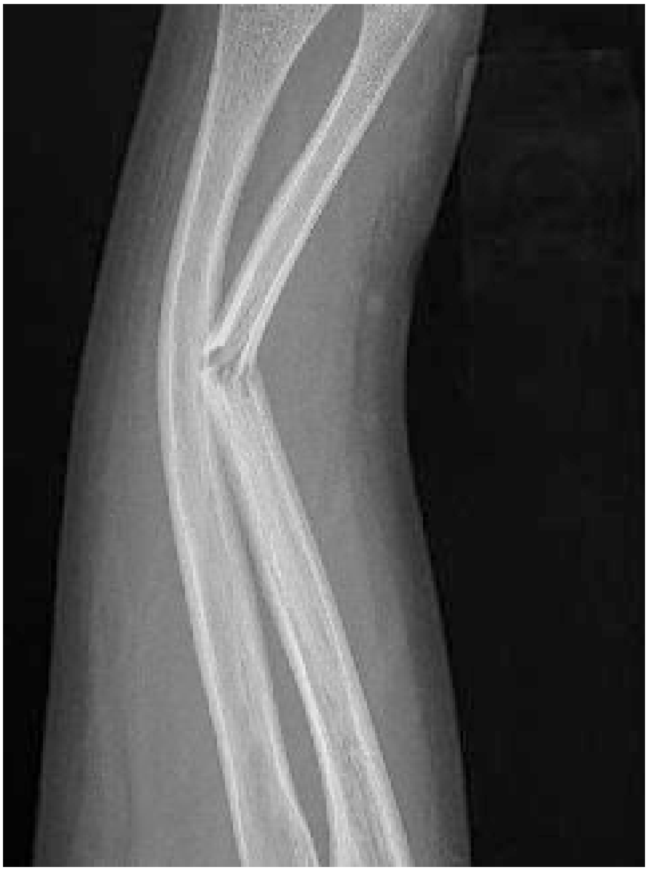

Fig. 20.7 Bowing fracture of radius. Plain radiograph shows bowing fracture of the radial diaphyses, adjacent to ulnar fracture

Table 20.5 Fractures of the forearm

Fracture	Description
Galeazzi	Fracture in the midshaft of the radius Associated subluxation or dislocation of the distal radioulnar joint Uncommon in children
Monteggia	Fracture of the ulnar diaphysis with dislocation of the radial head Associated dislocation of the radial head Involves a proximal ulnar fracture with anterior apex angulation and anterior radial head dislocation
Essex–Lopresti complex	Combination of a fracture of the radial head and dislocation at the distal radioulnar joint
Nightstick fracture	Isolated fracture of the ulna in the distal shaft

Monteggia fracture dislocation is defined as fracture of the ulnar diaphysis with dislocation of the radial head (Fig. 20.6b). It most commonly involves a proximal ulnar fracture with anterior apex angulation and anterior radial head dislocation. As a rule, an angulated fracture of the radius or ulna is seen with fracture or dislocation of the other bone in the forearm. The combination of a fracture of the radial head and dislocation at the distal radioulnar joint is known as the Essex–Lopresti complex (Fig. 20.6c). A nightstick fracture is defined as an isolated fracture of the ulna, often in the distal shaft (Table 20.5).

Distal Radius Fractures

The majority of forearm fractures are at the distal radius and typically occur from a fall on an outstretched hand in pronation and dorsiflexion (Figs. 20.8 and 20.9). The radial fracture is most commonly extra-articular and transversely oriented.

The pronator quadratus sign suggests a distal radius fracture that may be otherwise radio-occult. This sign is identified on lateral radiographs as anterior displacement, bowing, or obliteration of the pronator quadratus fat stripe, which parallels the pronator quadratus muscle and represents accumulation of fluid, usually blood, within the pronator quadratus muscle (Fig. 20.8a).

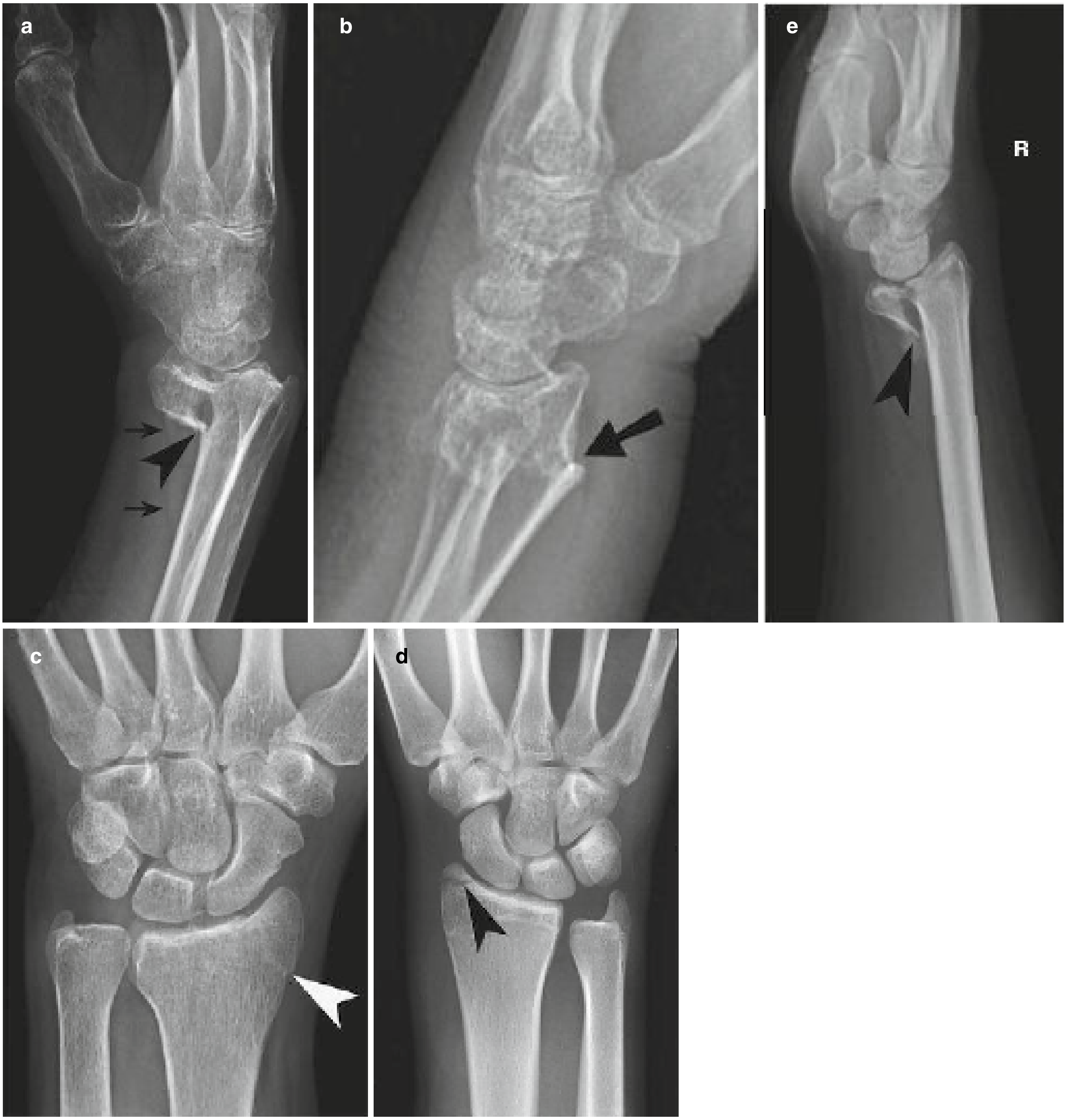

Fig. 20.8 Distal radius fractures. (**a**) Pronator quadratus sign: the radiolucent stripe of fat (*arrows*) along the anterior border of the pronator quadratus is bowed anteriorly because of edema/hemorrhage in the pronator quadratus muscle, secondary to the distal radial fracture (*arrowhead*). (**b**) Colles' fracture: lateral view of the distal radius demonstrates a transversely oriented fracture (*arrow*) of the distal radius with dorsal displacement of the distal fragment. (**c**, **d**) Chauffeur's fracture: AP view of the wrist joint in two different patients demonstrates acute fractures of the radial styloid process (*arrowheads*). (**e**) Reverse Barton's fracture: there is intra-articular fracture of the distal radius (*arrowhead*) through the volar aspect of the articular surface. Compared to Barton's fracture which is an intra-articular fracture through the dorsal rim of the distal radius

Colles' Fracture

It involves dorsal impaction and angulation of the distal radius fracture fragment, leading to the "dinner fork" deformity (Fig. 20.8b). Smith fracture or reverse Colles' fracture is characterized by volar impaction, displacement, and angulation of the distal radial fracture fragment.

Chauffeur's Fracture

It is an intra-articular fracture of the radial styloid due to avulsion of radiocarpal ligament and is also known as "Hutchinson" fracture (Fig. 20.8c, d). It results from direct trauma or axial loading. These fractures are usually displaced due to pulling of radiocarpal ligaments; however, they can be nondisplaced and subtle.

Barton's Fracture

It refers to an intra-articular fracture involving the dorsal aspect of the distal radius and may be accompanied by fracture of the radial styloid (Fig. 20.8e).

Torus (buckle) fracture (Fig. 20.9a) of the distal radius is the most common fracture of distal forearm in children. It is a greenstick fracture where the cortex buckles on the compressed side and is intact on the opposite side.

Salter–Harris type 1 fracture (Fig. 20.9b) of distal radius occurs due to fall on outstretched hand and occurs in the first decade of life. The hyperextension and supination cause dorsal displacement of the distal epiphyseal center. It is often associated with fracture of distal radius (50%). After healing, abnormalities in the growth of the radius are uncommon.

Treatment is based on reestablishing normal radius length, with appropriate radial volar tilt and congruence at the radiocarpal and distal radioulnar joint. Acute carpal tunnel syndrome with median nerve palsy is a known complication of Colles' fracture, and carpal tunnel syndrome has been reported to develop even many years after the initial injury [10].

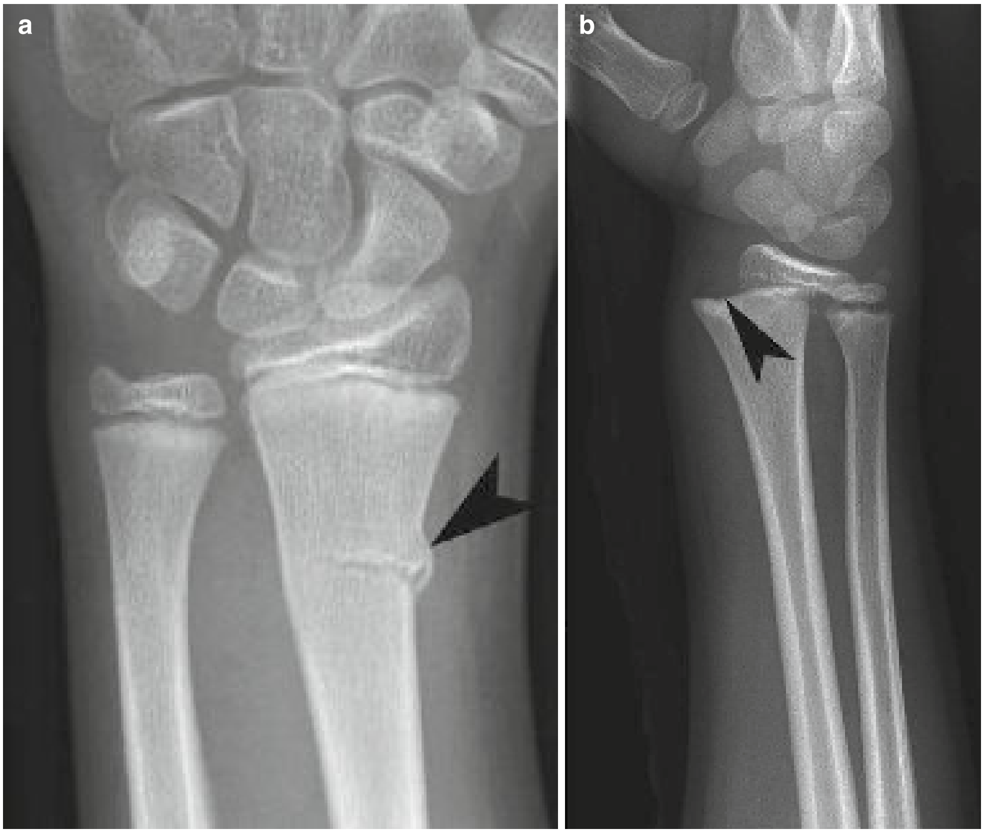

Fig. 20.9 Distal radial fractures. (**a**) Buckle fracture: AP view of the wrist demonstrates a greenstick buckle fracture (*arrowhead*) of the distal radial metaphyses. (**b**) Salter–Harris type 1 fracture: radiograph of the wrist demonstrates dorsal displacement of the distal radial epiphyseal center due to Salter–Harris type 1 injury through the physis (*arrowhead*)

Carpal Fractures

Scaphoid fracture is the most common isolated carpal bone fracture, representing approximately 75% of carpal bone fractures [11–13]. Fall onto a dorsiflexed wrist is the usual mechanism and results in impingement of the scaphoid by the radial styloid with tensile loading of the scaphoid waist. Thus, 70% of fractures occur through the scaphoid waist [11].

Triquetral fractures make up the second most common carpal fracture (approximately 15%) and result from severe dorsiflexion with ulnar deviation of the wrist. The mechanism of injury involves impaction of the triquetrum against the ulnar styloid with avulsion of a bone fragment from the dorsal triquetral surface. Transverse or sagittal fractures of the triquetral body are less common.

Hamate bone fractures are less common and result from a direct blow to the ulnar aspect of the wrist when an individual is holding an object such as a golf club or baseball bat. Fractures can occur commonly through the base of the hamate hook or through the body of the hamate. Fracture of the hook of hamate can be due to direct trauma or avulsion through the transverse carpal ligament. These fractures can present with persistent pain, but can also occur acutely. Treatment may be conservative or surgical.

Fractures of the remaining carpal bones including the capitate, lunate, and pisiform are less common and may be seen following a direct forceful blow to the wrist in the setting of other fracture dislocations.

Imaging

In the setting of acute scaphoid fracture, initial radiographs may be normal. A dedicated scaphoid view may be helpful and involves positioning the wrist in maximal ulnar deviation with the X-ray beam directed in an anteroposterior direction with approximately 15° of craniocaudal angulation. Alternatively, a repeat radiograph can be obtained 7–10 days later and may show bone resorption at the fracture site (Fig. 20.10a, b). CT or MRI may be more sensitive for depiction of the acute fracture.

Triquetral fractures are typically occult on frontal radiographs, but a lateral projection may show a bone chip dorsal to the proximal carpal row with associated soft tissue swelling (Figs. 20.10c, d and 20.11). A hamate hook fracture may be suggested on a frontal radiograph by indistinctness or lack of the normally seen “eye” of the hamate hook. Alternatively, a carpal tunnel view or CT with axial reconstruction may show this fracture to better advantage.

Since the blood supply of the scaphoid is via a single artery passing from the distal pole to feed the proximal pole, a fracture through the scaphoid waist predisposes to AVN. Although the initial radiograph may be normal, later they show changes of AVN, such as cystic change, sclerosis, cortical collapse, and fragmentation. MRI may initially show heterogeneous areas of low signal on T1- and T2-weighted sequences, indicative of areas of sclerosis (Fig. 20.10b). Homogenous gadolinium enhancement indicates an intact blood supply, whereas lack of enhancement confirms irreversible necrosis.

Nonunion of a scaphoid fracture may result from a delay in diagnosis or fixation. Ultimately, a fibrous union may form between the two scaphoid poles with low-signal material filling the fracture gap on T1- and T2-weighted imaging. Scaphoid nonunion with advanced collapse (SNAC wrist) represents end-stage nonunion and involves carpal collapse with proximal migration of the capitate between the two scaphoid poles with dorsal angulation of the lunate.

Hamate fractures are often not visualized on plain radiography. Carpal tunnel view, 20° supine oblique view, and reverse oblique views can be used to increase sensitivity of plain radiography in demonstrating hamate fractures. Statistically, the most common fracture of hamate involves the hook and can be best seen on carpal tunnel view (Fig. 20.12). CT or MRI can be performed if the plain radiography findings are nondiagnostic for hamate fracture.

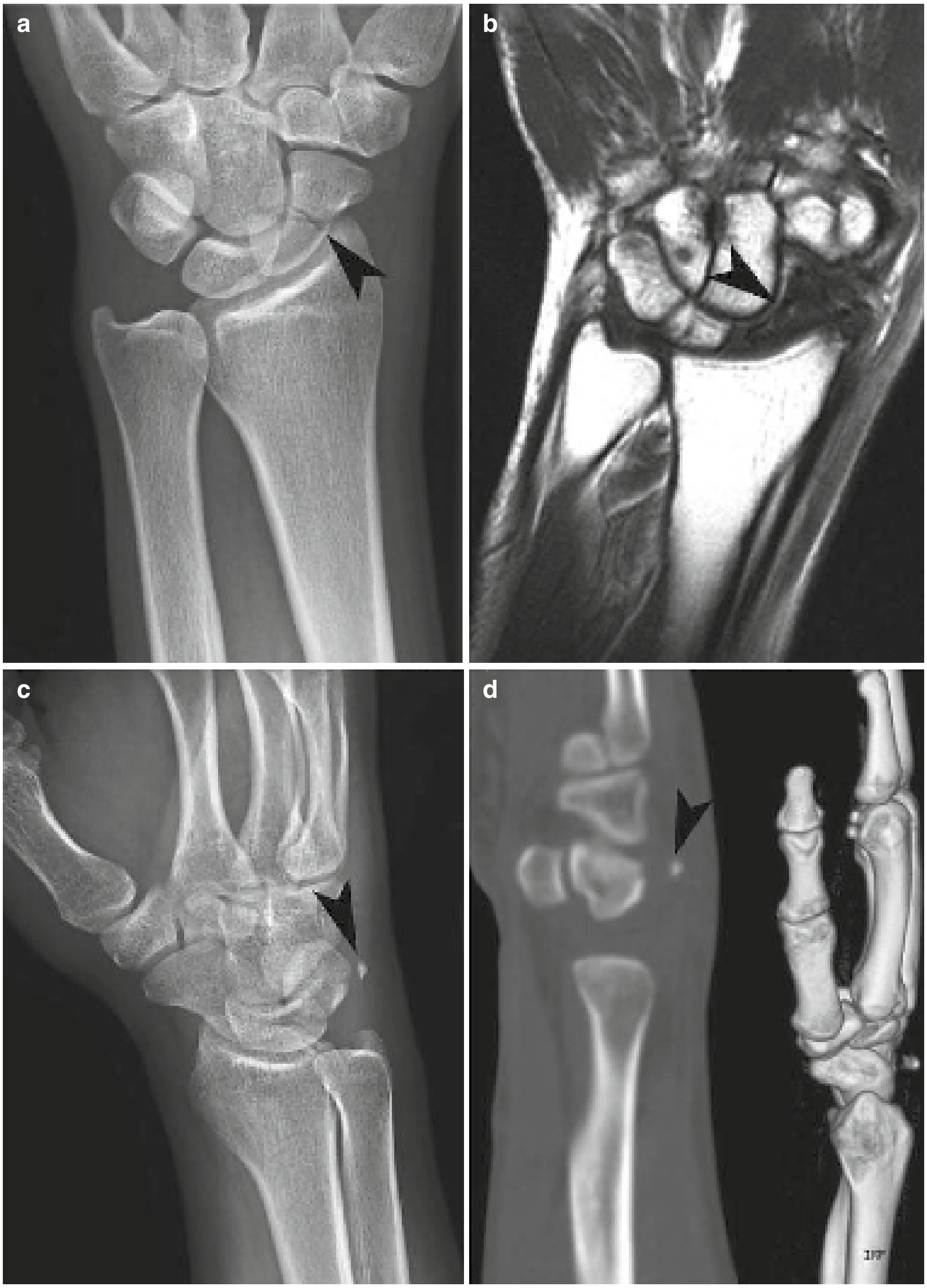

Fig. 20.10 Carpal bone fractures. (**a**) Scaphoid fracture: AP view of the wrist demonstrates a fracture lucency extending through the scaphoid waist (*arrowhead*), the most commonly fractured site in the scaphoid bone. (**b**) Avascular necrosis of scaphoid: coronal T1-weighted sequence demonstrates diffuse low signal within a collapsed scaphoid bone (*arrowhead*) secondary to avascular necrosis. (**c**) Triquetrum fracture: oblique view of the wrist shows a small fracture fragment (*arrowhead*) dorsal to the triquetrum. (**d**) Triquetrum fracture: sagittal reformation and 3D volume-rendered reconstruction demonstrate a small fracture fragment (*arrowhead*) dorsal to the triquetrum

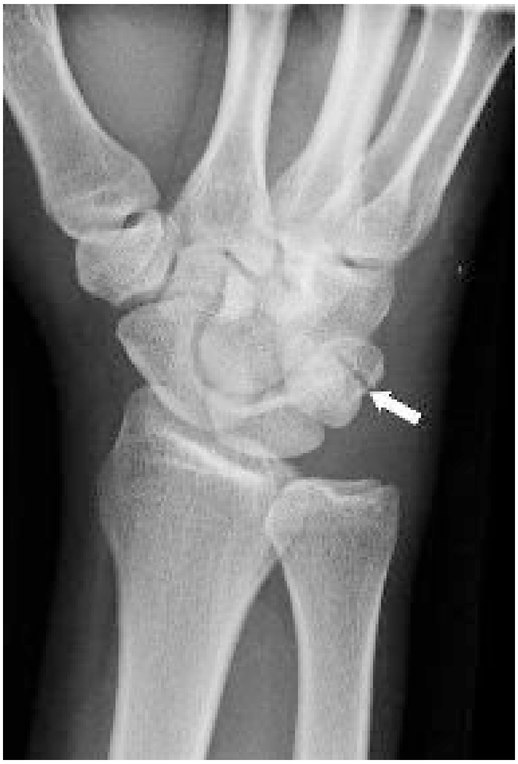

Fig. 20.11 Triquetrum fracture. Plain radiograph demonstrates fracture of the triquetrum (*arrow*)

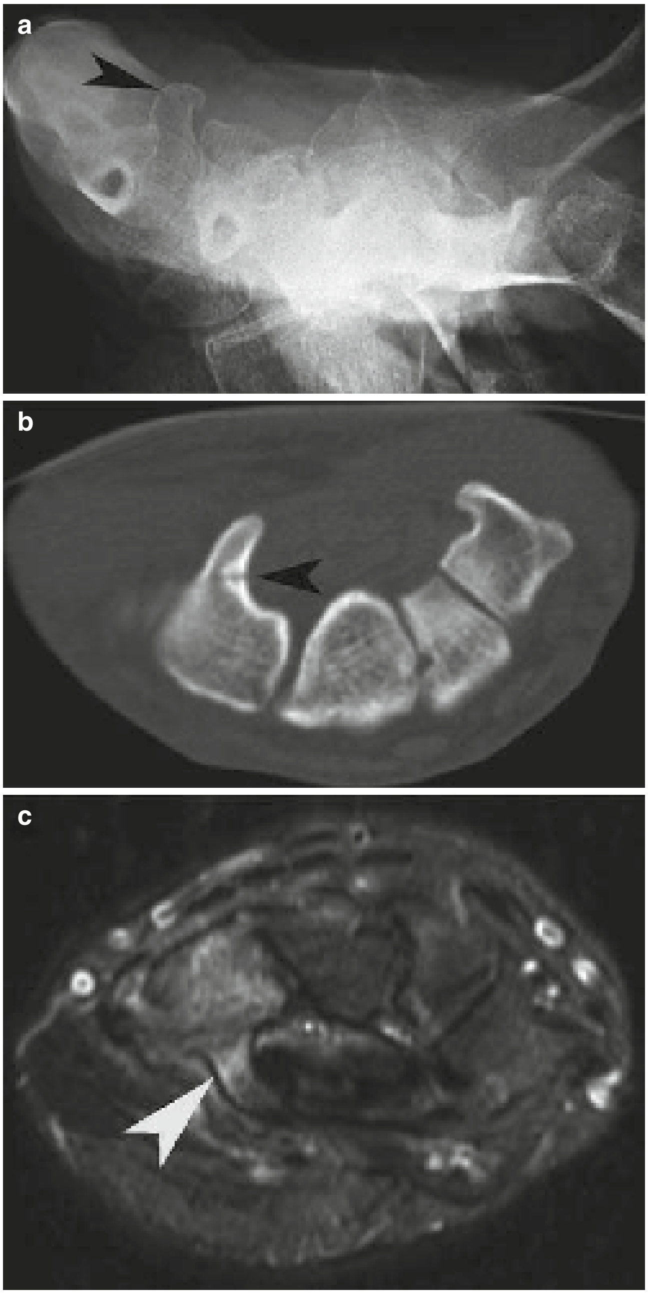

Fig. 20.12 Hamate fracture. (**a**) Carpal tunnel view of the wrist showing a fracture through the hook of hamate (*arrowhead*). (**b**) Axial CT through the wrist shows a fracture through the hook of hamate (*arrowhead*). (**c**) Axial T2-weighted sequence with fat suppression shows linear high signal (*arrowhead*) intensity bone marrow edema due to the fracture of the hook of hamate

Perilunate Instability Injuries

The mechanism of perilunate instability injuries typically involves falling on an outstretched hand or extreme loading applied to a hyperflexed or extended wrist. Mayfield et al. identified four stages of perilunate instability based on the severity of injury (Fig. 20.13a, b). These include (1) scapholunate dissociation, (2) capitolunate dislocation, (3) lunotriquetral dissociation, and (4) lunate dislocation [12].

Scapholunate dissociation is the least severe injury and involves disruption of the scapholunate and radioscaphoid ligaments, leading to the dorsal intercalated segmental instability (DISI) injury pattern. Normally, on the lateral projection, the scapholunate angle measures 30°–60°. The DISI pattern represents volar tilt of the scaphoid with dorsal tilt of the lunate, which increases the scapholunate angle above 60°. On the posteroanterior radiograph, widening of the scapholunate interval >3 mm gives rise to the "Terry-

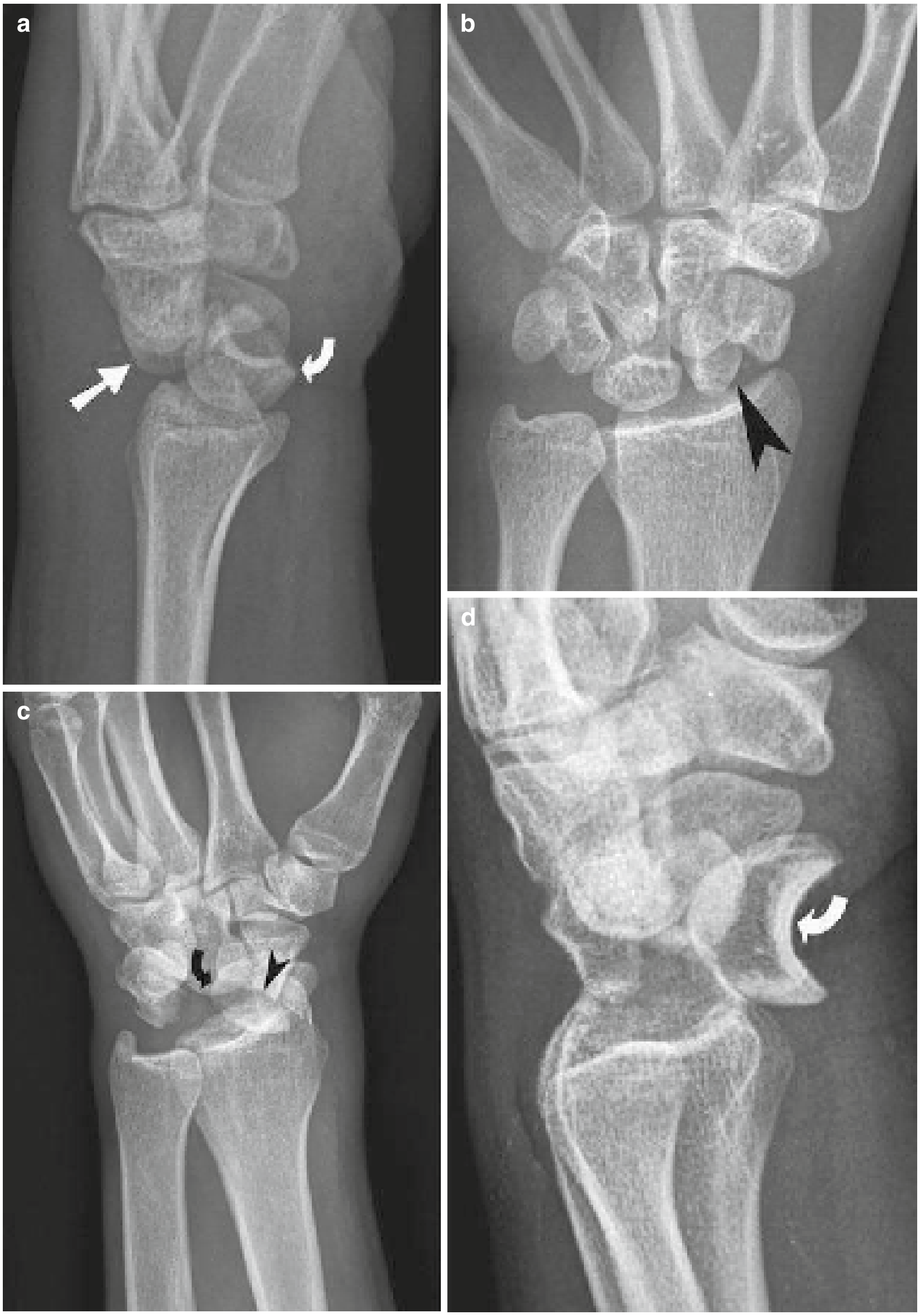

Fig. 20.13 Perilunate instability injuries. (**a**, **b**) Lateral and frontal view of the wrist shows the classic appearance of perilunate dislocation with dorsal dislocation of the capitate (*straight arrow*). Note that the lunate (*curved arrow*) maintains a normal alignment with the radius. There is fracture seen through the waist of the scaphoid with displacement of the proximal fragment (*arrowhead*). (**c**, **d**) Lateral and frontal view of the wrist shows volar dislocation of lunate (*curved arrow*) in a "spilled teacup" configuration. The capitate remains well aligned with the radius. The AP view in the same patient depicts an abnormal pie-shaped appearance of the lunate secondary to volar flexion. There is fracture seen involving the scaphoid (*arrowhead*)

Thomas" sign. Associated volar rotation of the scaphoid leads to the distal scaphoid pole viewed en face giving rise to the "signet ring" sign on the AP projection. Scapholunate dissociation eventually leads to further widening of the scapholunate interval with loss of cartilage at the radioscaphoid joint and proximal migration of capitate (scapholunate advanced collapse or SLAC wrist).

Capitolunate dislocation, also known as perilunate dislocation, is defined as dorsal dislocation of the capitate, while the longitudinal alignment of the lunate and radius is preserved (Fig. 20.13a).

Lunotriquetral dissociation results from rupture of lunotriquetral ligaments and may include perilunate dislocation but is considered more severe. On the AP view, the scaphoid is volar flexed, and so the "signet ring" sign may be identified. On the lateral radiograph, the lunate is volar flexed, leading to a scapholunate angle <30° or volar intercalated segmental instability (VISI deformity).

Lunate dislocation, the most severe injury in the perilunate instability spectrum, involves volar dislocation of the lunate, while the capitate remains in normal alignment with the radius. On the lateral projection, the lunate appears as a "spilled teacup" and is oriented approximately 90° with respect to the radius. On the frontal projection, the lunate takes on a triangular or "pie" shape, in contrast to its normal trapezoidal appearance (Fig. 20.13c, d and Table 20.6).

Table 20.6 Perilunate instability injuries

Condition	Description
Scapholunate dissociation	Least severe injury Disruption of the scapholunate and radioscaphoid ligaments Leading to the dorsal intercalated segmental instability "Terry-Thomas" sign "Signet ring" sign
Capitolunate dislocation	Also known as perilunate dislocation Dorsal dislocation of the capitate The longitudinal alignment of the lunate and radius is preserved
Lunotriquetral dissociation	Results from rupture of lunotriquetral ligaments Involves perilunate dislocation but more severe "Signet ring" sign
Lunate dislocation	The most severe injury Volar dislocation of the lunate Capitate in normal alignment with the radius "Spilled teacup" Triangular or "pie" shape on the frontal projection

Metacarpal Injuries

A transverse fracture of the neck of the fifth metacarpal, and less frequently the fourth metacarpal, with volar angulation is the most common metacarpal fracture and is called boxer's fracture. It typically results from axial loading of the metacarpal when the closed fist strikes a wall or jaw. Often, a butterfly fragment that is impacted volarly can be identified. A posteroanterior view of the hand will demonstrate shortening at the metacarpal neck (Fig. 20.14). A lateral view will demonstrate volar angulation at the fracture site.

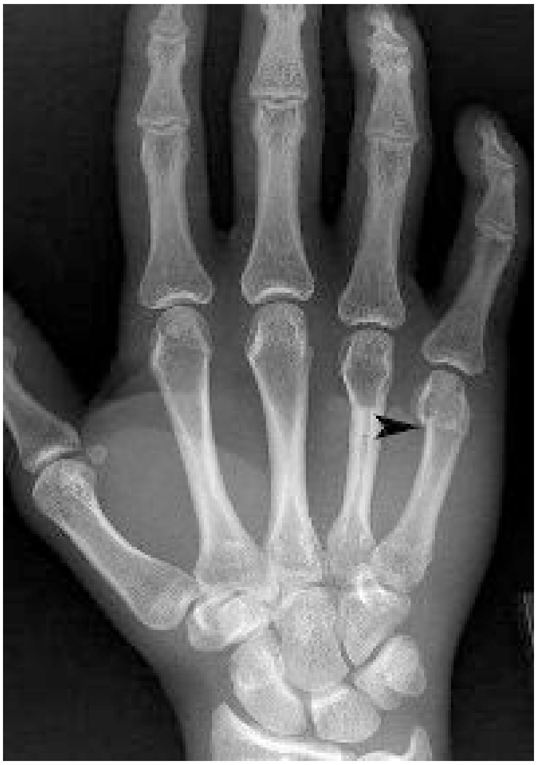

Fig. 20.14 Boxer's fracture. AP view of the hand depicts an impacted fracture through the neck of the fifth metacarpal (*arrowhead*) with shortening of the overall length of the metacarpal

Gamekeeper's Thumb

A complete or partial tear of the UCL of the thumb ("gamekeeper's thumb") classically occurs when a falling skier improperly plants his pole resulting in sudden abduction and valgus stress at the first metacarpophalangeal (MCP) joint. Disruption most commonly occurs at the distal attachment of the UCL, at the base of the proximal phalanx. Radial collateral ligament injury is significantly less common than UCL injury and results from forceful adduction at the MCP joint irrespective of thumb position.

Initial radiographic evaluation may reveal an avulsed bone fragment from the proximal phalanx at the distal attachment site of the UCL (Fig. 20.15). Abduction stress radiographs can demonstrate >30° of radial deviation at the MCP joint or >20° difference compared to the contralateral side, findings indicative of complete disruption of the ulnar collateral ligament. MRI may reveal abnormal signal within the ligament in the case of a partial tear. In the setting of a complete tear, discontinuity with proximal retraction of the ligament may be seen, referred to as the "yo-yo on a string" appearance.

A complete tear with proximal retraction of the ulnar collateral ligament may lead to abnormal interposition of the adductor aponeurosis between the retracted proximal UCL and its distal attachment, a complication known as the Stener lesion which complicates approximately 29% of cases [13]. This lesion mandates surgical repair to avoid chronic instability of the joint.

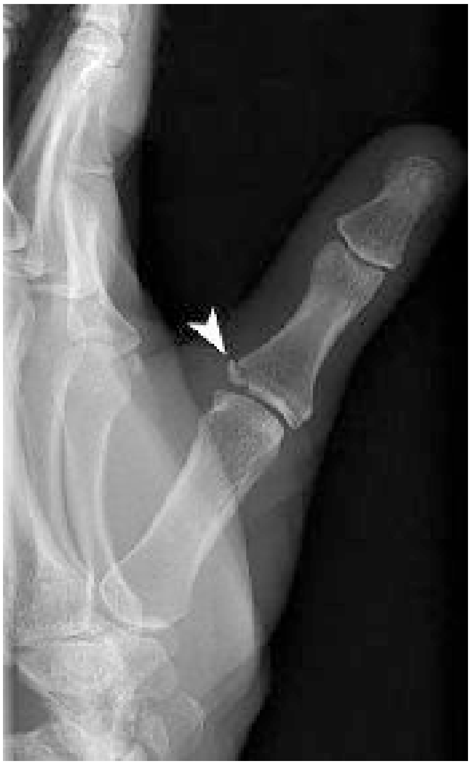

Fig. 20.15 Gamekeeper's thumb. AP view of the thumb shows an avulsed fragment (*arrowhead*) at the base of the proximal phalanx, at the attachment site of the ulnar collateral ligament

Injury at the Carpometacarpal Joint of the Thumb

An intra-articular fracture at the base of the first metacarpal, known as a Bennett fracture, is often accompanied by displacement or distraction of the metacarpal shaft due to continued traction by the adductor pollicis and abductor pollicis longus muscles, while the small ulnar fracture fragment is held in place by ligamentous attachments (Fig. 20.16). A Bennett fracture is treated with open reduction and fixation.

A Rolando fracture is a comminuted fracture of the metacarpal base. Soft tissue swelling in isolation may be indicative of injury to the anterior longitudinal ligament, which is the most important stabilizer at the base of the thumb. MRI may depict a partial or complete thickness tear of the ligament. Surgical repair of the comminuted Rolando fracture may be more challenging than Bennett fracture, with a higher likelihood of eventually developing post-traumatic osteoarthritis.

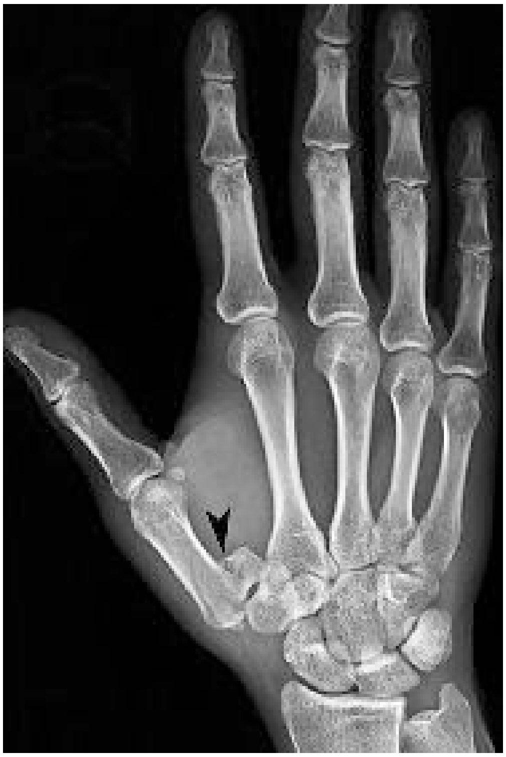

Fig. 20.16 Bennett fracture. AP view of the hand shows an intra-articular fracture at the base of the thumb (*arrowhead*). Note that the metacarpal shaft is displaced in a radial direction, secondary to traction by abductor pollicis longus

Phalangeal Injuries

Phalangeal tuft fractures are commonly associated with occupational injury and result from a direct loading mechanism such as having a heavy object drop on the finger. These fractures may be simple or comminuted. Formation of an epidermoid cyst secondary to dermal elements seeding the fracture site is a known complication [14].

Disruption of the extensor mechanism with an avulsion fracture at the dorsal base of the distal phalanx can occur when the finger is maximally extended and a sudden forceful flexion is caused, such as when the fingertip is struck by a baseball (Fig. 20.17a). This injury is known as mallet finger deformity due to the fixed flexion deformity at the distal interphalangeal (DIP) joint.

A similar injury occurs when the finger is in a flexed position and undergoes abrupt extension, classically occurring when an athlete grabs an opponent's jersey, leading to an avulsion fracture at the distal attachment of the volar plate at the DIP joint at the insertion of the flexor digitorum profundus tendon (Fig. 20.17b). This injury most commonly occurs at the ring finger and results in loss of ability to flex the DIP joint.

In descending order of frequency, phalangeal dislocations may occur dorsally ("coach's finger"), laterally, or volarly. Phalangeal dislocations most commonly occur at the proximal interphalangeal (PIP) joint. Dorsal or volar dislocations are often associated with volar plate disruption with or without avulsion fracture at its distal attachment site at the base of the middle phalanx. Lateral dislocation secondary to valgus or varus stress leads to disruption of one of the collateral ligaments.

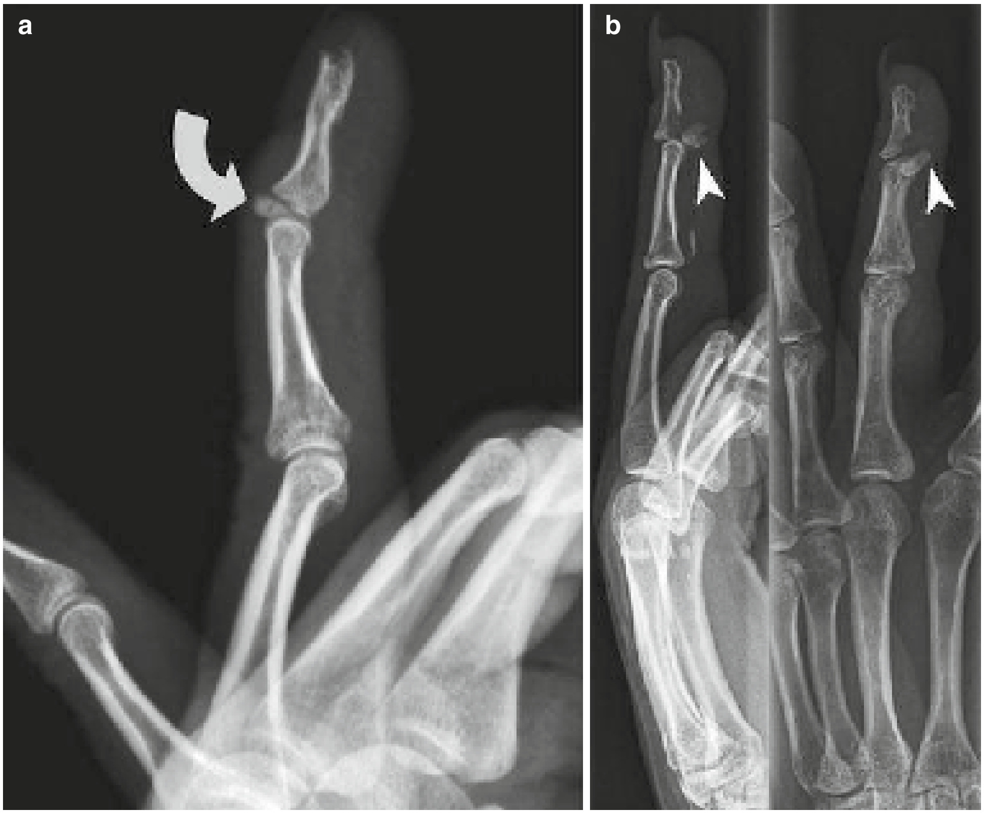

Fig. 20.17 Phalangeal fractures. (**a**) Baseball fracture: lateral view of the index finger shows fixed flexion deformity at the distal interphalangeal joint due to an avulsion fracture (*arrow*) at the extensor tendon attachment site. (**b**) Lateral view depicts an avulsion fracture at the site of attachment of flexor digitorum profundus (*arrowhead*) with fixed extension at the distal interphalangeal joint

Eponymous Fractures of Upper Extremity

Numerous fractures continue to be known by the eponyms of physicians who first described them. Table 20.7 outlines common eponymous fractures of upper extremity.

Teaching Points

- In scapulothoracic dissociation, radiograph shows lateral displacement of the scapula, as indicated by wide separation between the medial edge of the scapula and the spinous processes.
- AP radiographs with a 10°–15° cephalic tilt (Zanca view) are recommended for the assessment of the acromioclavicular region.
- The Neer classification system describes the severity of proximal humerus fractures according to the displacement of the four bone segments (greater tuberosity, lesser tuberosity, head, and surgical neck).
- In radial head fractures, lateral radiographs may reveal anterior and posterior fat pad signs, which indicate hemarthrosis and are suggestive of an underlying radial head fracture.
- Fractures of the condyles in the pediatric population are often Salter–Harris type IV fractures with involvement of epiphysis, physis, and metaphysis.
- Galeazzi fracture dislocation involves fracture through the midshaft of the radius with associated subluxation or dislocation of the distal radioulnar joint.
- Monteggia fracture dislocation is defined as fracture of the ulnar diaphysis with dislocation of the radial head.

Table 20.7 Eponymous fractures of upper extremity

Fracture name	Description
Bankart	Fracture of anterior-inferior glenoid cavity secondary to anterior dislocation of humeral head
Barton	Intra-articular distal radial fracture with extension to the dorsal articular surface and associated dislocation of radiocarpal joint
Bennett	Intra-articular fracture at the base of the first metacarpal with separation of palmar ulnar fragment at the base from the remaining distal metacarpal shaft
Chauffeur's	Intra-articular fracture of the radial styloid due to avulsion of radiocarpal ligament
Colles	Extra-articular, transversely oriented fracture of the distal radius with dorsal impaction, angulation, and displacement of distal radial fragment
Essex–Lopresti	Combination of a fracture of the radial head with interosseous membrane rupture and dislocation of the distal radioulnar joint
Galeazzi	Fracture through the midshaft of the radius with associated subluxation or dislocation of the distal radioulnar joint
Hill–Sachs	Impaction fracture of posterolateral humeral head in the setting of anterior shoulder dislocation
Holstein–Lewis	Spiral fracture of distal third of the humerus with significant association with radial nerve palsy
Monteggia	Fracture of the ulnar diaphysis with dislocation of the radial head
Rolando	Comminuted, intra-articular fracture of the first metacarpal base, fragments of which can produce "Y"- or "T"-shaped morphologies
Smith	Transverse fracture of distal radius with volar impaction, displacement, and/or angulation of the distal radial fracture fragment. Also known as reverse Colles' fracture

Questions

1. Medial segment of clavicle displaces toward which of the following directions in clavicle fractures?
   (A) Superolateral
   (B) Superomedial
   (C) Inferomedial
   (D) Inferolateral
   Ans.wer: B

2. Stanmore triangle classification is used in which of the following conditions?
   (A) Sternoclavicular dislocation
   (B) Acromioclavicular dislocation
   (C) Glenohumeral joint dislocation
   (D) Proximal humerus fractures
   Answer: A

3. Which of the following glenohumeral joint dislocations can cause reverse Bankart lesion?
   (A) Anteroinferior
   (B) Luxatio erecta
   (C) Superior
   (D) Posterior
   Answer: D

4. What pathology is depicted in the following plain radiograph (Fig. 20.18)?
   (A) Lunate fracture
   (B) Scaphoid fracture
   (C) Triquetrum fracture
   (D) Pisiform fracture
   Answer: B

5. What is the imaging diagnosis of the following lateral plain radiograph (Fig. 20.19)?
   (A) Lunate fracture
   (B) Colles' fracture
   (C) Perilunate dislocation
   (D) Triquetrum fracture
   Answer: C

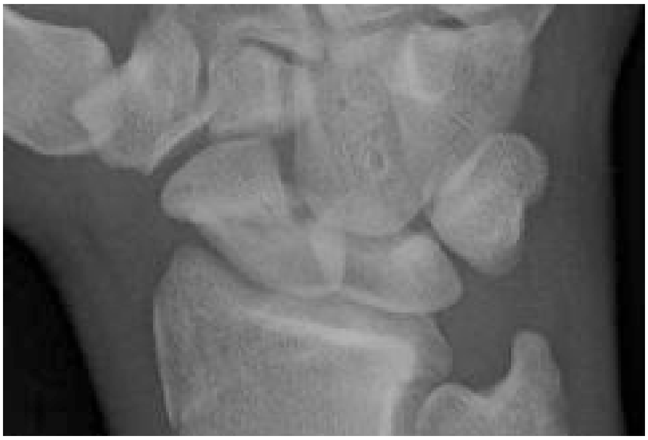

Fig. 20.18 Scaphoid fracture

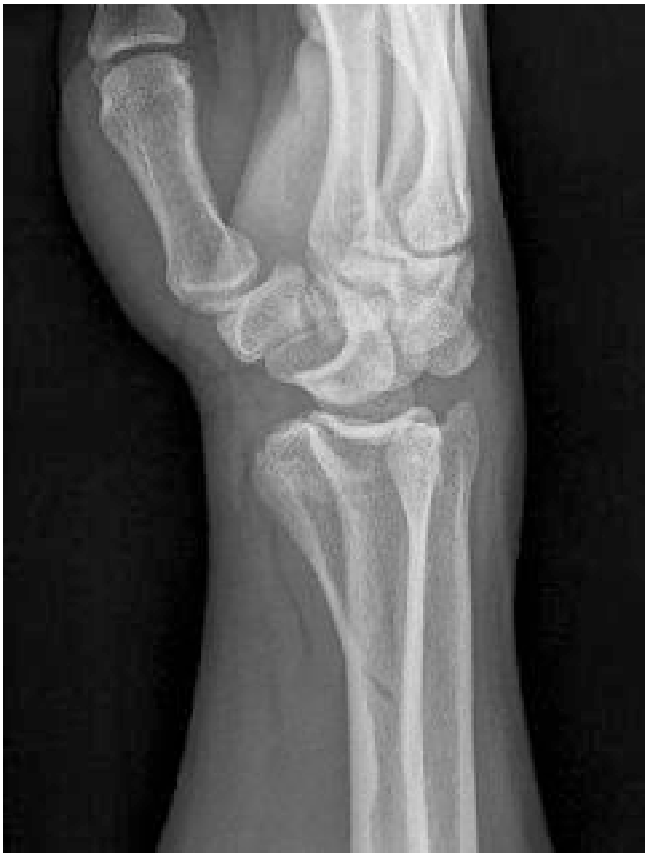

Fig. 20.19 Perilunate dislocation

6. Which of the following imaging findings is depicted in the following plain radiograph (Fig. 20.20)?
   (A) Clavicle fracture
   (B) Hill–Sachs lesion
   (C) Acromioclavicular dislocation
   (D) Glenohumeral joint dislocation
   Answer: B

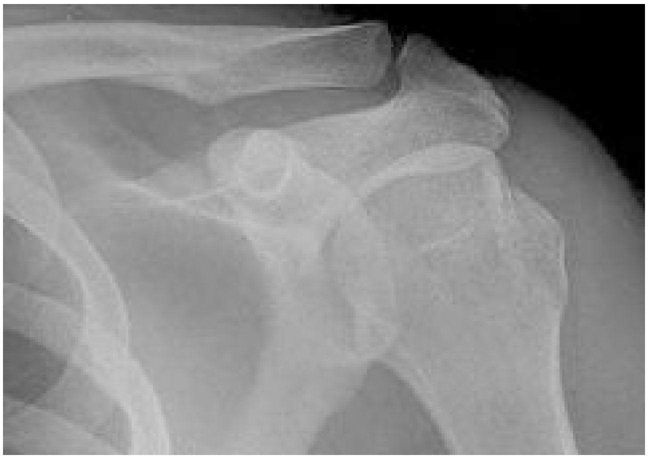

Fig. 20.20 Hill–Sachs lesion

References

1. Lavelle WF, Uhl R. Scapulothoracic dissociation. Orthopedics. 2010;33(6):417–21.
2. Preston CF, Egol KA. Midshaft clavicle fractures in adults. Bull NYU Hosp Jt Dis. 2009;67(1):52–7.
3. Smekal V. Shaft fractures of the clavicle: current concepts. Arch Orthop Trauma Surg. 2009;129(6):807–15.
4. Restrepo CS, Martinez S, Lemos DF, Washington L, McAdams HP, Vargas D, et al. Imaging appearances of the sternum and sternoclavicular joints. Radiographics. 2009;29(3):839–59.
5. Kuhn JE. Treating the initial anterior shoulder dislocation—an evidence-based medicine approach. Sports Med Arthrosc. 2006;14(4):192–8.
6. Neer CS. Displaced proximal humeral fractures. I. Classification and evaluation. J Bone Joint Surg Am. 1970;52(6):1077–89.
7. Mirzayan R, Skaggs DL. The posterior fat pad sign in association with occult fracture of the elbow in children. J Bone Joint Surg Am. 1999;81(10):1429–33.
8. Gartland JJ. Management of supracondylar fractures of the humerus in children. Surg Gynecol Obstet. 1959;109(2):145–54.
9. Walsh HP, McLaren CA, Owen R. Galeazzi fractures in children. J Bone Joint Surg Br. 1987;69(5):730–3.
10. Goyal V, Bhatia M, Behari M. Carpal tunnel syndrome after 22 years of Colles' fracture. Neurol India. 2003;51(1):113–4.
11. Hauger O, Bonnefoy O, Moinard M, Bersani D, Diard F. Occult fractures of the waist of the scaphoid: early diagnosis by high-spatial-resolution sonography. AJR Am J Roentgenol. 2002;178(5):1239–45.
12. Mayfield JK, Johnson RP, Kilcoyne RK. Carpal dislocations: pathomechanics and progressive perilunar instability. J Hand Surg Am. 1980;5(3):226–41.
13. Hinke DH, Erickson SJ, Chamoy L, Timins ME. Ulnar collateral ligament of the thumb: MR findings in cadavers, volunteers, and patients with ligamentous injury (Gamekeeper's thumb). AJR Am J Roentgenol. 1994;163(6):1431–4.
14. Hamad AT, Kumar A, Anand KC. Intraosseous epidermoid cyst of the finger phalanx: a case report. J Orthop Surg (Hong Kong). 2006;14(3):340–2.

Lower Extremity Trauma

21

Rathachai Kaewlai, Mohammad Mansouri,
and Ajay Singh

Introduction

Imaging of extremity trauma usually starts with conventional radiography, which is a cornerstone of orthopedic trauma workup. Standard AP and lateral views are usually diagnostically adequate for the assessment of lower extremity trauma. However, superimposed bony structures in complex areas such as ankle and foot can make image interpretation difficult. Extensive bone and joint injuries, though visible on radiography, may also be challenging for accurate treatment planning. In this regard, multidetector computed tomography (MDCT) with multiplanar reformations (MPRs) will provide a more accurate detection of occult bone and joint injuries and better depiction of complex fractures and dislocations.

Magnetic resonance (MR) imaging has excellent soft tissue contrast and can provide valuable information on the identification of occult fractures, stress fractures, cartilaginous/labral injuries, compartment syndromes, and tendon/ligamentous disruptions. However, the use of MR imaging has mainly been limited by cost and availability. In this chapter, the authors discuss common fractures, easily missed fractures, fracture classifications, and their imaging characteristics.

Pelvis

Standard views: AP, PA with 25° caudal angulation (Ferguson) of the pelvis
Frequent types of fractures
Isolated fractures of the pubic rami
Pelvic ring disruption

Fractures of the pelvis are usually caused by direct injury or by force transmitted longitudinally through the femur. There are two major groups of pelvic fractures: isolated fractures and pelvic ring disruption.

Any part of the pelvis may be affected by an isolated fracture. The commonest one is through the pubic ramus (superior, inferior, or both). Isolated fractures can also be seen involving the iliac wing (Duverney), sacrum, anterior inferior iliac spine (rectus femoris avulsion), anterior superior iliac spine (sartorius avulsion), and ischial tuberosity (hamstring avulsion) (Fig. 21.1).

Pelvic ring disruption refers to osseous or joint disruption at two points of the pelvic ring (sacrum and two innominate bones) approximately opposite to one another. The anterior injury often involves either a fracture through both pubic rami or pubic symphysis diastasis. The posterior injury is usually a subluxation of the sacroiliac joint or a fracture through the ilium or sacral ala. The most widely used classification of pelvic ring disruption is the Young–Burgess system and describes four patterns, according to the direction of forces to the pelvis [1]:

1. Anteroposterior compression: Vertically oriented fractures of the pubic rami, pubic symphysis diastasis, and disruption of the sacroiliac joints. They may be associated with urethral and urinary bladder rupture (Fig. 21.2).
2. Lateral compression: It produces coronal or horizontal fractures of the pubic rami, sacral compression fracture, iliac wing fracture, and central hip dislocation.
3. Vertical shear: It results in vertically oriented fractures of the pubic rami, sacrum, and iliac wings. There is exten-

R. Kaewlai
Department of Diagnostic and Therapeutic Radiology,
Ramathibodi Hospital, Mahidol University, Bangkok, Thailand

M. Mansouri
Department of Radiology, Massachusetts General Hospital,
Boston, MA, USA

A. Singh (✉)
Division of Emergency Radiology, Department of Radiology,
Massachusetts General Hospital, Boston, MA, USA

Harvard Medical School, Massachusetts General Hospital,
Boston, MA, USA
e-mail: asingh1@partners.org

© The Author(s), under exclusive license to Springer Nature Switzerland AG 2024
A. Singh (ed.), *Emergency Radiology*, https://doi.org/10.1007/978-3-031-65770-2_21

   sive ligamentous disruption, often resulting in severe pelvic instability, sciatic nerve, and pelvic vascular injury.
4. Combined mechanism (Table 21.1).

In general, a single break in the pelvic ring is considered stable, while two or more breaks of the pelvic ring are unstable. Most sacral fractures are vertically oriented and are associated with fractures of the pelvis or lumbosacral dislocation.

Denis classification divides sacrum into three zones (Table 21.2) [2].

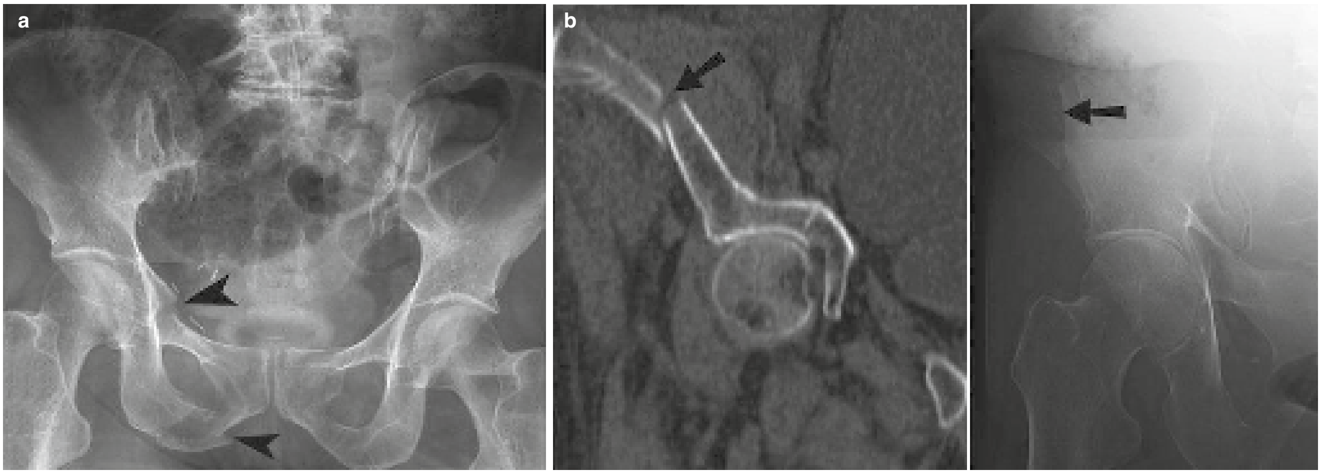

Fig. 21.1 Pelvic fracture. (**a**) An AP radiograph of the pelvis shows displaced vertically oriented fractures (*arrowheads*) of the right superior and inferior pubic rami and widening of the right sacroiliac joint, representing an anteroposterior compression (APC) type of pelvic ring disruption. (**b**) A focused AP radiographic view and corresponding CT image of the right iliac wing show an isolated fracture of the right iliac wing (*arrows*), which is considered a stable pelvic injury

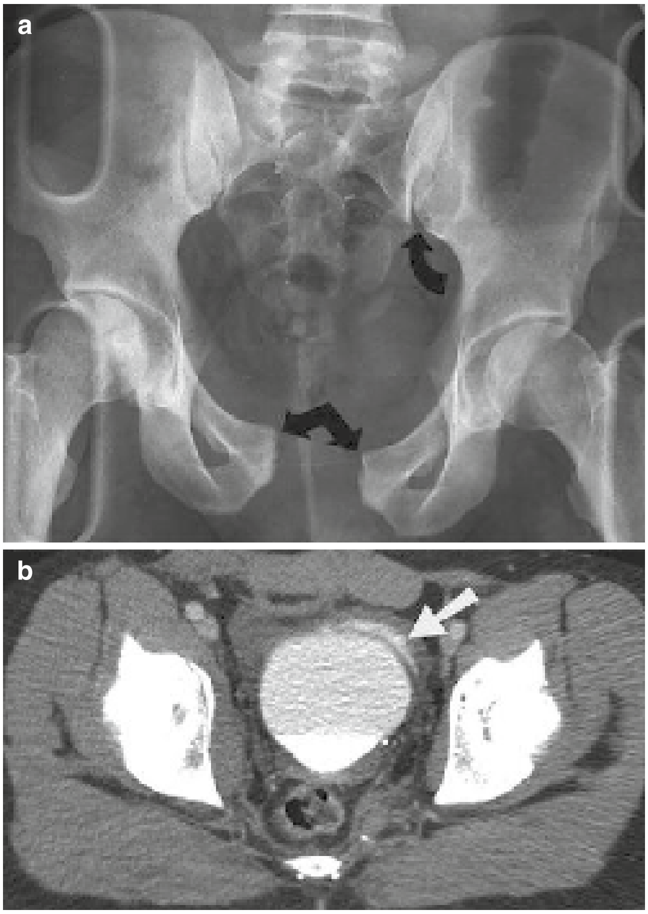

Fig. 21.2 Pelvic fracture. (**a**) An AP radiograph of the pelvis shows widening of the pubic symphysis (*double arrow*) and the left sacroiliac joint (*arrow*), indicative of an anteroposterior compression (APC) type of pelvic ring disruption. (**b**) An axial CT cystography image reveals an extraperitoneal bladder rupture (*arrow*)

Table 21.1 Young–Burgess classification

Direction	Description
Anteroposterior compression	Vertical Involves pubic rami, pubic symphysis diastasis, and sacroiliac joints
Lateral compression	Coronal or horizontal Involves pubic rami, sacral compression fracture, iliac wing fracture, and central hip dislocation
Vertical shear	Vertical Involves pubic rami, sacrum, and iliac wings Associated with ligamentous injury often resulting in severe pelvic instability and neurovascular injuries
Combined mechanism	Combination of above

Table 21.2 Denis classification

Zones	Description
Zone I	Lateral to the sacral foramina Neurological deficit uncommon
Zone II	Vertically pass through sacral foramina (Fig. 21.3a, b) L5 nerve root injury
Zone III	Central canal involvement Common neurological deficit

Acetabulum

Standard views: AP and Judet views of the hip (two oblique views centered on the hip, tilted 45° medially or laterally from a true AP direction)
Frequent types of fractures
Posterior wall
Transverse
Transverse plus posterior wall
T-shaped
Associated both columns

Imaging performed in acetabular fracture is to evaluate for wall involvement, intra-articular entrapped bone fragment, and associated femoral head fracture. On the AP view of the hip, six lines relating to the acetabulum and surrounding structures have been described: iliopubic or iliopectineal line, ilioischial line, radiographic teardrop, roof of the acetabulum, anterior rim of the acetabulum, and posterior rim of the acetabulum. Disruption of any of these normal lines indicates the possible presence of abnormality [3] (Fig. 21.3c).

1. Iliopectineal line: It extends from the sciatic notch to pubic tubercle and is discontinuous in anterior column fractures.
2. Ilioischial line: It is drawn from the sciatic notch to internal cortex of the ischium and is discontinuous with posterior column fracture. The breaks in the anterior and posterior rim of the acetabulum indicate either a column or a wall fracture. The radiographic teardrop is a composite U-shaped shadow at the anteroinferior portion of the acetabular fossa, without true structural correlate.

On lateral view, the pelvis is divided into anterior and posterior columns. The anterior column (iliopubic component) consists of pubis and ilium, whereas the posterior col-

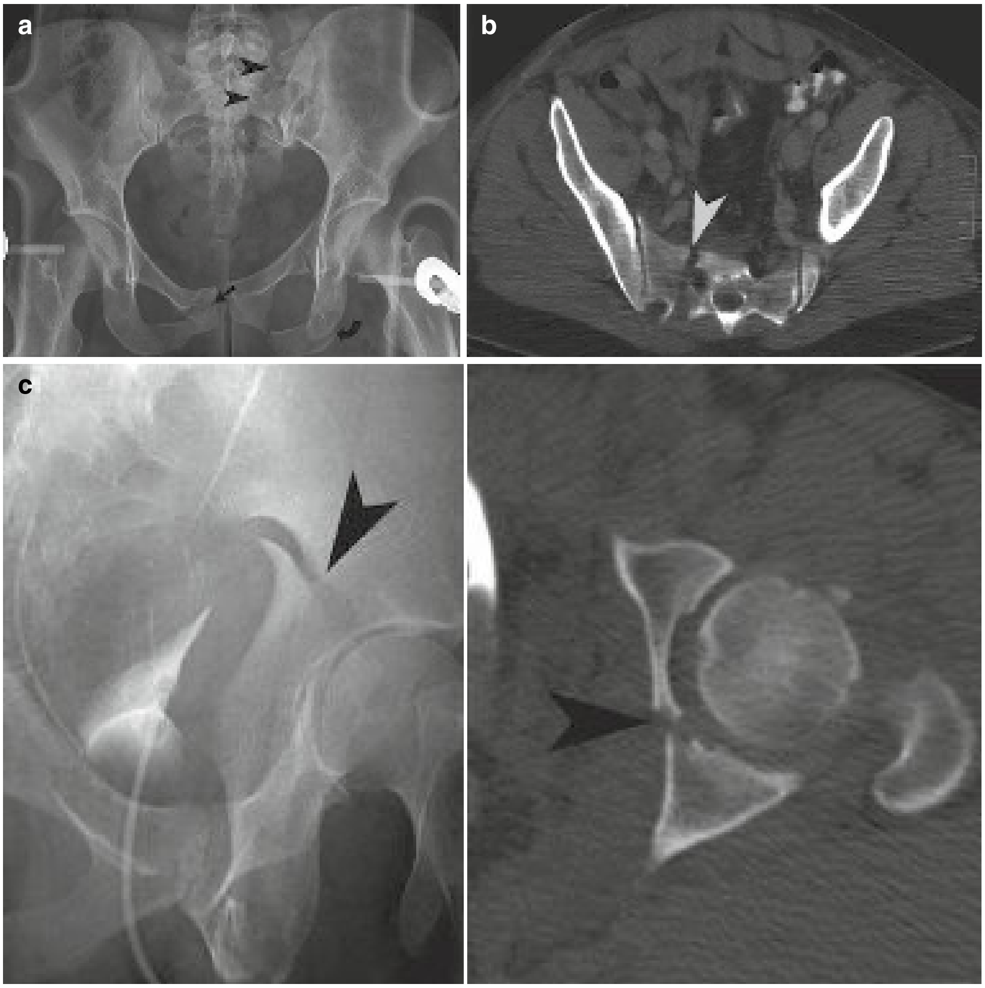

Fig. 21.3 Pelvic fractures. (**a**) An AP radiograph of the pelvis shows a vertical fracture through the left sacral ala (*arrowheads*), widening of the left sacroiliac joint, and multiple bilateral pubic rami fractures (*straight* and *curved arrow*). (**b**) An axial CT image of another patient shows a zone II right sacral fracture (*arrowhead*). (**c**) An iliac oblique Judet view of the left hip demonstrates a disrupted ilioischial line by a displaced posterior column fracture (*arrowhead*). An accompanying axial CT image confirms the finding of a column fracture, which is seen as a coronally oriented fracture line (*arrowhead*) through the posterior half of the acetabulum

umn (ischial component) consists of ischium, ischial spine, and ischial tuberosity. The posterior wall fractures are the most common acetabular fractures and are often associated with multiple fragments as well as posterior hip dislocation. The next most common fractures are transverse, anterior column, and posterior column fractures. The most common associated fractures are transverse and posterior wall fractures followed by both column fractures.

Hip

- Standard views: AP and true lateral views of the hip
- Frequent sites of fractures
  - Femoral neck fractures
  - Posterior hip dislocations
- Frequently missed injuries
  - Nondisplaced femoral neck fractures
  - Fractures of the greater trochanter
  - Fractures of the femoral head

Hip Dislocations

Dislocations of the hip are infrequent injuries since strong force is required to produce such trauma. There are several types of hip dislocations, which are defined by the relationship of the femoral head relative to the acetabulum.

Posterior dislocation, which is the most common type of hip dislocation, is characterized by posterior displacement of femoral head in relation to the acetabulum (Fig. 21.4). It is classically the result of a head-on motor vehicle collision, in which the occupant's knees strike the dashboard, while the knees are in flexed position. It commonly occurs in association with fractures of the posterior acetabular rim. On radiography, there is a lack of congruency of the femoral head and the acetabular fossa with the femoral head located superolateral to the acetabulum. In approximately half of the cases, there is associated fracture of the posterior acetabular rim. Common complications of posterior hip dislocation are injury to the sciatic nerve, femoral head fracture, avascular necrosis of the femoral head, post-traumatic ossification, and osteoarthritis.

Anterior hip dislocation is the second most common type of hip dislocation, accounting for 10%–15% of all hip dislocations. It is caused by forced abduction and lateral rotation of the limb, usually from motor vehicle collision. On radiography, the femoral head is often located inferomedial to the acetabulum. The dislocated femoral head appears slightly larger than on the contralateral side because of magnification (dislocated femoral head is located further away from the cassette), and the lesser trochanter is visualized in full profile. There is association with femoral head and acetabular fracture [4].

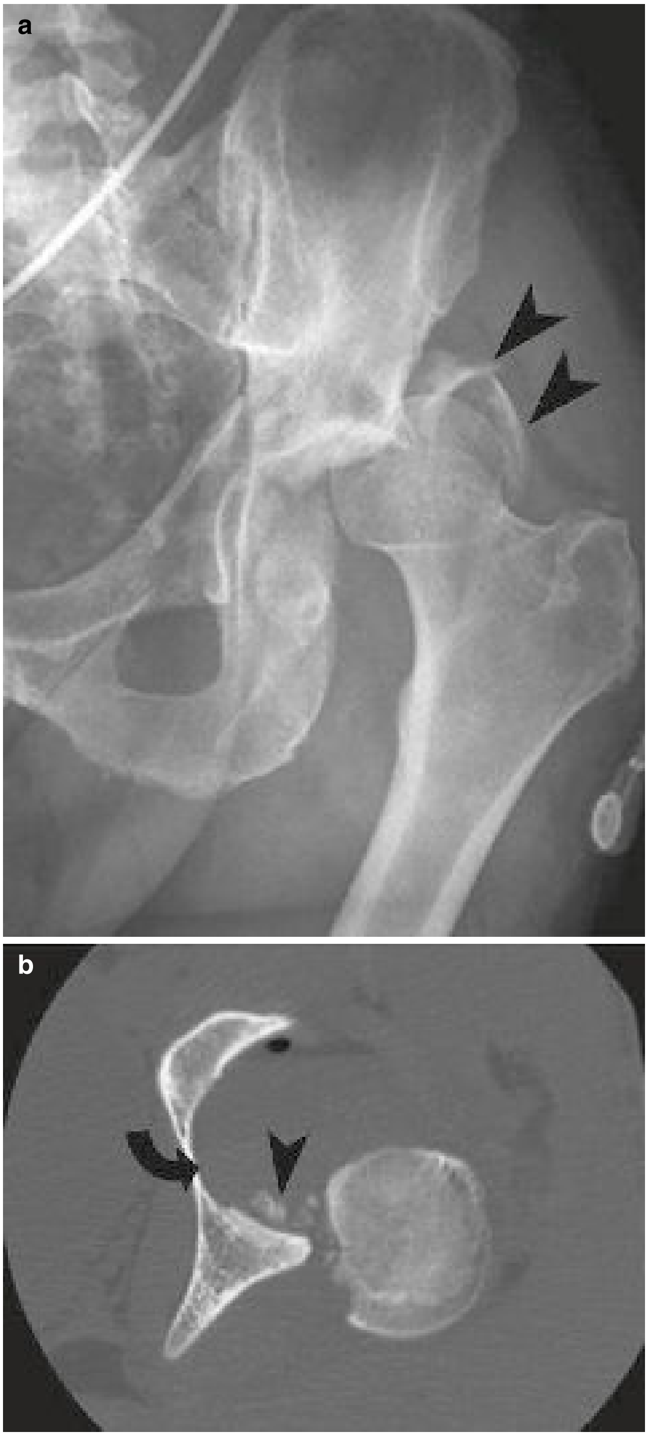

Fig. 21.4 Posterior dislocation at the hip joint. (**a**) An AP radiograph of the pelvis shows an apparent superolateral location of the left femoral head relative to the acetabulum, which is characteristic of posterior hip dislocation. *Arrowheads* point to associated acetabular fracture fragments. (**b**) An axial CT image shows an empty left acetabulum (*arrow*) with several bone fragments (*arrowhead*) in the hip joint from associated posterior wall acetabular fracture

Central hip dislocation describes the medial displacement of the femoral head into the pelvis, causing comminuted fracture of the medial wall of the acetabulum. It is usually

Table 21.3 Hip dislocations

Direction	Description
Posterior	Most common type Caused by dashboard injury in a motor vehicle collision Associated with fractures of the posterior acetabular rim Lack of congruency of the femoral head and the acetabular fossa Femoral head is located superolateral to the acetabulum Associated fracture of the posterior acetabular rim Complications include injury to the sciatic nerve, femoral head fracture and avascular necrosis, post-traumatic ossification, and osteoarthritis
Anterior	Second most common type Caused by forced abduction and lateral rotation of the limb Usually due to motor vehicle collision Femoral head is often located inferomedial to the acetabulum Associated with femoral head and acetabular fracture
Central	Medial displacement of the femoral head into the pelvis Associated with comminuted fracture of the medial wall of the acetabulum Complications: retroperitoneal bleeding or infection, and joint incongruity

caused by a heavy lateral blow upon the femur, for example, fall from height onto the side. Retroperitoneal bleeding, subsequent retroperitoneal infection, and residual joint incongruity frequently complicate this injury (Table 21.3).

Postreduction radiograph is required to determine the adequacy of reduction and to identify potential intra-articular fragments. Asymmetry of hip joint space or unequal widths between the radiographic teardrop and femoral head should raise suspicion of large effusion, interposed soft tissue, or intra-articular fragments. CT is the imaging method of choice to evaluate for intra-articular loose body.

Fractures of the Proximal Femur

Fractures of the femoral head are relatively infrequent in isolation given the protection of the femoral head by the acetabulum (Figs. 21.4b and 21.5a). When they occur, they are usually associated with hip dislocation and are caused by impaction or shearing by the acetabulum. Pipkin classification is the standard means to classify femoral head fractures, with a main criterion of whether the fracture is above or below the fovea [5].

Pipkin classification:

- Type 1 is a fracture below the fovea.
- Type 2 is the fracture above the fovea.
- Type 3 is a femoral head fracture associated with a neck fracture.
- Type 4 is a femoral head fracture associated with an acetabular fracture.

Type 3 and 4 fractures often require operative intervention, while the need for operative fixation of type 1 and 2 fractures depends on several factors including intra-articular fragment, irreducible dislocation, and involvement of the weight-bearing portion. The fractures of the femoral head are at an increased risk of avascular necrosis or nonunion because the main arterial supply (medial femoral circumflex artery) may be injured.

Femoral neck fractures may result from a significant injury such as a fall but can also be seen in minor trauma among osteoporotic individuals. Garden classification is most commonly used to describe these fractures (Table 21.4) [6].

While displaced fractures are readily visualized on radiography, imaging features of nondisplaced fractures are often subtle. These features include:

1. Disruption of a normal S or reversed S curve of the outline of the femoral head joining the concave outline of the femoral neck.
2. Sclerotic line of impacted fracture.
3. Abnormal angulation of the major trabeculae groups. On a lateral radiograph, one should look for posterior comminution of the fracture, since its presence indicates a higher chance of nonunion.

The blood supply to the femoral head is through three routes, including the vessels in the ligamentum teres, capsular vessels, and branches of the nutrient vessels. There is an increased risk of avascular necrosis following femoral neck fractures because of nutrient and capsular vessel disruption. The frequency of avascular necrosis in displaced and nondisplaced fractures is 30%–40% and 10%, respectively [7]. If radiography is negative but there is still a high clinical suspicion, CT with multiplanar reconstruction or MRI should be considered.

Intertrochanteric fractures occur along the line between greater and lesser trochanter (Fig. 21.5c). Since the joint cap-

Table 21.4 Garden classification

Type	Description
Garden I	Incomplete or impacted fracture Inferior aspect of the neck trabeculae is intact May cause valgus angulation of the neck
Garden II	Complete fracture No displacement (Fig. 21.5b)
Garden III	Complete fracture Partial displacement Associated with shortening and external rotation of the limb
Garden IV	Complete fracture Total displacement No continuity between the proximal and distal fragments

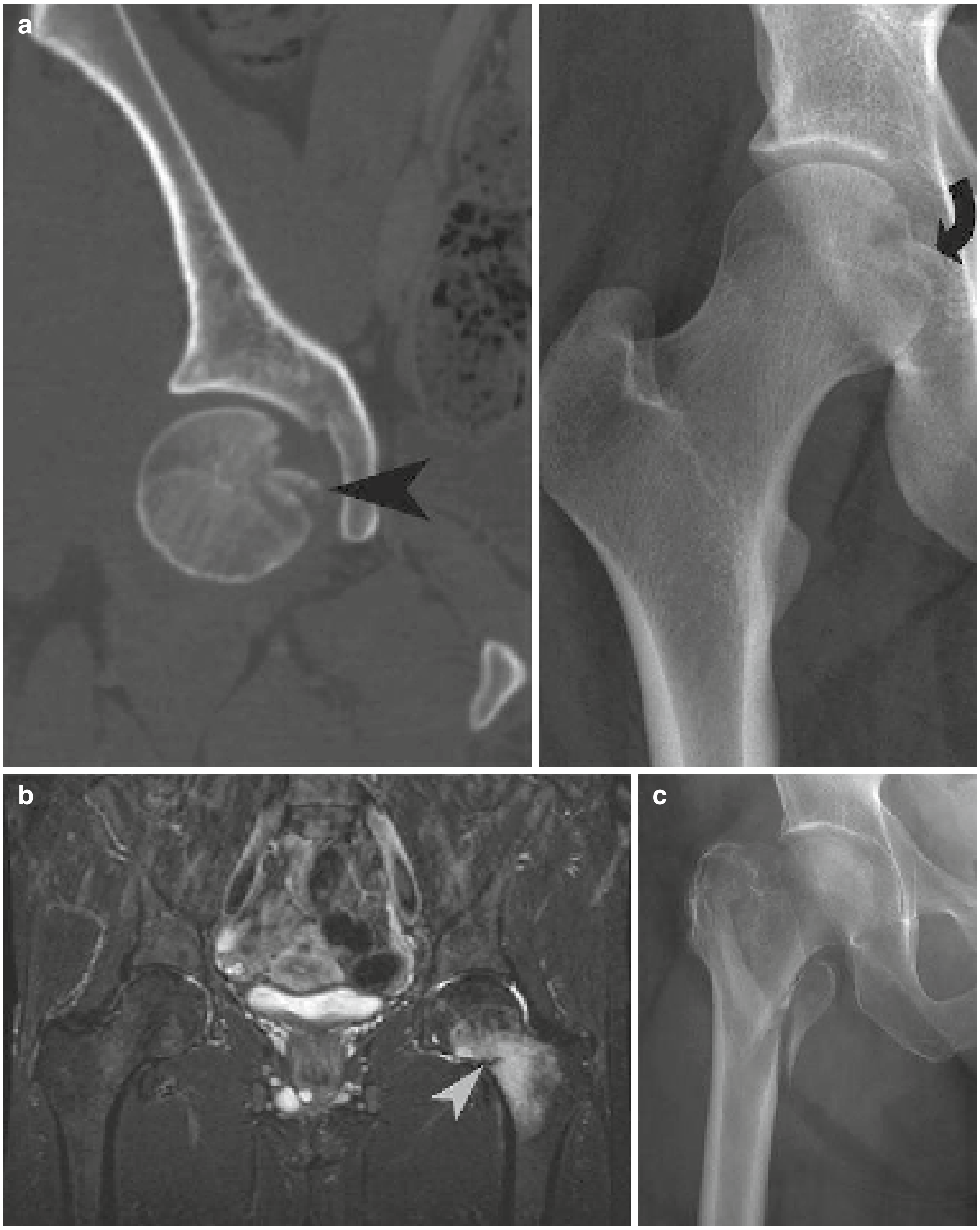

Fig. 21.5 Proximal femoral fractures. (**a**) An AP radiograph of the right hip reveals a depression at the femoral head (*arrow*), later confirmed by a corresponding CT scan as a depressed fracture (*arrowhead*) involving the fovea capitis. (**b**) A coronal STIR MR image of the pelvis in another patient demonstrates bone marrow edema of the left femoral neck with a linear hypointense line (*arrowhead*) in the medial aspect of the femoral neck, perpendicular to the bony cortex, representing a stress fracture. (**c**) An AP radiograph of the right hip of another patient shows an intertrochanteric fracture with a displaced lesser trochanter fragment

sule attaches anteriorly to the intertrochanteric line and posteriorly to the medial half of the femoral neck, trochanteric fracture is theoretically extracapsular and heals well relative to the femoral neck fractures. It is important to distinguish stable from unstable trochanteric fractures. This can be determined by assessing the medial cortex and comminution of the posterior cortex (on lateral view). Comminuted fracture line at the medial cortex, displaced lesser trochanter fracture, and lesser trochanter fragment containing calcar femorale are generally considered unstable. Presence of a fracture gap medially and posteriorly will allow fracture displacement into varus or retroversion, causing instability. Unlike fractures of the femoral neck, trochanteric fractures are almost free from serious complications.

Subtrochanteric fractures are fractures located between the lesser trochanter and 5 cm below. It is usually a result of direct trauma and may occur in isolation or with intertrochanteric fractures. The fractures are usually displaced by muscle pulls, resulting in shortening and varus deformity.

Fractures of the Femoral Shaft, Supracondyle, and Condyle

Fractures of the distal femur usually occur with high-velocity trauma in young adults and low-energy trauma in osteoporotic bone of elderly persons. Therefore, it is commonly associated with several other injuries such as fractures of the

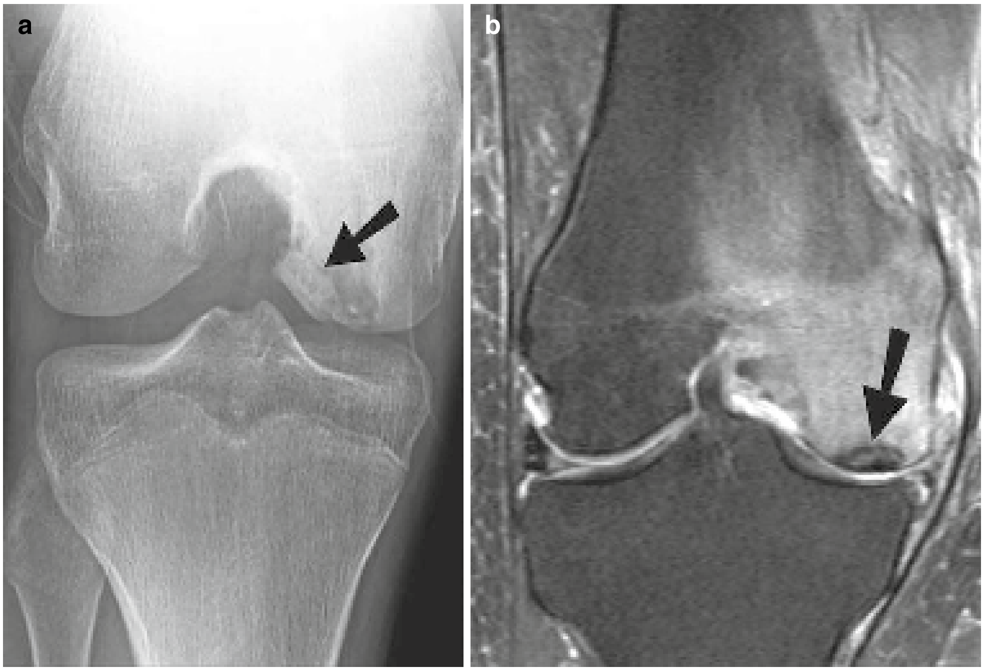

Fig. 21.6 Osteochondral injury. (**a**) A tunnel radiographic view of the right knee shows an osteochondral fracture (*arrow*) of the lateral aspect of the medial femoral condyle. (**b**) A coronal fat-suppressed T2W MR image of the right knee in a different patient reveals bone marrow edema of the medial femoral condyle with an osteochondral fragment in the subarticular portion (*arrow*). There is soft tissue edema in the medial aspect of the knee. The medial collateral ligament is intact

patella, hip and tibial shaft, and ligamentous disruptions of the knee. Femoral shaft fractures occur at any age and are equally common in the uppermost, middle, and lower thirds of the shaft. Their pattern may be transverse, oblique, spiral, comminuted, or greenstick. Radiographic evaluation must include the hip and knee joints since joint dislocations may coexist.

The fractures of the supracondylar and condylar regions are divided into three types: extra-articular (transverse), partial articular, and complete articular. The key components in dividing distal femoral fractures are presence of:

1. Fracture line extending into the intercondylar notch (intercondylar split).
2. Osteochondral fragments in the area of or between the intercondylar split.
3. Coronal-plane (Hoffa) fracture.

Partial articular fractures are an intra-articular fracture that involves either the medial, lateral condyle, or coronal plane (best seen on a lateral radiograph). Complete articular fractures produce separate articular and metaphyseal segments, in which each can be simple or multifragmentary.

Osteochondritis dissecans (OCD) of the knee (Fig. 21.6) may present in a similar fashion to acute traumatic osteochondral fractures, although they differ. The condition is characterized by sequential degeneration or aseptic necrosis and recalcification. It can occur in persons of any age group but is most frequent between 10 and 20 years old, with male predominance. Most of the cases (85%) involve the medial femoral condyle in the posterolateral aspect [8]. Radiography shows OCD as a well-circumscribed crescent-shaped area of radiolucency above the subchondral bone, separated from femoral condyle. MRI is helpful in determining the vascularity of the lesion, bilaterality, occult lesions, and degree of loosening of the lesion.

Knee

Standard views: AP, lateral, both obliques (optional patellar sunrise if suspicious for patellar injuries)
Frequent sites of fractures
Patellar fractures
Tibial plateau fractures
Frequently missed injuries
Tibial plateau fractures
Segond fractures
Maisonneuve fractures

Knee Dislocations

Knee dislocations may occur as a result of either high- or low-velocity trauma, in which the mechanism of injury will reflect the incidence of associated neurovascular injuries. Five types of knee dislocations are described with tibia in relation to the femur, which include anterior (most common), posterior (second most common), lateral, medial, and rotary.

On an initial radiographic assessment, the findings are usually obvious (Fig. 21.7a). One should look for associated

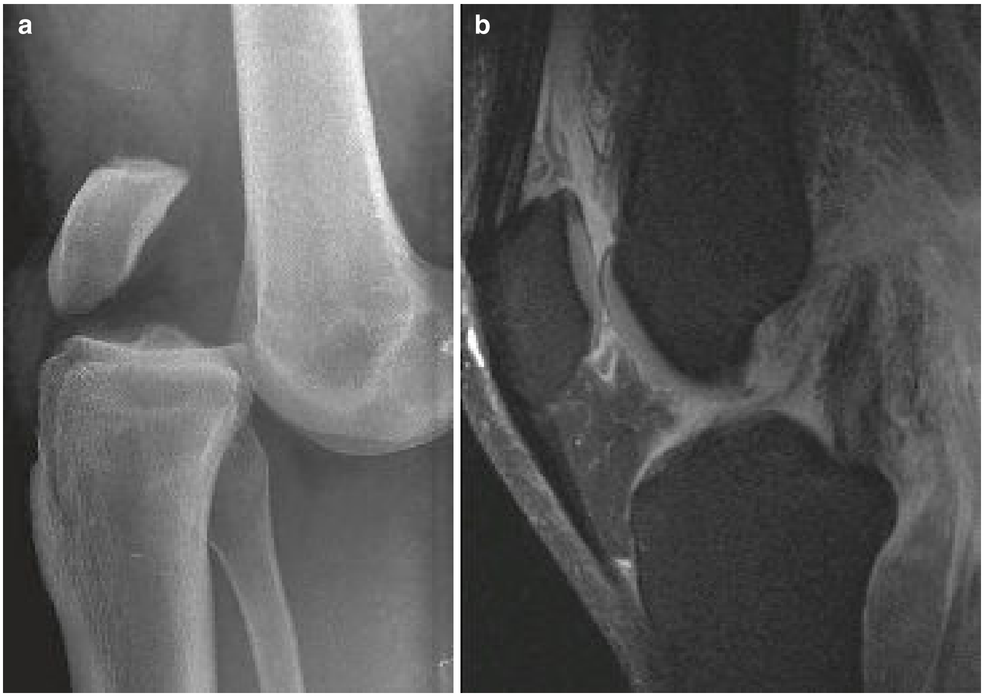

Fig. 21.7 Knee dislocation. (**a**) A lateral radiograph of the left knee demonstrates an apparent anterior knee dislocation with the tibia and fibula displacing anteriorly relative to the distal femur. The patella moves with the distal fragments. (**b**) A sagittal T2W MR image with fat suppression shows extensive ligamentous disruptions and soft tissue injuries of the knee joint

injuries such as fractures of the tibial plateau, proximal fibula, Gerdy's tubercle, intercondylar eminence, and fibular head. Tears of the ACL and PCL often occur along with at least one collateral ligament, which can be confirmed on MR imaging (Fig. 21.7b). Popliteal artery is at risk of intimal injury and subsequent occlusion [9]. Conventional or CT angiography is usually indicated in high-velocity knee dislocations to exclude intimal injury even if the distal pulse returns following the reduction.

Fractures of the Tibia Plateau

Tibial plateau fractures are the most common fractures of the proximal tibia. Since the lateral tibial plateau is weaker than the medial counterpart, it is more frequently fractured. This classically is a result of a direct trauma to the lateral side of the knee such as in pedestrian versus car collision (bumper fracture).

Schatzker et al. [10] classified the tibial plateau into six types according to the location and pattern of injury (Table 21.5 and Fig. 21.8a, b).

Table 21.5 Schatzker classification of the tibial plateau

Type	Description
Type I	Split fracture of the lateral plateau
Type II	Split-compression fracture
Type III	Isolated compression lateral plateau fracture (Fig. 21.8a, b)
Type IV	Depressed fracture of the medial plateau
Type V	Bicondylar fracture
Type VI	Diaphyseal-metaphyseal separation

The radiographic appearance of depressed-type fracture can be difficult to discern because the X-ray beam of a routine anteroposterior view of the knee is not tangential to the tibial joint surface. The secondary signs of tibial plateau fractures include the presence of a fat-blood level or fat-blood interface sign within the suprapatellar bursa, seen on the lateral crosstable radiographic view of the knee. CT with multiplanar reconstruction is helpful for detecting occult fractures, fracture staging, and treatment planning.

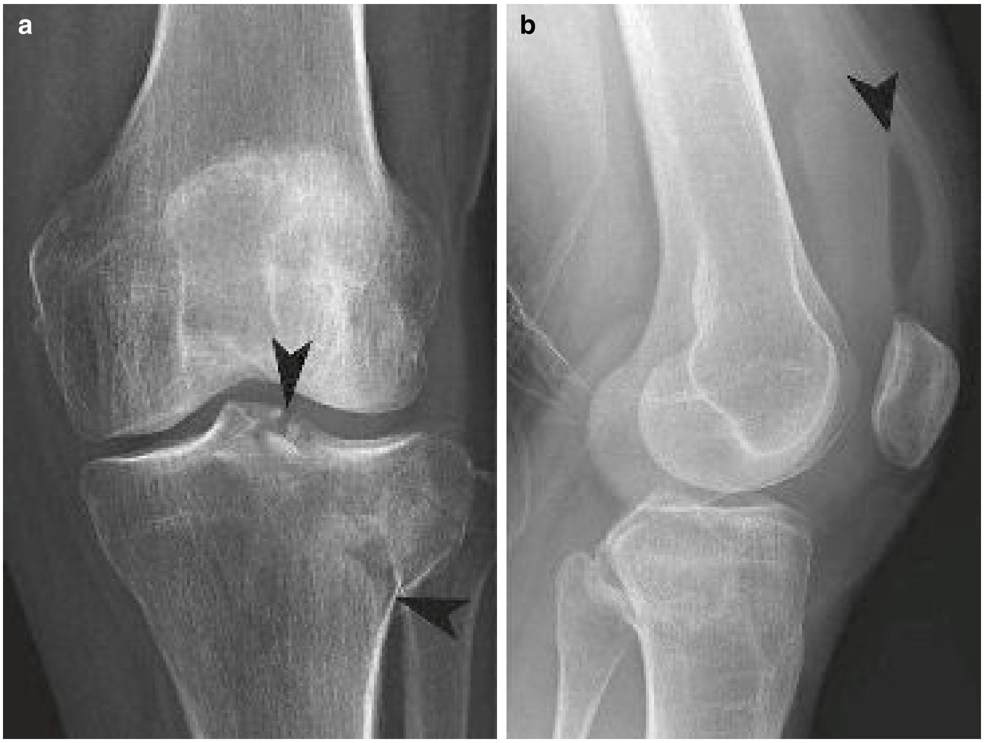

Fig. 21.8 Tibial plateau fracture. (**a**) An AP radiographic view of the left knee shows abnormal increased medullary sclerosis on the lateral plateau with cortical disruptions (*arrowheads*) at the plateau near the tibial spine and laterally at the metadiaphysis. (**b**) A lateral crosstable radiograph reveals a fat-blood interface (*arrowhead*) in the suprapatellar bursa, indicating lipohemarthrosis and implying an intra-articular fracture

Avulsion Fractures Around the Knee

Segond fracture is an avulsion of the lateral aspect of the proximal tibia due to a pull of lateral capsular ligament from the proximal tibia posterior to the Gerdy's tubercle. On AP radiography, it appears as a small elliptical bone fragment lying immediately distal to the lateral tibial plateau and parallel to the long axis of the tibia (Fig. 21.9a, b). It is often associated with more serious injuries such as anterior cruciate ligament or meniscal tear. The other similar entity that occurs on the medial side of the tibia, called medial Segond-type fracture, describes a cortical avulsion of the medial tibial plateau in association with posterior cruciate ligament tear.

Injury to the Gerdy's tubercle is an avulsion of the iliotibial tract at its attachment to the lateral proximal tibia. The detached fragment is usually much larger than and lies more anterior and distal to that of Segond fracture fragment. It is best seen on the oblique external rotation radiographic view and is associated with lateral capsular, lateral collateral, and ACL injuries.

Avulsion of the tibial eminence may involve anterior, posterior, or both tibial spines. The most common site is at the anterior aspect from a pull of ACL (Fig. 21.9c). The fragment may be displaced or nondisplaced, in which the degree of displacement dictates a different type of tibial eminence avulsion. The injury is commonly seen in children between ages of 8 and 14 but can also be seen in adults. Radiographic findings may be difficult to recognize and include a presence of small bone fragment in the intercondylar notch and hemarthrosis, best seen on lateral radiography. Avulsion of the fibular styloid process is the fracture at the attachment site of the biceps tendon and fibular collateral ligament, which is commonly associated with disruption of the ACL, popliteus tendon, and arcuate ligament.

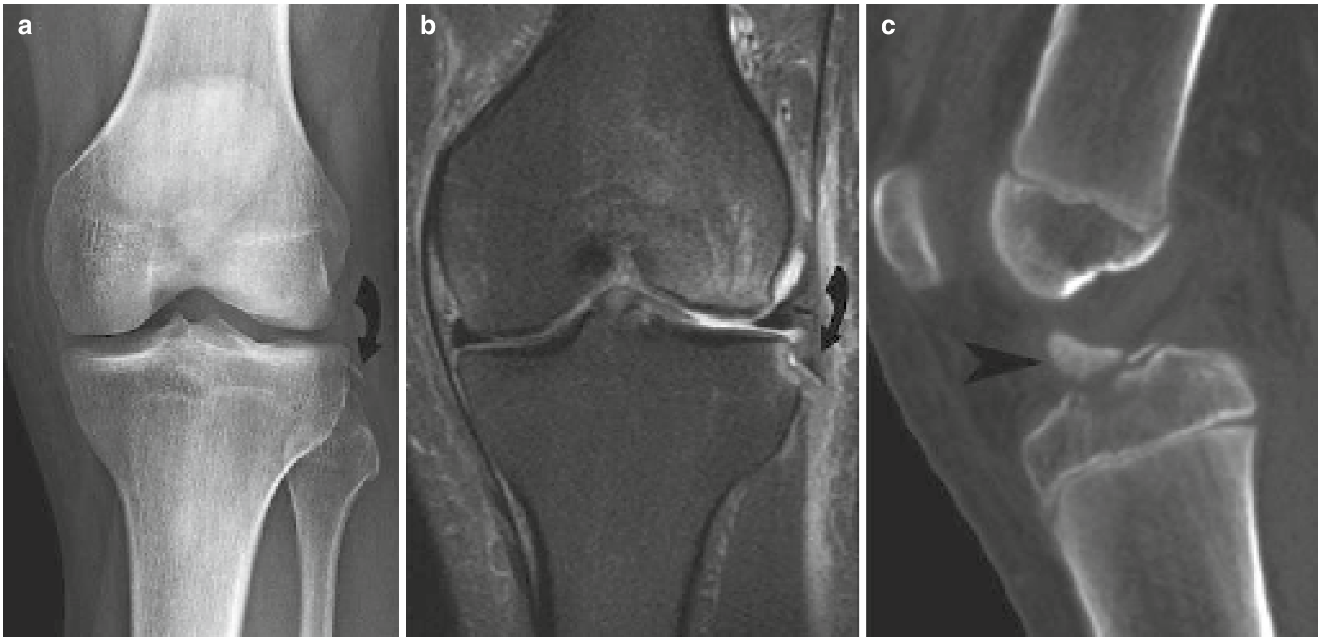

Fig. 21.9 Proximal tibial fractures. (**a**) An AP radiograph of the left knee shows a small flake of bone (*arrow*) just lateral to the edge of the lateral tibial plateau. (**b**) A coronal T2W MR image with fat suppression shows an avulsion of the lateral collateral ligament, joint effusion, and opposing bone contusions associated with a Segond fracture (*arrow*). (**c**) A sagittal CT image of the knee of a different patient shows an avulsion fracture (*arrowhead*) of the tibial spine due to a pull of the anterior cruciate ligament

Patellar Fractures

Patellar fractures account for 1% of skeletal fractures. Fractures due to a direct trauma usually result in stellate fractures, while indirect trauma causes transverse fractures. Patellar fractures may be a result of two types of injury:

1. A sudden violent contraction of the quadriceps (i.e., abnormal flexion of the knee against contracted quadriceps).
2. A fall or direct blow to the patella. The former tends to cause a clean fracture line with separation of the fragments, whereas the latter causes a comminuted fracture (Fig. 21.10a).

Based on the ACR appropriateness criteria, radiographs are recommended for initial step and should include AP, lateral, and patellar views. Displacement of the fracture fragments indicates disruption of the patellar retinaculum. Nondisplaced fracture can be difficult to visualize on AP radiographic view but usually can be discerned on the lateral projection. Small peripheral fractures may be confused with bipartite patella, which tends to have a sclerotic rim and is located in a characteristic superolateral aspect of the patella (Fig. 21.10b). If in doubt, a contralateral knee radiograph is usually helpful because bipartite patella often occurs bilaterally.

Soft tissue injuries to the extensor mechanism may occur to the quadriceps tendon or patellar tendon (Fig. 21.11a, b). The findings on radiograph include high- or low-lying patella, joint effusion, and thickening or distortion of the affected tendon. Chronic repetitive traction injury of the immature osteochondral junction at the inferior pole of the patella represents a Sinding–Larsen–Johansson disease [11] (Fig. 21.10c, d), in which it presents with point tenderness at the inferior pole of the patella associated with soft tissue swelling after strenuous sporting activity. This condition is seen in active adolescents typically between ages of 10 and 14. On radiography, there may be focal thickening of the proximal patellar tendon with hazy adjacent Hoffa's fat pad and osteolysis at the distal pole of the patella. Ultrasound and MRI may show thickening of the tendon with abnormal echogenicity and signal intensity representing tears of posterior fibers of the patellar tendon. The indirect force to the patellar tendon may cause acute bony avulsion at the inferior pole of the patella or tibial tubercle. Patellar sleeve avulsions are seen as thin, curvilinear bone fragment off the parent bone.

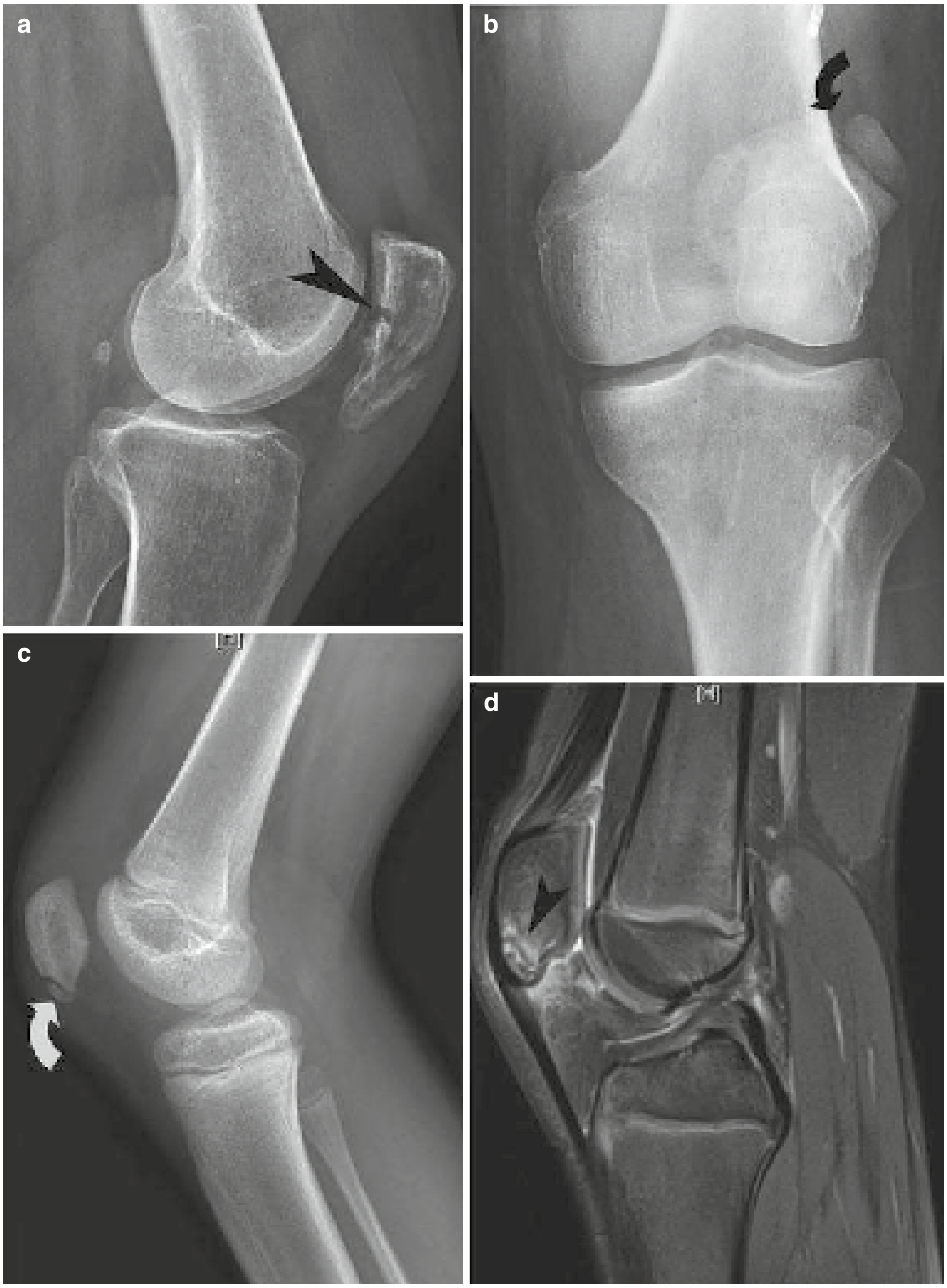

Fig. 21.10 Patellar fracture. (**a**) A lateral radiograph of the knee reveals a transverse nondistracting fracture of the patella (*arrowhead*) with a moderate-sized joint effusion. (**b**) An AP radiograph of the knee of another patient demonstrates a bipartite patella (*arrow*), which is a well-corticated bone fragment in a characteristic superolateral aspect of the patella. (**c**, **d**) Lateral knee radiograph and sagittal fat-suppressed T2W MR image of a patient with Sinding–Larsen–Johansson disease show a corticated fragment (*arrow*) at the inferior aspect of the patella with associated bone marrow edema (*arrowhead*) and thickened, T2 hyperintense patellar tendon at its deep portion of the patellar attachment

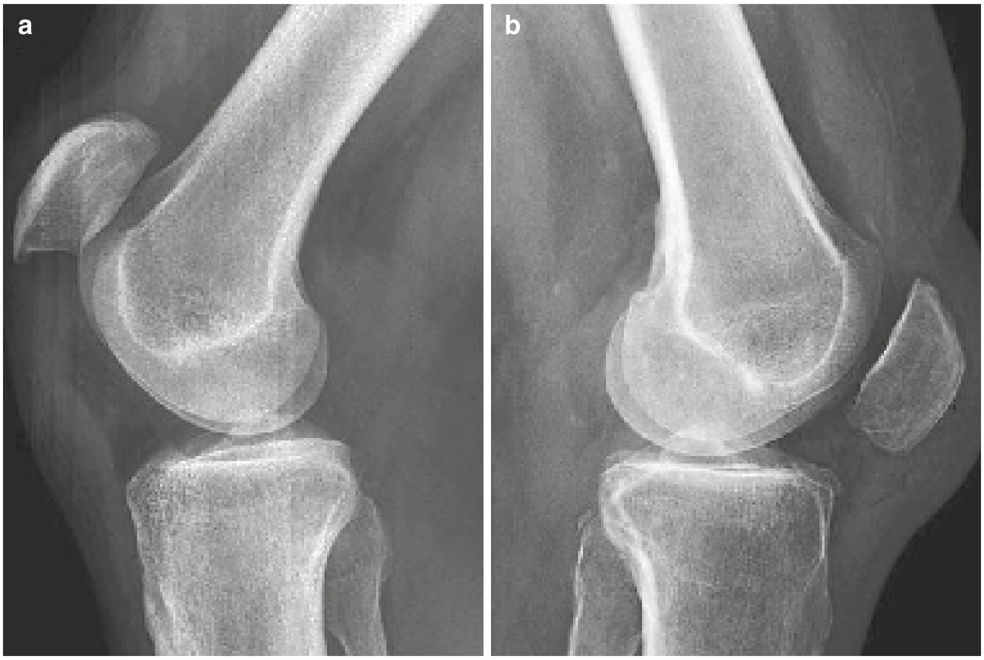

Fig. 21.11 Soft tissue injuries of the extensor mechanism. (**a**) A lateral radiograph of the right knee shows an abnormally high position of the patella with thickening of the patellar tendon, indicating a patellar tendon rupture in an acute setting. (**b**) A lateral radiograph shows low position of the patella with a soft tissue defect at the quadriceps attachment to the patella, representing a quadriceps tendon tear

Patellar Dislocations

The two major mechanisms that result in patellar dislocation are sudden forceful contraction of the quadriceps with sudden flexion and external rotation of the tibia on the femur and direct trauma to the patella with the knee in flexion. Majority of patellar dislocations are in lateral direction (Fig. 21.12a). The predisposing factors include patella alta, ligamentous insufficiency, and genu valgum.

When the patella is spontaneously relocated, the radiologic diagnosis is more difficult and the role of imaging is to search for associated injuries such as osteochondral or patellar fractures. On lateral radiographic view, there may be patella alta, osteochondral fragment, or joint effusion. Axial patellar (or sunrise) radiographic view may show patellar tilt or osteochondral fragment. The osteochondral fracture fragment often arises from the medial patellar facet or lateral femoral condyle and can be anywhere in the joint space, including in the suprapatellar pouch, posterior to the patella, intercondylar notch, and beside the femoral condyles.

Since the loose body may contain only cartilage, making it invisible on plain radiography, MR imaging is the most appropriate imaging method for detection and grading of this injury. The MR imaging appearance includes bone marrow edema in the inferomedial patella and anterolateral aspect of the lateral femoral condyle, rupture of the medial patellar retinacula, and abnormal patellofemoral cartilage (softening, fissuring, or focal defect) (Fig. 21.12b, c). MRI can also better detect bone contusion and osteochondral injuries.

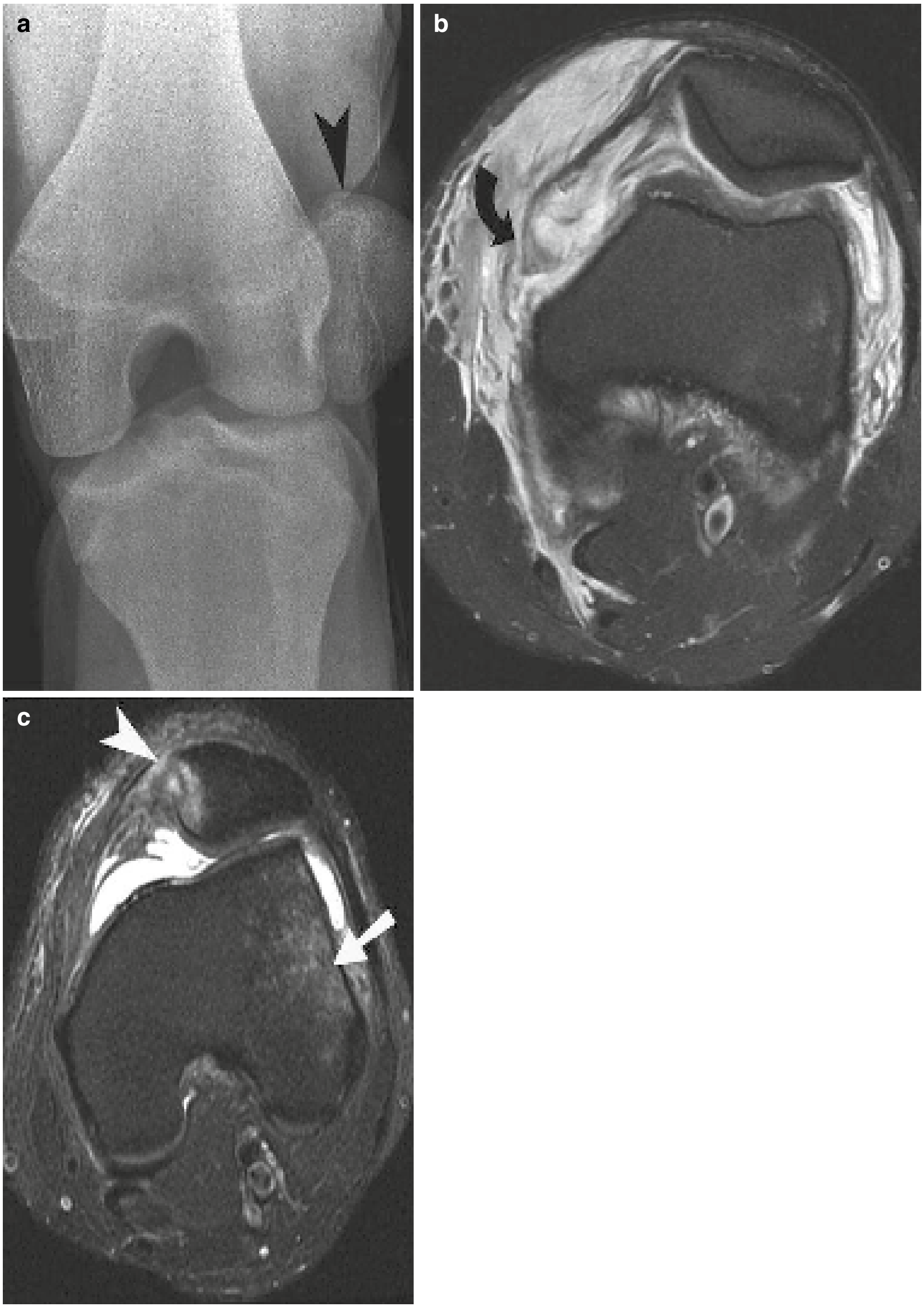

Fig. 21.12 Patellar dislocation. (**a**) An AP radiograph of the left knee shows an obvious lateral dislocation of the patella (*arrow*). (**b**, **c**) Axial fat-suppressed T2W MR images of other different patients demonstrate a tear of the medial patellar retinaculum (*arrow*), extensive soft tissue edema, and irregular cartilage of the femoral condyle (**b**) and characteristic pattern of bone marrow edema in the inferomedial aspect of the patella (*arrowhead*) and anterior aspect of the lateral femoral condyle (*arrow*) (**c**)

Fractures of the Shafts of the Tibia/Fibula

Most fractures of the shafts of the tibia and fibula occur from either angulatory force or rotational force. The former tends to cause transverse or short oblique fractures, while the latter often produces spiral fractures. They are usually displaced. The tibial fractures are usually open because the tibia is close to the skin and is poorly protected by muscles.

The fractures of the fibula alone often occur in association with injury to the lateral collateral ligament (LCL), peroneal nerve, and anterior tibial artery. It can also be the result of rotational injury of the ankle where there is significant ankle injury with transmission of force superiorly through the interosseous membrane, exiting through a proximal fibular fracture (Maisonneuve fracture) [12]. The ankle should always be imaged if an isolated fibular fracture is seen regardless of the level of the fibular fracture.

Tibia is among the most common site of stress fracture, caused by nonviolent, repetitive stress to tibia that does not allow sufficient recovery between stress applications. Tibial stress fractures are common in athletes in endurance and jumping sports because of their weight-bearing activities. Most early radiography shows no abnormality, especially when fractures are immature. Bone scan may help in diagnosing it by showing focal increased periosteal activity, but this is a nonspecific finding. Currently, MRI is the imaging method of choice because of its high sensitivity and specificity (Fig. 21.13).

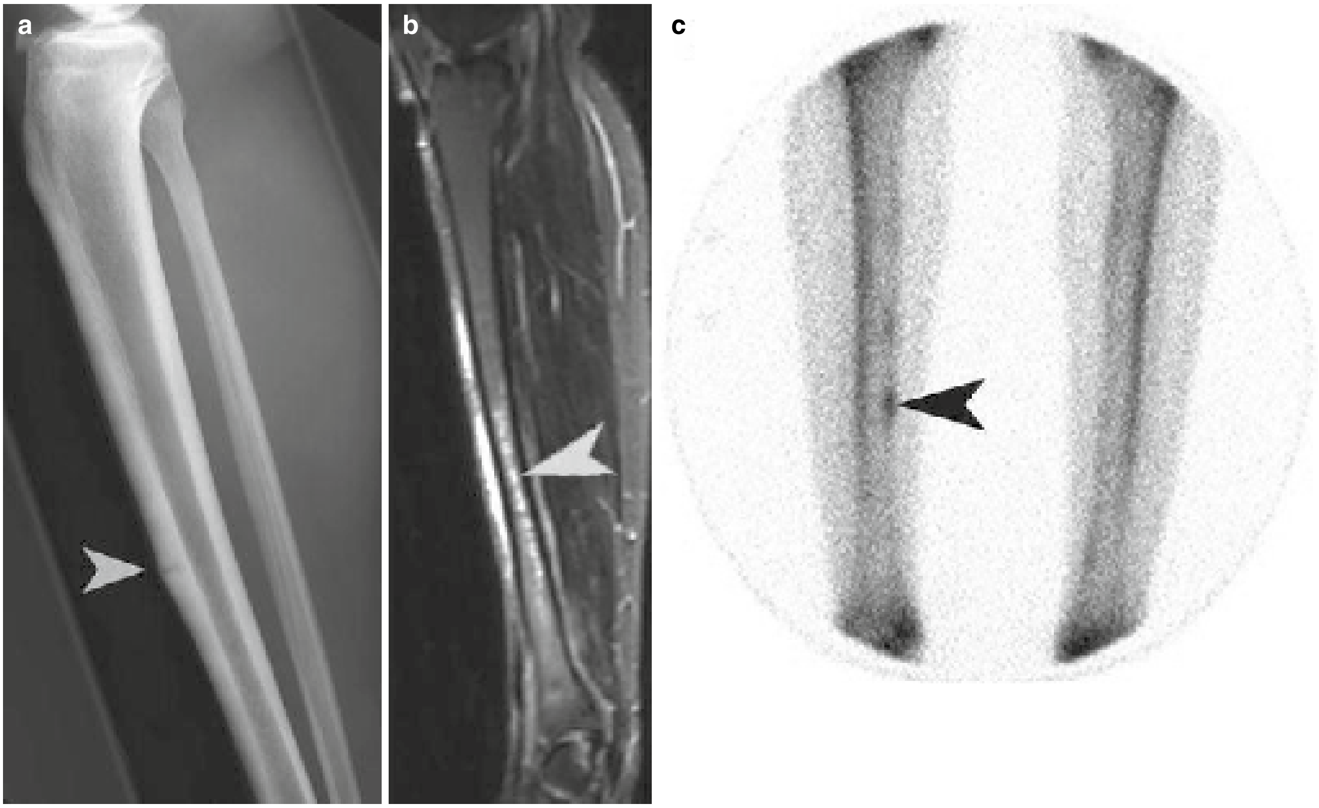

Fig. 21.13 Stress fracture of tibia. A lateral radiograph of the tibia/fibula (**a**), sagittal fat-suppressed STIR MR image (**b**), and bone scan (**c**) show characteristic imaging features of a tibial stress fracture. There is a linear lucent line perpendicular to the cortex at the anterior aspect of the mid-tibia with surrounding sclerosis, evidence of bone marrow edema on MRI, and localized increased uptake on bone scan (*arrowheads*)

Ankle and Foot

Standard views
Ankle: AP, lateral, mortise views of the ankle
Calcaneus: lateral and axial views of the calcaneus
Foot: PA, lateral, and oblique of the foot
Phalanx: PA, lateral, and oblique of the phalanx

Ankle Fractures

Ankle fractures resulting from an axial-loading force are called pilon or tibial plafond fractures (Fig. 21.14a). The fractures are a combination of ankle fracture (medial malleolus, anterior tibial margin, posterior tibial surface) with distal tibial metaphyseal fracture and intra-articular comminution. In most cases, there is an associated fibular fracture signifying the valgus shearing force that causes injuries to the lateral aspect of the ankle joint.

Tillaux fracture describes an avulsion of the lateral distal tibial margin seen as a vertical fracture line extending from the distal articular surface of the tibia superiorly to the lateral tibial cortex (Fig. 21.14b). In children, this is considered a Salter–Harris epiphyseal plate injury type III. The medial aspect of the distal tibial growth plate fuses earlier than the lateral counterpart; therefore, the lateral side is weaker and prone to trauma. In adults, this is usually a ligamentous injury without bony fractures, the so-called Tillaux lesion.

Ankle fractures often result from a combination of forces to the ankle joint, either rotational (less severe) or axial-loading types. The latter often results in comminuted intra-articular fracture of the distal tibia.

Rotational ankle fractures are divided into three types based on Weber classification into type A, B, and C injuries (Table 21.6) [13, 14]. It utilizes the level of the fibular fracture to determine the extent of injury to the tibiofibular ligamentous complex. In general, the higher the fibular fracture, the more extensive the damage to the tibiofibular ligament complex and greater the risk of ankle joint instability. An oblique fracture line is typically seen with impaction injuries, while a horizontal/transverse fracture line is characteristic of avulsion trauma.

Weber classification:

1. Weber type A: Inversion injury (supination-adduction), in which there is a horizontal fracture of the lateral malleolus, is below the level of the tibiofibular syndesmosis or rupture of the LCL. The syndesmotic ligaments are intact; therefore, the ankle mortise is stable. If the force is pro-

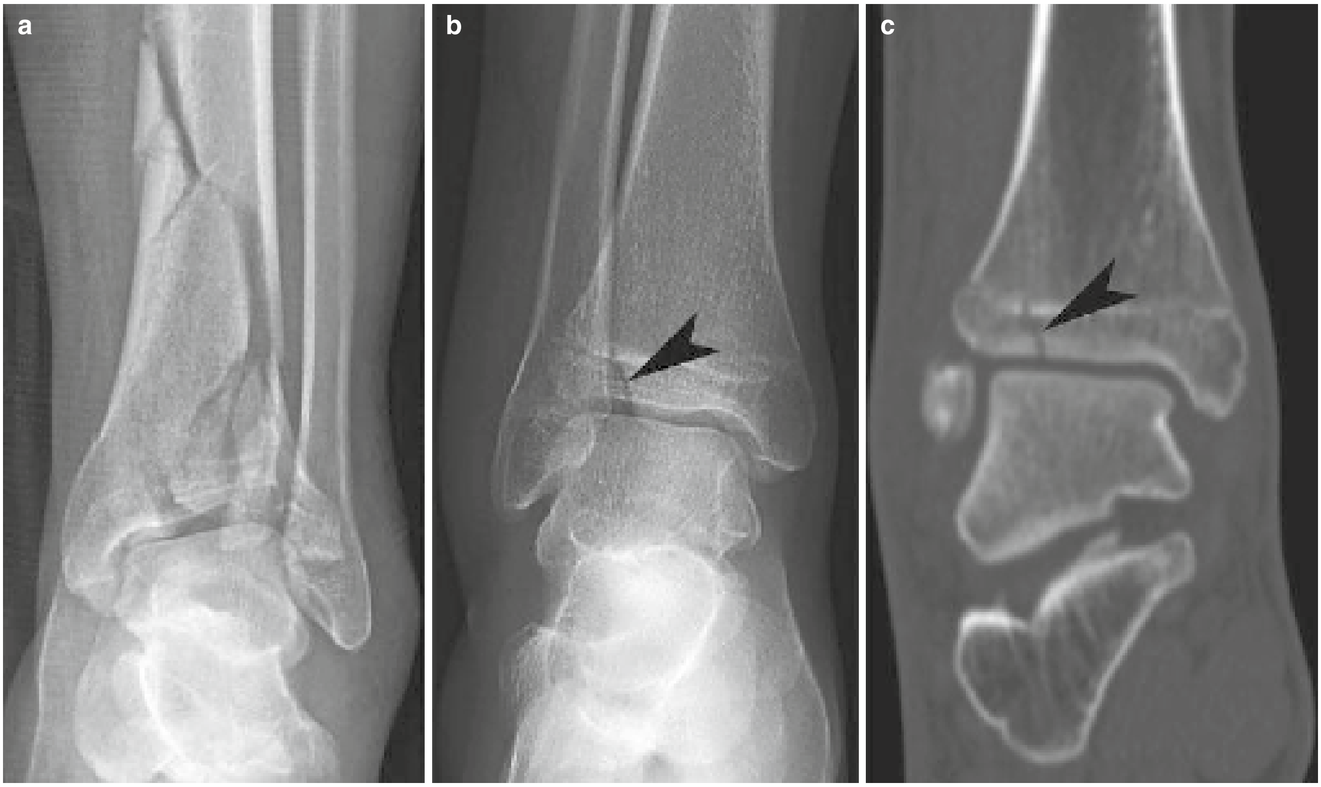

Fig. 21.14 Pilon and Tillaux fracture. (**a**) An AP ankle radiograph shows a comminuted fracture of the tibial plafond with disruption of the articular surface, or a pilon fracture. (**b**) An AP radiograph of the right ankle of another patient shows a vertical fracture line (*arrowhead*) involving the lateral aspect of the distal tibial epiphysis, which extends transversely and laterally along the physeal plate. (**c**) The coronal-reformatted CT image confirms the nature of the Tillaux fracture (*arrowhead*), which is a Salter–Harris type III epiphyseal plate injury

Table 21.6 Weber classification

Type	Description
Type A	Inversion injury Horizontal fracture of the lateral malleolus Below the level of the tibiofibular syndesmosis Rupture of the LCL Stable ankle mortise
Type B	Eversion injury Oblique fracture of the lateral malleolus At the level of the syndesmosis Possible horizontal fracture of the medial malleolus, fracture of the posterolateral tibia, and partial disruption of the tibiofibular ligament complex Deltoid ligament rupture if >5 mm widening of the medial clear space
Type C	Eversion injury Fibular oblique fracture above the level of the ankle joint Pronation-external rotation injury

gressive, there may be an oblique fracture of the medial malleolus or posteromedial aspect of the medial malleolus (Fig. 21.15a).

2. Weber type B: Eversion injury (supination-external rotation), in which there is an oblique fracture of the lateral malleolus at the level of the syndesmosis. In these injuries, there may be a horizontal fracture of the medial malleolus or deltoid ligament rupture, fracture of the posterolateral tibia, and partial disruption of the tibiofibular ligament complex. Injury to the deltoid ligament is assumed if there is a >5 mm widening of the medial clear space either on static or on stress radiograph.
3. Weber type C: Fibular fracture occurs above the level of the ankle joint and is oblique in orientation. It is an eversion injury that results from pronation-external rotation.

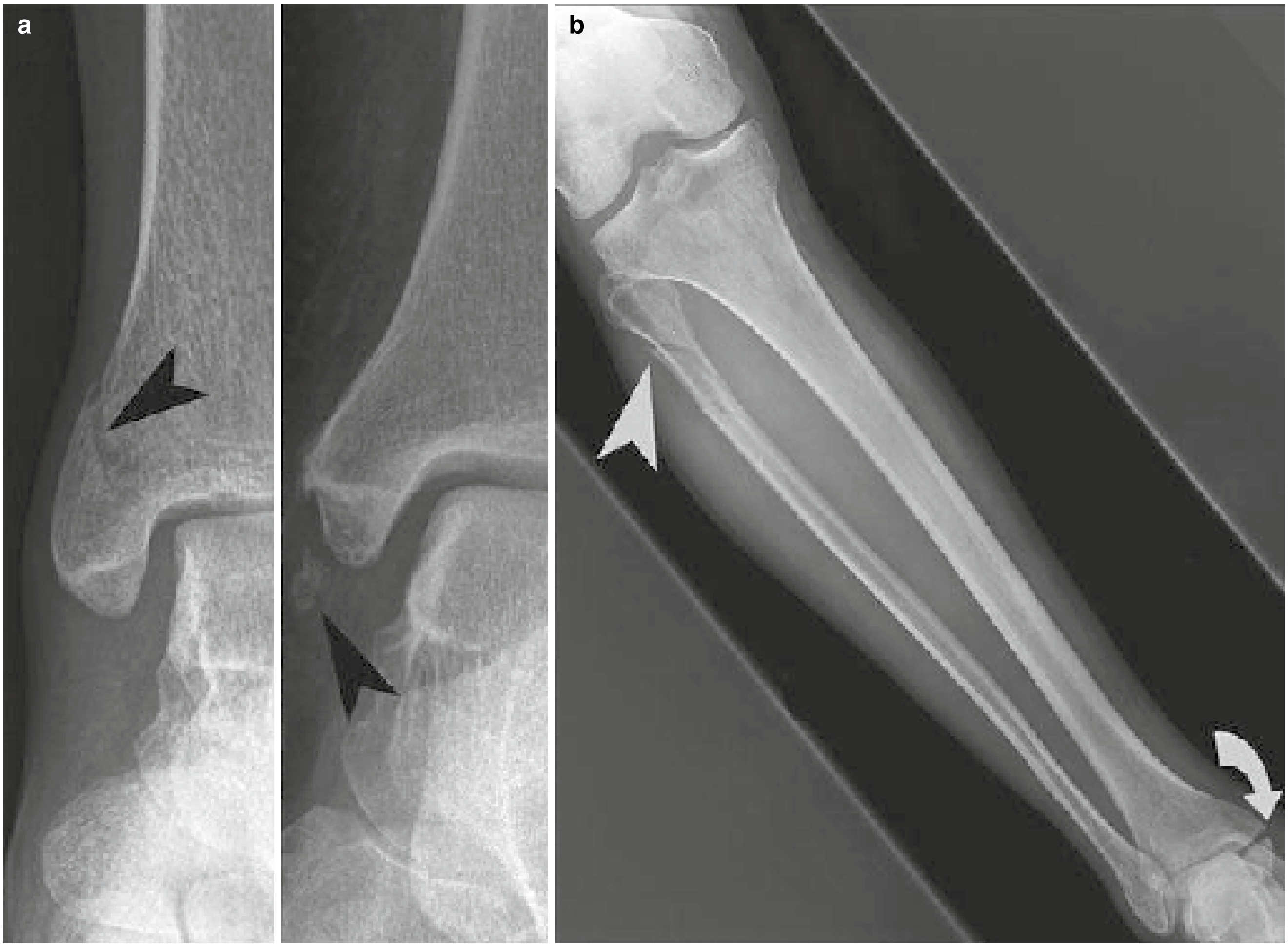

Fig. 21.15 Malleolar fracture. (**a**) Two focused radiographs of the right ankle demonstrate an oblique fracture of the medial malleolus (*arrowhead* in the *first picture*) compared with a well-corticated accessory ossicle (*arrowhead* in the *second picture*). (**b**) An AP radiograph of the right tibia/fibula shows a transverse fracture of the medial malleolus (*arrow*) and an oblique fracture of the fibular neck (*arrowhead*), representing a Maisonneuve fracture

Maisonneuve fracture [12] is a part of the spectrum of pronation-external rotation ankle injuries, in which the fibular fracture occurs proximally with a tear of the tibiofibular syndesmosis and distracting medial ankle injuries. The diagnosis of Maisonneuve fracture should be considered when one encounters an isolated fracture of the posterior lip of the distal tibia, isolated displaced fracture of the medial malleolus, and widening of the medial or lateral clear spaces without fracture of the lateral malleolus on ankle film (Fig. 21.15b). Full view of the tibia and fibula should be obtained to identify potential proximal fibular fractures.

Injuries of the Hindfoot

The calcaneus is the most frequently fractured tarsal bone, accounting for 60% of all tarsal fractures. Calcaneal fractures most frequently occur in young individuals (20–40 years), with axial-loading mechanism (most commonly falls from a height onto the heels). Both heels may be injured at the same time; bilateral calcaneal fractures are present in 5%–10% of cases. During trauma, the talus is driven down into the calcaneus causing a fracture.

There are two major forms of calcaneal fractures: an isolated fracture without displacement (usually in the tuberosity) and a compression injury (Fig. 21.16). Minor fracture without compression usually occurs in the tuberosity and can be overlooked if only a lateral projection of the calcaneus is taken. Avulsion fracture of the Achilles tendon may cause a tuberosity fracture particularly in diabetic patients.

Compression fracture of calcaneus is a serious injury that may cause significantly impaired function. On lateral radiograph, the upper surface of the calcaneus is flattened and Bohler's angle reduced. A Bohler's angle measures the angle between the line of the subtalar joint and the upper surface of the tuberosity to determine the severity of the compression and the status of the posterior facet of the calcaneus. The angle is normally between 20° and 40° [15].

Talar fractures are the second most common tarsal bone fractures. They are usually caused by forced dorsiflexion force, in which the force is transmitted to the head of the talus and the bone gives way in the neck. In severe injuries, the body of the talus may be dislocated posteriorly out of the ankle mortise. The most common site of talar fracture is the neck (Fig. 21.17). The fracture line is located anterior to the lateral process of the talus and is often vertically oriented. Hawkins classification divides talar neck fracture into four types (Table 21.7) [16].

The risk of developing AVN increases with higher fracture type due to damage to the nutrient vessels at the time of

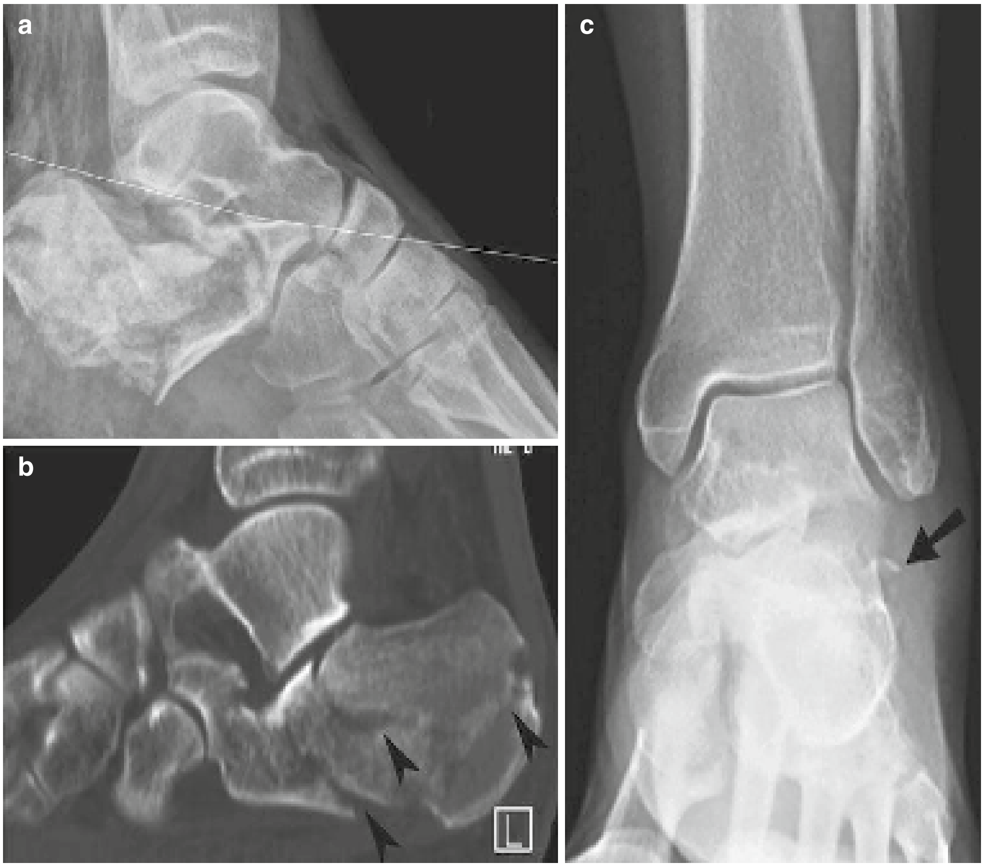

Fig. 21.16 Calcaneal fracture. (**a**, **b**) A lateral radiograph and sagittal-reformatted CT image of the calcaneus show a comminuted compression fracture of the calcaneus (*arrowheads*) with subtalar joint extension and reduced Bohler's angle. (**c**) An AP ankle radiograph of another patient demonstrates an avulsion fracture (*arrow*) of the dorsolateral aspect of the calcaneus at the origin of the extensor digitorum brevis muscle

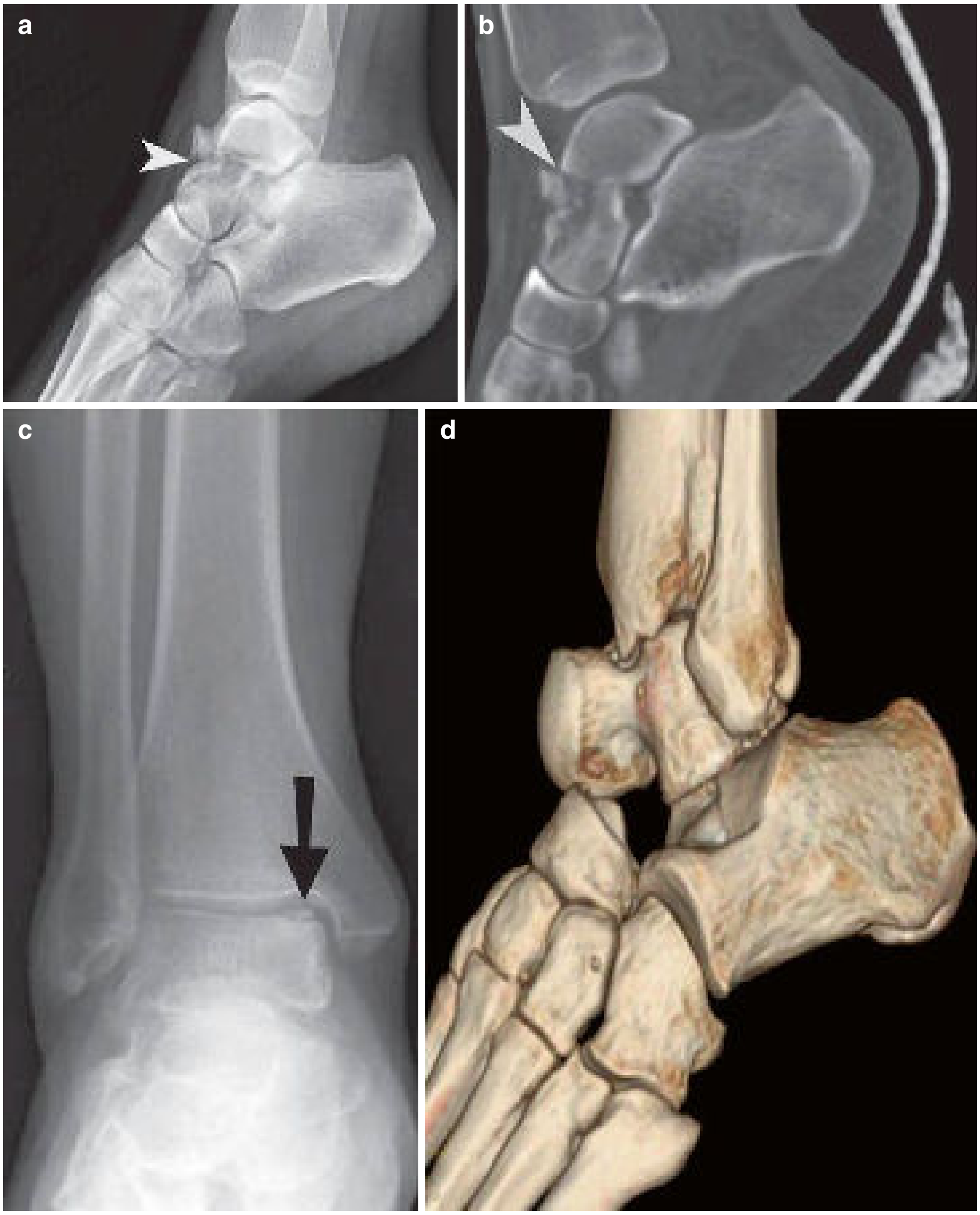

Fig. 21.17 Talar fracture. (**a**, **b**) A lateral radiograph and sagittal-reformatted CT image of the foot demonstrate a talar neck fracture (*arrowheads*) without subtalar or tibiotalar joint subluxation/dislocation. (**c**) An AP ankle radiograph of another patient shows a small bone fragment in the medial aspect of the talar dome (*arrow*), representing osteochondritis dissecans. (**d**) A 3D CT image of the ankle shows an obvious dislocation of the subtalar joint, in which there is disruption of the talonavicular and talocalcaneal articulations

Table 21.7 Hawkins classification of the talar neck fracture

Type	Dislocation or subluxation
Type I	None
Type II	Subtalar subluxation or dislocation
Type III	Subtalar and tibiotalar dislocation
Type IV	Subtalar subluxation and talonavicular dislocation

the injury. Fractures extending into or posterior to the lateral process of talus are defined as fractures of the body (intra-articular). The fractures of the lateral process are easily overlooked and can be misdiagnosed clinically as severe sprain. These fractures are best visualized on the mortise view.

Subtalar or peritalar dislocations are rare and describe concomitant dislocations of the subtalar and talonavicular joints but normal tibiotalar relationship. Medial dislocation is the most frequent type, but a lateral counterpart is more severe (Fig. 21.17d). Total talar dislocation is defined when there is concomitant dislocation of the subtalar, talonavicular, and tibiotalar joints, which is the most severe of all tarsal injuries.

Injuries of the Midfoot and Forefoot

The tarsal bones are responsible for maintaining the relationship between the forefoot and hindfoot. The navicular is the most frequently injured bone of the midfoot. These are commonly due to sports-related injuries, falls, or motor vehicle collisions. Uncommonly, navicular fractures occur from an avulsion force to the talonavicular or naviculocuneiform

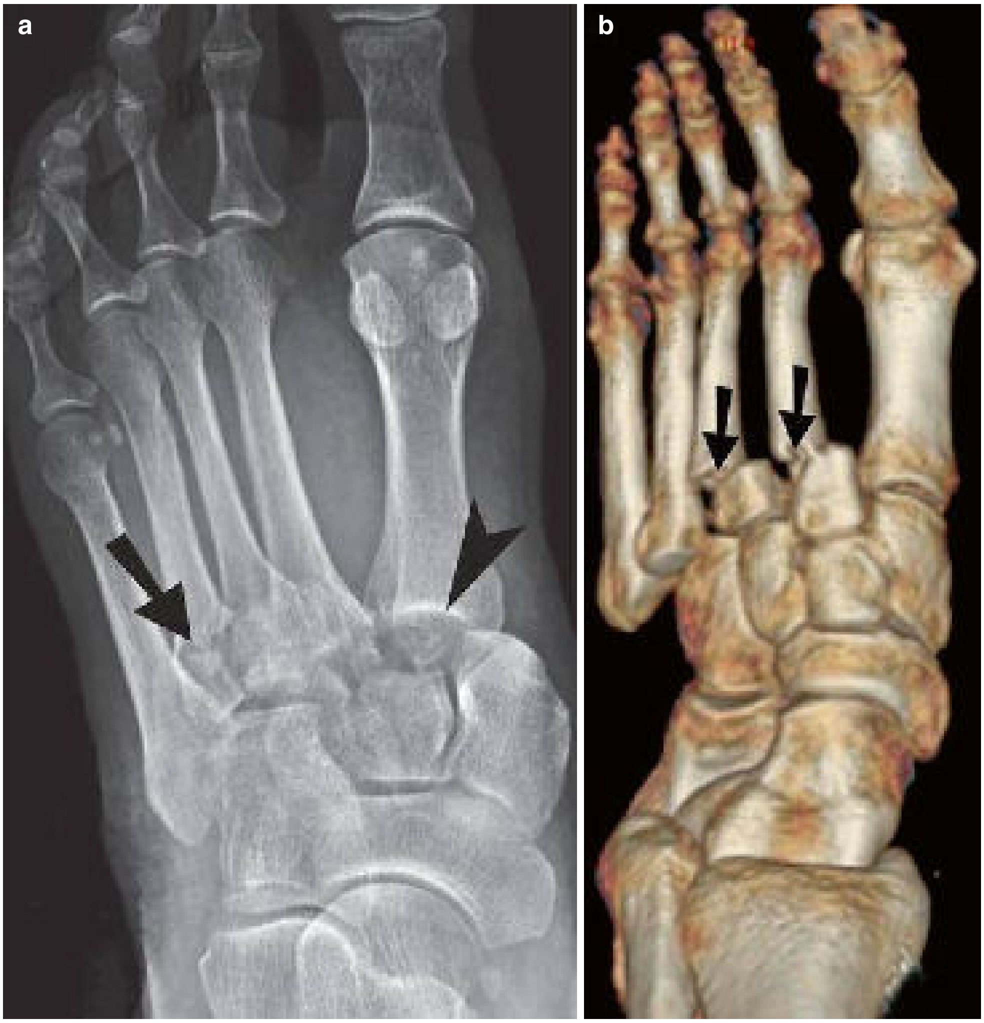

Fig. 21.18 Lisfranc fracture dislocation. (**a**, **b**) A PA radiographic view and 3D CT image of the foot demonstrate a disrupted alignment of the Lisfranc joint (*arrowhead*), with lateral/dorsal dislocation of the first through fifth digits and fractures of the metatarsal bases (*arrows*). This is a homolateral Lisfranc fracture/dislocation

Table 21.8 Fractures of the fifth metatarsal

Type	Dislocation or subluxation
Zone I	Avulsion fracture at the base
Zone II	Fracture of the metadiaphyseal junction (Jones fracture)
Zone III	Involvement of the proximal fifth metatarsal

ligaments. An accessory navicular (os tibiale externum) can be mistaken as a fracture, although this is bilateral in 90% of the time.

Lisfranc [17] (tarsometatarsal) injuries are a complex injury commonly resulting from plantar hyperflexion across the long axis of the foot. The key anatomic structure related to this injury is the Lisfranc ligament, which is a strong plantar ligament connecting the medial cuneiform and the second metatarsal base. Injuries may cause a tear of this ligament and/or fractures of the medial cuneiform or base of the second metatarsal. Two major types of Lisfranc injuries are homolateral and divergent (Fig. 21.18). When the four lateral metatarsals or all metatarsals dislocate laterally, this is called homolateral. If the first metatarsal dislocates medially but the rest is dislocated laterally, it is a divergent type.

There are three distinct patterns of fractures of the fifth metatarsal, according to the location of the fracture line (Table 21.8 and Fig. 21.19).

- Zone 1 injuries describe an avulsion fracture at the base of the fifth metatarsal due to a pull of a lateral band of the plantar aponeurosis during sudden inversion of the hindfoot.
- Zone 2 injuries are true Jones fractures, which involve the metadiaphyseal junction of this bone, extending to the intermetatarsal and/or tarsometatarsal joints.
- Zone 3 injuries are fractures of the proximal fifth metatarsal.

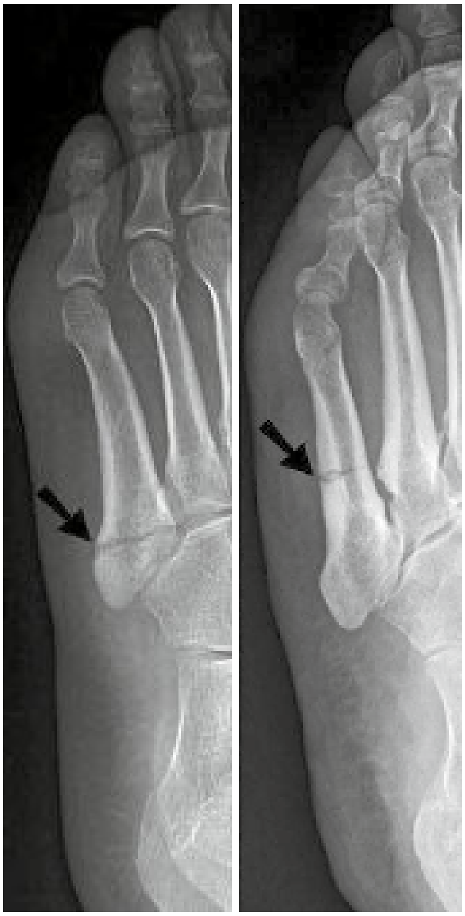

Fig. 21.19 Fifth metatarsal fracture. Two different cases demonstrate zone II (*left image*) and zone III (*right image*) fractures of the fifth metatarsal base (*arrows*)

Mimics of fractures of the fifth metatarsal base include an apophysis, which is oriented longitudinally to the axis of the metatarsal.

Phalangeal fractures are the most common injury to the forefoot with the proximal phalanx being the most frequent site. They are often a result of crushing injuries, as from the fall of a heavy object onto the foot. The former often causes a comminution, while the latter produces a spiral or oblique fracture with greater deformity due to varus or valgus forces.

Stress fractures (Fig. 21.20) are a result of repetitive trauma below the threshold for acute fracture but considerable enough to cause microtrabecular failure. Lower extremity stress fractures are common in athletes and military recruits. The diagnosis is based on the history of repetitive overuse and the lack of acute traumatic event. Frequent locations are metatarsals, calcaneus, and lower leg. The most frequently affected metatarsal bone is the second metatarsal, which typically occurs in the diaphysis. In the calcaneus, the posterior aspect (heel) is the most common location. The fracture line is perpendicular to the trabecular cancellous lines. Radiography has a poor sensitivity for detection in an early phase because of the lack of callus formation unless there is a superimposed acute fracture. MRI is very sensitive and specific for evaluation of these injuries. Linear region of T1 and T2 hypointensity (fracture line) with surrounding T2 hyperintensity (bone marrow edema) is characteristic.

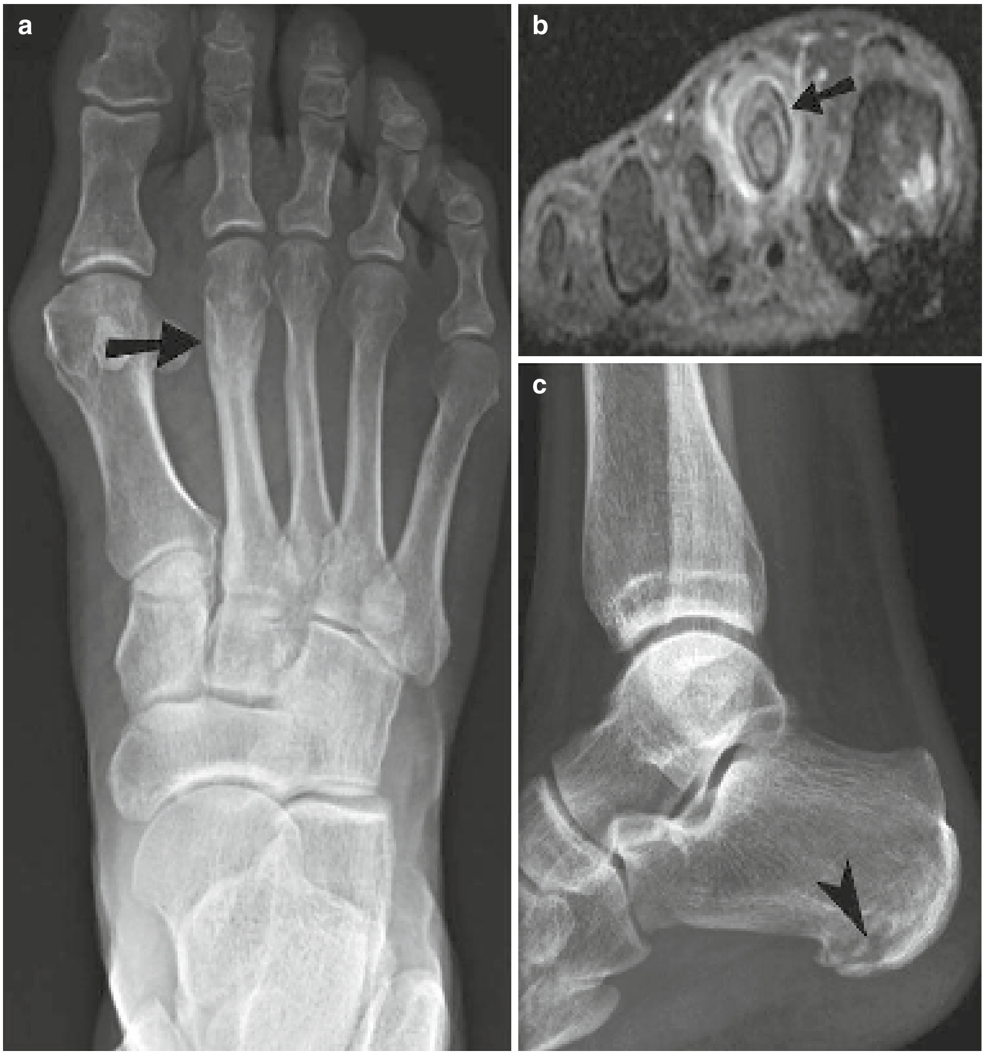

Fig. 21.20 Stress fracture. (**a**, **b**) A PA radiograph and axial fat-suppressed STIR MR image of the foot of two different patients show a stress fracture (*arrow*) of the second metatarsal bone at the neck. On radiography, there is bony callus formation of a healed stress fracture. On MRI, bone marrow edema with surrounding callus formation and T2 hyperintensity is seen. (**c**) A lateral calcaneal radiograph shows a linear lucent line at the heel with surrounding sclerosis (*arrowhead*), representing a calcaneal stress fracture

Nonaccidental Trauma

Fractures are the second most common findings in nonaccidental trauma after dermatologic findings such as bruises, contusions, and burns. Skeletal survey is commonly performed in children under the age of 2 years suspected of nonaccidental trauma. This study helps showing fractures, in which up to half can be clinically occult. The role of radiologists is to detect and describe fractures with knowledge of the clinical history in cooperation with other specialists such as pediatricians. Several fractures are highly specific for inflicted injury including rib (especially posterior), classic metaphyseal lesion (CML, also known as corner fracture or bucket-handle fracture), spiral fracture of the femur, and fractures of the sternum, spine, and scapula (Figs. 21.21 and 21.22). Other fractures that should raise a suspicion of nonaccidental trauma are bilateral fractures, multiple fractures at various ages of healing, vertebral body fractures, epiphyseal separation, and digital fractures [18]. The CML is a fracture through the immature metaphysis of the long bone, resulting from twisting injury. It is frequently found in the femur, tibia, and humerus. Radiographic appearance differs when one views it from a different angle. A bucket-handle fracture fragment is seen en face, while a triangular “corner” fracture is depicted when viewed in profile [19].

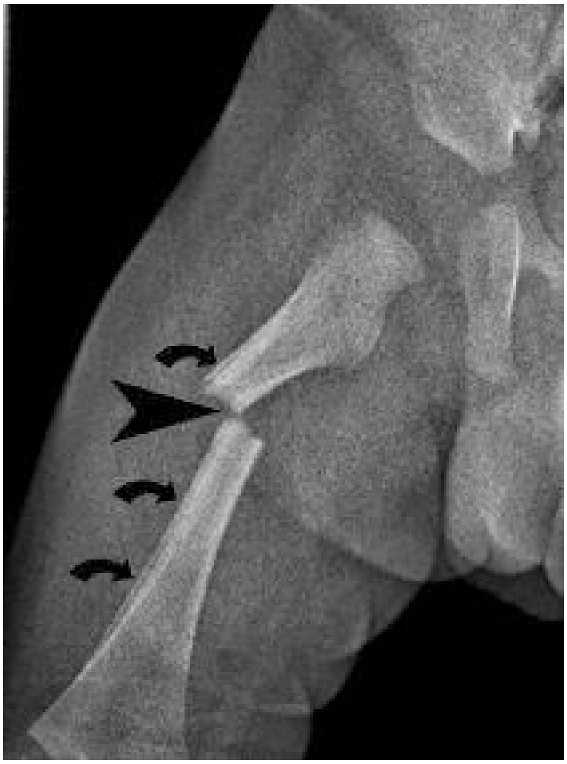

Fig. 21.21 Nonaccidental trauma. An AP radiograph of the right femur as a part of bone survey in a young child demonstrates a displaced transverse fracture (*arrowhead*) of the proximal third of the femur superimposed on an ongoing healing process as evident by solid periosteal reaction (*arrows*) along the femur

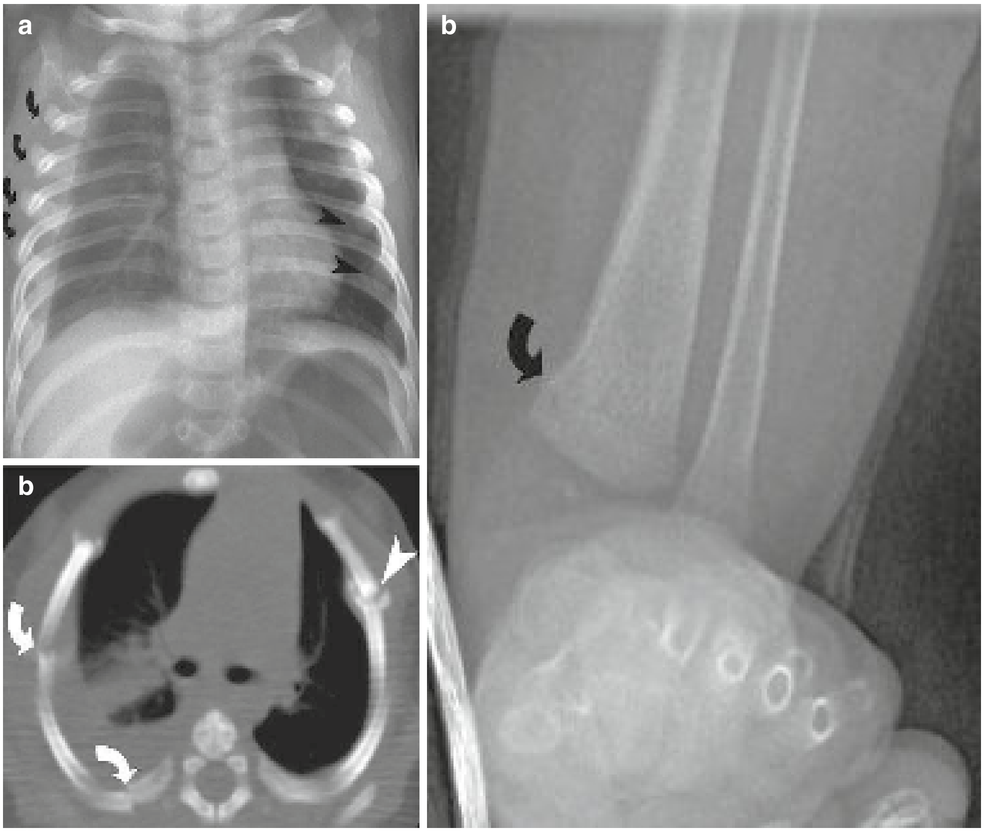

Fig. 21.22 Nonaccidental trauma. (**a**, **b**) Plain radiograph and CT of the chest demonstrate multiple right-sided acute rib fractures (*arrows*). There are multiple healing left-sided rib fractures (*arrowheads*). (**c**) Plain radiograph of the same patient demonstrates a healed distal tibial metaphyseal fracture (*arrow*)

Eponymous Fractures of Lower Extremity

Numerous fractures continue to be known by the eponyms of physicians who first described them. Table 21.9 outlines common eponymous fractures of lower extremity.

Teaching Points

- Two major groups of pelvic fractures are isolated fractures and pelvic ring disruption.
- On the AP view of the hip, six lines relating to the acetabulum and surrounding structures have been described: iliopubic or iliopectineal line, ilioischial line, radiographic teardrop, roof of the acetabulum, anterior rim of the acetabulum, and posterior rim of the acetabulum.
- Posterior hip dislocation is the most common type and is characterized by lack of congruency of the femoral head and the acetabular fossa with the femoral head located superolateral to the acetabulum.
- The fractures of the supracondylar and condylar regions of femur are divided into three types: extra-articular (transverse), partial articular, and complete articular.
- Five types of knee dislocations are described with tibia in relation to the femur, which include anterior (most common), posterior (second most common), lateral, medial, and rotary.
- The secondary signs of tibial plateau fractures include the presence of a fat-blood level or fat-blood interface sign within the suprapatellar bursa, seen on the lateral cross-table radiographic view of the knee.

Table 21.9 Eponymous fractures of lower extremity

Fracture name	Description
Chopart	Fracture dislocation at the midtarsal (talonavicular and calcaneocuboid) joints
Gosselin	Intra-articular distal tibial fracture with a V-shaped fractured fragment
Jones	Transverse fracture of fifth metatarsal at the metadiaphyseal junction
Lisfranc	Tarsometatarsal fracture dislocation. Homolateral and divergent are the two major types
Maisonneuve	Proximal fibular fracture with associated tear of the distal tibiofibular syndesmosis and distracting medial ankle injuries
Pipkin	Fractures of the femoral head with associated hip dislocation. Pipkin classification describes four types
Segond	Avulsion fracture of the lateral aspect of the proximal tibia involving the attachment site of lateral capsular ligament
Shepherd	Fracture of the lateral tubercle of the posterior talar process
Tillaux	Avulsion fracture of the anterolateral distal tibial tubercle

Questions

1. Which of the following statements is correct regarding pelvis fractures?
   (A) Lateral compression is a vertical fracture involving pubic rami and symphysis diastasis
   (B) Anteroposterior compression is commonly associated with central hip dislocation
   (C) Vertical shear injuries are associated with severe pelvic instability
   (D) Anteroposterior compression involves pubic rami, sacroiliac joints, and iliac wings
   Answer: C

2. Which of the following zones in Denis classification of pelvis fractures involves central canal?
   (A) Zone I
   (B) Zone II
   (C) Zone III
   (D) Zone IV
   Answer: C

3. Type 4 Pipkin classification of the proximal femur includes which of the following?
   (A) Fracture above the fovea
   (B) Fracture below the fovea
   (C) Femoral head fracture associated with an acetabular fracture
   (D) Femoral head fracture associated with a neck fracture
   Answer: C

4. What is the imaging diagnosis in the following plain radiograph (Fig. 21.23)?
   (A) Pilon fracture
   (B) Tibia and fibula fractures
   (C) Tillaux fracture
   (D) Weber fracture
   Answer: A

5. What is the pathology depicted in the following plain radiograph (Fig. 21.24)?
   (A) Pilon fracture
   (B) Deltoid ligament injury
   (C) Ankle fracture
   (D) Distal fibula fracture
   Answer: B

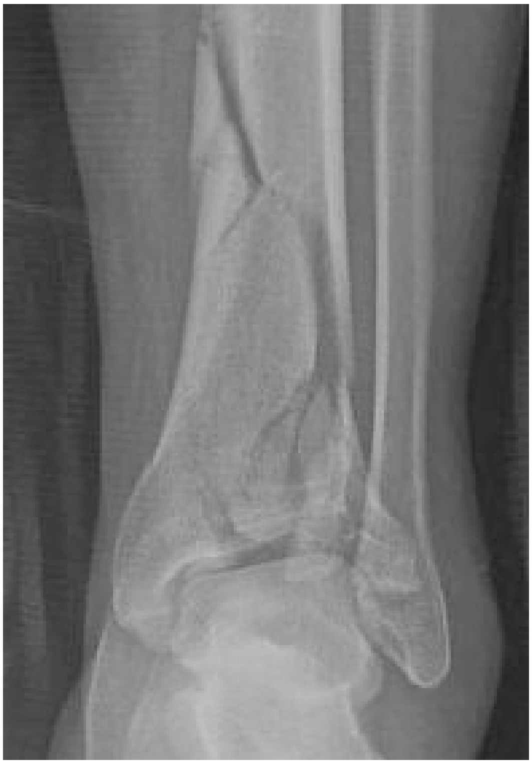

Fig. 21.23 Identify the plain radiograph—Pilons fracture

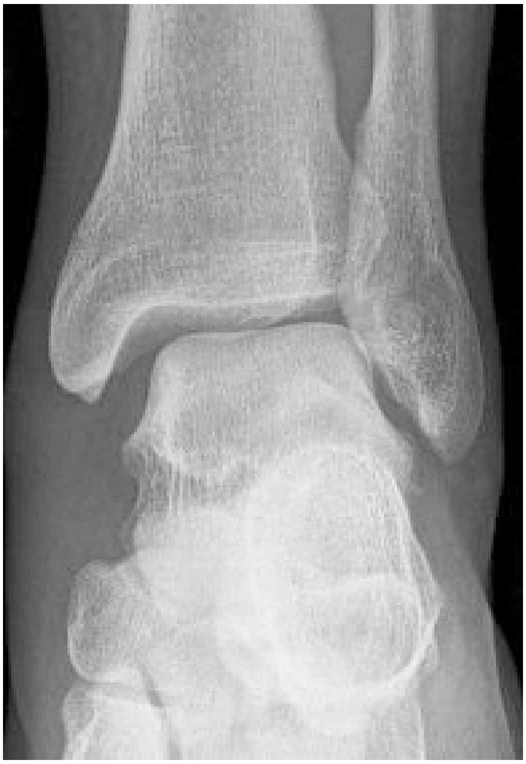

Fig. 21.24 Identify the plain radiograph—Deltoid ligament injury

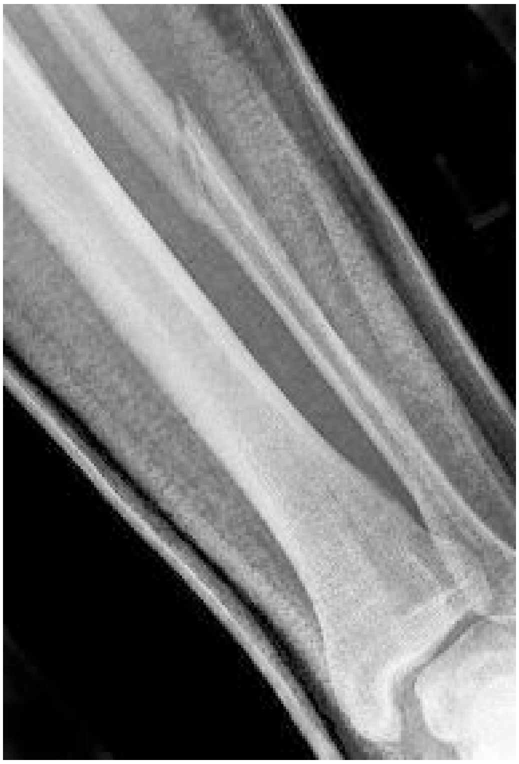

Fig. 21.25 Identify the plain radiograph—Fibular fracture and deltoid ligament injury

6. What is the imaging diagnosis of the following plain radiograph (Fig. 21.25)?
   (A) Fibular fracture alone
   (B) Deltoid rupture alone
   (C) Pilon fracture
   (D) Fibular fracture and deltoid ligament injury
   Answer: D

References

1. Young JW, Burgess AR, Brumback RJ, Poka A. Pelvic fractures: value of plain radiography in early assessment and management. Radiology. 1986;160:445–51.
2. Denis F, Davis S, Comfort T. Sacral fractures: an important problem. Retrospective analysis of 236 cases. Clin Orthop Relat Res. 1988;227:67–81.
3. Saks BJ. Normal acetabular anatomy for acetabular fracture assessment: CT and plain film correlation. Radiology. 1986;159:139–45.
4. DeLee JC, Evans JA, Thomas J. Anterior dislocation of the hip and associated femoral-head fractures. J Bone Joint Surg Am. 1980;62:960–4.
5. Pipkin G. Treatment of grade IV fracture-dislocation of the hip. J Bone Joint Surg Am. 1957;39-A:1027–42.
6. Garden RS. Low-angle fixation in fractures of the femoral neck. J Bone Joint Surg Br. 1961;43B:17.

7. Barnes R, Brown JT, Garden RS, Nicoll EA. Subcapital fractures of the femur. A prospective review. J Bone Joint Surg Br. 1976;58:2–24.
8. Aichroth P. Osteochondritis dissecans of the knee. A clinical survey. J Bone Joint Surg Br. 1971;53:440–7.
9. Green NE, Allen BL. Vascular injuries associated with dislocation of the knee. J Bone Joint Surg Am. 1977;59:236–9.
10. Schatzker J, McBroom R, Bruce D. The tibial plateau fracture. The Toronto experience 1968–1975. Clin Orthop Relat Res. 1979;138:94–104.
11. Medlar RC, Lyne ED. Sinding-Larsen-Johansson disease. Its etiology and natural history. J Bone Joint Surg Am. 1978;60:1113–6.
12. Pankovich AM. Maisonneuve fracture of the fibula. J Bone Joint Surg Am. 1976;58:337–42.
13. Danis R. Theorie et pratique de I' osteosynthese. Paris: Masson & Cie; 1949.
14. Weber BG. Die verletzungen des oberen sprunggelenkes. Bern: Huber; 1972.
15. Chen MY, Bohrer SP, Kelley TF. Boehler's angle: a reappraisal. Ann Emerg Med. 1991;20:122–4.
16. Hawkins LG. Fractures of the neck of the talus. J Bone Joint Surg Am. 1970;52:991–1002.
17. Lisfranc J. Nouvelle methode operatoire pour l'amputation partielle du pied dans son articulation tarso-metatarsienne: methode precedee des nombreuses modifications qu'a subies celle de Chopart. Paris: Gabon; 1815.
18. Kleinman PK, Marks SC Jr, Richmond JM, Blackbourne BD. Inflicted skeletal injury: a postmortem radiologic-histopathologic study in 31 infants. AJR Am J Roentgenol. 1995;165:647–50.
19. Kleinman PK, Marks SC, Blackbourne B. The metaphyseal lesion in abused infants: a radiologic-histopathologic study. AJR Am J Roentgenol. 1986;146:895–905.

Imaging of Spinal Trauma

22

Parul Penkar, Rathachai Kaewlai, Mohammad Mansouri,
Ajay Singh, Laura Avery, and Robert A. Novelline

Introduction

Spine trauma accounts for significant mortality and morbidity. The annual incidence of spinal cord injury (SCI), excluding those who died at the scene of the accident, is approximately 40 cases per million population in the USA or approximately 12,000 new cases each year [1]. Spine trauma can result from blunt or penetrating trauma such as motor vehicle collisions, falls, diving injuries, industrial accidents, gunshot wounds, assault, and other miscellaneous causes. Pathological fractures usually occur from underlying osteoporosis, rheumatoid arthritis, malignancy, infection, and metabolic or endocrine conditions and usually cause compression fractures.

Initial Cervical Spine Screening Modality

Most cervical spine fractures occur predominantly at two levels, at the level of C2 and at the level of C6 or C7. Unfortunately, 20%–30% of these fractures can be missed on plain radiographs. Current data and American College of Radiology Appropriateness Criteria recommend the use of multidetector-row computed tomography (MDCT) as the initial screening examination in suspected cervical trauma instead of radiographs [2].

The multicentric National Emergency X-Radiography Utilization Study (NEXUS) criteria, which were based on clinical data and radiography of 34,069 patients, found that their criteria had an overall sensitivity of 99.6% in identifying patients at risk for cervical spine injury [3, 4]. Another clinical prediction prospective study on 8924 patients, the Canadian C-Spine Rule Study (CCRS) which was based on three main questions, found that their clinical criteria had 100% sensitivity and 42.5% specificity for identifying clinically important cervical spine injuries [5]. New Orleans Criteria is an acceptable alternative criterion, which has the same sensitivity. It is debatable if radiography should be obtained in patients with low risk for cervical spine injury, but recent ACR Appropriateness Criteria recommend no imaging in patients who satisfy any of the “low-risk” criteria and CT imaging in patients who do not fall in the low-risk category (i.e., indicated imaging based on criteria, initial imaging study in moderate to severe head injury, follow-up studies) [2, 4, 5].

Based on the ACR appropriateness criteria, MRI is an appropriate study in:

- Short-term follow-up imaging of acute traumatic brain injury, neurologic deterioration, delayed recovery, or persistent unexplained deficits
- Subacute or chronic traumatic brain injury with new cognitive and/or neurologic deficits
- Suspected intracranial arterial or venous injury (Table 22.1)

P. Penkar · M. Mansouri · L. Avery · R. A. Novelline
Department of Radiology, Massachusetts General Hospital,
Boston, MA, USA
e-mail: ppenkar@partners.com; lavery@partners.org;
rnovelline@partners.org

R. Kaewlai
Department of Diagnostic and Therapeutic Radiology,
Ramathibodi Hospital, Mahidol University, Bangkok, Thailand

A. Singh (✉)
Division of Emergency Radiology, Department of Radiology,
Massachusetts General Hospital, Boston, MA, USA

Harvard Medical School, Massachusetts General Hospital,
Boston, MA, USA
e-mail: asingh1@partners.org

© The Author(s), under exclusive license to Springer Nature Switzerland AG 2024
A. Singh (ed.), *Emergency Radiology*, https://doi.org/10.1007/978-3-031-65770-2_22

Table 22.1 Recommendations of ACR appropriateness criteria in head trauma

Situation	Appropriate study
Minor or mild acute closed head injury (GCS ≥13), imaging not indicated by NEXUS clinical criteria	None
Minor or mild acute closed head injury (GCS ≥13), imaging indicated by NEXUS clinical criteria	CT head without IV contrast
Moderate or severe acute closed head injury (GCS <13)	CT head without IV contrast
Short-term follow-up imaging of acute traumatic brain injury. No neurologic deterioration	CT head without IV contrast (in patients with risk factors)
Short-term follow-up imaging of acute traumatic brain injury Neurologic deterioration, delayed recovery, or persistent unexplained deficits	CT head without IV contrast
	MRI head without IV contrast (complementary to CT)
Subacute or chronic traumatic brain injury with new cognitive and/or neurologic deficits	MRI head without IV contrast
	CT head without IV contrast (complementary to MRI)
Suspected intracranial arterial injury	CTA
	MRA
Suspected intracranial venous injury	CTV
	MRV
Suspected post-traumatic cerebrospinal fluid leak	CT maxillofacial without IV contrast
	CT temporal bone without IV contrast

NEXUS Criteria

Imaging is unnecessary if all of the five following criteria are met:

1. Absence of posterior midline cervical tenderness
2. No focal neurological deficits
3. Normal-level alertness
4. No evidence of intoxication
5. No painful distracting injures

A retrospective study at our institution showed that in patients with low clinical suspicion for cervical spine trauma who had plain-film radiography, the overall positivity rate for acute cervical spine fractures was 0.0%. This data indicates that radiography for patient with low risk for cervical spine trauma may have too low a yield to justify its use and could be explained by the fact that the radiographs were done on patients who do not meet the validated NEXUS criteria or Canadian C-Spine Rule (Fig. 22.1a) [6, 7]. In a meta-analysis of seven studies with strict inclusion criteria, the pooled sensitivity of radiography for detecting patients with cervical spine injury was 52%, while the combined sensitivity of CT was 98% [2, 8–10].

In case if cervical plain radiographs are obtained for trauma due to unavailability of emergent CT, an adequate cervical spine series must include five views: a true lateral view, which must include all seven cervical vertebrae and the cervicothoracic junction; an anteroposterior view; an open-mouth odontoid view; and both the oblique views. A swimmer's view may be necessary to adequately show the lower cervical spine. Any film series that does not include these five views or which does not visualize all seven cervical vertebrae and the junction of C7–T1 is inadequate.

Flexion and extension views of the cervical spine are contraindicated in case of cervical spine fracture. They were used in the past for suspected ligamentous injuries; however, currently they have been replaced by MRI for suspected soft tissue trauma. In rare instances, they have been used for detecting new malalignment or exaggeration of the existing listhesis in patients with degenerative changes and in patients with equivocal MRI findings.

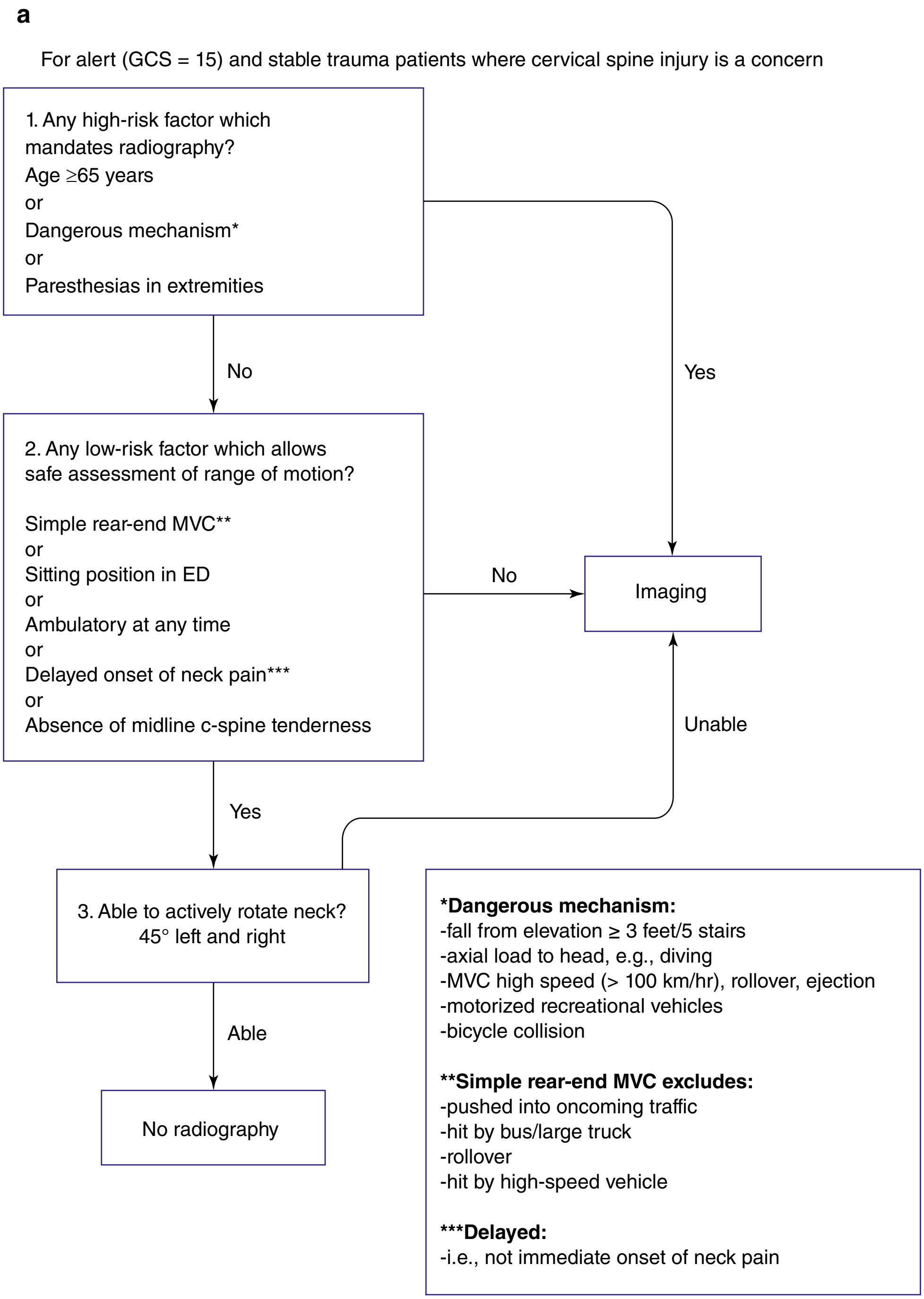
a
For alert (GCS = 15) and stable trauma patients where cervical spine injury is a concern
1. Any high-risk factor which mandates radiography?
Age ≥65 years
or
Dangerous mechanism*
or
Paresthesias in extremities
No
Yes
2. Any low-risk factor which allows safe assessment of range of motion?
Simple rear-end MVC**
or
Sitting position in ED
or
Ambulatory at any time
or
Delayed onset of neck pain***
or
Absence of midline c-spine tenderness
No
Imaging
Unable
Yes
3. Able to actively rotate neck? 45° left and right
Able
No radiography
*Dangerous mechanism:
-fall from elevation ≥ 3 feet/5 stairs
-axial load to head, e.g., diving
-MVC high speed (> 100 km/hr), rollover, ejection
-motorized recreational vehicles
-bicycle collision
**Simple rear-end MVC excludes:
-pushed into oncoming traffic
-hit by bus/large truck
-rollover
-hit by high-speed vehicle
***Delayed:
-i.e., not immediate onset of neck pain

Fig. 22.1 (**a**) The Canadian C-Spine Rule. Adapted from [27]. (**b**, **c**) Normal lines on lateral view of the cervical spine. (**b**) On the lateral radiograph of the cervical spine, the anterior spinal line (3), posterior spinal line (2), and spinolaminar line (1) are located along the anterior cortex of vertebral bodies, posterior cortex of vertebral bodies, and spinolaminar junctions, respectively. (**c**) Discontinuous anterior spinal line (3), posterior spinal line (2), and spinolaminar line (1) are seen on lateral radiograph of the cervical spine in a patient with type 2 dens fracture (*arrowhead*)

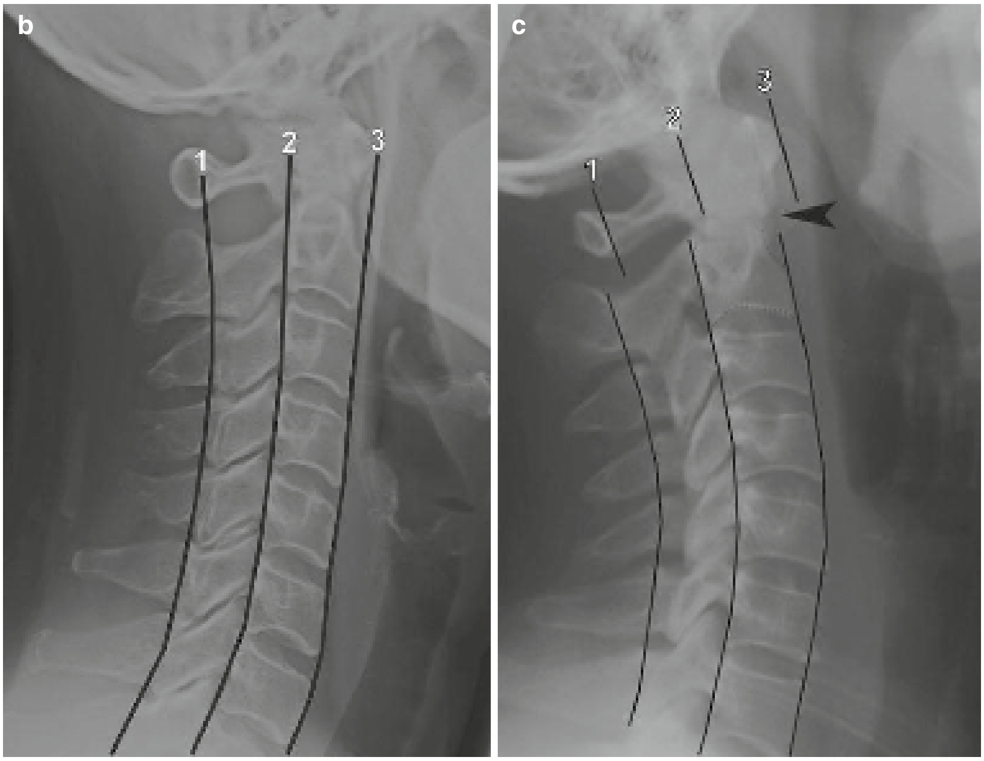

Fig. 22.1 (continued)

New Orleans Criteria (NOC)

NOC includes patients with GCS 15, who are >18 years old, and who had blunt head trauma occurring within 24 h and causing loss of consciousness, amnesia, or disorientation. Based on NOC, head CT is not required if all of the following are absent:

1. Headache
2. Vomiting
3. Age >60 years
4. Alcohol or drug intoxication
5. Deficits in short-term memory
6. Visible trauma above clavicles
7. Seizure

Cervical Spine Lines and Spaces

The cervical spine lines should be continuous curves through the bony elements regardless of the degree of flexion or extension, and any misalignment of these lines should be viewed as a sign of ligamentous injuries or occult fractures. The exception to this finding would be from anterior pseudosubluxation ligamentous laxity, which can occur at the C2–C3 level and less commonly at the C3–C4 level. Normal cervical spine lordosis can sometimes be reversed due to the presence of cervical collar, patient positioning, or muscle spasm.

There are four basic lines to evaluate alignment on lateral view of the cervical spine (Fig. 22.1b, c). These lines include anterior spinal line, posterior spinal line, spinolaminar line, and posterior spinous process line.

Predental Space or Atlanto-Dens Interval Space

The space between the odontoid process and the anterior portion of the ring of C1 should be <3.5 mm in adults and <5 mm in children. An increase in this space is presumptive evidence of a fracture of C1 or of the odontoid process, although it may also represent ligamentous injury at this level.

Prevertebral Space

Prevertebral soft tissue swelling (more than 6 mm at C2, more than 22 mm at C6) is highly specific for a fracture but not very sensitive. Soft tissue swelling in symptomatic patients should be considered an indication for further radiographic evaluation.

Table 22.2 Acceptable measures in cervical spine lines and spaces

Lines and spaces	Acceptable measures
Cervical spine lines (except pseudosubluxation ligamentous laxity)	Continuous
Predental space	Adults: <3.5 mm
	Children: <5 mm
Prevertebral space	C2: <6 mm
	C6: <22 mm
Intervertebral or interspinous distance or angulation	<10°
Vertical basion-dens distance	<12 mm
Basion-axial interval	<12 mm

Interspinous and Intervertebral Distance

The spinous processes are examined to evaluate for abnormal widening or fanning of the spinous processes. If abnormal widening of the intervertebral or interspinous distance or angulation of more than 10° is present, a ligamentous injury or fracture should be considered.

Basion-axial interval (BAI) is the distance from the basion (inferior tip of the clivus) to a line drawn along the posterior body of C2, which should measure <12 mm.

Vertical basion-dens distance should measure <12 mm (Table 22.2).

Indication for CT or MR Angiogram

Concomitant arterial injury although rare can occur with penetrating or blunt cervical spine injury causing intimal tears or rupture of the vasa vasorum leading to intramural hematoma, traumatic dissections, stenosis or occlusion, pseudoaneurysms, or rarely transection. CT or MR angiogram is noninvasive and should be obtained in patients with a high clinical suspicion and neurological deficits, if the cervical fracture is extending into the carotid canal or foramen transversarium, and in patients with severe trauma such as facet dislocation, vertebral subluxation, or multiple fractures. Vertebral arterial injury tends to be more common than carotid arterial injury due to close proximity to the spine. Imaging findings are depicted as intimal flaps, segmental or focal narrowing, or occlusions on CT or MR angiograms.

Indication for Spine MRI

In patients with severe fractures, neurological deficits, significant pain, or high clinical suspicion based on the mechanism of injury, MRI of the spine should be obtained to evaluate for ligamentous injuries, traumatic disk herniation, spinal cord edema, cord contusion or compression, spinal cord transection, or prevertebral, intramedullary, or epidural hematoma. The utility of obtaining MRI in obtunded patients with negative spine CT findings is still debatable; however, recent evidence suggests that if an adequate neurological exam cannot be carried out in the first 24 h, MRI of the spine should be obtained, especially in high-speed trauma where ligamentous or soft tissue injury of the cervical spine is a possibility. It should be noted that even MRI does not depict all major ligamentous injuries. The following sequences are usually obtained in trauma MRI, sagittal and axial T1-weighted images, sagittal and axial T2-weighted images, sagittal gradient sequence, and sagittal short tau inversion recovery (STIR) sequences.

Spinal anatomy and fractures are best demonstrated on T1W images. Edema is best observed on T2W images. STIR images provide more homogenous fat suppression and are therefore more sensitive than fat-suppressed T2W images for depiction of cord edema. STIR images are also utilized for demonstrating soft tissue changes and ligamentous injuries.

Classification of Cervical Spine Fractures

Cervical spine fractures are classified based on the mechanism of injury, and only the commonly encountered fractures will be discussed further [11, 12] (Tables 22.3, 22.4, 22.5, and 22.6).

Table 22.3 Cervical injury by flexion mechanism

Mechanism	Submechanism	Fracture
Flexion	Flexion-distraction and rotational forces	Unilateral or bilateral facet dislocation, anterior subluxation
	Hyperflexion and compression	Flexion teardrop fracture
	Hyperflexion avulsion forces	Clay-shoveler's fracture
	Anterior compression	Wedge compression fracture

Table 22.4 Cervical injury by extension mechanism

Mechanism	Submechanism	Fracture
Extension	Hyperextension with distraction	Hangman's fracture
	Hyperextension with axial loading	Hyperextension sprain and fracture dislocation
	Severe hyperextension	Lamina fracture
	Rotation and impaction	Pillar fracture
	Avulsion forces	Extension teardrop fracture
	Hyperextension and compression	Posterior arch of C1 fracture

Table 22.5 Cervical injury by axial loading

Mechanism	Submechanism	Fracture
Axial load	Burst compression	Jefferson fracture, Jefferson variants, and lateral mass fractures
	Vertical axial compression	Burst fractures

Table 22.6 Cervical injury by complex mechanism

Mechanism	Submechanism	Fracture
Complex	Severe extension or flexion with distraction and posterior translation	Atlanto-occipital dissociation
	Severe flexion-extension, distraction, and rotational forces	Atlantoaxial instability
	Flexion or extension loading	Odontoid fracture

Cervical Spine Fractures

Atlanto-Occipital Dissociation

Atlanto-occipital dissociation (AOD) usually occurs in high-energy trauma history such as motor vehicle accidents. Up to 33% of high-energy motor vehicle collisions are reported to have AOD. Complete dislocation is fatal due to stretching injury of the brain stem. Subluxation is rare and can be missed on plain films. It should be suspected in patients with severe facial trauma, and the current methods used to determine subluxation are based on the distances between the occiput and axis which are as follows: BAI is the distance from the basion (inferior tip of the clivus) to a line drawn along the posterior body of C2, which should measure <12 mm. Vertical basion-dens distance should measure <12 mm (Figs. 22.2 and 22.3). AOD is classified into three types:

- Type 1: The most common type. Includes ventral dislocation of occiput.
- Type 2: The most unstable type. Includes longitudinal distraction of occiput.
- Type 3: Dorsal dislocation of occiput.

AOD is classified into two grades:

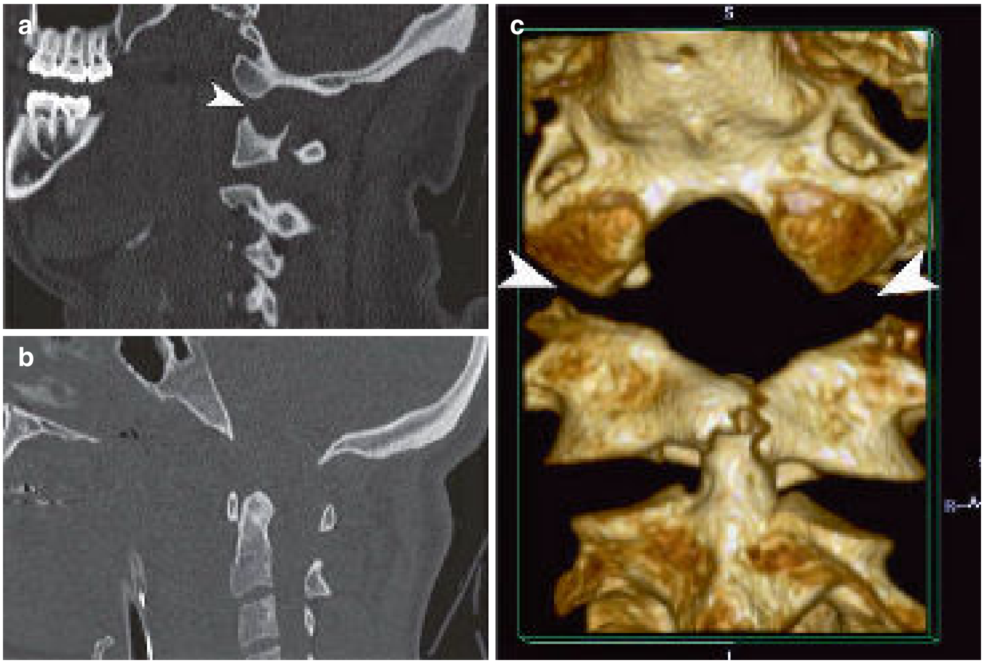

Fig. 22.2 Atlanto-occipital dissociation. (**a**–**c**) Midline sagittal CT reformation, parasagittal CT reformation, and 3D image show widening to the atlanto-occipital joint (*arrowheads*) and increased distance between the dens and the clivus

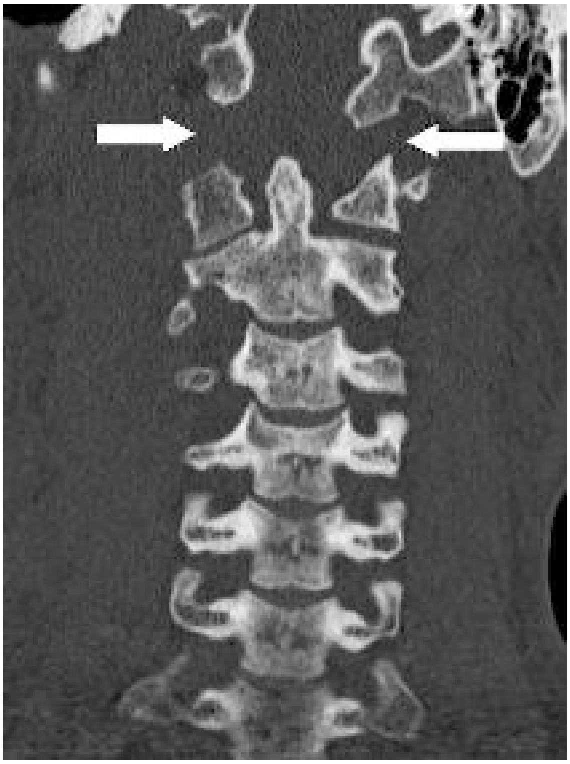

Fig. 22.3 Atlanto-occipital dissociation. Coronal CT reformation demonstrates widening of bilateral atlanto-occipital joint space (*arrows*)

- Grade 1: Normal CT findings and equivocal clinical findings of ligamentous injuries.
- Grade 2: At least one abnormal CT or MRI finding. This group is treated with internal fixation.

Occipital Condyle Fractures

These fractures are discussed with spine trauma due to the mechanism and their association with other cervical spine fractures. They occur from high-energy blunt trauma due to axial loading and lateral bending. Fractures of the occipital condyles are often undiagnosed on plain radiography, and prevertebral soft tissue swelling may be the only radiographic marker (Fig. 22.4). These fractures may extend into the hypoglossal canal or the jugular foramen; therefore, clinical signs of injury to cranial nerves IX–XII may be found. Anderson–Montesano divides occipital condyle fractures into three types (Table 22.7):

Tuli et al. suggested a new classification for occipital condyle fractures:

- Type 1: Nondisplaced fractures.
- Type 2A: Displaced fractures without ligamentous instability. Treatment is rigid collar.

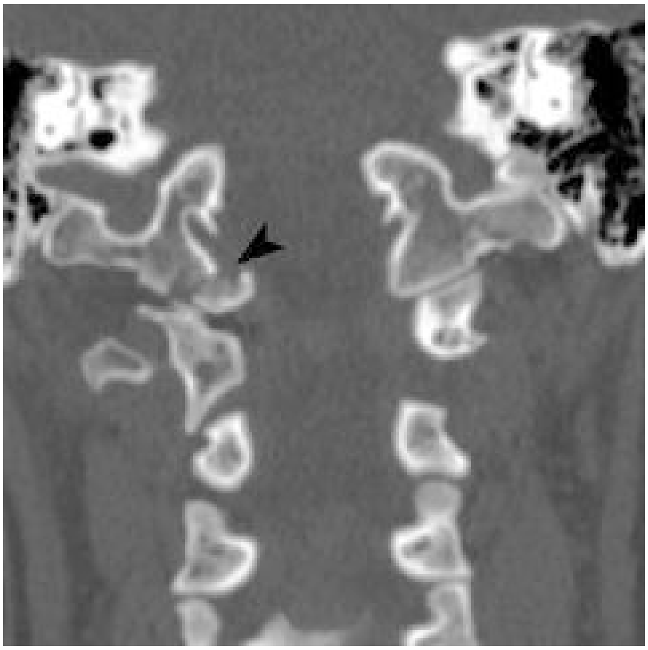

Fig. 22.4 Occipital condyle fracture. Coronal CT of the cervicothoracic junction shows minimal medially displaced oblique fracture (*arrowhead*) of the right occipital condyle

Table 22.7 Types of occipital condyle fractures

Types	Description
1	Comminuted impacted vertically oriented fracture without or with minimal displacement. Usually stable unless bilateral
2	More extensive skull base fracture extending into one or both the occipital condyles
3	Inferior medial avulsion fracture caused by a pull of the alar ligament with medial displacement of the fragment into the foramen magnum. Generally considered unstable since the contralateral alar ligament or tectorial ligament may be compromised and stressed resulting in partial or complete tear or if the degree of displacement is >5 mm, if concomitant atlanto-occipital dislocation is present, or if the fractures are bilateral

- Type 2B: Displaced fractures with ligamentous instability. Treatment is surgical.

Jefferson Fracture

This occurs with axial loading injury with downward compression forces to C1, through the occipital condyles which can cause Jefferson fracture, Jefferson variants, or lateral mass fractures. Jefferson fractures account for 2%–13% of acute cervical fractures. The classic Jefferson fracture is a four-part fracture of the anterior and posterior arches (Fig. 22.5a). Jefferson variants are two- and three-part fractures (Fig. 22.5b) with the most common one being fracture

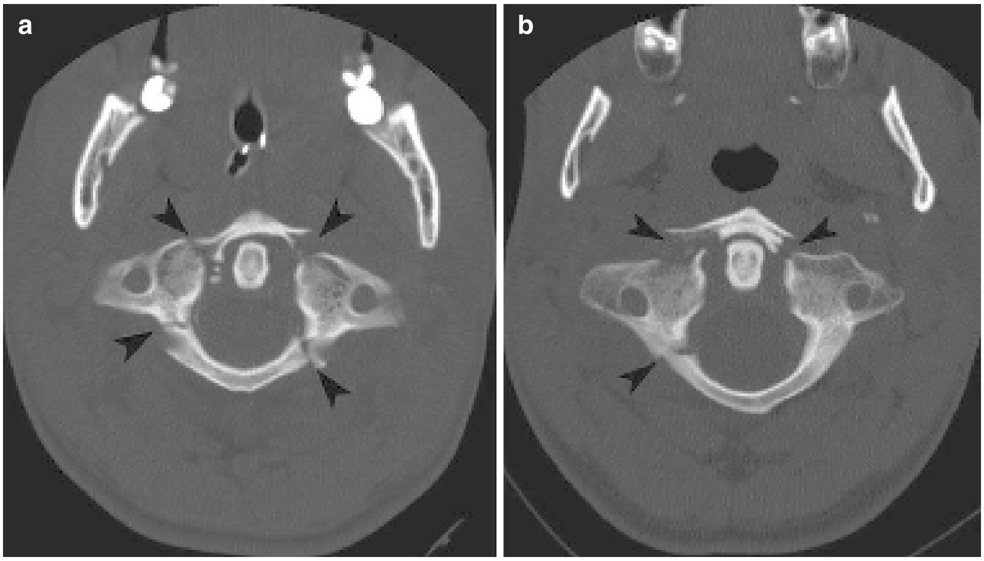

Fig. 22.5 Classic four-part Jefferson fracture. (**a**) Classic four-part Jefferson fracture. Axial CT shows four-part fracture (*arrowheads*) including bilateral fractures of the anterior arch of C1, minimally displaced fracture of the left posterior arch, and nondisplaced fracture of the right posterior arch of C1. (**b**) Three-part Jefferson fracture variant. Axial CT shows three-part fracture (*arrowheads*) including displaced bilateral fractures of the anterior arch of C1 and nondisplaced fracture of the right posterior arch of C1

of one anterior and two posterior arches. On frontal radiography, the presence of Jefferson fracture is implied by offset of the lateral masses of C1 relative to C2 and widening of the atlantodental interval. CT is the best imaging modality in acute injuries. On MDCT with reformats, the fracture is easy to identify. These fractures can be unstable, if they are associated with disruption of the transverse atlantal ligament which fixes the dens to the anterior arch of C1, when the lateral mass cumulative displacement is >7 mm, if the atlanto-dens interval is >5 mm, or when they are associated with C2 fractures. Neurological compromise is infrequent as the fractures cause widening of the C1, thereby limiting cord compression. If the axial loading force is eccentric, a lateral mass fracture may result. This fracture is often associated with fracture of the occipital condyle or articular process, and they are regarded as unstable fractures because the transverse atlantal ligament is often detached. MRI has a complementary role. On T2-weighted images, low signal intensity is seen in ligaments. In ligamental injuries, heterogeneous signal or complete disruption of the fibers is seen.

Table 22.8 Types of dens fracture

Types	Description
1	Rare oblique fracture that involves the superolateral aspect of the dens from avulsion of the alar ligaments and is usually stable injuries
2	Most frequent unstable transverse fracture involving the base of the dens
3	Unstable fracture involving the base of the dens extending into the lateral masses and body of the axis. It has a better prognosis for healing because of the larger surface involved

Dens Fracture

Anderson and D'Alonso classified dens fracture based on the location as types 1, 2, and 3 (Table 22.8). Type 1 fracture (Fig. 22.6a) is rare but stable. Type 2 (either acute or ununited) (Fig. 22.6b) and type 3 fractures (Fig. 22.7) are considered unstable because they can result in atlantoaxial instability (since the ligaments, proximal fragment, C1, and occiput act as a single unit during motion).

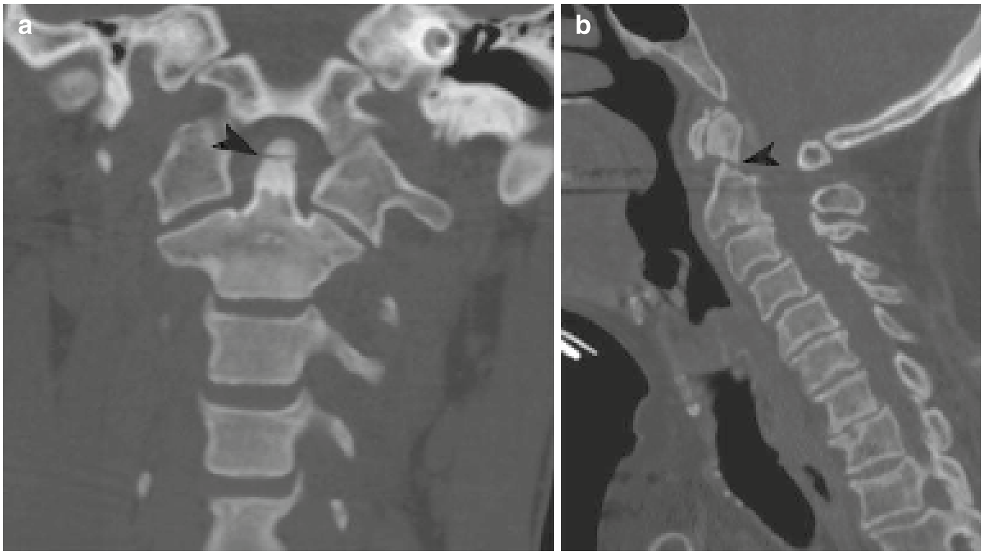

Fig. 22.6 Dens fracture. (**a**) Type 1 dens fracture. Coronal CT shows transverse fracture (*arrowhead*) through the tip of the dens. (**b**) Type 2 dens fracture. Sagittal CT shows oblique fracture (*arrowhead*) through the base of the dens, with mild anterior displacement and angulation of the superior dens

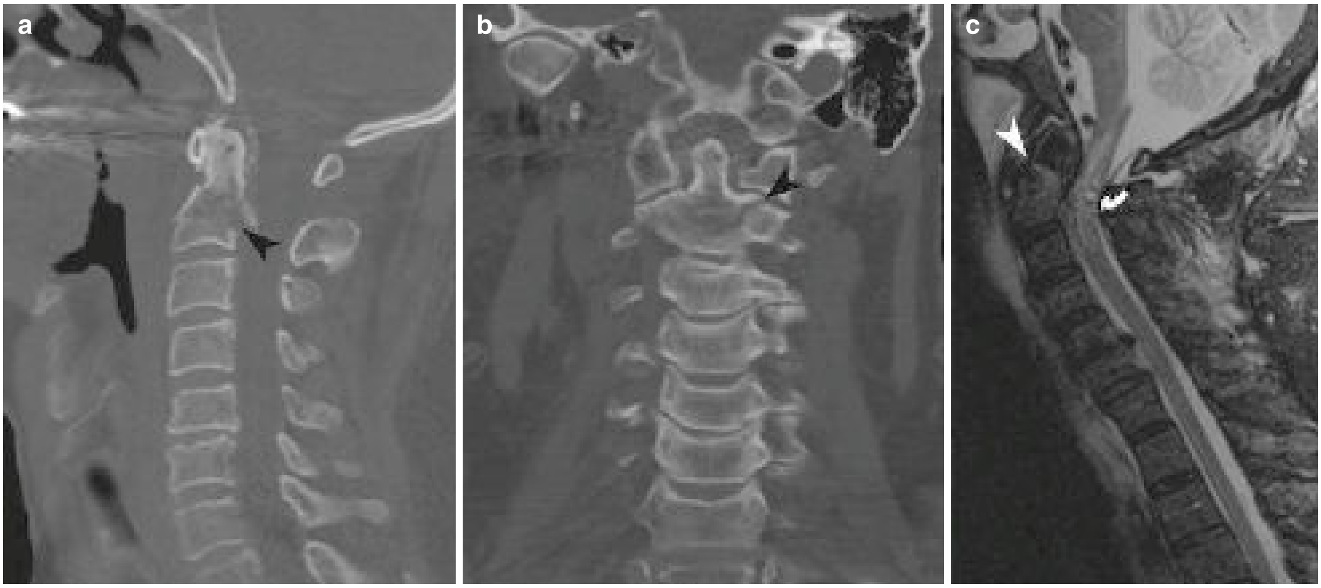

Fig. 22.7 Type 3 dens fracture. (**a**) Sagittal CT shows comminuted fracture (*arrowhead*) of the dens extending into the body with mild retropulsion of the superior dens into the spinal canal. Marked prevertebral soft tissue swelling is also noted. (**b**) Coronal CT shows the fracture (*arrowhead*) extending into the vertebral body and lateral mass of C2. (**c**) Sagittal MPGR MRI demonstrates fracture through the dens (*arrowhead*) with posterior displacement of the superior dens, spinal stenosis, cord edema (*curved arrow*), contusion, and hemorrhage

Anomalies of Dens

The os terminale is an ossification center at the tip of the dens, which normally fuses by 12 years of age but may remain unfused in adulthood and simulate a type 1 fracture. The os odontoideum formation is debatable as some authors think that it is congenital due to lack of fusion with the base of the dens or post-traumatic fracture of the synchondrosis before closure at age 5–6 years resulting in a large ossicle that is separated from the hypoplastic dens by a wide gap. It may be fixed to the arch of C1 or the clivus and may simulate a nonunited dens fracture or rarely result in atlantoaxial instability [8].

Hangman's Fracture

Bilateral pars interarticularis fracture at C2 is known as hangman's fracture and usually also involves the bilateral neural arches and the pedicles causing traumatic spondylolysis or spondylolisthesis (Fig. 22.8). They have been classified by Effendi and modified by Levine as follows (Table 22.9):

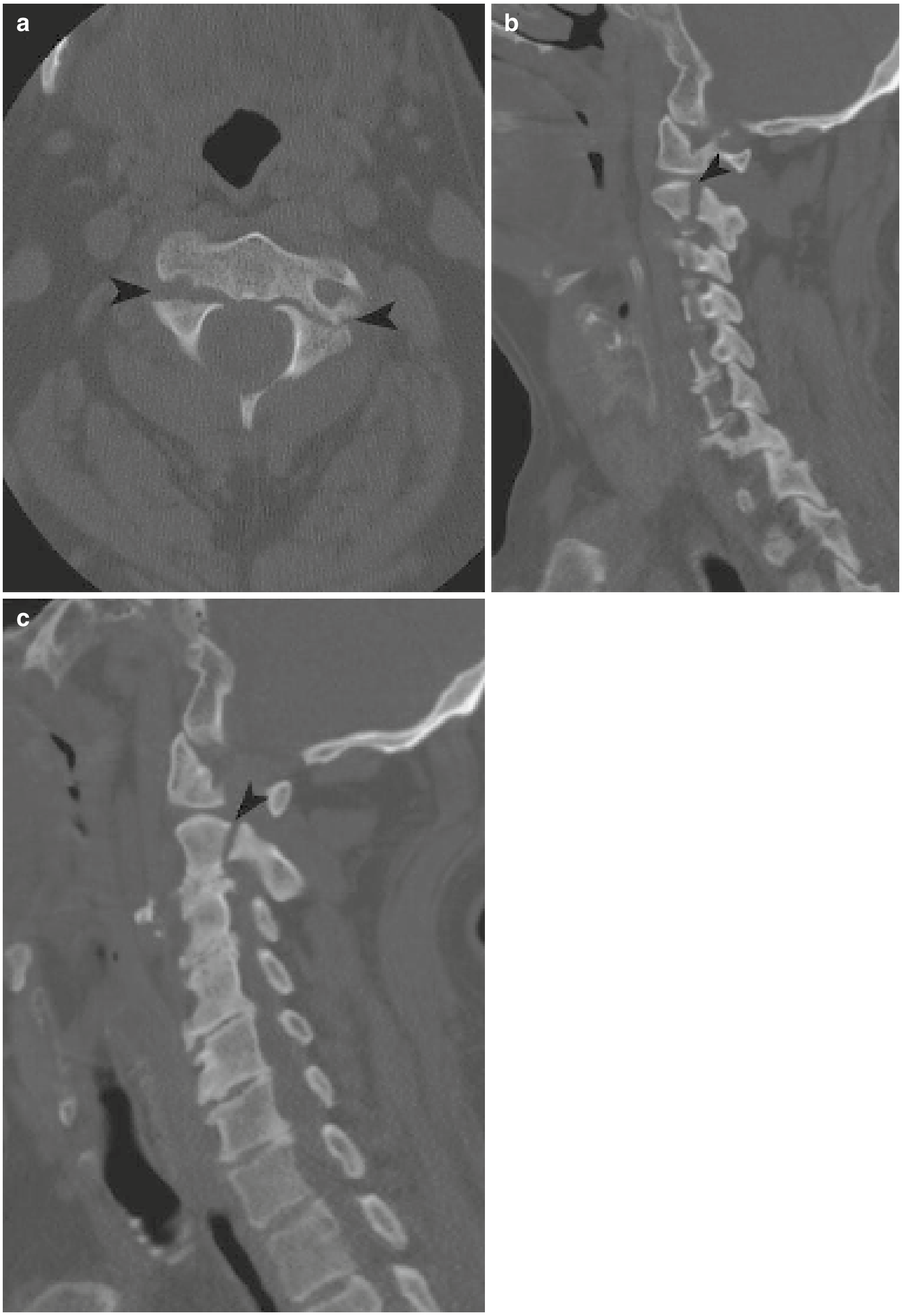

Fig. 22.8 Hangman's fracture. (**a**) Axial CT shows minimally displaced fracture (*arrowheads*) extending through the bilateral pars interarticularis of C2. (**b**, **c**) Parasagittal CT shows vertical fracture (*arrowhead*) through the C2 pars interarticularis

Table 22.9 Hangman's fracture classification

Types	Description
1	Normal C2–C3 disk space and <3 mm anterior translation of C2 on C3
2	Greater than 3 mm anterior translation, C2–C3 disk disruption, angulation of more than 10°, and significant disruption of the posterior longitudinal ligament and slight disruption of the anterior longitudinal ligament
3	Includes all the characteristics of type 2 plus unilateral or bilateral facet dislocation

Atlantoaxial Instability

Atlantoaxial instability can be post-traumatic, congenital, or secondary to rheumatoid arthritis. There is excessive movement at the C1–C2 junction ranging from subluxation to dislocation due to excessive laxity or rupture of the transverse ligament with or without alar and tectorial membrane involvement. Instability can lead to compression of the spinal canal between the dens and posterior arch of C1 or vertebrobasilar artery insufficiency. There is widening of the atlanto-dens interval with asymmetrical distance between the lateral masses of C1 and dens, misalignment of the lateral masses of C1 and C2, and discontinuity of the spinolaminar line. Associated dens fracture is common.

In atlantoaxial rotatory subluxation, there is fixation of the atlantoaxial joint, so that C1–C2 joint moves as a single unit instead of rotating independently [13–15]. Atlantoaxial rotatory subluxation is divided into four subtypes according to Fielding and Hawkins [14] (Table 22.10). Types 3 and 4 are rare but have fatal consequences. Fixed rotatory subluxation is diagnosed if the distance from the dens to the C1 lateral mass on one side is persistently widened on all images compared to the other side when the head is imaged in the neutral, left, and right positions (Fig. 22.9).

Grisel syndrome is a nontraumatic subluxation of the atlantoaxial joint in children. It occurs due to hyperemia and pathologic relaxation of the transverse ligament of the atlantoaxial joint. It is associated with pharyngitis, adenotonsillitis, tonsillar or cervical abscess, and otitis media.

Table 22.10 Types of rotatory fixation

Types	Description
1	Rotatory fixation without anterior displacement of the atlas
2	Rotatory fixation with anterior displacement of the C1 of 3–5 mm. Transverse ligament may be compromised
3	Rotatory fixation with more than 5 mm anterior displacement of C1 lateral masses, one greater than the other. Transverse and alar ligaments are compromised
4	Rotatory fixation with posterior displacement of the lateral masses of C1 on C2

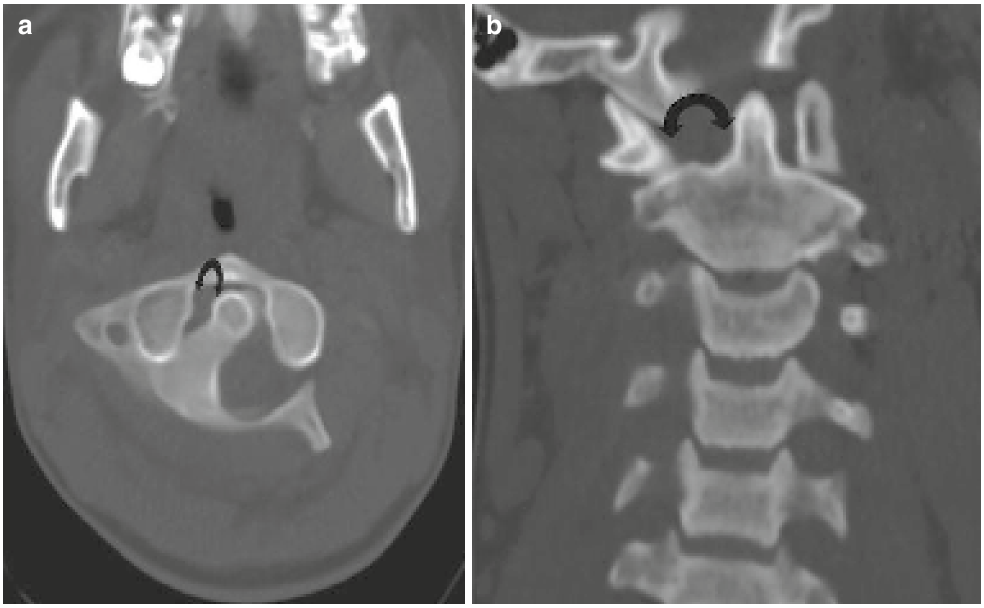

Fig. 22.9 Rotational subluxation. (**a**, **b**) Axial and coronal CT images show asymmetrical fixed widening (*curved arrows*) of the distance between the dens-lateral mass of C1 on the *right* when compared to the *left*. This is consistent with rotational subluxation

Flexion Teardrop Fracture

This is one of the most severe injuries of the cervical spine resulting from severe flexion and compression force injuries [8, 16]. This fracture most commonly occurs at C5–C6 and is characterized by a triangular teardrop fracture at the anterior–inferior aspect of the vertebral body with posterior displacement of the comminuted posterior vertebral body to varying degrees in the spinal canal, kyphosis, anterior subluxation, narrowing of the disk space, widening of the interspinous and interlaminar spaces, and disruption of the ligaments (Fig. 22.10). It can result in anterior cervical cord syndrome (quadriplegia, loss of pain, touch, and temperature with intact vibration, and proprioception).

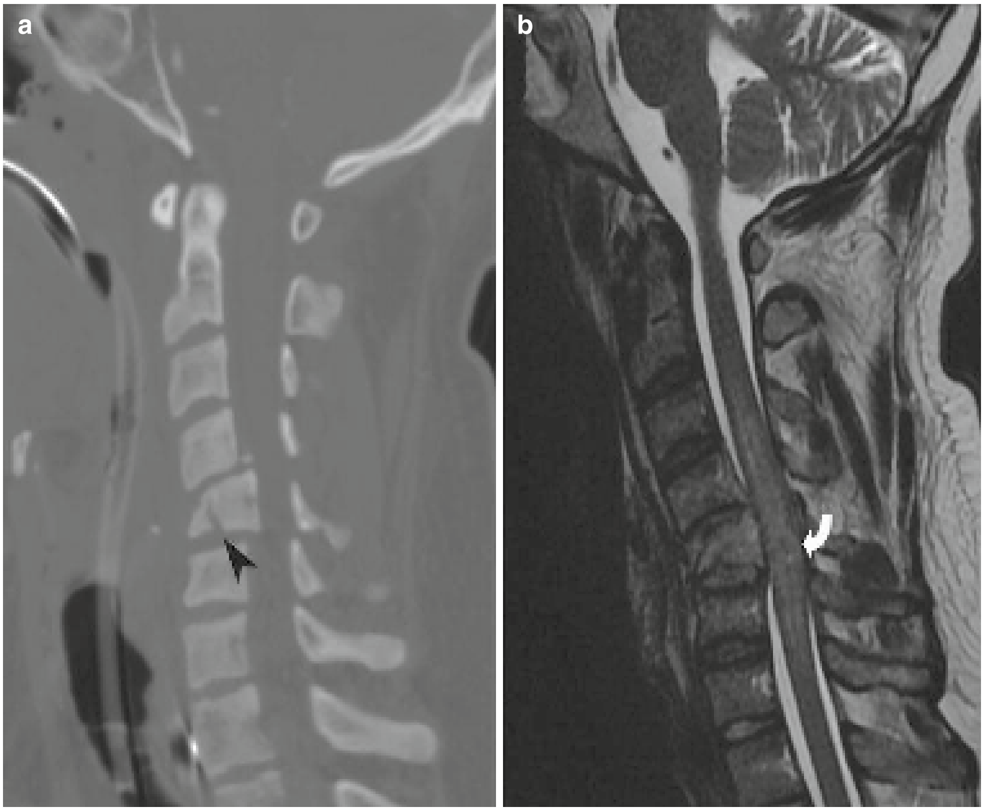

Fig. 22.10 Flexion teardrop fracture of C5. (**a**) Sagittal CT shows teardrop fracture (*arrowhead*) involving the anterior and inferior aspects of the C5 vertebral body with mild retropulsion of the posterior vertebral body into the spinal canal. Note the irregularity of the left posterior/inferior corner of the C4 vertebral body with small adjacent bony fragment (*arrow*) consistent with a small corner fracture. (**b**) Sagittal T2-weighted MRI shows abnormal signal in the spinal cord (*curved arrow*) consistent with edema and hemorrhagic contusion

Facet Dislocation

Unilateral interfacetal dislocation or unilateral locked facet results from flexion-distraction and rotation injury and usually occurs at C4–C5 and C5–C6 levels. It is characterized by focal kyphosis and anterior subluxation by approximately 25% of the vertebral body with the inferior articular facet of the superior vertebral body perched or locked anterior to the superior facet of the inferior vertebral body or in the intervertebral foramen, while the contralateral facet joint on the side of the rotational forces is fixed and acts as the pivot (Fig. 22.11). The spinous processes are malaligned at the level of the injury [13, 17]. There is concomitant injury of the posterior spinous ligamentous complex to varying degrees on the affected side (supraspinous and interspinous ligaments, posterior longitudinal ligament, annulus, ligamentum flavum, and facet joint capsule) and impaction fracture of the facets. Neurological deficits are rare and are of nerve root distribution.

Bilateral interfacetal dislocation results from more severe flexion-distraction injury. The dislocated facet joints may be

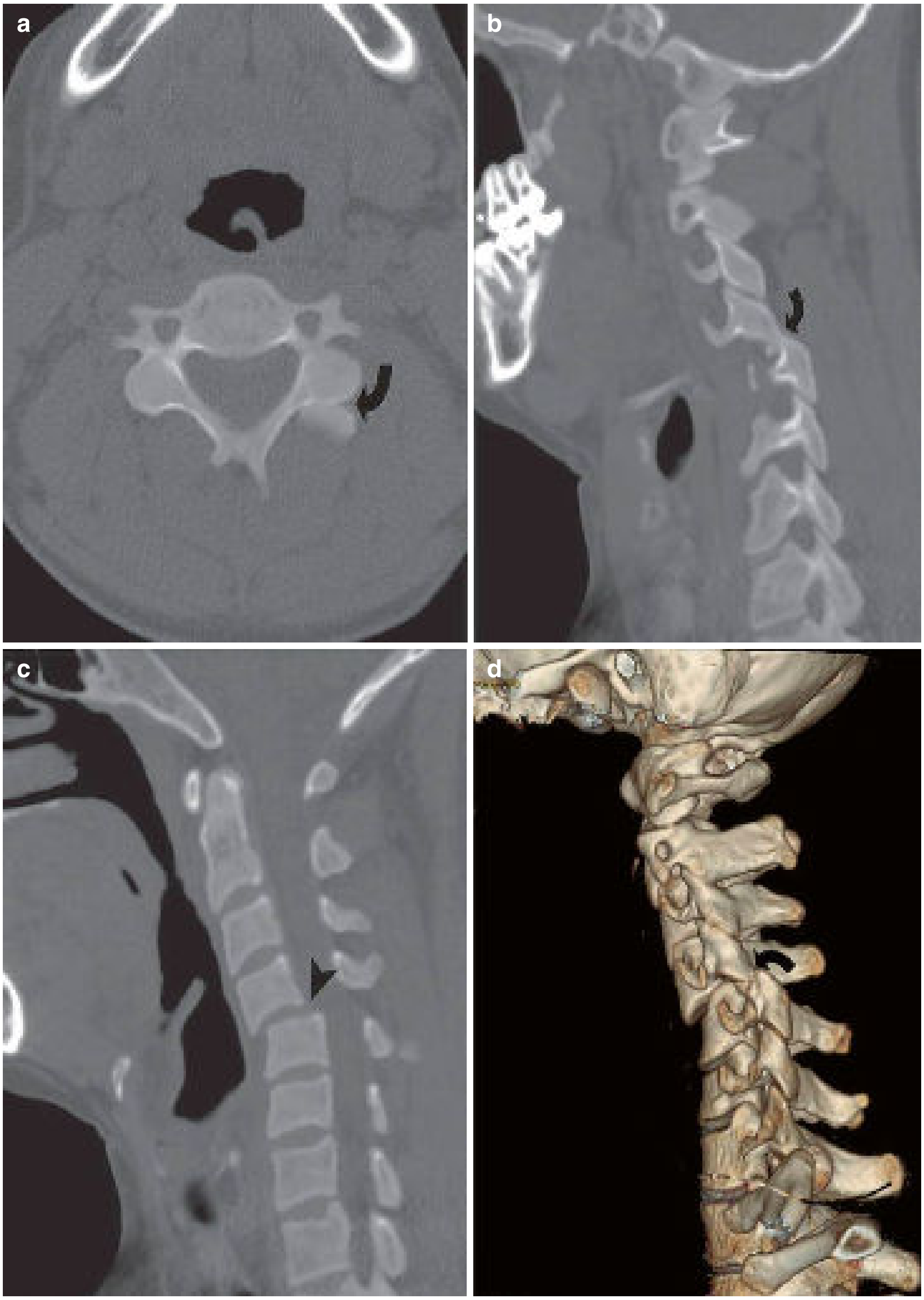

Fig. 22.11 Unilateral facet dislocation. (**a**) Axial CT shows reverse hamburger's bun sign (*curved arrow*); the left inferior articular facet of C4 is dislocated anterior to the superior articular facet of C5. (**b**) Left parasagittal CT shows unilateral left dislocated C4–C5 facets (*curved arrow*). A small fracture fragment in the left C4–C5 interfacet joint space from superior articular process of C5 is also noted. (**c**) Midline sagittal CT shows grade 2 anterolisthesis (*arrowhead*) of C4 on C5. (**d**) Right parasagittal CT shows subluxed right C4–C5 facets (*arrowhead*)

perched or "jump" over one another to become locked. There is subluxation of the vertebral body by more than 50%, and both the anterior and posterior ligamentous structures are disrupted at the site of the injury with fracture of the superior and inferior articular facets and disk extrusion (Fig. 22.12). There is a high degree of neurological deficits with this injury (Table 22.11). The "reverse hamburger bun sign" refers to reversal of the normal articulating facet relationship with the rounded instead of the flat surfaces of the facets facing each other at the site of facet dislocation and the "naked facet sign," which refers to uncovered articulating facet processes with loss of the joint space.

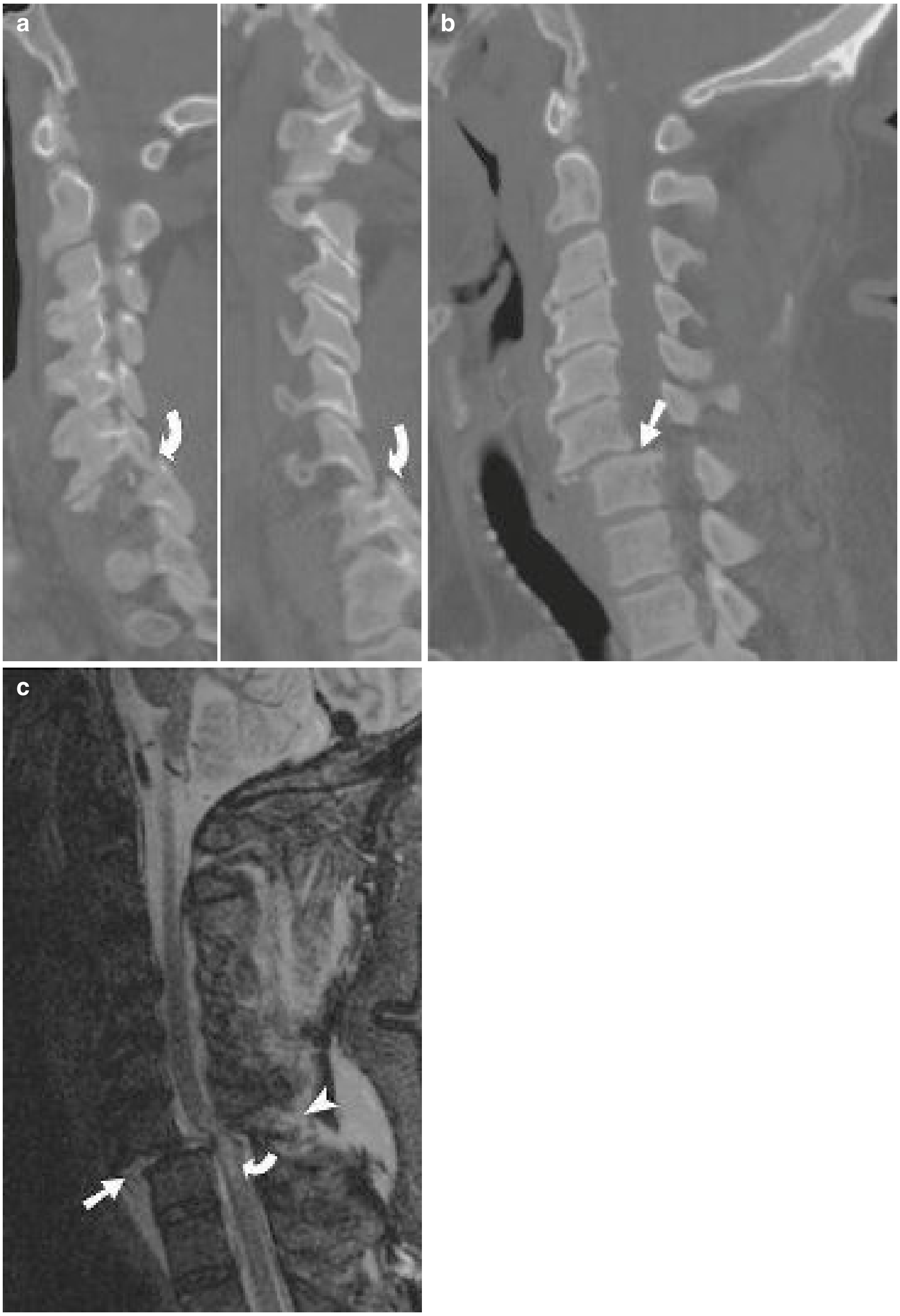

Fig. 22.12 Bilateral facet dislocation. (**a**) Parasagittal right and left CT shows bilateral anteriorly dislocated facets (*curved arrows*) at C6–C7. Note is also made of small bony fractures in the right C6–C7 joint space from inferior and superior articular facets of C6 and C7, respectively. (**b**) Midline sagittal CT shows grade 2 anterolisthesis (*arrow*) of C6 on C7. The small bony fragments (*arrow*) are from the fracture of the inferior end plate of C6. (**c**) Sagittal STIR MRI shows grade 2 anterolisthesis *(straight arrow*) at C6–C7, traumatic disk rupture, severe central canal stenosis, cord compression, and spinal cord compression (*curved arrow*) at this level. There is abnormal T2 hyperintensity consistent with anterior and posterior longitudinal ligaments and interspinous ligament disruption (*arrowhead*)

Table 22.11 Unilateral versus bilateral interfacetal dislocation

Unilateral	Bilateral
Results from flexion-distraction and rotation injury	Results from more severe flexion-distraction injury
Usually at C4–C5 and C5–C6	Dislocated facet joints “jump” over one another
Focal kyphosis and anterior subluxation by 25% of the vertebral body	Subluxation of the vertebral body by more than 50%
Injury of the posterior spinous ligamentous complex	Anterior and posterior ligamentous structures are disrupted
Neurological deficits are rare	High degree of neurological deficits

Clay-Shoveler’s Fracture

This is a stable fracture of the spinous processes of the lower cervical and upper thoracic vertebrae usually C6 to T1 from severe hyperflexion injury. There is sudden strenuous exertion of the paraspinal muscles, mainly the trapezius and rhomboid and the supraspinous ligaments causing avulsion of the spinous process (Fig. 22.13). A less common mechanism of injury is from direct trauma to the spinous process. The fracture is generally considered to be mechanically stable; however, if the fracture line extends to the lamina, there is a potential for spinal cord injuries.

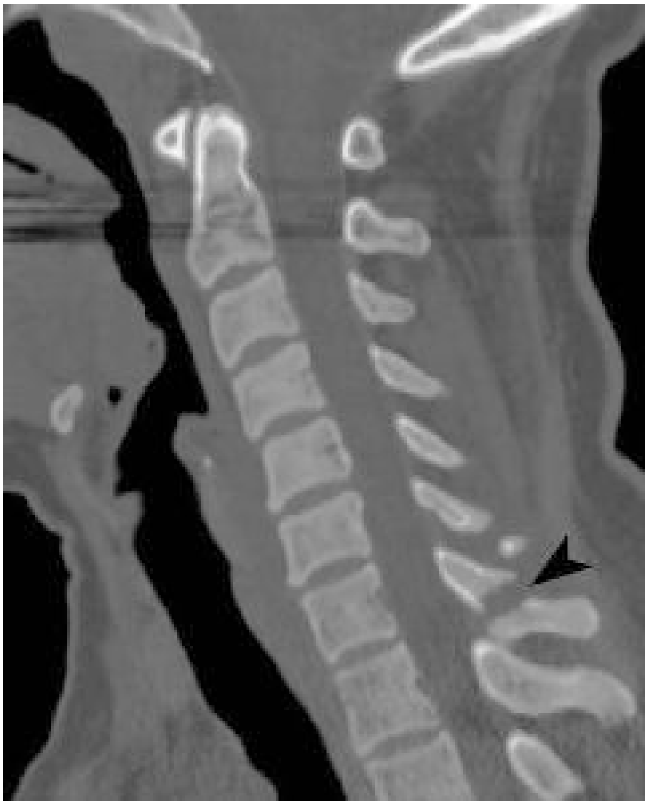

Fig. 22.13 Clay-shoveler’s fracture. Sagittal CT shows displaced fracture (*arrowhead*) involving the posterior spinous processes of C7

Hyperextension Teardrop Fracture and Sprains

There is a corner avulsion fracture of the anteroinferior aspect of the C2 or C3 vertebral body by the anterior longitudinal ligament and tear of the annulus fibrosis from hyperextension injury (Fig. 22.14). Hyperextension sprains are seen in young adults with high-energy trauma, and fracture dislocation occurs in elderly with underlying bone and joint diseases [ankylosing spondylitis, diffuse idiopathic skeletal hyperostosis (DISH), spondylosis, congenital spinal stenosis, and severe degenerative disk disease]. In young adults, the avulsion usually occurs in the lower cervical spine. Hyperextension sprains are soft tissue injuries occurring from blunt trauma to the face with resultant hyperextension of the cervical spine causing injury to the anterior column with intact tear or disruption of the longus colli, longus capitis, anterior longitudinal ligament, anterior annulus, detachment or tear of the intervertebral disk, anterior vertebral plate fracture, ligamentum flavum, and posterior longitudinal ligament [18, 19].

Momentary posterior dislocations may occur and reduce spontaneously but cause central cord syndrome (disproportionate greater neurological motor deficits in the upper extremities than in the lower extremities, variable sensory deficits below the level of the injury, and bladder dysfunction) due to compression of the spinal cord between the posterior vertebral body and ligamentum flavum.

Imaging findings may be subtle and show prevertebral soft tissue swelling, widening of the intervertebral disk space, and small avulsion fracture fragment arising from the anterior aspect of the inferior end plate of the dislocated vertebra (Figs. 22.15 and 22.16). In elderly patients with fracture dislocation, there is posterior displacement of the vertebral body, fracture of the posterior elements, and facet joint disruption. MRI helps depict spinal cord edema and contusion.

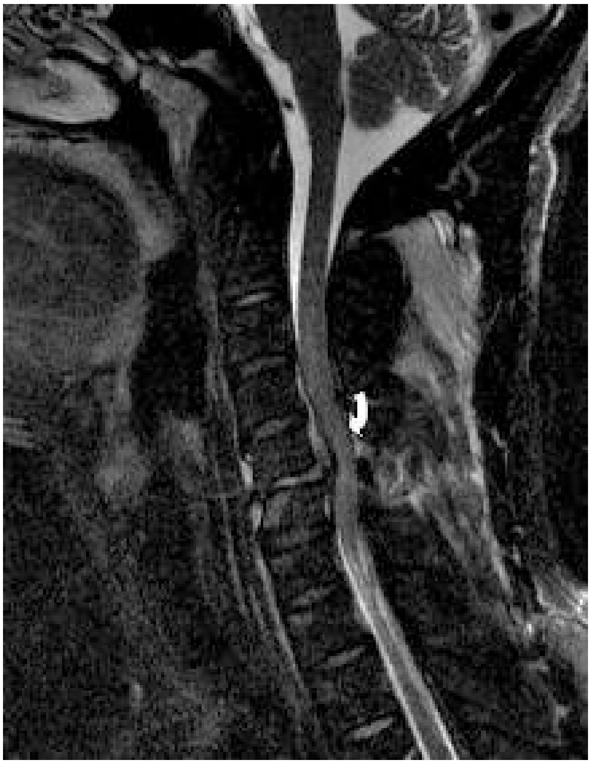

Fig. 22.15 Hyperextension injury. Sagittal T2-weighted FSE MRI shows mild kyphosis and grade 1 anterolisthesis of C5 on C6. Traumatic disk extrusion, severe central canal stenosis at C5–C6, and spinal cord contusion (*curved arrow*) from C4–C7 levels are also seen

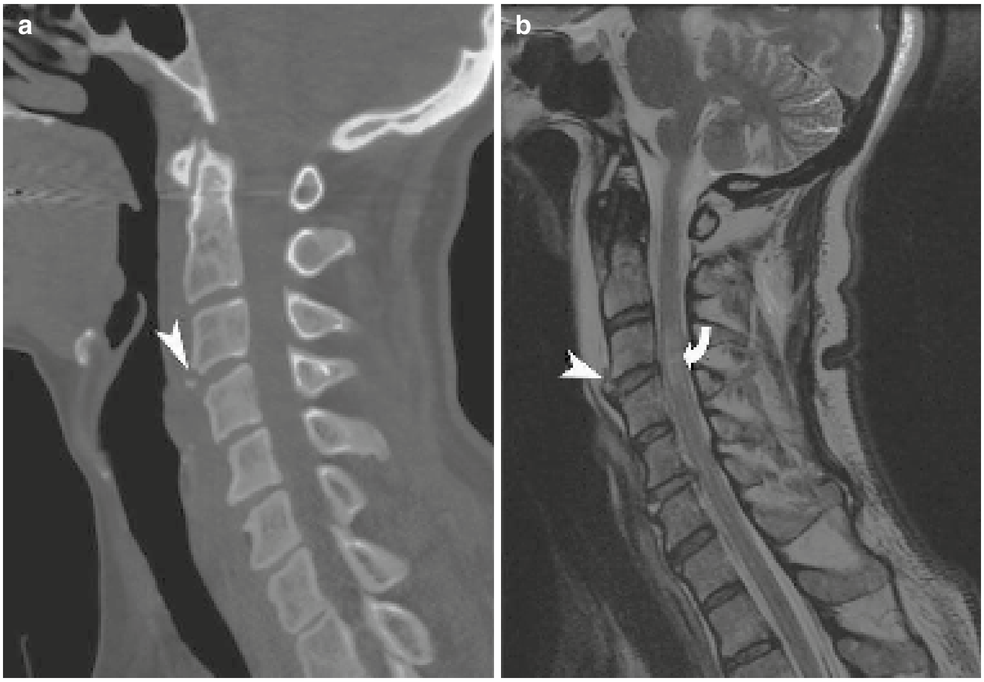

Fig. 22.14 Hyperextension teardrop fracture. (**a**) Sagittal CT reformation shows small displaced teardrop fracture (*arrowhead*) of the anterior and inferior aspects of the C3 vertebral body. (**b**) Sagittal T2 FSE MRI shows teardrop fracture with small tear (*arrowhead*) of the anterior longitudinal ligament and prevertebral edema. Associated spinal cord contusion (*curved arrow*) at the level of C3–C4

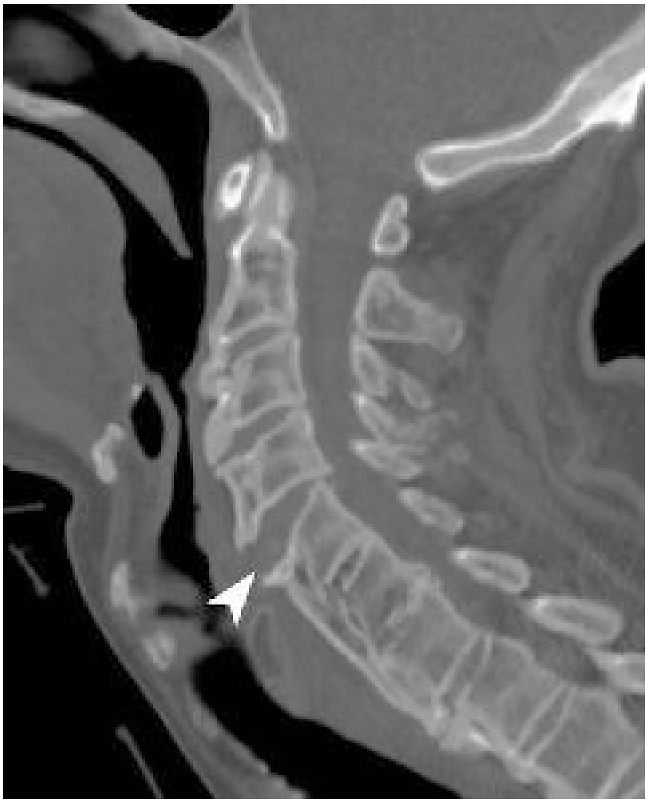

Fig. 22.16 Hyperextension injury in a patient with diffuse idiopathic spinal hyperostosis (DISH). Sagittal CT shows hyperextension injury, indicated by grade 1 retrolisthesis at C4–C5 with fracture through the anterior longitudinal ligament ossification (*arrowhead*) causing asymmetrical C4–C5 disk space widening

Pillar and Laminar Fractures

Pillar fracture is a type of articular facet impaction fracture from the suprajacent articular facet resulting from hyperextension and rotation injuries often extending into the transverse process or the lamina. Pillar fractures are not typically associated with neurologic impairment. However, patients with associated pediculolaminar separation are more likely to have a neurologic injury. Pillar fractures may be associated with instability due to ALL and PLL injuries.

Isolated lamina fractures are rare and are usually associated with other complex fractures and dislocations such as burst fractures, pedicolaminar fracture-separation, and flexion teardrop fracture. They can be further divided into vertical fracture with compression of the vertebral body usually due to axial loading with or without rotation and transverse fractures which are avulsion fractures due to tear of the ligamentum flavum. Isolated laminar fractures are mechanically stable, but neurological sequelae may result from fragments within the cervical spinal canal.

Posterior Arch of C1 Fracture

Isolated fracture of the posterior arch of C1 is due to hyperextension and compressive forces causing compression of the posterior arch of C1 between the occiput and the spinous process of C2. It is considered to be a stable fracture as there is lack of ligamentous involvement.

Wedge and Burst Compression Fracture

Wedge compression fracture is characterized by buckled anterior cortex with loss of the anterior vertebral body height. The posterior cortex and posterior ligaments are intact; therefore, the fracture is considered to be stable [20]. Burst fracture is more common in the thoracolumbar spine but can also occur in the cervical spine and results from axial compression forces. It is characterized by comminuted vertical fracture of the vertebral body with anterior wedging, retropulsion of the bony fragments into spinal canal to varying degrees, and associated fractures of the posterior elements [21].

Thoracic and Lumbar Spine Fractures

Screening for thoracolumbar spine injuries has become easier with the advent of MDCT in polytrauma patients, in whom reformatted images of the thoracic and lumbar spine can be obtained from the chest-abdomen-pelvis scans. Recent data indicates that the reformatted spine images obtained from the body scans have practically replaced plain radiographs as they provide more information and also avoid additional radiation to the patient [2]. Dedicated spine CTs are reserved for cases where concurrent body imaging was not indicated. MRI of the lumbar and thoracic spine is obtained in patients with significant fractures and suspected cord or ligamentous injuries. Since the mechanism of trauma in both the thoracic and lumbar spine is similar, they will be discussed together.

Anterior and Lateral Wedge Compression Fractures

This is a common stable fracture due to axial loading and varying degrees of flexion forces [13]. There is buckling of the anterior cortex with involvement of the superior end plate and/or the inferior end plate causing a wedge-shaped vertebral body. The middle and posterior columns are intact.

These fractures can occur at multiple levels in 20% of the cases and can be further classified based on the Denis system of classification [22], which is based on the involvement of the vertebral plate (Table 22.12).

In lateral wedge compression fractures, the wedge deformity involves the lateral instead of the anterior cortex. They usually occur in the mid-thoracic spine due to lateral flexion forces and are mostly insufficiency fractures.

Table 22.12 Denis system of classification of compression fractures

Types	Description
A	Involves both the superior and inferior end plates
B	Involves only the superior end plate (most common type)
C	Involves only the inferior end plate (rare and usually occurs with pathological fractures)
D	Buckling or wedging of the anterior cortex with sparing of the superior and inferior end plates

Burst Fracture

Burst fractures occur from vertical compression forces resulting in comminuted fracture of the vertebral body [13, 23]. It involves both the superior and inferior vertebral end plates with loss of height and bowing deformity of the posterior cortex or retropulsion of the bony fragments to varying degrees into the spinal canal (Figs. 22.17, 22.18, and 22.19). They may be associated with concomitant facet fractures, and there is a high risk of neurological deficits. There may be associated bilateral calcaneal fractures due to mechanism of the injury; therefore, in patients with bilateral calcaneal fractures, the thoracic and lumbar spines need to be imaged for additional fractures.

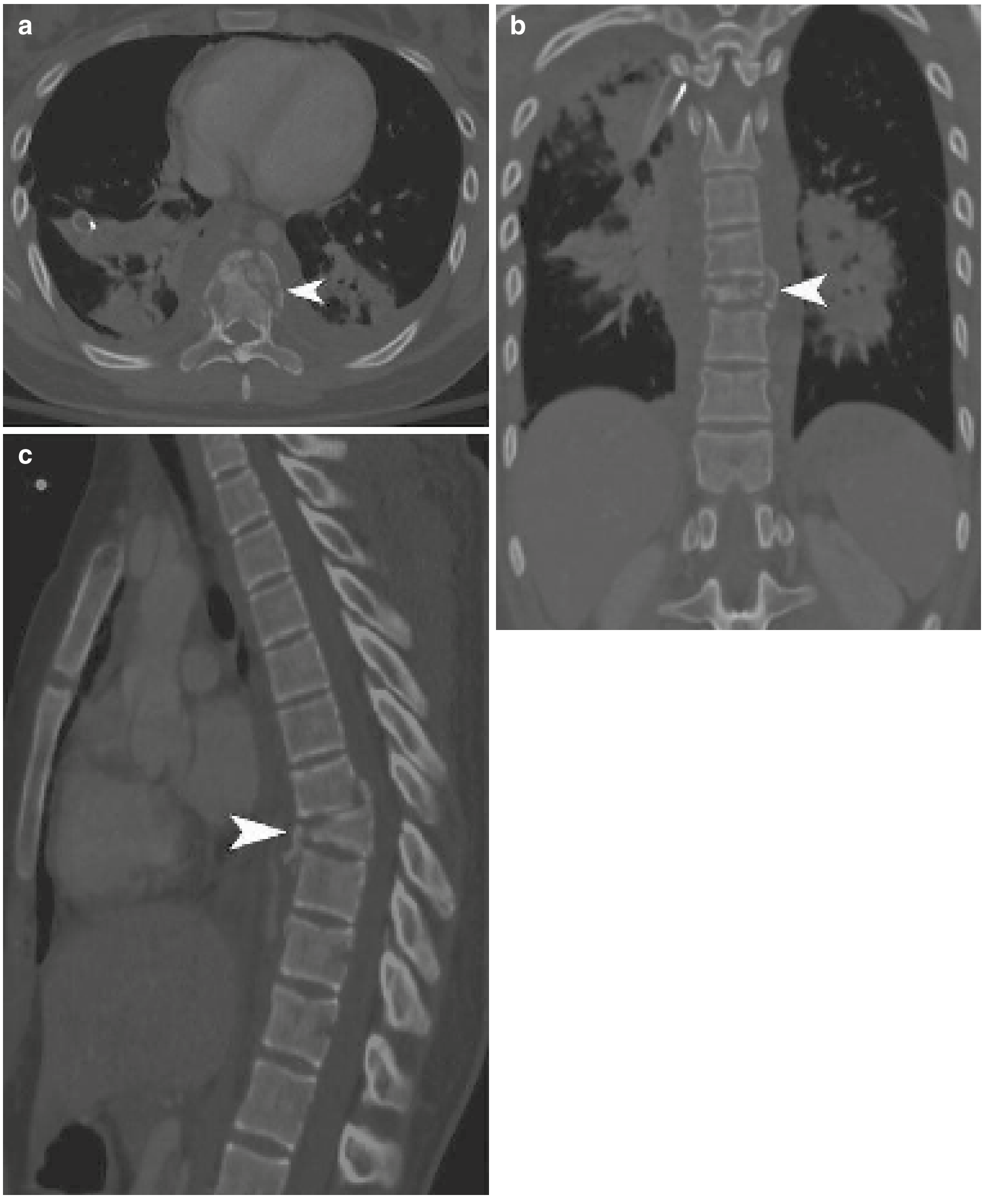

Fig. 22.17 Burst fracture with paraspinal hematoma. (**a**) Axial CT shows bilateral paraspinal hematoma adjacent to the T6 burst fracture (*arrowhead*). There are bilateral lower lobe pulmonary contusions. (**b**, **c**) Coronal and sagittal CT shows diffuse bilateral paraspinal hematoma due to burst fracture of T6 vertebral body (*arrowhead*). There is also fracture of the posteroinferior aspect of T5 vertebral body

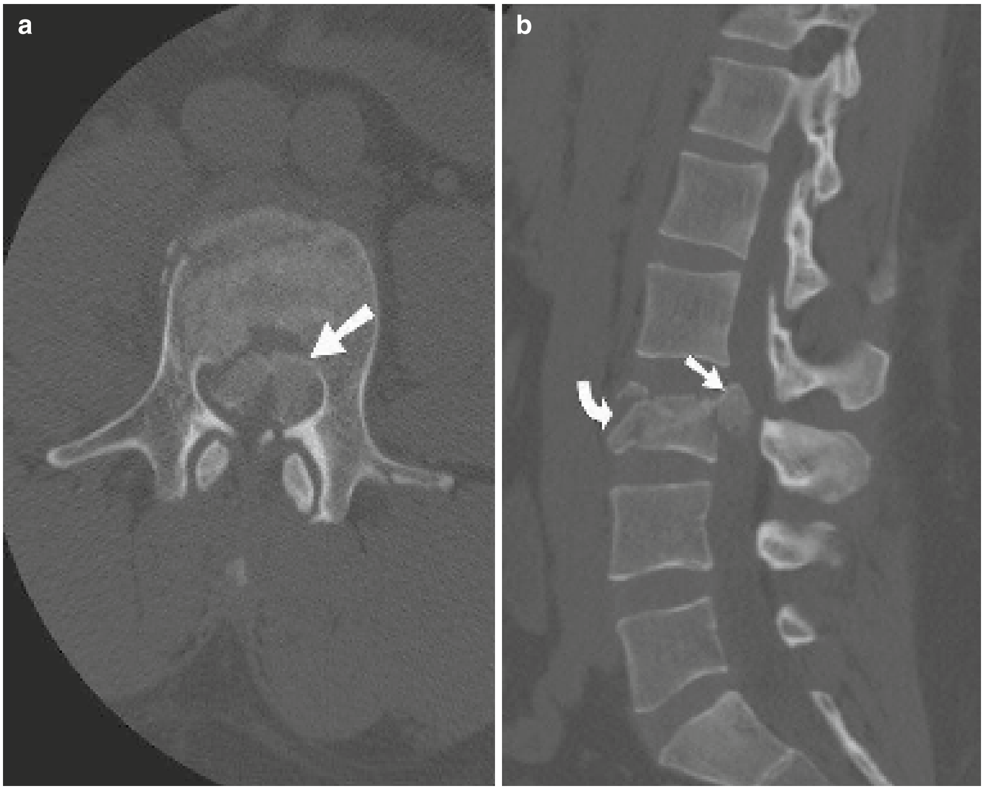

Fig. 22.18 Burst fracture. (**a**) Axial CT shows burst fracture of the L3 vertebral body with retropulsion of multiple bony fragments (*straight arrow*) into the spinal canal, causing severe spinal stenosis. (**b**) Sagittal CT shows similar findings of the L3 burst compression fracture (*curved arrow*) with significant loss of height and retropulsion (*straight arrow*)

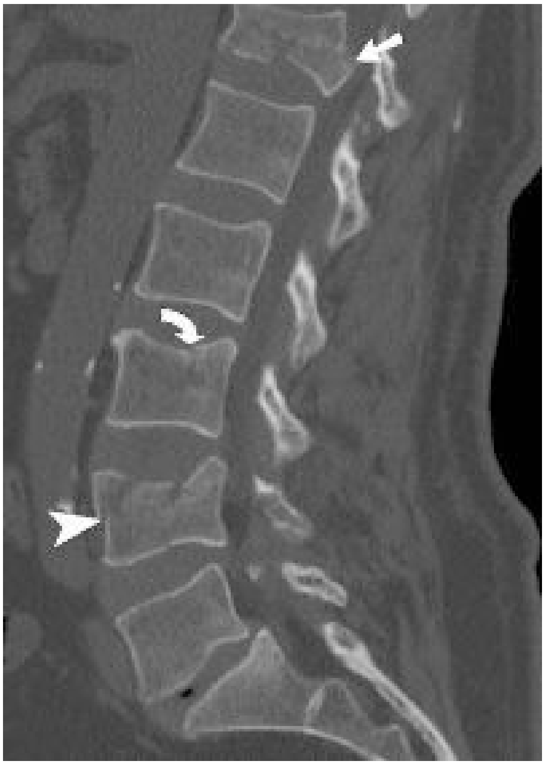

Fig. 22.19 Multiple vertebral body fractures. Sagittal CT shows burst fracture of T12 with retropulsion of the bony fragment (*straight arrow*) into the spinal canal. There is also superior end plate fracture of the L3 (*curved arrow*) and compression fracture of L4 vertebral bodies (*arrowhead*)

Chance Fracture

This is unstable horizontal fracture due to flexion-distraction impaction type of injury causing compression of the anterior vertebral body and distraction of the middle and posterior columns due to failure in tension of all the three columns (Fig. 22.20). The classic Chance fracture from seat belt trauma extends through the spinous process, lamina, pedicles, intervertebral disk space, posterior portion of the vertebral body or anterior wedging of the vertebral body and complex ligamentous involvement of the interspinous and supraspinous ligaments, posterior longitudinal ligament, posterior annulus, facet capsule, ligamentum flavum, and thoracodorsal fascia [13]. Fractures occur at the thoracolumbar junction or in the upper lumbar spine (T10 to L2). Neurological deficits depend on the severity of the fracture, but associated abdominal injuries (pancreatic, duodenal injuries) are common.

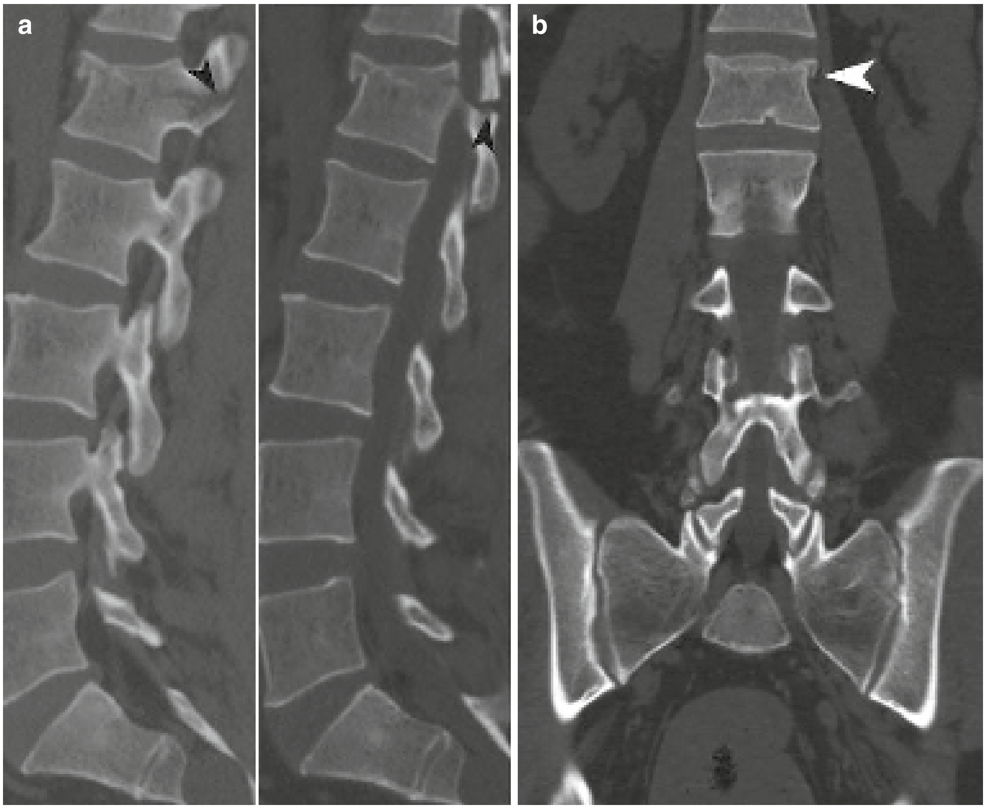

Fig. 22.20 Chance fracture. (**a**) Parasagittal CT reformations show the horizontal fracture of the L1 vertebral body extending through the posterior arch (*arrowheads*). (**b**) Coronal CT shows the horizontal fracture (*arrowhead*) through the L1 vertebral body

Other Miscellaneous Fractures

Fracture dislocations can occur from shearing distraction injuries or severe hyperflexion or hyperextension forces. They are characterized by ligamentous injuries with facet dislocation or posterior element involvement depending on the mechanism [24]. These are unstable fractures with associated severe neurological deficits, dural tears, and abdominal injuries.

Transverse process and spinous process fractures can occur in isolation or in association with other fractures and typically occur at multiple levels. They are stable fractures; however, depending on the mechanism of injury, there may be associated trauma to the thoracic, abdominal, or pelvic structures.

Spine MRI

Ligamentous Injury

MRI of the spine is useful for imaging of the ligamentous structures such as the anterior and posterior longitudinal ligaments, interspinous and supraspinous ligaments, and ligamentum flavum. Ligamentous injuries are usually depicted as discontinuity or tears of the anterior or posterior longitudinal ligaments with or without associated hematoma [25]. Diffuse prevertebral soft tissue swelling or hematoma may be seen with disruption of the anterior longitudinal ligament (Fig. 22.14).

Traumatic Disk Herniation

This usually involves the cervical and thoracic spine and can occur in isolation or in association with fractures, which is more common. MRI findings are characterized by intervertebral disk hemorrhage or edema, end plate avulsions, narrowing or asymmetrical widening of the intervertebral disk space, tear of the annulus fibrosus, and disk herniations [26]. There is a high association of traumatic disk herniation with facet subluxation or dislocation, and therefore, preoperative MRI is recommended before facet reduction is attempted (Figs. 22.12 and 22.15).

Epidural Hematoma

Spinal epidural hematomas are extra-axial extradural in location and occur spontaneously or due to trauma. The source of hemorrhage is unclear but may originate from the epidural venous plexus, arterial origin, or vascular malformations. MRI is the modality of choice for evaluating the extent of the spinal epidural hematoma and the degree of cord compres-

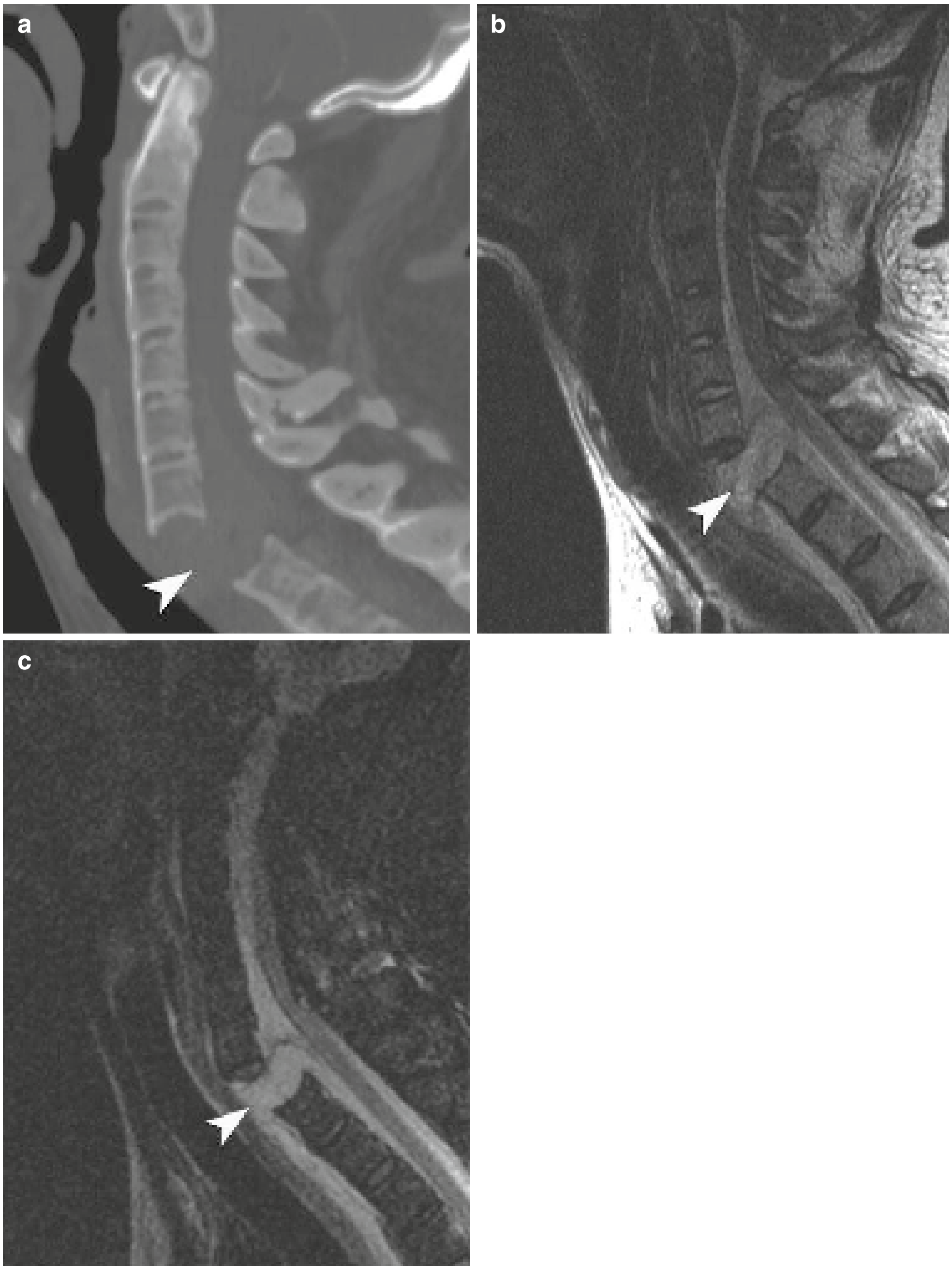

Fig. 22.21 Fracture distraction at C7–T1. (**a**) Sagittal CT shows complete fracture distraction injury at C7–T1 with distraction and anterior displacement of the superior cervical vertebral column (*arrowhead*). Bridging syndesmophytes are seen at all levels, consistent with ankylosing spondylitis. (**b**, **c**) Sagittal T2 FSE and sagittal T2 STIR MRI images in addition show large intervertebral (*arrowhead*) and epidural hematoma, causing central canal stenosis and cord compression from the C6 to the T1 vertebral level

sion (Fig. 22.21). The characteristic findings on the MRI depend on the age of the hemorrhage and vary accordingly on the T1- and T2-weighted images.

Spinal Cord Trauma

Spinal cord injury can result from direct or indirect trauma to the spinal cord. In patients with preexisting conditions such as spinal stenosis, ankylosing spondylitis, or rheumatoid arthritis, even minor trauma to the spine can lead to injury. MRI is the imaging method of choice when SCI is suspected. These findings may vary across intraspinal hematoma, cord edema, or contusion. Cord compression can result from epidural hematoma, traumatic disk herniation, or retropulsion of the bony fragments into the spinal canal. Spinal cord transection is rare. In acute cases, blood products are isointense to hyperintense on T1 and hypointense on T2 weighted due to deoxyhemoglobin and become hyperintense on T1 and T2 sequences, when the deoxyhemoglobin evolves into methemoglobin. Spinal cord edema is manifested as hyperintensity on T2-weighted sequences, and cord swelling is seen as abnormal focal expansion of the cord, best seen on T1-weighted sequences [3]. Spinal cord transection occurs from facet dislocations and shearing injuries and is seen as cord discontinuity or disruption on MRI. Diffusion-weighted MRI has recently been implemented in some centers to evaluate for spinal cord ischemia and the extent of axonal loss after spinal injury.

The term SCIWORA (spinal cord injury without radiological abnormality) is being used less commonly with the advent of MRI, which aids in the identification of spinal cord, soft tissue, and ligamentous injuries, and so has now become a diagnosis of exclusion. The overall prognosis of patients with SCIWORA without any imaging findings is better than in patients with positive findings.

Teaching Points

- Imaging of a wide variety of spinal fractures is now possible with the use of multidetector CT and MR imaging, which has essentially replaced radiography.
- Cross-sectional imaging is also more sensitive, accurate, and cost-effective in the long run.
- Current imaging guidelines recommend the use of CT for the initial assessment of suspected spine injury.
- MRI can be reserved for soft tissue and spinal cord injuries.
- This may decrease the incidence of missed injuries and aid in early diagnosis and management of spinal trauma.

Questions

1. Which of the following statements is correct?
   (A) Unilateral interfacetal dislocation is usually associated with neurological deficits
   (B) Clay-shoveler's fracture commonly involves C3–C5
   (C) In flexion teardrop fracture, vibration and proprioception senses are usually intact
   (D) Type 1 of atlantoaxial rotatory subluxation involves anterior displacement of atlas
   Answer: C

2. Which of the following fractures is the result of flexion mechanism?
   (A) Wedge compression
   (B) Hangman
   (C) Pillar
   (D) Jefferson
   Answer: A

3. Which of the Following Measures Is Acceptable in Cervical Spine Lines and Spaces?
   (A) Basion axial interval >14 mm
   (B) Intervertebral angulation >10°
   (C) Prevertebral space >8 mm at C2
   (D) Predental space <5 mm in children
   Answer: D

4. Which of the Following Abnormalities Is Depicted in the Following Noncontrast CT (Fig. 22.22)?
   (A) Facet fracture
   (B) Perched facet
   (C) Neural foramina stenosis
   (D) Clay-shoveler's fracture
   Answer: B

5. What Is the Imaging Diagnosis of the Following Noncontrast Cervical Spine CT (Fig. 22.23)?
   (A) Atlanto-occipital dislocation
   (B) Occipital condyle fracture
   (C) Jefferson fracture
   (D) Dens fracture
   Answer: A

6. Which of the Following Pathologies Is Depicted in the Following Sagittal Cervical Spine CT (Fig. 22.24)?
   (A) Atlanto-occipital dislocation
   (B) C5–C6 interfacet dislocation
   (C) Occipital condyle fracture
   (D) Jefferson fracture
   Answer: B

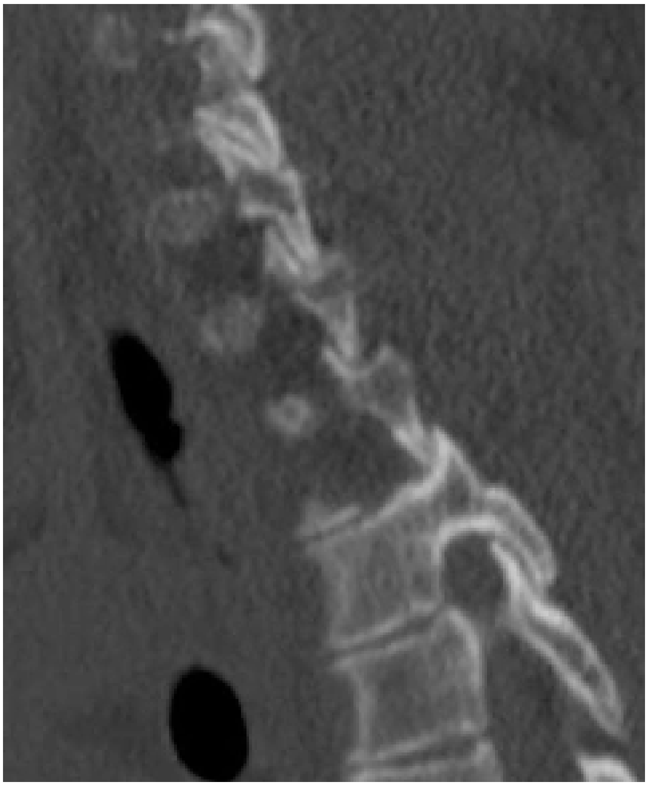

Fig. 22.22 Noncontrast CT

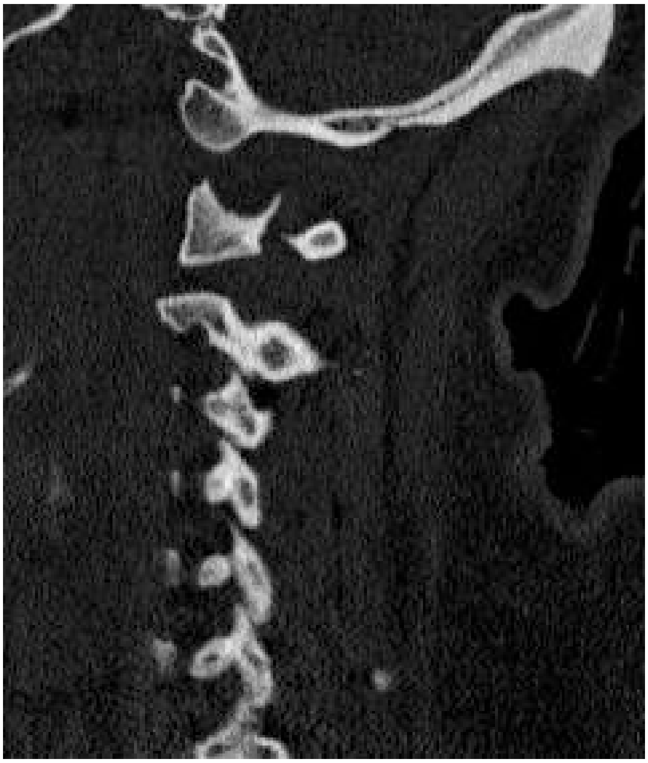

Fig. 22.23 Noncontrast cervical spine CT

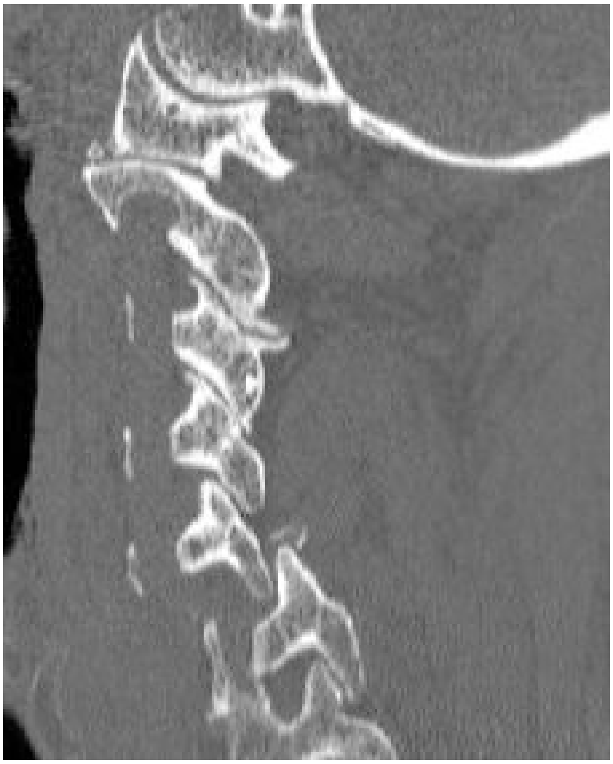

Fig. 22.24 Sagittal cervical spine CT

7. In the CT and MRI depicted below (Fig. 22.25a, b), which of the following is the most probable mechanism of injury?
   (A) Hyperflexion and compression
   (B) Anterior compression
   (C) Hyperextension with distraction
   (D) Rotation and impaction
   Answer: C

8. What Is the Imaging Diagnosis on the CT Depicted below (Fig. 22.26)?
   (A) Hyperextension fracture of thoracic spine
   (B) Burst fracture of thoracic spine
   (C) Fracture of spinous process in the thoracic spine
   (D) None of the above
   Answer: A

9. Which pathology is depicted in the following cervical spine CT (Fig. 22.27)?
   (A) Facet fracture
   (B) Jumped facet
   (C) Neural foramina stenosis
   (D) Clay-shoveler's fracture
   Answer: B

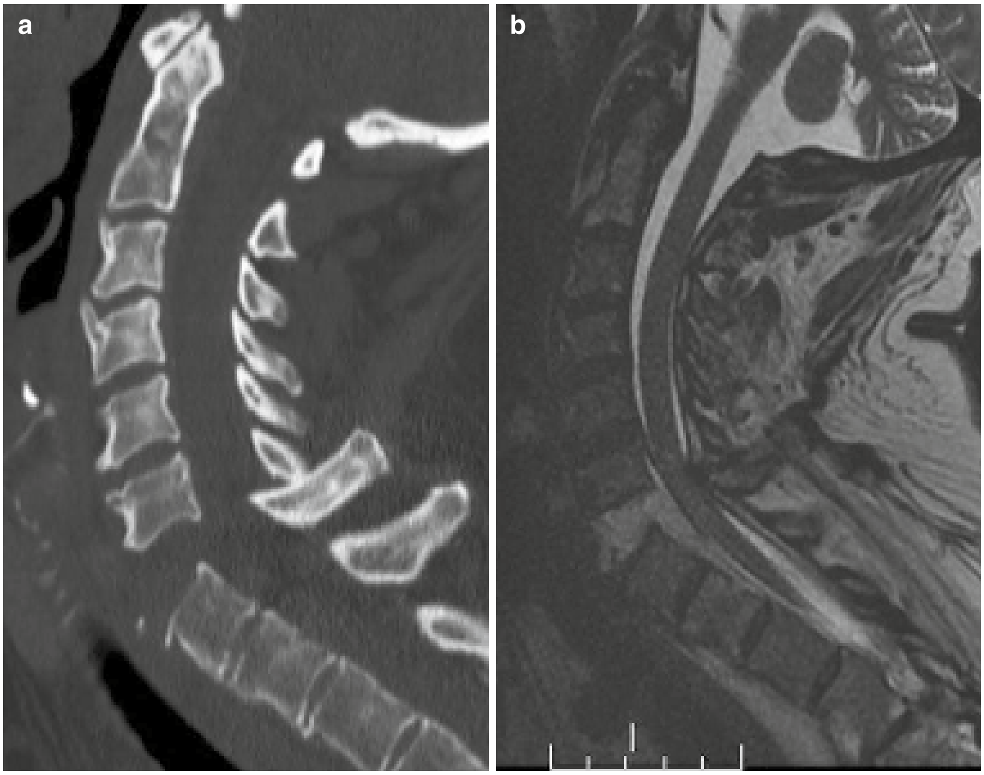

Fig. 22.25 (**a**) CT and (**b**) MRI depicted—Hyperextension with distraction

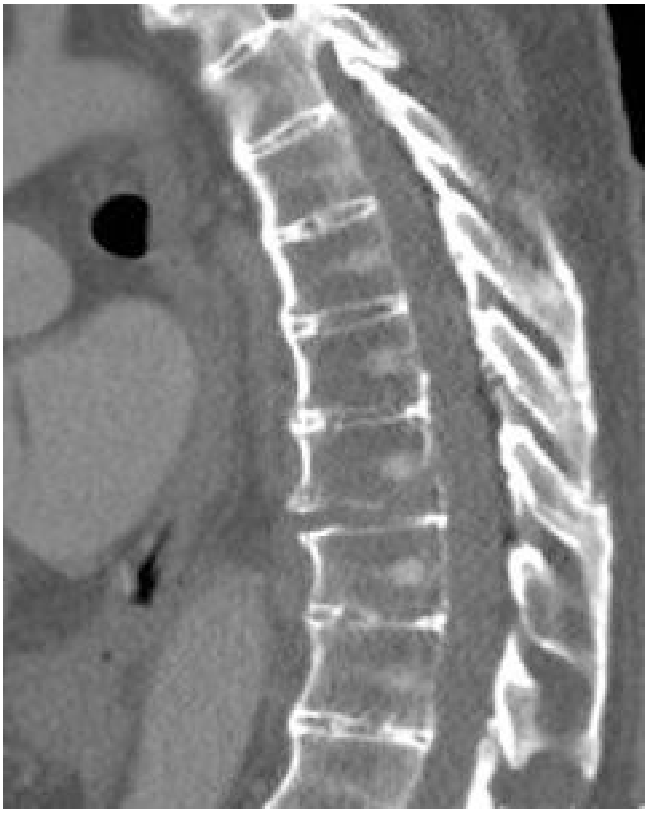

Fig. 22.26 Hyperextension fracture of thoracic spine

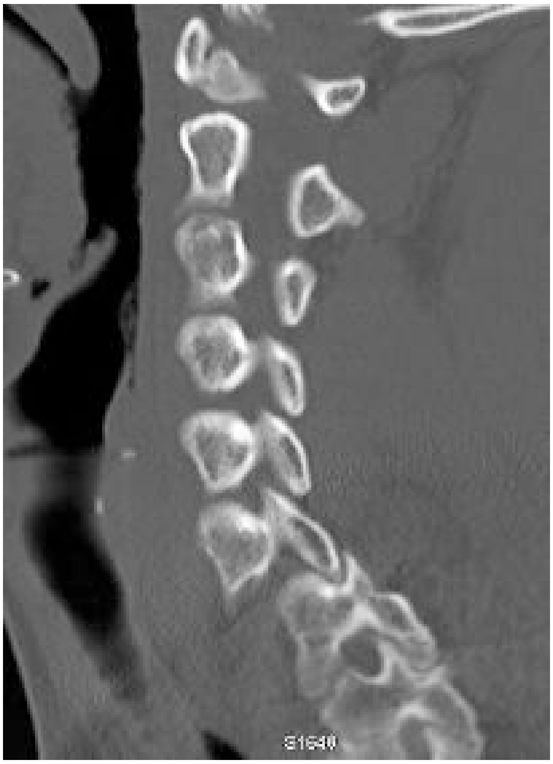

Fig. 22.27 Cervical spine CT

References

1. National Spinal Cord Injury Statistical Center. Spinal cord injury: facts and figures at a glance. www.spinalcord.uab.edu. Accessed 1 Mar 2011.
2. Daffner RH, Hackney DB. ACR appropriateness criteria on suspected spine trauma. J Am Coll Radiol. 2007;4(11):762–75. https://doi.org/10.1016/j.jacr.2007.08.006.
3. Looby S, Flanders A. Spine trauma. Radiol Clin North Am. 2011;49(1):129–60.
4. Hoffman JR, Mower WR, Wolfson AB, Todd KH, Zucker MI. Validity of a set of clinical criteria to rule out injury to the cervical spine in patients with blunt trauma. National Emergency X-Radiography Utilization Study Group. N Engl J Med. 2000;343(2):94–9. https://doi.org/10.1056/NEJM200007133430203.
5. Stiell IG, Clement CM, Wells GA, Vandemheen KL, Clement CM, Lesiuk H, et al. The Canadian C-spine rule for radiography in alert and stable trauma patients. JAMA. 2001;286(15):1841–8. https://doi.org/10.1001/jama.286.15.1841.
6. Lange BB, Penkar P, Binder WD, Novelline RA. Are cervical spine radiograph examinations useful in patients with low clinical suspicion of cervical spine fracture? An experience with 254 cases. Emerg Radiol. 2010;17:191–3. https://doi.org/10.1007/s10140-009-0830-x.
7. Nunez DB, Ahmad AA, Coin CG, Leblang S, Becerra JL, Henry R, et al. Clearing the cervical spine in multiple trauma victims: a time-effective protocol using helical computed tomography. Emerg Radiol. 1994;1(6):273–8. https://doi.org/10.1007/BF02614949.
8. Blackmore CC, Ramsey SD, Mann FA, Deyo RA. Cervical spine screening with CT in trauma patients: a cost effectiveness analysis. Radiology. 1999;212(1):117–25.
9. Holmes JF, Akkinepalli R. Computed tomography versus plain radiography to screen for cervical spine injury: a meta-analysis. J Trauma. 2005;58(5):902–5. https://doi.org/10.1097/01.TA.0000162138.36519.2A.
10. Vandemark RM. Radiology of the cervical spine in trauma patients: practice pitfalls and recommendations for improving efficiency and communication. AJR Am J Roentgenol. 1990;155:465–72.
11. Weissledder R, Wittenberg J, Harisinghani MG. Primer of diagnostic imaging. Philadelphia: Mosby; 2002. p. 370–8.
12. Manaster BJ, May DA, Disler DG. The requisites, musculoskeletal imaging. Spine trauma. Amsterdam: Elsevier Health Sciences; 2002. p. 164–77.
13. Wheeless CR III, Nunley JA II, Urbaniak JR, Nasca R, Fitch B, Furey C, Musante D, Urquia D. Wheeless' textbook of orthopaedics http://www.wheelessonline.com/. Accessed Mar 2011.
14. Fielding JW, Hawkins RJ. Atlanto-axial rotatory fixation. (Fixed rotatory subluxation of the atlanto-axial joint). J Bone Joint Surg Am. 1977;59:37–44.
15. Mirvis SE, Shanmuganathan K. Imaging of trauma and critical care, imaging of cervical spinal trauma. 2nd ed. New South Wales: Saunders; 2003. p. 185–289.
16. Kim KS, Chen HH, Russel EJ, Rogers LF. Flexion tear drop fracture of the cervical spine. AJR Am J Roentgenol. 1989;152:319–26. https://doi.org/10.2214/ajr.152.2.319.
17. Boyarsky I, Godorov G, Mueller B, Keenan MAE. Fractures of the cervical spine eMedicine article 1267150. Updated 20 Oct 2009.
18. Schwartz ED, Flanders AE. Spinal trauma: imaging, diagnosis, and management. Philadelphia: Lippincott Williams & Wilkins; 2006. p. 130–5.
19. Rao SK, Wasyliw C, Nunez DB Jr. Spectrum of imaging findings in hyperextension injuries of the neck. Radiographics. 2005;25:1239–54.
20. Johan OO. Cervical trauma. In: van Goethem WM, vanden Hauwe L, Parizel PM, editors. Spinal imaging: diagnostic imaging of the spine and spinal cord. New York: Springer; 2007. p. 302.
21. Bohndorf K, Imhof H, Pope TL. Musculoskeletal imaging: a concise multimodality approach. New York: Stuttgart; 2001. p. 48.
22. Denis F. The three column spine and its significance in the classification of acute thoracolumbar spinal injuries. Spine. 1983;8(8):817–31.
23. Bernstein MP, Mirvis SE, Shanmuganathan K. Chance-type fractures of the thoracolumbar spine: imaging analysis in 53 patients. AJR Am J Roentgenol. 2006;187:859–68.
24. Holdsworth F. Fractures, dislocations and fracture dislocations of the spine. J Bone Joint Surg Am. 1970;52:1534–51.
25. Schaefer DM, Flanders A, Northrup BE, Doan HT, Osterholm JL. Magnetic resonance imaging of acute cervical spine trauma. Correlation with severity of neurologic injury. Spine. 1989;14:1090–5.
26. Levitt MA, Flanders AE. Diagnostic capabilities of magnetic resonance imaging and computed tomography in acute cervical spinal column injury. Am J Emerg Med. 1991;9:131–5.
27. Stiell IG, Clement CM, McKnight RD, Brison R, Schull MJ, Rowe BH, et al. The Canadian C-spine rule versus the NEXUS low-risk criteria in patients with trauma. N Engl J Med. 2003;349:2510.

Imaging of Nontraumatic Mediastinal and Pulmonary Processes

23

Brett W. Carter, Victorine V. Muse,
and Mohammad Mansouri

Introduction

Thoracic complaints including cough, shortness of breath, and pleuritic chest pain are common but nonspecific presenting symptoms in the emergency department, and as many as 5% of visits are due to acute chest pain. Acute chest pain in the absence of trauma remains a diagnostic challenge because of extensive etiology that ranges from benign to potentially lethal. After cardiac and aortic etiologies are ruled out, three main categories of disease origin should be considered: mediastinum (including pulmonary vasculature only), lung, and pleura. Nontraumatic, noncardiac mediastinal processes which can present with chest symptoms include, but are not limited to, pulmonary embolism (technically lung but will be considered with mediastinum), esophageal perforation, mediastinitis, and abscess. Pulmonary pathology also tends to affect the pleural space, so these two categories will be considered together. Pneumonia and pulmonary edema are the most common pulmonary diagnoses in the emergency room. It is equally important to delineate any associated complications including pulmonary abscess and empyema. Pneumothorax can also be nontraumatic in etiology and present with acute thoracic symptoms.

Imaging

Although accurate clinical history and physical examination are essential, diagnostic imaging continues to be indispensable in helping to navigate nonspecific thoracic signs and symptoms and reach a more refined assessment (Table 23.1).

Table 23.1 Summary of imaging modalities in pulmonary and mediastinal evaluation

Modality	Description
CXR	Obtain PA and lateral
	Limited sensitivity and specificity
	Quickly evaluates emergencies
CT	Contrast-enhanced CT for mediastinal and vascular structures
	Contrast-enhanced CT helps separate pleural and parenchymal pathologies
MRI	DWI can characterize lung cancer, lymph nodes, and metastases
	Perfusion scan can be used in vascular and airway diseases. It can also predict postsurgical lung function in cancer
Ultrasound	Useful in delineating the pleural space
	Assist in guidance for procedures

B. W. Carter
Department of Diagnostic Radiology, The University of Texas MD Anderson Cancer Center, Houston, TX, USA
e-mail: bcarter2@mdanderson.org

V. V. Muse (✉)
Division of Thoracic Imaging, Department of Radiology, Harvard Medical School, Massachusetts General Hospital,
Boston, MA, USA
e-mail: vmuse@mgh.harvard.edu

M. Mansouri
Department of Radiology, Massachusetts General Hospital,
Boston, MA, USA

© The Author(s), under exclusive license to Springer Nature Switzerland AG 2024
A. Singh (ed.), *Emergency Radiology*, https://doi.org/10.1007/978-3-031-65770-2_23

Chest Radiograph

The first radiological examination obtained on a patient with chest symptoms should be a good quality PA and lateral chest radiograph. Portable technique should be reserved for only those patients who are truly obtunded or too critical to transport to the radiology department. While a CXR is limited in its sensitivity and specificity, it is the most efficient way to quickly evaluate the patient and be able to categorize the management as a surgical issue which may need to be imminently addressed such as a pneumothorax or a non-life-threatening medical process such as pneumonia. Correlation with the patient's clinical history, immune status, and comorbidities is critical to the proper interpretation of the film.

Chest CT Scan

Chest CT can be helpful to further elucidate subtle findings seen on the chest radiograph. Contrast-enhanced examination should be obtained when possible so that contrast enhancement can better delineate mediastinal and vascular structures and help define and separate pleural and parenchymal processes. Pulmonary embolism protocol is a separate technique and needs to be specifically requested if this diagnosis is a consideration.

MRI

MRI can be a radiation-free alternative to chest CT in assessing the lung and mediastinum. Diffusion-weighted imaging can characterize lung cancer, lymph nodes, and metastases, while perfusion images can be used in vascular diseases such as pulmonary embolism, airway diseases such as cystic fibrosis and chronic obstructive pulmonary disease, and can also predict postsurgical lung function in lung cancer.

Ultrasound

Ultrasound has limited application in the lung and mediastinum but is very useful in delineating the pleural space as to the nature of the contained process. Directed ultrasound can also assist in guidance for diagnostic thoracentesis or drainage catheter placement.

Mediastinum

Pulmonary Embolism

Acute pulmonary embolism (PE) is the third most common cause of cardiovascular death following coronary artery disease and stroke, with an average incidence in the USA of 1 per 1000 persons. Approximately 300,000 patients die from PE each year. The most common signs and symptoms at the time of presentation include dyspnea, pleuritic chest pain, tachypnea, and tachycardia [1]. The classic clinical triad of chest pain, dyspnea, and hemoptysis is only seen in a minority of patients. Common risk factors for PE include acute medial illness, prolonged immobilization, malignancy, and orthopedic surgery.

The chest radiograph is usually the first imaging examination obtained in the evaluation of patients presenting with chest pain and can be used to detect other potential causes of symptoms mimicking PE, including pneumonia, pulmonary edema, and pneumothorax. Several classic radiographic signs of PE have been described, but are infrequently encountered. These include Westermark's sign, which is increased lucency of all or portion of a lung secondary to decreased vascular flow in the setting of obstructive PE. Hampton's hump is a peripheral, wedge-shaped opacity that may represent pulmonary infarction in the setting of PE [2].

Ventilation-perfusion scintigraphy is performed with the intravenous injection and inhalation of radiopharmaceuticals for the purpose of identifying PE. It is most valuable in the setting of a normal chest radiograph, as pulmonary parenchymal disease limits its sensitivity and specificity. The presence of a ventilation-perfusion mismatch, or a defect on the perfusion study only, is suggestive of PE. The Prospective Investigation of Pulmonary Embolism II (PIOPED II) interpretation scheme is used in the reporting of the ventilation-perfusion scan. The diagnostic categories include normal, very low probability, low probability, intermediate probability, and high probability. Many patients have scans between low and high probability and require additional testing for diagnosis [3].

Pulmonary angiography has traditionally been considered the gold standard examination to evaluate for PE. However, multidetector computed tomography (MDCT) with intravenous contrast has now surpassed angiography and is the primary modality utilized for diagnosis of PE in most institutions. Factors contributing to the effectiveness of CT

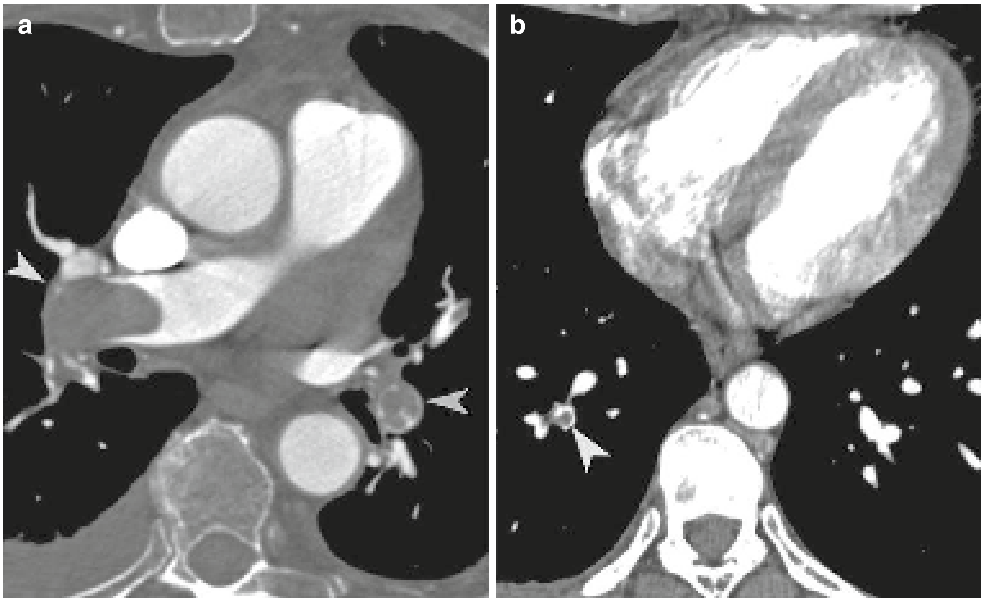

Fig. 23.1 Pulmonary embolism. (**a**, **b**) Axial CT images show filling defects (*arrowheads*) within the right and left pulmonary arteries, as well as segmental pulmonary arterial branch in right lower lobe

over pulmonary angiography include widespread availability and fast scan times. Additionally, ventilation-perfusion scintigraphy and pulmonary angiography do not accurately demonstrate subsegmental PE. In addition to demonstrating PE within the main, lobar, and segmental PE, MDCT is more accurate in identifying PE affecting the subsegmental pulmonary arteries. CT can also evaluate the remainder of the chest for abnormalities such as pneumonia, pulmonary edema, and pneumothorax. The most common finding on contrast-enhanced CT is hypodense filling defects within opacified pulmonary artery branches (Fig. 23.1) [4]. Saddle emboli, or pulmonary emboli bridging the main pulmonary arteries, may be seen. Abrupt vessel cutoff and complete occlusion may be identified. Cardiac dysfunction in the setting of massive acute PE may manifest as enlargement of the right atrium and ventricle, straightening of the interventricular septum, or bowing of the interventricular septum towards the left ventricle (Fig. 23.2) [5]. In partial filling defect, the emboli is usually centrally located, surrounded by contrast media and may produce the "polo mint" sign if the images are obtained perpendicular to the long axis of the vessel. "Railway-track" sign happens when the image is along the long axis of the affected vessel. In eccentrically located filling defect, embolus usually creates acute angles with the vessel wall. The most common finding within the lung parenchyma in patients with PE is atelectasis. Pulmonary infarction may be seen within the peripheral aspects of the lung parenchyma and typically manifests as wedge-shaped ground-glass or mixed ground-glass and solid opacities (Fig. 23.3). A thickened vessel may be seen extending to the margin of the opacity. "Reversed halo sign" represents ischemia and infarct. It is a nonspecific finding in which the centrally located ground-glass opacity is surrounded by peripheral soft tissue attenuation (Table 23.2). Infarction is more common in patients with impaired collateral circulation and pulmonary venous hypertension. Pleural effusions may also be present [6].

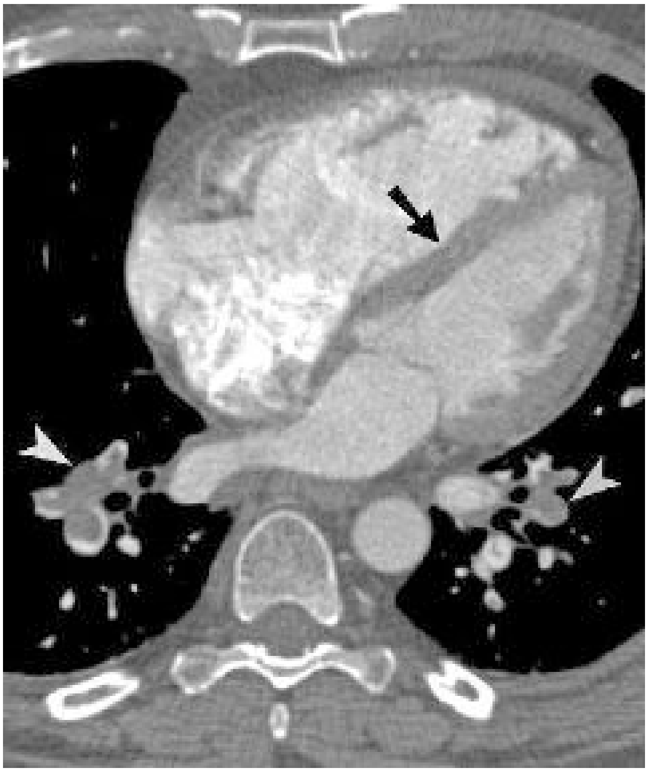

Fig. 23.2 Pulmonary embolism. Axial CT image shows extensive pulmonary emboli (*arrowheads*) within the lower lobes. Straightening of the interventricular septum (*arrow*) is consistent with right cardiac dysfunction

In pregnant patients, radiation dose can be reduced by using low kVp (100 kVp), no tube current modulation to decrease abdominal dose, and abdominal shielding.

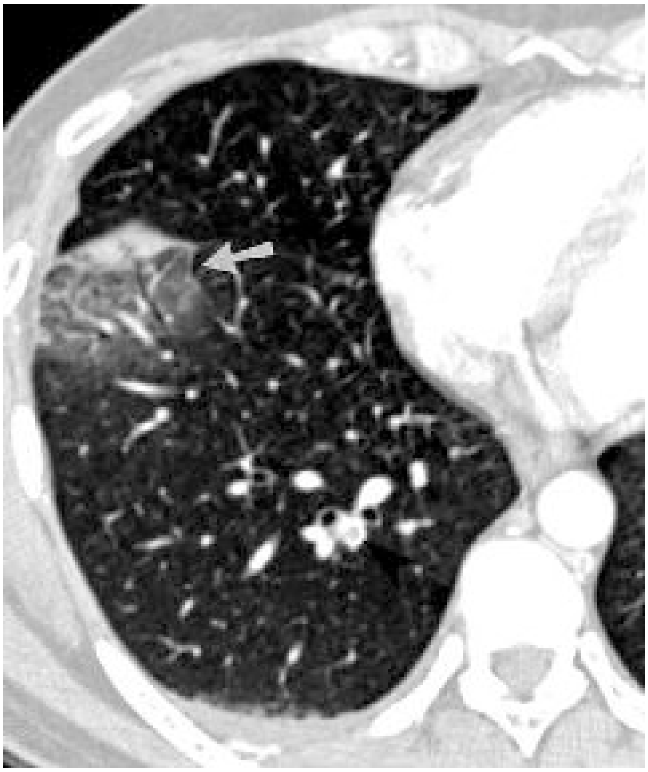

Fig. 23.3 Pulmonary embolism and infarction. Axial CT image demonstrates a mixed ground-glass and solid opacity within the right lower lobe along the major interlobar fissure. This opacity represents pulmonary infarction (*arrow*) in this patient with pulmonary emboli (*arrowhead*)

Table 23.2 Imaging signs in PE

Sign	Description
Westermark's sign	Increased lucency of all or portion of a lung secondary to decreased vascular flow
Hampton's hump sign	Peripheral, wedge-shaped opacity; represent pulmonary infarction
Polo mint sign	Centrally located emboli surrounded by contrast media; if images are obtained perpendicular to the long axis of the vessel
Railway-track sign	Same as "polo mint" sign; when the image is along the long axis of the affected vessel
Reversed halo sign	Centrally located ground-glass opacity is surrounded by peripheral soft tissue attenuation; represents ischemia and infarct

Strategies to improve opacification in pregnant patients include rapid injection (5 cm^3/s), higher contrast concentration, and minimizing contrast interruption.

Esophageal Perforation

Esophageal perforation is a potentially life-threatening phenomenon. The most common etiology of esophageal perforation is iatrogenic, usually associated with endoscopic instrumentation and thoracic surgery. The rate of perforation associated with endoscopy has been estimated at approximately 1 per 1000. In one series, perforation was iatrogenic in 55% of cases. Traumatic perforation is most common within the cervical portion of the thoracic esophagus, which is the narrowest portion. Other etiologies include spontaneous perforation (Boerhaave's syndrome) in 15%, foreign body in 14%, and blunt or penetrating trauma in 10%. Underlying esophageal disease, such as esophagitis or malignancy, appears to place patients at an increased risk of rupture [7].

Boerhaave's syndrome or spontaneous esophageal perforation is a rare phenomenon, affecting approximately one per 6000 patients [7]. Perforation is typically due to an episode of violent vomiting. In this scenario, the posterior esophagus ruptures, usually near the crus of the left hemidiaphragm. In imaging, left-sided mediastinal fluid and gas associated with left pleural effusion are commonly seen.

Food bolus (especially meat) is the most common reason for foreign body-induced esophageal perforation. Food bolus can perforate the thin sections of the esophageal wall. Strictures are usually found at the time of retrieval. Sharp foreign bodies can also penetrate the esophagus. Chicken or fish bones are the second most esophageal foreign bodies. Barium studies are discouraged in bone impaction due to obscuring the object.

Traumatic esophageal injury is uncommon due to great protection of esophagus. Clinical findings in traumatic patients are nonspecific. Imaging findings include esophageal mural defect with posterior pneumomediastinum.

The most common clinical symptoms include history of vomiting, chest pain, and fever. Subcutaneous emphysema may be present on physical examination [7, 8]. The role of conventional chest radiography in the assessment of esophageal perforation is limited, and initial radiographs may be normal. The most common abnormalities are characterized as indirect signs of esophageal perforation and include pneumomediastinum, pneumothorax, and pleural effusion (Fig. 23.4) [7, 8].

Pneumomediastinum may appear as visualization of the white pleural line adjacent to the mediastinum, areas of radiolucency in the soft tissues, and focal air collections within the mediastinum and retrosternal region. The "continuous diaphragm sign," a linear collection of air along the diaphragm, and "V sign" of Naclerio, a collection of air along the left paraspinal region above the left hemidiaphragm, are well-described signs of pneumomediastinum that are rarely seen. CT is definitive in demonstrating the presence of pneumomediastinum, pneumothorax, and pleural effusion complicating esophageal perforation.

If oral contrast material is used at the time of CT imaging, extravasation of contrast from the esophageal lumen into the mediastinum or pleura may be present (Fig. 23.5). Esophagography had previously been considered the initial examination of choice in the evaluation of uncomplicated esophageal disease. In the event of esophageal perforation, esophagography should be performed with water-soluble contrast material, which is rapidly absorbed by the mediastinum. However, water-soluble contrast material should not enter the tracheobronchial tree, as its hyperosmolar composition may result in pulmonary edema. Contrast esophagography may demonstrate extravasation of intraluminal contrast material into the mediastinum or pleura (Fig. 23.6). However, false-negative results may be encountered 10% of the time [7].

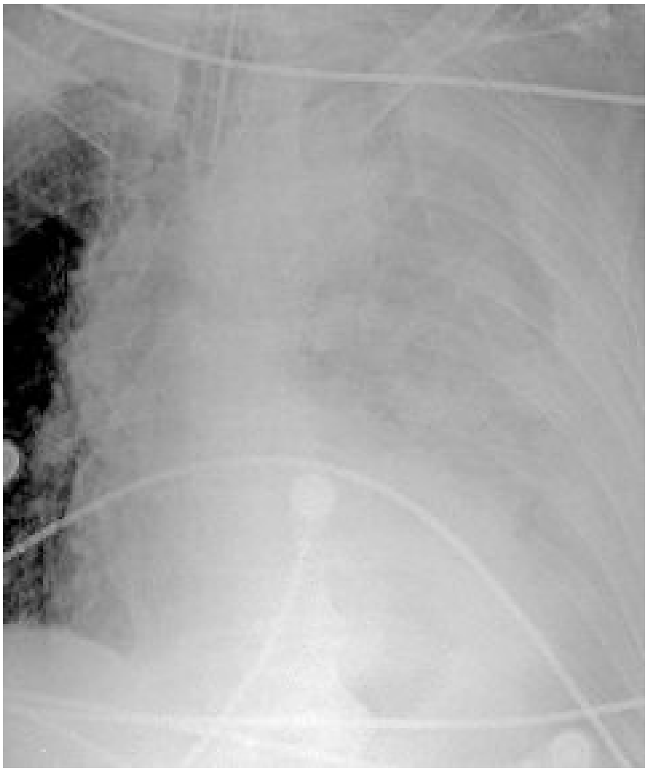

Fig. 23.4 Boerhaave's syndrome. Frontal chest radiograph demonstrates a left pleural effusion and near-complete opacification of the left hemithorax in this patient with Boerhaave's syndrome

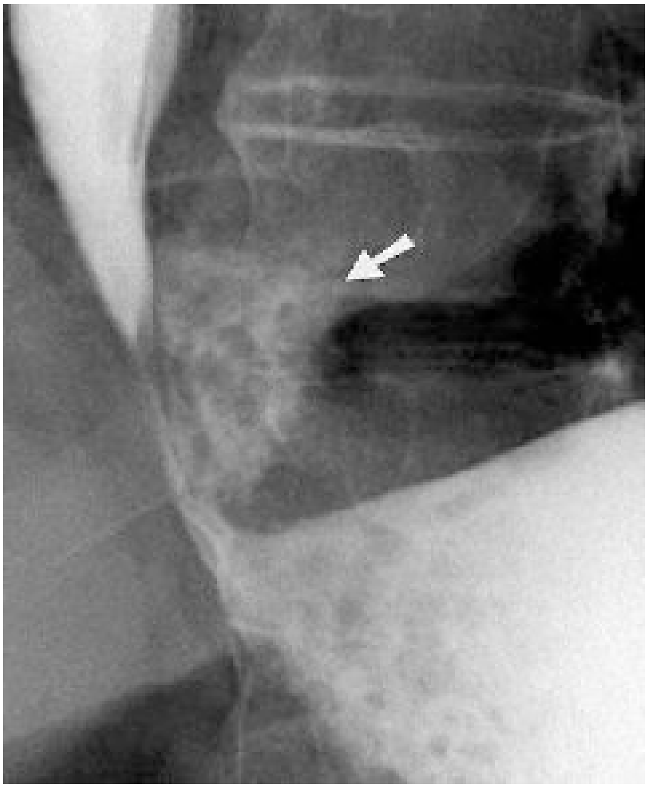

Fig. 23.6 Boerhaave's syndrome. A magnified image from an esophagram shows leakage of contrast material (*arrow*) from the distal thoracic esophageal lumen into the left hemithorax in this patient with Boerhaave's syndrome

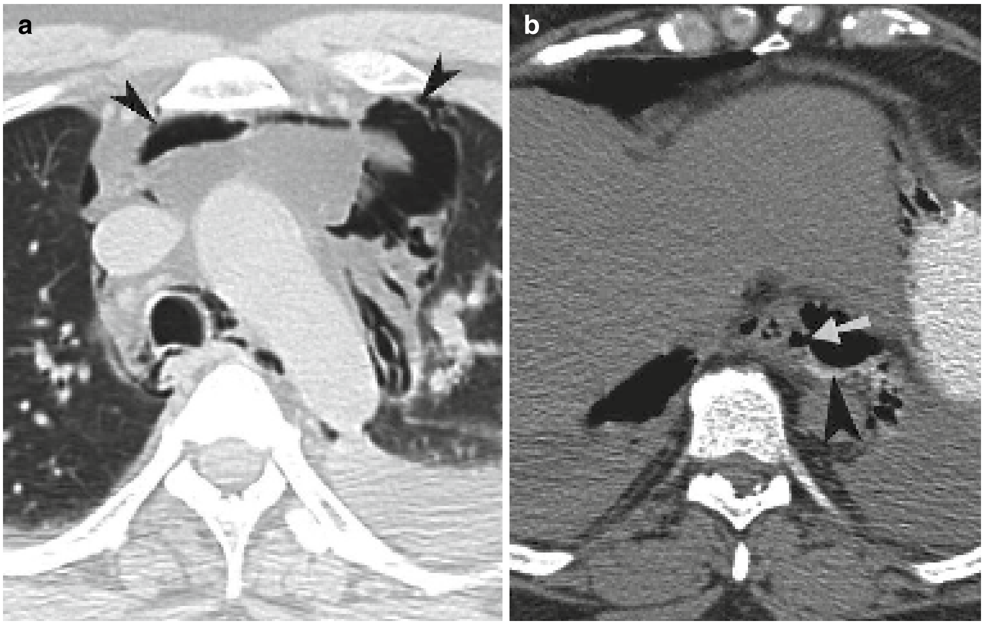

Fig. 23.5 Esophageal perforation. (**a**) Axial CT image through the upper chest shows extensive pneumomediastinum (*arrowheads*) and a left pleural effusion. (**b**) Axial CT images of the same patient demonstrate a defect (*arrow*) within the left lateral wall of the distal thoracic esophagus. An extraluminal collection of air and contrast material (*arrowhead*) is present to the left of the esophageal wall defect

Mediastinitis and Abscess

Acute mediastinitis, or infection of the mediastinum, may be caused by esophageal perforation, tracheobronchial injury, or direct extension from adjacent structures affected by infectious organisms. Hematogenous spread of infection is uncommon. The most common etiology of acute mediastinitis is esophageal perforation, with approximately 1% of patients developing mediastinitis and mediastinal abscess. Additional etiologies include postoperative infection following thoracic surgery for coronary artery bypass grafting, cardiac valve replacement, sampling of mediastinal lymph nodes, and pulmonary resection [7]. Signs and symptoms at the time of presentation are nonspecific and may be confused for those associated with myocardial infarction, acute aortic syndrome (including aortic dissection, intramural hematoma, and penetrating atherosclerotic ulcer), and pulmonary embolism. Patients may present with chest pain, fever, chills, shortness of breath, and leukocytosis. Early diagnosis and treatment are critical for patient survival.

Approximately 0.5%–5% of patients who undergo median sternotomy develop acute mediastinitis. Mortality rate is in the range of 7%–80%. The most common organism is reported to be Staphylococcus *aureus*. Risk factors include obesity, diabetes mellitus, and internal mammary artery grafts.

The most common abnormalities identified on chest radiography include widening of the superior mediastinum (Fig. 23.7) and loss of the normal mediastinal contours. Pneumomediastinum and focal mediastinal fluid collection may also be present. In the absence of these findings, the initial chest radiograph may be normal. In cases of esophageal perforation, contrast esophagography may demonstrate extravasation of intraluminal contrast material into the mediastinum or pleura. In postoperative mediastinitis, radiography may depict changes in the position of sternal wires in serial postoperative radiographs, and rarely, midsternal lucent stripe. CT is definitive in demonstrating mediastinal widening and increased attenuation of the mediastinal fat, both of which are secondary to edema and inflammatory

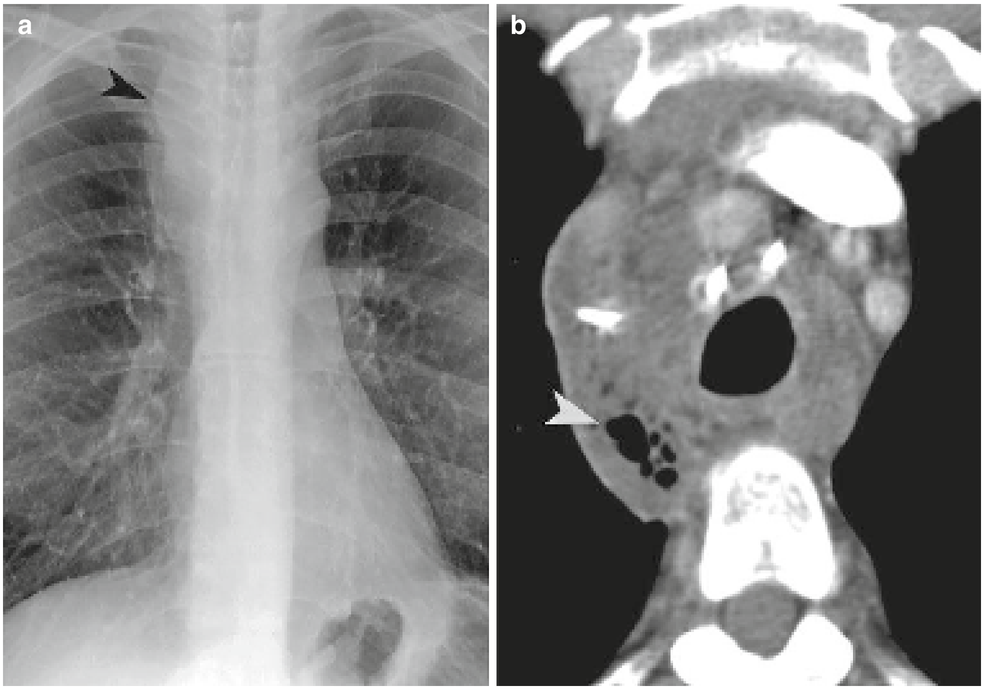

Fig. 23.7 Ediastinitis. (**a**) Frontal chest radiograph demonstrates widening (*black arrowhead*) of the superior mediastinum. (**b**) Axial CT image of the same patient shows extensive inflammatory stranding and edema within the mediastinum. Pneumomediastinum (*white arrowhead*) is also present in this patient with mediastinitis

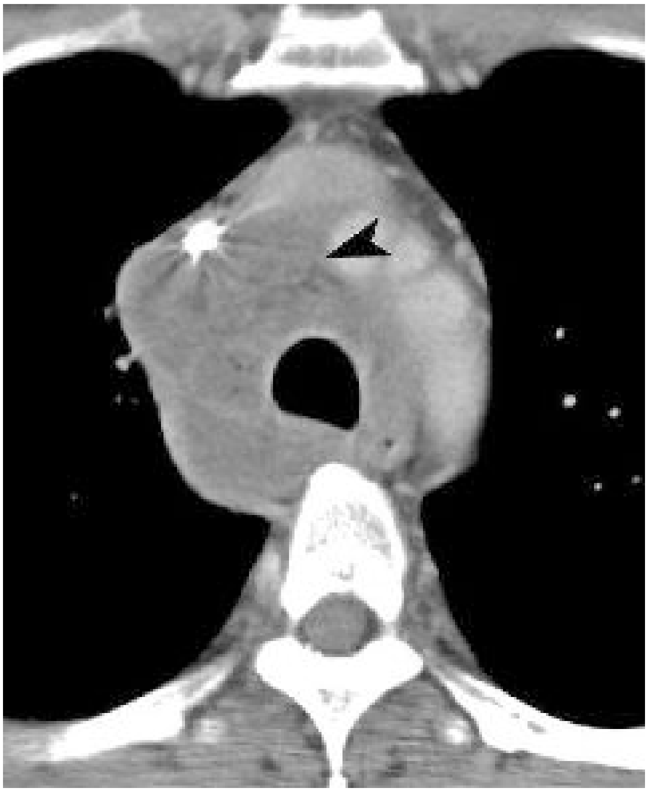

Fig. 23.8 Mediastinal abscess. Axial CT demonstrates inflammatory stranding and low density within the mediastinum (*arrowhead*), consistent with abscess

changes. Pneumomediastinum may be seen (see Fig. 23.7). CT is excellent for visualization of potentially drainable fluid collections such as abscesses and may be used to guide percutaneous drainage. Concomitant acute abnormalities of the lung parenchyma, such as bronchopneumonia, lobar pneumonia, abscess, and empyema, may be identified (Fig. 23.8). Secondary signs of mediastinal infection, including mediastinal lymphadenopathy, pleural effusions, and pericardial effusions, may also be identified. In patients with acute mediastinitis secondary to esophageal perforation, thickening of the esophageal wall, pneumothorax and pleural effusion, extravasation of intraluminal contrast material, and abscesses may be present. In patients with acute mediastinitis following thoracic surgery, CT is excellent for visualization of sternal dehiscence and pleuromediastinal fistulas [7].

Danger space is a potential space behind the retrolaryngeal space, extending from the clivus to the diaphragm. Anterior to the danger space is the alar fascia and posterior to the space is the prevertebral fascia. It connects the deep cervical spaces to the mediastinum and becomes visible when distended by fluid or pus (Fig. 23.9a, b). Infections in pharynx may spread through this space to the mediastinum.

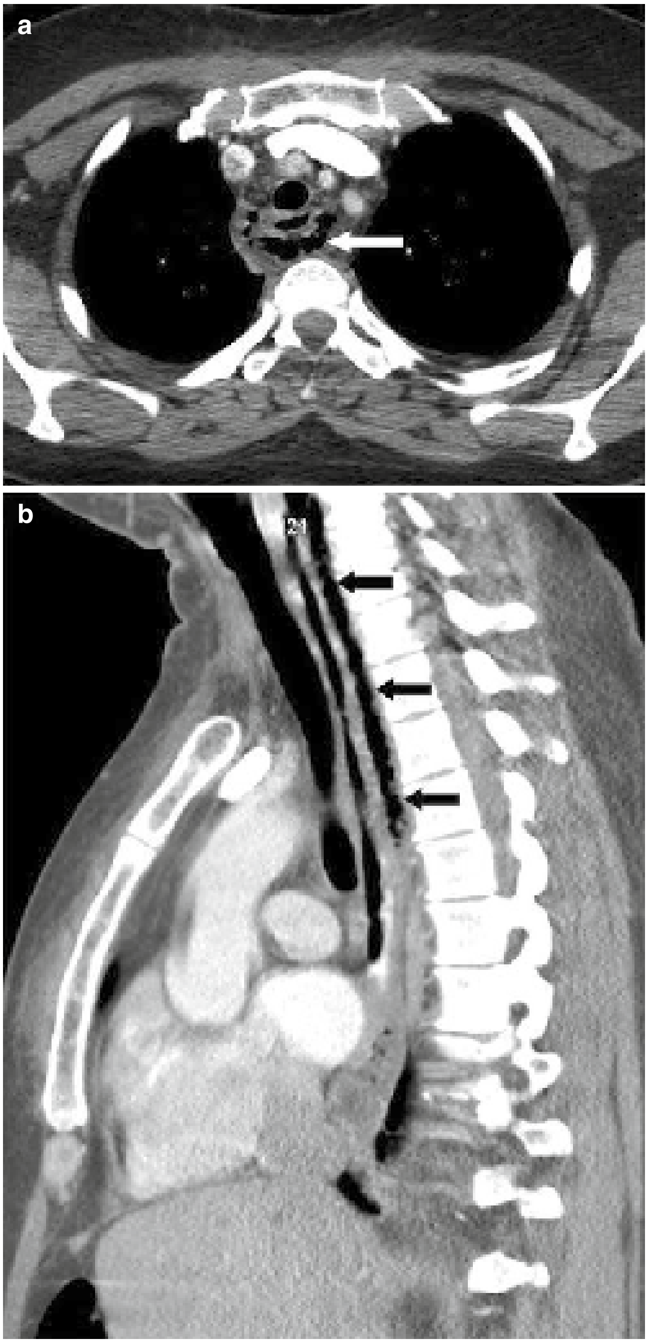

Fig. 23.9 (**a**, **b**) Danger space abscess. Contrast-enhanced CT demonstrates air-containing collection between esophagus and thoracic spine (*arrows*)

Lungs and Pleura

Pneumonia

There are over 4 million cases of pneumonia each year in the USA with 1 million hospitalizations a year. Pulmonary infections are the eighth leading cause of death in the USA and are the most common cause of infection-related mortality

[9]. Pneumonias can be classified into main four clinical groups: community acquired, aspiration, healthcare associated, and hospital acquired. Cough, fever, and dyspnea are the usual presenting symptoms, but 50% of patients also complain of pleuritic chest pain. Even with advances in current medical techniques, the specific etiology can be determined in only 50%–70% of cases [10].

Definitive diagnosis requires confirmation of pulmonary findings by imaging. ATS recommendations include PA and lateral chest radiographs which increase the sensitivity of the exam; portable technique should be reserved for truly obtunded patients. The main radiological patterns of lobar pneumonia, bronchopneumonia, and interstitial pneumonia are recognized with sufficient frequency and correlate enough with different causative organisms in enough cases, so their recognition is useful diagnostically [10]. CT is used to further characterize a complex pneumonia, visualize a process not seen on chest radiograph (Fig. 23.10a, b), and look for complications such as abscess or empyema [11].

Community-acquired pneumonia (CAP) is the most common cause of pulmonary infection in both immunocompromised and immunocompetent patients presenting to the emergency room [10]. *Streptococcus pneumoniae*, the most common bacterial cause, typically demonstrates a lobar pattern of consolidation (Fig. 23.11); air bronchograms are common, and pleural effusions are uncommon.

Left upper lobe pneumonia (lingular pneumonia) is associated with indistinct left paramediastinal silhouette and aortic arch, and clear demarcation of left oblique fissure on the lateral view (Fig. 23.12). Right middle lobe pneumonia is associated with indistinct right heart border and medial aspect of right hemidiaphragm. In right and left lower lobe pneumonia air-space opacity with air bronchograms obscure the right and left hemidiaphragms, respectively.

Staphylococcus aureus is a less common cause of CAP and usually is seen in debilitated patients. A multifocal lobar and bronchopneumonia pattern primarily in the lower lobes with pleural effusions can be seen on the CXR (Fig. 23.13a), and the presence of associated pneumatoceles and/or abscesses better seen on CT scan (Fig. 23.13b) may suggest this diagnosis. Atypical infections including *Mycoplasma pneumoniae* (Figs. 23.14 and 23.15) have an asymmetric patchy bilateral interstitial and alveolar pattern which sometimes can be hard to confirm by chest radiograph. CT findings include patchy ground-glass opacities, centrilobular nodules, and septal thickening: pleural effusions are uncommon. Viral pneumonias have a similar pattern and are becoming a much more common cause of CAP [9].

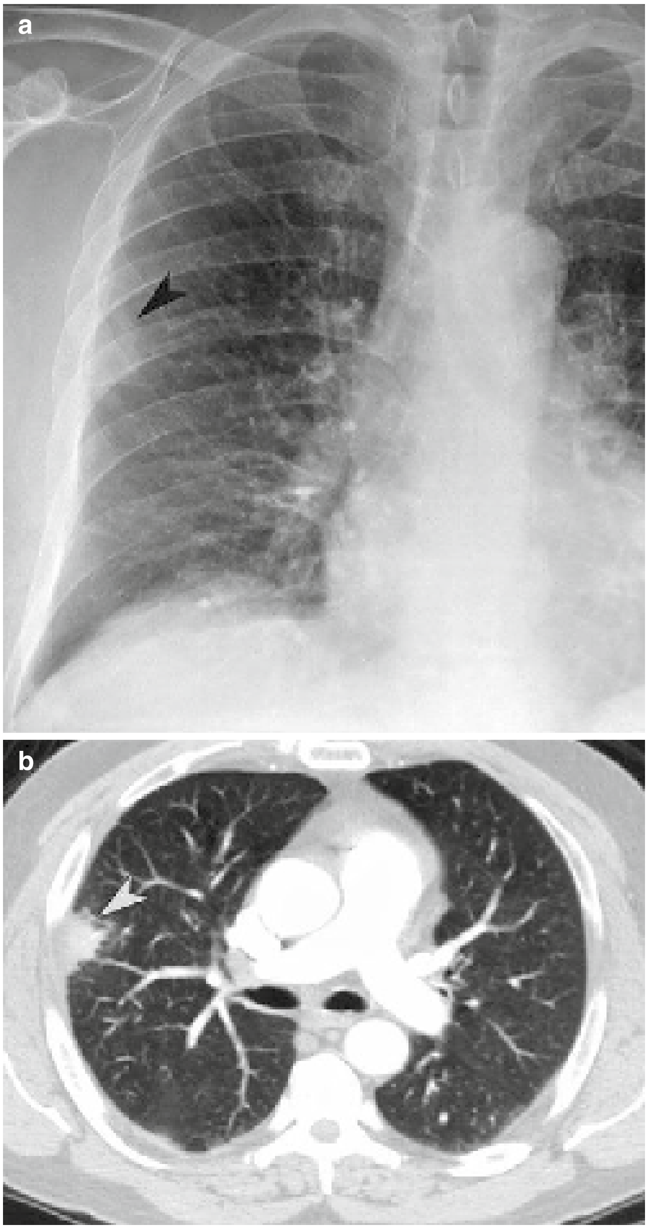

Fig. 23.10 Pneumonia. (**a**) Frontal chest radiograph shows a peripheral opacity (*arrowhead*) in the anterior segment of the right upper lobe. (**b**) Axial CT scan confirms a peripheral pneumonia (*arrowhead*) in the right upper lobe

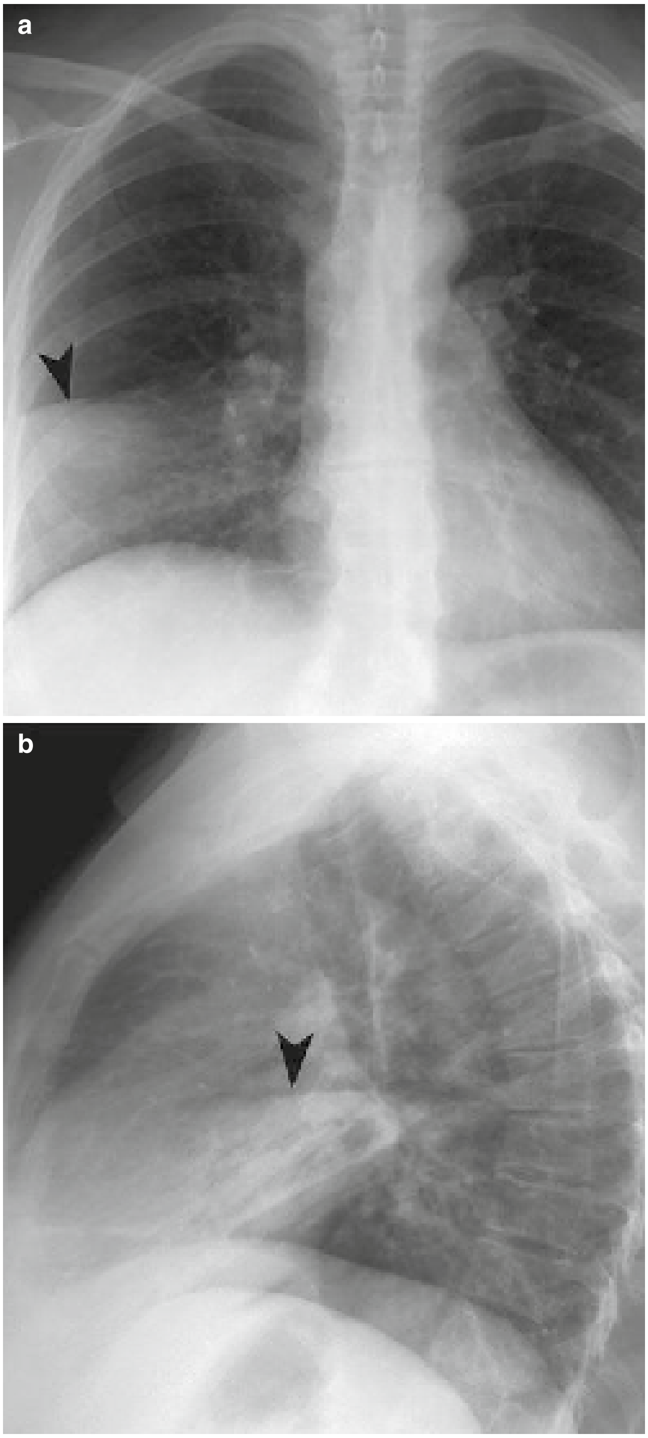

Fig. 23.11 Right middle lobe pneumonia. (**a**) Frontal radiograph of the chest demonstrates classic right middle lobe pneumonia (*arrowhead*) with ill definition of the right heart border. (**b**) The *right middle* lobe pneumonia (*arrowhead*) is seen projecting over the heart on the lateral view

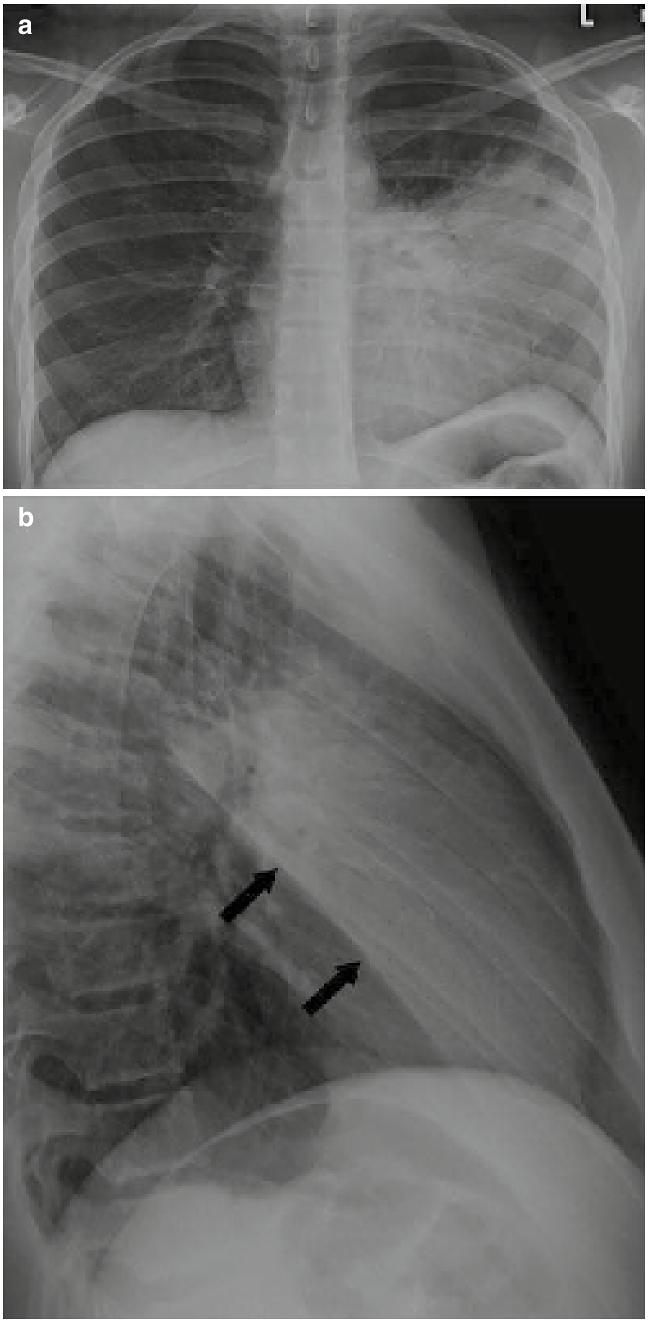

Fig. 23.12 Left upper lobe pneumonia. (**a**) PA chest radiograph demonstrates obscuration of left border of the heart by the consolidation. (**b**) Lateral view demonstrates clear demarcation of left major fissure (*arrows*)

Aspiration pneumonia has a more distinct pattern on chest radiograph (Fig. 23.16). It occurs in the dependent portion of the lower lobes, favoring the right lung because of the straight orientation of the right mainstem bronchus with respect to the trachea. In supine patients, the aspirated material collects in the posterior segments of the upper lobes and superior segments of the lower lobes. Pleural effusions are common (Fig. 23.17b and Table 23.3). Anaerobic organisms are the etiology of the resultant pneumonia 90% of the time [11].

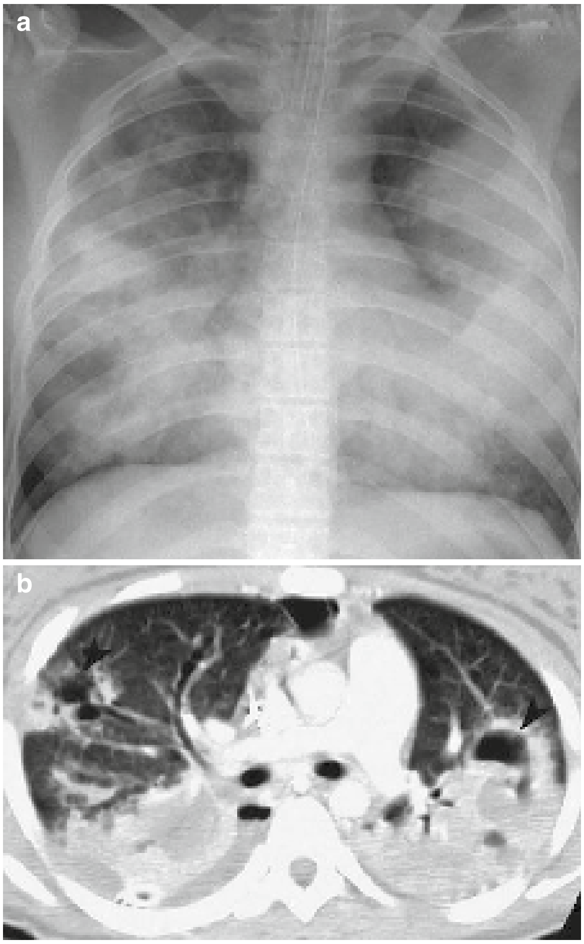

Fig. 23.13 Bronchopneumonia. (**a**) Plain radiograph of the chest demonstrates bilateral multifocal bronchopneumonia. (**b**) Axial CT demonstrates pneumatoceles (*arrowheads*) associated with the pneumonic process

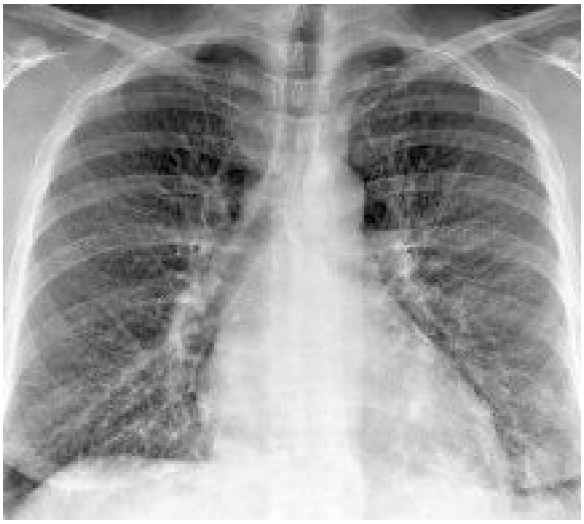

Fig. 23.15 Viral pneumonia. Chest radiograph shows bilateral central interstitial prominence along with some left lower lobe subsegmental air-space disease

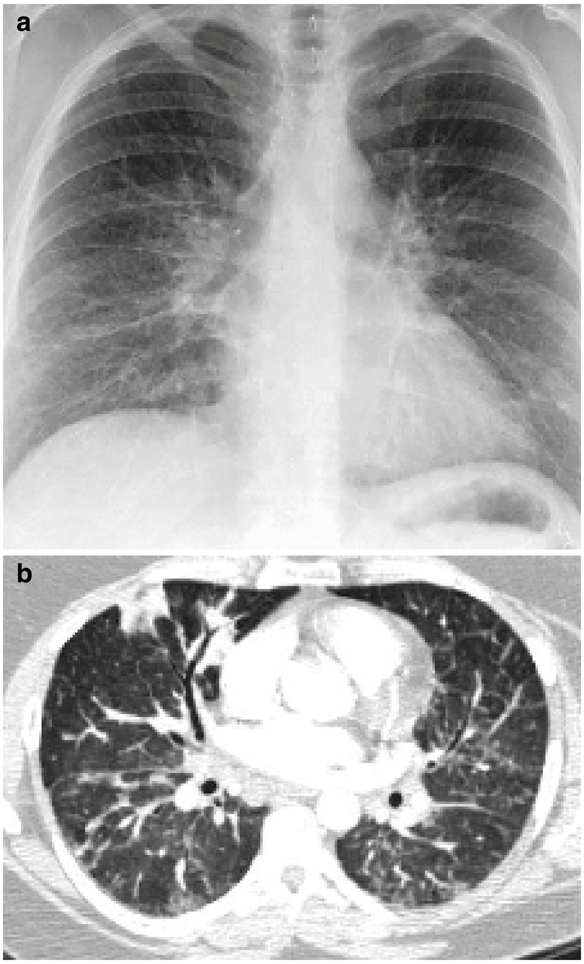

Fig. 23.14 *Mycoplasma pneumonia*. (**a**) Chest radiograph shows atypical *Mycoplasma pneumoniae* with bilateral patchy interstitial opacities. (**b**) Axial CT shows bilateral asymmetric septal thickening and ground-glass nodules. Note the absence of pleural effusions

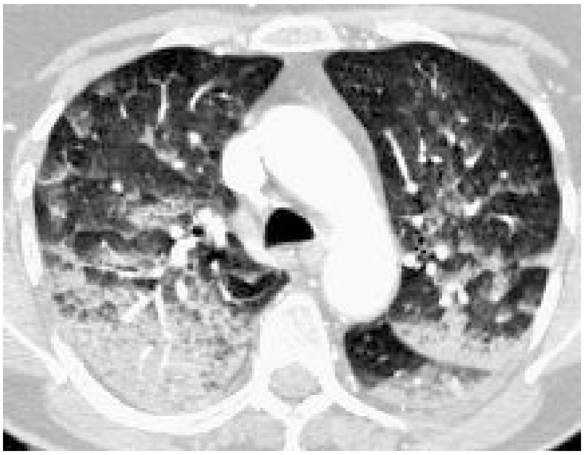

Fig. 23.16 Aspiration pneumonia. Axial CT demonstrates bilateral dependent confluent consolidation, greater on the right

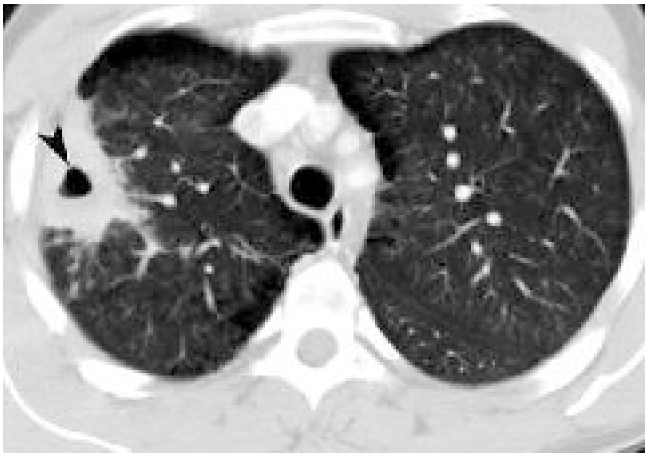

Fig. 23.17 Pulmonary abscess. Axial CT shows right upper lobe pulmonary abscess (*arrowhead*) which developed in a focus of consolidation

Table 23.3 Imaging features in pneumonia

Cause	Description
Streptococcus pneumoniae	Most common cause
	Lobar consolidation
	Air bronchograms
	Pleural effusions uncommon
Staphylococcus aureus	Seen in debilitated patients
	Multifocal lobar and bronchopneumonia pattern
	Lower lobes affected
	Possibly pleural effusions
	Associated pneumatoceles and/or abscesses
Mycoplasma pneumoniae	Atypical cause
	Asymmetric patchy bilateral interstitial and alveolar pattern
	Patchy ground-glass opacities
	Centrilobular nodules
	Septal thickening
	Pleural effusions uncommon
Viral pneumonia	Similar to *Mycoplasma pneumoniae*
Anaerobic	Aspiration pneumonia
	Dependent portion of the lower lobes
	Commonly affects right lung
	If supine: affects posterior segments of the upper lobes, and superior segments of the lower lobes
	Pleural effusions common

Pulmonary Abscess and Empyema

A lung abscess represents a localized infection that undergoes tissue destruction and necrosis. They are most common in mixed anaerobic infections, so should be suspected in patients at risk for aspiration. Multiple abscesses can also be seen in septic emboli. The chest radiograph may demonstrate an air-fluid level indicating communication with the tracheobronchial tree. Abscess is usually round-shaped, creating an acute angle with the costal surface or chest wall (Fig. 23.18). CT scan can better delineate the abscess (see Fig. 23.17) which typically manifests a smooth internal wall and develops within and is adjacent to parenchymal consolidation, an imaging feature which can help differentiate it from a cavitary neoplasm [11]. Lung abscess is typically treated with prolonged antibiotics and physiotherapy with postural drainage.

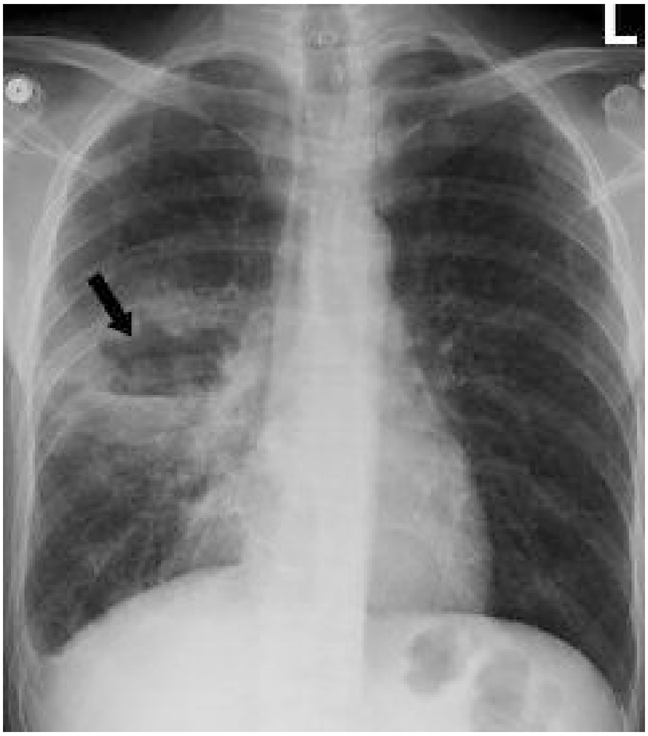

Fig. 23.18 Pulmonary abscess mimicking a cavitating neoplasm. Plain radiograph of the chest demonstrates an abscess cavity (*arrow*) containing air-fluid level. The irregular thick wall of the abscess raises the concern for cavitating neoplasm

Most pleural effusions associated with pneumonia are sterile sympathetic effusions. Empyemas develop when the pleural space becomes infected, usually from direct extension of a pulmonary parenchymal source. An empyema can also exhibit an air-fluid level, but since the fluid conforms to the pleural space, the air-fluid level is longer on the lateral view (Fig. 23.19a). Contrast-enhanced CT scan demonstrated adjacent compressed lung as well as the “split pleura” sign of thickened inflamed visceral and parietal pleura which is seen in over half of patients with empyema (Fig. 23.19b). Empyema usually creates an obtuse angle with the chest wall. Chest ultrasound combined with CT scan helps define the nature of fluid collections in the pleural space and better delineate the phase of empyema: exudative, fibropurulent, or organized, which will direct patient management as to drainage or more invasive surgical procedures [12]. Empyema is treated with percutaneous or surgical drainage.

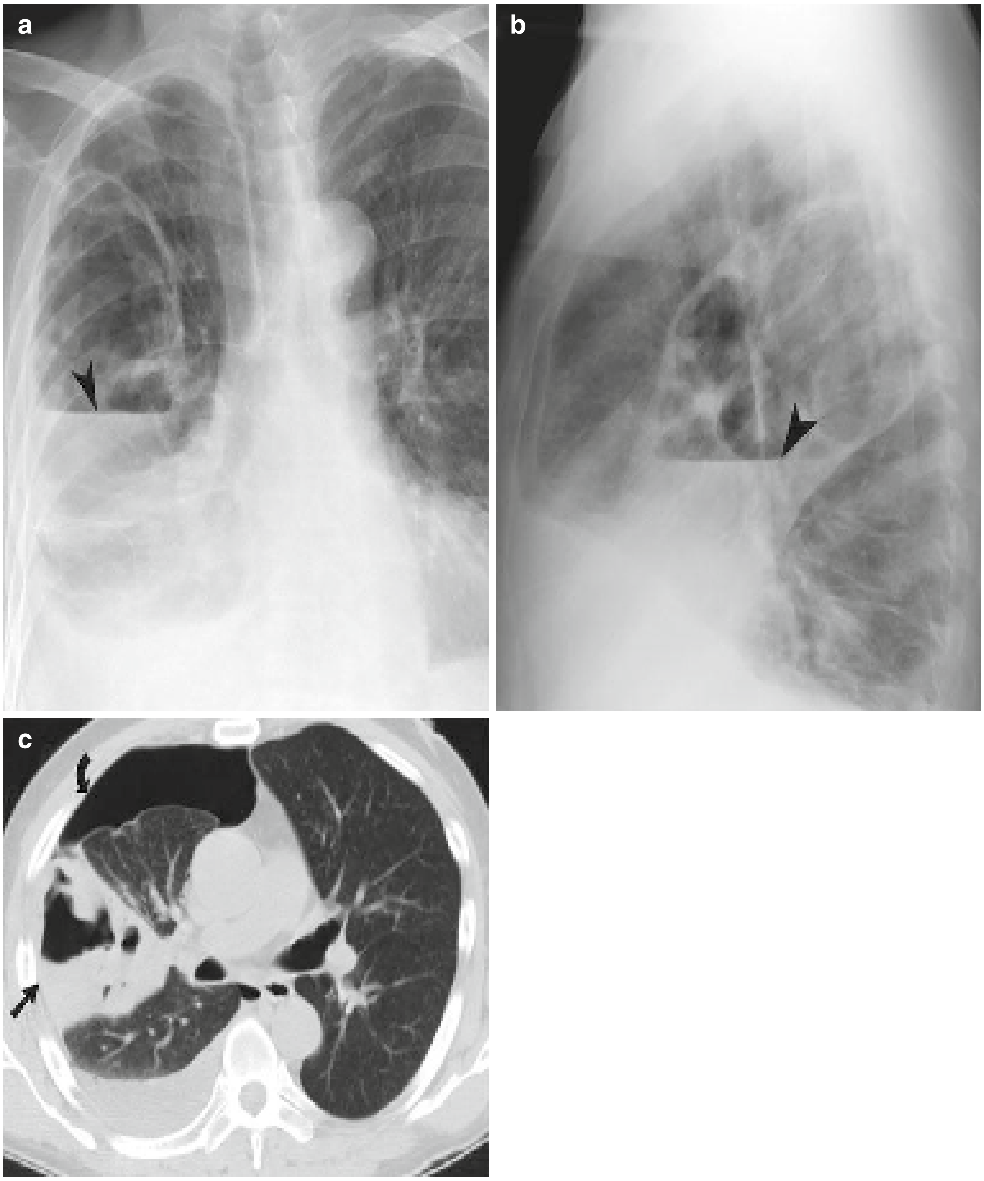

Fig. 23.19 Empyema. (**a**, **b**) Plain radiograph demonstrates empyema of the right pleural space with air-fluid levels (*arrowheads*). (**c**) Axial CT demonstrates empyema (*straight arrow*) in the oblique fissure with the complication of pneumothorax (*curved arrow*)

Neoplasms may have similar imaging features with pulmonary abscesses. Comparing with previous chest imaging may also be useful. Malignant cavitary nodules commonly have an irregular internal wall. Fiberoptic bronchoscopy may be necessary to distinguish the borderline cases.

Pulmonary Edema

Pulmonary edema can either be cardiogenic or noncardiogenic in etiology and although they have distinct causes, they can be indistinguishable by imaging so clinical correlation is critical. The majority of cases presenting to the emergency room are cardiogenic in nature due to heart failure. Noncardiogenic causes to consider include pneumonia, sepsis, inhalation injury, and aspiration of gastric contents [13].

Chest radiographs can be very nonspecific and tend to be the ones ordered with portable technique which further decreases their sensitivity. In cardiogenic edema, cardiomegaly with a widened vascular pedicle, bilateral symmetric septal thickening, coalescing alveolar opacities, and bilateral pleural effusions are common manifestations delineated on chest radiograph (Fig. 23.20a). Peribronchial cuffing and

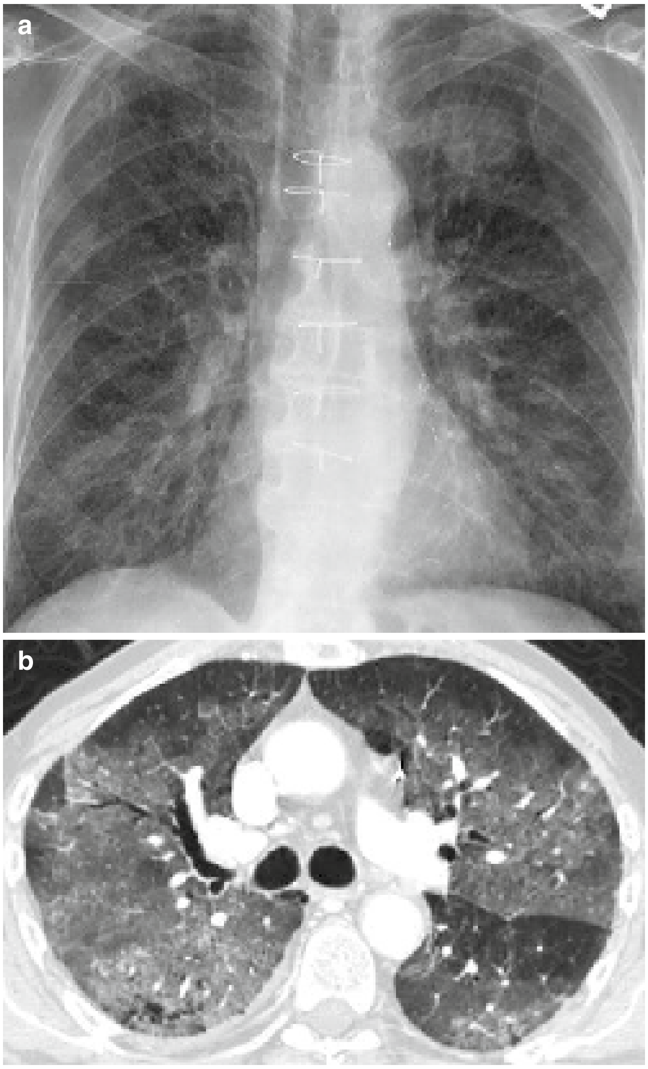

Fig. 23.20 Pulmonary edema. (**a**) Plain radiograph demonstrates diffuse bilaterally symmetrical central interstitial prominence. (**b**) Axial CT demonstrates bilateral ground-glass opacities

perihilar prominence are also present and may be a differentiating factor from a noncardiogenic cause [13]. CT scan can delineate further the septal thickening; air-space edema on CT can be ground-glass or frankly consolidative (Fig. 23.20b). Pulmonary edema tends to be symmetric except in cases where the patient has severe underlying emphysema. Noncardiogenic pulmonary edema tends to be less “wet” looking with no widened vascular pedicle or peribronchial cuffing minimal septal lines, a lack of pleural effusions, and a more patchy air-space appearance with air bronchograms (Fig. 23.21 and Table 23.4) [14].

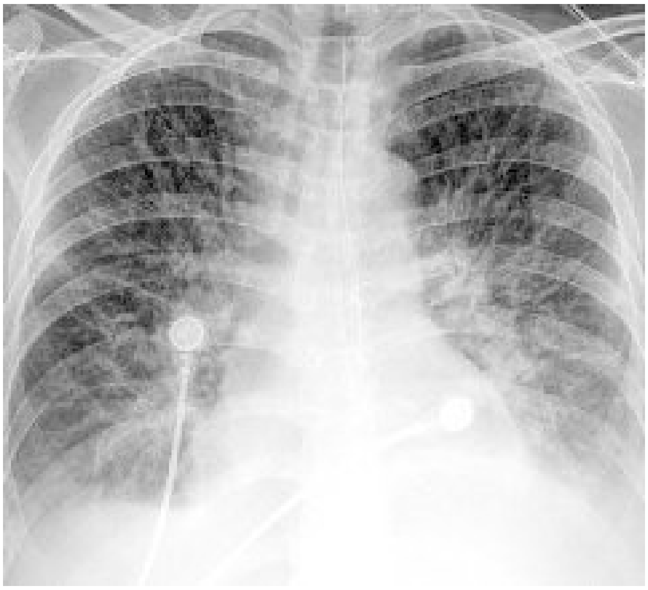

Fig. 23.21 Pulmonary edema. Plain radiograph demonstrates cardiomegaly with bilateral interstitial as well as alveolar edema and bilateral pleural effusions

Table 23.4 Cardiogenic versus noncardiogenic pulmonary edema

Cardiogenic	Noncardiogenic
Cardiomegaly with a widened vascular pedicle	No widened vascular pedicle
Bilateral symmetric septal thickening	Minimal septal lines
Coalescing alveolar opacities	Patchy air-space appearance with air bronchograms
Symmetric bilateral pleural effusions	Lack of pleural effusions
Peribronchial cuffing	No peribronchial cuffing
Perihilar prominence	
Ground-glass or consolidative air-space edema on CT	

Pneumothorax

Nontraumatic pneumothorax can be attributed to one of two categories: primary spontaneous or secondary to complications of underlying lung disease.

Primary spontaneous pneumothoraces occur most commonly in young, tall, thin males without predisposing factors although rupture of small bleb or bullae and smoking are thought to play roles. Secondary causes include COPD, metastatic disease, infection, and cystic lung disease [15]. Pneumomediastinum can cause pneumothorax but not vice versa.

An upright chest radiograph in most cases can confirm the presence of a pneumothorax by demonstrating the absence of lung markings from the edge of the visceral pleura to the chest wall (Fig. 23.22). In supine patients, a deep sulcus sign can develop as air layers out anteriorly and projects as an area of increased lucency that outlines the costophrenic sulcus (Fig. 23.23) [16]. Expiratory views have no additional diagnostic value and are not needed although lateral views can sometimes be helpful if it is uncertain whether a pneumothorax is present. Tension pneumothorax occurs if intrapleural pressure increases to a point where gas exchange and cardiac function become compromised. Radiographically, this manifests as contralateral mediastinal shift and diaphragmatic depression (Fig. 23.24), both of which should resolve with decompression. CT can be used to detect patients with small pneumothorax (<15%) as well as to further elucidate the possible underlying cause such as blebs, bullae, or pulmonary disease.

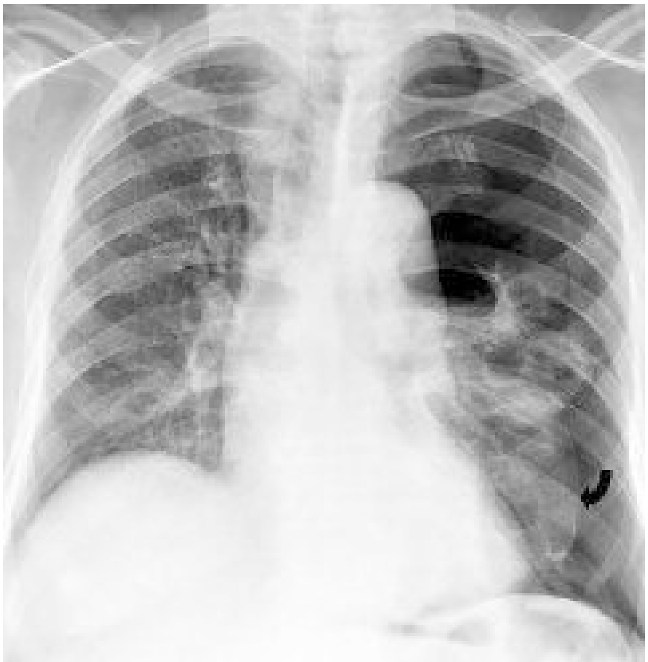

Fig. 23.22 Tension pneumothorax. Plain radiograph of the chest demonstrates visceral pleural line (*curved arrow*) with a left-sided tension pneumothorax. There is flattening of the left dome of diaphragm and partial collapse of the lung centrally with mediastinal shift

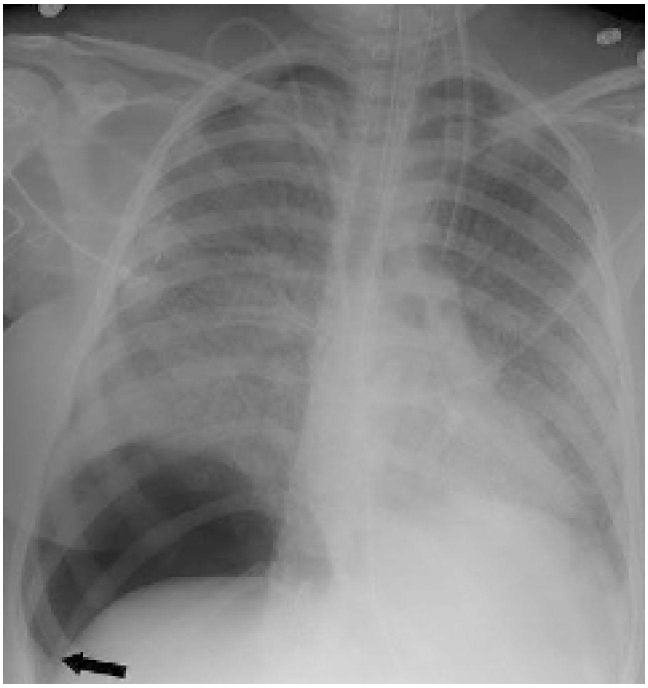

Fig. 23.23 Deep sulcus sign. Chest radiograph demonstrates collection of air in the pleural space at the right base, outlining the posterior costophrenic sulcus

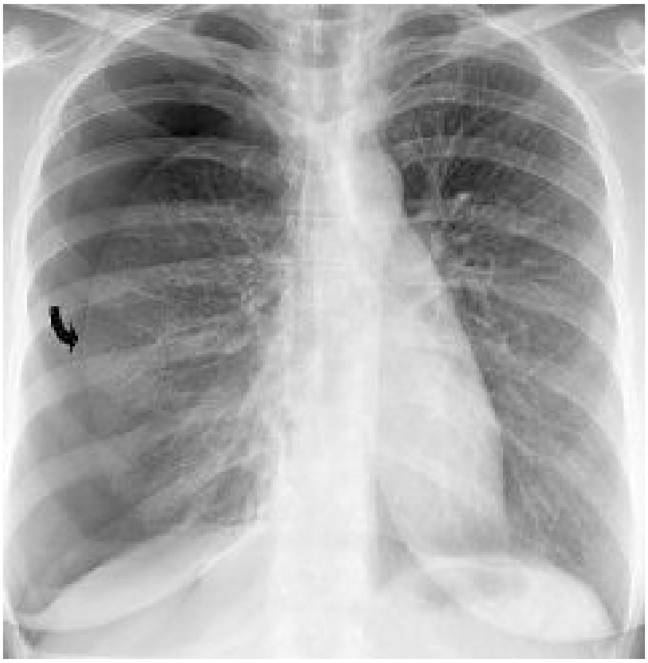

Fig. 23.24 Tension pneumothorax. Portable chest radiograph demonstrates large right-sided tension pneumothorax (*curved arrow*) with mediastinal shift to the left side

COVID-19 Pneumonia

First described in 2019 in Wuhan, China, COVID-19 was declared a pandemic in March 2020. Although gold standard for diagnosis is reverse transcriptase polymerase chain reaction (RTPCR), chest imaging plays a crucial role in assessing extent and evolution of the disease.

Characteristic chest radiograph findings include peripheral ground-glass opacities and consolidation (Fig. 23.25a), often bilateral, multifocal, and more commonly involving the lower lobes. Less common manifestations include reticular opacities and pneumothorax.

On chest CT, the most characteristic findings include ground-glass opacities, typically subpleural, followed by consolidation (Fig. 23.25b). Other findings include reticulation, crazy-paving pattern, pleural thickening, air bronchogram, halo sign, and reversed halo sign. In early stages, ground-glass opacities predominate which progresses to crazy-paving appearance and consolidation. After 14 days, ground-glass opacities and consolidation begin to gradually subside, and signs of fibrosis may become apparent [17, 18].

Teaching Points

- Chest radiograph should be the first imaging modality used in the assessment of nontraumatic thoracic emergencies.
- The most common CT finding of PE is hypodense filling defects within opacified pulmonary artery branches. Abrupt cutoff and complete occlusion may also be seen.
- The most common findings of esophageal perforation on chest radiograph and CT include pneumomediastinum, pneumothorax, and pleural effusion. If oral contrast material is administered, extravasation of contrast into the mediastinum or pleura may be seen.
- The radiographic pattern of pneumonia in CAP may help suggest a causative organism to better tailor treatment; CT is helpful to define subtle cases or detect superimposed complications.
- CT scan can better delineate the lung abscess which typically demonstrates a smooth internal wall and develops within and is adjacent to parenchymal consolidation.
- Noncardiogenic pulmonary edema tends to be less "wet" looking with no widened vascular pedicle or peribronchial cuffing minimal septal lines, a lack of pleural effusions, and a more patchy air-space appearance with air bronchograms.

Questions

1. A centrally located pulmonary emboli surrounded by contrast media creates which of the following signs?
   (A) Westermark's sign
   (B) Hampton's hump sign
   (C) Railway-track sign
   (D) Reversed halo sign
   Answer: C

2. Which of the following is the most common cause of foreign body-induced esophageal perforation?
   (A) Chicken bone
   (B) Food bolus
   (C) Fish bone
   (D) Sharp bodies
   Answer: B

3. Which of the following pulmonary segments is commonly affected in anaerobic pneumonia?
   (A) Right middle lobe
   (B) Lateral basal segment of right lower lobe
   (C) Posterior segment of left upper lobe
   (D) Superior segment of right lower lobe
   Answer: D

4. What Is the Imaging Diagnosis Based on the Chest CT (Fig. 23.26a, b) Performed Using Oral and IV Contrast?
   (A) Boerhaave's syndrome
   (B) Esophageal varices
   (C) Mallory-Weiss syndrome
   (D) Aortic rupture
   Answer: A

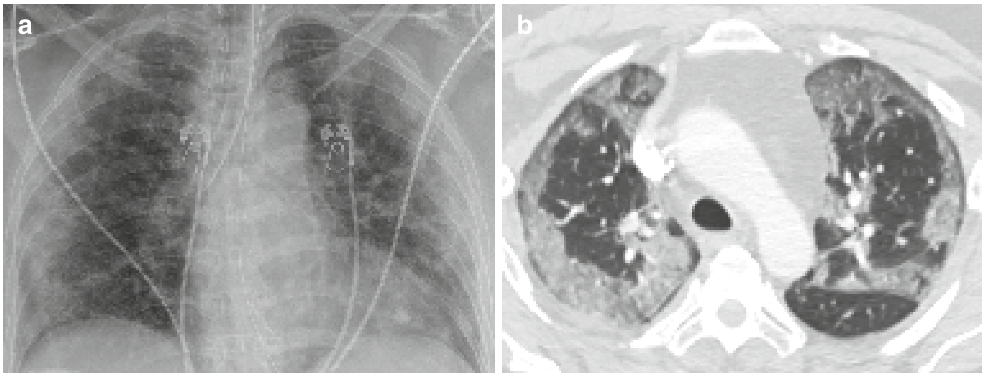

Fig. 23.25 COVID pneumonia. (**a**) Chest radiograph demonstrates bilateral peripheral consolidations. The endotracheal tube is seen extending in the right main bronchus. (**b**) Axial CT scan demonstrates bilateral, peripheral ground glass and consolidative densities from COVID-19 pneumonia

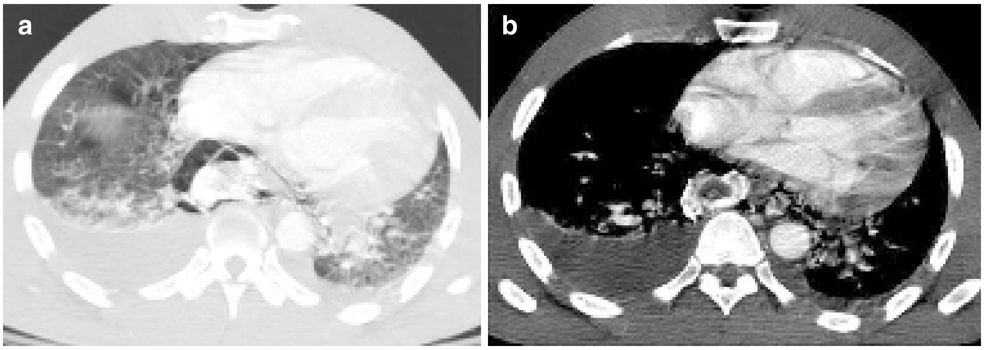

Fig. 23.26 Chest CT (**a**, **b**)

References

1. Tapson VF. Acute pulmonary embolism. N Engl J Med. 2008;358:1037–52.
2. Coche EE, Verschuren F, Hainaut P, Goncette L. Pulmonary embolism findings on chest radiographs and multislice spiral CT. Eur Radiol. 2004;14:1241–8.
3. Stein PD, Woodard PK, Weg JG, Wakefield TW, Tapson VF, Sostman HD, et al. Diagnostic pathways in acute pulmonary embolism: recommendations of the PIOPED II Investigators. Radiology. 2007;242(1):15–21.
4. Han D, Lee KS, Franquet T, Müller NL, Kim TS, Kim H, et al. Thrombotic and nonthrombotic pulmonary arterial embolism: spectrum of imaging findings. Radiographics. 2003;23:1521–39.
5. Wittram C, Maher MM, Yoo AJ, Kalra MK, Shepard JA, McLoud TC. CT angiography of pulmonary embolism: diagnostic criteria and causes of misdiagnosis. Radiographics. 2004;24(5):1219–38.
6. Coche EE, Müller NL, Kim KI, Wiggs BR, Mayo JR. Acute pulmonary embolism: ancillary findings at spiral CT. Radiology. 1998;207(3):753–8.
7. Giménez A, Franquet T, Erasmus JJ, Martínez S, Estrada P. Thoracic complications of esophageal disorders. Radiographics. 2002;22:S247–58.
8. Hingston CD, Saayman AG, Frost PJ, Wise MP. Boerhaave's syndrome—rapidly evolving pleural effusion; a radiographic clue. Minerva Anestesiol. 2010;76(10):865–7.
9. Nair GB, Niederman MS. Community-acquired pneumonia: an unfinished battle. Med Clin North Am. 2011;95:1143–61.
10. Tarver RD, Teague SD, Heitkamp DE, Conces DW. Radiology of community-acquired pneumonia. Radiol Clin North Am. 2005;43(3):497–512.
11. Waite S, Jeudy J, White CS. Acute lung infections in normal and immunocompromised hosts. Radiol Clin North Am. 2006;44:295–315.
12. Heffner JE, Klein JS, Hampson C. Diagnostic utility and clinical application of imaging for pleural space infections. Chest. 2010;137:467–79.
13. Ware LB, Matthay MA. Acute pulmonary edema. N Engl J Med. 2005;353:2788–96.
14. Glueker T, Capasso P, Schnyder P, Gudinchet F, Schaller MD, Revelly JP, et al. Clinical and radiologic features of pulmonary edema. Radiographics. 1999;19:1507–31.
15. Luh S. Diagnosis and treatment of primary spontaneous pneumothorax. J Zhejiang Univ Sci B. 2010;11(10):735–44.
16. Jeudy J, Waite S, White CS. Nontraumatic thoracic emergencies. Radiol Clin North Am. 2006;44:273–93.
17. Kwee TC, Kwee RM. Chest CT in COVID-19: what the radiologist needs to know. Radiographics. 2020;40(7):1848–65. https://doi.org/10.1148/rg.2020200159. [published correction appears in Radiographics. 2022;42(1):E32]
18. Churruca M, Martínez-Besteiro E, Couñago F, Landete P. COVID-19 pneumonia: a review of typical radiological characteristics. World J Radiol. 2021;13(10):327–43. https://doi.org/10.4329/wjr.v13.i10.327.

Imaging of Acute Thoracic Trauma

24

Neil Patel, Mohammad Mansouri, Sridhar Shankar,
and Ajay Singh

Introduction

Thorax injury remains the third most common type of injury in trauma patients [1]. With the number of trauma cases on the increase, the incidence of injuries to the thorax is proportionally increasing. The overall mortality rate of thoracic trauma is approximately 10% and is highest in patients with cardiac or tracheobronchial-esophageal injuries [1]. More than two-thirds of cases of trauma in developed countries are caused by motor vehicle collisions. The remaining cases are the result of falls or blows from blunt objects [2].

Historically, plain radiographs have been the imaging modality of choice because of their low cost and their ability to be done quickly. While they may be useful for the evaluation of many traumatic injuries including large pneumothoraces or fractures, CT has been shown to change the management in 20% of trauma cases [3]. Specifically, thoracic CT has shown improved accuracy over conventional radiography in the diagnosis of pneumothorax, subtle fractures, hemopericardium, detailed lung parenchymal injury, and both mediastinal hemorrhage and direct vascular injury, among other injuries. Furthermore, it is not uncommon for a plain radiograph to identify a possible injury that needs further evaluation with CT whether it be for surgical planning or to definitively assess the degree of the injury [4].

Injuries to the Pleural Space

The pleural space is defined as the space between the visceral pleura and the parietal pleura. In a healthy patient, this is a potential space that is not well visualized on radiograph or CT. When either the visceral pleura, parietal pleura, or possibly both are interrupted, the potential space can expand, most commonly with blood or air in the setting of trauma.

Pneumothorax

When air fills the pleural space, a pneumothorax results. The most common clinical presentation of this is shortness of breath with decreased breath sounds. They may be caused by ruptured alveoli which would allow air to enter the space from the visceral aspect or by external trauma to the chest which would allow air to enter from the parietal aspect [5]. Traumatic pneumothorax can be caused by a variety of mechanisms such as blunt trauma, penetrating injury, and iatrogenic causes such as biopsy procedures, central venous catheterization, thoracentesis, perforation due to feeding tube, and mechanical ventilation.

On chest radiograph, the visceral white line is visible, along with peripheral lack of lung markings (Figs. 24.1 and 24.2). Although pneumothorax is often accentuated on expiratory film, the British Thoracic Society does not recommend its routine. A lateral radiograph should be performed if the frontal view is negative for pneumothorax and there is

---

The original version of this chapter was revised. An erratum to this chapter can be found at https://doi.org/10.1007/978-3-319-65397-6_27. An erratum to this publication is available online at https://doi.org/10.1007/978-3-319-65397-6_27

N. Patel
University of Tennessee Health Science Center,
Memphis, TN, USA

M. Mansouri
Department of Radiology, Massachusetts General Hospital,
Boston, MA, USA

S. Shankar
Department of Radiology, Regional One Health Hospital,
University of Tennessee, Memphis, TN, USA
e-mail: sshankar@uthsc.edu

A. Singh (✉)
Division of Emergency Radiology, Department of Radiology,
Massachusetts General Hospital, Boston, MA, USA

Harvard Medical School, Massachusetts General Hospital,
Boston, MA, USA
e-mail: asingh1@partners.org

© The Author(s), under exclusive license to Springer Nature Switzerland AG 2024
A. Singh (ed.), *Emergency Radiology*, https://doi.org/10.1007/978-3-031-65770-2_24

high clinical suspicion of pneumothorax. The air in the pleural space tends to accumulate anteromedially on supine radiograph. A 2 cm or more rim of air is equivalent to approximately 50% of the hemithorax. Deep sulcus sign refers to the presence of air lucency between diaphragm and spine, resulting in prominence of costodiaphragmatic space. Tension pneumothorax is characterized by progressive flattening of the ipsilateral diaphragm and shift of mediastinum to the opposite side. CT is the gold standard modality to detect pneumothorax and can be used in uncertain cases.

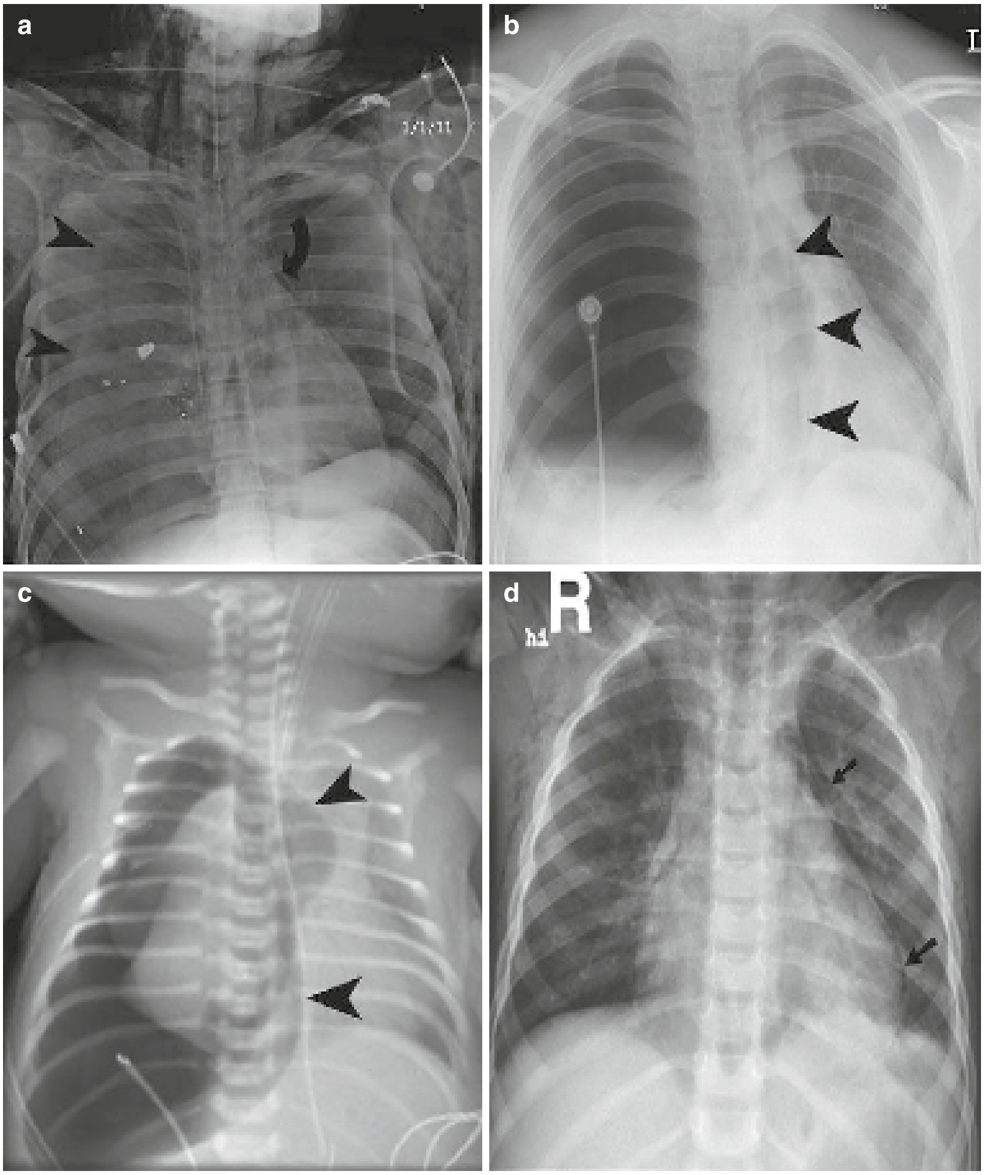

Fig. 24.1 (**a**) Pneumomediastinum and pneumothorax. Single frontal chest radiograph from a trauma patient after a gunshot wound reveals air between the epicardium and the pleura on the *left* (*curved arrow*). Pneumothorax on the *right* with collapsed lateral lung margin (*arrowheads*) and loss of peripheral lung markings. The ballistic fragment can be seen within the right mid-lung. Extensive subcutaneous emphysema is present. (**b**) Tension pneumothorax. Frontal radiograph shows relative lucency and loss of lung markings within the right hemithorax with shift of mediastinum to the *left*. The medial margin of the right tension pneumothorax is seen crossing the midline (*arrowheads*). (**c**) Tension pneumothorax. In this pediatric patient, there is a large lucency in the right hemithorax with loss of lung markings. There is associated shift of the mediastinal structures, including the heart to the *left*. Medial margin of the enlarged pleural cavity crosses the midline (*arrowheads*). (**d**) Pneumomediastinum. Frontal radiograph shows air outlining the heart (*arrows*) as well as extensive subcutaneous emphysema. (**e**) Pneumomediastinum and pneumopericardium. Frontal radiograph reveals are outline structures in the upper mediastinum outlined by air (*black arrow*). Pneumopericardium is best seen outlining the left ventricle (*white arrow*). (**f**) Pneumomediastinum. Lateral radiograph shows the pneumomediastinum (*arrow*) as a large lucent area posterior to the sternum and surrounding the heart

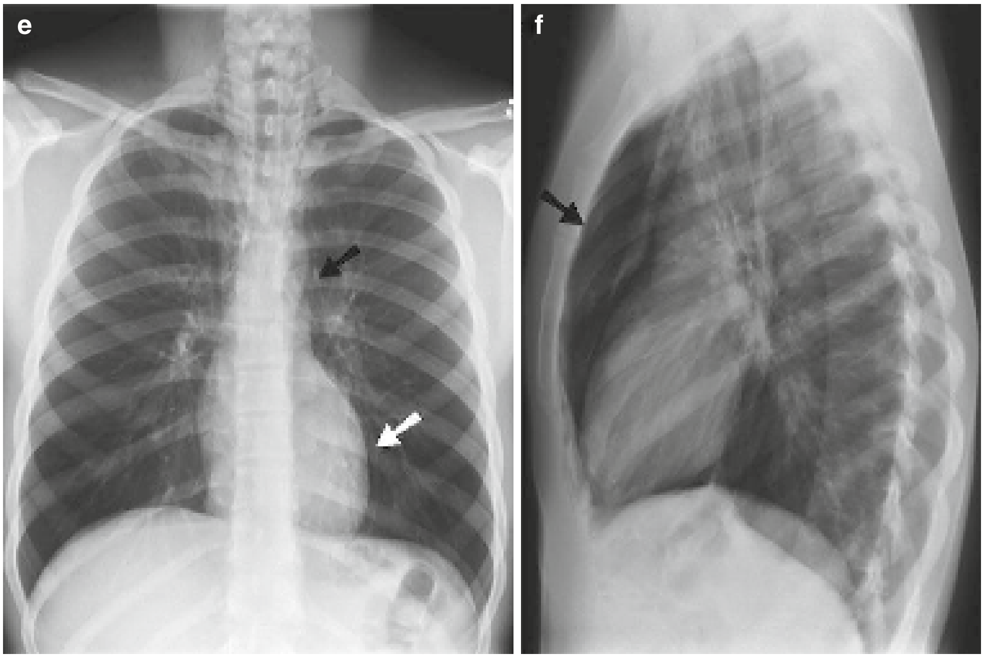

Fig. 24.1 (continued)

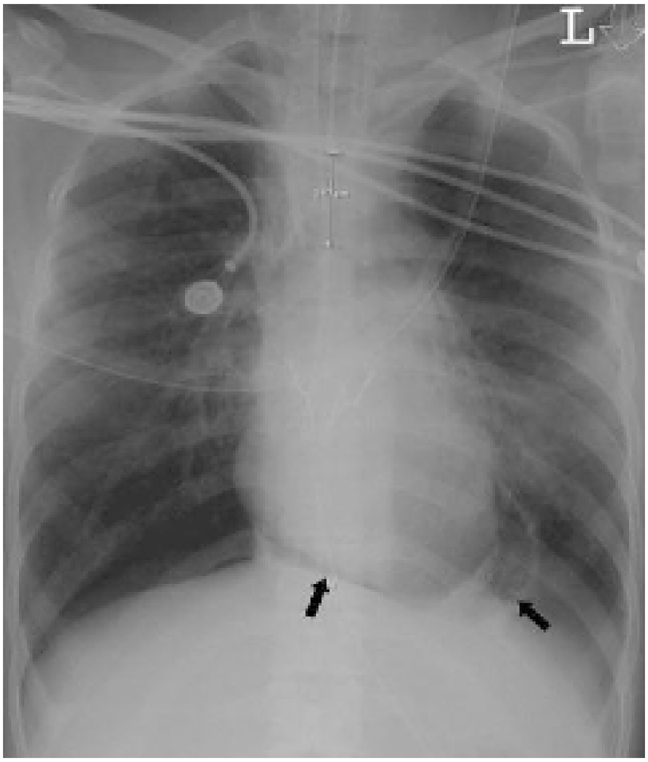

Fig. 24.2 Pneumopericardium. Chest radiograph demonstrates air (*arrows*) outlining the pericardium in a patient with history of penetrating trauma

Ultrasonography can also be used to accurately diagnose the pneumothorax. It is reported to be more sensitive, equally specific and faster compared with radiographs. Both of the following two signs in ultrasonography should be absent to establish the diagnosis of pneumothorax:

- The lung sliding sign: the sliding motion of the visceral pleura.
- Comet tail artifact: artifact from pleural line which radiates to the edge of screen.

The early diagnosis of a small pneumothorax can become clinically important especially if the patient is going to be mechanically ventilated as this can expand the pleural space leading to greater mass effect and mediastinal shift. This, in turn, can cause decreased blood return to the heart more likely from the loss of negative intrapleural pressure rather than the presence of positive intrapleural pressure [6]. Large, symptomatic pneumothoraces are usually treated with chest tube (24 Fr) or smaller caliber image-guided catheter (6–12 F). Smaller pneumothorax may be conservatively monitored with serial radiographs, provided the patient is not breathless. If the patient is breathless, a chest tube or catheter drainage should be performed irrespective of the size of pneumothorax.

Hemothorax

When blood fills the pleural space, a hemothorax results and occurs in approximately 50% of major thoracic trauma victims [7]. Blood may originate from injury to the lung, chest wall, heart, great vessels, or abdominal organs. Although

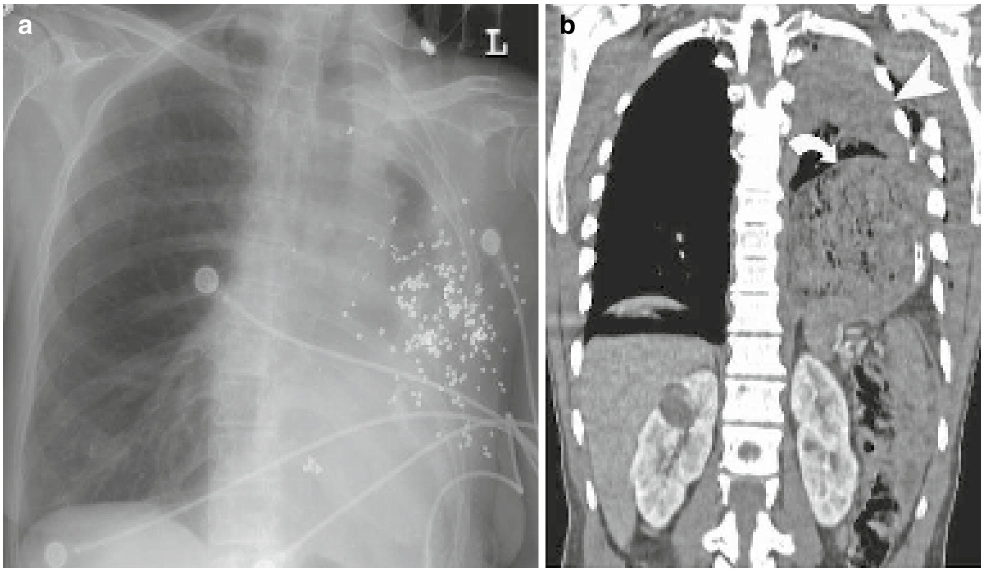

Fig. 24.3 (**a**) Hemothorax after gunshot injury. Frontal radiograph shows multiple shotgun pellets within the left hemithorax and a large hemorrhagic left pleural fluid collection. (**b**) Hemothorax and diaphragmatic rupture. Coronal CT reformation demonstrates left hemothorax (*arrowhead*) with left rib fractures and left diaphragmatic hernia (*curved arrow*)

bleeding from venous structures is often self-limiting secondary to the low pressure, hemorrhage from high-pressure arterial sources such as the internal mammary, intercostal, or subclavian arteries can cause rapid mass effect on the mediastinum.

CT can accurately identify a small hemothorax more readily than plain radiographs. On plain radiographs, the density of the pleural fluid is difficult to determine but with the use of CT, a density of 30–70 HU suggests blood with >90 HU indicative of acute blood (Fig. 24.3) [6]. Of note, hemorrhage of extrapleural origin is usually associated with rib fractures.

Injuries to the Lung Parenchyma

Pulmonary Contusion

Pulmonary contusion is seen in 17%–70% of trauma patients and represents the most common injury to the lung parenchyma [8]. Contusions result from the direct transmission of energy through adjacent solid structures and thus are usually found along the ribs, sternum, and vertebral bodies. They may be unilateral or bilateral, focal, multifocal, or diffuse depending on the mechanism of injury. Pathologically, the opacification of the lung is caused by hemorrhage and edema filling the alveoli which originates from damage and resultant leak from the alveolar-capillary membrane [9]. Radiographically, this is seen as peripheral focal ground-glass opacities or patchy consolidative opacities ("traumatic pneumonia") that are distributed along a bronchopulmonary segmental anatomy (Fig. 24.4a) [6]. Radiographic findings disappear within few days.

Plain radiograph tends to underestimate the size of pulmonary contusion and lag behind the clinical presentation by up to 6 h. Increase in the size of lung contusion on radiography is a negative prognostic factor. The appearance of pulmonary opacities >24 h after initial injury should suggest other possible diagnoses like pneumonia or fat embolism [7]. Resolution of contusions is within 24–48 h and is complete between 3 and 10 days. Patients with contusions visible on both CT and radiography have worse prognosis compared with cases visible on CT alone.

Pulmonary Laceration

Pulmonary lacerations are less common than contusions and result from disruption of the lung parenchyma, most commonly from penetrating trauma. The result is formation of a cavity within the lung as the surrounding parenchyma pulls back from the laceration itself (Fig. 24.4b, c). Because of this, they are more common in younger patients who have more optimal lung elasticity [10].

The formed cavity from the laceration may contain air, blood, or a combination of the two and the terms pneumatocele, hematocele, and hematopneumocele correlate to the contents of the cavity.

CT is more sensitive than radiograph in the evaluation of pulmonary laceration. Pulmonary lacerations are usually more difficult to diagnose on plain radiographs, often due to the presence of surrounding contusion. They become more apparent as the densities from contusion clears up. The pulmonary laceration classification by Wagner et al. is based on the mode of injury and the imaging indication (Table 24.1).

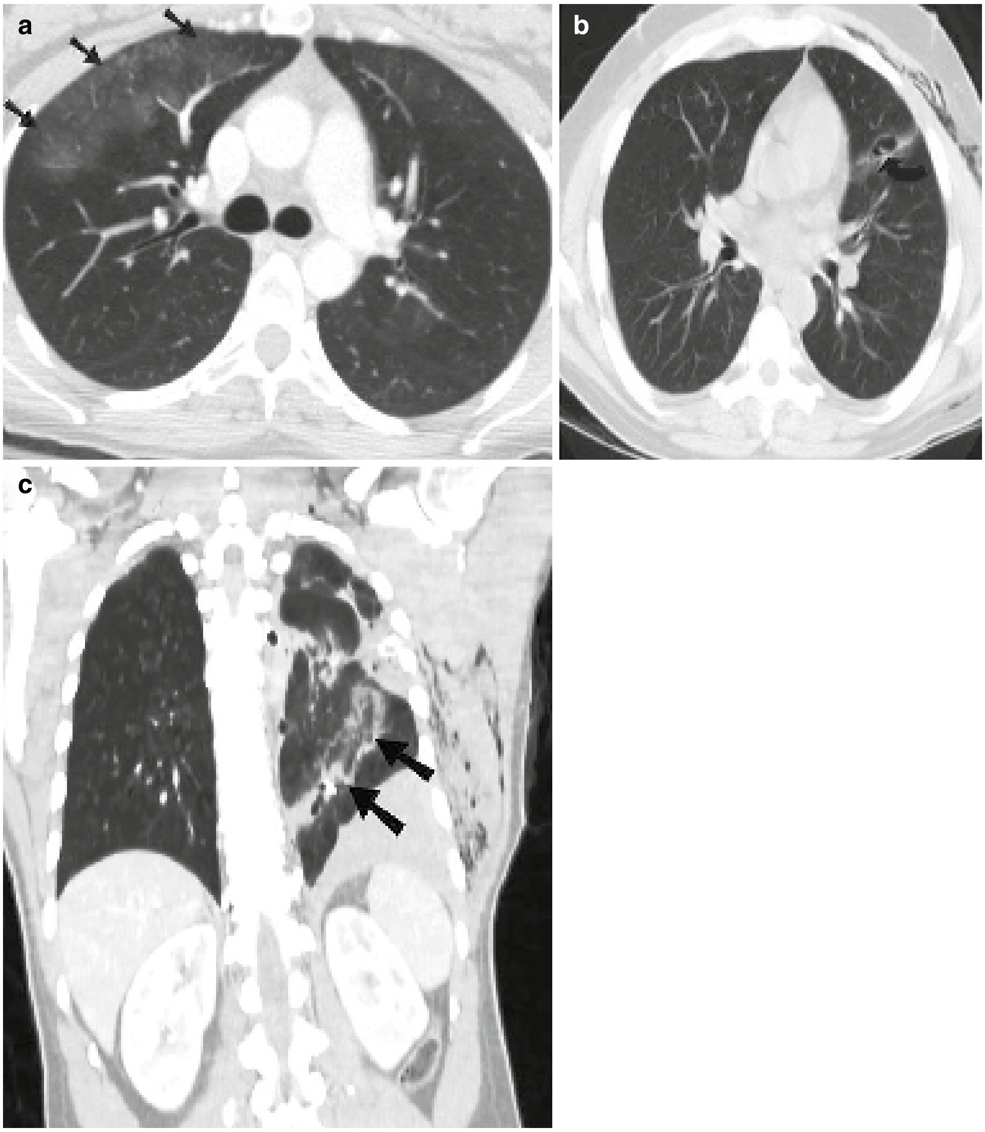

Fig. 24.4 (**a**) Pulmonary contusion. Axial CT shows non-segmental distribution of ground-glass opacification (*arrows*) in the right upper lobe, indicative of contusion. (**b**) Pneumatocele. Axial CT shows a pneumatocele (*curved arrow*) with adjacent hemorrhage in this patient who suffered a knife stab injury to the left anterior chest wall. The cavity is formed due to retraction of the edges of the lacerated lung. (**c**) Lung laceration. Coronal CT shows the linear pulmonary laceration (*arrows*) following the bullet path through the left lung as a central lucent area with adjacent hemorrhage. Subcutaneous emphysema is also present

Table 24.1 Classification of pulmonary laceration

Type 1	They are the most common laceration and are seen within the deep lung parenchyma. They tend to be large and result from direct compressive force to the lung
Type 2	They occur in paraspinal region and are caused by a sudden blow to the lower thorax, resulting in shift of the lower lobes across the spine
Type 3	They occur when the lung is torn by penetrating ribs and are thus usually seen in the lung periphery
Type 4	It occurs when the lung tears away from an adhesion

Traumatic Lung Herniation

A segment of the peripheral lung rarely can herniate outside the confines of the thoracic cavity either as the result of blunt or penetrating thoracic trauma. The anterior thorax is often the site of herniation because of a general lack of support (Fig. 24.5). Surgical reduction of intercostal lung hernia is recommended because of the potential for incarceration or strangulation. This potential risk is much greater in mechanically ventilated patients.

Injuries to the Airways

Injury to the tracheobronchial tree is rarely seen in clinical practice because up to 78% of the patients die before arriving at the hospital [10]. The majority of these cases occur during deceleration when the airways may be compressed against the sternum or spine or when elevated thoracic pressure from

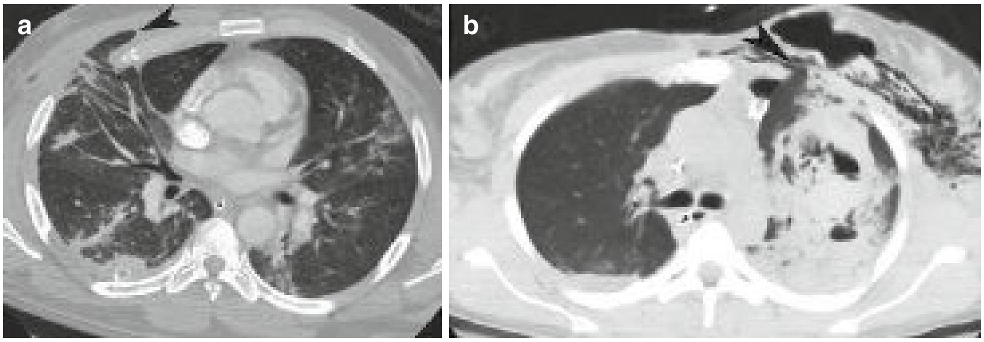

Fig. 24.5 (**a**) Lung herniation. Axial CT shows anterior herniation (*arrowhead*) of a portion of the right upper lobe, between consecutive ribs. An area of ground-glass density likely representing pulmonary contusion can be seen in the posterior left upper lobe. A chest tube is noted in the posterior right hemithorax. (**b**) Lung herniation. Axial CT shows herniation (*arrowhead*) of the medial portion of the left upper lobe into the adjacent anterior chest wall. Subcutaneous emphysema, pulmonary hemorrhage, and a pneumatocele are also present on the *right side*. There is a small left anterior pneumothorax present

compression occurs in the setting of a closed glottis. Anatomically, the thoracic trachea is more commonly affected than the cervical trachea and the right main stem bronchus is more commonly injured than the left. CT is an important tool for early diagnosis as up to 68% of injuries are not accurately diagnosed [11].

Clinically, these patients may present with respiratory distress, cough, and hemoptysis among other symptoms. These symptoms are more common in the setting of bronchial injuries as opposed to tracheal injuries.

Bronchial lacerations are more common than tracheal lacerations because the bronchial walls are not as strong as the tracheal walls. The common imaging manifestations of bronchial injuries include pneumomediastinum and pneumothorax, and bronchial lacerations should be considered when a pneumothorax persists even in the presence of a chest tube and suction. The “fallen lung” sign is seen when bronchial lacerations cause the ipsilateral lung to fall away from the hilum. This sign represents the most specific radiographic sign for tracheobronchial rupture [6].

Tracheal lacerations usually occur at the junction of the cartilaginous and membranous portions. Pneumomediastinum is the most common finding in the setting of tracheal lacerations (Fig. 24.6 and Table 24.2).

The Macklin effect, which can be seen in up to 40% of blunt chest trauma patients, involves alveolar rupture, with air dissection along the bronchovascular sheaths and spreading into the mediastinum. In 70%–100% of cases, overdistention or herniation of an endotracheal balloon reveals tracheal laceration [7]. Tracheal laceration should always be emergently confirmed with laryngoscopy or fiberoptic bronchoscopy. The potential complications include airway obstruction, pneumonia, bronchiectasis, abscess, and empyema.

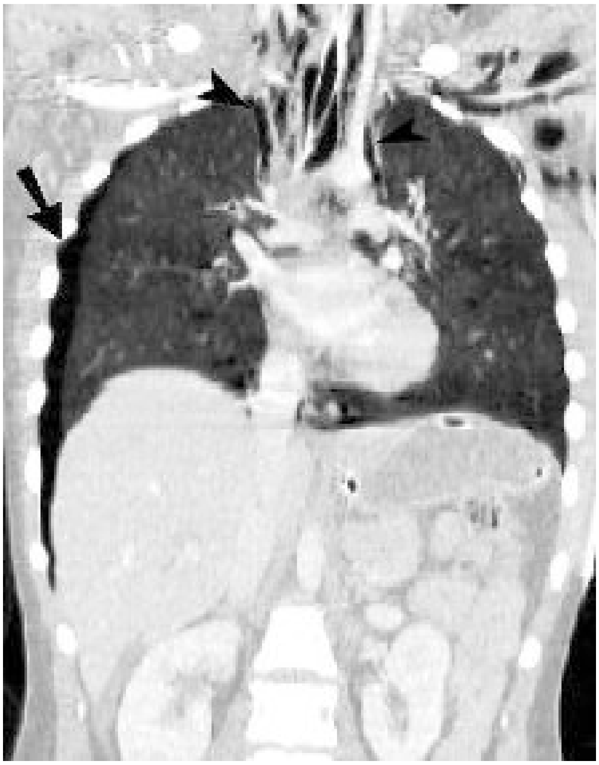

Fig. 24.6 Tracheal laceration. Chest coronal reformation in a patient with tracheal laceration demonstrates pneumothorax (*arrow*) and pneumomediastinum (*arrowheads*)

Table 24.2 Airway injuries

Bronchial lacerations	More common
	Associated with pneumomediastinum and pneumothorax
	Fallen lung sign: ipsilateral lung to fall away from the hilum; very specific
Tracheal lacerations	At the junction of cartilaginous and membranous portions
	Associated with pneumomediastinum

Cardiac Injuries

Injuries to the heart usually result from motor vehicle collisions and may range from cardiac contusion to frank rupture of the heart. Some of the earliest signs of injury are an abnormal EKG or elevated cardiac enzymes. Chest wall contusions or fractured ribs suggest adequate force to cause cardiac injury. Many of these patients are cardiovascularly asymptomatic, especially those with myocardial contusions and small pericardial tears. Pericardial tears are usually due to direct trauma or from increased intra-abdominal pressure. The most common site of pericardial injury is the left side of the pericardium, parallel to the phrenic nerve [12].

The imaging findings may include contrast material extravasation into the pericardium/mediastinum or pneumomediastinum. The patients with penetrating trauma may present with pneumopericardium (Fig. 24.7). Injury to the valves and chambers typically occur in the patients with preexisting cardiac disease. The right chambers are more commonly involved, and the aortic and mitral valves are the most commonly injured valves [12].

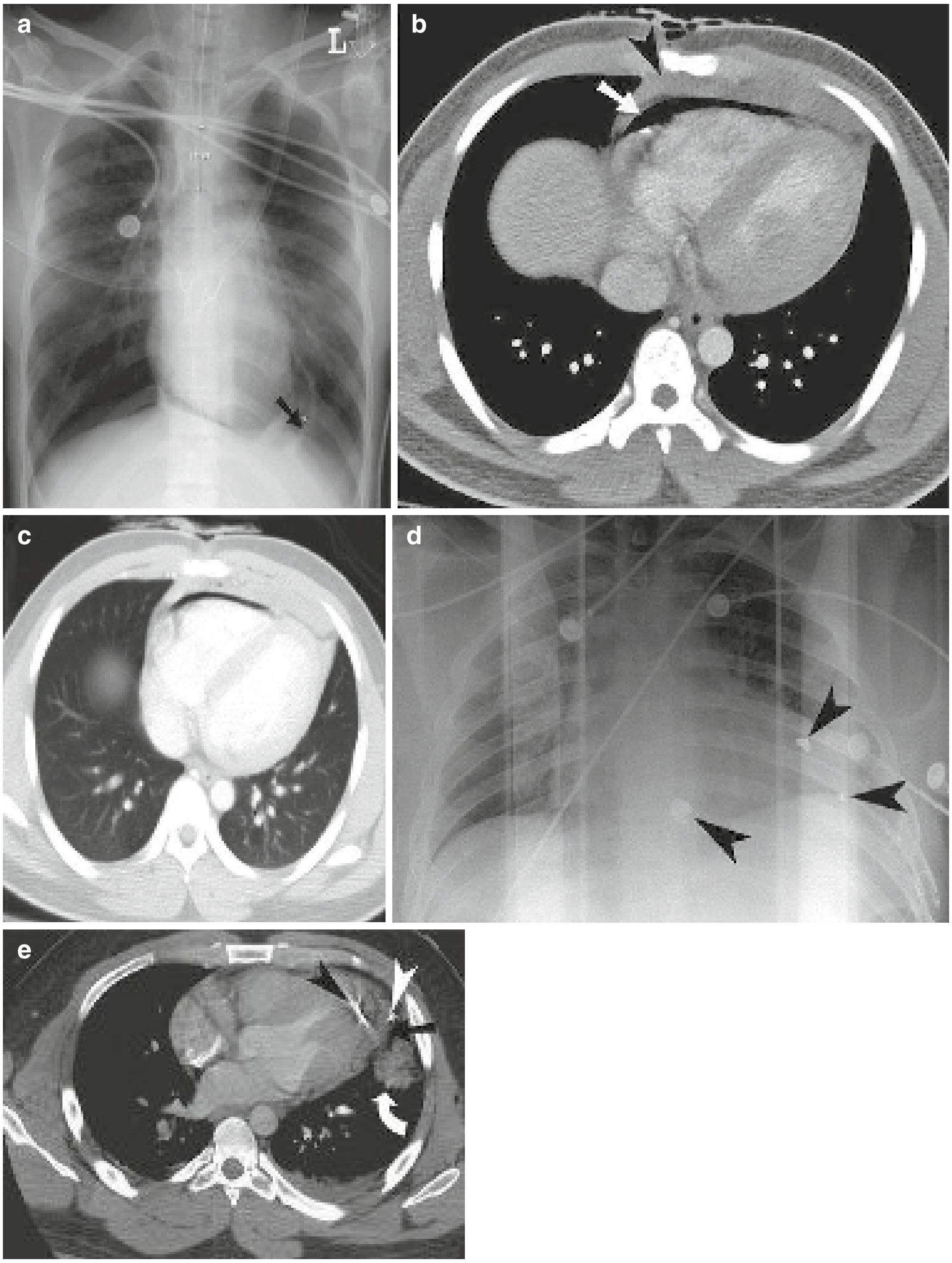

Fig. 24.7 (**a**) Pneumopericardium. Frontal radiograph shows air around the ventricles and displacing the parietal pericardium (*arrow*). (**b**, **c**) Pneumopericardium. Contrast-enhanced axial CT in a 16-year-old male stab victim shows air outlining the right ventricle (*arrow*) with retrosteral hemorrhage (*arrowhead*). (**d**) Cardiac injury from gunshot wound. Frontal chest radiograph shows three bullet fragments (*arrowheads*) overlying the cardiopericardial silhouette. (**e**) Hemopericardium. Axial contrast-enhanced CT shows a high-density pericardial effusion representing hemopericardium (*arrow*) in this gunshot wound patient. Bullet fragments can be seen in the left ventricle wall (*black arrowhead*) and pericardial space (*white arrowhead*). Adjacent pulmonary hemorrhage (*curved white arrow*) is also identified

Aortic Injury

The danger of rapid exsanguination remains a constant risk among patients who initially survive traumatic aortic injury. With progressively rapid transport to trauma centers, there are an increasing number of patients with aortic injury making it to the emergency department alive [13]. The most common theory proposed for aortic injury suggests that aortic injury is a combination of rapid decelerations and compression, producing rotational and shearing forces as well as transverse laceration at the vulnerable portions of the aorta [8]. Thoracic aorta injuries typically occur at the sites of aortic attachment, including (in descending order of frequency) the proximal descending aorta, aortic arch, aortic root, and distal descending aorta at the aortic hiatus.

Chest radiograph is usually the first imaging modality used in traumatic aortic injury. Mediastinal widening is defined by width >8 cm at the level of subclavian artery origin on AP view or a mediastinum to chest width ratio of >0.25. Widening of superior mediastinum has a high sensitivity (81%–100%) but low specificity (34%–60%) in detecting aortic injury. Mediastinal widening due to aortic injury usually involves the left paratracheal region or the entire superior mediastinum. Other radiographic findings which should raise suspicion about aortic injury include: indistinct aortic contour, loss of aorticopulmonary window, lower left mainstem bronchus, tracheal deviation, deviation of the nasogastric tube, first rib fracture, and increased density of the left subclavian artery reflection.

Contrast CT angiogram involves the IV administration of 120–150 mL of contrast at 5 mL/s followed by the initiation of the scan when the density in the descending thoracic aorta is at least 150 HU. The study should assess the presence, location, and extent of the mediastinal hemorrhage and aortic injury as well as any injury to adjacent vessels. Periaortic hematoma formation from rupture of the vasa vasorum can be seen on CT but is not always present. CT may also diagnose associated pseudoaneurysms, changes in the aortic contour or diameter, intimal flap consistent with dissection, thrombus, and active extravasation (Fig. 24.8). The aortic contour is often distorted by tearing of the wall and compression from the adjacent pseudoaneurysm or hematoma.

In most cases, the aortic injury presents as a pseudoaneurysm that projects anteriorly or anteromedially from the aortic lumen at the level of the left pulmonary artery. In addition, there is typically a surrounding collar of mediastinal blood [7].

Active extravasation is seen radiographically as any area of contrast outside the vascular lumen. If active extravasation is present, angiography is the next step to try and control the bleeding via coiling or other interventional methods.

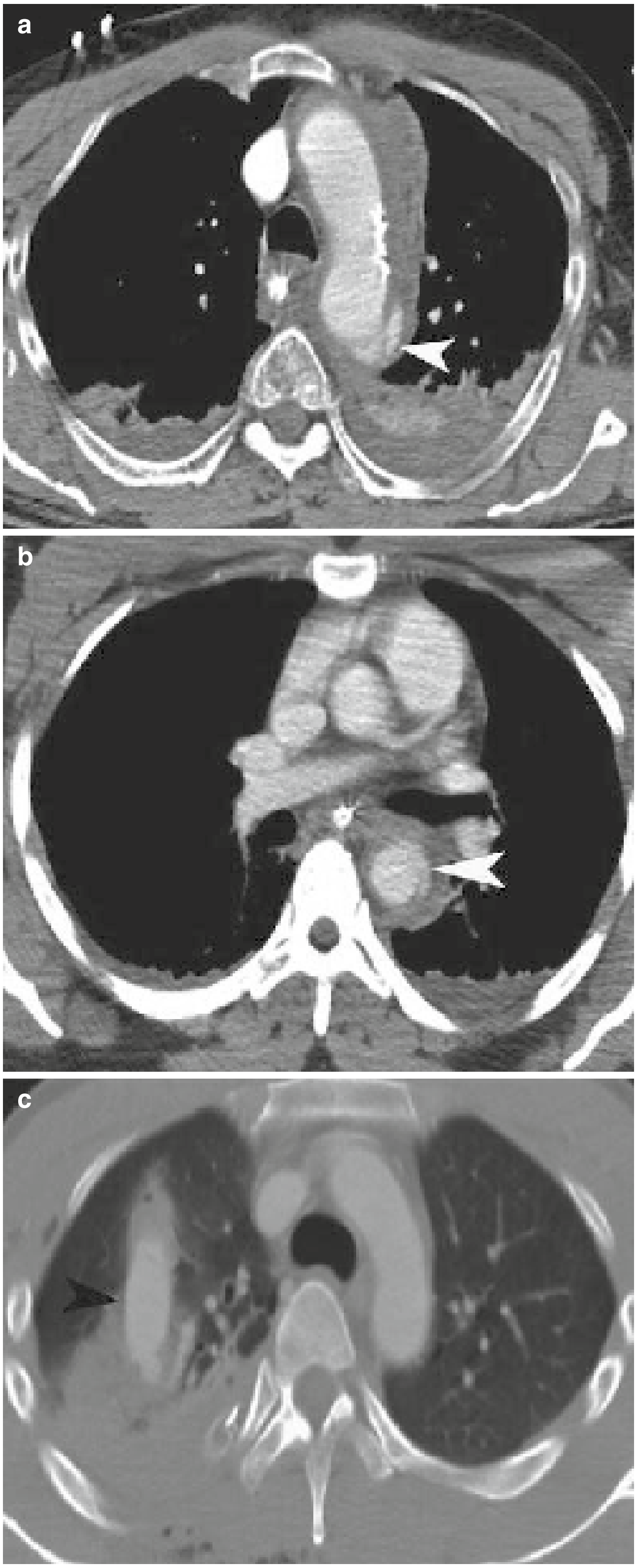

Fig. 24.8 (**a**) Aortic injury. Axial CT with contrast at the level of the aortic arch shows a focal extravasation of contrast (*arrowhead*) at the level of the posterior aortic arch with hemorrhage seen tracking anteriorly. (**b**) Aortic transection. Contrast-enhanced axial CT shows irregularity of the descending thoracic aorta with contrast leaking (*arrowhead*) outside the vessel. (**c**) Pseudoaneurysm of pulmonary artery branch in the right upper lobe. Axial CT shows a focal tubular contrast collection (*arrowhead*) with a saccular outpouching seen posteriorly

Transesophageal echocardiography (TEE) has sensitivity much lower than that of CT for the distal ascending aorta as well as the proximal aortic branches. TEE does offer a good alternative for patients who are too unstable to travel to the CT scanner [14]. Thoracic angiography is still commonly used because it has high sensitivity and specificity but relatively low morbidity. The major drawbacks of angiography include higher cost, invasiveness, and nonavailability in a timely fashion [7]. As a result, angiography is used for further investigation based on initial CT results.

Magnetic resonance imaging (MRI) is currently not commonly used in the everyday imaging of patients with suspected aortic injury because of its cost, difficulty in developing adequate protocols, and problems with having life support equipment in the presence of a strong magnetic field; rather, it is reserved for problem solving in difficult situations.

Injuries to the Diaphragm

Diaphragmatic Injury

Injuries to the diaphragm are uncommon with a prevalence of 0.16%–5% in trauma patients [7]. Injuries are most commonly caused by a sudden increase in intra-abdominal or intrathoracic pressure against a fixed diaphragm. Motor vehicle accidents are responsible for up to 90% of traumatic diaphragmatic injuries [15]. The left hemidiaphragm is more commonly injured compared to the right. Associated injury to the abdominal organs such as the spleen, kidneys, and liver are relatively common in trauma patients. In addition, coinciding thoracic injuries such as pneumothorax, hemothorax, and lung contusions are often seen. Displaced lower rib fractures should particularly increase the concern for possible left hemidiaphragm tears.

Table 24.3 CT findings in diaphragmatic rupture

1. Collar sign—The collar sign is produced by a waist-like constriction of herniated viscera at the site of herniation
2. Dependent viscera sign—The dependent viscera sign results from the abdominal viscera falling dependently against the posterior chest wall through the diaphragmatic tear
3. Diaphragmatic thickening due to hemorrhage
4. Peridiaphragmatic contrast material extravasation

Diagnosis of diaphragm injuries based on imaging can be difficult especially if herniation of abdominal contents is not present. Plain radiographs are normal or nonspecific in 25%–50% of cases [15]. Radiographic signs suggestive of rupture include elevation of the hemidiaphragm, distortion of diaphragmatic contour, and contralateral displacement of the heart and mediastinum. Presence of abdominal contents within the thorax is diagnostic for diaphragm rupture. CT is the mainstay for diagnosis because of its accuracy, speed, and cost (Table 24.3 and Figs. 24.9, 24.10, and 24.11). The sagittal and coronal reconstructions are especially valuable in diagnosing diaphragmatic rupture and should be carefully scrutinized in every trauma case. Other modalities used to augment diagnosis include ultrasound and MRI. Ultrasound is specifically helpful in evaluating the right hemidiaphragm as the liver acts as an acoustic window. On ultrasonography, the hyperechoic diaphragmatic line may be interrupted, edges of the diaphragm may be floating and visceral herniation may be seen.

In hemodynamically stable patients with inconclusive CT findings, MRI can be done. On T1-weighted images, the normal diaphragm is hypointense band surrounded by hyperintense abdominal and subpleural fat. Any discontinuity in diaphragm can be accurately detected on MRI.

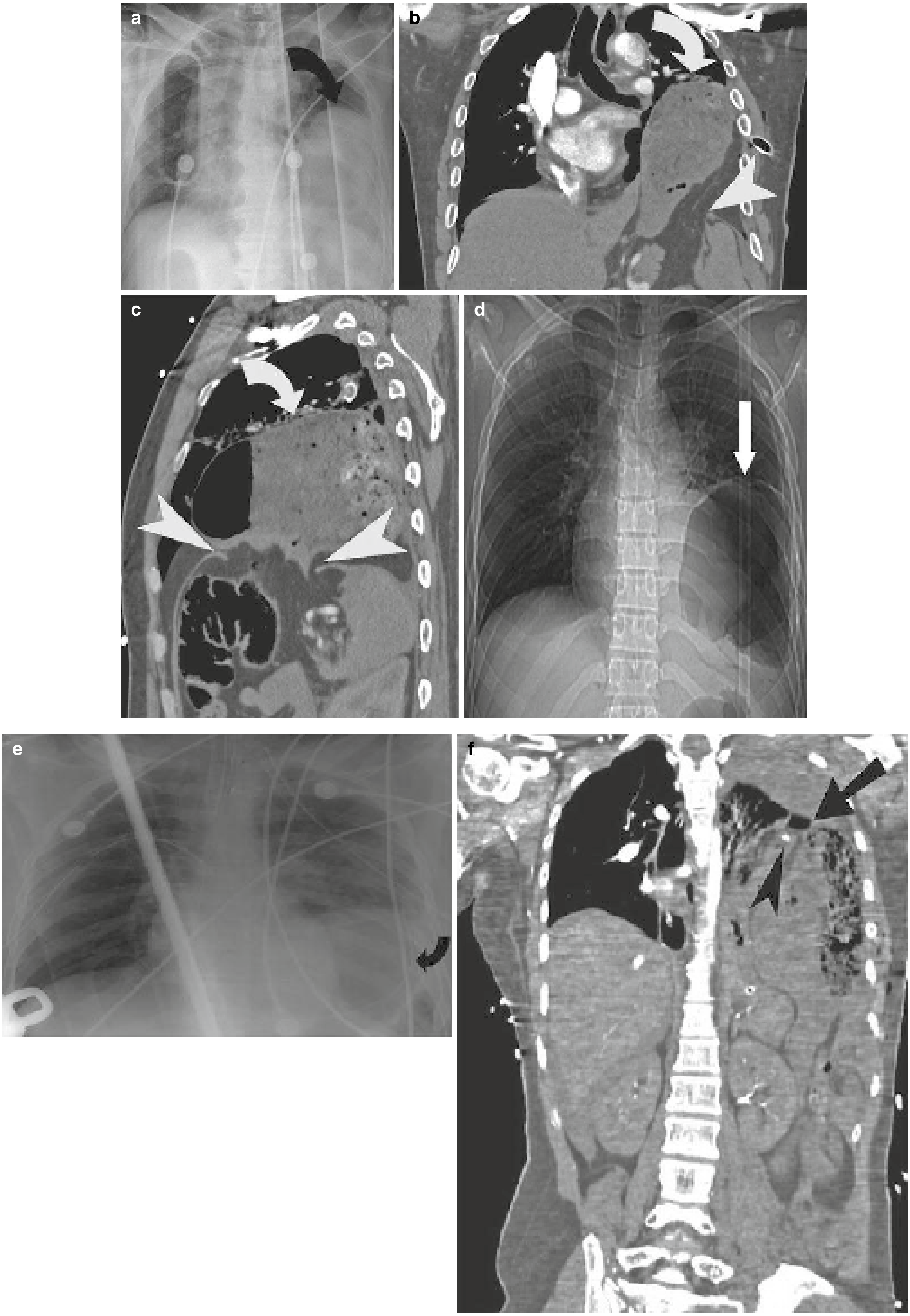
a
b
c
d
e
f

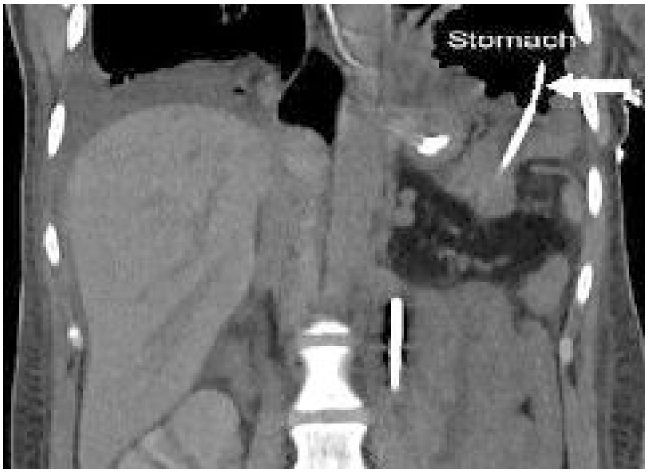

Fig. 24.10 Diaphragmatic injury. Contrast-enhanced CT demonstrates herniation of stomach into the left hemithorax. Nasogastric tube (*arrow*) is seen in the stomach

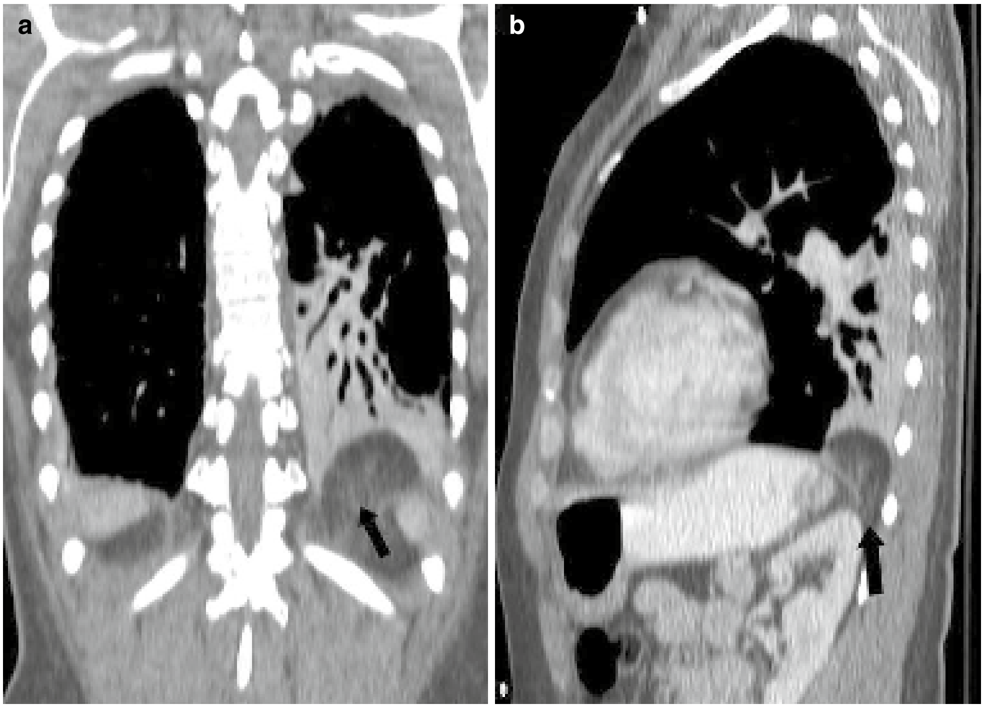

Fig. 24.11 Bochdalek hernia. CT demonstrates focal defect in the posteromedial left hemidiaphragm (*arrows*) with herniation of retroperitoneal fat on coronal (**a**) and sagittal (**b**) reformations

Fig. 24.9 (**a**) Diaphragmatic injury. Plain radiograph shows significantly elevated left hemidiaphragm (*curved arrow*) with elevation of gastric air bubble in a motor vehicle trauma victim. (**b**, **c**) Herniated stomach (*curved arrow*) is seen above the level of the diaphragm in this coronal-reformatted image. There is a large left diaphragmatic defect (*arrowhead*). (**d**) Chest CT scout film in a gunshot victim shows the gastric air bubble (*straight arrow*) well above the expected level of the left hemidiaphragm. (**e**) AP radiograph in a trauma patient demonstrates a raised left hemidiaphragm with bilateral chest tubes, and endotracheal and NG tubes (*curved arrow*) in place. (**f**) Coronal CT reformat in the same patient shows the large stomach herniation (*arrow*) through a diaphragmatic defect, bullet fragment (*arrowhead*), and left hemothorax

Injuries to the Chest Wall

Rib fractures are the most common skeletal injury in chest trauma and occur in approximately 50% of patients. While single rib fractures are rarely life threatening, multiple rib fractures have been associated with increased morbidity and mortality probably because of their coexistence with more severe thoracic injury [4]. Double fractures in three or more ribs can lead to “flail chest” and is clinically significant because it can impair respiratory mechanics, promote atelectasis, and impair pulmonary drainage. Fracture of the first three ribs is considered to be high-energy trauma because these ribs are well protected. Some common complications of rib fractures are pneumothorax, hemothorax, extrapleural hematoma, and lung contusions (Fig. 24.12).

Sternal fractures are usually the result of deceleration injuries or direct anterior chest trauma. Displaced sternal fractures and those with associated joint disruption frequently occur with cardiac and spinal injuries. Sternal fractures are best seen on sagittal CT images and should be suspected by the presence of an anterior mediastinal hemorrhage.

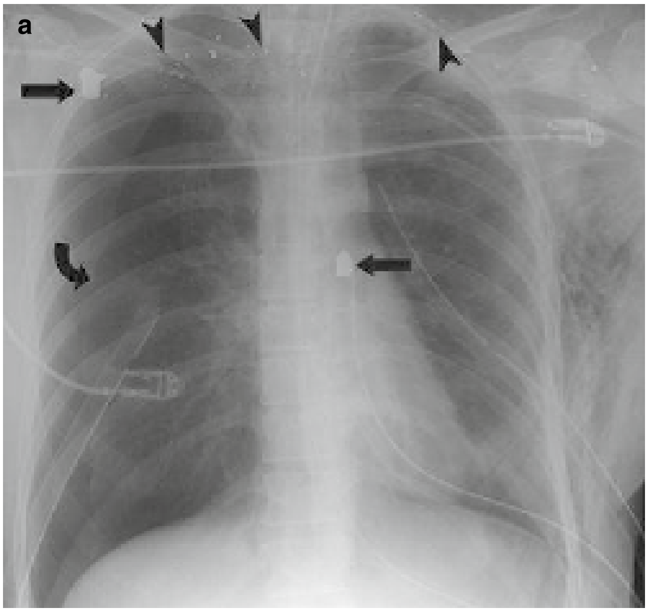

Fig. 24.12 (**a**) Gunshot injury to spinal canal. Right-sided pneumothorax (*curved arrow*) with chest tubes in place bilaterally. Bullets (*straight arrows*) are seen over the right upper chest and left paramediastinal locations. Small shrapnels (*arrowheads*) indicate the track of the bullet in the right and left upper chest. (**b**) Spinal cord injury. Axial CT scan in the same patient demonstrates shrapnels along the bullet track (*arrowheads*) passing through the spinal canal. Note also the pneumomediastinum, subcutaneous emphysema, endotracheal tube, and nasogastric tubes. (**c**) Gunshot injury to chest wall. Multiple shotgun pellets (*arrowheads*) are seen in the anterior chest wall and the pericardium

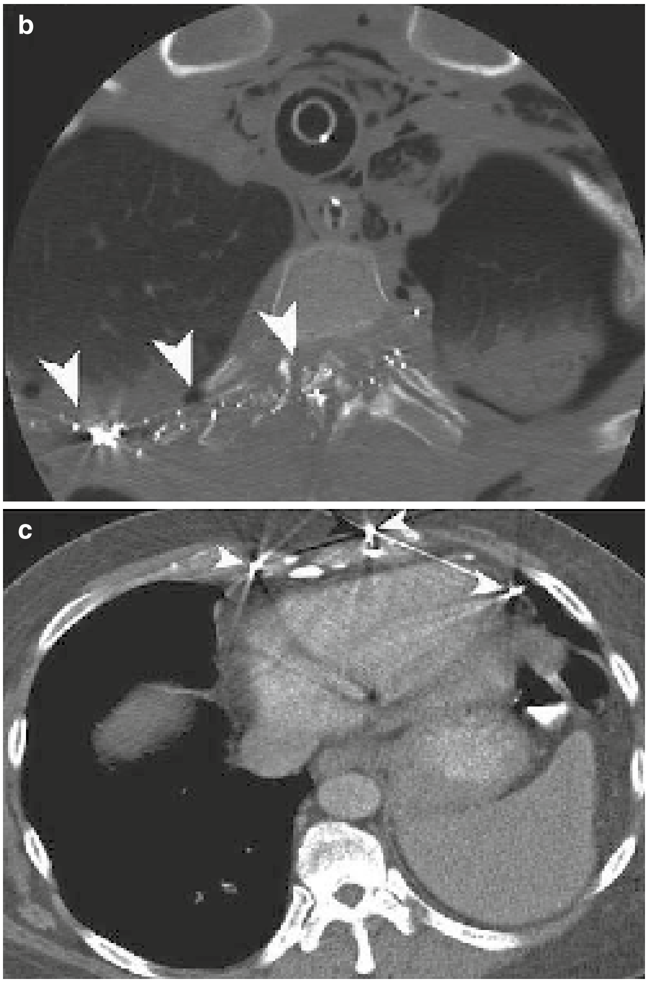

Fig. 24.12 (continued)

Sternoclavicular dislocations are not common but are clinically important because of injury to the mediastinal blood vessels, trachea, and esophagus secondary to posterior dislocations. Anterior dislocations usually result from anterior blows to the shoulders, for example, from a seat belt injury, and posterior dislocations result from posterior blows.

Injuries to the Esophagus

Injuries to the esophagus are much more common with penetrating thoracic trauma. Distal esophageal tears usually occur along the left side [6]. CT findings in the setting of esophageal rupture may include pneumomediastinum, mediastinitis, hydropneumothorax, or leakage of orally administered contrast into the mediastinal or pleural space (Fig. 24.13). Water-soluble contrast esophagram or flexible esophagoscopy is usually the next step in investigating esophageal rupture.

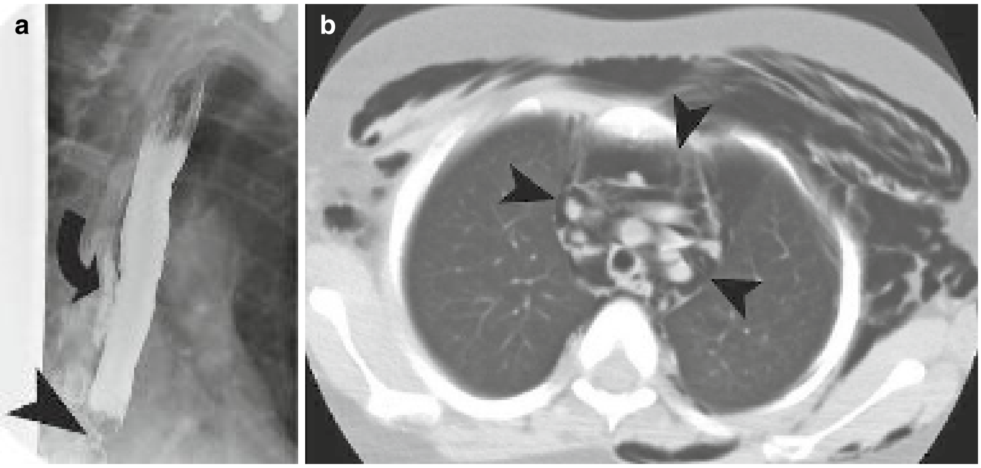

Fig. 24.13 (**a**) Esophageal perforation. Water-soluble contrast swallow demonstrates esophageal perforation in the mid posterior aspect of the esophagus (*curved arrow*) with impacted food located just proximal to a distal stricture (*arrowhead*). (**b**) Pneumomediastinum. Postcontrast axial CT demonstrates pneumomediastinum (*arrowheads*). Subcutaneous emphysema is present as well

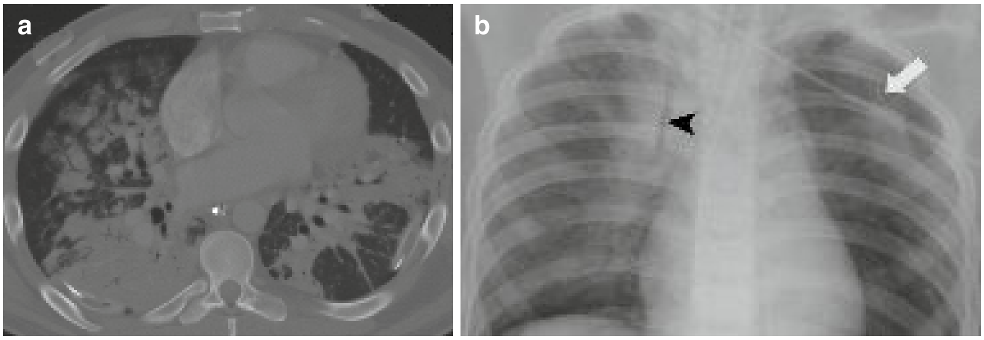

Fig. 24.14 Pulmonary barotrauma. (**a**) Axial CT of the lung demonstrates bilateral multifocal consolidation. There are bilateral chest tubes seen which were placed for the bilateral pneumothorax. The barotrauma in this patient was caused by an improvised explosive device. (**b**) Plain radiograph of the chest demonstrating left apical pneumothorax measuring 1 cm in thickness (arrow). Air space consolidation is seen medially in the right upper lobe which is marking the lateral margin of the pneumomediastinum (arrowhead). The barotrauma in this patient was caused by a gas explosion

Blast Injuries

Explosives can be categorized as high order explosives and low order explosives. Blast injuries can be subdivided into primary, secondary, tertiary, and quaternary based on the different mechanisms of injury infliction.

Primary blast injuries result from the effects of overpressure blast wave produced by the high order explosives. Air-filled organs and cavities, including ear, lungs, and gastrointestinal tract, are the most susceptible. Closed space explosions are associated with generation of an even stronger blast wave. Common primary blast injuries include tympanic membrane perforation, pulmonary barotrauma, rupture of globe of the eye, abdominal hemorrhage and perforation, and brain parenchymal injury (without any direct head injury). Pulmonary blast injuries account for 47% of the mortality in the immediate period following explosion and is the most common cause of death among the initial survivors. As the overpressure blast wave spreads through the pulmonary parenchyma, it disrupts the alveolar-capillary barrier resulting in alveolar hemorrhage and rupture. The lung-mediastinum *interface*, costophrenic angles, and peripheral lung regions at the intercostal spaces are the most susceptible sites for the injuries. The injuries include parenchymal hemorrhage, contusions, pneumothorax and subpleural cysts from alveolar rupture at peripheral lung, air embolism from traumatic alveolovenous fistulas, and lacerations (Fig. 24.14) [16]. Chest radiographs demonstrate bilateral, peri-hilar airspace opacities in the “batwing” or “butterfly” pattern.

Secondary blast injuries are produced by the bomb fragments and external debris that gets propelled by the blast wind of the explosion. Secondary injuries, major cause of mortality, are primarily associated with penetrating trauma which can affect any part of the body, often multiple. Blunt injuries, though less common, can also occur. Tertiary injuries are produced by the propulsion of individuals into the air and against solid objects by the strong blast wind, primarily resulting in blunt trauma. Tertiary injuries can include fractured bones, head injuries, traumatic injuries of chest, abdomen, and pelvis to name some. Quaternary blast injuries include all other explosion-related injuries that cannot be categorized as primary, secondary, or tertiary. Some examples include burn, inhalation, radiation, toxin, or environmental injuries [16].

Teaching Points

- Thoracic trauma continues to constitute a large percentage of life-threatening injuries in overall trauma patients, the number of which is on the rise.
- Because a variety and combination of injuries to the intrathoracic contents can lead to complications and possible death, efficient diagnosis is of the utmost importance.
- Multidetector CT remains the primary modality to quickly and accurately diagnose these injuries.
- CT has increased sensitivity over chest radiography and allows for a more complete analysis.

Questions

1. Which of the following is correct statement regarding diaphragmatic rupture?
   (A) On MRI of diaphragm, hyperintense band is surrounded by hypointense fat.
   (B) On CT, diaphragmatic thinning is a specific finding.
   (C) Diaphragmatic injuries usually occur on the right.
   (D) Dependent viscera sign results from the abdominal viscera falling dependently against the posterior chest wall through the diaphragmatic tear.
   Answer: D

2. Which of the following structure produces Comet tail artifact on ultrasonography in a patient with pneumothorax?
   (A) Pleura
   (B) Chest wall
   (C) Diaphragm
   (D) Lung
   Answer: A

3. What is the diagnosis based on the contrast-enhanced CT (Fig. 24.15) of a patient involved in motor vehicle collision?
   (A) Boerhaave’s syndrome
   (B) Diaphragm rupture
   (C) Tamponade
   (D) Aortic dissection
   Answer: B

4. What is the imaging diagnosis in the chest radiograph of a patient with acute chest pain after vomiting (Fig. 24.16)?
   (A) Aortic dissection
   (B) Pneumomediastinum
   (C) Tension pneumothorax
   (D) Pulmonary contusion
   Answer: B

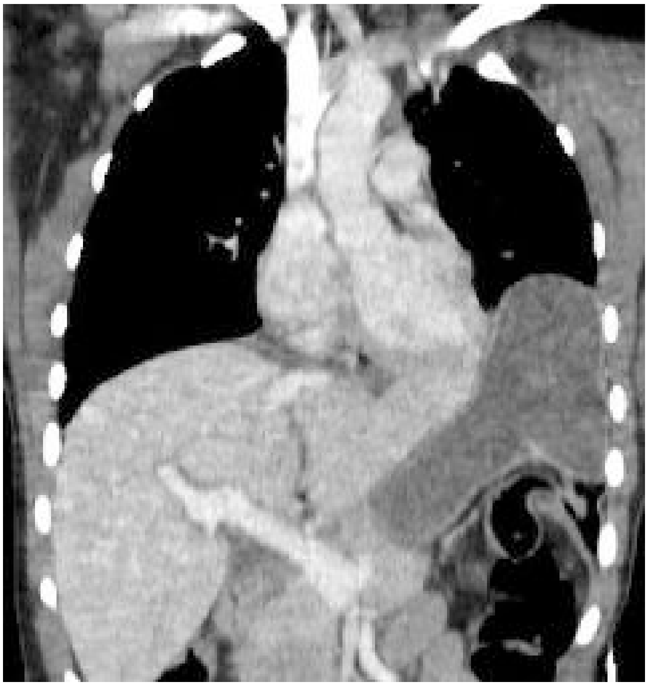

Fig. 24.15 Contrast-enhanced CT

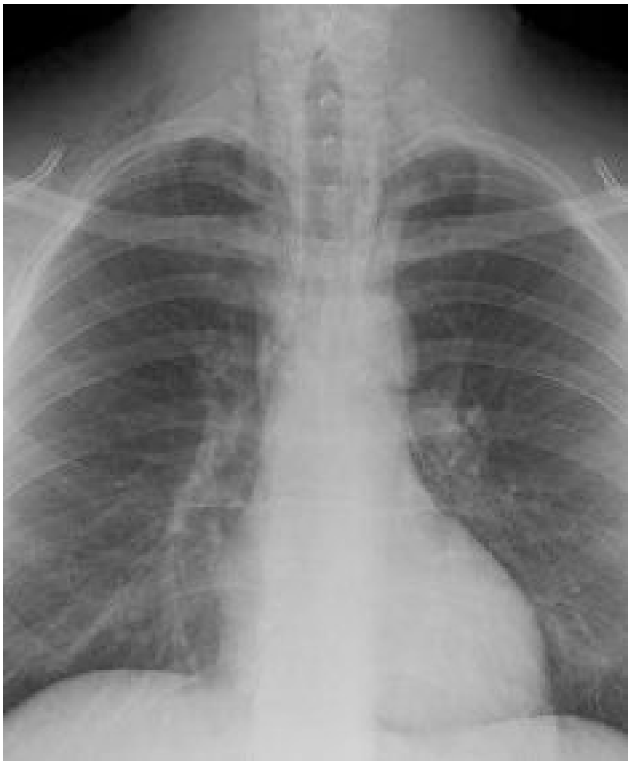

Fig. 24.16 Chest radiograph

5. What is the diagnosis based on the contrast-enhanced CT (Fig. 24.17) of patient with history of motor vehicle accident?
   (A) Tension pneumothorax
   (B) Pulmonary laceration
   (C) Pulmonary contusions
   (D) Bacterial pneumonia
   Answer: C

6. What is the diagnosis on the CT (Fig. 24.18) of a patient with history of motor vehicle collision?
   (A) Tension pneumothorax
   (B) Pulmonary contusion
   (C) Respiratory distress syndrome
   (D) Pulmonary laceration and pneumothorax
   Answer: D

7. On the chest radiograph (Fig. 24.19) of a patient with history of gunshot injury, what is the diagnosis which needs urgent communication?
   (A) Hemopericardium
   (B) Aortic rupture
   (C) Tension pneumothorax
   (D) Rib fractures
   Answer: C

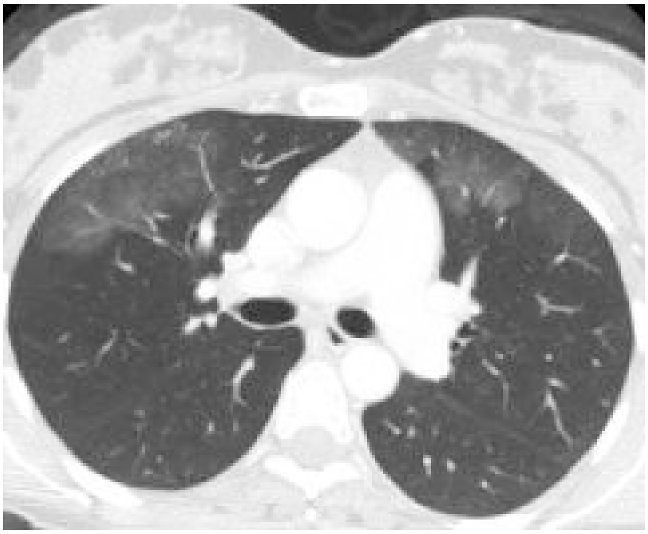

Fig. 24.17 Contusions CT scan

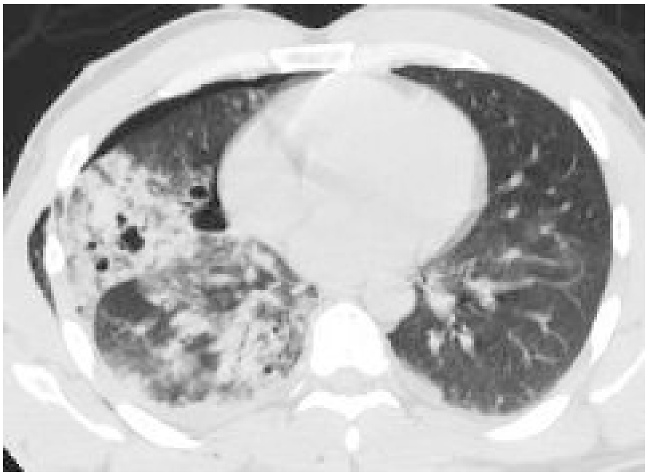

Fig. 24.18 Pulmonary laceration and pneumothorax

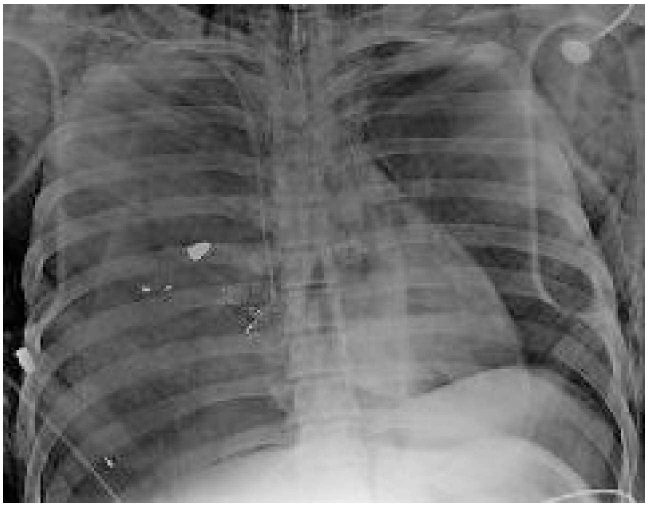

Fig. 24.19 Chest radiograph gunshot injury

References

1. The American College of Surgeons Committee on trauma leadership. In: Clark DE, Fantus RJ, editors. National Trauma Data Bank (NTDB) annual report 2007. Chicago: American College of Surgeons; 2007. pp. 1–64.
2. Report on injuries in America: all unintentional injuries; 2005. http://www.nsc.org/library/report_table_1.htm. Accessed 9 Dec 2007.
3. Omert L, Yeaney WW, Protetch J. Efficacy of thoracic computerized tomography in blunt chest trauma. Am Surg. 2001;67:660–4.
4. Livingston DH, Haurer CJ. Trauma to the chest wall and lung. In: Moore EE, Feliciano DV, Mattox KL, editors. Trauma. 5th ed. Philadelphia: McGraw-Hill; 2004. p. 507–37.
5. Miller LA. Chest wall, lung, and pleural space trauma. Radiol Clin North Am. 2006;44:213–24.
6. Kaewlai R, Avery LL, Asrani AV, Novelline RA. Multidetector CT of blunt thoracic trauma. Radiographics. 2008;28(6):1555–70.
7. Mirvis SE, Kathirkamanathan S. Imaging in trauma and critical care. 2nd ed. New York: Saunders; 2003. p. 297–367.
8. Wagner RB, Crawford WO Jr, Schimpf PP. Classification of parenchymal injuries of the lung. Radiology. 1988;167:77–82.
9. Green R. Lung alterations in thoracic trauma. J Thorac Imaging. 1987;2:1.
10. Goodman LR, Putman CE. The SICU chest radiograph after massive blunt trauma. Radiol Clin North Am. 1981;19:111.
11. Halttunen PE, Kostianen SA, Meurala HG. Bronchial rupture cause by chest trauma. Scand J Thorac Cardiovasc Surg. 1984;18:141.
12. Fulda G, Brathwaite CE, Rodriguez A, Turney SZ, Dunham CM, Cowley RA. Blunt traumatic rupture of the heart and pericardium: a ten-year experience (1979–1989). J Trauma. 1991;31:167–73.
13. Stark P. Traumatic ruptures of the thoracic aorta: a review. Crit Rev Diagn Imaging. 1984;21:221.
14. Read RA, Moore EE, Moore FA, Havernek EP, Veerakul G, Mestek M, et al. Intravascular ultrasonography for the diagnosis of traumatic aortic disruption: a case report. Surgery. 1993;114:624.
15. Kearney PA, Rouhana SW, Burney RE. Blunt rupture of the diaphragm: mechanism, diagnosis, and treatment. Ann Emerg Med. 1986;18:438.
16. Singh AK, Ditkofsky NG, York JD, et al. Blast injuries: from improvised explosive device blasts to the Boston Marathon bombing. Radiographics. 2016;36(1):295–307. https://doi.org/10.1148/rg.2016150114.

25

Imaging of Lines and Tubes

Ajay Singh, Mohammad Mansouri, and Chris Heinis

Introduction

The emergency room has evolved over the years, and the practice has become increasingly complicated, commonly turning them into mini ICUs. During rapid assessment and stabilization of the patients in acute setting, there is often a need to intubate the respiratory failure patients and provide intravenous fluid during resuscitation. With the growing volume of septic patients managed in the ED, central venous pressure monitoring has become more commonplace. This has led to the ED physicians placing more central line than ever. In this controlled chaos environment, the physicians are frequently exposed to anatomic variations which can lead to errors in line placement. Since image guidance is not routinely used during placement, the line or an endotracheal tube can be commonly malpositioned. However, we rely heavily on radiology to help confirm that the line or tube is where it should be without inadvertent damage to the surrounding tissue.

Endotracheal Tube

Once an endotracheal tube has been positioned, it is critical to evaluate its position on the chest radiograph. The endotracheal tube tip should be approximately 3–7 cm from the carina or at the level of the aortic arch. Flexion or extension of the chest can cause movement of the endotracheal tube by approximately 2–4 cm in either direction [1]. Ideally, when the neck is flexed, the endotracheal tube is 3 cm from the carina; conversely, when the neck is extended, the endotracheal tube should be 7 cm from the carina. Malpositioning [2] of the tube can occur in approximately 10%–20% of endotracheal intubations. Low placement of the endotracheal tube can cause bronchial intubation or carinal irritation. High placement of the tube can cause extubation, gastric distention, vocal cord injury, and ineffective ventilation. The carina is not always well seen on a portable radiograph of the chest. In these scenarios, other landmarks may be useful in determining the position of the endotracheal tube. In 95% of the cases (Fig. 25.1) [3], the positioning is proper when an endotracheal tube is 3.4–5 cm above the tangential line to the caudal edge of the aortic arch. Even when the carina is not visible, the endotracheal tube positioning can be confirmed if the tip ends at the level of T3 or T4 vertebral body. Goodman et al. found that carina projects over T5, T6, or T7 in 95% of the patients [1]. The endotracheal tube's diameter should be anywhere between one-half to two-thirds the width of the trachea. The radiolucency within the tracheal cuff should be confined to the lumen of the trachea, without distending it.

The original version of this chapter was revised. An erratum to this chapter can be found at https://doi.org/10.1007/978-3-319-65397-6_27. An erratum to this publication is available online at https://doi.org/10.1007/978-3-319-65397-6_27

A. Singh (✉)
Division of Emergency Radiology, Department of Radiology, Massachusetts General Hospital, Boston, MA, USA

Harvard Medical School, Massachusetts General Hospital, Boston, MA, USA
e-mail: asingh1@partners.org

M. Mansouri
Department of Radiology, Massachusetts General Hospital, Boston, MA, USA

C. Heinis
University of Massachusetts Memorial Medical Center, Worcester, MA, USA

© The Author(s), under exclusive license to Springer Nature Switzerland AG 2024
A. Singh (ed.), *Emergency Radiology*, https://doi.org/10.1007/978-3-031-65770-2_25

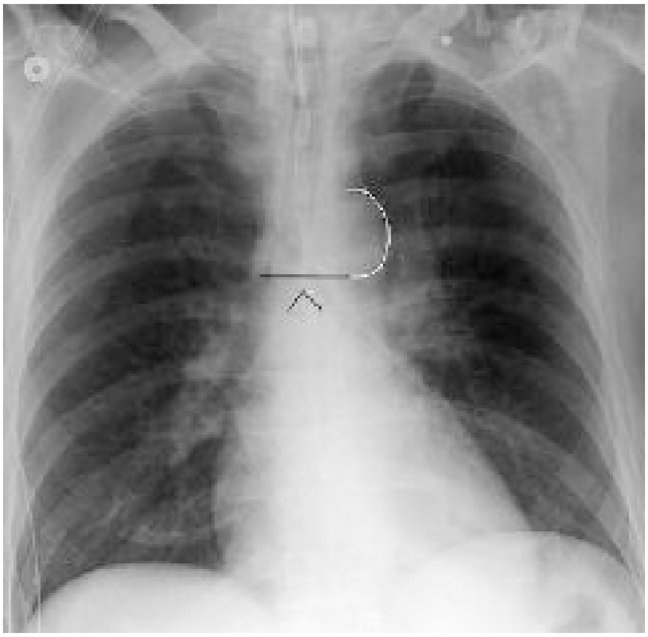

Fig. 25.1 Positioning of endotracheal tube when carina is obscured on a radiograph. Schematic representation of the left aortic arch outline which when extended horizontally at its inferior limit gives the landmark where the endotracheal tube should be placed. There is a nasogastric tube tip seen in the left bronchial tree

The radiographic findings of a right main stem bronchial intubation include hyperinflation of the right lung, atelectasis of the left lung, and atelectasis of the right upper lobe (with a right lower lobe intubation) (Fig. 25.2). Intubation of bronchus intermedius may cause right upper lobe atelectasis. Repositioning of the endotracheal tube in the trachea leads to rapid reexpansion of the collapsed lung in patients where inadvertent main stem bronchial incubation was performed.

Other complications of endotracheal intubation include pneumothorax, tracheal rupture, tracheal stenosis (secondary to ischemia), and esophageal intubation (Fig. 25.3). The balloon cuff of the endotracheal tube should fill but not distend the lumen of the trachea. The ratio of balloon cuff diameter to tracheal diameter of more than 150% is a predictor of tracheal damage [4]. Tracheal rupture typically occurs in the membranous posterior wall of the trachea, within 7 cm of the carina. Imaging findings are subcutaneous emphysema, pneumomediastinum, pneumothorax, overdistension of the endotracheal tube balloon, and reduced distance between balloon to the endotracheal tip (less than 1.3 cm; normal distance is 2.5 cm).

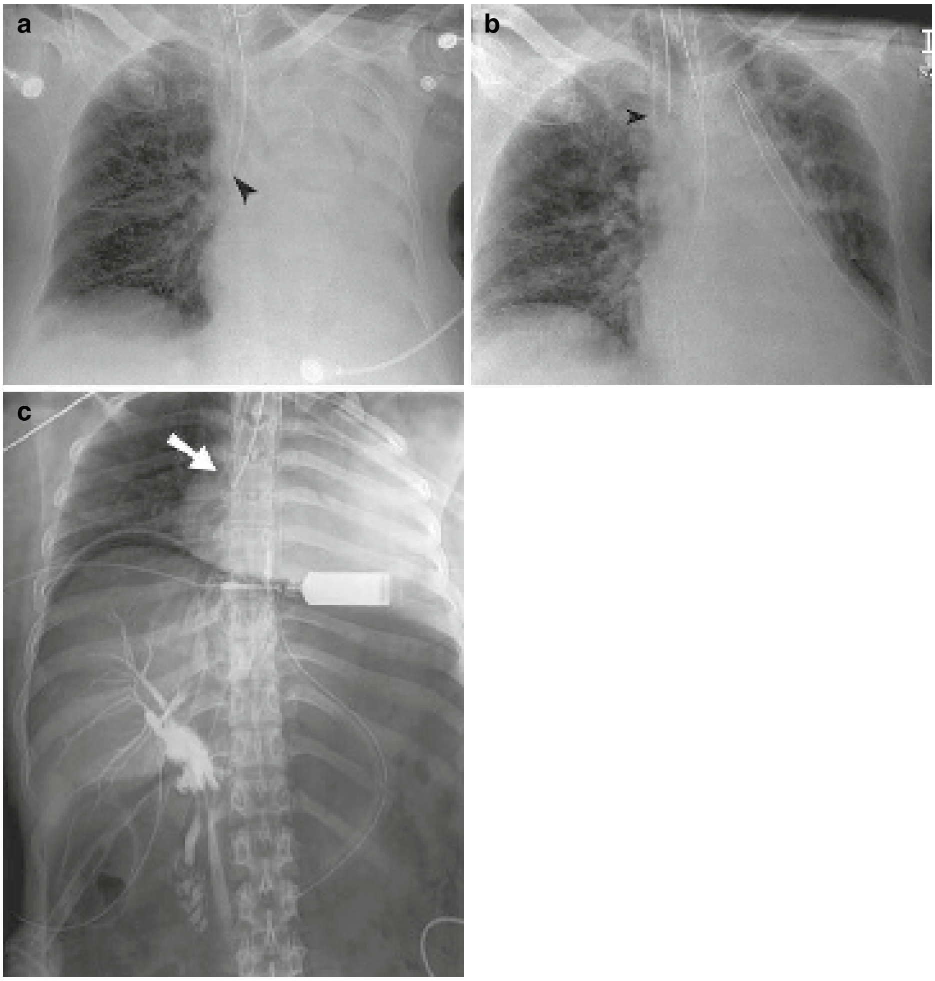

Fig. 25.2 Bronchial intubation. (**a**) Portable chest radiograph demonstrates the tip of the endotracheal tube (*arrowhead*) extending into the right main bronchus. There is lack of aeration in the left hemithorax with collapse of the left lung. (**b**) Follow-up chest X-ray after repositioning of the endotracheal tube into the trachea demonstrates reexpansion of the left lung. A left-sided chest tube was surgically placed based on the clinician's interpretation of the chest radiograph. (**c**) Intraoperative radiograph of the chest and abdomen, obtained during laparoscopic cholecystectomy, demonstrates right main bronchial intubation (*arrow*) with secondary collapse of the left lung

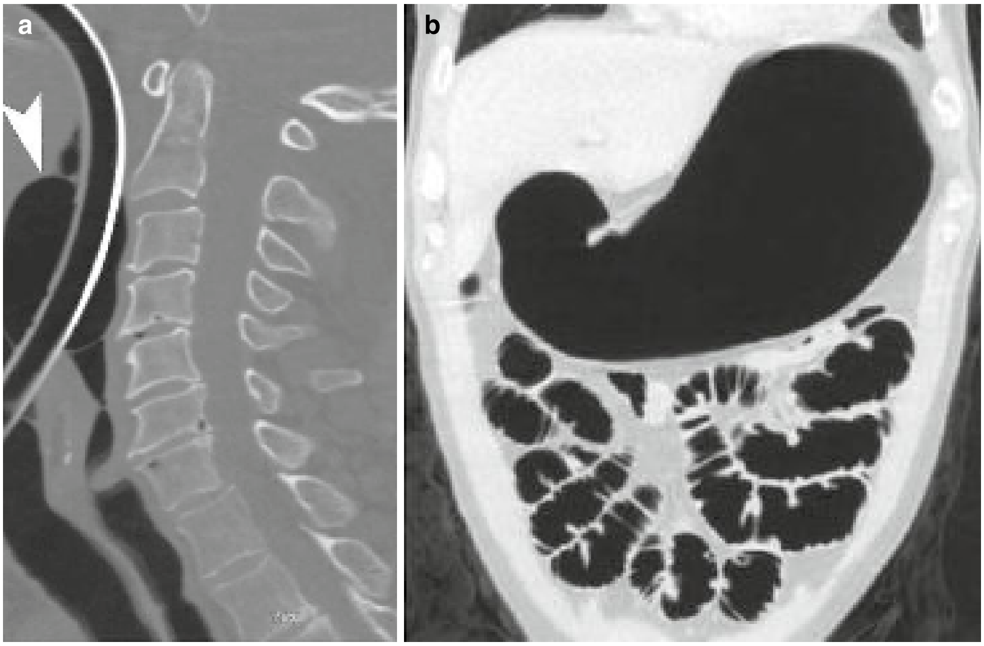

Fig. 25.3 High placed endotracheal tube. (**a**) Sagittal CT reformation demonstrates the cuff (*arrowhead*) of the endotracheal tube inflated in the hypopharynx. The upper esophagus is outlined by air from the endotracheal tube. (**b**) Coronal CT reformation of the abdomen demonstrates gaseous distention of the stomach and small bowel loops due to air leaking from the endotracheal tube

The imaging findings of esophageal intubation include endotracheal tube cuff diameter more than that of the trachea, distention of the bowel lumen, and the presence of air column in the esophagus. If an esophageal intubation is suspected, then a chest radiograph should be done after rotating the head to the right side and turning the patient to the right side by 25°. This obliquity results in esophageal air column projecting separate from the tracheal air column.

Tracheostomy Tube

Tracheostomy tube is used for long-term ventilation or in patients with laryngeal obstruction. Its caliber should be two-thirds the caliber of the trachea. It should be inserted at the level of the third tracheal cartilage with the tip placed above the level of the carina. It is not unusual to see pneumomediastinum and subcutaneous emphysema after placement of a tracheostomy tube. However, significant amount of emphysema may be due to complications. The tracheostomy tube position does not change with neck flexion or extension. The complications include tracheal perforation, fistulous communication between trachea and esophagus, and malpositioning (Fig. 25.4).

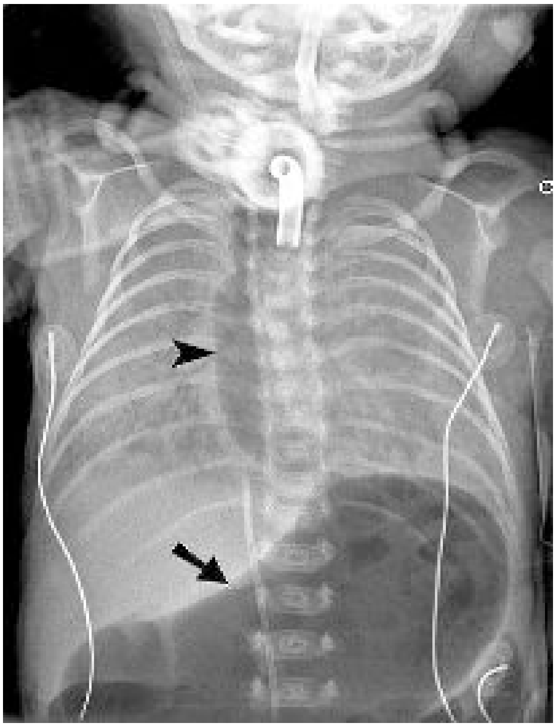

Fig. 25.4 Abnormal tracheostomy tube positioning. Plain radiograph of the chest and upper abdomen demonstrates marked distention of the esophagus (*arrowheads*) and stomach (*arrow*) due to leakage of air from the tracheostomy tube into the upper gastrointestinal tract

Nasogastric Feeding

Nasogastric tube is widely used to decompress the acidic gastric contents and reduce aspiration risk. It is recognized by the presence of a radiopaque line traversing the entire tube length. The side port of the nasogastric tube is approximately 8 cm from the tip. Ideal location of the nasogastric tube is in the stomach with the side port below the gastroesophageal junction. If the side holes of the tube are located in the distal esophagus, it can lead to aspiration pneumonia.

A feeding tube is recognized by the presence of a linear radiopaque tungsten band at the tip of the tube. It is ideally placed in the distal duodenum and is used for enteric feeding without the risk of gastroesophageal reflux. Placement of the tip distal to the gastric pylorus reduces the risk of aspiration.

Complications may be as high as 7.6% after placement of feeding tube. The enteric tubes may be coiled in the pharynx, esophagus, or stomach. They may be malpositioned into the bronchial tree, mediastinum, or pleural space (Fig. 25.5). If the post feeding tube or nasogastric tube placement radio-

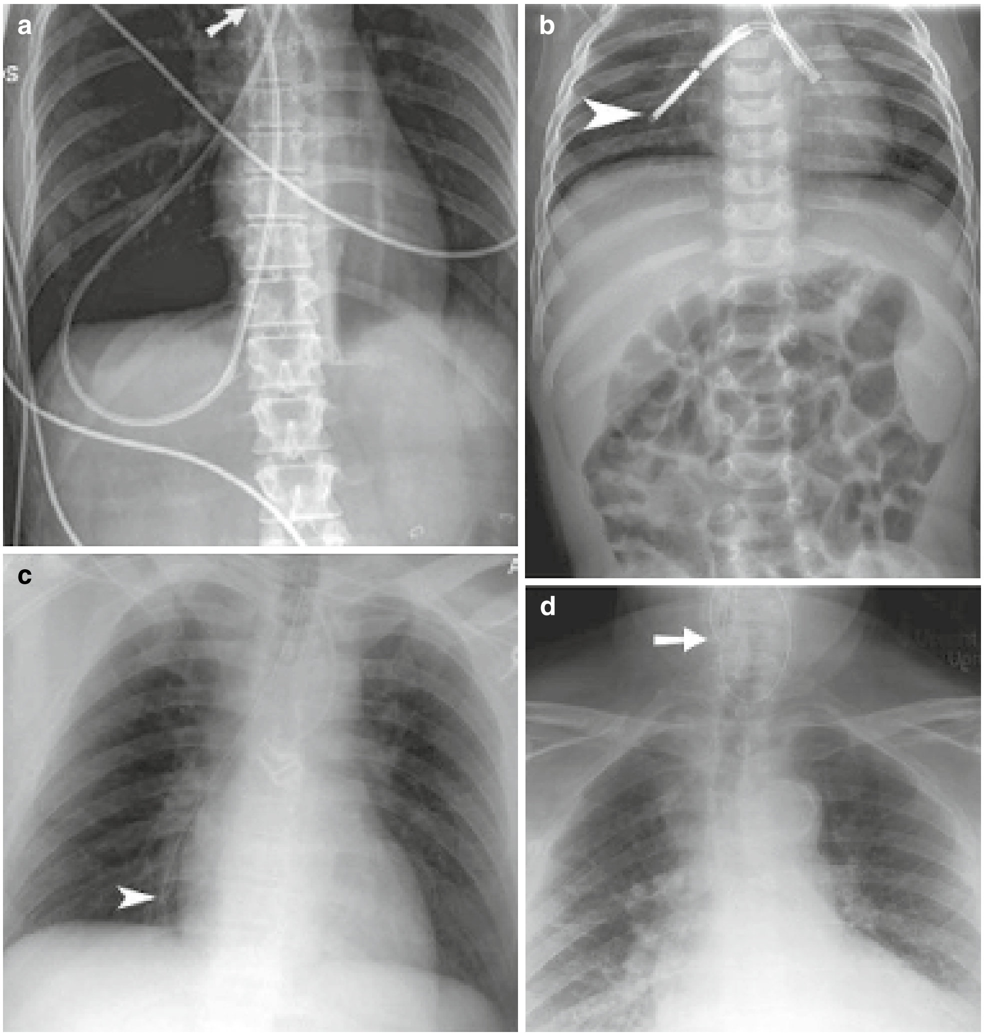

Fig. 25.5 Abnormal nasogastric and feeding tube positions. (**a**) Plain radiograph demonstrates a feeding tube (*arrow*) extending through the right main bronchus and penetrating into the pleural space. (**b**) Plain radiograph demonstrating feeding tube extending coiled in the left main bronchus and the tip (*arrowhead*) extending into the right main bronchus. (**c**) Plain radiograph demonstrating nasogastric tube (*arrowhead*) extending into the right lower lobe bronchus. (**d**) Plain radiograph demonstrating coiling of the nasogastric tube (*arrow*) in the hypopharynx. (**e**) Plain radiograph of the abdomen demonstrating tip of the feeding tube in the stomach on the first study and in the distending colon (*arrow*) on the second study. The patient had swallowed the feeding tube between the two studies

graph shows placement in the tracheobronchial tree, the tube should be withdrawn and a follow-up radiograph obtained to rule out a pneumothorax [5]. Other complications include esophageal perforation, swallowing of entire enteric tube, pulmonary laceration or contusion, pneumothorax, and hydropneumothorax. Secondary complications of tracheobronchial tube malposition include: aspiration, pneumonia, lung abscess, and empyema.

G and GJ Tubes

G and J tubes are widely used for long-term enteric feeding, often used in patients with failure to thrive, risk of aspiration, and swallowing dysfunction. An increasing number of these tubes are placed by interventional radiologist because of the advantage of their placement without the need for general anesthesia. There is 5% major complication rate associated with G-tube placement [6]. The complications include colonic perforation, tube dislodgement, tube migration, peritonitis, abscess formation, septicemia, tube site insertion infection, and GI bleeding (Fig. 25.6).

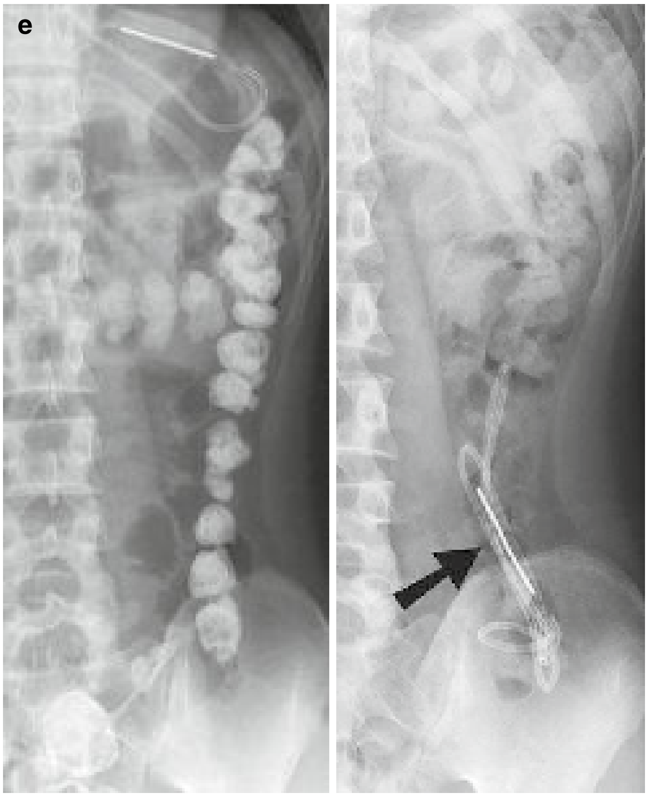

Fig. 25.5 (continued)

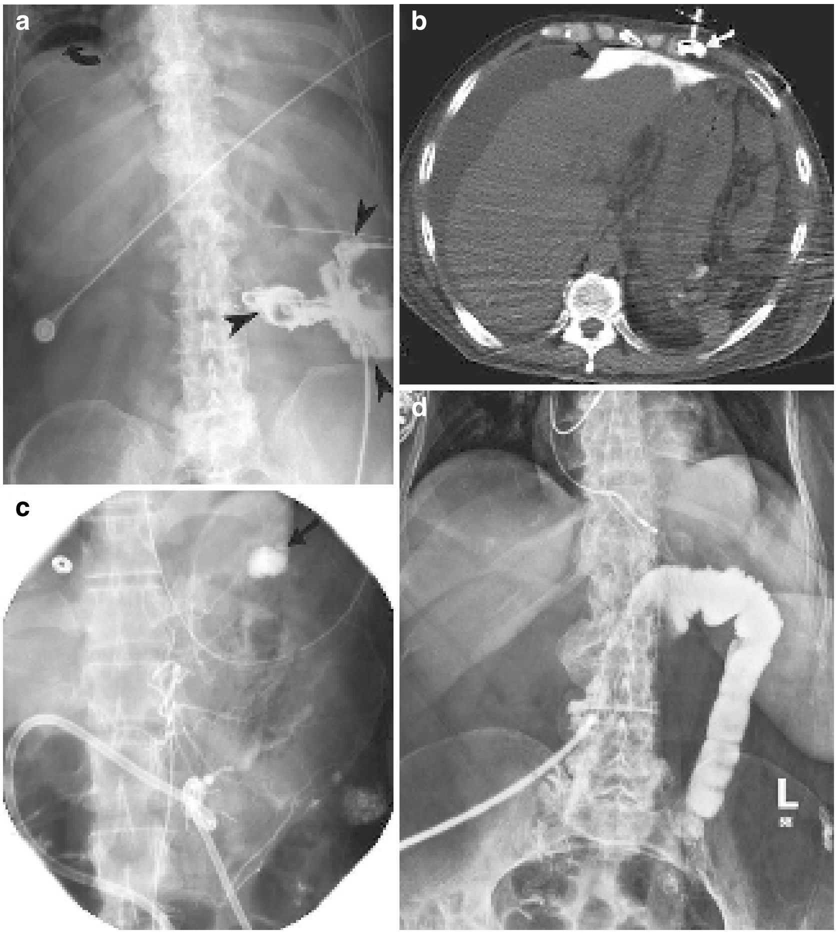

Fig. 25.6 G-tube malposition. (**a**) Tube injection study demonstrating the G tube located outside the stomach. There is contrast extravasation outside the bowel loops (*arrowheads*). There is free air (*curved arrow*) under the right dome of diaphragm. (**b**) Noncontrast CT after tube injection demonstrates the G tube (*arrow*) located in the left anterior abdominal wall. The contrast (*arrowhead*) injected through the G tube is present within the peritoneal cavity, anterior to the left lobe of the liver and the stomach. (**c**) Left gastric arteriogram demonstrates active arterial bleeding (*arrow*) after gastrojejunostomy tube insertion. (**d**) G-tube injection study demonstrates opacification of the colonic lumen from inadvertent colonic perforation

Central Venous Catheters

More than 5 million central venous catheters are placed by physicians in the USA, most often by surgeons and anesthesiologist, without image guidance [7]. While tunneled catheters are most often placed by surgeons or interventional radiologists, nontunneled catheters are most commonly placed by the surgeons and anesthesiologists. In 1999, interventional radiologists accounted for 20% of the tunneled and 15% of the nontunneled catheters placed in Medicare patients [8]. Subclavian, internal jugular, and femoral veins are the most common places to insert catheters.

The subclavian vein is separated from the subclavian artery by anterior scalenus muscle. The subclavian vein is separated from the pleura of the lung apex by only 5 mm. The needle placement at the time of subclavian central venous catheter insertion should be in inward and slightly upward direction (from the mid clavicle, aiming toward the sternoclavicular joint).

Imaging plays an important role in documenting correct position of the central venous line tip as between 10% and 30% of the catheters placed without imaging guidance are in suboptimal position. The right tracheobronchial angle is the best anatomic landmark to delineate the border of the superior vena cava and right atrium junction. The optimal position of central line tip is in the superior vena cava, adjacent to the cavoatrial junction. If the central venous line tip is placed too high from the cavoatrial junction, the tip may be above the venous valves or may be outside the vascular lumen. The valves are found in the subclavian vein and internal jugular vein, approximately 2.5 cm from their confluence to form the brachiocephalic vein. The placement of the catheter tip above the valves can lead to inaccurate measurement of central venous pressures (most commonly elevated pressures).

Although there is tendency among interventional radiologist to place the catheter tip in the upper right atrium, the FDA disagrees with this practice because of the potential for cardiac-related complications. According to 1989 FDA precautionary statement related to central venous catheter, the catheter tip should not be placed in the heart.

A chest radiograph should be obtained in every patient where subclavian venous catheter placement was attempted, irrespective of whether it was successful or not. Despite the presence of venous canals, central venous catheter may extend up the internal jugular vein or less commonly into the contralateral brachiocephalic, subclavian, internal jugular, or azygous veins. The most common location of a misplaced subclavian central line is the ipsilateral internal jugular vein (Fig. 25.7) [5]. Central venous catheter tip of which is located within the internal jugular vein should not be used, as there is a risk of thrombosis and vascular rupture. The extension of a left-sided central line into the right brachiocephalic vein can be seen, especially in patients where the left brachiocephalic vein is higher and more horizontally located. Right-sided central line placement does not usually extend to the left brachiocephalic vein as the right brachiocephalic vein course is more in line with the superior vena cava. A central venous catheter placed into the azygous vein can be best identified on the lateral view, as the catheter courses posteriorly at the level of the superior vena cava.

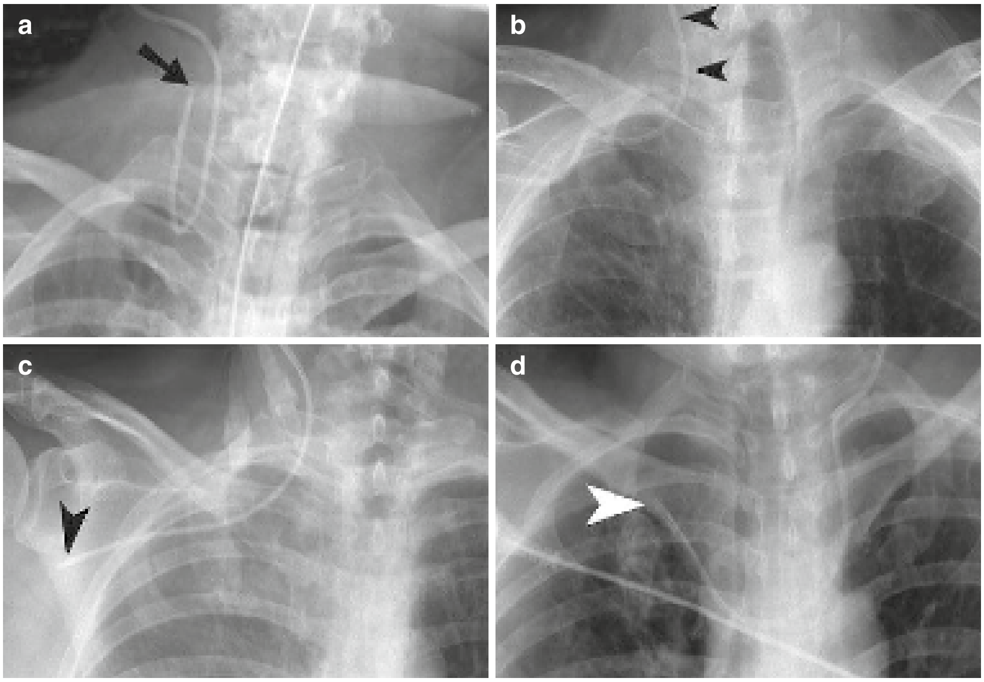

Fig. 25.7 Abnormal central venous line positions. Plain radiograph of the upper chest demonstrates: (**a**) Right internal jugular venous line tip (*arrow*) coiled in the internal jugular vein. (**b**) Right subclavian venous line extending up, into the right internal jugular vein (*arrowheads*). (**c**) Right internal jugular venous line extending into the right axillary vein (*arrowhead*). (**d**) Left internal jugular venous line extending into the right subclavian vein (*arrowhead*)

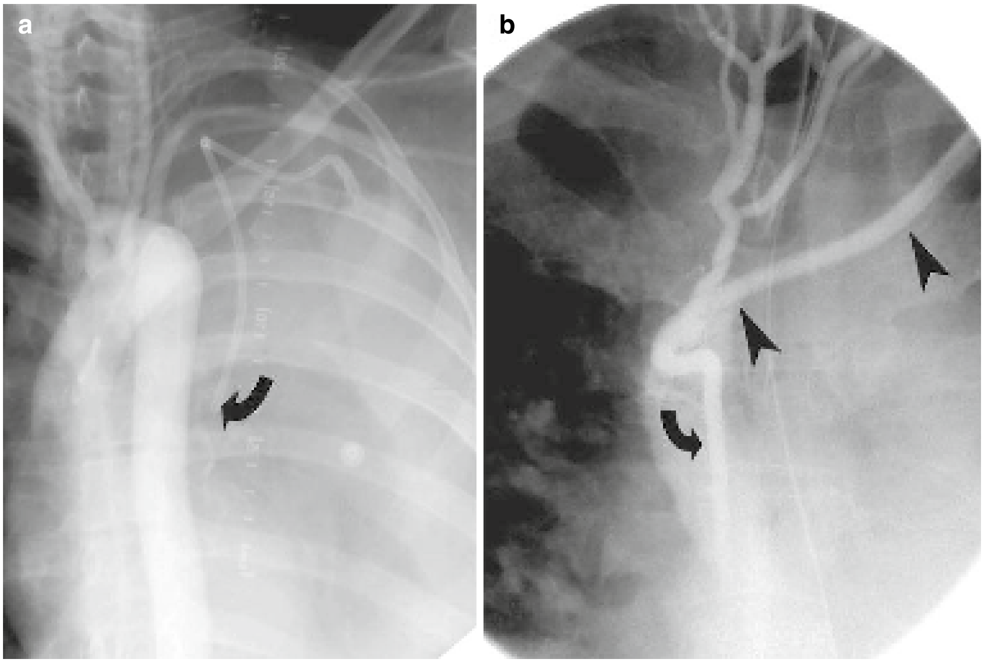

Fig. 25.8 Extravascular location of lines. (**a**) Aortogram study demonstrates left-sided Port-A-Cath tip (*curved arrow*) located in the left pleural space. The large left pleural effusion was produced by inadvertent usage of the left Port-A-Cath. (**b**) Venogram study through the left hemodialysis catheter (*arrowheads*) demonstrates opacification of the azygous vein (*curved arrow*)

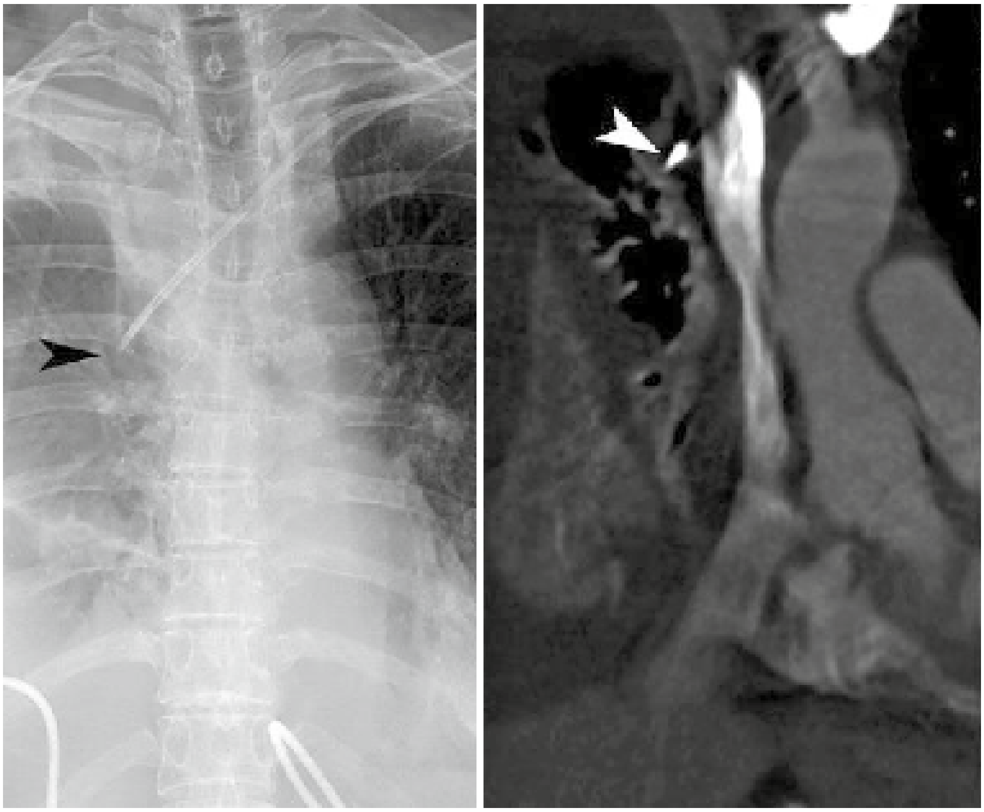

Fig. 25.9 Extravascular location of venous line. Plain radiograph of the chest (*left image*) demonstrates left-sided subclavian venous line tip (*arrowhead*) projecting beyond the right margin of the superior vena cava. There is moderate-size pleural effusion seen on the right due to infusion of saline through the central line. CT venogram (*right image*) demonstrates extension of the tip of the left subclavian venous line (*arrowhead*) beyond the margin of the superior vena cava

Central venous catheter tip located in the mediastinum and pleural space can result in infusion of the IV fluid into the mediastinal space or pleural cavity (Figs. 25.8 and 25.9). Rapid accumulation of pleural effusion is a clue to the diagnoses of pleural placement of the central line.

The complications of central venous line placement include arterial placement (Fig. 25.10), vascular perforation, SVC syndrome, knotting, looping, kinking, catheter break, and infection. Unusual trajectory of the catheter, apical cap due to extrapleural hematoma, new pleural

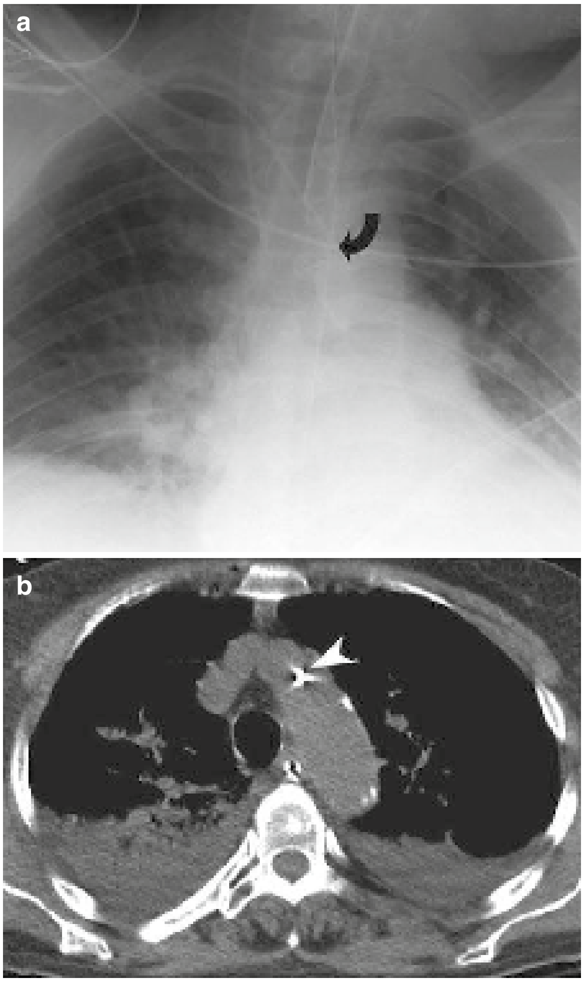

Fig. 25.10 Arterial location of central venous lines. (**a**) Plain radiograph of the chest demonstrates right subclavian line (*curved arrow*) extending across the midline to the left side. (**b**) Noncontrast CT of the chest confirms the arterial location of the central line (*arrowhead*)

effusion, and mediastinal widening may indicate vascular perforation.

Another common complication is pneumothorax which may occur in 5% of line placements. Acquiring chest radiograph after central venous catheter placement is recommended to rule out pneumothorax. Contralateral decubitus radiograph can detect small pneumothoraces. Curve of the catheter tip and position of the catheter against vascular wall may be signs of impending vascular perforation.

Uncommon locations of the catheter tip include pericardiophrenic vein, internal mammary vein, superior intercostal vein, left superior accessory vein, axillary vein, or left-sided superior vena cava (Figs. 25.11, 25.12, and 25.13). Left-sided superior vena cava is seen in 0.3% of the control population and will lead to placement of the left-sided central line along the left superior mediastinum, coursing posterior to the heart (coronary sinus), into the right atrium.

The placement of the catheter tip in the heart can lead to arrhythmia, myocardial rupture, and pericardial tamponade. Pneumothorax is seen in approximately 5% of patients after central line or port placement and is most commonly seen after subclavian rather than internal jugular line placement (Fig. 25.14). The majority of the pneumothorax from central venous line placement is asymptomatic and resolve spontaneously. Symptomatic or enlarging pneumothorax requires treatment with a pigtail drainage catheter.

Infections associated with central venous line catheters are most commonly related to staphylococcus species. The presence of sepsis usually mandates removal of the catheter and treatment with antibiotics. The single most common cause of catheter dysfunction is formation of a fibrin sheath, made up of eosinophilic material and inflammatory cells at

Fig. 25.11 Central venous line extending into the left superior intercostal vein. Plain radiograph (*left image*) and coronal CT (*right image*) reformation demonstrate left internal jugular venous line (*arrowhead*) extending into the left superior intercostal vein

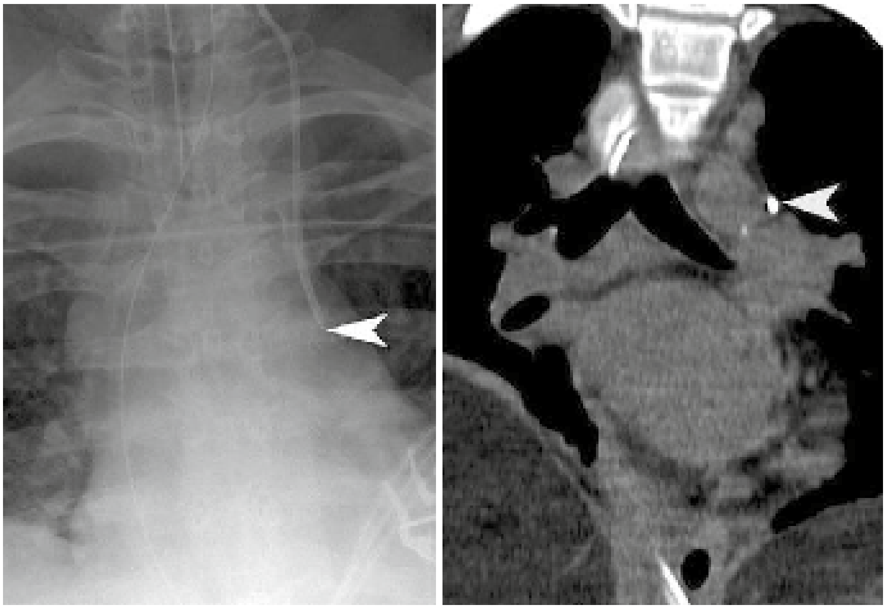

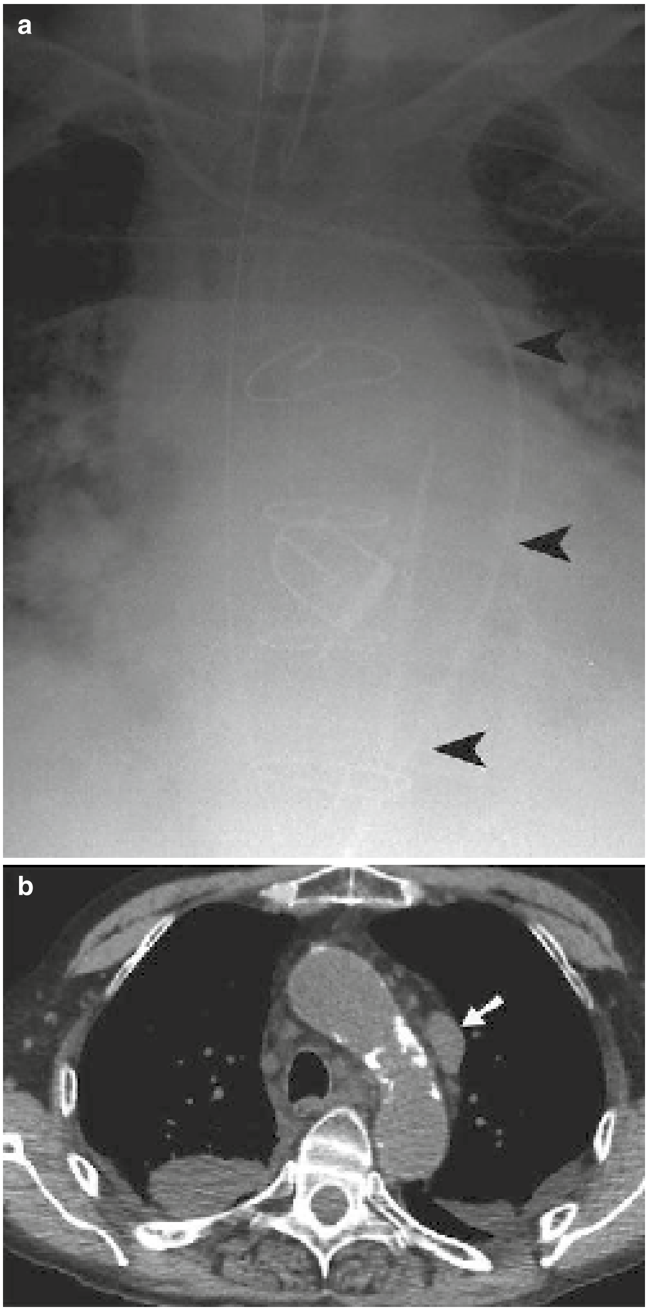

Fig. 25.12 Central line in left-sided superior vena cava. (**a**) Portable radiograph of the chest demonstrates right-sided internal jugular venous line (*arrowheads*) extending into left-sided superior vena cava and coronary sinus *arrowheads*. (**b**) Axial CT of the chest demonstrates a left-sided superior vena cava (*arrow*). There is no right-sided superior vena cava

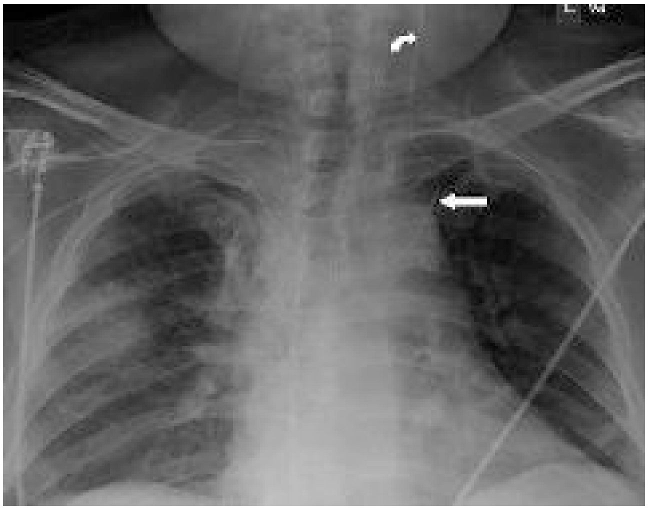

Fig. 25.13 Abnormal peripherally inserted central line position. A right-sided peripherally inserted central line is seen to cross the midline and extend into the left subclavian vein (*arrow*). A left-sided peripherally inserted central line is seen to extend in the left internal jugular vein (*curved arrow*)

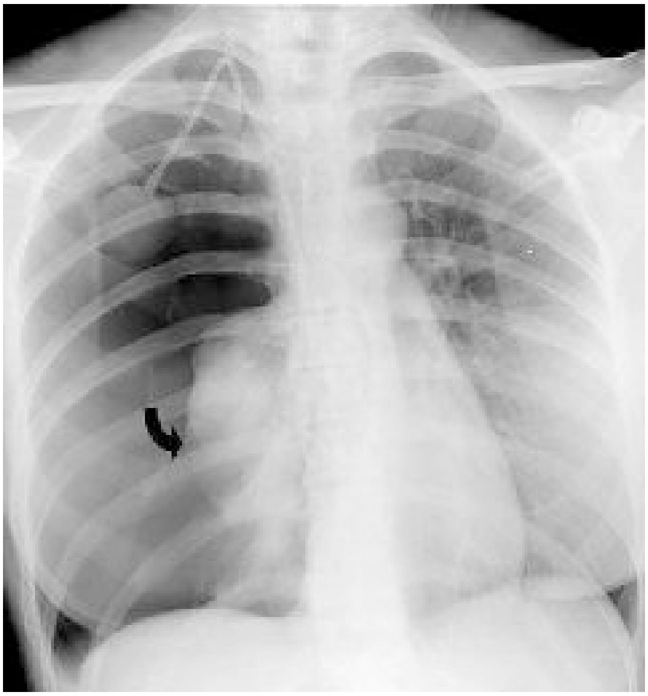

Fig. 25.14 Tension pneumothorax after Port-A-Cath placement. Plain radiograph of the chest demonstrates large right-sided pneumothorax with complete collapse of the right lung (*arrow*) due to visceral pleural puncture at the time of right Port-A-Cath placement

the catheter tip. It is often associated with thrombus and functions as a one-way valve which allows the catheter to be flushed but not aspirated. The treatment of a fibrin sheath is tissue plasminogen activator infusion into the catheter, which if not successful can be treated with catheter exchange over an Amplatz guidewire. The sheath can sometimes be removed using a loop snare or balloon angioplasty.

Catheter breakage can lead to embolization of the catheter fragment into the right atrium, right ventricle, or pulmonary circulation. These catheter fragments can be retrieved percutaneously using a snare (Fig. 25.15). Complications of venous line fragments include arrhythmia, vascular injury, and pulmonary embolism.

Long-term venous central venous access can lead to thrombosis and venous stenosis. The risk of thrombosis is less in patients with Broviac and Hickman catheters.

Umbilical venous catheters are used in the neonates as a route for venous access. The catheter passes through the umbilicus, umbilical vein, left portal vein, ductus venosus, middle or left hepatic vein, and inferior vena cava. The tip of the catheter should be at the junction of inferior vena cava and right atrium (Fig. 25.16).

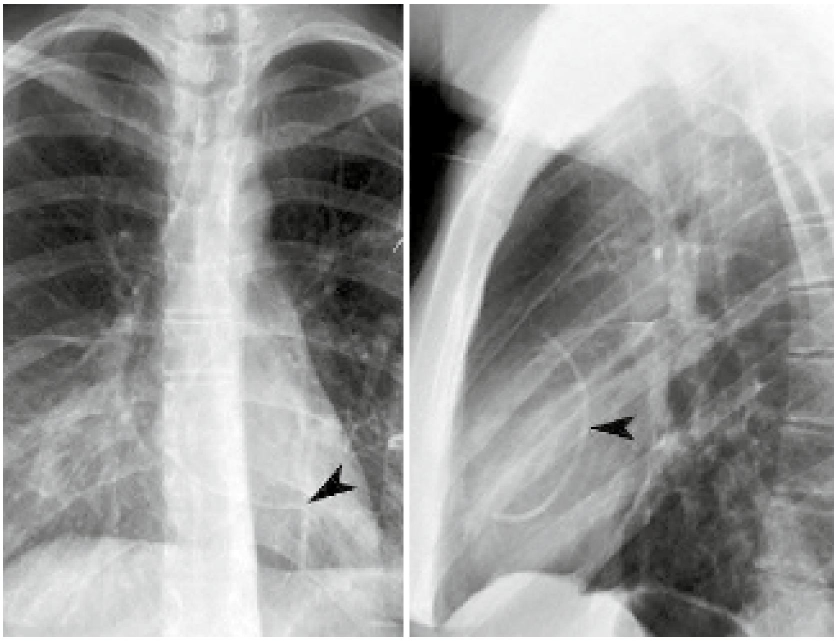

Fig. 25.15 Fractured central venous line. PA and lateral views of the chest demonstrate fractured central venous line tubing (*arrowheads*) located in the right ventricle. This was taken out using a snare

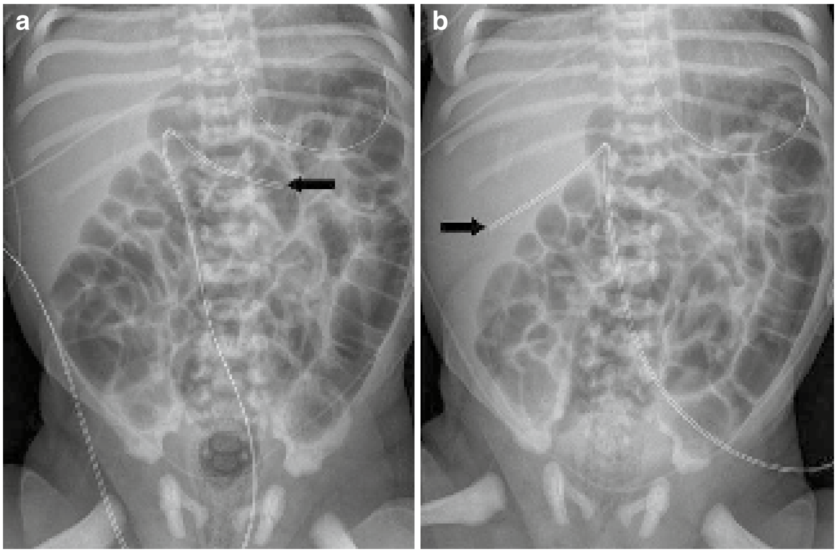

Fig. 25.16 Malpositioned umbilical venous catheters. (**a**) The tip of the umbilical venous catheter (*arrow*) is seen in the left branch of portal vein. (**b**) The tip of the umbilical venous catheter (*arrow*) is seen in the right branch of portal vein

Subcutaneous Ports and Tunneled Catheters

A subcutaneous port most often used is the Port-A-Cath. It is often used for repeated access of the venous system and is most often used either in oncology or in cystic fibrosis patients. Typical port is located subcutaneously in the anterior chest wall and is connected to the central vein by tubing which typically enters the thorax via the internal jugular vein. The complications include thrombosis of the port/tubing, disconnection of the tubing from the port, upward retraction of the tubing, infection, and fibrin sheath formation (Fig. 25.17).

Tunneled catheters offer a benefit over nontunneled versions. Tunneled catheters can be used for hemodialysis and other longer duration vascular access. If the internal jugular vein is punctured more than 3–4 cm above the clavicle, the tunneled catheter has high chance of kinking and occlusion. When the patient moves from supine to upright position, the tunneled central venous catheter has a tendency to migrate cranially by several centimeters. In female population, the downward pull on the tunneled catheter or the port by breast can exaggerate cranial migration of the catheter tip.

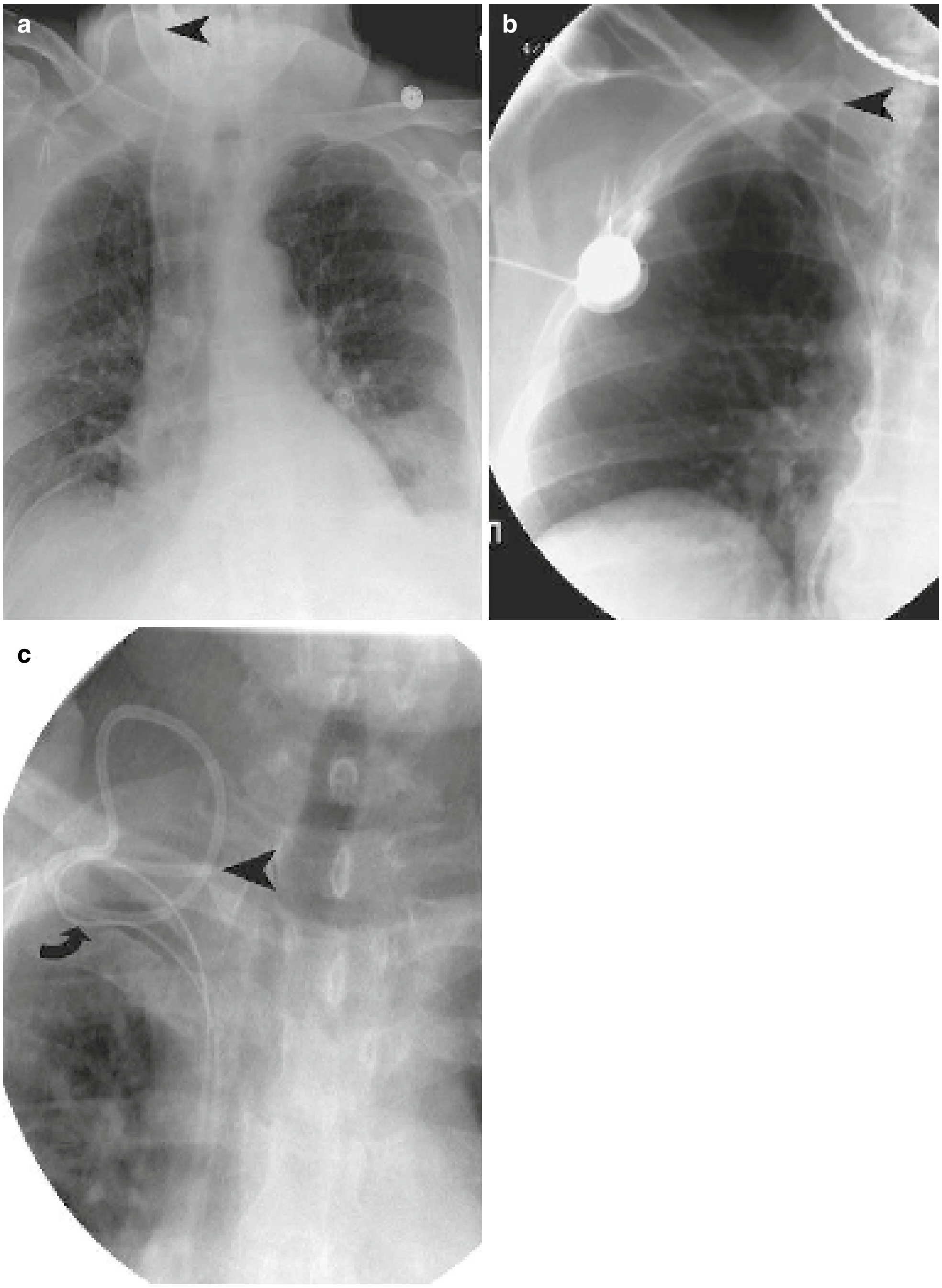

Fig. 25.17 Port-A-Cath abnormalities. (**a**) Plain radiograph of the chest demonstrates abnormally high loop (*arrowhead*) of the Port-A-Cath tubing. (**b**) Plain radiograph of the chest demonstrates separation of the port from the tubing (*arrowhead*). (**c**) Scout film of the upper chest demonstrates retraction of the right Port-A-Cath tubing (*arrowhead*) into the right subclavian vein. The spot film also demonstrates snare (*arrow*) which was used to pull the tip of the tubing back into the superior vena cava

Intra-Aortic Balloon Pump

The use of intra-aortic balloon pump has increased in recent times for the treatment of low cardiac output in patients with congestive heart failure. It inflates in diastole, increasing the coronary artery blood flow as well as peripheral vascular flow. It deflates in systole, decreasing the left ventricular afterload. The proximal tip of the balloon pump is marked with a metallic marker.

The tip of the intra-aortic balloon pump should be 1 cm distal to the origin of the left subclavian artery (Fig. 25.18a). The radiopaque tip marker should be at the level of the carina. If the tip is too proximally placed in the aortic arch, it can occlude the branches of the aortic arch. If the tip is too distally placed, then the IABP may not be effective enough in increasing coronary blood flow, and may also occlude the origin of visceral arteries.

The complications of intra-aortic balloon pump include aortic dissection, aortic wall laceration, embolic phenomenon, vascular insufficiency in the catheterized length, hemolysis, and improper positioning (Fig. 25.18b). Brain infarct may occur as a result of too proximal positioning of the intra-aortic balloon pump.

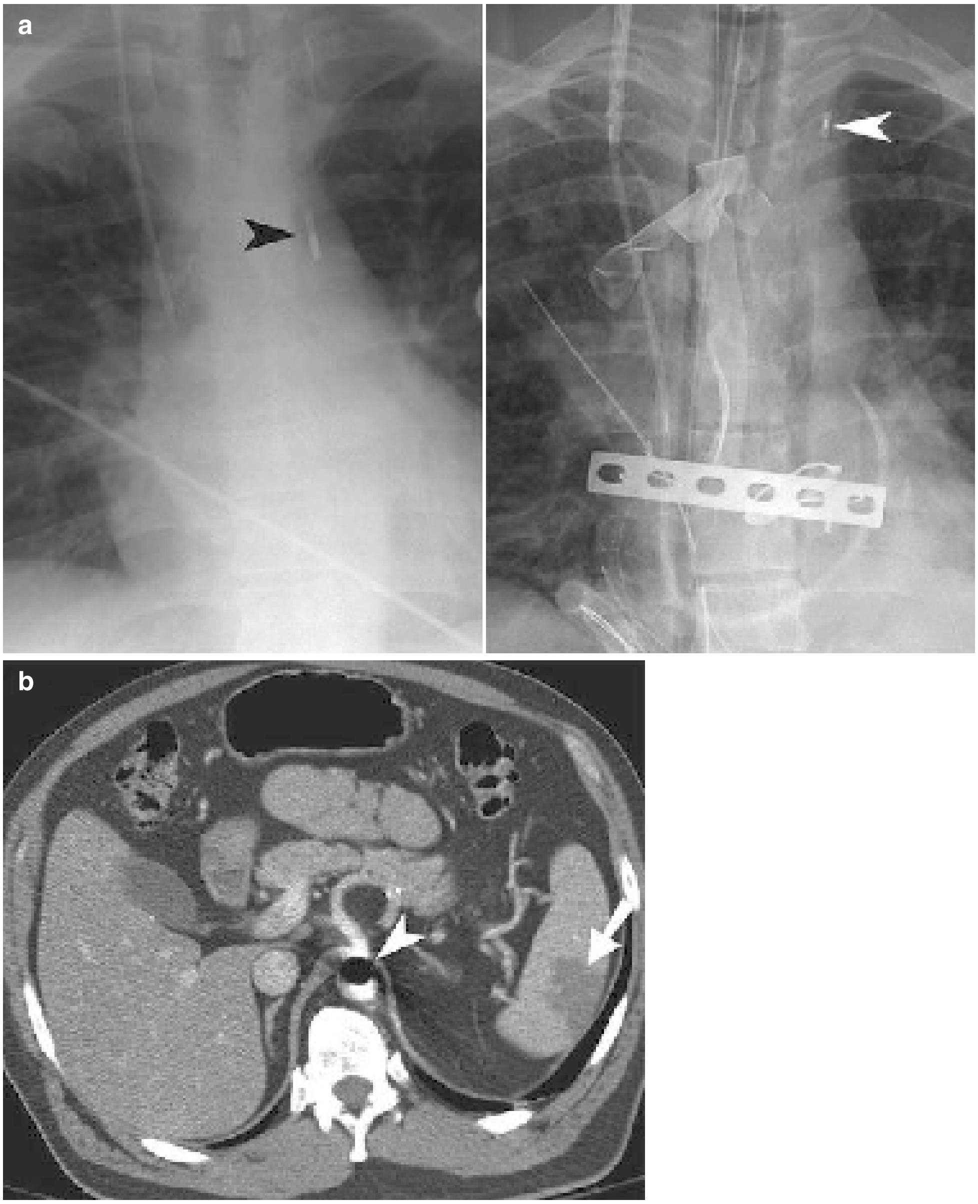

Fig. 25.18 Intra-aortic balloon pump. (**a**) The *left-sided* image demonstrates normal position of intra-aortic balloon pump (*arrowhead*), just below the aortic arch. The *right-sided* image demonstrates an abnormally high location of an intra-aortic balloon pump tip, extending into the left subclavian artery (*arrowhead*). (**b**) Axial contrast-enhanced CT scan study of the upper abdomen demonstrates wedge-shaped splenic infarct (*arrow*), secondary to the intra-aortic balloon pump (*arrowhead*) seen adjacent to the origin of the celiac artery

Swan-Ganz Catheter

Swan-Ganz catheter or pulmonary artery catheter is used to measure the pulmonary artery wedge pressure, which is useful in evaluating end-diastolic left ventricular pressure and pulmonary capillary hydrostatic pressure. Swan-Ganz catheter is helpful in distinguishing cardiogenic from noncardiogenic pulmonary edema. When the pressure is not being measured, the Swan-Ganz catheter is positioned in the right or left pulmonary artery (Fig. 25.19). The catheter tip should not reach beyond the proximal interlobar pulmonary artery. The catheter wedges into the distal pulmonary artery segment when the balloon is inflated, thereby giving the pulmonary artery wedge pressure. The balloon of the Swan-Ganz catheter should be kept deflated, unless pulmonary artery wedge pressure reading is required.

The complications of a Swan-Ganz catheter placement include cardiac arrhythmia, pulmonary infarction due to pulmonary artery branch occlusion, intracardiac knotting, balloon rupture, pseudoaneurysm formation, and rupture of the pulmonary artery. Other complications include misplacement of the catheter, looping, coiling, pneumothorax, and vascular injury.

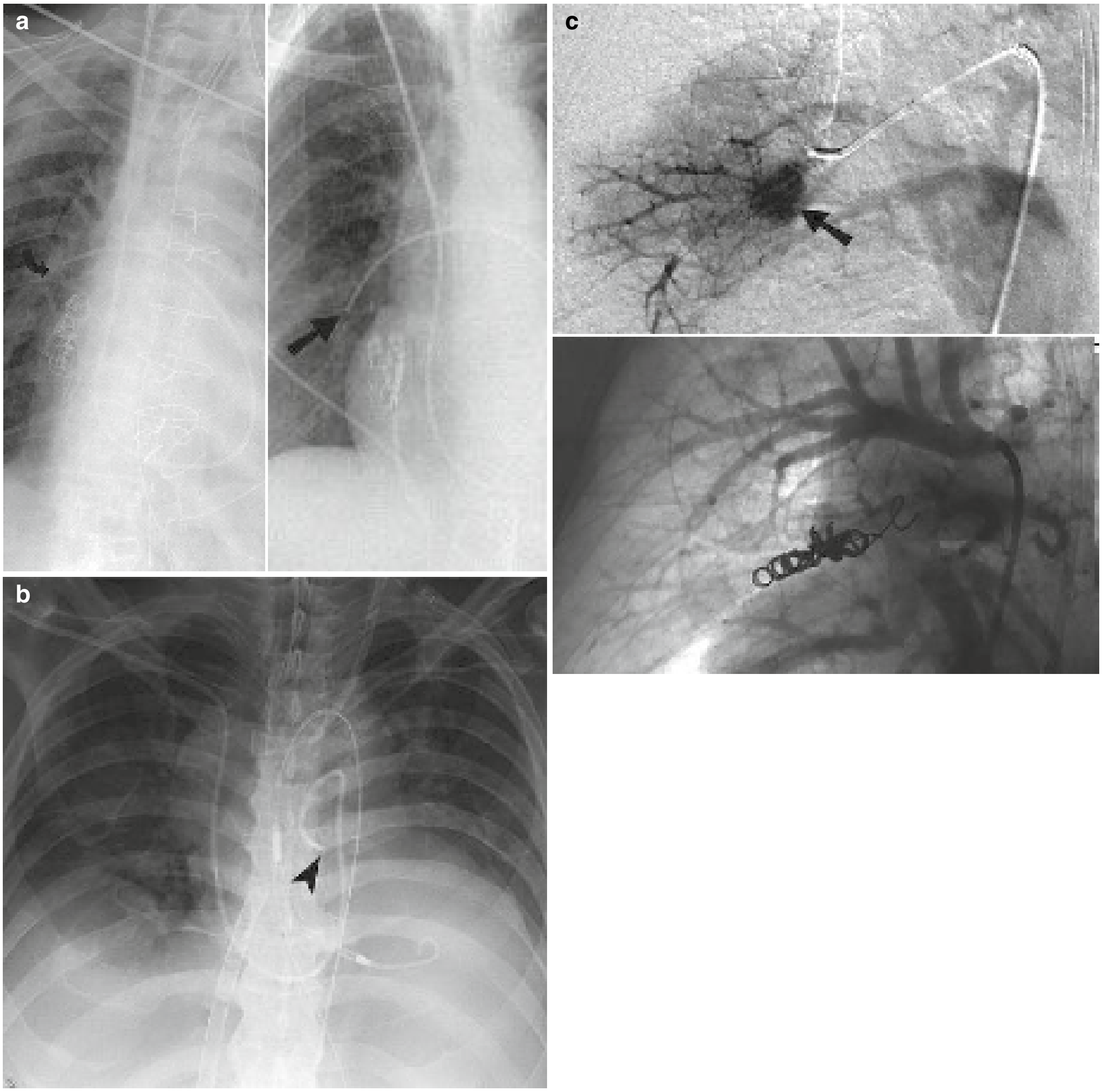

Fig. 25.19 Swan-Ganz catheter. (**a**) *Left-sided* image demonstrates Swan-Ganz catheter tip (*curved arrow*) in the right main pulmonary artery. The radiograph on the right demonstrates the tip of the Swan-Ganz catheter (*straight arrow*) into the interlobar artery branch of the right pulmonary artery. (**b**) Plain radiograph of the chest demonstrates Swan-Ganz catheter tip (*arrowhead*) coiled in the outflow tract of the right ventricle. (**c**) Pulmonary arteriogram before and after coil placement. The image on the *top* demonstrates a pseudoaneurysm (*arrow*) secondary to Swan-Ganz catheter placement in the past, supplied by the right middle lobe artery. The image at the *bottom* demonstrates placement of tornado coils into the arterial feeder of the pseudoaneurysm

Cardiac Conduction Devices

Cardiac conduction devices (CCD) include pacemakers and automatic implantable cardioverter defibrillator (ICD). Components of CCD include a pulse generator and one or more lead wires with electrodes. The cardiac pacing devices can be categorized as single chamber (one lead placed in right atrium or right ventricle), dual chamber (two leads placed in right atrium and right ventricle), and biventricular (additional lead placed into coronary sinus for left ventricular pacing). Right atrial lead is a J-shaped lead which curves upward with its tip into the right atrial appendage. For right ventricular pacing, the lead is placed in the right ventricular apex. Lateral chest radiograph demonstrating anteriorly oriented lead confirms the position of the lead tip in the right ventricle. Biventricular pacemaker utilizes lead for each ventricle and an optional right atrial lead. Left ventricular lead courses through coronary sinus and is placed in the left ventricular wall epicardial vein. Its position can be confirmed on lateral chest radiograph which demonstrates a posteriorly oriented lead.

ICDs can be categorized into transvenous ICD (T-ICD) and subcutaneous ICD (S-ICD). Leads of T-ICDs are wider with one or two metal shock coils, giving them a coiled-spring appearance. One electrode each is placed in right atrium and right ventricle. T-ICDs are frequently utilized with biventricular pacemakers with pacemaker lead placed in right atrial appendage and left ventricle, and ICD lead placed in the right ventricle. S-ICDs can also be used when cardiac pacing is not required. For S-ICD implantation, pulse generator is placed in the left lateral chest and subcutaneous lead, consisting of electrode and shock coils, is placed in left parasternal region [9].

The complications of CCD placement include lead misplacement, intracardiac knotting, lead fracture (Fig. 25.20) or kinking, infection of the generator pocket of lead, perforation, cardiac tamponade, tricuspid regurgitation, arrhythmias, implant vein occlusion, and pacer malfunction. Twiddler syndrome, a rare complication, refers to deliberate or unintentional patient manipulation of subcutaneously placed device causing rotation of CCD generator with resultant retraction of the normally positioned leads [9].

Teaching Points

- The endotracheal tube tip should be approximately 3–7 cm from the carina or at the level of the aortic arch.
- Tracheostomy tube should be inserted at the level of the third tracheal cartilage with the tip placed above the level of the carina.

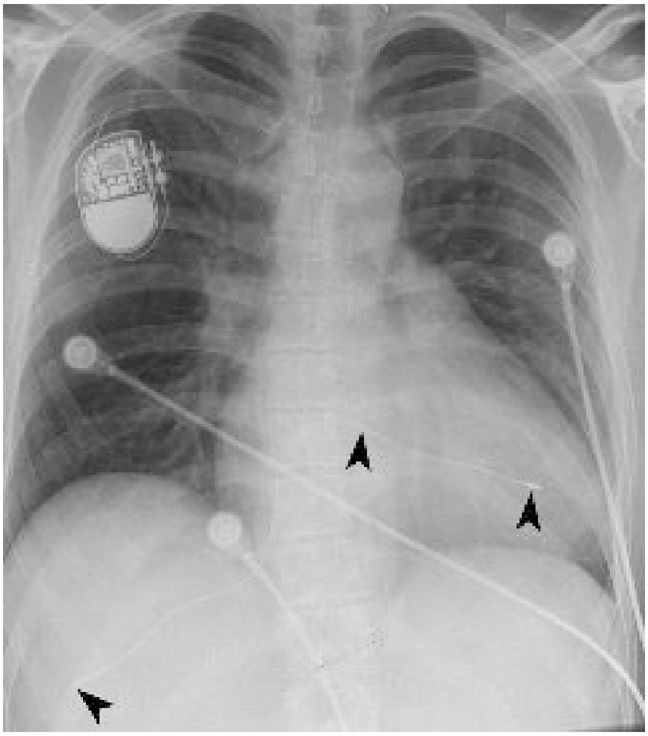

Fig. 25.20 Fractured pacemaker lead. Plain radiograph of the chest demonstrates a fractured pacemaker wire which is seen extending from the right hepatic vein to the right ventricle (arrowheads)

- Ideal location of the nasogastric tube is in the stomach with the side port below the gastroesophageal junction.
- The right tracheobronchial angle is the best anatomic landmark to delineate the border of the superior vena cava and right atrium junction.
- The optimal position of central line tip is in the superior vena cava, adjacent to the cavoatrial junction.
- The tip of the intra-aortic balloon pump should be 1 cm distal to the origin of the left subclavian artery.
- The Swan-Ganz catheter is positioned in the right or left pulmonary artery when the pressure is not being measured.

Questions

1. Which of the following is the correct position of intra-aortic balloon pump?
   (A) The tip should be in the ascending aorta.
   (B) The tip should be placed in the aortic arch.
   (C) The distal tip should be 1 cm from left common carotid artery.
   (D) The tip should be 1 cm distal to the subclavian artery.
   Answer: D

2. Which of the following is the best position for the tip of a central venous line?
   (A) Superior vena cava adjacent to the cavoatrial junction
   (B) Superior vena cava adjacent to the brachiocephalic vein confluence
   (C) Superior vena cava above the valves
   (D) Inferior vena cava below the right atrium.
   Answer: A

3. What tube or line is malpositioned in the following radiograph (Fig. 25.21)?
   (A) Nasogastric tube
   (B) Swan-Ganz catheter
   (C) Feeding tube
   (D) Endotracheal tube
   Answer: C

4. What is the location of endotracheal tube in the following radiograph (Fig. 25.22)?
   (A) Mediastinum
   (B) Pharynx
   (C) Trachea
   (D) Esophagus
   Answer: D

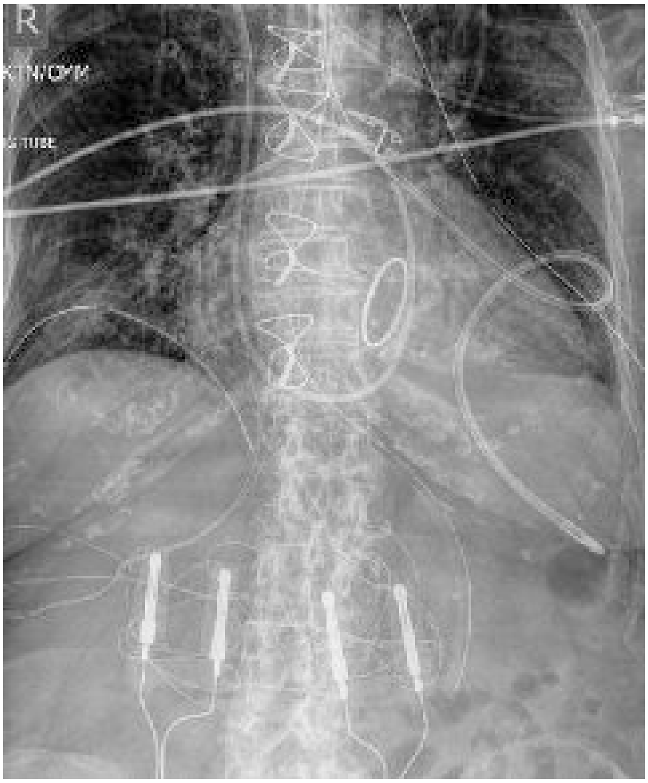

Fig. 25.21 Identify the tube or line malpositioned in the radiograph

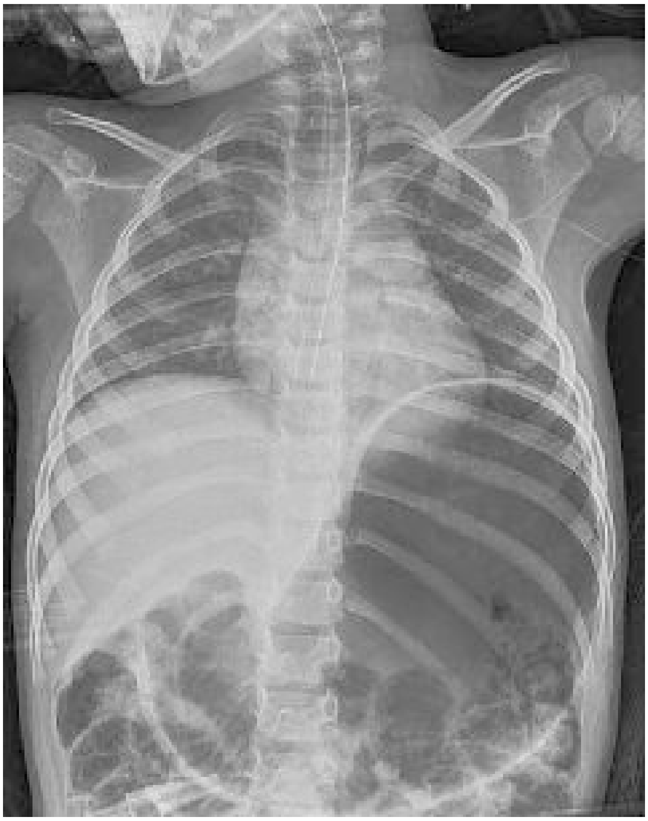

Fig. 25.22 Locate endotracheal tube in the radiograph

References

1. Goodman LR, Conrardy PA, Laing F. Radiographic evaluation of endotracheal tube position. Am J Roentgenol. 1976;127:433–4.
2. Stauffer JL, Olson DE, Petty TL. Complications and consequences of endotracheal intubation and tracheostomy: a prospective study of 150 critically ill adult patients. Am J Med. 1981;70:65–76.
3. Pappas JN, Goodman PC. Predicting proper endotracheal tube placement in underexposed radiographs: tangent line of the aortic arch. Am J Roentgenol. 1999;173:1357–9.
4. Price DB. Tubes in the alimentary and respiratory tracts: appearances on CT scans of the head and neck. Am J Roentgenol. 1991;156:1047–51.
5. Aronchick JM, Miller WT Jr. Tubes and lines in intensive care setting. Semin Roentgenol. 1997;32:102–16.
6. Friedman JN, Ahmed S, Connolly B, Chait P, Mahant S. Complications associated with image-guided gastrostomy and gastrojejunostomy tubes in children. Pediatrics. 2004;114(2):458–61.
7. McGee DC, Gould MK. Preventing complications of central venous catheterization. N Engl J Med. 2003;348:1123–33.
8. Reeves AR, Seshadri R, Trerotola SO. Recent trends in central venous catheter placement: a comparison of interventional radiology with other specialties. J Vasc Interv Radiol. 2001;12(10):1211–4.
9. Torres-Ayala SC, Santacana-Laffitte G, Maldonado J. Radiography of cardiac conduction devices: a pictorial review of pacemakers and implantable cardioverter defibrillators. J Clin Imaging Sci. 2014;4:74. Published 2014 Dec 31. https://doi.org/10.4103/2156-7514.148269.

Imaging of Pediatric Emergencies

26

John J. Krol, Ashvin Singh, Paul F. Von Herrmann,
Harigovinda R. Challa, Mohammad Mansouri,
and Johanne E. Dillon

Introduction

The diagnosis and management of pediatric patients in the emergency department has unique challenges that often require a different approach by the clinician than with an adult patient. Although children may develop many of the same illnesses as adults, certain life-threatening diagnoses are seen more often in the pediatric population. An immature immune system, small body size, and developmental anomalies are several factors that can place children at an increased risk for specific diseases. This chapter will focus on the imaging evaluation of diagnoses that occur more often or with a unique appearance in the pediatric population.

Neurology

Acute Disseminated Encephalomyelitis (ADEM)

Acute disseminated encephalomyelitis is a diagnostic challenge both to the clinician and the radiologist owing to its similarity in presentation with other diseases, specifically multiple sclerosis (MS). The disease is an acute demyelinating process (often preceded by a viral illness or vaccination) predominantly affecting the white matter, deep gray matter, brain stem, and spinal cord with an estimated mortality rate as high as 5% [1]. Because of the confusing and severe presentations of patients, imaging is frequently obtained for further evaluation.

Magnetic resonance imaging (MRI) of the head is the preferred modality for evaluation of the majority of patients with symptoms suggestive of ADEM, and further evaluation with MRI of the spine is often performed as well. The limited literature available comparing the sensitivity of computed tomography (CT) to MRI suggests that MRI is far superior both in sensitivity and specificity compared to CT [2]. CT may be performed initially to exclude neurosurgical emergencies, but CT will often underestimate the extent of disease and may not appropriately characterize the condition. On MRI, the imaging findings of ADEM are similar to other demyelinating disorders and typically include focally increased signal in the white matter on T2-weighted sequences, mild enhancement on postcontrast sequences, and restricted diffusion in acute lesions (Fig. 26.1). The distribution of lesions is variable though certain patterns of involvement may help favor the diagnosis of ADEM over MS. The thalamus (30%–40%), basal ganglia (30%–40%), cerebellum (30%–40%), and brain stem (45%–55%) are affected more frequently in ADEM than MS, and the periventricular white matter and corpus callosum are frequently spared (Table 26.1) [3, 4].

Treatment includes admission for administration of intravenous steroids and for some patients, intravenous immunoglobulin. The majority of patients will improve clinically with mild residual impairment in 57%–90% of patients [1]. Disease relapses are possible.

J. J. Krol
Virtual Radiologic Associates, Eden Prairie, MN, USA

A. Singh
Massachusetts General Hospital, Boston, MA, USA

P. F. Von Herrmann (✉)
Department of Radiology, North Alabama Medical Center, Florence, AL, USA
e-mail: pvh@lauderdaleradiology.com

H. R. Challa
Tennessee Interventional and Imaging Associates, Chattanooga, TN, USA

M. Mansouri
Department of Radiology, Massachusetts General Hospital, Boston, MA, USA

J. E. Dillon
University of Kentucky Health Care, Lexington, KY, USA

© The Author(s), under exclusive license to Springer Nature Switzerland AG 2024
A. Singh (ed.), *Emergency Radiology*, https://doi.org/10.1007/978-3-031-65770-2_26

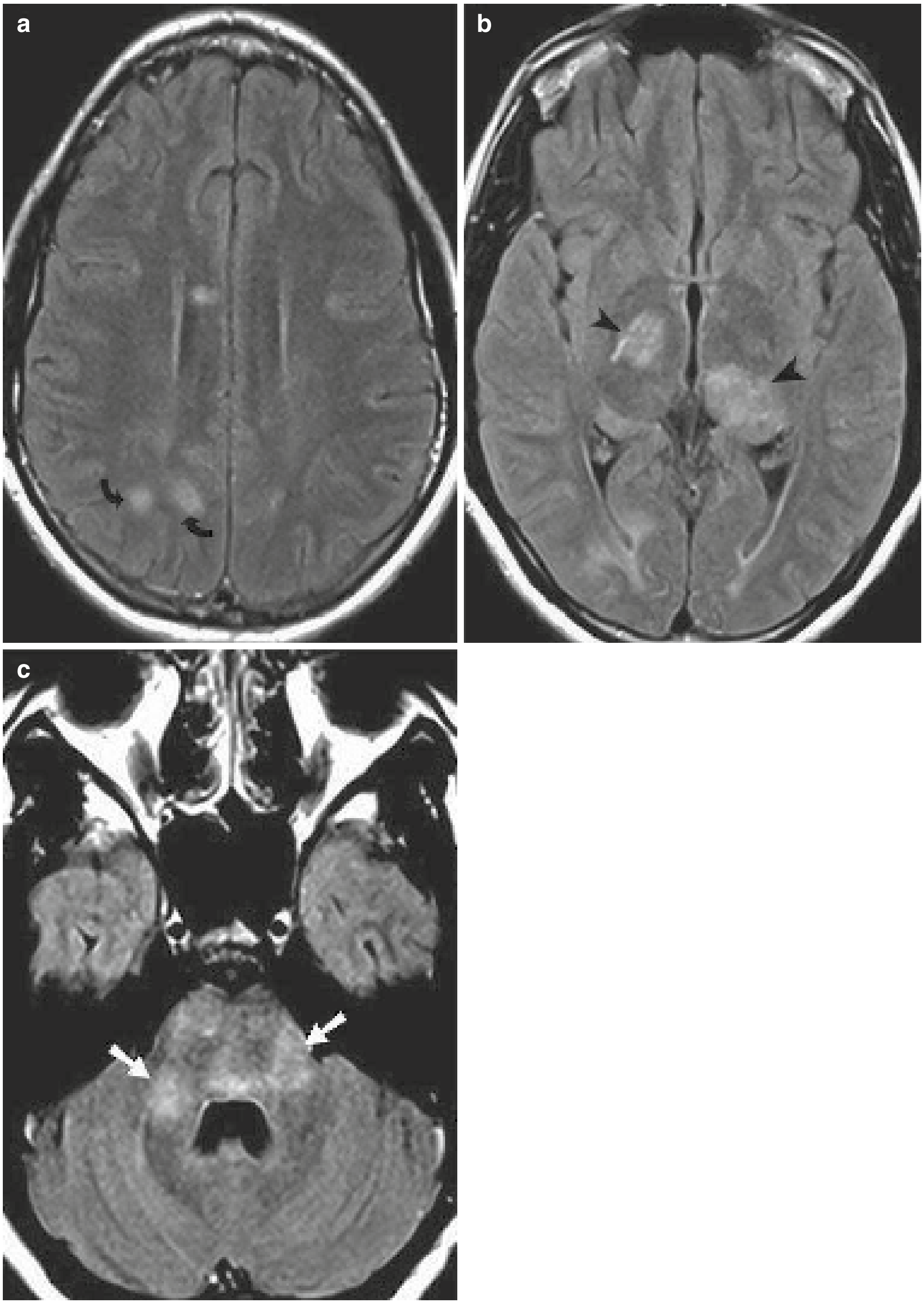

Fig. 26.1 ADEM. (**a–c**) Axial FLAIR sequence images in a 4-year-old girl demonstrate increased signal in the bilateral subcortical white matter (*curved arrows*), bilateral thalami (*arrowheads*), and middle cerebellar peduncle (*straight arrows*) involvement

Table 26.1 Imaging findings in ADEM

CT	Initial imaging modality Underestimates the extent of disease
MRI	Increased signal in the white matter on T2-weighted sequences Mild enhancement on postcontrast sequences Restricted diffusion in acute lesions

Intracranial Complications of Acute Otitis Media and Sinusitis

Due to the high prevalence of viral infections and the small diameter of draining pathways for the middle ear cavity and sinuses, children are at increased risk for developing acute otitis media (AOM) and acute sinusitis. In rare cases, the infection can extend intracranially. Meningitis, intracranial abscesses, and septic thrombosis of intracranial venous structures may result. Patients with known or suspected sinusitis or AOM presenting with sudden worsening of headache, visual symptoms, seizures, or neurologic deficits may necessitate imaging for further evaluation.

MRI of the head with contrast is the examination of choice to evaluate for intracranial spread of infection. The specificity of MRI is superior in evaluation for meningitis and intracranial abscesses and in differentiating dural reaction from extra-axial or intra-axial abscess. Early in the process, meningeal inflammation may be the first abnormality present, which typically appears as meningeal enhancement on both CT and MRI. As an extra-axial abscess develops, the appearance is typically a fluid collection with high T2 signal intensity and low T1 signal intensity on MRI and usually higher attenuation relative to cerebrospinal fluid (CSF) on CT (Fig. 26.2). Abscess on either modality generally demon-

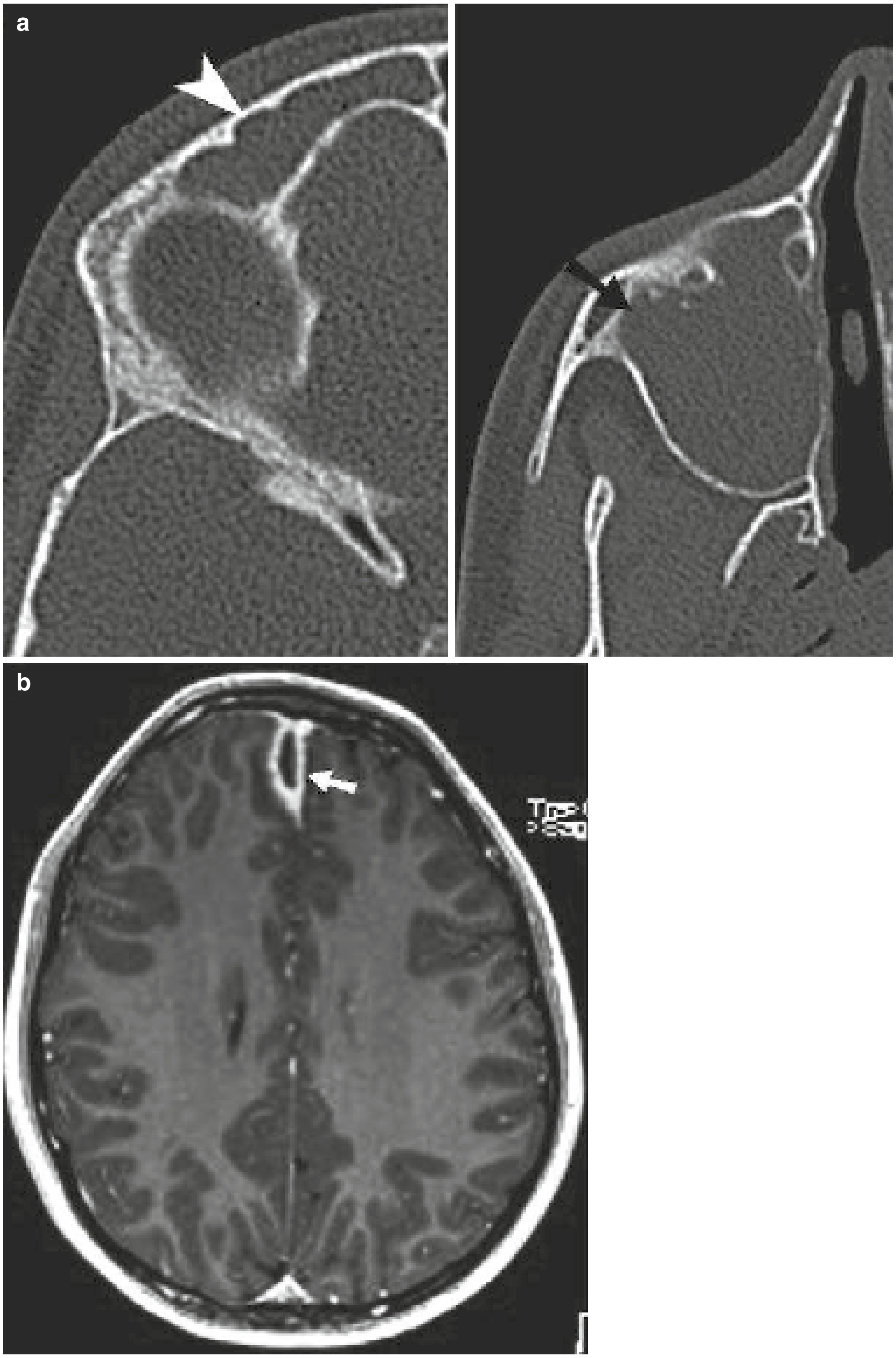

Fig. 26.2 Frontal sinusitis with subdural empyema. (**a**) Axial CT images of an 11-year-old boy exhibits opacification of the right maxillary (*arrow*) and frontal sinuses (*arrowhead*). (**b**) Axial post-gadolinium T1-weighted image demonstrates oval abscess (*arrow*) with meningeal enhancement in the interhemispheric fissure

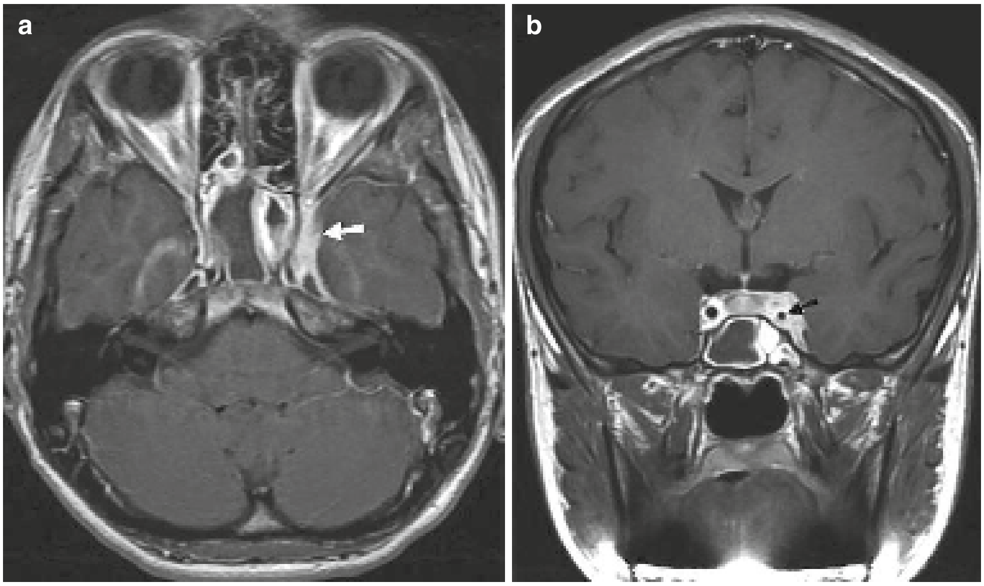

Fig. 26.3 Cavernous sinus thrombosis. (**a**, **b**) Axial and coronal T1-weighted post-gadolinium demonstrates enhancement and enlargement of the left cavernous sinus (*white arrow*) in a patient with marked mucosal enhancement of the adjacent sphenoid sinus. Note the diminished caliber of the left internal carotid artery (*black arrow*) relative to the right side due to mass effect

Table 26.2 Imaging findings in complications of acute otitis media and sinusitis

CT	The first abnormality: Meningeal enhancement Fluid collection has higher attenuation relative to CSF Thrombosis is best seen on CT venogram Cerebritis manifests as focally decreased attenuation
MRI	Imaging modality of choice: MRI with contrast The first abnormality: Meningeal enhancement Fluid collection has high T2 signal intensity and low T1 signal intensity Thrombosis is best established on postcontrast images on MR venogram Cerebritis manifests as increased T2 signal intensity in the brain parenchyma

strates peripheral enhancement on postcontrast images. Dural venous or cavernous sinus thrombosis are often challenging with either CT or MRI though thrombosis is best established on postcontrast images on either a CT or MR venogram examination appearing as a filling defect in the venous structure. Venous congestion may result from septic venous thrombosis and vasogenic and cytotoxic cerebral edema, sometimes with associated susceptibility artifact (representing hemorrhage) or restricted diffusion, may be seen in the parenchyma drained by the thrombosed dural venous sinus (Fig. 26.3) (Table 26.2) [5]. Cerebritis typically manifests as focally decreased attenuation on CT and increased T2 signal intensity in the brain parenchyma on MRI. As the process progresses to abscess formation, either modality will demonstrate progressive peripheral enhancement on postcontrast imaging along with surrounding vasogenic edema. Intracranial abscesses often exhibit restricted diffusion on MRI.

Intravenous antibiotics are indicated for intracranial spread of infection. Treatment of intracranial abscess typically involves surgical drainage. Septic thrombosis of the dural venous sinuses and cavernous sinus is managed with intravenous antibiotics and surgical drainage of the adjacent infectious source.

Orbital Infection: Subperiosteal Abscess and Orbital Cellulitis

Infection in the orbit constitutes an ophthalmologic emergency. Whether as a result of sinusitis or periorbital cellulitis extending across the orbital septum, this constitutes an emergency as the infection can cause blindness and spread intracranially. Imaging may be performed to determine the extent of the infection to localize an abscess or for surgical planning.

CT of the orbits is often the first imaging modality ordered because it is quick, accessible, and has a high sensitivity and specificity; however, according to the 2009 American College of Radiology (ACR) Appropriateness Criteria, contrast-enhanced MRI is recognized as a first-line imaging test to evaluate orbital infections. With periorbital cellulitis invading the orbit, the infection typically invades medially as the orbital septum is thinner in its medial portion. Orbital cellulitis will be seen on CT as obliteration of fat planes and soft tissue enhancement if contrast is administered. On MRI, the infection will demonstrate low T1 signal intensity, high T2 signal intensity, and soft tissue enhancement. In regard to subperiosteal abscess, the findings at CT generally include an extraconal fluid collection adjacent to an opacified sinus. Early orbital abscesses may not demonstrate peripheral enhancement on contrast-enhanced examinations on CT (Fig. 26.4) [6]. On MRI, subperiosteal abscesses have low T1 signal intensity, high T2 signal intensity, often peripherally enhance and often restricted diffusion (Fig. 26.5)

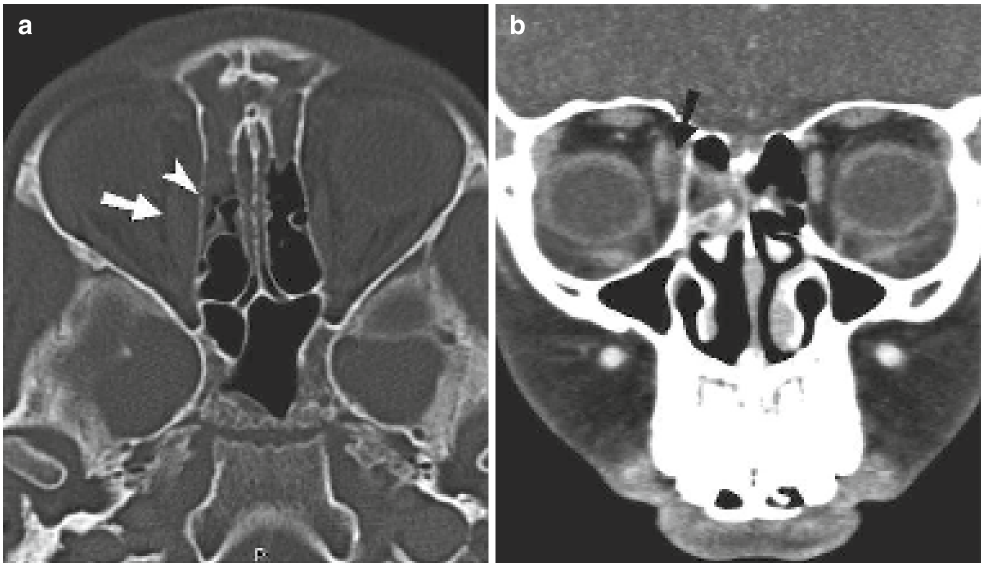

Fig. 26.4 Subperiosteal abscess. (**a**, **b**) Axial and coronal CT image demonstrates ethmoidal and frontal sinusitis with right extraconal subperiosteal abscess (*arrow*), adjacent to the medial rectus muscle. There is breech identified in the right lamina papyracea (*arrowhead*)

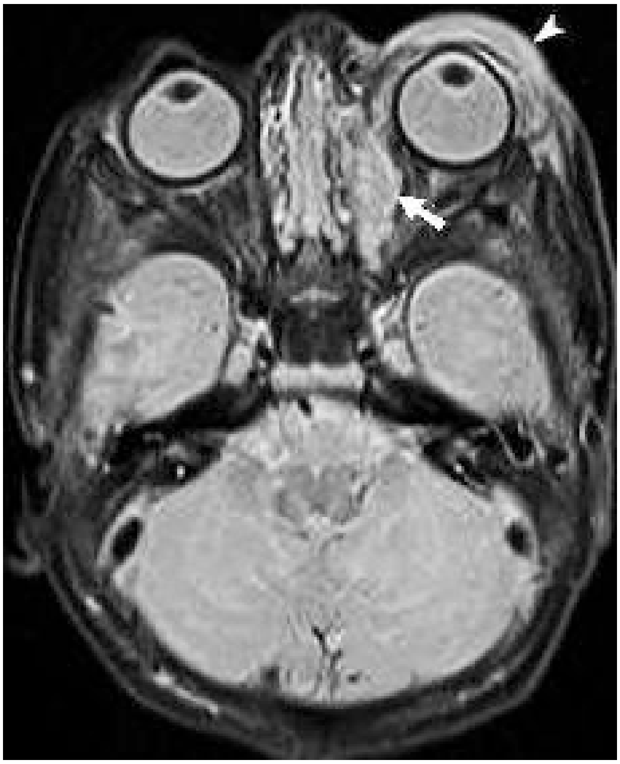

Fig. 26.5 Subperiosteal abscess. T2-weighted STIR sequence in an 8-day-old demonstrates subperiosteal abscess (*short white arrow*) along medial wall of the left orbit, secondary to ethmoidal sinusitis. There is left-sided proptosis with preseptal edema (*arrowhead*)

(Table 26.3). When contrast is administered, both MRI and CT are acceptable in diagnosing superior ophthalmic venous thrombosis.

Treatment for orbital cellulitis is intravenous antibiotics. Subperiosteal abscess typically warrants surgical intervention especially when there is visual acuity loss or paralysis of extraocular muscles.

Table 26.3 Imaging findings in orbital infection

CT	Obliteration of fat planes and soft tissue enhancement on contrast-enhanced CT Extraconal fluid collection adjacent to an opacified sinus In the early phase, peripheral enhancement is usually not seen
MRI	First-line imaging test: Contrast-enhanced MRI Low T1 signal intensity, high T2 signal intensity, and soft tissue enhancement Subperiosteal abscesses have: • Low T1 signal intensity • High T2 signal intensity • Peripherally enhance • Restricted diffusion

Transverse Myelitis

One of the more neurologically devastating diagnoses is transverse myelitis, which is defined as demyelination across the spinal cord that can occur at any level. Back pain and sensory deficits are common presenting symptoms. In addition to CSF analysis, imaging is often warranted to support the diagnosis and define its extent, as well as to exclude a mass in the spinal column that could produce similar symptoms but would have a different treatment.

MRI of the spine with contrast is the examination of choice in patients with suspected transverse myelitis, and MRI of the head is often also obtained. Affected portions of the spinal cord characteristically have increased signal on T2-weighted images and typically span at least two-thirds of the spinal cord in transverse dimensions (Fig. 26.6). There may be edema resulting in expansion of the cord. Contrast enhancement, usually peripherally around the lesion, may be seen in a significant percentage of patients [7].

Treatment generally includes intravenous steroids though some patients may also receive plasmapheresis. Prognosis is variable with approximately one-third of patients fully

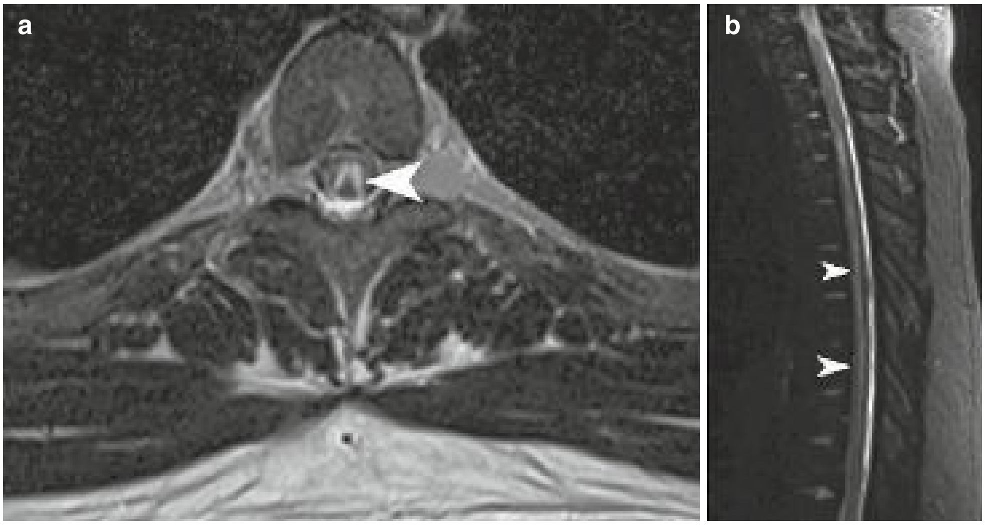

Fig. 26.6 Transverse myelitis. (**a**, **b**) Axial and sagittal T2-weighted images of the thoracic spine demonstrate multiple foci of abnormal increased signal (*arrowheads*) extending transversely through the spinal cord in an acutely paraplegic 18-year-old male

recovering and one-third of patients regaining minimal to no function.

Ventriculoperitoneal Shunt Malfunction

Ventriculoperitoneal (VP) shunts are usually placed to treat hydrocephalus. Shunting malfunction may manifest with either increased or decreased ventricle size with accompanying changes in intracranial pressure. Radiologically important causes of shunt malfunction include shunt valve malfunction, infection, tubing discontinuity, and loculated CSF accumulation in the peritoneal cavity (CSF pseudocyst), each of which are treated differently. Radiologic evaluation is usually indicated to confirm a change in size of the ventricles, evaluate for other intracranial abnormalities as well as to identify potential underlying mechanisms of disease.

VP shunt radiographic series usually includes images of the skull, neck, chest, and abdomen. If a discontinuity of the catheter exists at the level of the reservoir, a soft tissue mass may be seen within the scalp, representing a CSF leak into the scalp; however, most reservoirs are radiolucent, and radiolucency should not be confused with discontinuity in this location. Discontinuity, if present, will often be easily identified along the other portions of the tubing (Fig. 26.7). Within the abdomen, a new dense region located near the shunt tip is strongly suggestive of a CSF pseudocyst. This finding can be confirmed with ultrasound by demonstration of an anechoic to hypoechoic structure in the peritoneum without internal blood flow.

To assess interval change in size of ventricles, either CT or MRI may be utilized and comparison to prior examinations is helpful to assess for subtle changes from the patient's baseline examination. Considering the priority of limiting ionizing radiation in children and the regularity that children with shunts require advanced imaging of the brain, "rapid MRI" examinations have been developed at many institutions. Rapid MRI provides assessment of ventricular size equivalent to CT and is reasonable for excluding other intracranial causes of symptoms. The time commitment is much shorter than with routine MRI examinations. Rapid MRI examinations typically consist of T2-weighted images in the axial, sagittal, and coronal planes and typically require 5–10 min to acquire. In the absence of comparison studies, large ventricles and transependymal flow of CSF, seen as hypoattenuation on CT and high T2 signal intensity on MRI, in the periventricular white matter may suggest recent increase in ventricle size and pressure, though these are non-

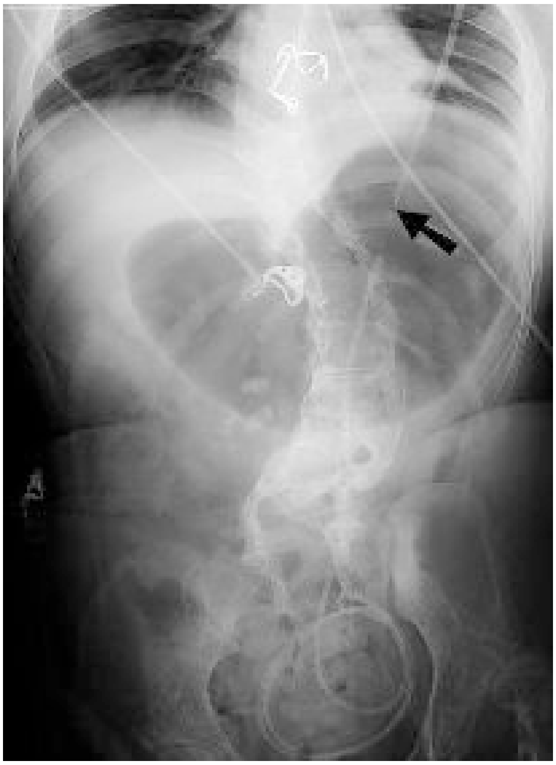

Fig. 26.7 Shunt catheter fragmentation. Abdominal radiograph in a patient with VP shunt malfunction shows fragmentation of the intra-abdominal portion of the shunt catheter (*arrow*)

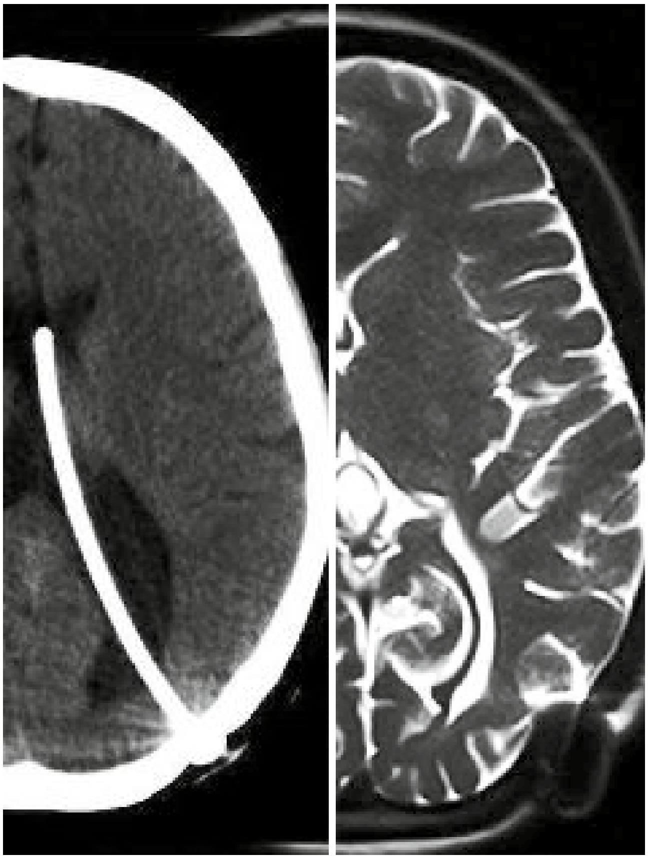

Fig. 26.8 Overshunting after shunt placement. Post-shunt placement baseline CT and follow-up rapid MR in an 11-year-old female shows marked decrease in the size of the lateral ventricles on follow-up imaging. The overshunting was believed to be the cause of the patient's acute episode of vomiting and headache

specific findings. Slit-like appearance of the ventricles may suggest overshunting in the absence of comparison examinations (Fig. 26.8) [8].

The main finding in the setting of ventriculitis on imaging is the abnormal appearance of CSF. On MRI, the infected CSF within the ventricles may retain signal characteristics on FLAIR and be relatively increased in signal to CSF on T1. On CT, infected CSF in the ventricles appears increased in attenuation relative to the rest of the CSF. The adjacent periventricular white matter usually appears edematous, with low attenuation on CT and high T2 signal on MRI.

Treatment of VP shunt malfunction is tailored to the specific cause of the malfunction though most complications require neurosurgical procedures.

Chest

Bronchiolitis

Bronchiolitis is an infection of the smaller airways, which produces thick secretions that can obstruct the airways. Chest radiography may be performed to support the diagnosis and to exclude other potential etiologies such as superimposed pneumonia.

The characteristic imaging findings of bronchiolitis result from thick secretions within the airways, which cause a combination of air trapping and atelectasis (Fig. 26.9). Air trapping results in a combination of focally and globally hyperexpanded lungs, which result in flattened diaphragms on both frontal and lateral radiographic views. Patchy atelectasis often results in streaky perihilar opacities although it may present as larger portions of collapsed lung. Peribronchial thickening is typically present due to airway inflammation.

Treatment is generally supportive though antiviral medication is used in severe cases of respiratory syncytial virus (RSV) infections.

Round Pneumonia

Pneumonia is common in the pediatric population, causing 13% of infectious illnesses in children under the age of 2 years, with its incidence decreasing with increasing age [9, 10]. Chest radiography is the primary radiologic examination for the evaluation of pediatric pulmonary infections.

Bacterial pneumonia in children produces pulmonary consolidation(s) with air bronchograms that may be similar in appearance to infections in adults. The pediatric lung differs from the adult lung in the number of microscopic communicat-

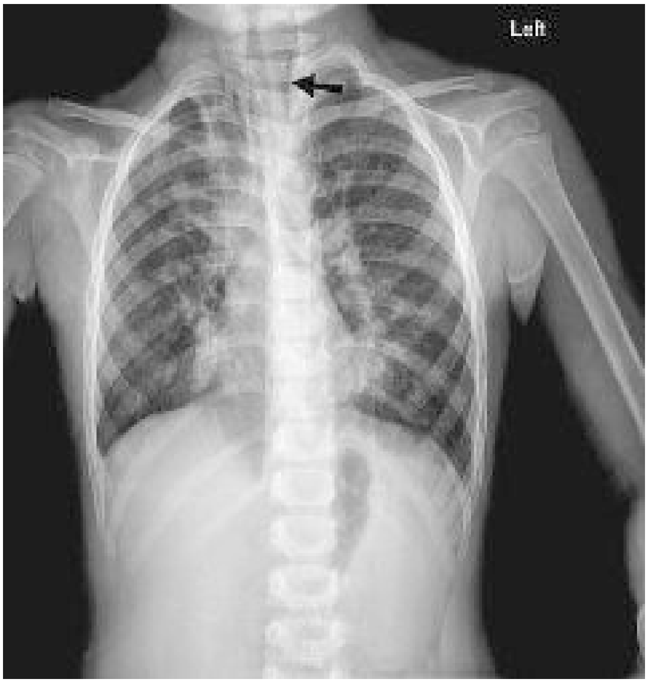

Fig. 26.9 Bronchiolitis and pneumomediastinum. Frontal chest radiograph in a patient with RSV infection demonstrates a combination of bilateral perihilar atelectasis and hyperexpanded lungs. Note the presence of pneumomediastinum (*arrow*) with gas tracking up the neck soft tissues

ing channels between alveoli, called the pores of Kohn and channels of Lambert. The decreased number of these communications between alveoli prohibits the spread of exudates between adjacent alveoli [11]. The result is that some pediatric patients with pneumonia will present with well-defined, rounded airspace consolidations termed "round pneumonia" (Fig. 26.10).

The appearance of round pneumonia may be disconcerting because its shape may mimic a mass. If a diagnosis of round pneumonia is not definitive, a follow-up chest radiograph may be considered in approximately 6 weeks to evaluate for resolution.

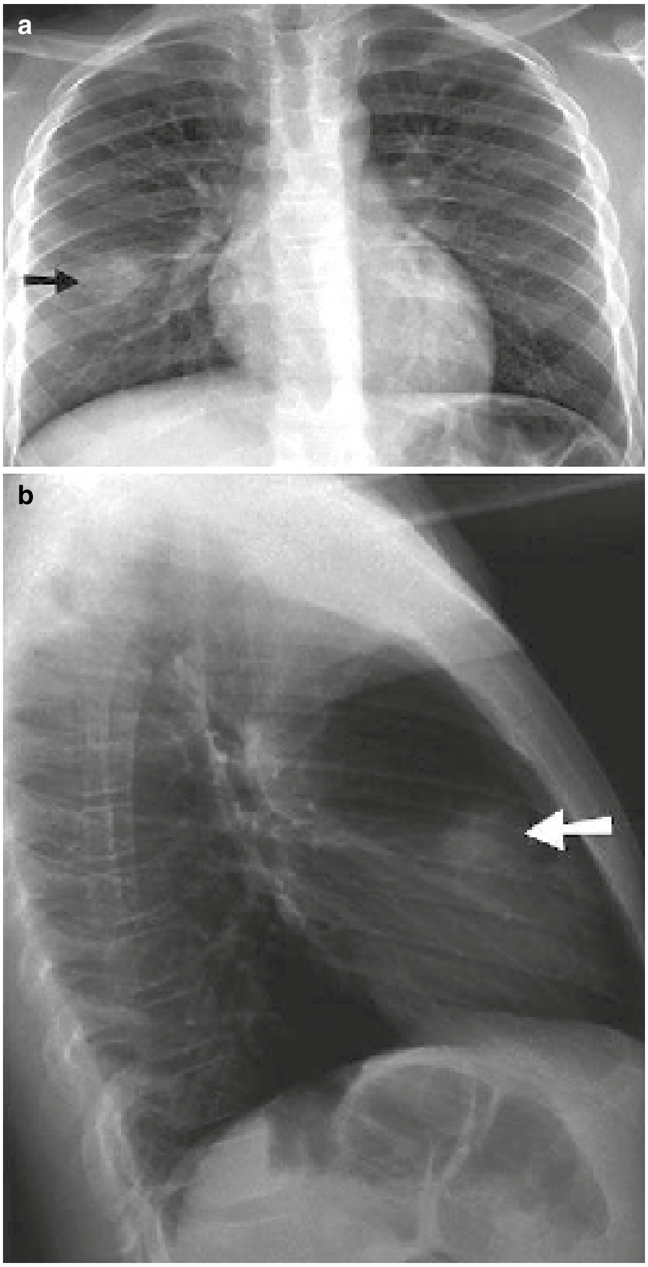

Fig. 26.10 Round pneumonia. (**a**, **b**) Frontal and lateral chest radiographs demonstrate a round consolidation in the right middle lobe (*arrows*)

Abdominal

Ingested Foreign Body

Due to the tendency for young children to place objects in their mouth, both accidentally and purposefully ingested foreign bodies are a relatively common occurrence in the pediatric population. The overall significance of the ingested foreign body depends on its nature [12]. The most common location of impaction is in esophagus. In esophagus, the most common location is upper esophageal sphincter, followed by midesophagus at the level of aortic arch impression, and lower esophageal sphincter. Most small objects, however, will pass harmlessly through the gastrointestinal tract.

Radiographic evaluation of suspected foreign body ingestion may include a neck and chest radiograph to evaluate the esophagus and airways as well as an abdominal radiograph to assess the remainder of the gastrointestinal tract. Some plastics and naturally occurring objects, such as wood, are radiolucent and may be radiographically undetectable. Most glass and metallic foreign bodies, excluding thin aluminum objects, are conspicuous (Fig. 26.11).

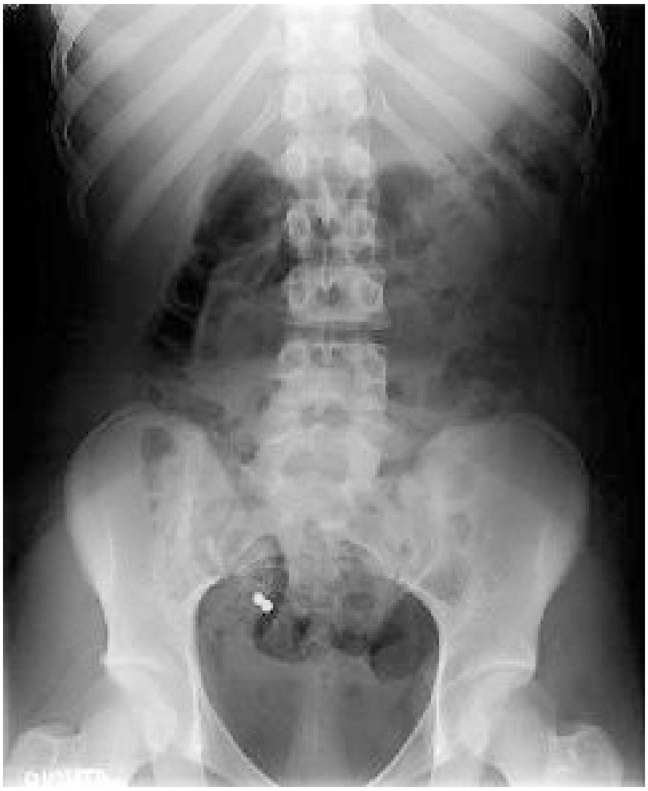

Fig. 26.11 Ingested metallic foreign bodies. Frontal radiograph of the abdomen and pelvis demonstrates two radiodense objects in the right lower quadrant. These were known to be batteries and when distal progression halted, surgery was performed and the batteries were found in the lumen of the appendix

Coins are the most common type of ingested foreign body in the pediatrics patients. On radiography, coins have metallic opacity and flat disk shape. Coins in the United States have standard sizes (Table 26.4). The main potential complication of ingested coins is esophageal obstruction and possibly secondary aspiration.

Disk batteries have a bilaminar structure, which appear as a double ring when seen en face on the radiographs (Figs. 26.12, 26.13, and 26.14). In profile, they have a beveled edge appearance on radiograph, which differentiates them from coins. Batteries can produce enough current to make liquefaction necrosis and thermal injury to the esophagus.

Management will depend on the object that has been ingested and its potential for harm. Obstruction and a high risk of perforation may be managed with endoscopy or surgery depending on the location of the foreign body. Smaller objects may warrant serial radiographs to assess distal progression. Batteries, particularly the disk varieties, may leak their contents and are therefore followed closely, with a low threshold for intervention. Magnets are unique in their ability to attract each other in adjacent segments of bowel, potentially causing focal pressure necrosis which may result in perforation and sepsis.

Table 26.4 Size of United States coins

Coin	Size (mm)
Penny	19
Nickel	21
Dime	18
Quarter	25

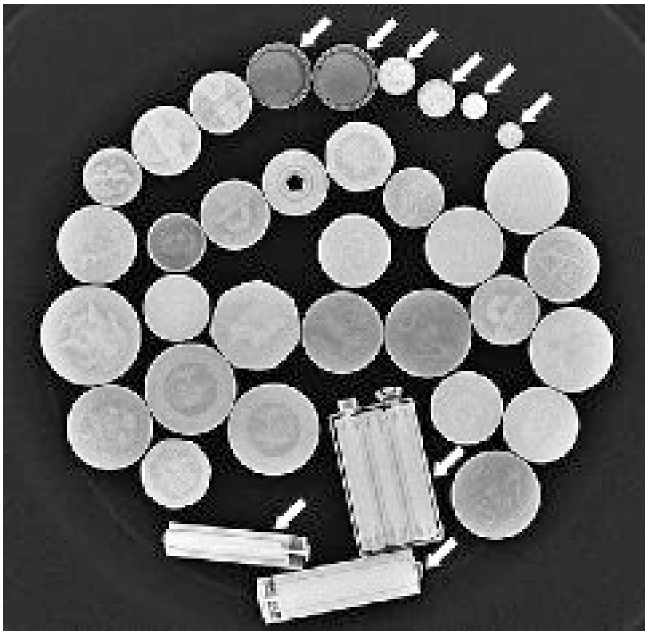

Fig. 26.12 Radiography of coins and batteries. Beveled edge appearance differentiates disk batteries coins. Batteries (disk, AA, A and 9-volt batteries) are identified with arrows in the radiograph

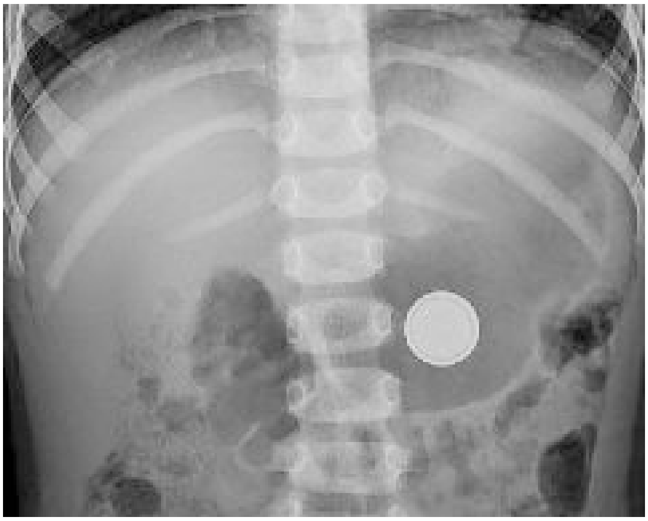

Fig. 26.13 Disk battery ingestion. Plain radiograph of abdomen shows a disk battery with peripheral double rings, located in the gastric lumen

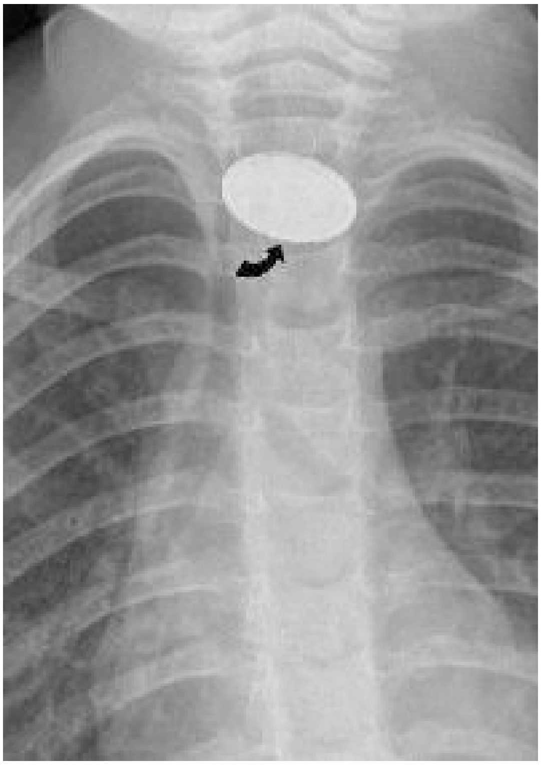

Fig. 26.14 Disk battery ingestion. A disk battery with eroded edges is demonstrated in the esophagus

Intussusception

Intussusception is one of the most common and important causes of an acute abdomen in the pediatric population, occurring most frequently at the ileocecal valve. The history and physical examination in patients with an intussusception is often nonspecific. The clinical threshold to proceed to imaging workup is low because of the potential for adverse outcome associated with failing to diagnose and treat an intussusception.

The initial imaging workup for a child with suspected intussusception is an abdominal ultrasound noting that when abdominal radiographs are performed, the bowel gas pattern may be abnormal and nonspecific. Ultrasound is estimated to have a 97.9% sensitivity, a 97.8% specificity, and a 99.7% negative predictive value (Fig. 26.15) [13]. Dilated, fluid-filled small bowel may be seen, suggesting obstruction. The intussusception will appear as a round mass with the imaging characteristics of its contents: Bowel wall is hypoechoic with a hyperechoic mucosa, but the appearance of the wall of the intussusceptum may be relatively hypoechoic due to congestion and edema. The mesentery contains fat, which is hyperechoic relative to bowel, and lymph nodes, which are oval and hypoechoic relative to fat. The classic bowel-within-bowel appearance of an intussusception is best appreciated on images obtained transverse to the bowel lumen (Table 26.5).

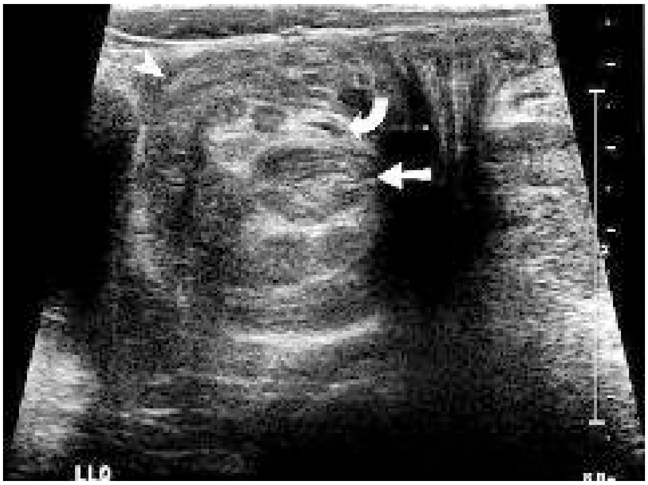

Fig. 26.15 Intussusception. Abdominal ultrasound of the descending colon demonstrates centrally located hypoechoic bowel (*straight arrow*) within the descending colon (*arrowhead*). Note the hyperechoic mesenteric fat (*curved arrow*) with internal hypoechoic lymph nodes associated with the intussusceptum

Table 26.5 Findings of intussusception on ultrasonography

Round mass
Hypoechoic bowel wall, hyperechoic mucosa
Intussusceptum wall may be relatively hypoechoic
Mesentery contains hyperechoic fat and hypoechoic oval lymph nodes
Bowel-within-bowel appearance

The treatment of intussusception is dependent on the patient's clinical status. If the patient presents relatively early in the process, air contrast or water-soluble contrast enema reduction may be attempted with high success rates. Patients who appear septic warrant surgical consultation [14].

Malrotation with Midgut Volvulus

The small and large bowel has ligamentous attachments, which tether it in place. In the case of malrotated bowel, these attachments are often absent. The bowel is therefore free to move and rotate, potentially on its axis, with resulting obstruction and vascular compromise. Volvulus is most commonly seen in the first few days of life although any young child with bilious vomiting warrants consideration of this diagnosis. If not recognized and treated promptly, the bowel supplied by the superior mesenteric vessels will infarct and bowel necrosis will ensue.

The initial test of choice in an infant younger than 6 weeks of age with bilious vomiting is the abdominal radiograph, which is used to evaluate for obstruction and to determine if the obstruction is proximal or distal. If there are findings suspicious for proximal obstruction, upper GI fluoroscopy is then performed in order to evaluate the anatomy, and specifically, the position of the ligament of Treitz. In malrotation with midgut volvulus, enteric contrast will empty into the proximal duodenum; however, instead of crossing the midline to the left and into the third portion of the duodenum, contrast will be descending inferiorly on the right. As small quantities of oral contrast advance through the proximal small bowel, a corkscrew configuration may be evident representing the bowel having been twisted upon its axis in a midgut volvulus [15] (Fig. 26.16).

Prompt surgical intervention is indicated; the classic intervention is the Ladd procedure.

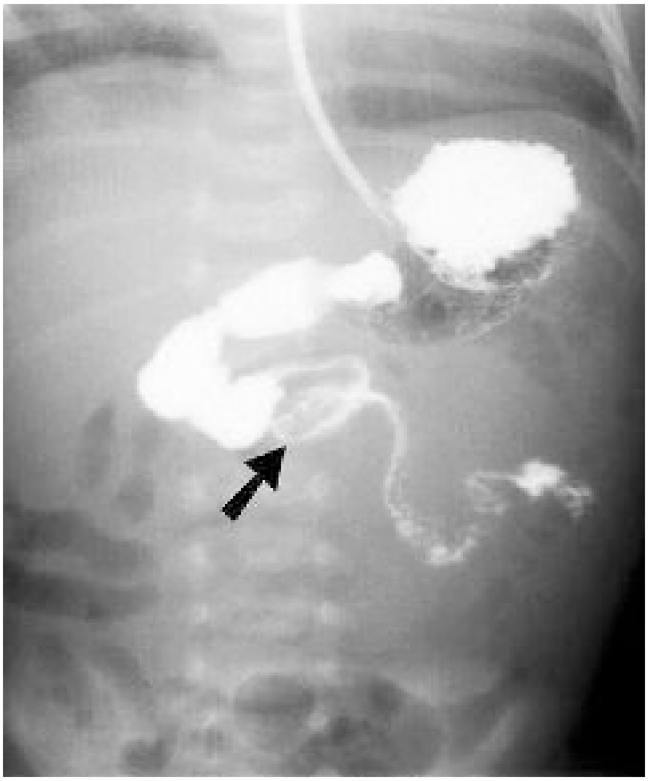

Fig. 26.16 Midgut volvulus. Frontal radiograph from an upper GI series demonstrates the proximal small bowel in a corkscrew pattern (*arrow*)

Hypertrophic Pyloric Stenosis

While hypertrophic pyloric stenosis does not necessarily represent a true surgical emergency, it is a commonly encountered problem in the emergency department due to its striking presentation and potential to lead to dehydration. Clinical suspicion of the hypertrophic pyloric stenosis generally merits ultrasound workup as this is nearly 100% sensitive and specific for the purpose of confirming or excluding hypertrophic pyloric stenosis [16].

Pyloric ultrasound is the preferred imaging test for an older infant (greater than 6 weeks) with a new onset of nonbilious vomiting. The length of the pyloric channel is measured in the longitudinal plane, while the pyloric muscle diameter is best obtained in the transverse plane relative to the pylorus. The upper limit of normal for thickness of the muscularis is approximately 3 mm (Fig. 26.17). The pyloric channel length is typically also reported for purpose of surgical planning [17]. Failure to demonstrate passage of gastric contents through the pylorus and into the duodenum during the examination further supports the diagnosis.

Surgical treatment consists of pyloromyotomy; long-term prognosis is excellent.

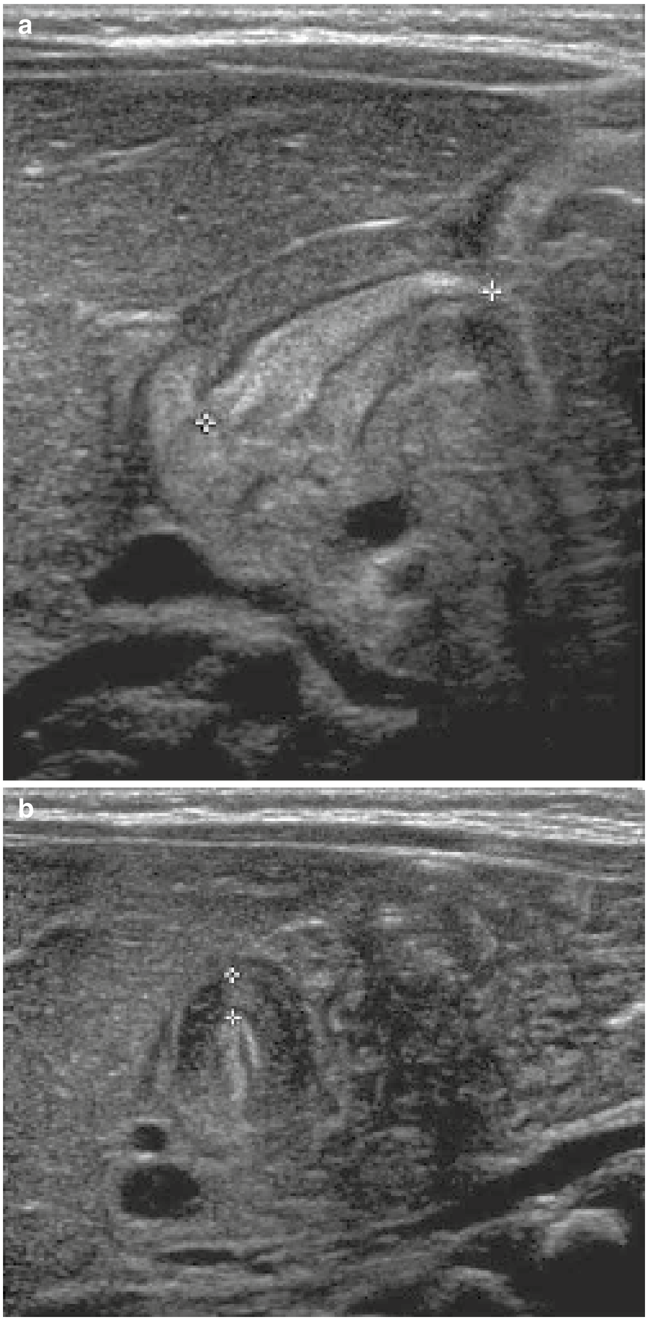

Fig. 26.17 Hypertrophic pyloric stenosis. (**a**, **b**) Longitudinal and transverse gray-scale ultrasonographic images of the pylorus in a child with projectile vomiting demonstrating a pylorus measuring 3.5 mm in thickness and a pyloric channel measuring 2 cm in length

Musculoskeletal

Septic Arthritis and Transient Synovitis

One of the most common pediatric musculoskeletal surgical emergencies is septic arthritis. A clinically similar condition, transient synovitis, is characterized by sterile joint fluid and synovial inflammation that may mimic the imaging features of septic arthritis. In both septic arthritis and transient synovitis, there is almost always a joint effusion present, and there may be accompanying warmth and erythema. It may not be possible to reliably examine the hip joint in some patients, especially when the patient is unable to tolerate movement of the joint. For this reason, the hip joint often receives more imaging consideration than other joints.

The predominant imaging findings in both transient synovitis and septic arthritis are joint effusion and synovial enhancement. Effusion is often easily identified in most joints, but small hip effusions may be occult both clinically and radiographically. Hip ultrasound is often performed initially. The affected side will demonstrate a hip joint capsule with increased fluid, which can vary in echogenicity from anechoic to hyperechoic (Fig. 26.18). Sonographic comparison to the unaffected side should always be made. If clinically indicated, an MRI with contrast may be obtained. The typical MRI findings of both septic arthritis and transient synovitis are a joint effusion with high T2 signal intensity and low T1 signal intensity and synovial enhancement on T1-weighted post-gadolinium images. On MRI, if there is abnormal bone marrow signal and enhancement in the bones adjacent to the affected joint, these findings favor the diagnosis of septic arthritis (Fig. 26.19) [18]. If septic arthritis is clinically suspected, joint fluid analysis should be obtained.

Septic arthritis warrants prompt surgical exploration, debridement, and treatment with intravenous antibiotics. Transient synovitis is usually self-limiting and does not necessitate surgical intervention.

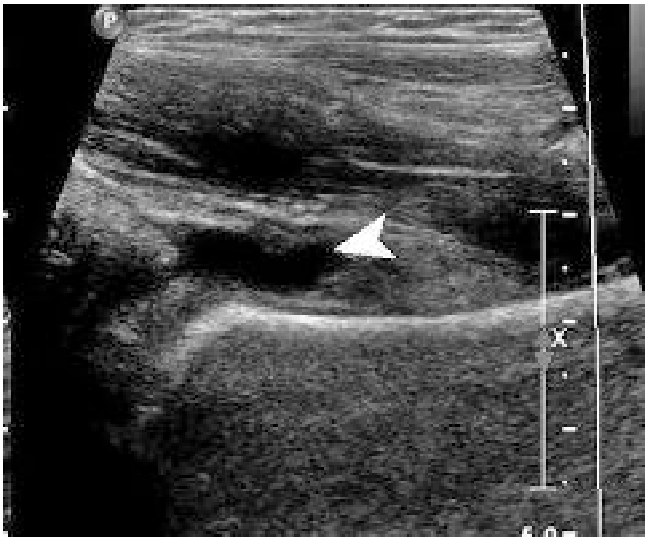

Fig. 26.18 Hip effusion. Gray-scale ultrasound evaluation of the right and left hips in a 4-year-old girl with acute pain and refusal to walk on the left leg demonstrates a left hip effusion (*arrowhead*)

Teaching Points

- ADEM is best diagnosed by combining clinical, radiological, and laboratory information.
- MRI of the head with contrast is the imaging test of choice when evaluating for intracranial spread of sinus or middle ear infections due to its better specificity compared to CT as well as its lack of ionizing radiation.
- MRI of the orbits with contrast is considered by the ACR to be the best initial imaging examination for evaluation of pediatric orbital infections for its detailed information of the patient's abnormalities and its lack of ionizing radiation.
- Patients with acute onset of severe neurologic deficits and back pain in the absence of trauma warrant MRI evaluation with contrast owing to its ability to define the location and extent of the abnormality as well as to evaluate for mass lesions that may produce similar symptoms.
- To assess the brain and ventricles of pediatric patients with VP shunts, order rapid MRI examinations when available and feasible as these patients often accumulate large radiation doses to the head over time.

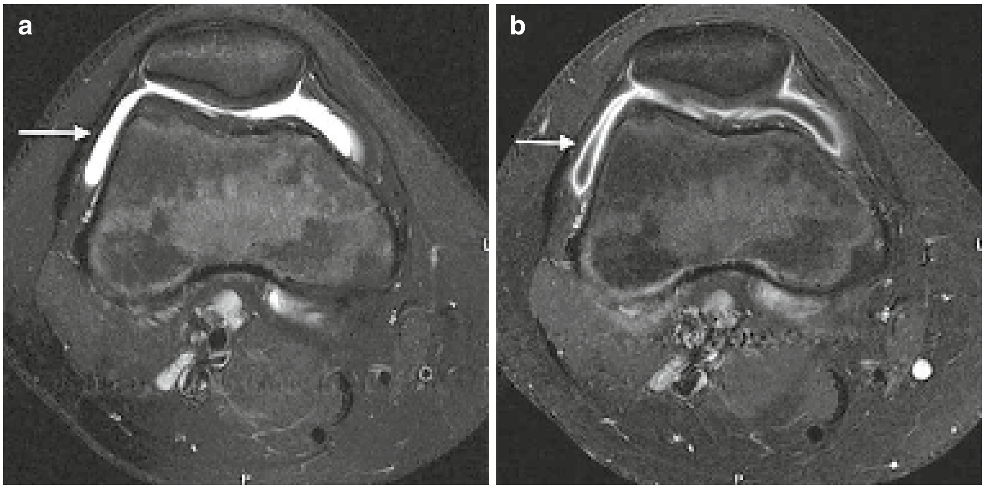

Fig. 26.19 Transient synovitis. (**a**) Axial T2-weighted fat-saturated image of the patient's right knee demonstrates normal bone marrow signal and a small suprapatellar knee effusion (*white arrow*). (**b**) Axial post-gadolinium T1-weighted image of the knee shows synovial enhancement (*arrow*), consistent with synovial inflammation

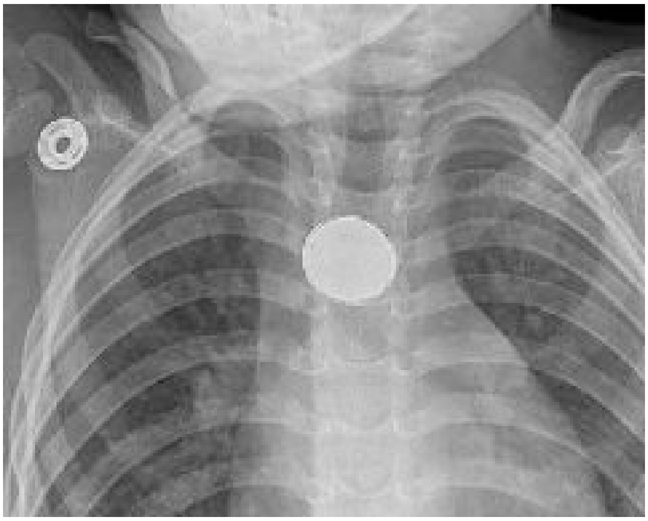

Fig. 26.20 abnormality seen in the radiograph is Disk battery.

- Ultrasound is an established first-line imaging modality for suspected intussusception that has an excellent sensitivity, specificity, and negative predictive value.
- When evaluating a young infant (<6 weeks) with bilious emesis, start with an abdominal radiograph to localize the obstruction.
- Pyloric ultrasound is almost 100% sensitive and specific in confirming or excluding hypertrophic pyloric stenosis.
- Especially when physical examination of a joint is limited, ultrasound may be extremely helpful in evaluating for joint effusions.

Questions

1. Based on the ACR Appropriateness Criteria, which of the following is the first-line imaging modality for assessing orbital infections?
   (A) Contrast-enhanced MRI
   (B) Noncontrast MRI
   (C) Contrast-enhanced CT
   (D) Noncontrast CT
   Answer: A

2. What abnormality is seen in the following radiograph (Fig. 26.20)?
   (A) Coin
   (B) Magnet
   (C) Disk battery
   (D) Battle cap
   Answer: C

3. Which of the following is the most common location of impaction of ingested foreign body?
   (A) Upper esophageal sphincter
   (B) Midesophagus at the level of aortic arch impression
   (C) Lower esophageal sphincter
   (D) Colon
   Answer: A

References

1. Menge T, Hemmer B, Nessler S, Wiendl H, Neuhaus O, Hartung HP, et al. Acute disseminated encephalomyelitis: an update. Arch Neurol. 2005;62:1673–80.
2. Madan S, Aneja S, Tripathi RP, Batra A, Seth A, Taluja V. Acute disseminated encephalomyelitis—a case series. Indian Pediatr. 2005;42:367–71.
3. Baum PA, Barkovich AJ, Koch TK, Berg BO. Deep gray matter involvement in children with acute disseminated encephalomyelitis. AJNR Am J Neuroradiol. 1994;15:1275–83.
4. Apak RA, Kose G, Anlar B, Turanli G, Topaloglu H, Ozdirim E. Acute disseminated encephalomyelitis in childhood: report of 10 cases. J Child Neurol. 1999;14:198–201.
5. Leach JL, Fortuna RB, Jones BV, Gaskill-Shipley MF. Imaging of cerebral venous thrombosis: current techniques, spectrum of findings, and diagnostic pitfalls. Radiographics. 2006;26(Suppl 1):S19–41; discussion S42–3.
6. Ludwig BJ, Foster BR, Saito N, Nadgir RN, Castro-Aragon I, Sakai O. Diagnostic imaging in nontraumatic pediatric head and neck emergencies. Radiographics. 2010;30:781–99.
7. Choi KH, Lee KS, Chung SO, Park JM, Kim YJ, Kim HS, et al. Idiopathic transverse myelitis: MR characteristics. AJNR Am J Neuroradiol. 1996;17:1151–60.
8. Goeser CD, McLeary MS, Young LW. Diagnostic imaging of ventriculoperitoneal shunt malfunctions and complications. Radiographics. 1998;18:635–51.
9. Eren S, Balci AE, Dikici B, Doblan M, Eren MN. Foreign body aspiration in children: experience of 1160 cases. Ann Trop Paediatr. 2003;23:31–7.
10. Denny FW, Clyde WA Jr. Acute lower respiratory tract infections in nonhospitalized children. J Pediatr. 1986;108:635–46.
11. Bramson RT, Griscom NT, Cleveland RH. Interpretation of chest radiographs in infants with cough and fever. Radiology. 2005;236:22–9.
12. Hunter TB, Taljanovic MS. Foreign bodies. Radiographics. 2003;23:731–57.
13. Hryhorczuk AL, Strouse PJ. Validation of us as a first-line diagnostic test for assessment of pediatric ileocolic intussusception. Pediatr Radiol. 2009;39:1075–9.
14. Niramis R, Watanatittan S, Kruatrachue A, Anuntkosol M, Buranakitjaroen V, Rattanasuwan T, et al. Management of recurrent intussusception: nonoperative or operative reduction? J Pediatr Surg. 2010;45:2175–80.
15. Houston CS, Wittenborg MH. Roentgen evaluation of anomalies of rotation and fixation of the bowel in children. Radiology. 1965;84:1–18.
16. Hernanz-Schulman M, Neblett WW. Imaging of infantile hypertrophic pyloric stenosis (IHPS). In: Medina LS, Applegate K, Blackmore CC, editors. Evidence-based imaging in pediatrics:

improving the quality of imaging in patient care. New York: Springer; 2009.

17. Cogley JR, O'Connor SC, Houshyar R, Dulaimy KA. Emergent pediatric us: what every radiologist should know. Radiographics. 2012;32:651–65.
18. Lee SK, Suh KJ, Kim YW, Ryeom HK, Kim YS, Lee JM, et al. Septic arthritis versus transient synovitis at mr imaging: preliminary assessment with signal intensity alterations in bone marrow. Radiology. 1999;211:459–65.

Signs in Radiology: Plain Radiographic Signs

27

Khyati Bidani, Gandharv Singh, Garima Chandra,
and Ajay Singh

Cupola Sign

Cupola sign, also known as the saddlebag sign or the moustache sign, is seen on a supine abdominal radiograph in patients with free intraperitoneal air.

It refers to the arcuate lucency that overlies the lower thoracic spine and extends caudally to the heart (Fig. 27.1). It results from non-dependant air accumulation in the median subphrenic space, especially underneath the central tendon of the diaphragm due to its anterior location. The term cupola is used to imply the "inverted cup"-shaped configuration of the lucency where the superior border is more well-defined than the inferior. Sometimes, the falciform ligament can also be seen contiguously with the superior border of the lucency.

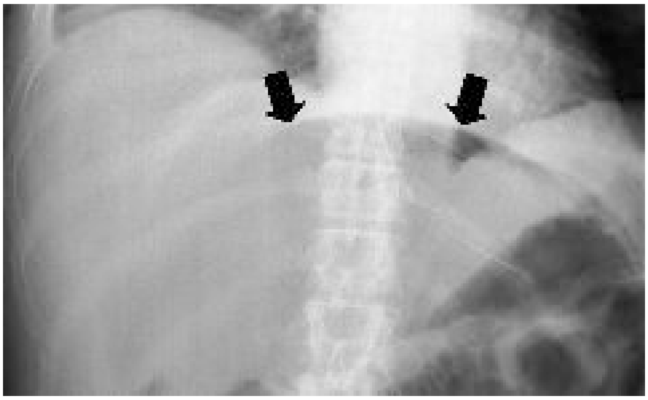

Fig. 27.1 Cupola sign. Upright plain radiograph of the abdomen demonstrating free air accumulation under the central tendon of the diaphragm (arrows)

Rigler Sign

Rigler sign, also known as the double wall sign or the bas-relief sign is seen on a supine abdominal radiograph in patients with free intraperitoneal air.

It refers to the visualization of both sides of the intestinal wall from the intraluminal bowel gas and the air within the peritoneal cavity (Figs. 27.2 and 27.3). The sign is relatively insensitive since it requires significant amounts of gas (up to

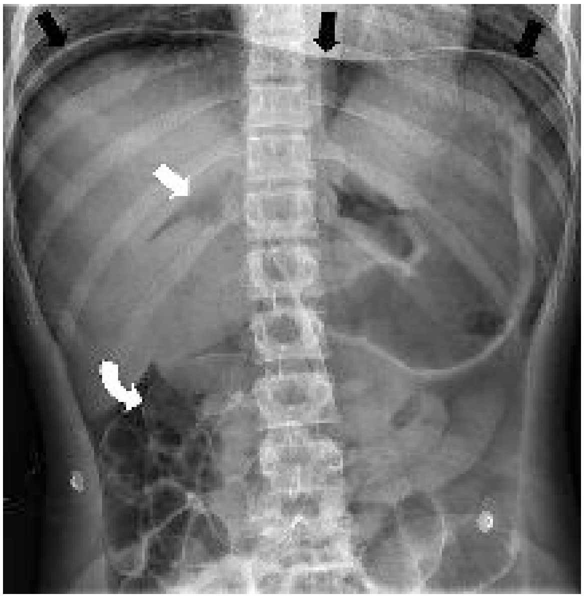

Fig. 27.2 Rigler sign, continuous diaphragm sign, and doge cape's sign. Supine plain radiograph of the abdomen demonstrating air outlining inside and outside of multiple small bowel loops (curved arrow). There is free air also outlining the diaphragm as well as the central tendon (continuous diaphragm sign) (black arrows). There is also a triangular collection of free air in the Morrison's pouch (doge cape's sign) (white arrow)

K. Bidani · G. Singh · G. Chandra
Department of Radiology, Massachusetts General Hospital,
Boston, MA, USA

A. Singh (✉)
Division of Emergency Radiology, Department of Radiology,
Massachusetts General Hospital, Boston, MA, USA

Harvard Medical School, Massachusetts General Hospital,
Boston, MA, USA
e-mail: asingh1@partners.org

© The Author(s), under exclusive license to Springer Nature Switzerland AG 2024
A. Singh (ed.), *Emergency Radiology*, https://doi.org/10.1007/978-3-031-65770-2_27

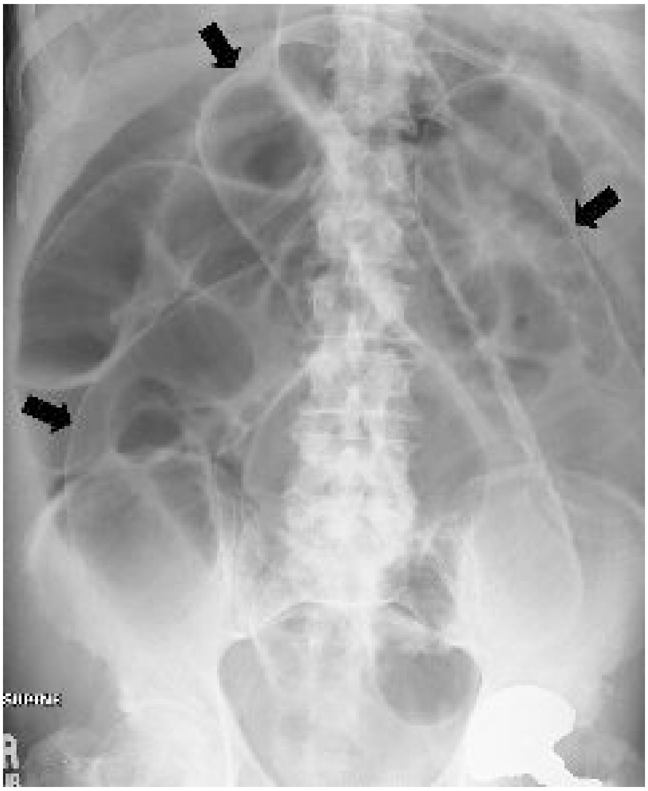

Fig. 27.3 **Rigler sign.** Supine plain radiograph of the abdomen demonstrating a large amount of free air outlining multiple small bowel loops (arrows). There is air distension of multiple small bowel loops due to paralytic ileus

1 L), such as in cases of colonic perforation, before becoming evident. Occasionally, two gas-distended bowel loop segments in contact with each other can produce a false positive Rigler sign, also known as the pseudo-Rigler sign. The presence of free air in Morrison's pouch can create a triangular-shaped lucency which is known as the doge cap sign (Fig. 27.2).

Football Sign and Falciform Ligament Sign

Football sign represents a massive pneumoperitoneum that distends the abdomen and is most frequently seen in cases of gastrointestinal perforation in neonates.

It refers to a large, vertically oriented oval radiolucency (Fig. 27.4) that, on a supine radiograph, outlines the peritoneal cavity's boundaries and creates a distinct interface with the parietal peritoneum. The radiological appearance resembles the shape of the American football, hence the name of the sign. Occasionally, free air can also delineate falciform and medial umbilical ligaments within the lucency, which are not apparent as distinct structures from the liver under normal circumstances.

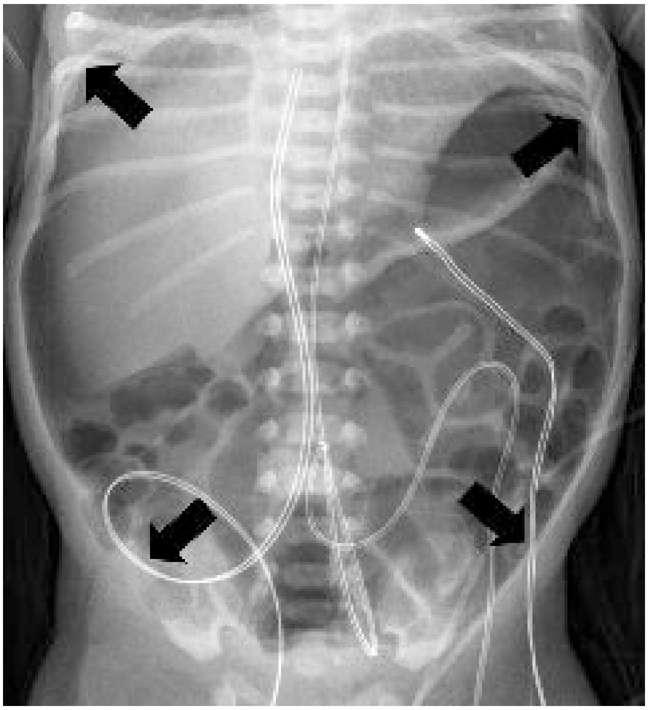

Fig. 27.4 **Football sign.** Supine plain radiograph of the abdomen demonstrating a massive amount of free air outlining the boundaries of the peritoneal cavity (arrows)

Triangle Sign

Triangle sign is a sign of free intraperitoneal air and is probably more sensitive than Rigler's sign since it requires less gas to become evident.

It refers to the triangular radiolucency (Fig. 27.5) resulting from the accumulation of free intraperitoneal air between three adjoining bowel loops or between two bowel loops and the parietal peritoneum.

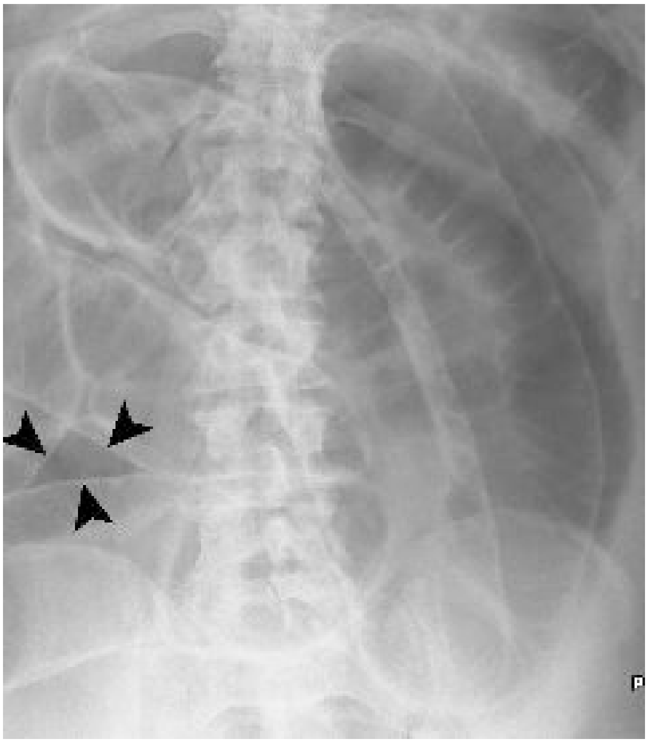

Fig. 27.5 **Triangle sign.** Supine plain radiograph of the abdomen demonstrating triangular free air accumulation between three adjoining small bowel loops (arrowheads)

Fissure of Ligamentum Teres Sign

Fissure of ligamentum teres sign, seen on supine abdominal radiographs, is a sign of free intraperitoneal air.

It refers to the visualization of the extrahepatic portion of the ligamentum teres (Fig. 27.6) from the free air in the peritoneal cavity. Ligamentum teres is a peritoneal ligament representing the remnant of the obliterated left umbilical vein. The free air around the ligament creates a slit-like hyperlucency on the right of vertebral bodies, most typically between the tenth and twelfth ribs.

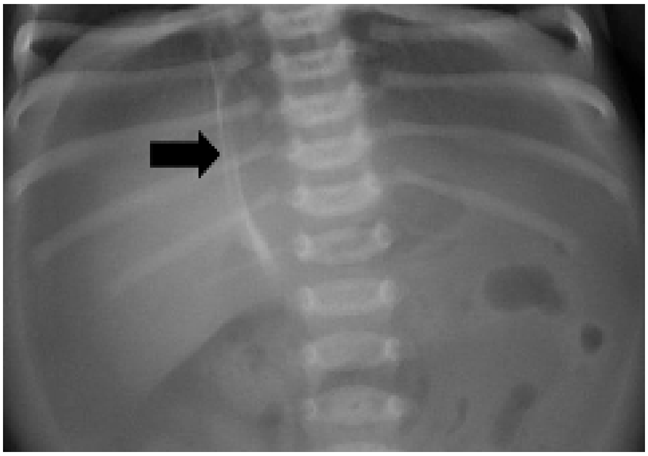

Fig. 27.6 **Fissure of Ligamentum Teres sign.** Supine plain radiograph of the abdomen demonstrating free air outlining the extrahepatic portion of ligamentum teres (arrow)

Continuous Diaphragm Sign

Continuous diaphragm sign, seen on chest radiograph, is a sign of free air abutting the diaphragm.

Typically, the central portion of the diaphragm blends with the cardiac silhouette on chest radiographs, making it difficult to distinguish. If the diaphragm is visible across the midline continually (Figs. 27.2 and 27.7), it is highly suspicious of the free gas in the mediastinum, pericardium, or peritoneal cavity. Lucency above the diaphragm suggests pneumomediastinum or pneumopericardium whereas lucency below the diaphragm indicates pneumoperitoneum.

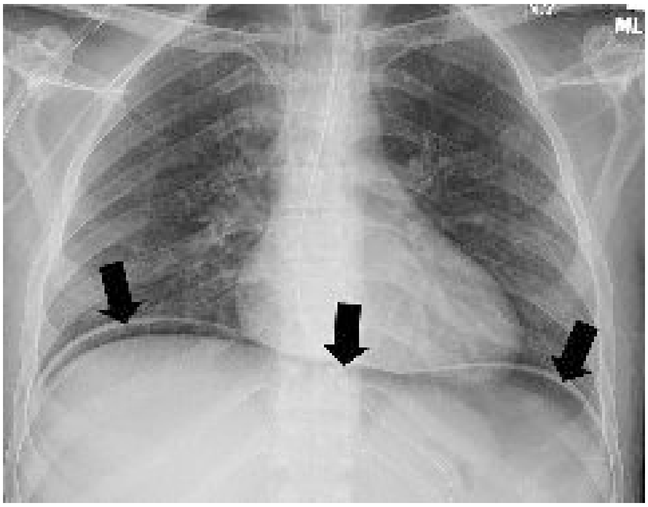

Fig. 27.7 **Continuous diaphragm sign.** Upright plain radiograph of the chest demonstrating free air outlining the entire diaphragm including the central tendon making it visible across the midline continually (arrows)

Steeple Sign

Steeple sign is most characteristic of acute laryngotracheobronchitis (croup). Plain radiographs are utilized to rule out other causes of stridor or croup mimics such as foreign body aspiration, epiglottitis, and congenital subglottic stenosis. The steeple sign can also be demonstrated in some other conditions, namely bacterial tracheitis, angioneurotic edema, epiglottitis, and thermal injuries.

It refers to the subglottic narrowing (Fig. 27.8) and is typically visualized on the anterosuperior radiograph of the soft tissues of the neck. It results from tracheal edema causing elevation of the tracheal mucosa which produces an inverted V appearance of the tracheal air column resembling a church steeple, hence the name of the sign.

Fig. 27.8 **Steeple sign.** (**a**, **b**) Plain radiographs of soft tissue neck demonstrating smooth steeple-shaped subglottic narrowing of the upper trachea (arrow)

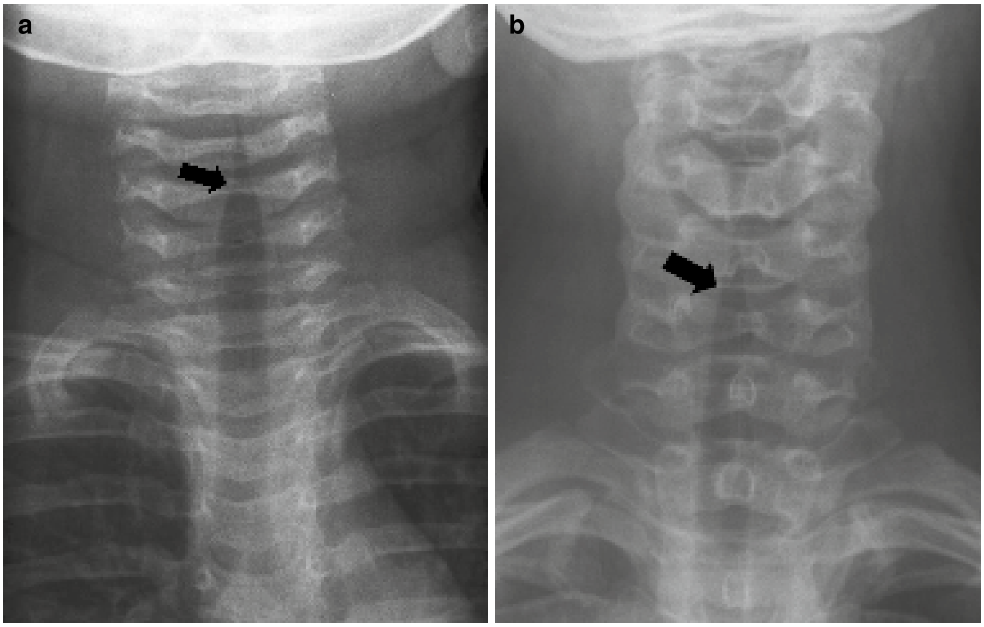

Thumb Sign

Thumb sign refers to edematous prominence of epiglottis seen with acute epiglottitis which carries a significant risk of acute airway compromise. As a result of routine pediatric immunization for *Haemophilus influenzae* serotype b, the incidence of acute epiglottitis has dramatically reduced in children but has increased in the adult population.

It refers to the thickened, edematous, thumb-shaped appearance of the epiglottis (Fig. 27.9) seen on the lateral radiograph of the soft tissues of the neck.

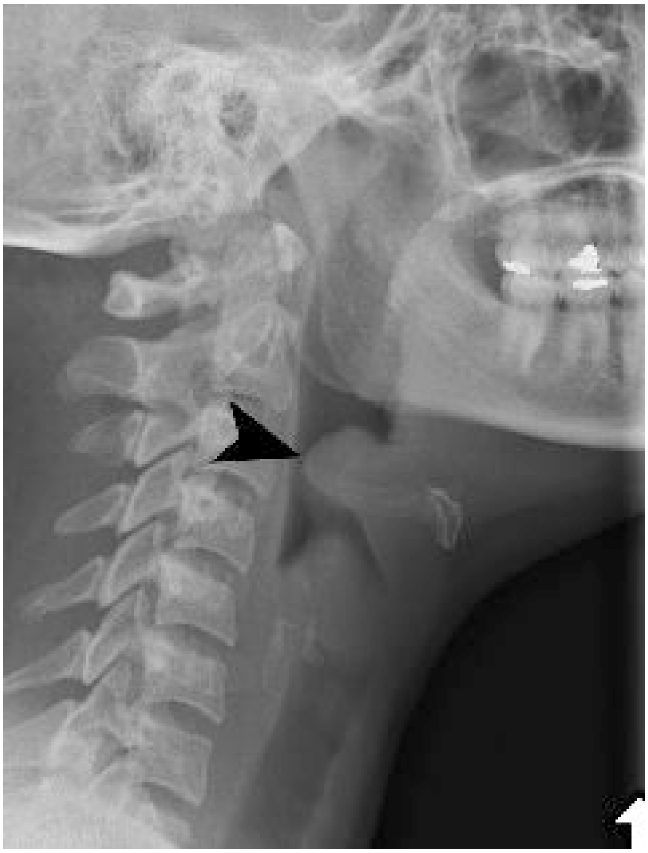

Fig. 27.9 Thumb sign. Lateral radiograph of soft tissue neck demonstrates lobulated thickening of the epiglottis (arrowhead) compromising the pharyngeal airway

Thumbprinting Sign

Thumbprinting sign is seen in numerous bowel conditions, most notably in ischemic colitis, pseudomembranous colitis, and inflammatory bowel disease, and can be usually demonstrated within 24 h of the bowel insult. It results from submucosal edema and/or bleeding, leading to nodular thickening of the colonic haustra which projects into the lumen of the involved large bowel segment.

It refers to the projection of multiple round, smooth, and scalloped defects into the air-filled colonic lumen imparting the appearance of regularly placed thumbprints (Fig. 27.10) on an abdominal radiograph.

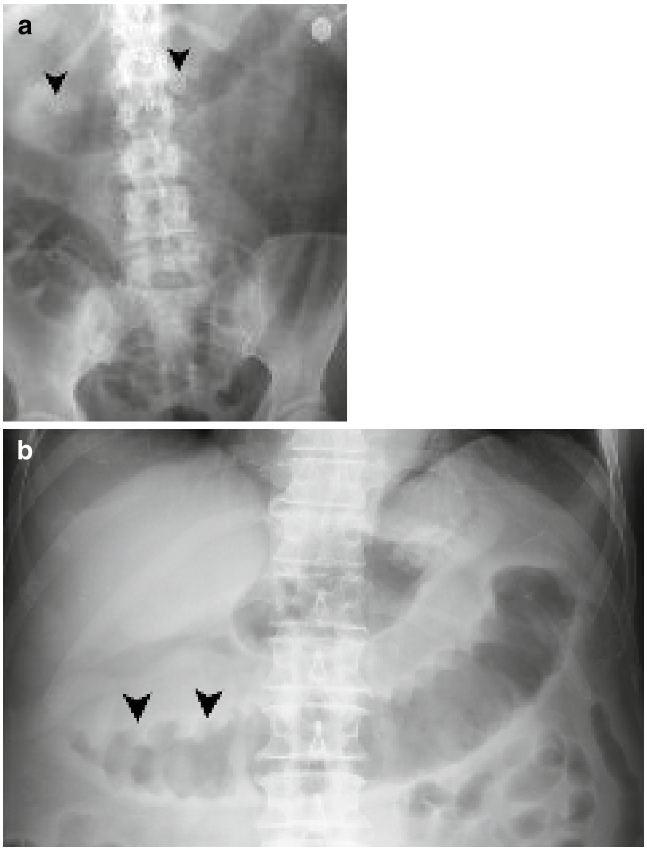

Fig. 27.10 Thumbprinting sign. (**a**, **b**) Supine radiograph of the abdomen demonstrates thumb-shaped nodular indentation (arrowheads) along the transverse colonic wall in two patients with acute colitis

Deep Sulcus Sign

Deep sulcus sign, seen on supine chest radiograph, is highly suggestive of pneumothorax.

It refers to an increased lucency and deepening of the lateral costophrenic sulcus toward the hypochondrium (Fig. 27.11) on the supine chest radiograph. In the supine position, the free air in the pleural space collects anteriorly and basally in the non-dependant regions of the pleural cavity, producing the deep, hyperlucent, ipsilateral costophrenic angle. In the upright position, the intrapleural air rises up and the pneumothorax is seen at the apex. The visceral pleural line visible on the upright chest radiographs is most often not seen on supine radiographs, making deep sulcus sign an important finding for diagnosing pneumothorax in supine patients.

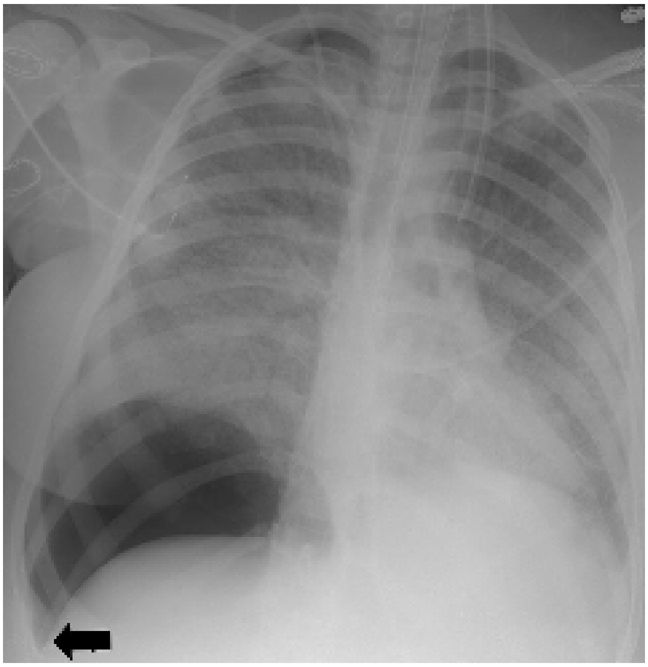

Fig. 27.11 **Deep sulcus sign.** Supine radiograph of the chest in a patient with pneumothorax demonstrates air accumulation in the pleural cavity producing a deep, hyperlucent ipsilateral costophrenic angle (arrow)

Golden S Sign

Golden S sign, also known as the “reverse S sign of the Golden,” seen on the posteroanterior chest radiographs, is a sign of right upper lobe collapse due to obstructive hilar mass. The presence of this sign is highly suspicious for primary lung malignancy and requires further evaluation with a chest CT.

It refers to the creation of a reverse S-shaped configuration of the minor fissure of the lung (Fig. 27.12) caused by right upper lobe collapse due to hilar mass. The lateral concave portion of the minor fissure is formed from the superior and medial pulling of the collapsed right lobe toward the superior mediastinum and the medial convex portion of the minor fissure represents the bulge from the central mass.

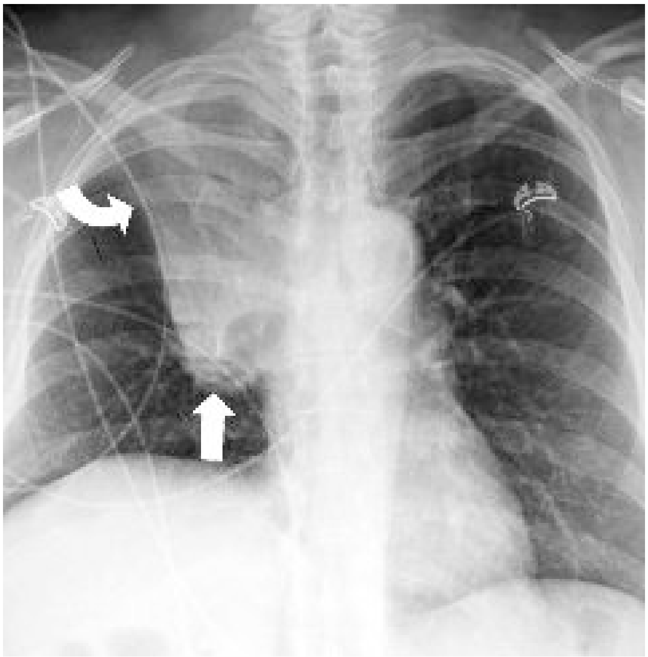

Fig. 27.12 **Golden S sign.** Frontal radiograph of the chest of a patient with right non-small cell carcinoma demonstrating an obstructive right hilar mass causing right upper lobe collapse. The right upper lobe collapse is causing cranial displacement of the right horizontal fissure (curved arrow). The medial aspect of the horizontal fissure is bulging caudally (arrow) due to the right hilar mass and producing a reverse S-shaped configuration of the minor fissure

String of Pearls Sign

String of pearls sign, seen on upright and decubitus abdominal radiographs, is suggestive of mechanical small bowel obstruction.

It refers to a row of multiple small air bubbles trapped in the valvulae conniventes (mucosal folds) of the dilated small bowel (Fig. 27.13). The obstruction results in gaseous distension of the small bowel proximally and the development of multiple air-fluid levels. This dilation causes valvulae conniventes to enlarge which then traps the small gas bubbles within them.

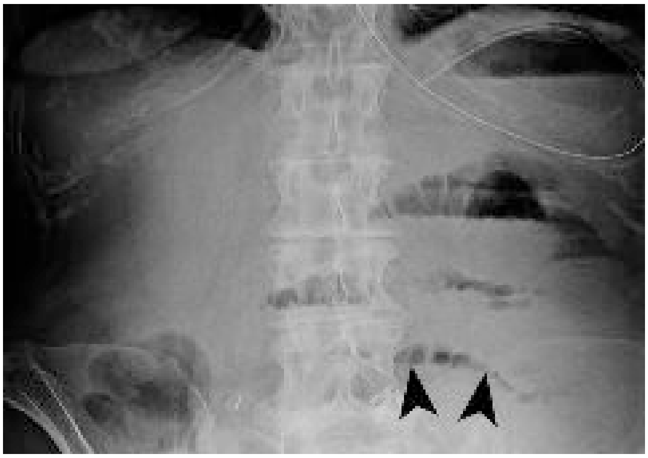

Fig. 27.13 String of pearls sign. Upright radiograph of the abdomen in a patient with partial distal small bowel obstruction demonstrates multiple non-dependent air bubbles (arrowheads) trapped between valvulae conniventes of fluid-distended small bowel loops

Coffee Bean Sign

Coffee bean sign, seen on abdominal radiograph, is a sign of sigmoid volvulus. If not managed emergently, it can result in colonic perforation.

It refers to the inverted U-shaped configuration of the dilated loop of the sigmoid colon (Fig. 27.14). It results from the twisting of the sigmoid colon on its mesenteric axis creating a closed-loop obstruction. The dilated bowel frequently extends from the pelvis into the right upper abdomen. The apposed inner walls of the sigmoid colon produce a central linear opacity pointing toward the pelvis and resembling the cleft of the coffee bean.

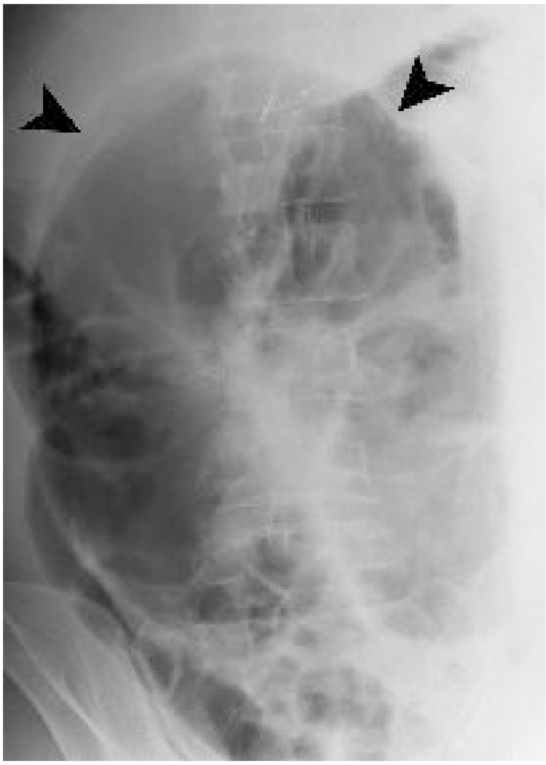

Fig. 27.14 Coffee bean sign. Supine radiograph of the abdomen demonstrating air-containing dilated inverted U-shaped configuration of the sigmoid colon resembling a coffee bean (arrowheads). This closed-loop obstruction is due to the twisting of the sigmoid colon on its mesenteric axis

Flexion Teardrop Fracture

Flexion teardrop fractures of the cervical spine are the most severe and unstable form of cervical spinal fractures given their high degree of association with spinal cord injury. These result from flexion injury with axial loading (compression) and typically involve C5-C6 vertebrae. Posterior displacement of the divided vertebral body into the spinal cord is responsible for the characteristic neurologic injury. Given the unstable nature of the fracture due to the disruption of both anterior and posterior ligaments, operative management is indicated.

It refers to the distinctive triangular-shaped fractured fragment (Fig. 27.15) involving the anterior-inferior aspect of the vertebral body. These are best seen on lateral view radiographs of the neck.

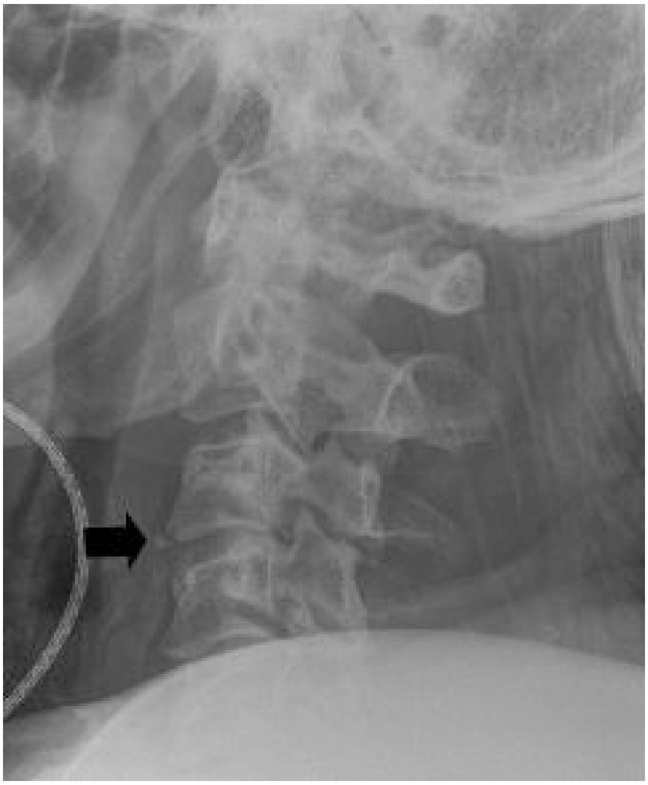

Fig. 27.15 **Flexion teardrop fracture.** Lateral radiograph of the cervical spine demonstrating triangular-shaped fractured fragment at the anterior-inferior aspect of the C3 vertebral body (arrow) due to flexion teardrop fracture

Luftsichel Sign

Luftsichel sign, seen on posteroanterior chest radiographs, is suggestive of upper lobe collapse, and is more characteristically seen with left upper lobe collapse than the right.

It refers to the paramediastinal crescent-shaped hyperlucency (Fig. 27.16) caused by hyperexpansion of the apical segment of the left lower lobe which gets pulled superiorly resulting in hyperlucency between the aortic arch medially and collapsed left upper lobe laterally. The term “Luftsichel” comes from the German words “Luft” and “Sichel” meaning air and crescent, respectively.

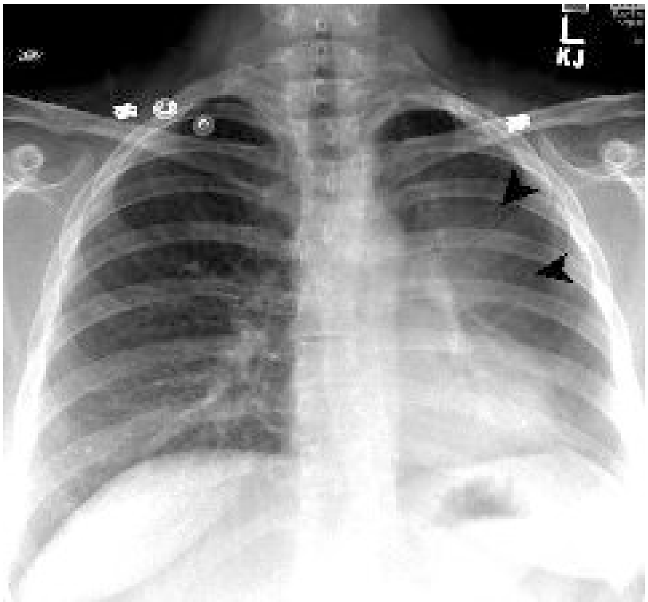

Fig. 27.16 **Luftsichel sign.** Frontal radiograph of the chest demonstrates ill-defined opacification in the left upper zone (arrowheads) due to left upper lobe collapse. There is hyperexpansion of the apical segment (arrow) of the left lower lobe between the collapsed left upper lobe and the arch of the aorta

Batwing Sign

Batwing sign, also known as angel wing appearance or butterfly appearance, is seen on frontal chest radiograph in patients with acute pulmonary edema. Less commonly, it can be seen in cases of pulmonary hemorrhage, alveolar proteinosis, pneumonia, sarcoidosis, inhalational injuries, and progressive massive fibrosis.

It refers to the presence of bilateral, symmetrical, perihilar airspace edema with sparing of the lung periphery (Fig. 27.17). The appearance resembles the spread wings of a butterfly or a bat, hence the name of the sign.

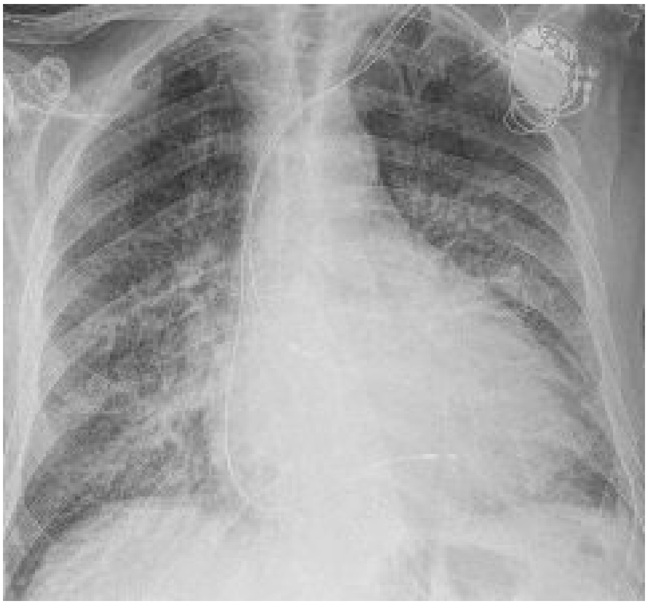

Fig. 27.17 **Angel wing sign.** Frontal radiograph of the chest demonstrating bilateral interstitial and alveolar prominence along with Kerley B lines consistent with pulmonary edema

Bulging Fissure Sign

The bulging fissure sign is seen on chest radiograph and is typically described in patients with Klebsiella pneumonia due to its propensity to produce enormous amounts of inflammatory exudate.

It refers to the intense consolidation of the upper lobes of the lung causing the interlobar fissure to bulge outwards in the posteroinferior direction (Fig. 27.18). Klebsiella most commonly involves the posterior segment of the right upper lobe, pushing the minor fissure downward.

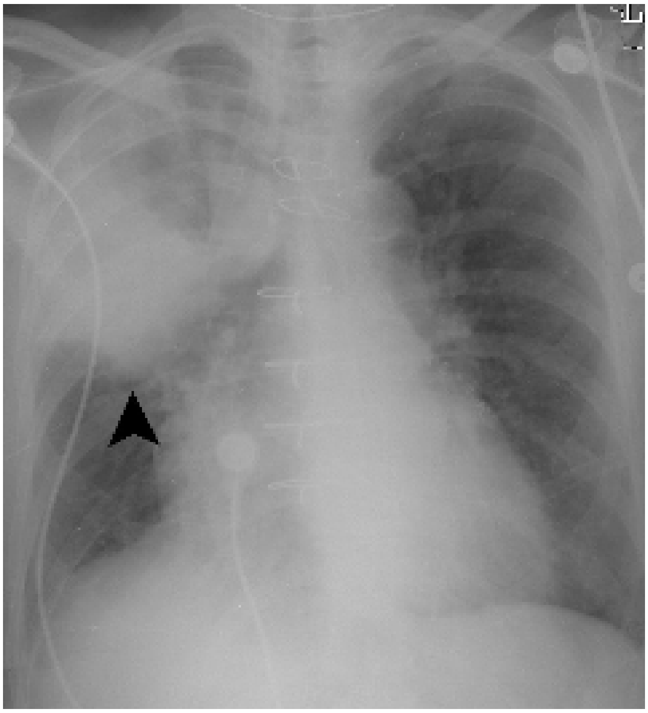

Fig. 27.18 **Bulging fissure sign.** Frontal radiograph of the chest in a patient with Klebsiella pneumonia demonstrates caudal bulging of the minor fissure (arrowhead) due to right upper lobe pneumonia

Terry Thomas Sign

Terry Thomas sign, also known as the David Letterman sign, seen on posteroanterior radiographs of the wrist, is a sign of scapholunate (SL) dissociation. It most commonly results from a fall on the outstretched hand causing the lunate and scaphoid bones to separate as a result of the scapholunate ligament disruption.

It refers to a widening of the intraosseous gap between the scaphoid and lunate to more than 3 mm (normal gap is 2 mm or less) (Fig. 27.19). Ulnar deviation on posteroanterior view or clenched fist anteroposterior position view can exacerbate this scapholunate gap. The sign was named after a British comedian, Terry Thomas, who had a wide gap between his front teeth.

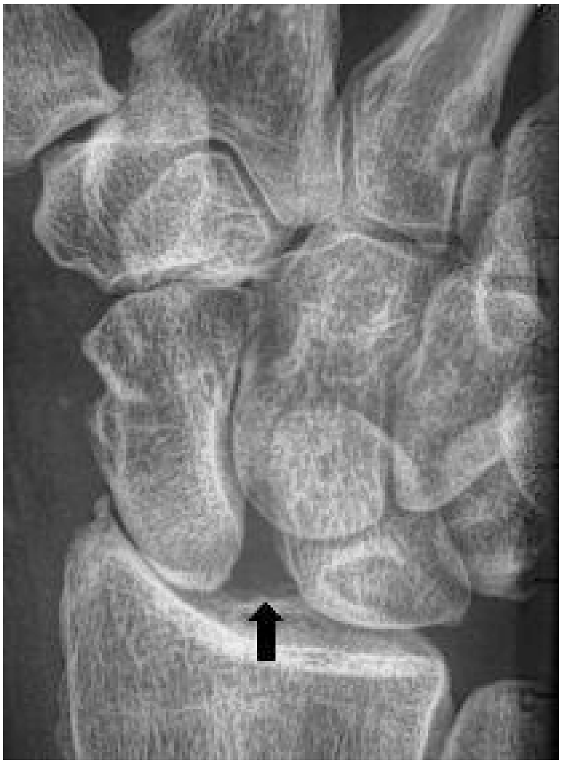

Fig. 27.19 Terry Thomas sign. Plain radiograph of the right wrist demonstrating an increased separation between the scaphoid and lunate (arrow) due to scapholunate ligament tear

Deep Lateral Femoral Notch Sign

The deep lateral femoral notch sign, sometimes also known as the deep lateral sulcus sign is seen on lateral knee radiographs and is a useful indirect sign of anterior cruciate ligament tear.

It refers to the abnormal deepening of the lateral condylopatellar sulcus or the lateral femoral notch (Fig. 27.20) from an osteochondral impaction fracture. The lateral femoral notch represents the junction between the tibial and the patellar articular surfaces of the lateral femoral condyle. Depth of the sulcus greater than 1.5 mm suggests anterior cruciate ligament tear.

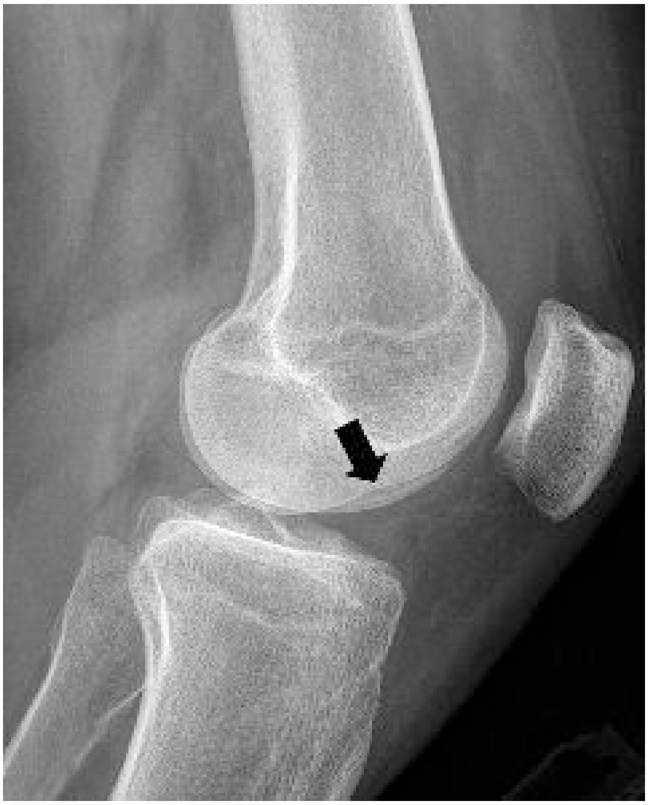

Fig. 27.20 Deep lateral femoral notch sign. Lateral radiograph of the knee demonstrating deepening of the lateral condylopatellar sulcus (arrow) due to impaction fracture. There is knee joint effusion seen in the suprapatellar bursa due to an associated anterior cruciate ligament tear

Fat Pad Sign

A positive fat pad sign, seen on a lateral radiograph of the elbow flexed at 90 degrees, is often suggestive of occult fractures of the elbow, most commonly, supracondylar fracture in children and radial head fracture in adults. The sign can also be seen in conditions like hemophilia, septic arthritis, rheumatoid arthritis, and gout.

It refers to the visualization of lucency along the posterior surface of the humerus and/or the elevated lucency along the anterior surface (Fig. 27.21). This lucency represents the displaced intra-articular, extra-synovial fat pad around the elbow joint resulting from joint effusion and distension. Under normal circumstances, the anterior fat pad is often visible, however, the posterior fat pad is located deep within the olecranon fossa and cannot be visualized on lateral radiographs.

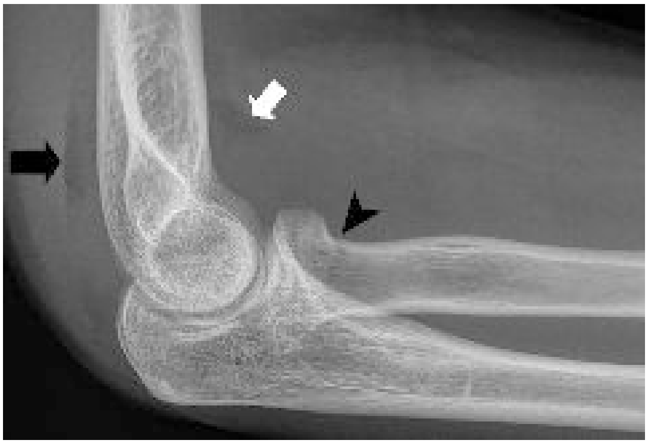

Fig. 27.21 **Fat pad sign.** Lateral radiograph of elbow flexed at 90° demonstrating prominence of the anterior (white arrow) as well as posterior (black arrow) fat pads due to outward displacement by the elbow joint effusion. There is an impacted fracture of the radial neck (arrowhead)

Lightbulb Sign

The lightbulb sign, seen on anteroposterior shoulder radiographs, is a sign of posterior shoulder dislocation. The most common mechanism includes violent muscle contractions from seizures or electrocution and a severe blow to the anterior shoulder. Posterior dislocations occur from a strength imbalance between more powerful internal rotators of the humerus (teres major, pectoralis major, and latissimus dorsi) and the less powerful external rotators (infraspinatus, teres minor, and posterior deltoid).

It refers to the persistently internally rotated humeral head causing its posterior dislocation from the glenoid fossa and loss of lateral projection of the tuberosities, giving the humeral head a circular appearance like that of a lightbulb (Fig. 27.22).

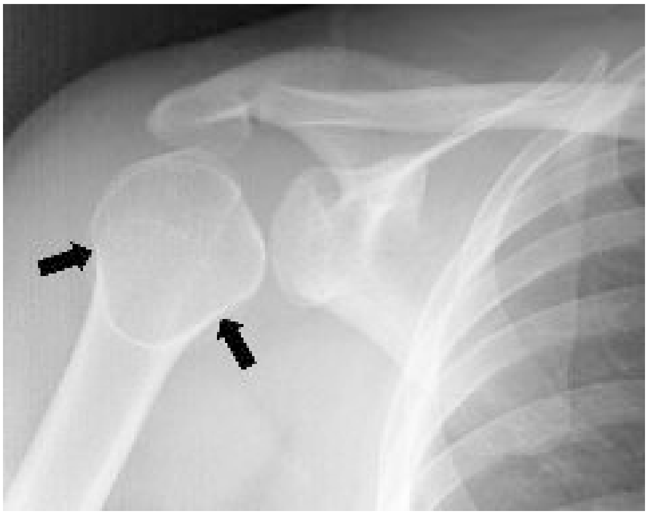

Fig. 27.22 **Lightbulb sign.** Plain radiograph of the shoulder demonstrating a lightbulb-like appearance of the humeral head (arrows) due to internal rotation and posterior dislocation of the humeral head from the glenoid fossa

Lateral Capsular Sign

The lateral capsular sign, also known as segond fracture, best seen on anteroposterior knee radiographs, is suggestive of severe lateral capsular ligament injury and is highly associated with anterior cruciate ligament tear. It may also be associated with medial and lateral meniscal tears. The mechanism of injury commonly involves flexion of the knee and internal tibial rotation.

It refers to an avulsion fracture involving the lateral surface of the lateral tibial condyle (Fig. 27.23). The fracture site involves the lateral tibial plateau at the site of attachment of the lateral capsular ligament. A longitudinal fracture line separating an avulsed tibial fragment from the tibia can be seen on the radiographs.

Pronator Quadratus Sign

Pronator quadratus sign, also known as the MacEwan sign, best seen on lateral radiographs of the wrist, refers to the obliterated or displaced fat pad lying parallel and superficial to the pronator quadratus muscle (Fig. 27.24) along the distal radius and ulna. This results from edema or hematoma within the pronator quadratus muscle secondary to trauma.

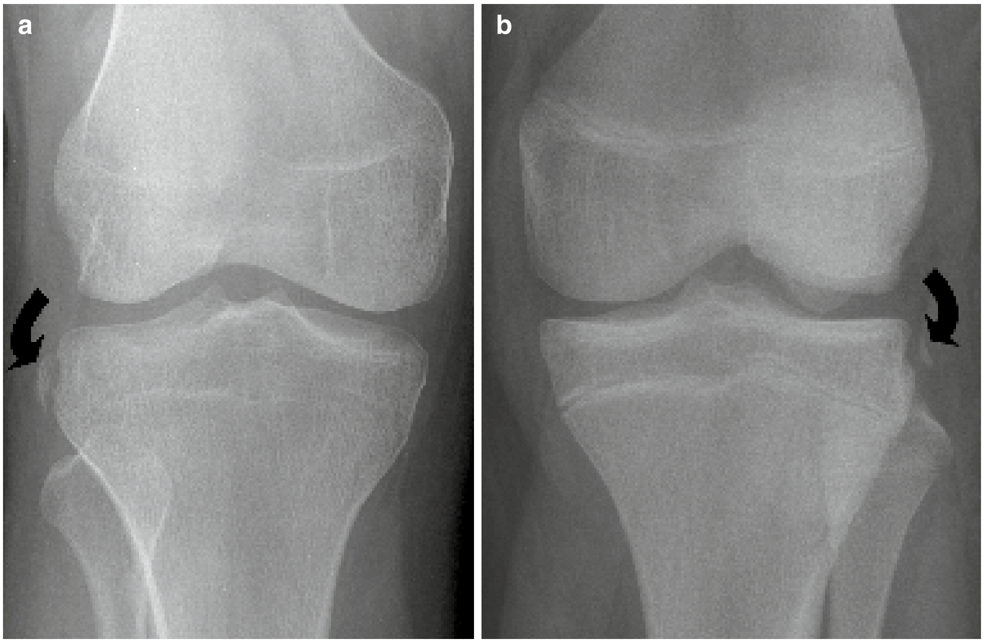

Fig. 27.23 Lateral capsular sign. (**a**, **b**) Plain radiographs of the knee demonstrating avulsion fracture of the lateral margin of the lateral tibial plateau (curved arrow). This sign is also called segond fracture and is associated with a severe lateral capsular ligament injury and concurrent anterior cruciate ligament tear

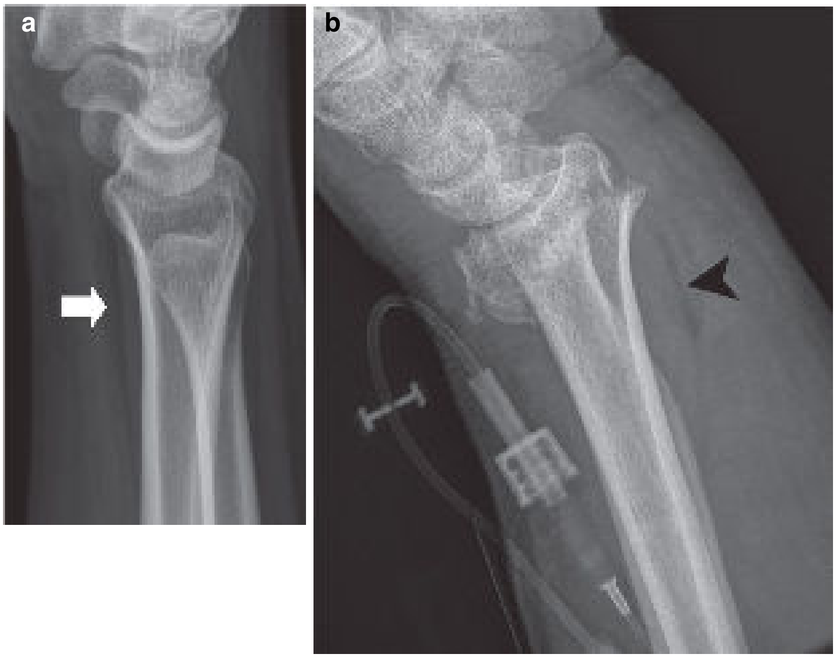

Fig. 27.24 MacEwan sign. (**a**) Lateral radiograph of the wrist demonstrating a normal, linear fat pad anterior to the pronator quadratus muscle (arrow). (**b**) Lateral radiograph of the wrist demonstrating bulging of the fat pad anterior to the pronator quadratus muscle (arrowhead) due to distal radial fracture

Reverse Batwing Sign

Reverse batwing sign, sometimes also known as reverse pulmonary edema sign, seen on frontal chest radiographs, refers to the presence of bilateral, peripheral airspace opacities (Fig. 27.25) with sparing of the perihilar regions of the lung. The presence of this sign is a rare occurrence and is usually seen in cases of chronic eosinophilic pneumonia, organizing pneumonia, pulmonary vasculitis, and adenocarcinoma of the lung. COVID-19 can also cause organizing pneumonia and present with peripheral consolidations with central sparing.

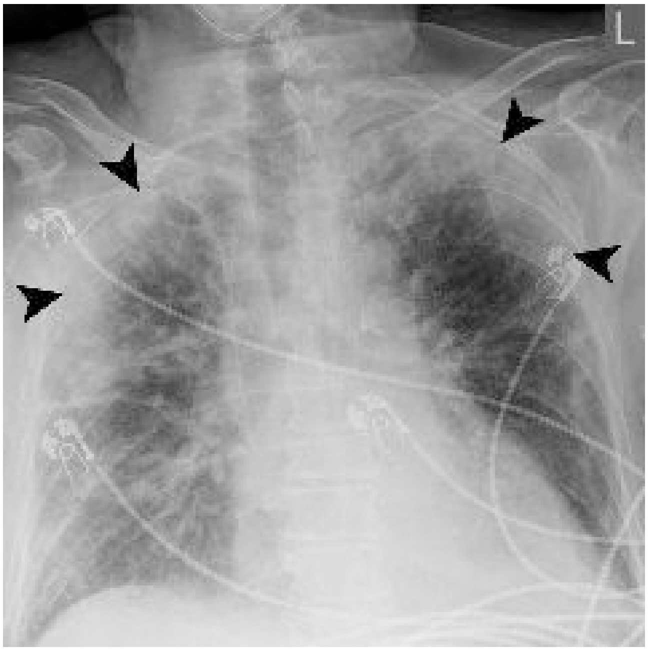

Fig. 27.25 **Reverse batwing sign.** Frontal radiograph of the chest in a patient with organizing pneumonia demonstrating bilateral peripheral reticular opacities with relative sparing of the central lungs (arrowheads)

Spilled Teacup Sign

The spilled teacup sign, seen on the lateral wrist radiographs, refers to the volar displacement of the dislocated lunate. The lunate "spills" forwards and loses its articulation with the distal radius (Fig. 27.26). This sign is specific for lunate dislocation and helps to differentiate it from perilunate dislocation where the articulation of the lunate with radius is preserved but is associated with displacement of other carpal bones. The most common mechanism of injury is a fall on the outstretched hand with the wrist in extension. Lunate dislocations carry a significant risk of neurological and vascular injuries and must be managed emergently.

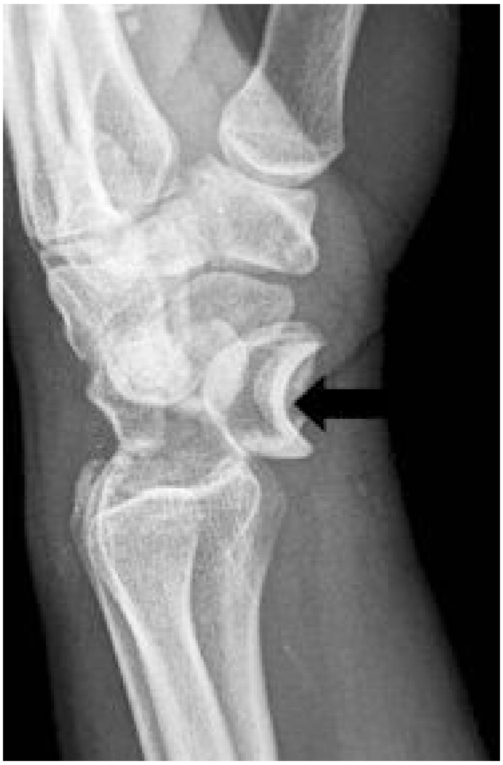

Fig. 27.26 **Spilled teacup sign.** Lateral radiograph of the wrist demonstrating anterior dislocation of the lunate with its concave surface directed anteriorly in a spilled teacup configuration (arrow)

Signs in Radiology: Cross-Sectional Signs

28

Khyati Bidani, Gandharv Singh, Garima Chandra, and Ajay Singh

Hyperdense Middle Cerebral Artery Sign

Hyperdense middle cerebral artery sign refers to the hyperdensity of the middle cerebral artery (Fig. 28.1) on a non-contrast CT scan of the head. It implies the presence of thromboembolism within the lumen of the artery. It is the earliest marker of acute ischaemic stroke. The hyper-density varies, making the proximal portion of the MCA, up to the terminal supraclinoid internal carotid artery denser as compared to the other side. Confirmation of this sign as an accurate finding is done by the analysis of thin-section CT and multiplanar reformation instead of thick axial slices. This sign has low sensitivity (approximately 30%) and high specificity (approximately 90%).

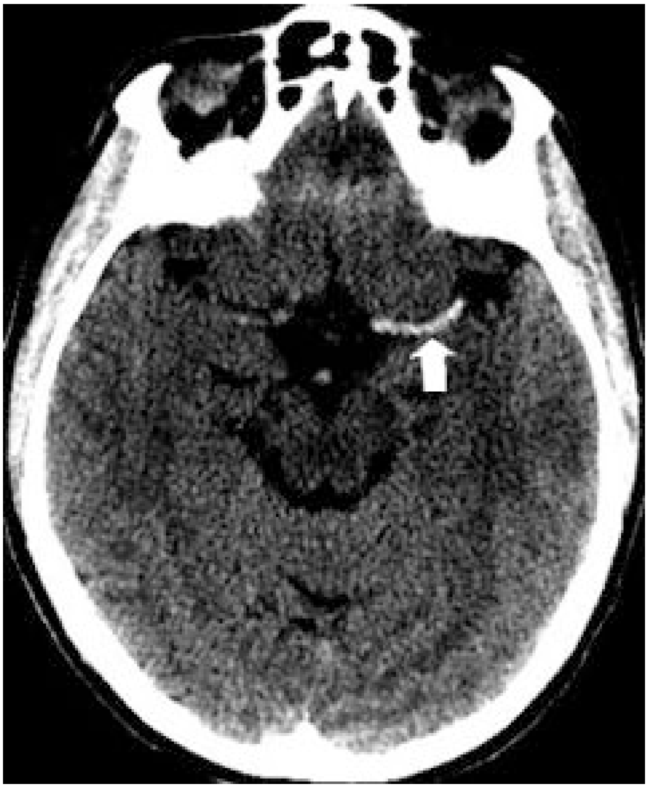

Fig. 28.1 Hyperacute left middle cerebral artery (MCA) infarct with hyperdense MCA sign. Non-contrast CT scan of the head demonstrating hyperdensity in the left M2 middle cerebral artery (arrow) due to the presence of thrombus within the arterial lumen

K. Bidani · G. Singh · G. Chandra
Department of Radiology, Massachusetts General Hospital,
Boston, MA, USA

A. Singh (✉)
Division of Emergency Radiology, Department of Radiology,
Massachusetts General Hospital, Boston, MA, USA

Harvard Medical School, Massachusetts General Hospital,
Boston, MA, USA
e-mail: asingh1@partners.org

© The Author(s), under exclusive license to Springer Nature Switzerland AG 2024

A. Singh (ed.), *Emergency Radiology*, https://doi.org/10.1007/978-3-031-65770-2_28

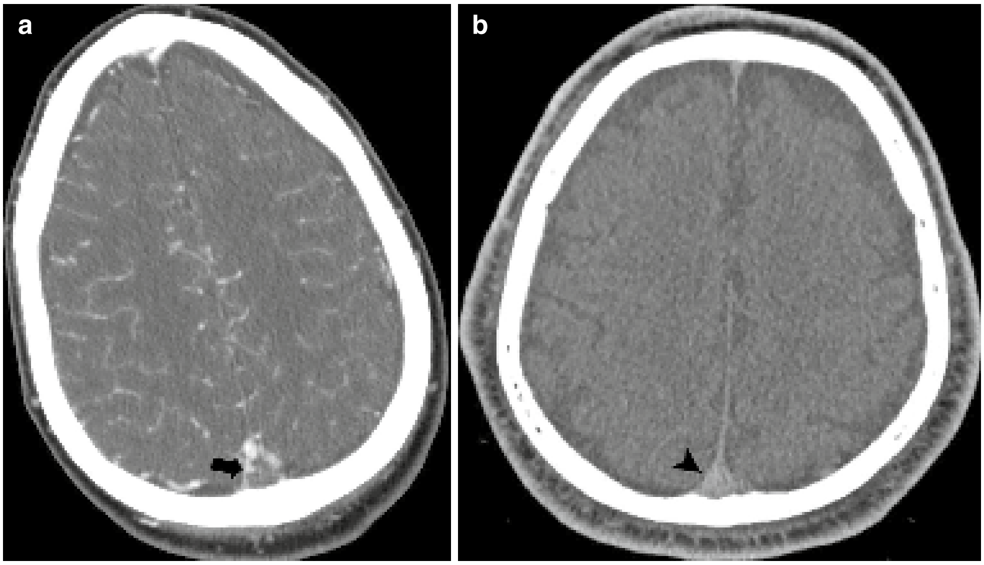

Fig. 28.2 Empty delta sign of dural venous sinus thrombosis. (**a**) CT venogram study of the head demonstrating the triangular filling defect (arrow) within the superior sagittal sinus. (**b**) CT venogram study of the head demonstrates the normal enhancement pattern (arrowhead) of the superior sagittal sinus

Empty Delta Sign

Empty delta sign refers to the triangular area of enhancement with a low attenuating centre (Fig. 28.2), representing a thrombosed sinus. It is seen in cerebral dural venous sinus thrombosis, most commonly being superior sagittal sinus thrombosis. It is only visualised with the help of a contrast-enhanced CT scan. Its name is inspired by the Greek letter Delta "Δ" having a triangular shape. The exact pathological reason behind this sign is not certain, the most popular theory being recanalisation around an organising clot along with peridural small veins enlargement.

Reversal Sign

Reversal sign refers to the appearance of reduced density of cerebral cortical grey matter, compared to adjacent white matter, which appears hyperdense, leading to inversed attenuation relationship between white and grey matter (Fig. 28.3) when compared to a normal CT scan. It is visualised on a non-contrast CT scan. This sign is suggestive of a diffuse hypoxic-ischaemic cerebral injury carrying irreversible brain damage. The presence of a reversal sign implies poor prognosis and high mortality. Its pathogenesis is uncertain, the most common theories being post-ischaemic hypervascularity and raised intracranial pressure leading to partial venous obstruction which further causes distension of deep medullary veins.

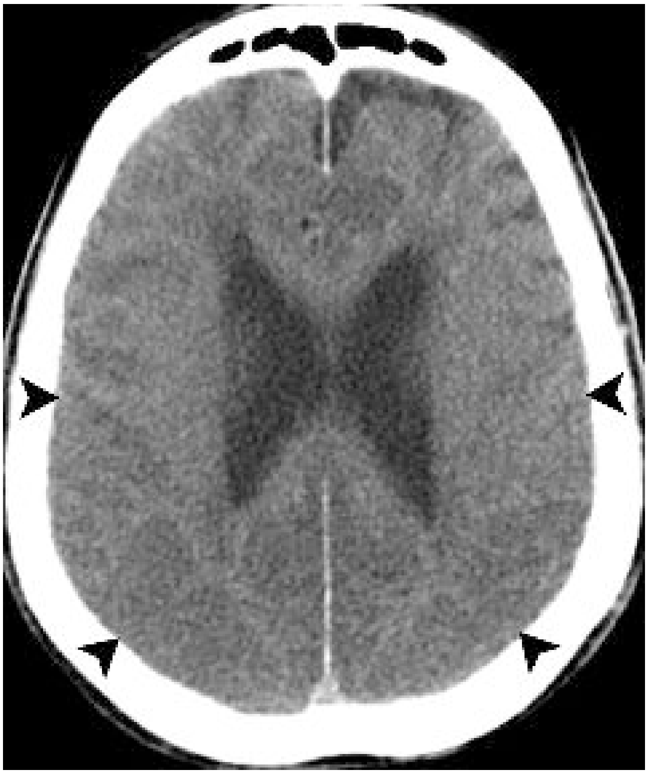

Fig. 28.3 Reversal sign of diffuse hypoxic-ischaemic brain injury. Non-contrast CT scan of the head demonstrates lower attenuation of the cerebral cortex compared to the cerebral white matter (arrowheads) in a patient with irreversible ischaemic brain injury caused by cardiac arrest

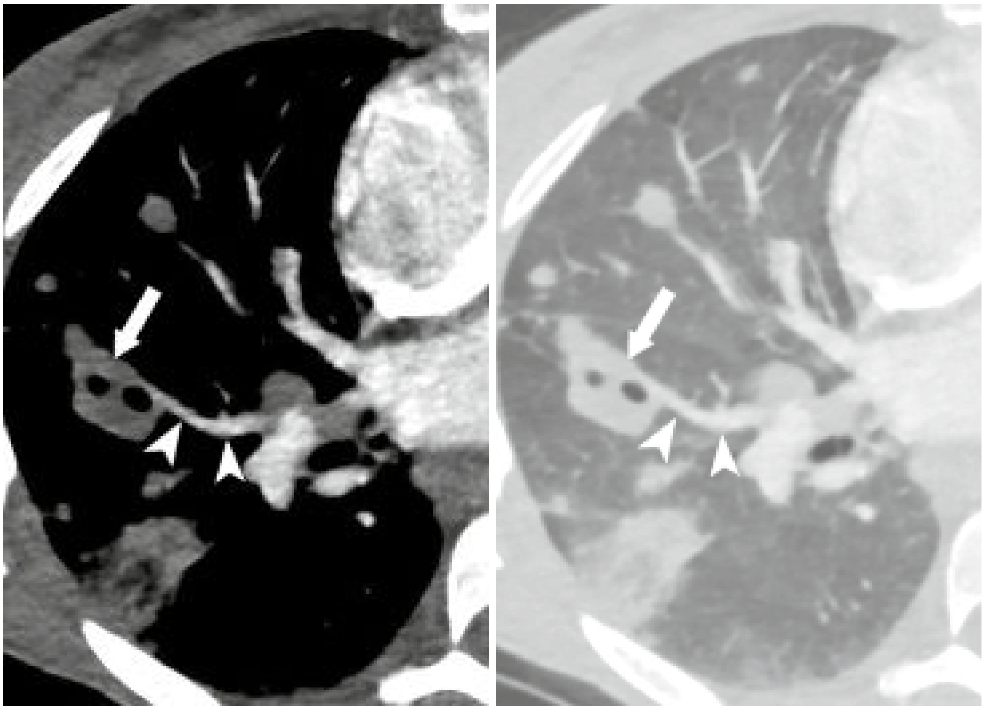

Fig. 28.4 Feeding vessel sign of septic embolism. CT angiogram of the chest demonstrates enhancing artery (arrowheads) feeding a focus of septic embolism (arrow). There are multiple nodular lesions seen in the right lung, some of which demonstrate central liquefaction and air

Feeding Vessel Sign

Feeding vessel sign refers to the visualisation of a pulmonary artery branch which leads to the centre of a nodule or a mass (Fig. 28.4). It is seen in a chest CT scan and is a reliable indicator of septic embolism. It is also known as the fruits on the branch sign. Pathogenesis involves the lodgement of an infective thrombus in a blood vessel, followed by inflammation, thereby leading to abscess formation. Abscesses are commonly formed by staphylococcal species. This sign is consistent in approximately 65% of the cases. This sign can also be seen in secondary metastasis to lungs, pulmonary infarcts, and pulmonary arterio-venous malformations.

Barber Pole Sign

Barber pole sign refers to the clockwise twisting of the superior mesenteric artery and its branches, showing a typical corkscrew appearance (Fig. 28.5), seen with the help of CT angiography, in the case of midgut volvulus. Nowadays, mesenteric angiography has limited use in the diagnosis of suspected volvulus, due to its high cost and invasive nature, whereas, angiographic CT volume rendering reconstructions provide similar findings as well as help in the assessment of the anatomy of the mesenteric vascular supply, thereby, aiding in diagnosis, and surgical approach of treatment.

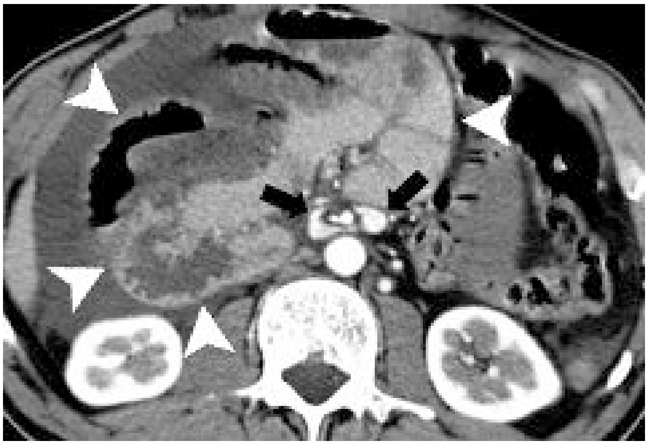

Fig. 28.5 Barber pole sign of midgut volvulus. CT angiogram of the abdomen demonstrates a corkscrew appearance (arrows) due to twisting of the superior mesenteric artery and venous branches. There is clustered appearance of dilated small bowel loops (arrowheads) in the right abdomen with surrounding fluid and mesenteric oedema

Whirl Sign

Whirl sign refers to the radial whirl-like encircling distribution (Fig. 28.6) of the loops of the small bowel along with mesenteric soft tissue and fat; with the superior mesenteric artery being the centre of the whirl. It is seen in the case of midgut volvulus. It is a highly specific but poorly sensitive sign and indicates a closed-loop obstruction. The presence of this sign also implies the need for surgical management of volvulus. The affected mesenteric vessels are typically at a different anatomic level because a closed-loop obstruction is pinched off at the constriction site.

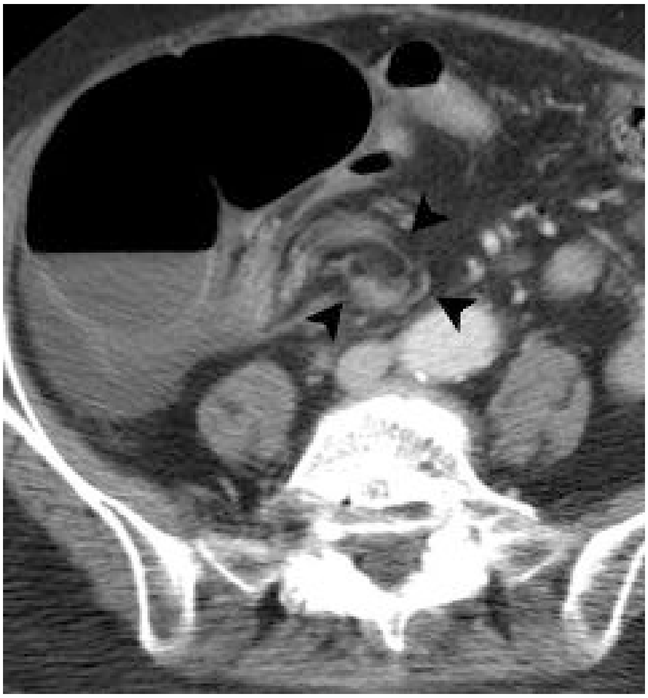

Fig. 28.6 Whirl sign of midgut volvulus. CT abdomen demonstrates twisting of the small bowel loop along with mesenteric soft tissue and fat

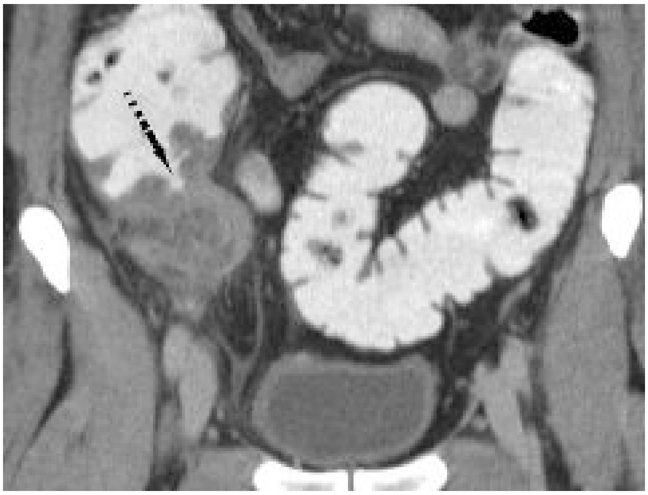

Fig. 28.7 Arrowhead sign of acute appendicitis. Contrast-enhanced CT scan of the abdomen demonstrates a triangular configuration (arrow) of GI contrast in the caecal lumen due to inflammation of the caecal wall caused by acute appendicitis

Arrowhead Sign

Arrowhead sign refers to the triangular arrowhead-like formation (Fig. 28.7) of contrast material present in the caecal lumen, which points towards the inflamed appendix, at the caecal-appendiceal junction. It is obtained via helical CT combined with contrast material. The contrast material is administered orally or per rectal. It is a highly specific sign of appendicitis. This sign appears due to the focal and symmetrical thickening of the caecal wall at the level of the root of the appendix, resulting from the inflammatory changes of acute appendicitis.

Caecal Bar Sign

Caecal bar sign refers to the separation of the base of the appendix from the caecum (Fig. 28.8) which is contrast filled, due to the presence of inflammatory soft tissue and oedema. The separation is present in the shape of a bar-like thickening/soft tissue density on axial imaging, thereby, naming this sign as caecal bar sign. Pathogenesis involves proximal lodgement of calcified appendicolith which provokes surrounding inflammation of the apex of the caecum. This sign is positive in approximately 60% of the cases.

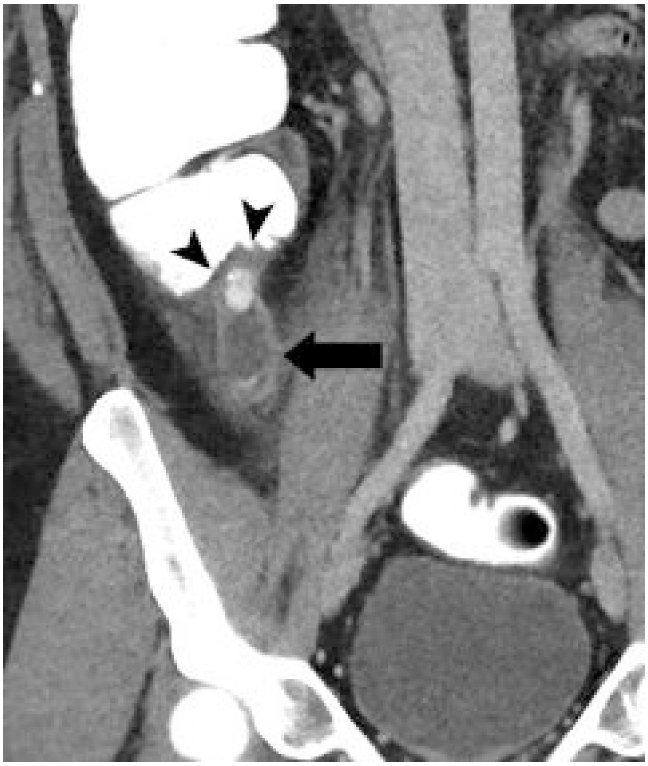

Fig. 28.8 Caecal bar sign of acute appendicitis. Contrast-enhanced CT scan of the abdomen demonstrates plaque-like thickening (arrowheads) of the caecal wall at the junction of the inflamed appendix and the caecal lumen. The appendix (arrow) is dilated up to 13 mm in diameter and contains a 9 mm appendicolith at the base

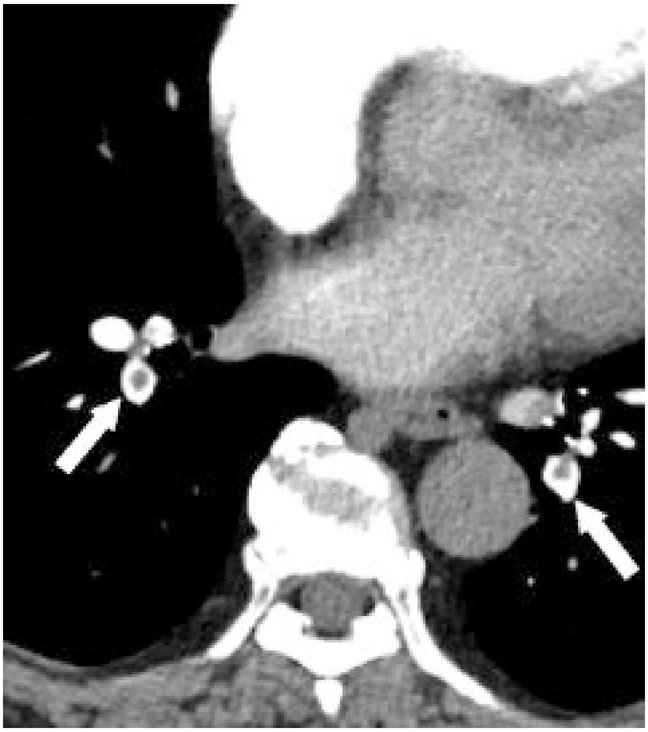

Fig. 28.9 Polo mint sign of acute pulmonary embolism. CT angiogram of the chest demonstrates round, centrally placed thrombus surrounded by concentric rim of contrast (arrows) in right as well as left lower lobes

Polo Mint Sign

Polo mint sign refers to the presence of a thin peripheral rim of contrast as a hyperattenuating area around a central filling defect (Fig. 28.9) representing the thrombus, resembling a Polo Mint candy, when visualised on the axial plane of contrast-enhanced CT scan. Polo mint sign represents a partial filling defect in a blood vessel and can be indicative of conditions like pulmonary embolism and portal vein thrombosis. This sign is also known as mint with a hole.

Railway Track Sign

Railway track sign refers to the visualisation of a partial filling defect (Fig. 28.10) due to a centrally placed thrombus in a pulmonary arterial vessel. It is seen on the longitudinal section (parallel to the long axis of the vessel) of contrast-enhanced CT angiography, in case of acute pulmonary embolism. The contrast is present at the periphery as a hyperattenuating area, resembling a railway track.

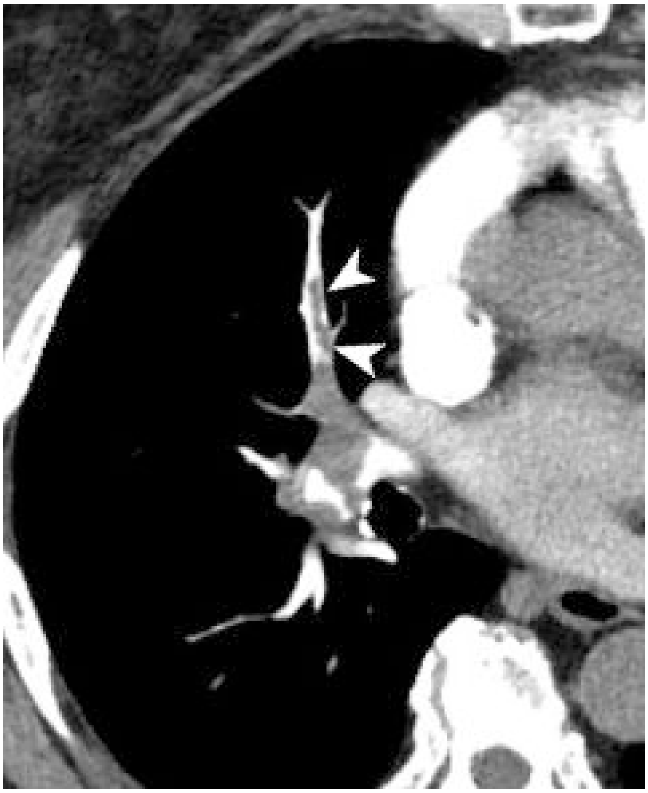

Fig. 28.10 Railway tract sign of acute pulmonary embolism. CT angiogram of the chest demonstrates linear hypoattenuation due to the presence of a centrally placed linear thrombus (arrowheads) in the anterior segment of the right middle lobe surrounded on both sides by contrast

Halo Sign

Halo sign is also known as the target sign and is seen on contrast-enhanced CT of the abdomen. It contains three concentric rings (Fig. 28.11) formed due to inflammatory pathology in the bowel. The inner layer represents to the enhancement of mucosa, the outer layer represents the muscularis propria and serosa, and the middle layer conforms to the submucosal oedema. All three give a stratified appearance on CECT. Initially described for Crohn's disease, it can also be seen in ulcerative colitis, *Clostridium difficile* colitis, radiation-induced colitis, and ischaemic bowel disease.

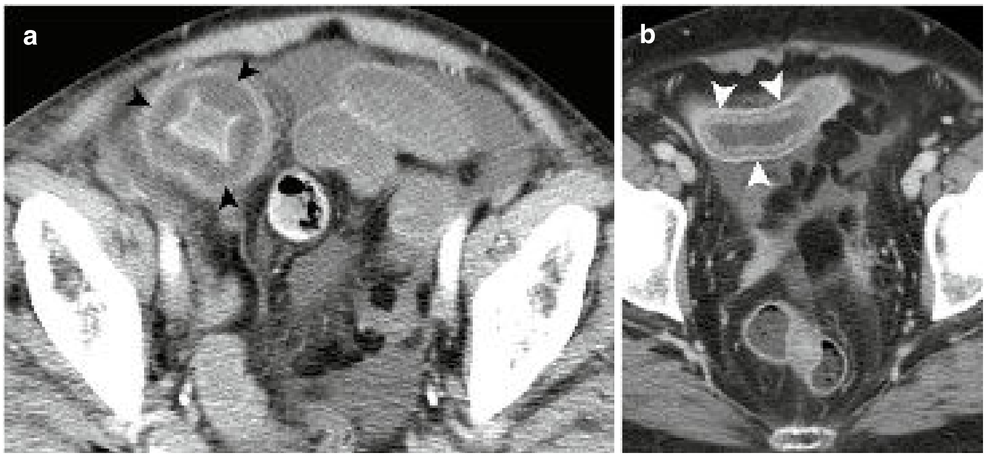

Fig. 28.11 (**a**, **b**) Halo sign in small bowel enteritis. Contrast-enhanced CT of the abdomen demonstrates stratified appearance of the bowel. Mucosa (arrowheads) and muscularis propria form the inner and outer hyperdense rings, respectively. The central low density sandwiched between the muscularis propria and the mucosa represents the edematous submucosa

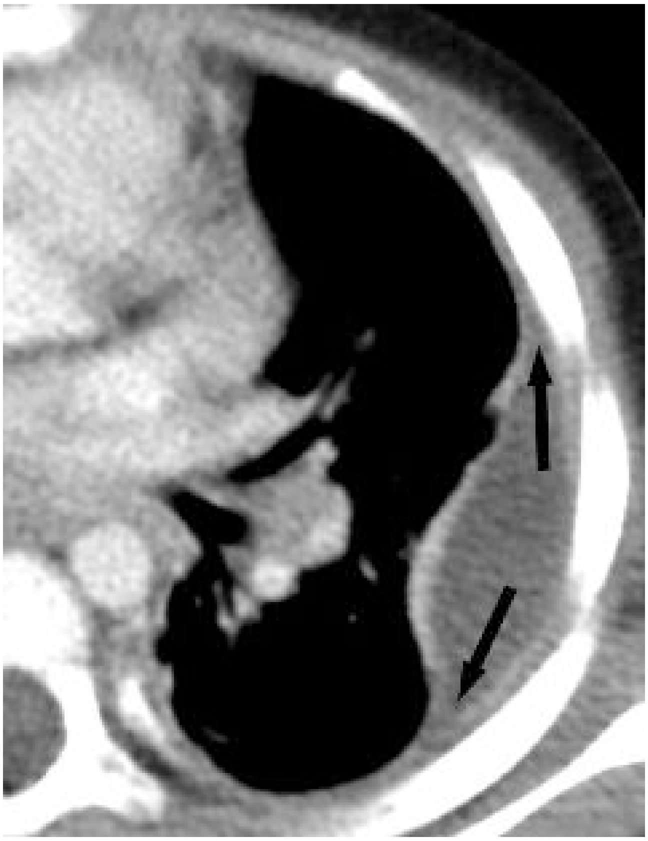

Fig. 28.12 Split pleura sign of empyema. Contrast-enhanced CT scan of the chest demonstrates separation of the parietal and the visceral pleura (arrows) at the edges of an empyema

Split Pleura Sign

Split pleura sign is a characteristic sign of empyema and is visualised best on contrast-enhanced CT of the chest. As the name suggests, there is thickening and subsequent separation of parietal and visceral pleura encasing a lenticular or elliptical-shaped fluid collection (Fig. 28.12) in a non-dependent location between both layers. Fibrothorax may manifest as a long-term complication.

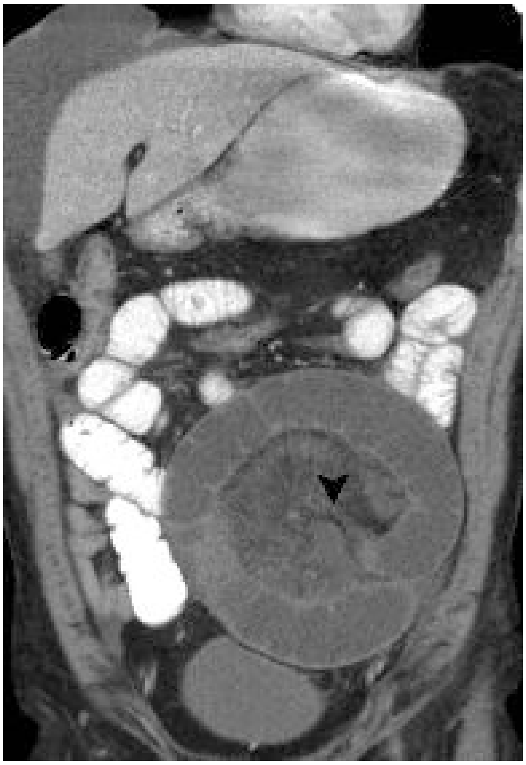

Fig. 28.13 Beak sign of small bowel obstruction. Contrast-enhanced CT scan of the abdomen demonstrates tapered narrowing (arrowhead) of a dilated small bowel loop in a patient with closed-loop obstruction

Beak Sign

Beak sign is a CT finding of small bowel obstruction and is defined as the sudden beak-like tapering of a dilated loop to a compressed, narrowed loop (Fig. 28.13) with an intertwining transition point present between the two. Adhesions in the bowel are responsible for up to 70% of small bowel obstructions and can cause obstruction of two adjacent small bowel loops. The presence of adhesions is not directly appreciated on CT but the presence of abrupt narrowing of bowel loop in the absence of any recognisable cause is suggestive of adhesions as the cause.

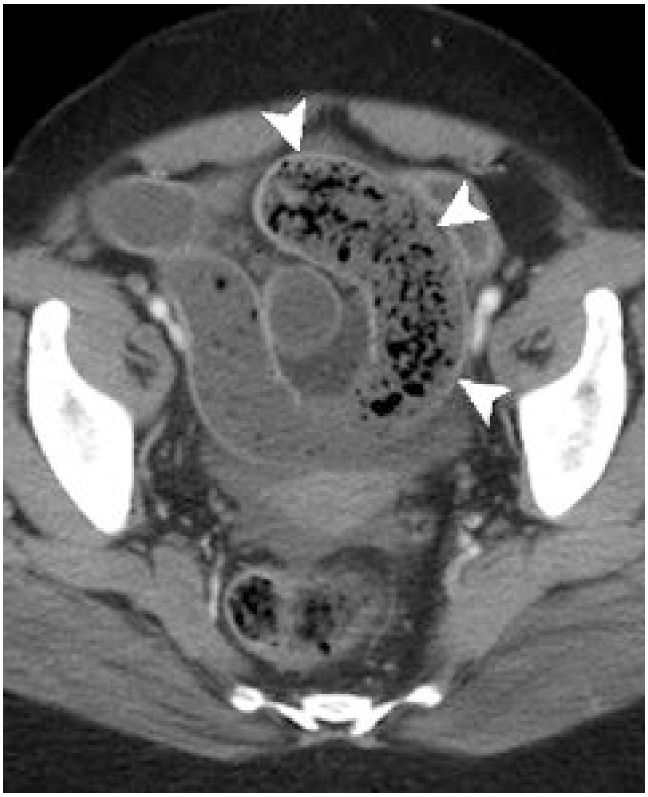

Fig. 28.14 Small bowel faeces sign of small bowel obstruction. Contrast-enhanced CT scan of the abdomen demonstrates particulate matter and gas bubbles (arrowheads) within a dilated small bowel loop located just proximal to the site of small bowel obstruction

Small Bowel Faeces Sign

Small bowel faeces sign is seen on the CT abdomen and is suggestive of small bowel obstruction. It refers to the mixture of particulate matter and gas bubbles present in the lumen of dilated loops (Fig. 28.14) found just proximal to the site of small bowel obstruction. It results from delayed transit through the bowel loops causing accumulation of incompletely digested food, giving a colonic stool-like appearance within the small bowel loop just proximal to the transition site.

Comb Sign

Comb sign refers to the prominent mesenteric vascularity resembling the teeth of a comb (Fig. 28.15), best seen on contrast-enhanced CT of the abdomen. The mesenteric arterial vessels appear dilated and tortuous with broadly spaced vasa recta. This sign can be used to diagnose acute exacerbations in known cases of Crohn's disease. Similar findings can also be seen in mesenteric thromboembolism, bowel strangulation, and vasculitis.

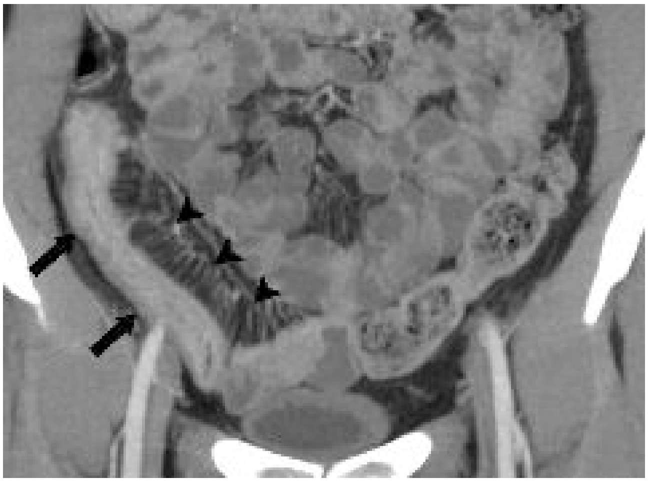

Fig. 28.15 Comb sign of acute exacerbation of Crohn's disease. Coronal MIP CT image of the abdomen demonstrates prominent mesenteric arterial branches (arrowheads) along the mesenteric border of the inflamed terminal ileum (arrows) in this patient with active Crohn's disease

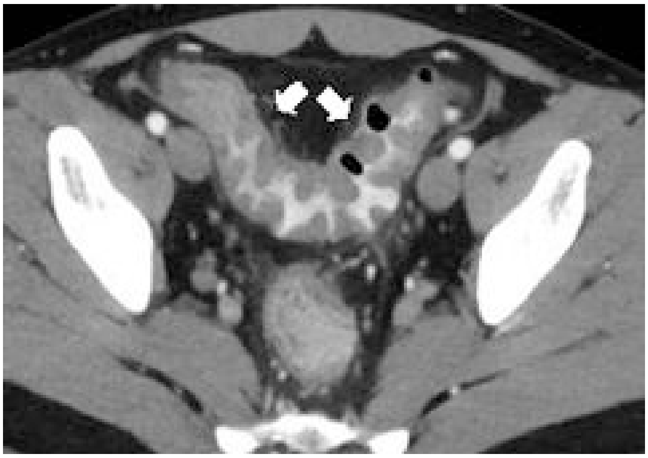

Fig. 28.16 Accordion sign of pseudomembranous colitis. Contrast-enhanced CT scan of the abdomen demonstrates trapped oral contrast in the appearance of accordion (arrows) within the edematous haustral folds of the colon

Accordion Sign

Accordion sign is also known as the concertina sign. It is observed in patients who have been given oral contrast which gets trapped between the haustral folds of the colon (Fig. 28.16), mimicking the folds of an accordion, thus its name. The haustral fold prominence is due to hyperenhancing mucosa and relatively hypodense edematous submucosa. It is usually seen with *C. difficile* infection causing pseudomembranous colitis but can also be found in other aetiologies that lead to diffuse oedema of the colon.

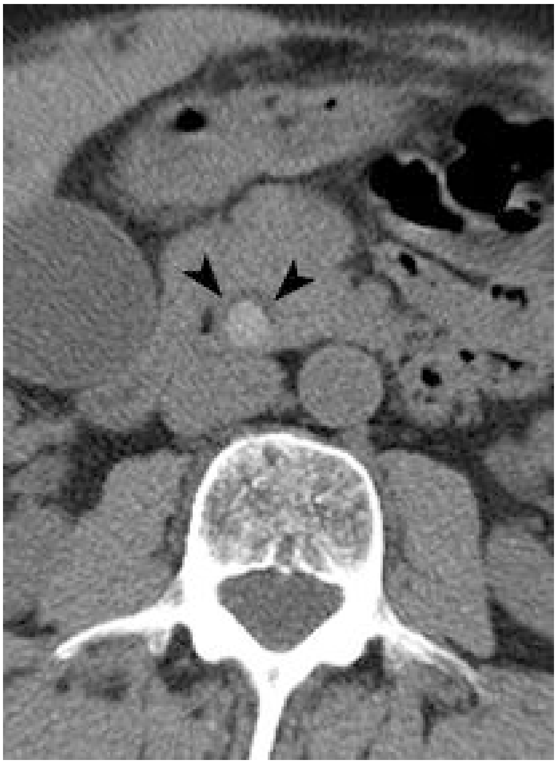

Fig. 28.17 Crescent sign of choledocholithiasis. Contrast-enhanced CT of the abdomen demonstrates high-density stone in the common bile duct surrounded by a crescent of hypodense bile (arrowheads)

Crescent Sign

Crescent sign is a characteristic sign of choledocholithiasis where the biliary calculus is separated from the wall of the biliary duct by a crescent of fluid-density bile (Fig. 28.17). A variant of crescent sign is the target sign where central density present within the bile duct suggestive of calculi is surrounded by a complete outer rim of hypodense bile or mucosa.

Sentinel Clot Sign

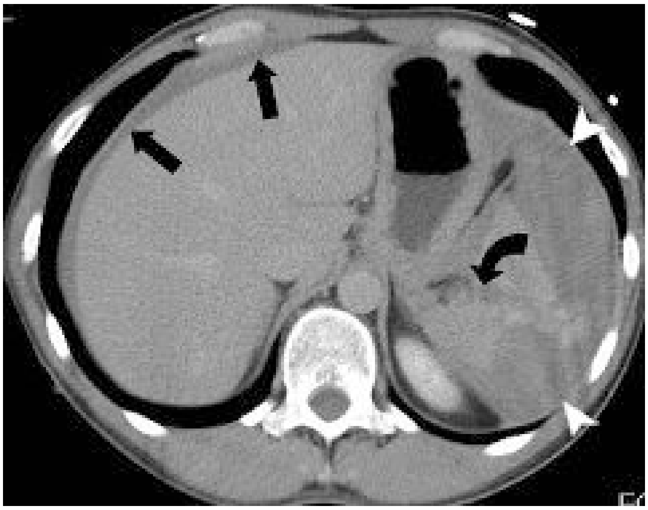

Fig. 28.18 Sentinel clot sign of haemoperitoneum. Contrast-enhanced CT scan of the abdomen demonstrates higher density haemorrhagic blood products (arrowheads) lateral to the site of splenic laceration (curved arrow). The haemorrhagic fluid anterior to the liver has a relatively lower density (arrows), indicating that the source of the bleed is in the left upper quadrant of the abdomen

Sentinel clot sign is a sign depicting the site of origin of intraperitoneal haemorrhage on CT abdomen and pelvis. The blood contiguous to the site of bleeding gets clotted (therefore has higher viscosity and greater haemoglobin content) and shows higher attenuation (45–70 U) (Fig. 28.18) as opposed to the unclotted blood (35–40 U) located away from the site of bleeding. This sign can be seen with solid visceral organ laceration, intraperitoneal rupture of the bladder, and pelvic fractures.

Crazy Paving Pattern

Crazy paving pattern is a finding that was initially described for pulmonary alveolar proteinosis and is seen on the HRCT chest. This sign is characterised by polygonal opacities formed by ground-glass attenuation with intra- and interlobular septal thickenings and proteinaceous debris filling up the air spaces (Fig. 28.19). The affected geographical part is sharply delineated from the normal lung parenchyma.

This finding can also be seen in ARDS, UIP, pneumonia, alveolar haemorrhage, cariogenic pulmonary oedema, lymphangitis carcinomatosis, pulmonary veno-occlusive disease, and COVID-19 pneumonia.

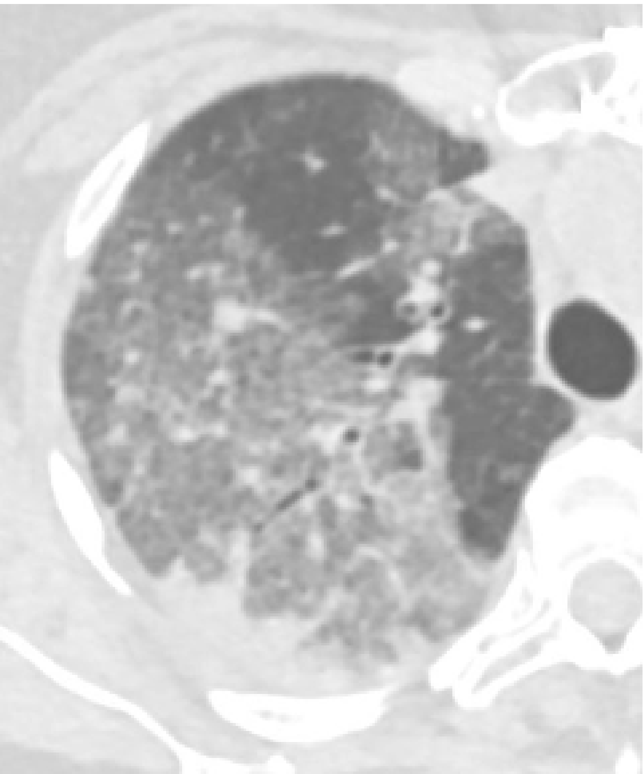

Fig. 28.19 Crazy paving pattern. Contrast-enhanced CT of the chest demonstrates interlobular septal prominence on a background of diffuse ground glass inflammatory densities in a patient with COVID-19 pneumonia

Draped Aorta Sign

Draped aorta sign is a characteristic sign of contained aortic aneurysmal leak and is highly suggestive of inadequacy in the aortic wall. The posterior wall of the aorta containing the rupture site drapes around the contour of the anterior margin of the adjacent vertebral body (Fig. 28.20) and is accompanied by the loss of normal fat planes between them.

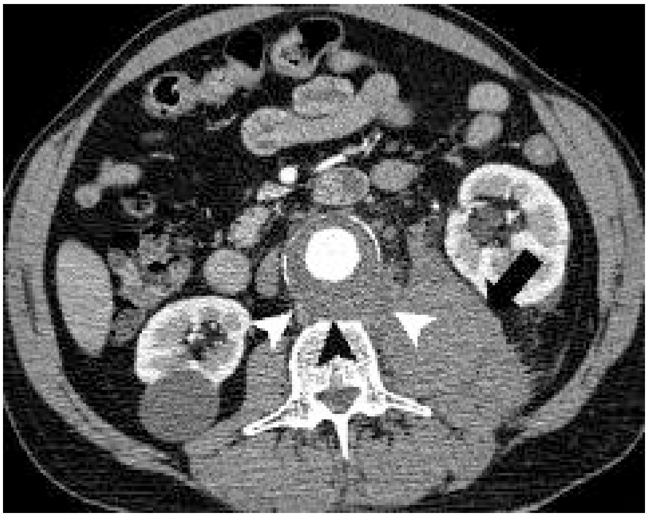

Fig. 28.20 Draped aorta sign of contained abdominal aortic aneurysmal leak. Contrast-enhanced CT scan of the abdomen demonstrates an infrarenal aortic aneurysm, the posterior margin of which is seen draping (arrowheads) over the adjacent lumbar vertebral body. There is haemorrhage (arrow) in the left psoas compartment from contained rupture of the abdominal aortic aneurysm

Hyperdense Crescent Sign

Hyperdense crescent sign is seen when intraluminal blood dissects through the thrombus to lie against the feeble arterial wall and appears as a hyperdense crescent (Fig. 28.21) either beneath the thrombus or within the vessel wall. Blood coming in contact with the already weakened aortic wall heightens the probability of rupture.

The appearance of this sign on unenhanced CT is suggestive of impending aortic rupture. The crescent has greater attenuation than the psoas muscle on enhanced CT. CT of severely anaemic patients may mimic this sign due to decreased attenuation of the lumen attributable to their fairly low haematocrit. A similar false picture may be found in the intramural hematoma of the abdominal aorta and false lumen thrombosis in the case of aortic dissection.

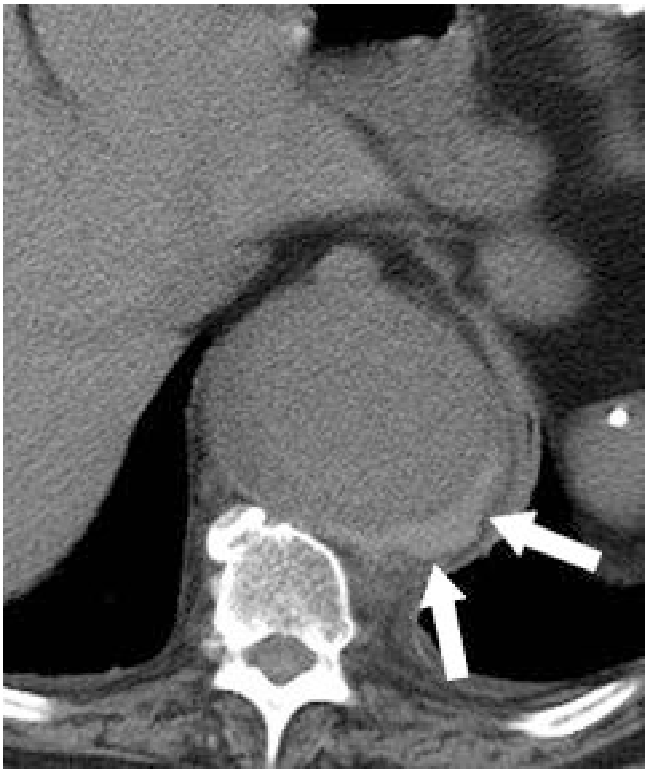

Fig. 28.21 Hyperdense crescent sign of impending aortic rupture. Contrast-enhanced CT scan of the abdomen demonstrates aortic aneurysm at the level of the diaphragmatic hiatus containing a crescentic hyperdense clot (arrows) in the wall

Tangential Calcium Sign

Tangential calcium sign is a finding indicative of an unstable aneurysm. It describes a focal break in the continuity of the calcification of the intimal wall of the vessel. The CT shows a displaced portion of the calcified atheromatous plaque pointing tangentially away from the lumen of the aneurysm (Fig. 28.22). This sign can also be found in case of contained leaks or impending aneurysmal ruptures.

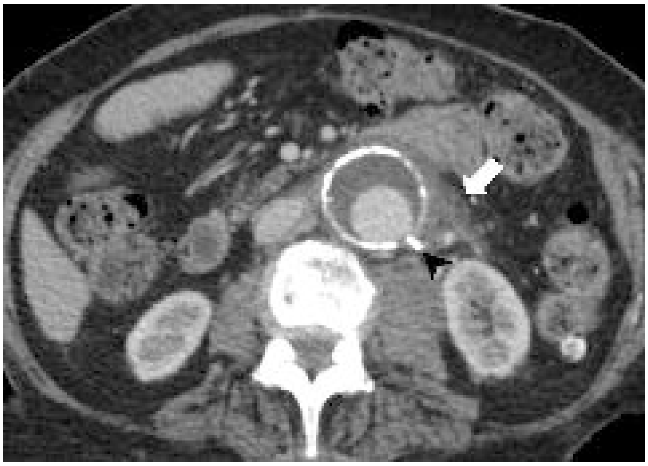

Fig. 28.22 Tangential calcium sign of unstable aneurysm. Contrast-enhanced CT of the abdomen demonstrates vertical orientation of a calcified atherosclerotic plaque (arrowhead) at the site of contained aortic rupture. A small amount of haemorrhage (arrow) is seen in the left para-aortic location from the contained rupture

Reverse Hamburger Sign

Reverse hamburger sign is also known as the naked facet sign and refers to the bare part of the inferior articular facet directed away from the superior articular facet in patients with facet joint dislocation. Each half of a whole facet joint forms the ‘half-buns’ of a whole hamburger which gets disrupted on dislocation forming the ‘reverse hamburger’ sign (Fig. 28.23) seen on axial CT of the cervical spine. There is

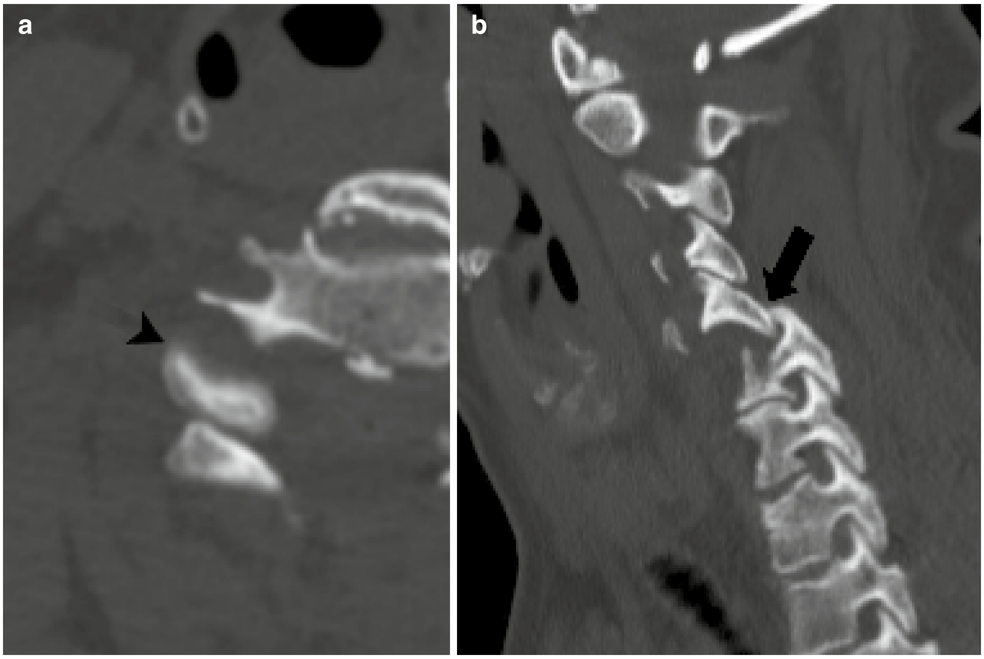

Fig. 28.23 Reverse hamburger sign of facet joint dislocation. (**a**, **b**) Axial CT scan of the cervical spine demonstrates a right-sided jumped facet (arrow) at the C5-C6 junction resulting in anteriorly directed naked articular surface of the right C5 inferior articular facet. The sagittal reformation demonstrates anteriorly positioned inferior C5 articular facet (arrowhead) in relation to the superior C6 articular facet

a loss of congruity between the articular surfaces of the apophyseal joints. The articular surface of the superior facet of the inferior vertebra is directed posteriorly. The inferior facet of the superior vertebra is directed anteriorly.

Halo Sign

Halo sign, also known as the double target sign, is one of the characteristic signs of a liver abscess visualised on contrast-enhanced CT of the abdomen. It is composed of a central part representing the abscess cavity, encircled by two rims (Fig. 28.24). The inner rim having higher attenuation is hyperdense and displays early contrast enhancement. The outer rim is formed as a result of oedematous liver parenchyma and has low attenuation.

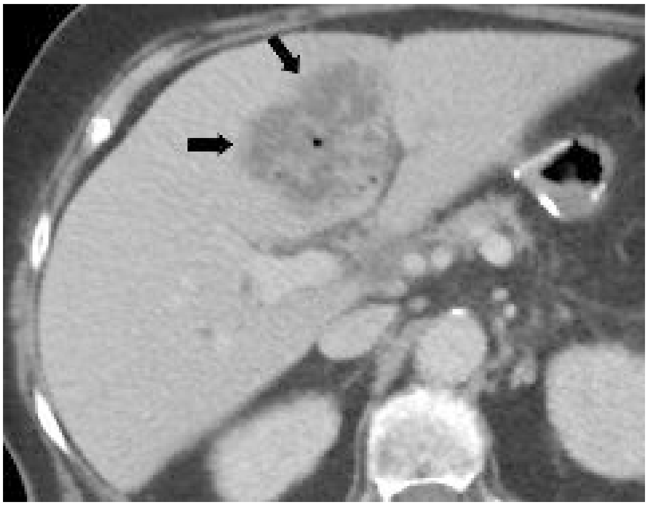

Fig. 28.24 Halo sign of liver abscess. Contrast-enhanced CT of the abdomen demonstrates an abscess cavity in segment 4 of the liver. The abscess cavity is multiseptated, containing a small focus of air within it, and surrounded by oedema (arrows)

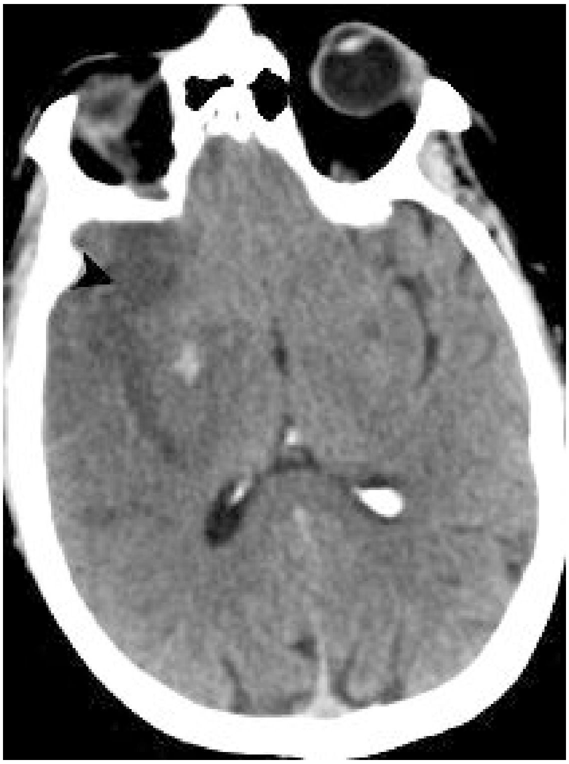

Fig. 28.25 Insular ribbon sign of acute MCA infarct. Non-contrast CT of the head demonstrates loss of grey-white matter differentiation (arrowhead) at the right insula. There is a 1.3 cm focus of haemorrhage seen in the right basal ganglia

Insular Ribbon Sign

Insular ribbon sign is found in cases of acute infarcts in the part of the brain supplied by MCA. There is an obscuration of grey-white confluence at the insula (Fig. 28.25) due to disruption of the insular blood supply of the MCA. Acute oedema secondary to infarction leads to loss of grey-white matter differentiation.

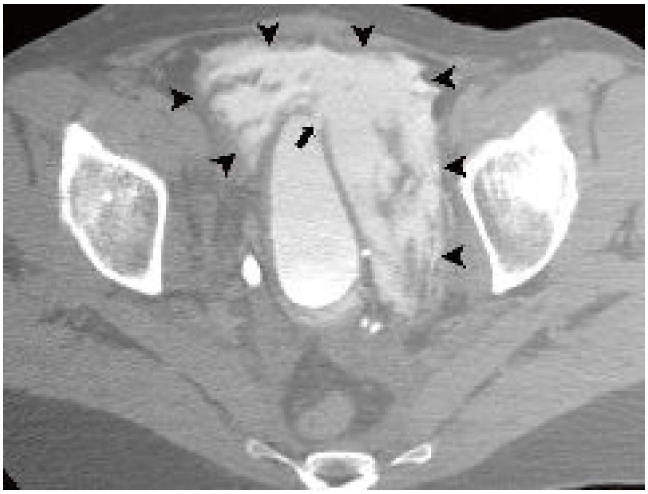

Fig. 28.26 Molar tooth sign of extraperitoneal urinary bladder rupture. CT cystogram demonstrates extraperitoneal rupture of the bladder resulting in leakage of contrast (arrowheads) anterior and lateral to the urinary bladder in the configuration of a molar tooth. There is a focal discontinuity (arrow) of the anterior urinary bladder wall which represents the site of rupture of the bladder

Molar Tooth Sign

Molar tooth sign is seen with the extraperitoneal rupture of the bladder (type 4A simple extraperitoneal rupture as classified by Sandler et al.). CT cystography of the bladder reveals flame-shaped areas of extravasation in peri-vesicle and pre-vesicle areas (Fig. 28.26) that can be traced all the way up to the umbilicus thus giving it a molar tooth appearance.

Yin Yang Sign

Yin yang sign is observed on Doppler ultrasound in patients with true or false aneurysms. It represents the bidirectional flow due to swirling of the blood within the aneurysm in a yin yang pattern (Fig. 28.27). Blood flowing towards the transducer appears red whereas blood flowing away from the transducer appears blue.

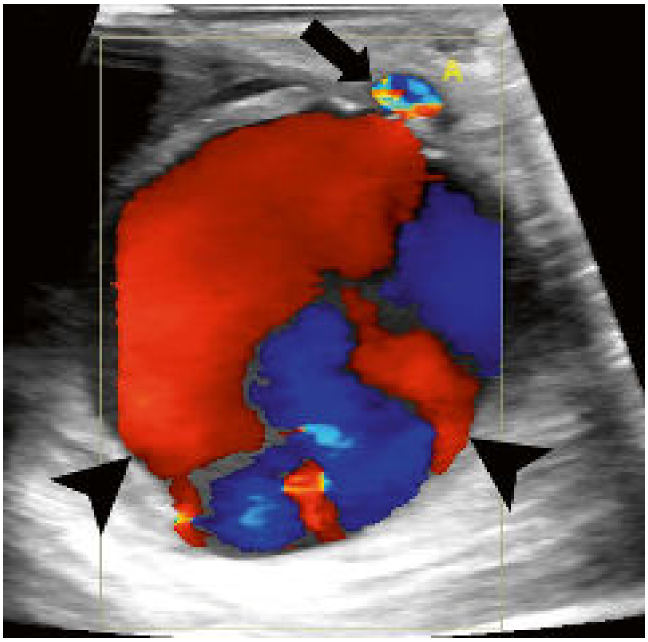

Fig. 28.27 Yin Yang sign of pseudoaneurysm. Colour Doppler ultrasound of the left common femoral artery (arrow) demonstrates a pseudoaneurysm containing yin yang pattern (arrowheads) of blood flow. The blood flowing away from the Doppler probe appears blue in colour and the blood flowing towards the probe appears red in colour

Tip of the Iceberg Sign

Tip of the iceberg sign refers to the characteristic sonographic appearance of the ovarian dermoid cysts, also known as teratomas. The contents of the dermoid cysts, including hair, calcifications (e.g. teeth), and sebum produces an appearance of poorly defined, highly echogenic mass. However, these echogenic contents, especially macroscopic fat, cause marked posterior acoustic attenuation, obscuring the posterior structures (Fig. 28.28). Therefore, multiple tissue interfaces within the lesion and the resultant posterior shadowing results in non-visualisation of the major portion of the cyst, much like an iceberg where the witnessed portion above the water represents less than 10% of its whole volume, and thus the name of the sign.

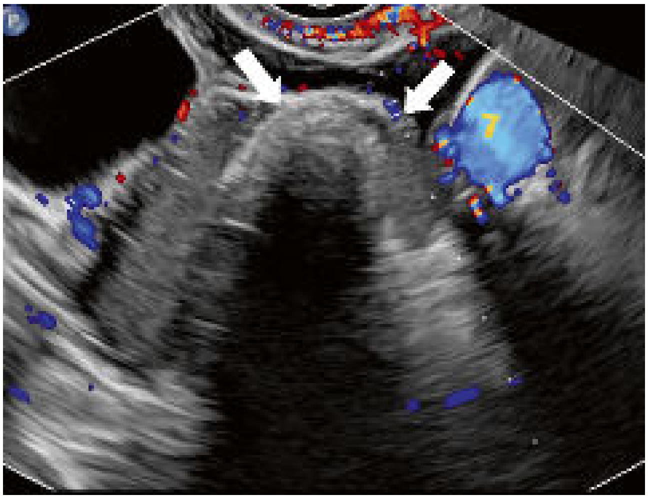

Fig. 28.28 Tip of the iceberg sign of ovarian dermoid. Ultrasound pelvis demonstrates a curvilinear band of hyperechogenicity (arrows) with posterior acoustic shadowing caused by fat within the dermoid

Linguine Sign

Linguine sign is a sign of intracapsular rupture of a silicone breast implant on MR imaging. It refers to the appearance of multiple, diffusely scattered, curvilinear lines of low signal intensity within the silicone gel of high signal intensity (Fig. 28.29). The breast implant consists of an outer elastomeric shell filled with silicone gel. A fibrous capsule forms around the implant, which contains the silicone gel released from the rupture of the elastomeric shell. This collapsed elastomeric shell floating in the silicone gel produces an appearance of wavy lines.

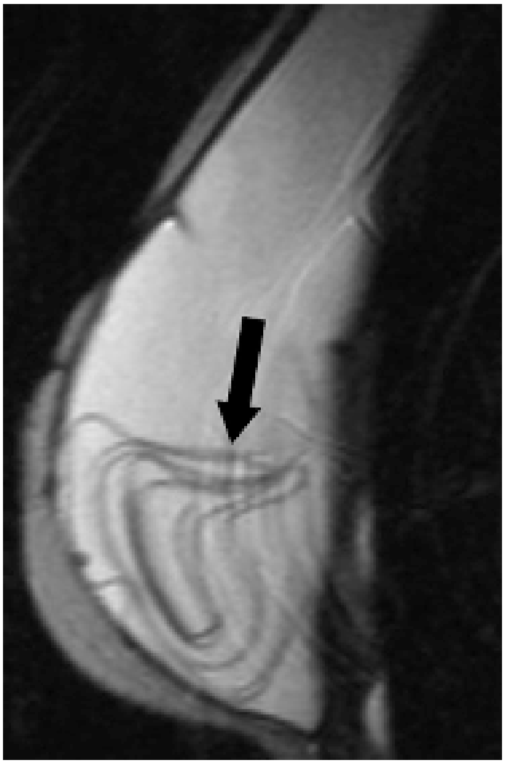

Fig. 28.29 Linguine sign of intracapsular breast implant rupture. MRI of the breast demonstrating multiple hypointense curvilinear lines (arrow) within high-intensity silicone gel caused by collapsed breast implant

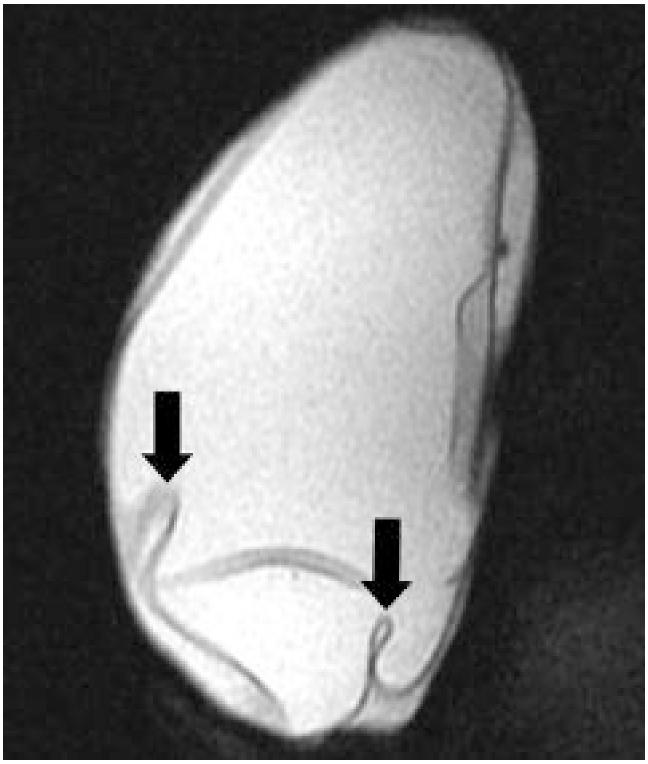

Fig. 28.30 Keyhole sign of intracapsular breast implant rupture. MRI of the breast demonstrates a small contained leak of silicone gel through the tear of the elastomer shell of the breast implant in a keyhole configuration (arrows)

Keyhole Sign

Keyhole sign, also known as the noose sign or the teardrop sign, is an early MR imaging sign of intracapsular rupture of silicone breast implant and represents the uncollapsed rupture of the outer elastomer shell. A silicone breast implant consists of a silicone gel filling surrounded by an outer elastomer envelope. A fibrous layer (scar tissue) forms around the implant following placement of the implant. In uncollapsed ruptures, there is a minor tear in the elastomeric shell causing a small and contained leak of silicone between the elastomeric and the fibrous layer giving the appearance of a teardrop or keyhole (Fig. 28.30), hence the name. This sign is more commonly observed with intracapsular ruptures than the linguine sign.

Rim Sign

Rim sign, seen on cholescintigraphy, refers to the increased enhancement of hepatic parenchyma surrounding the gallbladder fossa (Fig. 28.31). The presence of this sign is a useful secondary marker of acute cholecystitis. The increased radiotracer uptake in the surrounding liver parenchyma occurs due to increased blood flow to the area as a result of the extension of severe inflammation of the gallbladder to the adjacent liver. The presence of this sign correlates with the severity of cholecystitis, as it is observed with more severe forms including gangrenous and perforated cholecystitis.

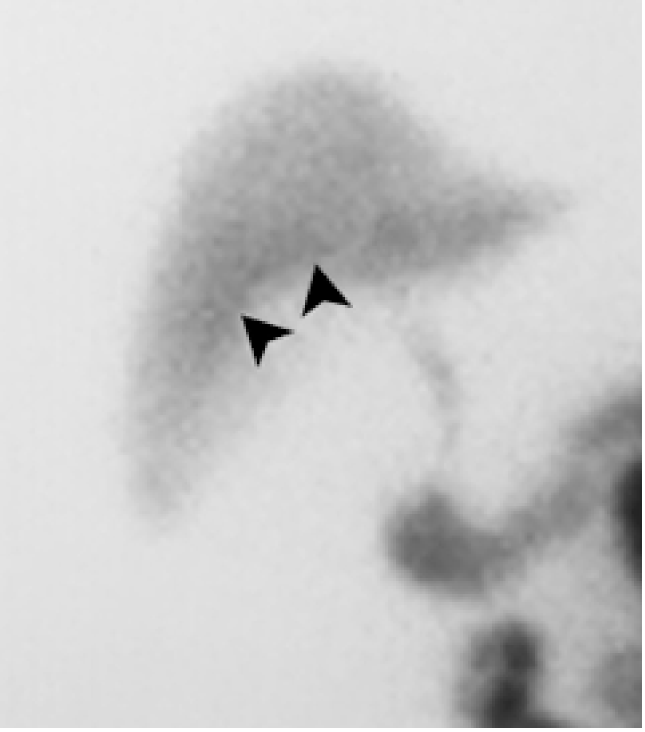

Fig. 28.31 Rim sign of gangrenous cholecystitis. Cholescintigraphy study demonstrates a curvilinear band (arrowheads) of increased radiotracer activity in the pericholecystic liver parenchyma. This increased activity is due to cholestasis in the inflamed liver parenchyma adjacent to the gallbladder fossa

Hot Nose Sign

Hot nose sign, seen on radionuclide brain perfusion scans, refers to the increased observed radiotracer activity in the nasopharyngeal region (Fig. 28.32). Secondary to absent or diminished blood flow in the internal carotid artery due to its functional obstruction caused by increased intracranial pressure, blood flow in the external carotid artery increases which results in significantly increased perfusion in the nasal region. In the absence of any intracerebral perfusion, the presence of this sign is considered a secondary marker of brain death.

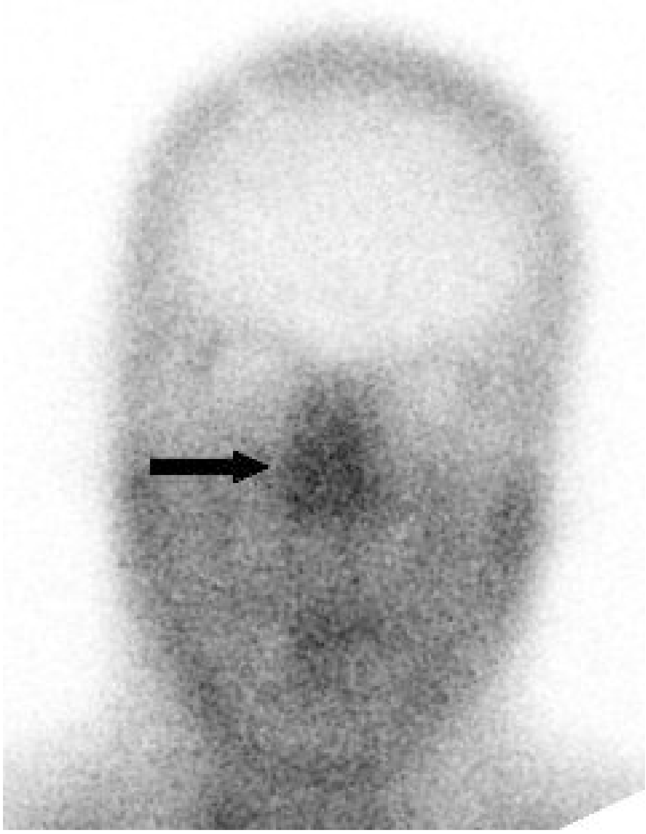

Fig. 28.32 Hot nose sign of brain death. 99mTc-HMPAO study demonstrates increased radiotracer activity in the nasopharyngeal region (arrow) due to shunting of blood flow from internal carotid arteries to the external carotid arteries. There is absent intracranial perfusion due to functional internal carotid artery obstruction caused by increased intracranial pressure

Target Sign

Target sign, also known as the doughnut sign or bulls-eye sign, observed on abdominal ultrasound, refers to the visualisation of alternating hyperechoic and hypoechoic concentric bands (Fig. 28.33) resulting from the invagination of the bowel. The presence of this sign is suggestive of intestinal intussusception. Mucosal and muscularis layers are observed as echogenic bands whereas the submucosal layer forms the hypoechoic bands.

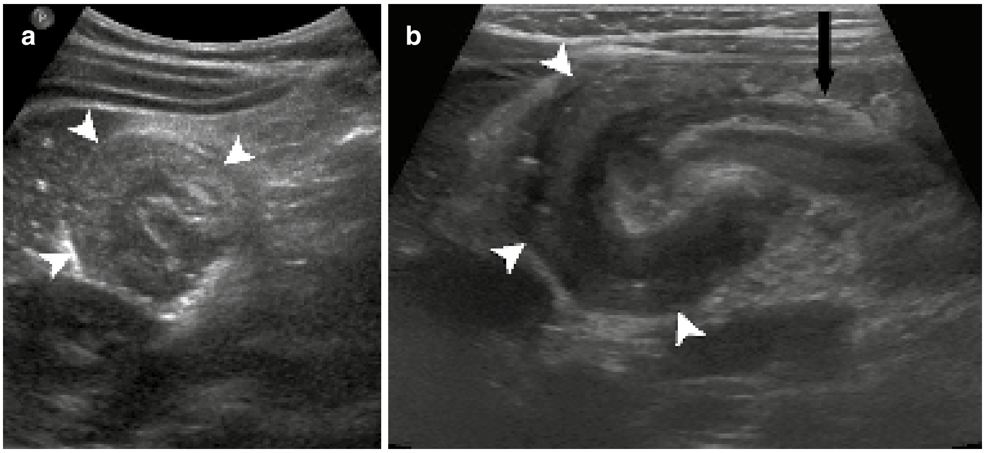

Fig. 28.33 (**a**, **b**) Target sign of intussusception. Ultrasound of the abdomen demonstrates concentric hyperechoic and hypoechoic layers (arrowheads) of the bowel wall in a patient with ileocolonic intussusception. Hyperechoic bands represent mucosa and muscularis propria layers of the bowel and hypoechoic band represents submucosa

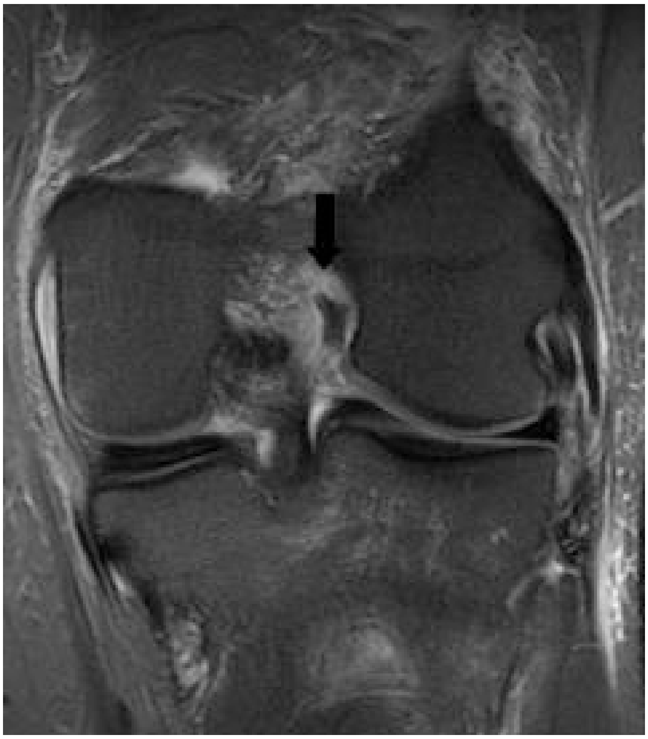

Fig. 28.34 Empty notch sign of anterior cruciate ligament (ACL) tear. Coronal T2-WI of the knee demonstrates fluid density at the lateral intercondylar notch of the femur. There is fluid (arrow) surrounding the femoral end of the torn ACL ligament

Empty Notch Sign

Empty notch sign, observed on MR imaging, refers to the visualisation of an unusual fluid signal instead of the anterior cruciate ligament attachment at the lateral intercondylar notch (fossa) of the femur (Fig. 28.34). It is a direct sign of ACL tear/avulsion at its femoral attachment site. ACL is the most commonly injured ligament of the knee. The sign is best observed on axial and coronal images on fluid-sensitive MRI sequences.

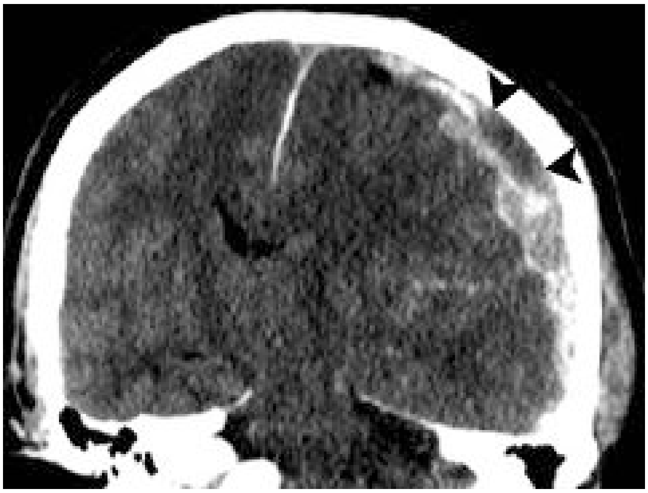

Fig. 28.35 Swirl sign in subdural haematoma. Non-contrast coronal CT reformation of the head demonstrates subdural haemorrhage over the left cerebral convexity. The oval low-density focus (arrowheads) within the subdural haematoma represents active bleeding

Swirl Sign

Swirl sign, seen on non-contrast CT of the head, refers to a focal area of hypo- or isoattenuation within the hyperattenuating haemorrhagic collection (Fig. 28.35) and represents active bleeding within an acute haematoma. Fresh, unclotted blood appears hypodense whereas clotted blood appears hyperdense. The sign was initially defined for epidural haematoma but is also seen with subdural haematoma and intracerebral haemorrhage. Demonstration of swirl sign in intracerebral haemorrhage is an independent predictor of poor prognosis and is associated with a higher incidence of haematoma expansion and midline shift.

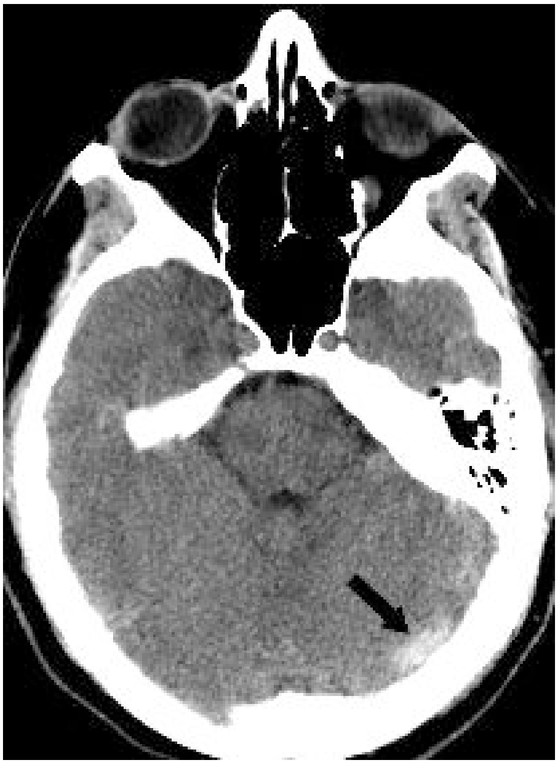

Fig. 28.36 Cord sign of dural venous sinus thrombosis. Non-contrast CT of the head demonstrates linear high density (arrow) in the expected location of the left transverse sinus due to the presence of blood clot within the transverse sinus lumen

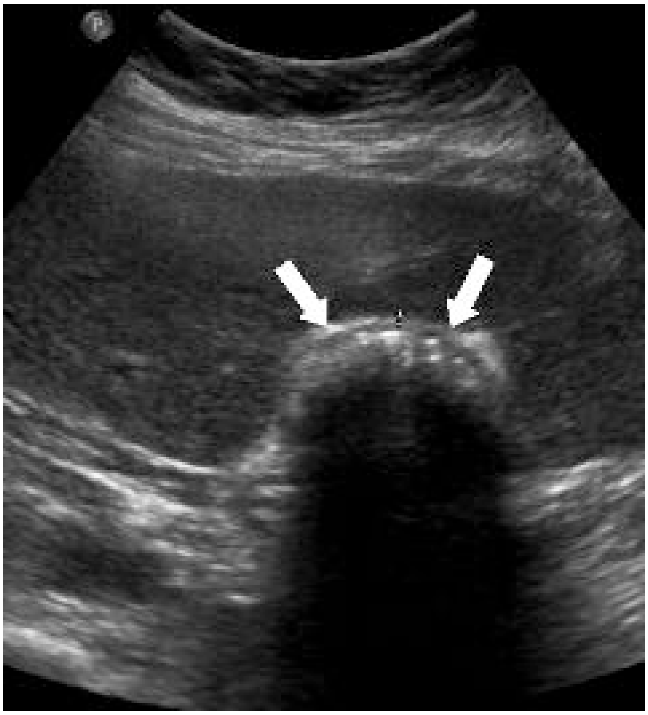

Fig. 28.37 Wall-echo-shadow sign of cholelithiasis. Ultrasound of the gallbladder demonstrates two curvilinear bands of hyperechogenicity (arrows) representing the gallbladder wall and gallstones, respectively, separated by a thin hypoechoic layer of bile. The acoustic shadowing, seen posterior to the posterior hyperechoic layer, is caused by the gallstones

Cord Sign

Cord sign, seen on non-contrast CT of the head, is a sign of central venous sinus thrombosis and refers to the cord-like hyperattenuation (Fig. 28.36) of the thrombus within the involved dural venous sinus. The sign is appreciated more in sinuses running parallel to the axial plane, most commonly the transverse sinus. The presence of cord sign is suggestive of acute venous thrombosis since the hyperattenuation of the thrombus begins to fade after 7–14 days of its formation and therefore will not be observed in subacute or chronic cases.

Wall-Echo-Shadow (WES) Sign

Wall-echo-shadow sign refers to characteristic sonographic findings of cholelithiasis. Two parallel, curvilinear, hyperechogenic bands separated by a narrow hypoechoic space and marked posterior acoustic shadowing is observed within the gallbladder fossa (Fig. 28.37). The two hyperechogenic bands represent the gallbladder wall (W) and the echoes (E) from gallstones subjacent to the gallbladder wall. A thin layer of hypoechoic bile separates these two layers. The prominent posterior shadowing (S) results from sound attenuation by the highly reflective gallstones. WES sign suggests either a large or multiple gallstones within the gallbladder.

Middle Cerebral Artery (MCA) Dot Sign

Middle cerebral artery (MCA) dot sign, also known as the Sylvian fissure sign, observed on non-contrast CT of the head, refers to the visualisation of a hyperattenuating dot within the Sylvian fissure (Fig. 28.38). The Sylvian fissure contains the M2 and M3 segments of the MCA, and the visualisation of the dot sign represents thromboembolism within these segmental branches. The sign is seen on axial images when the occluded vessel lies perpendicular to the cross-sectional plane of imaging. The MCA dot sign is considered a variant of the hyperdense MCA sign with the former representing thromboembolism within more distal branches of MCA and the latter involving the more proximal portions of the artery (M1 segment) and therefore, being associated with larger territories of infarction.

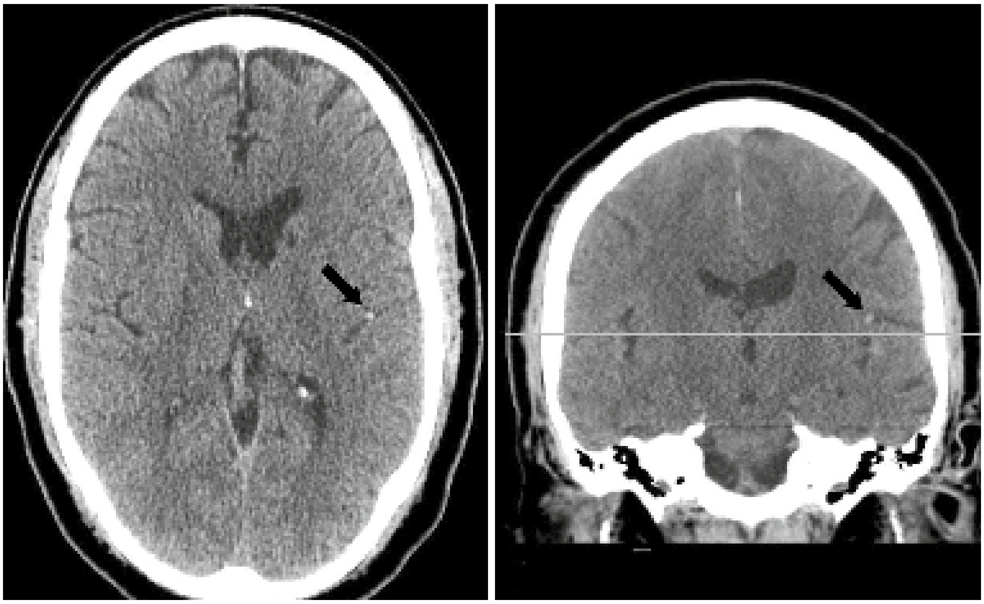

Fig. 28.38 Middle cerebral artery (MCA) dot sign of acute MCA infarct. Non-contrast CT scan of the head demonstrates a punctate focus of hyperattenuation (arrows) located within the M2 branch of left MCA

Mount Fuji Sign

Mount Fuji sign, seen on CT scan of the head, is a characteristic sign of tension pneumocephalus, a surgical emergency. It refers to the presence of bilateral subdural collections of large amounts of air resulting in compression and separation of frontal lobes (Fig. 28.39). The resultant expansion of interhemispheric space between tips of frontal lobes gives the conical appearance like that of a volcanic mountain in Japan, Mount Fuji, hence the name. The presence of the sign suggests that pressure of the air exceeds the surface tension of cerebrospinal fluid between the frontal lobes. This sign is highly valuable in differentiating tension pneumocephalus from nontension pneumocephalus. Surgical evacuation of the subdural haematoma is the most common cause of tension pneumocephalus. Other common causes include paranasal sinus surgery, brain trauma, and skull base surgery.

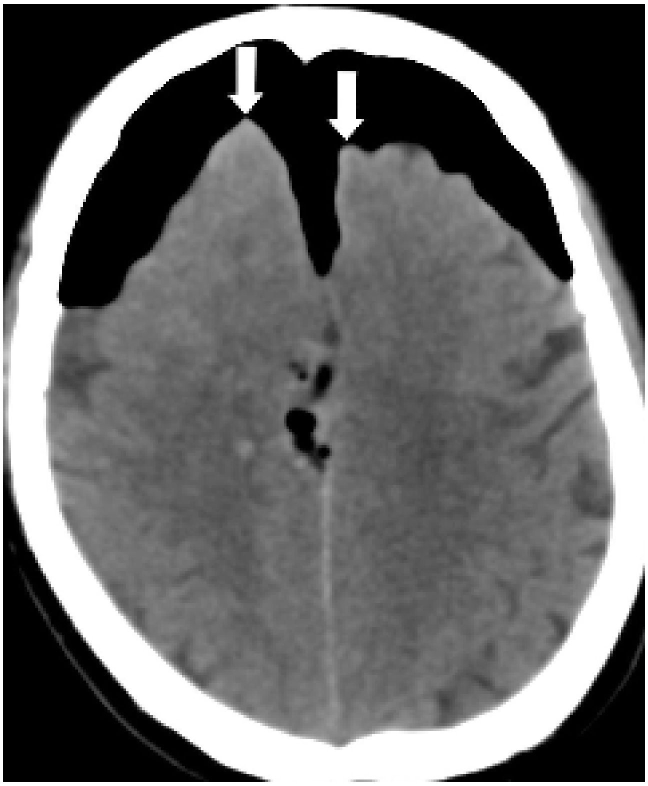

Fig. 28.39 Mount Fuji sign of tension pneumocephalus. Non-contrast CT scan of the head demonstrates compression and separation of frontal lobes (arrows) due to the presence of subdural air under pressure giving frontal lobes the heaped-up appearance

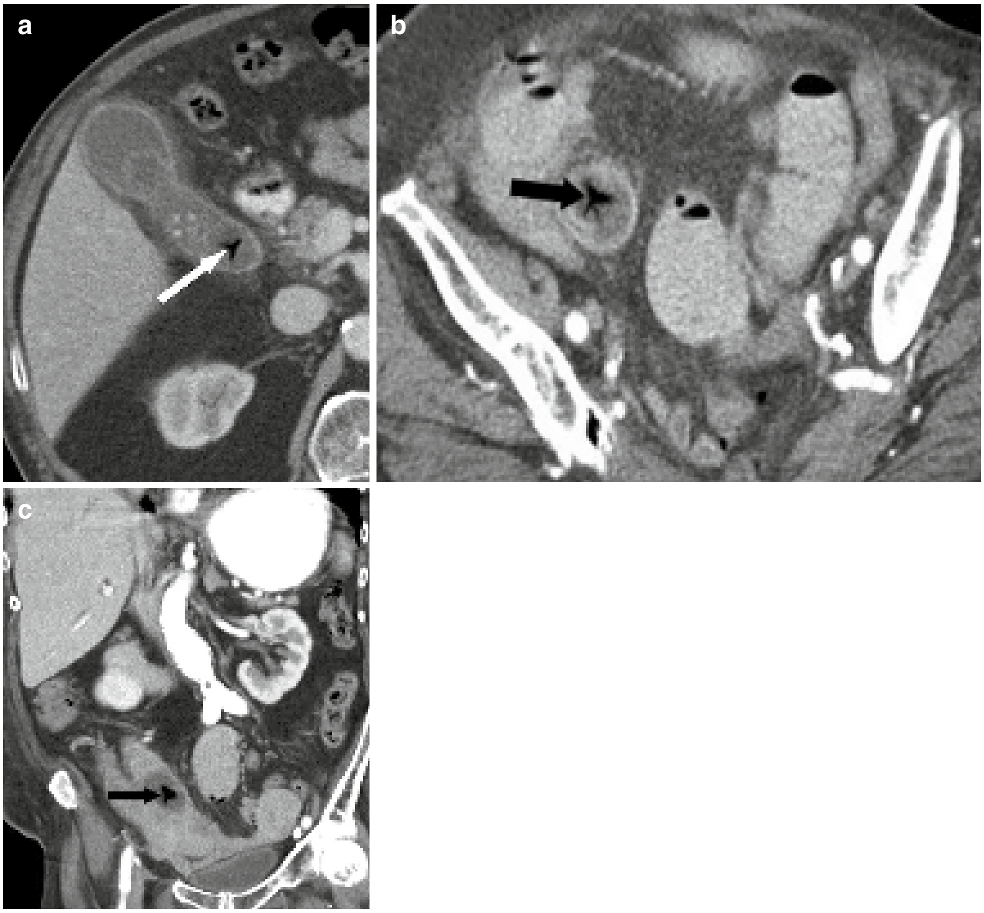

Fig. 28.40 Mercedes-Benz sign of cholelithiasis. (**a**) Contrast-enhanced CT scan of the abdomen demonstrates triradiate radiolucency (arrow) due to the presence of nitrogen gas within the central crevice of the gallstone. (**b**, **c**) Axial and coronal images demonstrate small bowel obstruction caused by a gallstone lodged in the distal small bowel. Mercedes-Benz sign (arrows) is demonstrated within this gallstone

Mercedes-Benz Sign

Mercedes-Benz sign, seen on abdominal radiographs or CT scan of the abdomen, refers to the presence of triradiate radiolucency within the fissured gallstones giving an appearance of Mercedes-Benz logo (Fig. 28.40), hence the name. In most cases, fluid fills up the clefts of the fissures, however, radiolucency is produced when these crevices contain air, typically the nitrogen gas. These fissures are usually widest at the centre and taper outwards like points of a star. It is believed that the gas is released as a result of negative pressure generated during fissuring or shrinkage of cholesterol stones owing to their crystalline structure.

Beak Sign

Beak sign, seen on contrast-enhanced CT images, is a characteristic sign of aortic dissection. An intimomedial flap is formed as a result of aortic dissection which produces two communicating channels. The beak sign refers to the acute angle formed between the walls of the true lumen and the false lumen of the aorta (Fig. 28.41).

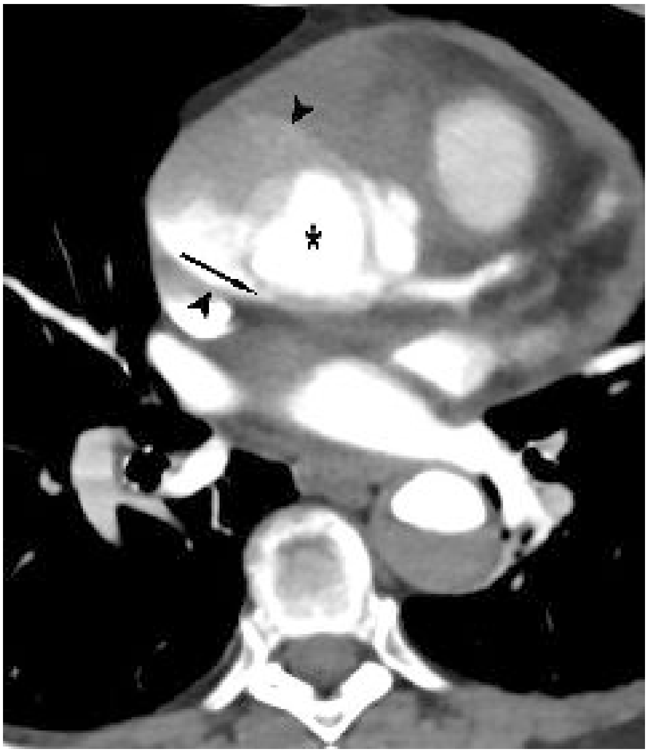

Fig. 28.41 Beak sign of aortic dissection. Contrast-enhanced CT of the chest demonstrates a partially thrombosed false lumen in a patient with type A aortic dissection. The beak sign (arrow) is indicated by the acute angulation between the wall of the true lumen (*) and false lumen (arrowhead) in the ascending aorta

Cystic Duct Sign

Cystic duct sign, also known as the nubbin sign, seen on cholescintigraphy, refers to the focus of increased radiotracer activity in the cystic duct (Fig. 28.42) with no evidence of radiotracer uptake by the gallbladder. The sign is suggestive of cystic duct/gallbladder neck obstruction and must not be mistaken for gallbladder filling. The focus of radiotracer activity observed would be medial to the gallbladder fossa and smaller than that anticipated for the gallbladder filling. When the diagnosis is not clear on cholescintigraphy, SPECT/CT should be utilised to confirm the diagnosis.

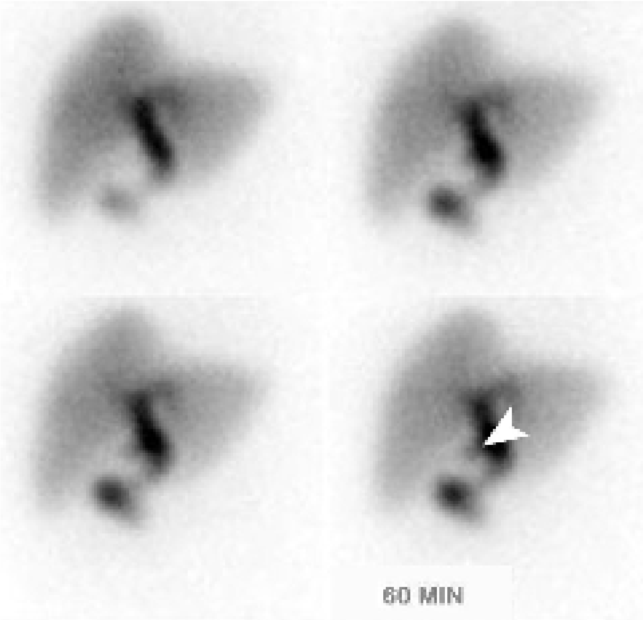

Fig. 28.42 Cystic duct sign of acute cholecystitis. Cholescintigraphy study demonstrates nonvisualisation of the gallbladder with a focus of increased radiotracer activity (arrowhead) in the expected location of the cystic duct

Reversed Halo Sign

Reversed halo sign, also known as the atoll sign, seen on the CT chest, refers to the visualisation of a denser ring or crescent of consolidation containing a focus of ground-glass opacities at its centre (Fig. 28.43). In cryptogenic organising pneumonia, the central ground-glass opacity represents alveolar septal inflammation and peripheral consolidation represents granulomatous tissue. Although first described for cryptogenic organising pneumonia, the sign is observed with various infectious and non-infectious pulmonary pathologies including fungal infections, community-acquired pneumonia, tuberculosis, COVID-19 pneumonia, sarcoidosis, tumours, radiofrequency ablation, lymphomatoid granulomatosis, and Wegener granulomatosis.

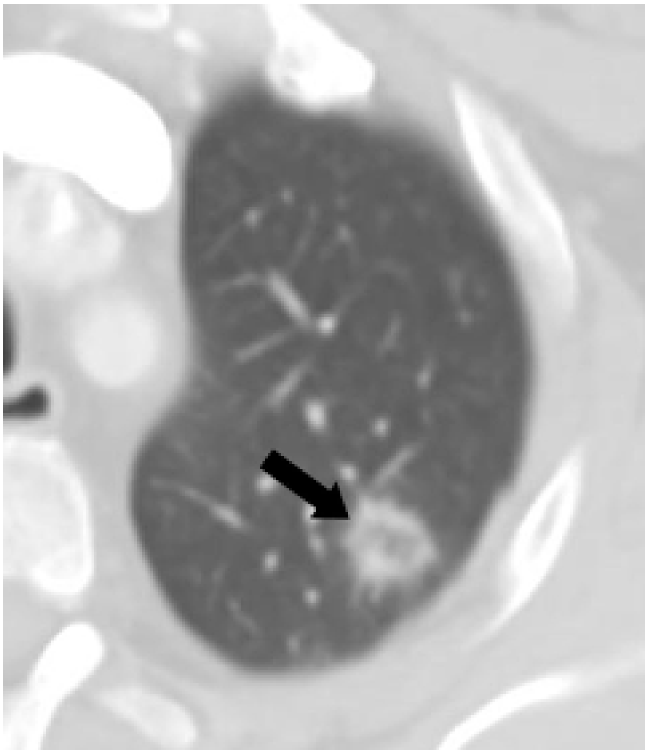

Fig. 28.43 Reversed halo sign. Contrast-enhanced CT of the chest demonstrates a rim of consolidation (arrow) containing central ground-glass opacity in this patient with COVID-19 pneumonia

Collar Sign

Collar sign, also known as the hourglass sign, seen on sagittal or coronal CT images, is a sign of diaphragmatic rupture. It refers to the waist-like constriction of the herniating intra-abdominal organs at the rupture site (Fig. 28.44). This sign is more frequently observed with left-sided ruptures due to buffering effect of the liver on the right. However, when right-sided herniation of the liver occurs, it produces two variants of the collar sign, namely, the hump sign and the band sign. The hump sign refers to the hump-shaped appearance of the herniated portion of the liver. The band sign refers to a thin linear band of hypoattenuation intersecting the liver at the rupture site and represents a zone of low perfusion secondary to compression.

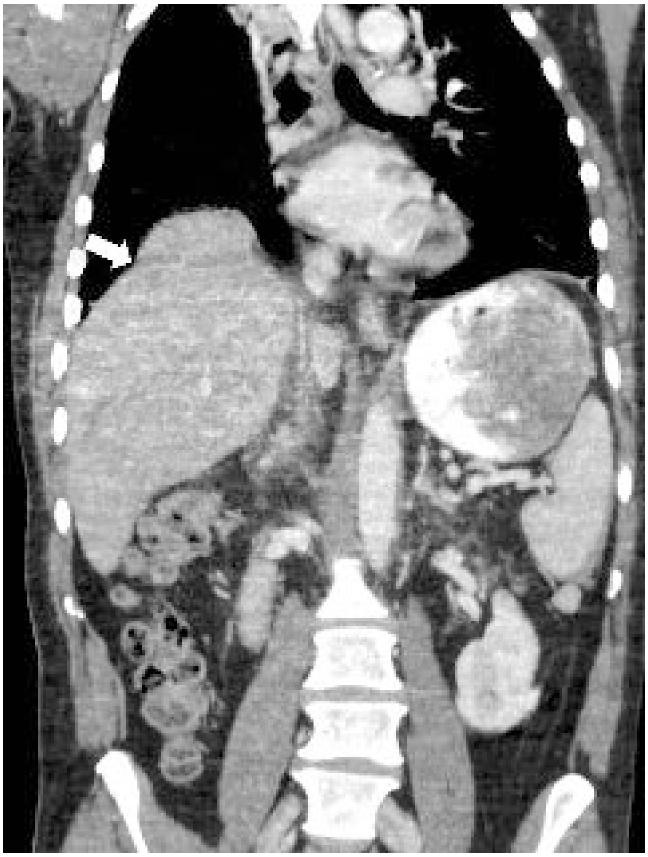

Fig. 28.44 Collar sign of diaphragmatic rupture. Coronal contrast-enhanced CT reformation demonstrates a waist-like constriction (arrow) at the site of hepatic herniation through the diaphragmatic rupture

Dangling Diaphragm Sign

Dangling diaphragm sign, seen on the CT scan of the chest or abdomen, is considered a direct sign of diaphragmatic rupture. It refers to the inward curling of the torn free edge of the hemidiaphragm which appears as a comma-shaped fragment (Fig. 28.45). Cut edges of the diaphragm can display focal thickening as well. This sign is associated with blunt diaphragmatic injuries which typically produce large radial tears.

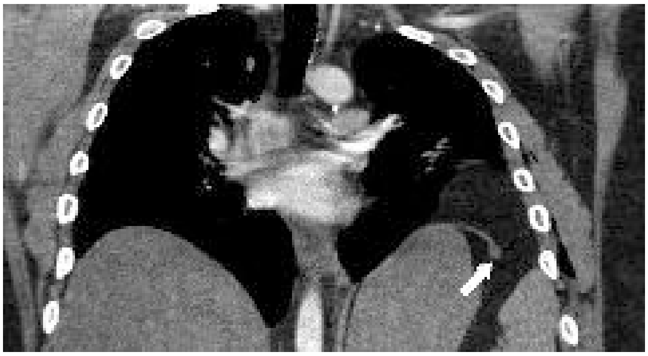

Fig. 28.45 Dangling diaphragm sign of diaphragmatic rupture. Coronal contrast-enhanced CT reformation demonstrates inward curling of the torn free edge (arrow) of the diaphragm

Cobweb Sign

Cobweb sign, seen on contrast-enhanced CT scans, is a characteristic sign of aortic dissection. It refers to thin hypoattenuating ribbon-like filling defects within the false lumen (Fig. 28.46). These slender lines represent incompletely dissected strands of aortic tunica media. This sign is specifically observed within the false lumen. However, the sensitivity of the sign is low as it is not encountered often.

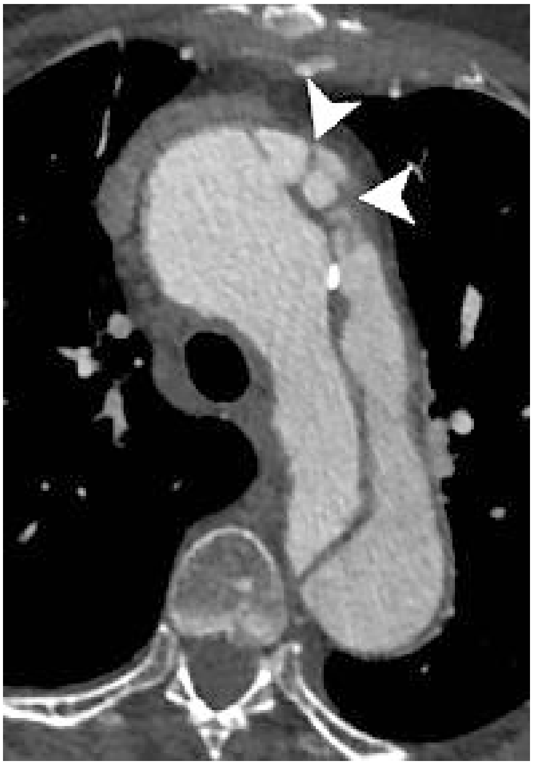

Fig. 28.46 Cobweb sign of aortic dissection. Axial contrast-enhanced CT of the chest demonstrates type A aortic dissection. Multiple low-density ribbon-like structures (arrowheads) traversing the false lumen of the aorta represent strands of aortic tunica media

Index

A
Abdominal aortic aneurysm (AAA), 1, 3
  aortic pathology, 12
  causes, 1
  diagnosis, 12
  factor, 12
  indicator, 12
Abdominal trauma
  bowel and mesentery, 137–139
  FAST, 127, 128
  gunshot injuries, 140
  kidney, 133–135
  liver, 128–130
  pancreas, 132, 133
  spleen, 130, 131
  urethral injury, 136, 137
  urinary bladder, 135, 136
Abnormal central venous line positions, 416
Abnormal tracheostomy tube positioning, 413
Accordion sign, 461
Acetabular fracture, 329
Acromioclavicular dislocation, 308, 309
Actinomyces israelii, 184
Active bile leak, 211
Active contrast extravasation (ACE), 129
Acute abdomen, 75
Acute aortic conditions
  AAA, 1–3
  aortic dissection, 6, 7
  aortic rupture, 1–3
  calcification, 4
  causes, 12
  dissection, 7
  draped aorta sign, 2
  endoleak, 8
  hyperdense crescent sign, 2, 5
  imaging, 2, 4, 7
  intramural hematoma, 8, 9
  lumen, 7, 8
  mycotic aneurysm, 4
  penetrating ulcer, 11
  risk factors, 2, 4
  traumatic aortic transection, 4, 6
Acute aortic syndrome, 384
Acute appendicitis, 39, 46
  abdominal pain and fever, 46
  anatomy, 33
  barium enema, 34
  complications, 37, 38
  CT, 35–37, 46, 47
  diverticular disease, 45, 46
  imaging algorithm, 43
  imaging findings, 39
  interventional management, 43, 44
  MR findings, 42
  MR imaging, 41–43
  pathophysiology, 34
  postoperative complications, 43, 44
  in pregnancy, 39, 41
  radiographic findings, 34
  stages, 35
  ultrasound, 35, 38, 39, 46
  variants, 39, 40
  vermiform process, 33
Acute chest pain, 210
Acute cholecystitis
  overview, 16
  ultrasound, 17, 18
Acute colonic disorders
  acute epiploic appendagitis, 81, 82
  barium enema, 89
  complications, 77–79, 84
  Crohn’s disease, 83, 84
  CT, 77, 78
  diagnosis, 91
  diverticulum, 77
  enterography, 84
  GI bleeding, 92, 93
  imaging, 82
  inflammatory bowel disease, 82, 84
  intussusception, 89–91
  ischemic colitis, 91, 92
  omental torsion, 80
  pseudomembranous colitis, 84, 85
  segmental omental infarction, 79–81
  sigmoid, 77
  sigmoid volvulus, 86
  treatment, 79
  typhlitis, 85, 86
  ulcerative colitis, 83, 84
  volvulus, 86–89
Acute coronary syndrome (ACS), 201, 202
Acute disseminated encephalomyelitis (ADEM), 427, 428
Acute diverticulitis, 93
Acute edematous pancreatitis, 161
Acute epiploic appendagitis, 94
  clinical management, 81
  imaging, 81, 82
  location, 81
  vascular occlusion and infarction, 81

© The Editor(s) (if applicable) and The Author(s), under exclusive license to Springer Nature Switzerland AG 2024

A. Singh (ed.), *Emergency Radiology*, https://doi.org/10.1007/978-3-031-65770-2

Acute fulminant invasive fungal sinusitis (AFIFS), 302
Acute gynecologic disorders, 191, 192
  cogwheel sign, 183
  cystitis, 187, 188
  endometriosis, 185, 186
  functional ovarian cysts, 181
  hematometrocolpos, 191
  hydrometrocolpos, 191
  imaging, 181–183, 186
  OHSS, 188
  ovarian cycle, 181
  ovarian torsion, 186, 187
  ovarian vein thrombosis, 189
  pelvic pain, 181
  PID, 183–185
  torsion, 186
  tubo-ovarian abscess, 184
  ultrasound, 181, 183, 185
  uterine fibroids, 189, 190
Acute head emergencies
  acute hypertensive encephalopathy, 251
  basilar skull fractures, 252
  brain death, 252
  carbon monoxide poisoning, 236
  central nervous system infections, 237–239
  cerebral arterial air embolism, 248, 249
  cerebral contusions, 247, 248
  CSF leak, 251
  extra-axial hemorrhages, 244, 245
  giant MCA aneurysm, 242
  herniation syndromes, 245–247
  herpes encephalitis, 240
  obstructive hydrocephalus, 249, 250
  pseudo-subarachnoid hemorrhage, 235, 236
  spontaneous intracranial hypotension, 243
  tension pneumocephalus, 241
Acute hepatitis, 145
  HU, 146
  hypoattenuating regions, 146
  imaging, 145
Acute hepatitis B, 146
Acute hepatitis C, 146
Acute hypertensive encephalopathy, 251
Acute ischemic stroke, 272, 273
Acute liver failure (ALF), 153
Acute mesenteric ischemia, 52
  clinical presentation, 52
  CT, 53–56
  pathogenesis, 53
  radiograph, 53
  risk factor, 53
  treatment, 55
Acute obstetric disorders
  anembryonic gestation, 171, 172
  ectopic pregnancy, 174, 175
  gestational age, 169
  heterotopic pregnancy, 176
  interstitial ectopic pregnancy, 175, 176
  molar pregnancy, 177
  normal pregnancy, 169–171
  placenta previa, 178
  pregnancy termination failure, 172, 173
  subchorionic hemorrhage, 173, 174
Acute obstructive uropathy, 98
Acute otitis media (AOM), 428, 430
Acute pancreatitis, 164
  AIP, 166, 167
  causes, 159
  classification, 159
  complications, 160, 163, 164
  CT severity index, 160
  embolization, 168
  grading, 164–167
  imaging, 160–162, 167
  MRCP, 166
  MRI, 167
  pancreatic cancer, 164
  pancreatic contusions, 164, 166
  peripancreatic fluid collections, 159
  ultrasonography, 160
Acute pyelonephritis
  imaging, 101–103
  MDCT, 102
  MRI, 103
  overview, 101
  treatment, 103
Acute sinusitis (AS), 428, 430
Adenoidal hypertrophy, 223
Adenomas, 151
Air embolism, 248, 249
Airway injuries, 400
Amebic abscess, 148, 156
American Association for the Surgery of Trauma (AAST), 127, 128, 131, 133, 137, 141, 142
American College of Radiology (ACR) appropriateness criteria, 353, 354
Amplatz guidewire, 420
Amyand's hernia, 39, 41
Anembryonic pregnancy, 178
Aneurysms, 286
Angel wing sign, 449
Angiography, 13
Ankle fractures, 341
Anterior hip dislocation, 330
Anteroinferior dislocation, 309
Aortic dissection, 6, 7
Aortic injury, 402–403
Aortic rupture, 1–3
  CT findings, 4
  risk factors, 2, 4
Aortic transection, 6, 402
Aortic ulcer, 11
Appendiceal caliber, 35
Appendicoliths, 35
Appendix testis, 119
Arrowhead sign, 36, 458
Aspiration pneumonia, 388
Asymmetrically thickened small bowel wall, 63
Atlantoaxial instability, 363
Atlantoaxial rotatory subluxation, 363
Atlanto-Dens interval space, 356
Atlantooccipital dissociation (AOD), 358–359
Autoimmune pancreatitis (AIP), 162, 166, 167
Avascular necrosis (AVN), 311

B
Bacterial meningitis, 239
Bacterial pneumonia, 433
Bacteriuria, 101
Bacteroides, 117
Barber pole sign, 457

Barium study, 50
Barton's fracture, 316
Basilar skull fractures, 252
Basion-axial interval (BAI), 357
Batwing sign, 449
Beak sign, 460, 473, 474
Bezold's abscess, 231
Bilateral facet dislocation, 366
Bilateral interfacetal dislocation, 365
Biliary tract, 30
  acute cholecystitis
    overview, 16
    ultrasound, 17, 18
  bacterial cholangitis, 23, 24
  cholecystitis, 19
  complications, 27, 28
  CT, 15
  emphysematous cholecystitis, 21
  gallbladder torsion, 22
  gallstone ileus, 25–27
  gallstones, 15, 16
  gangrenous cholecystitis, 19, 20
  hemobilia, 25
  imaging, 15, 16
  Mirizzi syndrome, 19
  MRI role, 29
  obstruction, 22, 23
  perforation, 21, 22
Black turbinate sign, 302
Blast injuries, 407–410
Bloody stools, 94
Blow-in fracture, 257–259
Blow-out fracture, 257, 258
Bochdalek hernia, 405
Boerhaave's syndrome, 382, 383
Bowel and mesenteric surgery, 137, 139
Bowel hypoperfusion, 139
Bowel obstruction, 26
Bowel perforation, 57–62
Bowel spasm, 63
Bowing fracture, 313
Boxer fracture, 321
Brain death, 252
Branchial cleft, 226–228
British Thoracic Society, 395
Bronchial intubation, 412
Bronchial lacerations, 400
Bronchiolitis, 433
Bronchopneumonia, 388
Broviak and Hickman catheters, 420
Bubbly gas and fluid accumulation, 110
Budd–Chiari syndrome, 151, 155, 156
Bulging fissure sign, 449
Burst fractures, 369–371

C
Calcaneal fractures, 343
Campylobacter ileocolitis, 62
Canadian C-spine Rule Study (CCRS), 353–355
Capitolunate dislocation, 321
Carbon monoxide poisoning, 236
Cardiac conduction devices (CCD), 424
Cardiac Injuries, 401–403
Cardiogenic vs. noncardiogenic pulmonary edema, 391
Carotid cavernous fistula, 302–303
Carpal bone fractures, 318
Carpal fractures, 317–320
Carpometacarpal joint, 322
Catheter angiogram, 288
Catheter angiography, 283
Catheter breakage, 420
Cavernous sinus thrombosis, 430
Cecal bar sign, 36, 47, 458
Cecal volvulus, 86, 87
Central cord syndrome, 368
Central high-attenuation, 81
Central hip dislocation, 330
Central nervous system infections, 237–239
Central venous catheters, 416, 417
Central venous lines, 418
Cerebral amyloid angiopathy, 282
Cerebral arterial air embolism, 248, 249
cerebral blood volume (CBV), 275
Cerebral contusions, 247, 248
Cerebritis, 430
Cervical injury
  axial loading, 358
  complex mechanism, 358
  extension mechanism, 358
  flexion mechanism, 357
Cervical spine fractures, 353–354
  anterior and lateral wedge compression fractures, 369–370
  AOD, 358–359
  atlantoaxial instability, 363
  burst fracture, 370–371
  chance fracture, 371–372
  classification, 357–358
  Clay-Shoveler's fracture, 367–368
  dens fracture, 360–361
  facet dislocation, 365–367
  flexion teardrop fracture, 364–365
  Hangman's fracture, 361–363
  hyperextension teardrop fracture and sprains, 368–369
  Jefferson fracture, 359–360
  occipital condyles, 359
  pillar and laminar fractures, 369
  posterior arch of C1 fracture, 369
  severe hyperflexion/hyperextension forces, 372
  shearing distraction injuries, 372
  thoracic and lumbar spine fractures, 369
  transverse process and spinous process fractures, 372
  wedge and burst compression fracture, 369
Cervical spine lines, 356, 357
Chance fracture, 371–372
Chauffeur's fracture, 316
Chest radiograph, 402
Cholangitis, 23, 24
Choledocholithiases, 23
Cholescintigraphy, 17
Cholesteatoma, 230
Choroidal detachment (CD), 298
Classic 4-part Jefferson fracture, 360
Clavicle fractures, 307, 308
Clay-Shoveler's fracture, 367–368
Closed loop obstruction, 74
Clostridium difficile infection, 63, 84, 85
Cobweb sign, 476
Coffee bean sign, 447
Coins, 435
Collar button lesions, 93
Collar sign, 475

Colles' fracture, 316
Colonic ischemia, 92
Color Doppler imaging, 101
Color Doppler ultrasound, 114
Comb sign, 461
Comminuted fracture, 332
Communicating rupture, 155
Community-acquired pneumonia (CAP), 386
Computed tomography angiography (CTA), 287
Congenital diverticula, 49
Continuous diaphragm sign, 63, 443, 444
Cord sign, 471
Corpus luteal cyst, 182
Cortical laminar necrosis, 247–248
COVID-19 pneumonia, 393–394
Craniofacial trauma, 269
  anatomy, 256
  blow-in fracture, 257–259
  blow-out fracture, 257, 258
  dentoalveolar and maxillary sagittal fractures, 267
  frontal fractures, 263, 264
  imaging, 255, 256
  isolated arch fracture, 260, 261
  Le Fort fractures, 265, 266
  mandible fractures, 267, 268
  maxillary fractures, 265
  nasal fractures, 261, 262
  NOE fractures, 262, 263
  orbital fractures, 257
  ZMC fracture, 259, 260
  zygoma fractures, 259
Crazy paving pattern, 462, 463
Crescent sign, 462
Creutzfeldt-Jakob disease, 236
Crohn's disease, 82
Cross-sectional signs
  accordion sign, 461
  arrowhead sign, 458
  barber pole sign, 457
  beak sign, 460, 473
  cecal bar sign, 458
  cobweb sign, 476
  collar sign, 475
  comb sign, 461
  cord sign, 471
  crazy paving pattern, 462
  crescent sign, 462
  cystic duct sign, 474
  dangling diaphragm sign, 475
  draped aorta sign, 463
  empty delta sign, 456
  empty notch sign, 470
  feeding vessel sign, 457
  halo sign, 459, 465
  hot nose sign, 469
  hyperdense crescent sign, 463
  hyperdense middle cerebral artery sign, 455
  insular ribbon sign, 466
  keyhole sign, 468
  Linguine sign, 467
  MCA dot sign, 471
  Mercedes Benz sign, 473
  molar tooth sign, 466
  Mount Fuji sign, 472
  polo mint sign, 459
  railway track sign, 459
  reversal sign, 456
  reverse hamburger sign, 464
  reversed halo sign, 474
  rim sign, 468
  sentinel clot sign, 462
  small bowel feces sign, 461
  split pleura sign, 460
  Swirl sign, 470
  tangential calcium sign, 464
  target sign, 469
  tip of the iceberg sign, 467
  Wall echo shadow sign, 471
  Whirl sign, 457
  Yin yang sign, 466
Croup, 224, 225
Cryptosporidium, 61
CSF leak, 251
Cupola sign, 58, 441
Cystic duct sign, 474
Cystic fibrosis, 75
Cystitis, 187, 188
Cytomegalovirus, 61
Cytomegalovirus enteritis, 61
Cytoxan assay, 85

D
Danger space, 219, 220, 385
Dangling diaphragm sign, 475, 476
David Letterman sign, 450
Deep lateral femoral notch sign, 450
Deep sulcus sign, 392, 446
Degenerating uterine fibroid, 190
Denis classification, 329
Denis system, 370
Dense artery sign, 273
Dens fracture, 360, 361
  anomalies, 361
  atlantoaxial instability, 360
  classification, 360
  types of, 360
Dermoid cyst, 192
Diabetes mellitus, 110
Diaphragmatic injury, 403, 405
Diaphragmatic rupture, 403
Diaphragm injuries, 403
Diaphragm muscle slip sign, 60
Diaphragm rupture, 408
Disk batteries, 435
Disk battery ingestion, 435
Dislodged denture, 232
Distal interphalangeal (DIP) joint, 323
Distal radial fractures, 316
Distal radius fractures, 314, 315
Doge's cap sign, 60
Doppler colors, 99
Doppler imaging, 109, 183, 186
Dorello's canal, 230
Double-decidual sac sign, 171
Draped aorta sign, 2, 463
Dropped appendicolith, 43
Dropped gallstones, 27
Duodenal diverticulum, 49
Duodenal hematoma, 73

E
Ectopic pregnancy, 174, 175, 178
Elbow dislocation, 313
Emphysematous cholecystitis, 21
Emphysematous cystitis (EC), 106, 111
  radiography, 106
  symptoms, 106
  treatment, 107
Emphysematous pyelonephritis, 105, 111
  CT imaging types, 105
  sonographic evaluation, 105
  symptoms, 105
  treatment, 105
Empty delta sign, 456
Empty notch sign, 470
Empyema, 19, 390
  cavitary neoplasm, 389
  CT scan, 389
  neoplasms, 390
  parenchymal consolidation, 389
  pleural effusions, 389
  septic emboli, 389
  tissue destruction and necrosis, 389
Endoleak, 8, 10
Endometriomas, 178, 185
Endometriosis, 185, 186
Endotracheal tube, 411–413
Epididymitis, 115, 116
Epididymo-Orchitis, 115, 116
Epidural hematoma, 244, 372–373
Epiglottitis, 225
Epiploic appendages, 81
Escherichia coli, 117
Esophageal perforation, 383, 407
  clinical symptoms, 382
  endoscopic instrumentation and thoracic surgery, 382
  esophagography, 383
  etiology, 382
  food bolus, 382
  left hemidiaphragm, 382
  pleural effusion, 382
  pneumomediastinum, 382
  pneumothorax, 382
  strictures, 382
  subcutaneous emphysema, 382
  traumatic patients, 382
Esophagography, 382
Esophagus, 406–407, 425
European Cooperative Acute Stroke Study (ECASS), 279, 280
Extra-axial hemorrhages, 244, 245
Extrapleural hematoma, 406
Extravaginal torsion, 118
Extravascular location of venous line, 417

F
Falciform ligament sign, 442
Fat pad sign, 451
Feeding tube, 425
Feeding vessel sign, 457
Femoral neck fractures, 331
Fiberoptic bronchoscopy, 390
Fifth metatarsal fracture, 346
Fissure of ligamentum teres sign, 443
Fistula, 305
Fitz-Hugh–Curtis syndrome, 150
Flexion-distraction injury, 365
Flexion teardrop fracture, 364–365, 448
Fluid-filled diverticulum, 77
Focused assessment with sonography for trauma (FAST), 127, 128
Follicular ring sign, 186
Football sign, 58, 442
Forniceal rupture, 99
Fossa of Landzert, 75
Fournier gangrene, 117, 118
Fractured central venous line, 420
Fracture distraction, C7–T1, 373
Fractured pacemaker, 424
Fractures of forearm, 314
Frontal fractures, 263, 264
Frontal sinusitis, 429
Frontobasal fractures, 252
Fungal abscess, 148

G
G and GJ tubes, 415–416
Galeazzi fracture dislocation, 313
Gallbladder carcinoma, 20
Gallbladder empyema, 19
Gallbladder perforation, 22
Gallbladder torsion, 22
Gallstone ileus, 25–27, 73
Gallstones, 15
Gamekeeper's thumb, 322
Gangrenous cholecystitis, 19, 20
Garden classification, 331
Gastroduodenal artery aneurysm, 163
Gastrointestinal (GI) bleeding, 92, 93, 206, 207
Genitourinary emergencies, 110
  abdominal pain, dysuria and urinary frequency, 110
  acute pyelonephritis
    imaging, 101–103
    overview, 101
    treatment, 103
  emphysematous cystitis, 106, 107
  emphysematous pyelonephritis, 104–106
  obstructive uropathy
    clinical presentation, 97
    complications and treatment, 101
    definition, 97
    imaging, 97–101
    infections, 101
  renal infarction, 107, 108
  renal/perinephric abscesses, 103, 104
  renal transplantation, 108–110
  renal vein thrombosis, 108
  striated nephrogram, 110
Gerdy's tubercle, 334, 335
Giant intracranial aneurysms, 242
Glenohumeral joint dislocation, 309, 310, 324
  classification of, 311
  imaging, 309–311
Globi pallidi, 236
Golden S sign, 446
Goldman's classification, 137
Gonadal vein thrombosis, 189
Graded-compression ultrasound, 38, 77
Gradenigo syndrome, 230
Grisel syndrome, 363
G-tube malposition, 415
G-tube placement, 415
Gunshot injury, 406

H
Halo sign, 459, 460, 465
Hamate fractures, 317, 319
Hampton's hump, 380
Hangman's fracture, 361–363
Hawkins classification, 343, 344
Hemangioma, 156
Hematochezia, 212
Hematoma, 129, 155
Hematometrocolpos, 191
Hemicolectomy, 71
Hemobilia, 25
Hemoperitoneum, 182
Hemorrhagic adenoma, 152
Hemorrhagic infarct (HI), 279
Hemorrhagic ovarian cyst, 182
Hemorrhagic products, 283
Hemorrhagic transformation, 279, 280
Hemothorax, 397–398, 406
Hepatic abscesses, 149
Hepatic infarcts, 150
Hepatic injuries, 128, 130
Hepatic laceration, 128, 129
Hepatobiliary scintigraphy (HBS)
  bile duct injury, 205
  common bile duct obstruction, 203–205
  cystic duct obstruction, 203–205
Hepatocellular carcinoma, 152
Herniation syndromes, 245–247
Herpes encephalitis, 240
Herpes simplex virus infection, 240
Heterotopic pregnancy, 176
High placed endotracheal tube, 413
Hip dislocations, 330–331
Hip effusion, 438
Hot nose sign, 469
Hounsfield Unit (HU), 146
Hydatid cyst, 149, 150, 239
Hydrocele, 113, 114
Hydrometrocolpos, 191
Hydronephrosis, 100
Hydrosalpinx, 192
Hyoid bone fracture, 229
Hyperacute left middle cerebral artery (MCA), 455
Hyperbaric oxygen, 118
Hyperdense appendix, 37
Hyperdense crescent sign, 2, 5, 463, 464
Hyperdense middle cerebral artery sign, 455
Hyperechoic mucosa, 436
Hyperemesis, 179
Hyperextension injury, 368, 369
Hyperextension teardrop fracture, 368
Hyperintense hematoma, 125
Hypertension, 282
Hypertensive hemorrhage, 282
Hypertrophic pyloric stenosis, 437
Hypodensity, 273
Hypopharynx, 217
Hypotension, 212

I
Image-guided pigtail catheter drainage, 43, 79
Implantable cardioverter defibrillator (ICD), 424
Incarcerated hernia, 69
Infarct evolution, 281
Infected thymic cyst, 228
Infectious enteritis, 60, 61
Inferior vena cava (IVC), 130
Inflammatory bowel disease, 84
Ingested foreign body, 434–435, 439
Insular ribbon sign, 466
Internal border zone, 281
Internal hernia, 69, 70
Interspinous and intervertebral distance, 357
Interstitial ectopic pregnancy, 175, 176
Intertrochanteric fractures, 331
Intra-aortic balloon pump, 422
Intracranial hemorrhage, 244
Intracranial hypotension, 243
Intracranial vasospasm, 288
Intradecidual sign, 169
Intramural hematoma, 8, 9
Intraocular foreign body, 295–297
Intraparenchymal hematomas, 129
Intraparenchymal hemorrhage, 246
Intraperitoneal bladder rupture, 141
Intravaginal torsion, 118
Intussusception, 72, 89–91, 436
Ischemic colitis, 91, 92
Ischemic stroke, 271, 272

J
Jaundice, 22
Jefferson fracture, 359–360
Jejunoileal diverticula, 50

K
Keyhole sign, 468
Kidney, 133–135
Knee dislocations, 333, 334

L
Landzert's fossa, 69
Laparoscopy, 185
Laparotomy, 52
Lateral capsular sign, 452
Latrerobasal fractures, 252
Le Fort fractures, 265, 266, 269
Left upper lobe pneumonia, 386, 387
Leigh syndrome, 236
Lemierre's syndrome, 221, 232
Lens dislocation, 293–294
Less common herniations, 245
Leukocytosis, 41
Ligamentous disruption, 313
Ligamentous injury, 372
Ligamentum teres sign, 57
Lightbulb sign, 451
Linguine sign, 467, 468
Lisfranc (tarsometatarsal) injuries, 345
Lisfranc fracture dislocation, 345
Liver abscess, 156
Longitudinal fractures, 228
Lower extremity trauma
  acetabular fracture, 329
  ankle fractures, 341
  calcaneal fractures, 343
  eponymous fractures, 349

- fractures of distal femur, 332
- fractures of proximal femur, 331–332
- hip dislocations, 330–331
- knee dislocations, 333, 334
- lisfranc injuries, 345
- maisonneuve fracture, 343
- nonaccidental trauma, 347, 348
- patellar dislocations, 338, 339
- patellar fractures, 336, 337
- pelvic fracture, 327, 328
- stress fracture of tibia, 340
- talar fractures, 343, 344
- tibial plateau fractures, 334, 335

Luftsichel sign, 448
Lunate dislocation, 321, 453
Lung contusions, 406
Lung herniation, 400
Lungs and pleura
- pneumonia (*see* Pneumonia)
- pneumothorax, 391–393
- pulmonary abscess and empyema, 389–390
- pulmonary edema, 390–391

Lunotriquetral dissociation, 321
Lymphoceles, 109

M
MacEwan sign, 452
Macklin effect, 400
Magnetic resonance angiography (MRA), 287
Magnetic resonance imaging (MRI), 18, 181, 403
Maisonneuve fracture, 343
Malleolar fracture, 342
Malpositioned umbilical venous catheters, 420
Malpositioning, 411, 413
Malrotation, 436
Malrotation of bowel, 71
Mandible fractures, 267, 268
Marfan syndrome, 71
Mastoiditis, 231
Maxillary fractures, 265
Meckel's diverticulum, 49, 51–53
Medial and lateral condyle fractures, 312
Medial epicondyle avulsion, 313
Mediastinal abscess, 385
Mediastinitis and abscess, 384
- chest radiography, 384
- esophageal perforation, 384
- etiology, 384
- lung parenchyma, 385
- mortality rate, 384
- retrolaryngeal space, 385
- risk factors, 384
- signs and symptoms, 384
- sternal dehiscence and pleuromediastinal fistulas, 385

Mediastinum
- esophageal perforation (*see* Esophageal perforation)
- mediastinitis and abscess, 384–385
- PE (*see* Pulmonary embolism (PE))

Meningeal cysts, 237
Mercedes Benz sign, 473
Mesenteric arterial vasoconstriction, 139
Mesenteric venous thrombosis, 52
Metacarpal injuries, 321–322
Microabscesses, 147
Middle cerebral artery (MCA) dot sign, 471, 472
Midgut volvulus, 436, 437
Mirizzi syndrome, 19
Molar pregnancy, 177
Molar tooth sign, 466
Momentary posterior dislocations, 368
Monteggia fracture dislocation, 314
Morison's pouch, 43
Motor vehicle collision, 13
Mount Fuji sign, 472
MR perfusion imaging techniques, 278, 279
Multidetector computed tomography (MDCT), 97, 127, 327, 353, 380
Multiplanar reformations (MPRs), 327
Multiple sclerosis (MS), 305, 427
Multiple vertebral body fractures, 371
Murphy's sign, 17
Mycobacterium avium-intracellulare (MAI), 61
Mycoplasma pneumoniae, 386, 388
Mycotic aneurysm, 4
Myocardial infarction, 384
Myocardial perfusion imaging (MPI), 201, 202

N
Naked facet sign, 366
Nasal fractures, 261, 262
Nasogastric and feeding tube, 414
Naso-orbital-ethmoid (NOE) fractures, 262, 263, 269
National Emergency X-Radiography Utilization Study (NEXUS), 353, 354
Neck emergencies, 232
- adenoidal hypertrophy, 223
- branchial cleft, 226–228
- cholesteatoma, 230
- croup, 224, 225
- danger space abscess, 219, 220
- epiglottitis, 225
- hyoid fracture, 229
- Lemierre's syndrome, 221
- mastoiditis, 231
- oral cavity infections, 217, 218
- petrous apicitis, 230
- pharynx and esophagus, 215–217
- retropharyngeal space abscess, 219–221
- sialadenitis, 218, 219
- temporal fracture, 228, 229
- thyroglossal duct cyst, 225, 226
- tonsillitis and peritonsillar abscess, 221, 222

Necrotizing enterocolitis, 55
Necrotizing pancreatitis, 160
Neer classification system, 311
Neurocysticercosis, 237
New Orleans Criteria (NOC), 356
Nonaccidental trauma, 347, 348
Noncontrast CT (NCCT), 273, 274
Nonocclusive bowel ischemia, 53
Nontraumatic intracranial hemorrhage (ICH), 282
- etiology, 282, 283
- imaging evaluation, 283–285

Nontraumatic liver and spleen imaging
- acute hepatitis, 145, 146
- ALF, 153
- Budd–Chiari syndrome, 151
- Fitz-Hugh–Curtis syndrome, 150
- fungal abscess, 148, 149
- hematoma, 155
- hepatic abscess, 147, 148

Nontraumatic liver and spleen imaging (*cont.*)
  hepatic infarcts, 150
  hydatid cyst, 149, 150
  portal vein thrombosis, 152, 153
  splenic infarction, 153, 154
  splenic torsion, 154
  spontaneous hepatic hematoma, 151, 152
Nontraumatic mediastinal
  acute chest pain, 379
  cardiac and aortic etiologies, 379
  imaging
    chest CT scan, 380
    chest radiograph, 380
    MRI, 380
    ultrasound, 380
  pneumonia and pulmonary edema, 379
  thoracic complaints, 379
Nontraumatic urinary tract, 97
Nontunelled catheters, 416
Nuclear medicine (NM), 196
  ACS, 201, 202
  clinical indications, 195, 196
  in emergency setting, 195
  GI bleeding, 206, 207
  HBS
    bile duct injury, 205
    common bile duct obstruction, 203–205
    cystic duct obstruction, 203–205
  Meckel's diverticulum scintigraphy, 207, 213
  pulmonary embolism, 197–201
  scintigraphy, 195

O
Obstructive hydrocephalus, 249–251
Obstructive uropathy, 97
  complications and treatment, 101
  imaging, 97–101
  infections, 101
  MRI, 99
Occipital condyle fractures, 359
Odontogenic infection, 217
Omental contusion, 138
Omental infarction, 79
Omental torsion, 80
Open-globe injury, 294–295
Optic nerve injury, 302
Optic neuritis, 305
Oral cavity infections, 217
Orbital blow-in fracture, 306
Orbital blow-out fracture, 306
Orbital cellulitis, 430–431
Orbital fractures, 257
Orbital infections, 303, 305, 431
Orbital pathology, 306
  advantages and disadvantages, imaging modalities, 292
  AFIFS, 302
  anterior segment injury, 293–294
  blow-out fractures, 299, 300
  carotid cavernous fistula, 302–303
  choroidal detachment (CD), 298
  classification and mechanism, 291
  imaging protocol, 293
  intraconal and extraconal hemorrhage, 301
  intraocular dislocation, 293
  intraocular foreign body, 295–297
  Le Fort fractures, 299
  lens dislocation, 293–294
  MRI and CT, 292
  normal anatomy, 291, 292
  open-globe injury, 294–295
  optic nerve injury, 302
  optic neuritis, 305
  orbital infections, 303
  orbital subperiosteal abscess, 304
  radiographic assessment, 292
  retinal detachment (RD), 297–298
  traumatic eye injuries, 291
  ultrasound, 292
Orbital subperiosteal abscess, 304–305
Orbital wall fractures, 299, 300
Organ injury scales (OISs), 127
Ossicular disruption, 229
Osteochondral injury, 333
Osteochondritis dissecans (OCD), 333
Ovarian cysts, 183, 186
Ovarian dermoid, 187
Ovarian hyperstimulation syndrome (OHSS), 188
Ovarian torsion, 186, 187
Ovarian vein thrombosis, 189
Overshunting, 433
Ovulation, 141

P
Page kidney, 133
Palatal fractures, 269
Pancreatic collection, 161
Pancreatic duct stone, 164
Pancreatic injuries, 132, 133, 164
Pancreatic laceration, 132, 166
Parasitic infection, 237
Parenchyma, 273
Parenchymal neurocysticercosis, 237
Partial articular fractures, 333
Patellar dislocations, 338, 339
Patellar fractures, 336, 337
Pediatric emergencies
  acute sinusitis, 428
  ADEM, 427, 428
  AOM, 429
  bacterial pneumonia, 433
  bronchiolitis, 433
  disk batteries ingestion, 435
  frontal sinusitis, 429
  hypertrophic pyloric stenosis, 437
  ingested foreign body, 434–435
  intussusception, 436
  malrotation, 436
  midgut volvulus, 436
  orbital cellulitis, 430
  overshunting, 433
  round pneumonia, 434
  subperiosteal abscess, 431
  transient synovitis and septic arthritis, 438
  transverse myelitis, 431–432
  VP shunt, 432
Pediatric supracondylar fractures, 311
Pelvic fracture, 327, 328
Pelvic inflammatory disease (PID), 183–185
Pelvic ring disruption, 327
Penetrating ulcer, 11

Penile fracture, 121, 122, 125
Penumbra, 272
Peptic ulcer disease, 58
Perforated appendicitis, 37
Perforation, 21, 22
Periaortic hematoma, 402
Peribronchial thickening, 433
Perilunate instability injuries, 320, 321
Periodontal abscess, 218
Peripheral enhancement of vein, 155
Peritonsillar abscess, 221, 222
Petrous apicitis, 230
Petrous temporal fracture, 228
Phalangeal fractures, 346
Phalangeal tuft fractures, 323
Pharynx and esophagus, 215
Phlegmon, 46
Pilon and Tillaux fracture, 341
Pipkin classification, 331
Placenta previa, 178
Plain radiographic signs
  Batwing sign, 449
  bulging fissure sign, 449
  coffee bean sign, 447
  continuous diaphragm sign, 443
  Cupola sign, 441
  deep lateral femoral notch sign, 450
  deep sulcus sign, 446
  falciform ligament sign, 442
  fat pad sign, 451
  fissure of ligamentum teres sign, 443
  flexion teardrop fractures, 448
  football sign, 442
  golden S sign, 446
  lateral capsular sign, 452
  lightbulb sign, 451
  Luftsichel sign, 448
  pronator quadratus sign, 452
  reverse bat wing sign, 453
  Rigler sign, 441
  spilled teacup sign, 453
  steeple sign, 444
  string of pearls sign, 447
  Terry Thomas sign, 450
  thumbprinting sign, 445
  thumb sign, 445
  triangle sign, 442
Plain radiography, 216
Pleural effusions, 382, 393
Pleural space, 395
Pneumatosis, 85
Pneumatosis cystoides intestinalis, 56
Pneumatosis intestinalis, 56
  bowel perforation, 57–62
  causes, 56–57
  patterns, 56
  portal venous gas, 57
  ultrasound study, 57
Pneumobilia, 57
Pneumomediastinum, 382, 384, 385, 393, 396, 408
Pneumonia, 386, 389
  air bronchograms, 386
  aspiration, 387
  CAP, 386
  causative organisms, 386
  classification, 386
  diagnosis, 386
  multifocal lobar and bronchopneumonia pattern, 386
  pleural effusions, 387
  pulmonary infections, 385
  right and left hemidiaphragms, 386
  viral, 386
Pneumopericardium, 397, 401
Pneumoperitoneum, 50, 60, 61, 64
Pneumothorax, 379, 382, 391–393, 395–397, 406, 409, 418
Polo mint sign, 459
Port-A-Cath abnormalities, 421
Portal vein thrombosis, 152, 153
Postanginal sepsis, 221
Post appendectomy abscess drainage, 44
Postcholecystectomy bile leaks, 28
Postcholecystectomy biloma, 28
Postcholecystectomy hemorrhage, 28
Posttreatment imaging, 282
Predental space, 356
Prevertebral space, 356
Primary blast injuries, 407
Progressive aneurysmal dilatation, 2
Pronator quadratus sign, 452
Prospective Investigation of Pulmonary Embolism II (PIOPED II), 380
Proximal femoral fractures, 332
Proximal humerus fractures, 311
Proximal interphalangeal (PIP) joint, 323
Proximal tibial fractures, 336
Pseudoaneurysm, 141
Pseudodiverticula, 49
Pseudomembranous colitis, 84
Pseudo-subarachnoid hemorrhage, 235, 236
Pulmonary abscess, 389
  See also Empyema
Pulmonary and mediastinal evaluation, 379
Pulmonary angiography, 380
Pulmonary contusion, 398, 399, 409
Pulmonary edema, 390–391, 393
Pulmonary embolism (PE), 197–201, 209, 381, 384
  cardiac dysfunction, 381
  chest radiograph, 380
  coronary artery disease and stroke, 380
  CT, 381
  diagnosis, 380
  imaging, 382
  infarction, 381, 382
  lung parenchyma, 381
  opacification, 382
  partial filling defect, 381
  pleural effusions, 381
  pulmonary angiography, 380
  risk factors, 380
  ventilation-perfusion scintigraphy, 380
  Westermark's sign, 380
Pulmonary lacerations, 398, 399, 409
Pyloric ultrasound, 437
Pyogenic abscesses, 147, 148, 155
Pyogenic cholangitis, 24
Pyosalpinx, 184
Pyuria, 101

R
Radial head fractures, 312
Radiography, 105
Radiopaque coins, 216
Railway track sign, 459

Red degeneration, 189
Renal infarction, 107, 108
Renal injury, 135
Renal laceration, 133, 134
Renal/perinephric abscesses, 103
Renal transplantation, 108–110
Renal vein thrombosis, 108
Renovascular emergencies, 107
Respiratory syncytial virus (RSV) infections, 433
Retinal detachment (RD), 297–298
Retrograde urethrography, 123
Retroperitoneal air, 62
Retropharyngeal space, 219–221
Retzius space, 110
Reversal sign, 456
Reverse bat wing sign, 453
Reversed halo sign, 381, 474, 475
Reverse hamburger bun sign, 366
Reverse hamburger sign, 464, 465
Rib fractures, 406
Right middle lobe pneumonia, 386, 387
Right upper quadrant gas sign, 57
Rigid endoscopy, 231
Rigler's sign, 58, 59, 441, 442
Rim sign, 468, 469
Rotational subluxation, 363
Rotatory fixation, 363
Round pneumonia, 434

S
Saccular abdominal aortic aneurysm, 2
Saddle emboli, 381
Salivary gland duct, 218
Salter–Harris type IV fractures, 312
Scaphoid fracture, 317
Scapholunate dissociation, 320
Scapular fracture, 311
Scapulothoracic dissociation, 307
Schatzker classification, 334
Scintigraphy, 92
Scout film, 93
Scrotal appendage, 124
Scrotal pain, 125
Scrotal trauma, 120
Secondary blast injuries, 407
Segmental omental infarction, 79–81
Segond fracture, 335, 452
Segond-type fracture, 335
Sentinel clot sign, 462
Septic arthritis, 437–439
Shock bowel syndrome, 138, 139, 142
Shunt catheter fragmentation, 432
Sialadenitis, 218, 219
Sialolithiasis, 219
Sigmoid colon, 93
Single-contrast barium enema, 93
Small bowel diverticulitis, 51, 63, 64
  acute mesenteric ischemia
    clinical presentation, 52
    CT, 53–56
    pathogenesis, 53
    radiograph, 53
    risk factor, 53
    treatment, 55
  clinical presentation, 50
  congenital diverticula, 49, 50
  CT scan, 50, 51
  duodenal diverticulum, 49, 50
  infection, 60, 61
  Meckel's diverticulum, 51–53
  NSAID, 51
  overview, 49
  pathogenesis, 50
  pneumatosis intestinalis
    causes, 56, 57
    patterns, 56
    portal venous gas, 57
    ultrasound study, 57
Small bowel feces sign, 461
Small bowel obstruction, 74, 75
  bowel malrotation, 71
  causes, 67, 69
  closed loop obstruction, 74
  CT scan, 67–69
  duodenal hematoma, 73
  gallstone ileus, 73
  imaging findings, 68
  incarcerated hernia, 69
  internal hernia, 69, 70
  intussusception, 72
  MRI, 67
  radiographic findings, 67, 68
  small bowel volvulus, 70, 71
Small bowel volvulus, 70, 71
Soft tissue injuries, 336, 338
Spermatic cord torsion, 118
Spilled teacup sign, 453
Spinal cord injury (SCI), 353, 373, 406
Spinal cord injury without radiological abnormality (SCIWORA), 374
Spine MRI, 357
  epidural hematoma, 372–373
  ligamentous injury, 372
  spinal cord trauma, 373–377
  traumatic disk herniation, 372
Spine trauma
  blunt/penetrating trauma, 353
  compression fractures, 353
  mortality and morbidity, 353
Spleen, 130, 131
Splenic artery pseudoaneurysm, 167
Splenic infarction, 153, 154, 156
Splenic injury, 131
Splenic pseudoaneurysm, 131
Splenic torsion, 154
Splenic vascular injuries, 130
Split pleura sign, 460
Spontaneous esophageal perforation, 382
Spontaneous hepatic hematoma, 151, 152
Spontaneous intracranial hypotension, 243
Spontaneous splenic hematoma, 155
Staphylococcus aureus, 384, 386
Steeple sign, 224, 444
Stenmore triangle classification, 324
Stensen's duct, 218
Sternal fractures, 406
Sternoclavicular dislocation, 308, 406
Streptococcus pneumoniae, 386
Stress fracture, 346, 347
Striated nephrogram, 102, 110
String of pearls sign, 447
Stroke, 288, 289

  acute infarct, 276
  CTA, 274, 275
  CTP, 275
  definition, 271
  hemorrhagic transformation, 279, 280
  hypertension, 289
  imaging goals, 272, 273
  infarct evolution, 281
  ischemia, 271, 272
  MR imaging, 276–278
  MR perfusion, 278, 279
  NCCT, 273, 274
  NECT, 289
  nontraumatic ICH, 282
    etiology, 282, 283
    imaging evaluation, 283–285
  penumbra, 272
  posttreatment imaging, 282
  SAH
    catheter angiogram, 288
    CTA, 287
    etiology, 285, 286
    imaging evaluation, 286
    MRA, 287
    MRI, 287
    vasospasm, 288
  septic emboli infarction, 280
  watershed infarction, 280, 281
Stump appendicitis, 40
Subarachnoid hemorrhage (SAH)
  catheter angiogram, 288
  CTA, 287
  etiology, 285, 286
  imaging evaluation, 286
  MRA, 287
  MRI, 287
  vasospasm, 288
Subcapsular hematoma, 141
Subchorionic hemorrhage, 173, 174
Subclavian central line, 416
Subclavian vein, 416
Subdural hematomas, 244
Subfalcine herniation, 245
Subperiosteal abscess, 430–431
Subtalar/peritalar dislocations, 344
Subtrochanteric fractures, 332
Superficial border zone, 280
Superior mesenteric artery occlusion, 53
Supracondylar fracture, 312
Swan-Ganz catheter, 423
Swirl sign, 470
Sylvian fissure sign, 471

T
Talar fractures, 343, 344
Tangential calcium sign, 464
Target sign, 469, 470
Tc99m HMPAO study, 252
Temporal fracture, 228, 229
Tension pneumocephalus, 241
Tension pneumothorax, 392, 409, 419
Terry Thomas sign, 450
Testicular anatomy, 113
Testicular fracture and rupture, 120, 121
Testicular laceration, 121
Testicular torsion, 118, 119
Thoracolumbar spine injuries, 369
Thorax injury
  esophageal rupture, 406
  extravasation, 402
  laceration, 398
  pleura, 408
  pleural space, 395
  pneumothorax, 397
  radiographs, 395
  rib fractures, 406
  sulcus sign, 396
  TEE, 403
  tracheobronchial tree, 399
  type, 395
  viscera sign, 408
Thrombosed varicocele, 115
Thumbprinting sign, 91, 445
Thumb sign, 445
Thyroglossal duct cyst, 225, 226
Tibial plateau fractures, 334, 335
Tibial stress fractures, 340
Tillaux fracture, 341
Tip appendicitis, 39, 40
Tip of the iceberg sign, 467
Tonsillar herniation, 245
Tonsillitis abscess, 221, 222
Trachea and esophagus, 413
Tracheal laceration, 400
Tracheal rupture, 412
Tracheobronchial tube malposition, 415
Tracheostomy tube, 413
Transesophageal echocardiography (TEE), 403
Transient synovitis, 437–439
Transvenous ICD (T-ICD), 424
Transverse myelitis, 431–432
Trauma, 120
Traumatic aortic transection, 4, 6
Traumatic disk herniation, 372
Traumatic lung herniation, 399
Traumatic spondylolysis/spondylolisthesis, 361
Traumatic subarachnoid hemorrhage, 244
Triangle sign, 58, 442, 443
Triquetral fractures, 317
Triquetrum fracture, 319
Tubo-ovarian abscess, 183, 184
Tunneled catheters, 421
Type A aortic dissection, 7
Type B aortic dissection, 7
Type 3 dens fracture, 361
Typhlitis, 85, 86

U
Ulcerative colitis, 82, 93
Ultrasonography (US), 19, 46, 57, 72, 98, 109, 119, 120, 124, 145, 164, 221, 397
Ultrasound, 1, 17, 18, 23, 77, 160
Umbilical venous catheters, 420
Uncal herniation, 245
Unilateral vs. bilateral interfacetal dislocation, 367
Unilateral facet dislocation, 365
Unilateral interfacetal dislocation, 365
Unilateral locked facet, 365
United States coins, 435
Upper extremity, 324

Ureterovesicular junction (UVJ), 98
Urethral injury, 122–124, 136, 141
Urinary bladder, 135, 136
Uterine fibroids, 189, 190

V
Varicocele, 114, 115
Vascular occlusion, 91
Vasospasm, 288
Venous congestion, 430
Ventilation-perfusion scintigraphy, 380
Ventriculoperitoneal (VP) shunts, 432
Vermiform process, 33
Viral pneumonia, 388

W
Waldeyer's fossa, 69
Wall echo shadow (WES) sign, 471
Wandering spleen and splenic torsion, 154
Watershed infarction, 280, 281
Weber classification, 341, 342
Wedge compression fracture, 369
Westermark's sign, 380
Whirl sign, 70, 457, 458
Wilson's disease, 236
Witch nitinol basket, 43

Y
Yin Yang sign, 466, 467
Young–Burgess classification, 328

Z
Zygoma fractures, 259
Zygomaticomaxillary complex (ZMC) fracture, 259, 260, 269